# THE PHYSICAL REVIEW

VOLUME 94 Second Series NUMBER 5

JUNE 1, 1954

Published for the

AMERICAN PHYSICAL SOCIETY

by the

AMERICAN INSTITUTE OF PHYSICS

Lancaster, Pa., and New York, N. Y.

A journ

Published by the American Ins
for the

AMERICAN PHYSICAL

Officers

*President*

S. A. Bertis
Cornell University
Ithaca, New York

*Vice-President*

E. T. Birge
University of Californ
Berkeley, California

*Secretary*

K. K. Darrow
Bell Telephone Labora
Office:
Columbia University
New York 27, New Yo

*Treasurer*

G. B. Pegram
Columbia University
New York 27, New Yo

*Local Secretary*
*for the Pacific Co*

J. Kaplan
University of Califor
Angeles
Los Angeles, California

*Managing Editor*

S. A. Goudsmit
Brookhaven National L
Upton, Long Island
New York

The Physical

Entered as second-class

Acceptance for mailing at special

THE
PHYSICAL REVIEW

*A journal of experimental and theoretical physics established by E. L. Nichols in 1893*

SECOND SERIES, VOL. 94, NO. 5 JUNE 1, 1954

# Superfluid Dynamics of Liquid He II

J. G. DASH
*University of California, Los Alamos Scientific Laboratory, Los Alamos, New Mexico*
(Received January 15, 1954)

Some implications of the cooperative cluster model are explored. Supercritical flow of liquid He II through capillaries is discussed and compared with experiment, as a test of the theory and as a means for deducing some information on the postulated wall friction mechanism. The general flow characteristics of the actual mobile film of He II and the present film model flowing under the influence of gravity are found to be in substantial agreement.

## I. INTRODUCTION

THIS paper is intended as a supplement to an earlier one,[1] in which the author proposed a phenomenological theory of the dynamics of flow of the superfluid component in liquid He II. We will present here some additional evidence in support of the model and certain arguments amplifying the original ideas. The reader is referred to the first paper for a presentation of the assumptions and derivations. The earlier results will be summarized here.

The production of "quantum excitations" by a frictional process between the superfluid and a solid wall immersed in the liquid is energetically possible when the superfluid velocity $v_s$ exceeds a "critical velocity" $v_c$. The transformed energy $E_f$ per unit volume has the functional dependence:

$$E_f=0, \quad v_s<v_c; \quad E_f \propto \rho_s(v_s^2-v_c^2), \quad v_s>v_c. \tag{1}$$

The quantum excitations involved in the establishment of the critical velocity are assumed to be sound quanta, or phonons of energy $hc/\lambda$, where $c$ is the velocity of sound in the liquid and $\lambda$ is the wavelength. On the basis of this assumption, the relative velocity required to produce excitations is given by $v=[2hc/\lambda\rho_s\sigma^3]^{\frac{1}{4}}$, $\sigma^3$ representing the volume of each "cluster" within which the moving atoms may cooperate in the production of phonons. The *critical* velocity is determined by the weakest, or longest wavelength quanta that may be produced in large quantities; for liquid geometries of characteristic dimension $a$, the longest wavelength is of the order of $a$. On the basis of a comparison between the above equation and critical velocities observed over a wide range of characteristic liquid dimensions and upon the assumption of the temperature independence of the cluster volume, we obtain the semi-empirical formula

$$v_c \simeq 0.087(a\rho_s/\rho)^{-\frac{1}{4}} \text{ cm sec.} \tag{2}$$

The precise value of the constant is still very much in doubt, however; its better determination must await critical velocity studies under conditions of more precisely known geometries.

## II. THE TEMPERATURE DEPENDENCE OF CRITICAL VELOCITIES IN FILMS AND SLITS

Supporting evidence for the temperature dependence of $v_c$ [Eq. (2)] was previously drawn from oscillating disk experiments[2] in liquid helium volumes of about 1-cm characteristic dimension, or "bulk liquid." The predicted temperature behavior should not depend upon the liquid dimensions, however, and it is desirable to compare with experimental data, if available, on considerably smaller liquid regions.

The temperature behavior of the critical velocity in the He II mobile film can be given, in principle, by the simultaneous measurement of the flow rate and the thickness of the film, for we may express the volume flow rate $R_v$ in terms of its thickness $d$, the mobile fraction $\rho_s/\rho$, and $v_c$:

$$R_v \text{ cc/cm sec} = (\rho_s/\rho)v_c d.$$

[1] J. G. Dash, Phys. Rev. **94**, 825 (1954).

[2] A. C. Hollis-Hallett, Proc. Roy. Soc. (London) **A210**, 404 (1951).

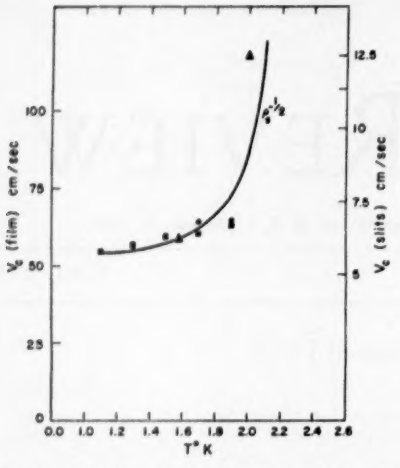


FIG. 1. The variation of critical velocity with temperature. ●, ■: from film flow, Jackson and Henshaw. ▲: from flow through a 1.6-micron slit, Hung, Hunt, and Winkel.

By assuming that $\rho_s/\rho$ for the film is identical with that of bulk liquid, given empirically by $\rho_s/\rho=1-(T/T_\lambda)^{5.5}$,[2] the critical velocity is directly obtainable from $R_v$ and $d$. Jackson and Henshaw[3] have carried out such simultaneous studies of mobile films on stainless steel containers at a number of temperatures between 1.1 and 1.9°K. They have deduced values for $v_c$ which decrease toward higher temperatures, contrary to the present theoretical predictions. The calculated decrease is due, however, to an inadvertent error in their values for $\rho_s/\rho$.[4] Supplying $\rho_s/\rho$ values according to the 5.5 power law to the flow rates and thicknesses measured by Jackson and Henshaw, one finds that the critical velocity rises as the λ point is approached. The scaled critical velocities so obtained are given in Fig. 1, together with the scaled function $\rho_s^{-1}$. Additional points in the graph are taken from the measurements of Hung, Hunt, and Winkel,[5] from a study of flow through a slit of $1.6\times10^{-4}$ cm separation.

The experimental and theoretical variations with temperature appear to be well correlated. A clearer test of the theory would be provided by additional experimental information in the region close to the λ point. At the present time one can only say that the theoretical temperature dependence is provisionally verified.

## III. SUPERCRITICAL FLOW THROUGH CAPILLARIES

The dissipation function, Eq. (1), may be modified to permit a comparison with experimental studies of capillary flow. Under the influence of a pressure difference $\Delta P$, a volume flow rate $dV/dt$ through a capillary leads to a rate of energy loss of $dE/dt=\Delta P(dV/dt)$: this loss rate is independent of the mechanism of the frictional force that produces the dissipation. Capillary flow data on liquid He II may therefore be compared with the functional Eq. (1) in the hope that the details of the correlations may yield some hints of the frictional process involved in the supercritical flow of the superfluid.

In order to employ capillary flow data for a test of Eq. (1), we will assume that the energy $E_f$ is dissipated per unit volume flow rate, or that $dE/dt=E_f(dV/dt)$. Following our postulate that $E_f$ arises from a frictional process with the walls, the rate of energy conversion should, in addition, be proportional to $L$, the length of the capillary. Supplying a constant of proportionality $k$, the equation between the pressure drop and the superfluid velocity is

$$\Delta P/L=\nabla P=k(\rho_s/\rho)(v_s^2-v_c^2). \tag{3}$$

The flow of He II through capillaries of different internal diameters and lengths has been studied by Allen and Misener[6] and Atkins.[7] Their data have been utilized for the present discussion in the following fashion. The flow rates observed by Allen and Misener at the lowest temperature (1.20°K) and the lowest pressure gradient (0.75 dynes/cm²), and those rates observed by Atkins at 1.22°K and 1 dyne/cm² were then used to solve for the "friction" constant $k$ in Eq. (3). The critical velocities belonging to the various capillaries were calculated according to Eq. (2), where $a$ was taken as the capillary radius. Choosing these low values of temperature and pressure effectively reduced the possibility of errors arising from the contribution of the normal viscous component $\rho_n$ to the total observed flow rates. The calculated values of the friction constant for the various tubes are shown, in

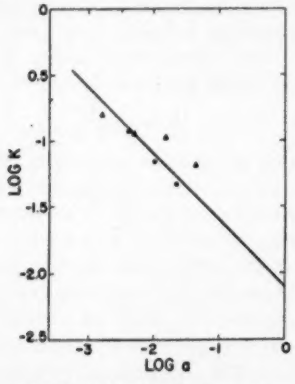


FIG. 2. The variation of friction constant with capillary radius. ●: from flow measurements of Atkins. ▲: from flow measurements of Allen and Misener.

[3] L. C. Jackson and D. G. Henshaw, Phil. Mag. **41**, 1081 (1950); **44**, 14 (1953); D. G. Henshaw and L. C. Jackson, Proceedings of the International Conference on Low Temperature Physics, Oxford, 1951 (unpublished).

[4] L. C. Jackson (private communication). I am grateful to Dr. Jackson for authorizing this revision.

[5] Hung, Hunt, and Winkel, Physica **18**, 629 (1952).

[6] J. F. Allen and A. D. Misener, Proc. Roy. Soc. (London) **A172**, 467 (1939).

[7] K. R. Atkins, Proc. Phys. Soc. (London) **A64**, 833 (1951).

Fig. 2, plotted logarithmically against the tube radii. The curve of best fit to the experimental points appears to be the function $k=8\times10^{-3}/\sqrt{a}$ g cm$^{-4}$, if one attaches more importance to the more recent investigation.

The possible significance of this functional form of $k$ will be discussed in a later section of the paper; at present we shall accept it provisionally as an adequate description of the frictional dependence.

Certain additional features of the observations may be compared with Eq. (3). By using Eq. (2) to calculate $v_c$ and the above expression for $k$, the flow velocity is explicitly determined by the pressure drop. As a check on the linearity of the frictional force with the length of the capillary, we compare Eq. (3) with the results given by Allen and Misener on the variation of flow velocity with capillary length, at constant pressure drop. A good agreement is obtained for both sets of measurements, taken at total pressure drops of 15 dynes/cm$^2$ and 160 dynes/cm$^2$, as compared with the theory, in Fig. 3. There is considerable disagreement, however, at the shortest length, 1 mm, studied by Allen and Misener, the predicted velocities exceeding those observed by about a factor of three. The ratio of capillary radius to length is quite large in this case, i.e., 0.153, and it seems likely that our long capillary formula should not be applicable. For the long capillary approximation assumes that the longest wavelength phonons that can be produced in large quantities have wavelengths comparable with the tube diameter. While this assumption may be reasonable in the case of very small ratios of diameter to length, the ratio is large for the 1-mm length, and the capillary radius alone cannot be used to describe the liquid geometry.

The variation of flow rate with pressure gradient in the neighborhood of zero gradient is an effective test of the existence of the critical velocity term in Eq. (3). We have therefore compared the equation with Atkins' flow measurements at small gradients. The empirical value of the friction constant and the semi-empirical critical velocity [Eq. (2)] were used to calculate flow rates in all three capillaries. Calculated and observed velocities are shown in Fig. 4. The velocities through

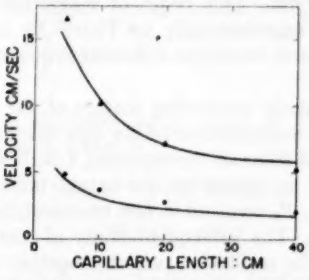


FIG. 3. The variation of velocity with capillary length at constant pressure head, from flow measurements of Allen and Misener. Capillary radius $1.53\times10^{-2}$ cm. ●: $\Delta P=15$ dynes/cm$^2$. ▲: $\Delta P=160$ dynes/cm$^2$. ——: calculated from theory.

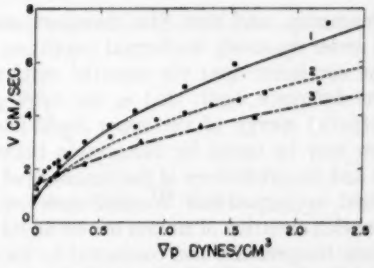


FIG. 4. The variation of flow velocity with pressure gradient, from measurements of Atkins. ■: capillary radius $2.2\times10^{-2}$ cm (Tube 1). ●: capillary radius $1.0\times10^{-2}$ cm (Tube 2). ▲: capillary radius $4.1\times10^{-3}$ cm (Tube 3). ——: calculated from theory.

the tube of largest bore, Tube 1, have been calculated for mixed flow of superfluid and normal fluid, computing the contribution of the normal fluid as given by Poiseuille flow of a liquid of 16-micropoise viscosity.[8] Experimental data on a fourth, and narrowest capillary have been judged unreliable by Atkins, and have accordingly not been included here. Although the data are gathered from only three tubes, whose diameters differ by a maximum factor of five, the details of the pressure gradient-velocity behavior, except for Tube 2 at intermediate gradients, are well described by Eq. (3), together with the "universal" expressions for $k$ and $v_c$.

## IV. THE DYNAMICS OF FILM TRANSPORT

Film flow between regions of bulk liquid presents certain general aspects that may be discussed in terms of the present model. Some of the functional dependences of the critical velocities and flow rates upon temperature and geometry have been treated in this and the preceding paper. We shall now put forth some general arguments concerning the driving force that produces the liquid transport. The discussion will be, in part, a generalization of an analysis presented by Atkins,[9] whose conclusions are correct, in the author's opinion.

Numerous independent observations[10–12] on the film transport into or out of open vessels suspended in liquid He II are universally characterized by the final establishment of equal heights (within surface tension rise) of the film-connected liquid regions. It is conceivable that minute temperature differences may sometimes exist between the helium bath and the liquid contained in a vessel immersed in it, and that such temperature differences depend upon the height differences of the menisci. In view of the high thermal conductivity of He II and the precautions sometimes taken to minimize such temperature differences,[12] it appears that the thermal gradients are not an essential feature of the

[8] A. C. Hollis-Hallett, Proc. Cambridge Phil. Soc. **49**, 717 (1953).
[9] K. R. Atkins, Proc. Roy. Soc. (London) **A203**, 119 (1950).
[10] J. G. Daunt and K. Mendelssohn, Proc. Roy. Soc. (London) **A170**, 423, 439 (1939).
[11] Webber, Fairbank, and Lane, Phys. Rev. **76**, 609 (1949).
[12] J. G. Dash and H. A. Boorse, Phys. Rev. **82**, 851 (1951).

flow phenomenon, and that film transport would be observed under rigorously isothermal conditions. One is led to the conclusion that the essential motivation is the height difference itself; that is, the extra gravitational potential energy of the upper liquid level. The conclusion may be tested by comparison between experiment and the predictions of the equations of motion for idealized, isothermal flow. We shall therefore inspect the Lagrangian equation of motion of two liquid regions at the same temperature and connected by the present film model.

We consider a cylindrical beaker of constant internal cross section $A$, internal perimeter $P_1$ and external perimeter $P_2$ partially immersed in a liquid bath of large cross section. The liquid level in the beaker is higher by a distance $h$ than the bath level, giving an extra gravitational potential energy

$$\Delta V = A\rho g h^2/2,$$

where $g$ is the acceleration of gravity. The kinetic energy of the film of varying thickness $d$ that covers the exposed surface of the beaker is

$$T=\tfrac{1}{2}\int_h^{H_0}\rho_s v_s^2 P_1 d(l)dl+\tfrac{1}{2}\int_0^{H_0}\rho_s v_s^2 P_2 d(l)dl,$$

where $l$ is measured along the film, $d(l)$ is the film thickness along the path, and $H_0$ is the height of the vessel rim above the bath level. The velocity $v_s$ of the superfluid may be expressed in terms of the time rate of change $\dot{h}$ of the beaker meniscus height by the equation of continuity,

$$A\rho\dot{h}=P\rho_s v_s d,$$

where $P$ is the inside or outside vessel periphery, depending on the surface over which the integration is carried out. Assuming that $\rho_s$ is a function of temperature only, we obtain the Lagrangian,

$$L=\frac{A\rho}{2}\left\{\frac{A\dot{h}^2}{(\rho_s/\rho)}\left[\frac{1}{P_1}\int_h^{H_0}\frac{dl}{d(l)}+\frac{1}{P_2}\int_0^{H_0}\frac{dl}{d(l)}\right]-gh^2\right\}. \quad (4)$$

The equation of motion of the liquid level when $h \ll H_0$ is approximately

$$\frac{d^2h}{dt^2}+\frac{g(\rho_s/\rho)P_1 h}{A(1+P_1/P_2)\int_0^{H_0}dl/d(l)}=0. \quad (5)$$

The above equation, without dissipative terms, should represent conditions of flow at subcritical rates. It reduces, in the case of a smooth-walled cylindrical beaker ($P_1$ and $P_2$ calculated as the macroscopic peripheries), to the equation of motion deduced by Atkins and employed by him to analyze the oscillations of the liquid level about its equilibrium position. We shall assume, as does Atkins, that the film thickness is a function of height above the bulk liquid, as $d=d_1 l^{-1/n}$, where $d_1$ is the film thickness at 1-cm height. The thickness at the rim of the vessel is $d_r=d_1 H_0^{-1/n}$, and, in terms of this thickness, the solution of Eq. (5) is

$$h=h_0\sin\omega t, \quad \omega=\left[\frac{P_1 g d_r(1+1/n)\rho_s/\rho}{AH_0(1+P_1/P_2)}\right]^{\frac{1}{2}}. \quad (6)$$

The maximum time rate of change of $h$, $(dh/dt)_0=\dot{h}_0$ is related to the maximum amplitude $h_0$ of the oscillations by $\dot{h}_0=\omega h_0$, and to the critical mass flow rate $R_c$ by $A\rho\dot{h}_0=P_1R_c=P_1\rho_s(v_s d)_{\text{critical}}$. The variation of critical velocity with thickness is given by Eq. (2); substituting for $v_c$, the critical rate as a function of film thickness is given by $R_c(d)=0.087(\rho_s\rho d)^{\frac{1}{2}}$. The actual flow rate of the film is limited to the smallest critical rate along the film path and according to the above relation, is established by the minimum thickness of film connecting the bulk liquid regions. Adopting the empirical variation of thickness with height, as given above, the minimum thickness is found at the rim of the vessel. Denoting this thickness by $d_r$, the critical mass flow rate and the rate of change of liquid level corresponding to the critical rate are given by

$$R_c=0.087(\rho_s\rho d_r)^{\frac{1}{2}}, \quad \dot{h}_0=0.087(d_r\rho_s/\rho)^{\frac{1}{2}}P_1/A. \quad (7)$$

Combining Eqs. (6) and (7) for the oscillation amplitude, we obtain

$$h_0=\dot{h}_0/\omega=0.087\left[\frac{P_1H_0(1+P_1/P_2)}{Ag(1+1/n)}\right]^{\frac{1}{2}}. \quad (8)$$

$h_0$ represents the liquid level difference required to accelerate the film to the critical flow rate, the maximum rate at which the frictionless equation of motion is applicable. An expression similar to Eq. (8), but without the use of our general Eq. (2), has been found by Atkins to agree with the experimental oscillation amplitudes. The predicted "critical height" $h_0$ for typical experimental geometry used in transport studies is quite small; a smooth-walled cylindrical beaker of 2-mm diameter, with its rim 2 cm above the source liquid yields a calculated critical height of approximately 0.3 mm. This order of magnitude has been determined experimentally by Picus[13] by a technique which measures the height difference required to initiate critical flow.

A particularly interesting feature of the expression for $h_0$ is its independence of the film thickness, except for the small effect of the exponent $1/n$. It should then be possible to determine the actual microscopic peripheries $P_1$, $P_2$ involved in film transport, by measurements of $h_0$. The subsequent study of film thickness, by timing the oscillation periods, together with measurements of the critical flow rates can serve to check the velocity-thickness dependence.

[13] G. S. Picus, Phys. Rev. **90**, 719 (1953).

The preceding treatment is concerned with film flow behavior in the subcritical or critical region; we shall now speculate on its supercritical behavior. Indeed, it seems likely that much of the experimental information has been derived from supercritical rate studies, for the level differences generally employed far exceed the magnitudes of the critical heights discussed above. We will here make use of the dissipation Eq. (3), treating the film as a layer of parallel capillaries arranged on the surface of a beaker. The total pressure difference between the ends of the film is given by the liquid level difference $h$, and may be related to the dissipation equation by

$$\rho g h = \int_l \nabla p dl = \int_h^{H_0} k(\rho_s/\rho)(v_s^2 - v_c^2) dl + \int_0^{H_0} k(\rho_s/\rho)(v_s^2 - v_c^2) dl, \quad (9)$$

where $H_0$ is the distance between the vessel rim and the surrounding bath. The solution of Eq. (9) requires a knowledge of the friction constant $k$. At the present time, the only information on $k$ is the empirical $k = 8\times10^{-3}/\sqrt{a}$, found from capillary flow data. Although its application to liquid dimensions corresponding to film thicknesses represents a considerable extrapolation from the data, it will be employed here in an attempt to obtain a crude estimate of magnitudes. Approximating $v_s^2 - v_c^2 \simeq 2v_c\delta v = 2v_c\delta R/\rho_s d(l)$, where $\delta R = R - R_c$, and substituting the empirical friction constant, Eq. (9) becomes

$$\delta R = \frac{63\rho^2 g h}{\int_l v_c dl/[d(l)]^3}. \quad (10)$$

The critical velocity varies with the film thickness along the path; substituting for $v_c$ according to Eq. (2) and for the film thickness according to $d(l) = d_1 l^{-1/n}$, we obtain

$$\delta R = \frac{720\rho^2 g h d_1^2(\rho_s/\rho)^3}{\int_l l^{2/n} dl} = \frac{720(1+2/n)\rho^2 g h d_1^2}{2H_0^{1+2/n} - h^{1+2/n}}. \quad (11)$$

For a film thickness $d_1$ at 1 cm of $4\times10^{-6}$, the increased mass flow rate is

$$\delta R = \frac{2.4\times10^{-7}(1+2/n)h(\rho_s/\rho)^3}{2H_0^{1+2/n} - h^{1+2/n}}. \quad (12)$$

The excess flow rate for vessel heights of a few centimeters and for $n>1$ is of the order of 2 percent of the critical flow rate. Assuming that we have used a realistic friction constant for this calculation, experimental film transport might appear to be very nearly independent of the applied gravity heads. This apparent independence, together with the smallness of the level differences required to produce critical flow, indicate the reasons that transport by He II films should exhibit such marked dissimilarities to a siphon, while retaining a siphon's intrinsic character.

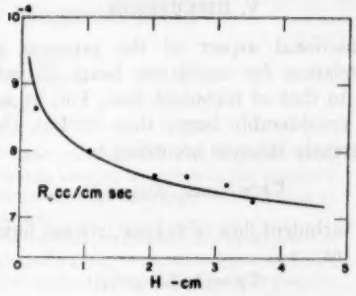


FIG. 5. Variation of film flow rate with height of vessel rim. ●: from measurements of Atkins. ——: scaled curve $R \propto H^{-1/14}$.

If we may approximate film flow under typical conditions by the equality $R = R_c$, ignoring the effect of pressure head, it is still possible that the observed flow rate should vary with the height of the liquid levels. For the critical flow rate is determined by the film thickness at the vessel rim, as in Eq. (7). If the film thickness varies with the height $H$ of the rim above the upper liquid level, according to $d(l) = d_1 l^{-1/n}$, then the thickness $d_r = d_1 H^{-1/n}$. The critical rate will therefore vary with the height as

$$R_c \propto H^{-1/2n}. \quad (13)$$

A transport rate having such a functional dependence on height is, in fact, a possible explanation of the so-called "lip effect."[10] The lip effect is seen as a markedly higher transport rate into or out of a container when the upper (source) liquid is close to the limiting perimeter of the film path. An investigation possibly checking this argument has been carried out by Atkins.[14] The thickness-height variation was determined by the oscillation technique as $d \simeq d_1 H^{-1/7}$ for a particular vessel, and under particular cryostat conditions. The same vessel was later used for a study of film flow rate-height dependence. The predicted variation is $R_c \propto H^{-1/14}$ in this case; this function is shown in Fig. 5, together with Atkins' experimental values. The agreement suggests the validity of the suggested mechanism for the lip effect. In addition, the theoretically direct connection between the film thickness at the rim and the critical rate implies an alternative method for obtaining the functional dependence of thickness upon height; by the simpler method of determining the height dependence of the volume flow rate.

[14] K. R. Atkins, Proc. Roy. Soc. (London) **A203**, 240 (1950).

## V. DISCUSSION

The functional aspect of the pressure gradient-velocity relation for capillaries bears an interesting similarity to that of turbulent flow. For, at superfluid velocities considerably larger than critical, the superfluid apparently behaves according to

$$\nabla p \simeq (\text{const}/d^{\frac{1}{2}})(\rho_s v_s^2),$$

while the turbulent flow of normal, *viscous* fluids is well described by

$$\nabla p = (\lambda/2d)(\rho v^2),$$

in circular channels of diameter $d$, $\lambda$ expressing the "pipe friction coefficient,"[15] which is relatively insensitive to $d$. If we may investigate the analogies somewhat further, it is well to point out that the turbulent flow of $\rho_s$ in the supercritical velocity region is not forbidden. The Kelvin circulation theorem[16] may indeed preclude the onset of turbulence in the subcritical velocity region if the viscosity of the $\rho_s$ component is identically zero. The circulation theorem is valid, however, under the assumption that the only forces acting upon the fluid are derivable from a single valued potential, i.e., $\nabla \times \mathbf{F} = 0$. The postulated frictional interaction between the walls and the superfluid does not necessarily have this property. We are not implying that the supercritical region *is* turbulent, the energy dissipation formula having been arrived at by somewhat different considerations, and the dissipated energy assumed to be of directly phonon character. The possibility that turbulence may exist in this region, however, should not be ignored.

The dependence of the pressure drop upon the channel size might be considered in the following fashion. A quantity of energy conversion per unit volume of fluid (per unit time) arises from a frictional interaction with the surface of the confining tube. The quantity, or rate of energy converted is therefore proportional to the tube surface area available per unit volume of fluid within which the conversion takes place. Should the process occur at an equal rate throughout the liquid in a circular tube, this factor would be simply $2\pi r/\pi r^2 = 2/r$. In the equally simple case that the liquid involved is limited to a thin (compared with the diameter) film of constant thickness adjacent to the wall, the factor is independent of $d$. The flow of superfluid in the range of capillary sizes considered in the text appears to be an intermediate case—that of energy conversion proceeding in a region of liquid adjacent to the walls, the thickness of the region varying with the tube diameter as $d^{\frac{1}{2}}$. The argument is, of course, extremely tenuous. It does not appear possible at the present time to provide any more than these simple speculations on the frictional mechanism. Additional data over a wider range of capillary sizes and perhaps of different shapes may eventually yield additional clues to the interaction.

An important body of experimental phenomena, i.e., the mobilities of unsaturated He films, has not been included in the present considerations. Information on unsaturated films is at present not easily applied for detailed comparison with the theory. It is encouraging, however, that the general dynamical behavior of unsaturated films, that their volume flow rates decrease with decreasing thickness,[17] is in accord with the present theory.

In conclusion, the success of the present model in describing the numerous aspects of superfluid dynamics appears to point to the possible validity of the underlying assumptions. The most unique assumption is that of the cooperative clusters, representing the spatial bounds of the effective liquid mass involved in the phonon creation, and whose significance has been only briefly discussed. No attempt has been made to account for their existence on the basis of the fundamental theories of liquid helium.[18] It is hoped that they may be indicated by a re-examination of the quantum-statistical models.

The present theory owes much to the general properties of the quantum models. In particular, we have adopted the two-fluid representation, together with the special character of the superfluid component, as our description of the static liquid. The independence of the velocity fields of the normal and superfluid components and the phonon character of the possible thermal excitations in the liquid are essential to the present dynamical theory, to which we have added the *a priori* assumptions of the wall friction and the cooperative clusters. The present treatment does not examine the foundations of the two-fluid model; it assumes the validity of this representation and then attempts to describe the dynamical behavior of the superfluid component.

[15] B. A. Bakhmeteff, *The Mechanics of Turbulent Flow* (Princeton University Press, Princeton, 1941).
[16] H. Lamb, *Hydrodynamics* (Dover Publications, New York 1945).
[17] E. A. Long and L. Meyer, Phil. Mag. **2** (1953).
[18] R. B. Dingle, Phil. Mag. **1**, 111 (1952).

# Motion of Arc Cathode Spot in a Magnetic Field*

ROBERT M. ST. JOHN AND J. G. WINANS
*University of Wisconsin, Madison, Wisconsin*

(Received Februrary 19, 1954)

The motion of the cathode spot of a mercury arc was observed under various transverse magnetic fields, arc currents, and inert gas pressures. With no inert gas, the retrograde velocity increased as the magnetic field strength increased. Addition of an inert gas at low pressures reduced the retrograde velocity and at higher pressures caused a forward (direction of magnetic force) motion.

The motion of the cathode spot in a magnetic field can be associated with electrostatic forces on positive ions produced by electron impact. A cathode spot assembly consisting of a group of electrons in the cathode, a positive ion sheath separated by a dark space from the cathode, and an electron cloud between the positive ion sheath and anode is postulated.

Electrons after acceleration through the cathode dark space would travel a curved path due to the magnetic field and produce new positive ions on the forward side of the cathode spot. These new positive ions would be attracted by the cathode spot assembly with a resultant force that would cause them to overshoot the positive ion sheath before being pulled into the cathode to start a new spot in the retrograde direction.

Addition of an inert gas reduces the mobility of positive ions to the order of that of the cathode electrons thus permitting forward motion of the cathode spot assembly to reduce the overshooting. Higher pressures would cause a forward spot motion.

## INTRODUCTION

THE motion of the cathode spot of an electric arc in a transverse magnetic field has been previously investigated by Minorsky,[1] Smith,[2] Gallagher and Cobine,[3–5] Himler and Cohn,[6] and Miller.[7]

Minorsky[1] observed that under some conditions the cathode spot moves in a direction opposite to the force on the charges due to their motion in a magnetic field. This type of spot motion has been termed retrograde. Motion of the spot in the direction of the force due to the motion of the charges through a magnetic field will be called a forward motion.

With a special cathode Smith [reference 2e] found that the velocity of the arc spot in the retrograde direction increased with magnetic field strength, leveling off at about 120 m/sec and then suddenly rising at about 9000 oersteds to about 250 m/sec. Under special conditions the speed went to about 800 m/sec. Smith [reference 2(c)] also found that retrograde motion of the cathode spot occurred only for cold cathodes arcs.

Gallagher and Cobine[3–5] observed that with the addition of an inert gas to a mercury arc the retrograde velocity of the arc spot decreased. There was a certain pressure at which the arc stopped, and at pressures greater than this, the spot moved in the forward direction. They obtained an indication of a proportionality between the pressure needed to reverse the motion and the energy of the first excited state of the admixed gas.

## APPARATUS

Figure 1 shows a cross section of the discharge tube mounted in the magnet. Not shown is an outlet to the vacuum system and inert gas supply. The tube elements are circular when viewed from above. The cathode is composed of a molybdenum stump standing in a pool of mercury. When the molybdenum has a very clean surface it is wet by the mercury which then rises around the stump. The arc spot is formed at the junction of the mercury and the molybdenum stump. Thus, the electric field and the path of the charged particles near the cathode are both horizontal. Since the magnetic field is vertical, the charged particles near the cathode have a horizontal force exerted on them because of their motion through the magnetic field. The force is in the same direction for both positively and negatively charged particles, since they travel in opposite directions. The cathode spot moves around the stump

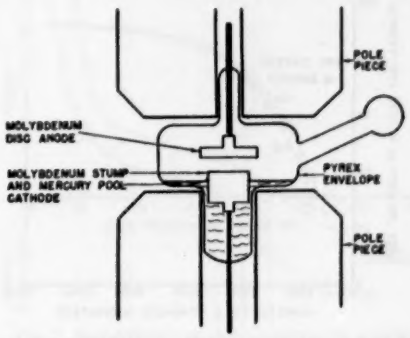


FIG. 1. Arc discharge tube mounted in magnet.

* Reported in large part at conference on Gaseous Electronics, Washington, D. C., October 24, 1953 [Phys. Rev. **93**, 653 (1954)].

[1] N. Minorsky, J. de phys. et rad. (Paris) **9**, 127 (1928).

[2] C. G. Smith, (a) Phys. Rev. **62**, 48 (1942); (b) Phys. Rev. **69**, 96 (1946); (c) Phys. Rev. **73**, 543 (1948); (d) Phys. Rev. **83**, 194 (1951); and (e) Phys. Rev. **84**, 1075 (1951).

[3] C. J. Gallagher, Special publication of General Electric Company, and J. Appl. Phys. **21**, 768 (1950).

[4] C. J. Gallagher and J. D. Cobine, Phys. Rev. **71**, 481 (1947).

[5] J. D. Cobine and C. J. Gallagher, Elec. Eng. **68**, 469 (1949).

[6] G. J. Himler and G. I. Cohn, Elec. Eng. **67**, 1148 (1948).

[7] C. G. Miller, Report at Gaseous Electronics Conference October 24, 1953. [Phys. Rev. **93**, 654 (1954)].

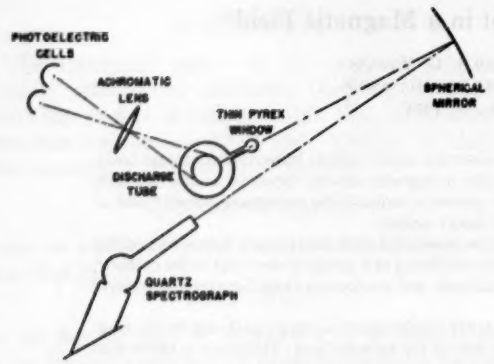


FIG. 2. Apparatus used in observing the arc.

at the junction between the mercury and the molybdenum stump.

Figure 2 is a top view of the apparatus used in observing the arc. Light from the arc is focused on two photoelectric cells close together. The output of these cells is fed into a cathode-ray oscilloscope along with the output of an audio oscillator to produce Lissajou figures. When the frequency of the audio oscillator is such as to give a single closed loop on the oscilloscope screen, the frequency of the cathode spot equals that of the audio oscillator. The spot velocity is determined from this frequency and the diameter of the stump. The use of two photoelectric cells permitted the determination of the direction of the spot motion and showed that there was but one spot. When the output of the photoelectric cells was fed into the vertical deflection channel of the oscilloscope with the horizontal sweep frequency set at the arc spot frequency, a stationary trace having two close peaks was obtained on the oscilloscope. Each peak could be associated with the cell whose output produced it by partially covering one of the cells and noting the peak whose height was reduced. This showed which cell received light first from the arc spot and thus showed the direction of motion of the arc spot.

The spectrum of the cathode spot region was obtained by focusing an image of the spot on the slit of a spectrograph as shown in Fig. 2.

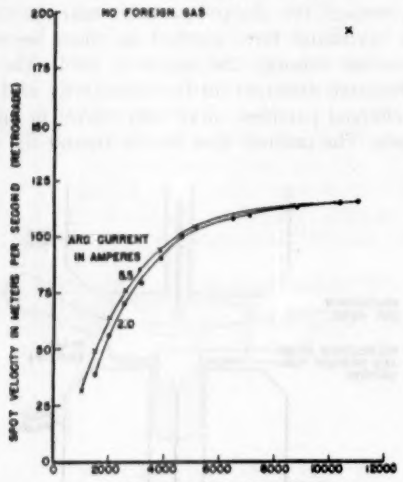


FIG. 3. Spot velocity *vs* magnetic field strength for constant arc currents. No inert gas.

## RESULTS

The spot velocity as found by previous investigators and also in this work depends upon (a) magnetic field strength, (b) arc current, and (c) pressure of inert gas.

Figure 3 shows a plot of the spot velocity as a function of magnetic field strength for constant arc currents of 5.5 and 2.0 amperes and no inert gas in the tube. An increase in magnetic field strength is accompanied by an increase in retrograde velocity.

With the higher arc current (5.5 amperes) the spot velocity changes discontinuously to a value nearly twice as great at a certain magnetic field strength. The change was from about 112 m/sec to about 193 m/sec at a field strength about 10 500 oersteds. The magnetic field strength at which the break occurs changes with arc current as shown in Fig. 4. A decrease in arc current increases the field strength needed to produce the velocity discontinuity.

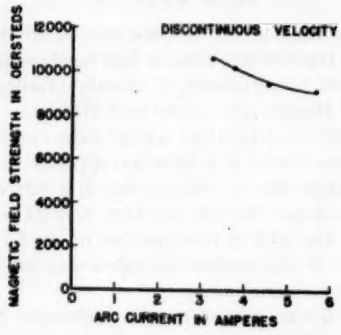


FIG. 4. Magnetic field strength *vs* arc current for the discontinuity in spot velocity. No inert gas.

Figure 5 shows the spot velocity plotted as a function of arc current for various constant magnetic field strengths and no inert gas present. The spot velocity increases in the retrograde direction as the arc current is increased.

With an inert gas (argon) in the tube at a pressure of 150 mm Hg the spot velocity depends on the magnetic field strength as shown in Fig. 6 for several values of the arc current. The shape of these curves is similar to those for no inert gas present (Fig. 3). However, the curves are shifted downward along the velocity axis toward the forward velocities, and the velocities are about one hundredth of the velocities with no inert gas.

For a given magnetic field strength, an increase in arc current increases the forward velocity, thus changing the velocity toward the forward direction. When there was no inert gas and the velocity was retrograde an increase in arc current increased the retrograde velocity (Fig. 3). With inert gas present there was no discontinuity in velocity at high magnetic field strengths.

Figure 7 shows a plot of the spot velocity as a function of argon pressure for two constant magnetic field strengths. With a low inert gas pressure the spot moves in the retrograde direction. Increasing the pressure causes the spot to slow down, stop, and then move in the forward direction.

The conditions required for a zero-spot velocity are shown in Fig. 8. The magnetic field strength to give

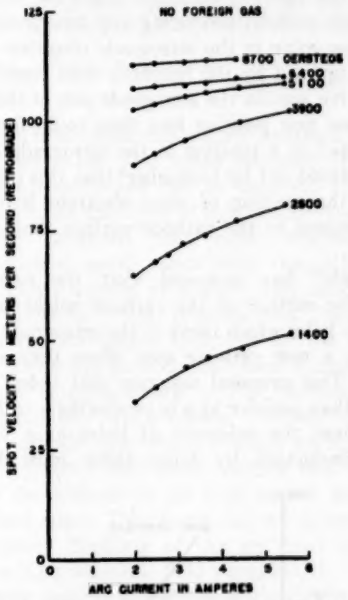


FIG. 5. Spot velocity *vs* arc current for constant magnetic field strengths. No inert gas.

zero-spot velocity is plotted as a function of arc current for constant gas pressures. In general, an increase in arc current requires an increase in magnetic field strength to hold the spot at rest. For a high gas pressure a small change in arc current requires a large change in magnetic field strength to compensate it, while for a low gas pressure the same change in arc current requires a small change in magnetic field strength to compensate it. If curves like these had been plotted for a constant retrograde velocity instead of zero velocity, the curve for zero gas pressure would have had a negative slope as may be seen from Fig. 3. and Fig. 5. For a constant retrograde velocity and no inert gas an increase in arc current requires a decrease in magnetic field strength to compensate it.

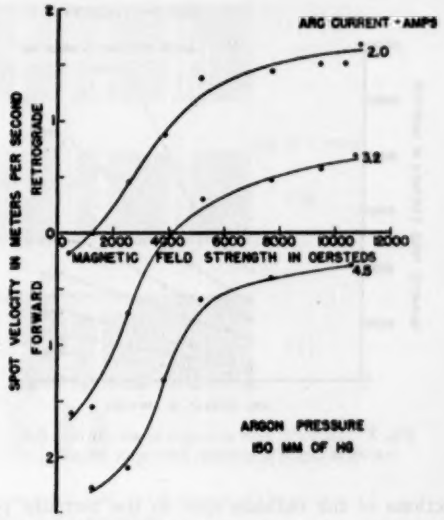


FIG. 6. Spot velocity *vs* magneitc field strength for constant arc currents. Argon pressure 150 mm Hg.

Figure 9 shows the inert gas (argon) pressure required to produce a zero-spot velocity at various arc currents for three constant magnetic field strengths. An increase in arc current requires a decrease in pressure to compensate it.

Spectra of Hg are shown in Fig. 10. Figure 10(a) shows the spectrum of the arc in a weak magnetic field. The central continuous spectrum is from the cathode spot while the lower part is due to the negative glow. (The part above the continuous spectrum is from

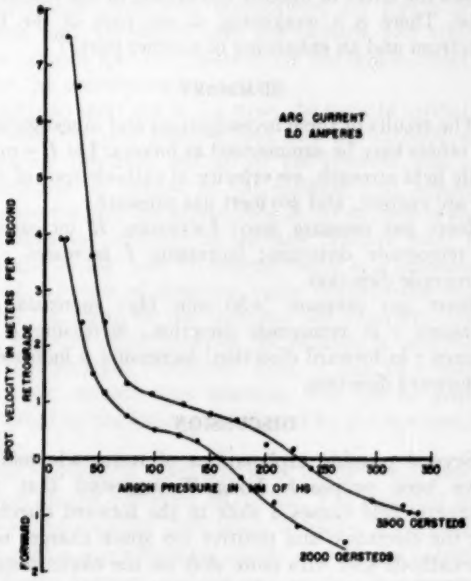


FIG. 7. Spot velocity *vs* argon pressure for constant magnetic field strengths.

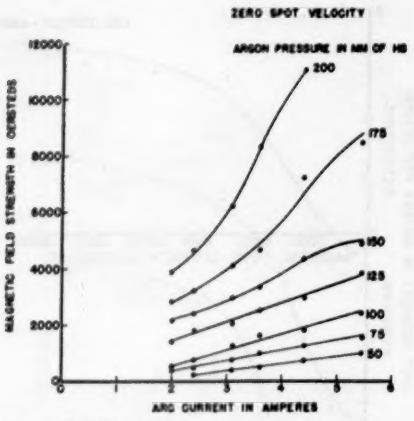


FIG. 8. Magnetic field strength *vs* arc current for constant argon pressures. Zero-spot velocity.

reflections of the cathode spot in the mercury pool.) The spectrum shown in Fig. 10(b) is of the arc in a magnetic field of about 12 000 oersteds. In the spectrum of the arc in a strong magnetic field several new lines appear and several others are greatly enhanced. These are Hg II lines. Smith [reference 2(d)] observed both Hg II and Hg III lines in the spectrum of the arc in a magnetic field of 10 000 oersteds.

The continuous spectra for the strong and weak magnetic fields are similar. That this continuous spectrum is not due to a high concentration of mercury molecules near the cathode is shown by comparing it with the continuous spectrum of mercury molecules shown in Fig. 10(c). (The center part of Fig. 10(c) shows the effect of heating the middle of the discharge tube. There is a weakening of one part of the $Hg_2$ spectrum and an enhancing of another part.[8])

## SUMMARY

The results of these investigations and investigations by others may be summarized as follows: Let $H$ = magnetic field strength, $v$ = velocity of cathode spot of arc, $I$ = arc current, and $p$ = inert gas pressure.

Inert gas pressure zero: Increasing $H$ increases $v$ in retrograde direction; increasing $I$ increases $v$ in retrograde direction.

Inert gas pressure >50 mm Hg: Increasing $H$ increases $v$ in retrograde direction; increasing $I$ increases $v$ in forward direction; increasing $p$ increases $v$ in forward direction.

## DISCUSSION

Several possible explanations of retrograde motion have been proposed. Longini[9] suggested that the magnetic field causes a shift in the forward direction for the electronic and positive ion space charges near the cathode spot with more shift for the electron space charge near the cathode surface than for the positive ion sheath above the cathode spot. This would neutralize part of the positive ion sheath in the forward direction and thus produce a maximum of electric field at a retrograde position for all but very strong magnetic fields. Longini assumed that the arc spot occurred at the position of highest electric field strength. Thus, the arc spot would move in the retrograde direction along with the maximum of the electric field strength. Longini recognized that according to this explanation the motion should change from retrograde to forward with very strong magnetic fields. Later observations show only an increase in retrograde velocity with increase in magnetic field strength.

H..nler and Cohn[6] have suggested that if electrons are ejected from the cathode spot in all directions, those going in the forward direction might be returned to the cathode without producing any new positive ions, while those going in the retrograde direction although deflected upward by the magnetic field could produce new positive ions on the retrograde side of the cathode spot. These new positive ions then could form a new cathode spot at a position in the retrograde direction. It was pointed out by Gallagher[3] that this explanation required the ejection of more electrons in directions nearly tangent to the cathode surface then would be plausible.

Rothstein[10] has proposed that the current just outside the surface of the cathode might be carried in part by holes which move in the retrograde direction and start a new cathode spot when they strike the cathode. This proposal assumes that holes are more effective than positive ions in producing a cathode spot and assumes the existence of holes in a vapor. To obtain conduction by holes there must be many

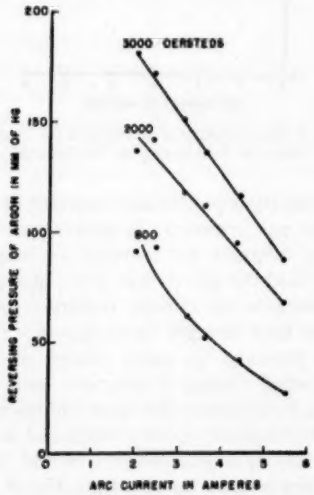


FIG. 9. Argon pressure *vs* arc current for constant magnetic field strengths. Zero-spot velocity.

[8] J. G. Winans, Phys. Rev. 42, 800 (1932).
[9] R. L. Longini, Phys. Rev. 71, 642 (1947); 72, 184 (1947).
[10] J. Rothstein, Phys. Rev. 78, 331 (1950).

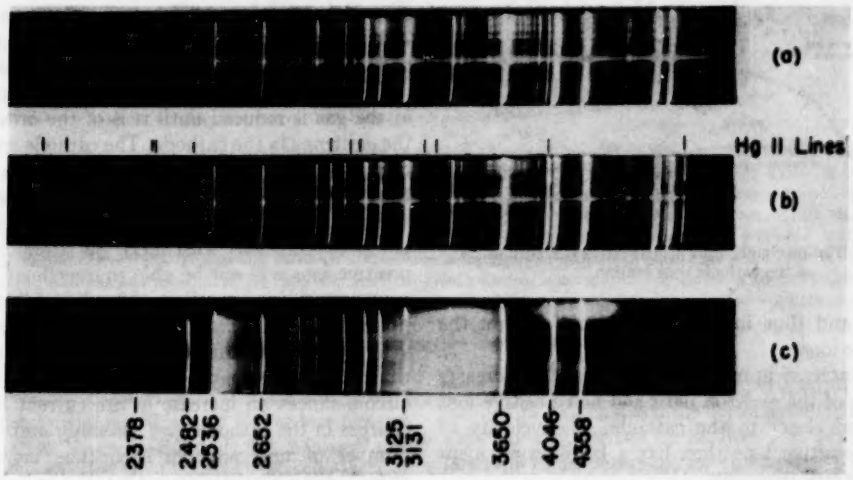


FIG. 10. Spectra of Hg. (a) Spectrum of the arc in a weak magnetic field, (b) Spectrum of the arc in a stong magnetic field and (c) Spectrum of $Hg_2$ molecules.

neutral particles which can supply electrons and thus becomes new holes. The vapor pressure of mercury near the cathode would not be expected to be high enough to permit this type of hole conduction.

Tanberg[11] proposed that rapid evaporation of partially ionized metal vapor from the cathode spot could provide a stream of positive ions moving away from the cathode. These positive ions could be deflected in the retrograde direction by the magnetic field and strike the cathode and form a new cathode spot on the retrograde side of the previous cathode spot. It is unlikely that a stream of atoms evaporated from the cathode spot would contain an appreciable number of positive ions since positive ions would be held near the cathode by the high electric field in the cathode dark space. This theory also would not account for the nearly doubling of the arc spot retrograde velocity at high magnetic field strengths.

A possible mechanism which is consistent with all observations of retrograde and forward motion so far made is illustrated in Fig. 11. The magnetic field is normal to the drawing. The potential difference across the cathode dark space from the spectral evidence shown in Fig. 10 must be about 20 or 30 volts while the total potential difference across the arc is about 12 or 15 volts. This potential distribution requires a positive ion sheath very near the cathode and an electron cloud between this sheath and the anode.

The proposed mechanism for the case in which no inert gas is present is as follows. Electrons emitted from the cathode spot are accelerated through the cathode dark space, and bent into a curved path by the force from their motion through the magnetic field. At the end of a free path for ionization they collide with atoms to produce new positive ions on the forward side of the cathode spot as shown in Fig. 11. These new positive ions are drawn toward the cathode spot region by the forces exerted on them by the electrons in the cathode, the positive ion sheath, the electron cloud above the sheath, and the electrons streaming toward the new positive ions ($F_1$, $F_2$, $F_3$, $F_4$, in Fig. 11). This gives the new positive ions a velocity which has a component in the retrograde direction. As these positive ions approach the cathode spot region they are shielded from the electrons in the cathode spot by the positive ion sheath and attracted toward the electron cloud. Their tangential velocity then carries them over the positive ion sheath after which they are pulled into the cathode and start a new cathode spot at a point in the retrograde direction from the previous cathode spot.

With no inert gas in the tube, the force of attraction between the new positive ions and the cathode spot assembly produces motion of the positive ions and practically no motion of the cathode spot assembly because the mobility of electrons in the cathode is much less than the mobility of the new positive ions. The mobility of $Hg^+$ ions in mercury vapor at a pressure of about 0.3 mm of mercury (tube temperature about 100°C) is about 10 000 (cm/sec) per (volt/cm) while the mobility of electrons in the cathode is near 40 or 50 (cm/sec) per (volt/cm). Also, it can be expected that the cathode spot assembly will not be greatly distorted by the forces exerted on it by the new positive ions.

An increase in magnetic field strength has several effects on the operation of the arc. The potential drop across the cathode dark space increases considerably, but only a slight increase results in the total potential difference between cathode and anode. This increases the charge in the electron cloud above the positive

[11] R. Tanberg, Nature **124**, 371 (1929).

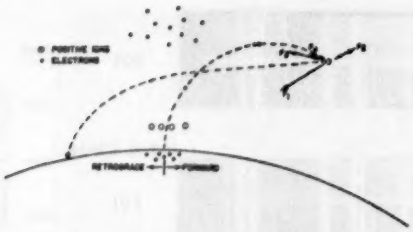

FIG. 11. The mechanism for a qualitative description of the cathode spot motion.

ion sheath and thus increases the total force on the new positive ions.

Also, an increase in magnetic field strength increases the bending of the electron path and new positive ions are produced closer to the cathode. The velocity of these new positive ions then has a larger component in the retrograde direction.

These effects cause the positive ions to overshoot the cathode spot to a greater distance in the retrograde direction when the magnetic field strength is increased. Thus, an increase in the retrograde velocity of the arc spot results from an increase in the magnetic field strength.

The approximate doubling in the retrograde spot velocity with an increase in magnetic field strength beyond 11 000 oersteds when no inert gas is present can be attributed to the production of $Hg^{++}$ ions. The spectrum shows that excited $Hg^{+}$ ions are produced. It is to be expected that $Hg^{++}$ ions are also produced. The tangential force on $Hg^{++}$ being twice that on $Hg^{+}$, the retrograde velocity should be nearly doubled when $Hg^{++}$ ions are formed.

With an inert gas present high-energy electrons can be expected to ionize or excite gas atoms and not gain enough energy to produce doubly-charged ions like $Hg^{++}$. Thus, with an inert gas present, there should be no sudden increase in retrograde velocity with increase of magnetic field strength. This agrees with observations.

An increase in the arc current causes an increase in the total charge in the cathode spot assembly, and this in turn increases the force on each of the positive ions. With no inert gas present they overshoot further in the retrograde direction before starting a new cathode spot, and thus there results an increase in the retrograde velocity of the cathode spot.

The introduction of an inert gas into the discharge tube reduces the mobility of the positive ions very greatly since the mobility is inversely proportional to the gas pressure. Addition of argon to a pressure of 760 mm Hg reduces the positive-ion mobility from about 10 000 (cm/sec) per (volt/cm) to 1 or 2 (cm/sec) per (volt/cm). Thus, the mobility of the positive ions in the gas is reduced until it is of the order of that of the electrons in the cathode. The cathode spot assembly can then move in the forward direction during the time of motion of the positive ions. Also the tangential velocity acquired by the positive ions is rapidly dissipated by collisions with inert gas atoms, so that the positive ions will not be able to overshoot the cathode spot assembly as much as they did with no inert gas present. These effects produce a reduction in retrograde velocity and, if sufficiently large, cause a motion of the cathode spot in the forward direction. Under these circumstances an increase in arc current increases the charges in the cathode spot assembly and increases the number of new positive ions, thus increasing these effects. Experiment shows that the velocity increases in the forward direction with an increase in arc current when an inert gas is present.

## CONCLUSIONS

The retrograde motion of the cathode spot of an electric arc in a transverse magnetic field when little or no inert gas is present can be described in terms of positive ions overshooting the cathode spot assembly.

A substantial amount of inert gas retards the movement of the positive ions to the extent that the movement of the cathode spot assembly in the forward direction is greater than the overshooting of the positive ions. This can account for the forward motion of the cathode spot with an inert gas present.

The writers wish to thank Dr. C. G. Smith for the use of a magnet and one of his arc tubes, and also for some pure molybdenum that was used in making electrodes of other tubes.

Work is continuing with the support of the Research Corporation.

*Note added in proof.*—A. E. Robson and A. von Engel [Phys. Rev. **93**, 1121 (March 1, 1954)] suggest that retrograde motion may result from a local reversal of magnetic field due to sharp bending of the electron current. While the process might give retrograde motion it would not account for the doubling of retrograde velocity at high magnetic fields. Also this mechanism requires that the retrograde velocity be nearly proportional to the square of the arc current while measurements (Fig. 5) show it to be less than proportional to the first power of arc current.

# Second Virial Coefficients of $He^3$ and $He^4$†

JOHN E. KILPATRICK,* WILLIAM E. KELLER, EDWARD F. HAMMEL, AND NICHOLAS METROPOLIS
*Los Alamos Scientific Laboratory, University of California, Los Alamos, New Mexico*
(Received February 10, 1954)

The second virial coefficients of $He^3$ and $He^4$ have been calculated at closely spaced temperatures over the range 0.3°K to 60°K using the Lennard-Jones 12–6 potential with constants determined by de Boer and Michels. The necessary phase shifts were calculated on a high-speed electronic digital computer. The resulting $He^4$ second virial coefficients agree very well with the available experimental data. They also join nicely at 60°K with the coefficients calculated from the high-temperature classical equation with quantum corrections. The second cross virial coefficients for $He^3$, $He^4$ have also been calculated. The deviation of a gaseous solution of $He^3$ and $He^4$ from an ideal solution is comparatively small at temperatures above about 2°K, while at very low temperatures pronounced quantum solution imperfection appears.

## I. INTRODUCTION

THE second virial coefficient of $He^4$ at low temperatures has been calculated by Massey and Buckingham[1] and by Buckingham, Hamilton, and Massey,[2] from several intermolecular potentials, the constants of which are theoretical or semitheoretical in origin. A similar calculation has been made by de Boer and Michels[3] with the Lennard-Jones 12–6 potential. The constants of this equation were determined empirically by fitting the high-temperature statistical equations (with quantum corrections) to experimental (above 50°K) virial coefficient data. Of these several calculations, that of de Boer and Michels best fits the experimental low-temperature virial coefficient data. The same Lennard-Jones potential has also been used by de Boer, van Kranendonk, and Compaan[4] to calculate the second virial coefficients of $He^3$. There are as yet no experimental data in this case.

The most difficult and lengthy part of such a calculation is the determination of the very large number of phase shifts needed to describe the binary atomic collision. Most of the phase shifts given by de Boer and co-workers[3,4] were determined by numerical integration of the one-dimensional radial Schrödinger equation with the Lennard-Jones potential. Relatively few details are given of the numerical technique used, so that it is difficult for one to judge the probable accuracy of the calculation. However, it is safe to assert that at least a lifetime of work on a desk calculator would be needed to achieve moderately high accuracy in the results. This problem obviously calls for the use of a modern high-speed digital computer.

Although one observes that the second virial coefficients of de Boer and Michels[3] for $He^4$ are a pretty good representation of the experimental results, we decided to recalculate these coefficients for $He^4$ and $He^3$, using constants given by de Boer and Michels[5] for the Lennard-Jones potential, for two reasons: (1) to establish how much of the small deviation of the previous work[3] from the experimental data is due to the potential and how much is due to accumulated numerical error, and (2) to extend the temperature range of the calculated second virial coefficients. In addition, we have calculated the cross $He^3$, $He^4$ coefficients using the same Lennard-Jones potential.

## II. THEORY

The equation of state of a gas may be expressed in either the pressure or the inverse volume expansion:

$$Pv=RT+BP+CP^2+\cdots, \tag{1}$$

$$Pv=RT(1+B'/v+C'/v^2+\cdots, \tag{2}$$

where $B=B'$ is the second virial coefficient ($C\neq C'$, etc.). In this section the method used to obtain $B$ will be briefly developed inasmuch as the several aspects of this theory have not been consolidated in the earlier literature. In Part (a), an expression for $B$ in terms of the density of energy levels for an ideal gas relative to that for a real gas is derived from the statistical mechanical relationship for $B$. In Part (b), the potential energy between the two particles is inserted into the radial wave equation from the solution of which one obtains the relative energy density. In Part (c), the results of the quantum-mechanical operations are introduced into the formula for $B$.

### (a) Transformation of the $B$ Equation

The statistical mechanical expression for $B$ is given by[6]

$$B=-NV(Z_2-\tfrac{1}{2}Z_1^2)/Z_1^2, \tag{3}$$

where $N$ is Avogadro's number, $Z_1$ is the partition function for one molecule, and $Z_2$ is the partition function for two molecules. This expression is correct

† Work performed under the auspices of the U. S. Atomic Energy Commission.
* Department of Chemistry, The Rice Institute, Houston, Texas.
[1] H. S. W. Massey and R. A. Buckingham, Proc. Roy. Soc. (London) **A168**, 378 (1938); **A169**, 205 (1939).
[2] Buckingham, Hamilton, and Massey, Proc. Roy. Soc. (London) **A179**, 103 (1941).
[3] J. de Boer and A. Michels, Physica **6**, 409 (1939).
[4] de Boer, van Kranendonk, and Compaan, Phys. Rev. **76**, 998 (1949); **76**, 1728 (1949); Physica **16**, 545 (1950).
[5] J. de Boer and A. Michels, Physica **5**, 945 (1938).
[6] J. E. Kilpatrick, J. Chem. Phys. **21**, 274 (1953).

both quantum-mechanically and classically. $Z_1$ is given by

$$Z_1=(2s+1)\lambda^{-3}V, \tag{4}$$

where[7]

$$\lambda^2=h^2/2\pi mkT, \tag{5}$$

and $s$ is the nuclear spin.[8]

In the following discussion we shall use the term "ideal" to refer to a hypothetical gas identical with the real gas except that the potential of interaction is zero for all distances. Properties of such a gas will be denoted by attaching an asterisk to the appropriate symbols. It is convenient to divide $B$ into two parts, $B^*$ and $B-B^*$. Equation (3) then takes the form

$$B=\mp\frac{2^{-5/2}N\lambda^3}{2s+1}-\frac{N\lambda^6(Z_2-Z_2^*)}{(2s+1)^2V}. \tag{6}$$

The sign of the first (ideal gas) term is negative for a Bose-Einstein gas and positive for a Fermi-Dirac gas. In general

$$Z_2=\sum{}' e^{-E/kT}=Z_{2(\text{trans})}\cdot Z_{2(\text{rel})}=2^{\frac{1}{2}}\lambda^{-3}V\cdot Z_{2(\text{rel})}, \tag{7}$$

where the prime on the summation indicates it is to be taken over all quantum states, $Z_{2(\text{trans})}$ is the partition function of the translatory motion of the center of gravity of the two-molecule system, and $Z_{2(\text{rel})}$ is the partition function of the two-molecule system summed over only the quantum states due to the relative motion. We can then write Eq. (6) as

$$B=\mp\frac{2^{-5/2}N\lambda^3}{2s+1}-\frac{2^{\frac{1}{2}}N\lambda^3(Z_{2(\text{rel})}-Z_{2(\text{rel})}^*)}{(2s+1)^2}. \tag{8}$$

The only term in Eq. (8) that offers any difficulty is $Z_{2(\text{rel})}-Z_{2(\text{rel})}^*$. Its value depends principally upon the difference in density of the energy levels of relative motion between the two cases.

### (b) The Quantum-Mechanical Relations

The energy levels of relative motion are the eigenvalues of the radial wave equation

$$-\frac{\hbar^2}{2\mu}(r\psi)''+\frac{l(l+1)\hbar^2}{2\mu r^2}r\psi+V(r)r\psi=Er\psi, \tag{9}$$

where $\mu$ is the reduced mass and $V(r)$ is the actual intermolecular potential for the real pair of molecules and is identically zero for the ideal pair. It is convenient to reduce Eq. (9) to a dimensionless form by the substitutions

$$R=r/\rho, \tag{10}$$

$$U(R)=(2\mu/\hbar^2)\rho^2V(r), \tag{11}$$

$$q^2=(2\mu/\hbar^2)\rho^2E, \tag{12}$$

$$R\psi(R)=r\psi(r). \tag{13}$$

Here we introduce the symbol $\rho$, rather than the usual $\sigma$, to emphasize the fact that in the above expressions $\rho$ is an arbitrary parameter, whereas the $\sigma$ in the Lennard-Jones potential (see further on) has special significance; for this potential it is convenient to let $\rho=\sigma$.

We then obtain

$$-(R\psi)''+[-q^2+l(l+1)R^{-2}+U(R)]R\psi=0. \tag{14}$$

The energy levels fall into two classes: (1) a finite number (possibly zero) of negative levels for the real pair of molecules (there are never any negative levels for the ideal pair) whose contribution to $Z_2$ can be directly summed, and (2) an infinite number of very closely spaced positive levels for both the real and the ideal pair. The relative density of these two near-continua can best be treated by the method of phase shifts, introduced for this problem by Gropper[9] and by Beth and Uhlenbeck.[10]

For values of $R$ large enough that $l(l+1)R^{-2}+U(R)$ is negligible,

$$R\psi=\sin(qR-\tfrac{1}{2}\pi l+\eta_l). \tag{15}$$

The phase shift $\eta_l$ of course is zero for the case $U(R)=0$. With very little loss in generality[11] we can set a boundary condition of $R\psi=0$ at $R=L$, a fairly large number. The possible values of $q$ for the two cases [real $U(R)$ and ideal $U\equiv0$] are given by

$$qL-\tfrac{1}{2}\pi l+\eta_l=n\pi, \tag{16}$$

$$qL-\tfrac{1}{2}\pi l=n\pi, \tag{17}$$

where $n$ is a positive integral quantum number and is equal to the number of zeros of the wave function (excluding the one at the origin). The difference in density of the energy levels between the real and the ideal cases is obtained by taking the variation of these two equations and rearranging:

$$(\delta n/\delta q)-(\delta n/\delta q)^*=(1/\pi)(\delta\eta_l/\delta q). \tag{18}$$

This difference in density then is measured by the rate of change of the phase shift $\eta_l$ with the energy parameter $q$.

### (c) Final Expression for $B$

We may divide $Z_{2(\text{rel})}$ into two sums, one extending over the discrete negative states (if any) and the other extending over the positive states. Since the positive levels are so very close together no appreciable error is introduced into $Z_{2(\text{rel})}$ by replacing the sum over all

[7] Values of the fundamental physical constants used in this paper were obtained from F. D. Rossini *et al.*, J. Am. Chem. Soc. **74**, 2699 (1952). The values employed for the isotopic masses were obtained from C. W. Li *et al.*, Phys. Rev. **83**, 512 (1951).

[8] We assume a monatomic gas since this theory is of interest principally for helium.

[9] L. Gropper, Phys. Rev. **51**, 1108 (1937).

[10] E. Beth and G. E. Uhlenbeck, Physica **4**, 915 (1937).

[11] The error is only in the very minor shape-of-container effect upon the equation of state.

quantum states by an integration with respect to $n$. We then convert to an integration with respect to $q$ and obtain

$$Z_{2(\mathrm{rel})}=\sum' \exp(-E_{n,l}^-/kT)+\sum' \exp(-E_{n,l}^+/kT)$$
$$=\sum_l \Omega(s,l)\left[\sum_n \exp(-E_{n,l}^-/kT)+\int_{q=0}^{\infty}\exp(-q^2/q_0^2)\frac{dn}{dq}dq\right], \quad (19)$$

where $\Omega(s,l)$ gives the appropriate quantum weighting factors, the summation in $n$ is over all negative energy levels of the system, and $E_{n,l}^+$ has been replaced by its equivalent according to Eq. (12), so that

$$q_0^2=2\mu\rho^2kT/\hbar^2=2\pi\rho^2\lambda^{-2}. \quad (20)$$

The corresponding expression for $Z_{2(\mathrm{rel})}^*$ may then be combined with Eq. (19) using Eq. (18) to obtain $Z_{2(\mathrm{rel})}-Z_{2(\mathrm{rel})}^*$ in terms of the phase shifts $\eta_l$.

The degeneracy $\Omega(s,l)$ of a particular energy level depends on the statistics of the two atoms, their nuclear spin, and the value of the angular-momentum quantum number. For a pair of identical Fermi-Dirac atoms, each with nuclear spin $s$, the weight is $(s+1)(2s+1)(2l+1)$ for $l$ odd and $s(2s+1)(2l+1)$ for $l$ even [the factor $(2l+1)$ arises from the spatial degeneracy]; these two weights are interchanged for a pair of Bose-Einstein atoms.

We may now write for a pair of Fermi atoms, for example,

$$Z_{2(\mathrm{rel})}-Z_{2(\mathrm{rel})}^*$$
$$=(s+1)(2s+1)\sum_{l\ \mathrm{odd}}(2l+1)\left\{\sum_n \exp(-E_{n,l}^-/kT)+\frac{1}{\pi}\int_{q=0}^{\infty}\exp(-q^2/q_0^2)\frac{d\eta_l}{dq}dq\right\}$$
$$+s(2s+1)\sum_{l\ \mathrm{even}}(2l+1)\left\{\sum_n \exp(-E_{n,l}^-/kT)+\frac{1}{\pi}\int_{q=0}^{\infty}\exp(-q^2/q_0^2)\frac{d\eta_l}{dq}dq\right\}. \quad (21)$$

Integration of Eq. (21) by parts, insertion of the resulting expression into Eq. (18) and re-arrangement with the aid of Eq. (20), yields the final expression for $B$,

$$B=\frac{N\pi^{\frac{1}{2}}\rho^3}{2(2s+1)q_0^3}-\frac{8N\pi^{\frac{1}{2}}\rho^3}{q_0^3}$$
$$\times\sum_n\left\{\frac{s+1}{2s+1}\sum_{l\ \mathrm{odd}}(2l+1)[\exp(-E_{n,l}^-/kT)-1]+\frac{s}{2s+1}\sum_{l\ \mathrm{even}}(2l+1)[\exp(-E_{n,l}^-/kT)-1]\right\}$$
$$\mp\frac{16N\pi^{\frac{1}{2}}\rho^3}{q_0^5}\int_0^{\infty}(\sum)\exp(-q^2/q_0^2)qdq, \quad (22)$$

were

$$(\sum)=\frac{s+1}{2s+1}\sum_{l\ \mathrm{odd}}(2l+1)\eta_l+\frac{s}{2s+1}\sum_{l\ \mathrm{even}}(2l+1)\eta_l. \quad (23)$$

Again, Eqs. (22) and (23) apply to a pair of identical Fermi atoms. The nuclear spin weighting factors $s+1$ and $s$ are to be interchanged for a pair of Bose atoms. The Boltzman factors arise directly from $Z_2$, but the associated minus unity comes from the integration by parts of the phase shift integral. Phase shifts in general are arbitrary to the extent of any integral multiple of $\pi$. They are made definite by the convention that (1) $\eta_l=0$ for all $q$ and $l$ when $U(R)\equiv 0$, and (2) $\eta_l$ be continuous for all $q$ and $l$ as $U(R)$ varies. This convention necessitates that $\eta_l=\pi n_l$ for $q=0$, when $n_l$ is the number of discrete negative energy states associated with the angular quantum number $l$.

If the same analysis[6] that led to Eq. (3) is applied to a gaseous solution such as a mixture of $He^3$ and $He^4$, the following equation is obtained for the second virial coefficient:

$$B=N_3^2B_{33}+2N_3N_4B_{34}+N_4^2B_{44}. \quad (24)$$

The mole fractions of the two components are $N_3$ and $N_4$. $B_{33}$ and $B_{44}$ are the second virial coefficients of pure $He^3$ and pure $He^4$. $B_{34}$, the second cross virial coefficient of the mixture, is defined by

$$2B_{34}=-NV(Z_{2(3,4)}-Z_{1(3)}Z_{1(4)})/Z_{1(3)}Z_{1(4)}, \quad (25)$$

where $Z_{2(3,4)}$ is summed over all of the states of a system composed of an $He^3$ and an $He^4$ atom. The initial ideal gas term of Eq. (22) is exactly zero since the two atoms are distinguishable. The sum $(\sum)=\frac{1}{2}\sum(2l+1)\eta_l$ is taken over all values of $l$ and the nuclear spin weighting factors cancel identically.

## III. NUMERICAL SOLUTION OF EQUATIONS

With the exception of some preliminary, exploratory calculations that were performed on an IBM CPC computer, all of the numerical calculations of this work were carried out on the MANIAC, the Los Alamos electronic digital computer. This is a single address, binary, fixed decimal machine with electrostatic storage. The access time of a word in storage is about 10 $\mu$sec, and the multiplication time of two forty place binary numbers (approximately twelve decimal places) is about 1000 $\mu$sec.

The radial wave equation in the reduced form of Eq. (14) was integrated by a method given by Milne.[12] This method is quite advantageous in that it requires relatively few operations, only two starting values, and has the same error term as the more commonly used three-point closed double integration formula. We used the integration pattern $R=0.625(1/128)1.5(1/64)4\times(1/32)8$, since it was necessary to use a finer inte-

[12] W. E. Milne, Amer. Math. Mon. 49, 96 (1942).

gration interval when $R$ was small. This choice was made after considerable experimentation in order to determine the effect of integration interval pattern upon the phase shifts. The numerical procedure was so arranged that the integration interval was doubled automatically at the preselected values of $R$.

The potential term was so coded that with relatively little work any new potential function, even one given in the form of a numerical table, could be easily substituted. The Lennard-Jones potential used has the form

$$V(r)=4\epsilon[(\sigma/r)^{12}-(\sigma/r)^{6}]. \tag{26}$$

The two parameters were determined from the statement of de Boer *et al.*[4] that for helium $\epsilon/k=10.22°\text{K}$ and $N\sigma^3=10.06$ cc.

The reduced Lennard-Jones 12–6 potential may be written as

$$U(R)=p^2(R^{-12}-R^{-6}), \tag{27}$$

where $\rho=\sigma$ and $p^2=8\mu\epsilon\sigma^2/\hbar^2$. In the region of small $R$,

$$R\psi=\exp(-pR^{-5}/5). \tag{28}$$

For the Milne integration formula the first-order error per cycle is $\delta^6(R\psi)/240$. To obtain accurate phase shifts, it is necessary in solving the wave equation to preserve accuracy in $R\psi$ or in $(R\psi)'/R\psi$. Whereas a prohibitively small integration interval would be necessary in the region of small $R$ to obtain $R\psi$ exactly, only a moderately coarse interval ($\Delta R=1/128$) is sufficient to preserve accuracy in $(R\psi)'/R\psi$. Furthermore, the phase shift in the wave function (determined at large $R$) is pretty nearly independent of the particular starting values of $R\psi$ used in the neighborhood of $R=0.6$. For example, the phase shifts for $He^3$ for $q=1$ and $l=0$, 1, 2, 3, etc., were determined using the following arbitrarily chosen starting values: $R_0$ and $R_1=0.625$ and $0.625+1/128$; $(R\psi)_0$ and $(R\psi)_1=$ (1) $2^{-12}$ and $2^{-4}$; (2) $2^{-4}$ and $2^{-4}$; (3) $2^{-4}$ and $2^{-12}$. The phase shifts for each value of $l$ were the same to at least six significant (decimal) figures in all three trials.

It would be necessary to integrate out to a prohibitively large value of $R$ in order that $R\psi$ be given accurately by Eq. (15). For much smaller values of $R$ [namely, when $U(R)$ is negligible] an expression in half-integral Bessel functions may be used,

$$R\psi=AR^{\frac{1}{2}}J_{l+\frac{1}{2}}(qR)+BR^{\frac{1}{2}}J_{-l-\frac{1}{2}}(qR), \tag{29}$$

$$\eta_l=\tan^{-1}[(-)^{l}B/A]. \tag{30}$$

To obtain $B/A$, two equations of the form of Eq. (29) were solved simultaneously, using values of $R\psi$ corresponding to two values of $R$ separated by two integration intervals. In the course of our exploratory work we observed a smooth systematic trend in the apparent value of $\eta_l$ (determined in the region of some particular value of $R$) as $R$ increased. This error in $\eta_l$, due to stopping at a finite value of $R$, was shown to be

$$\eta_l(\text{true})-\eta_l(\text{apparent})=p^2/10qR^5+\cdots. \tag{31}$$

This error expression is the first term of an asymptotic series. The integration proceeded until the error term was less than 0.0001 radian, at which point $\eta_l$ (apparent) was obtained. This value of $\eta_l$ was corrected by means of Eq. (31). The proper quadrant for $\eta_l$ was determined automatically by a series of discriminations upon the trend in the apparent value of $\eta_l$ from Eq. (30).

The Bessel functions of Eq. (29) are simple algebraic functions in $qR$, $\sin qR$ and $\cos qR$. Since according to Eq. (31) the same stopping point in $R$ for a particular value of $q$ can be used for all $l$, it was possible to have the computer first generate the necessary trigonometric functions and then higher-order Bessel functions by recursion as they were needed.

The over-all pattern of operation was as follows. Starting with some particular value of $q$, the first integration would be carried out with $l=0$; the phase shift would be calculated; the necessary Bessel functions for the next higher value of $l$ would be generated, $l$ advanced by unity (by two in the case of $He^4$) and the next integration begun. At the end of each integration the following information was printed out: $q$, $l$, $(2l+1)\eta_l$ and the running sum of $(2l+1)\eta_l$ (over even and odd $l$ separately). Whenever $(2l+1)\eta_l$ reached a predetermined small value, $q$ was advanced by $\Delta q=1/16$, $l$ set to zero, the paper spaced and a new series begun at once. The running time required per phase shift was about 7 seconds.

The phase shift $\eta_l$ was probably determined (for a given value of $q$) to the same number of decimal places accuracy for all $l$. It is the sum with respect to $l$ of $(2l+1)\eta_l$ that is needed. For each value of $q$ a value of $l$ was soon reached at which it was better to use phase shifts calculated from the Born approximation in preference to those determined by numerical integration. The Born approximation[13] becomes good whenever $l$ is several times $q$ in magnitude. The definite integral can be evaluated in a simple form by means of equations given by Watson[14] to yield

$$\eta_l=3\pi p^2q^4/(2l+5)(2l+3)(2l+1)(2l-1)(2l-3), \tag{32}$$

where $p^2$ is interpreted as the coefficient of $R^{-6}$ in $U(R)$. The repulsive term contributes essentially nothing. For each value of $q$ the summation over $l$ of $(2l+1)\eta_l$ was extended until $(2l+1)\eta_l<0.00001$ radian.

A curious relation was observed between the phase shifts computed by numerical integration and those obtained from the Born approximation. For sufficiently large values of $l$ these two series always agreed very well in the mean. However, although $\eta_l$(Born) is a smooth function of $l$, $\eta_l$(num. int.) continued to oscillate about $\eta_l$(Born) with a wavelength of perhaps ten units in $l$. This effect is perfectly real and was not affected by drastic changes in the integration pattern or in the

[13] L. I. Schiff, *Quantum Mechanics* (McGraw-Hill Book Company, Inc., New York, 1949).

[14] G. N. Watson, *Theory of Bessel Functions* (Cambridge University Press, Cambridge, 1952), p. 396.

value of $R$ at which $\eta_l$ was determined. It probably contributes very little error to $\sum(2l+1)\eta_l$.

To obtain $\sum(2l+1)\eta_l$, for a given value of $q$, the procedure was to join

$$\sum_{l=0}^{l=l_0}(2l+1)\eta_l(\text{num. int.}) \quad \text{to} \quad \sum_{l=l_0+\Delta}^{l=\infty}(2l+1)\eta_l(\text{Born})$$

at a value of $l=l_0$ when $\eta_l$(num. int.) was very nearly equal to $\eta_l$(Born). For example, for $He^4$, $q=10$,

$$l_0=34; \qquad \eta_{l_0}(\text{num. int.})=0.09215;$$

$$\eta_{l_0}(\text{Born})=0.09206; \qquad \sum_{l=0}^{l=\infty}(2l+1)\eta_l=-63.6064.$$

The values of $l_0$ chosen were roughly proportional to $q$.

Phase shifts and the sums $\sum(2l+1)\eta_l$ were calculated directly at intervals of $\Delta q=1/16$ from $q=1/16$ to $q=10$. From $q=10$ to $q=15$, numerical integrations were performed at intervals of $\Delta q=0.5$ and the values of $\sum(2l+1)\eta_l$ at intervals of 1/16 determined by interpolation.

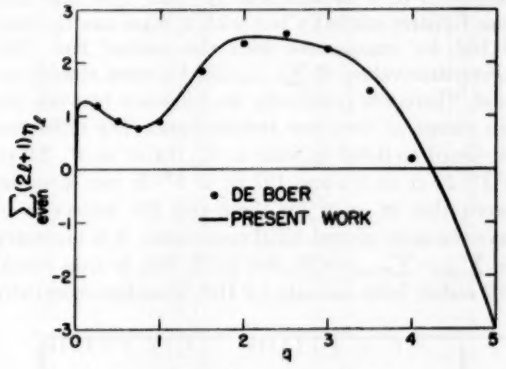


FIG. 1. $\Sigma(2l+1)\eta_l$ *versus* $q$ for $He^4$.

A total of about 15 000 individual phase shifts were calculated by numerical integration in the course of this work, with an even larger total calculated from the Born approximation. Fortunately this tremendous mass of numbers did not have to be handled in detail by hand; the computer tabulated the final sums $\sum(2l+1)\eta_l$ in a form convenient for examination and checking. Periodically, detailed spot checks were run on individual phase shifts.

It is difficult to make an estimate of the accuracy of our final values of $(\sum)$ [as defined in Eq. (23)]. In the region around $q=1$ they are probably good to better than 0.0005 radian. The accuracy decreases as $q$ increases until at $q=10$, the error may be as large as 0.05 radian.

The radial wave equation for a pair of $He^3$ atoms certainly has no discrete negative energy levels. The $He^4$ system, with the Lennard-Jones potential we used, almost has a negative level but clearly just fails to have one. Our value of $p^2$ in this case is 22.049. The critical value for the appearance of a negative level is 22.37 according to calculations of Kilpatrick and Kilpatrick.[15]

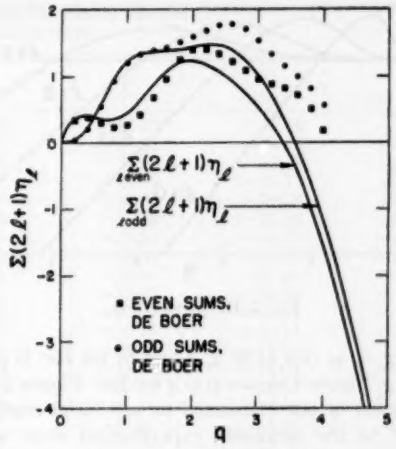


FIG. 2. $\Sigma(2l+1)\eta_l$ *versus* $q$ for $He^3$.

The phase shift integral of Eq. (22) was evaluated numerically by both Simpson's and Weddle's rules. At all temperatures between 0.1° and 60°K results were very nearly the same.

## IV. RESULTS

The results of our phase shift calculations are presented graphically. In Fig. 1, $\sum_e[\sum(2l+1)\eta_l$ summed over even $l]$ for $He^4$ is plotted against $q$. The sums calculated by de Boer and Michels[3] are shown as solid circles. The agreement is fairly good. In Fig. 2, $\sum_e$ and $\sum_o$ for $He^3$ are plotted against $q$. De Boer's[4] sums are shown in squares and circles. The agreement in certain ranges, particularly for large $q$ is not so good.

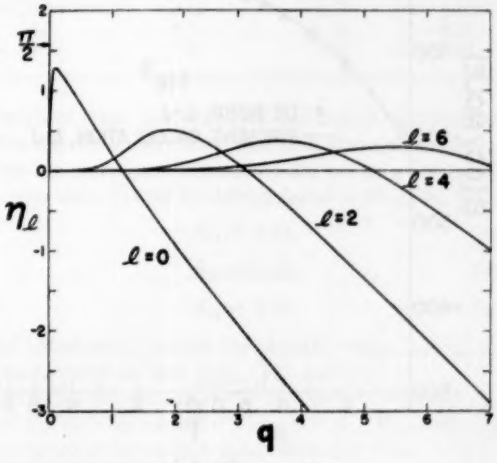


FIG. 3. $He^4$ phase shifts.

[15] J. E. Kilpatrick and M. F. Kilpatrick, J. Chem. Phys. **19**, 930 (1951).

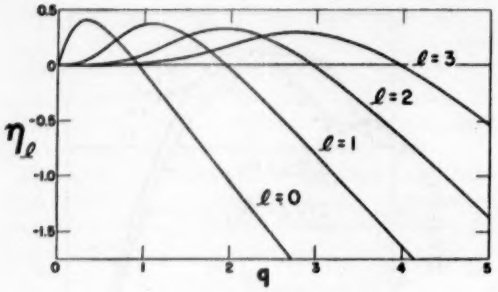


FIG. 4. $He^3$ phase shifts.

In Fig. 3, $\eta_l$ (for $l=0$, 2, 4 and 6) for $He^4$ is plotted against $q$. Figure 4 shows $\eta_l$ *vs* $q$ for $He^3$. Figure 5 shows the relation of our calculated second virial coefficients for $He^4$ to the available experimental data and to de Boer and Michels'[3] calculated points. In the case of $He^3$, there is no experimental data. The agreement between our calculations and those of de Boer *et al.*[3,4] is fairly good. This was surprising, since for $He^3$ there is considerable disagreement in the phase shifts. The small disagreement between de Boer and Michels' $He^4$ calculations and the experimental data appears to be almost wholly accumulated numerical error. Here our curve gives a somewhat better representation of the experimental data.

In Table I we give our final virial coefficients at closely spaced temperature intervals. They probably represent the second virial coefficient (for the exact potential used) correct to the number of figures given. Between 40°K and 60°K it was necessary to add a small correction to our virial coefficients, due to the fact that we directly determined phase shifts only up to $q=15$. This correction was evaluated by fitting a quadratic expression in $q$ to the values of $(\sum)$ from $q=10$ to 15 and then integrating the phase integral analytically from $q=15$ to infinity. This correction had a maximum value of 0.19 cc/mole for $He^4$ at 60° and of 0.03 cc/mole for $He^3$ at the same temperature.

The Boyle points of $He^3$ and $He^4$, interpolated from our $B_{33}$ and $B_{44}$ tables, are 19.64°K and 23.18°K, respectively. By means of de Boer's[16] quantum theory of corresponding states we extrapolate a value of $T$(Boyle) for $He^3$ of 19.9°K. The agreement is satisfactory considering the uncertainty in the extrapolation curve.

The theory of corresponding states does not include the effect of nuclear spin or of statistics. We thought it would be of interest to calculate the second virial coefficients of a hypothetical He with zero spin and Bose-Einstein statistics but with a mass exactly that of $He^3$ for comparison with the normal $He^3$. The appropriate values of $\sum_{l\ \mathrm{even}}(2l+1)\eta$ were already on hand. There was practically no difference between the two except at very low temperatures. The difference amounted to 0.003 cc/mole at 8°, 0.4 cc at 4°, 2.0 cc at 3°, 22 cc at 2°, and 107 cc at 1°. It can easily be shown that in order for these two $He^3$ molecules to have the same second virial coefficients, it is necessary for $\sum_{\mathrm{odd}}-\sum_{\mathrm{even}}=\pi/8$. For $q\geq 5$, this is true within 0.02 radian from our data for $He^3$. Therefore essentially

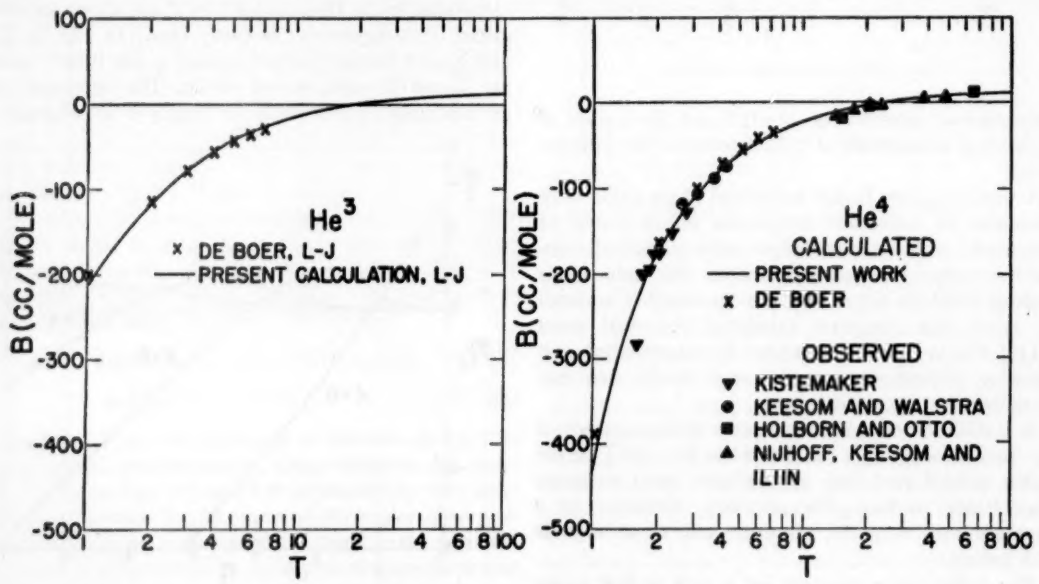


FIG. 5. Low-temperature second virial coefficients for $He^3$ and $He^4$.

[16] J. de Boer, Physica 14, 139 (1948); J. de Boer and B. S. Blaisse, Physica 14, 149 (1948); J. de Boer and R. J. Lunbeck, Physica 14, 520 (1948).

TABLE I. Second virial coefficients of $He^4$ and $He^3$ and the solution imperfection as a function of temperature.

| $T$°K | $B_{44}$ cc/mole | $B_{33}$ cc/mole | $\Delta$ cc/mole | $T$°K | $B_{44}$ cc/mole | $B_{33}$ cc/mole | $\Delta$ cc/mole |
|---|---|---|---|---|---|---|---|
| 0.3 | −2715.4 | −375.1 | 352.6 | 5.8 | −48.70 | −35.74 | −0.66 |
| 0.4 | −1712.8 | −348.6 | 175.0 | 6.0 | −46.53 | −34.11 | −0.64 |
| 0.5 | −1203.2 | −320.0 | 95.3 | 6.2 | −44.50 | −32.57 | −0.62 |
| 0.6 | −906.6 | −293.5 | 54.8 | 6.4 | −42.59 | −31.13 | −0.60 |
| 0.7 | −717.6 | −269.9 | 32.4 | 6.6 | −40.80 | −29.78 | −0.58 |
| 0.8 | −589.0 | −249.1 | 19.4 | 6.8 | −39.12 | −28.50 | −0.56 |
| 0.9 | −497.2 | −230.7 | 11.5 | 7.0 | −37.53 | −27.29 | −0.55 |
| 1.0 | −428.9 | −214.4 | 6.6 | 7.2 | −36.03 | −26.14 | −0.53 |
| 1.1 | −376.5 | −200.0 | 3.5 | 7.4 | −34.61 | −25.05 | −0.52 |
| 1.2 | −335.2 | −187.08 | 1.5 | 7.6 | −33.27 | −24.02 | −0.50 |
| 1.3 | −302.0 | −175.53 | 0.2 | 7.8 | −31.99 | −23.04 | −0.49 |
| 1.4 | −274.6 | −165.13 | −0.6 | 8.0 | −30.78 | −22.11 | −0.48 |
| 1.5 | −251.7 | −155.73 | −1.1 | 8.5 | −28.00 | −19.95 | −0.45 |
| 1.6 | −232.34 | −147.21 | −1.41 | 9.0 | −25.53 | −18.04 | −0.42 |
| 1.7 | −215.69 | −139.45 | −1.61 | 9.5 | −23.32 | −16.31 | −0.40 |
| 1.8 | −201.25 | −132.36 | −1.71 | 10.0 | −21.34 | −14.75 | −0.38 |
| 1.9 | −188.58 | −125.86 | −1.76 | 10.5 | −19.54 | −13.34 | −0.36 |
| 2.0 | −177.39 | −119.89 | −1.76 | 11.0 | −17.90 | −12.05 | −0.34 |
| 2.1 | −167.41 | −114.38 | −1.74 | 11.5 | −16.41 | −10.87 | −0.33 |
| 2.2 | −158.47 | −109.29 | −1.71 | 12.0 | −15.04 | −9.78 | −0.31 |
| 2.3 | −150.39 | −104.57 | −1.67 | 12.5 | −13.79 | −8.78 | −0.30 |
| 2.4 | −143.06 | −100.18 | −1.62 | 13.0 | −12.63 | −7.86 | −0.28 |
| 2.5 | −136.38 | −96.10 | −1.56 | 13.5 | −11.55 | −7.00 | −0.27 |
| 2.6 | −130.26 | −92.28 | −1.51 | 14.0 | −10.56 | −6.21 | −0.26 |
| 2.7 | −124.62 | −88.72 | −1.46 | 14.5 | −9.63 | −5.46 | −0.25 |
| 2.8 | −119.42 | −85.38 | −1.41 | 15.0 | −8.77 | −4.77 | −0.24 |
| 2.9 | −114.60 | −82.24 | −1.36 | 15.5 | −7.96 | −4.12 | −0.24 |
| 3.0 | −110.13 | −79.29 | −1.31 | 16.0 | −7.20 | −3.51 | −0.23 |
| 3.1 | −105.96 | −76.51 | −1.26 | 17.0 | −5.82 | −2.40 | −0.21 |
| 3.2 | −102.06 | −73.88 | −1.22 | 18.0 | −4.60 | −1.41 | −0.20 |
| 3.3 | −98.40 | −71.40 | −1.19 | 19.0 | −3.51 | −0.52 | −0.19 |
| 3.4 | −94.98 | −69.05 | −1.15 | 20.0 | −2.53 | 0.28 | −0.18 |
| 3.5 | −91.75 | −66.83 | −1.12 | 21.0 | −1.65 | 1.00 | −0.17 |
| 3.6 | −88.71 | −64.72 | −1.08 | 22.0 | −0.85 | 1.65 | −0.16 |
| 3.7 | −85.84 | −62.71 | −1.05 | 23.0 | −0.12 | 2.25 | −0.15 |
| 3.8 | −83.12 | −60.80 | −1.02 | 24.0 | 0.54 | 2.79 | −0.14 |
| 3.9 | −80.55 | −58.98 | −0.99 | 25.0 | 1.15 | 3.29 | −0.14 |
| 4.0 | −78.11 | −57.25 | −0.97 | 26.0 | 1.71 | 3.76 | −0.13 |
| 4.1 | −75.79 | −55.59 | −0.95 | 27.0 | 2.23 | 4.18 | −0.12 |
| 4.2 | −73.58 | −54.01 | −0.92 | 28.0 | 2.71 | 4.58 | −0.12 |
| 4.3 | −71.48 | −52.49 | −0.90 | 29.0 | 3.15 | 4.94 | −0.11 |
| 4.4 | −69.47 | −51.04 | −0.88 | 30.0 | 3.57 | 5.28 | −0.11 |
| 4.6 | −65.72 | −48.32 | −0.84 | 35.0 | 5.25 | 6.67 | −0.09 |
| 4.8 | −62.29 | −45.81 | −0.81 | 40.0 | 6.49 | 7.70 | −0.08 |
| 5.0 | −59.14 | −43.49 | −0.77 | 45.0 | 7.43 | 8.47 | −0.07 |
| 5.2 | −56.22 | −41.34 | −0.74 | 50.0 | 8.16 | 9.07 | −0.06 |
| 5.4 | −53.53 | −39.34 | −0.71 | 55.0 | 8.74 | 9.55 | −0.05 |
| 5.6 | −51.03 | −37.48 | −0.69 | 60.0 | 9.20 | 9.93 | −0.05 |

all of the difference between $B_{33}$ and $B_{44}$ above 4°K is a mass rather than a statistical effect.

It is of interest to compare our virial coefficients with those calculated from classical theory corrected by de Boer and Michels[5,17] for quantum effects. The most convenient temperature for this comparison is 61.32°K (corresponding to a reduced temperature of $T^*=kT/\epsilon=6$). From de Boer's equations we calculate

$$B_{44}=6.804-0.147+2.756-0.457=8.96, \quad (33)$$

$$B_{33}=6.804+0.139+3.662-0.805=9.80, \quad (34)$$

$$B_{34}=6.804+0.000+3.137-0.592=9.35. \quad (35)$$

The first term is from the high-temperature, classical equation; the second is the (ideal-gas) nuclear spin—statistical term; and the third and fourth, the first two quantum deviation terms. The next quantum correction term is positive, so these results are low by a few tenths cc. Our data (Table I), extrapolated to 61.32°K, yield

$$B_{44}=\ 9.34, \quad (36)$$

$$B_{33}=10.04, \quad (37)$$

$$B_{34}=\ 9.64. \quad (38)$$

The agreement is within the probable magnitude of the missing terms of Eqs. (33), (34), and (35).

For an ideal solution of $He^3$ and $He^4$, $B_{34}=\frac{1}{2}(B_{33}+B_{44})$ and Eq. (24) becomes $B=N_3B_{33}+N_4B_{44}$. Equation (24) can therefore be written in an alternate form

$$B=N_3B_{33}+N_4B_{44}+2N_3N_4\Delta, \quad (39)$$

$$\Delta=B_{34}-\tfrac{1}{2}(B_{33}+B_{44}). \quad (40)$$

[17] J. de Boer and R. B. Bird, University of Wisconsin Report CF 1509-A, 1952 (unpublished), Chap. 6.

TABLE II. The effect on $B_{44}$ of varying $\sigma$ and $\epsilon$.

| | $B_{44}$ cc/mole | | |
|---|---|---|---|
| $T$°K | $p^2=22.049$ $\sigma_1, \epsilon_1$ | $p^2=22.300$ $\sigma_1, \epsilon_2$ | $\sigma_2, \epsilon_1$ |
| 0.5 | −1203.2 | −1245.2 | −1244.6 |
| 1.0 | −428.93 | −441.54 | −442.27 |
| 1.5 | −251.72 | −258.57 | −259.40 |
| 2.0 | −177.39 | −182.03 | −182.73 |
| 3.0 | −110.13 | −112.91 | −113.36 |
| 4.0 | −78.11 | −80.07 | −80.36 |
| 5.0 | −59.14 | −60.67 | −60.85 |
| 6.0 | −46.53 | −47.76 | −47.87 |
| 8.0 | −30.78 | −31.66 | −31.67 |
| 10.0 | −21.34 | −22.05 | −22.00 |
| 15.00 | −8.77 | −9.21 | −9.08 |

The quantity $\Delta$ (tabulated in Table I) is a good measure of the deviation of the solution from ideality. $\Delta$ approaches plus infinity at very low temperature, passes through zero at about 1.33°K, and stays small and negative at all higher temperatures.

Our data, extrapolated to 61.32°K [Eqs. (36), (37), and (38)] give a value for $\Delta$ of −0.05 cc/mole. Equations (33), (34), and (35) yield $\Delta=-0.03$. This latter value of $\Delta$ is more accurate than the individual values of the virial coefficients from which it is derived since the effects of the missing higher terms tend to cancel.

We also considered it of interest and importance to determine what effect changes in the potential constants $\epsilon$ and $\sigma$ would have on the low-temperature values of $B_{44}$. To accomplish this, we first obtained phase shifts for $He^4$ using a value of $p^2=22.300$ instead of 22.049 and then carried out the quadratures for two cases, both corresponding to the new $p^2$: (1) $\sigma_1=2.571\times10^{-8}$ cm, $\epsilon_2=1.428\times10^{-15}$ erg; (2) $\sigma_2=2.557\times10^{-8}$ cm, $\epsilon_1=1.411\times10^{-15}$ erg. (The subscript 1 refers to the parameters as used in the original potential.) A brief summary of the results is given in Table II, where some original values of $B_{44}$ are repeated for easy comparison.

Several points are worthy of mention. First, it is seen that for the two cases corresponding to $p^2=22.300$ the $B_{44}$'s are nearly the same; but curves representing the two sets of points cross at about 0.7°K and at 8.5°K. Next we observe that a $\delta\sigma$ ($\epsilon$ constant) of 0.6 percent or a $\delta\epsilon$ ($\sigma$ constant) of 1.2 percent may change $B_{44}$ by about 3 percent and that the effect on $B_{44}$ is nearly temperature independent (up to 15°K). Simultaneously changing $\sigma$ and $\epsilon$ within the above limits and subject to $p^2=22.300$ would introduce no larger variations in $B_{44}$. Thus the values of $B_{44}$ computed with this $p^2$ would adequately fit the existing experimental data but not quite so well as those computed with the original $p^2$.

A similar analysis, employing only the classical Lennard-Jones treatment, shows that the above variations in $\sigma$ and $\epsilon$ may produce variations in the high-temperature values of $B_{44}$ as great as 5 percent; but this too is within experimental error. We may therefore safely conclude that de Boer and co-workers have chosen parameters for the Lennard-Jones potential which best fit experimental values of the second virial coefficient for $He^4$ for the temperature range up to 400°K.

Mason and Rice[18] have recently obtained constants for a Slater-type potential which give a fit for the experimental second virial coefficients of $He^4$ from 40 to 1500°K as good as or better than the Lennard-Jones (12–6) potential. In addition, the three-constant potential gives a clearly superior representation of the observed viscosity and thermal conductivity of $He^4$ above 100°K. It is therefore of considerable interest to investigate the low-temperature virial coefficients and transport properties calculated from this new potential. Such an undertaking will be the subject of a forthcoming paper from this Laboratory.

[18] E. A. Mason and W. E. Rice, J. Chem. Phys. **22**, 522 (1954).

# Solution of the Schrödinger Equation in Periodic Lattices with an Application to Metallic Lithium*

W. KOHN AND N. ROSTOKER†
*Department of Physics, Carnegie Institute of Technology, Pittsburgh, Pennsylvania*
(Received December 23, 1953)

The problem of solving the Schrödinger equation in a periodic lattice is studied from the point of view of the variation-iteration method. This approach leads to a very compact scheme if the potential $V(r)$ is spherically symmetrical within the inscribed spheres of the atomic polyhedra and constant in the space between them. The band structure of the lattice is then determined by (1) geometrical structure constants, characteristic of the type of lattice and (2) the logarithmic derivatives, at the surface of the inscribed sphere, of the $s$, $p$, $d$, . . . functions corresponding to $V(r)$. By far the greater part of the labor is involved in the calculation of (1), which needs to be done only once for each type of lattice; (2) can be obtained by numerical integration or directly from the atomic spectra. Although derived from a different point of view, this scheme turns out to be essentially equivalent to one proposed by Korringa on the basis of the theory of lattice interferences. The present paper also contains an application to the conduction band of metallic lithium.

## 1. INTRODUCTION

ONE of the central problems in the band theory of solids is to find the propagating solutions of a Schrödinger equation,

$$[-\nabla^2+V(\mathbf{r})-E]\psi(\mathbf{r})=0, \tag{1.1}$$

in which the potential has the periodicity of the lattice under consideration. Exact solutions of this problem are in general not possible, and so a number of approximation methods have been used in the past.[1] The present paper deals with the application of the variation-iteration method to this problem, a method which has in recent years been found to be a very useful tool for the approximate solution of the wave equation in nuclear and electromagnetic theory and whose practicability in solid state physics is just beginning to be explored.[2–5]

A straightforward application of this method was used by one of us [W. Kohn (unpublished); see reference 3] to find the ground-state energy ($k=0$) of metallic Na. While the result was very satisfactory, the labor involved discouraged him from calculating the rest of the band in this way.

Dank and Callen[4,5] have proposed a technique based on repeated iteration. Apart from orthogonality questions, not yet fully clarified, which arise from the fact that the wave functions of interest in band theory do not correspond to the lowest eigenvalues, their method has the advantage of being a general and systematic technique. It involves, however, a major computational effort for each physical problem, requiring the assistance of large scale computing machines.

After our original attempts we noticed that under two conditions the whole problem simplified enormously, namely when the effective potential was spherically symmetrical within the inscribed spheres of the atomic polyhedra and constant in the space between them. Both of these are rather well satisfied in many solids. If necessary, small deviations from these conditions can be taken into account by a perturbation calculation.

The most attractive feature of the scheme which then emerges is that by far the greater part of the work of calculating energy bands consists of the calculation of certain geometrical "structure constants" which must be calculated once and for all for each type of lattice. Beside these, the only other information required are the logarithmic derivatives $L_l$, at the surface of the inscribed sphere, of the $s$, $p$, $d$, . . . solutions of the Schrödinger equation with the given $V(r)$. These can be easily obtained either by numerical integration or, in some cases, directly from the atomic spectra[6] without explicit introduction of $V(r)$.

It should be emphasized that in spite of the assumption of a spherical $V(r)$ the method is not equivalent to the spherical approximation of Wigner and Seitz in which also the atomic polyhedron is approximated by a sphere. The present method takes the actual shape of the polyhedron exactly into account.

We have used this method to calculate the filled part of the conduction band of metallic lithium (Sec. 5). On the basis of our experience with this calculation, we believe that once the structure constants are tabulated, the method affords a very convenient way of calculating energy bands when the potential satisfies approximately the aforementioned conditions.

A program of preparing systematic tables of the structure constants for body- and face-centered cubic

* Supported in part by the U. S. Office of Naval Research. Preliminary reports were given at the 1953 Durham and Rochester meetings of the American Physical Society, Phys. Rev. **91**, 234 (1953) and Phys. Rev. **92**, 847 (1953).

† Now at Armour Research Foundation, Chicago 16, Illinois.

[1] See, e.g., W. Kohn, Phys. Rev. **87**, 472 (1952) where many references are given; also C. Herring, Phys. Rev. **57**, 1169 (1940).

[2] D. S. Saxon and R. A. Hutner, Philips Research Repts. **4**, 81 (1949).

[3] R. Silverman and W. Kohn, Phys. Rev. **80**, 912 (1950).

[4] M. Dank and H. B. Callen, Phys. Rev. **86**, 622 (1952).

[5] M. Dank, Office of Naval Research Report, University of Pennsylvania, December, 1952 (unpublished).

[6] T. S. Kuhn and J. H. Van Vleck, Phys. Rev. **79**, 382 (1950).

lattices has been started, and the results will be published when available.

When this work was completed, a paper by Korringa[7] was brought to our attention[8] in which an essentially equivalent scheme was developed from a different point of view. We have felt, however, that a presentation of our work in substantially its original form was advisable, since it brings out a number of new points which did not appear in Korringa's work.

## 2. RESUMÉ OF GENERAL THEORY

Consider a monatomic lattice of nuclei at the equivalent positions,

$$\mathbf{r}_s = s_1\boldsymbol{\tau}_1 + s_2\boldsymbol{\tau}_2 + s_3\boldsymbol{\tau}_3, \quad s_i = 0, \pm 1, \pm 2, \cdots, \tag{2.1}$$

where the $\boldsymbol{\tau}_i$ are three fundamental translation vectors of the lattice. Let $V(\mathbf{r})$ be an effective potential with the periodicity property:

$$V(\mathbf{r}+\mathbf{r}_s) = V(\mathbf{r}). \tag{2.2}$$

We shall look for the "propagating" solutions,

$$\psi(\mathbf{r}+\mathbf{r}_s) = e^{i\mathbf{k}\cdot\mathbf{r}_s}\psi(\mathbf{r}), \tag{2.3}$$

of the Schrödinger equation,

$$[-\nabla^2 + V(\mathbf{r}) - E]\psi(\mathbf{r}) = 0. \tag{2.4}$$

These solutions satisfy the following boundary conditions in the central polyhedron, which surrounds the origin:

$$\begin{aligned} \psi(\mathbf{r}^c) &= \exp(i\mathbf{k}\cdot\boldsymbol{\tau}_r)\psi(\mathbf{r}), \\ \partial\psi(\mathbf{r}^c)/\partial n^c &= -\exp(i\mathbf{k}\cdot\boldsymbol{\tau}_r)\partial\psi(\mathbf{r})/\partial n, \end{aligned} \tag{2.5}$$

where $\mathbf{k}$ is the wave vector of the solution, $\mathbf{r}^c$ and $\mathbf{r}$ are conjugate points on the surface of the polyhedron, and $\boldsymbol{\tau}_r$ is the fundamental translation vector joining them. (See Fig. 1.) From here on, it will be sufficient to consider the solution of (2.4) and (2.5) in the central polyhedron only.

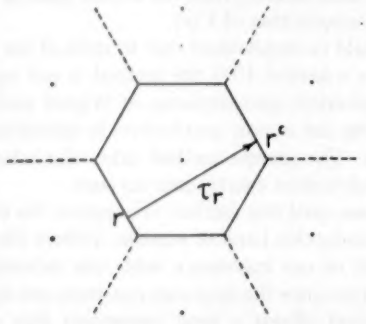


FIG. 1. Conjugate boundary points.

We now introduce the Green's function $G(\mathbf{r},\mathbf{r}')$ defined by

$$(-\nabla^2 - E)G(\mathbf{r},\mathbf{r}') = -\delta(\mathbf{r}-\mathbf{r}'), \tag{2.6}$$

and, for conjugate boundary points $\mathbf{r}$ and $\mathbf{r}^c$

$$\begin{aligned} G(\mathbf{r}^c,\mathbf{r}') &= \exp(i\mathbf{k}\cdot\boldsymbol{\tau}_r)G(\mathbf{r},\mathbf{r}'), \\ \partial G(\mathbf{r}^c,\mathbf{r}')/\partial n^c &= -\exp(i\mathbf{k}\cdot\boldsymbol{\tau}_r)\partial G(\mathbf{r},\mathbf{r}')/\partial n. \end{aligned} \tag{2.7}$$

Let $\mathbf{K}_n$ be the vectors of the reciprocal lattice defined by

$$\mathbf{K}_n\cdot\boldsymbol{\tau}_i = 2\pi\times(\text{integer}), \quad i = 1, 2, 3. \tag{2.8}$$

Then $G$ can be written as

$$G(\mathbf{r},\mathbf{r}') = -\frac{1}{\tau}\sum_n \frac{\exp[i(\mathbf{K}_n+\mathbf{k})\cdot(\mathbf{r}-\mathbf{r}')]}{(\mathbf{K}_n+\mathbf{k})^2 - E}, \tag{2.9}$$

where $\tau$ is the volume of the atomic polyhedron. Alternatively, $G$ can be expressed in the form,

$$G(\mathbf{r},\mathbf{r}') = -\frac{1}{4\pi}\sum_s \frac{\exp[i\kappa|\mathbf{r}-\mathbf{r}'-\mathbf{r}_s|]}{|\mathbf{r}-\mathbf{r}'-\mathbf{r}_s|}\exp(i\mathbf{k}\cdot\mathbf{r}_s), \tag{2.10}$$

where

$$\begin{aligned} \kappa &= +\sqrt{E}, & E>0, \\ &= +i\sqrt{(-E)}, & E<0. \end{aligned} \tag{2.11}$$

The correctness of (2.9) and (2.10) may be verified by direct substitution. Equation (2.9) is the standard expansion of a Green's function in terms of the eigenfunctions of the homogeneous boundary value problem and (2.10) can easily be derived from it. (See Appendix 2.) The Green's function has the hermitian property,

$$G(\mathbf{r}',\mathbf{r}) = G^*(\mathbf{r},\mathbf{r}'), \tag{2.12}$$

as is apparent from (2.9).

To replace the boundary value problem (2.4), (2.5) by an integral equation, we multiply (2.4) by $G^*(\mathbf{r},\mathbf{r}')$, and the complex conjugate of (2.6) by $\psi(\mathbf{r})$, subtract and integrate over $\mathbf{r}$ in the interior of the polyhedron. This leads to

$$\psi(\mathbf{r}') = \int_\tau G^*(\mathbf{r},\mathbf{r}')V(\mathbf{r})\psi(\mathbf{r})d\tau, \tag{2.13}$$

which, by (2.12) is equivalent to

$$\psi(\mathbf{r}) = \int_\tau G(\mathbf{r},\mathbf{r}')V(\mathbf{r}')\psi(\mathbf{r}')d\tau. \tag{2.14}$$

Our further considerations are based on this equation.[9]

[7] J. Korringa, Physica **13**, 392 (1947).

[8] We are greatly indebted in this connection to Drs. E. M. Baroady and R. J. Harrison of the Batelle Memorial Institute. We understand that Drs. Harrison and Trefftz are engaged in applications of Korringa's method which are similar to the work reported here.

[9] The final secular equation (3.17) is derived in the following from a variational formulation, which shows that the energy calculated from it will have an error of the second order compared to that of the trial function. A briefer, nonvariational derivation is given in Appendix 1. The reader who wishes to omit the variational discussion should proceed from here to the beginning of Sec. 3 up to (3.7) and then to Appendix 1.

The integral Eq. (2.14) is equivalent to the variational principle:

$$\delta\Lambda=0, \tag{2.15}$$

where

$$\Lambda\equiv\int_\tau\psi^*(\mathbf{r})V(\mathbf{r})\psi(\mathbf{r})d\tau - \int_\tau\int_{\tau'}\psi^*(\mathbf{r})V(\mathbf{r})G(\mathbf{r},\mathbf{r}')V(\mathbf{r}')\psi(\mathbf{r}')d\tau d\tau', \tag{2.16}$$

as may be directly verified. It should be noted that $\delta\Lambda$ vanishes for arbitrary variations of $\psi$, in particular also such as do not satisfy the boundary conditions (2.5). This allows one much greater freedom of choice of the trial functions.

The variational formulation has considerable practical usefulness. For let $\psi$ be a solution of (2.14) corresponding to $\mathbf{k}$ and $E$ (the latter enter through $G$); then, clearly,

$$\Lambda(\psi,\mathbf{k},E)=0. \tag{2.17}$$

If now $\psi_t$ is a trial function,

$$\psi_t=\psi+\epsilon\chi,$$

where $\epsilon$ is a parameter of smallness, then by (2.15),

$$\Lambda(\psi_t,\mathbf{k},E)=O(\epsilon^2). \tag{2.18}$$

Hence if for given $\mathbf{k}$ we calculate $E_t$ from the equation,

$$\Lambda(\psi_t,\mathbf{k},E_t)=0, \tag{2.19}$$

then clearly,

$$E_t-E=O(\epsilon^2), \tag{2.20}$$

i.e., the error of the energy is of the second order compared to that of the trial function. Similarly, if we considered $E$ given and calculated $\mathbf{k}_t$ from

$$\Lambda(\psi_t,\mathbf{k}_t,E)=0, \tag{2.21}$$

we would have

$$\mathbf{k}_t-\mathbf{k}=O(\epsilon^2). \tag{2.22}$$

The variational principle (2.15) lends itself to an application of the Rayleigh-Ritz technique. We use a trial function of the form:

$$\psi=\sum_0^n c_i\varphi_i, \quad c_i=a_i+ib_i, \tag{2.23}$$

and substitute into (2.16). Calling

$$\Lambda_{i;j}\equiv\int_\tau\varphi_i^*(\mathbf{r})V(\mathbf{r})\varphi_j(\mathbf{r})d\tau - \int_\tau\int_{\tau'}\varphi_i^*(\mathbf{r})V(\mathbf{r})G(\mathbf{r},\mathbf{r}')V(\mathbf{r}')\varphi_j(\mathbf{r}')d\tau d\tau', \tag{2.24}$$

where $\Lambda_{i;j}$ is Hermitian, we have

$$\Lambda=\sum_{i,j=0}^n c_i^*\Lambda_{i;j}c_j. \tag{2.25}$$

The conditions,

$$\partial\Lambda/\partial a_i=\partial\Lambda/\partial b_i=0, \quad i=0,1,\cdots n, \tag{2.26}$$

which follow from (2.15), give the linear equations

$$\sum_{j=0}^n\Lambda_{i;j}c_j=0, \quad i=0,1,\cdots n, \tag{2.27}$$

which are compatible only if

$$\mathrm{Det}\Lambda_{i;j}=0. \tag{2.28}$$

Since, for given functions $\varphi_i$, the $\Lambda_{i;j}$ are functions only of $\mathbf{k}$ and $E$, Eq. (2.28) gives the required stationary connection between $\mathbf{k}$ and $E$.

If desired, the coefficients $c_i$ can be determined from (2.27) after (2.28) has been solved.

### 3. SIMPLIFICATION FOR A CERTAIN CLASS OF POTENTIALS

While the method described in the preceding section does formally represent a solution of our problem its practicability depends on whether the $\Lambda_{i;j}$ (2.24) can be evaluated with a reasonable effort. Unfortunately this is in general quite a formidable task, involving first of all the calculation of the Green's function for various $\mathbf{k}$ and $E$ but then also the evaluation of the 6-dimensional integrals occurring in (2.24); the latter is made harder by the fact that the Green's function is singular for equal arguments, and that the region of integration is the rather complicated atomic polyhedron.

A great simplification can be achieved if one confines oneself to potentials $V(\mathbf{r})$ with the following properties:

$V(\mathbf{r})$ = spherically symmetrical,

$$r<r_i=\text{radius of inscribed sphere}; \tag{3.1}$$

$V(\mathbf{r})=V_0=\text{constant}, \quad r\geq r_i.$

In that case we can first of all shift our zero of energy to make

$$V_0=0, \tag{3.2}$$

and can therefore restrict our discussion to potentials which vanish for $r\geq r_i$. We then notice from (2.16) that the contribution to $\Lambda$ come only from the spheres $r<r_i$, $r'<r_i$.

Now for $r<r_i$ the true solution of our problem, for energy $E$, can be expanded in spherical harmonics,

$$\sum_{l=0}^\infty\sum_{m=-l}^l C_{lm}R_l(r)Y_{lm}(\theta,\varphi), \tag{3.3}$$

where $R_l(r)$ is defined by

$$\left[-\frac{1}{r^2}\frac{d}{dr}r^2\frac{d}{dr}+\frac{l(l+1)}{r^2}+V(r)-E\right]R_l(r)=0, \tag{3.4}$$

$$R_l(0)=\text{finite}, \quad R_l(r_i)=1;$$

and

$$Y_{lm}(\theta,\varphi)=\left[\frac{2l+1}{4\pi}\frac{(l-|m|)!}{(l+|m|)!}\right]^{\frac{1}{2}}P_l^{|m|}(\cos\theta)e^{im\varphi}, \quad (3.5)$$

which is normalized to unity:

$$\int_0^{\pi}d\theta\int_0^{2\pi}d\varphi\,|Y_{lm}(\theta,\varphi)|^2\sin\theta=1. \quad (3.6)$$

It is therefore natural to use as trial function a finite series of the form (3.3),

$$\psi=\sum_{l=0}^{\bar{l}}\sum_{m=-l}^{l}C_{lm}R_l(r)Y_{lm}(\theta,\varphi), \quad (3.7)$$

which satisfies the wave equation exactly.

To deal properly with the singularities of $G$ we must use a limiting procedure in evaluating $\Lambda$. We set

$$\Lambda=\lim_{\epsilon\to 0}\Lambda_\epsilon, \quad (3.8)$$

where

$$\Lambda_\epsilon=\int_{r<r_i-2\epsilon}d\tau\psi^*(\mathbf{r})V(\mathbf{r})\times\left[\psi(\mathbf{r})-\int_{r'<r_i-\epsilon}d\tau'G(\mathbf{r},\mathbf{r}')V(\mathbf{r}')\psi(\mathbf{r}')\right]. \quad (3.9)$$

With the trial function (3.7), the volume integrals in (3.9) can be transformed into surface integrals by using the wave equation (2.4) satisfied by the trial $-\psi$ and (2.6) satisfied by $G$. Thus,

$$\begin{aligned}\psi(\mathbf{r})-\int_{r'<r_i-\epsilon}d\tau'G(\mathbf{r},\mathbf{r}')V(\mathbf{r}')\psi(\mathbf{r}')&=\psi(\mathbf{r})-\int_{r'<r_i-\epsilon}d\tau'G(\mathbf{r},\mathbf{r}')(\nabla'^2+E)\psi(\mathbf{r}')\\&=-\int_{r'=r_i-\epsilon}ds'\left[G(\mathbf{r},\mathbf{r}')\frac{\partial}{\partial r'}\psi(\mathbf{r}')-\psi(\mathbf{r}')\frac{\partial}{\partial r'}G(\mathbf{r},\mathbf{r}')\right]. \quad (3.10)\end{aligned}$$

Substituting into (3.9) and noting that, for $r>r'$,

$$\begin{aligned}\int_{r<r_i-2\epsilon}d\tau\psi^*(\mathbf{r})V(\mathbf{r})G(\mathbf{r},\mathbf{r}')&=\int_{r<r_i-2\epsilon}d\tau(\nabla^2+E)\psi^*(\mathbf{r})\cdot G(\mathbf{r},\mathbf{r}')\\&=\int_{r=r_i-2\epsilon}ds\left(\frac{\partial\psi^*(\mathbf{r})}{\partial r}G(\mathbf{r},\mathbf{r}')-\psi^*(\mathbf{r})\frac{\partial G(\mathbf{r},\mathbf{r}')}{\partial r}\right), \quad (3.11)\end{aligned}$$

we find

$$\Lambda_\epsilon=\int_{r<r_i-2\epsilon}ds\int_{r'<r_i-\epsilon}ds'\left[\frac{\partial\psi^*(\mathbf{r})}{\partial r}-\psi^*(\mathbf{r})\frac{\partial}{\partial r}\right]\times\left[\psi(\mathbf{r}')\frac{\partial}{\partial r'}G(\mathbf{r},\mathbf{r}')-G(\mathbf{r},\mathbf{r}')\frac{\partial}{\partial r'}\psi(\mathbf{r}')\right]. \quad (3.12)$$

Now it is shown in Appendix 2 that, for $r<r'<r_i$, $G$ can be expanded in the form

$$G(\mathbf{r},\mathbf{r}')=\sum_{l,m}\sum_{l',m'}[A_{lm;l'm'}j_l(\kappa r)j_{l'}(\kappa r')+\kappa\delta_{ll'}\delta_{mm'}j_l(\kappa r)n_l(\kappa r')]\times Y_{lm}(\theta,\varphi)Y^*_{l'm'}(\theta',\varphi'), \quad (3.13)$$

where

$$\begin{aligned}j_l(x)&=(\pi/2x)^{\frac{1}{2}}J_{l+\frac{1}{2}}(x),\\n_l(x)&=(\pi/2x)^{\frac{1}{2}}J_{-l-\frac{1}{2}}(x);^{10}\end{aligned} \quad (3.14)$$

$\theta$, $\varphi$ and $\theta'$, $\varphi'$ are polar angles of $\mathbf{r}$ and $\mathbf{r}'$, relative to some fixed system of coordinates; and the "structure constants" $A_{l,m;l',m'}$ which are functions of $E$ and $\mathbf{k}$ are characteristic for the lattice under consideration. They are explicitly given in the form of infinite sums (for details see Appendix 2).

When (3.13) and (3.7) are substituted into (3.12) and the limit $\epsilon\to 0$ is taken, one obtains for the matrix elements of $\Lambda$:

$$\Lambda_{lm;l'm'}=(L_lj_l-j_l')[(A_{lm;l'm'}j_{l'}+\kappa\delta_{ll'}\delta_{mm'}n_{l'})-(A_{lm;l'm'}j_{l'}+\kappa\delta_{ll'}\delta_{mm'}n_{l'})L_{l'}], \quad (3.15)$$

where

$$\begin{aligned}L_l&\equiv\frac{dR_l(r)}{dr}\Big/R_l(r)\Big|_{r=r_i},\\j_l'&\equiv\frac{dj_l(\kappa r)}{dr}\Big|_{r=r_i},\quad\text{etc.}\end{aligned} \quad (3.16)$$

In deriving (3.15) we have used the normalization $R_l(r_i)=1$. Before equating the determinant of (3.15) to zero, we divide each row by $(L_lj_l-j_l')$, and each column by $(L_{l'}j_{l'}-j_{l'})$ which gives the secular equation,

$$\mathrm{Det}\left|A_{lm;l'm'}+\kappa\delta_{ll'}\delta_{mm'}\frac{n_l'-n_lL_l}{j_l'-j_lL_l}\right|=0. \quad (3.17)$$

This equation contains the required connection between $E$ and $\mathbf{k}$. It is shown to be equivalent to Korringa's Eq. (19)[7] in Appendix 3.

In practice, (3.17) may be used as follows:

(1) The structure constants $A_{lm,l'm'}$ are tabulated once and for all, for each type of lattice, as functions of $E$ and $\mathbf{k}$.

[10] For explicit expressions in terms of sin$x$ and cos$x$ see, e.g., L. I. Schiff, *Quantum Mechanics* (McGraw-Hill Book Company, Inc., New York, 1949), first edition, 77.

(2) For the first few $l$, the logarithmic derivatives $L_l$ are obtained as functions of the energy. [It is understood here that the energy zero has already been shifted to make $V(r)=0$, $r\geq r_i$.] This may be done by numerical integration of (3.4) or directly from the observed term values of the atomic spectrum.[6]

(3a) If the energy is required for general $\mathbf{k}$'s (i.e., $\mathbf{k}$'s which are not invariant under any of the symmetry operations of the lattice), the most convenient way of solving (3.17) is to fix $E$ (and hence $\kappa$) and to find those $\mathbf{k}$'s which make (3.17) vanish. Note that $\mathbf{k}$ enters only through the $A$'s.

(3b) Certain points in $\mathbf{k}$ space are invariant under some of the symmetry operations of the lattice. The procedure (3a) does, of course, still apply to such points, but in general (3.17) can now be factored and it is advantageous to perform this factorization in advance.

Suppose then we know from group-theoretical considerations[11] that the wave function must have the form,

$$\psi=\sum_{l,i} C_l^{(i)} R_l(r) \sum_m \alpha_{lm}^{(i)} Y_{lm}(\theta,\varphi),\ l=l_1, l_2, \cdots, \tag{3.18}$$

where the $\alpha_{lm}^{(i)}$ are given by group theory and may be chosen so that

$$\sum_m \alpha_{lm}^{*(i)} \alpha_{lm}^{(j)}=\delta_{ij}. \tag{3.19}$$

Substituting (3.18) into (3.12) and demanding that $\delta\Lambda/\delta C_l^{(i)}=0$ gives, in the limit $\epsilon\to 0$,

$$\text{Det}\left|B_{li;l'j}+\kappa\delta_{ll'}\delta_{ij}\frac{n_l'-n_lL_l}{j_l'-j_lL_l}\right|=0,$$
$$l=l_1, l_2, \cdots, \tag{3.20}$$
$$l'=l_1, l_2, \cdots,$$
$$B_{li;l'j}=\sum_{m,m'} \alpha_{lm}^{*(i)} A_{lm;l'm'} \alpha_{l'm'}^{(j)}.$$

The order of this secular equation equals the number of independent functions (i.e., the number of $C_l^{(i)}$) introduced in (3.18).

If the energy is wanted at an isolated point of high symmetry, e.g., $\mathbf{k}=0$, then (3.20) must be solved by varying $E$. If however the energy is required on a symmetry axis or plane, e.g., along the axis $k_x=k_y=0$, along which the $\alpha_{lm}^{(i)}$ remain constant, it is simpler to fix $E$ and solve (3.20) for $k_z$.

For definitions of the $A_{lm;l'm'}$ see Appendix 2.

### Wave Functions

For some purposes one requires, besides the energy $E(\mathbf{k})$, also the wave functions $\psi_{\mathbf{k}}$. As usual, these can be obtained from the set of linear equations (2.26), after the secular equation (3.17) or (3.20) has been solved.

For a "general" $\mathbf{k}$, the coefficients $C_{lm}$ in (3.7) are given by

$$\sum_{l',m'}\left(A_{lm;l'm'}+\kappa\delta_{ll'}\delta_{mm'}\frac{n_l'-n_lL_l}{j_l'-j_lL_l}\right)\bar{C}_{l'm'}=0, \tag{3.21}$$
$$C_{lm}=\bar{C}_{lm}/(j_l'-j_lL_l).$$

Similarly, for a symmetrically located $\mathbf{k}$, the coefficients $C_l^{(i)}$ in (3.18) are given by

$$\sum_{l',j}\left(B_{li;l'j}+\kappa\delta_{ll'}\delta_{ij'}\frac{n_l'-n_lL_l}{j_l'-j_lL_l}\right)\bar{C}_{l'}^{(j)}=0, \tag{3.22}$$
$$C_l^{(i)}=\bar{C}_l^{(i)}/(j_l'-j_lL_l).$$

One should remember, however, that in a variational procedure such as the present one the accuracy of the wave function is much poorer than that of the energy.

### 4. USEFULNESS AND LIMITATIONS

In this section we shall try to appraise the advantages and limitations of the method just described.

In cases where an effective potential is given which has the properties (3.1) to a sufficient degree of approximation we believe that the present method offers an extremely convenient way of calculating the energy bands. By far the greatest part of the work consists of the calculation of the structure constants $A_{lm;l'm'}$ which are characteristics of the geometry of the lattice and whose computation is well suited for high-speed calculating machines.

The only other ingredients necessary for obtaining the band structure are the logarithmic derivatives of the radial functions, which are easily obtained.

The convergence of the procedure is very good, as illustrated in the application to metallic lithium which is described in the following section. Very accurate results for the energies are obtained there with as few as 2 or 3 trial functions. There are three factors which favor rapid convergence:

(1) The secular equation results from a variational principle so that the error of $E$ (or $\mathbf{k}$) is of the second order compared to the error of the trial function.

(2) As a rule, variational principles based on the integral equation, as the present one is, give much more accurate results than those based on the differential equation.[1]

(3) The trial function is required only inside the inscribed sphere. In this limited region a smaller number of partial waves will give a good approximation to the correct function than is needed to describe the wave function in the entire polyhedron.

The chief limitation of the method is, of course, its restriction to potentials of the class (3.1). When the actual potential violates these conditions radically the

[11] F. C. Von der Lage and H. A. Bethe, Phys. Rev. **71**, 612 (1947).

TABLE I. The lithium potential.

| $r$ (atomic units) | $-rV$ (atomic units) | $r$ (atomic units) | $-rV$ (atomic units) |
|---|---|---|---|
| 0.02 | 5.727 | 0.92 | 2.4242 |
| 0.04 | 5.544 | 1.00 | 2.3766 |
| 0.06 | 5.450 | 1.08 | 2.3058 |
| 0.08 | 5.351 | 1.16 | 2.2458 |
| 0.10 | 5.253 | 1.24 | 2.2035 |
| 0.12 | 5.157 | 1.32 | 2.1661 |
| 0.14 | 5.058 | 1.40 | 2.1350 |
| 0.16 | 4.960 | 1.48 | 2.1090 |
| 0.18 | 4.862 | 1.64 | 2.0697 |
| 0.20 | 4.762 | 1.80 | 2.0466 |
| 0.24 | 4.563 | 1.96 | 2.0325 |
| 0.28 | 4.360 | 2.12 | 2.0288 |
| 0.32 | 4.1584 | 2.28 | 2.0292 |
| 0.36 | 3.9463 | 2.44 | 2.0228 |
| 0.40 | 3.7360 | 2.60 | 2.0124 |
| 0.44 | 3.5429 | 2.76 | 2.0065 |
| 0.48 | 3.3797 | 2.92 | 2.0031 |
| 0.52 | 3.2417 | 3.08 | 2.0015 |
| 0.56 | 3.1209 | 3.24 | 2.0008 |
| 0.60 | 3.0138 | 3.40 | 2.0004 |
| 0.68 | 2.8342 | 3.56 | 2.0002 |
| 0.76 | 2.6881 | 3.72 | 2.0001 |
| 0.84 | 2.5662 | | |

procedure is not suitable. In many cases, however, the deviations from these conditions are small. One can then write

$$V(\mathbf{r})=V^{(0)}(r)+V^{(1)}(\mathbf{r}), \tag{4.1}$$

where $V^{(0)}$ satisfies (3.1), and $V^{(1)}$ is small. Thus for $r<r_i$ one might take for $V^{(0)}(r)$ the angular average of $V(\mathbf{r})$, and for $r>r_i$ the average value of $V(\mathbf{r})$ in the space between the inscribed sphere and the polyhedron. One then solves the problem with $V^{(0)}$, and adds to this a first-order perturbation correction using the wave functions determined by (3.21), (3.22).

## 5. APPLICATION TO METALLIC LITHIUM

As a first test of this method we have calculated the filled part of the $2s$ conduction band of metallic lithium.

As potential we took that which was used by Seitz[12] in his original calculation, but due to an error was not correctly printed in his published paper. It is correctly listed in Table I.

This potential, while spherically symmetrical, is not strictly constant outside the inscribed sphere. We have therefore replaced it by the potential:

$$\begin{aligned} V'(r)&=V(r), \quad r\leq r_i, \\ &=V_0, \quad r>r_i, \end{aligned} \tag{5.1}$$

where $V_0$ was chosen as the average value of $V(r)$ in the space between the inscribed sphere and the boundary of the polyhedron:

$$V_0=-0.6629 \text{ ry}. \tag{5.2}$$

[12] F. Seitz, Phys. Rev. 47, 400 (1953). In Table II of the paper by Seitz, the quantity $rV_{II}$ was obtained from $rV_I$ incorrectly by adding a small corrective potential with the wrong sign. Thus the correct $rV_{II}$ can be obtained from the $rV_I$ given by adding the difference $(rV_I-rV_{II})$ derived from Table II to the value of $rV_I$ given in the table.

Figure 2 shows that this replacement is not likely to introduce an appreciable error, an expectation borne out by the calculation.

In the subsequent work the energy zero was shifted to $V_0$, so that the effective potential in our calculation was

$$\begin{aligned} \bar{V}(r)&=V(r)-V_0, \quad r\leq r_i, \\ &=0, \quad r>r_i, \end{aligned} \tag{5.3}$$

and the effective energy was

$$\bar{E}=E-V_0. \tag{5.4}$$

The lattice parameter (cube edge) was taken as

$$a=6.5183a_0, \tag{5.5}$$

where $a_0$ is the Bohr radius.

At $\mathbf{k}=0$, we used the trial function,

$$\psi=C_{00}(4\pi)^{-\frac{1}{2}}R_0(r), \tag{5.6}$$

which, when substituted into (3.17), gave

$$E=-0.6832 \text{ ry}. \tag{5.7}$$

This agrees to four figures with the energy calculated in the spherical approximation.[3] Since it is known that for $\mathbf{k}=0$ the spherical approximation gives very accurate results for the alkalis, this agreement represents a good check on the validity of replacing $V$ by $V'$, Eq. (5.1). We may also note that $\bar{E}$, the value of $E$ relative to $V_0$, is very small ($-0.0203$ ry) for the ground-state.

Next the energy was fixed at $\bar{E}=2(a_0/a)^2$ ry and the corresponding $\mathbf{k}$ along the (1,0,0) direction was determined. As trial functions we used

$$\psi=\sum_{l=0}^{l} C_l R_l(r) Y_{l0}(\theta,\varphi), \tag{5.8}$$

with the $Y_{l0}$ referred to the (1,0,0) direction. To test the convergence, $l$ was taken as 1 and 2 (2 and 3 trial functions). The results are listed in Table II.

Finally $\bar{E}$ was taken as $10(a_0/a)^2$ ry (near the Fermi level) and the corresponding $\mathbf{k}$'s were found along the (1,0,0) and (1,1,1) directions. The trial functions were again of the form (5.8) with the $Y_{l0}$ referred to the

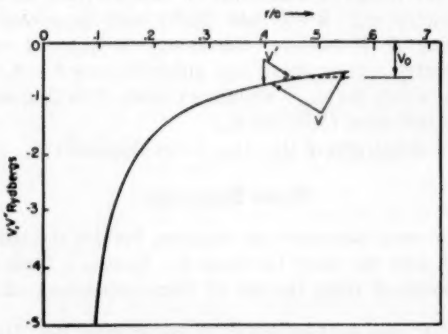


FIG. 2. The potentials $V$ and $V'$.

(1,0,0) and (1,1,1) directions, respectively. The results are listed in Table II.

It will be seen that the convergence is very rapid. With 2 trial functions the error is less than 2 percent, so that with 3 functions it is presumably quite negligible.

Adopting the three values of $|k|$ calculated with $l=2$ and the $\bar{E}$ for $k=0$ [Eq. (5.7)], we can fit an expression

$$E=E_0+E_2k^2+E_4^{(1)}k^4 + (5E_4^{(2)})(k_x^2k_y^2+k_y^2k_z^2+k_z^2k_x^2-\tfrac{1}{5}k^4) \quad (5.9)$$

to these points. (The smallness of $E_4^{(1)}$ and $E_4^{(2)}$ justifies the use of this form, which is strictly correct only for small $\mathbf{k}$'s.) The result is listed in Table III, where it is also compared with the corresponding result obtained in the spherical approximation.[3]

As was to be expected, the band is not strictly spherically symmetrical in $\mathbf{k}$ space, i.e., $E_4^{(2)}\neq 0$. (In the spherical approximation the band has, of course, spherical symmetry.) However, the smallness of both fourth order coefficients is quite remarkable. It means that the entire filled part of the band is very nearly parabolic, although the top of the filled region is quite close to the boundary of the Brillouin zone.

From a physical standpoint the $E_4^{(1)}$ and $E_4^{(2)}$ terms are too small to be taken very seriously.[13] We believe, however, that the present method is useful when the band shape differs considerably from spherical symmetry as a result of the nonsphericity of the polyhedron. Such deviations from spherical symmetry, when substantial, play an important role in the theories of the Hall coefficient and of magnetoresistance.

We should like to express our thanks to Miss Alice Carroll for her expert assistance with the numerical calculations.

TABLE II. Three points of the energy band.

| $\bar{E}$ (ry) | $\lvert k\rvert a_0/(a/a_0)^2$ (1,0,0) | (1,1,1) |
|---|---|---|
| + 2.0 | $l=1$: 0.3026<br>$l=2$: 0.3037 | |
| +10.0 | $l=1$: 0.5757<br>$l=2$: 0.5844 | $l=1$: 0.5845<br>$l=2$: 0.5920 |

TABLE III. Expansion coefficients of the energy, Eq. (5.9).

| | Spherical approximation | Present method |
|---|---|---|
| $E_0$ | −0.6832 | −0.6832 |
| $E_2$ | 0.7270 | 0.723 |
| $E_4^{(1)}$ | −0.029 | 0.039 |
| $E_4^{(2)}$ | 0.000 | −0.033 |

## APPENDIX 1. NONVARIATIONAL DERIVATION OF THE SECULAR EQUATION 3.17

Let us consider a potential $V(r)$ with the properties:

$$V(r)=\text{spherically symmetrical}, \quad \text{for } r\leq r_i-\epsilon$$
$$=0, \quad \text{for } r>r_i-\epsilon \quad (A1.1)$$

(in the end $\epsilon\to 0$). Then (2.14) becomes

$$\psi(\mathbf{r})=\int_{r'<r_i-\epsilon} G(\mathbf{r},\mathbf{r}')V(r')\psi(\mathbf{r}')d\tau'. \quad (A1.2)$$

Now consider an $\mathbf{r}$ for which $r=r_i-2\epsilon$, and use (2.4) and (2.6). This gives

$$0=\psi(\mathbf{r})-\int_{r'<r_i-\epsilon} G(\mathbf{r},\mathbf{r}')(\nabla'^2+E)\psi(\mathbf{r}')d\tau'$$

$$=\int_{r'=r_i-\epsilon}\left\{G(\mathbf{r},\mathbf{r}')\frac{\partial}{\partial r'}\psi(r')-\psi(r')\frac{\partial}{\partial r'}G(\mathbf{r},\mathbf{r}')\right\}ds'. \quad (A1.3)$$

In this equation, we substitute (3.13) for $G$ and (3.3) for $\psi$, multiply by $Y_{lm}^*(\theta,\varphi)$ and integrate over the sphere $r=r_i-2\epsilon$. Finally, we let $\epsilon\to 0$ and obtain:

$$\sum_{l',m'} j_l[A_{lm;l'm'}(j_{l'}L_{l'}-j_{l'}') + \kappa\delta_{ll'}\delta_{mm'}(n_{l'}L_{l'}-n_{l'}')]C_{l'm'}=0, \quad (A1.4)$$

where the symbols are explained in (3.13), (3.14), and (3.16). These linear equations lead at once to the compatibility condition (3.17).

## APPENDIX 2. EXPANSION OF THE GREEN'S FUNCTION

We begin by setting down three standard results which will be used in what follows:

*Addition Theorem:*

$$P_l(\cos\Theta)=\frac{4\pi}{2l+1}\sum_{m=-l}^{l} Y_{lm}(\theta,\varphi)Y_{lm}^*(\theta',\varphi'), \quad (A2.a)$$

where $\Theta$ is the angle between the directions $(\theta,\varphi)$ and $(\theta',\varphi')$ and the $Y_{lm}$ are defined in (3.5).

*Expansion of Plane Wave:*

$$e^{i\mathbf{K}\cdot\mathbf{R}}=4\pi\sum_{l,m} i^l j_l(KR)Y_{lm}(\theta_R,\varphi_R)Y_{lm}^*(\theta_K,\varphi_K), \quad (A2.b)$$

where $j_l$ is defined in (3.14), and $\theta_R$, $\varphi_R$ and $\theta_K$, $\varphi_K$ are the polar angles of $\mathbf{K}$ and $\mathbf{R}$ relative to some fixed coordinate system.

[13] A very rough estimate shows, for example, that the neighboring ions contribute a small term of the form $c(x^2y^2+y^2z^2+z^2x^2-\frac{1}{5}r^4)$ to the potential which gives rise to an $E_4^{(2)}$ whose order of magnitude (probably within a factor of 5) is −0.006. Furthermore, it is very doubtful if the band picture can be trusted for such fine effects.

*Expansion of Free Space Green's Function:*

$$-\frac{1}{4\pi}\frac{e^{i\kappa|\mathbf{r}-\mathbf{r}'|}}{|\mathbf{r}-\mathbf{r}'|}=\kappa\sum_{l,m} j_l(\kappa r)[n_l(\kappa r')-ij_l(\kappa r')] \times Y_{lm}(\theta,\varphi)Y_{lm}^*(\theta',\varphi'), \quad \text{(A2.c)}$$

for $r<r'$, and a symmetrical expression when $r'<r$.

We now turn to the expansion of the Green's function in spherical harmonics. For this, either (2.9) or (2.10) can be used as a starting point, leading to alternative expressions for the expansion coefficients.

We begin with (2.9),

$$G(\mathbf{r},\mathbf{r}')=-\frac{1}{\tau}\sum_n \frac{\exp[i(\mathbf{K}_n+\mathbf{k})\cdot(\mathbf{r}-\mathbf{r}')]}{(\mathbf{K}_n+\mathbf{k})^2-E}, \quad (2.9)$$

and introduce

$$D(\mathbf{r},\mathbf{r}')=G(\mathbf{r},\mathbf{r}')-G_0(\mathbf{r},\mathbf{r}'), \quad \text{(A2.1)}$$

where

$$G_0(\mathbf{r},\mathbf{r}')=-\frac{1}{4\pi}\frac{\cos(\kappa|\mathbf{r}-\mathbf{r}'|)}{|\mathbf{r}-\mathbf{r}'|} =\begin{cases}\kappa\sum_{l,m} j_l(\kappa r)n_l(\kappa r')Y_{lm}(\theta,\varphi)Y_{lm}^*(\theta',\varphi'); & r<r',\\ \kappa\sum_{l,m} n_l(\kappa r)j_l(\kappa r')Y_{lm}^*(\theta,\varphi)Y_{lm}(\theta',\varphi'); & r'<r,\end{cases} \quad \text{(A2.2)}$$

[see (A2.c)] and satisfies the same inhomogeneous wave equation as $G(\mathbf{r},\mathbf{r}')$ for $\mathbf{r}$, $\mathbf{r}'$ inside the atomic polyhedron. Consequently $D$ satisfies the homogeneous wave equation in $\mathbf{r}$ and $\mathbf{r}'$, and hence for $r$, $r<r_i$ must have an expansion of the form

$$D(\mathbf{r},\mathbf{r}')=\sum_{l,m}\sum_{l',m'} A_{lm;l'm'}j_l(\kappa r)j_{l'}(\kappa r') \times Y_{lm}(\theta,\varphi)Y_{l'm'}^*(\theta',\varphi'). \quad \text{(A2.3)}$$

Together with (A2.1) and (A2.2), this gives the form (3.13) for $G$. The Hermitian property of $G$, (2.12), implies the relationship

$$A_{l'm';lm}=A_{lm;l'm'}^*. \quad \text{(A2.4)}$$

Explicit expressions for the $A$'s can be obtained by expanding each of the factors $\exp[i(\mathbf{K}_n+\mathbf{k})\cdot\mathbf{r}]$ and $\exp[-i(\mathbf{K}_n+\mathbf{k})\cdot\mathbf{r}']$ occurring in (2.9) in spherical harmonics and comparing the result with the expansion (3.13). Thus one finds

$$A_{lm;l'm'}=-\frac{(4\pi)^2}{\tau}i^{(l-l')}[j_l(\kappa r)j_{l'}(\kappa r')]^{-1} \times\sum_n \frac{j_l(|\mathbf{K}_n+\mathbf{k}|r)j_{l'}(|\mathbf{K}_n+\mathbf{k}|r')Y_{lm}(\theta_n,\varphi_n)Y_{l'm'}(\theta_n,\varphi_n)}{(\mathbf{K}_n+\mathbf{k})^2-E} -\kappa\delta_{ll'}\delta_{mm'}\frac{n_l(\kappa r')}{j_l(\kappa r)}, \quad r<r'<r_i, \quad \text{(A2.5)}$$

where $\theta_n$, $\varphi_n$ are the polar angles of $\mathbf{K}_n+\mathbf{k}$ relative to the fixed coordinate system. The right-hand side is of course independent of the particular choice of $\mathbf{r}$ and $\mathbf{r}'$. It should be noted that in view of the asymptotic behavior,

$$x\to\infty: \quad j_l(x)\to\frac{1}{x}\sin\left(x-l\frac{\pi}{2}\right), \quad \text{(A2.6)}$$

the sum in (A2.5) is absolutely convergent.

Apart from the Hermitian relationships (A2.4) the $A$'s are not all independent but are derivable from a smaller number of independent constants. It may be noted that $G$ is a function only of the single vector,

$$\mathbf{R}=\mathbf{r}-\mathbf{r}'. \quad \text{(A2.7)}$$

We shall now show how the $A$'s can all be expressed in terms of the expansion coefficients of $G$ relative to $\mathbf{R}$.

Proceeding exactly as before, we find that $G$ can be written in the form

$$G(\mathbf{R})\equiv-\frac{1}{\tau}\sum_n \frac{\exp[i(\mathbf{K}_n+\mathbf{k})\cdot\mathbf{R}]}{(\mathbf{K}_n+\mathbf{k})^2-E} =-\frac{1}{4\pi}\frac{\cos\kappa R}{R}+\sum_{L,M} D_{L,M}j_L(\kappa R)Y_{LM}(\Theta,\Phi), \quad \text{for } R<r_s \ (s=1,2,\cdots), \quad \text{(A2.8)}$$

where $\Theta$, $\Phi$ are the polar angles of $\mathbf{R}$. The $D_{L,M}$ are given by

$$D_{L,M}=-\frac{4\pi}{\tau}i^L[j_l(\kappa R)]^{-1} \times\sum_n \frac{j_L(|\mathbf{K}_n+\mathbf{k}|R)Y_{LM}^*(\theta_n,\varphi_n)}{(\mathbf{K}_n+\mathbf{k})^2-E} +\frac{\kappa}{4\pi}\delta_{L0}\delta_{M0}\cot\kappa R,$$
$$D_{L,-M}=(-1)^L D_{L,M}^* \quad \text{(A2.9)}$$

where $\theta_n$, $\varphi_n$ are the polar angles of $(\mathbf{K}_n+\mathbf{k})$.

The infinite sum in (A2.9) converges, but only slowly. A convenient practical scheme of evaluating this sum is based on Ewald's method.[14] We consider

$$S(\eta)=\sum_n \frac{j_L(|\mathbf{K}_n+\mathbf{k}|R)Y_{LM}^*(\theta_n,\varphi_n)}{(\mathbf{K}_n+\mathbf{k})^2-E} \times\exp\{[E-(\mathbf{K}_n+\mathbf{k})^2]/\eta\}. \quad \text{(A2.10)}$$

We require $S(\infty)$. Now Ewald has shown that $S(\eta)-S(\infty)$ approaches zero exponentially as $\eta\to\infty$. Hence, by choosing for $\eta$ a sufficiently large value (which in practice turns out to be remarkably small), we can without appreciable error evaluate $S(\eta)$ instead of

[14] P. Ewald, Ann. Physik **64**, 253 (1921).

$S(\infty)$. This is a great practical advantage since the sum for $S(\eta)$, because of its exponential factor, converges much more rapidly than that for $S(\infty)$.

The $A_{lm;l'm'}$ are expressible in terms of the $D_{L,M}$. Comparing (3.13) with (A2.8), we see that

$$\sum_{L,M} D_{L,M} j_L(\kappa R) Y_{LM}(\Theta,\Phi) = \sum_{l,m} \sum_{l',m'} A_{lm;l',m'} j_l(\kappa r) j_{l'}(\kappa r') \times Y_{l,m}(\theta,\varphi) Y_{l'm'}(\theta',\varphi'). \quad \text{(A2.11)}$$

Now by a double application of (A2.b),

$$\begin{aligned} & j_L(\kappa R) Y_{LM}(\Theta,\Phi) \\ &= \frac{1}{4\pi i^L} \int \exp(i\boldsymbol{\kappa}\cdot\mathbf{R}) Y_{LM}(\theta_s,\varphi_s) d\Omega_s \\ &= \frac{1}{4\pi i^L} \int \exp(i\boldsymbol{\kappa}\cdot\mathbf{r}) \exp(-i\boldsymbol{\kappa}\cdot\mathbf{r}') Y_{LM}(\theta_s,\varphi_s) d\Omega_s \\ &= \frac{4\pi}{i^L} \sum_{l,m} \sum_{l',m'} i^{(l-l')} j_l(\kappa r) j_{l'}(\kappa r') Y_{lm}(\theta,\varphi) \times Y_{l'm'}^*(\theta',\varphi') C_{LM;lm;l'm'}, \end{aligned} \quad \text{(A2.12)}$$

where

$$C_{LM;lm;l'm'} = \int Y_{LM}(\theta,\varphi) Y_{lm}^*(\theta,\varphi) Y_{l'm'}(\theta,\varphi) d\Omega. \quad \text{(A2.13)}$$

Substituting (A2.11) into (A2.10) and comparing coefficients of $Y_{lm}(\theta,\varphi) Y_{l'm'}(\theta',\varphi')$, gives

$$A_{lm;l',m'} = 4\pi i^{(l-l')} \sum_L \frac{1}{i^L} D_{L,m-m'} C_{L,m-m';lm;l'm'}. \quad \text{(A2.14)}$$

Here we have used the fact that

$$C_{LM;l,m;l',m'} = 0, \quad M \neq m-m'. \quad \text{(A2.15)}$$

The sum over $L$ runs only over the values,

$$L = |l-l'|, |l-l'|+2, \cdots |l+l'|, \quad \text{(A2.16)}$$

as, by (A2.13), the $C$'s vanish for other $L$'s.

In summary, the structure constants $A_{lm;l'm'}$ in the secular equation (3.17) are given either directly by (A2.5) or in terms of the smaller number of constants $D_{L,M}$ by (A2.14, 13 and 9). A practical method for evaluating the sum in (A2.9) is indicated in connection with (A2.10).

*Alternative Definitions of Structure Constants*

As already mentioned, the Green's function can also be expanded by starting from the expression (2.10).

We begin by deriving (2.10) from (2.9).[13] For this purpose we use the standard results:

$$\frac{1}{(2\pi)^3} \int \exp[i(\mathbf{K}_n+\mathbf{k}-\mathbf{K})\cdot\boldsymbol{\rho}] d\boldsymbol{\rho} = \delta(\mathbf{K}_n+\mathbf{k}-\mathbf{K}), \quad \text{(A2.17)}$$

$$\frac{1}{\tau} \sum_n \exp(i\mathbf{K}_n\cdot\boldsymbol{\rho}) = \sum_s \delta(\boldsymbol{\rho}-\mathbf{r}_s), \quad \text{(A2.18)}$$

$$\lim_{\epsilon\to+0} \frac{1}{(2\pi)^3} \int \frac{\exp[i\mathbf{K}\cdot(\mathbf{R}-\mathbf{r}_s)]}{K^2-(E+i\epsilon)} d\mathbf{K} = +\frac{1}{4\pi} \frac{\exp(i\kappa|\mathbf{R}-\mathbf{r}_s|)}{|\mathbf{R}-\mathbf{r}_s|}, \quad \text{(A2.19)}$$

$$\kappa = \begin{cases} \sqrt{E}, & E>0 \\ i\sqrt{-E}, & E<0. \end{cases}$$

Then,

$$\begin{aligned} G(\mathbf{R}) &= \lim_{\epsilon\to+0} -\frac{1}{\tau} \sum_n \frac{\exp[i(\mathbf{K}_n+\mathbf{k})\cdot\mathbf{R}]}{(\mathbf{K}_n+\mathbf{k})^2-(E+i\epsilon)} \\ &= \lim_{\epsilon\to+0} -\frac{1}{\tau} \sum_n \int \delta(\mathbf{K}_n+\mathbf{k}-\mathbf{K}) \frac{\exp(i\mathbf{K}\cdot\mathbf{R})}{K^2-(E+i\epsilon)} d\mathbf{K} \\ &= \lim_{\epsilon\to+0} -\frac{1}{\tau} \frac{1}{(2\pi)^3} \sum_n \int\int \exp[i(\mathbf{K}_n+\mathbf{k}-\mathbf{K})\cdot\boldsymbol{\rho}] \times \frac{\exp(i\mathbf{K}\cdot\mathbf{R})}{K^2-(E+i\epsilon)} d\boldsymbol{\rho} d\mathbf{K} \\ &= \lim_{\epsilon\to+0} -\frac{1}{(2\pi)^3} \sum_s \exp(i\mathbf{k}\cdot\mathbf{r}_s) \times \int \frac{\exp[i\mathbf{K}\cdot(\mathbf{R}-\mathbf{r}_s)]}{K^2-(E+i\epsilon)} d\mathbf{K} \\ &= -\frac{1}{4\pi} \sum_s \exp(i\mathbf{k}\cdot\mathbf{r}_s) \frac{\exp(i\kappa|\mathbf{R}-\mathbf{r}_s|)}{|\mathbf{R}-\mathbf{r}_s|}. \end{aligned} \quad \text{(A2.20)}$$

If $\epsilon$ had been chosen negative, then for $E>0$, $\kappa$ in (A2.20) is replaced by $-\kappa$. Both of these expressions are correct since their difference is evidently a solution of the homogeneous problem and hence zero. Thus, instead of (2.10) we can also write

$$G(\mathbf{r},\mathbf{r}') = -\frac{1}{4\pi} \sum_s \exp(i\mathbf{k}\cdot\mathbf{r}_s) \frac{\cos(\kappa|\mathbf{r}-\mathbf{r}'-\mathbf{r}_s|)}{|\mathbf{r}-\mathbf{r}'-\mathbf{r}_s|}, \quad E>0, \quad \text{(A2.21)}$$

which, in contrast to (2.10), is manifestly Hermitian.

If (A2.20) is expanded in spherical harmonics relative to $\mathbf{R}$, using (A2.c), the following alternative expression

is found for the coefficients $D_{L,M}$ of (A2.8):

$$D_{L,M}=\kappa\sum_{s\neq 0}\exp(i\mathbf{k}\cdot\mathbf{r}_s)[n_L(\kappa r_s)-ij_L(\kappa r_s)]Y_{LM}^*(\theta_s,\varphi_s)$$
$$-\frac{i\kappa}{(4\pi)^{\frac{1}{2}}}\delta_{L0}\delta_{M0}, \quad \text{(A2.22)}$$

where $\theta_s$, $\varphi_s$ are the polar angles of $\mathbf{r}_s$. It may be noted that this series converges exponentially for $E<0$ since $n_L(ix)-ij_L(ix)\sim e^{-x}/x$ for large $x$. Hence it provides a good check on evaluations of $D_{L,M}$ by (A2.9).

*Convergence of the Green's Function Expansion*

It has already been remarked that $D(\mathbf{r},\mathbf{r}')$, (A2.1) has an expansion of the form (A2.3) which converges, provided both $\mathbf{r}$ and $\mathbf{r}'$ are inside the inscribed sphere of the polyhedron. On the other hand, a consideration of (2.10) shows that the expansion does not converge for all other $\mathbf{r}$ and $\mathbf{r}'$ inside the atomic polyhedron. This must be borne in mind when one considers applications of the integral equation method to potentials which are not constant outside the inscribed sphere.

## APPENDIX 3. CONNECTION WITH THE WORK OF KORRINGA[7]

Consider the scattering in free space by the potential

$$V=V(r), \quad r\leq r_i,$$
$$=0, \quad r>r_i, \quad \text{(A3.1)}$$

at an energy $E$. Let $R_l$ be the radial part of the solution corresponding to angular momentum $l$, which for $r\leq r_i$ satisfies (3.4) and for $r>r_i$ has the form

$$R(r)=A[j_l(\kappa r)-\tan\eta_l n_l(\kappa r)], \quad \text{(A3.2)}$$

where $\eta_l$ is the phase shift. An elementary calculation shows that if $L_l$ is the logarithmic derivative of $R$ at $r_i$, then

$$\cot\eta_l=\frac{n_l'(\kappa r_i)-n_l(\kappa r_i)L_l}{j_l'(\kappa r_i)-j_l(\kappa r_i)L_l}. \quad \text{(A3.3)}$$

When this is introduced into (3.17), together with the constants,

$$G_{lm;l'm'}=\kappa^{-1}A_{lm;l'm'}-i\delta_{ll'}\delta_{mm'}, \quad \text{(A3.4)}$$

(3.17) becomes

$$\mathrm{Det}\left|G_{lm;l'm'}+\delta_{ll'}\delta_{mm'}\frac{e^{i\eta_l}}{\sin\eta_l}\right|=0, \quad \text{(A3.5)}$$

which corresponds to Korringa's Eq. (19). Equation (3.17) appears to be slightly more convenient than (A3.5), as its elements are Hermitian for positive and negative $E$, and as it involves the logarithmic derivatives which are the quantities directly obtained from numerical integration or extrapolation of atomic data.[6]

*Note added in proof.*—Recently a calculation of the lithium conduction band was published by B. Schiff.[15] This author used a potential which differs from that constructed by Seitz, on which previous calculations by Seitz,[12] Bardeen,[16] Silverman and Kohn,[3] as well as the present work were based.

The results of Schiff for the position of the lowest level in the conduction band, relative to the ionization energy of the atom, and for the width of the filled part of the band, differ from the results of the other authors by 13 and 23 percent, respectively. However, the cohesive energies are in good agreement.

This discrepancy is presumably due to the difference between the potentials used. According to the theory of Wigner and Seitz the potential should be the best effective potential for the valence electron in the free atom. The potential of Seitz does indeed reproduce all atomic energy levels with great accuracy. Schiff's potential is substantially weaker than that of Seitz in the vicinity of the nucleus, in places by as much as 15 percent. As a result his calculated ionization energy for the atomic 2$s$ electron is 8 percent smaller than the observed value, while the Seitz potential gives agreement with experiment within a fraction of a percent.

[15] B. Schiff, Proc. Phys. Soc. (London) **A67**, 2 (1954).
[16] Bardeen, J. Chem. Phys. **6**, 367 (1938).

# New Galvanomagnetic Effect

COLMAN GOLDBERG AND R. E. DAVIS
*Westinghouse Research Laboratories, East Pittsburgh, Pennsylvania*

(Received February 5, 1954)

A galvanomagnetic effect is described which is observed by measuring the induced voltage normal to the direction of current flow as in the Hall effect but with the magnetic field in the current-voltage plane. The measurements enable us to test the assumptions of spherical energy surfaces and spherical relaxation time surfaces for semiconductors. If these assumptions are correct, the effect should be isotropic. Preliminary room temperature measurements show this effect to be anisotropic in both *p*- and *n*-type germanium, in agreement with magnetoresistance measurements.

## I. INTRODUCTION

THE galvanomagnetic effect to be discussed here is not new in the sense that it is based on new principles, but is new because it apparently has not been previously discussed and investigated. As will be shown in the following sections, if a crystal carrying an electric current is placed in a magnetic field, an electric field will be induced perpendicular to the current in the current-magnetic field plane. We call this field the "planar Hall field" since the experimental conditions are similar to those used in Hall experiments, except that in observing the Hall effect the magnetic field, electric field, and current are mutually perpendicular.

The electric field induced by the planar Hall effect analytically involves the same coefficients (but in a different arrangement) as does magnetoresistance. The magnetoresistance effect, of course, is concerned with a change in electric field parallel to the current direction.

## II. GENERAL

In the absence of temperature gradients the electric current carried by a crystal with cubic symmetry is[1]

$$\mathbf{i}=\sigma_0\mathbf{E}+\alpha\mathbf{E}\times\mathbf{H}+\beta\mathbf{E}H^2+\gamma\mathbf{H}(\mathbf{E}\cdot\mathbf{H})+\delta M\mathbf{E}, \quad (1)$$

$$M=\begin{bmatrix} H_1^2 & 0 & 0 \\ 0 & H_2^2 & 0 \\ 0 & 0 & H_3^2 \end{bmatrix}, \quad (1a)$$

where $E$ and $H$ are the electric and magnetic field, respectively, and the subscripts 1, 2, and 3 refer to the axes of cubic symmetry. Equation (1) is actually an approximation obtained by ignoring terms containing $E$ to a power higher than the first or $H$ to a power higher than the second. The coefficients in (1), $\sigma_0$, $\alpha$, $\beta$, $\gamma$, and $\delta$ are expressed in terms of integrals which can be evaluated, in principle, if assumptions are made concerning the statistics to be used and the dependence of relaxation time and energy upon the wave vector $\mathbf{k}$. If $\delta$ is nonzero, the presence of the tensor $M$ complicates this equation since the current passing through the crystal in the presence of electric and magnetic fields will be anisotropic, being dependent upon the orientation of the crystal.

Equation (1) gives the current density in terms of the electric and magnetic fields. Since in an experiment it is customary to fix the current and magnetic field and to measure the resulting electric field, it is more useful to have an equation of the following form[2]:

$$\mathbf{E}=\rho_0[\mathbf{i}+A\mathbf{i}\times\mathbf{H}+BiH^2+C\mathbf{H}(\mathbf{i}\cdot\mathbf{H})+DM\mathbf{i}]. \quad (2)$$

Here we have the electric field as a function of the current and magnetic field. If we substitute this equation for the electric field into Eq. (1), we can determine the coefficients in Eq. (2) in terms of the coefficients in the current Eq. (1).

$$\rho_0=1/\sigma_0, \quad (3a)$$

$$A=-\alpha\rho_0, \quad (3b)$$

$$B=-(\beta+\rho_0\alpha^2)\rho_0, \quad (3c)$$

$$C=-(\gamma-\rho_0\alpha^2)\rho_0, \quad (3d)$$

$$D=-\delta\rho_0. \quad (3e)$$

In obtaining Eqs. (3) we ignore terms containing the magnetic field to a power higher than the second.

If for a semiconductor we assume Maxwell-Boltzmann statistics for the carriers and a mean free path independent of energy, and if we assume that the energy and relaxation time surfaces in $\mathbf{k}$ space are spherical, then we can integrate the coefficients of (1). If the resulting values for $\sigma_0$, $\alpha$, $\beta$, $\gamma$, and $\delta$ are substituted into Eqs. (3), we have the following as the coefficients of (2) for these assumptions:

$$\rho_0=1/ne_0\mu, \quad (4a)$$

$$A=-(3\pi/8c)(q/e_0)\mu, \quad (4b)$$

$$B=-C=(9\pi/16c^2)(1-\pi/4)\mu^2, \quad (4c)$$

$$D=0, \quad (4d)$$

where

$$\mu=4e_0\lambda/3(2\pi mkT)^{\frac{1}{2}}$$

is the mobility, $n$ is the carrier density, $c$ is the velocity of light, $\lambda$ is the mean free path, and $q$ is the charge of the current carrier, being $+e_0$ for holes and $-e_0$ for electrons. Since for these assumptions, $D$ is zero, the field as given by Eq. (2) will be isotropic. The only

[1] F. Seitz, Phys. Rev. **79**, 372 (1950).

[2] G. L. Pearson and H. Suhl, Phys. Rev. **83**, 768 (1951).

crystal parameter involved in the coefficients $A$, $B$, or $C$ is the mobility so that these parameters should not vary too much from one crystal to another of the same type but of different resistivity, as long as we are concerned only with relatively pure crystals. Thus, measurement of $A$, $B$, or $C$ should enable us to calculate the mobility. Essentially (4b) is used to calculate mobility from Hall and conductivity measurements and (4c) is used to calculate mobility from magnetoresistance measurements. From (4c) we see that

$$\mu=1.623B^{\frac{1}{2}}, \tag{5a}$$

$$\mu=1.623(-C)^{\frac{1}{2}}, \tag{5b}$$

and, anticipating Eq. (13), it is found from (4b) that

$$(3\pi/8)\mu=R\sigma_0. \tag{5c}$$

The mobilities calculated from (5a), (5b), and (5c) should be equal to the mobility determined from drift measurements.[3] Since mobilities determined by (5c) for germanium do not agree with the mobilities determined by drift measurements, the isotropic assumptions must be incorrect for germanium. The correct set of assumptions must lead to the observed experimental relations between $R\sigma_0$, $B$, and $C$ and must give the observed value for $D$. If the correct assumptions enable us to calculate the mobility from $B$, $C$, and $R\sigma_0$, the mobilities obtained should equal the drift mobility. Experimental values for $B$, $C$, and $D$ will thus be useful in checking assumptions made about energy and relaxation time surfaces.

Experimentally it is convenient to set up a coordinate system in a crystal which may or may not coincide with the axes of cubic symmetry. If the axes we define experimentally are $x$, $y$, and $z$, then the components of the electric field in these directions are represented by

$$E_r=\rho_0[i_r+A(\mathbf{i}\times\mathbf{H})_r+Bi_rH^2+CH_r(\mathbf{i}\cdot\mathbf{H})$$

$$+D\sum_{g=1}^{3}\sum_{r'=x}^{g}\sum_{r''=x}^{g}\sum_{r'''=x}^{g}i_{r'}a_{gr'}a_{gr''}a_{gr'''}H_{r''}H_{r'''}], \tag{6}$$

where $r$ may equal $x$, $y$, or $z$ and where the $a_{gr}$ are the direction cosines of the $x$, $y$, $z$ axes with respect to the 1, 2, 3 axes of cubic symmetry.

The coefficients $B$, $C$, and $D$ can be calculated from magnetoresistance measurements.[2] These measurements give $B$ directly, but $C$ and $D$ always appear in additive combinations with $B$ or with each other and $B$. Hence, the accuracy of the values of $C$ and $D$ obtained from magnetoresistance measurements will depend upon the relative magnitudes of the three coefficients.

## III. THE NEW EFFECT

If we use the experimental conditions that $i=i_x$, $H_x=i_y=i_z=0$, i.e., the current is along the $x$ axis and the magnetic field is in the $xy$ plane, we find from Eq. (6) that the field in the $y$ direction is

$$E_y=\rho_0Ci_xH_xH_y+\rho_0Di_x[(\sum_g a_{gx}{}^3a_{gy})H_x{}^2$$

$$+(\sum_g a_{gx}a_{gy}{}^3)H_y{}^2+2H_xH_y(\sum_g a_{gx}{}^2a_{gy}{}^2)]. \tag{7a}$$

If $H_z=0$ and we define $\psi$ as $\arctan(H_y/H_x)$, then (7a) may be written as

$$E_y=i_xH^2[G\sin(2\psi+\Delta)+g], \tag{7b}$$

where

$$G=\rho_0\{[\tfrac{1}{2}C+D\textstyle\sum_g a_{gx}{}^2a_{gy}{}^2]^2$$

$$+\tfrac{1}{4}D^2[\textstyle\sum_g (a_{gx}{}^3a_{gy}-a_{gx}a_{gy}{}^3)]^2\}^{\frac{1}{2}}, \tag{7c}$$

$$g=\tfrac{1}{2}D\rho_0[\textstyle\sum_g (a_{gx}{}^3a_{gy}+a_{gx}a_{gy}{}^3)], \tag{7d}$$

$$\Delta=\arctan\frac{[\sum_g (a_{gx}{}^3a_{gy}-a_{gx}a_{gy}{}^3)]}{[\tfrac{1}{2}C+D\sum_g a_{gx}{}^2a_{gy}{}^2]}. \tag{7e}$$

It is the field given by Eq. (7b) that we wish to investigate. This field which has apparently not been previously discussed or investigated, will be anisotropic unless $D=0$, and measurements of it for crystals with known orientations should enable us to calculate the coefficients $C$ and $D$.

If we use a crystal in which $x$, $y$, $z$ coincide with the (100) axes of cubic symmetry, (7b) becomes simply

$$E_y=Gi_xH^2\sin(2\psi), \tag{8}$$

with

$$G=C\rho_0/2. \tag{9}$$

If $x$ coincides with the (110) axis, $y$ with the $(\bar{1}10)$ axis, and $z$ with the (001) axis, (7) again reduces to (8) only for this crystal orientation:

$$G=(C+D)\rho_0/2. \tag{10}$$

Equation (8) shows that the field should have a maximum at $\psi=45°$ for crystals with the two orientations mentioned above. $G$ can be calculated by making measurements at this angle and by using the relation,

$$G=(V_yt/H^2I)\times10^{16}, \tag{11}$$

where $t$ is the sample thickness. Equation (11) follows directly from (8). The factor $10^{16}$ is used so that $G$ and hence $C$ and $(C+D)$ calculated by (9) and (10) will be in laboratory units (cm$^5$/joule sec) if the units of $V_y$, $t$, $H$, and $I$ are volts, centimeters, gauss, and amperes, respectively.

Thus, this new effect enables us to calculate $C$ directly and $D$ indirectly and enables us to check our assumptions of isotropy discussed in Sec. I. It should be pointed out that crystal orientations other than those discussed above could be used in studying this effect. The orientations discussed in this section, however, are readily obtainable, at least for germanium, and also lead to simple expressions for $G$, $g$, and $\Delta$ of Eq. (7b).

[3] J. R. Haynes and W. Shockley, Phys. Rev. **81**, 835 (1951).

## IV. PRELIMINARY EXPERIMENTS

In order to investigate the effect described in Sec. III several properly oriented samples of both $n$- and $p$-type germanium were prepared. The samples had their $x, y, z$ axes parallel to either the (100), (010), (001) axes or the (110), ($\bar{1}$10), (001) axes. Several samples of both orientations were cut from a single slice of a single-crystal germanium ingot grown by the method of Teal and Little.[4] By preparing the samples in this way it was hoped to obtain a group of samples that had the same characteristics except for orientation. Three groups of samples were prepared from three ingot slices: 9.5 and 20.5 ohm cm $p$ type and 13 ohm cm $n$ type. Leads were soldered to the samples as in a Hall measurement. For the effect we wish to investigate (which we shall refer to as the "planar Hall effect") the magnetic field lies in the $xy$ plane, i.e., the plane of the sample. The voltage developed in the $y$ direction may contain a contribution from the Hall effect if the magnetic field does not lie precisely in the $xy$ plane. By proper reversals of the magnetic field and sample current we can obtain that component of the voltage in the $y$ direction which is a function of $H^2$ and $I$, thus eliminating any Hall voltage.

All measurements were made at room temperature. The planar Hall voltage was found to vary linearly with the sample current and sinusoidally with $2\psi$ as predicted by Eq. (7b). The dependence upon the angle $\psi$ is shown in Fig. 1. The coefficient $G$ was calculated by means of Eq. (13) and Fig. 2 shows the dependence of $G$ upon $H^2$. The horizontal lines obtained from $n$-type samples indicate that $E_y$ is proportional to $H^2$. The finite slope obtained for the $p$-type samples indicates the presence of an $H^4$ contribution to $E_y$ which is not unexpected since our derivation has ignored higher-order terms. (The values of $G$ for $n$ type indicate a very small $H^4$ contribution which is not detectable in Fig. 2.) If we consider the (100) $p$-type samples we see that for a ratio of resistivity of 2.19 the $G$ values have a ratio of 2.17 which is in good agreement with Eq. (9).

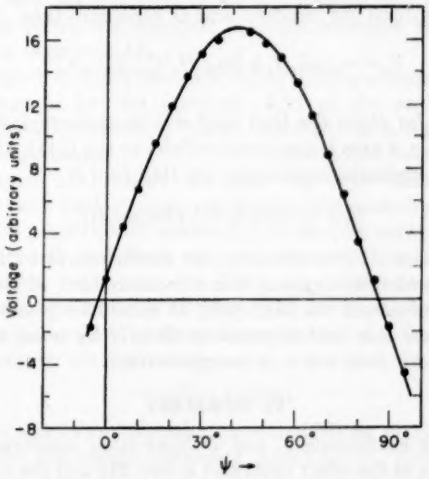


FIG. 1. Dependence of the planar Hall voltage upon the angle between current and magnetic field. The solid line fits the equation $V=16.47\sin2(\psi+3°)-0.50$. [Compare with Eq. (7b).]

[4] G. K. Teal and J. B. Little, Phys. Rev. 78, 647 (1950).

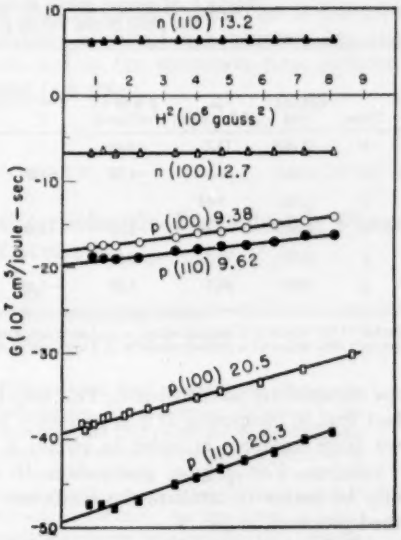


FIG. 2. Dependence of coefficient $G$ on magnetic field for germanium at room temperature. The numbers in parentheses refer to the crystal orientation (see footnotes to Table I). The letter before the parentheses indicates whether the particular curve is for an $n$- or $p$-type sample and the number after the parentheses is the resistivity in ohm-cm.

The $G$ values for the two $n$-type crystals in Fig. 2 show a decided anisotropy. Not only the magnitude of $G$ but also its sign is dependent upon crystal orientation. The anisotropy is also evident in the $p$-type samples.

The values of $C$ and $D$ obtained by means of (9) and (10) from Fig. 2 are shown in Columns I of Table I. In order to compute $D$ it is, of course, necessary to use data from two samples with different orientations. Since the values obtained for $C$ and $D$ differed from those obtained by Pearson and Suhl[2] by magnetoresistance measurements (Table II), magnetoresistance measurements were made on the same samples for which the coefficient $G$ had been measured. With these data it was possible to obtain $B$ and $C$ from measurements on single samples while $D$ could be obtained by combining measurements on the two samples with different orientation. The results of these magnetoresistance measurements are shown in columns II of Table I. By combining planar Hall measurements with magnetoresistance measurements it is possible to determine all three coefficients by measurements on a single sample as shown in columns III. The values of $B$ and $C$ for $n$- and $p$-type crystals and of $D$ for $n$-type material are fairly consistent for the different crystals and the different techniques of measurement. The values of $D$

TABLE I. Measured values of the coefficients for germanium (room temperature). (The units of the values given for $B$, $C$, and $D$ are $10^7$ cm$^4$/volt$^2$ sec$^2$.)

| Sample | Type | Orientation | $\rho_0$ (ohm cm) | $R\times10^{-4}$ (cm$^3$/coul) | (I) Planar Hall effect $C$ | (I) Planar Hall effect $D$ | (II) Magnetoresistance $B$ | (II) Magnetoresistance $C$ | (II) Magnetoresistance $D$ | (III) Magnetoresistance plus planar Hall effect $B$ | (III) Magnetoresistance plus planar Hall effect $C$ | (III) Magnetoresistance plus planar Hall effect $D$ | (IV) $\mu_H$ (cm$^2$/volt sec) |
|---|---|---|---|---|---|---|---|---|---|---|---|---|---|
| 33–2 | $n$ | (110)[a] | 13.2 | −4.44 | | | | −0.98 | | +1.08 | −0.98 | +1.93 | |
| Both | | | | | | +2.04 | | | +1.82 | | | | |
| 33–5 | $n$ | (100)[b] | 12.7 | −4.36 | −1.09 | | +1.14 | | | +1.14 | −1.09 | +2.02 | 5400 |
| 9–7 | $p$ | (110) | 9.62 | | | | | −3.22 | | +4.62 | −3.22 | −0.88 | |
| Both | | | | | | −0.24 | | | −0.84 | | | | |
| 9–9 | $p$ | (100) | 9.38 | 2.94 | −3.86 | | +4.60 | | | +4.60 | −3.86 | −0.20 | 10 100 |
| 9–2 | $p$ | (110) | 20.3 | 5.56 | | | | −3.64 | | +5.23 | −3.64 | −1.22 | |
| Both | | | | | | −1.03 | | | −0.70 | | | | |
| 9–6 | $p$ | (100) | 20.5 | 5.60 | −3.83 | | +4.97 | | | +4.97 | −3.83 | −0.80 | 10 000 |

[a] The symbol (110) refers to a crystal whose $x$, $y$, $z$ axes are parallel to the (110), ($\bar{1}$10), and (001) crystallographic axes.
[b] The symbol (100) refers to a crystal whose $x$, $y$, $z$ axes are parallel to the (100), (010), (001) crystallographic axes, respectively.

for $p$-type material are not consistent. This may be due to the fact that in computing $D$ it is necessary to subtract two large numbers in order to obtain a much smaller number. For $p$-type germanium it would apparently be better to measure the coefficient $D$ by the method proposed in Sec. V.

The mobilities as calculated by the isotropic formula from the value of $C$ obtained by the planar Hall effect (columns I of Table I) are given in column IV of Table I. These values are appreciably different from those obtained from drift experiments or the Hall coefficient. As pointed out in Sec. I, this indicates that the assumptions used in evaluating the coefficients of Eq. (4) are incorrect. Furthermore, the nonzero values of $D$ obtained for both $n$- and $p$-type germanium also indicate that either the energy surfaces or the relaxation time surfaces in $\mathbf{k}$ space or both are not spherical. Seitz[1] has derived expressions for $B$, $C$, and $D$ by assuming that the energy surfaces are spherical and that the expression for relaxation time as a function of the wave vector $\mathbf{k}$ has a spherically symmetrical term plus a term containing the simplest cubically symmetric anisotropy. He finds that with these assumptions $D$ and $C$ should be of the same sign. Our experimental results show this to be true for $p$-type germanium but not $n$-type so that Seitz's theory does not describe the proper situation for electrons in germanium. It can also be shown[2] from Seitz's derivation that for his assumptions the ratio $(B+C+\frac{1}{2}D)/(B+C+D)$ should equal 2.5. For our data of Table I we find this ratio varies from 1.19 to 2.65 in $p$-type germanium. The uncertainty in the ratio is due to the uncertainty in the value of the coefficient $D$. Seitz's theory, however, does not (but should) explain the serious discrepancy in mobility between Hall and drift measurements for $p$-type germanium.

TABLE II. Values of the coefficients for germanium (room temperature) obtained by Pearson and Suhl.[a] (Units are $10^7$ cm$^4$/volt$^2$ sec$^2$.)

| Type | $B$ | $C$ | $D$ |
|---|---|---|---|
| $p$ | 1.3 | −1.09 | 0 |
| $n$ | 1.03 | −0.69 | 1.3 |

[a] See reference 2.

## V. A METHOD FOR DIRECT MEASUREMENT OF COEFFICIENT $D$

As indicated in Sec. IV, it would be useful to have a method for measuring the coefficient $D$ directly. In this section it will be shown that this can be done by observation of the dependence of the Hall field upon $H^2$.

The experimental conditions when measuring the Hall coefficient are $i=i_z$, $H=H_z$, i.e., $i_y=i_z=H_x=H_y=0$. If our assumptions of Sec. I are correct, then (6) shows that for these experimental conditions

$$E_y=-A\rho_0 i_z H_z, \tag{12}$$

and $R$, the Hall coefficient, is

$$R=-A\rho_0=\alpha\rho_0^2. \tag{13}$$

There will be no terms quadratic in the magnetic field in the expression for the Hall field. However, if the assumptions are incorrect and $D$ is nonzero then

$$E_y=-A\rho_0 i_z H_z+D\rho_0 i_z H_z^2\Big(\sum_s a_{sx}a_{sy}a_{sz}^2\Big). \tag{14}$$

Thus for $D\neq0$ the Hall field will be anisotropic.[5] For the $x$, $y$, $z$ axes respectively parallel to the (2$\bar{1}$1), ($\bar{1}$1$\bar{1}$), (011) crystallographic axes the Hall field is

$$E_y=-A\rho_0 i_z H_z+0.236D\rho_0 i_z H_z^2. \tag{15}$$

Equation (15) shows that the coefficient $D$ could be obtained directly by a direct measurement of the $H^2$ dependence of the Hall field. It should be possible to measure this field dependence directly by using an ac magnetic field and a dc sample current.

## VI. SUMMARY

The coefficients $C$ and $D$ have been measured by means of the effect described in Sec. III and the values obtained agree with values calculated from magneto-

[5] This anisotropy has been pointed out by Mason, Hewitt, and Wick, J. Appl. Phys. **24**, 166 (1953).

resistance measurements except for the coefficient $D$ in $p$-type germanium. The coefficient $D$ could probably be evaluated most accurately by the method proposed in Sec. V.

The nonzero values obtained for $D$ indicate that the assumptions of Sec. I are incorrect, i.e., the energy surfaces and/or the relaxation time surfaces are not spherical in $\mathbf{k}$ space.

PHYSICAL REVIEW VOLUME 94, NUMBER 5 JUNE 1, 1954

# Threshold Field and Free Energy for the Antiferroelectric-Ferroelectric Phase Transition in Lead Zirconate

A. P. DEBRETTEVILLE, JR.
*Signal Corps Engineering Laboratories, Fort Monmouth, New Jersey*
(Received May 20, 1953; revised manuscript received February 9, 1954)

Sawaguchi and Kittaka obtained the threshold field of $PbZrO_3$—that field necessary to change the antiferroelectric to the ferroelectric phase—below the Curie temperature. The free-energy difference is the difference between the area under the ferroelectric portion of the curve and that under the antiferroelectric portion. An expression for free-energy difference has been obtained as a function of voltage, by eliminating the temperature parameter. This experimental relationship is compared with the author's theoretical expression—one that involves the product of the constant spontaneous polarization ($16\times10^{-6}$ coulomb/cm$^2$ in the ferroelectric phase), the threshold voltage, and the molar volume (43 cm$^3$); the free energy so calculated is small—of the order of 4 calories/mole at 25 kv/cm. Equations are given for calculating the threshold field-strength and free-energy difference as functions of temperature. The equation for threshold field-strength resembles the Clapeyron-Clausius equation, with field strength analogous to pressure and spontaneous polarization analogous to volume. The threshold voltage *versus* the downward shift of the Curie temperature is in good agreement with the experimental results of Sawaguchi and Kittaka.

## I. INTRODUCTION

IT is known that pure lead zirconate has an antiferroelectric phase below and a paraelectric phase above 230°C, the Curie point. Sawaguchi and Kittaka have shown that one can apply a field of the order of 10 kv/cm to pure lead zirconate ceramic and cause the ferroelectric phase to appear below the Curie point.[1]

Below the Curie point the sample is normally antiferroelectric; the dielectric constant $\epsilon_a$ is approximately 200, and has a positive temperature coefficient. At the Curie point, the dielectric constant increases sharply about twenty-fold.[2]

Figure 1 shows the experimental data obtained by Sawaguchi for the threshold field of the antiferroelectric-to-ferroelectric phase transition, as a function of temperature.[1]

Figure 2(b) shows the point $O$, from which the threshold field $E_t$ was calculated; the cross-hatched area is proportional, essentially, to the free energy.[1]

The author intends to calculate the value of the threshold field, and the free-energy difference $\Delta F$, between the ferroelectric phase and the more stable or lower free-energy antiferroelectric phase, as a function of temperature and voltage.

## CALCULATION[3]

Sawaguchi and Kittaka have derived an expression for the free-energy difference $\Delta F=(F_f-F_a)$ between the ferroelectric state $F_f$ and the antiferroelectric state $F_a$, in terms of the internal energy of the antiferroelectric state $U_a$ and the internal energy of the ferroelectric state $U_f$[1]

$$F_f(T_m)-F_a(T_m)=U_f(T_f)-U_a(T_a). \qquad (1)$$

The temperatures of the antiferroelectric and ferro-

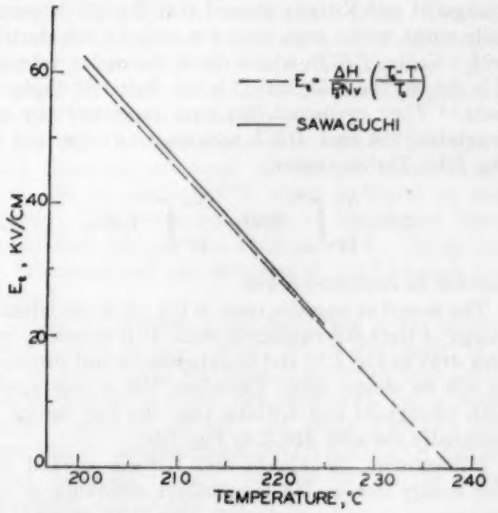


FIG. 1. Relation between threshold field and Curie temperature.

[1] E. Sawaguchi and T. Kittaka, J. Phys. Soc. Japan **7**, 336–337 (1952); E. Sawaguchi, J. Phys. Soc. Japan **8**, 615–629 (1953).
[2] Shirane, Sawaguchi, and Takagi, Phys. Rev. **84**, 476–481 (1951).
[3] Background for this type of calculation can be found in the field of low-temperature physics. See J. C. Slater, *Quantum Theory of Matter* (McGraw-Hill Book Company, Inc., New York, 1951), pp. 504–508; E. T. Jaynes, *Ferroelectricity* (Princeton University Press, Princeton, 1953), pp. 70–80.

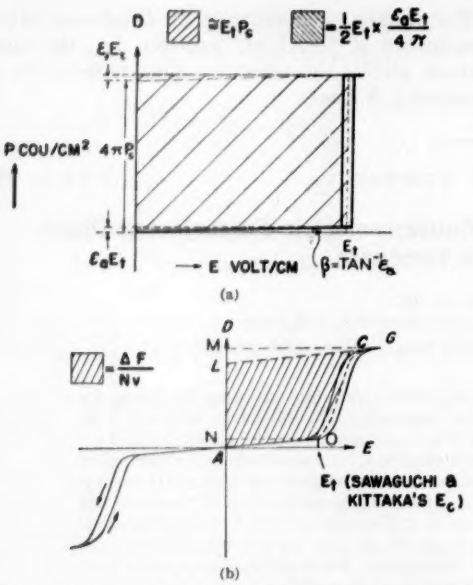


FIG. 2. (a) An idealized hysteresis loop and the method of calculating free-energy difference between the two phases. $D$ is the dielectric displacement; $E$ is the electric field strength. (b) The experimental data on which the free-energy difference can be calculated. Shaded area is that area used by Sawaguchi and Kittaka to calculate free-energy difference.

electric states are $T_a$ and $T_f$, respectively, while $T_m$ is the mean of the two temperatures. The temperature difference is small and amounts to only 3°C and is obtained by dividing the latent heat by the specific heat for lead zirconate with 3 percent lead titanate. Sawaguchi and Kittaka showed that Eq. (1) is essentially equal to the work done per mole by the electric field, $(Nv/4\pi)\int EdD$, where $Nv$ is the molar volume, $E$ is the electric field, and $D$ is the dielectric displacement.[1,4] They evaluated this term experimentally by integrating the area $AOCL$ surrounded by the loop in Fig. 2(b). The expression

$$\Delta F = \frac{Nv}{4\pi}\int_{P_t}^{P_m} EdD_f - \frac{Nv}{4\pi}\int_0^{E_t} EdD_a, \qquad (2)$$

and will be evaluated below.

The second or negative term in Eq. (2) is the internal energy of the antiferroelectric state. It is shown by the area $AON$ in Fig. 2(b) and is negligible for lead zirconate as will be shown later. Therefore, the author agrees with Sawaguchi and Kittaka that the free energy is essentially the area $AOCL$ in Fig. 2(b).

Furthermore, Sawaguchi and Kittaka showed the free energy due to the temperature difference of the two states could be neglected. This term amounts to only 0.01 calorie compared to several calories for the electrostatic work term.

[4] H. Fröhlich, *Theory of Dielectrics* (Oxford University Press, London, 1949), pp. 160–161.

The internal energy of the antiferroelectric state per unit volume is[4]

$$U_a = \frac{Nv}{4\pi}\int_0^{E_t} E\epsilon_a dE = \epsilon_a E_t^2 Nv/8\pi, \qquad (3)$$

and this energy is shown graphically in Fig. 2. The author has neglected the term

$$\frac{Nv}{4\pi}\int_0^{E_t} E^2 d\epsilon_a = \frac{Nv}{4\pi}\int_0^{E_t} E^2\left(\frac{\partial\epsilon_a}{\partial T}dT + \frac{\partial\epsilon_a}{\partial E}dE\right),$$

because $\partial\epsilon_a/\partial T \approx 1$, and $\partial\epsilon_a/\partial E \approx 0$; therefore it can be neglected compared to (3).

For the ferroelectric state, $dU_f = (E/4\pi)dD_f Nv$, and the limits of integration are derived from Fig. 2(a). The idealized Fig. 2(a) is only an approximation for the purpose of calculation. One is here dealing with a ceramic material, which gives a lower value of the spontaneous polarization, $P_s$, than the true value which is approached more nearly with single crystals and will be discussed later. The limits will be

$$U_f = \frac{Nv}{4\pi}\int_{E_t}^{E_t} EdE + NvE_t\int_{P_t}^{P_m} dP,$$

where $P_m$ is the maximum polarization namely $P_s + \epsilon_f E_t/4\pi$. $P_t$ is the threshold polarization or $\epsilon_a E_t/4\pi$. The maximum polarization cannot be used, because only values of spontaneous polarization $P_s$ are available. The integrated equation is

$$U_f = E_t P_s Nv + (2\epsilon_f - 2\epsilon_a)E_t^2 Nv/8\pi. \qquad (4)$$

The area $LMCG$ in Fig. 2(b) corresponds to slightly more than half the value of the first part of the second term in Eq. (4). The slope $LCG$ is proportional to $\epsilon_f$, or equal to $4\pi(\partial P/\partial E)$.

Inserting the internal energy difference per mole [Eq. (4) minus Eq. (3)] into the expression for the free energy per mole [Eq. (1)], one obtains

$$\Delta F = P_s E_t Nv + (2\epsilon_f - 3\epsilon_a)E_t^2 Nv/8\pi. \qquad (5)$$

This is the fundamental expression for the free-energy difference. The term due to the internal energy of the antiferroelectric phase, $\epsilon_a E_t^2 Nv/8\pi$, is negligible for the region in which the experimental data were taken, and amounts to only 3 percent of the first term for the maximum threshold field.

The value of $\epsilon_f$ is approximately the same as $\epsilon_a$ for lead zirconate so that the last two terms in (5) tend to cancel each other out.

Threshold field strength is calculated from (5), by using the relation $S = -\partial F/\partial T$. The new equation then becomes, assuming $P_s$ constant, and $\Delta\epsilon = (2\epsilon_f - 3\epsilon_a)$,

$$\Delta S = -P_s\frac{\partial E_t}{\partial T}Nv - \left(\frac{\partial\Delta\epsilon}{\partial T}\frac{E_t^2}{8\pi} + \frac{\Delta\epsilon E_t}{4\pi}\frac{\partial E_t}{\partial T}\right)Nv. \qquad (6)$$

Substituting the increase of entropy per mole, $\Delta S$

$=\Delta H/T$, Eq. (6) becomes

$$\frac{\partial E_t}{\partial T}=-\left[\frac{\Delta H}{TNv}+\frac{\partial \Delta\epsilon}{\partial T}\frac{E_t^2}{8\pi}\right]\Big/\left[P_s+\frac{\Delta\epsilon}{4\pi}E_t\right]. \quad (7)$$

This is the most general form for the equilibrium slope. For lead zirconate the last two terms in (6) can be neglected; then (7) becomes

$$\partial E_t/\partial T=-\Delta H/P_sTNv. \quad (8)$$

This is equivalent to the familiar Clapeyron-Clausius equilibrium equation, with electric field analogous to pressure and spontaneous polarization analogous to volume. This equation was first pointed out by Shirane, Sawaguchi, and Takagi as being applicable to $PbZrO_3$ in studying the dc field-dependence of transition temperature from ferroelectric to antiferroelectric state.[5]

Equation (8) expresses the fact that the phase transition is a first order one which is due to the large jump of spontaneous polarization.

In Fig. 2(b) the polarization ordinates are compressed and do not give the reader a true picture of the magnitude of the jump in spontaneous polarization compared to the threshold polarization. The spontaneous polarization is fifteen times greater than the maximum threshold polarization. This ratio was computed by dividing $P_s$ by $\epsilon_a E_t/4\pi$, using $P_s=16\times10^{-6}$ coulomb/cm$^2$, $E_t=60$ kv/cm and $\epsilon_a=200$. Inserting 135 calories/mole from calorimetric measurements on $Pb(Zr_{0.97}\text{-}Ti_{0.03})O_3$ which is ferroelectric without an applied field, using $T_c=511$°K obtained by extrapolating the curve of $\Delta F$ *versus* $t$ to zero, and using the value of $P_s=16\times10^{-6}$ coulomb/cm$^2$, we obtain

$$\partial E_t/\partial T=-1.61 \text{ kv/cm°C}.$$

The experimental value obtained from the solid curve of Fig. 1 is $-1.65$ kv/cm°C.

Integrating (8) with respect to $T$, assuming that $\Delta H$, $P_s$, and $v$ are constants, gives

$$E_t=(-\Delta H/P_sNv)\ln T+\text{constant}.$$

Using $T=T_c$ for $E_t=0$ to determine the constant, one obtains

$$E_t=(\Delta H/P_sNv)\ln(T_c/T).$$

To the author's knowledge, this equation has not been published elsewhere. The logarithm is expanded and only the first term is retained. This is justified because the second term amounts to only 3 percent of the first term with respect to a 30°C lowering of the Curie temperature. This gives

$$E_t=\frac{\Delta H}{P_sNv}\left(\frac{T_c-T}{T_c}\right). \quad (9)$$

Equation (9) is plotted in Fig. 1. The equation is in good agreement with the experimental data.

[5] Shirane, Sawaguchi, and Takagi, J. Phys. Soc. Japan **6**, 208 (1951), and Sawaguchi, Shirane, and Takagi, J. Phys. Soc. Japan **6**, 337 (1951).

Equation (9) is plotted in Fig. 1, where 238°C is used for the "ferroelectric" Curie point. In a private communication to the author, Y. Takagi and E. Sawaguchi state that they have investigated the $PbZrO_3$-$PbTiO_3$ system. They found the free energies of the antiferroelectric-paraelectric phase became equal at 230°—"antiferroelectric" Curie point; and the free energies of the ferroelectric-antiferroelectric phase became equal at 238°C—"ferroelectric" Curie point. The more stable paraelectric phase actually replaces the ferroelectric phase at 238°C. Hence, the Curie point used in Eq. (9) was determined by extrapolating the temperature-composition line of the ferroelectric-antiferroelectric phase boundary.[1]

## DISCUSSION

Sawaguchi and Kittaka[1] estimated the heat of transition from their free energy data by taking the product of the slope and the Curie temperature of pure $PbZrO_3$ and obtained 80 cal/mole. They then compared this with 130 cal/mole obtained by their calorimetric measurement with $Pb(Zr_{0.97}\text{-}Ti_{0.03})O_3$. They attributed this discrepancy between 130 (135 for Sawaguchi's latest value) and 80 cal/mole to their material, a ceramic.

Some discussion of the $E_t$ *versus* $T$ graph for pure $PbZrO_3$ is in order, to explain why the values of $\Delta H$ and $P_s$ are not those of $PbZrO_3$ but those of $Pb(Zr_{0.97}\text{-}Ti_{0.03})O_3$. The phase change for pure $PbZrO_3$ is from an antiferroelectric state to a paraelectric state, and therefore the value of or 440 cal/mole could not be used.[6] However, when 3 mole-percent $PbTiO_3$ is added, a ferroelectric phase appears between the antiferroelectric phase and the paraelectric phase. Therefore the value of the heat of transition, 135 cal/mole, of this latter antiferroelectric-ferroelectric phase change is used.[1] For a full discussion of the phase diagram and the heats of transition see Sawaguchi.[1]

The value of spontaneous polarization $P_s$ is practically constant and equal to $16\times10^{-6}$ coulomb/cm$^2$ from 170 to about 220°C, where it begins to drop slightly. This value was given to the author before publication through the kindness of Y. Takagi and E. Sawaguchi and was obtained by the hysteresis loop method.

Earlier in the paper, it was stated that $\epsilon_f$ was approximately equal to $\epsilon_a$ or about 200. A calculation of $\epsilon_f$ can be made using the expression $4\pi(\partial P/\partial E)$, which can be written as $4\pi(\partial P/\partial T)/(\partial E/\partial T)$. Using Sawaguchi's[1] value of $(\partial P/\partial T)$, or about $3.4\times10^{-8}$ coulomb/cm$^2$ °C obtained from $Pb(Zr_{0.97}\text{-}Ti_{0.03})O_3$, and the value $1.65\times10^3$ v/cm°C for $(\partial E/\partial T)$ in the above expression, one obtains 230 for $\epsilon_f$.

Since the temperature coefficient of polarization is so small, Eq. (9) is unaffected. It was assumed that $\partial P/\partial T$ was zero in the derivation of (9).

[6] G. Shirane, Phys. Rev. **86**, 226 (1952).

## CONCLUSIONS

The fundamental equation for the free energy is given by (5), from which a general equation for other ferroelectrics expressing the equilibrium slope of the threshold field with respect to temperature can be derived.

## ACKNOWLEDGMENTS

The author wishes to thank Dr. V. F. Payne of the Chemical Physics Branch, Squier Signal Laboratory, for his constant encouragement, and Ellis L. Manning and Erwin D. Harris for helpful discussion. The author also wishes to thank Professor Y. Takagi of the Tokyo Institute of Technology, Oh-Okayama, Tokyo, Japan, for the reprint of an exceedingly interesting paper by Dr. E. Sawaguchi and his colleague Dr. T. Kittaka of the same institute. The paper served as a foundation for this work; to Professor Takagi and Dr. Sawaguchi go thanks for supplying the author with data pertaining to this work.

PHYSICAL REVIEW VOLUME 94, NUMBER 5 JUNE 1, 1954

# Pressure Dependence of the Resistivity of Germanium

WILLIAM PAUL* AND HARVEY BROOKS
*Division of Applied Science, Harvard University, Cambridge, Massachusetts*
(Received January 26, 1954)

The effect of hydrostatic pressure on the resistivity of a sample of 35 ohm-cm germanium has been investigated up to 30 000 kg/cm² pressure at temperatures between 25°C and 76°C, and up to 7000 kg/cm² pressure at temperatures down to −195°C. The results indicate an increase in the total energy gap to 15 000 kg/cm² at a rate in agreement with earlier experimental determinations at lower pressures. A rapid rise in resistivity above 15 000 kg/cm² that seems to apply to *n*-type germanium crystals of any purity has also been investigated. Explanations based on the deionization of impurities and on a decrease in electron mobility are discussed.

THE effect of hydrostatic pressure on the electrical properties of germanium has been investigated experimentally by measurements of *p-n* junction resistance,[1] the resistivity of impure samples,[2] and the resistivity of high-purity material at elevated temperatures.[3,4] It has also been estimated theoretically by a deformation potential method.[5] Both experiment and theory indicated a uniform increase of resistivity with pressure in the intrinsic conduction range, corresponding to a widening of the energy gap between valence and conduction bands. Bridgman's results also showed interesting behavior at pressures above 15 000 kg/cm² where the resistivity of *n*-type samples of a wide range of purity increased rapidly with increasing pressure. In the present work new measurements are reported at elevated temperature which extend the effective pressure range for intrinsic conduction. New measurements are also reported for temperatures down to liquid nitrogen. An attempt is made to correlate the new and the older measurements and to clarify the behavior above 15 000 kg/cm².

## APPARATUS AND METHOD

The pressure apparatus used in the present set of experiments is that developed by Bridgman. The first, which allowed resistivity determinations up to 30 000 kg/cm², has been sufficiently described already in the literature,[6] so that only a general discussion of it, and of any features peculiar to this experiment, need be set down here. The chamber in which the high pressure is generated is slightly coned on its external surface. As the main moving piston produces high hydrostatic pressure in a central cylindrical hole, this cone is simultaneously thrust into coned receiving sleeves by a second piston; the external support of the chamber compensates the effect of the internal pressure and allows its prolonged operation at pressures higher than a single unsupported cylinder can stand.

The pressure, which was produced in liquid isopentane, was measured by a manganin wire gauge previously calibrated by Bridgman at 30°C and 75°C; sufficient data were therefore available for a determination of the pressure at any of the temperatures of the present set of experiments.

The sample, a germanium single crystal of 35 ohm-cm room temperature resistivity, had been previously investigated by Bridgman,[3] and was originally supplied by Bell Telephone Laboratories through the interest of Dr. W. Shockley. The crystal dimensions were 3 cm×3 mm², and the contacts to it were soldered with pure tin. The resistance was measured by a potentiometric method for both increasing and decreasing pressure; care was taken that temperature equilibrium had been reestablished after each alteration of pressure. No hysteresis was found, and no variation of resistivity

* Carnegie Research Fellow of the Universities of Scotland.
[1] Hall, Bardeen, and Pearson, Phys. Rev. **84**, 129 (1951).
[2] P. Miller and J. Taylor, Phys. Rev. **76**, 179 (1949).
[3] P. W. Bridgman, Proc. Am. Acad. Arts Sci. **79**, 139 (1951); **82**, 71 (1953).
[4] W. Paul, Phys. Rev. **90**, 336 (1953).
[5] W. Shockley and J. Bardeen, Phys. Rev. **77**, 407 (1950); **80**, 72 (1950).
[6] P. W. Bridgman, Proc. Am. Acad. Arts Sci. **72**, 157 (1938).

with time when both temperature and pressure were constant. The resistivities to be quoted were derived from the measured resistances at high pressure and the dimensions at atmospheric pressure and room temperature. The error involved in disregarding any changes in dimensions of the crystals with pressure and temperature is usually small.[7] Readings of resistivity were usually made at 5000 kg/cm² intervals up to 30 000 kg/cm², and on reducing pressure at 27 500 kg/cm² and at 5000 kg/cm² intervals thereafter. An initial pressure of about 100 kg/cm² was applied before the temperature was raised above 25°C in the high-temperature experiments, to prevent boiling of the isopentane.

For runs at elevated temperatures, the apparatus was immersed in a symmetrically-heated, continuously stirred oil bath to a point above the top of the carboloy piston transmitting pressure to the central cavity. A mercury regulator switched the heating current to a very low value when the temperature rose too high. The variation of temperature in the bath was less than 0.02°C, and doubtless the regulation at the sample was better than this because of the very large mass of metal shielding it from the oil. As indicated above, it is necessary to wait for the heat of compression to be dissipated after each increase of pressure; ten minutes was generally found to be sufficient time for all the pressures and pressure increments of these experiments.

The second pressure apparatus[8] yielded pressures up to 7000 kg/cm² with temperatures from −80°C to 350°C using commercial nitrogen as transmitting gas; its use for this purpose has been described by Bridgman.[3] Below −80°C, commercially produced helium was used as transmitting fluid, necessitating some changes in technique: for example, a pressure of some 4–5000 kg/cm² was applied at −80°C before the temperature was further lowered, in order to flow the lead washers that formed part of the sealing mechanism for the pressure chamber. Without this device the washers become stiff at zero pressure at the temperature of boiling nitrogen, and will not seal effectively.

The experiments here described were all carried out at temperatures below room temperature so that cryostats with ice, $CO_2$, and nitrogen coolants could conveniently be used. The pressure is produced in a cavity some 2 in. long by $\frac{1}{4}$ in. diameter in a cylindrical tube 4 in. long by 1 in. diameter. This is connected to an upper cylinder, in which the main pressure producing piston moves, by a slim tube 12 in. long by $\frac{1}{4}$ in. diameter pierced by a $\frac{1}{32}$ in. hole. Before the main piston is operated the cavity is filled to a pressure of 2000 kg/cm² by two precompressors. The thermostatting bath liquid covers the bottom cylinder and most of the connecting tube; the upper cylinder is at room temperature. A pressure increase therefore produces a rise in temperature of the germanium by virtue of the compression, and also by the addition of warmer gas to the cold lower chamber. It was found in practice that the resistivity reading settled very quickly—within minutes—to its final value, so that any temperature variation would seem to be unimportant here. It must be noted, however, that in this temperature range the germanium was relatively insensitive to temperature change; a more careful consideration of these variations might be necessary for a semiconductor with a high temperature coefficient at the temperature of the experiment. The thermoelectric emf's present were small in comparison with the applied ones, and were conveniently eliminated by suitable switching.

The connections to the crystal were made by Teflon covered copper wires threaded through the slim connecting tube and out by way of insulated plugs in the upper cylinder. The manganin gauge was also located in the upper cylinder. Both pressure and resistivity were determined as in the experiments to 30 000 kg/cm². Again no hysteresis or time variation in the readings was found. Except at −195°C, readings were usually taken at 1000 kg/cm² intervals from 0 to 7000 kg/cm² and from 6500 kg/cm² down to zero pressure.

## THEORY

It can be shown that the resistivity of an intrinsic semiconductor is given by

$$\rho=[1/e(\mu_e+\mu_p)](1/2A)\exp(E_g/2kT), \qquad (1)$$

where $\mu_e$ and $\mu_p$ are the electron and hole mobilities, respectively, $e$ the electronic charge, $E_g$ the energy gap between the valence and conduction bands, $k$ Boltzmann's constant, $T$ the absolute temperature, and $A$ given by

$$A=(2\pi kT/h^2)^{\frac{3}{2}}(m_e m_p)^{\frac{3}{4}},$$

where $m_e$ and $m_p$ are the effective masses for electrons and holes, respectively. The assumption is made that the energy *vs* crystal momentum curves for both bands are nonmultiple; multiplicity of branches would result in a more complicated expression for $A$, and an alteration in the estimated values of $m_e$ and $m_p$.

When donor or acceptor impurities contribute to the conductivity, the expression for $\rho$ is altered; in the case of a single donor level, the resistivity is given by

$$\rho=1/e(n\mu_e+p\mu_p), \qquad (2)$$

where $n$ and $p$, the number densities of electrons and holes, are given by

$$n=n_0/2+[(n_0/2)^2+n_i^2]^{\frac{1}{2}},$$
$$p=-n_0/2+[(n_0/2)^2+n_i^2]^{\frac{1}{2}}, \qquad (3)$$

and

$$n_i^2=4A^2\exp[-E_g/kT], \qquad (4)$$

where $n_0$ is the number density of ionized donors.

$E_g$, the minimum energy gap between valence and conduction bands, we assume dependent on both tem-

[7] However, in two of the low-temperature experiments the corrections are not inconsiderable. These will be indicated later in the text.

[8] P. W. Bridgman, Proc. Am. Acad. Arts. Sci. **67**, 305 (1932).

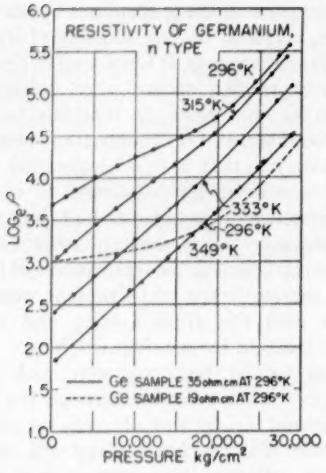


FIG. 1. Resistivity of high-purity germanium *vs* pressure, at several temperatures, (with two runs at 349°K). Also shown is the resistivity *vs* pressure curve for a less pure sample at room temperature.

perature $T$ and pressure $P$

$$E_g^{P,T}=E_g^{0,0}+\int_0^P\left(\frac{\partial E_g}{\partial P}\right)_T dP+\int_0^T\left(\frac{\partial E_g}{\partial T}\right)_P dT. \quad (5)$$

Under certain conditions of low temperature and/or high pressure we shall see that the contribution of the intrinsically derived carriers ($n_i$) will become negligible compared to that of the impurity derived carriers. For a single donor level of depth below the conduction band,

$$\epsilon^{P,T}=\epsilon^{0,0}+\int_0^P\left(\frac{\partial \epsilon}{\partial P}\right)_T dP+\int_0^T\left(\frac{\partial \epsilon}{\partial T}\right)_P dT, \quad (6)$$

the value of $p$ tends to zero and $n$ to the solution of

$$n^2+A_e n\exp(\epsilon/kT)-n_0A_e\exp(\epsilon/kT)=0, \quad (7)$$

where

$$A_e=(2\pi m_e kT/h^2)^{\frac{3}{2}}.$$

## RESULTS

Figure 1 shows the resistivity—pressure relation at several temperatures, Fig. 2 the corresponding resistivity—temperature curves at several pressures. Figure 3 shows the results to 7000 kg/cm² at low temperatures. $\text{Log}_e R$ is plotted here: the conversion to $\log_e\rho$ involves a correction of some 10 percent of the total change under pressure at −80°C, and 20 percent at −195°C, due to the change in dimensions of the sample. This change is insignificant at the other temperatures.

Figure 2 shows that at 76°C the sample is intrinsic over the entire pressure range; in this case the log resistivity *vs* pressure relation is almost linear. Figure 3, and room temperature experiments by Bridgman on less pure samples,[3] suggest that up to about 15 000 kg/cm² the carrier mobility is substantially independent of pressure. If we assume that both the mobilities and effective masses are independent of pressure, we can deduce from Eqs. (1) and (5) that in the pressure range to 15 000 kg/cm²,

$$(\partial E_g/\partial P)_T=5.5\times10^{-12}\text{ ev dyne}^{-1}\text{ cm}^{-2}\text{ at }76°\text{C}. \quad (8)$$

This compares reasonably well with previously determined values: for example, Bridgman found $5.6\times10^{-12}$ and Miller and Taylor, $5.2\times10^{-12}$. It also agrees with the value deduced by Shockley and Bardeen from the hole and electron mobilities by the deformation potential method,[5] although in view of the probable complexity of the energy band structure, it seems likely that this last agreement is coincidental.

As the temperature is reduced from 76°C, the curve of log resistivity *vs* pressure tends to become $S$ shaped, approaching a plateau below 15 000 kg/cm², and then bending upwards back towards parallelism with the 76°C curve above 15 000 kg/cm². This effect is barely visible at 42°C, but becomes quite definite at room temperature. Above 15 000 kg/cm² the curves, which are fairly parallel, have a slope about equal to that found by Bridgman in this pressure range for less pure samples (see the 19 ohm-cm sample in Fig. 1). Although this slope is very close to the slope of the intrinsic curve, a consideration of the resistivity-temperature relation shows that at the low temperatures and high pressures the sample is not intrinsic. Bridgman's results for less pure samples[3] support the view that in the pressure range above the bend the conduction is by impurity-derived electrons.

## DISCUSSION

The data appear to warrant the conclusion that the increase of $E_g$ with pressure extends to at least 15 000

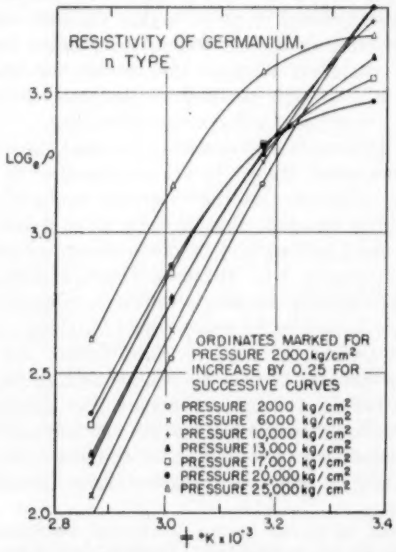


FIG. 2. Resistivity of high-purity germanium *vs* temperature, at several pressures.

kg/cm², and our value for $(\partial E_g/\partial p)_T$ agrees with those previously determined. The unexplained element in the situation is the increase of resistivity above 15 000 kg/cm², even for impure samples, and in view of this any interpretation of the intrinsic curve above 15 000 kg/cm² in terms of energy gap variation is not necessarily justified. It is to these aspects of the situation that attention will now be directed. We examine several alternative hypotheses.

(a) First let us suppose that the total energy gap is changing at the rate quoted above throughout the entire pressure range, that the impurity activation energy is constant, and that the carrier mobilities are unaffected by pressure.

The curves of Fig. 3, in conjunction with Bridgman's earlier results,[3] support the assumption that the mobility is independent of pressure up to about 15 000 kg/cm² for electrons[9] while Bridgman's experiments on relatively impure $p$-type samples[3] indicate that to a first approximation the hole mobility may be considered independent of pressure up to 30 000 kg/cm². If we attempt to ascribe the entire resistivity variation in Figs. 1 and 2 to changes in carrier concentration, resulting from change in energy gap, then Eqs. (2), (3), (4), and (5) apply.

$n_0$, the number of electronic carriers at low temperatures, is determined from the resistivity values of Fig. 3, assuming an electron mobility of 3600 cm²/volt sec at 300°K and a $T^{-\frac{3}{2}}$ law of variation with temperature: its value is $2\times10^{13}$ cm$^{-3}$. The determination of $n_i^2$ involves some uncertainty. In practice $E_g^{0.0}$ and $\beta=(\partial E_g/\partial T)_{P=0}$ can be found from the slope and intercept on the $1/T$ axis of curves of $\log_e n_i^2$ *vs* $1/T$ at zero pressure. In germanium such a curve follows

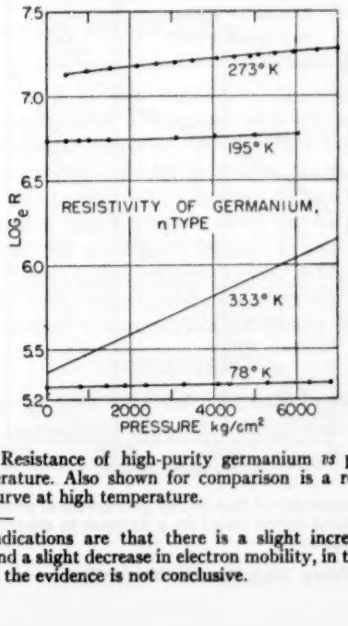


FIG. 3. Resistance of high-purity germanium *vs* pressure, at low temperature. Also shown for comparison is a resistance *vs* pressure curve at high temperature.

[9] The indications are that there is a slight increase in hole mobility and a slight decrease in electron mobility, in this pressure range, but the evidence is not conclusive.

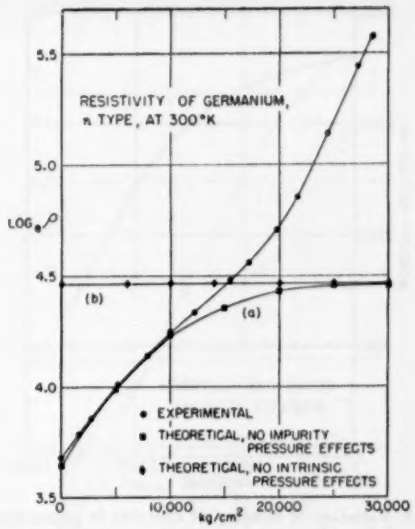


FIG. 4. Resistivity of high-purity germanium *vs* pressure, at room temperature, along with theoretical curves for two hypothetical cases quoted in the text.

the rule[10]

$$n_i^2=9.3\times10^{31}T^3\times\exp(-0.75/kT)\ \text{cm}^{-3}\ \text{at temperature}\ T, \quad (9)$$

where $E_g^{0.0}=0.75$ ev, and $4A^2\exp(\beta/K)=9.3\times10^{31}$. Comparison of (4) and (9) give $E_g^{0.0}$ and $\beta$ ($\beta$ is assumed independent of $T$) if $A$ is assumed. The value for $\beta$ thus depends on the assumed band structure, and on the assumed effective masses. The value for $\beta$ normally assumed, $-0.0001$, is a good round figure, but is not exactly consistent with $E_g^{0.0}=0.75$ ev and with an $A$ deduced assuming $m_e=m_p=m$ the free electron mass.

When the pressure is varied at a temperature $T$, (9) becomes

$$n_i^2=9.3\times10^{31}T^3\exp[(-E_g^{0.0}-\alpha P)/kT], \quad (10)$$

where $\alpha=(\partial E_g/\partial P)_T$ and $P$ is the pressure. Throughout the following discussion we shall use Eq. (10) where a value of $n_i^2$ at pressure $P$ and temperature $T$ is required.

$n$ and $p$ are thus determined from (3) and (10), and thence $\rho$, at any pressure. Figure 4 (a) represents the expected room temperature behavior of $\log_e\rho$ with pressure. Although it describes the actual low-pressure behavior well, and the flattening predicted around 15 000 kg/cm² is obtained, it is clearly inadequate at the higher pressures.

(b) The analysis above indicates that above 15 000 kg/cm² conduction should be largely by impurity-derived electrons. Thus the high-pressure resistivity behavior must be ascribed to a change of impurity activation energy with pressure or a pressure variation of electron mobility or a combination of the two. Let

[10] E. M. Conwell, Proc. Inst. Radio Engrs. 40, 1327 (1952).

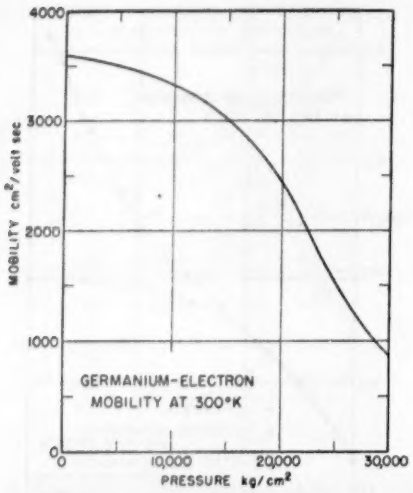


FIG. 5. Variation of mobility of electrons in germanium with pressure, deduced from conductivity of a relatively impure $n$-type sample.

us first examine the possibility of a change of activation energy with pressure. It is necessary to suppose that the activation energy changes with pressure at the same rate as the total energy gap; we assume that in Eq. (6), $\epsilon^{0,T}=0.01$ ev. Then, ignoring any contribution from the intrinsically derived electrons, $n$ is given by (7). The resultant variation of $\log_e\rho$ with pressure, given by (2), is that of Fig. 4 (b). There is but 2 percent deionization by 40 000 kg/cm² at room temperature, and the sharp rise in resistivity due to rapid deionization does not set in until we are beyond attainable hydrostatic pressures. Also, the effect of deionization would appear at lower pressures the lower the temperature. The curves in Fig. 3 which should show the rapid rise in resistivity, indicate only a very slow uniform increase.

(c) We have concluded that the hole mobility is substantially constant to 30 000 kg/cm², and the electron mobility to 15 000 kg/cm². However, it is not possible to infer anything about the electron mobility above 15 000 kg/cm². Let us, then, examine the supposition that the behavior of $n$-type Ge above 15 000 kg/cm² is due entirely to a decrease of electron mobility with pressure. At 76°C, the rate of increase of resistivity above 15 000 kg/cm² would then be due both to the decreasing carrier density and to the decreasing mobility of the electronic carriers, and should be somewhat greater than the rate due to energy gap change alone. In fact, there is a slight increase of slope in the 76°C curve around 15 000 kg/cm², but still the slope of the curve above 15 000 kg/cm² at this temperature is little different from that at room temperature in impure $n$-type germanium samples.

We can derive the supposed change of electron mobility with pressure from 0–30 000 kg/cm², assuming constant carrier density, from Bridgman's results for impure $n$-type samples, avoiding the complication of intrinsic carrier depopulation in the 35-ohm-cm sample. This is shown in Fig. 5. For this derivation we used the curve of $\log_e\rho$ *vs* pressure for a 4-ohm cm sample [see second reference under (2)]. If we then suppose that the total energy gap increases at the quoted rate, that the impurity activation energy is constant, and that the mobilities of electrons and holes are as indicated, (corrected for $T^{-\frac{1}{2}}$ and $T^{-2.3}$ law of variation[11] with temperature for electrons and holes, respectively, and with $\mu_e^{P,T}/\mu_e^{0,T}$ assumed independent of temperature) we can derive the curve of Fig. 6 for $\log_e\rho$ *vs* pressure at 76°C. Clearly, although there *is* a slight increase in slope of the experimental curve above 15 000 kg/cm² the fit of the theoretical curve is not very good. In order to account for the nearly constant slope of the intrinsic curve it would be necessary to suppose that in the same region where the mobility change begins there is a reduction in the rate of increase in band gap with pressure. Such a change is, in fact, not too unlikely if it is assumed, as seems probable, that the change in mobility is associated with a change of the point in $k$ space at which the minimum energy in the conduction band comes.

(d) An explanation based on the presence of a large number of $p$-$n$ junctions in the material is excluded by the absence of any resistance change with pressure at very low temperatures, and by the fact that the rapid resistance increase above 15 000 kg/cm² at and above room temperature also occurs in very impure samples.

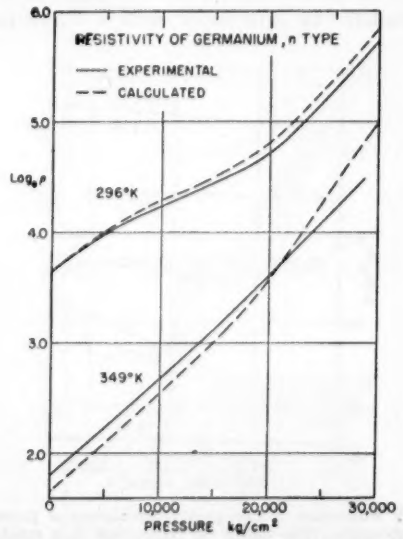


FIG. 6. Resistivity of high-purity germanium *vs* pressure, along with theoretical curves based on a decrease in electron mobility at high pressures.

[11] M. B. Prince, Phys. Rev. 91, 208 (1953).

Bridgman[12] found a sharp maximum in the resistivity-pressure relation for $n$-type germanium in experiments out to 100 000 kg/cm² pressure, but the interpretation of this result may be complicated by the nonhydrostatic nature of the pressure.

The suppositions of (c) can be used somewhat differently. From (2) and (3), $[(n_0/2)^2+n_i^2]^{\frac{1}{2}}=1/(\mu_e+\mu_p)\times[(1/\rho e)-(n_0/2)(\mu_e-\mu_p)]$. Hence, with the assumptions of (c), and using the experimentally determined values of $\rho$ *vs* $P$ at 76°C, we can find $n_i^2$ *vs* $P$ and hence $E_g$ from (4). Figure 7 shows $E_g$ *vs* $P$ determined in this way. We note that in the linear range the rate of change of $E_g$ with $P$ is nearly 10 percent less than when constant carrier mobility was assumed. It is suggested that the flattening in the $E_g$ *vs* $P$ curve at high pressures is not an unreasonable additional hypothesis on which to base a full explanation of the experimental facts.

The small differences between the slopes of the experimental curves above 15 000 kg/cm² at the various temperatures measured are not implausible. Although it is not obvious from the general expression for the slope of $\log_e\rho$ *vs* $P$, derived from Eq. (2), how the slope will change with temperature, some idea of the change can be obtained from the two cases (a) where the conduction above, say 20 000 kg/cm², is by impurity derived electrons. This corresponds to our sample at room temperature; (b) where the conduction above, say 20 000 kg/cm², is mostly by intrinsic electrons and holes. This corresponds to our sample at 76°C. In (a) $\rho=1/en_0\mu_e$, and

$$\frac{d\log_e\rho}{\partial P}=-\frac{1}{\mu_e}\frac{\partial\mu_e}{\partial P}.$$

This expression is nearly temperature independent. For (b) $\rho=1/[en_i(\mu_e+\mu_p)]$, and

$$(d/dP)\log_e\rho=(1/2kT)(\partial E_g/\partial P)_T-\{1/(\mu_e+\mu_P)\}\{\partial\mu_e/\partial P\}.$$

The first term in this expression decreases as the temperature is raised. The second term is also temperature dependent because of the $T^{-2.3}$ law for holes as opposed to a $T^{-1.5}$ law for electrons; since $d\mu_e/dP$ is negative, this term tends to increase $d\log_e\rho/dP$ as the temperature is raised. The net effect can be greater or smaller than the slope given by (a). In fact the slope of the 76°C curve above 15 000 kg/cm² is smaller than that of the room temperature case, while the slopes for the 42°C and 60°C experiments are greater than both.

## CONCLUSION

The energy gap between conduction and valence bands in germanium increases with hydrostatic pressure up to at least 15 000 kg/cm² at a rate in agreement with earlier determinations at lower pressures. A rapid increase of resistivity with pressure above 15 000 kg/cm² found in $n$-type germanium, but not in $p$ type, cannot be explained by a change in impurity activation energy, and is not wholly consistent with a change in mobility, unless the additional assumption is made that the rate of increase of energy gap decreases at the same pressure at which the reduction of electron mobility sets in. Any theoretical explanations must also ultimately be consistent with the possibility of a maximum in the resistivity at 50 000 kg/cm² found by Bridgman, and with the relative insensitivity of the resistivity to pressure at low temperatures.

Experiments to determine the Hall constant and the drift mobility under pressure are planned, in addition to experiments to examine the pressure shift of the optical absorption edge.

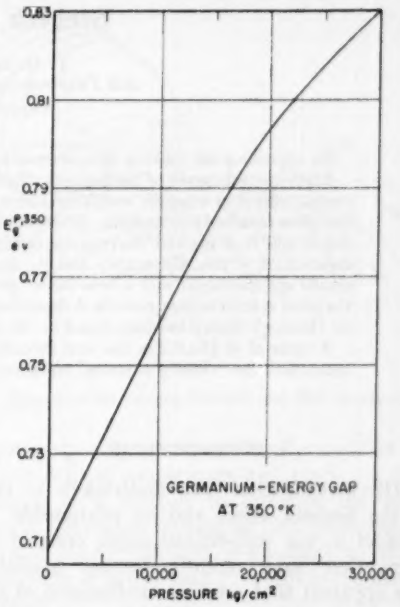


FIG. 7. Variation of energy gap in germanium, deduced from resistivity data, and assuming the decrease in electron mobility with pressure indicated in Fig. 5.

## ACKNOWLEDGMENTS

It is a pleasure to acknowledge the assistance of Professor P. W. Bridgman in making available his apparatus and experience in high-pressure measurements. We are also much indebted to Mr. L. H. Abbot and Mr. Charles Chase for help in the high-pressure instrumentation

[12] P. W. Bridgman, Proc. Am. Acad. Arts Sci. 81, 221 (1952).

# Seebeck Effect in Germanium

T. H. GEBALLE AND G. W. HULL
*Bell Telephone Laboratories, Murray Hill, New Jersey*
(Received Februrary 19, 1954)

An apparatus for making measurements of the Seebeck effect between 20°K and 375°K is described. Experimental curves of the Seebeck effect are given for a series of germanium crystals in which various concentrations of acceptor and donor atoms have been incorporated. The Seebeck data are compared with Hall data obtained concurrently. Above 250°K the two effects can be correlated by means of existing theory. Below 250°K a marked discrepancy occurs between existing theory and experiment. The temperature dependence of this discrepancy and its dependence upon concentration of added atoms are given. The results are consistent with a new theory proposed by C. Herring which considers an interaction between the phonon and electron systems. A dependence of Seebeck voltage upon sample dimension which is predicted by Herring's theory has been found in the temperature region below 50°K.

A value of $(0.75\pm0.2)m$ has been determined for the mass parameter of both holes and electrons which enters into the "density of states" equation.

## I. INTRODUCTION

THIS investigation[1] was undertaken to examine the Seebeck effect and its relationship to the Hall effect in the well-defined single crystals of germanium that have recently become available. It will be apparent that a major modification of existing theory is necessary to explain the results presented here and elsewhere[2] in order to account for the very large Seebeck voltages measured below room temperature. Measurements have been made between 20°K and 375°K on a series of $p$-type germanium crystals which have varying excess amounts of acceptor atoms and $n$-type germanium crystals which have varying excess amounts of donor atoms incorporated into the lattice. Near room temperature it is found that the results can be explained by existing theory.

## II. THEORETICAL RELATIONSHIPS

The energy flux[3] relative to the electrochemical potential carried through the thermoelectric circuit per carrier of charge $e$ is given by $eQT$, where $Q$ is the Seebeck voltage per degree difference in junction temperature, or the thermoelectric power, and $T$ the absolute temperature. The Wilson-Sommerfeld theory applied to a nondegenerate extrinsic semiconductor gives[4]

$$eQ_eT=\Delta E_F-\Delta E_T. \tag{1}$$

The subscript $e$ is used to emphasize that we are considering the contribution of current carriers only. The terms on the right-hand side refer to potential and kinetic energy respectively. $\Delta E_T$ is the average kinetic energy transported by the carriers and $\Delta E_F$ is their Fermi level, both measured relative to the energy of the edge of the band (conduction or valence) in which the carriers move. $\Delta E_F$ is the same parameter which enters into the equation for the density of mobile carriers in an extrinsic, nondegenerate semiconductor.

$$n=2N_v\left(\frac{2\pi m^*kT}{h^2}\right)^{\frac{1}{2}}\exp(-\Delta E_F/kT), \tag{2}$$

where $N_v$ is a statistical weight factor and $m^*$ is an inertial effective mass. The density of mobile carriers, $n$, is also inversely proportional to the Hall constant and thus the $n$ determined from Hall measurements can be related to the thermoelectric data by means of Eqs. (1) and (2). The data to be presented below yield a value for the product $N_v^{\frac{2}{3}}m^*$. This product is referred to as the "density of states" effective mass.

## III. EXPERIMENTAL PROCEDURE

The crystals were grown by pulling from the melt by the method of Teal and Little.[5] In some cases, the samples were taken from the same crystals used by Debye.[6] We are indebted to J. P. Maita for some help with the sample preparation. Briefly, this is done as follows: A slab is cut perpendicular to the pulled direction of the crystal and lapped to approximately 0.13 cm thick. The [110] direction which is perpendicular to the developed faces is conveniently located. The long axis of the cutting die is lined up in the [110] direction and the sample shown in Fig. 1 cut out using the magnetostriction device developed by W. L. Bond.[7]

Two of the arms shown in Fig. 1 are spares. The two control arms, $F$, are used as Hall probes and the two outside arms, $E$, as electrical conductivity probes

[1] Some results were presented at the Rochester meeting of the American Physical Society, June, 1953 [Phys. Rev. **92**, 857 (1953)].
[2] H. P. R. Frederikse, Phys. Rev. **92**, 248 (1953).
[3] C. Herring and M. H. Nichols, Revs. Modern Phys. **21**, 5506 (1949).
[4] This equation is discussed in detail in a forthcoming paper by C. Herring, Phys. Rev. (to be published). The theoretical investigation carried out by Herring and the experimental investigation reported here were carried out cooperatively and it will be convenient to make frequent reference to that paper.
[5] G. K. Teal and J. B. Little, Phys. Rev. **78**, 647 (1950).
[6] P. P. Debye and E. M. Conwell, Phys. Rev. **93**, 693 (1954).
[7] W. L. Bond, Phys. Rev. **78**, 646 (1950).

in the manner developed by Pearson.[8] All samples used, or samples cut from sections of the crystals near to the samples used are probed at room temperature at 0.05- or 0.1-cm intervals to insure uniform resistivity along the axis. The sample is gold-plated from aqueous solution and then tinned with an indium alloy solder a distance of 0.18 cm on the upper and lower surface of each end. In a few cases, the solder has been secured directly to the germanium surface using acid flux. Gold lead wires are welded to the arms. The sample is washed in distilled water and lightly sand-blasted using 180-mesh silicon carbide powder and soldered in the holder shown schematically in Fig. 1. The hollow heater $A$ is sufficiently light to be supported by the sample. The thermal sink $B$ is made from copper-filled lead in order to have sufficient thermal stability at the lower temperatures. The copper thermocouple blocks $C$ are soldered to the upper surface of the germanium. To facilitate assembly, they are held in place by phosphor-bronze springs that are electrically and thermally insulated from the rest of the system. The thermocouples are constructed from No. 30 constantan and No. 36 copper wires. They are soldered in 0.06-cm holes drilled close to the lower inside corner of each block as indicated. It proved desirable to incorporate the differential thermocouples $G$ in order to keep track of the thermal impedance across each junction. The whole system is surrounded by a radiation shield and placed in a container connected to a high vacuum system. The vacuum is usually maintained at $5\times10^{-6}$ mm except at the higher temperatures where out-gassing causes the pressure to rise slightly above $10^{-5}$ mm.

## IV. METHOD OF MEASUREMENT

The Hall and electrical conductivity measurements are made in the usual manner.[6] The Seebeck effect is measured in the steady state with a few hundredths of a watt dissipated at the heater $A$. For a period of about 10 minutes, the power dissipated at the heater, the thermocouple readings, and the Seebeck voltage across the two thermocouple copper leads are followed as a function of time. The system inside the container drifts upward about 0.02° per minute at room temperature with a gradient of 2° between the thermocouples when in a vacuum. The decreasing thermal capacity of the thermal sink and increasing thermal conductivity of the germanium cause the drifts to increase as the temperature is lowered. To maintain the 2° gradient between the junctions, the heat introduced causes a 0.05° drift at nitrogen temperatures and 0.3° drift per minute at 30°K. However, it is possible to stabilize the system between 20 and 30°K, and also in the liquid nitrogen range, by introducing a small pressure of helium into the container and utilizing the heat capacity of the liquid refrigerant surrounding the container.

[8] G. L. Pearson and J. Bardeen, Phys. Rev. **75**, 865 (1949).

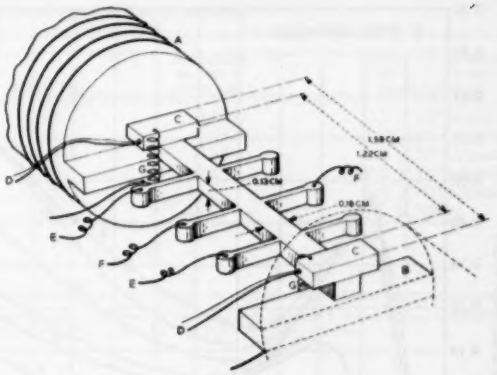


FIG. 1. Apparatus for making Seebeck and Hall measurements.

The system quickly reaches a steady state in which there is no drift of temperature with time.

Although it is difficult to estimate the absolute accuracy of the measurements, we have made numerous checks and taken sufficient precautions to insure a reproducibility of better than 2 percent in the measured values of $QT$.

The chief source of error is in measuring the temperature exactly at the electrical junctions. The all-copper circuit which is used to measure the thermocouple voltages originally consisted of a type K potentiometer and a high sensitivity galvanometer. Parasitic emf's in the measuring circuit were measured and corrected for. Parasitic emf's introduced by rotation of the potentiometer drum were allowed to decay before taking drifts. Later measurements have been taken with a White double potentiometer and agree with the earlier results. The thermocouples have been calibrated at the boiling and triple points of hydrogen and nitrogen near the beginning and end of the measurements reported here and a temperature scale prepared from the table of Giauque *et al.*[9] The thermocouples are intercompared during each run.

It is possible to perform the following experiments without changing the measured $QT$ value more than 2 percent.

(a) Vary the temperature gradient several fold.

(b) Make a drastic change in the container temperature (for instance from nitrogen temperatures to either hydrogen temperatures or room temperature) without changing the sample temperature. This shows that radiation and heat conduction losses are not affecting the results.

(c) Remove the sample, clean off all the contacts and remount. This indicates the thermocouples are measuring the temperature at (or reproducibly close to) the electrical junctions of the copper and the germanium.

(d) Have either 1 mm of the gas in the container

[9] Giauque, Buffington, and Schulze, J. Am. Chem. Soc. **49**, 2343 (1927).

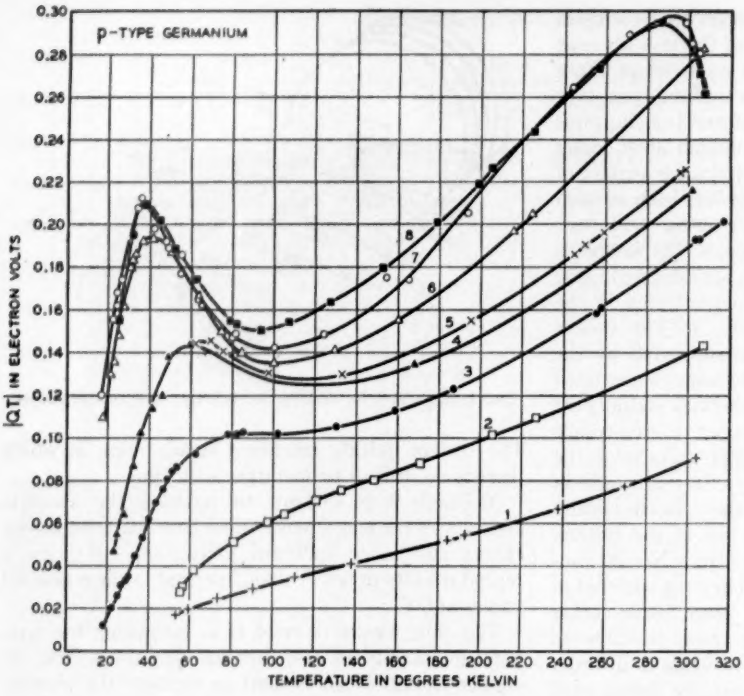


FIG. 2. Measured values of the $QT$ product for eight $p$-type samples listed in Table I.

(no drift conditions, see above) or less than $10^{-5}$ mm residual pressure in the container. This shows the thermocouple blocks are in excellent thermal contact with the sample.

One can compare the ratio of the Seebeck voltages measured between the thermocouple blocks and between the arms $E$ (Fig. 1) with the ratio of the distances between the blocks and between the insides of the arms $E$. At room temperature, the ratios are the same. In some samples, the Seebeck voltage ratio remains the same at low temperatures whereas in other samples it increases by as much as 10 percent. In a few cases, the ratio changed several hundred percent and in such cases the results have been discarded.

## V. EXPERIMENTAL RESULTS AND ANALYSIS

The measured values of $Q$ show a remarkable rise as the temperature is lowered below room temperature for a wide range of donor and acceptor concentrations. The $QT$ product is plotted as a function of temperature between 20°K and 300°K for the series of $p$-type crystals in Fig. 2 and for the $n$-type crystals in Fig. 3. The room temperature resistivities of the samples are given in Table I. Also in Table I the excess donor or acceptor atom concentrations are given for each sample. These values are assumed equal to the number of mobile carriers determined by Hall measurements in the saturation temperature range. This assumption has been verified for the antimony-germanium system by Pearson, Struthers, and Theuerer using radioactive techniques.[10] By saturation temperature range is meant the temperature range over which the donor or acceptor atoms are almost completely ionized giving a constant number of mobile carriers which is much larger than the number of mobile carriers resulting from intrinsic ionization. In the purer samples the saturation range extends from below 50°K to room temperature. In the upper temperature range the measured $QT$ values are almost proportional to $T$. The Wilson-Sommerfeld theory predicts this type of behavior throughout the saturation temperature range, i.e., from about 40°K to almost 300°K for the purer samples. It appears that this theory can be reasonably complete only above 250°K. For a given temperature the absolute value of $QT$ decreases as the number of acceptors or donors increases as is also predicted by the Wilson-Sommerfeld treatment. The rapid increase in $Q$ for the purer materials as the temperature decreases from 200°K to 35°K cannot be accounted for by this theory. It is postulated by Frederikse[3] and Herring[4] that there is an interaction between the anisotopic lattice vibrations, which exist of necessity in the thermal gradient, and the mobile charge carriers. The carriers are preferentially scattered toward the cold end of the sample by the nonequilibrium phonon distribution. The electrostatic field established within the semiconductor by the normal diffusion of the mobile carriers from hot to cold is thus enhanced by an interaction between

[10] Pearson, Struthers, Theuerer, Phys. Rev. 77, 809 (1950).

TABLE I. Room temperature resistivities and composition of samples.

| Sample No.[a] | Resistivity at 300°K (ohm cm) | Excess No. of donor atoms per cc (from Hall measurements) | Sample No.[a] | Resistivity at 300°K (ohm cm) | Excess No. of atoms per cc (from Hall measurements) |
|---|---|---|---|---|---|
| 1 | 0.0033 | $7.1\times10^{18}$ gallium | *A* | 0.0050 | $2.3\times10^{16}$ arsenic |
| 2 | 0.016 | $6.0\times10^{17}$ gallium | *B* | 0.032 | $1.08\times10^{17}$ arsenic |
| 3 | 0.066 | $8.0\times10^{16}$ gallium | *C* | 0.38 | $6.4\times10^{15}$ arsenic |
| 4 | 0.18 | $2.1\times10^{16}$ gallium | *D* | 2.5 | $7.8\times10^{14}$ arsenic |
| 5 | 0.23 | $1.5\times10^{16}$ gallium | *E* | 18.5 | $8.9\times10^{13}$ arsenic |
| 6 | 1.7 | $1.5\times10^{15}$ gallium | *F* | 46.0 | $8\times10^{13}$[b] |
| 7 | 21.5 | $1.6\times10^{14}$ gallium | | | |
| 8 | 20.0 | $1.9\times10^{14}$ indium | | | |
| 9 | 34.5 | $8.0\times10^{13}$ gallium | | | |

[a] All samples are cut in the 110 direction from crystals pulled from the melt as described in the text except sample 8. Sample 8 is cut in some direction perpendicular to the 111 direction from a zone-leveled [see W. G. Pfann and K. M. Olsen, Phys. Rev. 89, 322 (1953)] single crystal.
[b] Identity of excess donor not known.

the mobile carriers and the lattice. Indeed, the experimental values to be presented show that at the lower temperatures the latter effect must dominate almost completely.

The discrepancy between existing theory and experiment, which presumably is the result of the phonon-electron interaction, and will be referred to as such in the subsequent discussion, can be estimated by setting the measured $QT$ product equal to two terms,

$$(QT)_{\text{meas}}=Q_eT+Q_pT, \tag{4}$$

where $Q_eT$ is the contribution of the mobile carriers arising from the Wilson-Sommerfeld treatment, and $Q_pT$ is the contribution arising from the phonon-electron effect. Combining Eqs. (1) and (2) and transforming to convenient units gives

$$\pm Q_eT=\left[\log 4.70\times10^{15}T^{\frac{3}{2}}N_v\left(\frac{m^*}{m}\right)^{\frac{3}{2}}-\log n\right]T/5037+AkT, \tag{5}$$

where $A$ is a constant specifying the kinetic energy transported and which can be calculated, and $n$ is the number of mobile carriers per cc. The theoretical limits of $A$ in the final term of Eq. (5) are discussed by Herring.[4] Following him, $A$ is taken as 2.0 for high purity $n$-type material and as 2.0 for high purity $p$-type material below 125°K. Between 125°K and 300°K, $A$ for $p$-type material is assumed to decrease linearly from 2.0 to 1.7. It should be noted that the whole $AkT$ term is only 15 percent of $Q_eT$ for the high purity samples. The number of mobile carriers per cc, $n$, is calculated from the Hall constant $R_H$ using the equation[11]

$$n=\frac{\mu_H}{\mu_e}\frac{1}{R_He}. \tag{6}$$

The Hall to conductivity mobility ratio $\mu_H/\mu_e$, has been determined by Morin[12] and differs somewhat from $3\pi/8$ which is correct only when the mean free path is independent of energy. The $Q_eT$ values are insensitive to small uncertainties in $n$ since a 10 percent variation in $n$ changes $Q$ by only 10 microvolts.

In Figs. 4 and 5 are plotted isotherms of $Q_pT$ determined from Eqs. (4) and (5) as functions of acceptor and donor atom concentrations, respectively. The unspecified effective mass parameter $N_v^{\frac{2}{3}}m^*$ occurring in Eqs. (2) and (5) is chosen as 0.75 of the free electron mass $m$ for both $n$ and $p$ material on the basis of measurements in and near the intrinsic range which are discussed below.

It is apparent from Figs. 2 through 5 that the behavior of $p$- and $n$-type material is qualitatively similar. The dependence of $Q_pT$ on donor or acceptor concentration is small until a concentration range is

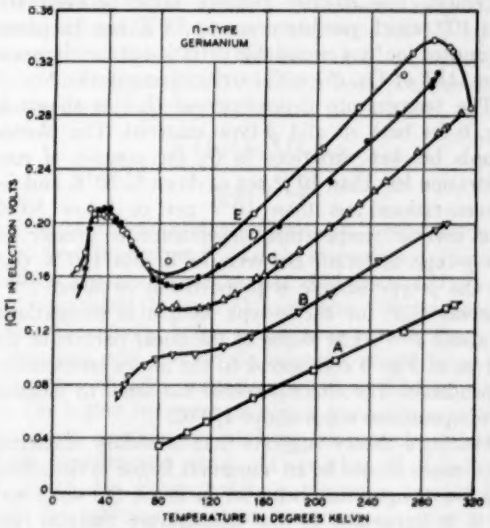


FIG. 3. Measured values of the $QT$ product for five $n$-type samples listed in Table I.

[11] W. Shockley, *Electron and Holes in Semiconductors* (D. Van Nostrand Company, Inc., New York, 1950), p. 215.

[12] F. J. Morin, Phys. Rev. 93, 62 (1954).

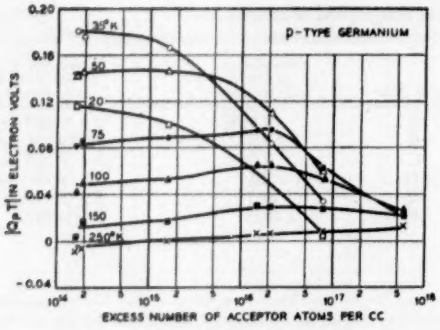


FIG. 4. Isotherms of $Q_pT$, Eq. (4), as function of concentration of excess acceptor atoms.

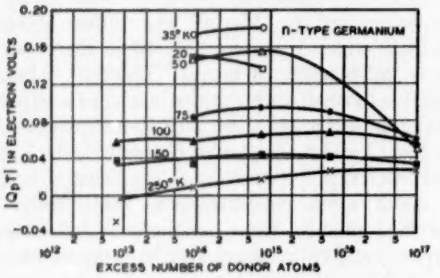


FIG. 5. Isotherms of $Q_pT$, Eq. (4), as function of concentration of excess donor atoms.

reached beyond which $Q_pT$ falls rapidly. This concentration range becomes lower as the temperature decreases. $Q_p$ becomes small when the concentration becomes large enough to approach Fermi-type degeneracy. The slightly positive slope between $10^{14}$ and $10^{16}$ which persists down to 75°K can be partly accounted for by a reasonable variation of the transport term $AkT$ of Eq. (5) with carrier concentration.[4]

The temperature dependence of $Q_pT$ is shown in Fig. 6 for both $n$- and $p$-type material. The plotted chords bracket variations in $Q_p$ for samples of concentration less than $10^{+15}$ per cc down to 50°K and for concentrations less than $10^{+14}$ per cc below 50°K. The inverse temperature dependence is greater for the $p$-type material. Between 75°K and 150°K $Q_pT$ for the $p$-type sample is proportional to about $T^{-2.2}$, whereas $Q_pT$ for the $n$-type sample is proportional to about $T^{-1.4}$. The slopes of the linear portion of the curves of Fig. 6 correspond to the above temperature dependence. The effect becomes too small to measure at temperatures much above 150°K.

Herring's theory suggests that boundary scattering of phonons should be an important factor in describing the low temperature behavior in much the same way as it is important in low temperature thermal conductivity.[13] Reference to Fig. 6 shows that departure from the inverse temperature dependence given by the straight lines occurs at between 50°K and 70°K. This is a considerably higher temperature range than that at which phonon boundary scattering becomes important in thermal conductivity experiments. This is what one would expect if the low energy phonons predominantly are interacting with the mobile carriers. In order to determine whether boundary scattering can be used to explain the low temperature curvature in Fig. 6, and, in fact, to provide experimental corroboration of Herring's model,[4] the thicknesses of $p$-type sample 7 and $n$-type sample $E$ were reduced by sand blasting and the samples remeasured. Sample 7 was reduced from 0.125 cm to about 0.069 cm for a distance of about 1.0 cm. Sample $E$ was reduced from 0.148 cm to about 0.025 cm for a distance of about 1.0 cm.[14] In order to avoid breakage the thin portion of the sample was supported by a sheet of 0.005 in. mica using an epoxy-resin cement. The curves for the "thin" samples are within 2 percent of the originals shown in Figs. 2 and 3 down to 80°K. The results below 80°K are shown in Fig. 7 on a somewhat enlarged scale for both

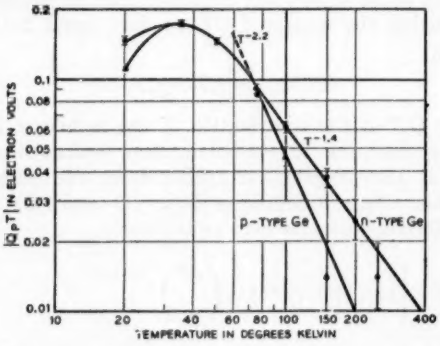


FIG. 6. Dependence of $Q_pT$, Figs. 4 and 5 on temperature for the purer samples.

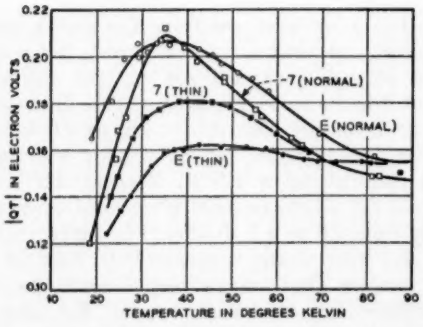


FIG. 7. Dependence of measured values of $QT$ upon sample dimension.

[13] R. Berman, Advances in Physics 2, 103 (1953).

[14] All samples except $E$ were between 0.12 cm to 0.13 cm thick. However, breakage was encountered while measuring high purity $n$-type samples (for example, sample $F$, which did not break until after measurements shown in Fig. 8 were completed). Sample $E$ was purposely made thicker in order to reduce the chance of breakage.

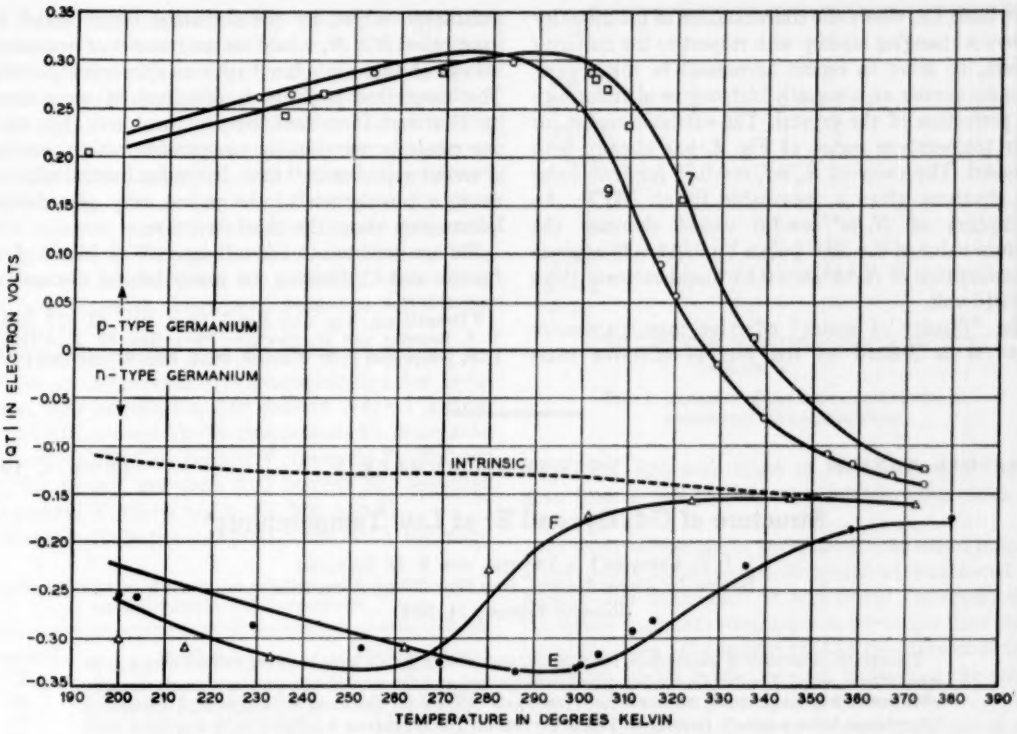


FIG. 8. Calculated values (curves) and measured values in the temperature range where the sample changes from extrinsic to intrinsic.

the normal (original) size and the "thin" size. It appears that the measurements below about 75°K are not typical of bulk germanium alone. The values are smaller for the smaller dimensions as is expected on the basis of Herring's model. The curvature in the low temperature portion of the curves of Fig. 6 is a property of the samples used, presumably much larger samples would follow the inverse temperature relations to lower temperatures. Similarly the maxima in Figs. 2 and 3 would shift to lower temperatures and higher values. The availability of large crystals of sufficient uniformity makes possible a more complete investigation of the effect of the sample dimensions. We hope to be able to report on this in the near future.

We now consider data near room temperature, where $Q_p$ is small, in order to determine a value of $N_v^{\frac{1}{3}}m^*$ occurring in Eq. (5). It can be seen from Figs. 3 and 4 that the choice of $N_v^{\frac{1}{3}}(m^*/m)=0.75$ for both $n$- and $p$-type samples satisfies Eq. (1) to about $\pm 0.01$ ev for the purer samples at 250°K after making a small allowance for $Q_p$. It has already been noted that the positive slope of these curves, indicating a slow, possibly logarithmic variation with impurity concentration, can be partly explained by a variation of the transport term $AkT$ of Eq. (5). Additional confidence in this value of $N_v^{\frac{1}{3}}(m^*/m)$ can be obtained by considering the results above room temperature where the purer samples become intrinsic. The purer samples have been measured to 375°K, and the results shown in Fig. 8. The curves are calculated using only the 1 adjustable parameter $N_v^{\frac{1}{3}}m^*=0.75m$ for both the $n$ and $p$ samples. To make this calculation, equation (5) must be generalized to include both positive and negative mobile carriers:

$$Q_eT=\frac{T(Q_+n_+\mu_+ + Q_-n_-\mu_-)}{n_+\mu_+ + n_-\mu_-}. \tag{7}$$

The concentration product of holes, $n_+$, and electrons, $n_-$, at the temperature $T$, and the respective mobilities $\mu_+$ and $\mu_-$ are taken from the data of Morin and Maita.[15] The quantities $Q_+$ and $Q_-$ are the thermoelectric powers the mobile holes would have in the absence of electrons, and the mobile electrons would have in the absence of holes, respectively, calculated from Eq. (5). The higher temperature points where the samples are almost completely intrinsic fall on the curves within experimental error. A variation of $N_v^{\frac{1}{3}}m^*/m$ by $\pm 0.15$ for either holes or electrons separately would be sufficient to cause a systematic deviation of the points from the curves in the almost intrinsic region. The agreement is not so good in the temperature region where the sample is changing from extrinsic

[15] F. J. Morin and J. P. Maita, Phys. Rev. (to be published).

to intrinsic, i.e., where the concentration of the minority carriers is changing rapidly with respect to the majority carriers. In order to expect agreement in this region, one must assume an unusually high degree of uniformity and perfection of the crystal. The extrinsic region, or lower temperature region of Fig. 8, has already been discussed. The value of $N_v^{\frac{1}{3}}m^*/m=0.75$ for both holes and electrons gives a reasonable fit at 300°K. An assumption of $N_v^{\frac{1}{3}}m^*/m=1.0$ would decrease the absolute value of the 300° points by 0.011 volt whereas an assumption of $N_v^{\frac{1}{3}}m^*/m=0.55$ would increase them by 0.015 volt.

The "density of states" effective mass parameter $N_v^{\frac{1}{3}}m^*/m$ is related to the inertial effective mass parameter, $m^*/m$, by the statistical factor which we have called $N_v^{\frac{1}{3}}$, $N_v$ would be the number of equivalent valleys or edges in a band with no spin-orbit splitting. The theoretical problem is discussed in some detail by Herring.[4] It suffices here to point out that while our result is not directly comparable with a number of recent experiments[16] that determine inertial effective mass, a comparison of the values may give further information about the band structure.

We are indebted to our colleagues F. J. Morin, J. A. Burton and C. Herring for many helpful discussions.

[16] Dresselhaus, Kip, and Kittel, Phys. Rev. **92**, 827 (1953); T. S. Benedict and W. Shockley, Phys. Rev. **89**, 1152 (1953); P. P. Debye and E. M. Conwell, Phys. Rev. **93**, 693 (1954).

PHYSICAL REVIEW VOLUME 94, NUMBER 5 JUNE 1, 1954

# Structure of Gd, Dy, and Er at Low Temperatures*

J. R. BANISTER,† S. LEGVOLD, AND F. H. SPEDDING
*Institute for Atomic Research, Iowa State College, Ames, Iowa*

(Received February 24, 1954)

The crystal structures of gadolinium, dysprosium, and erbium metals have been determined over a wide temperature range. The metals are hexagonal close packed and the $a_0$ unit axis contracts nearly linearly with decreasing temperature, whereas the $c_0$ unit axis exhibits an abnormal expansion with decreasing temperature below magnetic transformations of the metals. The $c_0$ behavior is believed to be associated with the magnetic properties of the metals.

## I. INTRODUCTION

MAGNETIC transformations in metals are usually accompanied by crystal structure changes which may be of different types.[1] In view of the fact that some of the rare earth metals have been reported to be ferromagnetic it was felt that an x-ray study of the structures of these over a wide temperature range should be made. This report covers such studies for gadolinium, dysprosium, and erbium.

Gadolinium has been reported[2–5] to have a ferromagnetic Curie point of 16°C. Dysprosium exhibits[6–9] a magnetic anomaly at about 175°K and a ferromagnetic Curie point near 90°K. Erbium has recently been found[10] to have a magnetic susceptibility anomaly of the dysprosium type near 80°K, and it is further reported that the susceptibility becomes strongly field-dependent below 55°K.

Dilatometric studies on gadolinium and dysprosium have been reported by Trombe and Foex.[11,12] For gadolinium they report an abrupt decrease in the coefficient of thermal expansion below the Curie point. A similar phenomenon was displayed by dysprosium below the magnetic anomaly near 175°K.

The electrical resistivities[4] of the three metals also exhibit peculiarities near the temperatures cited above, showing the influence of the transformations on the conduction process. This is also in evidence in the study of the Hall effect as reported by Kevane *et al.*[13]

## II. EXPERIMENTAL METHODS

The metal samples used were prepared by methods reported earlier.[14,15] Metal filings annealed under vacuum at 550°C for about 30 hours were mixed with pulverized

* Contribution No. 309 from the Institute for Atomic Research and Department of Physics, Iowa State College, Ames, Iowa. Work was performed in the Ames Laboratory of the U. S. Atomic Energy Commission.

† Present address, Sandia Corporation, Albuquerque, New Mexico.

[1] R. M. Bozorth, *Ferromagnetism* (D. Van Nostrand Company, Inc., New York, 1951).
[2] Urbain, Weiss, and Trombe, Compt. rend. **200**, 2132 (1935).
[3] F. Trombe, Ann. phys. **7**, 385 (1937).
[4] Legvold, Spedding, Barson, and Elliott, Revs. Modern Phys. **25**, 129 (1953).
[5] Elliott, Legvold, and Spedding, Phys. Rev. **91**, 28 (1953).
[6] F. Trombe, J. phys. et radium **12**, 222 (1951).
[7] F. Trombe, Compt. rend. **221**, 19 (1945).
[8] F. Trombe, Compt. rend. **236**, 591 (1953).
[9] Elliott, Legvold, and Spedding, this issue, Phys. Rev. **94**, 1143 (1954).
[10] Elliott, Legvold, and Spedding, "Some of the Magnetic Properties of Erbium Metal" (to be published).
[11] F. Trombe and M. Foex, Compt. rend. **235**, 42 (1952).
[12] F. Trombe and M. Foex, Compt. rend. **235**, 163 (1952).
[13] Kevane, Legvold, and Spedding, Phys. Rev. **91**, 1372 (1953).
[14] Spedding, Voight, Gladrow, and Sleight, J. Am. Chem. Soc. **69**, 2777, 2786, 2812 (1947).
[15] F. H. Spedding and A. H. Daane, J. Am. Chem. Soc. **74**, 2783 (1952).

NaCl crystals which served as an internal standard for the exposures. The mixed samples were placed in thin-walled glass capillaries approximately 0.035 cm in diameter. A Debye-Sherrer powder camera capable of operating at various temperatures was used for the exposures. A temperature-controlled, helium gas stream flowing past the sample was used to obtain the different temperatures. The temperature fluctuation during a given exposure was less than four degrees and mean temperatures for exposure have been used in reporting the results. Cu-$\alpha$ radiation was employed in the study and long exposure times gave negatives suitable for analysis.

The metal samples used showed the following impurities as determined spectrographically: for gadolinium, 0.02 percent Ca, 0.05 percent Nd, 0.1 percent Sm and 0.02 percent Tb; for dysprosium, Ca detectable, 0.01 percent Ho, 0.07 percent Y, traces of Fe, Ta, and Mg; for erbium, less than 0.02 percent Ho, less than 0.02 percent Y, traces of Ca, Fe, Mg, and Si.

To obtain the lattice constants of the NaCl, the calculated $a_0$'s were extrapolated to $\theta=90°$. The values so obtained were found to be commensurate with the values which would be anticipated from the thermal expansion coefficient of sodium chloride. The $\sin^2\theta$ values for the metal were then modified by using the correction curve obtained by comparing the observed and calculated $\sin^2\theta$'s for the NaCl lines. Lattice parameters of the metals were calculated using the corrected $\sin^2\theta$ of the reflections and expressions derived by minimizing the sum of the squares of the deviations of the calculated angles from the observed angles. The calculation was checked, and errors estimated by substituting the calculated values back in the $\sin^2\theta$ of the individual reflections.

TABLE I. Variation of the lattice constants of gadolinium and sodium chloride with temperature.

| Temperature (°K) | Gadolinium $a_0$(A) | Gadolinium $c_0$(A) | Sodium chloride $a_0$(A) |
|---|---|---|---|
| 106 | 3.629±0.002 | 5.796±0.004 | 5.603±0.001 |
| 175 | 3.630±0.002 | 5.798±0.005 | 5.614±0.001 |
| 183 | 3.631±0.002 | 5.786±0.005 | 5.615±0.001 |
| 216 | 3.629±0.002 | 5.780±0.005 | 5.623±0.001 |
| 231 | 3.633±0.002 | 5.782±0.005 | 5.625±0.001 |
| 283 | 3.633±0.002 | 5.776±0.005 | 5.636±0.001 |
| 285 | 3.633±0.002 | 5.781±0.005 | 5.637±0.001 |
| 298 | 3.635±0.002 | 5.776±0.005 | 5.641±0.001 |
| 299 | 3.633±0.002 | 5.771±0.005 | 5.640±0.001 |
| 300 | 3.636±0.002 | 5.779±0.005 | 5.641±0.001 |
| 324 | 3.634±0.002 | 5.778±0.005 | 5.645±0.001 |
| 349 | 3.639±0.002 | 5.777±0.005 | 5.653±0.001 |

## III. RESULTS AND DISCUSSION

### Gadolinium

It was difficult to obtain clear negatives for the gadolinium analysis. It appeared that the absorption coefficient of gadolinium metal for Cu-$\alpha$ radiation was very high. Exposure times of twenty to forty hours gave from seven to thirteen readable metal lines for the analysis.

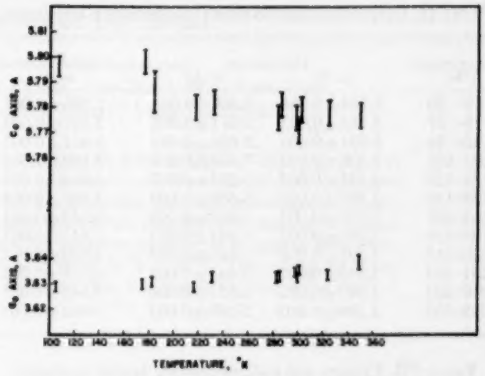


FIG. 1. Variation of the lattice parameters of gadolinium with temperature.

At room temperature, gadolinium was found to have a hexagonal, close-packed structure as was noted by Klemm and Bommer.[16] It was found, however, that the lattice constants were appreciably larger than those found by them. The largest part of this difference may be accounted for by the upward revision of the wavelength values in angstroms since their study.

It was found that there was no gross change in the structure of gadolinium across the Curie point, but it was noted that the $c_0$ unit axis increased with decreasing temperature in the region between the Curie point and 175°K as seen in Table I and in Fig. 1. The behavior of the $a_0$ unit axis appeared to be normal, within experimental error, showing an increase with increasing temperature. Assuming linear trends above and below the Curie temperature, the macroscopic coefficient of thermal expansion may be estimated as $-2\times10^{-6}$ per degree K below the Curie point and about $10\times10^{-6}$ per degree K above the Curie point. This is in rough agreement with the dilatometric study of Trombe and Foex.[11]

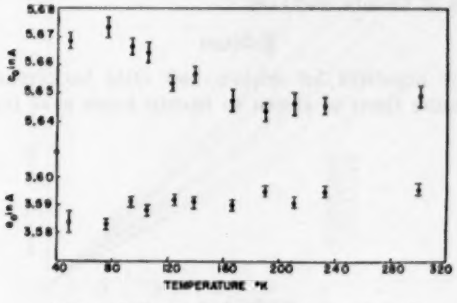


FIG. 2. Variation of the lattice parameters of dysprosium with temperature.

[16] W. Klemm and H. Bommer, Z. anorg. u. allgem. Chem. **231**, 138 (1937).

TABLE II. Dysprosium and sodium chloride lattice constants.

| Temperature (°K) | Dysprosium $a_0$(A) | Dysprosium $c_0$(A) | Sodium chloride $a_0$(A) |
|---|---|---|---|
| 48– 50 | 3.584±0.004 | 5.668±0.003 | 5.596±0.001 |
| 75– 77 | 3.583±0.002 | 5.673±0.004 | 5.597±0.001 |
| 92– 94 | 3.591±0.002 | 5.666±0.003 | 5.601±0.001 |
| 103–107 | 3.590±0.002 | 5.664±0.004 | 5.602±0.001 |
| 122–124 | 3.595±0.002 | 5.653±0.003 | 5.604±0.001 |
| 138–140 | 3.591±0.002 | 5.656±0.003 | 5.607±0.001 |
| 165–167 | 3.595±0.002 | 5.647±0.004 | 5.613±0.001 |
| 188–192 | 3.595±0.002 | 5.643±0.003 | 5.617±0.001 |
| 210–212 | 3.591±0.002 | 5.646±0.004 | 5.620±0.001 |
| 231–235 | 3.595±0.002 | 5.645±0.003 | 5.627±0.001 |
| 299–301 | 3.595±0.002 | 5.657±0.006 | 5.641±0.001 |
| 298–302 | 3.596±0.002 | 5.649±0.003 | 5.641±0.001 |

TABLE III. Erbium and sodium chloride lattice constants.

| Temperature (°K) | Erbium $a_0$(A) | Erbium $c_0$(A) | Sodium chloride $a_0$(A) |
|---|---|---|---|
| 42.5–43.5 | 3.558±0.001 | 5.590±0.002 | 5.595 ±0.001 |
| 64 –66 | 3.562±0.002 | 5.582±0.003 | 5.597 ±0.001 |
| 83 –87 | 3.561±0.001 | 5.582±0.002 | 5.798 ±0.001 |
| 102 –104 | 3.563±0.001 | 5.581±0.002 | 5.601 ±0.001 |
| 151 –153 | 3.563±0.001 | 5.586±0.002 | 5.6095±0.0015 |
| 199 –201 | 3.565±0.001 | 5.591±0.002 | 5.6195±0.001 |
| 300 –302 | 3.562±0.002 | 5.602±0.003 | 5.641 ±0.001 |

## Dysprosium

The x-ray negatives obtained using dysprosium samples showed some background, but were considerably clearer than the negatives for gadolinium. From eight to fourteen metal lines were observable on the negatives with exposure times of twelve to twenty hours. The lines indicated a hexagonal, close-packed structure for all exposures. This is in fair agreement with results reported by Klemm and Bommer[16] when account is taken of the wavelength revision reported above.

Results are summarized in Table II and Fig. 2. If linear trends above and below 190°K are assumed, a least mean square analysis gives a macroscopic coefficient of expansion of $9\times10^{-6}$ per degree K above 190°K, and $0.5\times10^{-6}$ per degree K below that temperature. This is comparable with the dilatometric result of Trombe and Foex.[11]

## Erbium

The negatives for erbium had little background. Exposure times of eleven to twenty hours gave from twelve to twenty-three detectable metal lines. The structure of erbium metal was hexagonal, close-packed for all exposures. This structure has also been reported by Klemm and Bommer.[16] Their lattice constants, when revised as indicated previously, are in fair agreement with the values reported here.

Results of the x-ray exposures are summarized in Table III and Fig. 3. Assuming linear trends and using a least mean square analysis, the macroscopic coefficient of thermal expansion may be estimated as about $10\times10^{-6}$ per degree K above 100°K, and about zero below that temperature.

In general, it would appear that the unusual behavior of the $c_0$ parameter below the Curie point or magnetic anomaly is probably due to the internal fields of the domain and may be regarded as a form of magnetostriction due to that field. It also suggests that there is a correlation between the crystal directions and the directions of easy magnetization. This effect has been observed in other ferromagnetic elements. If the rare earth metals are similar to the hexagonal, close-packed phase of cobalt at room temperature, the direction of easy magnetization would be parallel to the $c_0$ axis.

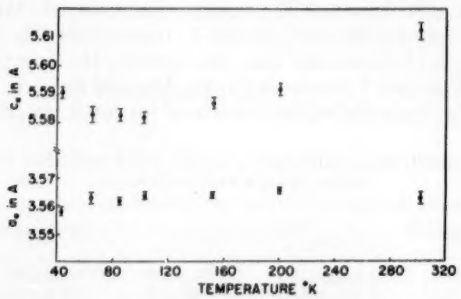


FIG. 3. Variation of the lattice parameters of erbium with temperature.

It should be noted that sodium chloride might be useful as a temperature index as well as an internal standard because of its large and relatively uniform expansion coefficient.

The authors wish to thank J. Powell for preparing the rare earth salts, and A. H. Daane, D. Dennison, and R. Barton for preparing the metal samples.

# Some Magnetic Properties of Dy Metal*

J. F. Elliott,† S. Legvold, and F. H. Spedding
*Institute for Atomic Research and Department of Physics, Iowa State College, Ames, Iowa*

(Received August 10, 1953; revised manuscript received January 25, 1954)

The magnetic moment of dysprosium has been measured in applied fields of 4000–18 000 oersteds, over the temperature range of 4.2–202°K. The susceptibility of dysprosium was found to be field dependent below about 175°K. Below 90°K, dysprosium appeared to have true though abnormal ferromagnetic properties, confirming the previous work of Trombe. At hydrogen and helium temperatures the magnetization isotherms fell below the 31°K isotherm. An absolute saturation magnetic moment of at least 8 Bohr magnetons was indicated by the data obtained in the temperature range of 31°K to 80°K. The magnitude of the measured values of the magnetic moment of dysprosium indicated that the orbital angular momentum of the 4*f* electrons contributes to the ferromagnetism.

## I. INTRODUCTION

THE magnetic properties of metallic dysprosium have been studied by Trombe[1–3] above 70°K. He has reported a magnetic anomaly at about 175°K. Below 175°K he notes that the susceptibility is field dependent and that the susceptibility *vs* temperature curve is such as to indicate an antiferromagnetic Curie temperature (Néel point) at 175°K. He further reports a transition to the ferromagnetic state at 85°K, this being the zero field ferromagnetic Curie temperature. This paper confirms the results of Trombe and extends the measurements to lower temperatures and higher fields.

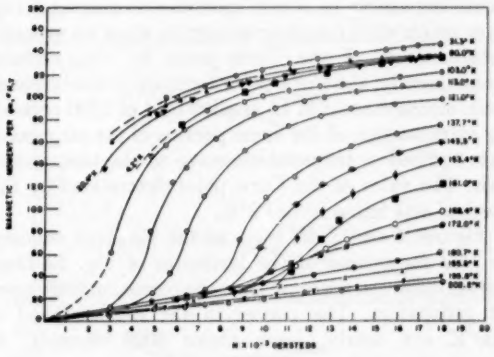

FIG. 1. Magnetic moment isotherms of dysprosium as a function of applied field.

The metal used in this study was prepared by methods previously reported.[4,5] Spectrographic analysis showed the following impurities: calcium, detectable but less than 100 ppm (parts per million); iron, detectable but less than 2000 ppm; holmium, detectable but less than 2600 ppm; erbium, detectable but less than 200 ppm; yttrium, detectable but less than 200 ppm; nickel, cobalt, and other rare earths not detected. Complete spectrographic standards for determining accurate quantitative amounts of impurities in dysprosium are not yet available; thus, the amounts of impurities cited are estimated upper limits.

The experimental procedure was similar to that used to measure the magnetic properties of gadolinium and is described elsewhere.[6,7]

## II. EXPERIMENTAL RESULTS

Figure 1 shows a number of the magnetic isotherms of dysprosium as a function of applied field. Figure 2 is an enlarged portion of the low field region of Fig. 1. The initial susceptibility (i.e., the susceptibility calculated from the low field linear portion of the curves in Fig. 2) from 113°–202°K plotted as a function of temperature is shown in Fig. 3. One notes in Figs. 1 and 2 that for applied fields up to 18 000 oersteds the magnetization *vs* $H$ isotherms remain linear down to about 175°K. Below 175°K the isotherms are linear

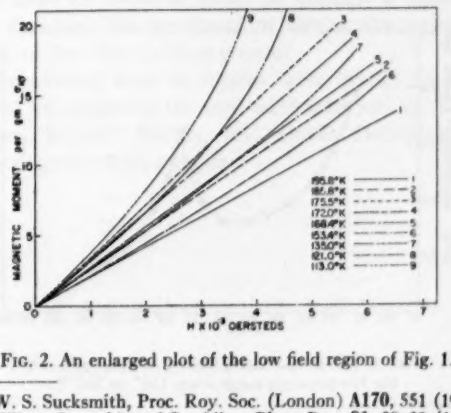

FIG. 2. An enlarged plot of the low field region of Fig. 1.

* Contribution No. 307 from the Institute for Atomic Research and Department of Physics, Iowa State College, Ames, Iowa. Work was performed in the Ames Laboratory of the U. S. Atomic Energy Commission.

† Now at General Electric, Syracuse, New York.

[1] F. Trombe, Compt. rend. **221**, 19 (1945).

[2] F. Trombe, J. phys. et radium **12**, 222 (1951).

[3] F. Trombe, Compt. rend. **236**, 591 (1953).

[4] Spedding, Voight, Gladrow, and Sleight, J. Am. Chem. Soc. **69**, 2777 (1947).

[5] F. H. Spedding and A. H. Daane, J. Am. Chem. Soc. **74**, 2783 (1952).

[6] W. S. Sucksmith, Proc. Roy. Soc. (London) **A170**, 551 (1939).

[7] Elliott, Legvold, and Spedding, Phys. Rev. **91**, 28–30 (1953).

in the low field region, but at some higher field the susceptibility becomes field dependent. As the temperature is lowered below 175°K, the susceptibility becomes field dependent in progressively lower fields.

Below 110°K the magnetization curves for dysprosium as shown in Fig. 1 are much the same as those of gadolinium,[6] and are nearly typical of a ferromagnetic substance. It is observed that the element is very magnetically "hard" in comparison to iron, or even gadolinium, and is far from saturation in a field of 18 000 oersteds. One also notes that below 103°K, dysprosium becomes rapidly temperature saturated, i.e., temperature has little effect upon the magnitude of the magnetization.

Of particular interest is the fact that the 20.4°K and the 4.2°K data fall below the 31.2°K isotherm.

The anomaly observed by Trombe is quite evident in Figs. 2 and 3. The general shape of the curve in Fig. 3 is not unlike the corresponding curve for an antiferromagnetic substance in the neighborhood of its Néel temperature.[8]

In order to discuss the magnetic behavior of dysprosium, four temperature regions or magnetic states may be distinguished. The first state *A* occurs above 176°K where the element appears to be truly paramagnetic. The second state (hereafter called state *B*) occurs in the temperature range bounded by the anomaly at 176°K and by the ferromagnetic Curie point at 92°K. (The Curie point determination is discussed below.) The magnetic behavior of dysprosium in this temperature range is characterized by the field dependence of the susceptibility, and the apparent lack of spontaneous magnetization.

The third magnetic state of dysprosium (hereafter called state *C*) occurs below about 92°K. Here the element appears to be in a true though abnormal ferromagnetic state, characterized by spontaneous magnetization, saturation effects, and hysteresis effects.

The fourth magnetic state for dysprosium (hereafter called state *D*) is in the temperature range below about

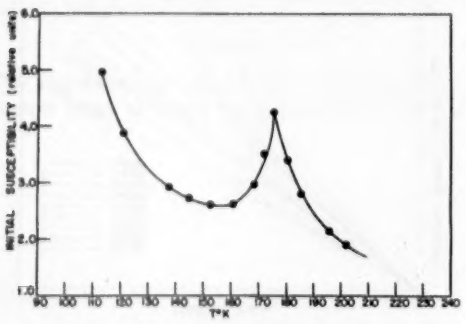


FIG. 3. The initial susceptibility of dysprosium in the temperature range from 110° to 200°K.

[8] F. Trombe, Compt. rend. 236, 591 (1953).

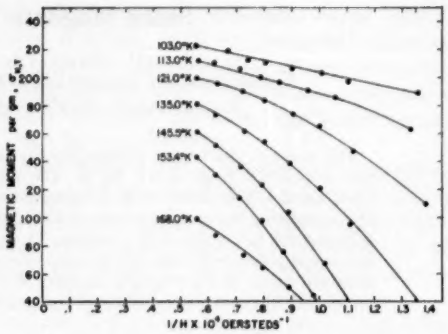


FIG. 4. Representative curves of the isothermal variation of the magnetic moment of dysprosium with $1/H$ in the temperature range 103° to 168°K.

25°K as indicated by the anomalous behavior of the isotherms in this temperature region.

The difficulty encountered in attempting to obtain the Curie point from spontaneous magnetization data may be seen from the magnetization curves (Fig. 1). In order to determine the Curie point by this method it is necessary to obtain spontaneous magnetization curves above and below the Curie point. Because of the strange behavior of dysprosium immediately above its ferromagnetic Curie point (i.e., in state *B*), it was found impossible to obtain spontaneous magnetization data which were complete enough to allow an accurate determination of the Curie point by this method. Consequently, the Curie point for state *C* was obtained from measurements in an applied field of 1200 oersteds by extrapolation of the linear portion of the magnetization squared *vs* temperature curve to the temperature axis. The value of the Curie point determined by this method was found to be 92°K.

Figures 4 and 5 are plots of the magnetic moment *vs* $1/H$ for several of the isotherms of Fig. 1. These curves differ considerably from the corresponding curves of gadolinium. The curves in the neighborhood of 100°K are nearly linear above 5000 oersteds. At temperatures above 100°K, the curves are concave downward. The curves below 80°K seem to consist of two nearly straight intersecting lines although it is also possible that the upward trend of the data at higher fields (low $1/H$) might continue. Both of the linear sections of the curves below 80°K have been extrapolated to infinite fields to estimate the saturation moments.

In Fig. 6 the saturation moments obtained from Fig. 5 are plotted as a function of $T^{\frac{1}{2}}$ to obtain the absolute saturation moment. The saturation moment at absolute zero for dysprosium appears to be about 299±5 cgs units if one uses saturation moments from the high field extrapolations, and about 273±3 cgs units, if one uses the low field extrapolated saturation moments. These moments correspond to 8.7 and 8.0 Bohr magnetons, respectively.

It is noted that these absolute saturation moments were obtained using data from the temperature range of 31°–80°K only, and therefore only attempt to point out what the approximate magnitude of the saturation moment at absolute zero would be assuming no anomalies between 0°–31°K. The magnitudes of the standard deviations cited are estimates based on attempts to fit various straight lines to the experimental data.

## III. DISCUSSION

The nature of the magnetization data for dysprosium particularly in the temperature range below 30°K might indicate ferromagnetism with two sublattices accounting for the decreasing saturation magnetization with decreasing temperature. On the other hand, it is also possible that a decrease in temperature could cause a change in the population of split 4f electron states of different magnetic moments.

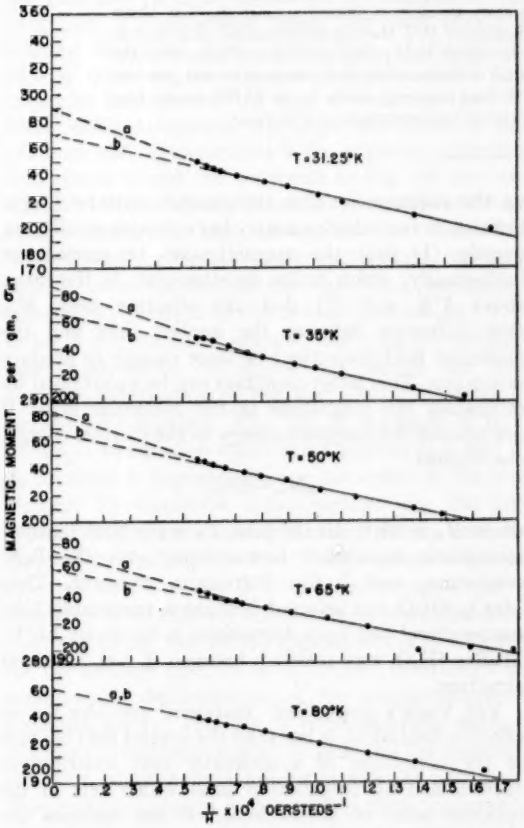


FIG. 5. Representative curves of the isothermal variation of the magnetic moment of dysprosium with $1/H$ in the temperature range 31° to 80°K.

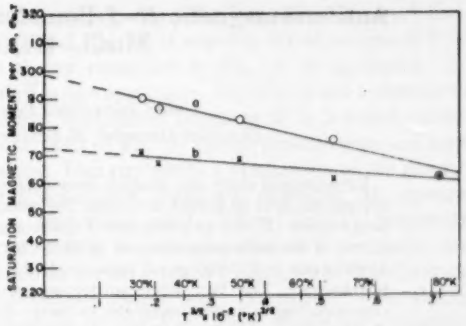


FIG. 6. The saturation magnetic moment of dysprosium as a function of $T^{\frac{1}{2}}$, open circles are values obtained from high field extrapolations and crosses are values obtained from low field extrapolations.

The high magnetic moment of dysprosium is of considerable significance. Magnetic moments have been measured of the order of 245 cgs units. Such a magnetic moment corresponds to about 7 Bohr magnetons. The spectrographic state of the dysprosium ion is a $^6H_{15/2}$, and from the paramagnetic theory of Hund and Van Vleck, one would expect an absolute saturation moment of 10 Bohr magnetons. These data indicate that the absolute saturation moment of dysprosium is probably not this large, which may be interpreted as meaning that the 4f electrons are not completely free from the influence of neighboring atoms. On the other hand, the measured values of the magnetic moment are much larger than the 5 Bohr magnetons expected on the basis of spin only.

While the above data suggest interesting modifications in the present theories of magnetism, we feel more data must be obtained before an attempt is made in this direction. We are therefore leaving the interpretation of the data for later papers.

The authors wish to express their thanks to Jack Powell for preparing the rare earth salts and to A. H. Daane, Richard Barton, and David Dennison for preparing the metal samples.

# Antiferromagnetic $H-T$ Boundaries and Apparent Molecular Fields for $MnCl_2 \cdot 4H_2O$ and $MnBr_2 \cdot 4H_2O$

WARREN E. HENRY
*United States Naval Research Laboratory, Washington, D. C.*

(Received December 18, 1953; revised manuscript received March 3, 1954)

Experimental study and analysis have been made of non-Brillouin magnetic moments of two hydrated manganous salts of similar structure. The moment ($M$) was measured as a function of field at constant temperature ($T$) and as a function of temperature at constant field ($H$). From the former, analysis of the extent of the nonsuperposition of $M(H/T)$ for different temperatures gave apparent molecular fields of 14 000 gauss and 18 000 gauss, respectively, for manganous chloride tetrahydrate and manganous bromide tetrahydrate. The Van Vleck antiferromagnetic exchange coefficient $\gamma$ is experimentally determined, corresponding to antiferromagnetic exchange energy densities of the order of $10^6$ ergs/cm$^3$. The constant field measurements gave points on antiferromagnetic transition curves such that $H_m/T_N$ was about 8000 gauss per degree for each salt. If the constant temperature moment is plotted against the Van Vleck parameter $(H-\gamma M)/T$ instead of the usual Brillouin parameter $H/T$ there is superposition of isotherms for points in the $H$-$T$ plane outside the antiferromagnetic region, thus giving experimental support to the Van Vleck model for simple antiferromagnetics. The method of measurement is the same as for our previous measurements. The temperature range was 1.3°–4.2°K and magnetic fields up to 58 000 gauss were applied, the greater part of the range being such as to prevent antiferromagnetic ordering.

## INTRODUCTION

THE magnitude of magnetic interaction has been estimated from high field magnetization measurements on $Mn^{++}$ ($^6S_{\frac{5}{2}}$ state for the free ion) in two manganous salts in which only a small effect of the crystalline electric field is to be expected and in which the anisotropy energy is small. This estimation is based on observation of the departures from a Brillouin function since previous measurements[1] of magnetization of salts with small interionic interactions have shown the applicability of the free spin Brillouin function for magnetic moments up to over 99.5 percent saturation for $Cr^{+++}$, $Fe^{+++}$, and $Gd^{+++}$. The Brillouin moment is given by

$$M = Ng\mu\left[(2S+1)\coth\frac{(2S+1)\mu H}{kT} - \coth\frac{\mu H}{kT}\right], \quad (1)$$

where $N$ is the number of paramagnetic ions, $g$ (having been taken as 2 for free spin and $J=S$) is the Landé factor, $\mu$ is the Bohr magneton, $S$ is the spin, $H$ is the magnetic field, $k$ is the Boltzmann constant, and $T$ is the absolute temperature. It can be noted from Eq. (1) that a necessary though not sufficient condition for the applicability of the formula is that $M$ be a function of $H/T$, implying superposition of magnetic moment isotherms. It has been observed both from adiabatic[2] and isothermal[3] moment measurements that copper sulphate pentahydrate is characterized by nonsuperposition of moment isotherms. This immediately suggests the possibility of using the extent of nonsuperposition of isotherms to estimate molecular fields.[4] A choice of substance to be used for study is based not only on the requirement that the ground state be simple but also on two other necessary but opposing conditions, namely (1) that the magnetization be carried out isothermally, which limits measurements to the range above 1°K and (2) that the effective field, $H_{eff}$ (the difference between the applied field and the molecular field projection) be large enough to produce saturation. This latter condition can be ascertained by estimating the magnitude of the molecular field: If one equates the magnetic energy to the thermal energy, one obtains

$$\mu H_m \sim kT_N, \quad (2)$$

where $H_m$ is the molecular field, $T_N$ is the Néel (antiferromagnetic transition) temperature, $\mu$ is the Bohr magnetion, and $k$ the Boltzmann constant. Thus $MnCl_2 \cdot 4H_2O$ was selected because a reasonable Néel temperature[5] had been determined to be about 1.6°K. $MnBr_2 \cdot 4H_2O$ was selected because it has a similar structure.

Van Vleck's generalized treatment[6] provides for an effective field which is less than the applied field because of the opposition of a molecular field contribution (determined by neighboring ions) which acts in the opposite sense of Weiss fields.[7] If one assumes the simplest case of one type of neighbor, i.e., two sublattices, and if one uses the simplified Van Vleck[8] treatment of this case, one has

$$H_{eff} = H_0 - \gamma M, \quad (3)$$

where $H_0$ is the applied field, $M$ is the magnetization and $\gamma$, the Van Vleck antiferromagnetic exchange

[1] W. E. Henry, Phys. Rev. **88**, 559 (1952).
[2] T. H. Gaballe and W. F. Giauque, J. Am. Chem. Soc. **74**, 3513 (1952).
[3] W. E. Henry, Phys. Rev. **87**, 1133 (1952).
[4] W. E. Henry, Phys. Rev. **90**, 492 (1953).
[5] S. A. Friedberg and J. D. Wasscher, Physica **19**, 1072 (1953).
[6] J. H. Van Vleck, J. Chem. Phys. **9**, 85 (1941); also see L. Néel, Ann. Phys. **17**, 64 (1932); **5**, 256 (1936); F. Bitter, Phys. Rev. **54**, 79 (1937).
[7] P. Weiss, J. phys. et radium **6**, 667 (1907).
[8] J. H. Van Vleck, J. phys. et radium **12**, 282 (1951).

coefficient, is given by

$$\gamma = ZA/(Ng^2\beta^2), \tag{4}$$

where $Z$ is the number of neighbors, $A/2$ is the antiferromagnetic exchange integral, $N$ is the density of magnetic ions, $g$ the Landé factor, and $\beta$ is the Bohr magneton. The first part of the investigation involved experimental investigation of magnetic moments of manganous chloride tetrahydrate and manganous bromide tetrahydrate as a function of magnetic field at selected constant temperatures. This enables one to plot $M$ against $H/T$, and to determine the dispersion in the magnetic moment isotherms; by analysis of the data over a considerable range, one may obtain a limiting molecular field contribution at saturation. This is taken as the apparent molecular field. This molecular field can now be used to obtain $\gamma$, the Van Vleck antiferromagnetic exchange coefficient in Eq. (3) since $\gamma M_0$ at saturation is the apparent molecular field. From $\gamma$ and the constants in Eq. (4) one can calculate $ZA$, which is the antiferromagnetic exchange energy density. To test the applicability of the Van Vleck model for simple antiferromagnetics, one may plot $M$ as a function of the Van Vleck parameter, $(H-\gamma M)/T$, instead of the Brillouin parameter, $H/T$ to see if the magnetic moment isotherms are brought into superposition. It should be pointed out that although substitution of the Van Vleck parameter in the moment equation [Eq. (1)] in the place of $H/T$ results in an equation which is not explicit in $H$ and $T$, no hardship is imposed, for one can arrive at the true moment by successive approximation. For the first approximation, one starts with the Brillouin moment (explicit in $H$, $T$) in the Van Vleck expression for the effective field Eq. (3). The moment so calculated is then used in the effective field for the second approximation, and so on. The second approximation is sufficient for the average case. It is of interest to attempt an experimental determination of the antiferromagnetic exchange energy. This can be done relatively easily if one has the exchange energy density and the magnetic structure which determines the number of neighbors. The exchange energy is determined from the experimental value of $\gamma$ and the magnetic structure can be obtained by a method such as that of Shull and Smart.[9]

The second part of the experiment consisted in measuring moments as a function of temperature at fixed constant fields. From these measurements one can obtain the field dependence of the antiferromagnetic transition temperatures. The transition temperature is taken to be the temperature at which

$$\left(\frac{\partial M}{\partial T}\right)_H = 0. \tag{5}$$

That is to say, from the Van Vleck theory,[8] the left member of Eq. (5) is negative for all values of $T$ when the theory embodied in Eq. (3) is applicable. If the theory is not applicable, i.e., if $\gamma$ is not a constant but becomes sufficiently larger as $T$ is lowered, then the left member of Eq. (5) can go through zero and become positive. This represents a breakdown of the theory for the paramagnetic phase and therefore the appearance of a transition point. These critical temperatures corresponding to various sufficiently low fields can be plotted in the $H$-$T$ plane to look for a transition curve predicted by Sauer and Temperley[10] and Garrett's extension[11] of the Van Vleck model and implied by Garrett's adiabatic experiments[12] on cobalt ammonium sulphate below 1°K. The advantage of using manganous salts here chosen is that isothermal conditions can be maintained and the $H$ intercept in the $H$-$T$ plane is taken as the molecular field by assuming that no spontaneous antiparallel alignment takes place at the absolute zero in an applied field greater than the aligning molecular field. Also, from the Van Vleck theory, if $H > H_m$, there is no failure of the theory. The $T$ intercept of the transition curve may be obtained by extrapolation of the curve to zero field. This is permissible since the points in this range fall on practically a straight line.

## EXPERIMENTAL PART

The relative moments were measured on a spherical aggregate of small crystals; the technique employed in our previous measurements[1] was used. The temperature of the sample was kept at desired points in the liquid helium range (1.3°−4.2°K) with the help of a metal Dewar for liquid helium. The magnetic field was produced by a Bitter type magnet which gave fields to over 58 000 gauss. The moment was measured by a differential fluxmeter which consisted of a ballistic galvanometer, a coil system, and a precision lift[13] for motion of the sample with respect to the coil system. Since manganous bromide tetrahydrate is more unstable than the chloride, extra precautions were taken. First, the salt is recrystallized from water at a temperature slightly above room temperature, to insure production of the proper hydrate; then the crystals are kept in a moist atmosphere until just before the experiment is performed. The remainder of the experiment is carried out with the usual care with respect to loss of water of hydration.

## INTERPRETATION OF RESULTS

The results are obtained for $MnCl_2 \cdot 4H_2O$ and $MnBr_2 \cdot 4H_2O$ from the measurement of moments as a

[9] C. G. Shull and J. S. Smart, Phys. Rev. **76**, 1256 (1949).

[10] J. A. Sauer and H. N. V. Temperley, Proc. Roy. Soc. (London) **A176**, 203 (1940).

[11] C. G. B. Garrett, J. Chem. Phys. **19**, 1154 (1951).

[12] C. G. B. Garrett, Proc. Roy. Soc. (London) **A206**, 242 (1951).

[13] W. E. Henry, National Bureau of Standards Circular No. 519, 1952 (unpublished), p. 237.

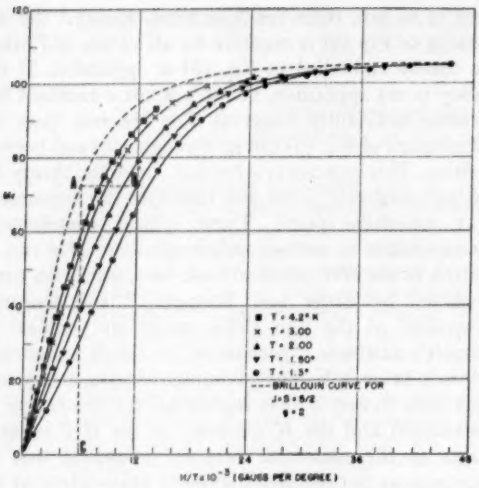


FIG. 1. Plot of relative magnetic moment ($M_r$) against $H/T$ for manganous chloride tetrahydrate.

function of field at constant temperatures and as a function of temperature at constant fields.

## Manganous Chloride Tetrahydrate

### *Field Dependence of Moment for Fixed Temperatures*

Figure 1 shows magnetic moment plotted against $H/T$. It is seen that

$$\left(\frac{\partial M}{\partial H}\right)_T \to 0 \tag{6}$$

at the high fields and low temperatures so that saturation is being approached. By estimating the saturation moment (very little different from the highest measured moment) one can draw a Brillouin curve from Eq. (1) with $S=J=5/2$ and $g=2$. Now it is seen from Fig. 1 that the isotherms do not superpose and that no isotherm falls on the theoretical Brillouin curve using the applied field in the argument. If it is assumed that an effective field is constructed from the applied field and a molecular field contribution, then the displacement of the experimental curve for a given temperature from the Brillouin curve is used to estimate the apparent molecular field as follows: An arbitrary test point is chosen on any of the five isotherms. From this arbitrary point, say point $B$ (Fig. 1) on the 1.50°K isotherm, one follows a constant moment line, $BA$, to the point $A$ on the Brillouin function where the value of $H/T$ is read at the point $C$. This value of $H/T$, when multiplied by $T$ (1.50°K in this case), gives the effective field, $H_{eff}$. The difference between the applied field and the effective field is taken as the contribution of the molecular field. This process is repeated for many arbitrary points on each isotherm. With these data, one is in position to apply the Van Vleck model for the effective field [Eq. (3)] and if one assumes $\gamma M$ to be the contribution of the molecular field,

$$\mathbf{H}_m = \gamma \mathbf{M}, \tag{7}$$

with $\gamma$ a constant, then the molecular field projection divided by the moment should be a constant over the range of applicability. We use the apparent molecular field contribution obtained by the graphical analysis mentioned previously, and find that

$$\mathbf{H}_m^{(i)}/\mathbf{M}^{(i)} = \text{constant} \pm 10 \text{ percent}, \tag{8}$$

over a very large range of temperatures and fields, corresponding to quadrupling $H/T$. The value of $\mathbf{H}_m^{(i)}$ corresponding to $\mathbf{M}_0$ (the saturation moment) is the apparent molecular field. As saturation is approached, the error becomes large and indeterminable but one may use the value of the constant in Eq. (8) to extrapolate the $\mathbf{H}_m^{(i)}$ to saturation to obtain an apparent molecular field of about 14 000 gauss. From this value of the molecular field we compute an antiferromagnetic exchange energy density from the Van Vleck model[8] for simple antiferromagnetics as follows: We take the experimental molecular field as $\gamma M_0$, where $M_0$ is the saturation moment (5 Bohr magnetons). The computed $\gamma$ is now substituted into Eq. (4) to compute $ZA$ (the antiferromagnetic exchange energy density). If $N$ in Eq. (4) is taken to be $6\times10^{21}$ ions/cm³ for manganous

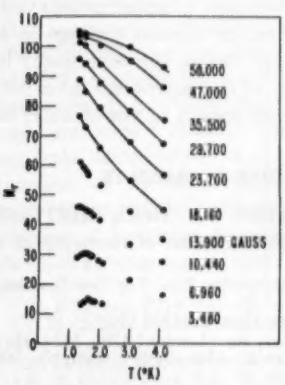


FIG. 2. Plot of relative magnetic moment ($M_r$) against temperature ($T$) for fixed fields ($H$) for manganous chloride tetrahydrate.

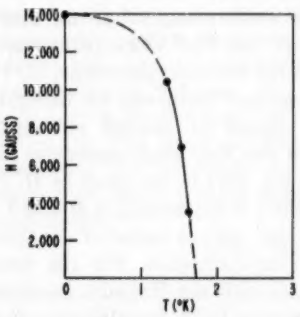


FIG. 3. Plot of critical field ($H$) against temperature ($T$) for manganous chloride tetrahydrate.

chloride tetrahydrate,[14] $ZA$ turns out to be $0.6\times10^6$ ergs/cm$^3$, $A/2N$ being the exchange integral and of the order of 2.5 cm$^{-1}/Z$ where $Z$ is the number of nearest neighbors.

### *Temperature Dependence of Moment for Fixed Fields*

The dependence of magnetic moment on temperatures for fixed fields is shown in Fig. 2. For low fields it is seen that a change in sign of the slope takes place in the temperature range used. Following the convention of Bizette, Squire, and Tsai[15] of looking for the maximum in susceptibility for monotonic change in temperature, we call the temperature at which Eq. (5) holds the transition temperature for the field $H$. Thus, by measuring the moment as a function of temperature for various fixed fields it is possible to obtain the field dependence of the antiferromagnetic transition temperature. While one cannot in practice obtain the moment for $T=0$ or $H=0$, it is possible to get these two intercepts ($H$ and $T$ intercepts) as follows: The apparent molecular field is taken as the critical field at absolute zero on the assumption that no spontaneous antiparallel alignment can take place in applied fields greater than the aligning field, namely, the molecular field. This is in accord with the Van Vleck model. Extrapolation of the experimental curve to zero field (the experimental curve seems to approach a straight line in this region) gives a critical temperature in zero field. Thus, one can plot a complete curve (Fig. 3) which serves as a boundary between the paramagnetic and antiferromagnetic regions in the $H$-$T$ plane. Having this separation between the antiferromagnetic and paramagnetic regions we can see whether or not this separation has a relation to the region of applicability of certain aspects of the Van Vleck theory of antiferromagnetic exchange. That is, we can now use a theoretical curve based on the Van Vleck parameter, $(H_0-\gamma M)/T$, as opposed to the Brillouin parameter, $H/T$ to test the applicability of the Van Vleck model. We do this by plotting $M$ against the Van Vleck parameter to obtain a theoretical curve. Now, all points in the $H$-$T$ plane not enclosed by the antiferromagnetic transition boundary fall on the theoretical curve Fig. 4.

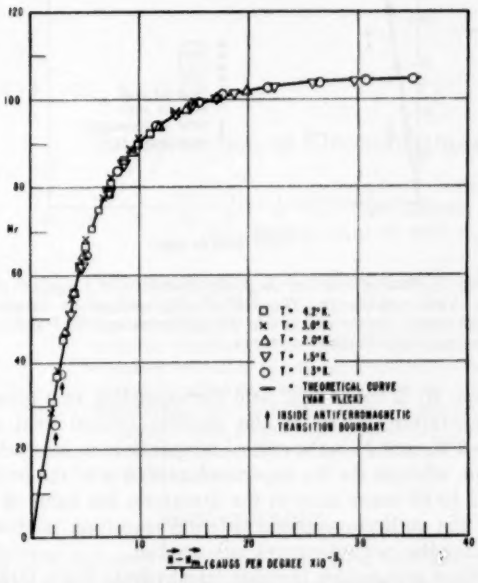


FIG. 4. Plot of relative magnetic moment ($M_r$) against the Van Vleck parameter $(H_0-\gamma M)/T$ for manganous chloride tetrahydrate. Points well inside the antiferromagnetic transition boundary are indicated by arrows.

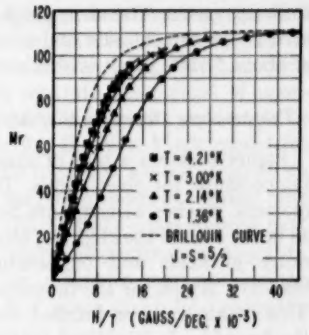


FIG. 5. Plot of relative magnetic moment ($M_r$) against $H/T$ for manganous bromide tetrahydrate.

## Manganous Bromide Tetrahydrate

### *Field Dependence of Moment for Fixed Temperatures*

A graphical representation of the field dependence of moment for fixed temperatures is shown for $MnBr_2\cdot4H_2O$ in Fig. 5. Although the highest moments for manganous bromide tetrahydrate do not come as near to exhibiting a vanishing slope as the chloride, saturation is sufficiently near to make a good approximation for the saturation moment and thus to construct a

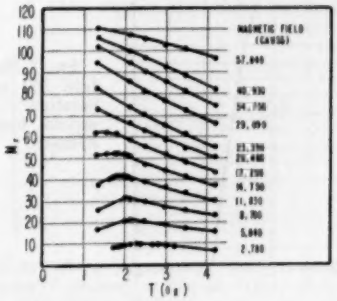


FIG. 6. Plot of relative magnetic moment ($M_r$) against temperature ($T$) for fixed fields ($H$) for manganous bromide tetrahydrate.

[14] National Research Council, *International Critical Tables* (McGraw-Hill Book Company, Inc., New York, 1926), Vol. I, p. 127.

[15] Bizette, Squire, and Tsai, Compt. rend. **207**, 449 (1938).

Brillouin curve. The same graphical technique is used here as for the chloride and a limiting molecular field of about 18 000 gauss is obtained.

*Temperature Dependence of Moment for Fixed Field*

Figure 6 shows a plot of magnetic moment against temperature for fixed fields. It is noticed that the moment reaches a maximum for the lower fields just as in the case of the chloride, but that there is a greater range of fields and temperatures in the antiferromagnetic region for the bromide than for the chloride. This makes a more detailed examination possible for the bromide. It is noticed that slopes of the curves at temperatures below the maxima are different for different fields, and lends support to the suggestion of Van Vleck[8] that the ratio of the average susceptibility at absolute zero to the susceptibility at the critical temperature is field dependent and might be expected in some cases to vary from $\frac{2}{3}$ to unity as higher and higher fields are applied.

Again taking the antiferromagnetic transition temperature corresponding to a given field as the point at which the slope of the moment curve goes through zero, we obtain a series of transition temperatures for the bromide. If the temperatures so obtained are plotted against the fields, one obtains a plot shown in Fig. 7, which represents the antiferromagnetic transition boundary in the $H$-$T$ plane for manganous bromide tetrahydrate. The apparent molecular field of 18 000 gauss is taken as the critical field for the suppression of antiparallel alignment at the absolute zero. It is of interest that Fig. 7 (as well as Fig. 3) shows the same qualitative features as the critical field curve for the suppression of superconductivity.[16] That is, in both cases, fields exceeding the appropriate critical fields prevent the spontaneous ordering which would otherwise occur. Let us assume that there exists an analytical expression for the two types of ordering of the form

$$H_c = H_0[1-(T/T_0)^n], \tag{9}$$

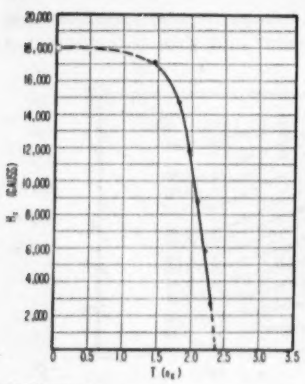


FIG. 7. Plot of critical field ($H$) against temperature ($T$) for manganous bromide tetrahydrate.

[8] D Shoenberg, *Superconductivity* (Cambridge University Press, Cambridge, 1952), p. 9.

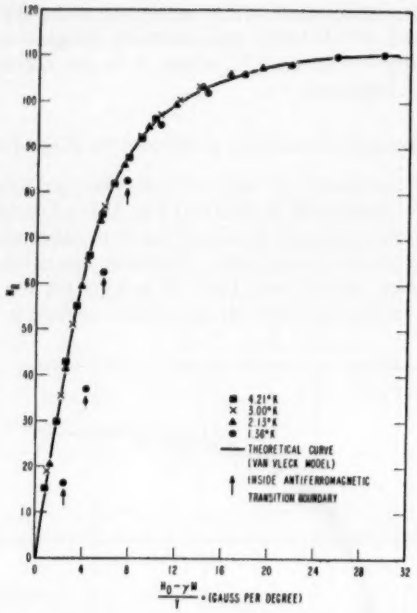


FIG. 8. Plot of relative magnetic moment ($M_r$) against the Van Vleck parameter $(H_0-\gamma M)/T$ for manganous bromide tetrahydrate. Points well inside the antiferromagnetic transition boundary are indicated by arrows.

where $H_c$ is the critical field corresponding to a given temperature $T$, $H_0$ is the limiting critical field at $T=0°$K, and $T_0$ is the critical temperature in zero field. Now, whereas for the superconductor, $n$ is of the order of 2 to fit many data in the literature, the value of $n$ for the antiferromagnetic ordering transition is about 5.3 for the two substances here studied.

Since manganous bromide tetrahydrate has a larger area in the antiferromagnetic region of the $H$-$T$ plane, one may see in bold relief the difference between the antiferromagnetic and paramagnetic regions with respect to the use of the Van Vleck parameter for the calculation of the moment; one uses the method of successive approximation and the product of the Van Vleck antiferromagnetic exchange coefficient and the Brillouin moment is taken as the first approximation to the molecular field contribution. Figure 8 is a plot of magnetic moment against the Van Vleck parameter, and it is seen that for all points outside of the antiferromagnetic transition boundary, the experimental points for all isotherms fall on the theoretical curve calculated from the Van Vleck model. If the points are well inside the antiferromagnetic transition boundary of Fig. 7, the points do not fall on the theoretical curve as illustrated in the points associated with arrows, but these points deviate more, percentagewise, the greater the distance inside the antiferromagnetic transition boundary.

## SUMMARY

Magnetization data have been obtained for two manganous salts. Analyses of these data for manganous chloride tetrahydrate and manganous bromide tetrahydrate have been carried out by (1) plotting magnetic moments against $H/T$ and observing nonsuperposition of magnetic moment isotherms, (2) construction of Brillouin curves from the saturation magnetization and determining graphically the departures of the moments from the Brillouin moments; from these departures, we obtain molecular fields, Van Vleck antiferromagnetic exchange coefficients and exchange energy densities, (3) plotting magnetic moments against temperature for fixed fields and determining geometrically the transition temperatures corresponding to these fields; this leads to antiferromagnetic transition boundary curves which separate the regions of spontaneous antiparallel alignment from the paramagnetic regions and, (4) subjecting the Van Vleck model for simple antiferromagnetics to critical examination which consisted in plotting magnetic moment against the Van Vleck parameter, $(H_0-\gamma M)/T$; this showed that the model for simple antiferromagnetics gives a quantitative evaluation of the magnetic moment for the group of points in the $H$-$T$ plane which lie outside the antiferromagnetic transition boundary.


PHYSICAL REVIEW VOLUME 94, NUMBER 5 JUNE 1, 1954

# Interpretation of Electroluminescence Effects in an Excited Phosphor*

FRANK MATOSSI
*U. S. Naval Ordnance Laboratory, White Oak, Maryland*

(Received September 10, 1953; revised manuscript received February 17, 1954)

The consideration of electron transitions between valence band, conduction band, and traps as presented by Randall and Wilkins' theory of luminescence growth is extended by including terms which take into account the emptying of traps by an electric field and the draining off of electrons by field-induced, nonradiative transitions. The result of the mathematical analysis corresponds to effects observed in a ZnS phosphor, embedded in a dielectric matrix, under the influence of a periodic electric field while continuously excited by ultraviolet radiation. These are a momentary illumination, an extinguishing effect, and the superposition of a ripple with twice the frequency of the field, whose amplitude decreases with increasing frequency. Some further observations are discussed qualitatively, utilizing the following assumptions: the draining effect ceases after some time; at low frequencies and for dc fields, a current effect counteracts the draining effect.

## INTRODUCTION

THE influence of an electric field on luminescence can be expected to reveal fundamental properties of phosphors. However, in spite of much experimental research in this field, or rather because of the abundance of complex results, the understanding of these processes is still very limited. The present paper attempts a theoretical approach to one particular electroluminescence effect, the change of light output of a continuously excited phosphor by alternating electric fields.

The observations referred to may be briefly summarized as follows:[1] A ZnS(Cu) phosphor, embedded in a dielectric matrix and excited to equilibrium output, is subjected to a sinusoidal electric field while the excitation continues. Then a momentary illumination ("electrically stimulated luminescence" = electric stimulation) is followed by an extinguishing effect ("electric quenching"). After this, the light output recovers slowly to a new equilibrium ("intermediate recovery"). Cutting the field off may stimulate a second momentary illumination ("cut-off stimulation"), after which the original equilibrium is finally attained again ("final recovery").

The essential features of the observations are schematically illustrated in Fig. 1 and Fig. 2. The large time scale of Fig. 2 reveals the superposition, upon the "basic effect" of Fig. 1, of a periodic "ripple" whose frequency is twice the frequency of the field. The amplitude of this ripple decreases with increasing

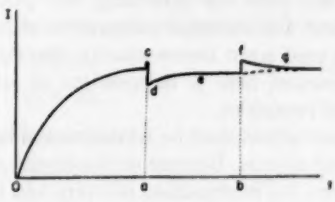


FIG. 1. Basic effect, schematical. $I$ = luminescent output; $t$ = time (in order of minutes); $a$: field on; $b$: field off; 0: ultraviolet on; $c$: electric stimulation; $d$: electric quenching; $e$: intermediate recovery; $f$: cut-off stimulation; $g$: final recovery at high (———) and at low (– – – –) frequencies.

* Presented at the Rochester Meeting of the American Physical Society, June, 1953 [Phys. Rev. **92**, 846 (1953)]. A preliminary account appeared in Naturwiss **40**, 239 (1953).

[1] G. Destriau and J. Mattler, J. phys. et radium **11**, 529 (1950); F. Matossi and S. Nudelman, Phys. Rev. **89**, 660 (1953). Similar results for decaying phosphors are reported by K. W. Olson, Phys. Rev. **92**, 1323 (1953).

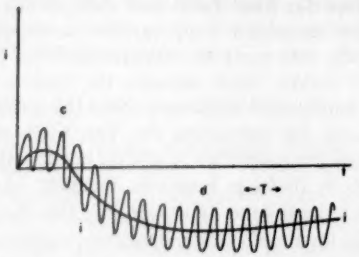


FIG. 2. Region $c$ and $d$ of Fig. 1 in large time scale. Ripple superimposed on basic effect, schematical. $T=2\pi/\omega$, $\omega$=frequency of field.

frequency at high frequencies. At low frequencies ($\omega$ about 200 cps), the amplitude reaches a maximum.

The time for reaching the peak of the electric stimulation is of the order of magnitude of a few periods of the field. It decreases, therefore, with increasing frequency. The minimum is reached very slowly compared to the time for the peak, but fast compared to the time of the intermediate recovery, which is of the order of magnitude of the growth time of the phosphor.

Phase shifts between field and ripple have not yet been measured, but observations with a decaying phosphor[2] seem to indicate that phase shifts exist and that they depend on frequency.

At low frequencies, up to several hundreds of cps, some of the results may have been influenced by "polarization effects" since dc experiments showed that a dc field ceases to be effective after about 1/100 of a second. No quenching was observed in a dc field.

It may be pointed out that the qualitative features of the above described observations seem to be a quite general property of ZnS and related phosphors. (Our own experiments refer to a DuPont ZnS-phosphor No. 1300 prepared as described previously[1] and excited by a dc ultraviolet source.) Only the quantitative details vary from sample to sample. This is in particular so for the effects at field removal, while for "field on" the observations of different investigators with different substances agree very well. For phosphors of short persistence, the stimulation effects are not observed, but only quenching.[3] Phosphors of very low conductivity do not show the quenching, but only Gudden-Pohl flashes.[4] The chemical composition of most of the phosphors used is not known exactly. But the interpretation presented here is independent of any specific contents of impurities.

The observations shall be related to the band model of sulfide phosphors. Because of the empirical relationship between the intermediate recovery and the growth curve, the theory of the growth curve, as given by Randall and Wilkins[5] seemed to be a reasonable starting point of a theoretical analysis.

[2] G. Destriau and J. Mattler, J. phys. et radium **13**, 205 (1952).
[3] G. Destriau, J. Appl. Phys. **25**, 66 (1954).
[4] G. Dechêne, J. phys. et radium **9**, 109 (1938).

## BASIC ASSUMPTIONS

As usual, the properties of the phosphor will be described by the distribution of electrons among the filled or valence band, the conducting band, and the traps. The electrons are excited by external radiation from emission centers in the valence band. For the purpose of this analysis, it is not necessary to consider separate impurity levels near the valence band.

The number of electrons in the conduction band may be designated by $N$; the number of traps, which is considered to be constant, by $n$; and the number of empty emission centers, by $m$. All these numbers refer to unit volume. Then the following equations govern the number of electrons in the conduction band and the number of empty traps $(n-m+N)$:

$$\begin{aligned} dN/dt&=\eta-A_1Nm-A_2N(n-m+N),\\ d(n-m+N)/dt&=-d(m-N)/dt\\ &=-A_2N(n-m+N). \end{aligned} \tag{1}$$

These equations are essentially identical with those of Randall and Wilkins.[5] $A_1$ and $A_2$ are two constants of the nature of transition probabilities, which, according to Randall and Wilkins, are of the same order of magnitude. $\eta$ is the number of electrons transferred per unit time to the conduction band by the exciting energy. The equations take into account the spontaneous transitions from the conduction band to the valence band or to the traps, assuming a "bimolecular" type of recombination.[6] But spontaneous (thermal) transitions from the traps to the conduction band are not included. Their explicit consideration is not necessary here, since we are not interested in temperature effects. With Randall and Wilkins, we assume $N$ to be small compared with $n$ and $m$, and the total number of centers to be larger than the number of traps. Equilibrium is reached if $m=n$.

The electric field disturbs this equilibrium. It seems to be reasonable to assume the following possibilities for the action of the field:

(a) The field may empty the traps. This would add a term of the form $\epsilon|\cos\omega t|$ in both Eqs. (1). $\epsilon$ is some function of the amplitude of the field strength[7] $E_0$. It is further assumed to be proportional to $m-N$, the

[5] J. T. Randall and M. H. F. Wilkins, Proc. Roy. Soc. (London) **A184**, 390 (1945).
[6] There is doubt whether the recombination is strictly of second order. But the applicability of a bimolecular approximation in the case of a phosphor during excitation seems to be assured also if other processes are assumed for the description of the decaying phosphor. See, e.g., D. Curie, Ann. phys. **7**, 746 (1952).
[7] The field is assumed to be $E=E_0\cos\omega t$. There may be a phase shift between the applied field and its effect on the traps, which is not considered here. It would not affect the essential results.

number of filled traps. It may or may not be proportional to $N$, depending on whether the emptying of traps is due to collisions with conduction electrons accelerated by the field or to processes independent of the conduction electrons. That collision processes may indeed be responsible for the excitation of electroluminescence effects, has recently been discussed by Curie[8] who removed one of the difficulties in understanding these processes for the low fields that apparently are effective in producing electroluminescence. But it is not necessary to specify the model in this respect since the particular form of $\epsilon=\epsilon(E_0,N)$ is immaterial. This gives the treatment the character of a phenomenological description rather than that of a specific physical interpretation. Similar considerations apply also to the other terms discussed hereafter.

Because the effect of the field is supposed not to depend on its direction, the absolute value of $\cos\omega t$ appears in the additional term. This may safely be approximated by $\cos^2\omega t$, in order to simplify the mathematical treatment. To be sure, there are directional effects observed, insofar as the cathode side of the phosphor seems to be the main seat of the phenomena.[9] However, the observations combine the light output of both surfaces of the phosphor, which alternately become cathodes.

(b) The mathematical analysis reveals that we have to introduce a term $-\beta\cos^2(\omega t+\varphi)$ in the equation for $dN/dt$ and that this term, which describes a loss of conduction electrons, must appear also as a loss of empty centers if results agreeing with experiment shall be obtained. Therefore, the term introduced here should be formally interpreted as describing "field-induced nonradiative transitions." Although again it is not necessary to think of a particular mechanism as the cause of the effect assumed here, we may imagine that the field drains conduction electrons to the surface where they may undergo nonradiative transitions to empty surface centers. Nonradiative transitions which would possibly occur also without the field are neglected. They are considered to be in equilibrium, not contributing to the net changes of electrons by the field. Formally, they may be included in the $\eta$ term.

The terms discussed above are sufficient to describe the ripple and the basic curve up to the beginning of the intermediate recovery. The other observations will be discussed in more general terms using the results of the analysis of the better understood parts of the effect as a frame of reference. This will lead to some additional information about the relative importance of the several terms during different stages of the effect. The uncertainty that will remain in the interpretation of the later parts of the basic curve does not affect the main results for the other parts of the observed effects.

[8] D. Curie, J. phys. et radium **13**, 317 (1952).
[9] W. W. Piper and F. E. Williams, Phys. Rev. **87**, 151 (1952).

## MATHEMATICAL ANALYSIS

According to the foregoing section, we have the following equations:

$$dN/dt=\eta-A_1Nm-A_2N(n-m+N)+\epsilon\cos^2\omega t-\beta\cos^2(\omega t+\varphi), \quad (2)$$

$$-dm/dt+dN/dt=-A_2N(n-m+N)+\epsilon\cos^2\omega t.$$

The emitted intensity is given by

$$I=A_1Nm,$$

if, as mentioned before, we assume the recombination process as "bimolecular."

We put $N=N_0+\Delta$, $m=m_0+\delta$, $I=I_0+i$ with $I_0=A_1N_0m_0$ [except in $\epsilon=\epsilon(N_0,m_0)$ and $\beta=\beta(N_0,m_0)$], where $N_0$ and $m_0$ shall satisfy the original Eqs. (1). $\Delta$ and $\delta$ are small deviations from the values $N_0$ and $m_0$, respectively, caused by the field. We assume that equilibrium is reached before the field is applied, so that $m_0=n$. For $I_0$, $N_0$, and $m_0$, we write again $I$, $N$, and $m$, respectively, in all succeeding equations.

We omit terms quadratic in $\Delta$ and $\delta$, and utilize the conditions $N\ll n$, $N\ll m$, $m=n$. The solution obtained for $\Delta$, $\delta$, and $i=A_1(N\delta+m\Delta)$ by standard and straightforward methods consists of a part $\tilde{i}$ that is periodic with frequency $2\omega$ and a nonperiodic part $\bar{i}$. We take up first the periodic part, which after a sufficient time is the only one remaining, apart from a constant. It corresponds, of course, to the ripple. We give the result for the periodic solution only for the case $\beta=0$, which is the only important one, as the discussion will show. See the general result in the Appendix.

We write

$$\tilde{i}=A_1(p\cos2\omega t+q\sin2\omega t),$$

and obtain

$$\sigma^2=p^2+q^2=\epsilon^2\frac{4\omega^4A_1^2m^4+\omega^2m^2[16\omega^4+A_1^2A_2^2N^2m^2]}{[16\omega^4+4\omega^2A_1^2m^2+A_1^2(A_2-A_1)^2N^2m^2]^2}, \quad (3)$$

$$q/p=(4\omega^2-A_1A_2Nm)/2\omega A_1m.$$

$\sigma$ measures the amplitude of the ripple; $q/p$, the phase shift against the field (or more accurately, against $\cos2\omega t$).

For small frequencies, we have

$$\sigma_0^2=\epsilon^2A_2^2\omega^2/(A_2-A_1)^4A_1^2N^2, \quad (\text{if } A_1\neq A_2);$$
$$\sigma_0^2=\epsilon^2N^2/16\omega^2, \quad (\text{if } A_1=A_2); \quad (4a)$$
$$(q/p)_0=-A_2N/2\omega.$$

For large frequencies,

$$\sigma_\infty^2=\epsilon^2m^2/16\omega^2, \quad (q/p)_\infty=2\omega/A_1m. \quad (4b)$$

From this, we see that for very large and for very low frequencies as well, $p$ disappears, so that there should be a phase shift of $\pm90°$ against $\cos2\omega t$. In between, at a certain critical frequency $\omega_0$, the phase

shift is zero. This critical frequency is given by

$$\omega_0=\tfrac{1}{2}(A_1A_2Nm)^{\frac{1}{2}}. \quad (5)$$

The amplitude decreases with $1/\omega$ if $A_1=A_2$. Or, if $A_1\neq A_2$, it may show a maximum at another critical frequency $\omega_m$, which is given by the equation

$$\omega^6+(1/4)\omega^6A_1^2m^2+(1/16)\omega^4A_1^3N^2m^2(6A_2-3A_1) -(1/64)\omega^2A_1^4N^2m^4(A_2^2+2A_1^2-4A_1A_2) -(1/256)A_1^4A_2^2N^2m^4(A_2-A_1)^2=0. \quad (6)$$

$\omega_m$ depends on the ratio $A_1/A_2$. For $A_1=2A_2$, for instance, we have $\omega_m\cong\frac{1}{2}A_1(Nm)^{\frac{1}{2}}$.

We now turn to the unperiodic part of the solution. The constants are determined so that $\Delta=0$ and $\delta=0$ for $t=0$. We have

$$\bar{\imath}=\mu_1[e^{-A_1Nt}-e^{-A_1mt}] +\mu_2[(N/m)(1-e^{-A_1Nt})-(1-e^{-A_1mt})], \quad (7)$$

in which the same approximations as before are applied, and where $\mu_1=\frac{1}{2}\epsilon(A_1/A_2)$, $\mu_2=\beta/2$.

The first term yields an intensity curve like that shown as curve "$a$" in Fig. 3. Its maximum occurs at

$$t_\epsilon=(1/A_1m)\ln(m/N). \quad (8)$$

The second term is also shown, as curve "$b$." It gives an extinguishing effect if $\mu_2$ is positive. The minimum of that curve is at $t_\beta=2t_\epsilon$. It is much less pronounced than the maximum of the $\epsilon$ term.

The superposition of both terms gives a curve with either one maximum only, near $t_\epsilon$, or one minimum only, near $t_\beta$, depending on the ratio $\mu_2/\mu_1$. The time $t_m$ of the extreme value of $\bar{\imath}$ is given by

$$t_m=(1/A_1m)\ln\left[\frac{m}{N}\,\frac{(\mu_2/\mu_1)-1}{(N\mu_2/m\mu_1)-1}\right]. \quad (9)$$

If the $\epsilon$ term prevails, we obtain curves like those shown as $c$ or $c'$ in Fig. 3, which are similar to those obtained experimentally for times before the intermediate recovery.

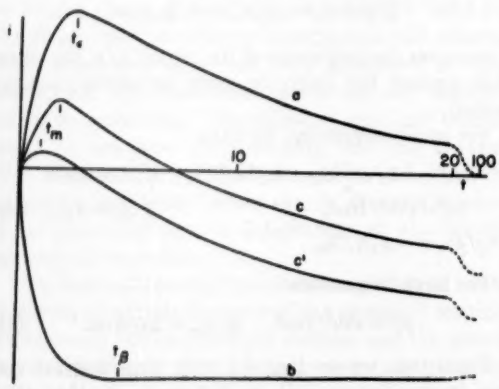


FIG. 3. Theoretical curves for basic effect. $a$: emptying effect in arbitrary units; $b$: draining-off effect; $c$: resultant effect $(a+\frac{1}{2}b)$; $c'$: resultant effect $(a+\frac{3}{2}b)$; $N/m=1/10$.

## DISCUSSION

### 1. Effects with Field "On"

From the results of the previous section, it is obvious that the general features of the observations are adequately described qualitatively, at least with respect to electrical stimulation, quenching, and ripple. The details depend, of course, on the numerical values of the controlling parameters, about which not much is known accurately enough.[10]

*Vice versa*, the results, particularly the expressions for the different critical frequencies or for the time at which the peak of the basic curve occurs, might be utilized to obtain better information about these parameters. In comparing the experimental and theoretical results, however, the interference of polarization effects has to be taken into account. This particularly applies to the ripple amplitude, where the maximum of $\sigma$ that is actually observed, probably has nothing to do with the maximum required by Eq. (6).

The results are derived for sinusoidal fields. One may think of discussing the effect of nonsinusoidal fields on the same basis applying Fourier analysis to the field and using for every component equations corresponding to Eq. (3). Actually, the results obtained by this method are at variance with the observations with square wave fields,[11] because the effective field is not identical with the applied field. Also in the sinusoidal case, of course, these fields will be different, but both can be supposed to be sinusoidal, and this is sufficient for the applicability of the results of the previous section.

We now want to discuss some more details of the observations in the light of the results gained above. As mentioned before, the unperiodic part of the theoretical solution agrees reasonably well with the shape of the basic curve as seen in the large time scale of Fig. 2. However, the observed minimum, as seen in Fig. 1, is obviously not described by this theory. This leads to the hypothesis that the draining-off effect is effective only over a certain time range. Formally, this interpretation can be expressed by admitting that $\mu_2$ in Eq. (7) is time dependent.[12] It may be imagined that after a certain number of field-induced nonradiative transitions has occurred, the available empty surface centers are filled, so that no further transitions

[10] Estimates of $A_1$ and $A_2$ differ within several orders of magnitude [see, e.g., F. Stoeckmann, Naturwiss **39**, 246 (1952)] and the same can be said about the ratio $A_1/A_2$. We have followed the data of Randall and Wilkins with $A_2\cong A_1$. If other data should be preferred, there would be no formal difficulty in solving the Eqs. (2). The fundamental results will not differ very much from those of our approximations. Equations (16) and (17) of the Appendix may serve as an example for this statement.

[11] S. Nudelman (unpublished).

[12] It can be considered as "slowly variable," so that $\beta$ may be retained as a constant in Eq. (2).

of this kind will take place. Any nonradiative transitions that would occur from this time on are considered to be in equilibrium and are, therefore, neglected as being immaterial, just as we have neglected such transitions from the beginning. The phosphor can now be considered as a "modified" one whose continued excitation would yield a growth curve like the original one but starting from another level and reaching another equilibrium. A more detailed picture of this phase of the basic curve would be premature.[13] But it may be said that, after equilibrium is reached, only the $\epsilon$ effect would remain, so that Eq. (3) and (6) or Eq. (16) of the Appendix may safely be used for the description of the ripple.

According to the observations, $t_m$ increases with decreasing frequency. In view of Eq. (9), this would mean that also $\mu_2/\mu_1$ decreases with decreasing frequency. The contribution of the $\beta$ effect should, therefore, become less important at low frequencies. This would be in agreement with the observation that in dc fields no quenching at all could be observed. A possible mechanism for this decrease of $\mu_2$ at low frequencies will be discussed farther below.

If the phosphor contains only few traps or none at all (phosphors of short persistence), we do not expect the $\epsilon$ effect to be present, which is in accordance with observations.[3] Of course, for any specific phosphor, even of long persistence, $\mu_2/\mu_1$ may be so large that the $\epsilon$ effect would not be manifest. On the other hand, the extinguishing effect may be weaker or even be absent if the conductivity is low, which would explain Dechêne's statement.[4]

### 2. Effects at Field "Off"

While so far the discussion seems to be on reasonably firm ground and has led to additional information about the presumed actions of the field, the electroluminescence effects at removing the field, i.e., the second momentary illumination followed by the final recovery, can be treated in very general terms only. The interpretation suggested is as follows.

Removing the external field restores the "modified phosphor" to its original properties, and the final recovery is the growth curve of the phosphor from the intermediate equilibrium to the original one. If there is no competing effect, the intensity will rise gradually, as it is observed at low frequencies (see the dotted curve of Fig. 1). Apparently, at such frequencies, this recovery is the only process taking place.

The momentary illumination which is observed at higher frequencies must then be due to another process. We may assume that there are, in the average, more electrons in the conduction band while the field is applied. These excess electrons may partly be due to those electrons that fail to recombine with the more or less localized holes because these electrons are moved by the field too fast across the region of a hole; partly they may be polarization charges piled up by the field near the surface; partly they may be produced by an effect considered by Krömer,[14] who showed that the tilting of the boundaries of the conduction band by the field results in an increase of the electron density. The polarization effect is probably the main contribution to the number of excess electrons. If the external field is removed, the excess electrons are released for transitions, producing a luminescent flash.[15]

But why does this effect not operate at lower frequencies, where no cut-off stimulation is observed? It is remarkable in this respect that this stimulation diminishes with decreasing frequency faster than the first stimulation and the quenching do. More light on this problem may be shed by discussing some results with dc fields described presently.

The most significant result of the application of a dc field was the production of excess illumination only, without any trace of a quenching effect. The initial excess output gradually decreased with a time constant in the order of magnitude of several hundredths of a second. No flash at removal of the field occurred. The fading off may easily be ascribed to polarization effects of some kind which need not be specified. But if we remember that the quenching effect could still be observed at 60 cps, we would expect that the dc field, although fading out, would last long enough to give at least some indication of the $\beta$ effect if there was one at all at $\omega=0$.

This contradiction may be reconciled with our picture if we assume that for $\omega=0$ the loss of electrons by the draining-off effect is compensated by electrons drawn into the phosphor from the electrodes, maintaining a constant electron density or a constant current. Thus, the draining effect would be made ineffective, while the emptying effect remains. Moreover, this "current effect" would also remove all excess electrons so that cutting the field off will not have any effect.

The existence of currents is, of course, not surprising in a semiconductor. But what is important in relation to the problem discussed here is the possibility of drawing electrons off or into the phosphor particle. At low frequencies, this will be a source for compensating any electron losses or excesses at one place by contributions from other, more distant parts of the phosphor. At higher frequencies, however, the current does not have this far-reaching effect.

The current effect acts in addition to any polarization effects (effects caused by more or less localized space charges that diminish the effective field) which alone would yield only a gradual decrease of all luminescence

[13] The complexity of the processes involved during the intermediate recovery can also be seen from the discussion of the field and temperature dependence of the intermediate equilibrium by Destriau and Mattler (see reference 1).

[14] H. Krömer, Z. Physik **134**, 435 (1953).

[15] The interpretation of experiments with electroluminescent Sylvania lamps leads to the same conclusion. See F. Matossi and S. Nudelman, Helv. Phys. Acta **26**, 573 (1953) and D. Curie, J. phys. et radium **14**, 672 (1953).

phenomena because of the decreased effective field, but not a selective action on some of them. It may be easily understandable that the combination of the two effects will have different results for the quenching and for the cut-off stimulation because of the different origin which we assumed for these two phenomena (field-induced nonradiative transitions and release of excess electrons, respectively). Furthermore, we understand that the individual behavior of a specific phosphor is governed by the relative importance of the several field actions considered above. This may depend on the specific contents of impurities and the method of preparation.

Whatever the correct interpretation of the effects at "field off" may be, it will probably not invalidate the conclusions reached for the stimulating and quenching effects at the beginning of the actions of the electric field. As the essential result of these considerations, therefore, it may be stated that trap emptying and inducing nonradiative transitions are the main actions of an electric field causing the phenomena observed in some ZnS-phosphors while under the simultaneous influence of the field and excitation by radiation.


## ACKNOWLEDGMENTS

I thank Mr. Sol Nudelman of this Laboratory for many discussions and for providing some as yet unpublished data.


## APPENDIX

The differential equations for $\delta$ and $\Delta$ have the form

$$\begin{aligned} d\delta/dt &= a\Delta+b\delta+c+d\cos 2\omega t+f\sin 2\omega t,\\ d\Delta/dt &= a\Delta+g\delta+h+k\cos 2\omega t+f\sin 2\omega t, \end{aligned} \tag{12}$$

with

$$\begin{gathered} a=-A_1m,\quad b=-A_1N,\quad c=-\tfrac{1}{2}\beta,\quad d=-\tfrac{1}{2}\beta\cos 2\varphi,\\ f=\tfrac{1}{2}\beta\sin 2\varphi,\quad g=(A_2-A_1)N,\quad h=(\epsilon-\beta)/2,\\ k=\tfrac{1}{2}(\epsilon-\beta\cos 2\varphi). \end{gathered}$$

The general solution can be written as

$$\begin{aligned} \delta &= A+B_1e^{\rho_1 t}+B_2e^{\rho_2 t}+C\cos 2\omega t+D\sin 2\omega t,\\ \Delta &= A'+B_1'e^{\rho_1 t}+B_2'e^{\rho_2 t}+C'\cos 2\omega t+D'\sin 2\omega t, \end{aligned} \tag{13}$$

where $A$ to $D'$ are constants that depend on $\omega$ and the other parameters. $\rho_1$ and $\rho_2$ are solutions of the equation

$$(\rho-a)(\rho-b)=ag.$$

In our approximation we have

$$\rho_1=-A_1m,\quad \rho_2=-A_1N, \tag{14}$$

if $A_2$ is not too different from $A_1$.

For the periodic part of the solution we have

$$i=A_1(p\cos 2\omega t+q\sin 2\omega t),$$

with

$$p=NC+mC',\quad q=ND+mD',$$

and

$$\begin{aligned} C &= (1/M)[-8\omega^3f-4\omega^2(ak+bd)\\ &\quad +2\omega fa(b-g)+a^2(b-g)(k-d)],\\ C' &= (1/M)[-8\omega^3f-4\omega^2(ak+gd)\\ &\quad -2\omega fb(b-g)-ak(b-g)^2],\\ D &= (d/2\omega)-(1/2\omega M)[8\omega^3f(a+b)\\ &\quad +4\omega^2(a^2k+abk+adg+b^2d)+a^2d(b-g)^2],\\ D' &= (k/2\omega)-(1/2\omega M)[8\omega^3f(a+g)\\ &\quad +4\omega^2(a^2k+agk+adg+bdg)\\ &\quad +2\omega fa(b-g)^2+a^2k(b-g)^2],\\ M &= 16\omega^4+4\omega^2(a^2+2ag+b^2)+a^2(b-g)^2. \end{aligned} \tag{15}$$

These formulas can be simplified some more by again taking advantage of the smallness of $N$.

The unperiodic part of the solution was obtained by using the conditions $A+B_1+B_2=0$ and $A'+B_1'+B_2'=0$. This introduces new integration constants, $-C$ and $-C'$, into Eq. (13). In deriving Eq. (7), the approximations must not be applied too early, but in the final result only.

Similar results are obtained also with other assumptions with respect to $N$. If $N\gg m-N$, for instance,[16] we have (for $A_1=A_2$)

$$p=-6\epsilon\omega^2A_1N/M',\quad q=2\epsilon(2\omega^3-A_1^2N^2\omega)/M',$$

$$M'=(4\omega^2+2A_1^2N^2)^2, \tag{16}$$

$$i=(\epsilon/2)(e^{-A_1Nt}-e^{-2A_1Nt})-(\beta/2)(1-e^{-2A_1Nt}). \tag{17}$$

Equation (16) is valid for $\beta=0$ only.

[16] G. F. J. Garlick, in *Solid Luminescent Materials* (John Wiley and Sons, Inc., New York, 1948), pp. 87 ff. In equilibrium, $N\cong m$.

# Graphical Representation of the Semiconductor Hall Effect

L. P. HUNTER
*International Business Machines Corporation, Poughkeepsie, New York*
(Received February 2, 1954)

The semiconductor Hall effect is represented in terms of an ellipse relating the Hall mobility and resistivity. Various uses and extensions of this representation are given which serve to correlate the important features of the Hall effect in semiconductors. The effects of excess current carrier lifetime and the nonequality of Hall and drift mobility ratios are discussed.

DUNLAP[1] has given a graphical representation of the semiconductor Hall effect in terms of an ellipse (Fig. 1) relating the Hall mobility $\mu=R/\rho$ and $\rho$ at constant temperature. This representation is limited to samples in which the excess carrier lifetime is infinitesimal and the Hall mobility ratio equals the drift mobility ratio, but it still serves to correlate the most important features of the Hall effect in semiconductors. Various uses and extensions of this representation will be given in the present paper.

Following Dunlap we define the Hall coefficient $R$ and the resistivity $\rho$ as

$$R=\frac{p-b^2n}{e(p+bn)^2}, \quad \frac{1}{\rho}=e(p+bn)\mu_p. \tag{1}$$

Proper algebraic manipulation gives the ellipse

$$\frac{[\frac{1}{2}(\mu_n-\mu_p)+\mu]^2}{(\mu_n+\mu_p)^2/4}+\frac{\rho^2}{1/(4e^2\mu_n\mu_p np)}=1, \tag{2}$$

where $p$=density of free holes, $n$=density of free electrons, $\mu_p$=mobility of free holes, $\mu_n$=mobility of free electrons, $b=\mu_n/\mu_p$, $\mu=R/\rho$, and $e$=electronic charge.

The product $np$ is constant for a given temperature regardless of the conductivity type.

Equation (2) is plotted in Fig. 1 showing the various relationships involved. It is seen that the origin of Hall mobility $\mu$ is not at the center of the ellipse unless the mobility ratio $b=1.0$. For the case illustrated, $b=1.5$ and the Hall mobility ($\mu_i$) of a sample which is intrinsic for this temperature would be negative and equal to $\frac{1}{3}$ of the electronic mobility. The value of the intrinsic resistivity $\rho_i$ corresponding to the mobility $\mu_i$ is seen to be equal to the resistivity of a sample which has zero Hall mobility at this temperature (point $B$, Fig. 1). A $p$-type sample which at this temperature falls between the points $B$ and $I$ will have a resistivity greater than intrinsic resistivity. In the familiar resistivity-temperature plot of Fig. 3B there is a region of temperature where the measured resistivity exceeds the intrinsic value. If an ellipse is constructed for some temperature in this range, the sample represented by the data of Fig. 3B would fall in the region of resistivity overshoot shown in Fig. 1. This effect has been noted in data in the literature.[2,3]

A similar overshoot of the Hall coefficient is also shown by this model. If we ask for the locus of points in the plane of Fig. 1 which represents a fixed value of the intrinsic Hall coefficient $R_i$, we must pass an equilateral hyperbola through the intrinsic point $I$ since $R=\mu\rho$. This hyperbola intersects the ellipse in two points $A$ and $I$. Any sample which falls between these two points will show a Hall coefficient which is greater than the intrinsic Hall coefficient at the same temperature.

So far we have considered the ellipse as significant only at a fixed temperature. If we recognize that the choice of the scales of $\mu$ and $\rho$ is arbitrary and independent, it is clear that we can normalize these variables in such a way that we eliminate their temperature dependence. To do this we will plot $\mu'=\mu/\mu_p$ against $\rho'=\rho/\rho_i$. If now the mobility ratio is independent of temperature, we can consider a single ellipse and its associated hyperbola as representing all samples of the same mobility ratio for all temperatures. This will allow us to interpret Hall and resistivity data with considerable facility.

In Fig. 2 is shown the effect of mobility ratio on both the resistivity and Hall coefficient overshoot. Here it is seen that the resistivity overshoot increases steadily for increasing $b$ and occurs only in $p$-type

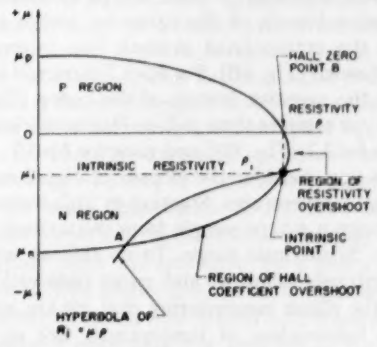


FIG. 1. Variation of Hall mobility $\mu=R/\rho$ with $\rho$ at a constant temperature for the mobility ratio $b=1.5$.

[1] W. C. Dunlap, Phys. Rev. **79**, 286 (1950).

[2] L. P. Hunter, Phys. Rev. **91**, 579 (1953).

[3] P. G. Herkart and J. Kurshan, RCA Rev. **14**, 427 (1953).

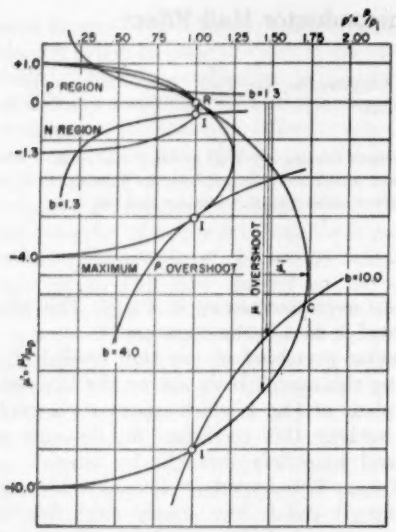


FIG. 2. Variation of Hall mobility with resistivity for several values of mobility ratio $b$.

samples. The equation relating the ratio $\rho_{max}/\rho_i$ to $b$ and the absolute value of $\mu_p$ is easily derived. From equation (2) the maximum value of $\rho$, $\rho_{max}$, is seen to be $[1/(4e^2n_i^2\mu_p^2b)]^{\frac{1}{2}}$, where $n_i^2=np$. Also from Eq. (1), $\rho_i=1/[en_i\mu_p(b+1)]$, since in the intrinsic range $n=p=n_i$. The ratio then becomes

$$\rho_{max}/\rho_i=(b+1)/2b^{\frac{1}{2}}. \tag{3}$$

The behavior of the Hall coefficient overshoot is much more complex. For small mobility ratios we must consider both branches of the hyperbola. When this is done, it can be seen that for $p$-type samples with mobility ratios less than 1.46, the extrapolated intrinsic Hall coefficient line will intersect the positive branch of the curve as is shown in Fig. 3A, but there will be no overshoot in the negative branch of the curve. For values of $b$ between 1.46 and 3.7 there will be no overshoot in the negative branch of the curve for $p$-type samples nor will the extrapolated intrinsic line intersect the positive branch (Fig. 3B). For $b>3.7$ there will be overshoot in the negative branch of the curve (Fig. 3C). With $n$-type samples there will be Hall coefficient overshoot for $b<3.7$ (Fig. 3D) and none for $b>3.7$.

Let us now consider the ellipses of Fig. 2 as representing all temperatures. Starting at high temperature we will trace a $p$-type sample from the intrinsic region well into its extrinsic range. To do this we will start at the intrinsic point, $I$, and move counterclockwise around the ellipse remembering that we are assuming $b$ to be independent of temperature. Let us choose $b=10$ as our example. Since $\rho'=\rho/\rho_i$, we will relate the variations along the ellipse to the intrinsic lines in the $1/T$ plot of Fig. 3C. Considering first resistivity variations, we will start on the intrinsic line at very high temperatures and will have exceeded intrinsic resistivity by 75 percent when we reach the maximum resistivity value of the ellipse. As we proceed along the ellipse we come to the point $B$ which is the Hall zero. The resistivity at point $B$ is exactly equal to the intrinsic value so that we see that the point of intersection $D$ of the resistivity curve in Fig. 3C with the extrapolated intrinsic resistivity line must occur at the temperature of the Hall zero. Proceeding beyond $B$ on the ellipse the resistivity falls rapidly below the intrinsic value as we enter the extrinsic region.

Considering now the Hall coefficient variation for the same sample, we note that there is also a Hall coefficient overshoot as we leave the intrinsic point. The intersection point $E$ of Fig. 3C occurs at the second intersection point $C$ of the hyperbola and the ellipse in Fig. 2. This is seen to be near the maximum of the resistivity overshoot. The maximum value of the Hall overshoot is seen to be about $R/R_i=1.21$ from Fig. 2. Since the other branch of the hyperbola is quite remote from the $P$ region of the ellipse, the extrinsic $R$ value levels off far below the intrinsic line, $R_i$, in Fig. 3C.

Similar reasoning applies to $n$-type samples as one moves clockwise from the intrinsic point of the ellipse with decreasing temperature.

The correlations shown here are very useful in interpreting Hall and resistivity data. For example, it is often desirable to calculate the energy gap in a semiconductor from the slope of the intrinsic Hall or resistivity line.[1] If a sizable overshoot is present, a large error will be made unless it is properly accounted for. If the mobility ratio is known, an ellipse can be constructed and the overshoot determined. The true extrapolated intrinsic line may then be constructed from the data using the proper overshoot. The accuracy of this determination of the slope of the intrinsic line will thus be improved.

For use in interpreting Hall and resistivity data the

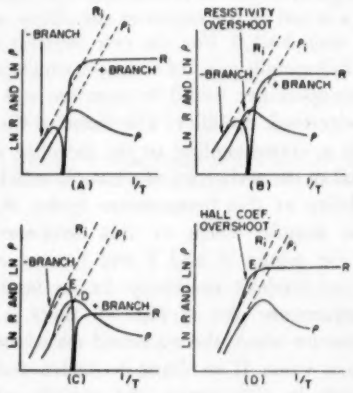


FIG. 3. Variation of the natural logarithms of the Hall coefficient and resistivity as functions of $1/T$ for; (A) $p$-type sample, $b=1.3$; (B) $p$-type sample, $b=2.5$; (C) $p$-type sample, $b=10$; (D) $n$-type sample, $b=2.5$.

curves of Fig. 4 have been computed from the elliptical construction. In the upper two curves the Hall coefficient overshoot and crossover point are plotted as a function of mobility ratio for the negative $\mu$ side of the ellipse. The Hall coefficient overshoot is defined as the maximum value of $R/R_i$ in the region of overshoot (Fig. 1), and the Hall coefficient crossover point is defined by the ratio of resistivities $\rho_i/\rho$ at the temperature of the point $E$ of Fig. 3C or 3D which corresponds to point $A$ of Fig. 1. At the mobility ratio $b=3.7$ the intrinsic point $I$ and the point $A$ of Fig. 1 coincide and the hyperbola is tangent to the ellipse. Below $b=3.7$ this Hall overshoot occurs in $n$-type samples only (Fig. 3D), and above $b=3.7$ this Hall overshoot occurs in the negative branch of the Hall curve for $p$-type samples (Fig. 3C).

At this point it should be emphasized that all of the above considerations apply quantitatively only under the conditions of:

1. infinitiesimal excess carrier lifetime;
2. mobility ratio $b$, independent of temperature;
3. the drift mobility ratio, $b$, = Hall mobility ratio, $b_H$.

The first condition can be met in practice by the proper choice of the geometry of the sample coupled with a surface treatment giving a high recombination velocity. The second condition can be met or, at least, corrected for by determining $b$ as a function of temperature. In this connection it should be mentioned that in the example of germanium the mobility ratio varies as $T^{0.8}$. Between 300° and 400°K, where most practical work is done with this semiconductor, $b$ increases from 2.10 to 2.37. This corresponds to approximately a 15 percent increase in crossover resistance ratio. From this it seems that a correction for the temperature variation of $b$ is not difficult for germanium.

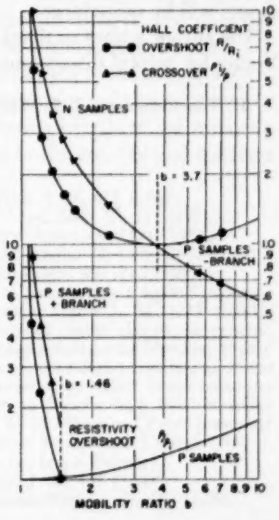


FIG. 4. Hall and resistivity overshoot as a function of mobility ratio.

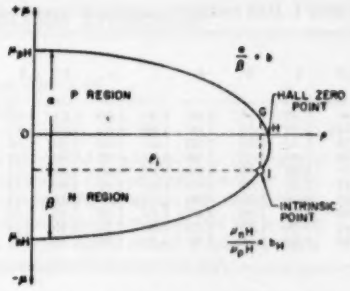


FIG. 5. The relation of the Hall zero point to the intrinsic point when $b \neq b_H$.

The third condition that $b=b_H$ must be considered in some detail.

We will now show that taking proper account of $b$ and $b_H$ without assuming them equal still leaves us with an ellipse. Equation (1) becomes

$$R=\frac{\mu_{pH}}{\mu_p}\frac{p-bb_Hn}{e(p+bn)^2}, \quad \frac{1}{\rho}=e(p+bn)\mu_p. \tag{4}$$

Proper algebraic manipulation gives an ellipse equivalent to that of Eq. (2):

$$\frac{[\frac{1}{2}(\mu_{nH}-\mu_{pH})+\mu]^2}{(\mu_{nH}-\mu_{pH})^2/4}+\frac{\rho^2}{1/(4e^2\mu_n\mu_pnp)}=1. \tag{5}$$

The only difference being the substitution of the Hall mobilities $\mu_{nH}$ and $\mu_{pH}$ for the drift mobilities $\mu_n$ and $\mu_p$ in the first term. The essential difference between this ellipse and the ellipse of Fig. 1 is that the Hall zero point and the intrinsic point no longer occupy symmetrical positions of equal resistivity value on the ellipse. In Fig. 5 the new relationship is shown. The case shown is for $b_H<b$; here the Hall zero point $H$ falls in the region of resistivity overshoot. If $b_H>b$, the Hall zero point $H$ will fall on the other side of the resistivity crossover point $G$. The intrinsic point $I$ is determined by dividing the mobility axis of the ellipse into two lengths, $\alpha$ and $\beta$, whose ratio, $\alpha/\beta$, equals the drift mobility ratio $b$, as shown. A line parallel to the resistivity axis is drawn through this dividing point until it intersects the ellipse at the intrinsic point $I$.

From the foregoing discussion it is clear that only in the case that $b=b_H$ will the resistivity crossover point fall at the same temperature as the Hall zero. The equilateral hyperbola of constant $R_i$ passing through the intrinsic point will still have the $\rho$ and $\mu$ axes for asymptotes. This means that the Hall coefficient crossover and overshoot are functions of both $b$ and $b_H$, while the resistivity overshoot is a function of $b$ alone. In Table I are given values of the Hall coefficient overshoot as a function of both $b$ and $b_H$.

We can use the intrinsic resistivity $\rho_i$ and the sample resistivity $\rho_0$ at the temperature of the Hall zero, to

TABLE I. Hall coefficient maximum overshoot.

| $b/b_H$ | 1.0 | 2 | 3 | 4 | 5 | 6 | 7 | 8 | 9 | 10 |
|---|---|---|---|---|---|---|---|---|---|---|
| 1.0 | ∞ | 1.59 | 1.152 | 1.04 | 1.00 | 1.00 | 1.01 | 1.02 | 1.04 | 1.05 |
| 2.0 | 2.245 | 1.19 | 1.04 | 1.00 | 1.00 | 1.02 | 1.04 | 1.07 | 1.10 | 1.12 |
| 3.0 | 1.76 | 1.12 | 1.02 | 1.00 | 1.01 | 1.04 | 1.07 | 1.10 | 1.13 | 1.15 |
| 4.0 | 1.60 | 1.09 | 1.01 | 1.00 | 1.01 | 1.04 | 1.08 | 1.11 | 1.14 | 1.17 |
| 5.0 | 1.52 | 1.08 | 1.00 | 1.00 | 1.01 | 1.05 | 1.08 | 1.12 | 1.15 | 1.18 |
| 6.0 | 1.47 | 1.07 | 1.00 | 1.00 | 1.02 | 1.05 | 1.09 | 1.12 | 1.16 | 1.19 |
| 7.0 | 1.45 | 1.06 | 1.00 | 1.00 | 1.02 | 1.06 | 1.10 | 1.13 | 1.17 | 1.19 |
| 8.0 | 1.43 | 1.06 | 1.00 | 1.01 | 1.02 | 1.06 | 1.10 | 1.13 | 1.17 | 1.20 |
| 9.0 | 1.41 | 1.05 | 1.00 | 1.01 | 1.03 | 1.06 | 1.10 | 1.14 | 1.17 | 1.20 |
| 10.0 | 1.40 | 1.05 | 1.00 | 1.01 | 1.03 | 1.06 | 1.10 | 1.14 | 1.16 | 1.21 |

give a relation between $b$ and $b_H$. The condition for the Hall zero is

$$nbb_H = p. \tag{6}$$

The condition for the intrinsic point is

$$n = p. \tag{7}$$

Since $1/\rho$ is proportional to $nb+p$, we will evaluate $nb+p$ at the two points using the conditions 6 and 7 and the relation $np$ and $n_i^2$.

At the Hall zero,

$$nb+p = nb+nbb_H = n_i(1+b_H)(b/b_H)^{\frac{1}{2}} \sim 1/\rho_0. \tag{8}$$

At the intrinsic point,

$$nb+p = nb+n = n_i(b+1) \sim 1/\rho_i \tag{9}$$

giving

$$\frac{\rho_0}{\rho_i} = \frac{b+1}{b_H+1}\left(\frac{b_H}{b}\right)^{\frac{1}{2}}. \tag{10}$$

With $b$ given, the resistivity overshoot can be determined from Eq. (3) and the proper intrinsic line constructed on the resistivity plot. The value of $\rho_0/\rho_i$ can then be measured at the temperature of the Hall zero and $b_H$ computed from Eq. 10.

The effect of a finite lifetime of excess current carriers[4] is shown in Fig. 6 for the case of $b=b_H$. The cases of infinite and infinitesimal lifetimes are contrasted. All cases of finite lifetime would lie between. It is seen that the primary effect is to distort the ellipse in such a way that the Hall zero moves into the region of resistivity overshoot, and in the case of infinite lifetime coincides with the maximum overshoot. This is a situation similar to that obtaining for $b>b_H$ with infinitesimal lifetime. Since this is the case, care must be taken to keep the lifetime short if one is interested in determining the relation between the $b$ and $b_H$ by means of the relative positions of the intrinsic point and the Hall zero.

## CONCLUDING REMARKS

The foregoing analysis has proven very useful in fitting Hall and resistivity data to the usual semiconductor model. It was this analysis that revealed the lack of agreement between good data and the traditional Hall effect model and caused Landauer and Swanson to develop their recent theory of the Hall effect for finite lifetime semiconductors.[4] It should prove useful in analyzing the new III–V group semiconducting compounds since the mobility ratio seems quite high[5] in these materials and hence the Hall and resistivity overshoots will be quite large.

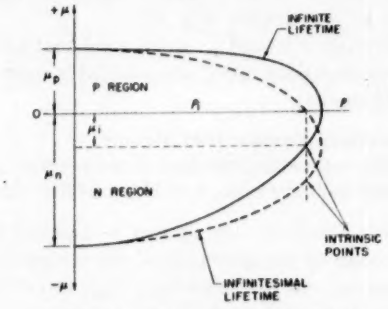


FIG. 6. Comparison of the infinite and infinitesimal lifetime relations.

The author wishes to thank J. A. Swanson and D. R. Young for helpful discussions.

[4] R. Landauer and J. Swanson, Phys. Rev. **91**, 555 (1953).

[5] M. Tanenbaum and J. P. Maita, Phys. Rev. **91**, 1009 (1953).

# Extension of the Theory of the Junction Transistor

EDMUND S. RITTNER
*Philips Laboratories, Irvington on Hudson, New York*
(Received December 24, 1953)

An examination of the validity range of the Shockley theory reveals that it is applicable to the emitter and collector regions for all current values of interest, whereas it is valid in the base region only for very small currents. In the present paper the treatment of the base region is extended so as to apply to arbitrary injection level and to include the effect of surface recombination. Two predictions are made: (a) the surface recombination velocity should increase with injection level; and (b) the alpha cut-off frequency for a transistor with plane parallel junctions should increase with emitter current by a factor of two.

## I. INTRODUCTION

A SIMPLE physical theory of the junction transistor was presented by Shockley in 1949.[1] This theoretical treatment had the unusual merit of preceding by a period of two years the first experimental realization and study of the device.[2] In the course of reporting[2] these experiments, the theory was somewhat further elaborated. Since that time only minor extensions or modifications of the physical theory have been published; Steele[3] has restated the theory concisely with slight modification of the treatment of the frequency response; Early[4] has made the point that space charge widening of the collector junction with collector voltage has important consequences in the small-signal behavior; and Hall[5] has attempted to extend the theory to cover power transistors.[6]

The simplicity of the Shockley theory follows primarily from the restriction of the treatment to low injection levels (i.e., levels for which the density of minority carriers is much smaller than the density of majority carriers) and to one-dimensional flow of charge carriers. The first of these restrictions is presumed to permit neglect of all conduction currents relative to diffusion currents. The validity of this procedure is examined in some detail in Sec. III, based upon a general formulation[7,8] of the problem of the injection of minority carriers into a semiconductor (see Sec. II). Our conclusion is that Shockley's procedure is indeed valid provided that the dimension of the specimen is large compared to the diffusion length of the minority carrier, a condition fulfilled in the emitter and collector regions but not in the base. In the latter case the neglect of the electric field is justified only for very small injection levels. Moreover, on translating the injection level conditions into electric current terminology, it turns out that Shockley's theory is applicable to the emitter and collector regions for all realizable values of current, whereas it is applicable to the base region only for extremely small currents.[9]

In order to extend the theory to cover currents of the magnitude commonly employed we present in Sec. IV a steady-state solution in the base region for arbitrary injection level subject, however, to the restriction of no recombination. (An estimate of recombination effects is deferred to Sec. VI.) In Sec. V the solution in the base is combined with Shockley's solutions in the emitter and collector regions to yield the steady-state current-voltage relations of a *p-n-p* transistor, which are then briefly discussed.

Section VI is devoted to the problem of recombination in the base. First (paragraph A) we estimate the recombination current by a perturbation method and thereby learn that for carefully prepared base material surface recombination is much more important than volume recombination. Moreover, this calculation permits us to account for the magnitude of alpha experimentally observed as well as the initial increase in $\alpha$ with emitter current[2,10,11] resulting from the buildup of a field which aids the transit of minority carriers. The decrease in $\alpha$ with emitter current occurring at still higher values of the latter[10,11] is attributable mainly to a decrease in emitter efficiency as has already been pointed out by Webster.[6] Also, a secondary contribution to this decrease may result from an increase in surface recombination velocity with injection level, which is a consequence of a recent theory by Brattain and Bardeen[12] of the surface recombination process. Then in paragraph B we present a three-dimensional theory in the spirit of Shockley's approach, which is

[1] W. Shockley, Bell System Tech. J. **28**, 435 (1949).
[2] Shockley, Sparks, and Teal, Phys. Rev. **83**, 151 (1951).
[3] E. L. Steele, Proc. Inst. Radio Engrs. **40**, 1424 (1952).
[4] J. M. Early, Proc. Inst. Radio Engrs. **40**, 1401 (1952).
[5] R. N. Hall, Proc. Inst. Radio Engrs. **40**, 1512 (1952).
[6] While this manuscript was in preparation a second paper by J. M. Early appeared [Bell System Tech. J. **32**, 1271 (1953)] dealing extensively with small-signal design theory. In general, this treatment follows along the same lines as the Shockley theory with some extensions in the directions of high-frequency and base resistance effects. Also it has recently been called to our attention that an extension of the theory to include high level injection effects has been carried out by W. M. Webster. [Paper presented at Transistor Research Conference, Penn. State College (July 6, 1953); Proc. Inst. Radio Engrs. (to be published)].
[7] C. Herring, Bell System Tech. J. **28**, 401 (1949).
[8] W. van Roosbroeck, Bell System Tech. J. **29**, 560 (1950).
[9] It is worth mentioning that comparison between theory and experiment (reference 2) has been made with sufficiently small applied voltages so that the above condition applied.
[10] Law, Mueller, Pankove, and Armstrong, Proc. Inst. Radio Engrs. **40**, 1352 (1952).
[11] D. A. Jenny, Proc. Inst. Radio Engrs. **41**, 1728 (1953).
[12] W. H. Brattain and J. Bardeen, Bell System Tech. J. **32**, 1 (1953).

TABLE I. Partial list of symbols used.

| Symbol | Meaning |
|---|---|
| $p_0$, $p_b$ | Equilibrium hole density in a semiconductor, in an $n$-type base region. |
| $n_0$, $n_i$, $n_e$, $n_c$ | Equilibrium electron density in a semiconductor, in an intrinsic semiconductor, in a $p$-type emitter region, in a $p$-type collector region. |
| $N_d$, $N_a$ | Density of donor centers, of acceptor centers. |
| $L_p$, $L_e$, $L_c$ | Diffusion length of holes in an $n$-type semiconductor, of electrons in a $p$-type emitter region, of electrons in a $p$-type collector region. |
| $w$, $2a$ | Width of base region, length of side of square of transistor cross section. |
| $\tau_p$, $\tau_n$, $\tau_0$ | Volume lifetime for arbitrary injection of holes into $n$-type material, of electrons into $p$-type material, volume lifetime of minority carriers for low injection levels. |
| $\tau_p'$, $\tau_e$ | Combined surface and volume lifetimes for arbitrary injection of holes into $n$-type material, of electrons into $p$-type emitter region. |
| $s$, $s_0$ | Surface recombination velocity for arbitrary injection level, for low injection level. |
| $J_{ne}$, $J_{nc}$; $J_{pe}$, $J_{pc}$ | Electron component of emitter current density, of collector current density; hole component of emitter current density, of collector current density. |
| $V_e$, $V_c$ | dc bias potential relative to base on emitter, on collector. |
| $I_e$, $I_c$, $I_r$ | Emitter current, collector current, recombination current in base. |
| $i_e$, $i_c$, $v_e$, $v_c$ | Small-signal emitter current, collector current, emitter voltage, collector voltage. |
| $A$, $A_s$ | Conduction area, area available for surface recombination. |

applicable in the base region for plane parallel junctions and for very small injection levels. This calculation permits precise numerical evaluation of the diminution factor $\beta$ as a function of the surface recombination velocity as well as an appraisal of the accuracy of the results of the perturbation calculation under very low injection level conditions.

Finally, in Sec. VII we take up the problem of the frequency response to a very small sinusoidal signal in the presence of either an extremely small or a large steady injection level. In the first of these cases we show that the injection factor, $\gamma$, has a negligible influence on the alpha cut-off frequency. In the second case we first neglect the injection factor but take into account the possibility of transit time dispersion resulting from surface recombination effects at high emitter currents. For values of the surface recombination velocity not exceeding a known upper limit this transit time dispersion proves to be negligible. Under these circumstances the alpha cut-off frequency should increase monotonically with emitter current reaching a limiting value at high currents just twice the low current value. We then consider the possible effects of the injection factor and find that this might cause the cut-off frequency to decrease slightly with increasing emitter current.

The scheme that has been adopted with respect to notation is illustrated by the partial list of symbols shown in Table I. In addition, the symbol $\mu$ has been employed for charge carrier mobility, $D$ for diffusion constant, $b$ for the ratio of electron to hole mobility, and $q$ for the electronic charge; other symbols are defined in the text as required.

A compilation of assumed numerical values of geometric and material parameters, which have been used throughout the paper for illustrative computation, is given in Table II.

## II. FORMULATION OF THE PROBLEM OF INJECTION OF MINORITY CARRIERS INTO A SEMICONDUCTOR

The problem of the injection of minority carriers into a semiconductor has been studied theoretically by Herring[7] and by van Roosbroeck.[8] In this section we shall recapitulate the main results of their formulation in a form suitable for subsequent use in this article.

The equations governing the behavior of injected minority carriers and the excess majority carriers drawn in to neutralize space charge are as follows:

$$\partial p/\partial t = -(p-p_0)/\tau_p - q^{-1}\,\mathrm{div}J_p,$$
(continuity equation for holes) (1)

$$\partial n/\partial t = -(n-n_0)/\tau_n + q^{-1}\,\mathrm{div}J_n,$$
(continuity equation for electrons) (2)

$$J_p = q\mu_p pE - qD_p\,\mathrm{grad}p,$$
(definition of current density of holes) (3)

$$J_n = q\mu_n nE + qD_n\,\mathrm{grad}n,$$
(definition of current density of electrons) (4)

$$J = J_p + J_n,$$ (definition of total current density) (5)

$$\mathrm{div}E = (4\pi q/\epsilon)(p-n+N_d-N_a)$$
(Poisson equation for semiconductor with completely ionized impurities). (6)

These six equations constitute an exact formulation of the problem.

To simplify the problem it is assumed that:

(a) electrons and holes disappear by mutual recombination at identical rates, i.e.,

$$(p-p_0)/\tau_p = (n-n_0)/\tau_n; \quad (7)$$

TABLE II. Assumed values of geometric and material parameters (appropriate to germanium) for illustrative computation.

| | |
|---|---|
| $w$ | $5.0\times10^{-3}$ cm |
| $a$ | $1.76\times10^{-2}$ cm[a] |
| $A$ | $4a^2=1.24\times10^{-3}$ cm$^2$ |
| $A_s$ | $8aw=7.04\times10^{-4}$ cm$^2$ |
| $D_p$ | 44 cm$^2$/sec |
| $D_n$ | 93 cm$^2$/sec |
| $n_i$ | $2.5\times10^{13}$/cm$^3$ |
| $p_b$ | $1.25\times10^{13}$/cm$^3$ |
| $n_e=n_c$ | $4.0\times10^{9}$/cm$^3$ |
| $s_0$ | 400 cm/sec |
| $\tau_0$ | $5\times10^{-4}$ sec |
| $L_e=L_c$ | $10^{-2}$ cm |

[a] This seemingly weird choice greatly facilitates the determination of the roots of Eq. (87).

(b) space charge neutrality is preserved at every point,

$$p-n+N_d-N_a=0, \tag{8}$$

which has as a consequence:

$$\partial p/\partial t=\partial n/\partial t, \tag{9}$$

$$\text{grad}p=\text{grad}n. \tag{10}$$

(Although Herring[7] has presented a convincing argument that the approximation represented by Eq. (8) is an excellent one, it is perhaps useful to demonstrate that div$E$ is indeed negligible for each solution based upon its use.)

It follows from the preceding equations that

$$\text{div}J=0, \tag{11}$$

and also for an $n$-type semiconductor with $N_a \ll N_d$ that

$$E=\frac{J-qD_p(b-1)\,\text{grad}p}{q\mu_p\{p(b+1)+bN_d\}}, \tag{12}$$

$$J_p=\frac{pJ-qbD_p(2p+N_d)\,\text{grad}p}{p(b+1)+bN_d}, \tag{13}$$

$$\frac{\partial p}{\partial t}+\frac{p-p_0}{\tau_p}=-\text{div}\left[\frac{pJ-qD_pb(2p+N_d)\,\text{grad}p}{q\{p(b+1)+bN_d\}}\right]. \tag{14}$$

This last equation reduces for the one-dimensional case to:

$$-\{\partial p/\partial t+(p-p_0)/\tau_p'\}=\frac{1}{qbN_d\{1+p(b+1)/bN_d\}^2}$$
$$\times[J(\partial p/\partial x-qbD_pN_d\{1+p(b+1)/bN_d\}$$
$$\times(1+2p/N_d)(\partial^2 p/\partial x^2)-qD_p(b-1)(\partial p/\partial x)^2]. \tag{15}$$

Here $\tau_p'$ is written instead of $\tau_p$ to take account of the effect of surface recombination in the one-dimensional theory.

In general, the procedure is to find a solution to (14) or (15) satisfying the boundary conditions and to put this back into (13) in order to obtain the current-voltage relations. This is usually an extremely difficult feat owing to the nonlinearity of the differential equation unless further simplification can be achieved with the use of additional restrictions.

## III. VALIDITY RANGE OF SHOCKLEY'S THEORY

Shockley[1,2] has greatly simplified the problem for the case of low-level injection ($p/N_d \ll 1$) and one-dimensional flow of carriers by dealing only with Eqs. (1) and (3) for injection into an $n$-type semiconductor (or with (2) and (4) for injection into $p$-type material) and by assuming that the conduction current is negligible relative to the diffusion current, i.e., $E=0$. In this case the resulting differential equation for $p(x,t)$ is

$$\partial p/\partial t+(p-p_0)/\tau_p'=D_p\partial^2 p/\partial x^2, \tag{16}$$

and the expression for the current density is simply

$$J_p=-qD_p\partial p/\partial x. \tag{17}$$

Although Eq. (13) readily reduces to (17) for the condition $p/N_d \ll 1$, this is not the case with respect to Eq. (15), which does not reduce to (16) for this condition but rather to

$$\frac{\partial p}{\partial t}+\frac{p-p_0}{\tau_p'}=\frac{-J\partial p/\partial x+qbD_pN_d\partial^2 p/\partial x^2+qD_p(b-1)(\partial p/\partial x)^2}{qbN_d}. \tag{18}$$

Indeed, Eq. (16) cannot be valid unless the terms in (18) involving $(\partial p/\partial x)$ are negligible. It therefore becomes of interest to check whether Shockley's solutions satisfy Eq. (18) to a good approximation without the imposition of additional conditions.

For a semi-infinite ($0<x<\infty$) $n$-type semiconductor (representing either emitter or collector regions) and for steady-state conditions the solution to (16) is

$$p-p_0=(p_1-p_0)e^{-x/L_p}, \tag{19}$$

where $p_1$ is the appropriate boundary value of $p$ at $x=0$ and $L_p=(D_p\tau_p')^{\frac{1}{2}}$. Equations (17) and (19) yield

$$J_p=qD_p(p_1-p_0)/L_p. \tag{20}$$

The condition $p/N_d \ll 1$ thus requires that

$$J_p \ll qN_dD_p/L_p. \tag{21}$$

Now, trying (19) as a steady-state solution of (18), we obtain

$$\frac{p-p_0}{\tau_p'}=\frac{J(p-p_0)/L_p+qbD_pN_d(p-p_0)/L_p^2+qD_p(b-1)\{(p-p_0)/L_p\}^2}{qbN_d}. \tag{22}$$

Thus, we find that (19) is indeed a solution of (18) provided that

$$(b-1)(p-p_0)/bN_d \ll 1, \tag{23}$$

$$J \ll qbN_dD_p/L_p. \tag{24}$$

Equation (23) is obviously satisfied by the low-level injection condition; however, Eq. (24) represents a more severe restriction than (21) owing to the fact that the total currents flowing through the emitter and collector regions are much larger than the currents injected from the base into the emitter or from the collector into the base. Nevertheless, numerical evaluation of (24) with the use of values of $N_d$ and $L_p$ appropriate to well-doped emitter and collector regions (see

Table II) reveals that this condition is satisfied provided that the total emitter (or collector) current is small compared to about 25 amperes. Hence, it is clear that Shockley's treatment of the emitter and collector regions represents a valid approximation for all realizable values of current. That this is the case is in part a consequence of the fact that the terms involving the first derivative,

$$dp/dx=-(p-p_0)/L_p, \tag{25}$$

are very small.

However, the situation in the base region is quite different. For an $n$-type semiconductor of finite width $w$ the steady-state solution to (16) may be written in the form

$$p-p_0=\frac{(p_1-p_0)\sinh((w-x)/L_p)+(p_2-p_0)\sinh(x/L_p)}{\sinh(w/L_p)}, \tag{26}$$

where $p_2$ is the boundary value of $p$ at $x=w$. The corresponding current density expression (evaluated at $x=0$) is

$$J_p=(qD_p/L_p)\{(p_1-p_0)\coth(w/L_p)-(p_2-p_0)\operatorname{csch}(w/L_p)\} \tag{27}$$

$$\cong qD_p(p_1-p_0)/L_p \quad (\text{for } w/L_p\ll 1,\ p_1\gg p_0\gg p_2). \tag{28}$$

Thus, again the condition $p/N_d\ll 1$ leads to condition (21).

Now, trying (26) as an approximate solution of (18), we find that the solution is valid provided that

$$J\ll qbN_dD_pw/L_p^2, \tag{29}$$

$$(b-1)(p-p_0)L_p^2/bN_dw^2\ll 1. \tag{30}$$

Both conditions require smaller current densities than is called for by (21). Equation (30) is the more stringent of the two conditions and implies that Eq. (26) can be justified only for extremely small injection levels such that $p/N_d\ll(w/L_p)^2$, corresponding to

$$J\ll qN_dD_pw^2/L_p^3. \tag{31}$$

The reason for this is that the terms involving the first derivative,

$$dp/dx\cong-(p-p_0)/w, \tag{32}$$

are no longer negligible when $w$ becomes small compared to the diffusion length $L_p$.

Putting numbers into (31) appropriate to relatively pure base material (see Table II) we find that Shockley's solution in the base is valid only for total emitter currents small compared to about $4\times10^{-6}$ ampere. Thus, it is important that existing theory be extended so as to apply to currents of the order employed technically.

## IV. STEADY-STATE SOLUTION IN THE BASE REGION FOR ARBITRARY INJECTION LEVEL NEGLECTING RECOMBINATION

It is clear from the fact that the current amplification factor in junction transistors is quite close to unity that recombination cannot be a very important process in the base region. If recombination is completely neglected, then a solution to the steady-state problem of the flow of minority carriers in the base region may be readily obtained for arbitrary injection level.

Although it is possible to derive the desired result starting with the general equation (15), it proves to be more convenient to return to the fundamental equations (1)–(6) inclusive. With the neglect of recombination and for the steady-state case (1) and (2) become

$$\operatorname{div}J_p=0, \tag{33}$$

$$\operatorname{div}J_n=0. \tag{34}$$

Furthermore, since neglecting recombination renders the carrier flow strictly one-dimensional, Eqs. (33) and (34) lead to

$$J_p=\text{constant}, \tag{35}$$

$$J_n=\text{constant}. \tag{36}$$

The value of $J_n$ is known immediately from the boundary conditions to be

$$J_n=J_{ns}-J_{nc}. \tag{37}$$

Since Shockley's theory is valid in the emitter and collector regions, we may express (37) for $p$-type material as[13]

$$J_n=qD_n(n_1-n_e)/L_e+qD_n(n_1-n_e)/L_e, \tag{38}$$

where the index 1 refers to boundary values at the emitter-base and at the base-collector junctions, respectively. Returning now to the fundamental equations it follows from (3), (4), (8), and (10) that

$$E=\frac{J_p+qD_pdp/dx}{q\mu_pp}=\frac{J_n-qbD_pdp/dx}{qb\mu_p(p+N_d)}. \tag{39}$$

Solving (39) for $dx$, we obtain:

$$dx=-\frac{qD_p}{J_p}\left\{\frac{(2p+N_d)dp}{p(1-J_n/bJ_p)+N_d}\right\}. \tag{40}$$

Direct integration yields

$$x+K=-\frac{2qD_p\{N_d+p(1-J_n/bJ_p)-N_d\ln\{N_d+p(1-J_n/bJ_p)\}}{J_p(1-J_n/bJ_p)^2}-\frac{qD_pN_d\ln\{N_d+p(1-J_n/bJ_p)\}}{J_p(1-J_n/bJ_p)}, \tag{41}$$

[13] The sign of the currents has been so chosen that a conventional current flowing from the emitter into the base or from the base into the collector is considered positive.

which is an equation for $p(x)$ containing two unknown constants $J_p$ and $K$ (a constant of integration). Since the equation is transcendental, it cannot be solved directly for $J_p$. We can obtain an approximate solution by neglecting the term $J_n/bJ_p$ relative to unity, a step which we shall justify later. In this manner we obtain

$$x+K\cong(qD_pN_d/J_p)\ln(p+N_d) -2qD_p(p+N_d)/J_p. \quad (42)$$

The two constants may now be evaluated with the use of the usual boundary conditions:

$$x=0, \quad p=p_1=p_b e^{qV_a/kT}, \quad (43)$$

$$x=w, \quad p=p_2=p_b e^{-qV_c/kT}. \quad (44)$$

Eliminating from (42) the expression for $K$ obtained in this manner, we arrive at

$$x=\frac{qD_pN_d}{J_p}\left\{\frac{2(p_1-p)}{N_d}-\ln\left(\frac{1+p_1/N_d}{1+p/N_d}\right)\right\}, \quad (45)$$

$$J_p=\frac{qD_pN_d}{w}\left\{\frac{2(p_1-p_2)}{N_d}-\ln\left(\frac{1+p_1/N_d}{1+p_2/N_d}\right)\right\}. \quad (46)$$

Note that for small injection levels ($p/N_d\ll1$) Eq. (45) indicates a linear dependence of $p$ on $x$ and Eq. (46) reduces to

$$J_p=qD_p(p_1-p_2)/w. \quad (47)$$

Similarly for high injection levels, $p$ is again a linear function of $x$ and Eq. (46) reduces to

$$J_p=2qD_p(p_1-p_2)/w. \quad (48)$$

We are now in a position to check the magnitude of $J_n/bJ_p$. Equations (38) and (46) indicate that this quantity is of the order of $(1-\gamma)$ and therefore its neglect relative to unity is well justified.

Hence, Eq. (46) represents the desired result for the $J$-$V$ characteristics of the base region for arbitrary injection level and should yield correct values of the conductance parameters apart from a small error of the order of $(1-\alpha)$.

There still remains the problem of demonstrating that $dE/dx\cong0$ in accordance with the assumption of space charge neutrality [Eq. (8)]. For both low and high injection levels, since $p$ is a linear function of $x$ and since $J_n$ is small, it follows from (39) and the Einstein relation that

$$dE/dx\cong kT(dp/dx)^2/q(p+N_d)^2. \quad (49)$$

For $p/N_d\ll1$, Eq. (49) becomes

$$dE/dx\cong kTp_1^2/qN_d^2w^2, \quad (50)$$

which quantity must be small compared to the total charge density expressed in appropriate units,

$$\rho=4\pi qN_d/\epsilon. \quad (51)$$

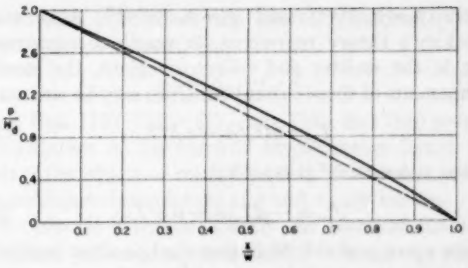


FIG. 1. Concentration of holes in $n$-type base region as a function of distance for intermediate injection level, illustrating largest deviations from linearity (see dashed curve).

Equations (50) and (51) lead to the condition:

$$p_1/N_d\ll2qw(\pi N_d/\epsilon kT)^{\frac{1}{2}}. \quad (52)$$

Since for relatively pure base material the right-hand side of (52) is of the order of 20 (see Table II) and since $p/N_d\ll1$ for this case, condition (52) is well fulfilled.

For $p/N_d\gg1$, Eq. (49) becomes

$$dE/dx\cong kT/qw^2, \quad (53)$$

which must be small compared to the total charge density,

$$\rho=4\pi qp/\epsilon. \quad (54)$$

Equations (53) and (54) lead to the condition:

$$p/N_d\gg\epsilon kT/4\pi q^2w^2N_d. \quad (55)$$

Since numerical evaluation of the right-hand side of (55) yields the value $2\times10^{-3}$ and since $p/N_d\gg1$ for this case, condition (55) is also well fulfilled.

For intermediate injection levels (i.e., $p/N_d\sim1$) the dependence of $p$ on $x$ may be obtained by plotting Eq. (45). We thereby find (see Fig. 1) that at worst only small deviations from linearity occur. Hence $d^2p/dx^2$, while no longer zero, is small and $dE/dx$ will likewise be small for this case as well.

## V. TRANSISTOR CURRENT-VOLTAGE CHARACTERISTICS

### A. General Relations

With the neglect of recombination in the junctions, an excellent approximation for abrupt impurity transitions, the total emitter and collector current densities are given by

$$J_e=J_{pe}+J_{ne}, \quad (56)$$

$$J_c=J_{pc}+J_{nc}. \quad (57)$$

As we have shown in Sec. IV, the larger components of these current densities are given to a good approximation by the expression:

$$J_{pc}=J_{pc}=\frac{qD_pN_d}{w}\left\{\frac{2(p_1-p_2)}{N_d}-\ln\left(\frac{1+p_1/N_d}{1+p_2/N_d}\right)\right\}, \quad (46)$$

where $p_1=p_be^{qV_c/kT}$ and $p_2=p_be^{-qV_c/kT}$. Also, since Shockley's theory represents an excellent approximation in the emitter and collector regions, the smaller components of these current densities may be written as

$$J_{ne}=qD_n(n_1-n_e)/L_e \tag{58}$$

where $n_1=n_ee^{qV_c/kT}(1+p_1/N_d)$,

$$J_{nc}=-qD_n(n_1-n_c)/L_c \tag{59}$$

where $n_1=n_ce^{-qV_c/kT}$. Note that the boundary condition at the emitter-base junction differs from Shockley's by a correction term which becomes important as the injection level in the base region becomes high. Equations (56), (57), (46), (58), and (59) represent the desired result for the $J$-$V$ characteristics of the junction transistor. If emitter and collector regions are well doped, these equations are applicable for any values of emitter current realizable in practice. The only essential feature missing from the simple theory leading to these equations is the small amount of recombination in the base region, which we shall discuss in detail in Sec. VI.

### B. Small-Signal Relations

The small-signal equations are readily derived from the general $J$-$V$ equations by differentiation. The important point made by Early,[4] namely that the base width $w$ is a function of the collector voltage owing to space charge broadening, is readily introduced into the theory at this point by noting that both $J_e$ and $J_c$ are functions of $w$ and that

$$dw=(\partial w/\partial V_c)dV_c+(\partial w/\partial V_e)dV_e \cong(\partial w/\partial V_c)dV_c. \tag{60}$$

On carrying out the differentiation, converting from current densities to currents with the use of the conduction area $A$, and neglecting all terms containing $e^{-qV_c/kT}$ since $qV_c/kT\gg1$, we obtain

$$i_e=g_{11}v_e+g_{12}v_c, \tag{61}$$

$$i_c=g_{21}v_e+g_{22}v_c, \tag{62}$$

where

$$g_{11}=\frac{q^2A}{kT}e^{qV_e/kT}\left\{\frac{2D_pp_b}{w}-\frac{D_pp_b}{w}\left(\frac{1}{1+(p_b/N_d)e^{qV_e/kT}}\right)+\frac{D_nn_e}{L_e}\left(1+\frac{2p_b}{N_d}e^{qV_e/kT}\right)\right\}, \tag{63}$$

$$g_{12}=g_{22}=\left(-\frac{\partial w}{\partial V_c}\right)\left(\frac{qAD_p}{w^2}\right)\times\{2p_be^{qV_c/kT}-N_d\ln(1+(p_b/N_d)e^{qV_c/kT})\}, \tag{64}$$

$$g_{21}=\frac{q^2A}{kT}e^{qV_e/kT}\left\{\frac{2D_pp_b}{w}-\frac{D_pp_b}{w}\times\left(\frac{1}{1+(p_b/N_d)e^{qV_e/kT}}\right)\right\}. \tag{65}$$

(Expressions for the quantity $(-\partial w/\partial V_c)$ may be obtained from reference 4.) Equations (61) and (62) are the starting point for transistor circuit theory.

### C. Current Amplification Factor

The current amplification factor is defined by

$$\alpha=\left(\frac{\partial I_c}{\partial I_e}\right)_{V_c=\text{const.}}=\left(\frac{i_c}{i_e}\right)_{v_c=0}=\frac{g_{21}}{g_{11}}. \tag{66}$$

Thus, it follows from (63) and (65) that

$$\alpha=\frac{2D_pp_b/w-(D_pp_b/w)(1+(p_b/N_d)e^{qV_e/kT})^{-1}}{2D_pp_b/w-(D_pp_b/w)(1+(p_b/N_d)e^{qV_e/kT})^{-1}+(D_nn_e/L_e)(1+(2p_b/N_d)e^{qV_e/kT})}. \tag{67}$$

For small injection levels, (67) reduces to

$$\alpha\cong\{1+(D_nn_ew/D_pp_bL_e)\}^{-1}, \tag{68}$$

which is just the injection factor,

$$\gamma=J_{pe}/(J_{pe}+J_{ne}), \tag{69}$$

similarly reduced for $p/N_d\ll1$, $qV_e/kT\gg1$, and $qV_c/kT\gg1$.[14] For large injection levels, Eq. (67) becomes

$$\alpha\cong\{1+(D_nn_ew/D_pN_dL_e)e^{qV_e/kT}\}^{-1}. \tag{70}$$

Thus $\alpha$ decreases with emitter current at high injection levels because of a decrease in injection efficiency.

Since the theory of Sec. IV is based on the assumption of no recombination in the base, the diminution factor,

$$\beta=J_{pc}/J_{pe}, \tag{71}$$

is of course equal to unity in this approximation.

[14] Shockley's interpretation of $\gamma$ as the injection factor and $\beta$ as the diminution factor in the equation $\alpha=\beta\gamma$ tacitly involves these same assumptions.

## VI. RECOMBINATION IN THE BASE REGION

### A. Approximate Solution for Arbitrary Injection Level

The volume recombination rate (No./cm³ sec) is obviously given by the expression $(p-p_b)/\tau_p$ while the surface recombination rate (No./cm² sec) is represented by $s(p-p_b)$. The total recombination current in the base is then evidently given to a good approximation by

$$I_r=qA_s\langle s(p-p_b)\rangle_w+qAw\langle(p-p_b)/\tau_p\rangle_w, \tag{72}$$

where the quantities in brackets are to be averaged so

as to take into account the spatial dependence of the injected carriers. It should be kept in mind that both $s$ and $\tau_p$ may be concentration dependent.

We shall base our estimate of $I_r$ on the solution in the base region without recombination (see Sec. IV), since the recombination process may be considered to be only a small perturbation upon the main flow of minority carriers from emitter to collector. Thus, the value of $p$ to be put into Eq. (72) is that given by Eq. (45). Note that to a good approximation (see Fig. 1 for the worst case) $p$ may be taken to be a linear function of $x$, thereby simplifying greatly the task of averaging.

Equation (72) may then be employed to obtain a first order correction to the hole current arriving at the collector, as the latter current will be smaller than the current injected at the emitter junction by the recombination current, i.e.,

$$J_{pc}=J_{pe}-I_r/A. \tag{73}$$

Thus, Eqs. (72), (73), (45), (46), (58), and (66) permit a calculation of the current amplification factor including the effects of recombination, provided that the concentration dependences of $s$ and $\tau_p$ are known.

In order to bring out clearly the essential features associated with alpha we shall first compute its value on the supposition that the surface recombination velocity and the volume lifetime are independent of minority carrier concentration and have their low injection level values $s_0$ and $\tau_0$, respectively. It is then readily shown with the use of the afore-mentioned equations that

$$1-\alpha=\frac{s_0A_e p_b/2A+wp_b/2\tau_0+(D_n n_e/L_e)(1+(2p_b/N_d)e^{qV_e/kT})}{2D_p p_b/w-(D_p p_b/w)(1+(p_b/N_d)e^{qV_e/kT})^{-1}+(D_n n_e/L_e)(1+(2p_b/N_d)e^{qV_e/kT})}. \tag{74}$$

For low injection levels and for a well-doped emitter region, (74) reduces to

$$1-\alpha\cong\frac{s_0A_e w}{2AD_p}+\frac{w^2}{2D_p\tau_0}+\frac{D_n n_e w}{D_p p_b L_e}, \tag{74a}$$

the terms on the right-hand side evidently representing contributions from surface recombination, volume recombination, and injection, respectively.

Numerical evaluation of the terms of (74a), with the use of the values assumed in Table II, yields

$$\frac{s_0A_e w}{2AD_p}=1.3\times10^{-2},\quad \frac{w^2}{2D_p\tau_0}=5.7\times10^{-4},\quad \frac{D_n n_e w}{D_p p_b L_e}=3.4\times10^{-3}.$$

It is evident that the surface recombination term is much larger than the volume recombination term[15] and is of the correct magnitude to account for observed values of $\alpha$ at low levels.

Plots of $1/(1-\alpha)$ *vs* $I_e$, computed with the use of Eq. (74), are shown in Fig. 2. Curve 1 was obtained with the use of the values of the parameters assumed in Table II; curve 2 results from increased doping of the emitter region relative to case 1 by an order of magnitude; while curve 3 corresponds to such high doping of the emitter that the terms arising from $J_{ne}$ may be neglected. The initial increase in $\alpha$ with emitter current is a consequence of the buildup in the base region of a field which assists the transit of minority carriers. At higher emitter currents $\alpha$ passes through a maximum and then declines with increasing emitter current owing to the decrease in injection efficiency, except for case 3 where the injection efficiency has been deliberately taken to be unity in order to show just the field-aided transit effect. Curves 1 and 2 are sufficiently similar to those experimentally observed[10,11] as to suggest that the theory is adequate in its present simple form. It is of some interest, however, to examine the consequences of the concentration dependences of $s$ and $\tau$.

The dependence of $\tau_p$ on $p$ has already been derived by Shockley and Read[16] based upon a recombination mechanism involving trapping states near the middle of the forbidden band. They find an expression of the form

$$\tau_p=\tau_0\{1+c(p-p_0)\}/\{1+d(p-p_0)\}, \tag{75}$$

where $c$ and $d$ are constants, the latter having the

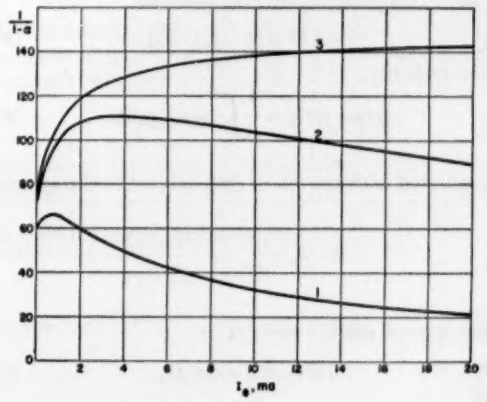


FIG. 2. Current amplification factor *vs* emitter current. Curve 1, assuming values of the parameters given in Table II; curve 2, increasing the doping of the emitter region by a factor of 10; curve 3, assuming an injection efficiency of unity for all currents.

[15] The dominance of surface recombination relative to volume recombination in carefully prepared, relatively pure germanium base material is assured even for the smallest values of $s_0$ that have been thus far realized (see reference 12).

[16] W. Shockley and W. T. Read, Jr., Phys. Rev. 87, 835 (1952).

simple value $1/(n_0+p_0)$.[17] For $c<d$, a condition which is likely to occur in relatively pure material, the lifetime decreases monotonically with injection level. Although this dependence tends to produce a decrease in $\alpha$, it is probably a very small effect relative to those already discussed.

No published information appears to be available concerning the concentration dependence of $s$. However, it is interesting to note that a recent theory of the surface recombination process by Brattain and Bardeen[12] leads to a decrease in $s$ with injection level, somewhat analogous to the case for $\tau$. Their theory is based upon the assumptions that there exist donor-type surface traps near the conduction band and acceptor-type surface traps near the full band, that the recombination rate is limited by the rate of trapping, and that the traps are largely unoccupied (which restricts the validity range to relatively low injection levels). The following expression is derived for the surface recombination rate $U$,

$$U=C(pn-p_0n_0), \tag{76}$$

where $C$ is a constant involving recombination cross sections, trap concentrations, etc.

We may rewrite Eq. (76) in the form

$$U=C\{n_0+p_0+(p-p_0)\}(p-p_0), \tag{77}$$

and then define an effective surface recombination velocity as follows:

$$s=U/(p-p_0). \tag{78}$$

We thereby obtain an expression for $s$ displaying a marked dependence on injection level, namely,

$$s=C\{n_0+p_0+(p-p_0)\}. \tag{79}$$

It is convenient to express Eq. (79) in terms of the low injection level value of the recombination velocity $s_0$; for an $n$-type base region (79) becomes

$$s=s_0\{1+(p-p_b)/N_d\}. \tag{80}$$

If the quantity,

$$\langle s(p-p_b)\rangle_{Av}=\frac{1}{w}\int_0^w s(p-p_b)dx, \tag{81}$$

is evaluated with the use of (80) subject to the assumptions that $p$ is a linear function of $x$, $qV_e/kT\gg 1$, and $qV_e/kT\gg 1$, one obtains

$$\langle s(p-p_b)\rangle_{Av}=(s_0p_1/2)(1+2p_1/3N_d). \tag{82}$$

If (82) is used to evaluate the dependence of $1/(1-\alpha)$ on $I_e$, it is found that the computed curve displays a maximum at much too small a value of current and then falls well below the experimental curve even if an injection efficiency of unity is assumed for all values of $I_e$. This is a consequence of the fact that $s$ is overestimated by the above theory when the injection level becomes appreciable. It is intuitively obvious that the traps must become completely filled at sufficiently high injection levels so that $s$ will reach a limiting value and will not increase indefinitely with $I_e$ as is implied by Eq. (80).

Therefore the possible importance of the concentration dependency of $s$ on the $\alpha$ *vs* $I_e$ characteristic cannot be assessed until experimental information bearing on this point becomes available. The similarity between the curves of Fig. 2 and the experimental data suggests that it may play only a secondary role.

### B. Three-Dimensional Theory for Very Small Injection Level[18]

For sufficiently small injection levels (see Sec. III), the electric field and the $n$-type currents in the base region become negligible and it suffices to deal only with Eqs. (1) and (3), which yield, for the steady-state case,

$$\text{div grad}p-(p-p_b)/D_p\tau_p=0. \tag{83}$$

For convenience let us consider a rectangular parallelepiped bounded by the planes $x=0$, $x=w$, $y=\pm a$, $z=\pm a$. The boundary conditions are

$$x=0,\quad p=p_1; \tag{43}$$

$$x=w,\quad p=p_2; \tag{44}$$

$$y=\pm a,\quad \partial p/\partial y\pm s_0(p-p_b)/D_p=0; \tag{84}$$

$$z=\pm a,\quad \partial p/\partial z\pm s_0(p-p_b)/D_p=0. \tag{85}$$

The solution to (83) satisfying these boundary conditions is

$$p-p_b=\sum_{i,j=0}^{\infty}\frac{a_{ij}[(p_1-p_b)\sinh((w-x)/L_{ij})+(p_2-p_b)\sinh(x/L_{ij})]\cos\beta_i y\cos\beta_j z}{\sinh(w/L_{ij})}, \tag{86}$$

where $\beta_i a=\theta_i$ are the roots of

$$\beta_i a\tan\beta_i a=s_0a/D_p, \tag{87}$$

and

$$1/\tau_{ij}=D_p(\beta_i^2+\beta_j^2)+1/\tau_p, \tag{88}$$

$$L_{ij}=(D_p\tau_{ij})^{\frac{1}{2}}, \tag{89}$$

$$a_{ij}=\frac{4\sin\theta_i\sin\theta_j}{(\theta_i+\frac{1}{2}\sin2\theta_i)(\theta_j+\frac{1}{2}\sin2\theta_j)}. \tag{90}$$

[17] It is worth mentioning that Hall's lifetime measurements[5] as a function of injection level for pure germanium may be well fitted by Eq. (75) with $c=8\times10^{-16}$ cm$^3$ and $d=2\times10^{-14}$ cm$^3$, both of which values are entirely reasonable from the point of view of the theory.

[18] The argument of this paragraph represents an extension to a semiconductor of finite width of the theory presented in Appendix V of Shockley's paper (see reference 1).

The current densities of holes may be determined from (86) as follows:

$$J_{pc}=-(qD_p/4a^2)\int_{-a}^{a}\int_{-a}^{a}(\partial p/\partial x)_{x=0}dydz$$

$$=qD_pp_b\sum_{i,j=0}^{\infty}\frac{A_{ij}}{L_{ij}}\left\{(e^{qV_c/kT}-1)\coth\left(\frac{w}{L_{ij}}\right)\right.$$

$$\left.-(e^{-qV_c/kT}-1)\operatorname{csch}\left(\frac{w}{L_{ij}}\right)\right\}, \quad (91)$$

$$J_{pe}=-(qD_p/4a^2)\int_{-a}^{a}\int_{-a}^{a}(\partial p/\partial x)_{x=w}dydz$$

$$=qD_pp_b\sum_{i,j=0}^{\infty}\frac{A_{ij}}{L_{ij}}\left\{(e^{qV_e/kT}-1)\operatorname{csch}\left(\frac{w}{L_{ij}}\right)\right.$$

$$\left.-(e^{-qV_e/kT}-1)\coth\left(\frac{w}{L_{ij}}\right)\right\}, \quad (92)$$

where

$$A_{ij}=\frac{4\sin^2\theta_i\sin^2\theta_j}{\theta_i^2\theta_j^2[1+(\sin 2\theta_i)/2\theta_i][1+(\sin 2\theta_j)/2\theta_j]}. \quad (93)$$

Note that for $s_0=0$, $\theta_i=0$, $A_{ij}=1$, $\tau_{ij}=\tau_p$, and hence Eqs. (91) and (92) reduce properly to the well known expressions of the simple theory.[1-3]

The diminution factor is given approximately ($qV_e/kT\gg 1$, $qV_c/kT\gg 1$)[14] by

$$\beta\cong\frac{\sum_{i,j=0}^{\infty}(A_{ij}/L_{ij})\operatorname{csch}(w/L_{ij})}{\sum_{i,j=0}^{\infty}(A_{ij}/L_{ij})\coth(w/L_{ij})}. \quad (94)$$

Equation (94) has been evaluated numerically for various values of $s_0$ with the results shown in Table III. In these computations $\tau_p$ has been taken to be infinite in order to permit comparison with the surface recombination term of the perturbation theory [first term of (74a)], which for the particular geometry considered here, assumes the form $s_0w^2/aD_p$. It may readily be seen from the table that the one-dimensional perturbation theory yields quite acceptable results for values of $\beta$ encountered in present day practice.

TABLE III. Diminution factor vs surface recombination velocity and comparison of perturbation theory with three-dimensional theory.

| $s_0$, cm/sec | $1-\beta$ | $s_0w^2/aD_p$ |
|---|---|---|
| 100 | $3.10\times10^{-3}$ | $3.23\times10^{-3}$ |
| 250 | $7.86\times10^{-3}$ | $8.07\times10^{-3}$ |
| 500 | $1.54\times10^{-2}$ | $1.61\times10^{-2}$ |
| 1000 | $3.03\times10^{-2}$ | $3.23\times10^{-2}$ |
| 2500 | $6.96\times10^{-2}$ | $8.07\times10^{-2}$ |
| 5000 | $1.22\times10^{-1}$ | $1.61\times10^{-1}$ |

## VII. FREQUENCY RESPONSE

Despite the fact that it is usually a valid procedure to neglect recombination[19] in the base region in computing the response to a periodic signal of varying frequency, nevertheless an enormous simplification similar to that resulting from omission of the recombination term in the steady-state case does not occur in the time dependent case. The reason for this is that in the latter case Eqs. (1) and (2) become

$$\partial p/\partial t=-q^{-1}\operatorname{div}J_p, \quad (95)$$

$$\partial n/\partial t=q^{-1}\operatorname{div}J_n. \quad (96)$$

Hence, it is no longer true that $J_p$ and $J_n$ are constants and as a consequence we are confronted with the formidable differential equation (14) or (15).

We shall content ourselves with a solution to the problem of the alpha cut-off frequency only for the limiting cases of very small and very large injection levels in a transistor with plane parallel junctions. Since it may readily be shown that the magnitude of the field in the base region varies monotonically with injection level between zero and a value of the order of $kT/qw$, it is to be expected that the alpha cut-off frequency should also vary monotonically between the values found for these limiting cases.

### A. Very Small Injection

For sufficiently small injection levels (see Sec. III) the field and the $n$-type currents in the base become negligible, and Eqs. (1) and (3) yield, for the one-dimensional case (including recombination),

$$\partial^2p/\partial x^2-(p-p_b)/L_p^2=D_p^{-1}\partial p/\partial t. \quad (97)$$

If it is assumed that the voltage applied at the emitter consists of an extremely small sinusoidal signal superimposed on a very small steady bias,

$$V=V_e+V_ae^{i\omega t}\quad(V_a\ll kT/q), \quad (98)$$

the boundary condition for the base region at $x=0$ becomes

$$p=p_b\exp[(q/kT)(V_e+V_ae^{i\omega t})]$$

$$\cong p_1+Pe^{i\omega t}, \quad (99)$$

where $p_1=p_be^{qV_e/kT}$ [by Eq. (43)] and

$$P=qV_ap_1/kT. \quad (100)$$

Since we are interested only in computing alpha, the short circuit current amplification factor, the boundary condition at $x=w$ remains simply

$$p=p_2=p_be^{-qV_c/kT}. \quad (44)$$

[19] Unless $s$ becomes too large at very high injection levels; see paragraph B.

The solution of (97) satisfying (44) and (99) is

$$p-p_b=\frac{(p_1-p_b)\sinh((w-x)/L_p)+(p_2-p_b)\sinh(x/L_p)}{\sinh(w/L_p)}+\frac{Pe^{i\omega t}\sinh\{(1+i\omega\tau_p')^{\frac{1}{2}}(w-x)/L_p\}}{\sinh\{(1+i\omega\tau_p')^{\frac{1}{2}}w/L_p\}}. \quad (101)$$

The analogous solution in the emitter ($-\infty<x<0$) is

$$n-n_e=(n_1-n_e)e^{x/L_e}+Qe^{i\omega t}\exp[(1+i\omega\tau_e)^{\frac{1}{2}}x/L_e], \quad (102)$$

where

$$n_1=n_e e^{qV_a/kT}, \quad Q=qV_a n_1/kT. \quad (103)$$

Since we are interested only in the ac component of the currents, it is unnecessary to consider the steady electron current in the collector and the first term on the right in each of Eqs. (101) and (102). The resulting expressions for the ac current densities are

$$J_e(\sim)=Pe^{i\omega t}(qD_p/L_p)(1+i\omega\tau_p')^{\frac{1}{2}}\times\coth\{(1+i\omega\tau_p')^{\frac{1}{2}}w/L_p\}+Qe^{i\omega t}(qD_n/L_e)(1+i\omega\tau_e)^{\frac{1}{2}}, \quad (104)$$

$$J_e(\sim)=P_e^{i\omega t}(qD_p/L_p)(1+i\omega\tau_p')^{\frac{1}{2}}\times\operatorname{csch}\{(1+i\omega\tau_p')^{\frac{1}{2}}w/L_p\}. \quad (105)$$

Evaluation of $\alpha$ from (104) and (105) yields

$$\alpha=\left[\cosh\left\{\frac{(1+i\omega\tau_p')^{\frac{1}{2}}w}{L_p}\right\}+\frac{D_n n_e L_p}{D_p p_b L_e}\frac{(1+i\omega\tau_e)^{\frac{1}{2}}}{(1+i\omega\tau_p')^{\frac{1}{2}}}\times\sinh\left\{\frac{(1+i\omega\tau_p')^{\frac{1}{2}}w}{L_p}\right\}\right]^{-1}. \quad (106)$$

For frequencies approaching the cut-off value it is not a very good approximation to expand the hyperbolic terms for small arguments; however, we may neglect unity relative to $i\omega\tau_p'$ (which is equivalent to neglecting recombination) and $i\omega\tau_e$ relative to unity.

On defining the following quantities:

$$\eta=(w/L_p)(\omega\tau_p'/2)^{\frac{1}{2}}, \quad (107)$$

$$\zeta=(D_n n_e L_p)/D_p p_b L_e(2\omega\tau_p')^{\frac{1}{2}}, \quad (108)$$

expanding the hyperbolic products, collecting terms, and extracting the modulus, we find that cutoff occurs when

$$2=(\cosh\eta\cos\eta+\zeta\sinh\eta\cos\eta+\zeta\cosh\eta\sin\eta)^2+(\sinh\eta\sin\eta+\zeta\cosh\eta\sin\eta-\zeta\sinh\eta\cos\eta)^2. \quad (109)$$

We shall derive an approximate solution to (109) by neglecting the $\zeta$ terms since $\zeta$ is obviously a small quantity, thus obtaining

$$2=\cosh^2\eta\cos^2\eta+\sinh^2\eta\sin^2\eta=(\cos2\eta+\cosh2\eta)/2. \quad (110)$$

The solution to (110) is $\eta=1.103$ which leads, with the use of (107), to a cut-off frequency,[20,21]

$$\omega_0=2.434D_p/w^2. \quad (111)$$

This approximate root permits the evaluation of $\zeta$ at the cut-off frequency; one finds that

$$\zeta=0.462D_n n_e w/D_p p_b L_e\cong2\times10^{-3}.$$

Since all of the other terms in (109) are of the order unity, neglect of the $\zeta$ terms is justifiable to an excellent approximation, which means that the influence of the injection factor on the cut-off frequency is negligible.

### B. High Steady Injection Level

It follows from Eqs. (3), (4), (8), (10), and the condition $N_a\ll N_d$ that

$$E=\frac{J_n-qbD_p\operatorname{grad}p}{qb\mu_p(p+N_d)}, \quad (112)$$

$$J_p=\frac{J_n-qbD_p(2+N_d/p)\operatorname{grad}p}{b(1+N_d/p)}. \quad (113)$$

For a high steady injection level ($p/N_d\gg1$), Eqs. (112) and (113) become

$$E=\frac{J_n-qbD_p\operatorname{grad}p}{qb\mu_p p}, \quad (114)$$

and

$$J_p=J_n/b-2qD_p\operatorname{grad}p\cong-2qD_p\operatorname{grad}p, \quad (115)$$

since as shown in Sec. IV, $J_n/bJ_p\ll1$.

Consider now the superposition on the high-level steady bias an extremely small ac signal. This will not have a significant influence on the electric field (114), but it will introduce a time dependence of $p$. Combining (1) and (115) we obtain

$$2D_p\operatorname{div}\operatorname{grad}p-(p-p_b)/\tau_p=\partial p/\partial t, \quad (116)$$

an equation which will be employed in the three-dimensional form in order to take into account possible transit time dispersion effects due to surface recombination, since $s$ may become large at high injection levels. The boundary conditions are given by Eqs. (99), (44), (84), and (85) with $s_0$ replaced by $s$.

The solution to (116) satisfying the boundary conditions contains two terms, a dc term given by Eq. (86)

[20] This result, which has already been obtained by Pritchard (reference 21), is 22 percent higher than the commonly cited value (see references 2 and 3).

[21] R. L. Pritchard, Proc. Inst. Radio Engrs. **40**, 1476 (1952).

plus an ac term represented by the expression

$$Pe^{i\omega t}\sum_{i,j=0}^{\infty} \times \frac{a_{ij}\sinh\{(1+i\omega\tau_{ij})^{\frac{1}{2}}(w-x)/L_{ij}\}\cos\beta_i y\cos\beta_j z}{\sinh\{(1+i\omega\tau_{ij})^{\frac{1}{2}}w/L_{ij}\}}, \quad (117)$$

where the symbols are defined by Eq. (87) with $s_0$ replaced by $s$ and by Eqs. (88), (89), and (90) with $D_p$ replaced by $2D_p$.

Since the influence of the injection factor on the frequency response will be small, we shall defer for a moment consideration of the analogous solution in the emitter. Also we need be concerned only with the ac component of the current density at the emitter and collector junctions, which may readily be derived from (117) with the use of (115). Thus, we obtain finally

$$\alpha \cong \frac{\sum_{i,j=0}^{\infty}(A_{ij}/L_{ij})\,\mathrm{csch}\{(1+i\omega\tau_{ij})^{\frac{1}{2}}w/L_{ij}\}}{\sum_{i,j=0}^{\infty}(A_{ij}/L_{ij})\coth\{(1+i\omega\tau_{ij})^{\frac{1}{2}}w/L_{ij}\}}, \quad (118)$$

with $A_{ij}$ defined by (93).

For values of $s$ which are not too high (i.e., up to $s=2500$ cm/sec for the cross-sectional area assumed in Table II) the quantity $i\omega\tau_{ij}$ will be much greater than unity for all of the terms of the series that contribute significantly to the sums. In this case Eq. (118) reduces to

$$\alpha \cong \mathrm{sech}(i\omega w^2/2D_p)^{\frac{1}{2}}, \quad (119)$$

which leads to a cut-off frequency,

$$\omega_0 = 4.868 D_p/w^2, \quad (120)$$

just twice the value found for very small injection.

If the asymptotic value of $s$ at very high emitter currents proves to be much higher than the above limit, then (118) must be evaluated numerically and the cut-off frequency may become somewhat smaller than the value indicated by (120).

A somewhat more important correction to $\omega_0$ is likely to result from a fall-off in injection efficiency at high currents. Neglecting three dimensional effects in the base, it may readily be shown that an expression for $\alpha$ results given by Eq. (106) except that $D_p$ becomes multiplied by 2, $L_p$ by $\sqrt{2}$, and $n_e$ by the factor

$$1+p_{b0}e^{qV_e/kT}/N_d.$$

The cut-off frequency may then be obtained from this equation by the method outlined in paragraph A. The result for $\omega_0$ is the value given by Eq. (120) slightly diminished by a correction factor which increases with increasing emitter current.

## ACKNOWLEDGMENTS

It is a pleasure for the writer to express his indebtedness to Dr. F. K. du Pré for a large number of valuable discussions; to Professor G. E. Uhlenbeck for several helpful suggestions; to the latter, Professor J. Bardeen, Dr. J. M. Early, and Mr. W. van Roosbroeck for critical readings of the manuscript; and to Dr. W. M. Webster for pointing out an error in an earlier version of the manuscript, as a consequence of which the decrease in injection efficiency with emitter current had been missed.

# de Haas-van Alphen Effect in Cadmium

TED G. BERLINCOURT
*United States Naval Research Laboratory, Washington, D. C.*
(Received February 18, 1954)

The de Haas-van Alphen effect (periodic dependence of magnetic susceptibility upon magnetic field) has been investigated in single crystals of cadmium in the liquid helium temperature range and in magnetic fields up to 25 kilogauss. The orientation dependence of the effect in cadmium was found to be different from all other known cases and cannot be interpreted in terms of ellipsoidal constant energy surfaces or other constant energy surfaces obtainable by the usual transformations from the isotropic case. The susceptibility oscillations of maximum period $\beta/E_0=1.88\times10^{-7}$ gauss$^{-1}$ occur whenever the magnetic field makes an angle of 28.5° with the hexagonal axis. The chemical potential of the pertinent electrons is $E_0=69.6\times10^{-14}$ erg$=0.435$ electron volt to an estimated accuracy of $\pm1$ percent.

Unsuccessful attempts were made to observe the de Haas-van Alphen effect in single crystals of Ta, Mo, and hexagonal Ti.

## INTRODUCTION

THE low-temperature oscillatory dependence of magnetic susceptibility upon magnetic field characteristic of the de Haas-van Alphen effect was observed in cadmium at liquid helium temperatures in 1950 by Verkin, Lazarev, and Rudenko[1,2] and independently shortly thereafter by Shoenberg.[3,4] These investigations were largely exploratory, and there was no detailed study of the dependence of the effect upon temperature, magnetic field, and crystallographic orientation. The present work was undertaken in order to study these dependences and thereby ascertain values for the effective masses and chemical potential of the electrons participating in the susceptibility oscillations. However, the orientation dependence of the effect in cadmium was found to be quite different from all other known cases and was amenable to only a partial analysis in terms of existing theory. It is in this respect that the measurements are chiefly of interest.

The theory of the de Haas-van Alphen effect is sufficiently general to indicate that the characteristic susceptibility oscillations should be a universal property of metal single crystals, and indeed, fifteen metals (if graphite may be so classified) have exhibited such behavior to date. Negative findings on several other metals[4,5] are very likely the result of experimental limits existing on the attainment of low temperatures and high magnetic fields. As will be evident from the theoretical expression describing the effect, small anisotropic effective electronic masses and low values of chemical potential favor easy detection of the oscillations. Such conditions exist chiefly in polyvalent metals where the Fermi surface overlaps Brillouin zone boundaries.

A free electron model was used in the development of the theory by Peierls,[6] Blackman,[7] and Landau,[8] the effect of the periodic field of the lattice being taken into account by the introduction of generally anisotropic effective electronic masses. Equation (1), obtained from Landau's theory (see reference 4), gives the difference between the magnetic susceptibilities ($\Delta\chi$) per unit mass in two directions at right angles to each other. (Recent modifications of this theory and methods for determining electronic parameters from the experimental data will be discussed in a later section.)

$$\Delta\chi=\sum\frac{A\Delta m}{\rho}\left\{\frac{\pi^2}{6}\left(\frac{k}{E_0}\right)^{\frac{1}{2}}-\frac{1}{T^{\frac{1}{2}}}\left(\frac{2\pi^2kT}{\beta H}\right)^{\frac{1}{2}}\times\sum_{p=1}^{\infty}\frac{(-1)^{p+1}\sin(2\pi pE_0/\beta H-\pi/4)}{2p^{\frac{1}{2}}\sinh(2\pi^2pkT/\beta H)}\right\},\quad(1)$$

where $A$ is a constant given by

$$A\equiv e^2E_0/[\pi^4c^2\hbar(2k)^{\frac{1}{2}}m'^{\frac{1}{2}}],\quad(2)$$

$\rho$ is the density, $\beta$ is an effective double Bohr magneton given by

$$\beta=e\hbar/m''c,\quad(3)$$

and $m'$, $m''$, and $\Delta m$ are functions of the relevant effective masses. These functions depend upon the geometry of the experiment and the shape of the electronic constant energy surface in momentum space for the crystal under investigation. $E_0$ is the energy at this surface of constant energy measured from the bottom of the relevant zone and is given by a quadratic function of the momenta. It is this function which determines the definitions of $m'$, $m''$, and $\Delta m$. The remaining symbols in Eq. (1) have their usual meanings.

In most cases thus far amenable to comparisons between theory and experiment[4] it has been possible to represent the constant energy surface in momentum space by one, two, or three ellipsoids, and, in fact, the

[1] Verkin, Lazarev, and Rudenko, J. Exptl. Theoret. Phys. (U.S.S.R.) **20**, 93 (1950).
[2] Verkin, Lazarev, and Rudenko, J. Exptl. Theoret. Phys. (U.S.S.R.) **20**, 995 (1950).
[3] D. Shoenberg, Nature **166**, 652 (1950).
[4] D. Shoenberg, Trans. Roy. Soc. (London) **245**, 1 (1952).
[5] Ted G. Berlincourt, Phys. Rev. **88**, 242 (1952).
[6] R. Peierls, Z. Physik **81**, 186 (1933).
[7] M. Blackman, Proc. Roy. Soc. (London) **A166**, 1 (1938).
[8] L. D. Landau, see appendix of D. Shoenberg, Proc. Roy. Soc. (London) **A170**, 341 (1939).

first summation sign in Eq. (1) is included in order to account for the existence of several surfaces characterized by different values of the parameters $\beta$, $m'$, $m''$, $\Delta m$, and $E_0$. For a suitable choice of axes with respect to the crystallographic directions, one such possible surface can be described by

$$E_0=\frac{1}{2m_0}(\alpha_{11}p_x^2+\alpha_{22}p_y^2+\alpha_{33}p_z^2), \tag{4}$$

where the $\alpha$'s are the ratios of the true electronic mass $m_0$ to the relevant components of the effective mass tensor and the $p$'s are components of the momentum. Recently, Onsager[9] has pointed out that one negative principal effective mass is permissible and would indicate a hyperboloid of one sheet and also that Shoenberg's[4] data on graphite might be interpreted in terms of a tube of variable cross section spanning the entire length of a cell in wave number space. The possibility that one effective mass might be infinite with a resultant cylindrical constant energy surface was also considered. However, as will be evident in a later section, the experimental data on cadmium cannot be interpreted in terms of any of the surfaces discussed above and therefore pose some interesting questions on the theory.

## THE EXPERIMENTAL WORK

### I. The Torsion Balance Method

The torsion balance method (which is adequately described elsewhere[4,5]) was employed in measuring the couple $C$ per unit mass in a vertical direction acting on the crystal placed in a homogeneous horizontal magnetic field. This couple is related to the difference $\Delta\chi$ [as given by Eq. (1)] between the mass susceptibilities along perpendicular directions in the crystal by the expression

$$C=\Delta\chi H^2\sin\phi\cos\phi, \tag{5}$$

where $H$ is the magnetic field strength and $\phi$ is the angle between a given crystallographic axis and the magnetic field. For example, denoting the hexagonal axis in cadmium by $c$, digonal axes of type I by $a$, and digonal axes of type II by $b$, the couple in a vertical direction is given by

$$C=(\chi_c-\chi_b)H^2\sin\phi\cos\phi, \tag{6}$$

if the $c$ axis, one $b$ axis, and $H$ are in a horizontal plane (i.e., an $a$ axis is vertical) and $\phi$ is the angle between the $c$ axis and $H$. This was the first of three modes of suspension of the crystal used in this work. A $b$ axis was vertical in the second mode, and the $c$ axis was vertical in the third. All three modes are illustrated in Fig. 1.

The torsion balance used in this investigation and the method of mounting crystals on the balance were described in an earlier communication[5] on tin, and consequently will not be described again. It should be mentioned, however, that the maximum angular displacements of the crystal were never greater than 0.5°, and angular displacements of approximately 0.0005° were detectable. Values of $\phi$ were corrected for these displacements, and measurements were carried out over relatively small ranges of field in order to avoid complications due to the sensitive orientation dependence of the susceptibility oscillations.

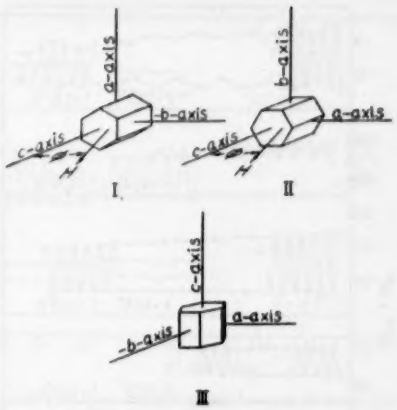


FIG. 1. Schematic representation of the three modes of suspension of the cadmium crystals. The $a$ axis is a digonal axis of type I; the $b$ axis is a digonal axis of type II; the $c$ axis is the hexagonal axis; the axis of suspension is vertical, and $H$ is in a horizontal plane.

All the measurements were made at liquid helium temperatures, the temperature being determined by observation of the vapor pressure of the liquid helium bath with mercury and oil manometers. The Mond vapor pressure tables[10] were used, and temperatures were maintained constant to better than 0.01°K.

### II. The Magnet and Its Calibration

An Arthur D. Little electromagnet capable of rotation through 360° about a vertical axis supplied horizontal magnetic fields up to 25 kilogauss in strength. Pole pieces $5\frac{3}{4}$ inches in diameter and a gap of $1\frac{3}{4}$ inches assured field homogeneity to a few gauss over the volumes of the crystals which approximated spheres roughly 3 mm in diameter. Time variations of the field were limited to less than 5 gauss at 25 kilogauss during the course of a single measurement by means of a degenerative feedback voltage regulator used in conjunction with two generators which supplied current to the magnet. A Varian nuclear fluxmeter used with a General Radio frequency meter permitted calibration of the magnet to an accuracy of better than 0.02 percent.

### III. The Crystals

Two cadmium single crystals (Cd 1 weighing 99.3 milligrams and Cd 2 weighing 108.8 milligrams) were

[9] L. Onsager, Phil. Mag. **43**, 1006 (1952).

[10] H. Van Dijk and D. Shoenberg, Nature **164**, 151 (1949).

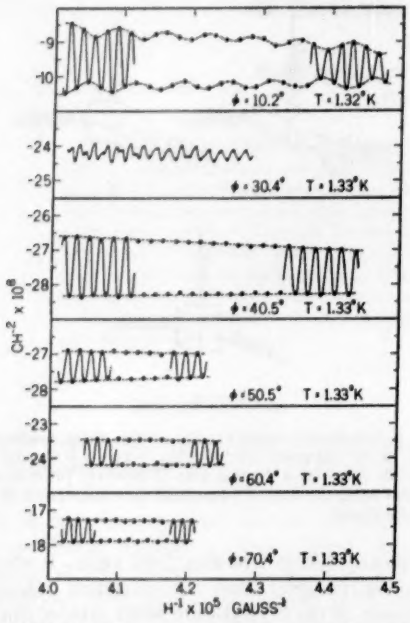


FIG. 2. $CH^{-2}$ in dyne cm g$^{-1}$ gauss$^{-2}$ *versus* $H^{-1}$ for Cd 1 with an $a$ axis vertical. $\phi$ is the angle between the $c$ axis and the magnetic field. The presence of two periodic terms accounts for the beats.

used in this investigation. They were grown by melting small beads of cadmium (Johnson, Matthey and Company, JM 170, Lab. No. 2572, 99.999 percent pure) under silicone oil under a helium atmosphere in a furnace which was allowed to cool slowly (in about 20 hours) to room temperature. Etching in concentrated hydrochloric acid with sufficient potassium chlorate added to produce liberal bubbling followed by a short etch in concentrated hydrochloric acid alone produced

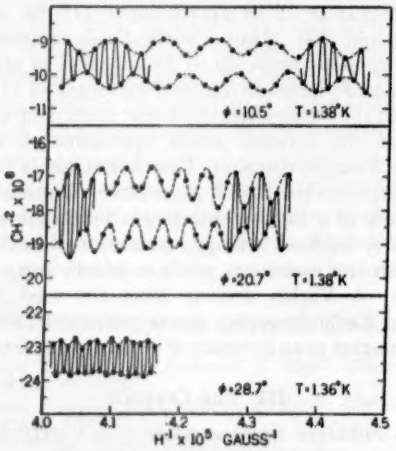


FIG. 3. $CH^{-2}$ in dyne cm g$^{-1}$ gauss$^{-2}$ *versus* $H^{-1}$ for Cd 1 with a $b$ axis vertical.

good reflections from the (0001) plane and the {101$l$} (where $l$ has many values) planes. The crystals were then oriented to an accuracy of better than 2° by means of an optical method described by Chalmers.[11] A Laue back-reflection x-ray picture of Cd 1 confirmed the orienting technique and, incidentally, revealed only slight asterism, so it is doubtful that further refinement of the crystal growing technique would have proved worth while.

## EXPERIMENTAL RESULTS

The general features of the susceptibility oscillations are illustrated in Figs. 2, 3, and 4. Because the constant energy surface does not fit the usual ellipsoidal scheme and the applicability of Eqs. (5) and (6) is therefore in question, $CH^{-2}$ (the product of the couple per unit mass and the square of the reciprocal field) rather than $\Delta\chi$ has been plotted as a function of reciprocal field. Only maxima, minima, and a few points of inflection were measured inasmuch as the short period of the oscillations (as little as 30 gauss from a maximum to a minimum at 25 kilogauss) made accurate determination of the detailed form of the susceptibility oscillations difficult and time consuming, and in any event this detailed form is not of very great interest at this stage.

The curves in Fig. 2 were obtained by using Cd 1 with an $a$ axis vertical (mode I, Fig. 1). $\phi$ is then the angle in a horizontal plane between the hexagonal axis and the magnetic field. For small values of $\phi$ modulations are present indicating the coexistence of two periodic terms, while for larger values of $\phi$ only one term is important. The curves in Fig. 3 were obtained using Cd 1 with a $b$ axis vertical (mode II, Fig. 1) and with $\phi$ again measuring the angle between the $c$ axis and the magnetic field. That this orientation (mode II) is equivalent to the earlier one (mode I) will be illustrated later. Figure 4, obtained using Cd 2 with one of its $a$ axes vertical, illustrates the dependence of the susceptibility upon temperature and magnetic field strength.

According to Eq. (1) the susceptibility oscillations should be periodic in $H^{-1}$. This was verified by plotting values of $H^{-1}$ for which maxima in $CH^{-2}$ occur against integers. This procedure yielded straight lines of slope $\beta/E_0$. Wherever beats were present the period of the subordinate term could usually be ascertained from the beat period.

The dependence of the period upon orientation is best illustrated by means of polar plots of $\beta/E_0$ against $\phi$ such as those appearing in Fig. 5 for the various runs. Figure 5(a) applies to Cd 1 with an $a$ axis vertical; Fig. 5(b) applies to Cd 1 with a $b$ axis vertical; Fig. 5(c) applies to Cd 2 with an $a$ axis vertical; Fig. 5(d) applies to Cd 1 with its $c$ axis approximately 7° off horizontal and the directions of the $a$ axes undetermined. The last case illustrates the effect of inaccuracies in orientation. The angle $\phi$ was measured in this last case between the

[11] B. Chalmers, Proc. Phys. Soc. (London) **47**, 733 (1935).

magnetic field and the projection of the $c$ axis on a horizontal plane. In all cases the circles are given by the expression

$$(\beta/E_0)_{\pm} = (1.88\times10^{-7})\,|\cos(\phi\pm28.5°)|, \qquad (7)$$

where the + sign corresponds to one circle and the − sign corresponds to the other. The proximity of the experimental points to the circles in Figs. 5(a), (b), and (c) indicates that the period is quite reproducible from one crystal to another, and also that the modes of suspension used in Figs. 5(a) and (b) are equivalent as far as period is concerned. Twelvefold symmetry about the $c$ axis is dictated by the latter fact since the orientations used in Figs. 5(a) and (b) (i.e., modes I and II) differ only by a rotation of 30° about the $c$ axis. Such high symmetry suggests that cadmium is magnetically isotropic in the basal plane. That this is so to a high degree of approximation was established by measurements on Cd 2 with its $c$ axis vertical (mode III, Fig. 1). A weak suspension capable of detecting oscillations in $CH^{-2}$ of the order of $10^{-11}$ dyne cm g$^{-1}$ gauss$^{-2}$ revealed no oscillations in fields up to 25 kilogauss and at temperatures down to 1.3°K. The evidence strongly suggests then that for both the $c$ axis and the magnetic field in a horizontal plane, the period is independent of the orientation of the $a$ axes and is closely approximated by Eq. (7).

The behavior noted in Figs. 2 and 3 is now clear if it is remembered that in general the amplitude of the oscillating couple for a given de Haas-van Alphen term increases with increasing period as $\phi$ is varied, reaching a maximum amplitude at a period a bit less than the maximum period and then approaching zero as the period approaches its maximum value. Thus, for small $\phi$ the longer period oscillations predominate, but as $\phi$ nears 28.5° the amplitude suddenly decreases, vanishing completely at 28.5° so that in a small region around 28.5° the short period oscillations in the couple are dominant. However, as $\phi$ increases beyond 28.5° the longer period oscillations again regain supremacy.

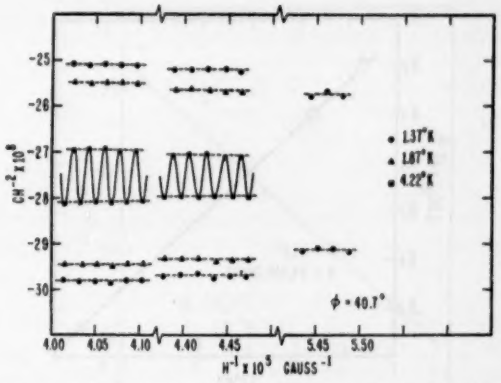


FIG. 4. $CH^{-2}$ in dyne cm g$^{-1}$ gauss$^{-2}$ *versus* $H^{-1}$ for Cd 2 with an $a$ axis vertical. The temperature and field dependences are illustrated.

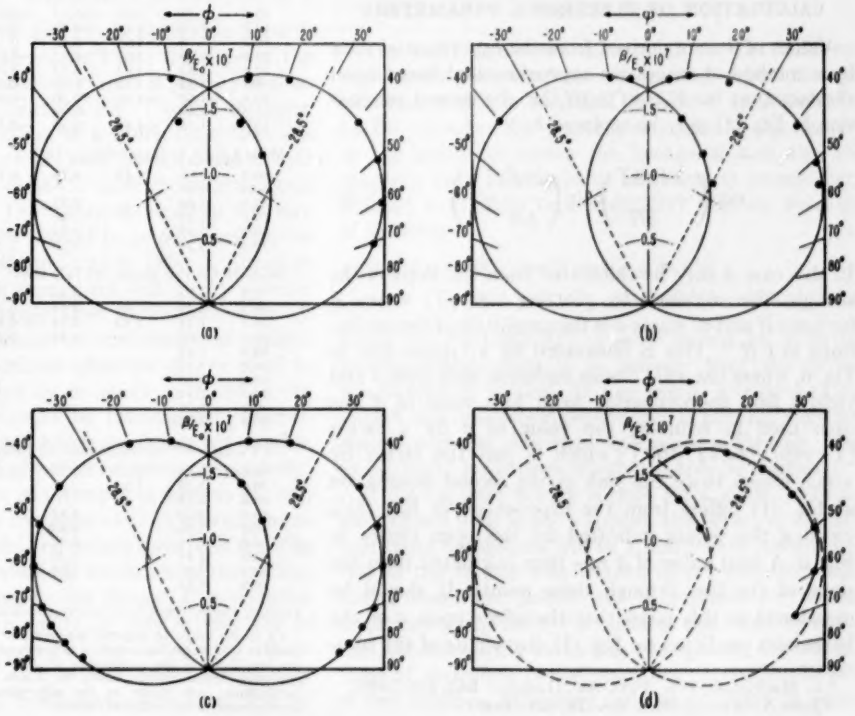


FIG. 5. Polar plots of the period $\beta/E_0$ in gauss$^{-1}$ *versus* the angle $\phi$ between the magnetic field and the hexagonal or $c$ axis. The circles whose centers occur at $\phi = \pm28.5°$ are given by Eq. (7). (a) Cd 1 with an $a$ axis vertical; (b) Cd 1 with a $b$ axis vertical; (c) Cd 2 with an $a$ axis vertical; (d) Cd 1 with the $c$ axis ~7° from the horizontal.

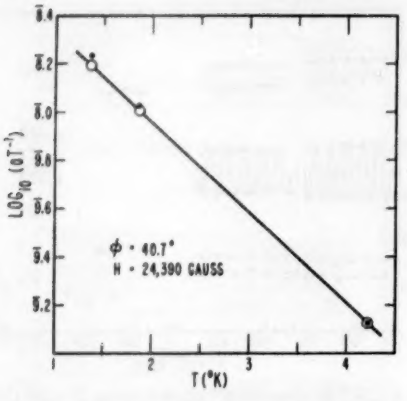


FIG. 6. $\log_{10}(a/T)$ at 24.39 kilogauss and $\phi=40.7°$ *versus* $T$. Values of $\beta$ are derived from the slopes of such plots. The open circle points were obtained by adjusting the solid circle points for the difference between the sinh in Eq. (1) and the exponential in Eq. (8).

The values obtained for the steady anisotropy $\Delta\chi = -1.00\times10^{-7}$ emu per g at 300°K and $\Delta\chi=-5.6\times10^{-7}$ emu per g at liquid helium temperatures are in good agreement with earlier determinations.[12,13]

Before proceeding to a discussion of the electronic parameters it should be mentioned that unsuccessful attempts were made to observe the de Haas-van Alphen effect in single crystals of Ta, Mo, and hexagonal Ti.

## CALCULATION OF ELECTRONIC PARAMETERS

Values of $\beta$ were derived from the experimental data by a method of successive approximation[4] based upon the fact that for $E_0 \gg kT \gg \beta H/2\pi^2$ the second summation in Eq. (1) may be replaced by

$$\exp\left(-\frac{2\pi^2 kT}{\beta H}\right)\sin\left(\frac{2\pi E_0}{\beta H}-\frac{\pi}{4}\right). \qquad (8)$$

In this case $\beta$ may be calculated from the slope of the straight line obtained by plotting $\log(a/T)$ *versus* $T$ for fixed $H$ and $\phi$, where $a$ is the amplitude of the oscillations in $CH^{-2}$. This is illustrated by a typical plot in Fig. 6, where the solid circles represent such points and yield a first approximation to $\beta$. This value of $\beta$ was then used in reducing the value of $a$ by a factor $[1-\exp(-4\pi^2kT/\beta H)]$ [which is just the factor by which minus twice the sinh in the second summation of Eq. (1) differs from the exponential in Eq. (8)], yielding the points indicated by the open circles in Fig. 6. A final value of $\beta$ was then calculated from the slope of the line through these points. It should be mentioned at this point that the effect upon $a$ of the harmonics predicted by Eq. (1) (by virtue of the summation over $p$) was shown by a simple calculation to be negligible even when the amplitude of the strongest harmonic was as great as 0.1 that of the fundamental.

Once $\beta$ had been determined, $E_0$ was readily obtained from the period, $\beta/E_0$. Values of $\beta$ and $E_0$ derived in this way are listed in Table I along with the experimentally measured quantities $\beta/E_0$ and $a$. The latter apply to a field strength of 24 390 gauss and are included because of the possibility that future modifications of the theory could invalidate the foregoing analysis. In any event, the most reliable values (to an

TABLE I. Summary of data on cadmium.[a]

| $\phi$ | $(\beta/E_0)\times10^7$ dom. | $(\beta/E_0)\times10^7$ sub. | $a\times10^8$ dom. | $a\times10^8$ sub. | $\beta\times10^{19}$ dom. | $E_0\times10^{14}$ dom. | $x$ dom. | $T$ |
|---|---|---|---|---|---|---|---|---|
| Mode I Cd 2 *bc* plane—29 July 1953 | | | | | | | | |
| 10.4 | 1.78 | 1.45 | 0.64 | 0.07 | | | | 4.22 |
| 20.6 | 1.86 | ~1.22 | 0.71 | 0.08 | | | | 4.22 |
| 40.7 | 1.84 | | 0.56 | | | | | 4.22 |
| 40.7 | 1.84 | | 1.97 | | 1.29 | 70.1 | | 1.87 |
| 40.7 | 1.84 | | 2.35 | | | | 1.1 | 1.37 |
| 50.7 | 1.74 | | | | | | | 1.36 |
| 60.6 | 1.60 | | | | | | | 1.36 |
| 70.6 | 1.39 | | | | | | | 1.36 |
| 75.5 | 1.26 | | | | | | | 1.36 |
| 80.4 | 1.13 | | 0.40 | | | | | 1.37 |
| 83.4 | 1.04 | | | | | | | 1.37 |
| −9.8 | 1.78 | | | | | | | 4.22 |
| −20.0 | 1.84 | | | | | | | 4.22 |
| −40.1 | 1.84 | | | | | | | 4.22 |
| −50.1 | 1.75 | | | | | | | 4.22 |
| −60.0 | 1.60 | | | | | | | 4.22 |
| −70.0 | 1.41 | | | | | | | 1.37 |
| −74.9 | 1.29 | | | | | | | 1.37 |
| −79.8 | 1.16 | | | | | | | 1.87 |
| −84.8 | 1.00 | | | | | | | 1.87 |
| Mode I Cd 1 *bc* plane—2 July 1953 | | | | | | | | |
| 10.2 | 1.75 | 1.42 | ~0.13 | ~0.04 | | | | 4.22 |
| 10.2 | 1.75 | 1.42 | 0.38 | 0.09 | 1.22 | 69.5 | 1.1 | 2.56 |
| 10.2 | 1.75 | 1.42 | 0.63 | 0.23 | | | 1.8 | 1.32 |
| 20.4 | 1.83 | 1.22 | 0.27 | ~0.01 | | | | 4.22 |
| 20.4 | 1.83 | 1.22 | 0.73 | ~0.08 | 1.26 | 69.1 | | 2.56 |
| 20.4 | 1.83 | 1.22 | 1.20 | 0.36 | | | | 1.32 |
| 30.4 | ~1.80 | ~1.04 | ~0.20 | ~0.09 | | | | 2.56 |
| 50.5 | 1.74 | | 0.99 | | | | | 1.32 |
| −10.0 | 1.75 | ~1.42 | 0.40 | ~0.10 | | | | 2.56 |
| Mode I Cd 1 *bc* plane—9 July 1953 | | | | | | | | |
| 10.2 | 1.78 | 1.41 | 0.76 | 0.15 | | | | 1.32 |
| 30.4 | ~1.88 | | | | | | | 1.33 |
| 40.5 | 1.83 | | 0.82 | | | | | 1.33 |
| 50.5 | 1.74 | | 0.40 | | | | | 1.33 |
| 60.4 | 1.58 | | 0.37 | | | | | 1.33 |
| 70.4 | 1.39 | | 0.30 | | | | | 1.33 |
| Mode II Cd 1 *ac* plane—22 July 1953 | | | | | | | | |
| 5.5 | 1.74 | | 0.46 | | | | | 1.39 |
| 10.5 | 1.79 | 1.45 | 0.51 | 0.23 | | | | 1.38 |
| 20.7 | 1.24 | 1.82 | 0.78 | 0.42 | | | | 1.38 |
| 28.7 | 1.06 | | 0.46 | 0.10 | | | | 1.38 |
| 40.8 | 1.81 | | | | | | | 1.38 |
| 50.8 | 1.72 | | | | | | | 1.38 |
| 55.8 | ~1.63 | | | | | | | 1.38 |
| −4.7 | 1.74 | | | | | | | 1.38 |
| −9.7 | 1.77 | | | | | | | 1.38 |
| −40.0 | 1.84 | | | | | | | 1.38 |
| Cd 1 *c* axis ~7° off horizontal—25 June 1953 | | | | | | | | |
| 10.0 | 1.71 | 1.33 | 1.23 | 0.45 | | | | 4.22 |
| 20.0 | 1.78 | 1.17 | | | | | | 4.22 |
| 30.0 | 1.79 | | | | | | | 4.22 |
| 40.0 | 1.76 | | 0.82 | | | | | 4.22 |
| 40.0 | 1.76 | | 3.13 | | 1.23 | 70.0 | 1.2 | 1.93 |
| 50.0 | 1.71 | | 0.55 | | | | | 4.22 |
| 50.0 | 1.71 | | 2.29 | | 1.19 | 69.5 | 0.7 | 1.93 |
| 60.0 | 1.52 | | 1.03 | | | | 0.7 | 1.93 |
| 70.0 | 1.23 | | | | | | | 1.93 |

[a] $\phi$ is the angle in degrees between the $c$ axis and the magnetic field; positive and negative values of $\phi$ are equivalent; $\beta/E_0$ is in gauss$^{-1}$; $a$ is the amplitude of the oscillations of $CH^{-2}$ in dyne cm g$^{-1}$ gauss$^{-2}$; $\beta$ is in ergs gauss$^{-1}$; $E_0$ is in ergs; $x$ is in °K; $T$ is in °K; dom. refers to the dominant oscillations; sub. refers to the subordinate oscillations; ~ designates approximate or less reliable values.

[12] L. Mackinnon, Proc. Phys. Soc. (London) **B62**, 170 (1949).
[13] Jules A. Marcus, Phys. Rev. **76**, 621 (1949).

estimated ±1 percent) for the electronic parameters at present are

$$E_0 = 69.6\times10^{-14} \text{ erg} = 0.435 \text{ electron volt}, \quad (9)$$

$$\beta = 1.31\times10^{-19} \text{ erg gauss}^{-1} \text{ (at } \phi = 28.5°), \quad (10)$$

$$m'' = 0.141 m_0 \text{ (at } \phi = 28.5°). \quad (11)$$

It should be remembered however that $m''$ is just the average effective mass in a plane normal to the magnetic field rather than the effective mass in a single direction. The above value for $E_0$ is greater by a factor of 3 than Shoenberg's value[4] which was intended only as a rough preliminary estimate.

As evidenced by Fig. 6 and by the small spread in values of $E_0$ listed in Table I, the temperature dependence of $a$ is described quite adequately by Eq. (1). It is also of interest to compare experiment with theory as regards the dependence of $a$ upon magnetic field strength, but first a modification of the theory by Dingle (see reference 4) must be considered. According to this modification, broadening of the electronic energy levels resulting from the presence of impurities and strains has the effect of reducing the amplitude of each term in the summation over $p$ in Eq. (1) by a factor

$$\exp(-2\pi^2 pkx/\beta H),$$

where $x$ has the dimension of temperature and is related to the collision time $\tau$ by the expression

$$x = h/(2\pi^2 k\tau). \quad (12)$$

It can be shown that if Eq. (8) is applicable $T+x$ is given by the product of $-\beta/2\pi^2 k$ and the slope of the straight line obtained when $\log(aH^{\frac{1}{2}})$ is plotted against $H^{-1}$. One such plot appears in Fig. 7 where the open circles correspond to values of $a$ which have been adjusted for the difference between the exponential and the sinh (as in Fig. 6) while the dark circles correspond to unadjusted values. The values obtained in this way for $x$ (which incidentally proved to be quite insensitive to the above correction) are listed in Table I. Although the agreement between experiment and theory appears satisfactory in that straight lines were obtained on all such plots as Fig. 7, it should be mentioned that straight lines could also be obtained when the power of $H$ in the ordinate was varied by as much as 1. Since the range of fields which could be investigated conveniently was limited to 6 or 7 kilogauss, it was not possible to test this aspect of the theory more conclusively. Furthermore, inasmuch as attempts to express $m'$, $m''$, and $\Delta m$ in terms of the components of an effective mass tensor were unsuccessful, no comparison was possible between the observed absolute amplitude of the oscillations and that predicted by the theory. It is doubtful that such a comparison would be very satisfactory in any event, for the amplitude was not a very reproducible feature from run to run under supposedly identical experimental conditions. This is typical of

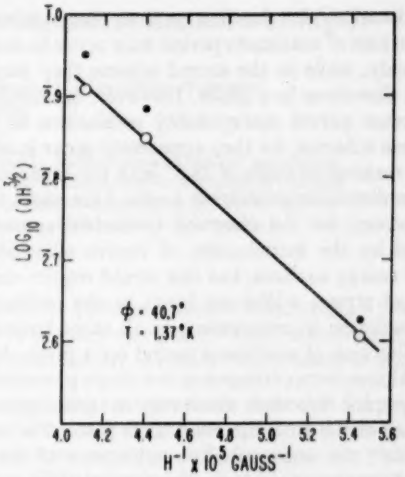


FIG. 7. $\text{Log}_{10}(aH^{\frac{1}{2}})$ for $\phi = 40.7°$ *versus* $H^{-1}$. Values of the amplitude damping parameter $x$, resulting from collision broadening of the energy levels, are derived from the slopes of such plots. The open circle points were obtained by adjusting the solid circle points for the difference between the sinh in Eq. (1) and the exponential in Eq. (8).

crystals exhibiting short period susceptibility oscillations[4,5] and may be due to a variety of causes such as inexact positioning of the crystal in the slightly inhomogeneous field and also strains introduced by successive coolings and warmings.

## DISCUSSION

The most significant feature of the de Haas-van Alphen effect in cadmium is its unusual orientation dependence which is described to a first approximation by Eq. (7) when the couple is measured at right angles to the plane containing the hexagonal axis and the magnetic field. It is probable (although at present very difficult to confirm experimentally) that an equation of the form

$$(\beta/E_0)_{\pm}^2 = (1.88\times10^{-7})^2 \cos^2(\phi \pm 28.5°) + P^2 \sin^2(\phi \pm 28.5°), \quad (13)$$

where $0 < P \ll 1.88\times10^{-7}$ gauss$^{-1}$ would be a better representation, since it is unlikely that the period would ever go to zero. In any event, attempts to interpret this orientation dependence in terms of constant energy surfaces described by existing theories were unsuccessful for reasons which will now be discussed.

If the constant energy surface for a given de Haas-van Alphen term is not a sphere, the period of the susceptibility oscillations will be a function of the orientation of the crystal with respect to the magnetic field, and a maximum period will be attained for certain directions of the field. For surfaces described by existing theories (again excluding the sphere) the oscillations of maximum period may occur according to one of two schemes, depending upon what surface is under

consideration. In the first scheme the susceptibility oscillations of maximum period may occur in one direction only, while in the second scheme they may occur in all directions in a plane. However, in cadmium the maximum period susceptibility oscillations fit neither of these schemes, for they apparently occur in all directions making an angle of 28.5° with the hexagonal axis, i.e., in directions generating a cone. One might attempt to account for the observed twelvefold symmetry in period by the introduction of twelve ellipsoidal constant energy surfaces, but this would require the existence of strong additional beats in the oscillations in contradiction to experiment. In all other known cases[4] the direction of maximum period for a given de Haas-van Alphen term corresponds to a single prominent crystallographic direction, which may in turn suggest where overlap of the Brillouin zone takes place. For example, in zinc[14] the susceptibility oscillations of maximum period occur along a single direction only, the hexagonal axis. It is interesting to note, however, that the angle $\phi = 28.5°$ at which the period exhibits its maximum value in cadmium is very nearly equal to $\cot^{-1}(c/a)$ (where $c/a$ is the axial ratio for cadmium), which has the value 27.9° at room temperature and a slightly greater value at liquid helium temperatures. In spite of this coincidence in angles the juxtaposition of the constant energy surface for the pertinent electrons with respect to the Brillouin zone boundaries is not at all clear.

Nevertheless the comparison between cadmium and zinc is of further interest, for they are both divalent (each with two $s$ electrons in its outer shell), they form hexagonal crystals, and their $c/a$ ratios differ by less than 2 percent. However, their lattice constants differ by roughly 10 percent and not only do the orientation dependences of the susceptibilities differ as discussed above, but the maximum period in zinc is greater than that in cadmium by a factor of roughly 350. One might conclude on these bases that the electronic structures of these crystals differ quite radically from each other. Thus, in the light of recent investigations[15–17] which have revealed an intimate relation between the de Haas-van Alphen effect and magnetoresistance for certain specific crystallographic orientations (in bismuth, graphite, and zinc) one might expect the orientation dependences and magnitudes of the magnetoresistance to differ quite markedly in cadmium and zinc. On the contrary, low-temperature magnetoresistance measurements performed by Lazarev, Nachimovich, and Parfenova[18] on single crystals of cadmium and zinc in transverse fields show remarkably similar features both as regards orientation dependence and magnitude. A possible explanation is that for certain orientations (i.e., those for which the correlation between susceptibility and magnetoresistance is observed) the electronic structure, as described by the chemical potential and effective masses, is the important factor in determining the magnetoresistance while in general the geometry of the lattice alone is most important. A second possible explanation is that still other de Haas-van Alphen terms, observable only at higher magnetic fields and lower temperatures and characterized by comparable electronic parameters, exist in cadmium and zinc.

In any event, the failure of attempts to account for the orientation dependence of the de Haas-van Alphen effect in cadmium suggests that (1) a more general application of the free electron theory is needed to provide for a greater variety of constant energy surfaces, or (2) possibly the relation between the susceptibility oscillations and specific features of the Fermi surface may be more subtle than has heretofore been hoped.

## ACKNOWLEDGMENTS

It is a pleasure to acknowledge the help of Mr. Peter Siebenmann in growing the cadmium crystals. I also wish to thank Professor L. Onsager of Yale University for his interest, Dr. F. D. Rosi of the Sylvania Research Center for the single crystal of hexagonal titanium, and Dr. R. Maddin of Johns Hopkins University for the tantalum and molybdenum single crystals. Finally, my sincere thanks are due the members of the Cryogenics Branch for many helpful suggestions and long hours of assistance during helium runs.

[14] S. G. Sydoriak and J. E. Robinson, Phys. Rev. **75**, 118 (1949). See also references 4 and 12.
[15] P. B. Alers and R. T. Webber, Phys. Rev. **91**, 1060 (1953).
[16] Ted G. Berlincourt, Phys. Rev. **91**, 1277 (1953).
[17] Ted G. Berlincourt and John K. Logan, Phys. Rev. **93**, 348 (1954).
[18] Lazarev, Nachimovich, and Parfenova, J. Exptl. Theoret. Phys. (U.S.S.R.) **9**, 1169 (1939).

# Energy and Temperature Dependence of the Secondary Emission of MgO†

A. J. DEKKER
*Department of Electrical Engineering, University of Minnesota, Minneapolis, Minnesota*
(Received January 18, 1954)

It is shown that the data on the energy and temperature dependence of the secondary yield of magnesium-oxide single crystals, recently published by Johnson and McKay, can be understood on the basis of a simple model. In fact, quantitative agreement is obtained for the temperature coefficient of the yield. The importance of measurements far away from either side of the maximum of the yield curve is stressed.

## 1. INTRODUCTION

A NUMBER of accurate measurements on the secondary emission coefficient of magnesium-oxide single crystals has recently been published by Johnson and McKay[1] in his journal. Their measurements of the secondary yield $\delta$ extend over a primary range up to 5 kev and over a temperature range between room temperature and 740°C. In view of the fact that the yield curves have been measured far beyond the maximum, it seems of interest to attempt to explain these observations on the basis of a simple model and, as we shall see below, this is indeed possible. The reasons why in secondary emission the regions far away on either side from the maximum are of particular interest in setting up suitable models for the secondary emission process will be made clear below.

The fact that the specimens used by Johnson and McKay showed variations in $\delta_{max}$ between about 5.5 and 7.1 is probably of no consequence for the considerations given in the present paper. Johnson and McKay ascribe these variations to possible changes in the physical structure or in the work function resulting from the treatment after cleavage. Another possible factor may be sought in variations in the concentration of excess oxygen in the crystals.[2] Whatever be the cause, experience in this laboratory indicates that vacuum heating of MgO to a temperature of 740°C over periods required for the $\delta$ measurements does not alter its physical properties. It thus seems safe to assume that the values of $\delta$ given by Johnson and McKay for a given crystal actually pertain to a crystal with a fixed set of physical properties. From the measured points published in Fig. 5 of the paper referred to above, the following table may be set up for one of their samples in the high primary energy region:

$E_{p0}$ represents the energy of the bombarding primaries. We note that for the sample under consideration the maximum yield at room temperature is 7.0, occurring for $E_{p0}\simeq 1100$ ev; at 740°C the maximum yield of 6.2 is obtained for $E_{p0}\simeq 900$ ev. From the table the following conclusions may be drawn:

(a) For primary energies $\gtrsim 2$ kev the ratio $\delta_{740}/\delta_{20}$ is practically constant; the average value is $0.79\pm 0.04$ if we exclude the perhaps doubtful value at $E_{p0}=3.0$ kev.

(b) For primary energies $\gtrsim 3$ kev the secondary yield varies approximately inversely proportional to $E_{p0}$.

Moreover, their measurements show that for primary energies below 500 ev the temperature effect is negligible, whereas the value of $E_{p0}$ at which the yield is a maximum shifts to lower values at higher temperatures. For a qualitative explanation of the temperature effect we refer to the paper of Johnson and McKay.

## 2. THE LOW PRIMARY ENERGY REGION

Before discussing the conclusions drawn from the table a few remarks about the low primary energy region may be in order. Denoting the number of secondary electrons produced by a primary at a depth between $x$ and $x+dx$ below the surface by $n(x)dx$ and the probability of escape by $f(x)$, the secondary yield may be written as

$$\delta=\int_0^\infty n(x)f(x)dx. \tag{1}$$

If the penetration depth $x_p$ of the primaries is very small compared with the range $x_s$ of the secondaries, the function $f(x)$ is approximately a constant and (1) reduces to

$$\delta\simeq nf(0), \quad x_p\ll x_s, \tag{2}$$

where $n$ is the total number of secondaries produced per incident primary electron. Now, for primary energies larger than several times the energy required to produce a secondary, it seems reasonable to assume that the

TABLE I. Values of the secondary emission coefficient of MgO as function of the primary energy $E_{p0}$ at room temperature and at 740°C. The data are taken from Fig. 5 in the paper by Johnson and McKay and only refer to the region beyond the maximum of the yield curve.

| $E_{p0}$ (kev) | $\delta_{740°C}$ | $\delta_{20°C}$ | $\delta_{740}/\delta_{20}$ | $(E_{p0}\delta)_{20°C}$ (kev) |
|---|---|---|---|---|
| 5.0 | 2.18 | 2.74 | 0.79 | 13.7 |
| 4.5 | 2.18 | 2.86 | 0.76 | 12.9 |
| 4.0 | 2.74 | 3.64 | 0.75 | 14.6 |
| 3.5 | 2.89 | 3.69 | 0.78 | 13.0 |
| 3.0 | 3.19 | 4.69 | 0.68 | 14.1 |
| 2.5 | 3.81 | 4.92 | 0.77 | 12.4 |
| 2.0 | 4.61 | 5.55 | 0.83 | 11.1 |
| 1.75 | 5.15 | 6.15 | 0.84 | 10.8 |

† Work supported by the U. S. Army Signal Corps.
[1] J. B. Johnson and K. G. McKay, Phys. Rev. **91**, 582 (1953).
[2] K. C. Nomura, Phys. Rev. **89**, 894 (1953).

total number of secondaries produced is proportional to $E_{p0}$. For such primary energies then (as long as $x_p \ll x_s$), the yield should according to (2) be proportional to $E_{p0}$. For MgO this seems to be approximately the case up to $E_{p0} \simeq 400$ ev, according to the results of Johnson and McKay. The importance of yield measurements in the low primary energy region is primarily that they may be used to study possible changes in the electron affinity of a crystal, because the latter determines in part the escape probability. For example, at present it is not known whether a stoichiometric excess of oxygen in the MgO crystals as a whole is correlated with a change in electron affinity.

A tentative indication about the electron affinity of MgO may be inferred from the first crossover point ($\delta = 1$) which for the sample under consideration occurs at a primary energy of 32.8 ev. Primaries of this energy may be expected to produce about two secondaries, indicating that $f(0) \simeq 0.5$. Now, the probability of escape of an electron at the surface with an energy $\epsilon$ in the conduction band is $0.5[1-(X/\epsilon)^{\frac{1}{2}}]$, where $X$ is the electron affinity. Although this formula cannot be applied immediately to the case under consideration, the implication seems to be that $X \ll \epsilon$, i.e., $X$ is probably only a fraction of an ev.

### 3. THE HIGH PRIMARY ENERGY RANGE

Beyond the maximum in the yield curve, the range of the secondaries $x_s$ is smaller than the penetration depth of the primaries. It will be assumed that, at any rate over the secondary range, the primaries move essentially along straight lines. Also, it will be assumed that the number of secondaries produced per unit depth is proportional to the energy loss per unit length of the primaries. As is well known, the primaries lose energy in accordance with the equation[3]

$$-\frac{dE_p}{dx} = \text{const}\frac{1}{E_p}\log\frac{2E_p}{\epsilon}, \tag{2}$$

where $\epsilon$ represents an excitation energy. Over a limited range of $E_p$ this expression may be approximated fairly well by Whiddington's law:

$$-\frac{dE_p}{dx} = \frac{A}{E_p}, \quad \text{or} \quad E_p(x) = (E_{p0}^2 - 2Ax)^{\frac{1}{2}}. \tag{3}$$

For the yield at large values of $E_{p0}$ one is in fact only interested in the production of secondaries over a depth range over which the primaries have lost only a fraction of their total energy, because the function $f(x)$ decreases rapidly beyond a certain value. From (3) it follows that

$$n(x) = -\frac{1}{\epsilon_e}\frac{dE_p(x)}{dx} = \left(\frac{A}{2}\right)^{\frac{1}{2}}\frac{1}{\epsilon_e(x_p - x)^{\frac{1}{2}}}, \tag{4}$$

[3] See A. J. Dekker and A. van der Ziel, Phys. Rev. **86**, 755 (1952).

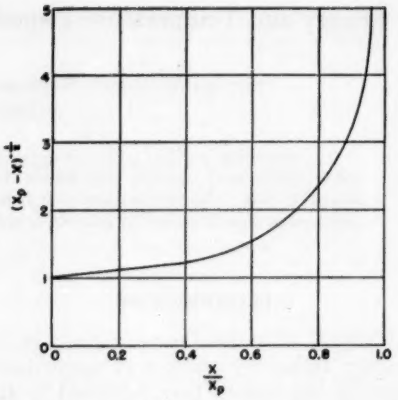


FIG. 1. The function $(x_p - x)^{-\frac{1}{2}}$ *versus* $x/x_p$ which determines the production of secondaries as function of depth for a Whiddington law.

where $\epsilon_e$ is the average energy required to produce a secondary and $x_p = E_{p0}^2/2A$. Thus, as long as the range of the secondaries is small compared with $x_p$, the production of secondaries is practically constant over this range and equal to

$$n(x) \simeq A/(\epsilon_e E_{p0}), \tag{5}$$

as may be seen from Fig. 1. For a primary energy of 3 kev, for example, $x_s/x_p \simeq 0.1$ in MgO; and for 5 kev, $x_s/x_p \simeq 0.04$. From (1) and (5) we thus obtain for the yield at high primary energies,

$$\delta = \frac{A}{\epsilon_e E_{p0}} f, \quad \text{with} \quad f = \int_0^{x_p} f(x)dx \simeq \int_0^{\infty} f(x)dx. \tag{6}$$

The integral $f$ is determined by the crystal under consideration and depends on its temperature, electron affinity, density of electron traps, etc. However, if these quantities are fixed, the product $E_{p0}\delta$ should be constant according to (6), in agreement with the findings of Johnson and McKay. It also shows the importance of yield measurements for primary energies far beyond the maximum, because such measurements provide direct information about the integrated probability of escape. One example is the influence of temperature on the secondary yield for high primary energies, discussed below. In a similar fashion, the influence of electron traps may be studied and models for the escape mechanism may be checked. Unfortunately, most yield measurements have been carried out too close to the maximum yield to allow a quantitative interpretation because in such cases one is not permitted to employ the simplifying assumption made here.

### 4. THE TEMPERATURE DEPENDENCE OF THE YIELD AT HIGH PRIMARY ENERGIES

As a first step it seems reasonable to attempt an explanation of the temperature effect on the basis of electron-lattice scattering alone, neglecting possible

trapping, etc. It seems that indeed this provides already a quantitative interpretation of the results obtained by Johnson and McKay, as shown below. From the theory of electron-lattice scattering (see appendix) in ionic crystals it follows that per collision a secondary loses on the average an amount of energy

$$-(d\epsilon/dx)\lambda = h\nu/(2n_\nu+1) = \alpha(T), \tag{7}$$

where $\lambda$ represents the mean free path and $\nu$ the frequency of the longitudinal optical vibrational modes. The quantum numbers $n_\nu$ are given by

$$n_\nu = 1/[e^{h\nu/kT}-1]. \tag{8}$$

From the optical data[4] on MgO one finds that $h\nu \simeq 1300k$, where $k$ is Boltzmann's constant. It should be noted that $\alpha(T)$ in (7) is a function of temperature alone and independent of the energy of the electron. If for simplicity it is assumed that all secondaries are produced with the same energy $\epsilon_0$, it follows from (7) that the energy of a secondary after $N$ collisions is equal to

$$\epsilon(N) = \epsilon_0 - N\alpha(T). \tag{9}$$

Moreover, the mean free path of the secondaries may be written as

$$\lambda = \lambda_0\epsilon/(2n_\nu+1), \tag{10}$$

where for the energy range of interest $\lambda_0$ is approximately constant as indicated in Fig. 2. According to the last two equations, the mean free path as function of the number of collisions suffered by the secondary after its birth is

$$\lambda = [\lambda_0/(2n_\nu+1)](\epsilon_0 - N\alpha). \tag{11}$$

For the escape mechanism the following, admittedly simplified, model will be adopted: on their way to the surface the secondaries carry out a one-dimensional random walk perpendicular to the surface, with steps decreasing in accordance with (11). Furthermore, it will be assumed that secondaries that have lost an energy $\epsilon_0'$ do not take part in the secondary emission process any longer. In other words, the life of the secondaries is limited to a maximum number of collisions $N_m$ given by

$$N_m\alpha = \epsilon_0'. \tag{12}$$

Two remarks may be injected at this point. From (7) it follows that the energy lost per collision at room temperature and 740°C is respectively

$$\alpha(298°\text{K}) = 0.108 \text{ ev}, \quad \alpha(1013°\text{K}) = 0.063 \text{ ev}.$$

In other words, the energy loss is smaller at the higher temperature. This by itself would lead to an increase in yield with increasing temperature and the observed decrease must thus result from a decrease in $\lambda$ which swamps this effect. In this connection it is interesting to consider the requirement (12) for the hypothetical case that the secondaries move in straight lines towards the surface, rather than in a random walk fashion. Under these circumstances the secondary range would be equal to $N_m\langle\lambda\rangle_{Av}$, where $\langle\lambda\rangle_{Av}$ represents the average mean free path during the life of the electron measured in numbers of collisions. It follows immediately from (7), (11), and (12) that $N_m\langle\lambda\rangle_{Av}$ is independent of temperature. One thus concludes that the observed temperature effect is essentially determined by the zig-zag nature of the paths of the secondaries.

Continuing now with the random walk model, one can readily show that the mean square displacement corresponding to $N$ steps, the length of which decreases with a fixed amount for each collision in accordance with (11), is given by

$$\langle x^2\rangle_{Av} = N\langle\lambda^2\rangle_{Av}, \tag{13}$$

where the average of $\lambda^2$ is taken over $N$ collisions. If $N = N_m$ the corresponding quantity $\langle x^2\rangle_{Av}$ will be considered as the square of the secondary range $x_s$ in the model adopted here. According to (11) and (13) the range of the secondaries for a given temperature is then equal to

$$x_s = \left[N_m\frac{\lambda_0^2}{(2n_\nu+1)^2}(\epsilon_0^2+\alpha^2\langle N^2\rangle_{Av} - 2\epsilon_0\alpha\langle N\rangle_{Av}\right]^{\frac{1}{2}}, \tag{14}$$

where the average value of $N$ is $N_m/2$ and where for $N_m \gg 1$ one may write

$$\langle N^2\rangle_{Av} = \int_0^{N_m}\frac{N^2dN}{N_m} = \frac{1}{3}N_m^2. \tag{15}$$

By employing (7) and (12), expression (14) may then be written as

$$x_s = \text{const}(2n_\nu+1)^{-\frac{1}{2}}. \tag{16}$$

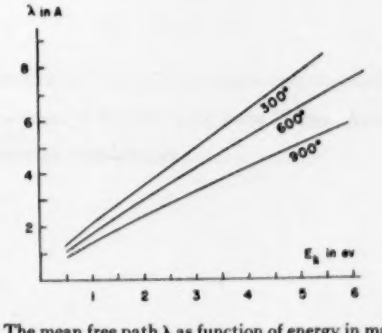


FIG. 2. The mean free path $\lambda$ as function of energy in magnesium oxide as calculated from (26a) and (26b) for $T = 300°$, $T = 600°$, and $T = 900°$ absolute.

[4] See H. Frohlich, *Theory of Dielectrics* (Oxford University Press, Oxford, 1949), pp. 155 and 158. [The maximum optical absorption (transverse waves) has been observed at $17.3\times10^4$A. For longitudinal waves the frequency is larger by a factor $(K/K_0)^{\frac{1}{2}}$ where $K$ and $K_0$ are, respectively, the static and high-frequency dielectric constant. For MgO these constant are $K \simeq 10$ and $K_0 \simeq 3$, leading to $h\nu \simeq 1300k$.]

Hence, as $T$ increases, $n_r$ increases and the range of the secondaries decreases. Now, for high primary energies the number of secondaries produced at a depth $x$ is given by (5) so that the yield is proportional to

$$(A/\epsilon_0 E_{p0})x_s. \tag{17}$$

For a given value of $E_{p0}$ the ratio of the yields at two temperatures $T_1$ and $T_2$ will thus be given by

$$\delta_1/\delta_2=[(2n_{r2}+1)/(2n_{r1}+1)]^{\frac{1}{2}}. \tag{18}$$

The fact that $\delta_1/\delta_2$ is independent of the primary energy far enough beyond the maximum in the yield curve is in agreement with the observations of Johnson and McKay. Also, for the ratio corresponding to $T_1=1013°K$ and $T_2=298°K$ (18) yields $\delta_1/\delta_2=0.76$, in good agreement with the experiments. It may be noted that (18) is also in agreement with the observations of Johnson and McKay in so far as $\delta$ is approximately a linear function of $T$ over the range between room temperature and 740°C.

One may raise objections to the one-dimensional model employed here. In view of the fact that only the ratio of the ranges of the secondaries at the two temperatures is involved, it would seem, however, that a three-dimensional treatment would lead to the same result because both (11) and (12) retain the same form so that the temperature dependence of $\langle\lambda^2\rangle_{Av}$ is the same as in the case treated above. The simple model employed here thus gives a quantitative interpretation of the observations.

## APPENDIX

A summary of the theory of interaction between slow electrons and lattice vibrations in ionic crystals, initiated by Frohlich,[5] may be found in a paper by Seitz.[6] Let Ze be the charge per ion, $M$ the effective mass per ion pair, $a$ the shortest interionic distance, $n$ the number of ion pairs per unit volume, $\nu$ the frequency of the optical vibrations, $q$ the wave vector of a particular vibrational mode, and $E$ the energy of the electron. The mean free path between collisions may then be shown to be given by

$$\frac{1}{\lambda}=\frac{\pi mZ^2e^4}{2nMa^6h\nu}\frac{2n_\nu+1}{E}\int\frac{dq}{q}. \tag{19}$$

The lower limit of the integration over $q$ is equal to $2\pi m\nu/hk$, where $k$ is the wave vector of the electron. The maximum wave vector of the phonons is about equal to $\pi/a$ and this value may be employed as the upper limit as long as $2k\geqslant\pi/a$. If, however, $2k<\pi/a$, the upper limit must be taken as $2k$. For MgO the mean free path has been plotted in Fig. 2 as function of the energy of the electron for three different temperatures, assuming (19) to be valid. This shows that $\lambda$ is approximately a linear function of $E$ over the energy range of interest and thus justifies Eq. (10). It must be admitted, however, that because the mean free path turns out to be small, it is doubtful whether the perturbation method employed by Frohlich is valid.[7] On the other hand, the treatment by Seeger and Teller[8] leads to a similar energy dependence of $\lambda$ and it would seem therefore that (10) is formally correct.

Although the loss of energy by an electron per unit time is an essential quantity in calculating mobilities, the energy loss per unit path length is essential in the escape mechanism. One can show on the basis of the ideas developed by Frohlich that

$$-\frac{dE}{dx}=\frac{\pi mZ^2e^4}{2nMa^6}\cdot\frac{1}{E}\int\frac{dq}{q}. \tag{20}$$

Equation (7) then follows immediately from (19) and (20).

The author wishes to acknowledge the interest of Drs. W. G. Shepherd and A. van der Ziel in this problem.

[5] H. Frohlich, Proc. Roy. Soc. (London) **160**, 230 (1937); **172**, 94 (1939).
[6] F. Seitz, Phys. Rev. **76**, 1376 (1949).
[7] See F. Seitz, *The Modern Theory of Solids* (McGraw-Hill Book Company, Inc., New York, 1940), p. 534.
[8] R. Seeger and E. Teller, Phys. Rev. **54**, 515 (1938); **56**, 352 (1939).

# Alpha-Particle Ionization Yields in a Gridded Chamber*

LLOYD O. HERWIG† AND GLENN H. MILLER
*Institute for Atomic Research and Department of Physics, Iowa State College, Ames, Iowa*

(Received Februrary 8, 1954)

The energy per ion pair for natural uranium alpha particles has been measured for several gases in a gridded parallel-plate ion chamber. Electron collection was used. The gases employed were He, Ne, A, Kr, $N_2$, A+3 percent $CO_2$, and A+5 percent $N_2$. On a relative basis, the results are in good agreement with those obtained by Jesse and Sadauskis using heavy ion collection. The absolute values herein reported are about 6 percent higher than those resulting from slow chamber measurements.

IN recent years, the average energy per ion pair for alpha particles in various gases has been measured by a number of investigators.[1–6] All of these measurements, except for the last, were made in ionization chambers utilizing heavy ion collection. The measurements herein presented were accomplished by means of electron collection, and so it is interesting to compare them with the results of other investigators.

The ionization chamber employed a grid which was located 8 cm from the source electrode and 1.25 cm from the collector. The grid consisted of parallel wires 0.008 cm in diameter, spaced 0.2 cm apart. The alpha source was of natural uranium and was about 50 microgram-cm$^{-2}$ thick. It was collimated so that the angle of emission measured from the normal to the source did not exceed 77 degrees. The amplifier had equal rise and clipping times of 30 microseconds. The rise time of pulses coming from the chamber did not exceed 15 microseconds. Dots representing the peak of each pulse were displayed on a cathode ray tube and photographed. The film was analyzed using a photoscanning device developed in the Ames Laboratory.[7] The inert gases were purified continuously by passage through chips of a Ca-Mg alloy at a temperature of 470°C. Unpurified tank gases, passed through a cold trap, were used in mixtures.

The results are shown in Table I, along with those of other investigators. The probable error was ±2 percent for our values. The number to the right of the absolute energy per ion pair in each case is the energy per ion pair relative to that of nitrogen. Nitrogen was chosen because the agreement between investigators appears to be best for this gas. It is to be noted that the present results agree well with those of Jesse and Sadauskis on a relative basis, but appear to be high in absolute value. This seems to be consistent with the findings of Bertolini, Bettoni, and Bisi, who also used electron collection in a gridded chamber. It appears from this that there may be some process, as yet unidentified, which affects one type of measurement and not the other.

TABLE I. Energy per ion pair for alpha particles in various gases. The numbers in parentheses are the energies per ion pair relative to that of nitrogen.

| Gas \ Investigator | Our value ev | Jesse and Sadauskis ev | Bortner and Hurst ev | Haeberli *et al.* ev | Valentine and Curran ev | Bertolini *et al.* ev |
|---|---|---|---|---|---|---|
| Argon | 27.7(0.714) | 26.4(0.721) | 26.4(0.727) | 26.25(0.723) | 25.9(0.720) | 28.9(0.763) |
| Helium | 44.2(1.139) | 42.7(1.167) | 46.0(1.267) | 30.86(0.850) | 31.7(0.881) | |
| Krypton | 25.7(0.662) | 24.1(0.659) | | | | |
| Neon | 38.6(0.995) | 36.8(1.006) | | | | |
| Nitrogen | 38.8(1.000) | 36.6(1.000) | 36.3(1.000) | 36.3(1.000) | 36.0(1.000) | 37.9(1.000) |
| Argon +3% $CO_2$ | 27.4(0.706) | | | | | |
| Argon +5% $N_2$ | 28.5(0.735) | | | | | |

* Contribution No. 291 from the Institute for Atomic Research and Department of Physics, Iowa State College, Ames, Iowa. Work was performed in the Ames Laboratory of the Atomic Energy Commission.

† Present Address: Atomic Power Division, Westinghouse Laboratories, Pittsburgh, Pennsylvania.

[1] T. E. Bortner and G. S. Hurst, Phys. Rev. **90**, 160 (1953).
[2] W. P. Jesse and J. Sadauskis, Phys. Rev. **90**, 1120 (1953).
[3] J. Sharpe, Proc. Phys. Soc. (London) **A65**, 859 (1952).
[4] J. M. Valentine and S. C. Curran, Phil. Mag. **43**, 964 (1952).
[5] Haeberli, Huber, and Baldinger, Helv. Phys. Acta **25**, 467 (1952).
[6] Bertolini, Bettoni, and Bisi, Nuovo cimento (9) **9**, 1004 (1952).
[7] Hunt, Rhinehart, Weber, and Zaffarano, Rev. Sci. Instr. (to be published).

# Hyperfine Structure in the Spectrum of $N^{14}H_3$.† I. Experimental Results

G. R. GUNTHER-MOHR,* R. L. WHITE, AND A. L. SCHAWLOW,‡ *Radiation Laboratory, Columbia University, New York, New York*

AND

W. E. GOOD AND D. K. COLES, *Westinghouse Research Laboratories, East Pittsburgh, Pennsylvania*

(Received December 28, 1953)

The structure of the hyperfine spectrum of $N^{14}H_3$ in the microwave region has been carefully re-examined. It has been found that the $N^{14}$ quadrupole line spacings for $K \neq 1$ can be fitted within experimental error to previously developed theory, provided a small change in the quadrupole coupling constant $eqQ$ due to centrifugal distortion of the molecule is allowed for. For $K=1$; and $J=2,3,4$, a doubling of each line of the quadrupole pattern has been found which increases from about 70 to 150 kc/sec with increasing $J$. It has been possible to explain these new features of the spectrum in terms of the interactions of the magnetic moments of the protons with the molecular magnetic field caused by rotation and with the magnetic moment of the $N^{14}$ nucleus.

## I. INTRODUCTION

SINCE the first measurements by Cleeton and Williams[1] on the inversion spectrum of the symmetric top molecule $NH_3$ in the radio-frequency range, a great number of increasingly detailed investigations of this spectrum have been made.[2] A hyperfine spectrum arising from the interaction of the nitrogen quadrupole moment $Q_N$ with the gradient of the molecular electric field $q$ at that nucleus was found and explained. Later a more extended and careful set of measurements[3] showed that a simple quadrupolar interaction would not completely fit the data. The addition of a term $c\mathbf{I}\cdot\mathbf{J}$ to the molecular Hamiltonian by Henderson[4] ($I_N$ is the nitrogen spin, $J$ the total angular momentum of the molecule exclusive of nuclear spin) accounted for discrepancies within their experimental accuracy. However, experimental errors were on the average about 25 percent of the $\mathbf{I}_N\cdot\mathbf{J}$ corrections applied to the quadrupole line spacings. Further, a doubling of the main absorption lines for $J=3,4$ and $K=1$ ($K$ is the projection of $J$ on the molecular symmetry axis) had been observed[5] and were still completely unexplained.

A careful re-examination of the hyperfine $NH_3$ spectrum shows that the quadrupole line spacings for $K\neq 1$ can be fitted to within our experimental error of $\pm 3$ kc/sec provided that, in addition to Henderson's $\mathbf{I}_N\cdot\mathbf{J}$ term, a change in the quadrupole coupling constant $eqQ$, due to centrifugal distortion of the molecule is allowed for. For $K=1$, the above mentioned doubling was found in both the main lines and their satellites for $J=2, 3, 4$. This doubling differs for each line of the quadrupole pattern and increases with $J$, representative values being from 70 to 150 kc/sec. It has been possible to explain these new features of the spectrum in terms of the interaction of the magnetic moments of the three protons with the molecular magnetic field caused by rotation and with the magnetic moment of the $N^{14}$ nucleus. We shall present the details of the theory in the following article, which we shall refer to as paper II, and make use of the results therein without further justification here.

## II. HYPERFINE STRUCTURE IN $N^{14}H_3$ WHEN $K\neq 1$

### Experimental Results

Energy due to hyperfine interactions between the nitrogen and the remainder of the $NH_3$ molecule is given to a good approximation by

$$W_{JKF_1}=-eqQ\left[1-\frac{3K^2}{J(J+1)}\right]\times\frac{3\mathbf{I}_N\cdot\mathbf{J}+\frac{3}{2}\mathbf{I}_N\cdot\mathbf{J}-I_N(I_N+1)J(J+1)}{2I_N(2I_N-1)(2J-1)(2J+3)}+\left[a+\frac{(b-a)K^2}{J(J+1)}\right]\mathbf{I}_N\cdot\mathbf{J}. \quad (1)$$

The first term of (1) is due to the interaction between the nuclear quadrupole moment $Q$, and the gradient of the electric field $q=\partial^2V/\partial z^2$ at the nucleus due to other molecular charges.[6] The second terms represent the interaction between the magnetic moment of the nitro-

† Work at Columbia University supported by the U. S. Atomic Energy Commission.

* U. S. Atomic Energy Commission Predoctoral Fellow. Now at the Watson Laboratory, Columbia University. This work is submitted in partial fulfillment of the requirements for the degree of Doctor of Philosophy at Columbia University.

‡ Present address: Bell Telephone Laboratories, Murray Hill, New Jersey.

[1] C. E. Cleeton and N. H. Williams, Phys. Rev. **45**, 234 (1934).

[2] We refer the reader to C. H. Townes and P. Kisliuk—Molecular Microwave Tables, National Bureau of Standards Circular 518, June 23, 1952 (unpublished), in which will be found a summary of the experimental and theoretical work on this molecule together with a survey of the literature and a tabulation of microwave transition frequencies.

[3] J. W. Simmons and W. Gordy, Phys. Rev. **73**, 713 (1948).

[4] R. S. Henderson, Phys. Rev. **74**, 107 (1948); Erratum: Phys. Rev. **74**, 626 (1948); also see J. M. Jauch, Phys. Rev. **74**, 1262 (1948).

[5] W. E. Good reported this finding to the Ohio State Symposium on Molecular Structure and Spectroscopy in 1947 (unpublished).

[6] J. Bardeen and C. H. Townes, Phys. Rev. **73**, 97 (1948).

gen nucleus and magnetic fields produced by molecular rotation.[4] Magnetic interactions associated with the hydrogen nuclei can be neglected to a good approximation, as will be shown in the following.

The transition $\Delta F=0, \pm 1$ which are allowed give from (1) three strong lines of identical frequency and two weaker satellites on either side of these.

The experimental data for $K \neq 1$ listed in Table I were initially fitted by the method of least squares to the satellite intervals predicted from Eq. (1). The deviations found between experimental satellite separations and the calculated separations showed a decreasing trend with increasing $J$ and $K$. The square root of the average square deviation, $\delta$, of the inner satellite to main line separation is 3.3 kc/sec and this quantity is 5 kc/sec for the outer satellite to main line separations. The experimental error was estimated to be $\pm 3$ kc/sec for $K \neq 1$ (see Sec. III).

An investigation of the theoretically predicted proton effects (see below) revealed that these systematic deviations could not be attributed to them. Previous molecular beam investigations of $\mathbf{I}_N \cdot \mathbf{J}$ interactions[7] have indicated a possible dependence of the coefficient, $c$, on $J$. Calculation of the corrections needed to a pure quadrupole hyperfine line pattern in order to secure agreement with the experimental data clearly shown that the $\mathbf{I}_N \cdot \mathbf{J}$ coefficient would have to increase with $J$ for the outer satellites and decrease with $J$ for the inner ones. The dependence of this coefficient on $J$ could be caused by a rotational perturbation of the molecular electronic wave functions but such a perturbation should be independent of the orientation of the nitrogen spin relative to $J$.

Centrifugal distortion of the molecule may be expected to cause the gradient of the electric field $q$ at the nitrogen to be a function of $J$ and $K$. This effect depends on the molecular rotational energy and we may therefore write

$$q=\bar{q}[d_0+d_1J(J+1)+d_2K^2].$$

The values of $d_0, d, d_2$ which minimize $\delta=\frac{1}{2}(\sum_{i=1}^{n}\delta_i^2/n)^{\frac{1}{2}}$, where $\delta_i$ is the deviation of the experimental separation from the calculated one, are $d_0=1-4\times10^{-3}$, $d_1=10^{-4}$, $d_2=10^{-4}$. These values reduce $\delta$ to 1.7 kc/sec for the inner satellites and 2.8 kc/sec for the outer ones. The coupling constants are then:

$$eqQ=-4084.2(1+10^{-4}J(J+1)+10^{-4}K^2)\pm0.3 \text{ kc/sec},$$
$$a=6.1\pm0.2 \text{ kc/sec}$$
$$b=6.5\pm0.2 \text{ kc/sec}.$$

Calculated separations of the satellites from the main lines using the values above, are given in Table I. The errors listed are believed to be random.

On the basis of the above fit of theory and experiment, one can say that the $\mathbf{I}_N \cdot \mathbf{J}$ coefficient is constant within 5 percent from $J=2$ to $J=7$. This is in contrast to the results of some molecular beam experiments[8] in which, for the same range of rotation energies,[9] changes of the coefficient by a factor of as much as 2 have been reported.

It should be noted that the quadrupole coupling constant, $eqQ$, contains a small percent of pseudo-quadrupole effect[10] in addition to the pure quadrupole coupling of the nitrogen since these two effects are indistinguishable in their dependence on the quantum numbers (see $NH_3$, paper II).

TABLE I. Comparison of experiment and theory not including effects due to proton magnetic moments. Intervals are given in kc/sec relative to the inversion transition frequency without hyperfine structure. Theoretical positions were calculated with the aid of (1) assuming

$eqQ=-4084.2[1+10^{-4}J(J+1)+10^{-4}K^2]\pm0.3$ kc/sec,
$a=6.1\pm0.2$ kc/sec, $(b-a)=0.4\pm0.2$ kc/sec.

| | Inner satellites | | | Outer satellites | | |
|---|---|---|---|---|---|---|
| $JK$ | Experimental | Calculated | Deviation | Experimental | Calculated | Deviation |
| 21[a] | 675 | 675.0 | +0.0 | 1010 | 1009.4 | −0.6 |
| 22 | 1294 | 1294.7 | +0.7 | 2060 | 2056.5 | −3.5 |
| 31[a] | 1045 | 1046.5 | +1.5 | 1358 | 1361.4 | +3.4 |
| 33 | 1682 | 1679.3 | −2.7 | 2319 | 2320.6 | +1.6 |
| 41[a] | 1216 | 1214.3 | −1.7 | 1456 | 1465.7 | +9.7 |
| 55 | 2093 | 2092.6 | −0.4 | 2597 | 2597.5 | +0.5 |
| 65 | 1084 | 1085.6 | +1.6 | 1362 | 1359.0 | −3.0 |
| 76 | 1297 | 1298.9 | +1.9 | 1585 | 1589.0 | +4.0 |

[a] Adjusted for proton effects (See IV B) and added for comparison.

## III. APPARATUS AND EXPERIMENTAL DETAILS

### A. Apparatus

Part of the above measurements were made with a high-resolution balanced bridge spectrometer designed and built by S. Geschwind. A detailed account of the considerations involved in the construction of such an instrument will be found in Geschwind's thesis.[11] The measurements were completed with a modified version of Geschwind's instrument incorporating low-frequency Stark modulation. The original instrument's sensitivity had been limited to minimum detectable absorptions of the order of $\alpha_0 \cong 3\times10^{-8}$ because it was not possible to completely eliminate spurious signals arising from bridge unbalances caused by frequency dependent reflections. In addition the sensitivity was also reduced by other undesired signals originating in unsymmetric guide vibrations, minor unstabilities in the sensitive detecting circuits and in pick up on these circuits.

[7] J. C. Swartz and J. W. Trischka, Phys. Rev. **88**, 1085 (1952).

[8] M. Danos and S. Geschwind, Phys. Rev. **91**, 1159 (1953).

[9] This change is reported between $J=1$ and $J=25$ for $Li^6F^{19}$. Since the moment of inertia of LiF is about nine times that of $NH_3$, $J=7$ for $NH_3$ involves approximately the same rotational energy as $J=25$ for LiF.

[10] H. M. Foley, Phys. Rev. **72**, 504 (1947). He has discussed this effect for diatomic molecules.

[11] S. Geschwind, thesis, Columbia University, 1951 (unpublished). See also S. Geschwind, Ann. N. Y. Acad. Sci. **55**, 751 (1952).

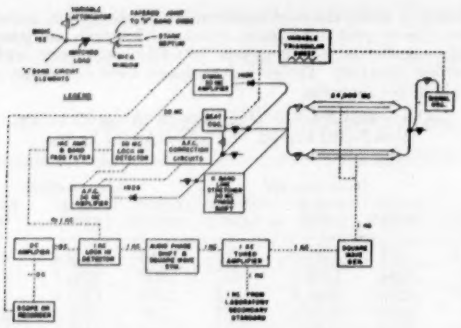

FIG. 1. Schematic diagram of high-resolution spectrometer.

In order to circumvent these difficulties and yet maintain the advantages of the original system, the spectrometer was adapted to use Stark modulation at 1 kc/sec as shown in Fig. 1. An appreciably higher Stark modulation frequency would have caused some broadening of very narrow lines.[12]

In spite of being very carefully constructed, the Stark septums in the arms of the new microwave bridge (Fig. 1) caused a very large increase in the amplitude of microwave reflections even at bridge balance and thus of the spurious signals associated with them. Though their fundamental frequency was equal to the repetition rate of the sawtooth sweep voltage ($\cong$1 cps), these signals had Fourier components of sufficiently large amplitude at 1 kc/sec to make discrimination against them difficult. In addition, their amplitude at 30 Mc/sec caused the high-gain first I.F. amplifier used in the detection system to saturate. The detection circuits described by Geschwind[11] were modified, therefore, by transferring a large fraction of the first I.F. amplifier's gain to a 1 kc/sec second I.F. amplifier. Because of the resulting low signal levels at the 1st lock-in-detector's control grid, it was necessary to drive that grid with a cathode follower to minimize pick up from the gating reference signal. A set of stagger-tuned twin $T$ narrow band amplifiers was inserted after the first lock-in to discriminate against the undesired signals at a low signal level.

Frequency was measured with marker pips generated in the usual manner[11] except that these were obtained by multiplying up directly from the primary laboratory standard which was monitored directly against WWV. The pips obtained at $K$ band starting with a 50 kc/sec standard frequency from a quartz crystal oscillator were 10 kc/sec wide.[13] The triangular sweep made it possible to set pips on the lines with both directions of sweep, thus completely eliminating errors in frequency measurements due to delays or phase shifts in the circuits.

[12] R. Karplus and J. Schwinger, Phys. Rev. **73**, 1020 (1948).

[13] We are indebted to Mr. R. Blume who designed and built the frequency standard used.

The spectrometer described above can detect a minimum gas absorption, $\alpha_g$, of $\alpha_g \cong 5\times10^{-9}$ for an effective band width of 10 cps, and has maintained the high resolution of the original instrument. At present it is impossible to use a recorder with the accompanying reduction in band width of the detecting system because the signal klystron, the source of microwave power, is not sufficiently stable in frequency.

### B. The Measurements

#### For $K\neq1$

The data given in Table I were taken at room temperature with satellite lines 100 kc/sec wide at half-amplitude and with main lines, which was slightly power saturated, 150 kc/sec wide. The tabulated separations are one-half the measured intervals between symmetrically placed satellites. In each case the position of the main line was also measured as a check on the expected symmetry of the line pattern. A careful re-examination of the lines for $J=2$, $K=2$; $J=3$, $K=3$; $J=5$, $K=5$ at $-78$°C with satellite line widths of 80 kc/sec revealed no additional features of the spectrum beyond those already discussed. The stated experimental error of $\pm3$ kc/sec represents the average deviations of several measurements. For a few values of $J$ and $K$, measurements first made on the original spectrometer and associated frequency measuring devices

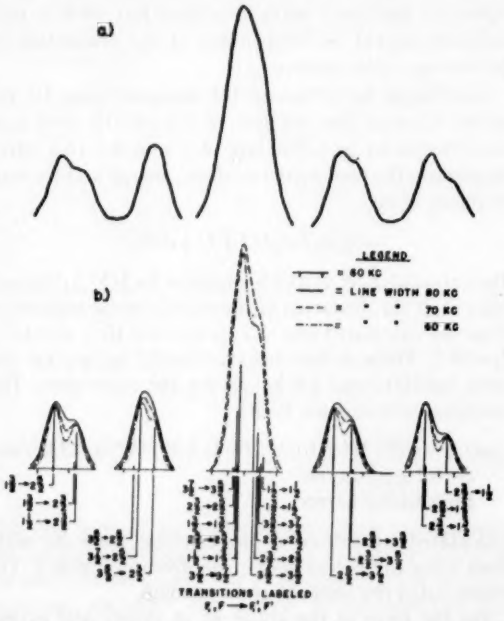


FIG. 2. Hyperfine structure of $N^{14}H_3$ inversion spectrum for $J=2$, $K=1$. (a) Photograph of oscilloscope trace. (b) Calculated hyperfine spectrum and corresponding line shapes. Frequency increases from left to right.

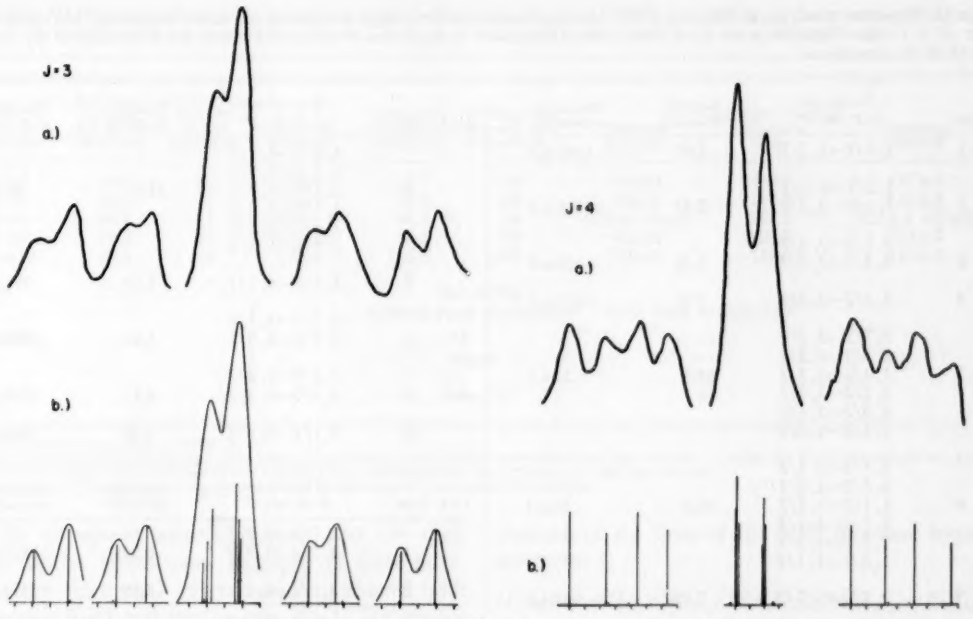


FIG. 3. Hyperfine structure of $N^{14}H_3$ inversion spectrum for $J=3$, $K=1$ and for $J=4$, $K=1$. (a) Photographs of oscilloscope traces. (b) Calculated transitions. For $J=3$, $K=1$ a line of half-widths $2\Delta\nu=80$ kc/sec was used to calculate the pattern. Frequency increases from left to right with 60 kc/sec intervals indicated.

were repeated to within 2 kc/sec on the rebuilt machine and frequency measuring system one year later.

### For $K=1$

As described above the splittings encountered here ranged from 70 to 150 kc/sec and thus were of the order of magnitude of the line widths. For this reason every effort was made to obtain narrow lines even at a large sacrifice in their intensity. All the measurements were made at $NH_3$ pressures of less than $10^{-4}$ mm, at power levels of the order of 10 $\mu$w/cm$^2$, and at a temperature of $-78$°C. Under these conditions the mean free path of the gas molecules was several times the cross-sectional dimensions of the $x$-band Stark guide which was used. Line widths, to which intermolecular collisions contributed negligibly, were determined by wall collisions and Doppler effect. The maximum absorptions, which at these pressures are proportional to the gas density, were down by a factor of about 50 from those given[2] for lines broadened only by intermolecular collisions. Theoretical line widths under these conditions are:[5] Doppler width at half-amplitude=60 kc/sec$=2\Delta\nu_D$; wall collision width at half-amplitude $=30$ kc/sec$=2\Delta\nu_w$ and total line width $2\Delta\nu=2((\Delta\nu_D)^2+(\Delta\nu_w)^2)^{\frac{1}{2}}=67$ kc/sec.

Experimentally these line widths were difficult to attain. In order to completely avoid saturation of the lines, the power level had to be reduced to such a low value that the automatic frequency control system did not function very satisfactorily. This, plus the theoretically expected decrease in sensitivity with a decrease in power resulted in rather poor sensitivity under conditions of optimum resolution. The observed spectra reproduced in Figs. 2 and 3 were taken at gas pressures sufficiently high to reduce the above difficulties and hence not at maximum resolution.

In Figs. 2 and 3 the theoretical patterns are drawn for various assumed line widths. At maximum resolution, the separations between line peaks or points of maximum curvature were measured for $J=2$, 3, 4 with special attention to the case $J=2$ from which most information could be hoped to be gained. These separations are listed in Table II. Measurements for $J=3$ were made with a line pattern approximately as drawn in the theoretical plots. In the case $J=4$, it was possible to completely resolve line No. 7 of the pattern and a direct measurement of its width gave

$$2\Delta\nu=64\pm8 \text{ kc/sec}.$$

Choice of the theoretical plots which gave the best fit of the measurements in the case $J=2$ indicate a line width at maximum resolution of

$$2\Delta\nu=68\pm5 \text{ kc/sec}.$$

These measurements confirm the theoretical line widths given above which were calculated according to the theory of Danos and Geschwind.[5]

TABLE II. Hyperfine spectrum of $NH_3$ for $K=1$. Lines are numbered by groups in order of increasing frequency. Measured intervals are all in kc/sec. Separations are given from a line undisplaced by hyperfine structure. Intensities are in percent of the total intensity of all the transitions.

| $J=2$ Line | Transitions $F_1,F\rightarrow F_1',F'$ | Relative intensity | Measured separation |
|---|---|---|---|
| 1 | 1, 3/2→2, 5/2 | 3.01 | −1047±3 |
| 2 | 1, 3/2→2, 3/2<br>1, 1/2→2, 3/2 | 2.35 | −968±3 |
| 3 | 3, 7/2→2, 5/2<br>3, 5/2→2, 5/2 | 3.26 | −689±3 |
| 4 | 3, 5/2→2, 3/2 | 2.07 | −652±3 |
| 5 | 3, 7/2→3, 7/2<br>2, 5/2→2, 5/2<br>1, 3/2→1, 3/2<br>3, 7/2→3, 5/2<br>2, 3/2→2, 5/2<br>1, 1/2→1, 3/2 | 47.5 | −24±3 |
| 6 | 3, 5/2→3, 5/2<br>2, 3/2→2, 3/2<br>1, 1/2→1, 1/2<br>3, 5/2→3, 7/2<br>2, 5/2→2, 3/2<br>1, 3/2→1, 1/2 | 32.0 | 36±3 |
| 7 | 2, 5/2→3, 7/2 | 2.96 | 646±3 |
| 8 | 2, 5/2→3, 5/2<br>2, 3/2→3, 5/2 | 2.22 | 708±3 |
| 9 | 2, 5/2→1, 3/2<br>2, 3/2→1, 3/2 | 3.34 | 978±3 |
| 10 | 2, 3/2→1, 1/2 | 1.68 | 1065±3 |

| $J=3$ Line | Transitions $F_1,F\rightarrow F_1',F'$ | Relative intensity | Measured separation |
|---|---|---|---|
| 1 | 2, 3/2→3, 5/2 | 1.07 | −1426±3 |
| 2 | 2, 5/2→3, 5/2<br>2, 5/2→3, 7/2 | 1.60 | −1312±3 |
| 3 | 4, 7/2→3, 5/2<br>4, 7/2→3, 7/2 | 1.19 | −1098±3 |
| 4 | 4, 9/2→3, 7/2 | 1.50 | −1004±3 |
| 5 | 4, 7/2→4, 7/2<br>3, 5/2→3, 5/2<br>2, 3/2→2, 3/2<br>4, 9/2→4, 7/2<br>3, 5/2→3, 7/2<br>2, 3/2→2, 5/2 | 38.3 | −53±3 |

| $J=3$ Line | Transitions $F_1,F\rightarrow F_1',F'$ | Relative intensity | Measured separation |
|---|---|---|---|
| 6 | 4, 9/2→4, 9/2<br>3, 7/2→3, 7/2<br>2, 5/2→2, 5/2<br>4, 7/2→4, 9/2<br>3, 7/2→3, 5/2<br>2, 5/2→2, 3/2 | 51.1 | 40±3 |
| 7 | 3, 5/2→4, 7/2 | 1.15 | 997±3 |
| 8 | 3, 7/2→4, 7/2<br>3, 7/2→4, 9/2 | 1.54 | 1080±3 |
| 9 | 3, 5/2→2, 3/2<br>3, 5/2→2, 5/2 | 1.14 | 1294±3 |
| 10 | 3, 7/2→2, 5/2 | 1.52 | 1406±3 |

| $J=4$ Line | Transitions $F_1,F\rightarrow F_1',F'$ | Relative intensity | Measured separation |
|---|---|---|---|
| 1 | 3, 7/2→4, 9/2<br>3, 7/2→4, 7/2 | 0.89<br>0.026 | −1518±4 |
| 2 | 3, 5/2→4, 7/2 | 0.69 | −1371±4 |
| 3 | 5, 11/2→4, 9/2<br>5, 9/2→4, 9/2 | 0.89<br>0.017 | −1267±4 |
| 4 | 5, 9/2→4, 7/2 | 0.73 | −1152±4 |
| 5 | 5, 11/2→5, 11/2<br>4, 9/2→4, 9/2<br>3, 7/2→3, 7/2<br>5, 9/2→5, 11/2<br>4, 7/2→4, 9/2<br>3, 5/2→3, 7/2 | 51.9 | −56±4 |
| 6 | 5, 9/2→5, 9/2<br>4, 7/2→4, 7/2<br>3, 5/2→3, 5/2<br>5, 9/2→5, 4/2<br>4, 9/2→4, 7/2<br>3, 7/2→3, 5/2 | 41.6 | 71±4 |
| 7 | 4, 9/2→5, 11/2<br>4, 9/2→5, 9/2[a] | 0.89<br>0.017 | 1159±4 |
| 8 | 4, 7/2→5, 9/2 | 0.73 | 1285±4 |
| 9 | 4, 9/2→3, 7/2<br>4, 7/2→3, 7/2[a] | 0.89<br>0.026 | 1393±4 |
| 10 | 4, 7/2→3, 5/2 | 0.69 | 1539±4 |

[a] Theory shows that these transitions though not observed are not to be associated with the stronger satellites. See Fig. 3.

## IV. A COMPARISON OF EXPERIMENT AND THEORY ALLOWING FOR EFFECTS DUE TO THE PROTON MAGNETIC MOMENTS

### Case $K=1$

Inspection of Figs. 2 and 3 reveals that the spectrum for $K=1$ is quite different from that for other values of $K$. For low $J$, the splitting of the quadrupole lines into pairs is small. It is too small for our spectrometer to resolve when $J=1$ but becomes of the same order as the intersatellite spacings for $J=4$. A splitting of the same magnitude was found in the microwave lines of $N^{15}H_3$ as shown in Table IIIb. Since $N^{15}$ has a spin of 1/2 and hence no quadrupole moment, the spectrum of $N^{15}H_3$ is considerably simpler than that of $N^{14}H_3$. The similarity between observed splittings in $N^{15}H_3$ and in $N^{14}H_3$ indicates clearly that they are not primarily due to the nitrogen nucleus. Since the protons interact with the rest of the molecule by virtue of their magnetic moments, one is led to consider (1) the interaction of the protons with the molecular fields due to rotation—an $\mathbf{I}\cdot\mathbf{J}$ type interaction, (2) their dipolar interactions

TABLE III. Splittings of the $NH_3$ hyperfine spectra (kc/sec) when $K=1$. (a) $N^{14}H_3$. Comparison of theory and experiment, assuming $A=\alpha+\rho=-10\pm10$ kc/sec, $B=\rho-\alpha=-14.4\pm0.2$ kc/sec, and $C=\gamma-(\alpha+\rho)=0\pm60$ kc/sec.

| | $J=2$ | | | $J=3$ | | | $J=4$ | |
|---|---|---|---|---|---|---|---|---|
| Interval[a] | Calculated splitting for strong lines only | Splitting from composite plot of spectrum[b] | Observed splitting | Calculated splitting for strong lines | Splitting from composite plot of spectrum | Observed splitting | Calculated splitting for strong lines | Observed splitting |
| 1→2 | 84.6 | 80 | 79±4 | 116.1 | 116 | 114±4 | 142.2 | 147±5 |
| 3→4 | 58.7 | 48 | 51±6 | 98.0 | 93 | 94±4 | 118.0 | 115±5 |
| 5→6 | 66.1 | 58 | 60±6 | 98.2 | 94 | 93±4 97±4[c] | 127.5 | 127±3 121±5[c] |
| 7→8 | 72.2 | 64 | 62±5 | 88.1 | 83 | 83±4 | 126.9 | 126±5 |
| 9→10 | 89.6 | 88 | 87±4 | 112.8 | 113 | 112±4 | 142.9 | 147±5 |

(b) $N^{15}H_3$.

| $J$ | Without stark modulation[c] | With stark modulation[c] |
|---|---|---|
| 2 | 85 | ... |
| 3 | 99±4 | ... |
| 4 | ... | 160 |
| 5 | 168±10 | 180 |

[a] Lines numbered according to Table II.
[b] Includes addition of all transitions. Line widths were taken as those which gave best fit to data for each $J$ value: for $J=2$, $2\Delta\nu=68$ kc/sec; for $J=3$, $2\Delta\nu=80$ kc/sec; for $J=4$, the resolution was sufficient that splittings were not influenced by the line breadth.
[c] Data taken at Westinghouse Laboratories. Other measurements were made at Columbia.

with the nitrogen magnetic moment and (3) their mutual dipolar interactions. In paper II these interactions and other small effects are all considered both for the case $K\neq1$ and for the case $K=1$. The energy levels are derived there in terms of the geometrical parameters of the molecule, of certain magnetic coupling parameters dependent on the electronic states (the $a$, $b$ of Henderson mentioned above and similar coefficients $\alpha$, $\beta$, $\gamma$ for the protons) and of the angular momentum quantum numbers of the molecule. In order to save space the reader will be referred to this paper for the formulas we are about to discuss. The parameters $\alpha$, $\beta$, $\gamma$ which are dependent on the ground- and excited-state electronic wave functions cannot be evaluated theoretically since little is known about these functions. Because these constants can most readily be evaluated experimentally for the case $K=1$, and because this evaluation does not depend on the coefficients, $a$, $b$, we shall discuss the case $K=1$ first, returning to the case $K\neq1$ to show that the proton perturbations do not significantly alter the results obtained from this case.

Close inspection of Figs. 2 and 3 will reveal the following qualitative features. (1) The relative intensities of the two members of each doublet alternates as $J$ varies from odd to even. (2) The splittings of the outer satellites are greatest in all cases. (3) For $J=2$ the lower-frequency satellites are less split than the higher-frequency ones. This effect reverses with $J$ and decreases with increasing $J$. As shown in the following pages, the alternation of relative intensities of the two members of each doublet with $J$ is a consequence of the requirement that the total wave function must be antisymmetric to proton exchange. The formulas for the energy levels are calculated in paper II and an energy level diagram is shown in Fig. 5 of paper II. These lead to the following expressions for the frequencies of the lines of the $NH_3$ inversion hyperfine spectrum:

$$\begin{aligned}\nu=\nu_0&+\{a+(b-a)K^2/[J(J+1)]\}[\mathcal{C}(F_1',J)-\mathcal{C}(F_1,J)]\\&+\{A+CK^2/[J(J+1)]\}[\mathcal{G}(J,F_1',F')-\mathcal{G}(J,F_1,F)]\\&+\mathfrak{D}_1[\mathcal{F}(J,F_1',F')-\mathcal{F}(J,F_1,F)]\{1-3/[J(J+1)]\}\\&+\delta_{K1}(-1)^J\{B[\mathcal{G}(J,F_1,F')+\mathcal{G}(J,F_1,F)]\\&\qquad+\mathfrak{D}_2[\mathcal{F}(J,F_1',F')+\mathcal{F}(J,F_1,F)]\},\end{aligned}$$

where

$$\mathcal{C}(F_1,J)=\mathbf{I}_N\cdot\mathbf{J},\quad A=\alpha+\rho,\quad B=\rho-\alpha,\quad C=\gamma-(\alpha+\rho).$$

$$\mathcal{G}(J,F_1,F)=(\mathbf{I}\cdot\mathbf{F}_1)(\mathbf{F}_1\cdot\mathbf{J})/[F_1(F_1+1)],$$

$$\mathfrak{D}_1=g_Hg_N\mu_0^2\langle v|r^{-3}(1-\tfrac{3}{2}\sin^2\beta)|v\rangle,$$

$$\mathcal{F}(J,F_1,F)=2(\mathbf{F}_1\cdot\mathbf{I})\Omega_2(J,F_1)/[F_1(F_1+1)],$$

$$\mathfrak{D}_2=g_Hg_N\mu_0^2\langle v|\tfrac{3}{2}r^{-3}\sin^2\beta|v\rangle,$$

$$\delta_{K1}=1\quad\text{for}\quad K=1$$
$$=0\quad\text{for}\quad K\neq1.$$

$\nu_0$ represents the transition frequency due to the usual inversion energy plus the quadrupole hyperfine structure of the nitrogen nucleus. The parameters employed above which have not been described are identified in paper II, Eqs. (13), (10), and (B1). The first four terms of (2) arise from the parts of the total molecular Hamiltonian which are diagonal in $K$ while the last two terms express the removal of the $K$ degeneracy when $K=1$. The term involving $\mathcal{C}(\mathbf{F}_1\cdot\mathbf{J})$ arises in the nitrogen $\mathbf{I}_N\cdot\mathbf{J}$ interaction [*cf* (1)]; terms involving the function $\mathcal{G}(J,F_1,F)$ are due to the proton interaction with magnetic field due to molecular rotation $(\mathbf{I}\cdot\mathbf{J})$; and finally terms involving the $\mathcal{F}(J,F_1,F)$ function are due to the nitrogen-proton dipolar interaction. As can be seen from Figs. 2 and 3 the theoretical plots for the line pattern which are discussed below are in good agreement with the experimentally observed patterns. The splitting of the main lines is almost wholly de-

pendent on the $\mathbf{I}\cdot\mathbf{J}$ parameter, $B$, while the satellite splittings are largely but not so exclusively dependent on this parameter. The different splitting of the lower-frequency satellites from the higher-frequency ones depend on the $A$ and $C$ terms which are diagonal in $K$. Finally, the different splitting of the outer and inner satellites is caused by the proton-nitrogen dipolar interaction. Because the order of the allowed energy levels and hence the sequences of line intensities depends on the proton statistics and because the splittings due to the latter interaction can be calculated from the geometrical constants of the molecule, the experiment constitutes another corroboration of these statistics as being Fermi-Dirac (incidentally, this corroboration shows that the phases of the rotational wave functions given in paper II are correct).

Keeping in mind the above discussed dependence of the splittings on the parameters $A, B, C$, we very carefully measured the splitting of the transition $\Delta F_1=0$ (main line) for $J=4$ under conditions of maximum resolution. This gave a reliable value of the constant $B$. The values of $A, C$ were then determined so as to give the best fit to the measured splittings under highest resolution for $J=2$ where they are most important. We then used the values so determined, which are independent of the constants $a, b$ of the Henderson effect, to draw up the predicted spectral patterns assuming several different line widths in cases in which the measured separations would have depended on these line widths. These drawings were used to obtain final values of $A, B, C$ essentially by a method of trial and error and to check on the measured line widths. It should again be remarked that the photographs given in Figs. 2 and 3 were not obtained under conditions of maximum resolution. For instance for $J=2$ the intermediate set of theoretical curves with a line width 70 kc/sec comes closest to the pattern actually observed during the course of the measurements. Unfortunately, the splittings are only weakly dependent on $A, C$ so that these constants could not be precisely determined. The best fit was obtained with

$$A=-10\pm10 \text{ kc/sec}, \quad B=14.4\pm0.2 \text{ kc/sec},$$
$$C=0\pm60 \text{ kc/sec},$$

where the stated errors indicate the range of values for which the fit obtained was still within the experimental error.

The measured, calculated, and corrected splittings are given in Table III(a) together with the similar splittings in $N^{15}H_3$ in Table III(b) for comparison. The fit is within our experimental error but is not as good for $J=4$ as it is for $J=2, 3$, probably because of the greater difficulty in making the measurements in this case. Using the above data, and the calculated intensities listed in Table II we have calculated the position of the "centers of gravity" of the unsplit lines for $K=1$ and have included them in Table I for comparison with the cases for $K\neq1$. It will be seen that the agreement is approximately as good as that found for $K+1$ in spite of the larger experimental errors for $K=1$. The deviation of the calculated average position of the outer satellites for $J=4$ is several times the probable error of the whole set of measurements. We have not found a satisfactory explanation for this discrepancy.

### Case $K\neq1$

In this case the expected is obtained from the first four terms of (2) and has been plotted for a typical case in Fig. 4.

In spection of Fig. 4 might lead one to expect that for $K\neq1$ the results listed in Table I should still show systematic deviations because of the unsymmetrical nature of the actual satellites which experimentally were not resolved. The splittings of a satellite line in this case as shown in Eq. (2) depend on the constants $A, C$. The fact that no structure was found is consistent with the line widths which we were able to achieve and with the values of the constants $A$ and $C$ determined above. Calculation of the shift of the peak of the lines due to the small displaced subsatellites shows that for low $J$ they are separated by about 40 kc/sec from the other two satellite components and, not being resolved, caused negligible shift in the center of gravity, while for higher $J(\simeq7)$ their intensities are so small that this effect is again negligible. We conclude therefore that Eq. (1) represents the results of our experiment satisfactorily when $K\neq1$.

### Other Effects

The formula (2) contains, we believe, all the features of the $NH_3$ hyperfine spectrum observable with a microwave spectrometer of sensitivity and resolving power comparable with what is now available. In the derivation of these relations we have neglected all effects which could reasonably be estimated to be too small to observe by at least two orders of magnitude (see paper II). The only interactions which should be mentioned in addition to those discussed above are the

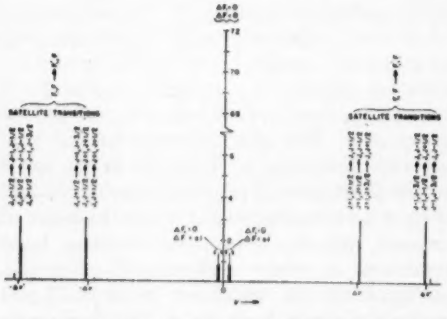

FIG. 4. Schematic drawing of the calculated structure of $N^{14}H_3$ inversion spectrum for a low value of $J$ and $K\neq1$.

pseudo-quadrupole effect,[12] and the interaction of the nuclear magnetic moments with each other through the intermediary of the electronic magnetic moments.[14] The former effect is not separable from the true nuclear quadrupole effect. The energy involved in the latter effect is less than 1 kc/sec in most known cases. In order to obtain more precise information a few cubic centimeters of liquid $NH_3$ were sealed in a thick walled glass tube and Hahn of the Watson Laboratories kindly examined the proton resonance in the $NH_3$ vapor in equilibrium with the liquid by means of the spin echo technique.[15] The resonance was observed with a sample vapor pressure of several atmospheres to a sample vapor pressure of the order of 40 atmospheres. The strong resonance signal was found to be without a trace of the modulations which would be caused by the above-mentioned effect. From this result Hahn was able to inform us that the magnitude of the interaction is certainly less than 300 cps and most probably less than 100 cps. Thus it would not be experimentally detectable by us.

The authors at Columbia University would like to thank Professor C. H. Townes for suggesting this problem and for his active support in carrying it through. We are also grateful to Mr. C. Dechert and his staff for help in construction of the apparatus.

[14] N. F. Ramsey and E. M. Purcell, Phys. Rev. **85**, 143 (1952).
[15] E. L. Hahn, Phys. Rev. **80**, 580 (1950); **88**, 1070 (1952).

PHYSICAL REVIEW VOLUME 94, NUMBER 5 JUNE 1, 1954

# Hyperfine Structure in the Spectrum of $N^{14}H_3$.† II. Theoretical Discussion

G. R. GUNTHER-MOHR* AND C. H. TOWNES, *Radiation Laboratory, Columbia University, New York, New York*

AND

J. H. VAN VLECK, *Harvard University, Cambridge, Massachusetts*

(Received December 28, 1953)

The new features in the hyperfine spectrum of $N^{14}H_3$ described in the preceding paper are shown to be due to the interactions of the magnetic moments of the three protons with the molecular magnetic field caused by rotation and with the magnetic moment of the $N^{14}$ nucleus. Since the protons are off the molecular symmetry axis, these interactions are of a form different from that usually encountered. They possess matrix elements connecting states differing by two units in symmetric top quantum number $K$ and are capable, therefore, of lifting the degeneracy between states for which $K=-1$ and $K=1$. A systematic treatment of the problem of the hyperfine interactions in this molecule has been made in order to find any other effects detectable with present equipment.

## I. INTRODUCTION

EARLY measurements of the hyperfine structure of the inversion spectrum of ammonia were interpretable[1] as due to an interaction between molecular electric fields and the quadrupole moment of $N^{14}$. More accurate measurements[2] indicated that small interactions between the $N^{14}$ magnetic moment and a magnetic field due to molecular rotation were also present.[3] The new experimental data presented in the previous paper (which we shall refer to as I) shows that several other types of effects are also of importance. Hence, a systematic and comprehensive treatment of the problem has been undertaken in order to find all effects which could conceivably be observed with a microwave spectrometer of sensitivity and resolving power comparable with what is now available. Doubling of the $K=1$ lines is shown to be a new manifestation of magnetic hyperfine interactions.

## II. FORMULATION OF THE PROBLEM

For the purposes of this calculation, the molecular Hamiltonian based on the Pauli approximation to the wave equation can be written as:[4,5]

$$\mathcal{H}=A(J_x-L_x)^2+A(J_y-L_y)^2+C(J_z-L_z)^2 \qquad (1.0)$$

$$+(e\mu_0/c)\sum_{Ki} r_{iK}^{-3}(\mathbf{r}_i-\mathbf{r}_K)\times\left(\mathbf{v}_i-\left(1+\frac{Z_K M_p}{g_K M_K}\right)\mathbf{v}_K\right)\cdot g_K\mathbf{I}_K \qquad (1.1)$$

† Work at Columbia University supported by the U. S. Atomic Energy Commission.
* U. S. Atomic Energy Commission Predoctoral Fellow. Now at Watson Laboratory, Columbia University. This work is submitted in partial fulfillment of the requirements for the degree of Doctor of Philosophy at Columbia University.
[1] W. E. Good and D. K. Coles, Phys. Rev. **70**, 979 (1946); J. H. Van Vleck, Phys. Rev. **71**, 468 (1947).
[2] J. W. Simmons and W. Gordy, Phys. Rev. **73**, 713 (1948).
[3] R. S. Henderson, Phys. Rev. **74**, 107, 626 (1948); see, also, J. M. Jauch, Phys. Rev. **74**, 1262 (1948).
[4] J. H. Van Vleck, Revs. Modern Phys. **23**, 213 (1951).
[5] L. H. Thomas, private communication. The equation derived on the basis of footnote (35) of Van Vleck's paper (reference 4) is not entirely correct since factors of $1/r_{jK}^3$ and $1/r_{iK}^3$ were inadvertently left out of his Eq. (37) and the factor $(1+Z_K M_P/g_K M_K)$ replaces the factors $\frac{1}{2}$ in a fashion evident by comparing the expressions (1.1) and (1.3) with his Eq. (37).

$$+g_e\mu_0\mu_e\sum_{j,K} r_{jK}^{-5}(g_K\mathbf{I}_K\cdot\mathbf{S}_j r_{jK}^2 - 3g_K\mathbf{I}_K\cdot(\mathbf{r}_K-\mathbf{r}_j)\mathbf{S}_j\cdot(\mathbf{r}_K-\mathbf{r}_j) \quad (1.2)$$

$$-(e\mu_0/c)\sum_{K,L\,K\neq L} Z_L r_{KL}^{-3}(\mathbf{r}_K-\mathbf{r}_L) \times\left[\left(1+\frac{Z_K M_P}{g_K M_K}\right)\mathbf{v}_K-\mathbf{v}_L\right]\cdot g_K\mathbf{I}_K \quad (1.3)$$

$$+\mu_0^2\sum_{K,L\,K>L} r_{KL}^{-5}[g_K\mathbf{I}_K\cdot g_L\mathbf{I}_L r_{KL}^2 - 3g_K\mathbf{I}_K\cdot(\mathbf{r}_K-\mathbf{r}_L)g_L\mathbf{I}_L\cdot(\mathbf{r}_K-\mathbf{r}_L)] \quad (1.4)$$

$$+\mathcal{H}_{\text{nitrogen quadrupole interaction}} \quad (1.5)$$

$$+\tfrac{1}{3}(16\pi\mu_0\mu_e)\sum_{K,j} g_K\delta(\mathbf{r}_K-\mathbf{r}_j)\mathbf{S}_j\cdot\mathbf{I}_K. \quad (1.6)$$

In (1), capital subscripts refer to nuclei and to electrons. These particles have, respectively, position vectors $\mathbf{r}_K$, $\mathbf{r}_j$, and velocities $\mathbf{v}_K$, $\mathbf{v}_j$ relative to the molecular center of mass which is assumed to coincide with the center of mass of the nuclei. They have charges $Z_K e$, $-e$; spins $\mathbf{I}_K$, $\mathbf{S}_j$, and $g$ factors $g_K$, $g_e$, respectively. $\mu_e$ and $\mu_0$ are the Bohr and nuclear magnetrons, respectively, while $M_P$ is the proton mass and $M_K$ the mass of the $K$th nucleus.

The inversion vibration which gives rise to the microwave spectrum ($\approx$24 000 Mc/sec) is a "tunnelling" of the nitrogen, which is normally at the apex of the $NH_3$ pyramidal structure, through the plane of the three protons. This inversion energy[6] has been omitted from (1) since it has a negligible effect on the hyperfine interactions.

The terms (1.0) represent the rotational energy of the nuclei.[7] $A$ and $C$ are the transverse and axial rotational constants exclusive of the electrons; $J_x$, $J_y$, $J_z$ are the components of the total molecular angular momentum exclusive of nuclear spin; and $L_x$, $L_y$, $L_z$ are the total electronic orbital angular momentum operators. The cross terms of (1.0),

$$-2[A(J_xL_x+J_yL_y)+CJ_zL_z], \quad (2)$$

represent the interactions of rotational and electronic angular momenta neglected in the Born-Oppenheimer approximation and cause the excitation of electronic states above the ground $^1\Sigma$ state. The presence of such excited states gives rise to a magnetic field at the nuclei and consequently contributes to hyperfine effects.[8] The effect of terms (1.1) which express the interaction of the nuclear magnetic moments with electronic currents, does not vanish because of the rotational perturbation terms (2) and is partly responsible for the experimentally observed doubling. Terms (1.2) and (1.6)[9] are interactions between electron and nuclear magnetic moments with the currents set up by the rotation of nuclear charges. We shall not discuss the nitrogen quadrupolar interaction (1.5) since it has been treated elsewhere.[1]

## III. THE MOLECULAR WAVE FUNCTIONS

Fortunately, the complexity of (1) can be greatly reduced by considering the relative magnitude of the energies involved, by eliminating effects which are too small to be observed experimentally by present techniques, and by taking into account the symmetry of the molecule and the statistics of the protons.

From its geometry it is clear that the molecule $NH_3$ is left unchanged in any physically observable way when transformed by any of the members of the rotation-reflection point group $C_{3v}$ which is isomorphic to the permutation group $P_3$ of the protons. We are concerned here only with the ground electronic state and the ground vibrational states (excepting the inversion, which can be considered a type of vibration). Hence, the electronic and vibrational parts of the wave function are symmetric (symmetry $A_1$) relative to the group $C_{3v}$. In addition the nitrogen spin function has symmetry $A_1$. We need only to examine in detail the product function of the other variables

$$\psi=\psi_R(\phi,\theta,\chi)\psi_V(z)\psi(\sigma_1)\psi(\sigma_2)\psi(\sigma_3), \quad (3)$$

where $\phi$, $\theta$, $\chi$ are the Eulerian angles of the nuclear framework, $\sigma_1$, $\sigma_2$, $\sigma_3$ represent the proton spin coordinates, and $z$ is the inversion coordinate. The coordinate system used is that of Hund.[10] It is described, the Eulerian angles defined, and the symmetric top rotation functions $\psi_R(\phi,\theta,\chi)$ given in Appendix I. Hund[10] and Dennison[11,12] have shown that for the lowest of the two inversion states between which the microwave transition occurs,

$$\psi_{V=0}(z)=\psi_{V=0}(-z), \quad (4)$$

and for the upper inversion state $\psi_{V=1}(z)=-\psi_{V=1}(-z)$.

From the results of the symmetry operations $P_3$ on the coordinate space of the functions of (3), the representative matrices of the group for each of these functions belonging to the same energy level can be found and reduced to its irreducible constituents.[13] If the direct products of these irreducible representations are in turn reduced, the total irreducible representations of the molecule can be identified. There results a set of functions which have definite symmetry with respect to the

[6] Sheng, Barker, and Dennison, Phys. Rev. **60**, 786 (1941).

[7] H. B. G. Casimir, *The Rotation of a Rigid Body in Quantum Mechanics* (J. B. Wolters, Groningen, 1931).

[8] The "physical" basis of these interactions has been given by G. C. Wick, Phys. Rev. **73**, 51 (1948).

[9] For diatomic molecules this term is more carefully considered by R. A. Frosch and H. M. Foley, Phys. Rev. **88**, 1337 (1952).

[10] F. Hund, Z. Physik **43**, 823 (1927).

[11] G. Herzberg, *Infrared and Raman Spectrum* (D. Van Nostrand Company, Inc., New York, 1945) describes these modes and gives their symmetries relative to the point group $C_{3v}$ of the molecule.

[12] Z. I. Slawsky and D. M. Dennison, J. Chem. Phys. **7**, 509 (1939); D. M. Dennison, Revs. Modern Phys. **3**, 281 (1931).

[13] E. Wigner, *Gruppentheorie und ihre Anwendung* (F. Vieweg, Braunschweig, 1931). See also E. B. Wilson, J. Chem. Phys. **3**, 276 (1935) for applications to molecules. Note that he uses a different coordinate system from ours.

group $P_3$ and of these only those belonging to the irreducible representation $A_2$, are to be kept in accord with the statistics of the protons.

The wave functions of (3) form irreducible representations of the three-dimensional rotation group and of the various angular momenta involved in the problem. Since the permutation and rotation groups commute, these wave functions must form simultaneous irreducible representations of these groups. The order in which the reductions of the direct products of these simultaneous irreducible representations are made will depend on the choice of coupling scheme. We shall choose it as follows: since magnetic interactions are much smaller than the nitrogen quadrupole coupling energy, the nitrogen spin, $\mathbf{I}_N$ is first coupled to $\mathbf{J}$ to give $\mathbf{F}_1$. The protons can then be numbered according to their positions relative to the chosen molecular axes and coupled together to give a resultant $\mathbf{I}$, which is in turn coupled to $\mathbf{F}_1$ to give the total angular momentum of the molecule $\mathbf{F}$. We are thus led to the coupling scheme in Fig. 1 which is

$$\mathbf{J}+\mathbf{I}_N=\mathbf{F}_1, \quad \mathbf{I}_1+\mathbf{I}_2+\mathbf{I}_3=\mathbf{I}, \quad \mathbf{I}+\mathbf{F}_1=\mathbf{F}. \qquad (5)$$

The symmetry properties of all the possible wave functions of the molecule were found in accordance with the above discussion and are listed in Table I. This table shows that when $K$ is a multiple of 3 ($|K|=3n$), $I=\frac{3}{2}$ and only $\frac{1}{4}$ of the possible functions are physically allowed while when $|K|=3n\pm1$, $I=\frac{1}{2}$ and only $\frac{1}{8}$ of the possible functions are allowed. It may be seen from this table that when $|K|=3n$ the two rotational levels have different symmetry and hence can be split by rotation-vibration interactions as found by Dennison and Nielsen.[14] When $|K|=3n\pm1$ the rotation-vibration part of the wave function is degenerate and the levels cannot be split by the same type of effect.[14] The levels can be split, however, by the effects of nuclear spin since the total wave functions including spin have a variety of symmetries as shown in Table I.

Before making detailed calculations of the effect of the Hamiltonian (1), it may be helpful to give a simple

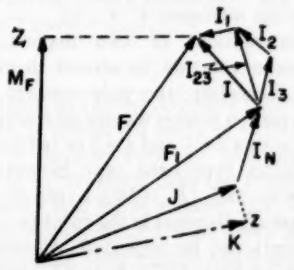


FIG. 1. $N^{14}H_3$ molecular coupling scheme referred to laboratory axis. $Z$ is the fixed direction in the laboratory, $z$ is the axis coinciding with the molecular symmetry axis, and $K$ is the projection of $J$ on the molecular symmetry axis.

[14] D. M. Dennison and H. H. Nielsen, Phys. Rev. 72, 86, 1101 (1947).

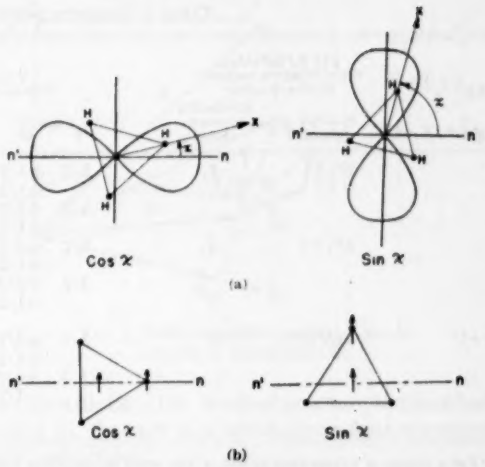


FIG. 2. (a) Azimuthal molecular wave functions ($M_J=0$, $K=1$). (b) Variation of magnetic energy with $\chi(K=1)$.

physical argument for the lifting of the $K$ degeneracy by the magnetic interactions. For each value of $|K|$ the molecular wave function can contain a factor of either $\sin K\chi$ or $\cos K\chi$, where $\chi$ is the azimuthal angle about the molecular symmetry axis.

A plot of the probability of a given value of $\chi$ is given in Fig. 2(a) for $K=1$, with the nuclear position superimposed. If the molecule is in one or the other of the above two possible degenerate states, its most probable orientation relative to the fixed laboratory axis is different even though classically the probabilities of clockwise and counter clockwise rotation are equally represented. Picturing the molecule projected on the plane of the protons in Fig. 2(b), indicating a proton spin by an arrow at the vertex of the triangle, we can see why the interaction between the proton and nitrogen magnetic moments gives the two states different energies.[15] The central arrow indicates the orientation of the magnetic moment of the nitrogen nucleus which can be assumed, neglecting the precession of $\mathbf{I}_N$ about $\mathbf{F}$ to remain fixed during the molecular rotation. For any constant assumed orientation of the proton spin relative to the fixed laboratory frame, clearly the two states have different energies, and thus the $K$ degeneracy is removed.

The number of lobes of the $\chi$ dependence of the wave function increases with $K$ and consequently the variation in dipolar interaction energy becomes essentially zero for $K>1$.

## IV. THE PERTURBATION CALCULATION

### Introduction

The perturbation problem can be solved to second order[4] in the ratio of hyperfine to electronic energies by

[15] Interaction between the protons and the magnetic field due to molecular rotation gives the same type of effect if, as may be expected, the magnetic field at the proton varies with $\chi$.

TABLE I. Symmetry properties of the $N^{14}H_3$ wave functions.

| | $\psi(VKJI_NF_1M_{F_1})$ Wave function exclusive of proton spins[a] | | $\psi(I_1I_2I_{12}IM_I)$ Proton spin functions | | | | $\Psi(VKJI_NF_1IFM_F)$ Total molecular wave function | | |
|---|---|---|---|---|---|---|---|---|---|
| $\lvert K\rvert$ | Number of functions | Irreducible representation | $I$ | Value of $M_I$ | Number of functions | Irreducible representation | Value of $F$ | Number of functions | Irreducible representation |
| $3n$ | $2F_1+1$ | $A_1$ | 3/2 | $\pm 3/2$ | 4 | $A_1$ | $F_1\pm 3/2$ | $4(2F_1+1)$ | $A_1$ |
| | | | | $\pm 1/2$ | | | $F_1\pm 1/2$ | | |
| | | | 1/2 | $+1/2$ | 2 | $E$ | $F_1\pm 1/2$ | $4(2F_1+1)$ | $E$ |
| | | | | $-1/2$ | 2 | $E$ | | | |
| | $2F_1+1$ | $A_2$ | 3/2 | $\pm 3/2$ | 4 | $A_1$ | $F_1\pm 3/2$ | $4(2F_1+1)$ | $A_2$ |
| | | | | $\pm 1/2$ | | | $F_1\pm 1/2$ | | |
| | | | 1/2 | $+1/2$ | 2 | $E$ | $F_1\pm 1/2$ | $4(2F_1+1)$ | $E$ |
| | | | | $-1/2$ | 2 | $E$ | | | |
| $3n+1$[b] | $2(2F_1+1)$ | $E$ | 3/2 | $\pm 3/2$ | 4 | $A_1$ | $F_1\pm 3/2$ | $8(2F_1+1)$ | $E$ |
| | | | | $\pm 1/2$ | | | $F_1\pm 1/2$ | | |
| | | | 1/2 | $+1/2$ | 2 | $E$ | $F_1\pm 1/2$ | $2(2F_1+1)$ | $A_1$ |
| | | | | $-1/2$ | 2 | $E$ | $F_1\pm 1/2$ | $2(2F_1+1)$ | $A_2$ |
| | | | | | | | $F_1\pm 1/2$ | $4(2F_1+1)$ | $E$ |

[a] For a change of $v$ from even to odd or vice versa the functions identified by the symbols $A_1$, $A_2$ would be interchanged.
[b] A similar tabulation holds for $|K|=3n-1$.

diagonalizing an effective Hamiltonian $G$, obtained from the true Hamiltonian, $H$ of (1) by the relations between matrix elements

$$\langle l_0 i|G|l_0 i'\rangle=\langle l_0 i|G_1|l_0 i'\rangle+\langle l_0 i|G_2|l_0 i'\rangle, \tag{6.1}$$

$$\langle l_0 i|G|l' i'\rangle=0,$$

$$\langle l_0 i|G_1|l_0 i'\rangle=\langle l_0 i|\,\mathfrak{IC}\,|l_0 i'\rangle, \tag{6.2}$$

$$\langle l_0 i|G_2|l_0 i'\rangle=\sum_{l\neq l_0}(E_{l_0}-E_l)^{-1}\Big(\sum_{i''}\langle l_0 i|\,\mathfrak{IC}\,|l i''\rangle \times\langle l i''|\,\mathfrak{IC}\,|l_0 i'\rangle\Big), \tag{6.3}$$

where $E_{l_0}$ = energy of the ground electronic state and $E_l$ = energy of an excited electronic state.

In our problem the $l$ refer to excited electronic states, to the ground electronic state ($^1\Sigma$) and the quantum numbers $i$, to the rotation, vibration, and hyperfine quantum numbers $J$, $K$; $v$; $F_1$, $F$. Once the matrix $G$ has been calculated, the energy of the ground state can be found by diagonalizing the matrix:

$$G=G_1+G_2=\{\langle l_0 i|G|l_0 i'\rangle\}. \tag{7}$$

The matrix elements of the hyperfine interactions in $G$ which are off-diagonal in the rotation or vibration energies off-diagonal in $J$, $K$, or $v$ can be neglected relative to those which are diagonal since their contribution in the perturbation calculation is smaller by a factor of at least $10^{-5}$. Similarly, the matrix elements of the magnetic hyperfine interactions off-diagonal in the quadrupole interaction energy (off diagonal in $F_1$) make contributions smaller by a factor of at least 1/40 than those of their diagonal elements and thus they too will be neglected.

The total Hamiltonian (1) can be broken up into two parts: $\mathfrak{IC}_1$ involving only these terms which are diagonal in the electronic quantum numbers and hence contribute to $G_1$, and the terms $\mathfrak{IC}_2$ involving the remaining off diagonal terms which contribute to $G_2$ defined in (6.3).

## Terms Involving Only the Ground Electronic States ($G_1$)

Terms which make up what we have called $G_1$ cannot include any operators involving either electronic velocities or angular momenta, for such operators are known to be off-diagonal in the electronic quantum numbers in a $^1\Sigma$ molecule.[16] The matrix $G_1$ is thus made up of those terms which are left in (1) after the electronic velocities and angular momenta have been set equal to zero. The expression so obtained will contain the rotational energy (from 1.0), the quadrupole interaction energy (1.5), that part of the electron current terms diagonal in 1 (from 1.1), the nuclear current terms (1.4). The first two of these we have assumed are well known.[1] The next two can readily be calculated in the molecular representation using the substitution,[4]

$$\mathbf{v}_K=\boldsymbol{\omega}\times\mathbf{r}_K, \tag{8}$$

where $\omega_x=2AJ_xh^{-1}$, $\omega_y=2AJ_yh^{-1}$, $\omega_z=2CJ_zh^{-1}$. Appendix II shows details of this calculation. The dipolar terms (1.4) are conveniently separated into the dipolar interactions of the protons with each other and of the protons with the nitrogen.

Dipolar interactions of two magnetic moments transform under rotation as second degree spherical harmonics.[17] Therefore, the only nonzero matrix elements of the proton proton dipolar interaction are those between the states $I=\frac{3}{2}$ and $I=\frac{3}{2}$ or between $I=\frac{1}{2}$ and $I=\frac{1}{2}$. The latter type exist only between states for which $|K|=3n$ and $|K|=3n\pm 1$, respectively. Since such states are off diagonal in the rotation energy, these matrix elements can be neglected. Allowed states for which $I=\frac{3}{2}$ must have $|K|=3n$ and for such states the $K$ degeneracy is lifted by a vibrational interaction.[14]

[16] J. H. Van Vleck, *Theory of Electric and Magnetic Susceptibilities* (Oxford University Press, London, 1932), p. 274.
[17] J. H. Van Vleck, Phys. Rev. **74**, 1168 (1948).

Thus because of the small magnitude of the dipolar interaction ($\mu_H^2/hr_{NH_3}\approx 7$ kc/sec) matrix elements of the second type will not cause detectable splittings of these $|K|=3n$ lines. For these reasons we shall drop the dipolar interactions of the protons with each other from further consideration. The nitrogen proton dipolar interaction produces a measurable effect on the spectrum and is discussed in Appendix II.

In order to be able to use matrix elements tabulated by Condon and Shortley[18] we shall carry out the calculation of the coupling of the angular momenta referred to molecular axes.[4] Angular momenta then have the same addition laws as in atomic cases if the internal angular momenta are reversed in sign.[4] Let then the angular momenta $\mathbf{J}$, $\mathbf{F}_1$, $\mathbf{F}$ previously defined relative to laboratory axes (capital subscripts $X$, $Y$, $Z$) be referred to molecular axes. Let $\bar{\mathbf{O}}$ be the total reversed internal angular momentum defined by

$$\bar{O}_\nu=\bar{L}_\nu+\bar{I}_{N\nu}+\bar{I}_\nu=-(L_\nu+I_{N\nu}+I_\nu),$$
$$J_\nu=F_\nu+\bar{O}_\nu, \quad \nu=x,y,z; \tag{9.1}$$

then

$$[\bar{O}_\nu,F_\rho]=0, \quad [J_Z,J_z]=0, \quad T_xT_y-T_yT_x=-ihT_z, \tag{9.2}$$
$$\nu=x,y,z; \quad \rho=x,y,z; \quad T=F,F_1,J,\bar{O}.$$

These relations lead to the "molecular frame coupling scheme" given in Fig. 3 which should be compared with the "laboratory coupling scheme" of Fig. 1.

Based on the above considerations the calculation of the matrix elements of $G_1$ in the molecular representation gives

$$\{\langle l_0 i|G_1|l_0 i'\rangle\}=A(J_x^2+J_y^2)+CJ_z^2 \tag{10.0}$$
$$-(a_1+a_2)(J_x\bar{I}_{Nx}+J_y\bar{I}_{Ny})-b_2J_z\bar{I}_{Nz} \tag{10.1a}$$
$$-(\alpha_1+\alpha_2)(J_x\bar{I}_{1x}+J_{x'}\bar{I}_{2x'}+J_{x''}\bar{I}_{3x''}) \tag{10.3a}$$
$$-(-\rho_1+\rho_2)(J_y\bar{I}_{1y}+J_{y'}\bar{I}_{2y'}+J_{y''}\bar{I}_{3y''}) \tag{10.1b}$$
$$-(\gamma_1+\gamma_2)(J_z\bar{I}_{1z}+J_{z'}\bar{I}_{2z'}+J_{z''}\bar{I}_{3z''}) \tag{10.3b}$$
$$+\mu_0^2g_Ng_H[\langle v|r^{-3}|v\rangle\bar{\mathbf{I}}_N\cdot\bar{\mathbf{I}}-3\langle v|r^{-3}\sin^2\beta|v\rangle$$
$$\times\{\bar{I}_{Nx}\bar{I}_{1x}+\tfrac{1}{4}\bar{I}_{Nx}(\bar{I}_{2x}+\bar{I}_{3x})-\tfrac{1}{4}\sqrt{3}\bar{I}_{Nx}(\bar{I}_{2y}-\bar{I}_{3y})$$
$$-\tfrac{1}{4}\sqrt{3}\bar{I}_{Ny}(\bar{I}_{2x}-\bar{I}_{3x})+\tfrac{3}{4}\bar{I}_{Ny}(\bar{I}_{2y}+\bar{I}_{3y})\}$$
$$+3\langle v|r^{-3}\cos^2\beta|v\rangle\bar{I}_{Nz}\bar{I}_z] \tag{10.4}$$
$$+\mathcal{H}_{QN}. \tag{10.5}$$

The terms listed in (10.0–10.5) have their origins in the correspondingly numbered terms of (1.0–1.5), $\langle v|r^{-3}|v\rangle$ indicates the inverse cube of the nitrogen-proton distance is to be averaged over the vibration. $\beta$ is the angle between $r$ and the symmetry axis. All other constants not previously identified are given in Appendix II and are dependent only on the electronic states. The meaning of the primes on the coordinate subscripts of the proton angular momenta will be discussed in connection with Eq. (12). We shall now turn to the calculation of $G_2$, the part of $G$ which comes from the second-order calculation.

[18] E. U. Condon and G. H. Shortley, *Theory of Atomic Spectra* (Cambridge University Press, Cambridge, 1951).

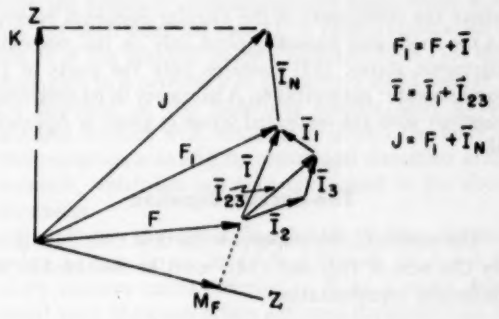


FIG. 3. $N^{14}H_3$ molecular coupling scheme referred to laboratory axis.

## Terms Off-Diagonal in Electronic States ($G_2$)

Terms of $G_2$ are of two types: (1) those off-diagonal in the electronic orbital quantum numbers and (2) those off-diagonal in the total electronic spin quantum numbers. (1.0) and (1.1) contain the terms of the first mentioned type while (1.2) and (1.6) contain the second-type terms. The perturbation of the electronic states by molecular rotation finds expression in Eq. (6.3) which will contain cross products of terms of type (2) and (1.1). The effect of the terms (1.1) will therefore be appreciable. On the other hand, since the total electronic spin is zero, electronic spin states are not perturbed by rotation. Hence, these latter terms are orders of magnitude smaller than the former and can be neglected. With this approximation, discussed in more detail in Appendix II, the off-diagonal terms left for consideration are

$$\mathcal{H}_2=A(L_x^2+L_y^2)+CL_z^2-2A(L_xJ_x+L_yJ_y)-2CL_zJ_z$$
$$+(l\mu_0/c)\textstyle\sum_{K,i}[\mathbf{r}_{iK}{}^{-3}(\mathbf{r}_i-\mathbf{r}_K)\times\mathbf{v}_i]\cdot g_K\mathbf{I}_K. \tag{11}$$

The first two terms above do not affect the hyperfine structure and thus will be dropped. The interaction of the protons with the electrons expressed in the last term is the same at points separated by a 120° rotation about the molecular symmetry axis. Advantage can be taken of this fact by employing initially three molecular coordinate systems: $x$, $y$, $z$ (described in Appendix I) in which proton (1) lies in the $xz$ plane; $x'$, $y'$, $z'$ in which proton (2) lies in the $x'z'$ plane; and $x''$, $y''$, $z''$ in which proton (3) lies in the $x''z''$ plane. These systems all have a common $z$ axis (see Fig. 4). If advantage is taken of the above symmetry and the terms of (11) are substituted into (6), $G_2$ becomes

$$\{\langle l_0 i|G_2|l_0 i'\rangle\}=-a_3(\bar{I}_{Nz}J_z+\bar{I}_{Ny}J_y)-b_3\bar{I}_{Nz}J_z \tag{12.1}$$
$$-\alpha_3(\bar{I}_{1x}J_x+\bar{I}_{2x'}J_{x'}+\bar{I}_{3x''}J_{x''})$$
$$-\rho_3(\bar{I}_{1y}J_y+\bar{I}_{2y'}J_{y'}+\bar{I}_{3y''}J_{y''}) \tag{12.2}$$
$$-\gamma_3(\bar{I}_{1z}J_z+\bar{I}_{2z'}J_{z'}+\bar{I}_{3z''}J_{z''}),$$

where the coefficients of the angular momenta referred to the molecular frames depend only on the molecular electronic states. (12) contains only the parts of (6) significant for our purposes. A summary of its derivation together with the neglected terms is given in Appendix II.

### The Secular Equation

The matrix $G$, the important parts of which are given by the sum of (10) and (12), must be obtained in the molecular representation

$$|vM_F\bar{I}_1\bar{I}_{23}\bar{I}FF_1\bar{I}_NJ_K\rangle.$$

According to the discussion in the introduction to this section, only matrix elements diagonal in $J$, $K$, and $F_1$ need be considered. Using the coupling scheme of Fig. 3, the appropriate matrix elements of $G$ can be found by standard methods given in Condon and Shortley.[18] The result of this calculation which is described in Appendix III is:

$$G=AJ(J+1)+(C-A)K^2 \tag{13.0}$$

$$+eq_NQ_N\left[1-\frac{3K^2}{J(J+1)}\right]\Omega_1(J,I_N) \tag{13.5}$$

$$+\left[a+\frac{(b-a)K^2}{J(J+1)}\right]\mathbf{I}_N\cdot\mathbf{J} \tag{13.1a, 13.3a}$$

$$+\frac{2g_ng_N\mu_0^2\mathbf{F}_1\cdot\mathbf{I}}{F_1(F_1+1)}\Omega_2(J,I_N)$$

$$\times\left[\langle v|r^{-3}(1-\tfrac{3}{2}\sin^2\beta)|v\rangle\left(1-\frac{3K^2}{J(J+1)}\right)\right. \tag{13.4}$$

$$-\tfrac{3}{4}\langle v|r^{-3}\sin^2\beta|v\rangle\left(1+\frac{3(I_1^2-I_{23}^2)}{I(I+1)}\right)\frac{(J_x^2-J_y^2)}{J(J+1)}$$

$$\left.+\tfrac{3}{4}\sqrt{3}\langle v|r^{-3}\sin^2\beta|v\rangle\frac{(I_2-I_3)\cdot I}{I(I+1)}\,\frac{(J_xJ_y+J_yJ_x)}{J(J+1)}\right]$$

$$+\frac{(\mathbf{I}\cdot\mathbf{F}_1)(\mathbf{F}_1\cdot\mathbf{J})}{F_1(F_1+1)J(J+1)}\left[(\alpha+\rho)J(J+1)\right.$$

$$+[\gamma-(\alpha+\rho)]K^2+(\alpha-\rho)\left(1-\frac{3I_{23}\cdot I}{I(I+1)}\right)$$

$$\times(J_x^2-J_y^2)-\tfrac{1}{2}\sqrt{3}(\alpha-\rho)\left(\frac{(I_2-I_3)\cdot I}{I(I+1)}\right)$$

$$\left.\times(J_xJ_y+J_yJ_x)\right], \tag{13.1b,13.3b}$$

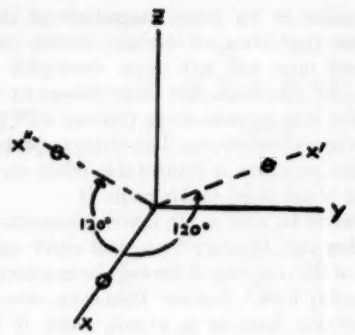


FIG. 4. The three initial proton coordinate systems.

where

$$\Omega_1(J,I_N)=\frac{3(\mathbf{I}_N\cdot\mathbf{J})^2+\frac{3}{2}(\mathbf{I}_N\cdot\mathbf{J})-I_N(I_N+1)J(J+1)}{(2J-1)(2J+3)2I_N(2I_N-1)},$$

$$\Omega_2(J,I_N)=\frac{3(\mathbf{I}_N\cdot\mathbf{J})^2+2J(J+1)\mathbf{I}_N\cdot\mathbf{J}-I_N(I_N+1)J(J+1)}{(2J-1)(2J+3)},$$

$$2\mathbf{I}_N\cdot\mathbf{J}=F_1(F_1+1)-J(J+1)-I_N(I_N+1),$$

$$2\mathbf{F}_1\cdot\mathbf{J}=F_1(F_1+1)+J(J+1)-I_N(I_N+1),$$

$$2\mathbf{F}_1\cdot\mathbf{I}=F(F+1)-F_1(F_1+1)-I(I+1).$$

$a=a_1+a_2+a_3$ is proportional to the transverse molecular magnetic field at the nitrogen nucleus and $b=b_2+b_3$ is proportional to the axial field. The terms with subscripts 1, 3 are due to the electron currents, the terms with subscript 2 to the nuclear currents.

$$\alpha=\alpha_1+\alpha_2+\alpha_3,$$

$$\rho=\rho_1+\rho_2+\rho_3,$$

$$\gamma=\gamma_1+\gamma_2+\gamma_3,$$

where $\alpha$ is proportional to the total $x$ molecular magnetic field at a given proton, and $\rho$ is proportional to the $y$ magnetic field and $\gamma$ is the $z$ magnetic field. The subscripts 1, 2, 3 have the same meaning as for $a$, $b$. Other quantities have been identified previously (see Appendix also). To find the energies of the perturbed levels in each inversion state, it is necessary to solve the secular equation:

$$\{\langle\bar{I}_{23}\bar{I}JK|G|\bar{I}_{23}'\,\bar{I}\,J\pm K\rangle - E\delta(I_{23},I_{23}')\delta(K,K')\}=0, \tag{14}$$

with the aid of the matrix elements given in Appendix III. For $K\neq1$ the Hamiltonian, to the approximations made above, is diagonal and the energy levels are given by

$$W_{vJKF_1F}=AJ(J+1)+(C-A)K^2$$
$$-eq_NQ_N\left(1-\frac{3K^2}{J(J+1)}\right)\Omega_1(J,I_N)$$
$$+\left(a+\frac{(b-a)K^2}{J(J+1)}\right)\mathbf{I}_N\cdot\mathbf{J}$$
$$+\left(\alpha+\rho+\frac{(\gamma-(\alpha+\rho))K^2}{J(J+1)}\right)\frac{(\mathbf{I}\cdot\mathbf{F}_1)(\mathbf{F}_1\cdot\mathbf{J})}{F_1(F_1+1)}$$
$$+2g_Hg_N\mu_0^2\langle v|r^{-3}(1-\tfrac{3}{2}\sin^2\beta)|v\rangle$$
$$\times\left(1-\frac{3K^2}{J(J+1)}\right)\frac{\mathbf{F}_1\cdot\mathbf{I}}{F_1(F_1+1)}\Omega_2(J_N,J), \quad (15)$$

where $I=\frac{3}{2}$ for $|K|=3n$, and $I=\frac{1}{2}$ for $|K|=3n\pm1$.

For $K\neq3n$, a typical set of levels whose $K$ and $I_{23}$ degeneracy has not been lifted is shown in Fig. 5b. This figure shows the effect of terms of (15) for a given $F_1$ value in the upper and in the lower inversion states. Note that when $K\neq1$ these are the final hyperfine levels and they are perfectly normal. They lead to a spectrum shown in full in Fig. 4 of I. For $K=3n$ there are twice the number of levels since $I=\frac{3}{2}$. Experimentally the presence of these multiple levels when $K\neq1$ has not been detected (see I). A close examination of the fit of the spectral pattern deduced from (15) does show that it is necessary to allow for a small change in the gradient of the molecular electric field at the nitrogen nucleus with rotation to obtain the best fit. This variation is caused by centrifugal distortion of the molecule, which has not been considered in the above discussion.

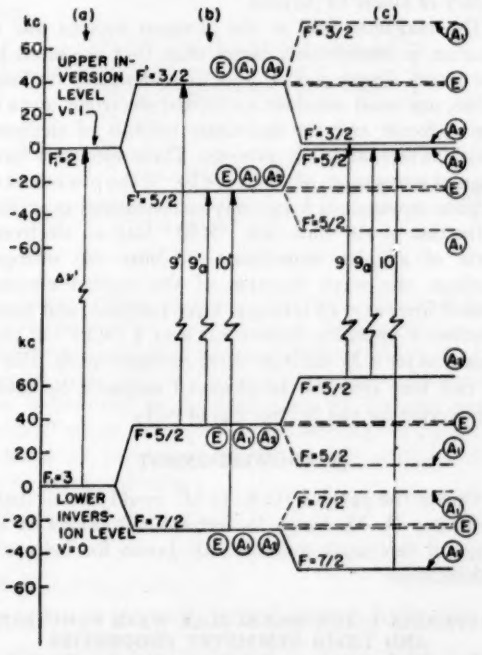


FIG. 5. Energy levels and transitions for the levels $J=3$, $K=1$ ($V=0$, $F_1=3$; $V'=1$, $F_1'=2$). (a) Energy levels omitting proton effects quadruply degenerate. (b) Energy levels including proton effects diagonal in $K$-neglecting lifting of $K$ degeneracy. (c) Actual energy levels—full lines; forbidden levels—dashed lines; $E$ levels are degenerate lines corresponding to allowed transitions shown in right-hand set of Fig. 3(b) of (I). $A_1$ refers to symmetric levels; $A_2$ refers to antisymmetric levels.

For $K=1$, the determinant (14) is not diagonal owing to the terms in $(J_x^2-J_y^2)$ and $(J_xJ_y+J_yJ_x)$ which connect states differing in $K$ by 2 units. Associated with these operators are ones dependent on $I_{23}$ which connect states $I_{23}=0$ with states $I_{23}=1$. The magnetic perturbations thus simultaneously lift the degeneracy in the levels of $K=\pm1$ and $I_{23}=0,1$. Employing the matrix elements calculated in Appendix III, one may easily solve the secular equation (14). Its roots are $E=W$, $W$, $W+2f$, $W-2f$, where $W$ is defined by Eq. (15) and

$$f=\tfrac{1}{2}\left\{\tfrac{3}{2}\langle v|r^{-3}\sin^2\beta|v\rangle+\frac{2g_Ng_H\mu_0^2\mathbf{F}_1\cdot\mathbf{I}}{F_1(F_1+1)}\Omega_2(J,I_N)\right.$$
$$\left.+(\rho-\alpha)\frac{(\mathbf{F}_1\cdot\mathbf{I})(\mathbf{F}_1\cdot\mathbf{J})}{F_1(F_1+1)J(J+1)}\right\}J(J+1). \quad (16)$$

With these roots the molecular wave functions can be determined and are given symbolically below in the laboratory frame:

$$\Psi_{E=W}=\frac{1}{\sqrt{2}}[|v\,K=1\,J\,I_N\,F_1\,I_{23}=1\,I=\tfrac{1}{2}\,FM_F\rangle$$
$$+i|v\,K=1\,J\,I_N\,F_1\,I_{23}=0\,I=\tfrac{1}{2}\,FM_F\rangle],$$
$$\Psi_{E=W\pm2f}=\tfrac{1}{2}[|v\,K=1\,J\,I_N\,F_1\,I_{23}=1\,I=\tfrac{1}{2}\,F\,M_F\rangle$$
$$\pm|v\,K=-1\,J\,I_N\,F_1\,I_{23}=1\,I=\tfrac{1}{2}\,F\,M_F\rangle$$
$$+i|v\,K=1\,J\,I_N\,F_1\,I_{23}=0\,I=\tfrac{1}{2}\,F\,M_F\rangle$$
$$\mp|v\,K=-1\,J\,I_N\,F_1\,I_{23}=0\,I=\tfrac{1}{2}\,F\,M_F\rangle]\equiv\Psi_2^1,$$

where the upper signs are to be associated together, etc. Inspection of Table I shows that the functions for $E=W$ clearly belong to the representation $E$ and have the same type energy levels as are found for $K\neq1$. The remaining two functions must then belong to the irreducible representations $A_1$ and $A_2$. Which of these they belong to can readily be determined by applying the permutation operator $P_{ij}$ or specifically $P_{23}$ to the wave functions. Let us express the wave functions $\Psi_{1,2}$ in the representation

$$\Psi_{1,2}=\tfrac{1}{2}[|v\,K=1\,JF_1M_{F_1}\rangle(|I_1I_{23}=1\,I=\tfrac{1}{2}\,M_I\rangle$$
$$+i|I_1I_{23}=0\,I=\tfrac{1}{2}\,M_I\rangle)\pm|v,\,K=-1\,J\,F_1\,M_{F_1}\rangle$$
$$\times(|I_1\,I_{23}=1\,I=\tfrac{1}{2}\,M_I\rangle-i|I_1\,I_{23}=0\,I=\tfrac{1}{2}\,M_I\rangle)]. \quad (17)$$

In this representation the operator $P_{23}$ can be expressed as[19]

$$P_{23}=P_{23}^{(x)}P_{23}^{(\sigma)}=P_{23}^{(x)}(\tfrac{1}{2}+2\mathbf{I}_2\cdot\mathbf{I}_3). \quad (18)$$

In the representation $|I_1,I_{23},I,M_I\rangle$, $\mathbf{I}_2\cdot\mathbf{I}_3$ can readily be calculated from the identity

$$\mathbf{I}\cdot\mathbf{I}=(\mathbf{I}_1+\mathbf{I}_2+\mathbf{I}_3)\cdot(\mathbf{I}_1+\mathbf{I}_2+\mathbf{I}_3)=I(I+1),$$

from which

$$\mathbf{I}_2\cdot\mathbf{I}_3=\tfrac{1}{2}[I(I+1)-3\cdot\tfrac{3}{4}-2(\mathbf{I}_1\cdot\mathbf{I}_{23})]=\tfrac{1}{2}(I_{23}(I_{23}+1)-\tfrac{3}{2}).$$

Thus,

$$\begin{aligned}P_{23}^{(\sigma)}|I_1\,I_{23}=1\;I=\tfrac{1}{2}\;M_I\rangle&=|I_1\,I_{23}=1\;I=\tfrac{1}{2}\;M_I\rangle,\\ P_{23}^{(\sigma)}|I_1\,I_{23}=0\;I=\tfrac{1}{2}\;M_I\rangle&=-|I_1\,I_{23}=0\;I=\tfrac{1}{2}\;M_I\rangle.\end{aligned} \quad (19)$$

Also, from Appendix I,

$$\begin{aligned}P_{23}^{(x)}|v\;K\;J\;F_1\;M_{F_1}\rangle&=(-1)^{J+v}|v\;-K\;J\;F_1\;M_{F_1}\rangle,\\ P_{23}^{(\sigma)}|v\;-K\;J\;F_1\;M_{F_1}\rangle&=(-1)^{J+v}|v\;K\;J\;F_1\;M_{F_1}\rangle,\end{aligned} \quad (20)$$

where $v=0$ for the lower inversion state and $v=1$ for the upper inversion state. Therefore, applying $P_{23}$ to $\Psi_{2'}$ expressed in (17a), we find

$$P_{23}\Psi_2{}^1=\pm(-1)^{J+v}\Psi_2{}^1. \quad (21)$$

Thus if $(-1)^{(J+v)}=-1$ the function $\Psi^1$ is physically allowed and the energy is $E=W+2f$ while when $(-1)^{J+(v+1)}=-1$ the function $\Psi_2$ is physically allowed and the energy is $E=W-2f$. These results can be summarized by writing

$$E=W-(-1)^{J+v}2f, \quad \text{for } |K|=1. \quad (22)$$

Note that if the levels marked $A_1$ were allowed, the intensity pattern would be reversed similar to that of Fig. 2b of I.

### Interpretation of the Magnetic Constants

Evaluation of the magnetic effects discussed above gives the three components of magnetic field at the hydrogen nuclei produced by rotation and the two independent components at the nitrogen nucleus. In addition, the magnetic moment of the molecule due to rotation about the symmetry axis or perpendicular to it are known from earlier work.[20] These seven pieces of information about the magnetic properties of $NH_3$ should in principle be interpretable in terms of its structure.

The electric currents which produce the magnetic fields associated with rotation of a $^1\Sigma$ molecule can be divided into those due to motions of the electrons and those due to the nuclei. The currents due to nuclear motion may be satisfactorily calculated from a knowledge of the equilibrium nuclear distances. Unfortunately a calculation of electronic currents is very difficult because it requires a fairly detailed knowledge of the ground and excited electronic states. However, the following simple model probably corresponds roughly to the behavior of the electron distribution as the molecule rotates and gives approximately correct values for the various magnetic effects.

Assume that the nitrogen nucleus, which stays essentially stationary at the center of mass as the molecule rotates, is surrounded by a fixed spherical cloud of electrons which includes all of its own valence electrons plus one-half of the valence electrons of the hydrogen atoms. Assuming further that the amount of electron charge in this fixed cloud at radii larger than the nitrogen-proton distance corresponds to one electron. The protons rotating about the nitrogen, then each carries one-half an electron around with them, slipping through the fixed spherical charge distribution (see slip effect).[8,20] The one-half electron carried around with each proton is assumed to spherically surround this proton, and hence will rotate about the nitrogen with the proton while staying fixed in orientation like the chair of a Ferris wheel (see slip effect again).[8,20] A simple classical calculation shows that this model gives the two different components of the molecular magnetic moment and the three different components of the magnetic field at the protons due rotation to an accuracy of about 15 percent.

The magnetic field at the nitrogen nucleus due to rotation is considerably larger than that produced by the above simple model, and to understand its large value, one must consider an excited electronic state of the molecule and the molecular orbitals of electrons which rotate with the protons. These electrons have angular momentum of about $3\times10^{-4}$ if the protons have angular momentum $\hbar$ and may be considered as excited a fraction of the time near $3\times10^{-4}$ into an electronic state of angular momentum $\hbar$. Near the nitrogen nucleus, the wave function of the excited electron should involve a $2p$ nitrogen wave function, and hence produce a hyperfine interaction near $1.5\times10^{-4}$ of that expected for a $2p$ electron in the nitrogen atom. This is in fact very close to the observed magnetic hyperfine interaction for the $N^{14}$ nucleus in $NH_3$.

#### ACKNOWLEDGMENT

One of the authors (G.R. G-M) would like to thank Professor H. M. Foley for helpful discussions at the start of this work and Mr. Ali Javan for help with calculations.

## APPENDIX I. THE MOLECULAR WAVE FUNCTIONS AND THEIR SYMMETRY PROPERTIES

### Molecular Coordinates and Eulerean Angles (see Fig. 6)

With the origin at the center of mass of the nuclei, the $z$ molecular axis is taken as positive in the direction of advance of a right-handed screw rotating in the

[19] P. A. M. Dirac, *The Principles of Quantum Mechanics* (Clarendon Press, Oxford, 1947), third edition.

[20] C. K. Jen, Phys. Rev. 81, 197 (1951); J. R. Esbach and M. W. P. Strandberg, Phys. Rev. 85, 24 (1952).

order of the numbering of the protons 1, 2, 3. The $x$ axis lies in the plane containing the axis and the proton numbered (1). The Eulerian angles are taken as follows relative to the fixed laboratory frame:

$\phi$—the fixed frame azimuthal angle, is measured from the fixed $x$ axis to the line of nodes, on;
$\theta$—the polar angle, is measured from the fixed $z$ axis to the molecular $z$ axis;
$\chi$—the molecular frame azimuthal angle, is measured from the line of nodes to the molecular $x$ axis.

The angles $\phi$, $\chi$ are defined in the range $0 \leqslant \phi, \chi < 2\pi$ and are positive in the direction of rotation $x \rightarrow y$. $\theta$ is defined in the range $0 \leqslant \theta \leqslant \pi$ and is positive for the rotation $y \rightarrow z$.

### The Symmetric Top Functions, $U_{kM}{}^{J}(\phi,0,\chi)$, and Their Properties

These functions are:[21]

$$U_{KM}{}^{J}(\phi,\theta,\chi) = (-1)^{K} e^{i(M+K)\pi/2} N_{JKM} \times e^{i(M\phi+K\chi)} P_{KM}{}^{J}(\theta) \quad \text{for } M \geqslant K$$
$$= (-1)^{M} e^{i(M+K)\pi/2} N_{JKM} \times e^{i(M\phi+K\chi)} P_{KM}{}^{J}(\theta) \quad \text{for } K \geqslant M,$$

where

$$N_{JKM} = \left[\frac{(2J+1)(J+\tfrac{1}{2}d+\tfrac{1}{2}s)!(J-\tfrac{1}{2}s+\tfrac{1}{2}d)!}{8\pi^2(J-\tfrac{1}{2}s+\tfrac{1}{2}d)!d!(J+\tfrac{1}{2}s-\tfrac{1}{2}d)!}\right]^{\frac{1}{2}},$$

$$P_{KM}{}^{J}(\theta) = t^{-\frac{1}{2}d}(1-t)^{-\frac{1}{2}s}\frac{d!}{(d+p)!}\frac{d^{p}}{dt^{p}}(t^{d+p}+(1-t)^{s+p}), \tag{A1}$$
$$d = |M-K|, \quad s = |M+K|,$$
$$t = (1-\cos\theta)/2, \quad 2p = 2J-(d+s).$$

The proper choice of phases has been discussed by Van Vleck[21] and by Casimir[7] and is determined for us by the requirement that the matrix elements of $J_z$, $J_y$, $J_x$ obtained from the above representation have the same phase convention as is established by Condon and Shortley[18] whose tabulated matrix elements of angular momenta we propose to use in further calculations. This choice is such that

$$\langle J\,M\,K|J_z \pm iJ_y|J\,M\,K\pm 1\rangle = [J(J+1)-K(K\pm 1)]^{\frac{1}{2}},$$
$$\langle J\,M\,K|J_z \mp iJ_y|J\,M\pm 1\,K\rangle = [J(J+1)-M(M\pm 1)]^{\frac{1}{2}}. \tag{A2}$$

By using the functions so defined, it can be shown that

$$U_{KM}{}^{J}(\phi,\pi-\theta,\chi) = (-1)^{J+M} U_{-KM}{}^{J}(\phi,\theta,\chi). \tag{A3}$$

[21] J. H. Van Vleck, Phys. Rev. 33, 467 (1929), especially p. 476 and 480. Also L. Pauling and E. B. Wilson, *Introduction to Quantum Mechanics* (McGraw-Hill Book Company, Inc., New York, 1935).

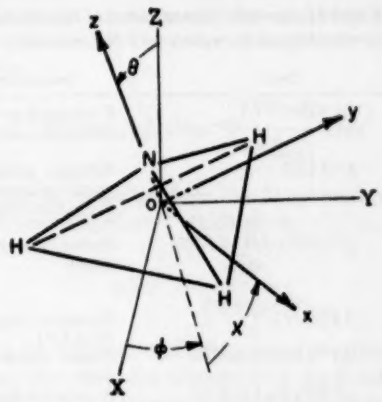


FIG. 6. Molecular coordinates and Eulerean angles.

We shall write

$$U_{KM}{}^{J}(\phi,\theta,\chi) = |vKJM\rangle \text{ in the laboratory frame}$$
$$= |vMJK\rangle \text{ in the molecular frame.}$$

The operator $P_{23}$ which exchanges protons 2, 3 and thus corresponds to the coordinate transformations

$$\phi \rightarrow \phi+\pi, \quad \chi \rightarrow \pi-\chi, \quad \theta \rightarrow \pi-\theta, \quad z \rightarrow -z, \tag{A4}$$

when applied to the rotation vibration function $|vKJM\rangle$, gives

$$P_{23}|v\,K\,J\,M\rangle = (-1)^{J+v}|v\,-K\,J\,M\rangle,$$
$$P_{23}|v\,-K\,J\,M\rangle = (-1)^{J+v}|v\,K\,J\,M\rangle. \tag{A5}$$

## APPENDIX II. CALCULATION OF THE TERMS IN EQ. (10) FROM EQ. (1)

### Terms Involving Only the Ground Electronic State ($G_1$)

The contribution of the term (1.3) and of the nuclear velocity dependent parts of the term (1.1) lead, respectively, to the terms (10.3a, b) and (10.1a, b) if the molecular coordinates are taken relative to the axis shown in Fig. 5 of Appendix I for the $I_N$ dependent parts (10.3a, 10.1a) and relative to the axes of Fig. 3 for the proton dependent parts (10.3b, 10.1b). The coefficients of (10.1) all involve integrals over the electronic wave functions, for example,

$$\gamma_1 = -2e\mu_0 g_H C(1/c\hbar)\langle vl_0|\textstyle\sum_i r_{i1}^{-3}(\mathbf{r}_i-\mathbf{r}_1)_x(\mathbf{r}_1)_z|vl_0\rangle, \tag{A6}$$

where $\mathbf{r}_1$ is the position vector of proton 1 relative to the axes $x$, $y$, $z$ of Fig. 3 or of proton 2 relative to the axis $x'$, $y'$, $z'$ of Fig. 4, etc. Because of our lack of knowledge of the electronic functions, these integrals cannot be evaluated and thus will be treated as unknown parameters. From (1.3) the following coefficients can be identified and evaluated approximately since the geo-

TABLE II. *Symbolic* representation of the second-order electron orbital contributions to the perturbation calculation.

| Matrix number | Term | Descriptive name usually applied—physical interpretation | Comments for $NH_3$ |
|---|---|---|---|
| $(G_2)_1$ | $(A'JL)^2$ | $L$ uncoupling—exchange of angular momentum between electrons and rotation of nuclei | Contribute to apparent moments of inertia, no hyperfine effects |
| $(G_2)_2$ | $a''(I_NL)^2$ | Nitrogen pseudoquadrupole[a] interaction of electron orbital origin—perturbation of precession of perpendicular components of electron orbital momenta of $N^{14}$ spin | Appears as part of the experimentally measured $eqQ$. Estimated upper limit about 5 cps |
| $(G_2)_3$ | $\alpha''(I_1^2I_1^2+I_2^2I_2^2+I_3^2I_3^2)$ | Proton pseudoquadrupolar interaction of electron orbital origin | Transforms like a 2nd degree spherical harmonic vanishes since $I_\nu=\frac{1}{2}$ |
| $(G_2)_4$ | $2A''I^2JI_N$ | Nitrogen magnetic moment interaction with molecular magnetic field | Discussed in detail below and in text |
| $(G_2)_5$ | $2A'''I^2J(I_1+I_2+I_3)$ | Proton magnetic moment interaction with molecular magnetic field | Discussed in detail below and in text |
| $(G_2)_6$ | $\alpha'''I^2I_N(I_1+I_2+I_3)$ | A pseudomagnetic dipolar interaction in which the nuclear spins are coupled to each other by their magnetic polarization of the magnetic orbitals | Estimated in the order of a few cycles |
| $(G_2)_7$ | $\rho'I^2(I_1I_2+I_1I_3+I_2I_3)$ | Similar to above (6) | Estimated negligible |

[a] So named by H. M. Foley, Phys. Rev. **72**, 504 (1947), who treated this term of diatomic molecules.

metrical structure of the molecule is known:

$$a_2=-6e\mu_0g_NA(1/ch)\langle v|\tfrac{1}{2}r^{-1}\{(14/17)r^{-1}+(3/17)r^{-1}(1+Z_NM_P/g_NM)_N\}\cos^2\beta|v\rangle$$
$$=-3.6\text{ kc/sec},$$
$$b_2=-6e\mu_0g_NC(1/ch)\langle v|r^{-1}\sin^2\beta|v\rangle=3.0\text{ kc/sec},$$
$$\alpha_2=-2e\mu_0g_HA(1/ch)\langle v|r^{-1}\{(2\sqrt{3}\sin\beta)^{-1}+(Z_N/17)[14(1+g_H^{-1})+3]\cos^2\beta\}|v\rangle$$
$$=-(8.0+4.0Z_N)\text{ kc/sec},$$
$$\rho_2=-2e\mu_0g_HA(1/ch)\langle v|r^{-1}\{[(3+g_H^{-1})(2\sqrt{3}\sin\beta)^{-1}]+Z_N(1+g_H^{-1}-(3/17g_H)\cos^2\beta]\}|v\rangle$$
$$=-(27.0+29.4Z_N)\text{ kc/sec},$$
$$\gamma_2=-2e\mu_0g_HC(1/ch)\langle v|r^{-1}\{[(2+g_H^{-1})(\sqrt{3}\sin\beta)^{-1}]+Z_N(1+g_H^{-1})\sin^2\beta\}|v\rangle$$
$$=-(21.6+16.1Z_N)\text{ kc/sec}.$$

Where the numerical values are obtained by substituting the geometrical constants of the molecule[11] and the nuclear constants[22] given below ($I_A$, $I_C$ transverse and axial moments of inertia, respectively)

$I_A=2.82\times10^{-40}$ g cm$^2$, $B=67°58'$, $A\equiv\hbar^2/2I_A$,
$I_C=4.43\times10^{-40}$ g cm$^2$, $g_H=2\times2.7896$, $C\equiv\hbar^2/2I_C$,
$r=1.014\times10^{-8}$ cm, $g_N=0.403$.

The effects of the "nuclear currents" which have thus been calculated can be subtracted from the experimentally measured effects to obtain those due to electronic currents only. This, of course, assumes that the effects of nuclear currents can be calculated from our model of $NH_3$ which disregards inversion. That this is a good approximation is demonstrated by the fact that the dipolar interaction calculated by this means gives good agreement with the data.

[22] *Segrè Chart* (Addison Wesley Press, Cambridge, 1948).

Using the position of the nuclei relative to the molecular frame of Fig. 5, we have from (1.4) for the nitrogen proton dipolar interaction the terms

$$-3\mu_0^2g_Ng_H\langle v|r^{-3}\sin\beta\cos\beta|v\rangle\times[\bar{I}_{Nx}\bar{I}_{1z}-\bar{I}_{Nz}(\bar{I}_{2x}+\bar{I}_{3x})+\tfrac{1}{2}\bar{I}_{Ny}(\bar{I}_{2z}-\bar{I}_{3z})-\bar{I}_{Nx}(\bar{I}_{2z}+\bar{I}_{3z})+\bar{I}_{Nz}\bar{I}_{1x}+\tfrac{1}{2}\sqrt{3}\bar{I}_{Nz}(\bar{I}_{2y}-\bar{I}_{3y})],$$

in addition to the terms given in (10.4). According to the discussion in Appendix III, these terms are only off-diagonal in $K$ by $\pm1$ and thus they may be dropped. The proton-proton dipolar interactions have been shown in the text to be negligible.

### Second-Order Terms Involving Excited Electronic States ($G_2$)

In a light molecule like $NH_3$ the Russell-Saunders system of representation is a good approximation, so that the terms involving the $L_x$, $L_y$, $L_z$ and the electron velocities will depend only on orbital quantum numbers $l$, while the operators $S_x$, $S_y$, $S_z$ will involve the spin quantum numbers $\sigma$. Because of their larger magnitude we shall consider the former terms first and return to the latter at the end of this Appendix.

Calculation of the orbital perturbations is based on the last three terms of (11) which are to be substituted into (6.3). Rather than writing out in detail the seven different kinds of terms to which such a substitution leads, we shall use a symbolism to describe them according to their dependence on angular momenta and molecular parameters. We represent Eq. (6.3) as

$$G_2=\{\sum_{l\neq l_0}(E_{l_0}-E_l)^{-1}(\langle l|AJL+a'L\bar{I}_N+\alpha'(L\bar{I}_1+L\bar{I}_2+L\bar{I}_3)|l_0\rangle)^2\},\quad\text{(A7)}$$

which when expanded in an equally symbolic way gives the contributions to $G_2$ listed in Table II.

To be specific, consider now the matrix $(G_2)_4$ as an example and define for convenience[4]

$$\eta_\nu = 2g_N e\mu_0(1/c)[\textstyle\sum_j r_{jN}^{-3}(\mathbf{r}_j-\mathbf{r}_N)\times\mathbf{v}_j]_{\nu=x,y,z}. \quad \text{(A8)}$$

In the molecular frame $\mathbf{r}_N$, the position vector of the nitrogen nucleus, is treated as a constant vector and its angular dependence relative to the laboratory axes is thrown over on the total angular momentum. Thus $\eta_\nu$ is, along with $L_\nu$, independent of the rotational quantum numbers. The matrix $(G_2)_4$, for instance, has elements

$$\begin{aligned}&\langle l_0 i|\,(G_2)_4\,|l_0 i'\rangle\\&=\sum_{l\neq l_0}(E_{l_0}-E_l)^{-1}[\sum_{i''}\{(\sum_\nu\langle l_0|A_\nu L_\nu|l\rangle\langle i|J_\nu|i''\rangle)\\&\quad\times(\textstyle\sum_{\nu'}\langle l|\eta_{\nu'}|l_0\rangle\langle i''|\bar{I}_{N\nu'}|i'\rangle)\\&\quad+(\textstyle\sum_\nu\langle l_0|\eta_\nu|l\rangle\langle i|\bar{I}_{N\nu}|i''\rangle)\\&\qquad\times(\textstyle\sum_{\nu'}\langle l|A_{\nu'}L_{\nu'}|l_0\rangle\langle i''|J_{\nu'}|i'\rangle)\}].\end{aligned} \quad \text{(A9)}$$

$\eta_\nu$ and $L_{\nu'}$ do not commute with each other if $\nu\neq\nu'$ but do commute with $J_\nu$ and $\bar{I}_\nu$. Because only matrix elements diagonal in $J$ and $|K|$ are needed, the lack of commutation of $I_\nu$ and $J_{\nu'}$ can be ignored. With the help of Eq. (A3), the matrix $(G_2)_4$ can be expanded as a sum of products of angular momentum operators $\bar{I}_\nu J_{\nu'}$ with coefficients dependent on the electronic states only.[4] A typical coefficient would be:

$$\begin{aligned}M_{\nu\nu'}=\sum_{l\neq l_0}(E_{l_0}-E_l)^{-1}(&\langle l_0|\eta_\nu|l\rangle\langle l|A_{\nu'}L_{\nu'}|l_0\rangle\\&+\langle l_0|A_\nu L_\nu|l\rangle\langle l|\eta_{\nu'}|l_0\rangle).\end{aligned} \quad \text{(A10)}$$

And so

$$(G_2)_4=\tfrac{1}{2}\textstyle\sum_\nu\sum_{\nu'}M_{\nu\nu'}J\bar{I}_{N\nu'}, \quad \text{(A11)}$$

where $M_{\nu\nu'}$ are the components of a symmetric tensor whose principal axes coincide with those of the molecule since the nitrogen nucleus is on the axis. From molecular symmetry, therefore,

$$M_{xx}=M_{yy}\neq M_{zz}, \quad M_{xy}=M_{xz}=M_{yz}=0, \quad \text{(A12)}$$

and so the result of Henderson, expression (12.1), is obtained with

$$M_{xx}=a_3=M_{yy}, \quad M_{zz}=b_3. \quad \text{(A13)}$$

Calculation of $(G_2)_5$ made in the manner above for each proton in turn in its "own" system of axes (Fig. 4) leads to the terms (12.2) if the reflection symmetry of the electronic functions in the $xz$ plane is considered. The coefficients appearing in (12.2) are:

$$\begin{aligned}\alpha_3=A\sum_{l\neq l_0}(E_{l_0}-E_l)^{-1}(&\langle l_0|\xi_x|l\rangle\langle l|L_x|l_0\rangle\\&+\langle l_0|L_x|l\rangle\langle l|\xi_x|l_0\rangle)\end{aligned} \quad \text{(A14)}$$

$$\xi_x=(1/c)eg_H\mu_0[\textstyle\sum_j r_{1j}^{-3}(\mathbf{r}_j-\mathbf{r}_1)\times\mathbf{v}_j]_x,$$

with similar definitions for $\rho_3$ and $\gamma_3$ in terms of $\xi_y$, $L_y$, and $\xi_z$, $L_z$, respectively. $\alpha_3$, $\rho_3$ are not equal because of the off-axis position of the protons. An order of magnitude calculation of the term $(G_2)_2$—the pseudoquadrupolar term, can be made[22] by assuming a case of "pure precession." The order of magnitude of $(G_2)_2$ is given by

$$(G_2)_2\simeq\mu_0^2\mu_e^2g_N^2\langle r_N^{-3}\rangle^2\frac{I^2l(l+1)}{4\Delta E_{\Sigma\to\pi}}\text{ ergs.} \quad \text{(A15)}$$

$\langle r_e^{-3}\rangle$ can be estimated from the fine structure separation of atomic spectra,[24] which gives

$$\mu_e^2\langle r_e^{-3}\rangle=\frac{\Delta\nu hc}{2(l+\frac{1}{2})Z_i^2},$$

$Z_i\simeq 3.5$ for nitrogen and assuming a $p$ orbital of the bonding electron at the nitrogen $l=1$. $\Delta\nu$ is not directly available from experiment but can be estimated to be $\simeq 120$ cm$^{-1}$ for a $p$ state,[25] while $\Delta E_{\Sigma\to\pi}$ is of the order of 40 000 cm$^{-1}$. One obtains with these values $(G_2)_2\simeq 5$ cps which is negligible. A similar reasoning indicates that $(G_2)_6$, $(G_2)_7$ are negligible, while $(G_2)_3$ vanishes and $(G_2)_1$ does not affect the hyperfine spectrum.

A calculation of the perturbation of the electronic spin states can be carried out in a manner entirely analogous to the above orbital calculation, using in Eq. (6.3) the terms of (1.2) and of (1.6) instead of the terms of (11). Employing the same rough-type symbolism as in (A1), we may write

$$G_{2S}=\{\sum_{\sigma\neq\sigma_0}(E_{\sigma_0}-E_\sigma)^{-1}(\langle\sigma|bS(I_N+I_1+I_2+I_3)|\sigma_0\rangle)^2, \quad \text{(A16)}$$

which leads to terms of the type listed in Table III.[24] The last two terms of Table III contain a part dependent on molecular orientation and a part independent of orientation both of about the same magnitude.[26] The orientation independent part has been determined experimentally for several molecules to be of the order of 1 to 100 cps. For $NH_3$ experimentally it is less than 300 cps (see I) and therefore we shall neglect these terms.

## APPENDIX III. REDUCTION OF EQS. (10) AND (12) TO THE FORM OF EQ. (13)

Equations (10), (12) are in the form of sums of products of angular momentum operators with coefficients independent of these operators. The matrices are to be diagonalized in a representation

$$|\bar{I}_2\bar{I}_3\bar{I}_{23}\bar{I}_1\bar{I}FF_1\bar{I}_NJK\rangle,$$

for which the vector coupling scheme of Fig. 3 is understood. We shall first calculate the important matrix elements contributed to $G(7)$ by a typical

[22] H. A. Bethe and R. F. Bacher, Revs. Modern Phys. **8**, 209 (1937).
[24] N. F. Ramsey and E. M. Purcell, Phys. Rev. **85**, 143 (1952).
[25] This estimate is discussed by C. H. Townes and B. P. Dailey, J. Chem. Phys. **17**, 782 (1949).
[26] N. F. Ramsey, Phys. Rev. **91**, 303 (1953).

TABLE III. Symbolic representation of the second-order electron spin contribution to the perturbation calculation.

| Matrix number | Term | Description | Comments for $NH_3$ |
|---|---|---|---|
| $(G_{2S})_1$ | $b'^2(I_N S)^2$ | Nitrogen pseudoquadrupolar interaction arising from the perturbation of electronic spin states by the nitrogen magnetic moment. | May not be negligible but not distinguishable from pure quadrupolar interaction. |
| $(G_{2S})_2$ | $b''S^2(I_1^2+I_2^2+I_3^2)$ | Proton pseudoquadrupolar interaction | Transforms like a 2nd degree spherical harmonic and therefore vanishes as $I_p=\frac{1}{2}$ |
| $(G_{2S})_3$ | $2b'''S^2 I_N(I_1+I_2+I_3)$ | A pseudo-dipolar interaction and an $\mathbf{I}_N\cdot\mathbf{I}$ interaction[a] due to magnetic interactions of the nuclei with electron spins which are exchange-coupled together[b] | Experimentally determined to be negligible. |
| $(G_{2S})_4$ | $2\rho S^2(I_1I_2+I_2I_3+I_1I_3)$ | Similar to above | |

[a] E. L. Hahn, Phys. Rev. **80**, 580 (1950).
[b] See reference 26.

product of two such operators. Then applying this result to the operators of Eqs. (10), (12) we shall deduce expression (13). Consider the matrix element from (10.4):

$$\mathfrak{M}=\langle \bar{I}_2\bar{I}_3\bar{I}_{23}\bar{I}_1\bar{I}FF_1\bar{I}_N JK|\,\bar{I}_{Nz}\bar{I}_{2y}|\,\bar{I}_2\bar{I}_3\bar{I}_{23}' \times\bar{I}_1\bar{I}'F'F_1'\bar{I}_N J'K'\rangle. \quad \text{(A17)}$$

By noting the commutation properties and approximations previously discussed and by using the matrix elements tabulated in Condon and Shortley, we can reduce the above typical matrix element to the form

$$\mathfrak{M}=\frac{I_2\cdot I_1}{I(I+1)}\frac{\mathbf{F}_1\cdot\mathbf{I}}{F_1(F_1+1)} \times\langle\gamma F_1\bar{I}_N JK|\,\bar{I}_{Nz}F_{1z}|\gamma F_1\bar{I}_N JK'\rangle, \quad \text{(A18)}$$

where we write for the coefficient

$$(\bar{I}_2\bar{I}_3\bar{I}_{23}\bar{I}_1\bar{I}|\,\bar{I}_2|\,\bar{I}_2\bar{I}_3\bar{I}_{23}'\bar{I}_1\bar{I})$$

its value $I_2\cdot I/I(I+1)$. The reduction of the terms (10.1a), (10.3a), and (12.1) to the corresponding terms (13.1a), (13.3a) can readily be accomplished with the help of the vector model of Fig. 3. Term (10.5) has been shown elsewhere[1] to be expressible as (13.5). The operators of (10.1b), (10.3b), and (12.2) can be transformed to a common system of axes (see Fig. 4) by expressing them in terms of the linear combinations:

$$T_1^{(1)}=J_x+iJ_y, \quad T_0^{(1)}=J_z, \quad T_{-1}^{(1)}=J_x-iJ_y,$$

and by noting that for a rotation $R(0,0,\chi)$ about the common $z$ axis,

$$T_1'^{(1)}=e^{i\chi i}T_1^{(1)}, \quad T_0'^{(1)}=T_0^{(1)}, \quad T_{-1}'^{(1)}=e^{i\chi i}T_{-1}^{(0)}.$$

The result of such a transformation is

$$\begin{aligned}[(12.2)+(10.1b)+(10.3b)]&\\ \equiv -G_\rho=2\sigma(J_z\bar{I}_z+J_y\bar{I}_y)+\gamma J_z\bar{I}_z+2\epsilon(J_z\bar{I}_{1z}&\\ -J_y\bar{I}_{1y}-\tfrac{1}{2}J_x(\bar{I}_{2x}+\bar{I}_{3x})-\tfrac{1}{2}J_y(\bar{I}_{2y}+\bar{I}_{3y})&\\ -\sqrt{3}\epsilon[J_x(\bar{I}_{2y}-\bar{I}_{3y})+J_y(\bar{I}_{2x}-\bar{I}_{3x})]. \quad \text{(A19)}&\end{aligned}$$

By (A18),

$$(\bar{I}_\rho)_\nu=-\frac{(\bar{I}_\rho\cdot\bar{I})}{I(I+1)}\cdot\left(\frac{\mathbf{I}\cdot\mathbf{F}_1}{F_1(F_1+1)}\right) \times\left(\frac{\mathbf{F}_1\cdot\mathbf{J}}{J(J+1)}\right)J_\nu \quad \begin{matrix}\nu=x,\,y,\,z\\ \rho=1,\,2,\,3,\end{matrix} \quad \text{(A20)}$$

and thus substitution of (A20) into (A19) yields (13.1b) and (13.3b).

When substitutions of the type (A18) are made in 10.4 one obtains after some rearranging [(10.4)$\equiv G_d$].

$$\begin{aligned}\frac{G_d}{\mu_0^2 g_H g_M}=&\frac{(\mathbf{F}_1\cdot\mathbf{I})(\mathbf{F}_1\cdot\mathbf{I}_N)}{F_1(F_1+1)}\langle v|r^{-3}(1-\tfrac{3}{2}\sin^2\beta)|v\rangle\\ &+\frac{3\mathbf{F}_1\cdot\mathbf{I}}{F_1(F_1+1)}\Big[\langle v|r^{-3}(1-\tfrac{3}{2}\sin^2\beta)|v\rangle\bar{I}_{Nz}F_{1z}\\ &+\langle v|(8r^3)^{-1}\sin^2\beta|v\rangle\left(1+\frac{3(I_1^2-I_{23}^2)}{I(I+1)}\right)\\ &\times(\bar{I}_{Nz}F_{1z}-\bar{I}_{Ny}F_{1y})-\langle v|(\sqrt{3}/4r^3)\sin^2\beta|v\rangle\\ &\times\frac{(I_2-I_3)\cdot I}{I(I+1)}(\bar{I}_{Nz}F_{1y}+\bar{I}_{Ny}F_{1z})\Big]. \quad \text{(A21)}\end{aligned}$$

Recalling that $\mathbf{J}+\mathbf{I}_N=\mathbf{F}_1$ and making use of the vector model, one obtains

$$\begin{aligned}\bar{I}_{Nz}F_{1z}=&-\{\mathbf{I}_N\cdot\mathbf{J}/[J(J+1)]\}J_z^2\\ &-\tfrac{1}{3}(3\bar{I}_{Nz}^2-\bar{I}_N^2)-\tfrac{1}{3}\bar{I}_N^2,\\ (\bar{I}_{Nz}F_{1z}-\bar{I}_{Ny}F_{1y})=&-\{\mathbf{I}_N\cdot\mathbf{J}/[J(J+1)]\}\\ &\times(J_z^2-J_y^2)-(\bar{I}_{Nz}^2-\bar{I}_{Ny}^2), \quad \text{(A22)}\\ (\bar{I}_{Nz}F_{1y}+\bar{I}_{Ny}F_{1z})=&-\{\mathbf{I}_N\cdot\mathbf{J}/[J(J+1)]\}\\ &\times(J_zJ_y+J_yJ_z)-(\bar{I}_{Nz}\bar{I}_{Ny}+\bar{I}_{Ny}\bar{I}_{Nz}).\end{aligned}$$

The matrix elements of $(3I_{Nz}^2-I_N^2)$, $(\bar{I}_{Nz}^2-\bar{I}_{Ny}^2)$, and $(\bar{I}_{Nx}\bar{I}_{Ny}+\bar{I}_{Ny}\bar{I}_{Nx})$ transform under rotation as certain linear combinations of second-degree spherical harmonics and may therefore be written as:[27]

$$\text{(a)}\quad \langle \bar{I}_N F_1 JK|\bar{I}_{Nz}^2-\bar{I}_{Ny}^2|\bar{I}_N F_1 JK'\rangle = (\Omega_2(J,I_N)/J(J+1))\langle JK|J_z^2-J_y^2|JK'\rangle,$$

$$\text{(b)}\quad \langle \bar{I}_N F_1 JK|(\bar{I}_{Nx}\bar{I}_{Ny}+\bar{I}_{Ny}\bar{I}_{Nx})\bar{I}_N F_1 JK'\rangle = (\Omega_2(J,I_N)/J(J+1))\langle JK|J_xJ_y+J_yJ_x)JK'\rangle,$$

$$\text{(c)}\quad \langle \bar{I}_N F_1 JK|3\bar{I}_{Nz}^2-\bar{I}_N^2|\bar{I}_N F_1 JK'\rangle = (\Omega_2(J,I_N)/J(J+1))\langle JK|3J_z^2-J^2|JK'\rangle, \quad \text{(A23)}$$

where the factor of proportionality $(\Omega_2(J,I_N)/J(J+1))$ is the same for all matrix elements of this type. $\Omega_2(J,I_N)$ can most readily be evaluated from (A23c) with the help of matrix elements tabulated in Condon and Shortley.[18] One finds after considerable algebra the result given in Eq. (13). Substituting relations (A22) and (A23) into (10.4) one obtains Eq. (13.4) of the text. (Note that the signs of $I$, $I_N$ have been restored to their normal values and compensating changes in sign made in their coefficients.)

Finally the proportionality factors of the type (A18) can be evaluated from Condon and Shortley.[18] Thus

$$\left(1+\frac{3(I_1^2-I_{23}^2)}{I(I+1)}\right)=\begin{pmatrix}-4 & 0\\ 0 & 4\end{pmatrix},$$

$$\left(1-\frac{3I_{23}\cdot I}{I(I+1)}\right)=\begin{pmatrix}-1 & 0\\ 0 & 1\end{pmatrix},$$

$$\frac{(I_2-I_3)\cdot I}{I(I+1)}=\begin{pmatrix}0 & 2/\sqrt{3}\\ 2/\sqrt{3} & 0\end{pmatrix},$$

where the rows and columns are to be labeled by values of $I_{23}=1, 0$ in that order.

Elements of the type $\langle \bar{I}_N F_1 JK|J_z^2|\bar{I}_N F_1 JK'\rangle$ are evaluated in a similar fashion substituting $K$ for $M$ in the Condon and Shortley matrix elements and changing the sign of $i$, thus:[27]

$$\langle JK|J_z^2-J_y^2|JK\rangle=0,\quad \langle JK|J_xJ_y+J_yJ_x|JK\rangle=0,$$
$$\langle J-1|J_z^2-J_y^2|J+1\rangle=\tfrac{1}{2}J(J+1),$$
$$\langle J+1|J_xJ_y+J_yJ_x|J-1\rangle=\tfrac{1}{2}iJ(J+1),$$
$$\langle J+1|J_z^2-J_y^2|J-1\rangle=\tfrac{1}{2}J(J+1),$$
$$\langle J-1|J_xJ_y+J_yJ_x|J\,1\rangle=-\tfrac{1}{2}iJ(J+1).$$

[27] See reference 13, Chap. XXI, Sec. 5.

PHYSICAL REVIEW VOLUME 94, NUMBER 5 JUNE 1, 1954

# Sulfur Bonds and the Quadrupole Moments of O, S, and Se Isotopes*

G. R. Bird† and C. H. Townes
*Columbia University, New York, New York*

(Received February 25, 1954)

Quadrupole couplings of $S^{33}$ in HDS, $SO_2$ and $CH_3SH$ have been measured. These and previously measured quadrupole couplings of $S^{33}$ in OCS, HNCS, CS, and $S_8$ are examined to determine the nature of sulfur bonds and the best value for the $S^{33}$ quadrupole moment. $s-p$ hybridization is found to be common, but not universal, in sulfur bonds. The $S^{33}$ quadrupole moment is $-0.064\pm0.01\times10^{-24}$ cm². If O and Se bonds are assumed to be similar to those of S, the quadrupole moments of $O^{17}$ and $Se^{79}$ are $-0.004\times10^{-24}$ cm² and $0.9\times10^{-24}$ cm², respectively.

## INTRODUCTION

COUPLING of the nuclear quadrupole moments of the halogens in molecules has been extensively studied and interpreted in terms of bond structure, but attention given to quadrupole hyperfine structure of O, S, or Se has been rather small by comparison. We have attempted to study the quadrupole coupling of $S^{33}$ in a variety of bond structures in order to obtain information about the nature of sulfur bonds, and in addition to obtain improved values for the nuclear quadrupole moments of $S^{33}$, $S^{35}$, and isotopes of the chemically similar elements, O and Se.

The most abundant sulfur nuclei, $S^{32}$ and $S^{34}$, have zero spin and hence no quadrupole moment, but the less common $S^{33}$ (0.75 percent abundance) has a spin of 3/2 and a quadrupole moment. Quadrupole hyperfine structure due to this isotope was first observed by Townes and Geschwind[1] in OCS, and its quadrupole coupling constant in this molecule has been determined with increasing accuracy by several workers, White's value[2] $eqQ=-29.130\pm0.008$ Mc/sec being the most

* This research was supported in part by the Army Signal Corps jointly with the U. S. Office of Naval Research under a Signal Corps contract.

† Formerly National Research Council Postdoctoral Fellow at the Columbia Radiation Laboratory. Now at Department of Chemistry, The Rice Institute, Houston, Texas.

[1] C. H. Townes and S. Geschwind, Phys. Rev. 74, 626 (1948).

[2] R. L. White, Columbia Radiation Laboratory Quarterly Report, March 31, 1953, p. 21 (unpublished).

accurate. Townes and Dailey[3] have discussed the bond structure of OCS in terms of two reasonable configurations and set upper and lower limits of 100 Mc/sec and 50 Mc/sec on the coupling constant per unbalanced $p$ electron for $S^{33}$. A corresponding uncertainty applies to the determination of the quadrupole moment from this coupling constant.

Measurements of hyperfine structure due to $S^{33}$ in the molecules HDS, $SO_2$, and $CH_3SH$ are reported and discussed below. Dousmanis, Sanders, Townes, and Zeiger[4] have recently determined the quadrupole coupling constant of $S^{33}$ in HNCS. Mockler and Bird are reporting the coupling in CS in a separate work to be published soon. Dehmelt[5] has recently determined the coupling constant in solid rhombic sulfur by measuring the pure quadrupole resonance.

Quadrupole effects in these six molecules and in OCS allow fairly extensive intercomparison between different types of bonds.

### HDS (Partially Deuterated Hydrogen Sulfide)

The microwave spectrum of HDS has been analyzed by Hillger and Strandberg.[6] From their measurements the frequencies of the transitions $2_{2,0}\leftarrow 2_{2,1}$ and $4_{3,1}\leftarrow 4_{3,2}$ of $HDS^{32}$ were known to be about 11 258 and 10 831 Mc/sec, and the difficulty of locating and identifying asymmetric rotor transitions was eliminated. The sample of HDS was prepared by Dr. G. Silvey from natural sulfur and hydrogen containing 50 percent deuterium. Nine weak lines were observed over a range of 15 Mc/sec centered about the predicted frequency of the $2_{2,0}\leftarrow 2_{2,1}$ line and one of these was partially resolved to give the required total of ten lines. Four lines corresponding to $\Delta F=0$ transitions were observed within one Mc/sec of the predicted frequency of the $4_{3,1}\leftarrow 4_{3,2}$ line. In this case the $\Delta F=\pm 1$ components should be very much weaker than the observed $\Delta F=0$ components and hence were not observed. The frequencies of the two rotational transitions without hyperfine structure were computed from the measurements to be 11 259.10 Mc/sec and 10 831.12 Mc/sec, but these absolute frequencies are probably less precise than the coupling constants since only frequency differences were desired and no precautions were taken against inaccuracies in absolute frequencies due to time-delays in the measurements. The eight fully-resolved lines of the $2_{2,0}\leftarrow 2_{2,1}$ transition were all measured at least twice and fitted by least squares to a first order quadrupole calculation with a rms deviation of 0.07 Mc/sec. Most of this deviation probably arises from distortion of the various lines by Stark components of adjacent lines, an effect which could not be completely eliminated.

Since closed expressions for $E(\kappa)$, the asymmetric rotor reduced energy, are available for all of the levels involved in these transitions, the expression given by Bragg and Golden[7] was more convenient than the alternative expression involving asymmetric rotor line strengths. That is, $W_Q=eQ\langle V_{22}\rangle_{Av}f(I,J,F)$, where $f(I,J,F)$ is Casimir's function, and

$$\langle V_{22}\rangle_{Av}=\frac{1}{J(J+1)}\left\{\frac{\partial^2 V}{\partial a^2}[J(J+1)+E(\kappa)-\kappa+1]+\frac{2\partial^2 V}{\partial b^2}\frac{\partial E}{\partial \kappa}+\frac{\partial^2 V}{\partial c^2}[J(J+1)-E(\kappa)+\kappa-1]\right\}.$$

Values of $x$ were obtained for $HDS^{32}$ and $HDS^{34}$ by rigid rotor calculations on the frequencies for the transitions $1_{1,0}\leftarrow 1_{1,1}$ and $2_{2,0}\leftarrow 2_{2,1}$ given by Hillger and Strandberg,[6] and these were simply averaged to give a value accurate enough for the calculations on $HDS^{33}$. The least square fit gave values for $eQ\langle V_{zz}\rangle_{Av}$ of $-23.4_3$ and $-31.1_6$ Mc/sec for the initial and final states respectively. Because of the mathematical symmetry of a $\Delta J=0$ transition, an equally good fit could be obtained by reversing the order and signs of these numbers, but this led to unreasonable values of the molecular coupling constants and was rejected. The coupling constants obtained are $eQ(\partial^2 V/\partial a^2)=-23.4_3$ Mc/sec and $eQ(\partial^2 V/\partial b^2)=-17.5_4$ Mc/sec. As a check on the accuracy of measurement, assignment, and calculation, these constants were used to calculate the fine structure of the $4_{3,1}\leftarrow 4_{3,2}$ transition. The calculated value of $-3.22$ Mc/sec compared favorably with the measured value of $-3.18$ Mc/sec for the single constant required to determine the splitting of the $\Delta F=0$ lines, with the difference representing an error of 0.01 Mc/sec in the splitting of the two strongest lines.

Before a final evaluation of this data could be made, it was necessary to carry out a rotation from the inertial axes of HDS to the electrical symmetry axes, which presumably coincide with the H−D direction and the bisector of the HSD angle. The angle of rotation must be calculated from molecular parameters, and these parameters may not simply be taken as identical with the infrared parameters of $H_2S$, since zero-point vibrations in such a light molecule will certainly produce some change in the effective structure of the molecule with isotopic substitution. For many other purposes these changes are negligible, but in this case the angle of rotation and the final coupling constants depend rather critically on the bond angle.

Angles of rotation have been calculated for several structures by Mr. George Dousmanis. One of these was obtained by taking Hillger and Strandberg's[6] frequencies for the $HDS^{32}$ transitions $1_{1,0}\leftarrow 1_{1,1}$ and $2_{2,0}\leftarrow 2_{2,1}$ and their calculated value of the inertial defect and determining the structure from $A$ and $B$

[3] C. H. Townes and B. P. Dailey, J. Chem. Phys. **17**, 782 (1949).
[4] Dousmanis, Sanders, Townes, and Zeiger, Columbia Radiation Laboratory Quarterly Report, March 31, 1953 (unpublished).
[5] H. Dehmelt, Phys. Rev. **91**, 313 (1953).
[6] R. E. Hillger and M. W. P. Strandberg, Phys. Rev. **83**, 575 (1951).
[7] J. K. Bragg and S. Golden, Phys. Rev. **75**, 735 (1949).

on a rigid rotor basis. This led to a bond angle of 93°18′ and bond distances (assumed equal) of 1.3455A. The angles of rotation calculated from these parameters were 36°29′ for $HDS^{32}$ and 36°51′ for $HDS^{33}$. In another structure the S−D distance from the first structure was shortened by 0.01A to test the dependence of rotation angle on such an inequality in effective bond distances as might be caused by zero-point vibrations. This changed the angle of rotation from 36°51′ to 36°24′ for $HDS^{33}$.

The coupling constants calculated from the first structure are

$$eQ(\partial^2V/\partial a'^2) = -31.0 \text{ Mc/sec},$$
$$eQ(\partial^2V/\partial b'^2) = -10.0 \text{ Mc/sec}.$$

Here $a'$ refers to the H−D direction and $b'$ to the bisector of the HSD angle. Those calculated from the second differ by about one Mc/sec from these values. The sum of the two constants is independent of the angle of rotation.

Essentially the above results were obtained some time ago and sent privately to Dehmelt, who has already commented[5] on the significance of the large difference between $eQ(\partial^2V/\partial a'^2)$ and $eQ(\partial^2V/\partial b'^2)$. Burrus and Gordy[6] have confirmed the experimental result by obtaining the similar quantities for $H_2S^{33}$ and also have discussed its significance. Their values for $H_2S$ are $eQ(\partial^2V/\partial a'^2) = -32.0$ Mc/sec and $eQ(\partial^2V/\partial b'^2) = -8.0$ Mc/sec, with an H−S−H angle of 92°6′. It is not clear whether the small differences between results for $H_2S$ and HDS are due to experimental uncertainties or to changes in the effects of zero-point vibrations. A change in bond angle as large as 1° is not unreasonable for substitution of D in place of H.

The importance of the observed difference between $eQ(\partial^2V/\partial a'^2)$ and $eQ(\partial^2V/\partial b'^2)$ lies in the fact that if $H_2S$ involved nearly pure $p$ bonds, as has often been assumed because the bond angle is so near to 90°, these two constants must necessarily be equal. The three $p$ orbitals would not be equally filled since the orbital perpendicular to the molecular plane would be occupied by two nonbonding electrons, which would give a field gradient symmetric about this direction and equivalent to that produced by one atomic $p$ electron. This is not as poor an approximation as it might seem since the observed difference between $eQ(\partial^2V/\partial a'^2)$ and $eQ(\partial^2V/\partial b'^2)$ may be accounted for by a small amount of $s$ hybridization for each bond. Assuming 4 percent ionic character for the S—H bond, and that the bond is an $s-p$ hybrid, one obtains from the above coupling constants a value 14.6 percent for the $s$-hybridization and a quadrupole coupling constant per pure $p$ bond of 50.0 Mc/sec. The rather small amount of ionic character assumed here has little effect on the quadrupole coupling and has been omitted from Table II for the sake of simplicity.

[6] C. A. Burrus, Jr., and W. Gordy, Phys. Rev. **92**, 274 (1953).

The difference between the observed HSD angle of 93°18′ and the angle of 100° required by the indicated $s-p$ hybridization is somewhat puzzling. Dehmelt[5] has suggested the possibility of $d$ hybridization, which might modify the angle. If this explanation is correct, the coupling constant per $p$ electron given above is too small by 10 to 20 percent. An alternative explanation might be that the localization of a bond along the internuclear line is a poor approximation for very light molecules. This idea is given some support by the difficulties in fitting the $NH_3$ coupling constant with a hybridization scheme determined by the bond angles, and by the fact that arsine and stibine also have HXH angles very nearly 90° but quadrupole coupling constants which require a sizeable degree of $s-p$ hybridization.[9,10] In contrast to arsine and stibine, the heavier molecules $AsF_3$ and $SbCl_3$ have bond angles which agree with the amount of hybridization indicated by their quadrupole coupling constants.[10]

## Sulfur Dioxide

Sulfur dioxide has been the subject of several investigations.[11] No transitions of the less abundant isotopic species of sulfur were identified in any of these researches, and this proved to be a major hindrance to the present work, since weak lines had to be found and identified.

The frequencies of the isotopic lines were calculated from Crable and Smith's frequencies for the $S^{32}O_2$ transitions $1_{1,1}\leftarrow 0_{0,0}$, $2_{1,1}\leftarrow 2_{0,2}$, and $4_{0,4}\leftarrow 3_{1,2}$ and the rigid rotor approximation. This calculation was performed with fifth power series in $\delta$, the prolate asymmetry parameter, and the following approximations were used:

$$I_B^{32} = I_B^{33}, \quad \Delta^{32} = \Delta^{33},$$
$$I_A^{32}\left(\frac{M_{S^{33}}}{M_{S^{32}}}\right)\left(\frac{M_{S^{33}}+2M_{O^{16}}}{M_{S^{32}}+2M_{O^{16}}}\right) = I_A^{33}.$$

The surprising feature of this calculation was the close agreement with the frequencies later measured, most of the difference being accounted for by the rigid rotor approximation used to calculate the moments of the principal isotopic species. The calculated and observed frequencies are given in Table I. Since the desired lines are weak, and the $J$ values fairly high, only the four hyperfine structure lines having $\Delta F = \Delta J$ had observable intensities when $SO_2$ with natural abundances was examined. Casimir's function has the peculiarity that for any value of $J$ and a spin of 3/2, $f(3/2, J, J+3/2) - f(3/2, J, J+1/2) = f(3/2, J, J-3/2) - f(3/2, J, J-1/2) = 1/4$. When only $\Delta F = \Delta J$ transitions are observed, this relation can prove whether or not a given

[9] C. C. Loomis and M. W. P. Strandberg, Phys. Rev. **81**, 798 (1951).
[10] P. Kisliuk, J. Chem. Phys. **22**, 86 (1954).
[11] Dailey, Golden, and Wilson, Phys. Rev. **72**, 871 (1947); M. H. Sirvetz, J. Chem. Phys. **19**, 938 (1951); G. F. Crable and W. V. Smith, J. Chem. Phys. **19**, 676 (1951).

TABLE I. Frequencies of $SO_2$ transitions.[a]

| Line | Observed frequency Mc/sec | Calculated frequency Mc/sec |
|---|---|---|
| $S^{32}O_2$ $4_{0,4}\leftarrow3_{1,3}$ | (29 321.22) | (29 321.2) |
| $S^{32}O_2$ $4_{0,4}\leftarrow3_{1,3}$ | 30 194.09 | 30 191.3 |
| $S^{34}O_2$ $4_{0,4}\leftarrow3_{1,3}$ | 31 011.19 | 31 006.4 |
| $S^{32}O_2$ $5_{2,4}\leftarrow6_{1,5}$ | (23 414.33) | 23 435.2 |
| $S^{32}O_2$ $5_{2,4}\leftarrow6_{1,5}$ | 20 605.97 | 20 632.1 |
| $S^{34}O_2$ $5_{2,4}\leftarrow6_{1,5}$ | 17 970.42 | 18 001.0 |

[a] ( ) indicates an observation by Crable and Smith (reference 11).

group of lines is a quadrupole pattern arising from a nucleus of spin 3/2, but prevents the identification of the $J$ values of the pattern from spacings observed. It also requires careful observation of the relative intensities of such a pattern to determine the assignment of $F$ values to the lines.

The four lines of the $4_{0,4}\leftarrow3_{1,3}$ transition centered at 30 194.09 Mc/sec were observed at room temperature and at $-70°$C. With these and all other frequency measurements on $SO_2$, slow triangular sweeps or stabilization were used to eliminate time delays in the frequency and line presentation circuits, since it was felt that other investigators might make use of the absolute frequencies so measured. The combination rule just mentioned was applied as a test of accuracy, and discrepancies not larger than about 0.05 Mc/sec were observed among the four frequencies thus compared. Here, too, the principal source of inaccuracy was probably distortion of the lines by Stark components from neighbors. The four lines of the $5_{2,4}\leftarrow6_{1,5}$ transition were observed at room temperature and at $-70°$C, and assignments based on calculations from the above transition verified by intensities and spacings. One of the four lines nearly coincided with a multiple of 30 Mc/sec and could not be measured accurately with the frequency standard available; for this reason the combination rule could not be applied.

Calculation of the coupling constants was performed with the expression given above. The earlier use of the $\delta$ series proved to be particularly helpful, since the necessary reduced energy terms $E(\kappa)$ and $\partial E/d\kappa$ could be obtained by differentiating the series and using the relationships $E(\kappa)=E(\delta)$ and $dE/d\kappa=\frac{1}{2}dE/d\delta$. The value of $\delta$ was obtained from the calculation of moments of inertia by the approximations already given. Since it predicted the location of the observed transitions satisfactorily, it was considered good enough for the less precise quadrupole data. This procedure is good only for small values of $\delta$ since the $dE/d\delta$ series will converge less rapidly than the original $E(\delta)$ series.

The calculated values of the coupling constants obtained from the $4_{0,4}\leftarrow3_{1,3}$ transition are as follows:

$$eQ(\partial^2V/\partial a^2)=-1.7\pm0.2 \text{ Mc/sec},$$
$$eQ(\partial^2V/\partial b^2)=+25.71\pm0.03 \text{ Mc/sec}.$$

The uncertainties given represent the average deviation of calculations based on different frequency measurements.

The electronic structure of $SO_2$ has been considered as mainly consisting of the two identical resonant forms,

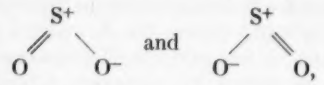


with $sp^2$ hybridization accounting for the observed bond angle of nearly 120°. The quadrupole coupling constants for such a structure would be $eQ(\partial^2V/\partial a^2)=-\frac{1}{6}eq_p{}^+Q$ and $eQ(\partial^2V/\partial b^2)=\frac{1}{3}eq_p{}^+Q$, where $eq_p{}^+Q$ is the coupling constant for one $p$ electron in $S^+$, or about 70 Mc/sec. This structure gives the correct signs for the coupling constants, but not precisely correct values.

In order to obtain the measured coupling constants, it is necessary to modify the above structure by decreasing the probability for an electron to be in the $p$ orbital about the S atom which is perpendicular to the plane of the molecule. The structure,

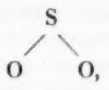


is not favorable, since it puts two electrons in this $p$ orbit. Some importance for the structure

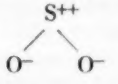


would give the correct effect as would also $d$-hybridization of the $\pi$ component of the double bond in the structure

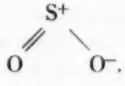


Assuming that the structure of primary importance is

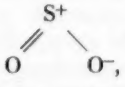


and that the probability for the electron being removed from the $\pi$ orbital by some mechanism such as those mentioned is $\epsilon$, one can obtain $\epsilon$ and $eq_pQ$ from the measured coupling constants. They are $\epsilon=0.27$ and $eq_pQ=55$ Mc/sec in reasonable agreement with the result from HDS.

### Methyl Mercaptan

Methyl mercaptan has been subjected to a number of microwave investigations, the most recent and exhaustive being that of Solimene and Dailey.[12] These authors kindly provided detailed information on their work and a sample of $CH_3SH$ with sulfur in natural abundance. They had identified a pair of lines at

[12] N. Solimene and B. P. Dailey, Phys. Rev. 91, 464 (1953).

25 291.87 Mc/sec and 25 290.92 Mev/sec as the transition $1_{0,1}\leftarrow 0_{0,0}$ (the line is double as a result of internal torsion) of the principal isotopic species, and a line at 25 879.08 Mc/sec as the unresolved doublet corresponding to the same transition for the species $CH_3S^{34}H$. With the high-sensitivity spectrograph described by Fletcher and Hardy[13] this line was easily resolved into a corresponding doublet (24 879.83 Mc/sec and 24 878.91 Mc/sec) confirming their assignment. Midway between these pairs of lines a group of three very weak doublets was found with appropriate doublet and quadrupole spacings. The central frequencies of the two groups of three lines were 25 079.64 Mc/sec and 25 078.70 Mc/sec. Only one of the two asymmetric rotor coupling constants may be obtained from this particular transition; it is $eQ(\partial^2V/\partial a^2)=-27.57\pm0.05$ Mc/sec. No other transitions of normal methyl mercaptan have been identified except for a $J=2\leftarrow1$ transition at about twice the frequency of the $J=1\leftarrow0$ transition. A search for the corresponding isotopic transitions was not attempted because of the difficulty of looking for a group of weak lines in a very dense spectrum.

The $a$ axis in methyl mercaptan coincides quite closely with the C−S direction, being tipped only 2.5° out of this direction by the hydrogen bonded to the sulfur.[12] The C−S−H bond angle is 99°26′ suggesting an $s$ hybridization of about 14 percent for the $p$ bonds as was found in HDS. If the electric fields surrounding the S in methyl mercaptan were similar to those in HDS, one would expect a value $eQ(\partial^2V/\partial a^2)=-23.2$ Mc/sec, which is not far different from the observed value of −27.6 Mc/sec. A measurement of the coupling constant $eQ(\partial^2V/\partial b^2)$ would permit a more complete interpretation of the sulfur bonds in this molecule.

## $S_8$, CS, and HNCS

Dehmelt[5] has observed the pure quadrupole resonance of $S^{33}$ in solid rhombic sulfur ($S_8$) from which a quadrupole coupling constant of ±45.8 Mc/sec is obtained. The coupling constant for a pure $p$ electron can be deduced from this if the amount of hybridization can be satisfactorily determined. Dehmelt argues against as much as 21 percent hybridization, which is indicated by the angle, and assumes 10 percent $s-p$ hybridization so that a coupling constant per $p$ electron of 50.4 Mc/sec is obtained. Dehmelt's argument against larger hybridization is based, however, on multiplying the total bond energy by a rough estimate of the percentage increase in overlap due to hybridization and comparing this product with the energy needed to promote 21 percent of one electron from an atomic $3s$ to a $3p$ orbit. The total bond energy of course involves repulsive interactions as well as overlap energies, and only a considerably more refined calculation would give good information about the hybridization. If 21 percent $s$ hybridization is assumed, the coupling constant per $p$ electron would be 58.0 Mc/sec rather than the 50.4 Mc/sec obtained by Dehmelt.

That $s$ hybridization in sulfur bonds can be large is strikingly demonstrated by the quadrupole coupling of $S^{33}$ in CS reported by Mockler and Bird.[14] In this case the most reasonable way of obtaining the correct sign for the coupling constant is to assume that the structure $C^-\equiv S^+$ is important and that the $\sigma$ component of this bond involves considerable $3s$ character. It is possible to obtain the positive coupling constant of CS by assuming the structure $C^-\equiv S^+$ to have $d$ hybridization in the $\pi$ orbitals rather than $s$ hybridization in the $\sigma$ orbital. However, there appears no reason why $d$ hybridization of the $\pi$ orbitals should not occur also in OCS, where it would be inconsistent with the measured coupling constant for $S^{33}$.

The various possible electronic structures for OCS were discussed some time ago by Townes and Dailey.[3] At that time, it was not clear whether or not the $\sigma$ orbital was hybridized, and hence structures with or without $s$ hybridization were suggested as alternatives. It now appears that if the coupling constant of $S^{33}$ in OCS is to be made consistent with those of the above molecules, very little $s$ hybridization can be allowed. This is in contrast to the case of CS, where $s$ hybridization of the $\sigma$ orbital seems essential. The difference between the OCS and CS cases is presumably connected with the difference between the carbon orbitals which are available. It illustrates the hazards involved in the simplifying assumption of an invariable amount of hybridization.

The coupling constant for HNCS is −27.5 Mc/sec which is very nearly equal to that for OCS, indicating the similarity of the sulfur bonds in the two cases. It is interesting that the small difference between the coupling constants in HNCS and OCS is fairly well predicted, however, from the variations in multiple bonding obtained by using the measured internuclear distances. This is shown in Table II.

## Summary of S Bonds

The most reasonable structures which fit all the measured quadrupole couplings of $S^{33}$ are listed in Table II. The quadrupole coupling per $p$ electron for atomic $S^{33}$ is assumed to be −55 Mc/sec for these cases. The sign of this coupling constant corresponds to a negative nuclear quadrupole moment for $S^{33}$. Most weight in determining the coupling constant has been given to hydrogen sulfide, $S_8$, and $SO_2$, in decreasing order of importance, since their structures seem to be most simply and uniquely interpretable. It is thought

[13] P. Fletcher and W. A. Hardy, Columbia Radiation Laboratory Quarterly Report, March 31, 1953, p. 20 (unpublished).

[14] R. Mockler and G. Bird (to be published).

TABLE II. Probable bond structures of molecules containing S and comparison between experimentally measured quadrupole coupling constants of $S^{33}$ and those predicted from the structures. The coupling constant per $p$ electron is assumed throughout to be $-55$ Mc/sec. Percentage importances of multiply bonded structures are determined from internuclear distances.

| Molecule | Structure | Importance (percent) | Hybridization of sulfur bonds (percent) | Predicted coupling constants (Mc) | Measured coupling constants (Mc) |
|---|---|---|---|---|---|
| $H_2S$ |  | 100 | 15 $s$ | $eQ(\partial^2V/\partial a'^2)=-34.2$ | $-31.0$ |
| (HDS) | | | | $eQ(\partial^2V/\partial b'^2)=-10.5$ | $-10.0$ |
| $CH_3SH$ | $H_3C-S-H$ | 100 | 15 $s$ | $eQ(\partial^2V/\partial a^2)=-24.4$ | $-24.6$ |
| $S_8$ | | 100 | 21 $s$ | $eQ(\partial^2V/\partial z^2)=-43.5$ | $\pm45.8$ |
| $SO_2$ | | 100 | 33 $s$ for $\sigma$ bonds See text for discussion of $\pi$ bond | $eQ(\partial^2V/\partial a^2)=-1.9$ | $\pm1.7$ |
| | | | | $eQ(\partial^2V/\partial b^2)=28.2$ | $+25.7$ |
| CS | $C=S$<br>$C^-\equiv S^+$ | 60<br>40 | 50 $s$ for $\sigma$ bond | $eQ(\partial^2V/\partial z^2)=13.8$ | $+12.84$ |
| OCS | $O=C=S$<br>$O^+\equiv C-S^-$<br>$O^-C\equiv S^+$ | 58<br>28<br>14 | none | $eQ(\partial^2V/\partial z^2)=-28.3$ | $-29.13$ |
| HNCS | $H-N=C=S$<br>$H-N^-C\equiv S^+$<br>$H-N^+\equiv C-S^-$ | 63<br>19<br>18 | none | $eQ(\partial^2V/\partial z^2)=-25.2$ | $-27.5$ |

that the coupling constant per $p$ electron is accurate to about 15 percent.

### Quadrupole Moments of $O^{17}$, $S^{33}$, $S^{35}$, and $Se^{79}$

The quadrupole coupling $eQ(\partial^2V/\partial z^2)$ per $p$ electron determined above may be used to evaluate the quadrupole moment of $S^{33}$ if the quantity $\partial^2V/\partial z^2=\frac{4}{5}e/\langle r^3\rangle_{Av}$ is known. By using the value of $\langle 1/r^3\rangle_{Av}$ given by Barnes and Smith,[15] we obtain a value $Q_{S^{33}}=-0.058\times10^{-24}$ cm². This should be further corrected by a factor of about 1.10 to allow for screening effects,[16] so that the corrected value is $Q_{S^{33}}=-0.064\times10^{-24}$ cm². This may be compared with the original value $-0.05\times10^{-24}$ given by Townes and Geschwind[1] and the very recent values $0.05\times10^{-24}$ and $0.06\times10^{-24}$ given by Dehmelt[5] and by Burrus and Gordy,[8] respectively. Since the ratio of the $S^{35}$ moment to that of $S^{33}$ is $-0.695$,[17] the $S^{35}$ moment is then $Q_{S^{35}}=0.045\times10^{-24}$ cm².

The quadrupole coupling constants of $O^{17}$ and $Se^{79}$ have been measured in OCS and OCSe.[18,19] Although the oxygen and selenium bonds are certainly not precisely like those of S, they may be assumed to be reasonably similar in the molecules OCS and OCSe. Previous evaluation of $Q$ for $O^{17}$ and $Se^{79}$ can hence be improved as a result of our more precise knowledge of the S bonds in OCS. Assuming that the structure of OCS is as given in Table II, that the oxygen bonds, like those of S, are not hybridized in this molecule, and using the measured[18] coupling constant of $O^{17}$ in OCS, the quadrupole coupling constant per $p$ electron for $O^{17}$ is $-3.30$ Mc/sec. Assuming that the bond structure of OCSe is similar to that of OCS, and using the measured coupling constant for $Se^{79}$, the quadrupole coupling per $p$ electron for $Se^{79}$ is 1430 Mc/sec. Using values of $\langle 1/r^3\rangle_{Av}$ from Barnes and Smith,[15] and applying corrections of 10 percent for screening,[16] one obtains the nuclear quadrupole moments $Q_{O^{17}}=-0.004\times10^{-24}$ cm² and $Q_{Se^{79}}=0.9\times10^{-24}$ cm².

[15] R. G. Barnes and W. V. Smith, Phys. Rev. **93**, 95 (1954).
[16] R. Sternheimer, Phys. Rev. **84**, 244 (1951).
[17] Cohen, Koski, and Wentink, Phys. Rev. **81**, 948 (1951).
[18] Geschwind, Gunther-Mohr, and Silvey, Phys. Rev. **85**, 474 (1952).
[19] Hardy, Silvey, and Townes, Phys. Rev. **85**, 494 (1952).

# Proton-Proton Scattering Near the Interference Minimum*

DANIEL I. COOPER,† DAVID H. FRISCH, AND ROBERT L. ZIMMERMAN
*Department of Physics and Laboratory for Nuclear Science, Massachusetts Institute of Technology, Cambridge, Massachusetts*

(Received Februrary 17, 1954)

The differential proton-proton scattering cross section at 45° in the laboratory system has been measured in the energy region 350–420 kev. The interference minimum occurs at 383.9±1.5 kev. The minimum in the ratio to the Mott cross section thus occurs at 382.8±1.5 kev, and at the latter energy the $S$-wave phase shift is $\delta_0=0.2527\pm0.0011$ radians, in good agreement with the most recent data in this energy region. The combination of our point with the Wisconsin data alone agrees with the previous analysis of data from a wide range of energies.

## I. INTRODUCTION

ONE of the time-honored[1] purposes of proton-proton scattering measurements[2] has been to determine the nuclear $S$-wave phase shift as a function of energy. Such measurements give a detailed description of the force field between two protons with antiparallel spins and no relative angular momentum.

It has been emphasized[3] that two parameters, the effective range and the scattering length, are sufficient alone to predict remarkably well the $S$-wave phase shift over a large energy range. Unfortunately, force fields derived from static potentials of widely different functional dependence on the separation between the protons, or even velocity-dependent forces, may well have the same best two-parameter fit to the low-energy data. The first information about the "shape" is given only when a third parameter becomes necessary to fit the data.

In order to choose, for example, between Yukawa potentials with and without a repulsive core the energy range of experiments must be wide and the low-energy data must be particularly accurate. High-energy measurements give large effects but are more difficult to interpret because they may have in them appreciable amounts of higher partial waves than $S$ wave, and because a comparison with low-energy data relies heavily on the assumption of a known velocity-dependence of the forces. On the other hand, the accuracy required in low-energy measurements necessitates the most painstaking work,[4] and the interpretation may still involve the velocity-dependence of the forces.

Proton-proton scattering experiments are particularly difficult at energies appreciably below 1 Mev, where the scattering and stopping powers of thin windows and of the scattering gas are relatively large. Because there is no bound state, because no experiments at thermal energies are possible, and because total cross section measurements would give negligibly little nuclear information even if possible technically, the measurements at energies below 1 Mev, as at higher energies, must be differential scattering experiments. Such experiments necessitate in general absolute measurements of the energy and numbers of incident protons, density, and volume of target protons, mean angle and solid angle subtended by the detector of scattered protons, and efficiency of the detector.

In practice accurate phase shifts may be obtained in this energy region by measuring[5] the relative yield of scattered protons as a function of angle. This requires absolute measurements of only energy and mean angle of scattering, but also requires considerable knowledge of the relative efficiency of the detector as a function of scattered proton energy, since the energy changes rapidly with angle.

There is in addition one set of exceptional energies and angles at which it is necessary to have absolute values for only the energy and mean angle, without an angular survey, and to correct if necessary for the change in the relative efficiency of detector and current monitor over a narrow energy interval only. These are combinations of energy and angle at which the repulsive electrostatic force[6] cancels out a part or all of the effect of the attractive $S$-wave nuclear force.[7] The destructive interference is most marked at an angle of 90° in the cm system. The energy of this minimum is determined in the present experiment by studying the relative

* Supported by the joint program of the U. S. Office of Naval Research and the U. S. Atomic Energy Commission.

† Now at Bell Telephone Laboratories, Murray Hill, New Jersey.

[1] Breit, Thaxton, and Eisenbud, Phys. Rev. **55**, 1018 (1939).

[2] Herb, Kerst, Parkinson, and Plain, Phys. Rev. **55**, 998 (1939).

[3] L. Landau and J. Smorodinsky, J. Phys. (U.S.S.R.) **8**, 154 (1944); Julian Schwinger, Phys. Rev. **72**, 742 (1947); H. A. Bethe, Phys. Rev. **76**, 38 (1949); and J. D. Jackson and J. M. Blatt, Revs. Modern Phys. **22**, 77 (1950).

[4] Worthington, McGruer, and Findley, Phys. Rev. **90**, 899 (1953).

[5] Yovits, Smith, Hull, Bengston, and Breit, Phys. Rev. **85**, 540 (1952) survey and interpret all the data and quote unpublished results of a thorough investigation by Heydenburg and Little in the low-energy regions.

[6] The dipole-dipole magnetic interaction has been treated as a perturbation on the nuclear interaction by J. Schwinger, Phys. Rev. **78**, 135 (1950).

[7] A rough optical analog to this experiment is the following: A spherically symmetric cloud of free electrons, of known density as a function of radius, is irradiated by light of wavelength comparable with the mean radius of the charge distribution. The scattered light is observed at a distant point at some fixed angle. Now a very small dielectric ball of scattering power comparable to that of the charge cloud is introduced at its center. The wavelength of the light is varied until the scattered intensity is a minimum at the angle of observation. The $S$-wave phase shift by the ball at one wavelength, and hence a single measure of the scattering properties of the dielectric ball, is thus determined.

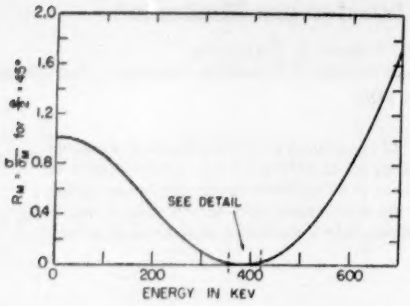


FIG. 1. Ratio of proton-proton cross section to Mott cross section at 45° laboratory angle.

yield of scattered protons at 90° c.m. (45° lab) as a function of energy from approximately 350 to 420 kev.

The laboratory cross section at 45° in the 0 to 1-Mev region may be predicted from the best fit to the combined data at higher energies.[5] For simplicity we chose to compute the cross section from the two-parameter ("shape independent") fit to the latest Wisconsin data[4] only. The quantity plotted in Fig. 1 is actually the ratio of the $p$-$p$ cross section computed in this way to the Mott cross section for protons with nothing but a pure Coulomb force between them. To get the differential cross section in millibarns per steradian in the laboratory, the ordinate in Fig. 1 must be multiplied by $20.73/E^2$, where $E$ is the bombarding energy in Mev.

An accurate determination of the cross-section minimum is not as difficult as it appears from Fig. 1. Plotted on a more appropriate scale in Fig. 2, the detail of the laboratory cross section shows a sharp minimum. We were preparing to do an accurate absolute cross section measurement until we observed experimentally this rapid variation of cross section with energy.

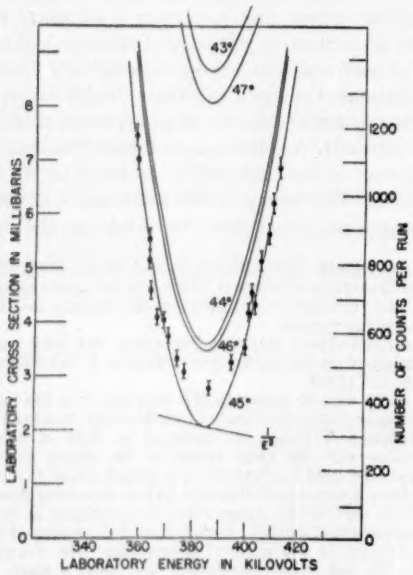


FIG. 2. Detailed proton-proton cross section at laboratory angles near 45°.

An order of magnitude estimate of the inaccuracies in the experiment and in its interpretation may be given as follows: At the 45° minimum the nuclear phase shift is approximately equal to $e^2/hv$, where $v$ is the relative velocity of the two protons at the energy of the minimum. We determined this energy to be $383.9\pm1.5$ kev, i.e., with 0.4 percent accuracy in $v^2$. Thus the nuclear phase shift at the minimum is obtained to about 0.2 percent. The 2- to 4-Mev data give phase shifts accurate at those energies to the order of 0.1 percent. When these data are used to predict the phase shift expected at the minimum the differences due to choice between popular static potentials are of the order of only a few tenths of a percent. A slightly velocity dependent force field—for example a nuclear "potential" the apparent depth of which changes by $\Delta v^2/c^2$ on going from one velocity to another—will also give comparable effects of a few tenths of a percent in phase shift in going over this energy range.

## II. EXPERIMENTAL DETAILS

### A. Machine

The proton beam was provided by a pressurized Van De Graaff generator[8] built with this experiment in mind. The beam from the radio-frequency ion source was focused in the conventional way and analyzed outside the machine by deflection through about 15° using a permanent magnet with an adjustable flux path to vary the magnetic field. Additional focusing of the mass-1 beam alone by an electrostatic alternating-gradient lens provided up to 5 microamperes through the collimator and to the scattering chamber (Fig. 3).

Voltage stabilization was provided by corona control operating on a signal from overlapping slits placed in the deflected mass-2 beam.

### B. Scattering Chamber

The fixed-angle scattering chamber was designed as small as possible to keep the path length of incident and scattered protons to a minimum in the scattering gas. Differential pumping was used at the beam entrance to give as little stopping power as possible in the entrance collimators. The counters were operated using the purified hydrogen scattering gas at the scattering chamber pressure with no windows to impede the scattered protons.

The proton beam entered the scattering chamber through a series of collimators which also served as impedances for gas flow in the differential pumping

[8] Cooper, Frisch, Storrs, and Strumski, Phys. Rev. **79**, 708 (1950). A letter describing the hydrogen supply for the ion source and the strong focusing electrostatic lens is being submitted to *Review of Scientific Instruments*.

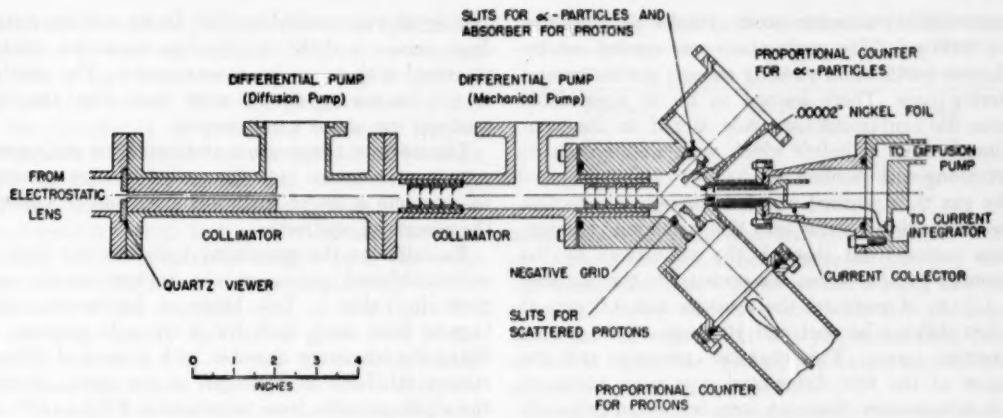


FIG. 3. Scattering chamber.

system. The first collimator was a brass tube 0.125 in. in diameter and four inches long. The next two consisted of a series of 0.040-in. holes in steel disks less than 0.001 in. thick at the inside edge, spaced $\frac{1}{4}$ in. apart. The angular spread thus defined was $\pm 0.5°$ about the central axis, or a maximum difference of angles of 1.0°. That there was no detrimental degradation of the energy of the protons by the walls of the collimator was indicated by the good functional form of the observed minimum in the $p$-$p$ cross section.

The current collector cup was kept at ground potential with a magnetic field to prevent secondary electrons from leaving the cup and a negative grid (a ring) to prevent secondary electrons from the nickel foil from entering the cup. The charge collected was measured with an electronic current integrator. By observing the Rutherford scattering of protons from argon, the rate and energy dependence of the current collecting system and of effects from the varying chamber pressure could be studied. Also in this way the correct value for the magnetic field and shielding voltage was determined.

The geometry was such that one could count the protons scattered through an angle of 45° on either side of the beam in each of two perpendicular planes. Coincidences between the two protons emerging from a single scattering were thus possible in each plane, and were used at first to check the identification by pulse height of the pulses coming from the counter.

Slits were provided in front of each of the counters such that only protons scattered through a narrow range of angles centered on 45° could enter. The first slit was located 0.625 in. from the beam along the line of the scattered protons; the second slit was 0.625 in. beyond the first. Typical slit dimensions were 0.012 in. × 0.200 in. and 0.018 in. × 0.200 in., respectively. There were no foils at this point; the counters operated in the scattering chamber gas at the scattering chamber pressure. The counters were especially designed for this (see Fig. 4); the center wire was $\frac{1}{8}$-inch drill rod 12 inches long cantilevered from a large Kovar-glass lead through and joined smoothly at the free end to a $\frac{3}{8}$-inch diameter rounded section. The operating voltage was in the vicinity of 1200 volts. When running the experiment with pure $H_2$ at about 1.5-cm Hg, typical pulses were 15 times noise with a pulse-height distribution that at best had a width at half-maximum about $\frac{1}{3}$ the most probable pulse height. The counters were adequately proportional so that the protons scattered from protons could be separated from protons scattered by heavier nuclei.

The counter output was amplified by a Model 100 amplifier and the pulses recorded on a 10-channel pulse-height analyzer in parallel with integral scalers Model 210. The availability of the 10-channel analyzer was of a far greater importance than would be indicated merely by the large statistical gain it gave over integral or even single differential channel analyzers.

### C. Gas Handling and Purification

At its minimum the 45° $p$-$p$ scattering cross section is only 1/1760 times that for the scattering of the protons by oxygen, the principal contaminant of the tank hydrogen used. Commercially available $H_2$ must be purified by more than a factor of 10 before the $p$-$p$ yield is comparable to the $p$-O yield. To purify the scattering gas, we used activated charcoal at liquid nitrogen temperature, passing the hydrogen through

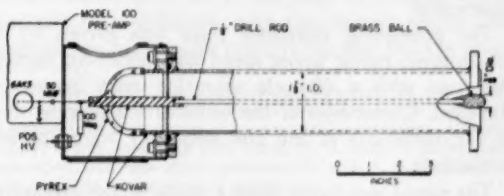


FIG. 4. Low-pressure proportional counter.

a charcoal-filled stainless steel cylinder at pressures above 1000 psi. This purification was carried out by batch, one purification yielding enough gas for several scattering runs. There seemed to be no appreciable increase in contamination while stored in the conventional metal cylinders which were well evacuated before filling with purified gas.

The gas thus purified was fed through a reduction valve and a needle valve into the scattering chamber. It was pumped out through the collimators by the differential pumps. When the pressure in the chamber was 1.5 cm of mercury, the pressure was 1.0 mm at the first differential port and $10^{-3}$ mm at the second differential pump. The chamber pressure and the pressure at the first differential port were measured by oil monometers. Since we were interested primarily in relative cross sections we did not need to know the pressure absolutely, although small corrections involving the ratio of pressures were made assuming the zero to be correct.

When large currents were passed through the collimators, the pressure in the chamber would rise significantly (approximately 10 percent for a current change from 1 to 5 microamperes) presumably because of the increase in viscosity of the hydrogen gas in the collimator. This effect is probably caused by the temperature rise from the additional energy lost in the gas by the more intense incident beam. It was therefore necessary to monitor the pressure to a few percent, and to keep the current fairly constant during a run.

### D. Energy Measurement

Originally it was intended to measure the energy of the beam by a time-of-flight method and to control by modulating an electron beam in a separate accelerating tube. We found, however, that with corona control operating from the mass-2 beam the generating voltmeter readings were remarkably reproducible, and that the fluctuations in beam energy about the average energy were not more than a few kilovolts (evidenced by the sharpness of the proton induced resonances described below). The average generating voltmeter galvanometer reading could be kept to about $\pm 300$ volts. Hence we felt no need at all of more rapid control equipment and no acute need of a more stable system. The energy measurement was therefore based entirely on the generating voltmeter readings, and no new absolute measurement of energy was made in this experiment.

The generating voltmeter rotor was driven by a synchronous motor whose speed was monitored during the runs with a 60-cycle vibrating reed frequency standard. Corrections of the order of 0.2 percent due to the variations in the line frequency were applied to the data.

The signal was taken from a stator whose geometry corresponded to that of the rotor, which was grounded. The signal was rectified by 6H6 diodes and the voltage drop across a 10K temperature-controlled resistor measured with a precise potentiometer. The resistors in the measuring circuit were such that the time constant was about a millisecond.

The machine temperature and insulating gas pressure were kept constant over the period of time necessary to complete a set of scattering runs and to calibrate the generating voltmeter.

To calibrate the generating voltmeter we used the well-established points on the nuclear energy scale[9] given in Table I. Two kinds of fluorine-containing targets were used, each for a separate purpose. By filling the scattering chamber with a trace of difluoroethane ($C_2H_4F_2$) in hydrogen at the usual pressure, the alpha particles from the reaction $F^{19}(p,\gamma\alpha)O^{16}$ may be observed in one of the proportional counters. A thin nickel window placed in front of the alpha-counter slit system absorbs the scattered protons, but allows the alpha particles from the 340.2-kev fluorine resonance to pass through. This scheme is not possible at the 483.1-kev resonance because the elastically scattered protons penetrate the foil.

Since the beam collimators were filled with essentially the same gas as they were during the actual proton-scattering run, this measurement provided a direct connection between the 340-kev proton energy at the scattering volume with the generating voltmeter reading.

To find the similar connection for the other proton energies we bombarded a LiF rotating target evaporated

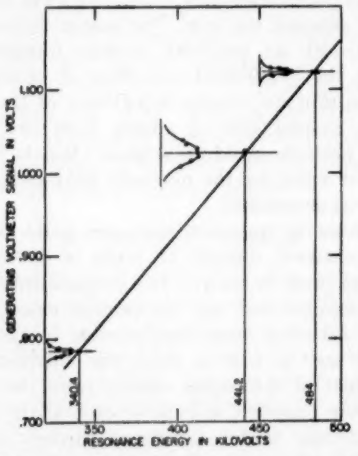


FIG. 5. Calibration of generating voltmeter using fluorine and lithium resonances. The values shown for the resonance energies are not the recent ones used in the calculation. Using 340.2 kev for the lower fluorine resonance and 441.2 kev for the lithium, we observe $482\pm2$ kev for the energy of the upper fluorine resonance, as compared with the $483.1\pm0.5$ kev in Table I. Not shown is a higher fluorine resonance at $873.5\pm0.8$ kev, which also indicated a linear calibration.

[9] A summary of the various measurements of these resonances is given by S. E. Hunt, Proc. Phys. Soc. (London) **A65**, 982 (1952).

in place at the scattering volume below the same beam collimators as were used during the proton scattering runs. The $\gamma$ rays from the three reactions in Table I were detected with a Victoreen Geiger tube. In this way the linearity of the generating voltmeter reading was checked. This target was not used for an absolute calibration because it was felt that we could not rely on a solid target being completely free from coatings when bombarded with high proton current densities. Actually, freshly evaporated targets gave the same calibration at 340.2 kev as did the gas target.

The solid target was also used to investigate the rate of energy loss in the various gases used in the scattering experiment by varying the position of the target along the beam. The shift in the 340.2- and 483.1-kev resonances was observed as the chamber was alternately evacuated or filled with $H_2$ gas or filled with various concentrations of $H_2-C_2H_4F_2$ mixture at various pressures.

Figure 5 shows the generating voltmeter readings plotted *versus* the published values of the resonances. These readings have all been corrected for energy loss in the gas or in the target coating. Because the generating voltmeter appears to be linear within the errors in Table I, we will express the energy of the minimum in terms of the energies of the two fluorine resonances so that possible future changes in their energies may be applied directly to our result. The lower resonance has the dominant effect in determining the energy of the nearby minimum.

### E. Experimental Procedure

After the current collector was calibrated by scattering from an argon-hydrogen mixture, the machine energy was calibrated and the $p$-$p$ scattering data taken according to the following procedure.

The chamber was filled with a 1 percent by volume mixture of $C_2H_4F_2$ in $H_2$ and the generating voltmeter was calibrated by observing the $F(p,\gamma\alpha)$ alphas from fluorine at 340.2 kev in the scattering volume. The chamber was then pumped out and pure hydrogen allowed to flow through. The yield of scattered protons was observed at each energy for two approximately five-minute intervals. Then the machine energy was shifted to an energy roughly symmetric about the minimum. After about five hours the generating voltmeter calibration was repeated with the fluorine-containing gas.

Immediately after this the solid target chamber was put in place of the scattering chamber below the collimator and the energy loss of the protons and generating voltmeter linearity were measured.

## III. RESULTS AND REDUCTION OF DATA

The points in Fig. 2 are our best run of $p$-$p$ laboratory cross section plotted against energy. Both ordinate and abscissa are absolute measurements, and the curves are computed from a best shape-independent fit to the Wisconsin data.[4] Three previous runs had been taken, all giving this same value for the minimum,[10] but since the experiment was not understood nearly so well in the earlier runs we will base our conclusions entirely on the data in Fig. 2.[11]

TABLE I. Established points on the nuclear energy scale.

| Reaction | $E_r$ in kev | Width in kev |
|---|---|---|
| $F(p,\gamma\alpha)$ | 340.2±0.5 | 2.9 |
| $Li(p,\gamma)$ | 441.2±0.5 | 12.2 |
| $F(p,\gamma\alpha)$ | 483.1±0.5 | 2.2 |

Our finite angular resolution should give an effective angle of about 44.4° for about half the protons and 45.6° for the other half. The effect of scattering in the hydrogen gas should make the deviation of the observed counts from the 45° curve even greater. The observed points thus lie too low by the order of 15 percent.

The value of the energy of the minimum is determined by folding the 45° curve to get the line of symmetry. A renormalization of absolute cross sections by a 15 percent increase would change the energy of the minimum by only about 0.2 kev, since the curves are almost symmetric about a line that is almost vertical.

A renormalization of 15 percent is outside the 8 percent or so we would have estimated as the absolute accuracy, except for a possible enrichment of the argon used in calibrating the current integrator by selective diffusion through the collimator of the hydrogen with which it was mixed. However, the comparison of our data on $p$-$d$ scattering[10] with that of Freier *et al.*[12] makes more than a 10 percent error in calibrations unlikely. Also if the points are all raised by the same factor the shape of the curve is not quite right; the resultant curve is too narrow at the top, touching the 46° curve at about 35 kev above and below the minimum. A better estimate for the correction for finite solid angle would make this distortion worse, and the energy resolution observed with the resonances seems too good (about 3 kev) to affect the curve appreciably.

This apparent difficulty with the absolute value of the observed cross section was not investigated thoroughly, and it may well all be instrumental. For it to be genuine the 45° theoretical $p$-$p$ cross section would have to be too high by roughly three-quarters of a millibarn over this energy region. For example, an improbable positive nuclear $D$-wave phase

[10] Cooper, Frisch, and Zimmerman, Phys. Rev. **90**, 339 (1953).

[11] The run plotted could have had five times as many counts in the same time with almost the same angular resolution. Unfortunately, it was done with slits which, for a study of pulse group separation, had been made unnecessarily narrow in the direction perpendicular to the plane of scattering.

[12] Freier, Stratton, Brown, Holmgren, and Yarnell, Phys. Rev. **86**, 593 (1952).

shift of the order of $10^{-3}$ radian in this energy region would bring the data and theory into better agreement.

The 45° curve as plotted is a fairly good match to the data for $S$-wave purposes. The curve could not be displaced by more than about a kilovolt up in energy or one and a half kilovolts down without being noticeably off the best fit to the points. A reasonable estimate of the best fit, combined with a 15 percent renormalization of the ordinates of the points, gives the minimum of the observed curve as about 0.4 kev lower than the minimum of the computed 45° curve. We assign an over-all error to the experimental value of about 1.5 kev, giving $E_{\min}(45°)=383.9\pm1.5$ kev. In terms of possible different values $E_1$ and $E_3$ of the fluorine resonances in the future, $E_{\min}=383.9+(99.2/142.9)(E_1-340.2)+(43.7/142.9)(E_3-483.1)$.

The minimum in ratio to Mott is less by 1.05 kev, giving 382.8 kev. An approximate expression for the phase shift at the energy of the minimum in ratio to Mott, is $\delta=\eta-0.156\eta^3$, where $\eta=e^2/v=0.2557$. Therefore, $\delta_0=0.2527\pm0.0011$ at 382.8 kev.

TABLE II. Values of $K$ at 382.8 kev, and the energy of the minimum in ratio to Mott.

| | $K$ at 382.8 kev | $E_{\min}$ |
|---|---|---|
| Yukawa | 3.905 | 381.6 |
| Observed | $3.917\pm0.016$ | $382.8\pm1.5$ |
| Shape independent | 3.924 | 383.4 |
| Square | 3.939 | 384.7 |

Table II gives the values of $K$ at 382.8 kev and the energy of the minimum in ratio to Mott which we calculate from the best fits to the Wisconsin data[13] for various assumptions of well shape.

Our determination of the energy of the minimum, in terms of the published *best* fits to the Wisconsin data, seems to exclude the possibility that the $p$-$p$ interaction might be described by a static square well, or Yukawa plus a very large repulsive core.[14] Less good fits to the Wisconsin data, but still within reason, give for any particular shape a spread in the values of the predicted $E_{\min}$ comparable with the spread in Table II. Hence, one cannot with certainty exclude a square well on the basis of these data alone.

Considered with all the data from a wide energy region, our datum fits in well with the conclusion, already indicated by Yovits *et al.*,[5] that the force field cannot be described by a potential shaped like a square well, or a Yukawa well with a large repulsive core.

We are particularly indebted to Peter Rose for considerable help with the experiment and to C. J. Strumski for a great part of the construction and operation of the machine.

[13] H. H. Hall and J. L. Powell, Phys. Rev. **90**, 912 (1953).
[14] Hafner, Hornyak, Falk, Snow, and Coor, Phys. Rev. **89**, 204 (1953).

# Doppler Effect in the Slow Neutron Resonance in Rhodium

H. H. LANDON
*Brookhaven National Laboratory, Upton, New York*
(Received December 31, 1953)

The variation in transmission of a rhodium foil to 1.26-ev neutrons has been measured as a function of foil temperature using a crystal spectrometer. A change in transmission of approximately two percent per 100-degree temperature change has been observed over a temperature range from 120°K to 860°K. After correction for instrument resolution and Doppler effect, a peak cross section of 4850±200 barns results. Comparison has been made with the theory of Bethe and Placzek as extended by Lamb.

## INTRODUCTION

MANY problems arise in the determination of accurate Breit-Wigner parameters for neutron capture resonances in the energy region above a few tenths of an electron volt. In addition to the problem of finite instrument resolution, the broadening of a resonance due to the thermal motion of the target atoms becomes increasingly important as the energy increases. Until recently it has not been possible to study a resonance with sufficiently high resolution so that such broadening was directly measurable. The results obtained with the BNL crystal spectrometer[1] have been such, however, as to require consideration of this problem in the determination of accurate parameters from direct line shape analysis. It was decided, therefore, to choose a suitable resonance and to study the effect of temperature on the measured cross section. The Doppler width[2] of a line is

$$\Delta = 2(E_0 kTm/M)^{\frac{1}{2}},$$

where $m$ is the neutron mass, $M$ the mass of the resonant isotope, $E_0$ the resonance energy, and $T$ the atom temperature. Since $\Delta$ increases with energy, while the resolution of a crystal spectrometer decreases, care must be taken in choosing a proper resonance.

The isolated 1.26-ev resonance in monoisotopic rhodium was chosen as the best compromise. Besides being suitably sensitive to temperature in the region of good spectrometer resolution, rhodium is available in metallic foil form, thus easing the experimental difficulties considerably. The resonance has been studied previously by several investigators, most recently by Sailor.[3]

## APPARATUS

A detailed description of the BNL spectrometer has been previously published.[1]

A temperature range 120°K to 860°K was covered by means of two sample chambers. The cryostat, which is shown schematically in Fig. 1, was mounted on the arm of the spectrometer in the monochromatic beam between collimating slits. The neutron beam passed through two aluminum foils in entering and leaving the evacuated chamber. The temperature of the rhodium foil was measured by means of a thermocouple placed just out of the well-defined neutron beam. The cylinder containing liquid nitrogen was thin-walled stainless steel, while the foil holder was an aluminum frame fabricated to have low heat capacity. At equilibrium the foil temperature was very constant, with only slow boiling of the nitrogen. Since moisture condensation on the aluminum windows would have caused serious errors in transmission measurements, careful sample out, sample in measurements were made to assure that any such effect was small. The windows were warmed by an air blower during measurements as a further precaution.

A simple method of raising the sample temperature was practical because the dimensions of a foil, chosen for appropriate neutron transmission, were such as to permit heating by means of an electric current passing through the foil. The oven is shown schematically in Fig. 2. The electrodes were connected to the secondary winding of a welding transformer whose primary was supplied from a Variac. It was found necessary to evacuate the chamber to keep the foil temperature from becoming nonuniform due to air convection currents. The foil temperature was measured by thermocouples and found to vary in all cases less than ten degrees over the region of the neutron beam.

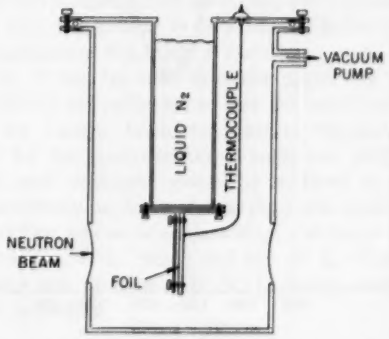


FIG. 1. Schematic diagram of the evacuated chamber for low-temperature transmission measurements.

[1] V. L. Sailor and L. B. Borst, Rev. Sci. Instr. **24**, 141 (1953).
[2] H. A. Bethe and G. Placzek, Phys. Rev. **51**, 462 (1937); H. A. Bethe, Revs. Modern Phys. **9**, 140 (1937).
[3] V. L. Sailor, Phys. Rev. **91**, 53 (1953). See R. R. Meijer, Phys. Rev. **75**, 773 (1949) for previous reference.

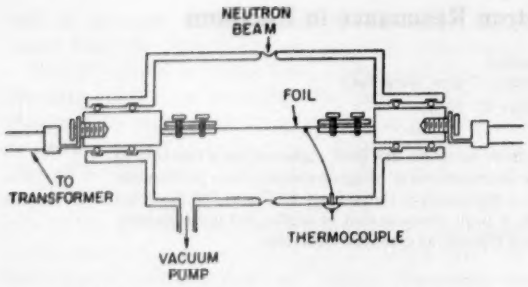


FIG. 2. Schematic diagram of the evacuated chamber for high-temperature transmission measurements.

Foil transmission measurements were then made at six temperatures in the diffracted beam from the $12\bar{3}1$ planes of a beryllium crystal monochromator. The Bragg angle for the 1.26-ev neutrons was ten degrees with an associated energy resolution of 2.6 percent.

## ANALYSIS

Bethe and Placzek[2] have modified a simplified one-level Breit-Wigner equation for the case where the target atoms can be treated as free, having velocities distributed according to a Maxwellian distribution. The effective cross section for neutrons of energy $E$ is then

$$\sigma(\xi,E)=\sigma_0\psi(\xi,x)[E_0/E]^{\frac{1}{2}}, \tag{1}$$

where

$$\psi(\xi,x)=\tfrac{1}{2}\xi\pi^{-\frac{1}{2}}\int_{-\infty}^{\infty}\frac{\exp[-\frac{1}{4}\xi^2(x-y)^2]}{1+y^2}dy, \tag{2}$$

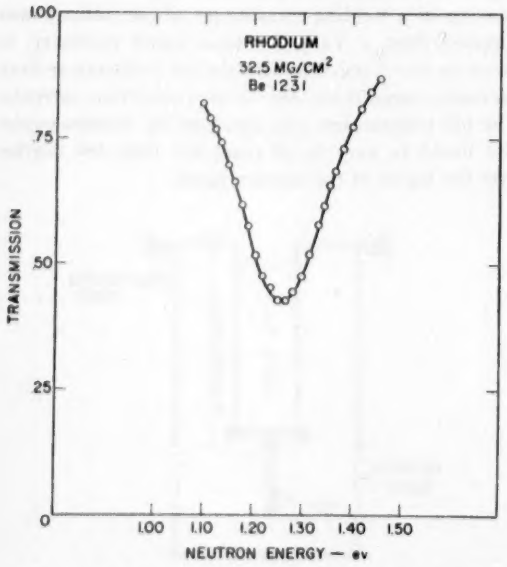


FIG. 3. Rhodium foil transmission *versus* neutron energy in the region of the 1.26-ev resonance.

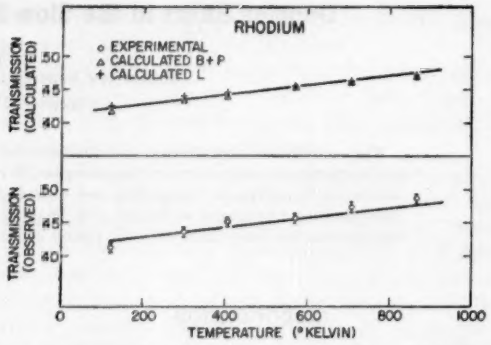


FIG. 4. Transmission *versus* temperature for the rhodium foil at the center of the resonance. The upper plot is calculated, while the lower compares the experimental data with the calculated data. The straight line is a calculated one (see text) and is not the "best" fit to the experimental points.

and

$$x\equiv(E-E_0)/\tfrac{1}{2}\Gamma,\quad y\equiv(E'-E_0)/\tfrac{1}{2}\Gamma,\quad \xi=\Gamma/\Delta.$$

Resonant scattering has been considered negligible and only energies near the resonant energy $E_0$ are considered. $\psi(\xi,x)$ is, in general, a complicated function of $x$. In the special case $x=0$, i.e., exact resonance, $\psi(\xi,0)$ reduces to the simple form

$$\psi(\xi,0)=\tfrac{1}{2}\pi^{\frac{1}{2}}\xi\exp(\tfrac{1}{4}\xi^2)[1-\Phi(\tfrac{1}{2}\xi)], \tag{3}$$

where $\Phi$ is the Gaussian error function:

$$\Phi(\tfrac{1}{2}\xi)=2\pi^{-\frac{1}{2}}\int_0^{\frac{1}{2}\xi}\exp(-t^2)dt. \tag{4}$$

This should be a reasonably good approximation if the resolution of the instrument is good. A test of Eq. (3) has been made for this case since the resolution width, $\Delta E=0.033$ ev, is small compared to the total width of the resonance, $\Gamma=0.156$.

Since the above results are valid only for free atoms, they are not expected to be exact for a rhodium foil. The characteristic or Debye temperature for rhodium is $\theta=370°$K, and consequently the chemical binding should be important at temperatures near room temperature and below. Lamb[4] has calculated the shape of an absorption line for an atom which is bound in a crystal lattice under the assumption that the crystal may be treated as a Debye continuum. He has shown that for sufficiently weak lattice binding, $\Delta+\Gamma\gg 2\theta$, the absorption curve has the same form as it would in a gas,

TABLE I. Peak cross section calculated at each temperature by using Eq. (3). No resolution correction has been applied.

| Temp.°K | 121 | 298 | 405 | 569 | 707 | 865 |
|---|---|---|---|---|---|---|
| $\sigma_0$ barns | 4650 | 4670 | 4660 | 4770 | 4660 | 4610 |

[4] W. E. Lamb, Jr., Phys. Rev. **55**, 190 (1939).

not at the temperature of the crystal, however, but at a temperature which corresponds to the average energy per vibrational degree of freedom of the lattice. He has plotted the effective temperature *versus* real temperature in units of the Debye temperature for any crystal under this condition of weak binding. In the case of strong binding, the line form is found to be more complicated, showing fine structure as well as a shift to lower energy accounting for a larger effective mass. In the case of rhodium the weak binding condition is satisfied so that Lamb's curve for effective temperature can be used.

It was desirable, however, to extend the analysis to account for instrument resolution. This was accomplished, following Sailor,[3] by operating on the true transmission,

$$T=e^{-N\sigma(\xi,E)},$$

by numerical integration over a resolution function $R(E-E_i)$ of the instrument. $N$ is the thickness of the sample expressed as the number of nuclei per cm.[2] The measured transmission $T_i$ will differ from the true transmission $T$ as follows:

$$T_i(E_i) = \int_0^\infty T(E,\psi)R(E-E_i)dE \Big/ \int_0^\infty R(E-E_i)dE, \quad (5)$$

where $E_i$ is the nominal energy setting of the spectrometer. The resolution function must include the reactor spectral distribution, the crystal reflectivity, and $1/v$ detector efficiency. By choosing trial values for $\sigma_0$ and $\Gamma$, the above integration can be performed approximately in order to adjust each point to best fit the experimental observation. For this work, measurements and calculations were made only at the resonance energy $E_0$. The $\psi$ functions were calculated by numerical integration for the particular values of the arguments obtaining in this experiment.

## RESULTS

The transmission of the rhodium foil as measured as a function of energy is shown plotted in Fig. 3. The cross section as directly measured at the resonance for this sample is 4370 barns. The spectrometer was then set at the minimum of the transmission curves, and the transmission measured as a function of temperature. The results are shown plotted in Fig. 4. The straight line drawn through the points is a calculated curve (see below) and is not the "best" fit to the experimental points. If Eqs. (3) and (4) are then applied to each of these points with no effective temperature correction, the resulting $\sigma_0$ as calculated for each is listed in Table I. The average $\sigma_0$ obtained from these is 4670 barns. If the transmission data are extrapolated linearly to a temperature of 0°K, a value of 4650 barns is found. It should be remembered that these values do not include a resolution correction. If this value of 4670 barns is corrected for resolution (see below), a cross section $\sigma_0=4820$ barns is obtained.

The more complete analysis including resolution correction was then applied to each point. For these calculations it is necessary to arrive at a best value for $\sigma_0$ and $\Gamma$. These were obtained by adjusting the calculations at the room temperature point, which was the best known point statistically. Values of $\sigma_0=4850\pm200$ barns and $\Gamma=0.156\pm0.005$ were obtained, and were then used for the correction of each successive point. The results are shown as calculated transmissions in Table II and are plotted in Fig. 4. Results are also shown using Lamb's correction to the measured temperature.

TABLE II. Transmission of the rhodium foil at the center of the resonance, as a function of temperature.

| Temp °K | Observed transmission | Calculated transmission | |
|---|---|---|---|
| | | Bethe | Lamb |
| 121 | 0.413 | 0.418 | 0.425 |
| 298 | 0.435 | 0.435 | 0.439 |
| 405 | 0.451 | 0.443 | 0.445 |
| 569 | 0.456 | 0.454 | 0.455 |
| 707 | 0.472 | 0.463 | 0.463 |
| 865 | 0.485 | 0.472 | 0.472 |

## CONCLUSIONS

The results of the calculations show, in general, good agreement with the theoretical predictions of Bethe and Lamb. This method of correction for Doppler effect should, therefore, be applicable in this energy region. The experimental curve is seen to have a slightly greater slope than the predicted curve. Part of this may come from thermal expansion in the sample. The linear dimensions of the sample change as the temperature increases. Consequently, if the sample were allowed to expand freely, the effective area of the sample would decrease about 0.5 percent for the full temperature interval, thus increasing the transmission. In this case the sample is constrained, however, and the importance of this effect is not clear.

Finally, it can be seen that the sensitivity of the experiment is not sufficient to test the modification of theory by Lamb. With the further improvements planned for the spectrometer, a sufficient increase in intensity and resolution should be achieved to permit the observations necessary for settling this question.

The author wishes to acknowledge the many discussions with Dr. V. L. Sailor and Mr. H. L. Foote, Jr., concerning this problem. Mr. R. L. Smith assisted in the data recording.

# Neutron Capture in the Separated Isotopes of Platinum*

J. M. Cork, M. K. Brice, L. C. Schmid, G. D. Hickman, and H. Nine
*Department of Physics, University of Michigan, Ann Arbor, Michigan*

(Received Februrary 23, 1954)

Using the separated isotopes of platinum, irradiated in the pile, the energies of the gamma rays for the activities of $Pt^{191}$, $Pt^{193}$, and $Pt^{195}$ have been evaluated. For $Pt^{191}$ fifteen gamma rays are found which fit well a simple level scheme. $Pt^{193}$ emits isomerically a gamma ray followed by $K$ capture to iridium, with the possible emission of a high-energy gamma. $Pt^{195}$ emits a highly converted gamma ray followed by two others in rapid succession decaying to the stable isotope. The half-lives of the three activities are found to be 2.90, 3.35, and 6 days, respectively.

THE irradiation of normal platinum with low-energy neutrons yields five radioactive isotopes in platinum as well as one activity in gold. The correct assignment of each activity to its proper isotopic mass has been a difficult problem. For example, there has been no positive criterion for distinguishing between the activities at masses 191 and 193. By bombarding iridium with either protons or deuterons both can be made. Fast neutron bombardments have been of value, but since four of the activities have half-lives differing not greatly from 3 days, the difficulty is apparent. Only by the separation or enrichment of the less abundant isotopes of platinum can the assignments be made with confidence. The Oak Ridge National Laboratory has recently made available these separated isotopes. Specimens enriched in each of the masses 190, 192, and 194 have been irradiated in the heavy-water pile at the Argonne National Laboratory, and quickly transported for studies in scintillation crystal and magnetic photographic spectrometers.

Table I. Summary of electron energies for $Pt^{191}$.

| Electron energy kev | Interpretation | Energy sum kev | Electron energy kev | Interpretation | Energy sum kev |
|---|---|---|---|---|---|
| 20.5 | $K$ | 96.2 | 164.9 | $L_1$ | 178.2 |
| 49.5 | Auger $KL_1L_1$ | | 168.8 | $M$ | 172.0 |
| 51.0 | Auger $KL_1L_2$ | | 175.0 | $N$ | 178.2 |
| 53.6 | $K$ | 129.6 | 192.9 | $K$ | 268.6 |
| 60.0 | $L_1$ | 73.7 | 206.0 | $L_1$ | 219.4 |
| | or Auger $KL_1M_1$ | | 216.4 | $M$ | 219.5 |
| 62.2 | $L_2$ | 73.7 | 255.0 | $L_1$ | 268.3 |
| | or Auger $KL_2M_1$ | | 274.8 | $K$ | 350.9 |
| 69.0 | $L_1$ | 82.6 | 284.0 | $K$ | 360.0 |
| 69.8 | $L_2$ | 82.6 | 333.3 | $K$ | 409.2 |
| 71.4 | $L_3$ | 82.7 | 338.0 | $L$ | 351.0 |
| 79.8 | $M_1$ | 82.7 | 346.0 | $L$ | 359.5 |
| 81.8 | $N$ | 82.7 | 356.8 | $M$ | 359.9 |
| 83.4 | $L_{1,2}$ | 96.4 | 380.0 | $K$ | 456.0 |
| 85.0 | $L_3$ | 96.4 | 396.0 | $L$ | 409.4 |
| | | | 442.6 | $L$ | 456.0 |
| 93.3 | $M$ | 96.3 | 463.2 | $K$ | 539.3 |
| 96.1 | $K$ | 172.2 | 476.0 | $K$ | 550 |
| 102.7 | $K$ | 178.6 | 525.5 | $L$ | 539.0 |
| 116.0 | $L_1$ | 129.4 | 535.7 | $M$ | 539.0 |
| 118.3 | $L_2$ | 129.8 | 547.5 | $K$ | 623.6 |
| 144.2 | $K$ | 220.1 | 609 | $L$ | 622.4 |
| 159.0 | $L_1$ | 172.5 | | | |

* This research was supported jointly by the U. S. Office of Naval Research and the U. S. Atomic Energy Commission.

## PLATINUM 191

The first assignment[1] of a 3-day activity to $Pt^{191}$, from the products formed in platinum by the bombardment of iridium with deuterons, has proved to be a fortunate choice. Subsequent studies[2,3] have shown this activity to yield many gamma rays, following $K$ capture, as shown in columns 1 and 2 in Table II. The gamma transitions are in iridium, following $K$ capture in platinum. In the present investigation most of the previously reported gamma rays are found, with only slight modification in their energies. However, no evidence can be found for the existence of gamma rays with energies of 42, 62, and 125 kev in $Pt^{191}$. In addition there appear to be gamma rays of energy 73.7 and 550 kev, which were not previously observed. The half-life is found to be $2.90\pm0.05$ days.

The energies of the conversion electrons taken with various magnetic fields are summarized in columns 1 and 4 in Table I. The interpretation of each line and the energy sums are given in following columns. By comparing the lower-energy lines in $Pt^{191}$ with the similar pattern obtained with $Pt^{193}$ it is possible to identify those electron lines that are due to Auger groups. Thus, the gamma ray reported by Hill *et al.*[2] as 62 kev is probably of this origin. No evidence whatever appeared to support the existence of a gamma ray at 42 kev, although its $L$ and $M$ lines should have been easily observed if present. The gamma reported at 125 kev is probably based upon the assumption that the electron group at 49.5 kev is a $K$ line. It is believed, however, that the better interpretation of this line is that it is of Auger origin corresponding to the very strong $K-L_1-L_1$ electron group. It thus appears that there are, in all, fifteen gamma rays, as shown in column 3, Table II.

The scintillation crystal spectrometer could of course not resolve these gamma energies when they are close together in value. It could, however, show broad peaks and yield valuable coincidence data. For example, the 172-kev gamma ray appears to be in sequence with radiation at 82, 96, and 178 kev but

[1] G. Wilkinson, Phys. Rev. **73**, 252 (1948).
[2] Swann, Portnoy, and Hill, Phys. Rev. **90**, 257 (1953).
[3] Tomlinson, Naumann, and Mihelich, Bull. Am. Phys. Soc. **29**, No. 1, 57 (1954).

not with 350-kev or higher-energy peaks. By observing that summations of certain of the reported energies yield other observed energies, it is readily possible to construct a very plausible array of levels as shown in Fig. 1, that will satisfy almost perfectly all fifteen gamma energies. Twelve of the transitions are definitely accommodated by only six levels. The three rather weak gamma rays at 73 550 and 623 kev seem to form a group whose ground state may be any of the other levels. If they are correctly placed in Fig. 1, then there must be three $K$-capture paths from the excited platinum level. This specimen was not entirely free from iridium as an impurity so that weak lines for the well-known $Ir^{192}$ spectrum were also obtained.

The ground state of $Ir^{191}$ with its 77 protons and 114 neutrons has been measured to be a $d_{\frac{3}{2}}$ level. The first excited level to be expected from shell theory would be an $s_{\frac{1}{2}}$ state. If the proposed level scheme is correct, then the 82.6-kev transition should be characterized as $M1$. Its $K$ electron group is too low in energy

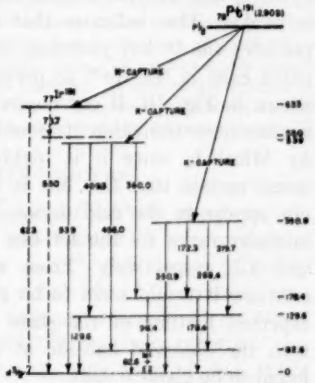

FIG. 1. Nuclear energy levels in $Ir^{191}$ following $K$ capture in $Pt^{191}$.

to be observed in the spectrometers but the $L_1$, $L_2$, and $L_3$ lines are well resolved and visually appear to be of almost equal intensity. The microphotometer could not well separate the $L_1$ and $L_2$ peaks but showed for the $(L_1+L_2)/L_3$ ratio a value of 1.8. This is compatible with a mixture of $M1+E2$ transitions as found[4] in a very similar case in gold 195 (61 kev) by Mihelich *et al.*

The $K/L_1$ intensity ratios for several of the remaining gamma rays are estimated visually as follows: 96.4 kev (~2), 129.6 kev (~3), 172.3 kev (~5), 350.8 kev (~9), 360 kev (~7), 409 kev (>10), 456 kev (~9), and 539 kev (~7). The $L_3/L_1$ ratio for the 129.6-kev gamma is ~0.12, which combined with its $K/L$ ratio and the low $L_2$ intensity indicates that it is probably an $M1$ transition. It is possible to make assignments of the multipole order of most of these transitions, which make possible consistent spin assignments to the levels in Fig. 1.

[4] Gillon, Gopalakrishnan, De-Shalit, and Mihelich, Phys. Rev. 93, 124 (1954).

TABLE II. Comparison of gamma energies (kev) in $Pt^{191}$.

| Observer | | |
|---|---|---|
| Swann *et al.*[a] | Tomlinson *et al.*[b] | Present |
| ... | 42 | ... |
| 62 | ... | ... |
| ... | ... | 73.7 |
| 82 | 82 | 82.6 |
| 94 | 96 | 96.4 |
| 125 | 125 | ... |
| 129 | ... | 129.6 |
| 171 | 172 | 172.3 |
| 178 | 179 | 178.4 |
| ... | 220 | 219.7 |
| 267 | 268 | 268.4 |
| 350 | 350 | 350.9 |
| 359 | 360 | 360.0 |
| 408 | 409 | 409.3 |
| 455 | 456 | 456 |
| 537 | 540 | 539 |
| ... | ... | 550 |
| ... | 620 | 623 |

[a] See reference 2.
[b] See reference 3.

## PLATINUM 193

By bombarding platinum with fast neutrons a radioactivity with half-life 3.4 days was observed[5] by Hole. He noted electron conversion lines for a gamma ray of energy 126 kev and believed the activity to be isomeric in one of the stable isotopes of platinum. A similar bombardment by fast neutrons, as carried out by Wilkinson[1] was found to yield a radioactive product whose half-life was 4.33 days. The gamma rays emitted were reported to have energies of 0.17 and 1.70 Mev and the responsible isotope was believed to be $Ir^{190}$ following $K$ capture in $Pt^{190}$. More recent studies[2] by Hill *et al.* have led to the conclusion that $Pt^{193}$ decays by an isomeric gamma transition of 134.9 kev, with an assumed half-life of 4.5 days.

In the present investigation, the enriched $Pt^{192}$ after irradiation showed a strong low-energy gamma ray which is highly converted. The energies of the $K$, $L_1$, $L_3$, $M$, and $N$ electron lines are 57.1, 121.6, 124.0, 132.3, and 134.8 kev, respectively, indicating a gamma energy of 135.5 kev. The intensity ratio for the $K/L_1$ lines is 0.25±0.1, and for the $L_3/L_1$ ratio, a value of 1.5±0.5 is found. This supports the interpretation[3] of the $M4$ nature of this radiation. Moreover the half-life appears to be not 4.5 days but 3.35±0.1 days. This is in better agreement with the lifetime expected for radiation of this nature as computed from the formula[6] of Moszkowski.

The scintillation crystal spectrometer showed a high-energy gamma ray in this source in the neighborhood of 1.6 Mev. This peak seemed to decay at the same rate as that for the 135-kev gamma. Because of the high sensitivity of the crystal detector and the possibility of impurities, it cannot be said with certainty that this gamma ray is in $Pt^{193}$. The ground state

[5] N. Hole, Arkiv. Mat. Astron. Fysik 36A, No. 9 29 (1948).
[6] S. A. Moszkowski, Phys. Rev. 89, 474 (1953).

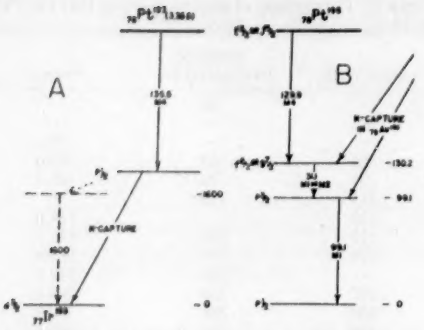


FIG. 2. A: Transitions in $Pt^{193}$; B: level scheme for $Pt^{195}$.

of $Ir^{193}$ is a $d_{\frac{3}{2}}$ level, so that the $K$ capture to the ground state from a $p_{\frac{1}{2}}$ level in $Pt^{193}$ would be only first forbidden. A number of gamma rays have been found[7] to exist in $Ir^{193}$ following beta emission from $Os^{193}$. None of these are observed in the present study of $Pt^{193}$, indicating that the main $K$-capture transition is to the ground state of $Ir^{193}$, as shown in Fig. 2(A).

### PLATINUM 195

Following the irradiation of normal platinum with neutrons, a group of electron lines was observed,[8] which with the work functions of platinum gave two gamma rays with energies of 99.1 and 129.8 kev. These energies were somewhat similar to values reported,[9] in the decay of $Au^{195}$ (185 day), and it was thus proposed that a metastable level probably exists in $Pt^{195}$ with a half-life of the order of 4 days. To verify this speculation, in the present investigation platinum enriched in mass 194 was irradiated in the pile. This specimen showed clearly the strong conversion electron lines for three gamma rays in platinum, whose energies are 31.1, 99.1, and 129.9 kev. The electron energies with their approximate intensities are shown in Table III.

In a later investigation Huber *et al.* reported[10] on the gamma energies from both $Pt^{195}$ and $Au^{195}$. The energies for the former were given as 29, 97, and 129 kev and for the latter 29, 97, and 126 kev. It was concluded that the 126-kev gamma ray was a crossover for the 29- and 97-kev transitions in sequence. The 129-kev radiation was assumed to precede the others, having its origin in a metastable state of $Pt^{195}$ of half-life 3.8 days. Each of these energies for $Pt^{195}$ appears to be too low by about 2 kev.

TABLE III. Electron energies associated with $Pt^{195}$.

| Electron energy (kev) | Intensity | Interpretation | Energy sum (kev) |
|---|---|---|---|
| 17.1 | 32 | $L_1$ | 31.0 |
| 20.8 | 23 | $K$ | 99.2 |
| 27.8 | 5 | $M_1$ | 31.1 |
| 51.6 | 10 | $K$ | 130.0 |
| 85.3 | 13 | $L_1$ | 99.1 |
| 87.6 | 1 | $L_2$ | 99.1 |
| 95.7 | 5 | $M$ | 99.0 |
| 116.0 | 50 | $L_1$ | 129.9 |
| 118.4 | 85 | $L_3$ | 129.9 |

From a consideration of our energies alone, namely, 31.1 plus 99.1 being so close in value to 129.9, one would confidently but mistakenly assert that the latter is a crossover for the other gammas. By comparing our photographic records for $Pt^{195}$ with similar plates obtained[4] by Mihelich *et al.* for $Au^{195}$ the arrangement can be quite definitely established. His energy values for the 31.1- and 99.1-kev gammas agree well with ours but he finds no gamma energy corresponding to their sum. Moreover, the relative intensity of the electron lines is quite different. In $Pt^{195}$ we find that the $L_1$ (31-kev) line is considerably stronger than the $K$ (99-kev) line, whereas he finds for $Au^{195}$ that the former is weaker. This indicates that the 31-kev transition precedes the 99-kev emission, so that two $K$-capture paths exist in the $Au^{195}$ as previously suggested[10] and shown in Fig. 2B. If our observed 130-kev gamma is a cross-over transition it would have been observed by Mihelich, since it is highly converted. It then seems certain that this line is in platinum and does not appear in the gold decay. The $K/L_1$ and $L_3/L_1$ intensity ratios for the 130-kev gamma are about 0.2 and 1.7, respectively. From established[11] empirical relations it would seem to be an $M4$ transition. The expected lifetime of the state would be compatible with the observed half-life of the activity, which is found to be about 6 days.

The 31- and 99-kev gamma rays are also highly converted. In both cases $L_1$ is very strong compared to $L_2$ or $L_3$, thus suggesting $M1$ or possibly $M2$ transitions. The $K/L_1$ ratio ($\sim$2) for the 99-kev gamma would favor an $M2$ assignment. The half-life of an $M2$ state for this radiation ($Z^2/W=61.5$) would be expected to be about 6 microseconds. Since coincidences were observed between the 31- and 99-kev radiations, no such delay exists. Moreover, the very small $L_3/L_1$ intensity ratio ($<0.1$) favors strongly an $M1$ assignment.

With the scintillation crystal spectrometer peaks were observed for the 30-, 60 (x-ray)-, 100-, and 130-kev gamma rays. Coincidences are observed between (30, 100), (30, x-ray), (x-ray, x-ray). No coincidences could be noted between the 130-kev radiation and either of the other gamma rays. This could be due to the very high conversion coefficient[12]

[7] Cork, LeBlanc, Nester, Martin, and Brice, Phys. Rev. **90**, 444 (1953).
[8] Cork, Le Blanc, Stumpf, and Nester, Phys. Rev. **86**, 415 (1952).
[9] Steffen, Huber, and Humbel, Helv. Phys. Acta **22**, 167 (1949).
[10] De-Shalit, Huber, and Schneider, Helv. Phys. Acta. **25**, 279 (1952).
[11] M. Goldhaber and A. Sunyar, Phys. Rev. **85**, 733 (1952): and J. Mihelich, Phys. Rev. **87**, 646 (1952).
[12] Rose, Goertzel, and Perry, Oak Ridge National Laboratory Report No. 1023, 1951 (unpublished).

(~800) for this radiation or to the possibility that the 30-kev gamma is an $M2$ transition, so that the delay would make coincidences unobservable. The very low value of the $L_3/L_1$ intensity ratio for this radiation favors but does not assure that it is an $M1$ transition.

The half-life of this radiation is considerably longer than the previously published values, which were undoubtedly influenced by the presence of other shorter-lived radioactivities. From a comparison of the intensities of the electron lines on a sequence of plates taken with known exposure times, the half-life appears to be approximately 6 days.

PHYSICAL REVIEW VOLUME 94, NUMBER 5 JUNE 1, 1954

# Radiations of AcK†

EARL K. HYDE
*Radiation Laboratory, University of California, Berkeley, California*

(Received February 26, 1954)

The gamma rays of AcK ($Fr^{223}$) were studied in a sodium iodide photomultiplier scintillation counter coupled to a 50-channel pulse-height analyzer. Photons of a 49.8-kev gamma ray appear in 40±10 percent and photons of an 80-kev gamma ray appear in 24±6 percent of the total beta disintegrations. In addition, low-intensity gamma rays appear at 215 and 310 kev. $L$ x-radiation is present in about the same intensity as the 49.8-kev gamma ray. Gamma-gamma coincidence studies proved that the 49.8- and 80-kev radiations were not in coincidence. It was also shown that the 215- and the 50-kev gamma rays are not in coincidence. The $L$ x-radiation was studied in a proportional counter coupled to a 50-channel analyzer and identified as radium x-rays. Since $Th^{227}$ decays to the same daughter as does AcK some measurements were made on its gamma spectrum. Prominent photopeaks were observed at 49.8, 87, and 235 kev. The 235- and 49.8-kev gamma rays were observed to be in coincidence. The known decay data for AcK and $Th^{227}$ cannot be fitted into a common decay scheme without additional information.

## I. INTRODUCTION

AcK ($Fr^{223}$) is a member of the $U^{235}$ decay chain in which it appears as a result of a 1.2 percent alpha branching in the decay of $Ac^{227}$. AcK decays primarily by beta emission with a half-life of 21 minutes into 11.2-day AcX ($Ra^{223}$), although recently a very slight alpha branching ($\sim 4\times10^{-5}$) has been reported.[1] Investigations of the gamma radiations of AcK have been carried out by Lecoin and co-workers[2] using absorption techniques. The present report concerns a more detailed study of these radiations using a scintillation crystal spectrometer and a proportional counter in combination with a multichannel pulse-height analyzer and also using gamma-gamma coincidence techniques.

## II. PREPARATION AND STANDARDIZATION OF SAMPLES

A stock solution of $Ac^{227}$ dissolved in 3 ml of saturated hydrochloric acid was used as a source of francium. Whenever a fresh sample of AcK was required one drop of a 0.4$M$ silicotungstic acid solution was added to the ice-cold $Ac^{227}$ solution. Silicotungstic acid precipitated, carrying the francium, and was centrifuged out. The precipitate was dissolved in distilled water and reprecipitated by saturating the solution with hydrogen-chloride gas. This process was repeated two or three times. A water solution of the last silicotungstic acid precipitate was quickly passed through a 1-cm×4-mm column of Dowex-50 ion exchange resin. The adsorbed AcK was washed free of silicotungstic acid by 2 ml of distilled water, then stripped from the column with 300 $\mu$l of 10$M$ hydrochloric acid. Aliquots of this solution were evaporated on platinum counting disks. These samples were weightless and of high radiochemical purity. Further details on this preparation method are given elsewhere.[3]

The samples were all counted with a Geiger counter using the third shelf of the Geiger tube mount standard to this laboratory. The tube used was an Amperex Geiger tube filled with a mixture of argon and chlorine. An aliquot of each preparation was followed for decay as a check on radiochemical purity. The observed counting rate was translated into disintegrations per minute by multiplying by the calibration factor 42.

This calibration factor was based on the determination of the alpha counting rate of the AcK daughters and was determined as follows. Samples of AcK isolated as described above were mounted on platinum plates. Asbestos washers were placed above the samples and a clean collector platinum plate was placed above. By touching a torch to the bottom plate for one second and bringing the platinum to a red glow for this instant the francium was volatilized to the collector foil leaving behind any traces of $Ac^{227}$, AcX or RdTh present at that time. This instant was taken as zero time. The

† This research was supported by the U. S. Atomic Energy Commission.

[1] E. K. Hyde and A. Ghiorso, Phys. Rev. **90**, 267 (1953).

[2] Lecoin, Perey, Riou, and Teillac, J. Phys. et radium **11**, 227 (1950).

[3] E. K. Hyde, J. Am. Chem. Soc. **74**, 4181 (1952).

Geiger counting rate of the volatilized francium sample was followed and back extrapolated to zero time. Several hours later the alpha disintegration rate of the sample was carefully measured in an alpha counter (52 percent geometry). One-fourth of this alpha activity was ascribed to the 11.2-day AcX daughter of AcK and by straightforward calculations the initial disintegration rate of AcK was determined. This method of standardization substitutes the uncertainties of alpha counting, which are considerably less, for the uncertainties of absolute beta counting arising out of the backscattering, window absorption, and other corrections. The purity of the alpha activity was checked by analysis of the alpha spectrum. This was done by introducing to a 48 channel differential pulse-height analyzer the alpha pulses developed in a large ionization chamber after suitable linear amplification. This analysis was performed by A. Ghiorso on equipment developed by him as an improvement of apparatus previously described.[4] The alpha spectrum curves verified that the alpha activity was pure $Ra^{223}$ plus daughters with no contribution from $Th^{227}$.

## III. SPECTROMETER EQUIPMENT

The spectrometer equipment used in this work was assembled by A. Ghiorso and A. E. Larsh of this laboratory. The gamma detection initially occurred in a 1.5-in. diameter by 1-in. thick crystal of sodium iodide (thallium-activated) procured from the Harshaw Chemical Company mounted below a Dumont 6292 tube using a method similar to that described by Borkowski.[5]

On the side of the crystal facing the photomultiplier tube was affixed a quartz disk; a layer of oil between the quartz and the outside surface of the tube provided optical coupling. The other surfaces of the tube were packed with a reflecting layer of magnesium oxide. The whole assembly was mounted in an aluminum-lined lead shield on top of a standard Geiger tube 5-position shelf assembly. Incident gamma rays penetrated a thin foil of beryllium ($\sim$150 mg/cm$^2$) and a thin layer of magnesium oxide (about $\frac{1}{16}$ in.) before entering the crystal.

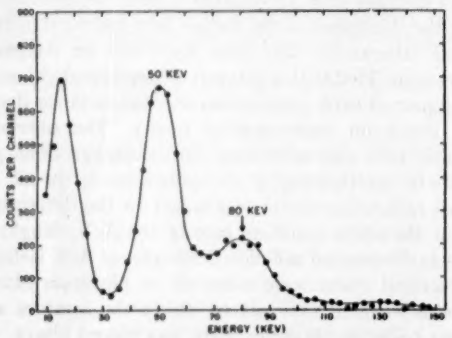


FIG. 1. Gamma spectrum of AcK in the 0-150 kev range. Data taken through 943-mg/cm$^2$ beryllium absorber.

The output pulse from the photomultiplier was amplified in a preamplifier, then in a linear amplifier. The final pulse was introduced to a 50-channel differertial pulse-height analyzer. This analyzer, based on a novel use of a 6BN6 as one arm of a gated univibrator, is a new design of Ghiorso and Larsh.[6] After proper alignment the channel width stability (operating at a 5-volt channel width) was better than 1 percent and remained so for periods of weeks. Gain and bias controls permitted the inspection of any predetermined energy interval with the full 50 channels. Further details on this equipment will be obtainable in a forthcoming publication.[6]

For measurements on the beta spectrum the sodium iodide detector was replaced by an anthracene crystal 1.5 in. in diameter by 0.25 in. thick mounted in front of an RCA-5819 photomultiplier tube.

A proportional counter was used to study $L$ x-rays. An Eck and Krebs tube 19 cm in diameter was filled to one atmosphere with a 90 percent xenon-10 percent methane mixture and operated at 1100 volts. After preamplification the pulse from the proportional counter was introduced to the linear amplifier of the 50-channel analyzer.

For study of gamma-gamma coincidences the apparatus assembled by A. E. Larsh and F. Asaro was used. In this equipment the sample was mounted between two sodium iodide crystals 1.5 in. in diameter and 1 in. thick with the front edge of the two crystals only 0.25 in. apart for maximum geometry. Each crystal had its own Dumont 6292 photomultiplier tube and preamplifier. The output from one crystal was fed to a single channel analyzer. The energy of the gamma rays recorded by this analyzer and the energy width of the "window" of this analyzer were both adjustable. The pulse from the second preamplifier was cabled to a linear amplifier. The signal pulse from this amplifier and that from the single-channel analyzer were led into a coincidence circuit, the signal pulse from the single-channel branch serving as the gate pulse. Only those signal pulses which were in coincidence with the gate pulses within the $10^{-6}$ sec resolving time were passed on to the differentiating circuit of the 50-channel analyzer. Hence the gamma spectrum in coincidence with a particular gamma ray could be examined.

The chance rate was determined by placing an absorber between the sample and the gate crystal and

[4] Ghiorso, Jaffey, Robinson, and Weissbourd, *The Transuranium Elements: Research Papers* (McGraw-Hill Book Company, Inc., New York, 1949), Paper No. 16.8, National Nuclear Energy Series, Plutonium Project Reord, Vol. 14B, Div. IV.

[5] C. J. Borkowski, Oak Ridge National Laboratory Report ORNL-1336, September 22, 1952 (unpublished).

[6] A. Ghiorso and A. E. Larsh (to be published). Brief preliminary description of pulse-height analyzer given in University of California Radiation Laboratory Report UCRL-1959, September 25, 1952 (unpublished).

applying a different radioactive source of about the same counting rate to the gate crystal. The usual calculation of the chance spectrum was carried out.

## IV. EXPERIMENTAL RESULTS

### 1. 49.8- and 80-Kev Gamma Rays

Figure 1 indicates the gamma spectrum of AcK in the 0-150 kev range. The energy scale was calibrated with the 60-kev gamma ray in the decay of $Am^{241}$ and the 87-kev gamma radiation of $Cd^{109}$. This and many similar curves were taken through 943-mg/cm² beryllium absorber to eliminate interference from the beta particles. There are prominent photopeaks at ~15, 50, and 80 kev, all decaying with the half-life of AcK. The ratio of the 80-kev/50-kev photopeaks was determined on several samples, the best value being 0.6±0.1. The overlapping of the two peaks causes some uncertainty in this ratio.

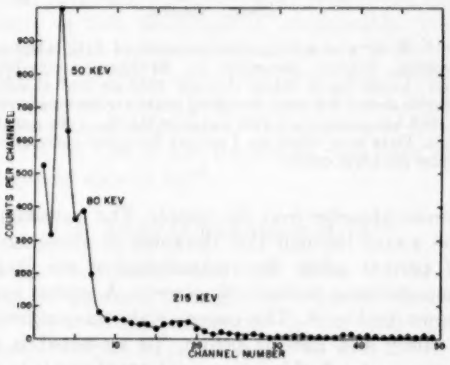


FIG. 2. Gamma spectrum of AcK in the 0–80 kev region. Data taken through 943-mg/cm² beryllium absorber.

The ratio of 50- and 80-kev photons to AcK disintegrations was determined in the following way. A sample of $Am^{241}$ with a known alpha disintegration rate mounted on platinum disk was placed in the scintillation spectrometer on the same shelf position used for the AcK samples and counted through the 943-mg/cm² beryllium absorber. The area under the 60-kev photopeak was determined. Using the information that 40 of the 60-kev photons are emitted per 100 alpha disintegrations of $Am^{241}$ the over-all counting efficiency was determined as 5.4 percent, i.e., 5.4 percent of the 60-kev photons emitted by the sample are registered in the photopeak.

The absolute disintegration rate of AcK samples mounted on platinum was determined by counting the samples in the Geiger counter and applying the calibration factor 42 as discussed above. The counting efficiency of the 50- and 80-kev photon peaks was taken as 5.4 percent. The resulting absolute abundances were: 40±10 of the 50-kev photons per 100 disintegrations of AcK and 24 of the 80-kev photons per 100 disintegrations. This calculation assumes that the variation in the ratio of the escape peak to the photopeak in the 50–80 kev range as a function of energy is negligible. Actually this is not true, but unpublished experimental results of F. Asaro using the identical apparatus and geometrical conditions indicate that the variation is not great. Asaro obtained a ratio of the observed escape peak to the observed photopeak of 20 percent at 50 kev dropping to 16 percent in the region 60–100 kev. Hence, the corrections to the above quoted abundances are only a few percent at most.

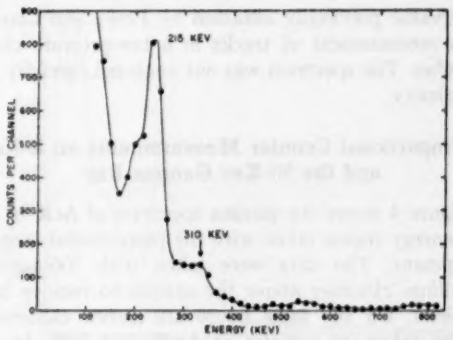


FIG. 3. Gamma curve showing 215-kev and 310-kev radiation in AcK sample. Data taken through 943-mg/cm² beryllium absorber.

### 2. 215- and 310-Kev Gamma Rays

Figure 2 shows the gamma spectrum from 0–800 kev. It is to be noted that some gamma radiation appears in the region of 215 kev in low abundance compared to the 50- and 80-kev radiation. There is no other radiation with abundance > 1 percent with respect to these peaks and additional curves showed this to be true through the 2-Mev range. The gamma radiation in the region of 215 kev was studied more carefully as shown in Fig. 3, after calibrating the energy scale with annihilation radiation from a $Na^{22}$ sample and with the 662-kev gamma radiation of $Cs^{137}$. A definite photopeak at 215 kev and a smaller peak at 310 kev were observed. The decay of these peaks was followed on numerous separately prepared samples to establish the 21-minute half-life. The ratios of these photopeaks to the 50-kev photopeak was determined correcting for the fact that the photoelectric efficiency of the crystal was not 100 percent for the 215- and 310-kev radiation. The absolute abundances were determined as 3–4 photons of 215-kev energy per 100 disintegrations and about 0.8 photon of 310-kev energy per 100 disintegrations of AcK.

### 3. Beta Spectrum

Several determinations of the maximum energy of the beta particles emitted by pure samples of AcK were made using the anthracene crystal. A visual end-point energy was 1.15±0.05 Mev. This confirms the 1.2±0.1

Mev value previously obtained by Perey and Lecoin[7] by a measurement of tracks in a low-pressure cloud chamber. The spectrum was not analyzed carefully for complexity.

## 4. Proportional Counter Measurements on X-Rays and the 50-Kev Gamma Ray

Figure 4 shows the gamma spectrum of AcK in the low-energy region taken with the proportional counter equipment. The data were taken with 706-mg/cm² beryllium absorber above the sample to remove beta particles. On the same figure are shown calibration curves taken on samples of $Am^{241}$ and $Io^{230}$. In the $Am^{241}$ curve are observed the prominent $L\alpha_1$ (13.94-kev)

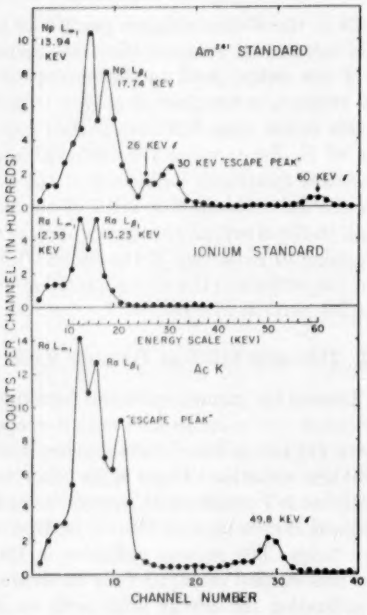


FIG. 4. X-ray and soft gamma spectrum of AcK taken with proportional counter connected to 50-channel pulse-height analyzer. Calibration runs on $Am^{241}$ and ionium are shown. The AcK sample was mounted on aluminum. 706-mg/cm² beryllium absorber was placed above sample to absorb $\beta^-$ particles.

and $L\beta_1$ (17.74-kev) lines of neptunium, a 26-kev gamma peak, and an "escape" peak at 30 kev caused by the photoelectric ejection of a $K$ electron from a xenon atom in the counter by the 59.8-kev gamma ray followed by the escape of the $K_\alpha$ x-ray of xenon from the tube. The ionium curve shows the prominent $L\alpha_1$ (12.39-kev) and $L\beta_1$ (15.23-kev) lines of radium. It can be noted that AcK gives rise to identical radium $L$ x-rays as well as to an escape peak at 20 kev resulting from the 50-kev gamma ray.

That this identification of the escape peak is correct was proved by redetermining the curve with a 1-g/cm²

[7] M. Perey and M. Lecoin, J. phys. et radium 7, 439 (1939).

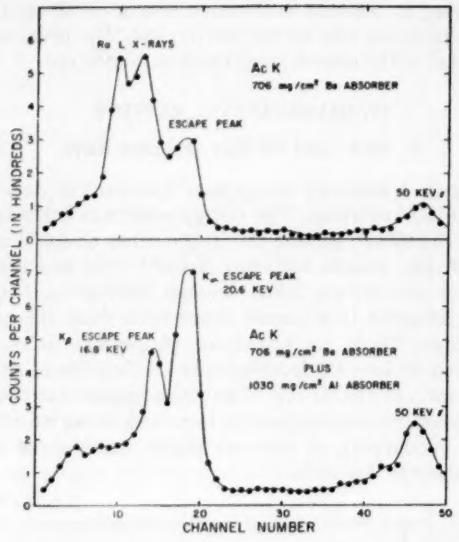


FIG. 5. X-ray and soft gamma spectrum of AcK taken with proportional counter connected to 50-channel pulse-height analyzer. Lower curve taken through 1032-mg/cm² aluminum absorber to absorb $L$ x-rays. Resulting peaks are the escape peaks of the 49.8-kev gamma ray with escape of the $K_\alpha$ or $K_\beta$ radiation of xenon. Data were taken for 1 minute for upper curve and for 4 minutes for lower curve.

aluminum absorber over the sample. The transmission of the x-rays through this thickness of aluminum is <0.1 percent while the transmission of the 50-kev gamma radiation is about 70 percent. A typical curve is shown in Fig. 5. The energy scale was calibrated with $Am^{241}$ and $Io^{230}$ as before. To be noted is the appearance of a double escape peak attributable to the escape of $K\alpha_1$ and $K\beta_1$ xenon x-radiation after absorption of the 50-kev gamma ray. These escape peaks serve as a better energy calibration than the sodium iodide crystal determinations of this value for the 50-kev gamma ray. The average of several determinations is 49.8±0.3 kev.

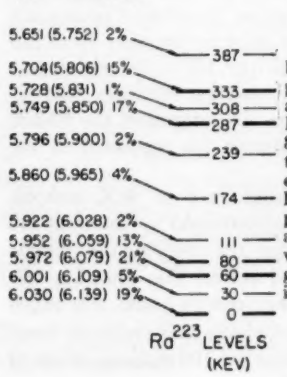


FIG. 6. $Ra^{223}$ levels reached by alpha decay of $Th^{227}$. Alpha particle energies (in Mev) and abundances as reported by Rosenblum *et al.* (see reference 8) are shown. Figures in parentheses are alpha disintegration energies (i.e., the recoil energy has been added to the alpha-particle energy). The accentuated $Ra^{223}$ levels are those which are reached by alpha groups greater than 10 percent in abundance.

### 5. Coincidence Studies on AcK

AcK samples mounted on quarter mil aluminum foils were placed between the two sodium iodide crystals of the coincidence apparatus and gamma-gamma coincidence spectra were run, gating in turn with the 50-, 80-, and 215-kev radiation. These measurements were performed by Mr. Frank Stephens. Some small coincidence peaks were observed but the order of intensity of these was very low. The 50–80 kev gamma-gamma coincidence peak was less than 1/100 of that to be expected if these rays were in coincidence. The 215–50 kev and 215–80 kev coincidences, with the 215 kev serving as the gate, were less than 1/30th of those to be expected of a true gamma-gamma coincidence. Of considerable importance to the consideration of various possible decay schemes is the presence or absence of a 50–30 kev coincidence or a 50-kev $L$ x-ray coincidence, the $L$ x-rays coming from the conversion of a 30-kev gamma ray. The absorption of the soft x-rays in the crystal cover and the fluorescence yield reduce the sensitivity of this determination considerably, but the intensity was conservatively a factor of 5 too low to indicate a 50-kev $L$ x-ray coincidence and within considerable larger limits there was no sign of a 50–30 kev gamma-gamma coincidence. The significance of this is that the 50- and 80-kev transitions must both lead to the ground state of $Ra^{223}$.

### 6. Study of Radiations of $Th^{227}$

Since $Th^{227}$(RdAc) and AcK decay to the same daughter product, it might be expected that some $Ra^{223}$ levels would be common to the decay schemes of both isotopes. In particular, levels with the 50- and 80-kev spacing of the two most prominent gamma rays in the decay of AcK might be expected among the lower-lying levels of $Ra^{223}$. The alpha spectrum of $Th^{227}$ is exceedingly complicated with 11 reported groups of greater than 1 percent abundance. Figure 6 displays the results of a study of the alpha groups carried out by Rosenblum *et al.*[8] The $Ra^{223}$ levels are labeled in kev above the ground state, if one makes the assumption that the most energetic alpha particle leads to the ground state, an assumption which may be false since alpha decay to the ground state of an odd-nucleon isotope is frequently more hindered than that to a higher-lying level.[9]

There are several literature reports on the gamma rays of $Th^{227}$. The absorption curve studies of Riou[10] showed a 50-kev gamma ray in 3 percent abundance, a 126-kev gamma ray in 13 percent abundance, and a 280-kev gamma ray in 50 percent abundance. Similar

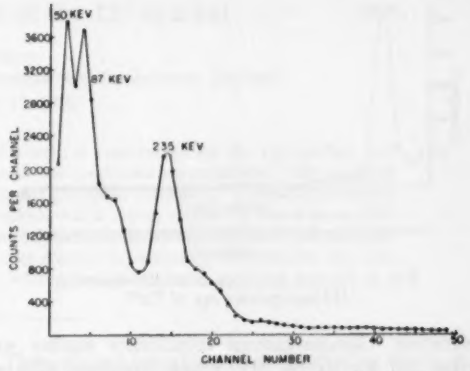


FIG. 7. Gamma spectrum of $Th^{227}$ as determined on sodium iodide crystal spectrometer in 0–800 kev region.

results were reported by Bachelet and Savel.[11] Studies on a crystal spectrometer were reported somewhat earlier by Frilley[12] who found gamma rays at 50, 57, 80, 101, 113, 119, 208, 240, and 258 kev. Magnetic analysis of the electron spectrum by Surugue,[13] and Te-Tschao and Surugue[14] showed 30 gamma rays between 30 and 638 kev.

Figures 7 and 8 indicate the gamma spectrum of a freshly purified sample of $Th^{227}$ as obtained in our sodium iodide crystal spectrometer. The sample was purified by extracting the thorium isotope from a dilute acid solution of $Ac^{227}$ into undiluted tributyl phosphate and washing the solvent repeatedly with 4$M$ nitric acid to remove possible radioactive contaminants. The most prominent photopeaks appear at 50, 87, and 235 kev. The last energy was determined to $\pm 5$ kev by calibration with the 662-kev gamma ray in the decay of $Cs^{137}$, annihilation radiation, the 59.6-kev gamma ray of $Am^{241}$, and the 184-kev gamma ray of $U^{235}$. The absolute abundance of the 50-kev gamma ray was determined to be $0.15 \pm 0.05$ photon per dis-

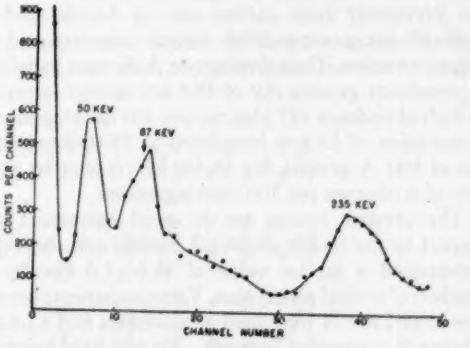


FIG. 8. Gamma spectrum of $Th^{227}$ in 0–300 kev region.

[8] Rosenblum, Perey, Valadares, and Guillot (private communication, October, 1952) as reported in Table of Isotopes by Hollander, Perlman, and Seaborg, Revs. Modern Phys. **25**, 469 (1953).
[9] Perlman, Ghiorso, and Seaborg, Phys. Rev. **77**, 26 (1950).
[10] M. Riou, J. phys. et radium **11**, 185 (1950).
[11] M. Bachelet and P. Savel, Cahiers phys. No. 19, 51 (1944).
[12] M. Frilley, J. phys. et radium **1**, 34 (1940).
[13] J. Surugue, thesé, Paris, 1936 (unpublished).
[14] Ouang Te-Tchao and J. Surugue, Compt. rend. **218**, 591 (1944).

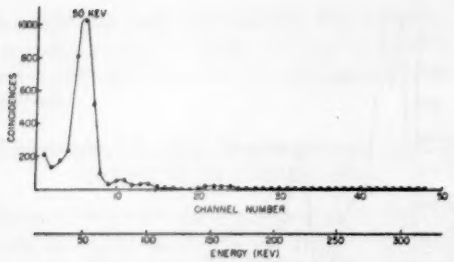


FIG. 9. Gamma spectrum in coincidence with 235-kev gamma ray of $Th^{227}$.

integration. Gamma-gamma coincidence studies were carried out for us by Mr. Frank Stephens with the equipment described previously, gating in turn with the 50- and 235-kev gamma rays. Figure 9 shows a prominent coincidence peak between the 50- and 235-kev radiations. This coincidence is so prominent and so easily reproduced that it has been found to be quite useful in our laboratory as a standard for other gamma-gamma coincidence studies. In the run with the 50-kev gate some coincidence peaks at ~90 and ~140 kev of much lower intensity (~1/20) were observed.

It seems likely that the 50-kev gamma ray is identical with the 49.8-kev gamma ray of AcK and this belief was strengthened by determining the energy of the gamma ray in the proportional counter. The $K_{\alpha 1}$ and $K_{\beta 1}$ escape peaks were determined as described above for AcK and as illustrated in Fig. 5. Freshly purified samples of $Th^{227}$ and of AcK were counted through 1 g/cm² of aluminum absorber within a few minutes of each other to eliminate any errors due to a drift in the calibration of the proportional counter. The curves of the escape peak were both identical with Fig. 5. It is believed that a difference of 1 kev could easily have been detected.

## V. DISCUSSION

A detailed study of the radiations of $Ac^{227}$ and AcK has previously been carried out by Lecoin and co-workers[2] using xenon-filled Geiger counters and absorption curves. Their findings on AcK were as follows. A prominent gamma ray of 48.6-kev energy is emitted in high abundance (27 photons per 100 disintegrations). $L$ radiation of 15 kev is emitted in 25 disintegrations out of 100. A gamma ray of 330 kev is emitted at the rate of 6 photons per 100 disintegrations.

The present results are in good agreement with respect to the 50-kev radiation. Lecoin and co-workers determined a precise value of 48.6±1.6 kev by the method of critical absorption. Various elements between $Z=53$ and $Z=74$ were used as absorbers and a marked change in absorption between $_{63}$Eu and $_{64}$Gd bracketed the gamma energy. The quoted value could be raised somewhat as the recent "Table of Critical X-Ray Absorption Energies" of Hill *et al.*[15] give 48.51 and 50.23 kev for the $K$ shell energies of europium and gadolinium. Our best value determined from the escape peak values as mentioned above is 49.8±0.3 kev.

The French authors also bracketed the 14.5-kev radiation by the method of critical absorption using $_{33}$As, $_{34}$Se, and $_{38}$Sr absorbers, and showed that it was the $L$ radiation of radium.

For radiation of energy greater than 50 kev the agreement between the two studies is not as good. The prominent radiation of 80–85 kev is not reported by Lecoin and co-workers.[2] The gamma ray of 330 kev reported by these authors with an intensity of 6 photons per 100 disintegrations may perhaps be identified with the 215-kev radiation with an intensity of 3–4 photons per 100 disintegrations, reported here since energy determinations by absorption measurements have a tendency to give high values.

It may be mentioned that the 80-kev radiation reported here is not $K$ x-radiation since the $K_{\alpha 1}$ and $K_{\alpha 2}$ lines of radium would be expected at 88.5 and 85.4 kev, although it is quite possible that some $K$ radiation is included in the high energy side of the 80-kev peak.

It was hoped that the gamma rays of AcK could be fitted into a decay scheme using the $Ra^{223}$ levels revealed by alpha-spectrum analysis of RdAc (Fig. 6) and consistent with the gamma radiation of $Th^{227}$. The chief facts which must be taken into account are: (1) The 49.8 and 80-kev gamma rays observed in the decay of AcK connect low-lying levels in $Ra^{223}$; (2) The 49.8-kev gamma ray is not in coincidence with 80-kev radiation, 30-kev gamma radiation or $L$ x-radiation; (3) The same 49.8-kev gamma transition is observed in the decay of AcK and RdAc ($Th^{227}$); (4) In the decay of RdAc the 49.8-kev gamma ray is in coincidence with a 235-kev gamma ray.

It was impossible to construct a partial decay scheme consistent with these data using only the levels of Fig. 6. It is necessary to postulate other low-lying levels and it is possible that the ground state of $Ra^{223}$ lies below the level so labeled on Fig. 6. This is not unreasonable in view of the well-established fact that alpha decay to the ground state is usually strongly hindered for alpha emitters with odd nucleons.[9] Further work to give more definite information on the low-lying levels of $Ra^{223}$ is contemplated.

## ACKNOWLEDGMENTS

Acknowledgment is made to A. Ghiorso and A. E. Larsh for the use of the spectrometer equipment. Also, thanks are owing to F. Stephens and F. Asaro for major assistance in the performance of the gamma-gamma coincidence experiments on their coincidence equipment.‡

[15] Hill, Church, and Mihelich, Rev. Sci. Instr. 23, 523 (1952).

‡ *Note added in proof.*—This paper was completed before the author read a recent paper by Frilley and co-workers, J. phys. et radium 15, 45 (1954). These authors discuss some new detailed studies of the low-energy conversion electrons of $Th^{227}$ and give a tentative partial decay scheme showing the 50-kev gamma ray to originate at the level labeled 80 kev in our Fig. 6. This assignment may be correct, but we are inclined to question it for the reasons discussed above.

# The Symmetry Relations of the 12$j$ Symbol

R. J. ORD-SMITH
*Department of Mathematics, University of Southampton, Southampton, England*

(Received January 15, 1954)

A triangular-condition diagram in the form of a Möbius strip is constructed for the 12$j$ symbol, and those geometrical transformations of the strip which preserve the conditions are considered. This suggests a revised notation for the 12$j$ symbol which exhibits clearly the triangular conditions. The transformations of the strip suggest a complete set of sixteen symmetry relations, which can be verified by use of an explicit expression for the symbol. In the new notation the symmetry relations are obtained easily as simple manipulative rules. The positions of the elements in the symbol also display the difference between the two sets of elements of the symbol with respect to degeneration by setting one element zero.

THE 12$j$ symbol was defined in an addendum to the note on the 9$j$ symbol by Hope and Jahn[1] by the relation

$$\frac{\langle\{r,(ab)e\}p,(cd)f,sm|\{r,(ac)g\}q,(bd)h,sm\rangle}{\{[e][f][g][h][p][q]\}^{\frac{1}{2}}}=\begin{Bmatrix}a&b&e&p\\c&d&f&q\\g&h&r&s\end{Bmatrix},$$

where $[e]=2e+1$, $\cdots$, etc.

An explicit expression as a sum over a 9$j$ and two 6$j$ symbols was given. An equivalent expression as the sum over four 6$j$ symbols has been given by J. P. Elliott (unpublished) as

$$(-1)^R\sum_x(-1)^{-x}[x]\begin{Bmatrix}b&c&x\\g&e&a\end{Bmatrix}\begin{Bmatrix}g&e&x\\p&q&r\end{Bmatrix}\begin{Bmatrix}p&q&x\\h&f&s\end{Bmatrix}\begin{Bmatrix}h&f&x\\c&b&d\end{Bmatrix},$$

where $R$ is the sum of the twelve elements of the symbol.

The eight triangular conditions which appear in the transformation can be represented by a diagram (Fig. 1) in the form of a Möbius strip. The conditions are given by the intersections at the vertices. The following geometrical transformations of the strip preserve these conditions: The strip may be reflected in a horizontal plane which bisects it. The strip may be reflected in a vertical plane through the twist and which bisects it. The strip may be rotated through 180° about the common line of these planes. The strip may be distorted by moving the twist round into the successive spaces between the vertical lines.

These sixteen transformations (including the identity) of the Möbius strip suggest:

(a) The revised notation for the 12$j$ symbol,

$$\begin{Bmatrix}a&b&e&p\\c&d&f&q\\g&h&r&s\end{Bmatrix}=\begin{Bmatrix}p&r&e&b&h\\q&g&a&c&d&f&s\end{Bmatrix},$$

which exhibits the eight triangular conditions: $(p,r,e)$, $(e,a,b)$, $(b,d,h)$, $(h,s,q)$, $(q,r,g)$, $(g,a,c)$, $(c,d,f)$, $(f,s,p)$.

(b) The sixteen symmetry relations, which may be verified by Elliott's formula, and which appear as simple manipulative rules in the new notation in closer line with the notation of Wigner for the 6$j$ and 9$j$ symbols:

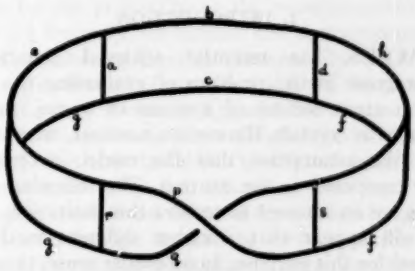

FIG. 1. Triangular-condition diagram in the form of a Möbius strip.

$$\begin{Bmatrix}p&r&e&a&b&d&h\\q&g&c&&&f&s\end{Bmatrix}=\begin{Bmatrix}q&r&g&e&c&d&f\\p&&a&b&&h&s\end{Bmatrix}=\begin{Bmatrix}q&s&h&f&d&b&e\\p&&&c&a&&g&r\end{Bmatrix}=\begin{Bmatrix}p&s&f&d&c&a&g\\q&&h&&b&&e&r\end{Bmatrix}$$

$$=\begin{Bmatrix}e&b&h&q&p\\g&a&c&d&f&s&&r\end{Bmatrix}=\begin{Bmatrix}g&c&f&p\\e&a&b&d&h&s&q&r\end{Bmatrix}=\begin{Bmatrix}g&q&h&b\\e&p&f&d&c&a\end{Bmatrix}=\begin{Bmatrix}e&p&f&c\\g&q&h&d&b&a\end{Bmatrix}$$

$$=\begin{Bmatrix}b&h&q&g\\c&d&f&s&p&r&e&a\end{Bmatrix}=\begin{Bmatrix}c&f&p&e\\b&d&h&s&q&r&g&a\end{Bmatrix}=\begin{Bmatrix}c&g&q&h\\b&a&e&r&p&s&f&d\end{Bmatrix}=\begin{Bmatrix}b&e&p&f\\c&a&g&r&q&s&h&d\end{Bmatrix}$$

$$=\begin{Bmatrix}h&q&g&c\\f&s&p&r&e&a&b&d\end{Bmatrix}=\begin{Bmatrix}f&p&e&b\\h&s&q&r&g&a&c&d\end{Bmatrix}=\begin{Bmatrix}f&c&g&q\\h&d&b&a&e&r&p&s\end{Bmatrix}=\begin{Bmatrix}h&b&e&p\\f&d&c&a&g&r&q&s\end{Bmatrix}.$$

[1] H. A. Jahn and J. Hope, Phys. Rev. 93, 318 (1954).

These symmetry relations show the equivalence in the positions occupied by the elements $r$, $a$, $d$, and $s$, and of the positions occupied by the elements $p$, $e$, $b$, $h$, $q$, $g$, $c$, and $f$. These two sets of positions differ from each other and this is shown by the different way in which the $12j$ symbol degenerates with one element zero in either type of position:

$$\begin{Bmatrix} e & 0 & e & a & b & d & h \\ g & g & a & c & d & f & s \end{Bmatrix} = \begin{Bmatrix} a & b & e \\ c & d & f \\ g & h & s \end{Bmatrix} \div \{[e][g]\}^{\frac{1}{2}},$$

$$\begin{Bmatrix} 0 & e & a & b & d & h \\ q & g & c & d & f & f \end{Bmatrix} = \frac{(-1)^{a+b+c+d+e+f+2q}}{\{[e][f]\}^{\frac{1}{2}}} \begin{Bmatrix} b & c & q \\ g & e & a \end{Bmatrix} \begin{Bmatrix} h & f & q \\ c & b & d \end{Bmatrix}.$$

The author is indebted to Professor H. A. Jahn for his help and encouragement, and to the Department of Scientific and Industrial Research for a scholarship, which have made this work possible.

The author would also like to thank Dr. J. P. Elliott for permission to quote his formula.

PHYSICAL REVIEW VOLUME 94, NUMBER 5 JUNE 1, 1954

# The Scattering of Neutrons by Systems Containing Light Nuclei*

G. C. WICK
*Carnegie Institute of Technology, Pittsburgh, Pennsylvania, and Institute for Advanced Study, Princeton, New Jersey*
(Received January 21, 1954)

The general expression for the slow-neutron cross section of a molecule is cast in a form which allows an explicit formulation of the assumption, that the duration of the collision is short compared to the natural periods of the molecule. It is shown that the assumption allows one to extend Placzek's results to molecules containing light nuclei, with only minor modifications. The limits of validity of the assumption are discussed, and the possibilities of exceptions are studied in detail on some examples.

## 1. INTRODUCTION

PLACZEK has recently[1] achieved considerable progress in the problem of evaluating the slow-neutron cross section of systems of nuclei, such as molecules or crystals. His results, however, are obtained under the assumption that the nuclei involved are heavy compared to the neutron. The following calculations are an attempt to remove this limitation.

It will appear that a rather different method is required for this purpose. In a broader sense, therefore, the present calculations may be offered as a contribution to the general technique for handling the scattering of a particle by a weakly bound system, when particles of comparable mass are involved.[2] The slow-neutron case here selected for study possesses, of course, some simplifying features (such as the constancy of the scattering length of each individual nucleus) the absence of which in other cases of interest may well restrict considerably the possibilities of the method here described.

In the following, the scattering system of nuclei will be referred to as a "molecule," although more complex systems may be implied. The reader is referred to Placzek's paper for all preliminaries; we shall borrow formulas and symbols from that paper without further explanation. We shall save some writing, however, by using units such that $\hbar=1$, and $m$ (mass of the neutron) $=1$. This removes the need of a special symbol $\mu$ for the ratio $M/m$ of nuclear mass to neutron mass.

The slow-neutron cross section $\sigma$ of a molecule is in general a complicated function of the energy $E_0$ of the neutrons; in particular the slope of this function changes abruptly whenever $E_0$ attains the threshold for the excitation of a new level of the molecule. The results of Placzek indicate, however, that when $E_0$ becomes large compared to the level spacing $\Delta$ of the scattering system, those changes in slope become negligible, so that $\sigma$ becomes a smooth function of $E_0$ which can be represented by means of simple asymptotic formulas.[3] For example in the case of a single nucleus, $\sigma(E_0)$ can be given as an expansion in falling powers of $E_0$, Eq. P(5.16).

In his argument, however, Placzek makes use of the fact that for a molecule composed of heavy nuclei the energy transfer is in general small (of the order $M^{-1}$) compared to the initial kinetic energy of the neutron. It is clear that this circumstance has a decisive role in preventing the excitation of any high level of the molecule from being felt in the total cross section until $E_0$ is well above the threshold for that particular level. Clearly this is a sufficient reason why no noticeable discontinuities in slope should occur. Placzek's calculations on heavy nuclei, therefore, offer no guarantee that a simple extension of his formulas to light nuclei is possible. This circumstance is strikingly illustrated

* Work partially supported by the Office of Ordnance Research.

[1] G. Placzek, Phys. Rev. 86, 377 (1952). This paper will be referred to with the abbreviation P, for example, in quoting formulas, thus: Eq. P(5.16).

[2] We have in mind, in particular, the high energy problems mentioned in reference 5.

[3] See also A. M. L. Messiah, Phys. Rev. 84, 204 (1951).

by the behavior of the cross section of a harmonically bound nucleus[4]; this case, because of its peculiar interest, will be again discussed in Sec. 4 of this paper.

In order to investigate the case of light nuclei it is necessary to perform the summation over the excited state $b$ of the molecule, without first resorting to an expansion in powers of the fractional energy transfer, Eqs. P(2.10), P(3–4), P(3.5). This may be done by means of a "symbolic method,"[5] leading to Eq. (3) below. Our problem is to find a suitable expansion of this expression.

## 2. BASIC FORMULAS AND ASSUMPTIONS

The total neutron cross section of the molecule in the state $a$ is given by P(1.1) based on Fermi's modified Born approximation. Notice that the summation over state $b$ is unrestricted. An essential role in this expression is played by the operator $F$, which according to P(1.2) is a linear combination, with coefficients $a_s$, of exponential operators corresponding to the transfer of a momentum $\kappa$ to the $s$th nucleus. Instead of $F_a{}^b$ for the matrix element P(1.4) we use the slightly more conventional notation $F_{ba}$. Using the Fourier representation of the $\delta$ function we write P(1.1) in the form

$$\sigma^{(a)}=(2\pi k_0)^{-1}\sum_b\int d\boldsymbol{\kappa}\int_{-\infty}^{+\infty}dt\,|F_{ba}|^2 \times\exp\{it(\tfrac{1}{2}\kappa^2-\boldsymbol{\kappa}\cdot\mathbf{k}_0+E_b-E_a)\}. \quad (1)$$

By means of the Hamiltonian operator P(7.1) we can write

$$e^{-itE_a}F_{ba}=(Fe^{-itH})_{ba}, \quad (2a)$$

$$e^{itE_b}(F_{ba})^*=(F^*e^{itH})_{ab}, \quad (2b)$$

$F^*$ being the Hermitean conjugate of $F$. The summation over $b$ is now simply a matrix multiplication, so that

$$\sigma^{(a)}=(2\pi k_0)^{-1}\int d\boldsymbol{\kappa}\int_{-\infty}^{+\infty}dt G_{aa}\exp[it(\tfrac{1}{2}\kappa^2-\boldsymbol{\kappa}\cdot\mathbf{k}_0)], \quad (3)$$

where $G_{aa}$ is the expectation value in the state "$a$" of the operator

$$G=F^*e^{itH}Fe^{-itH}=F^*(0)F(t), \quad F(t)=e^{itH}Fe^{-itH}. \quad (4)$$

These expressions are deceptively simple, since they are exact, and hence contain implicitly all the possible intricacies of the problem. We shall reduce them to a more truly simple form, by means of an approximation valid for large values of the neutron momentum $k_0$.

Such an approximation suggests itself naturally, if one examines the expressions (3) and (4) more carefully. The expectation value $G_{aa}$ can be recognized as a correlation function between momentum transfers $\kappa$ (operator $F$) and $-\kappa$ (operator $F^*$) applied $t$ seconds apart from one another. At first sight it may seem surprising that such a time lag between two momentum transfers should play any role at all in a first-order Born calculation, which essentially expresses the idea that the collision is effected in a single elementary interaction. In fact the presence of two transfer operators in the formulas appears to be merely the trivial result of the circumstance that the amplitudes of the partial scattered waves have to be squared to yield cross sections. A different viewpoint will be taken, however, after due consideration of the so-called optical theorem, according to which the total cross section is also related linearly to the imaginary part of the forward elastic scattered wave.

For obvious reasons, when proceeding in this manner, the lowest-order cross section in the Born method is obtained from the second Born approximation to the elastic amplitude. Now this has a bearing on our question in two respects. First, if $\sigma^{(a)}$ is calculated in this way, one gets, we think, a better insight into the reason for the possibility of the transformation from (1) to (3). Secondly, the formula now appears connected with the following physical picture. The total cross section is a measure of the attenuation of the neutron's DeBroglie wave in crossing a space filled with molecules. The optical theorem merely expresses the fact that the attenuation is due to destructive interference of the incident wave with the secondary coherent waves emitted in the forward direction by each molecule. The second-order process leading to forward elastic scattering is the successive transfer to the molecule of two equal and opposite momenta, the two elementary interactions being now physically related parts of a single process; it is thus not surprising that the time interval between the two should appear explicitly in the formulas.

In the second Born approximation the two interactions mark the beginning and the end of the collision, and $t$ may thus be properly viewed as the "collision time." The explicit appearance of this time in the formalism is perhaps the main advantage of Eq. (3). For it suggests at once an approximation based on the plausible physical idea that, for sufficiently large values of $k_0$, the duration of the collision must be short, and on the resultant assumption that large values of $t$ do not give a significant contribution to the integral over $t$ in Eq. (3). This specific assumption will be called for brevity the "short collision time approximation."

It is fitting to admit at this point, that having in Eq. (3) a complete mathematical statement of the problem, we should now supply, instead of a physical

[4] G. Placzek, Nuovo cimento (to be published). A brief qualitative statement of Placzek's result may be found in A. M. L. Messiah, J. phys. et radium **12**, 670 (1951).

[5] A. Akhiezer and I. Pomeranchuk, J. Phys. (U.S.S.R.) **11**, 167 (1947). My attention to this method was drawn in the course of conversations with Dr. Placzek and Dr. Chew. In particular I am indebted to Dr. Chew for showing me some unpublished calculations of his on the cross section of light nuclei for very energetic neutrons, following lines very similar to those in Sec. 3 of this paper.

plausibility argument, a formal proof that (3) has indeed the property postulated above. This, however, we are unable to do in a general manner. In fact we shall even find an interesting exception to the assumption, in the case of a harmonically and isotropically bound nucleus of mass $M=1$.

Nevertheless we believe that, apart from this rather unique exception, the assumption is fundamentally correct; the remaining part of this section will be devoted to a summary of all the arguments, besides physical plausibility, which can be brought forward in support of the assumption.

In Sec. 3 we shall examine the dependence on $t$ of the integrand of (3) by means of an expansion valid from $t=0$ up to values large compared to $E_0^{-1}$ but small compared to the natural periods of the molecule ($\sim\Delta^{-1}$ in Placzek's notation). Unfortunately this analysis tells us nothing about still larger values of $t$. Within the region examined, however, the short collision time assumption is fully confirmed. Indeed the integral over $t$ converges rapidly as soon as $t\gg E_0^{-1}$.

The assumption receives further support from a study (Sec. 4) of the special case of a harmonically bound nucleus, which, because of its simplicity, lends itself to a detailed and rigorous treatment. Here an explicit analytical expression can be given for the integrand of (3), and the integration over $\varkappa$ can be carried out exactly. The remaining integration over $t$ is then indeed found to possess the property postulated above, provided $M\neq 1$.

For an isotropic harmonic oscillator of mass $M=1$ the short collision time approximation breaks down, in the sense that, in addition to a small neighborhood of $t=0$ (which contributes the main term, i.e., the free $n$-$p$ cross section, plus the "normal" terms in $E_0^{-1}$, $E_0^{-3}$, etc.), also small intervals around $t=\pm T$, $\pm 2T$, $\cdots$ ($T$ being the oscillator's natural period) give significant contributions. This is just the kind of thing that the analysis of Sec. 3 could never reveal. Its significance for the general case thus requires careful consideration.

In addition it is noteworthy that the breakdown of the approximation for $M=1$ is directly connected (see Sec. 4) with the anomalous oscillatory behavior of the cross section, as a function of the energy, discovered by Placzek. This is indeed not very surprising; it is a well-known fact, often discussed, for example, in the theory of resonance cross sections, that rapid variations of a cross section, over a small interval $\Delta E$, are associated with phenomena involving long collision times, namely $t\sim\Delta E^{-1}$ as required by complementarity.

We may legitimately ask what the nature of the process is, which leads to long collision times in the present case. It turns out that a quite simple and convincing answer is possible in terms of the ding-dong picture of formula (3) developed above in connection with the optical theorem. It is clear in fact that the collision time can be long if, and only if, the neutron is left with almost zero velocity after the first momentum transfer. This is precisely possible if $M=1$, in a head-on collision (notice that the nucleus is assumed to be in the ground state before the collision; therefore it has only a small initial velocity). After the first collision[6] the nucleus swings with a large amplitude; the second collision can occur either immediately, or after 1, 2, 3$\cdots$ periods, when the nucleus passes again near the initial position (where it left the neutron at rest) and with the right direction of motion to kick the neutron again in the forward direction.

This picture also explains in a very simple manner various other features of the problem. For example it clearly shows why already for $M=2$ the importance of the longer collision times is rapidly damped with increasing energy (Sec. 4). Going back to $M=1$, it shows why the Placzek oscillation phenomenon is strongly reduced (it appears only in terms of higher order than $E_0^{-1}$) if the oscillator is anisotropic (Appendix 2). In fact in this case the nucleus, after being kicked, will perform a Lissajous motion which does not bring it back to the origin until a condition $t\approx n_1T_1\approx n_2T_2\approx n_3T_3$ is satisfied, where $T_1$, $T_2$, $T_3$ are the three different periods, and $n_1n_2n_3$ are three integers. Clearly this makes a delayed second collision much less probable.

These intuitive considerations can now be extended to other cases, in order to show that the exception of the isotropic harmonic oscillator is rather unique. Consider for example an isotropic but slightly anharmonic oscillator. Even starting from the more conventional formula (1) it is possible to argue that the cross section at high energies will oscillate far less than in the exactly harmonic case. In the latter case, in fact, the large oscillation is obviously tied to the high degeneracy of the levels. If the oscillator is anharmonic this degeneracy is removed (only the $2l+1$ degeneracy due to angular momentum conservation is left) with the result that the levels are much more closely spaced.[7] Hence also the kinks in the cross section diagram which occur at each possible excitation energy will be more closely spaced with the result that the curve is much closer to a smooth function. Now reverting to our time-

[6] The first collision is represented by the first operator from the right, i.e., $F$, the second by $F^*$. For the sake of simplicity we are assuming in the text that the integral is over negative values of $t$ only. This would give, apart from a factor $i$, the full forward scattered wave, instead of the imaginary part thereof.

[7] One can, of course, point out that not all levels can be easily excited in a collision. If the ground state is spread over a region of dimensions $\sim(M\omega)^{-\frac{1}{2}}$ and a momentum $\varkappa$ is transferred to the nucleus, only angular momenta up to $l_{\text{exc}}\sim\varkappa(M\omega)^{-\frac{1}{2}}$ can be excited. On the other hand, treating the oscillator as nearly harmonic, the state of energy $\varkappa^2/2M\approx n\omega$ contains angular momenta up to $l_{\max}\sim n$. Hence, $l_{\text{exc}}\sim l_{\max}^{\frac{1}{2}}$ apart from a numerical coefficient $\sim 1$. This means then, that while a level $n\omega$ of the harmonic oscillator splits into $n+1$ separate levels when the accidental degeneracy is removed by a small anharmonic term, only about $n^{\frac{1}{2}}$ of these appear as kinks in the $\sigma(E_0)$ function. While this is a considerable reduction, it still means that the amplitude of the oscillation decreases like $E_0^{-\frac{1}{2}}$, i.e., faster than the Doppler term.

dependent formalism, we have explained that the oscillations of the function are connected to the "long" collision times. Hence these must be relatively unimportant; our basic assumption must be essentially correct. In the double collision picture this can also be explained as follows. The difference between the harmonic and anharmonic case is that in the former case a wave packet always performs a strictly periodic motion; in the latter the wave packet undergoes the well-known diffusion phenomenon. Hence the probability that the nucleus hits again the neutron when it passes again near the initial position after one full oscillation is much reduced.

All of these arguments are admittedly only qualitative, but the gist of the matter seems to be that significant contributions from longer times (giving rise to "anomalous" asymptotic behaviors) may arise only for $M=1$. Furthermore, in the latter case, only for the isotropic harmonic oscillator does one find anomalies of the same order in $1/E_0$ as the Doppler term. In all other cases they are of a higher order. In the case of a molecule containing only heavy nuclei, moreover, we shall see that the approximation is exactly equivalent to the well-justified procedure of Placzek.

We now turn to the formal development of the preceding ideas, and in so doing we shall first examine (Secs. 3, 4) the "diagonal" terms in the cross section, i.e., the terms proportional to $a_s^2$ (see P, Sec. 7, Eq. P(7.13), etc.), postponing to Sec. 5 the discussion of the "nondiagonal" or "interference" terms, proportional to $a_{s'}\cdot a_s$ with $s'\neq s$. This separation is desirable not only for systematic reasons, but also and even more because the discussion is rather different in the two cases.

### 3. SINGLE NUCLEUS

For the sake of simplicity, we shall develop the treatment of a diagonal term for the example of a single nucleus bound by a fixed potential $V(r)$. The formula obtained is quite easily extended to the general case of a diagonal term, as is shown by the discussion in P; this point will be further elucidated at the end of this section.

Going back to Eqs. (3) and (4), and dropping the now useless index $s$ and the summation sign from the definition P(1.2) of the operator $F$, we shall ask for an expansion of the integrand, which exhibits the existence of an effective collision time, much shorter than the natural periods of the "molecule."

To this end we must identify within the integrand the strongly time-dependent factor or factors that are responsible for the shortness of the collision.

An obvious factor of this kind is the exponential of Eq. (3) which oscillates with a frequency given by

$$\Delta E=\mathbf{k}_0\cdot\boldsymbol{\kappa}-\tfrac{1}{2}\kappa^2=\tfrac{1}{2}k_0^2-\tfrac{1}{2}(\mathbf{k}_0-\boldsymbol{\kappa})^2, \qquad (5)$$

which is of course the energy lost by the neutron if it transfers a momentum $\boldsymbol{\kappa}$ to the nucleus. At this stage, however, $\Delta E$ is not the energy transfer which actually occurs, but an indeterminate quantity depending on the integration variable $\boldsymbol{\kappa}$. Similarly at this stage $\Delta E$ is not yet equal to the energy gained by the molecule, $\Delta E'=E_b-E_a$, the ultimate equality between the two being imposed upon them by the integration over $t$.

The justification for regarding the exponential factor as strongly time dependent is provided by the estimates $|\boldsymbol{\kappa}|\sim k_0$, $\Delta E\sim E_0=\frac{1}{2}k_0^2$, valid in the region of $\boldsymbol{\kappa}$ space which effectively contributes to the integral.[8] A simple example to show that this strongly oscillating factor, after integration over $\boldsymbol{\kappa}$, can indeed give a time dependence implying a finite and short collision time is provided by the case of infinitely tight binding; it is then easy to see that $G_{aa}=$ constant. Integration over $\boldsymbol{\kappa}$ then leaves an expression proportional to

$$\int t^{-1}e^{-iE_0t}dt,$$

which is indeed convergent at infinity and clearly indicates a collision time of the order of $E_0^{-1}$ (for the seeming divergence at $t=0$ see Sec. 4).

There are now cases in which $G_{aa}$, though not a constant, is a slow function of time and may be expanded in powers of $t$. The first term is then of the above type and gives the "bound" cross section $4\pi a^2$.[9] Furthermore, the successive terms reproduce the whole expansion in P exactly.[10] It is indeed quite obvious that the translation into our language of Placzek's assumption, that the energy transfer is $\ll E_0$, is the statement that the correlation function $G_{aa}$ is weakly time dependent.

In the case of light nuclei, of course, the assumption fails, i.e., the exponential in (3) is not the only rapidly variable term. In particular the elementary example of a free nucleus at rest, for which one has, apart from a proportionality factor $a^2$,

$$G_{aa}\sim\exp(i\hbar\kappa^2/2M), \qquad (6)$$

clearly indicates that the two factors in (3), namely the exponential and $G_{aa}$, are on very much the same footing. In the case of a bound nucleus, the analogy is slightly obscured, simply because of the different behavior of the two energy transfers $\Delta E$ and $\Delta E'$; while

[8] In this consideration it is essential that, since a time dependence is under discussion, the integration over $t$ has not been carried out. It is just for that reason that (contrary to a fairly common but slipshod formulation of the complementarity relationship for collisions) we cannot identify in general the $\Delta E$ that determines the time dependence (and hence the collision time according to the usual relation $t\sim\Delta E^{-1}$) with the actual energy transfer in the collision, or an average thereof. Clearly there is, for example, no reason why the collision time should become infinite when $M\to\infty$!

[9] More generally, for a molecule, the first term of the expansion of $G_{aa}$ in powers of $t$ gives Placzek's "static approximation," as one can see immediately.

[10] Again this is not hard to see, since an expansion of (4) in powers of $t$ is simultaneously an expansion in powers of the molecular excitation energies $E_b-E_a$, which is the essence of Placzek's expansion.

the former is a unique function (5) of the momentum transfer $\kappa$, the latter is not so, in general, so that $G_{aa}$ is a weighted sum of exponentials $e^{it\Delta E'}$ with all allowed values of $\Delta E'$.

For a fast incident neutron, however, that is, therefore, for large momentum transfers, we know on physical grounds, and from various examples, that the weights are strongly in favor of values in the neighborhood of

$$\Delta E' \approx \kappa^2/2M, \tag{7}$$

i.e., the transfer to a free nucleus which appears in (6).

Thus a natural extension of our previous assumption suggests itself, namely, that $G_{aa}$ is the product of the exponential in (6) times a slowly variable factor, which can be expanded in powers of $t$. It is also not difficult to make a rough guess about this latter factor. As we pointed out before, $G$, Eq. (4), is the product of two operators representing, respectively, momentum transfers $\kappa$ and $-\kappa$ to the nucleus but at different times, $t$ seconds apart. The first and most obvious effect of this time lag is the appearance of a phase factor such as (6) due to the temporary increase in energy (7) produced by the first "kick." Another obvious effect, however, is that, owing to the first kick, the wave packet representing the nucleus will be set in motion and travel a distance $\approx \kappa t/M$ in the time interval between the kicks. Since after the application of the second kick (which restores the average velocity of the wave packet approximately to its original zero value) we must take the scalar product of the resultant wave function with the original state, we see that the displacement suffered by the wave packet in the time $t$ will decrease the overlap integral by a factor roughly of the type

$$\exp(-\kappa^2 t^2/M^2D^2) = 1 - \kappa^2 t^2/M^2D^2 + \cdots, \tag{8}$$

if $D$ represents the average dimensions of the wave packet. Just such a term will in fact appear in the more detailed calculations of the next two sections. And it is worth noting that if $\kappa \gg D^{-1}$, i.e., if the momentum transfer is large compared to the average momenta of the nuclei in the initial bound state, the factor (8) may be regarded as slowly variable compared to (6). This allows one to use the expanded form on the right-hand side of (8).

It is now convenient to isolate a factor like (6) from the time dependence of $G$. This may be done as follows. The momentum transfer operator $\exp(i\boldsymbol{\kappa}\cdot\mathbf{r})$ may be used to generate a unitary transformation of the Hamiltonian

$$H' = \exp(-i\boldsymbol{\kappa}\cdot\mathbf{r})H\exp(i\boldsymbol{\kappa}\cdot\mathbf{r}) = H + L + \tfrac{1}{2}M^{-1}\kappa^2, \tag{9}$$

where

$$L = M^{-1}(\boldsymbol{\kappa}\cdot\mathbf{p}). \tag{10}$$

The same unitary transformation will transform a function of $H$: $f(H)$ into $f(H')$. Since $F = a\exp(i\boldsymbol{\kappa}\cdot\mathbf{r})$, we see that (4) becomes

$$G = a^2 e^{itH'} e^{-itH} = a^2 \exp(\tfrac{1}{2}it\kappa^2/M) e^{it(H+L)} e^{-itH}, \tag{11}$$

where our purpose is attained. Equation (3) becomes

$$\sigma^{(a)}/4\pi = (8\pi^2 k_0)^{-1} \int d\kappa \int g_{aa}(\kappa,t)\exp[il\alpha(\kappa)]dt, \tag{12}$$

where

$$\alpha(\kappa) = \tfrac{1}{2}\kappa^2(1+M^{-1}) - \boldsymbol{\kappa}\cdot\mathbf{k}_0 = \tfrac{1}{2}(1+M^{-1})\{(\mathbf{k}_r-\boldsymbol{\kappa})^2 - k_r^2\}, \tag{13}$$

$$\mathbf{k}_r = \mathbf{k}_0 M/(M+1),$$

and

$$g(\kappa,t) = a^2 e^{it(H+L)} e^{-itH}. \tag{14}$$

On the basis of previous considerations, we now expect (14) to be only weakly time dependent, compared to the exponential. In fact, if we neglect the time dependence of $g$ altogether, integration over $t$ gives $\delta[\alpha(\kappa)]$, which expresses energy conservation in a collision with a free nucleus at rest, an altogether reasonable first approximation.

We then proceed to expand:

$$g(\kappa,t) = \sum_{n=0}^{\infty} (it)^n g_n(\kappa)/n!, \tag{15}$$

where the coefficients are easily found[11] by means of the recursion formula and initial values:

$$g_{n+1} = g_n L + n g_{n-1}[H,L] + \tfrac{1}{2}n(n-1)g_{n-2}[H,[H,L]] + \cdots. \tag{16}$$

$$g_0 = a^2, \quad g_1 = a^2 L.$$

Before using (15) and (16) in Eq. (12) we must calculate expectation values of these operators in the state $a$. Furthermore we shall assume that the scattering system is randomly oriented. If necessary, this may be achieved by means of an average over states, Eq. P(3.8). Such an average will be implied by the notation $\langle\cdots\rangle$. One then gets, with the abbreviation $\langle g_n(\kappa)\rangle = s_n \equiv s_n(\kappa^2)$,

$$s_0 = a^2; \quad s_1/a^2 = \langle L\rangle = 0,$$

$$s_2/a^2 = \langle L^2 + [H,L]\rangle = \langle L^2\rangle = \kappa^2\langle p^2/3M^2\rangle = \tfrac{2}{3}(\kappa^2/M)\langle K\rangle,$$

$$s_3/a^2 = (\kappa^2/6M^2)\langle\nabla^2 V\rangle = B_{kn}\kappa^2/2M, \tag{17}$$

$$s_4/a^2 = \kappa^4\langle p^4/5M^4\rangle + (\kappa^2/3M^2)\langle(\nabla V)^2\rangle = (\kappa^2/M)^2\tfrac{4}{5}\langle K\rangle + (\kappa^2/M)C_{kn}.$$

These results include various simplifications; in the first place use is made of the fact that the expectation

[11] The easiest way to obtain (16) is to differentiate (14) thus: $dg/dt = ie^{it(H+L)}Le^{-itH} = igL(t)$, where $L(t) = e^{itH}Le^{-itH}$, and substitute (15) into the equation, using:

$$e^{itH}Le^{-itH} = L + it[H,L] + \tfrac{1}{2}(it)^2[H,[H,L]] + \cdots.$$

value, in a stationary state, of the time derivative $\dot{L}=i[H,L]$ vanishes. This applies also to $d^2L/dt^2=-[H,[H,L]]$ as well as to $L$ itself, since $L=[H,\boldsymbol{\kappa}\cdot\mathbf{r}]$ is also a time derivative. These remarks give at once the results for $g_1$ and $g_2$. The latter, however, was also averaged over the direction of $\boldsymbol{\kappa}$, which is allowed for randomly oriented systems. The calculation of $g_3$ and $g_4$ is more involved, but similar. $g_3$, for instance, contains a term $d^2L/dt^2$, which cancels as explained above, a term $L^3$, which cancels when one averages over the direction of $\boldsymbol{\kappa}$, and a term $\dot{L}L+2L\dot{L}$, which can be reduced to $\frac{1}{2}[L,\dot{L}]$ by using $\langle L\dot{L}+\dot{L}L\rangle=0$. The evaluation of the commutator leads to the result above. $g_4$ is handled in a similar manner.

With the notation P(5.7), (5.8), (5.9) we can also write

$$\begin{aligned} &s_1/s_0=0; \qquad s_2/s_0=(4/3)K_{\hbar}y, \\ &s_3/s_0=B_{\hbar}y; \quad s_4/s_0=(16/5)(K^2)_{\hbar}y^2+2C_{\hbar}y. \end{aligned} \tag{18}$$

The expressions $s_n$ play a similar role here as the expressions $S_n$ in Eqs. P(3.9), (3.10), and (18) is similar to P(5.6), but simpler. The reason the first terms on the right-hand side of P(5.6) are missing in (18) is that those terms merely represent the effect of the reduced mass factor, as explained by Placzek, an effect which is here separately included once and for all exactly in the exponent $\alpha(\kappa)$, Eq. (13).

When the cross section (12) is averaged over $a$ to produce isotropy (if necessary), and the Eqs. (15), (17), and (18) are used, the integration over $t$ can be performed for each term. The $n$th term is, apart from a factor,

$$I_n=\int s_n(\kappa^2)\delta^{(n)}[\alpha(\kappa)]d\kappa, \tag{19}$$

which, after a shift of the origin, $\boldsymbol{\kappa}=\mathbf{k}_r+\mathbf{q}$, may be integrated first over the solid angle $d\Omega_q$ (notice that the argument of the $\delta$ function does not depend on the direction of $q$) and then over $q$ by means of $n$ partial integrations. One gets

$$\begin{aligned} &I_n=(-1)^n[M/(M+1)]^{n+1}[(\partial/q\partial q)^n\Gamma_n(k_r,q)]_{q=k_r}, \\ &\Gamma_n(k_r,q)=q\int s_n(\kappa^2)d\Omega_q=(\pi/k_r)\int_{x^-}^{x^+}s_n(x)dx, \end{aligned} \tag{20}$$

with $x^{\pm}=(k_r\pm q)^2$.

Evaluating (20) explicitly up to $n=4$, and summing, with the appropriate factors, one gets a formula identical to P(3.11), apart from the following changes. (a) The right-hand side is multiplied with the reduced mass factor $[M/(M+1)]^2$. (b) The functions $S_n(\kappa^2)$ with the values P(5.2)(5.6) are replaced by the functions $s_n(\kappa^2)$, Eqs. (17), (18). (c) The parameters $u=4k_0^2$ and $E_0$ are replaced by $u_r=4k_r^2$, and $E_r=E_0M/(M+1)$.

The introduction of "relative" energy $E_r$ and momentum $k_r$ is of course to be expected in view of our approximation. Formula P(3.11) thus modified leads then, after trivial operations, to the result, in terms of the free cross section P(5.15):

$$\begin{aligned} \sigma/\sigma_{free}=1&+\tfrac{1}{3}K_{\hbar}M^{-1}E_0^{-1} \\ &-\tfrac{1}{3^2}[(M+1)/M]^2C_{\hbar}M^{-1}E_0^{-1}+\cdots, \end{aligned} \tag{21}$$

which now takes the place of P(5.16).

The result is changed by so little that we may be justified in pointing out some differences which do not strike the eye. The first two terms are exactly the same as before; the only difference here is that they are not obtained by rearrangement and summation of a series of partial terms as in P(5.14); they come out exactly and at once, which is perhaps a slight methodical advantage. There is in both P(5.16) and (21) an invisible third term, of order $E_0^{-2}$, and proportional to $B_{\hbar}$; that the coefficient of this term cancels is established by Placzek's calculation only to the lowest order in $M^{-1}$; one could of course push the approximation further, but there is then no simple argument to predict the general structure of the term as a function of $M$. Equation (21) shows, however, that the term vanishes identically. The last term of (21), finally, differs from the corresponding term in P(5.16) because of the appearance of the inverse of the reduced mass factor. This means that Placzek's $C$ term is proportional to the bound- rather than the free cross section. $C_{\hbar}$, see Eq. P(5.9), is proportional to the average square of the binding force. The result just mentioned is therefore physically plausible, but it could not have been inferred with certainty from an expansion in powers of $M^{-1}$.

We close this section with two more remarks. The first concerns another possible approximation method; it seems at first very tempting to use a "weak binding" approximation, expanding (14) in powers of the potential. The zero order then contains all terms of (15) obtained by neglecting systematically in (16) the commutator $[H,L]$ and commutators thereof. The result is both simple and physically plausible; it obviously describes the collision against a free nucleus, which is not initially at rest, but has instead a velocity distribution as found in the initial state. There the simplicity ends, however; already the next term looks rather complicated and not easily usable. It does not seem, therefore, that this approximation can be used to circumvent the difficulties of the "short collision time" method.

The second remark concerns the extension to a molecule containing several nuclei. We may use, of course, the discussion of P, Sec. 7, to separate the scattering into coherent and incoherent parts. The incoherent scattering is the sum of terms relating to individual nuclei, and for each of these terms a formula like (21) applies, or more precisely a formula which is related to (21) like P(7.8) to P(5.16), with the same change in the meaning of the symbol $C$. Finally, the formula can be extended to include the whole "diagonal"

term for a given nucleus simply by changing the value of the scattering length $a_s$.

## 4. ISOTROPIC OSCILLATOR

The main new result obtained in this section is to exhibit in detail the transition from the "normal" behavior of the asymptotic cross section of a heavy oscillator ($M\gg1$), Eqs. P(6.4) (6.8) (6.9) to the peculiar oscillating behavior discovered by Placzek[4] for the case of equal masses ($M=1$). This behavior may be described as follows: Writing the cross section in the form P(6.8) or, for $M=1$,

$$\sigma/\sigma_{free}=1+n_0^{-1}c(n_0), \tag{22}$$

where $n_0=E_0\omega^{-1}$ is the neutron energy measured in units of the oscillator's quantum, one would expect from the general formula P(6.9) that $c(n_0)\to\frac{1}{4}$ when $n_0\to\infty$. Placzek finds, instead, that $c(n_0)$ approaches asymptotically the periodic function of period one,

$$c_\infty(n_0)=1-\delta-\sum_{j=0}^{\infty}\Phi(x_j), \tag{23}$$

where $\delta=n_0-[n_0]$ is the fractional part of $n_0$, and $x_j=\sqrt{2}(j+\delta)^{\frac{1}{2}}$, while $\Phi$ is the error integral,

$$\Phi(x)=2\pi^{-\frac{1}{2}}\int_x^\infty \exp(-y^2)dy. \tag{24}$$

It is interesting to note that the function (23) has cusps at integer values of $n_0$. Thus the cusps which are present in the low-energy behavior of the cross section *vs* energy,[12] are also preserved in the asymptotic representation of the cross section.

The average of the function (23) over one period, however, is equal to $\frac{1}{4}$ and thus coincides with the constant limit expected from the general formula for $M>1$. This shows that if the cross section were measured with poor energy resolution ($\Delta E\gg\omega$) the asymptotic behavior would be found to be given by the general formula derived for $M>1$.

In principle, however, the oscillation of the $1/E_0$ term in the cross section for $M=1$ is observable, and the difference between the asymptotic behaviors in the cases $M=1$ and $M>1$ is quite real. On the other hand what one means by asymptotic behavior is partly a matter of definition. We shall see that the symbolic method leads to an asymptotic representation of the cross section by means of damped oscillations. The damping is zero for $M=1$ and increases with increasing $M$ (as one might expect from a comparison of the $M=12$ and $M=\infty$ curves in P Fig. 1), so that for large $M$ the function $c(n_0)$ very rapidly approaches a constant value. For $M>1$ but small, the asymptotic formula we shall give should be valid over a wider range of energies than the simple constant value $c(n_0)\sim\frac{1}{4}$.

In the case of a harmonic oscillator, the symbolic expression (3) can be transformed as follows. Having to do with a single nucleus, we omit the index $s$. In the ground state, or in any isotropic average over states, the expectation value of $G$ must be independent of the direction of $\kappa$, which we may therefore choose to be the $z$ axis, so that

$$F=ae^{i\kappa z}. \tag{25}$$

For a harmonic oscillator, one has:

$$e^{itH}ze^{-itH}\equiv z(t)=z\cos\omega t+\zeta\sin\omega t, \tag{26}$$

where $\omega$ is the proper frequency of the oscillator and $\zeta$ is, apart from a factor, the momentum associated to $z$. In fact,

$$[z,\zeta]=i(M\omega)^{-1}. \tag{27}$$

From (5), (25), and (26) one has:

$$\begin{aligned}&F(t)=ae^{i\kappa z(t)},\\ &G(t)=a^2e^{-i\kappa z}\exp(i\kappa z\cos\omega t+i\kappa\zeta\sin\omega t).\end{aligned} \tag{28}$$

This may be written with all the operators under a single exponential, remembering that if $[A,B]$ commutes with both $A$ and $B$ one has

$$e^Ae^B=e^{A+B+\frac{1}{2}[A,B]}=e^{A+B}e^{\frac{1}{2}[A,B]}. \tag{29}$$

In our case $[A,B]$ is a $c$ number, and

$$\begin{aligned}G=a^2\exp\{&i(\kappa^2/2M\omega)\sin\omega t\}\\ &\times\exp\{-i\kappa z(1-\cos\omega t)+i\kappa\zeta\sin\omega t\}.\end{aligned} \tag{30}$$

Furthermore, it is easy to see that the expectation value in the ground state[13] of an operator $\exp(i\alpha z+i\beta\zeta)$ depends only on $\alpha^2+\beta^2$, and may thus be calculated more simply as the expectation value of $\exp\{i(\alpha^2+\beta^2)^{\frac{1}{2}}z\}$, which, in the ground state, is $\exp\{-(\alpha^2+\beta^2)/4M\omega\}$. One thus finds, after simple reductions,

$$G_{aa}=a^2\exp\{(\kappa^2/2M\omega)(e^{i\omega t}-1)\}, \tag{31}$$

which, if the exponent is expanded in powers of $t$, gives the expected behavior, Eqs. (7) and (8). A similar formula is obtained for a thermal distribution over the energy levels of the oscillator. For simplicity, however, we shall stick to the case of the ground state.

Inserting (31) into (3), and expressing $\sigma$ in terms of the "bound" cross section $\sigma_b=4\pi a^2$ or later alternatively of the "free" cross section $\sigma_{free}=\sigma_bM^2/(M+1)^2$, we find

$$\begin{aligned}\sigma/\sigma_b=(8\pi^3k_0)^{-1}\int_{-\infty}^{+\infty}dt\int d\boldsymbol{\kappa}\exp\{&it(\tfrac{1}{2}\kappa^2-\mathbf{k}_0\cdot\boldsymbol{\kappa})\\ &-(\kappa^2/2M\omega)(1-e^{i\omega t})\}.\end{aligned} \tag{32}$$

[12] See, for example, E. Fermi, Ricerca sci. **7** (2), 13 (1936), and P, Fig. 1.

[13] Or more generally in an isotropic distribution over states.

We have assumed here that the $\kappa$ and $t$ integrations can be interchanged; if we first attribute to $t$ a small positive imaginary part, the integral over $\kappa$ becomes absolutely and uniformly convergent, and the interchange can be safely carried out.

Performing the $\kappa$ integration and introducing a nondimensional time variable $\xi=\omega t$, and a nondimensional energy measure $n_0=k_0^2/2m\omega$ as before, and with the abbreviations

$$\rho\equiv\rho(\xi)=\xi^2\lambda(\xi),$$
$$\lambda\equiv\lambda(\xi)=[M^{-1}(1-e^{i\xi})-i\xi]^{-1}, \tag{33}$$

we find

$$\sigma/\sigma_b=\tfrac{1}{4}(\pi n_0)^{-\frac{1}{2}}\int_{-\infty}^{+\infty}\lambda^{\frac{1}{2}}e^{-n_0\rho}d\xi. \tag{34}$$

The integrand of (34) has singularities (branch points) where $\lambda$ has poles or zeros. The only singularity on the real axis is at $\xi=0$, which according to a previous remark must be avoided by passing above it.[14]

For an asymptotic evaluation of (34) for large values of $n_0$, we can remark that any part of the integration path on which an inequality,

$$\mathrm{Re}(\rho)>c, \tag{35}$$

is satisfied, $c$ being a positive constant, will give a negligible contribution, of the order $e^{-cn_0}$, to the integral. We may derive the greatest benefit from this, if we deform the path in such a way as to have (35) satisfied over as much of the path and with as large a value of $c$ as is possible.

Now from (33) it is easy to see that $\mathrm{Re}(\rho)$ is positive over the whole real axis, except at the points $\xi=2\pi\nu$ ($\nu=0,\ \pm1,\ \pm2\cdots$) where it is zero. These points, therefore, must be examined more carefully.

Setting $\xi=2\pi\nu+\eta$, and expanding (33) in powers of $\eta$, one finds that, in the neighborhood of the real axis, the region where $\mathrm{Re}(\rho)>0$ has the structure represented by the shaded area in Figs. 1 and 2. We try to lay the path, as far as possible, within the shaded area; the place, where it must get out of it, is just above the origin. We may, however, deform the path in the manner indicated by the heavy line in the figures, so that the only part of the path where $\mathrm{Re}(\rho)<0$ is a small circular arc at the top of the loop around the origin.

It is best to divide the right-hand side of (34) into two parts, one $I_p$ corresponding to the loop which leads—from a point $\xi_i$ on the negative imaginary axis

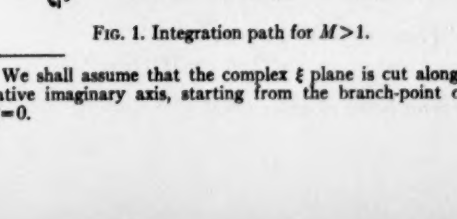


FIG. 1. Integration path for $M>1$.

[14] We shall assume that the complex $\xi$ plane is cut along the negative imaginary axis, starting from the branch-point of $\lambda^{\frac{1}{2}}$ at $\xi=0$.

FIG. 2. Integration path for $M=1$.

—around the origin—back to the same point, and one $I_h$ corresponding to the "horizontal" part of the path, which leads from $-\infty$ to the point $\xi_i$, and from $\xi_i$ on the right-hand side of the imaginary axis[14] to $+\infty$.

We can choose the point $\xi_i$ on the negative imaginary axis in such a way that the integrand is extremely small at $\xi_i$. We may choose, for instance, the point where $\rho$ has a maximum along the negative imaginary axis. For $M\gg1$, $\xi_i\approx-i\ln M$ and the maximum value of $\rho$ is also $\sim\ln M$, so that the exponential in the integrand has a very small value $M^{-n_0}$. As $M\to1$ the maximum value of $\rho$ decreases; for $M=1$ one has $\xi_i=-2i$, and $\rho(\xi_i)=0.48$. Even with this value the exponential, $e^{-0.48n_0}$, is asymptotically negligible as soon as $n_0\gg1$.

If $M\gg1$ it can now be shown that the contribution $I_h$ of the whole "horizontal path" is negligible. In fact, as $M$ increases, the lower boundaries of the shaded area, indicated in Fig. 1, move downwards, the distance from the real axis being of the order of $\ln M$; the path can be laid in such a way that an inequality (35) is satisfied over the whole path, with a value of $c$ of the order of $\ln M$. One then finds an upper limit to the integral along the horizontal path,

$$I_h<e^{-cn_0}\int|\lambda|^{\frac{1}{2}}d\xi\sim c_1e^{-cn_0}, \tag{36}$$

where $c_1$ is another constant. It should be noticed, to justify this, that $\lambda\sim|\xi|^{-1}$ when $\xi\to\pm\infty$, so that the integral in Eq. (36) is convergent. On the other hand, when $M$ approaches unity the "necks" through which the path must pass become narrower and narrower, until they reduce, see Fig. 2, for $M=1$, to points, where $|e^{-n_0\rho}|=1$. The neighborhood of these points gives then a contribution to (34), which is not exponentially small compared to the main term; it yields, in fact, terms of order $n_0^{-1}$, and is responsible for the oscillatory behavior discovered by Placzek.

Now to the actual evaluation: Beginning with the loop integral, we notice that for $|\xi|\ll1$ the exponent $-n_0\rho\approx-in_0\xi M/(1+M)$, so that the exponential rapidly vanishes on the negative imaginary axis as soon as $|\xi|\gg n_0^{-1}$. After the substitution $\tau=-i\xi n_0M/(1+M)$, an expansion of $\rho$ and $\lambda^{\frac{1}{2}}$ in powers of $\tau$ becomes simultaneously an expansion in powers of $n_0^{-1}$. Substituting into (34) and expanding the whole integrand with respect to $n_0^{-1}$, one then gets, apart from a factor, the expression

$$\int\tau^{-\frac{1}{2}}e^{\tau}[1+(Mn_0)^{-1}(\tfrac{2}{3}\tau+\tfrac{1}{3}\tau^2)$$
$$-(Mn_0)^{-2}\{\tfrac{1}{3\cdot2}(8M-7)\tau^2-\tfrac{1}{4\cdot3}(11-4M)\tau^3$$
$$-\tfrac{1}{8}\tau^4\}+\cdots]d\tau, \tag{37}$$

where the path runs in a loop around the origin from, and to, a point $\tau_l=-i\xi_l n_0 M/(1+M)$, which if $n_0\gg 1$ can be set $=-\infty$ without noticeable error. Using the integral representation of the reciprocal $\Gamma$ function[15] one finds for the loop part:

$$I_l=(1+M^{-1})^{-2}\{1+(4Mn_0)^{-1}+0(n_0^{-2})\}. \quad (38)$$

Notice the reduced mass factor $(1+M^{-1})^{-2}\equiv\sigma_{free}/\sigma_b$; notice also that the coefficient of the $n_0^{-2}$ term vanishes identically.

Turning now to $I_h$, we first assume $M=1$. Figure 2 clearly shows that the points $\xi=2\pi\nu$ ($\nu=\pm 1, \pm 2, \cdots$), are saddle-points for $\mathrm{Re}(\rho)$. This follows of course from the expansion already used, that is

$$\rho(2\pi\nu+\eta)=\rho_\nu+\rho_\nu'\eta+\tfrac{1}{2}\rho_\nu''\eta^2+\cdots,$$
$$\rho_\nu=2\pi i\nu, \quad \rho_\nu'=0, \quad \rho_\nu''=1+(i/\pi\nu). \quad (39)$$

The inequality (35) can be satisfied everywhere on the path, excluding the neighborhood of the saddle-points. It is therefore sufficient to evaluate asymptotically the contribution $I_h(\nu)$ from a small interval around each saddle-point. Here we shall content ourselves with the lowest order term, which is proportional to $n_0^{-1}$. This, together with the corresponding term in (38), will yield the function $c_\infty(n_0)$.

The evaluation is based, of course, on the familiar reduction to a Gauss integral.

One has:

$$\exp(-n_0\rho)\approx\exp(-n_0\rho_\nu)\exp(-\tfrac{1}{2}n_0\rho_\nu''\eta^2),$$

which has a sharp Gaussian peak of width $n_0^{-\frac{1}{2}}$ at the saddle-point, provided the path crosses the saddle in the right direction.[16] To the lowest order in $n_0^{-1}$ we are then allowed to replace $\lambda^{\frac{1}{2}}$ in the integral (34) by its value $\lambda_\nu^{\frac{1}{2}}$ at $\xi=2\pi\nu$, i.e., by $(i/2\pi\nu)^{\frac{1}{2}}$. Then, carrying out the Gauss integrals and remembering (34) and (38), we find that

$$\sigma/\sigma_b\approx I_l+\sum_{\nu=1}^{\infty}(I_h^{(\nu)}+\mathrm{cc})$$
$$=I_l+\tfrac{1}{4}\sqrt{2}n_0^{-1}\sum_{\nu=1}^{\infty}\{\lambda_\nu^{\frac{1}{2}}(\rho_\nu'')^{-\frac{1}{2}}\exp(-n_0\rho_\nu)+\mathrm{cc}\}. \quad (40)$$

Using $M=1$ in Eq. (38) and the values (39), and expressing $\sigma$ in terms of $\sigma_{free}=\frac{1}{4}\sigma_b$, we find, on comparison with (22),

$$c_\infty(n_0)=\tfrac{1}{4}+\sum_{\nu=1}^{\infty}(8\pi\nu)^{-1}\{(\pi\nu+i)^{-\frac{1}{2}}e^{-2\pi i\nu n_0+i\frac{\pi}{4}}+\mathrm{cc}\}. \quad (41)$$

We have now obtained two entirely different expressions (23) and (41) for the same function; but it is not difficult to verify by integration of (23) with a factor $\exp(2\pi i\nu\delta)$, that (41) is indeed the Fourier series for the function (23). The advantage of (23) is, of course, its much more rapid convergence.

We finally set ourselves the problem of bridging the gap between the two extreme cases $M=1$ and $M\gg 1$. The preceding discussion clearly points the way. As long as $M>1$, it is always possible to say that $I_h\sim\exp(-cn_0)$, but $c\to 0$ as $M\to 1$, so that neglecting $I_h$ entirely is not a good approximation. Looking at Fig. 1 we realize that there must be a saddle-point in the middle of each narrow "neck" of the shaded area. We can calculate $I_h$ approximately by a saddle-point method, just as we did for $M=1$.

We obtain again (40), the only difference being in the values of $I_l$, and of the coefficients $\lambda_\nu$, $\rho_\nu$, $\rho_\nu''$. The position of the saddle-points is quickly obtained as follows. The equation for a saddle-point $\xi$ is $\rho'(\xi)=0$, which one can rewrite using (33),

$$e^{i\xi}=M\{1-2i\epsilon/(\xi+2i)\}, \quad (42)$$

where $\epsilon=1-M^{-1}<1$. Taking the logarithm on both sides, and designating $\xi$ more specifically by $\xi_\nu$, if $\xi$ is the saddle-point which tends to $2\pi\nu$ when $M\to 1$, we get

$$\xi_\nu=2\pi\nu-i\ln M-i\ln\{1-2i\epsilon(\xi_\nu+2i)^{-1}\}, \quad (43)$$

where the principal value of each logarithm is meant. From (43) it is easy to obtain an expansion in powers of $M-1$ or of $\epsilon$, which converges rapidly if $(M-1)\ll 1$. For the practically more interesting case: $M$ equal a small integer, one can reach the goal more quickly by an iteration method. Starting from $\xi_\nu\approx 2\pi\nu-i\ln M$ as an approximate value, one feeds this into the right-hand side of (43) and gets a better value, and so on.

Another usable expansion is one in falling powers of $2\pi\nu$:

$$\xi_\nu=2\pi\nu-i\ln M+\sum_{n=1}^{\infty}a_n(2\pi\nu)^{-n},$$
$$a_1=-2\epsilon, \quad a_2=-2i\epsilon(\ln M-2+\epsilon)\cdots. \quad (44)$$

It is easy to see that (43) defines $\xi_\nu-2\pi\nu$ as an analytic function of $z=(2\pi\nu)^{-1}$ regarded as a complex variable, and that $z=0$ is not a singularity. Hence, (44) must have a nonzero radius of convergence and is in fact apparently quite usable down to $\nu=1$.

Knowing $\xi_\nu$ one can calculate the coefficients of the expansion (40). The most interesting one is the exponent $\rho_\nu$. Using (42), (23) can be transformed into

$$\rho_\nu\equiv\rho(\xi_\nu)=i\xi_\nu(1+2i\xi_\nu^{-1})[1+i(2-\epsilon)\xi_\nu^{-1}]. \quad (45)$$

This too can be expanded for large $\nu$:

$$\rho_\nu=i\{2\pi\nu-\epsilon^2(2\pi\nu)^{-1}+\cdots\}+\ln M-\epsilon$$
$$-\epsilon^2(2-\epsilon-\ln M)(2\pi\nu)^{-2}+\cdots, \quad (46)$$

the error being of order $(2\pi\nu)^{-3}$.

[15] E. T. Whittaker and G. N. Watson, *A Course of Modern Analysis* (The McMillan Company, New York, 1946), fourth edition, Sec. 12.22.

[16] For example at an angle $-\frac{1}{4}\arctan(1/\pi\nu)$ to the real axis. According to (33) the exponent $-\frac{1}{2}n_0\rho_\nu''\eta^2$ is then real and negative. This is indicated in Fig. 2.

Some numerical values for the exponents $\rho_\nu$ are given in Table I. The most noteworthy feature, of course, is the nonvanishing real part of $\rho_\nu$. Each term of the series (40) is a damped harmonic oscillation. The damping factor is only weakly dependent on $\nu$, and is roughly $\exp\{-n_0(\ln M-\epsilon)\}$. Also, the imaginary part of $\rho_\nu$ is only slightly different from $2\pi\nu$, so that the series is almost harmonic. The amount of damping indicated by Table I is in good agreement, as far as a comparison is possible,[17] with the numerical results of Placzek, as displayed in P (Fig. 1).

Finally, it is noteworthy that even for $M$ as low as 2, the damping is fairly rapid, the amplitude being reduced to $1/e$ when the energy increases by five oscillator quanta.

TABLE I. Values of $\rho_\nu$.

| | | | (a) Real part of $\rho_\nu$ | | |
|---|---|---|---|---|---|
| $M=$ | 1 | 2 | 3 | 6 | 12 |
| $\nu=1$ | 0 | 0.1880 | 0.4294 | 0.9694 | 1.598 |
| 2 | 0 | 0.1919 | 0.4313 | 0.9612 | 1.576 |
| $\infty$ | 0 | 0.1931 | 0.4320 | 0.9584 | 1.568 |
| | | (b) Imaginary part of $\rho_\nu$ divided by $2\pi\nu$ | | | |
| $\nu=1$ | 1 | 0.9937 | 0.9888 | 0.9825 | 0.979 |
| 2 | 1 | 0.9984 | 0.9972 | 0.9956 | 0.995 |
| $\infty$ | 1 | 1 | 1 | 1 | 1 |

## 5. NONDIAGONAL TERMS

In the discussion of these terms we have to rely to an even larger extent than before on purely qualitative arguments, except in special examples. Furthermore it turns out that in the present instance the "short collision time" approximation is essentially equivalent to the "small energy transfer" approximation of Placzek, and does not lead to any improvement over his formulas. One useful result emerges from the following discussion, however, namely that as far as the nondiagonal terms are concerned, Placzek's formulas are not essentially tied to the condition $M\gg1$, a fact which is not obvious from the discussion given in P. Thus we may say that we have a suitable treatment for all cases.

If we pick in the operator (4) the interference term relative to, say, nuclei 1 and 2, that is, apart from a factor $a_1a_2$, the expression

$$G_{21}=f_2^*e^{itH}f_1e^{-itH},\quad f_s=\exp(i\boldsymbol{\kappa}\cdot\mathbf{r}_s),\tag{47}$$

the first problem is to find its time dependence. The discussion will be clearer if we first get rid of an obvious pitfall.

There is, of course, no analog to an interference term in the classical theory of impacts, and thus no *a priori* argument for a time dependence such as in (6), based on the classical energy momentum relation (7); to begin with, if $M_1\neq M_2$, we would not even know which mass to use in these equations. Nevertheless if we apply the transformation (9)(11) to (47), we get

$$G_{21}=f_2^*f_1\exp(it\kappa^2/2M_1)e^{it(H+L_1)}e^{-itH},\tag{48}$$

$L_s$ being defined by (10) with $M$, and $\mathbf{p}$ replaced by $M_s$ and $\mathbf{p}_s$. The first exponential in (48) represents a strong (if $M_1\sim1$) time dependence of the type we have no good reason to expect. Alternatively, we may obtain a similar factor involving $M_2$ instead of $M_1$, if we notice that $G_{aa}=G_{aa}^1$, where

$$G^1=e^{-itH}F^*e^{itH}F,\tag{49}$$

and transform accordingly, pushing $F^*$ towards the right. The truth is, however, that the appearance of these strongly oscillating factors is without significance; they are canceled by compensating terms which occur in the expectation value of the remaining operators. More precisely we state that, if the time dependence of $\langle G_{21}\rangle$ is written as an exponential $\exp[if(t)]$, no linear term in $t$ is present in the exponent.

This can be seen most simply by showing that the time derivative of $\langle G_{21}\rangle$ is zero at $t=0$. And this follows immediately from P(7.17). Since the point is of some importance, however, it will be further explained by an alternative derivation. We rewrite (47) in the form

$$G_{21}=\exp(-i\kappa z_2)\exp\{i\kappa z_1(t)\},\tag{50}$$

taking the $z$ axis parallel to $\boldsymbol{\kappa}$. For comparison the diagonal term $G_{11}$ can be similarly written, by replacing $z_2$ with $z_1$ in (50). For small values of $t$ we expand in powers of $t$, neglecting terms of order $t^2$ or higher. Remembering (29) we obtain

$$\begin{aligned}G_{21}&\approx\exp(-i\kappa z_2)\exp(i\kappa z_1+il\kappa\dot z_1)\\&=\exp[i\kappa(z_1-z_2)+il\kappa\dot z_1],\end{aligned}\tag{51}$$

and similarly

$$\begin{aligned}G_{11}&\approx\exp(-i\kappa z_1)\exp(i\kappa z_1+il\kappa\dot z_1)\\&=\exp[il\kappa\dot z_1+\tfrac12 i\kappa^2M_1^{-1}t],\end{aligned}\tag{52}$$

where the main difference between the two operators is that the commutator term in (29) is zero for $G_{21}$, but not for $G_{11}$. It is just this term that gives the strong time dependent factor for $G_{11}$, but not for $G_{21}$. To complete this consideration, one has only to notice that under the assumption that the eigenfunction of state $a$ is real (i.e., invariant against time reversal; this assumption is essential, and is also made in P) the expectation value of an operator $\exp(\alpha z+\beta p_s)$ is an even function of $\beta$. Hence the exponential operators in (51) do not contribute any linear exponent in $t$.

The cancellation of the strong linear term in $G_{21}$ means that the first-order reduced mass correction does not apply to the interference terms, as pointed out in P. But for us it means, especially, that the transformation employed successfully in Sec. 3 is here not merely useless, but actually misleading. Under these circumstances it is more natural to expand the whole

[17] Owing to the omission of terms of order $n_0^{-2}$, our formula can only give a rough approximation for values of $n_0$ as low as those in P, Fig. 1.

$G_{21}$ in powers of $t$, but then of course we are back with the "small energy transfer" approximation and no improvement over P is obtained. The question we want to discuss, however, is whether such an improvement is really necessary.

The absence of a large linear term is in itself no guarantee that the time dependence of $G_{21}$ is weak. A strong time dependence could appear in higher powers of $t$ in the expansion or at later times, when the expansion is of no help. The case of long times has been examined in detail in Appendix 3 for a special case. There one can see in (A13), for example, that when $\kappa$ is large a strong time dependence can indeed appear for large $t$ values. That turns out to be unimportant, however, for the simple reason that the value of $G_{21}$ is at the same time quite negligible.

It is the latter circumstance that is decisive. Although in the general case this cannot be demonstrated as forcibly as in the special case of the appendix, we can at least show that quite improbable circumstances must occur for an exception to be possible.

Let us begin with the trivial case of two "independent" nuclei, for example two nuclei bound in a fixed external potential, but not interacting with each other, so that individual states can be assigned to each. In this well-known case the only coherent scattering is elastic; $G_{21}$ is not time dependent at all; this is so, of course, because the two factors of the matrix element

$$M_b=(f_2^*)_{ab}(f_1)_{ba} \tag{53}$$

associated with the energy transfer $E_b-E_a$ cannot both be $\neq 0$ unless $b=a$. Knowing this, we can see, furthermore, that the only nonzero matrix element $M_a$ becomes negligible as soon as $\kappa$ is large compared to the zero point momenta of 1 and 2 in the state $a$. This establishes our statement for this case.

Naturally, the example chosen is so special that its detailed features are of no special interest for the general case. If, for example, we add an interaction $\lambda V_{12}$ between the two particles, we expect to get the same result for the cross section in the limit $\lambda\to 0$; most of the detailed statements made above become invalid, however. In particular, it is necessary to remember the role of degeneracy in such a problem. Owing to degeneracy between levels of the unperturbed problem, even a weak interaction can lead to strong mixing of states, so that the matrix elements $M_b$ for individual states can be strongly affected. It is no longer true, for example, that for $\kappa$ large, every $M_b$ must become necessarily small. (The reader will find it instructive to consider in detail the possible effects of mixing between states in which either one of the two particles is strongly excited, while the remaining one is left in the ground state.) On the other hand, a sum over states such as the sum in Eq. (1) possesses a well-known stability against perturbations, so that for small $\lambda$ it will still be true that the contribution of large $\kappa$ values to the nondiagonal term can be neglected.

In the above example, a significant departure from our general assumption could only occur if the interaction becomes so large as to cause large splittings amongst the original degenerate levels, or, in more physical language, if momentum is exchanged rapidly between the two particles, more precisely, so rapidly that a momentum exchange $\kappa$ can occur during the short time available in a collision. If this necessary condition is examined more in detail, one finds that large $\kappa$ values can only contribute if the energy $E_0$ of the incident neutron is smaller than an expression of the type of $(\partial^2 V/\partial x^2)D^2$, where $V$ is the interaction and $D$ the distance between the two particles. This expression again may be taken to be of the order of binding energies if the particles are close to one another in the molecule and even smaller otherwise.

Although this necessary condition is better than nothing, it is not very strong and we have some reason to think that much more stringent conditions must be met, so that in practice we may safely assume that large momentum transfers are negligible quite in general.

We shall try to show this by means of a semiclassical consideration based again on the time-dependent picture. Reverting to the form (4) of the operator $G$ and using a configuration representation of the operator $e^{itH}$, we can write the expectation value of $G_{21}$ in the state $a$ in the form

$$\langle G_{21}\rangle=\int \psi_a^*(\mathbf{r}_1\mathbf{r}_2)\exp(-i\boldsymbol{\kappa}\cdot\mathbf{r}_2)d\mathbf{r}_1 d\mathbf{r}_2\langle \mathbf{r}_1\mathbf{r}_2|e^{itH}|\mathbf{r}_1'\mathbf{r}_2'\rangle \times d\mathbf{r}_1' d\mathbf{r}_2' \exp(i\boldsymbol{\kappa}\cdot\mathbf{r}_1')\psi_a(\mathbf{r}_1'\mathbf{r}_2')e^{-itE_a}. \tag{54}$$

For simplicity only the coordinates of the two particles involved have been indicated explicitly, but if other particles are present, additional coordinates $\mathbf{r}_3, \cdots$ and $\mathbf{r}_3'\cdots$ would have to be written in at the left and right, respectively. The following argument would not be affected. Let us now consider a classical motion leading from positions $\mathbf{r}_1'$, $\mathbf{r}_2'$ at time $t$ (it is convenient to fix our attention on the case $t<0$) to positions $\mathbf{r}_1$, $\mathbf{r}_2$ at time 0; let $S(\mathbf{r}_1\mathbf{r}_2;\mathbf{r}_1'\mathbf{r}_2';t)$ be the action integral for this motion. We now make the classical approximation

$$\langle \mathbf{r}_1\mathbf{r}_2|e^{itH}|\mathbf{r}_1'\mathbf{r}_2'\rangle=\exp\{iS(\mathbf{r}_1\mathbf{r}_2;\mathbf{r}_1'\mathbf{r}_2';t)\}, \tag{55}$$

neglecting a normalization factor, which would only complicate the formulas without much consequence. If a classical approximation is valid at all, the exponential on the right-hand side of (55) can be treated as a rapidly oscillating factor. We intend to discuss all the integrations in (3) and (54) (i.e., the integrations over $\boldsymbol{\kappa}$, $t$, $\mathbf{r}_1$, $\mathbf{r}_2$, $\mathbf{r}_1'$, $\mathbf{r}_2'$) by means of the method of stationary phase. This is, of course, very crude, but since we only intend to ascertain the conditions under which a "large" result can be obtained, the approximation seems legitimate. We recall that

$$\partial S/\partial \mathbf{r}_i=\mathbf{p}_i,\quad \partial S/\partial \mathbf{r}_i'=-\mathbf{p}_i',\quad \partial S/\partial t=E, \tag{56}$$

where $\mathbf{p}_i$ and $\mathbf{p}_i'$ $(i=1, 2)$ are the final and initial momenta of the two particles and $E$ is the energy in the classical motion envisaged above. We regard the momenta of 1 and 2 in state $a$ as negligible, that is we treat $\psi_a^*$ and $\psi_a$ as slowly variable (we neglect their derivatives). Then writing the stationarity condition for the integrations (in the order mentioned above) we find

$$\mathbf{r}_2-\mathbf{r}_1'=-t(\mathbf{k}_0-\boldsymbol{\kappa}), \tag{57}$$

$$\tfrac{1}{2}\kappa^2-\boldsymbol{\kappa}\cdot\mathbf{k}_0+E=E_a, \tag{58}$$

$$\mathbf{p}_1=0, \quad \mathbf{p}_2=\boldsymbol{\kappa}; \quad \mathbf{p}_1'=\boldsymbol{\kappa}, \quad \mathbf{p}_2'=0. \tag{59}$$

In addition we must require, of course, that $\mathbf{r}_1\mathbf{r}_2$ and, respectively, $\mathbf{r}_1'\mathbf{r}_2'$ be in a region of configuration space where the wave function of the ground state is large. The meaning of these equations is obvious. They say that there must be a classical motion of 1 and 2 (and if necessary of the remaining nuclei) which starting from a probable[18] configuration $\mathbf{r}_1'\mathbf{r}_2'$, with momentum $\boldsymbol{\kappa}$ for nucleus 1 and zero momentum for nucleus 2, leads as a result of the interactions to probable[18] final positions $\mathbf{r}_1\mathbf{r}_2$ with momenta 0 and $\boldsymbol{\kappa}$, respectively. Moreover, (58) is the energy conservation equation including the neutron, and (57) expresses the condition for the neutron to be able to travel, in the time $-t$, from position $\mathbf{r}_1'$ where it hits nucleus 1, to position $\mathbf{r}_2$ where it hits nucleus 2.

The result is thus by no means unexpected; in fact the above discussion is merely an explicit formalization of the intuitive considerations we have applied several times before. It will serve, perhaps, to show to what extent a classical description of the molecular motion is applicable to these essentially nonclassical interference terms.

If all this be granted, it will appear that (57) and (58) are additional requirements that will in general be hard to satisfy, even if the forces between 1 and 2 are strong enough to effect the momentum transfer that was discussed before, and is also exhibited in the conditions (59). While it is not true in general that the conditions are incompatible, they do turn out to be so, for example, in the case of the oscillator model of Appendix 3, where the conclusions reached have been checked by the direct quantum-mechanical calculation.

While it is not possible to state quite generally that the "classical" conditions (57) (58) (59) can never be satisfied, it seems reasonable to draw the following conclusions. The more complicated the system, the less likely it will be that the whole effect of a large blow applied to particle 1 can be undone by a counterblow applied simultaneously or at any other time, to a single other particle 2. Hence exceptions to the rule that large momentum transfers do not contribute significantly to interference terms will occur at most in very simple systems, like a diatomic molecule. Even so, they will play a role only under rather special conditions.

It follows then, that barring these special exceptions, and for neutrons satisfying the condition $E_0 \gg \Delta$, see P(2.3), the energy transfers effective in interference scattering will be $\ll E_0$, so that the approximation developed in P should be applicable, even to molecules containing very light nuclei. In particular the "static" approximation [first line of P(7.20)] should give an adequate representation of the cross section for most purposes.

Some comment is desirable, however, concerning the subsequent terms of Placzek's expansion, say, for instance, the 2nd and 3rd line of P(7.20). If our conclusions are correct, we should expect these terms to be small compared to the static approximation. Under the assumptions of P, the smallness of these terms is in fact warranted by the large mass of the nuclei, as for instance indicated by the factor $\mu_s\mu_{s'}$ in the last line of P(7.20). Such factors are of no help in our case. As pointed out in P, however, these terms are also small for other reasons, namely, because of factors $\sim\exp(-4E_0/M\omega)$, $\omega$ being a frequency of nuclear motion (Debye-Waller factors, etc.). Now as a rough rule of thumb, we may say the frequency $\omega$ varies with the mass as $M^{-\frac{1}{2}}$, so that the exponential varies $\sim\exp(-\alpha E_0/M^{\frac{1}{2}})$, $\alpha$ being roughly a constant. Thus this factor is actually much smaller for light nuclei and compensates for the absence of the mass denominators.

A different question, however, also arises. Namely, we may want to know not merely whether the second, third, $\cdots$ terms in the expansion are small, but also whether they effectively represent the error of the first, or static, approximation. This question is more difficult to answer in view of the energy dependence of the successive terms in P(7.20). Thus the first term is proportional to $E_0^{-1}$, while the second term and the terms in the second and third lines contain exponential factors of the type mentioned above. Proceeding further in the expansion, however, we would find the term $S_4'(0)$ in P(3.11) and other terms to be found later again yield simple reciprocal powers of $E_0$. Thus the series is definitely not an asymptotic expansion in the same sense as P(5.16) or (21). At very high energies we ought to leave out all exponential terms and keep the powers of $E_0^{-1}$; the series would then start as follows:

$$\sigma_{12}=4\pi a_1 a_2 k_0^{-2}\{\tfrac{1}{2}\langle r_{12}^{-2}\rangle_{\mathrm{Av}}-(1/96M_1M_2)E_0^{-2} \times\langle \mathrm{grad}_1 V\cdot\mathrm{grad}_2 V\rangle_{\mathrm{Av}}+\cdots\}. \tag{60}$$

For large masses and moderate energies, however, the terms thus thrown away are more important than the term added above.

For macroscopic bodies, such as crystals, there is in addition the question of the convergence of the sum over the indices $s, s'$. This question has been exhaustively discussed for the static approximation[19] but not

[18] Probable refers here to the space distribution in the ground state.

[19] Placzek, Nijboer, and Van Hove, Phys. Rev. 82, 392 (1951).

for the second and third line of P(7.20). A provisional estimate we have made shows that no special difficulty is encountered, but we hope to come back to this question later.

ACKNOWLEDGMENT

The author wishes to thank the members of the Institute for Advanced Study, and in particular Dr. G. Placzek, for several helpful discussions about the subject of this paper, which led to extensive modifications and improvements. Some of the formal results had been obtained earlier, at the Carnegie Institute of Technology; thanks are also due to Dr. F. Adler for help during the early stages of the work. Finally, the author wishes to acknowledge his indebtedness to the Institute for Advanced Study for a grant-in-aid and to Professor Robert Oppenheimer for the hospitality extended to him at the Institute.

## APPENDIX 1

### Single Nucleus, Differential Cross Section

One can, by means of the method of Sec. 3, also calculate the differential cross section or the effective differential cross section. In the case of light nuclei this means, of course, lumping together final neutrons of widely different energy. The result is, therefore, somewhat less significant and will be discussed only briefly. In order to obtain the differential cross section we must go back to Eqs. (12) and (19) and introduce as an integration variable the final momentum of the neutron $\mathbf{k}=\mathbf{k}_0-\boldsymbol{\kappa}$ in place of $\boldsymbol{\kappa}$. Writing then $d\mathbf{k}=k^2dkd\Omega$ in place of $d\boldsymbol{\kappa}$ and performing the integral over $k$, but not over $d\Omega$ we obtain

$$k_0d\sigma/d\Omega=\sum_n(n!)^{-1}\int_0^\infty k^2s_n(\kappa^2)\delta^{(n)}(\alpha)dk, \qquad \text{(A1)}$$

where $\kappa^2$ and $\alpha$ are now functions of $k$:

$$2M\alpha=(1+M)k^2-2k_0k\cos\theta-(M-1)k_0^2,$$
$$\kappa^2=k_0^2-2k_0k\cos\theta+k^2.$$

Inserting (18) into (A1) one can calculate each term explicitly. We give the result in an abbreviated form. Introduce a variable $x=(k/k_0)-\cos\theta/(M+1)$ and the value $x_0$ corresponding to the value of $k$ for which $\alpha=0$:

$$x_0=(M^2-\sin^2\theta)^{\frac{1}{2}}/(M+1). \qquad \text{(A2)}$$

Then, remembering that in Eq. (17), $s_n$ is a function $s_n(u)$ of $u=\kappa^2$, write $u$ as a function of $x$. This may be indicated explicitly by $u=k_0^2v_x$, where

$$v_x=1-2(k/k_0)\cos\theta+(k/k_0)^2$$
$$=[x-M\cos\theta/(M+1)]^2+\sin^2\theta. \qquad \text{(A3)}$$

Define functions

$$\phi_{n,m}(\theta)=(1+M^{-1})^{-n-1}$$
$$\times\left[\left(\frac{\partial}{\partial x^2}\right)^n\left\{x^{-1}\left(x+\frac{\cos\theta}{M+1}\right)^2v_x^m\right\}\right]_{x=x_0}. \qquad \text{(A4)}$$

In particular,

$$\phi_{0,0}(\theta)=(1+M^{-1})^{-1}x_0^2[x_0-(1+M)^{-1}\cos\theta]^{-1}. \qquad \text{(A5)}$$

We can now write the first terms of the expansion of the differential cross section

$$a^{-2}d\sigma/d\Omega=\phi_{0,0}(\theta)+(2/3ME_0)K_{\mathrm{H}}\phi_{2,1}(\theta)$$
$$-(B/6ME_0^2)\phi_{2,1}(\theta)+(2/15M^2E_0^2)\langle K^2\rangle_{\mathrm{H}}\phi_{4,2}(\theta)$$
$$+(C/12ME_0^3)\phi_{4,1}(\theta)+\cdots. \qquad \text{(A6)}$$

The effective differential cross section can be similarly obtained if one adds a factor $k_0/k$ to the integral in (A1). This leads to functions

$$\psi_{n,m}(\theta)=(1+M^{-1})^{-n-1}$$
$$\times\left[\left(\frac{\partial}{\partial x^2}\right)^n\left\{x^{-1}\left(x+\frac{\cos\theta}{M+1}\right)v_x^m\right\}\right]_{x=x_0}. \qquad \text{(A7)}$$

To get $d\sigma_{\mathrm{eff}}/d\Omega$, replace all $\phi$'s by $\psi$'s in Eq. (A6), thus,

$$a^{-2}d\sigma_{\mathrm{eff}}/d\Omega=\psi_{0,0}(\theta)+(2/3ME_0)K_{\mathrm{H}}\psi_{2,1}(\theta)+\cdots. \qquad \text{(A8)}$$

The formulas as written are not perhaps very explicit but the Eqs. (A5) to (A8) will give an explicit answer with a little work, but without difficulty, if needed.

One may wish to compare these formulas with P(5.19) and P(5.20). For this purpose bear in mind that the energy dependence in Eqs. (A6) and (A8) is given explicitly. And in fact one finds $K_{\mathrm{H}}$ divided by $E_0$, $B$ and $\langle K^2\rangle_{\mathrm{H}}$ divided by $E_0^2$, $C$ divided by $E_0^3$ as expected.

On the other hand, the $M$ dependence appears only in part. We have tried to write the $\phi$ and $\psi$ functions so that they are of zero order in $M$, when $M$ is large. Cancellations may occur, however, in the limit $M\to\infty$, so that a function may occasionally turn out to be of the order $M^{-1}$ or even smaller. One verifies easily, for instance, that in the limit $M=\infty$, $\phi_{2,1}\to 0$. Thus, the $B$ term in Eq. (A6) is not of first order in $M^{-1}$ as it seems to be, but higher, in agreement with P(5.19) where it appears to be of order $M^{-2}$. On the other hand, the $\psi_{2,1}$ function which multiplies $B$ in the effective cross section does not vanish in the limit $M=\infty$, in agreement with the $M$ dependence of the $B$ term in P(5.20).

## APPENDIX 2

### Nonisotropic Oscillator

For simplicity we assume $M=1$ from the start, since this is the critical case. We assume that the oscillator has three different frequencies $\omega_1$, $\omega_2$, $\omega_3$ along the Cartesian axes 1, 2 and 3. By an analysis completely

similar to that leading to (31), one finds

$$G_{aa}=a^2\prod_{j=1}^{3}\exp\{(\kappa_j^2/2\omega_j)(e^{i\omega_j t}-1)\},$$

and later, instead of (34),

$$\sigma/\sigma_b=\tfrac{1}{4}(\pi E_0)^{-1}\int_{-\infty}^{+\infty}dt\prod_{j=1}^{3}f_j(t), \tag{A9}$$

where

$$f_j(t)=(\omega_j\lambda_j)^{\frac{1}{2}}\exp(-f^2\omega_j k_j^2\lambda_j),$$
$$\lambda_j\equiv\lambda_j(t)=[1-e^{i\omega_j t}-i\omega_j t]^{-1},$$

$k_1k_2k_3$ being the components of the vector $k_0$. Leaving aside the neighborhood of $t=0$, which offers nothing essentially new, we examine the contribution from longer times. If a direction of $k_0$ is chosen at random, and $E_0$ is increased, it can be seen that the modulus of the integrand of (A9) goes to zero exponentially for any given $t\neq 0$ on the real axis. This is because the real parts of $f_1f_2f_3$ cannot be zero simultaneously if $\omega_1\neq\omega_2\neq\omega_3$ (barring the case $\omega_1:\omega_2:\omega_3=n_1:n_2:n_3$, where $n_1$, $n_2$, $n_3$ are three integers). However if $k_0$ is directed along one of the axes, then clearly the periodicity phenomenon of Sec. 4 reappears. Averaging the cross section over the direction of $k_0$, we see that "anomalous" terms will come from the neighborhood of the three axes.

Assume for example $k_1\approx k_0$, $k_2\ll k_0$, $k_3\ll k_0$. There are then saddle-points near the real axis; when $k_2$ and $k_3\to 0$ these saddle-points tend to $\omega_1 t=\pm 2\pi, \pm 4\pi, \cdots$. Writing for the saddle-point

$$t=2\pi\nu/\omega_1+\tau,$$

and expanding $\tau$ in powers of $k_2$ and $k_3$, we find

$$\omega_1\tau=k_0^{-2}(1+i/\pi\nu)^{-1}\{k_2^2A_2+k_3^2A_3\},$$

where

$$A_j=\xi_j\lambda_j(2-i\xi_j)(1+i\xi_j\lambda_j),$$
$$\xi_j=2\pi\nu\omega_j/\omega_1,\quad \lambda_j^{-1}=1-i\xi_j-e^{i\xi_j}.$$

The contribution of the saddle-point to the integral is again of the type of Eq. (40). Apart from less interesting factors, it is $E_0^{-1}$ times an exponential of $-f^2\sum_j\omega_jk_j^2\lambda_j$ calculated at the saddle-point. Neglecting again higher order terms in $k_2$ and $k_3$, however, it is obvious that the exponent can be calculated at the "unperturbed" saddle-point $t=2\pi\nu/\omega_1$. The exponent is then found to be

$$-4\pi\nu E_0\omega_1^{-1}\{i+(k_2/k_0)^2\xi_2\lambda_2+(k_3/k_0)^2\xi_3\lambda_3\}.$$

Since $\lambda_2$ and $\lambda_3$ have a positive real part, the correction terms in $k_2$ and $k_3$ have, of course, the effect to introduce an exponential damping with increasing energy. The anomalous terms are thus only important when $k_2^2k_3^2\ll k_0^2$, more precisely within a solid angle of the order of $\omega_1/E_0$. Averaging over the direction of the incident neutron, and including the similar contributions from the angular regions around axis 2 and 3, one finds that the anomalous term in the cross section is, roughly

$$(1/128)\textstyle\sum_\nu(\pi\nu)^{-5/2}(\omega_1/E_0)^2e^{-2\pi i\nu E_0/\omega_1},$$

plus two other similar terms in $\omega_2$ and $\omega_3$. For simplicity some factors of order of magnitude one, and some phase factors are omitted. This result shows that the anomalous oscillation does not entirely disappear from the asymptotic formula; however, two important differences emerge. First, the anomaly is removed from the $E_0^{-1}$ correction, and shifted to a term of order $E_0^{-2}$; secondly, the numerical factors are such as to make the effect quite insignificant.

## APPENDIX 3

### Oscillator Model for Interference Terms

We consider a diatomic molecule of total mass $M=M_1+M_2$ with the potential energy

$$V(\mathbf{r})=\tfrac{1}{2}M_{12}\omega^2\mathbf{r}^2, \tag{A10}$$

where $\mathbf{r}=\mathbf{r}_1-\mathbf{r}_2$ and $M_{12}=M_1M_2/M$. This would be a tolerably good model for a molecule, were it not for the unrealistic feature, that the equilibrium position is at $r=0$. It does provide us, however, with a simple and exact illustration of some interesting points. In terms of the total and relative momenta: $\mathbf{P}=\mathbf{p}_1+\mathbf{p}_2$ and $\mathbf{p}=M^{-1}(M_2\mathbf{p}_1-M_1\mathbf{p}_2)$ the Hamiltonian of the molecule is

$$H=\tfrac{1}{2}(M^{-1}\mathbf{P}^2+M_{12}^{-1}\mathbf{p}^2)+V(\mathbf{r}).$$

It is an easy matter to evaluate the expectation value of the operator $G$, Eq. (4), for the ground state of the molecule. For simplicity let us consider only the non-diagonal term, $a_1a_2G_{21}$. The factors referring to the center of mass can be separated; one gets then easily:

$$\langle G_{21}\rangle=\exp(it\kappa^2/2M)\langle\exp(i\boldsymbol{\kappa}\cdot\mathbf{r}M_1/M)\times\exp[i\boldsymbol{\kappa}\cdot\mathbf{r}(t)M_2/M]\rangle, \tag{A11}$$

which is, so far, independent of the assumption (A10). With that assumption, however, we get

$$\mathbf{r}(t)=\mathbf{r}\cos\omega t+(M_{12}\omega)^{-1}\mathbf{p}\sin\omega t. \tag{A12}$$

A calculation similar to that of Sec. 4 then gives

$$\langle G_{12}\rangle=\exp\{-(\kappa^2/4M_{12}\omega)+(\kappa^2/2M\omega)(1+i\omega t-e^{i\omega t})\}. \tag{A13}$$

Before we proceed, we may notice various properties of (A13). For $t=0$ the expression is exponentially small for large $\kappa$, which, of course, illustrates the fact that when momenta $\boldsymbol{\kappa}$ and $-\boldsymbol{\kappa}$ are applied to two different nuclei, it is unlikely that the molecule will be left in the ground state. For small $t$, the exponent may be expanded, and the absence of a linear term may be verified.

For any real value of $t$, one has, furthermore,

$$|\langle G_{12}\rangle|\leq\exp\{-(\kappa^2/4M_{12}\omega)(M_1-M_2)^2M^{-2}\}. \tag{A14}$$

Thus if $M_1\neq M_2$, the molecule is not likely to be restored to the ground state, even if there is an arbitrary

time lag between the two momentum transfers. The equality sign in (A14), i.e., a maximum value for the matrix element, is obtained for $\omega t=\pm\pi$, $\pm 3\pi$, $\cdots$. This result, which recalls to mind the behavior of the diagonal matrix element in Sec. 4, is easily understood, since it is just after a half-period, or an odd multiple thereof, that the maximum momentum transfer from 1 to 2 has taken place.

If moreover $M_1=M_2$, the two nuclei will have completely interchanged their momenta, at the times indicated, so that both can be brought to rest by a counterblow $-\varkappa$ applied to nucleus 2. In fact the absolute value of (A13) becomes, under these circumstances, equal to 1; one might think, therefore, that "long" times, of the order of the oscillator period, could give important contributions to the cross section, supplying us with a nondiagonal counterpart of the "anomalous" terms of Sec. 4. This is, however, not the case, no matter what values we choose for $M_1$ and $M_2$.

So far our discussion has only brought out the consequences of momentum conservation in the collisions and the initial and final values of the momenta. The subsequent integration over $\varkappa$ and $t$ will produce the additional requirements of coincidence in space and energy conservation expressed by (57) and (58) of Sec. 5. Even without calculation one can see that those requirements cannot be fulfilled here. Initially the two nuclei are at rest and close to each other (neglecting the zero point motion); immediately after the first collision, nucleus 1 is moving rapidly with a momentum $\varkappa$, which must be a value permissible in a free collision; nucleus 2 is at rest. Now when the second collision is supposed to occur, at a "favorable" time, say after a half-period, the two nuclei are again close together; hence the second collision can only occur if the velocity of the neutron after the first collision is equal to that of the center of mass. The reader can easily verify that this is incompatible with the condition $M_1=M_2$.

Now to the calculation. The integration over $\varkappa$ is trivial. Writing the cross section in the form $\sigma=4\pi\{a_1^2I_{11}+2a_1a_2I_{12}+a_2^2I_{22}\}$, and introducing the abbreviations $\xi=\omega t$, and

$$\lambda\equiv\lambda(\xi)=[(2M_{12})^{-1}-M^{-1}(1+i\xi-e^{i\xi})-i\xi]^{-1}, \quad \text{(A15)}$$

one finds

$$I_{12}=\tfrac{1}{4}(\pi n_0)^{-\frac{1}{2}}\int_{-\infty}^{+\infty}\lambda^{\frac{1}{2}}\exp(-n_0\xi^2\lambda)d\xi, \quad \text{(A16)}$$

i.e., an expression similar to (34), with a different function $\lambda$.

We must remember that (A16) includes the contribution of collisions with small momentum transfers. Thus it is not surprising that the integrand of (A16) is not now exponentially small for large energies $n_0$ in the neighborhood of time $\xi=0$. In fact, for small $\xi$, $\lambda\sim 2M_{12}$ and the contribution of small times to (A16) is

$$I_{12}\approx\tfrac{1}{4}(\pi n_0)^{\frac{1}{2}}(2M_{12})^{\frac{1}{2}}\int\exp(-2M_{12}n_0\xi^2)d\xi$$
$$=M_{12}\omega k_0^{-2}. \quad \text{(A17)}$$

Noticing that $\langle r_{12}^2\rangle=(2M_{12}\omega)^{-1}$, we recognize in (A17) the first and most important term of P(7.20). Other terms, of higher order in $n_0^{-1}$, can of course be obtained from the neighborhood of $\xi=0$ by a complete asymptotic expansion of the integral.

Leaving these terms aside, we now show that the remaining part of the integral, i.e., excluding the neighborhood of $\xi=0$, gives an exponentially small contribution (even for $M_1=M_2$). First, if $M_1\neq M_2$, and excluding a finite interval around the origin, it is easy to show that on the real axis an inequality like (35) is satisfied, which proves the statement. If $M_1=M_2$ we have to examine the neighborhood of the points $\xi=\pm\pi$, $\pm 3\pi$, $\cdots$ where the real part is equal to zero. One finds that at these points,

$$\frac{d}{d\xi}(\xi^2\lambda)=i\left(1+\frac{1}{M}\right)^{-2}\neq 0.$$

Hence, these points are not saddle points; if the integration path is deformed and caused to pass under the points $\xi=\pm(2n+1)\pi$, the inequality (35) can be re-established along the whole integration path, and the integral is thus $\sim\exp(-cn_0)$. This completes the proof of all our statements.

# Interaction of Polarized Neutrons with Polarized $Mn^{55}$ Nuclei

S. BERNSTEIN, L. D. ROBERTS, C. P. STANFORD, J. W. T. DABBS, AND T. E. STEPHENSON
*Oak Ridge National Laboratory, Oak Ridge, Tennessee*

(Received November 16, 1953; revised manuscript received February 15, 1954)

The dependence of the capture cross section of polarized $Mn^{55}$ nuclei for polarized neutrons upon relative orientations of incident and bombarded particles has been directly observed. The target material was the paramagnetic substance, manganous ammonium sulfate, which is known to have a large hyperfine structure coupling. It was placed in a magnetic field of 2350 oersteds at a temperature of 0.20°K. Under these conditions the polarization of the paramagnetic electrons is about 85 percent. Because of the large effective magnetic field created by the paramagnetic electrons at the Mn nucleus, the nuclei should achieve a polarization of 16 percent. The 2.6-hour activity of the residual nucleus, $Mn^{56}$, was measured after the sample had been bombarded with a beam of slow neutrons polarized to the extent of 32 percent by passage through magnetized iron. The activity for neutron polarizing field and sample polarizing field parallel was found to be 3.4 percent less than for the fields antiparallel. The difference in the two activities was found to depend upon the sample temperature in accordance with theory. The difference was found to be unaccompanied by a corresponding change in sample transmission. These results are interpreted to mean that the change in sample activity was due to the dependence of the capture cross section of the polarized Mn nuclei upon the relative orientation of the interacting particles. The observations are discussed in terms of available information about the energy level system of the compound nucleus, $Mn^{56}$.

## INTRODUCTION

THE spin dependence of nuclear forces was first demonstrated experimentally by the scattering of neutrons from ortho- and para-hydrogen,[1-4] in which experiment the effects observed are caused by the relative spin directions taken by the hydrogen atoms of each isolated hydrogen molecule. The spin dependence of scattering is exhibited also in the spin incoherent scattering of neutron diffraction experiments,[5] in which the random orientations of the nuclear spins of the sample cause an isotropic diffuse background in diffraction patterns. In both of these methods it is the spin dependence of the scattering cross section which is observed, and the bulk nuclear magnetization of the sample is zero. We have observed directly the spin dependence of the *capture* cross section by bombarding a sample possessing a bulk nuclear magnetization with a beam of polarized neutrons, and observing the dependence of the target activity upon relative spin orientations of the incident and bombarded particles. (The angular distribution of gamma rays from such polarized samples containing radioactive nuclei has been observed.[6] An experiment in which neutron effects of nuclear polarization in gadolinium sulfate were observed, has been mentioned briefly,[7] but no details of the experiment have been reported.)

For polarizing the nuclei we relied upon the method of Rose[8] and Gorter,[9] i.e., the use of the strong magnetic field produced at the nucleus by hyperfine structure coupling in an appropriate paramagnetic substance. An external magnetic field is applied to the sample merely for the purpose of polarizing the electronic moments. The sample used in this work was the deuterated paramagnetic salt, $Mn^{55}SO_4 \cdot (ND_4)_2SO_4 \cdot 6D_2O$. Its $Mn^{55}$ nuclei were polarized by partial adiabatic demagnetization of the salt. This substance was selected because its hyperfine structure is known to be large,[10] its low-temperature properties are suitable, the 13-barn neutron capture cross section of $Mn^{55}$ is acceptably large, and the 2.60-hour half-life of the radioactive compound nucleus, $Mn^{56}$, is convenient.

The electronic system of the $Mn^{++}$ ion possesses spin angular momentum only. The nuclear polarization is given by

$$f_N = \frac{S(I+1)hc}{3} \frac{A}{kT} \frac{M_e}{M_\infty} \tag{1}$$

in which $S$ is the electron spin quantum number, $I$ is the nuclear spin quantum number, $k$ is the Boltzmann constant, $T$ is the temperature, $M_e$ is the magnetic moment of the electron spin system, $M_\infty$ is the electronic magnetic moment at saturation, $h$ is Planck's constant, $c$ is the velocity of light, and $A$ is the hyperfine structure coupling constant. The spatial average value of $A$ for this substance has been calculated from measurements[10] to be 0.00932 $cm^{-1}$. Substituting the appropriate values $S=5/2$, $I=5/2$, expression (1) becomes

$$f_N = \frac{0.0391}{T} \frac{M_e}{M_\infty}. \tag{2}$$

[1] Halpern, Estermann, Simpson, and Stern, Phys. Rev. **52**, 142 (1937).
[2] Brickwedde, Dunning, Hoge, and Manley, Phys. Rev. **54**, 266 (1938).
[3] L. W. Alvarez and K. S. Pitzer, Phys. Rev. **58**, 1003 (1940).
[4] Sutton, Hall, Anderson, Bridge, DeWire, Lavatelli, Long, Snyder, and Williams, Phys. Rev. **72**, 1147 (1947).
[5] Shull, Wollan, Morton, and Davidson, Phys. Rev. **73**, 262 (1948).
[6] Ambler, Grace, Halban, Kurti, Durand, Johnson, and Lemmer, Phil. Mag. **349**, 216 (1953).
[7] J. A. Beun, Ned. Tijdschr. Natuurk. **18**, 245 (1952).
[8] M. E. Rose, Phys. Rev. **75**, 213 (1949).
[9] C. J. Gorter, Physica **14**, 504 (1948).
[10] B. Bleaney and D. J. E. Ingram, Proc. Roy. Soc. (London) **A205**, 336 (1951).

In this experiment the manganous ammonium sulfate sample was demagnetized from an initial temperature of 1.2°K and an initial magnetic field of 16 400 oersteds to a final magnetic field of 2350 oersteds. This demagnetization procedure gave a final temperature of 0.20°K in the final field of 2350 oersteds. The electron polarization, $f_e = M_e/M_\infty$, under these conditions of final field and temperature was measured to be $f_e = 85$ percent. The cryogenic aspects of this work, including the thermodynamic measurement of the final temperature and the measurement of the sample magnetic moment will be described in detail in a separate publication.[11] Substituting the measured values $f_e = 0.85$, $T = 0.20$°K in (2), a nuclear polarization $f_N = 16.6$ percent is to be expected.

The nuclear cross section, $\sigma$, for slow neutrons is given by[8]

$$\sigma = \sigma_1\left(1+\frac{I}{I+1}f_n f_N\right), \quad J = I+\tfrac{1}{2}, \tag{3a}$$

$$\sigma = \sigma_2(1-f_n f_N), \quad J = I-\tfrac{1}{2}, \tag{3b}$$

in which $f_n$ is the neutron polarization, $J$ is the angular momentum quantum number of the compound nucleus. $\sigma_1$ and $\sigma_2$ are the respective normal cross sections for $f_n$ or $f_N$ or both equal to zero. The polarization $f_n$ of the incident neutron beam was measured[12] to be 32 percent. Using $f_N = 0.16$, $f_n = 0.32$ in (3a) and (3b), the observed Mn capture cross section for spins of neutrons and nuclei parallel should be 7.2 percent greater than the cross section for antiparallel spins, if only a level of $J = I+\frac{1}{2}$ is effective, and should be 10.2 percent less, if only $J = I-\frac{1}{2}$ is effective. If only a single resonance level is effective, and if the product of the two polarizations ($f_n f_N$) is known, then we can directly deduce whether the angular momentum of the compound state is $I+\frac{1}{2}$ or $I-\frac{1}{2}$ from the observation of whether the neutron cross section increases or decreases with polarization. If more than one resonance level is effective, then terms of both types (3a) and (3b) may contribute to the cross section, $\sigma_0$. The measured relative change of cross section with polarization will then have to be interpreted in terms of the nuclear parameters of the effective resonance levels.

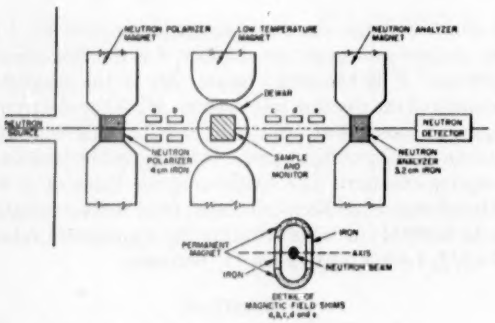


FIG. 1. Schematic arrangement of apparatus.

Our measurements of the capture cross section of $Mn^{55}$ showed a decrease of 3.4±0.3 percent, when the relative polarization directions (spin directions) of neutrons and nuclei were changed from the antiparallel to the parallel state. The interpretation of the measured negative 3.4 percent as compared to the calculated positive 7.2 percent for $J = I+\frac{1}{2}$, and the negative 10.2 percent for $J = I-\frac{1}{2}$, in terms of present knowledge of the energy level system of $Mn^{56}$, is given below.

A diagram of the experimental arrangement is shown in Fig. 1. The beam of neutrons emerging from the chain reactor is polarized in passing through 4 cm of highly magnetized iron. The polarized neutrons then pass through a Mn metal monitor and the deuterated manganous ammonium sulfate sample, which is at a temperature of 0.20°K in a magnetic field of 2350 oersteds. About 60 percent of the neutrons are scattered in the sample. A small fraction of the neutrons are captured by the manganese nuclei of the sample. The sample is first exposed to the beam of polarized neutrons for 50 minutes under such magnetic field conditions that the polarizations of $Mn^{55}$ nuclei and the neutrons are parallel. The sample is then removed from the system of Dewar flasks, and its activity is carefully measured. The procedure is later repeated with the neutron and nuclear polarizations antiparallel. The activities of the sample in the two exposures is a measure of the capture cross section of $Mn^{55}$ in the respective arrangements of relative spin orientations of neutron and nucleus.

## THE CRYOSTAT AND SAMPLE

The cryostat, which provided a simple arrangement for rapidly installing and removing the sample, was constructed entirely of metal. The sample and monitor assembly is shown in Fig. 2. The hydrogen of the sample material was replaced with deuterium in order to eliminate the depolarization of the neutron beam by the large incoherent scattering of the protons, and to make the total neutron scattering cross section of the sample as small as possible. The sample of $Mn^{++}(ND_4)_2(SO_4)_2 \cdot 6D_2O$ was prepared by recrystallizing the hydrated salt four times from heavy water. Mass spectrographic analysis showed the final sample material to be 99 percent deuterated. To preserve the deuteration from exchange with atmospheric light water, it was necessary to enclose the salt in an airtight container. The container had to meet several important requirements; namely, it must not be of metal, and it could not be made of a material which would appreciably depolarize the neutrons or be activated by them. The fluorocarbon plastic, Teflon, was used. In order to admit helium

[11] J. W. T. Dabbs and L. D. Roberts, Phys. Rev. **93**, 935 (1954).

[12] Stanford, Stephenson, Cochran, and Bernstein, Phys. Rev. **94**, 374 (1954).

exchange gas to the sample during the demagnetization procedure and have the container sealed when the sample was not in the cryostat, the container was fitted with a capillary vent which could be closed. The sample was pressed from small crystals (~0.5 mm in diameter) to within a few percent of crystal density into a right circular cylinder of 0.660-in. diameter and 0.247-in. height. The sample pellet weighed 2.96 g. A cylindrical recess 0.660-in. diameter when cold and 0.010-in. deep on the back of the Teflon box served to locate the manganese metal neutron beam monitor which was 0.660-in. in diameter and 0.060-in. thick. The common cylindrical axes of the sample and monitor coincided with the axis of the neutron beam. As is usual in demagnetization experiments, the sample was suspended on strings. In this experiment, since the sample and monitor had to be removed from the apparatus daily for counting the induced activities, the sample and the monitor were clamped into a holder which was in turn suspended by a number of cotton threads from a metal framework. The strings were arranged to give a rigid reproducible support to minimize vibration-induced heat leak to the sample and to give accurate day to day repositioning.

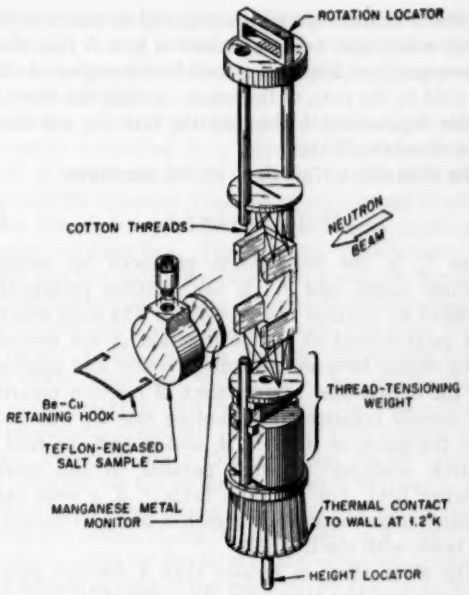


FIG. 2. Sample and monitor assembly.

## POLARIZED NEUTRONS

The beam of neutrons from the reactor was polarized by passage through 4 cm of highly magnetized cold-rolled steel. The transmission method was chosen rather than polarization by total reflection from a magnetized mirror[13] or by Bragg reflection from a magnetized crystal,[14] both of which methods give a higher polarization, for reasons of intensity. The neutron polarization was reversed with respect to the polarization of the nuclei simply by reversing the neutron polarizer magnetic field with respect to the sample polarizing magnetic field. Those neutrons which did not have any collision in the sample continued on their path through the analyzer, which was 3.2 cm of highly magnetized cold-rolled steel, and then into a $BF_3$ proportional counter neutron detector. The direction and magnitude of the magnetic field along the path of the neutron beam were controlled by means of the parallel plate shims shown in Fig. 1, so that the neutrons should maintain the desired state of polarization. The magnetic field between the plates was adjusted by numerous U-shaped permanent magnets placed at various points along the length of the shims, as shown in Fig. 1.

For those irradiations in which the magnetic fields of neutron polarizer and sample polarizer were parallel, the fields between pairs of shims *a* and *b* were adjusted so that the magnetic field in the region between neutron polarizer and Dewar flask was at least 100 oersteds in the same direction as the two polarizing fields. Under these conditions the magnitude and direction of the neutron polarization should be maintained along the neutron path.

When the magnetic fields of neutron polarizer and sample polarizer were antiparallel, the field of shim *a* was adjusted to be in the same direction as that of the neutron polarizer. The field of shim *b* was made to be parallel to the field of the sample polarizer. The permanent U-shaped magnets were adjusted so that the magnetic field reversed its direction in the small space between the adjacent ends of shims *a* and *b*. These conditions should induce the neutrons to make non-adiabatic transitions and strike the polarized nuclei of the sample with the opposite relative orientation to that described above when the field directions of neutron polarizer and sample polarizer were parallel. In order to obtain optimum conditions for nonadiabatic transitions or no transition depending upon the type of irradiation desired, magnetic field traverses were made with flip coil and compass in adjusting the strength and direction of the magnetic field in the region between the shim plates.

The runs were about equally divided between irradiations in which neutron polarizer field and sample polarizer field were parallel and those in which they were antiparallel. The state of polarization of the neutron beam transmitted by the sample was monitored throughout every sample irradiation by means of the "shim effect," $G$. Consider the case when neutron polarizer and sample polarizer are parallel. The field directions between all pairs of shims and the fields of the neutron polarizer, sample polarizer, and neutron analyzer were all adjusted to be in the same direction, and the counting rate, $C_1$, was taken. The three pairs

[13] D. J. Hughes and M. T. Burgy, Phys. Rev. **81**, 498 (1951).
[14] C. G. Shull, Phys. Rev. **81**, 626 (1951).

of shims $c$, $d$, and $e$ were then adjusted so that a region of very nearly zero field was achieved in $d$. A thin sheet of unmagnetized iron was placed in this region of near zero field in the path of the beam, causing the beam to become depolarized.[15] The counting rate, $C_2$, was taken under these conditions.

The shim effect, $G$, is given by the expression

$$G=C_1/C_2=1+f_n f_n', \tag{4}$$

where $f_n$ is the polarization produced by neutron polarizer alone, and $f_n'$ is the neutron polarization produced by neutron analyzer alone. The shim effect is thus proportional to the polarization of the neutrons in the region between neutron polarizer and analyzer. For the antiparallel arrangement of neutron polarizer and sample polarizer the counting rate $C_1$ was taken with the fields of shims $c$, $d$, and $e$, and the field of neutron analyzer adjusted parallel to the sample polarizer field. For $C_2$, shim fields $c$, $d$, $e$ were again adjusted to give a zero field region in which to depolarize the beam with the iron foil.

The shim effect is greater than 1 for the parallel field case and less than 1 for the antiparallel field case. $(G-1)$ will be symmetrical about 1, if the polarizations in the two cases have equal magnitude and opposite sign. The quantity $(G-1)$ was used as a relative measure of the polarization of the neutrons transmitted through the sample. Strictly speaking, the measured values of $(G-1)$ are proportional to the product of the neutron polarizations produced by polarizer alone and analyzer alone averaged over the continuous spectrum of neutrons emerging through 4.0 cm of polarizer iron plus 3.2 cm of analyzer iron, and weighted with the efficiency *vs* energy of the long $BF_3$ detector used. The polarization entering into the quantitative interpretation of the capture cross section data is the polarization detected by a $1/v$ detector averaged over the continuous spectrum emerging from the 4-cm thickness of polarizer. The measurement of this average polarization has been described.[12] About 80 percent to 95 percent of the continuous spectrum of neutrons were flipped. Under ideal conditions essentially all of the neutrons of approximately Maxwellian incident distribution filtered by a few cm of iron can be induced to make nonadiabatic transitions.[16] In our work the optimum magnetic field conditions for maximum efficiency of flipping were made somewhat difficult by the fact the the 11 000-oersted field at the neutron polarizer was only about 4 feet away from the oppositely directed 2350 to 10 500-oersted field of the sample polarizing magnet. The fraction of neutrons at the low and high energy ends of the spectrum was greater in our experiment than in the spectrum of reference 16 because the polarizing iron was thicker and the temperature of the incident Maxwell distribution of neutron velocities was higher.

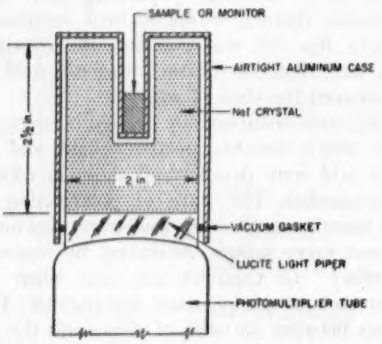


FIG. 3. Arrangement for measuring activities.

## MEASUREMENTS OF ACTIVITIES

In order to avoid the necessity for making absolute measurements, a Mn metal monitor was used. This monitor was fixed in an accurately reproducible position to the outside of the Teflon box containing the sample salt, as shown in Fig. 2, and was exposed simultaneously with the salt. The monitor was machined from a cast ingot of Mn metal containing about 3 percent Cu. The Cu was added to make the material more easily machinable and less porous. Activity due to the 12.9-hour $Cu^{64}$ was found to be unobservable in a series of test irradiations of 50 minutes made under the usual conditions of the experiment. The 4.3-minute $Cu^{66}$ activity gave no contribution during the counting period since this short life-time activity died away during the period of about 50 minutes elapsing between the end of irradiation and the beginning of the counting. Both sample and monitor were found to have the accepted value for the half-life of 2.60 hours to less than 1 percent. The neutron beam passed through the monitor before impinging upon the sample.

The activity of the 2.6-hour $Mn^{56}$ was measured by means of a NaI fluorescent crystal counting arrangement. The crystal was about 2-in. in diameter and $2\frac{1}{2}$-in. high. The samples were placed at the bottom of a reentrant "well" as shown in Fig. 3, to achieve greater efficiency. The walls of the sealed container surrounding the crystal were such that almost all of the pulses counted were due to three $\gamma$ rays emitted by $Mn^{56}$ and very few to $\beta$ rays. The usual arrangement of fluorescent crystal, light piper, photomultiplier tube, amplifier, and scaling circuit was used.

The requirement on the counting system was simply that its over-all sensitivity remain constant over the 6-hour period during which the activities of a sample and monitor from a single irradiation were being measured. The sensitivity was monitored and adjusted by means of the 0.669-Mev 37-year $Cs^{137}$ gamma ray. The observed integral and differential counting rate curves

[15] O. Halpern and T. Holstein, Phys. Rev. **59**, 960 (1941).

[16] Burgy, Hughes, Wallace, Heller, and Woolf, Phys. Rev. **80**, 953 (1950).

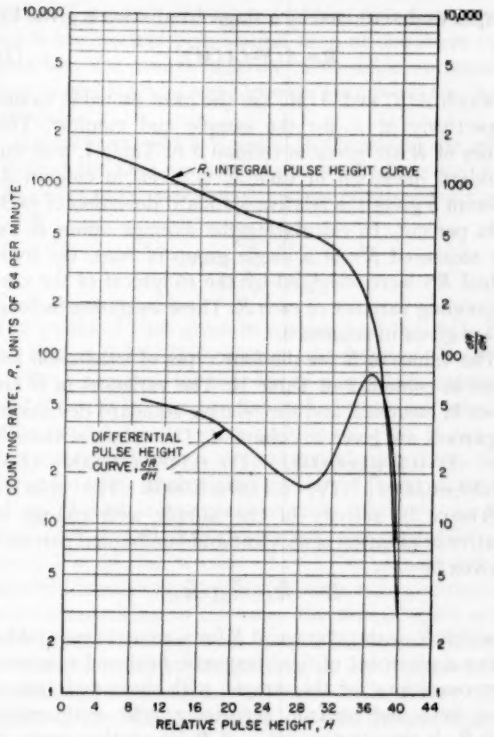
R, INTEGRAL PULSE HEIGHT CURVE
DIFFERENTIAL PULSE HEIGHT CURVE, dR/dH
COUNTING RATE, R, UNITS OF 64 PER MINUTE
RELATIVE PULSE HEIGHT, H
%/E

FIG. 4. Counting rate curves for $Cs^{137}$.

using $Cs^{137}$ are shown in Fig. 4, in which the peak of the differential curve corresponds to 0.669 Mev. The gain of a photomultiplier tube is a very sensitive function of its applied voltage. To maintain constant sensitivity the voltage on the tube was adjusted about once per hour during the counting schedule to make the $Cs^{137}$ peak of the differential curve occur at a fixed pulse height. In practice, one chooses the integral counting rate at a pulse-height setting corresponding to the peak and adjusts the voltage periodically to reproduce this counting rate.

The over-all gain of the system was actually tested with a much greater sensitivity than was used when counting the Mn activity. For Cs the pulse-height setting used was such that a small change in gain would cause a very large fractional change in counting rate. The pulse height used in counting the Mn activity was chosen to correspond to a rather flat portion of its integral counting rate *vs* pulse-height curve, thus making the Mn counting rate comparatively insensitive to gain changes. The Cs monitor count reproduced itself from hour to hour within 2 percent, or twice its statistical error. If this fluctuation were interpreted as being due to a true change in gain, then the Mn counting rate would have been affected by less than 0.05 percent. Differential counting rate curves were taken only for the purpose of checking and adjusting the equipment and finding optimum pulse-height settings for the integral counting rates taken during a run. For the irradiated samples all that was required was a number proportional to the saturated activity.

Counting rates of sample and monitor were taken alternately according to a planned schedule over a period of about six hours, starting 50 minutes after the end of the exposure. Positions of sample and monitor within the NaI crystal arrangement were made accurately reproducible. The relative orientations of sample and monitor obtaining during neutron irradiation were maintained during the activity measurements. This relative orientation was also kept the same from day to day. Initial counting rates for the sample were about 3000 counts per minute, and for the monitor were about 20 000 counts per minute. The NaI crystal background counting rate was about 100 counts per minute. For each run a total of about $3\times10^5$ counts were collected for the sample and about $10^6$ counts for the monitor. Typical decay curves for the sample and monitor are shown in Fig. 5. The result of a single irradiation is given by the ratio of the saturated activity of the sample to that of the monitor. By this procedure all activity measurements of the sample were made relative to the activity of the monitor. Fluctuations in neutron beam intensity due to fluctuations in pile power were canceled out.

## RESULTS AND ANALYSIS OF THE ACTIVATION MEASUREMENTS

Four types of irradiation were made. These are designated as I, II, III, and IV in the first column of Table I. The conditions listed in this column are the final temperature and magnetic field values of the sample, and the relative directions of sample-polarizing and neutron-polarizing fields. A comparison of the results of I and II should show the full effect of relative particle orientation. Under the temperature and field conditions of III and IV, the sample should have the same electron polarization but much less nuclear polarization than under the conditions of I and II. The relative change in sample activity exhibited by III and IV should be

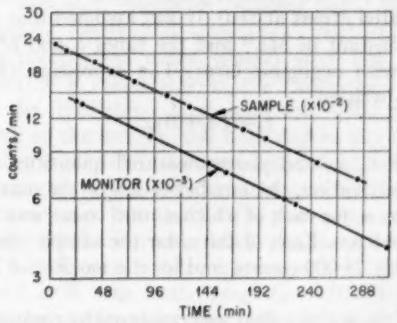


FIG. 5. Typical decay curves of sample and monitor.

TABLE I. Results and analyses of activation measurements.

| Experimental conditions (1.) | Run number (2.) | $R=\frac{A(S)}{A(M)}$ (3.) | Standard deviation of $R$, $\sigma(R)$ (4.) | Relative error in $R$, % $100\times\sigma(R)/R$ (5.) | Weighting factor, $w=[1/\sigma(R)]^2$ (6.) | Flipping efficiency factor; $q$ (7.) |
|---|---|---|---|---|---|---|
| I | 1 | 0.1443 | $8.66\times10^{-4}$ | 0.60 | $1.334\times10^{6}$ | |
| $T=0.20°K$ | 4 | 0.1446 | $7.95\times10^{-4}$ | 0.55 | $1.581\times10^{6}$ | |
| $H=2350$ | 5 | 0.1439 | $7.34\times10^{-4}$ | 0.51 | $1.857\times10^{6}$ | |
| oersteds | 8 | 0.1450 | $7.83\times10^{-4}$ | 0.54 | $1.631\times10^{6}$ | |
| Fields | 10 | 0.1439 | $14.82\times10^{-4}$ | 1.03 | $0.455\times10^{6}$ | |
| parallel | 11 | 0.1445 | $9.97\times10^{-4}$ | 0.69 | $1.006\times10^{6}$ | |
| | 14 | 0.1431 | $15.03\times10^{-4}$ | 1.05 | $0.443\times10^{6}$ | |
| | 16 | 0.1430 | $7.44\times10^{-4}$ | 0.52 | $1.809\times10^{6}$ | |
| | 34 | 0.1433 | $7.60\times10^{-4}$ | 0.53 | $1.733\times10^{6}$ | |
| | 36 | 0.1434 | $12.76\times10^{-4}$ | 0.89 | $0.614\times10^{6}$ | |
| II | 2 | 0.1519 | $14.28\times10^{-4}$ | 0.94 | $0.490\times10^{6}$ | 0.83 |
| $T=0.20°K$ | 3 | 0.1499 | $9.14\times10^{-4}$ | 0.61 | $1.196\times10^{6}$ | 0.91 |
| $H=2350$ | 6 | 0.1489 | $9.08\times10^{-4}$ | 0.61 | $1.212\times10^{6}$ | 0.86 |
| oersteds | 7 | 0.1471 | $7.65\times10^{-4}$ | 0.52 | $1.709\times10^{6}$ | 0.77 |
| Fields | 9 | 0.1488 | $8.04\times10^{-4}$ | 0.54 | $1.549\times10^{6}$ | 0.91 |
| antiparallel | 12 | 0.1482 | $10.82\times10^{-4}$ | 0.73 | $0.862\times10^{6}$ | 0.84 |
| | 13 | 0.1499 | $10.34\times10^{-4}$ | 0.69 | $0.935\times10^{6}$ | 0.85 |
| | 15 | 0.1498 | $13.33\times10^{-4}$ | 0.89 | $0.563\times10^{6}$ | 0.86 |
| | 17 | 0.1485 | $21.24\times10^{-4}$ | 1.43 | $0.122\times10^{6}$ | 0.84 |
| | 18 | 0.1458 | $16.18\times10^{-4}$ | 1.11 | $0.382\times10^{6}$ | 0.85 |
| | 35 | 0.1487 | $8.48\times10^{-4}$ | 0.57 | $1.392\times10^{6}$ | 0.83 |
| | 37 | 0.1491 | $7.01\times10^{-4}$ | 0.47 | $2.036\times10^{6}$ | 0.85 |
| III | 19 | 0.1463 | $7.31\times10^{-4}$ | 0.50 | $1.869\times10^{6}$ | |
| $T=1.2°K$ | 21 | 0.1462 | $12.57\times10^{-4}$ | 0.86 | $0.633\times10^{6}$ | |
| $H=10\,500$ | 23 | 0.1451 | $6.53\times10^{-4}$ | 0.45 | $2.345\times10^{6}$ | |
| oersteds | 25 | 0.1459 | $6.57\times10^{-4}$ | 0.45 | $2.320\times10^{6}$ | |
| Fields | 27 | 0.1478 | $13.60\times10^{-4}$ | 0.92 | $0.541\times10^{6}$ | |
| parallel | 30 | 0.1460 | $6.13\times10^{-4}$ | 0.42 | $2.660\times10^{6}$ | |
| IV | 20 | 0.1478 | $10.64\times10^{-4}$ | 0.72 | $0.883\times10^{6}$ | 0.71 |
| $T=1.2°K$ | 22 | 0.1460 | $7.45\times10^{-4}$ | 0.51 | $1.804\times10^{6}$ | 0.81 |
| $H=10\,500$ | 24 | 0.1452 | $7.12\times10^{-4}$ | 0.49 | $1.975\times10^{6}$ | 0.93 |
| oersteds | 26 | 0.1474 | $6.63\times10^{-4}$ | 0.45 | $2.273\times10^{6}$ | 0.92 |
| Fields | 28 | 0.1477 | $7.98\times10^{-4}$ | 0.54 | $1.572\times10^{6}$ | 0.92 |
| antiparallel | 29 | 0.1484 | $7.72\times10^{-4}$ | 0.52 | $1.679\times10^{6}$ | 0.84 |
| | 31 | 0.1471 | $7.36\times10^{-4}$ | 0.50 | $1.848\times10^{6}$ | 0.96 |
| | 32 | 0.1473 | $13.55\times10^{-4}$ | 0.92 | $0.545\times10^{6}$ | 0.99 |
| | 33 | 0.1454 | $9.60\times10^{-4}$ | 0.66 | $1.086\times10^{6}$ | 0.92 |

about $\frac{1}{6}$ of the change shown by comparison of I and II.

The total number of counts, $z_i$, accumulated during the time interval $(t_i-t_i^*)$ were recorded at various times in the course of the decay of the activity of sample and monitor. The intervals $(t_i-t_i^*)$ varied from 5 to 30 minutes, depending upon whether the sample or monitor was being counted and upon the elapsed time between the end of irradiation and time of counting. The counts, $z_i$, are given by the expression

$$z_i=A[\exp(-\lambda t_i)-\exp(-\lambda t_i^*)]+B(t_i-t_i^*). \quad (5)$$

In (5), $B$ is the background counting rate of the counting system, $A$ is a number proportional to the number of activated atoms at $t=0$. It was assumed that $\lambda$, the decay constant of $Mn^{56}$ and the times $t_i$ and $t_i^*$ were known with negligible error. The expression (5) can then be written

$$z_i=Ax_i+By_i, \quad (6)$$

in which $z_i$, $x_i$, and $y_i$ are measured quantities. For a typical activation, the number of $z_i$'s or the number of intervals, $n$, for each of which a total count was taken, was about ten. Each of the $z_i$ for the sample consisted of roughly 25 000 counts, and for the monitor of 75 000 counts.

All of the activity data were analyzed by conventional statistical procedures. The relative activity of the sample, as determined by a single irradiation is given by

$$R=A(S)/A(M), \quad (7)$$

in which $A(S)$ and $A(M)$ are the most probable values respectively of $A$ for the sample and monitor. The values of $R$ are given in column 3 of Table I, and the standard deviation of each $R$ is given in column 4. Column 5 gives the relative standard deviation of each $R$ in percent. In calculating the average value $\bar{R}$, of the measured $R$'s of a single group of runs, the individual $R$'s were weighted by the reciprocal of the corresponding variance of each $R$. These weighting factors, $w$, are given in column 6.

The values of $\bar{R}$ for the four types of irradiation are given in column 2 of Table II. The variances in $\bar{R}$ are given in column 3 and the relative standard deviations in percent are given in column 4. The values of the $\bar{R}$'s are: (I) $0.1440\pm0.0002$; (II) $0.1488\pm0.0004$; (III) $0.1459\pm0.0004$; (IV) $0.1469\pm0.0004$. The relative difference in activity of the sample with change in relative orientation of incident and bombarded particles is given by

$$D=(\bar{R}_a-\bar{R}_p)/\bar{R}_p, \quad (8)$$

in which $\bar{R}_a$ is the average of $R$ for a group of runs taken under a given set of final magnetic field and temperature conditions for the sample, with the sample polarizing field and neutron polarizing field antiparallel, and $\bar{R}_p$ is the average value of $R$ for another group of runs taken under the same final sample temperature and field conditions with the two polarizing fields parallel. The values of $D$ in percent are given in column 5. The standard deviations of the $D$'s are given in column 6. The final results state, then, that at 0.20°, the sample activity with fields antiparallel was $(3.38\pm0.34)$ percent greater than the activity with fields parallel. At 1.20°K, with the sample possessing,

TABLE II. Summary of statistical averages of the activity data.

| (1) | $\bar{R}$ (2) | $[\sigma(\bar{R})]^2$ (3) | $\frac{100\sigma(\bar{R})}{\bar{R}}$ (4) | $(\bar{R}_a-\bar{R}_p)/\bar{R}_p$ $D$,% (5) | $\sigma(D)$ (6) | $t$ (7) |
|---|---|---|---|---|---|---|
| I<br>$T=0.20°$,<br>$H=2350$,<br>parallel | 0.1440 | $4.87\times10^{-6}$ | 0.153 | | | |
| | | | | 3.38 | 0.34 | 9.3 |
| II<br>$T=0.20°$,<br>$H=2350$,<br>antiparallel | 0.1488 | $19.30\times10^{-6}$ | 0.295 | | | |
| III<br>$T=1.2°$,<br>$H=10\,500$,<br>parallel | 0.1459 | $15.03\times10^{-6}$ | 0.266 | | | |
| | | | | 0.66 | 0.33 | 1.7 |
| IV<br>$T=1.2°$<br>$H=10\,500$,<br>antiparallel | 0.1469 | $14.03\times10^{-6}$ | 0.255 | | | |

within 1 percent, the same electron polarization and much less nuclear polarization than at the lower temperature, the sample activity with fields antiparallel was (0.66±0.33) percent greater than with the fields parallel.

A parameter which is useful in discussing the reliability of the final results is the ratio, $t$, of the value of $(\bar{R}_a-\bar{R}_p)$ to the standard deviation of this difference.[17]

$$t=\frac{\bar{R}_a-\bar{R}_p}{\sigma(\bar{R}_a-\bar{R}_p)}. \tag{9}$$

The values of $t$ are given in column 7 of Table II. For the runs at 0.20°, 2350 oersteds, the value of $t$ is about 9. If one assumes, for purpose of illustration, that the two $R$'s at 0.20° for parallel and antiparallel orientations came from the same population, then it can be demonstrated by standard statistical procedures that the probability of obtaining a value of 9 or greater for $t$ from 22 runs, is extremely unlikely. Similarly, for the data of 1.2° and 10 500 oersteds, the probability is about 1 in 16 that a value of $t=1.7$ or greater will be obtained from 15 runs belonging to the same population, and corresponding to the same direction of effect as in 0.20° group. It seems, then, that the 3.38 percent change in activity obtained at 0.20°, and 2350 oersteds is, statistically at least, a "real" one with a very high degree of probability, whereas the 0.66 percent change in activity with relative orientation observed at 1.2° and 10 500 oersteds has a very much lower probability of being statistically "real".

Some aspects of the data are illustrated graphically in Fig. 6, a histogram of the $R_j$ values obtained with the four different experimental arrangements. The ordinate gives the relative number of runs, weighted with the weighting factor $w_j$. The width of the histogram interval is the value of $\sigma(R)$ averaged over all the runs of the four types. The areas enclosed by the histograms for the two types of irradiation at a single temperature were made equal. The average values $\bar{R}$ for each of the four types are indicated by the arrows along the axes of abscissas. The number above each histogram ordinate is the actual number of runs whose $R$ values fall in that interval.

Column 7 of Table I gives values of a flipping efficiency factor $q$, derived from the shim effect values measured during each irradiation. The value $q$ is the fraction of the neutrons which were induced to make the required nonadiabatic transition in the antiparallel runs. These $q$ values can be used to correct the values of $D$ to the values of $D$ which would have been obtained if all the neutrons had been flipped. When this correction is made the value $D=3.38$ percent is increased to the value $D=4.0$ percent.

The change in nuclear cross section on polarization is to a good approximation inversely proportional to

[17] A. M. Mood, *Introduction to Theory of Statistics* (McGraw-Hill Book Company, New York, 1950), p. 225.

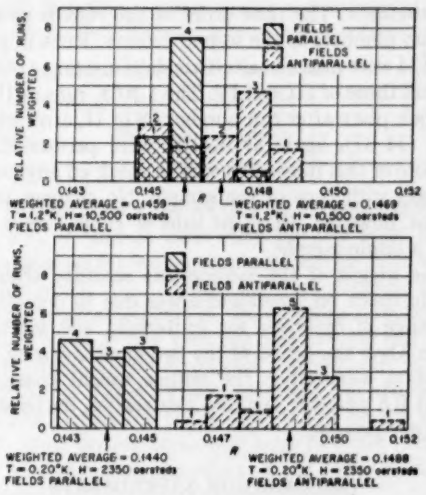


FIG. 6. Histogram of the experimental results. The ordinate is the relative frequency with which the relative activity given by the abscissa was obtained. The width of the interval is the average standard deviation of the activity.

the temperature at constant electronic magnetic moment. Although the fractional error on the 0.66 percent is large, the ratio $3.38/0.66\approx 5.1$ of the cross section changes observed at 0.20°K and 1.20°K, respectively, is close to the inverse ratio of the corresponding temperatures, $1.2°/0.20°=6.0$. This good agreement may be accidental but it does serve to emphasize that with constant neutron and electron polarizations the change in cross section with the two types of relative orientation of the particles decreased as the temperature increased in accordance with the theory. The average value $\frac{1}{2}(\bar{R}_p+\bar{R}_a)=0.1468$ of all runs at 0.20° including both parallel and antiparallel is very close to the value 0.1465 for the same average for all runs at 1.20°K. Both of these averages have been corrected for flipping efficiency. Throughout the entire experiment the distribution of repeated measurements of the same quantity compared very favorably with the distribution expected from a consideration of the counting statistics of a single measurement.

The electronic magnetic moment was measured immediately before and after each irradiation. The nuclear polarization varied slightly from run to run. For the 0.20°K measurements, the variations occurred during the irradiations because of the ~100 erg/min heat leak to the sample, and from day to day because of small variations in the initial and final fields and initial temperatures used. Variations in the field and temperature used for the 1.20°K measurements were extremely small. The calculated nuclear polarization for all 0.20°K runs fell in the range $f_N=0.16\pm0.01$, and the 1.20°K runs in the range $f_N=0.0265\pm0.0009$. Each of the sample to monitor activity ratios given in Table I required one day of work in preparation and

measurement. The time order of the runs is given by the run numbers in the second column. Runs in groups I and II were made on alternate days insofar as possible, as were those of III and IV. The 1.20°K runs of III and IV took place after run number 18 of II, after which 4 runs (34–37), again at 0.20°K were performed. The purpose of this time order was to check on any possible changes with time of the sample. No changes are apparent, however. All of the runs of Table I were taken with a single sample

The weight of the sample was recorded after each run to check on possible changes due to dehydration, exchange of hydrogen for deuterium, and mechanical losses. Over the period of the two months during which the data were taken the sample weight changed by about 0.6 percent, and the deuteration decreased less than one percent.

## TRANSMISSION EXPERIMENTS

The statistical analysis of the activation data suggests very strongly that the change in activity of the Mn as a function of relative orientation of neutrons and nuclei is real. The question can be raised as to whether or not the change in activity is correctly attributed to a change in the capture cross section of Mn. If, for some reason, there were a change of average path length through the sample of the scattered neutrons in going from the parallel to the antiparallel arrangement, the result would be a change in the activity of the sample, or an apparent change in capture cross section.

In order to determine if a change of total cross section accompanied the change of activity of the sample, a a series of transmission measurements for polarized incident neutrons were taken with the sample under the conditions described in Table III. The neutron polarizer magnetic field and the sample field were parallel for runs 2 and 4. The neutron detector slit, 1 inch wide and 2 inches high, was located about six feet behind the sample for the transmission measurements.

Comparison of the transmission in runs 1 and 2 should show the effect on the total cross section of the magnetic scattering due to electron polarization. Comparison of runs 3 and 4 should show the effect of nuclear polarization on the transmission. Comparison of runs 1 and 3 should show the effect of a change in sample temperature from 1.2°K to 0.2°K upon the transmission.

TABLE III. Conditions of sample during transmission measurements.

| Run | Temperature, °K | Magnetic field, oersteds |
|---|---|---|
| 1 | 1.20 | 0 |
| 2 | 1.20 | 16 400 |
| 3 | 0.12 | 0 |
| 4 | 0.20 | 2350 |

The transmission of the sample was found to be the same for all of the conditions listed in Table III, within the statistical error of the transmission measurements, which was ±0.2 percent showing that any changes in transmission due to the above mentioned causes were quite negligible compared to the observed change of 3.38 percent in sample activity with relative orientation of neutrons and nuclei. The transmission experiments show that the number of transmitted neutrons (and the number of scattered neutrons) remained unchanged with change of electron and neutron polarization. Any possible change of average path length must, therefore, take place without change in the number of scattered neutrons. Such a change in angular distribution of scattered neutrons with electron or neutron polarization without a corresponding change in the total cross section seems difficult to understand.

The transmission of the sample was 60.9 percent. This low value of the transmission is caused by scattering from the many atoms other than Mn making up the $MnSO_4 \cdot (ND_4)_2SO_4 \cdot 6D_2O$. Only about 2.5 percent of the neutrons incident upon the sample are captured by the Mn. A change of 3.38 percent in the number of neutrons captured by Mn would change the sample transmission by about 0.1 percent. Such a change is about equal to the statistical error of the transmission measurements and could not be detected. Any change in the scattering cross section of the Mn nucleus due to its polarization would be even less noticeable in the transmission measurements, since the nuclear scattering cross section of Mn is much smaller than its capture cross section for slow neutrons.

## DEPOLARIZATION OF THE NEUTRON BEAM BY COLLISIONS

The polarization of the neutron beam can be reduced by scattering collisions of the neutrons, with those constituents of the Dewar flask walls, the monitor, the sample itself, and other materials in the path of the beam, which have nonzero nuclear spins. We have calculated an extreme upper limit to the extent of this depolarization by following the average polarization through several collisions of those neutrons passing through the sample, on the basis of very pessimistic assumptions. Of those neutrons scattered by materials other than the sample, we have assumed that fully one-half pass through the sample, and that the average path length in the sample of all scattered neutrons is the same as for the unscattered neutrons. In the case of isotopes for which the spin dependent amplitudes were not known, the assumption was made that all those neutrons scattered incoherently were depolarized. For the case of *H* and *D* the published values of the spin dependent scattering amplitudes were used to calculate an upper limit of the probability[18] for the inversion of the spin during a scattering process.

[18] O. Halpern, Phys. Rev. 88, 232 (1952).

The most important factor in the depolarization is the initial scattering by the deuterons of the sample. Successive collisions with sample, monitor, and walls reduce the polarization an additional small amount. The result of the calculation is that the average polarization of those neutrons captured by the sample is, at the very least, about 85 percent of the initial neutron polarization.

## INTERPRETATION OF THE DATA IN TERMS OF THE NUCLEAR PROPERTIES OF Mn

The interpretation of our data will depend upon the sign of the hyperfine structure coupling constant, $A$, in the expression $A\mathbf{I}\cdot\mathbf{S}$ for the energy of interaction of the nuclear angular momentum of quantum number, $I$, and the angular momentum of the ionic electrons of quantum number, $S$. The sign of $A$ has been found to be negative,[10] so that the nuclear spin and electronic spin of Mn are parallel in the energy levels of greatest population. The interpretation depends also on the direction of the spins of the neutrons emerging from the polarizing block of iron. The direction of the spins of the neutrons emerging from the polarizing iron is known from theory and experiment[19] to be antiparallel to the direction of the magnetic field applied to the polarizing block. The result of these two statements is that the spins of the incident neutrons and the bombarded Mn nuclei are parallel when the magnetic fields applied to the neutron polarizing block and the sample are parallel.

When this experiment was being planned, the compound nucleus, $Mn^{56}$, was thought to have the resonance levels[20] with nuclear parameters[21] shown in Table IV. It was thought that the size of effect to be observed at thermal neutron energies would be determined largely by the 345 ev level for which $J=3$. On this basis, according to (3a) and (3b), the ratio, $\bar{R}_p/\bar{R}_a$, of the activity for magnetic fields (spins) parallel to the activity for fields (spins) antiparallel should be about 1.068. Actually, this ratio of $\bar{R}_p/\bar{R}_a$ was measured to be 0.966, and becomes 0.96 when corrected for neutron flipping efficiency.

If both the 345 ev and the 2400 ev levels influence the thermal capture cross section, then the cross section is given by the sum of the two expressions on the right side of relations (3a) and (3b), in which sum $\sigma_1$ is the capture cross section due to the 345 ev level only, $\sigma_2$ is the capture cross section due to the 2400 ev level only. The ordinary cross section for no polarization is $\sigma_0=\sigma_1+\sigma_2$. $\sigma_1$ and $\sigma_2$ each obey the one level Breit-Wigner relation for the capture cross section. The upper level for which $J=2$ affects the spin dependence of the capture cross section in the opposite direction to the lower level. If one uses the sum of (3a) and (3b) with the Breit-Wigner expression and the level parameters given in Table IV, considering $\Gamma_\gamma$ of the upper level as the unknown to be determined by the data, then $\Gamma_\gamma$ must become unusually large in order that the upper level over-ride the effect of the lower and give the observed $\sigma/\sigma_0=0.96$ at thermal energies.

TABLE IV. Breit-Wigner parameters for nuclear levels of $Mn^{56}$.

| $E_0$, Neutron energy ev | $\Gamma_n$, Neutron width, ev | $\Gamma_\gamma$, $\gamma$-ray width, ev | $J$, angular momentum |
|---|---|---|---|
| 345 | 21.6 | 0.6 | 3 |
| 2400 | 304. | about 1 ev | 2 |

Recent measurements[22] of the total cross section of Mn have brought to light another resonance level at about 1000 ev. The Breit-Wigner parameters of this level are not known yet. There is also the possibility of an unknown resonance level at negative energy influencing our results. It seems, then, that as of this date, there is not enough information available on the nuclear energy level system of $Mn^{56}$ to state definitely whether or not the nuclear properties and the hyperfine structure magnetic resonance measurements are consistent with our observation that those thermal neutrons whose spins are antiparallel to the spins of $Mn^{55}$ nuclei have a greater probability of being captured than those whose spins are parallel.

*Note added in proof.*—Recent mechanical velocity selector measurements of Bollinger, Palmer, and Dahlberg (Bulletin of the American Physical Society, Vol. 29, No. 4, 1954, Washington meeting) show neutron resonances in $Mn^{55}$ at 337, 1080, and 2360 ev, to which they assign the $J$ values of 2, 3, and 3, respectively.

## ACKNOWLEDGMENTS

We are very much indebted to Drs. M. E. Rose, J. M. Jauch, A. Simon, M. Hamermesh, G. Trammell, and T. A. Welton for discussions of the theoretical physical aspects of this work and to Drs. J. Moshman, C. L. Perry, and A. S. Householder for help with the statistical aspects. The mass spectrographic analyses of the sample were made by Dr. R. Baldock and his group. Miss T. Arnette assisted in taking the data. Mr. J. B. Capehart assisted with the cryogenic aspects of the work.

[19] Sherwood, Stephenson, Stanford, and Bernstein, Phys. Rev. **94**, 791 (1954).

[20] Neutron Cross Sections, Atomic Energy Commission Report AECU-2040. (Technical Information Service, Department of Commerce, Washington, D. C., 1952.)

[21] Harris, Hibdon, and Muehlhause, Phys. Rev. **80**, 1014 (1950).

[22] D. J. Hughes, Brookhaven National Laboratory (private communication).

# Gamma Rays from $Li^7$, $F^{19}$, $Ne^{22}$, and $Na^{22}$ Produced by Alpha-Particle Bombardment of Lithium and Fluorine*

N. P. HEYDENBURG AND G. M. TEMMER
*Department of Terrestrial Magnetism, Carnegie Institution of Washington, Washington, D. C.*

(Received February 23, 1954)

The study of the gamma radiation following the inelastic scattering of alpha particles in thin fluorine and lithium targets has led to the discovery of new levels in the compound nuclei $Na^{23}$ and $B^{11}$. The $(\alpha,p)$ and $(\alpha,n)$ reactions in $F^{19}$ have led to the establishment of the 1.28-Mev level as first-excited state of $Ne^{22}$, and the discovery of the first-excited state ($T=1$, $I=0^+$) of $Na^{22}$, respectively. Coulomb excitation is believed to be responsible for the low-energy part of the excitation function of the 196-kev second-excited state in $F^{19}$, whereas this effect is much weaker for the 113-kev first-excited state of $F^{19}$. No capture gamma rays exist above the known resonance at 0.958 Mev in the reaction $Li^7(\alpha,\gamma)B^{11}$.

## I. INTRODUCTION

THE purpose of the present investigation was to examine the energies of the gamma radiation emitted from lithium and fluorine under alpha-particle bombardment and to study the yield of these gamma rays as a function of the incident alpha-particle energy.

Fluorine-19 is known to have two low-lying excited states at about 110 and 190 kev, as found from a study of the alpha-particle groups in the reaction $Ne^{21}(d,\alpha)F^{19}$.[1] The gamma rays from these two levels have recently been observed by inelastic proton scattering on fluorine.[2] One expects to see these gamma rays by the inelastic scattering of alpha particles as well, via the formation of the compound nucleus $Na^{23}$. Further gamma radiation is to be expected from the reactions $F^{19}(\alpha,p)Ne^{22*}$ and $F^{19}(\alpha,n)Na^{22*}$ when the residual nuclei are left in excited states. Proton groups from the former reaction have indicated levels in $Ne^{22}$ at 0.4 and 1.4 Mev.[3] The latter reaction has a calculated ground-state threshold of 2.325 Mev.

Lithium-7 has its well-known first-excited state at 478 kev, which has been observed in various ways: in the $K$-capture decay of $Be^7$ (gamma ray), in the reaction $Li^6(d,p)Li^7$ (proton groups and gamma ray), in the reaction $Li^6(t,d)Li^7$ (deuteron groups), in the $B^{10}(n,\alpha)Li^7$ reaction (alpha groups), in the $Be^9(d,\alpha)Li^7$ reaction (alpha groups and gamma ray), as well as in the inelastic scattering of protons, deuterons, and 31-Mev alpha particles.[4] Alpha-particle capture gamma rays have also been observed from $Li^7$, with resonances occurring in the thick target yield of these gamma rays at 0.401, 0.819, and 0.958 Mev;[5] the decay takes place predominantly via the 4.46-Mev level in $B^{11}$.

## II. EXPERIMENTAL PROCEDURE

The gamma rays were detected by NaI(Tl) scintillation crystals mounted on a Dumont 6292 photomultiplier tube. We used either a 1-in.×1-in. or $1\frac{3}{4}$-in.×2-in. crystal, depending on the energy of the gamma ray under study. The output pulses were amplified and fed through a single-channel pulse-height analyzer. The energy calibration of the over-all system was achieved by locating the photopeaks of gamma radiation from known radioactive sources, as follows: ionium ($Th^{230}$), 68 kev and 142 kev; $In^{114}$, 190 kev; $Ba^{133}$, 300 kev and 357 kev;[6] $Cs^{137}$, 662 kev; $Na^{22}$, 511 kev (annihilation radiation) and 1.28 kev; $Co^{60}$, 1.17 and 1.33 Mev. We found the pulse height to be linear with energy. A 1-volt channel width was used throughout.

Thin targets were prepared by evaporating $CaF_2$ and $Li_2CO_3$ on nickel backing. The targets were bombarded by singly ionized helium ions produced in the rf ion source of our pressurized electrostatic generator. The target and NaI crystal were surrounded by a one-inch layer of lead to reduce general background

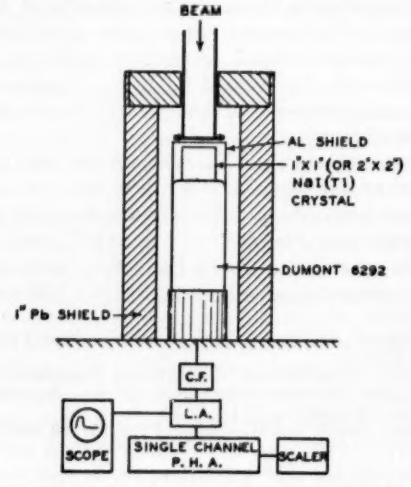


FIG. 1. Experimental arrangement for gamma-ray observation.

* Preliminary account presented at the American Physical Society New York meeting, Bull. Am. Phys. Soc. **29**, No. 1, 11 (1954).

[1] C. Mileikowsky and W. Whaling, Phys. Rev. **88**, 1254 (1952).

[2] Peterson, Barnes, Fowler, and Lauritsen, Phys. Rev. **93**, 951 (1954); R. F. Christy (private communication).

[3] B. J. Jolley and F. C. Champion, Proc. Phys. Soc. (London) **A64**, 88 (1951).

[4] F. Ajzenberg and T. Lauritsen, Revs. Modern Phys. **24**, 321 (1952).

[5] Bennett, Roys, and Toppel, Phys. Rev. **82**, 20 (1951).

[6] Hayward, Hoppes, and Ernst, Phys. Rev. **93**, 916 (1954).

radiation. A schematic of our experimental arrangement is shown in Fig. 1. It may be seen that our crystal subtended a solid angle approaching $2\pi$ in the forward direction. The neutrons from the reaction $F^{19}(\alpha,n)Na^{22}$ were detected with a $B^{10}F_3$ counter surrounded by paraffin ("long counter").[7]

## III. ALPHA-PARTICLE BOMBARDMENT OF FLUORINE

### A. $F^{19}(\alpha,\alpha'\gamma)F^{19}$

We observed the gamma rays from the de-excitation of the first- and second-excited states of $F^{19}$ to have energies of 113±2 kev and 196±2 kev, respectively. The photoelectric peaks for these gamma rays, taken at a bombarding energy of 2.55 Mev, are shown in

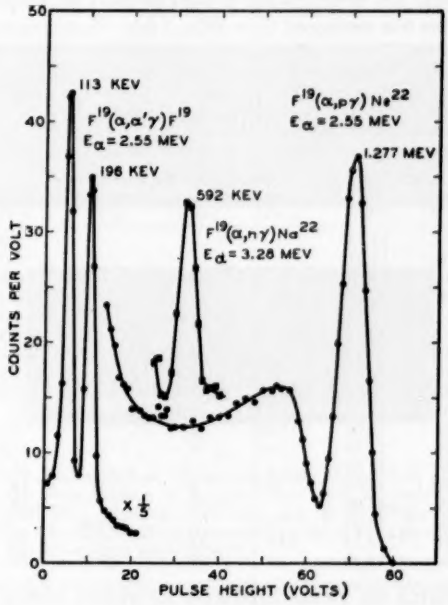


FIG. 2. Gamma-ray pulse-height distributions from alpha-particle reactions in fluorine. Circles refer to 2.55-Mev bombarding energy; squares refer to 3.28-Mev bombarding energy, showing the appearance of the 592-kev gamma ray from $Na^{22}$. See Fig. 7.

Fig. 2. The gamma-ray yields as a function of alpha-particle energy for the 113-kev and 196-kev lines are shown in Figs. 3 and 4, respectively. They were obtained by setting the single-channel analyzer on the peak of the gamma ray in question. We made a search for a possible 83-kev gamma ray connecting the two levels by taking a pulse-height distribution at an alpha energy of 2.1 Mev, (Fig. 5), where the ratio of the 196-kev to the 113-kev line is large (6.6). We are able to set an upper limit of 2 percent for the frequency of occurrence of any 83-kev gamma ray compared to the 196-kev line. The apparent peak to the left of the 113-kev peak

[7] A. O. Hanson and J. L. McKibben, Phys. Rev. **72**, 673 (1947).

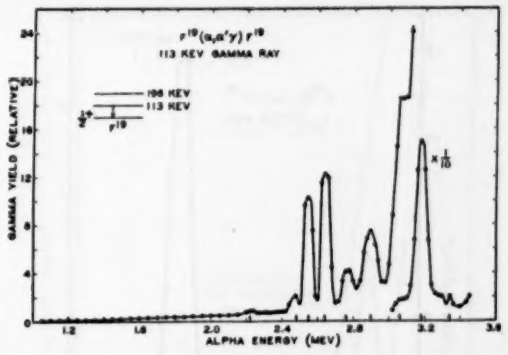


FIG. 3. Excitation curve of the 113-kev gamma ray from the first-excited state of $F^{19}$. Resonances correspond to levels in $Na^{23}$. Note slow rise from 1.1 Mev to 2.4 Mev. Thin target.

cannot be the cascade gamma ray, because sufficient amounts of absorber to cut the intensity of such a line by a factor of 10 merely reduced the intensity by about 2. This was the reduction suffered by the 196-kev line. A check with the 190-kev gamma ray from an $In^{114}$ source revealed a peak at about the same pulse height. We conclude that it is produced by the 196-kev gamma ray in the crystal.† Hence, for all practical purposes our yield curve for the first-excited state is not contaminated by cascade from the upper state. A rather striking behavior is seen in the yield of the 196-kev line up to about 2.2 Mev. We shall have more to say on this interesting feature in the light of some recent additional evidence. It may be seen that most but not all resonances occur for both gamma rays. The resonance energies, the corresponding excitation energies of the compound

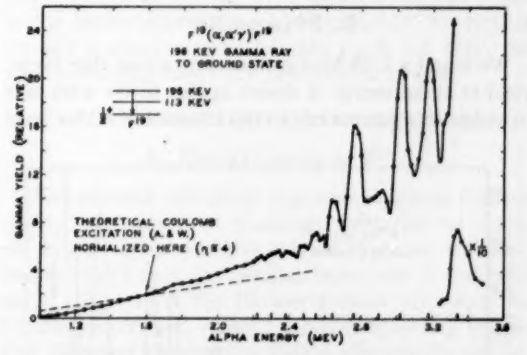


FIG. 4. Excitation curve of the 196-kev gamma ray from the second-excited state of $F^{19}$. Resonances correspond to levels in $Na^{23}$. Dashed curve is theoretical expression for Coulomb excitation (Alder and Winther) normalized at 1.6 Mev. $\eta = Z_1Z_2e^2/\hbar v \cong 4$. Note the general rise continuing under the resonances. Thin target. *Note added in proof.*—Dashed (theoretical) curve incorrectly plotted; correct $E2$ expression is in fair agreement with experiment.

† *Note added in proof.*—We have recently found this peak to be completely absent when using $4\pi$ geometry (target in well-type NaI crystal).

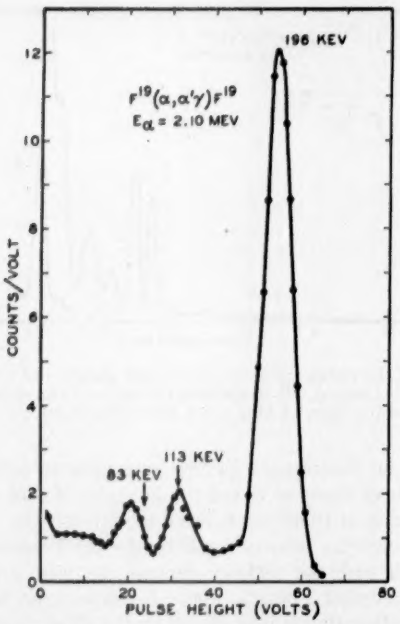


FIG. 5. Pulse-height distribution for low-energy gamma rays from fluorine taken at $E_\alpha = 2.1$ Mev. The first small peak was shown *not* to be an independent gamma ray but is produced in the crystal by the 196-kev line (see text). Arrow indicates where a possible 83-kev cascade between second- and first-excited states of $F^{19}$ would fall. Thin target.

nucleus $Na^{22}$ and relative intensities are summarized in Table I. The rising portion in Fig. 9 was subtracted out for this purpose. No gamma rays were observed between 196 kev and 1.28 Mev below the $F^{19}(\alpha,n\gamma)$ threshold.

### B. $F^{19}(\alpha,p\gamma)Ne^{22}$

We found a 1.28-Mev gamma ray, whose thin target yield *vs* alpha energy is shown in Fig. 6. We were able to assign this gamma ray to the known 1.277-Mev level in $Ne^{22}$ rather than to the third-excited state of $F^{19}$ at 1.37 Mev by a careful comparison with the energy of the gamma ray from a $Na^{22}$ source which connects the same two states. Furthermore, the photopeaks from $Co^{60}$ at 1.17 and 1.33 Mev were found to bracket the gamma ray. No gamma radiation corresponding to a 400-kev level in $Ne^{22}$ previously reported from a study of proton groups in this same reaction[5] was found. Recent observations on the $Ne^{22}(p,p'\gamma)Ne^{22}$ reaction also did not show this gamma line.[6] We can conclude that the 1.28-Mev level is the first-excited state of $Ne^{22}$.

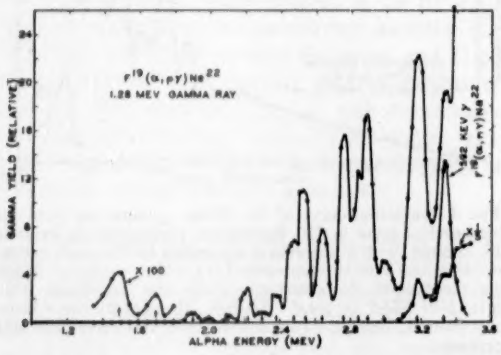


FIG. 6. Excitation curve for the 1.28-Mev gamma ray from the reaction $F^{19}(\alpha,p\gamma)Ne^{22}$. Peaks correspond to levels in $Na^{23}$. Square points show yield of the 592-kev gamma ray from the first-excited state of $Na^{22}$, with threshold around 3.05 Mev. Thin target.

### C. $F^{19}(\alpha,n\gamma)Na^{22}$

For alpha-particle energies greater than about 3.05 Mev, we noticed the appearance of a gamma ray which we could not detect at any lower energy. The energy of this line was measured to be $592\pm3$ kev. Photographs of the oscilloscope traces for equal exposures taken at alpha energies of 3.00 Mev and 3.33 Mev, respectively, are shown in Figs. 7(a) and (b). The pulse-height distributions at 2.55 Mev and 3.28 Mev are shown in Fig. 2. The yield curve for the 592-kev gamma ray is shown in Fig. 6. Our suspicion that this gamma ray might come from the hitherto unreported first-excited state of $Na^{22}$ was confirmed by the behavior of the neutron yield for the $F^{19}(\alpha,n)Na^{22}$ reaction. The yield curves for both thick and moderately thin $CaF_2$ targets are given in Fig. 8. The absolute neutron threshold is seen to occur at about the calculated value of 2.325 Mev. It must be remembered that such a threshold determination is obscured by (a) Coulomb barrier penetration for the incident alpha particles, (b) the presence of fairly well-defined resonances of the compound nucleus $Na^{23}$, and (c) the fact that the ground-state spin of $Na^{22}$ is

TABLE I. Energy levels in $Na^{23}$. $E_c$ is the excitation energy of the compound nucleus $Na^{23}$. Columns 3, 4, 5, and 6 are the relative resonant yields of the various competing outgoing channels. Each gamma-ray yield is independently normalized.

| | | Relative intensities of gamma rays | | | |
|---|---|---|---|---|---|
| $E$(lab) (Mev) | $E_c$ (Mev) | 113 kev $(\alpha,\alpha'\gamma)$ | 196 kev $(\alpha,\alpha'\gamma)$ | 592 kev $(\alpha,n\gamma)$ | 1.28 Mev $(\alpha,p\gamma)$ |
| 1.49 | 11.73 | ... | ... | ... | 0.04 |
| 1.70 | 11.91 | ... | ... | ... | 0.02 |
| 1.91 | 12.08 | ... | ... | ... | 0.8 |
| 2.00 | 12.15 | ... | ... | ... | 0.4 |
| 2.11 | 12.24 | ... | ... | ... | 0.5 |
| 2.22 | 12.32 | 0.4 | 0.4 | ... | 2.8 |
| 2.30 | 12.40 | ... | 0.5 | ... | 0.8 |
| 2.38 | 12.47 | ... | 0.5 | ... | 2.2 |
| 2.48 | 12.55 | 1.3 | 0.8 | ... | 6.8 |
| 2.55 | 12.60 | 9.4 | 1.0 | ... | 11 |
| 2.64 | 12.68 | 11.4 | 4 | ... | 7.5 |
| 2.76 | 12.78 | 3.2 | 9 | ... | 15.5 |
| 2.84 | 12.85 | ... | ... | ... | 12 |
| 2.90 | 12.90 | 6.5 | 3 | ... | 17 |
| 3.02 | 13.00 | ... | 12 | ... | 5 |
| 3.06 | 13.03 | 17.5 | ... | thresh | ... |
| 3.18 | 13.13 | 149 | 12 | 3.5 | 22 |
| 3.34 | 13.26 | 19 | 55 | 13 | 20 |

[5] Cox, vanLoef, and Lind, Phys. Rev. **93**, 925 (1954).

$3^+$, inhibiting emission of threshold ($s$-wave) neutrons. Nevertheless, the agreement of observed and calculated values is quite good. A rather pronounced additional rise in neutron yield can be seen around 3.05 Mev, probably corresponding to a new neutron group leading to the first-excited state of $Na^{22}$ and corresponding closely to the "threshold" for the 592-kev gamma radiation. Since this level has presumably spin $0^+$ (see following) threshold neutrons can emerge quite easily. The calculated gamma-ray threshold for the 592-kev radiation turns out to be at 3.04 Mev, in excellent agreement with our observations. A crude check on the angular distribution of the 592-kev gamma ray is not inconsistent with isotropy. The lifetime of the transition could be seen to be less than ~0.1 second. A measurement of this lifetime is in progress.‡

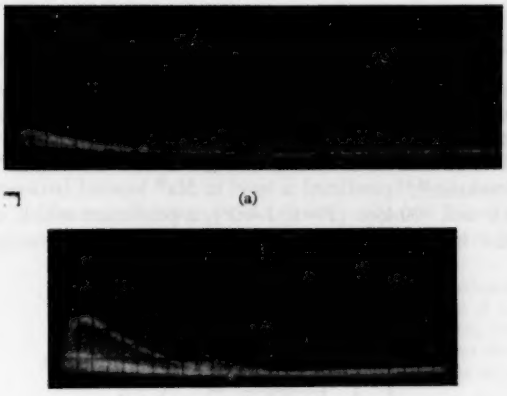


FIG. 7. Photograph of oscilloscope pulses produced by gamma radiation from fluorine in a 1¾-in.×2-in. NaI(Tl) crystal. (a) $E_\alpha = 3.00$ Mev, showing 1.28-Mev line from $F^{19}(\alpha,p\gamma)Ne^{22}$; (b) $E_\alpha = 3.33$ Mev, showing appearance of the 592-kev gamma ray from the first-excited state of $Na^{22}$.

## IV. ALPHA PARTICLE BOMBARDMENT OF LITHIUM

### A. $Li^7(\alpha,\alpha'\gamma)Li^7$

The thin target yield curve for alpha-particle excitation of the 478-kev level in $Li^7$ is shown in Fig. 9. Three prominent resonances at 1.91, 2.46, and 3.06 Mev are present, corresponding to excitation energies in $B^{11}$ at 9.88, 10.24, and 10.62 Mev. Some evidence of weak resonances at 2.60 and 2.70 Mev may also be discerned. This curve is in quite good agreement with some later work at the California Institute of Technology carried up to 2.8 Mev.[9]

### B. $Li^7(\alpha,\gamma)B^{11}$

We also investigated the high-energy gamma rays resulting from alpha-particle capture in a thin $Li_2CO_3$ target. The integral bias on our scintillation detector was set so as to accept gamma rays above 4.4 Mev, since it is known that the capture resonances lead to levels in $B^{11}$ decaying via the 4.46-Mev state in that nucleus.[5] The thin target yield for the 0.82-Mev and 0.96-Mev resonances are shown in the insert of Fig. 9. Their widths were found to be about 4 kev and 7 kev in the center-of-mass system, respectively. No further capture resonances were detected up to 2.5 Mev, the yield remaining essentially at background level.

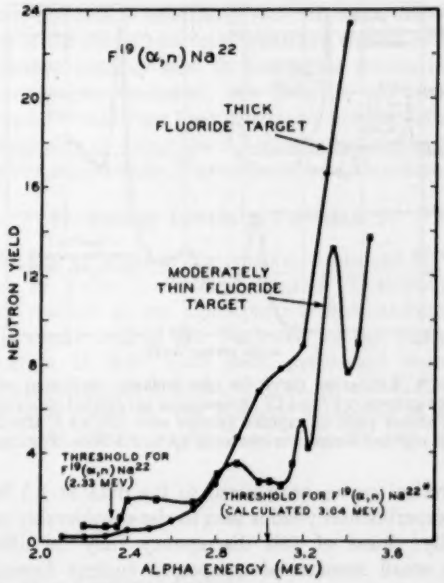


FIG. 8. Neutron yield for the reaction $F^{19}(\alpha,n)Na^{22}$ as a function of alpha-particle energy. Circles are for thick target; squares are for moderately thin target. Arrows indicate calculated thresholds for ground state and first-excited state neutrons (assuming 592-kev level separation).

## V. DISCUSSION OF RESULTS

### A. Energy Levels of $F^{19}$

We undertook this study of gamma rays from fluorine during our survey of Coulomb excitation of many nuclei by alpha particles,[10,11] so that we surmised immediately[10] that the peculiar linear rise in the yield curve (Fig. 4) for the 196-kev gamma ray might be Coulomb excitation without compound nucleus formation. The near absence of a similar effect in the yield of the 113-kev line (Fig. 2) was quite striking. Now the simple semiclassical theory of Coulomb excitation by electric quadrupole excitation given by Alder and Winther[12] is not expected to hold for this extremely light nucleus. The dotted line in Fig. 4 represents the

‡ *Note added in proof.*—From a motion picture record of the counting rate after beam was stopped we conclude that the lifetime is <0.01 second.

[9] C. W. Li (private communication).

[10] G. M. Temmer and N. P. Heydenburg, Phys. Rev. **93**, 351 (1954).

[11] N. P. Heydenburg and G. M. Temmer, Phys. Rev. **93**, 906 (1954).

[12] K. Alder and A. Winther, Phys. Rev. **91**, 1578 (1953).

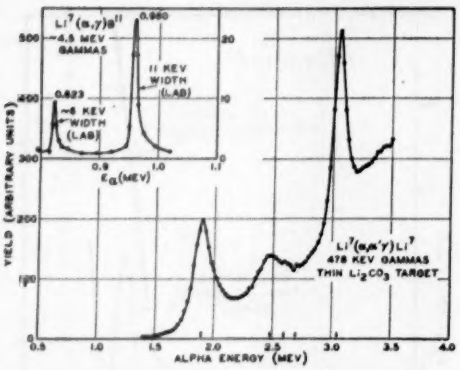


FIG. 9. Excitation curve for the inelastic excitation of the 478-kev gamma ray from $Li^7$. Resonances are excited states in $B^{11}$. Insert shows yield of capture gamma rays ($E_\gamma > 4.5$ Mev). No further capture resonances observed up to 2.5 Mev. Thin target.

theoretical curve, normalized to the data at 1.5 Mev. The experimental yield is seen to rise considerably more rapidly. Some of this discrepancy may be blamed on a small amount of compound nucleus formation which contributes to the yield.§ From the yield for the $F^{19}(\alpha,p\gamma)Ne^{22}$ reaction (Fig. 5), we know that there are levels of $Na^{23}$ below 2.2-Mev bombarding energy. The Coulomb barrier of fluorine for alpha particles is about 5 Mev, so that one might expect the bombarding particle to get *closer* than is considered in the semiclassical treatment, and hence to produce more excitation than predicted. We have evidence for a similar effect in $Na^{23}$, where the deviations from the theoretical prediction are considerably smaller. The general trend of the rise up to 2.2 Mev in $F^{19}$ can be seen to continue under the compound nucleus resonances to higher energies. This trend is very much weaker in the 113-kev excitation. Since the ground state of $F^{19}$ has spin $\frac{1}{2}^+$, a simple explanation of the smallness of this effect for the lowest level would be a $\frac{1}{2}$ assignment, since a quadrupole transition could not connect these two states. A spin of $\frac{3}{2}^+$ or $\frac{5}{2}^+$ would be indicated for the 196-kev level. We have just been informed of some important work on these levels using proton bombardment[13] and a recently reported method[14] for measuring lifetimes of excited states, yielding values of $\sim 10^{-7}$ second for the 196-kev level and $\sim 10^{-9}$ for the 113-kev state. These authors assign spins of $\frac{5}{2}^+$ and $\frac{1}{2}^-$ to these states on the basis of the lifetime values, their failure to observe any cascade gamma ray connecting the two levels, and an isotropic angular distribution of the 113-kev gamma ray. Our results thus find a very satisfactory explanation. It is interesting to note that this Coulomb excitation effect in light nuclei could not be clearly observed with protons because of the lower barrier of the nuclei and the consequent presence of strong compound nucleus resonances extending to practically zero bombarding energy.

The first-excited state of $F^{19}$ possibly constitutes the only clearcut example among the 72 nuclei we have studied where a low-lying level is accessible *only* by an electric dipole transition.

### B. Energy Levels of $Ne^{22}$

Since we do not find any evidence for any gamma ray of energy less than 1.28 Mev, (except for the 113-kev and 196-kev levels of $F^{19}$), we confirm the fact that the latter gamma ray comes from the first-excited state of the even-even nucleus $Ne^{22}$. In accordance with the systematics of these nuclei[15] this should be the level having spin 2 and even parity.

### C. Energy Levels of $Na^{22}$

In view of the evidence presented in Sec. III (C), we believe to have found the first-excited state of the odd-odd nucleus $Na^{22}$. In a recent survey of striking regularities in the isotopic spin singlets and triplets of odd-odd nuclei, extending from $H^2$ to $K^{38}$, Staehelin[16,17] predicted a level in $Na^{22}$ located between 600 and 700 kev ($T=1$, $I=0^+$), a prediction which is now believed to be confirmed. The Coulomb energy

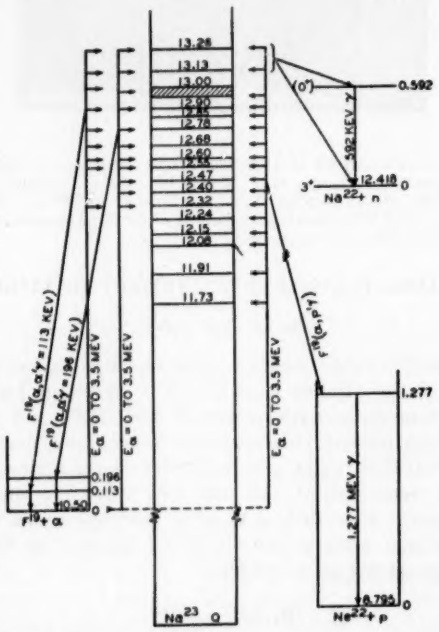


FIG. 10. Composite level diagram illustrating the various reactions investigated by observing gamma radiation from fluorine targets bombarded by alpha particles.

§ *Note added in proof.*—See, note added in proof, caption of Fig. 4.

[13] R. W. Peterson and R. F. Christy (private communications). We are grateful to Professor Christy for informative discussion.

[14] J. Thirion and V. L. Telegdi, Phys. Rev. **92**, 1253 (1953).

[15] G. Scharff-Goldhaber, Phys. Rev. **90**, 587 (1953).

[16] P. Staehelin, Helv. Phys. Acta **26**, 691 (1953).

[17] P. Staehelin, Phys. Rev. **92**, 1076 (1953).

difference between this $0^+$ level and the ground state ($0^+$) of $Ne^{22}$ leads to a value $r_0=1.40\times10^{-13}$ cm, in good agreement with those obtained from the other members of this series.[17]

The 592-kev transition connecting the $0^+$ state with the $I=3^+$ ground state of $Na^{22}$ (pure $M3$) has an expected lifetime[18] of 0.06 second. The internal conversion coefficient gives a negligible correction to this value.[19] Our upper limit of ~0.1 second is consistent with this prediction.[11] Considering the direct positron decay from the 592-kev state in $Na^{22}$ to the ground state of $Ne^{22}(0^+\rightarrow0^+)$, a lifetime of ~15 seconds is calculated on the basis of $\log ft=3.44$.[16] We see therefore that a theoretical branching ratio of about 190÷1 in favor of the electromagnetic transition should obtain.

Another missing level in this series occurs in $P^{30}$. Our attempts to detect this level in the reaction $Al^{27}(\alpha,n)P^{30}$* have not been conclusive to date, although we were able to detect the 2.5-minute positron activity from the ground state. These experiments are continuing.

### D. Energy Levels of $Na^{23}$ and $B^{11}$

The energy levels in the compound nucleus $Na^{23}$ are listed in Table I. A level diagram illustrating all states reached in the alpha-particle bombardment of $F^{19}$ is shown in Fig. 10. No levels in this region of excitation in $Na^{23}$ have been previously reported. New excited states in $B^{11}$ at 9.88, 10.24, and 10.62 Mev have been found by the inelastic scattering of alpha particles in lithium, as discussed in Sec. IV (A).

[18] M. Goldhaber and A. W. Sunyar, Phys. Rev. **83**, 906 (1951).
[19] Rose, Goertzel, Spinrad, Harr, and Strong, Phys. Rev. **83**, 79 (1951).
[11] *Note added in proof.*—See, however, note added in proof, galley 8.

PHYSICAL REVIEW VOLUME 94, NUMBER 5 JUNE 1, 1954

# Many-Particle Configurations in a Central Field*

C. SCHWARTZ† AND A. DE-SHALIT‡
*Department of Physics and Laboratory of Nuclear Science, Massachusetts Institute of Technology, Cambridge, Massachusetts*
(Received December 23, 1953)

Closed formulas are obtained for the fractional parentage coefficients of $j$-$j$ coupled configurations of three and four equivalent particles. In states of low seniority, these formulas can be used to simplify the calculation of familiar types of matrix elements. Some extension is made to the study of more complex configurations. In particular, it is shown that near the ground state the energy level spectrum of an even-even nucleus should be independent of the number of particles in the unfilled shell.

## INTRODUCTION

THERE are two well-known ways of describing an antisymmetric configuration of several equivalent particles bound in a central field. The first[1] is the permutational construction in which the wave functions of the several particles with the several sets of quantum numbers are arrayed in a Slater determinant to give directly an antisymmetric form. However, this structure proves to be quite unwieldy when one tries to calculate matrix elements of various operators, since a great many cross terms come into the expression.

The second[2,3] is the method of fractional parentage in which one considers just one particle of the configuration separated from all the others. The antisymmetry requirement is satisfied by leaving unspecified all the quantum numbers pertaining to the combination of the "other" particles and coupling the angular momentum of the one separated particle to some particular linear combination of all the allowed states of the "others." The fractional parentage coefficients which determine this particular linear combination for some given configuration are usually found as the solutions to a set of simultaneous algebraic equations and are tabulated for any particular problem.

However, it is clear that a direct (though formal) determination of the coefficients can be achieved by equating the wave function as written in the fractional parentage way to the permutational form mentioned first. The solution generally gives the fractional parentage coefficient in terms of the transformations which interrelate all the different vector coupling schemes of the several angular momenta. Using the techniques of Racah,[4] we have obtained formulas for the fractional parentage coefficients for configurations of three and four particles.

Using recursion relations, first derived by Racah[3] and extended in our Appendix, which are developed around the seniority concept, we can deduce formulas for the fractional parentage coefficients for some states of con-

* This work was assisted in part by the joint program of the U. S. Office of Naval Research and the U. S. Atomic Energy Commission.
† Gulf Oil Corporation Fellow.
‡ Now at the Weizmann Institute of Science, Rehovoth, Israel.
[1] E. U. Condon and G. H. Shortley, *The Theory of Atomic Spectra* (Cambridge University Press, Cambridge, 1951), p. 162 et seq.
[2] S. Goudsmit and R. F. Bacher, Phys. Rev. **46**, 948 (1934).
[3] G. Racah, Phys. Rev. **63**, 367 (1943).
[4] G. Racah, Phys. Rev. **62**, 438 (1942).

figurations of any number of particles. In particular, we consider states of low seniority number, which are presumed according to the shell model to describe the low-lying levels of nuclei.

With the fractional parentage coefficients thus simplified, we are able in many cases to carry out explicitly the sums involved in calculating matrix elements of one- and two-particle operators. Considering a short-range attractive two-body interaction with an arbitrary mixture of ordinary and spin-exchange forces, we find that to first order the energy difference between the ground state of spin zero and the states of spin 2, 4, etc. with seniority number 2 is independent of the (even) number of particles in the last unfilled shell.

In addition for the shell $j=7/2$, it is found that this same conclusion about the level structure for 2 and 4 particles holds for any two-body interaction whatsoever.

## ANTISYMMETRIC WAVE FUNCTIONS

It is well known that an antisymmetric wave function for two particles can be written in the form

$$\psi_{12}=N[\phi_1\chi_2-\phi_2\chi_1], \tag{1}$$

where the subscripts denote the particles described, and the normalization factor $N$ is $1/\sqrt{2}$ if $\phi$ and $\chi$ are orthogonal functions.

In describing the bound states in a central field, we say that two particles are equivalent if the wave functions $\phi$ and $\chi$ are identical in their radial dependence. If we wish to describe the state in which two equivalent particles, each of spin $j$,[5] are coupled so that the only good magnetic quantum number is that belonging to their total angular momentum $J$, we would write

$$\psi_{12}(j^2JM)=\sum_{m_1m_2}(jm_1jm_2|jjJM)N \times[\phi_1(jm_1)\phi_2(jm_2)-\phi_2(jm_1)\phi_1(jm_2)]. \tag{2}$$

However, due to the symmetry of the Clebsch-Gordon coefficient,

$$(j_1m_1j_2m_2|j_1j_2JM) =(-1)^{j_1+j_2-J}(j_2m_2j_1m_1|j_2j_1JM), \tag{3}$$

we can rename $m_1$ and $m_2$ (which are only summation variables) in the second term of (2) and reduce (2) to

$$\psi_{12}(j^2JM)=N[1-(-1)^{2j+J}] \times\sum_{m_1m_2}(jm_1jm_2|jjJM)\phi_1(jm_1)\phi_2(jm_2).$$

Here is the familiar result that the only allowed states for two equivalent particles of half-integral $j$ are those with an even total spin $J$.

For any number of particles an antisymmetric wave function can be written in the form[1]

$$N\sum_p(-1)^p\phi_1\phi_2'\phi_3''\cdots\equiv\mathcal{A}\phi_1\phi_2'\phi_3''\cdots, \tag{4}$$

where the sum extends over all the permutations of the arguments of the functions $\phi$, and $(-1)^p$ is the parity of each permutation. If $1, 2, 3, \cdots, n$ are all equivalent particles coupled to a resultant spin $J$, at least half of the $n!$ terms in the sum (4) are redundant because of (3), and in general some values of $J$ may not be allowed.

The expansion (4) allows the specification of all the intermediate resultant spins of the coupling sequence in an arbitrary way. However, these intermediate spins may not be good quantum numbers in a given problem, and a sum of several wave functions of the type (4) may be necessary to describe an eigenstate.

## THE METHOD OF FRACTIONAL PARENTAGES

An alternative procedure for describing the antisymmetrically vector-coupled state of $n$ equivalent particles is the method of fractional parentage.[2,3] In this approach it is not the identity of the particles which is used as the basis of an expansion as in (4), but instead one couples the $n$th particle to some linear combination of all the allowed states of the $n-1$ other particles.

Thus, for example, with three equivalent particles one would write

$$\psi_{123}(j^3JM)=\sum_{J'}(j^2(J')jJ\|j^3J) \times\sum_{m_1m_2m_3M'}\phi_1(jm_1)\phi_2(jm_2)\phi_3(jm_3) \times(jm_1jm_2|jjJ'M')(J'M'jm_3|J'jJM). \tag{5}$$

The coefficients of fractional parentage $(j^2(J')jJ\|j^3J)$ are, of course, zero for odd values of $J'$, and they are usually normalized according to

$$\sum_{J'}|(j^2(J')jJ\|j^3J)|^2=1. \tag{6}$$

Now since the evenness of $J'$ assures the antisymmetry of (5) with respect to interchange of particles 1 and 2, we need only require that (5) be also antisymmetric under an interchange of particles 2 and 3.[3]

Thus we must have

$$\sum_{J'}(j^2(J')jJ\|j^3J)\sum_{m_1'm_2'm_3'M'}\phi_1(jm_1')\phi_2(jm_2')\phi_3(jm_3') \times(jm_1'jm_2'|jjJ'M')(J'M'jm_3'|J'jJM) =-\sum_{J''}(j^2(J'')jJ\|j^3J)\sum_{m_1''m_2''m_3''M'''}\phi_1(jm_1'')\phi_2(jm_2'') \times\phi_3(jm_3'')(jm_1''jm_3''|jjJ''M'')(J''M''jm_2''|J''jJM).$$

Multiplying by

$$\phi_1^*(jm_1)\phi_2^*(jm_2)\phi_3^*(jm_3)(jm_1jm_2|jjJ'''M''') \times(J'''M'''jm_3|J'''jJM),$$

integrating over the coordinates of the three particles, and summing over the $m$'s, we have from the ortho-

[5] We will work here in the $j$-$j$ coupling scheme for simplicity of notation.

gonality of the $\phi$'s and the Clebsch-Gordon coefficients:

$$(j^3(J')jJ\|j^3J)=-\sum_{J''}(j^3(J'')jJ\|j^3J)$$
$$\times\sum_{m_1m_2m_3M'M''}(jm_1jm_2|jjJ'M')(jm_1jm_3|jjJ''M'')$$
$$\times(J'M'jm_3|J'jJM)(J''M''jm_2|J''jJM).$$

This sum over four Clebsch-Gordon coefficients has been defined by Racah[4] in terms of his $W$ coefficient. So,

$$(j^3(J')jJ\|j^3J)=-\sum_{J''}(j^3(J'')jJ\|j^3J)(2J'+1)^{\frac{1}{2}}$$
$$\times(2J''+1)^{\frac{1}{2}}W(jjjJ;J'J'')(-1)^{j+J+J'+J''}. \quad (7)$$

For convenience we shall use Wigner's form[6] of the Racah coefficient

$$\begin{Bmatrix}abe\\dcf\end{Bmatrix}=(-1)^{a+b+c+d}W(abcd;ef).$$

Thus,

$$(j^3(J')jJ\|j^3J)=\sum_{J''}(j^3(J'')jJ\|j^3J)(2J'+1)^{\frac{1}{2}}(2J''+1)^{\frac{1}{2}}$$
$$\times\begin{Bmatrix}jjJ'\\jJJ''\end{Bmatrix}(-1)^{J'+J''},\quad (J'\text{ even only}). \quad (8)$$

The coefficients $(j^3(J')jJ\|j^3J)$ are thus given as the solution to the system of Eqs. (8). However, this solution is rather involved, a more direct formula would be much desired.

We can write an antisymmetric wave function for the three particles in the form (4) [remembering that only half of the 3! terms are necessary since the evenness of $J_0$ leaves all pairs differing only in the permutation of particles 1 and 2 equivalent according to (3)]

$$\psi_{123}(j^3J_0jJM)=N\sum_{m_1m_2m_3M_0}(jm_1jm_2|jjJ_0M_0)$$
$$\times(J_0M_0jm_3|J_0jJM)[\phi_1(jm_1)\phi_2(jm_2)\phi_3(jm_3)$$
$$-\phi_1(jm_1)\phi_2(jm_3)\phi_3(jm_2)$$
$$-\phi_1(jm_3)\phi_2(jm_2)\phi_3(jm_1)]. \quad (9)$$

We can compare this expression with the expansion (5) to solve directly for the coefficients $(j^3(J')jJ\|j^3J)$.

One gets then§

$$(j^3(J')jJ\|j^3J)=C(J_0)\Big[\delta(J',J_0)(jjJ_0)(jJJ_0)$$
$$+(2J_0+1)^{\frac{1}{2}}(2J'+1)^{\frac{1}{2}}(1+(-1)^{J'})$$
$$\times\begin{Bmatrix}jjJ'\\jJJ_0\end{Bmatrix}\Big]\left(\frac{1+(-1)^{J_0}}{2}\right), \quad (10)$$

and in accordance with (6),

$$C(J_0)=\pm\left[3(jjJ_0)(jJJ_0)+6(2J_0+1)\begin{Bmatrix}jjJ_0\\jJJ_0\end{Bmatrix}\right]^{-\frac{1}{2}}, \quad (11)$$

§ This formula has also been derived recently by P. J. Redmond of Birmingham.

where the phases may be chosen to agree with the conventions of Racah.[3] The symbols $(jjJ_0)$ and $(jJJ_0)$ are "triangular delta functions,"

$$(abc)=\begin{cases}0 & \text{if } a,b,c \text{ cannot form a triangle}\\ 1 & \text{if } a,b,c \text{ can form a triangle.}\end{cases}$$

This solution can also be easily verified by direct substitution in (8) with the help of the following well-known relations[4,6] of the Racah coefficients§

$$\sum_{J'}\begin{Bmatrix}jjJ'\\jJJ_0\end{Bmatrix}\begin{Bmatrix}jjJ'\\jJJ''\end{Bmatrix}(2J'+1)=\frac{\delta(J_0,J'')}{2J_0+1}(jjJ_0)(jJJ_0),$$

$$\sum_{J'}\begin{Bmatrix}jjJ'\\jJJ_0\end{Bmatrix}\begin{Bmatrix}jjJ'\\jJJ''\end{Bmatrix}(2J'+1)(-1)^{J'}$$
$$=(-1)^{J_0+J''}\begin{Bmatrix}jjJ''\\jJJ_0\end{Bmatrix}.$$

The triangular conditions are also implied in the Racah coefficient; and although they will not always be written expressly, they will always be understood as a selection on the permissible values of the parameter $J_0$.

It remains to interpret the role of $J_0$ in Eq. (10). Equation (9) for all the different allowed values of $J_0$ yields the totality of wave functions which can be constructed for three particles which are antisymmetric in all three particles and which are eigenfunctions of $j_1^2$, $j_2^2$, $j_3^2$ $(j_1=j_2=j_3=j)$, $J^2$ and $J_z$. It is seen that (9) can be written in the symbolic form:

$$\psi_{123}(j^3JM)=N[\phi(j_1j_2(J_0)j_3JM)-\phi(j_1j_3(J_0)j_2JM)$$
$$-\phi(j_3j_2(J_0)j_1JM)], \quad (12)$$

which can be interpreted as describing a state in which there is always a pair of angular momenta coupled to $J_0$. To say that the definite pair (12) is coupled to $J_0$ would be inconsistent with the symmetry requirement among all three, but the statement that a pair is coupled to $J_0$ is sensible and may serve as an additional labeling of the state.

Since the different $\phi$'s in (12) are not necessarily orthogonal, one cannot say whether different choices of $J_0$ will lead to different $\psi$'s or not. The $\psi$'s defined by (9) will thus constitute generally a redundant basis for all the permissible states. For $j<9/2$ one knows that there is no further degeneracy in the states $\psi(j^3JM)$; thus different choices of $J_0$ should lead to identical sets of coefficients (10, 11). This implies a number of identities among the Racah coefficients with four half-integers (three of them identical) and two even integers.

In general we may consider the symmetric matrix,

$$(J_0|j^3J|J')=[1+(-1)^{J_0}]\delta(J',J_0)+(2J_0+1)^{\frac{1}{2}}(2J'+1)^{\frac{1}{2}}$$
$$\times[1+(-1)^{J'}][1+(-1)^{J_0}]\begin{Bmatrix}jjJ'\\jJJ_0\end{Bmatrix}, \quad (13)$$

[6] A. de-Shalit, Phys. Rev. **91**, 1479 (1953).

which satisfies the eigenvalue equation

$$\sum_{J'}(J_0|j^2J|J')\left[(2J'+1)^{\frac{1}{2}}(2J''+1)^{\frac{1}{2}}\begin{Bmatrix} jjJ' \\ jJJ'' \end{Bmatrix} -\delta(J',J'')\right]=0,$$

and so the coefficients (13) can describe at most $m$ independent states, if the matrix,

$$\lambda_{J'J''}=(2J'+1)^{\frac{1}{2}}(2J''+1)^{\frac{1}{2}}\begin{Bmatrix} jjJ' \\ jJJ'' \end{Bmatrix}, \quad (J', J'' \text{ even only}),$$

has $m$ eigenvalues $+1$.

It should be noted that if we take a linear combination of sets of coefficients (10) (given by different $J_0$'s), the normalization (11) is not correct.

## THE SENIORITY NUMBER

An additional quantum number which is useful in classifying the states of a number of equivalent particles, and one which is very practical in nuclear spectroscopy, is the seniority number.[3] The seniority number $v$ for the configuration $j^nvJ$ is given by[7]

$$\tfrac{1}{2}(n-v)(2j+3-n-v)=Q(n,v), \tag{14}$$

where $Q(n,v)$ is the eigenvalue of the operator $\sum_{i<j}q_{ij}$, and

$$(j^2J'|q_{ij}|j^2J')=(2j+1)\delta(J',0). \tag{15}$$

For three particles the seniority number $v$ is one if $(j^3(0)jJ]j^3J)\neq 0$ (therefore $J=j$) and three otherwise. There is never more than one state with $v=1$, though with larger values of $j$ the multiplicity of other states may increase.

We shall now show that $J_0=0$ and $J=j$ in Eq. (10), with the normalization (11), always represents just this state with seniority $v=1$.

Using the relation,

$$\begin{Bmatrix} jjJ' \\ jj0 \end{Bmatrix}=(-1)^{2j+J'}\frac{1}{(2j+1)}, \tag{16}$$

we have from (10) and (11) with $J_0=0$:

$$(j^3(J')jJ]j^3J) =\begin{cases}\left(\dfrac{2j-1}{3(2j+1)}\right)^{\frac{1}{2}}, & J'=0 \\ -\left(\dfrac{(2J'+1)}{3(2j+1)(2j-1)}\right)^{\frac{1}{2}}[1+(-1)^{J'}], & J'>0.\end{cases} \tag{17}$$

Calculating the eigenvalue $Q(3,v)$ we have [see reference 3, Eq. (42)]

$$\tfrac{1}{2}(3-v)(2j-v)=3(2j+1)|(j^3(0)jJ]j^3J)|^2,$$

or using the above value (17),

$$\tfrac{1}{2}(3-v)(2j-v)=(2j-1),$$

which is satisfied by $v=1$ only [$v$ can never be greater than $\frac{1}{2}(2j+1)$].

Using the general recursion relations first derived by Racah[3] [his Eqs. (58) here translated into the $j$-$j$ scheme], we can calculate explicitly the fractional parentage coefficients for the seniority one configuration of any (odd) number of particles

$$(j^{n-1}(v'=0\ J'=0)jJ=j]j^nv=1\ J=j) =\left(\frac{2j+2-n}{n(2j+1)}\right)^{\frac{1}{2}},$$
$$(j^{n-1}(v'=2J'\neq 0)jJ=j]j^nv=1\ J=j) =-\left(\frac{2(n-1)(2J'+1)}{n(2j-1)(2j+1)}\right)^{\frac{1}{2}}, \quad J' \text{ even only.} \tag{18}$$

## MATRIX ELEMENTS IN STATES OF SENIORITY ONE

The reduced matrix element of an operator of the type $F=\sum_i f_i$, where $f_i$ is a tensor operator of rank $r$, can be written:[3,4]

$$(j^n\alpha J\|F\|j^n\alpha'J')=n\sum_{J''\alpha''}(j^n\alpha J[j^{n-1}(\alpha''J'')jJ) \times(j^{n-1}(\alpha''J'')jJ']j^n\alpha'J')(-1)^{j+J''+J+r}(2J+1)^{\frac{1}{2}} \times(2J'+1)^{\frac{1}{2}}\begin{Bmatrix} jJJ'' \\ J'jr \end{Bmatrix}(j\|f\|j). \tag{19}$$

With the configurations $j^n\alpha J$, $j^n\alpha'J'$, both of seniority $v=v'=1$ $(J=J'=j)$. Substituting (18) in (19) and using the relations

$$\sum_{J'}\begin{Bmatrix} jjJ' \\ jjr \end{Bmatrix}(2J'+1)=1,$$
$$\sum_{J'}\begin{Bmatrix} jjJ' \\ jjr \end{Bmatrix}(2J'+1)(-1)^{J'}=(-1)^{2j}\delta(r,0)(2j+1), \tag{20}$$

we have

$$(j^nv=1\ J=j\|F\|j^nv=1\ J=j) =\frac{(j\|f\|j)}{(2j-1)}\{(n-1)(2j+1)\delta(r,0)+2j -1-(n-1)[1+(-1)^r]\}$$
$$=(j\|f\|j)\begin{cases}\times 1, & r \text{ odd} \\ \times\dfrac{2j+1-2n}{2j-1}, & r \text{ even} \neq 0 \\ \times n, & r=0\end{cases} \tag{21}$$

which is identical with Racah's equations (69).[3]

[7] All the formulas of Racah (see reference 3) on fractional parentage and seniority can be translated from the $LS$ scheme to the $j$-$j$ scheme by replacing $4l+2$ with $2j+1$ everywhere except in Eq. (15) above.

The matrix element of the two-particle scalar operator $G=\sum_{i<j} g_{ij}$ in the state $j^3\alpha J$ is given by

$$(j^3\alpha J|G|j^3\alpha J)=3\sum_{\alpha' J'}|(j^3(\alpha' J')jJ\}j^3\alpha J)|^2 \times(j^3J'|g_{ij}|j^3J').$$

So for the state of seniority $v=1$ using (17), we have

$$(j^3v=1\ J=j|G|j^3v=1\ J=j)$$
$$=\frac{2j-3}{2j-1}(j^2J=0|g_{ij}|j^2J=0)+\frac{2}{(2j+1)(2j-1)} \times\sum_{J'}(2J'+1)(1+(-1)^{J'})(j^2J'|g_{ij}|j^2J').$$

However, the sum

$$\sum_{J'}(2J'+1)\tfrac{1}{2}[1+(-1)^{J'}](j^2J'|g_{ij}|j^2J')$$

can be recognized as simply [see Appendix, Eq. (A5) *et seq.*]

$$(j^{2j+1}0|G|j^{2j+1}0),$$

the interaction in the filled shell.

For the configuration $j^nv=1\ J=j$ we have, using Eq. (A8)

$$(j^nv=1\ J=j|G|j^nv=1\ J=j)$$
$$=\frac{(n-1)(n-3)}{(2j-3)(2j+1)}(j^{2j+1}J=0|G|j^{2j+1}J=0) +\frac{(n-1)(2j-n)}{2(2j-3)}(j^3v=1\ J=j|G|j^3v=1\ J=j).$$

## THE CASE OF SENIORITY THREE

To calculate fractional parentage coefficients from Eq. (10) for states of seniority three when the state is not uniquely determined by the value of $J$ alone, we must take some linear combination of states described by different values of $J_0$. There are, for example, two states of the configuration $(9/2)^3$ with total spin $J=9/2$. The one of seniority $v=1$ is described by (17). With $J_0=2$ in (10), we get the values (not normalized):

$$-\frac{1}{10}(J'=0),\quad \frac{23}{132\sqrt{5}}(J'=2),\quad \frac{-1}{220}(J'=4),$$
$$\frac{8\sqrt{13}}{165}(J'=6),\quad \frac{\sqrt{17}}{55}(J'=8),$$

and with $J_0=8$

$$-\frac{1}{10}(J'=0),\quad \frac{1}{11\sqrt{5}}(J'=2),\quad \frac{93}{55\cdot 13}(J'=4),$$
$$\frac{5}{44\sqrt{13}}(J'=6),\quad \frac{289}{26\cdot 22\sqrt{17}}(J'=8).$$

The desired set of coefficients is that belonging to the state $v=3$, which should have $(j^3(0)jJ\}j^3v=3J)=0$. So subtracting the two above sets and normalizing, we get

$$0(J'=0),\quad -\frac{\sqrt{13}}{6\sqrt{11}}(J'=2),\quad \frac{7\sqrt{5}}{2\sqrt{143}}(J'=4),$$
$$\frac{-31}{6\sqrt{55}}(J'=6),\quad \frac{3\sqrt{17}}{2\sqrt{715}}(J'=8),$$

identical with the results of Flowers.[8]

In general, if two different values of $J_0$, say $J_0$ and $J_0'$, give two independent sets of coefficients (10), the state described by the linear combination of these with the coefficient for $J'=J_0$ equal to zero is orthogonal to the state described by $J_0$ alone.

To see this, consider one matrix $(J_0|j^3J|J')$ of the type defined in (13) and any other $F(J')$ formed from a linear combination of terms $(J_0'|j^3J|J')$. We then get for the cross sum

$$\sum_{J'}(J_0|j^3J|J')F(J')$$
$$=[1+(-1)^{J_0}]\Big[F(J_0)+\sum_{J'}F(J')(2J_0+1)^{\frac{1}{2}} \times(2J'+1)^{\frac{1}{2}}[1+(-1)^{J'}]\begin{Bmatrix} jjJ' \\ jJJ_0\end{Bmatrix}\Big],$$

but this second sum can be performed by the defining Eq. (8)

$$[1+(-1)^{J_0}]\sum_{J'}F(J')(2J_0+1)^{\frac{1}{2}}(2J''+1)^{\frac{1}{2}} \times[1+(-1)^{J'}]\begin{Bmatrix} jjJ' \\ jJJ_0\end{Bmatrix}=2[1+(-1)^{J_0}]F(J_0),$$

since $(-1)^J F(J')=F(J')$. So,

$$\sum_{J'}(J_0|j^3J|J')F(J')=3[1+(-1)^{J_0}]F(J_0),$$

which is zero if the linear combination $F$ has the coefficient for $J'=J_0$ equal to zero.

Looking for more complicated configurations, we find that for $(11/2)^3$ $J=9/2$ there are two independent states, both of seniority $v=3$. For $J_0=2$ we get the (normalized) values

I: $0.687(J'=2)$, $0.352(J'=4)$, $0.282(J'=6)$, $-0.105(J'=8)$, $-0.560(J'=10)$.

With $J_0=10$ we get another set of values, and taking the linear combination of these two described above, we get the orthogonal (normalized) set:

II: $0(J'=2)$, $-0.500(J'=4)$, $0.726(J'=6)$, $-0.452(J'=8)$, $0.141(J'=10)$.

In contrast with the convenient characterization of nuclear states afforded by the usual concept of seniority,

[8] B. H. Flowers, Proc. Roy. Soc. (London) **A215**, 398 (1952).

this division of the two states of the configuration $(11/2)^3_{9/2}$ does not appear to be very practical. That is, if we consider the effect of a perturbing short-range attractive force between all pairs of particles, the state of lowest energy in this configuration is not described by I alone or II alone, but by a mixture of both.

## MORE THAN THREE EQUIVALENT PARTICLES

In the fractional parentage description of a state of equivalent particles, the wave function is written

$$\psi(j^n\alpha_nJ_nM_n)=\sum_{\substack{J\cdots\\ \alpha\cdots}}(j^{n-1}(\alpha_{n-1}J_{n-1})jJ_n\|j^n\alpha_nJ_n)$$
$$\times(j^{n-2}(\alpha_{n-2}J_{n-2})jJ_{n-1}\|j^{n-1}\alpha_{n-1}J_{n-1})\cdots$$
$$\times(j^2(\alpha_2J_2)jJ_3\|j^3\alpha_3J_3)\delta(J_2\text{ even})$$
$$\times\sum_{m\cdots}\phi_1(jm_1)\phi_2(jm_2)\cdots$$
$$\times\phi_n(jm_n)(jm_1jm_2|jjJ_2M_2)\cdots$$
$$\times(J_{n-1}M_{n-1}jm_n|J_{n-1}jJ_nM_n). \quad (22)$$

If the fractional parentage coefficients for 3, 4, $\cdots n-1$ particles are known from earlier work, we can get the coefficients for $n$ particles by comparing (22) with (4). The antisymmetrization (4) can be interpreted as a series of changes in the coupling order of the several angular momenta. Thus, it is seen that the general coefficient $(j^{n-1}(\alpha'J')jJ\|j^n\alpha J)$ is given as sums over products of all the fractional parentage coefficients for less than $n$ particles and coefficients for all the transformations in the coupling scheme of $n$ angular momenta. These transformation coefficients can always be expressed as sums of products of Racah coefficients. There will be $n-2$ arbitrary parameters analogous to $J_0$ used before and these will help to describe the state.

For $n=4$ we compare the two developments

$$\psi(j^4JM)=\sum_{J'J''}(j^3(J')jJ\|j^4J)(j^2(J'')jJ'\|j^3J')$$
$$\times\sum_{\substack{m_1m_2m_3\\ m_4M'M''}}\phi_1(jm_1)\phi_2(jm_2)\phi_3(jm_3)\phi_4(jm_4)$$
$$\times(jm_1jm_2|jjJ''M'')(J''M''jm_3|J''jJ'M')$$
$$\times(J'M'jm_4|J'jJM), \quad (23)$$

and

$$\psi(j^4JM)=N\sum_{\substack{m_1m_2m_3\\ m_4M_2M_3}}(jm_1jm_2|jjJ_2M_2)$$
$$\times(J_2M_2jm_3|J_2jJ_3M_3)(J_3M_3jm_4|J_3jJM)$$
$$\times\phi_1(jm)\phi_2(jm)\phi_3(jm)\phi_4(jm),$$
$$[1234-1243+1423-1432+1342-1324$$
$$-2341+2314+2431-2413+3412-3421], \quad (24)$$

where the permutations have been written out symbolically. Then

$$(j^3(J')jJ\|j^4J)=\sum_{J''}(j^3J'\|j^2(J'')jJ')X(J''), \quad (25)$$

where $X(J'')$ is a series of sums of products of six Clebsch-Gordon coefficients. This can be evaluated in terms of Racah coefficients and $9-j$ symbols[6]

$$\begin{Bmatrix}j_{11}j_{12}j_{13}\\ j_{21}j_{22}j_{23}\\ j_{31}j_{32}j_{33}\end{Bmatrix}=\sum_j(2j+1)(-1)^{2j}\begin{Bmatrix}j_{11}j_{12}j_{13}\\ j_{23}j_{33}j\end{Bmatrix}$$
$$\times\begin{Bmatrix}j_{21}j_{22}j_{23}\\ j_{12}j\ \ j_{32}\end{Bmatrix}\begin{Bmatrix}j_{31}j_{32}j_{33}\\ j\ \ j_{11}j_{21}\end{Bmatrix}, \quad (26)$$

giving

$$X(J'')=N(2J'+1)^{\frac{1}{2}}(2J''+1)^{\frac{1}{2}}(2J_2+1)^{\frac{1}{2}}(2J_3+1)^{\frac{1}{2}}$$
$$\times(-1)^{J'-J''-J_3}\Bigg\{-\frac{\delta(J_2,J'')}{2J_2+1}\frac{\delta(J_3,J')}{2J_3+1}$$
$$+\frac{\delta(J_2,J'')}{2J_2+1}\begin{Bmatrix}jJ_2J_3\\ jJJ'\end{Bmatrix}-2\frac{\delta(J_3,J')}{2J_3+1}\begin{Bmatrix}jjJ_2\\ jJ_3J''\end{Bmatrix}$$
$$+2\begin{Bmatrix}jjJ_2\\ jJ'J''\end{Bmatrix}\begin{Bmatrix}jJ_3J_2\\ jJ'J\end{Bmatrix}+2\begin{Bmatrix}jjJ''\\ jJ_3J_2\end{Bmatrix}\begin{Bmatrix}jJ_3J''\\ jJ'J\end{Bmatrix}$$
$$+\begin{Bmatrix}jjJ_2\\ J'J''j\\ JjJ_3\end{Bmatrix}[1+(-1)^{j+J_2+J}]\Bigg\}. \quad (27)$$

Now substituting (10) and (27) in (25) and summing over $J''$ we obtain

$$[j^3(J')jJ\|j^4J]=N(J_2,J_3)(2J'+1)^{\frac{1}{2}}(2J_2+1)^{\frac{1}{2}}$$
$$\times(2J_3+1)^{\frac{1}{2}}(-1)^{J'+J_2}\Bigg\{\frac{-3\delta(J'J_3)}{2J_3+1}$$
$$\times\left[2\begin{Bmatrix}jjJ_2\\ jJ_3J_2\end{Bmatrix}+\frac{1}{2J_2+1}\right]+3\begin{Bmatrix}jJ_3J_2\\ jJ'J\end{Bmatrix}$$
$$\times\left[2\begin{Bmatrix}jjJ_2\\ jJ'J_2\end{Bmatrix}+\frac{1}{2J_2+1}\right]+[3+(-1)^{j+J_2+J}]$$
$$\times\Bigg\{\begin{Bmatrix}J_2J_2J\\ jJ_3j\end{Bmatrix}\begin{Bmatrix}J_2J_2J\\ jJ'j\end{Bmatrix}(-1)^{J'+J_2+J}$$
$$+\begin{Bmatrix}jjJ_2\\ jJ_3J_2\end{Bmatrix}\begin{Bmatrix}jJ'J_2\\ jJ_3J\end{Bmatrix}+\begin{Bmatrix}jjJ_2\\ J'J_2j\\ JjJ_3\end{Bmatrix}\Bigg\}\Bigg\}. \quad (28)$$

Here $J_2$ is equivalent to the earlier $J_0$, and $J_3$ is a new parameter of similar character. In general, to describe some particular state a linear combination of coefficients (28) given by different values of $J_2$, $J_3$ may be needed.

While the above method of breaking off a single particle is what one needs for calculating matrix elements of one-particle ($F$-type) operators, the two-particle operators ($G$-type) are best handled with the following description (for four particles).

$$\psi(j^4JM)=\sum_{J_{12}J_{34}}(j^2(J_{12})j^2(J_{34})J\|j^4J)\sum_{m\cdots}\phi_1(jm_1)\times\phi_2(jm_2)\phi_3(jm_3)\phi_4(jm_4)(jm_1jm_2|jjJ_{12}M_{12})\times(jm_3jm_4|jjJ_{34}M_{34})(J_{12}M_{12}J_{34}M_{34}|J_{12}J_{34}JM),\quad(29)$$

where the particles are grouped in pairs. With $J_{12}$, $J_{34}$ even, this description is antisymmetric in the pairs of particles (1,2) and (3,4). To determine the coefficients $(j^2(J_{12})j^2(J_{34})J\|j^4J)$ we shall exchange particles two and three and require the wave function to be $-1$ times (29)

$$(29)=-\sum_{J_{13}J_{24}}(j^2(J_{13})j^2(J_{24})J\|j^4J)\sum_{m\cdots}\phi_1(jm_1)\times\phi_2(jm_2)\phi_3(jm_3)\phi_4(jm_4)(jm_1jm_3|jjJ_{13}M_{13})\times(jm_2jm_4|jjJ_{24}M_{24})(J_{13}M_{13}J_{24}M_{24}|J_{13}J_{24}JM).\quad(30)$$

Comparing (29) and (30), we have the requirement

$$\sum_{J_{12}J_{34}}(j^2(J_{13})j^2(J_{24})J\|j^4J)[(2J_{13}+1)(2J_{24}+1)\times(2J_{12}+1)(2J_{34}+1)]^{\frac{1}{2}}\begin{Bmatrix}jjJ_{12}\\jjJ_{34}\\J_{13}J_{24}J\end{Bmatrix}=-(j^2(J_{12})j^2(J_{34})J\|j^4J),\quad(J_{12},\ J_{3t}\text{ even only}).\quad(31)$$

This is the 4-particle analog of Eq. (7).

By comparing (29) with (24), we could solve for the coefficient directly; but with the help of the relations,

$$\sum_{J_{12}J_{34}}\begin{Bmatrix}jjJ_{12}\\jjJ_{34}\\KLJ\end{Bmatrix}\begin{Bmatrix}jjJ_{12}\\jjJ_{34}\\J_{13}J_{24}J\end{Bmatrix}(2J_{12}+1)(2J_{34}+1)=\frac{\delta(K,J_{13})\delta(L,J_{24})}{(2K+1)(2L+1)}(jjJ_{13})(jjJ_{24})(J_{13}J_{24}J),\quad(32)$$

$$\sum_{J_{12}J_{34}}\begin{Bmatrix}jjJ_{12}\\jjJ_{34}\\KLJ\end{Bmatrix}\begin{Bmatrix}jjJ_{12}\\jjJ_{34}\\J_{13}J_{24}J\end{Bmatrix}(2J_{12}+1)(2J_{34}+1)(-1)^{J_{34}}=(-1)^{2j+J_{24}-L}\begin{Bmatrix}jjJ_{13}\\jjJ_{24}\\KLJ\end{Bmatrix},$$

it is easy to show that a general solution to (31) is

$$(j^2(J_{12})j^2(J_{34})J\|j^4J)=C(K,L)\Big\{\delta(J_{12},K)\delta(J_{34},L)+(-1)^J\delta(J_{12},L)\delta(J_{34},K)-[1+(-1)^{J_{12}}][1+(-1)^{J_{34}}][(2J_{12}+1)\times(2J_{34}+1)(2K+1)(2L+1)]^{\frac{1}{2}}\begin{Bmatrix}jjJ_{12}\\jjJ_{34}\\KLJ\end{Bmatrix}\Big\},\quad(33)$$

where $K$, $L$ are two (even) parameters similar to $J_0$ used before. The six triangular conditions implied in the $9-j$ symbols are understood to apply to the entire expression (33) although not written out expressly.

Equation (33) takes on a simple form when we set one of the parameters, say $L$, equal to zero; then, by the triangular conditions, we must have $K=J$ (even), and we get

$$(j^2(J_{12})j^2(J_{34})J\|j^4J)=C\Big[[\delta(J_{12},J)\delta(J_{34},0)+\delta(J_{12},0)\delta(J_{34},J)+[1+(-1)^{J_{12}}][1+(-1)^{J_{34}}]\times\frac{(2J_{12}+1)^{\frac{1}{2}}(2J_{34}+1)^{\frac{1}{2}}}{(2j+1)^{\frac{1}{2}}}\begin{Bmatrix}J_{12}J_{34}J\\j\ \ j\ \ j\end{Bmatrix}\Big].\quad(34)$$

If we require the normalization

$$\sum_{J_{12}J_{34}}|(j^2(J_{12})j^2(J_{34})J\|j^4J)|^2=1,$$

we have

$$C=\pm\left[6\delta(J,0)+6\frac{2j-3}{2j+1}\right]^{-\frac{1}{2}}.\quad(35)$$

Testing these values (34), (35) in Eqs. (14) and (15), we have

$$\tfrac{1}{2}(4-v)(2j-1-v)=6(2j+1)\sum_{J_{12}}|(j^2(J_{12})j^2(0)J\|j^4J)|^2=6(2j+1)\left[6\delta(J,0)+6\frac{2j-3}{2j+1}\right]^{-1}\left[1+\frac{-4\delta(J,0)}{2j+1}\right]^2=\begin{cases}2(2j-1) & J=0\\(2j-3) & J>0.\end{cases}$$

So that the fractional parentage coefficient (34), (35) describes the state of $j^4$ with seniority zero or two as $J$ is zero or greater. Using the recursion relations ($A_3$),

we have then for $n$ particles of seniority two:

$$(j^{n-2}(v'=0J')j^2(J'')J\|j^nv=2J)$$
$$=\left[\frac{2(2j+1-n)(2j+3-n)}{n(n-1)(2j-1)(2j+1)}\right]^{\frac{1}{2}}\delta(J',0)\delta(J'',J),$$
$$(j^{n-2}(v'=2J'\neq 0)j^2(J'')J\|j^nv=2J)$$
$$=\left[\frac{3\cdot 4(n-2)(2j+1-n)}{2n(n-1)(2j-3)}\right]^{\frac{1}{2}}\left[6\frac{2j-3}{2j+1}\right]^{\frac{1}{2}}$$
$$\times\left[\delta(J',J)\delta(J'',0)+[1+(-1)^{J'}][1+(-1)^{J''}]\right.$$
$$\left.\times\frac{(2J'+1)^{\frac{1}{2}}(2J''+1)^{\frac{1}{2}}}{(2j+1)^{\frac{1}{2}}}\begin{Bmatrix}J'J''J\\jjj\end{Bmatrix}\right]. \quad (36)$$

To calculate the matrix element of an operator of the type $G$ in a configuration of four equivalent particles with seniority two, we have

$$(j^4v=2J|G|j^4v=2J)$$
$$=6\sum_{J'J''}|(j^2(J')j^2(J'')J\|j^4v=2J)|^2(j^2J'|g_{ij}|j^2J')$$
$$=\sum_{J'}Z(J')(j^2J'|G|j^2J'), \quad (37)$$

where

$$Z(J')=6\sum_{J''}\left[6\frac{2j-3}{2j+1}\right]^{-1}\left[\delta(J',J)\delta(J'',0)\right.$$
$$+\delta(J',0)\delta(J'',J)-\frac{8}{(2j+1)}[\delta(J',J)\delta(J'',0)$$
$$\left.+\delta(J',0)\delta(J'',J)]+4[1+(-1)^{J'}][1+(-1)^{J''}]\right.$$
$$\left.\times\frac{(2J'+1)(2J''+1)}{(2j+1)}\begin{Bmatrix}J'J''J\\jjj\end{Bmatrix}^2\right]$$
$$=\frac{1}{2j-3}\left\{(2j-7)[\delta(J',J)+\delta(J',0)]\right.$$
$$+4(2J'+1)[1+(-1)^{J'}]$$
$$\left.\times\left[\frac{1}{2j+1}-\begin{Bmatrix}jjJ'\\jjJ\end{Bmatrix}\right]\right\}. \quad (38)$$

If $g_{ij}$ is $-\delta(\mathbf{r}_i-\mathbf{r}_j)$, then[6]

$$(j^2J'|g_{ij}|j^2J')=\frac{-F_0}{2}(2j+1)^2\frac{(j\tfrac{1}{2}j-\tfrac{1}{2}|jjJ'0)^2}{2J'+1}, \quad J' \text{ even},$$

and we can sum (37) and get

$$(j^4, v=2, J|G|j^4, v=2, J)$$
$$=-\tfrac{1}{2}F_0(2j+1)+(j^2J|g_{ij}|j^2J). \quad (39)$$

Using Eq. (A8), we have for $j^nv=2$:

$$(j^n, v=2, J|G|j^n, v=2, J)$$
$$=-\tfrac{1}{2}F_0(2j+1)(n-2)/2+(j^2J|g_{ij}|j^2J).$$

Also for states of seniority $v=0$, $J=0$:

$$(j^n, v=0, J=0|G|j^n, v=0, J=0)=-\tfrac{1}{2}F_0(2j+1)n/2.$$

Hence, for the configuration $j^n$, the energy level separation from the state $v=J=0$ to the state $v=2$, $J$ is given by

$$\Delta_{0J}^{(n)}=(j^2, v=2, J|g_{ij}|, j^2, v=2, J)+\tfrac{1}{2}F_0(2j+1)$$
$$=\Delta_{0J}^{(2)}. \quad (40)$$

Thus one would expect the $0-2-4\cdots$ energy level differences from the ground states of even-even nuclei to be independent of the number of particles in the unfilled outer shell. This conclusion may also be drawn from the more general analysis of Racah and Talmi.[9]

## THE 7/2 SHELL

The configuration $(7/2)^4$ is the simplest (i.e., lowest $j$) instance where the seniority number is needed to classify the states. There are two states each of spin $J=2$ and $J=4$; in each pair one state has seniority number $v=2$ and the other has $v=4$. We shall now show that in this case the seniority number $v$ is always a good quantum number. Consider any two-body symmetric interaction

$$G=\sum_{i<j}g_{ij}, \quad (41)$$

where, according to Racah, the angular and spin parts of $g_{ij}$ can be written as a sum of scalar products of tensor operators which act on each particle separately:

$$g_{ij}=\sum_r\tau_i^r\cdot\tau_j^r.$$

$G$ is now conveniently written in the following form

$$G=\sum_r\tfrac{1}{2}[\sum_i\tau_i^r\cdot\sum_j\tau_j^r-\sum_i\tau_i^r\cdot\tau_i^r]$$
$$=\sum_r\tfrac{1}{2}[|T^r|^2-\sum_i\tau_i^r\cdot\tau_i^r], \quad (42)$$

where $T^r=\sum_i\tau_i^r$. Taking the matrix element of $G$ between two states of the configuration $j^n$ with different seniorities, we have from the first term

$$(j^nvJ\|T^r\cdot T^r\|j^nv'J)=\sum_{J''v''}(2J+1)^{-\frac{1}{2}}(-1)^{J-J''}$$
$$\times(j^nvJ\|T^r\|j^nv''J'')(j^nv''J''\|T^r\|j^nv'J). \quad (43)$$

Racah has shown that the matrix elements of $T^r$ for odd $r$ are diagonal in the seniority; since $v\neq v'$, every term in (43) has $v''\neq v$ or $v''\neq v'$ so all these matrix elements vanish.

For the even values of $r$ we can use Racah's equation (74)[4] modified according to his discussions (76)[4] and (65).[3] For the half-shell, $n=(2j+1)/2$, the formula is

$$(j^nvJ\|T^r\|j^nv''J'')$$
$$=(-1)^{r+1+\frac{1}{2}(v''-v)}(j^nvJ\|T^r\|j^nv''J''). \quad (44)$$

[9] G. Racah and I. Talmi, Physica 18, 1097 (1952).

except for $r=0$. Hence, for even $r(\neq 0)$, these matrix elements vanish for $\Delta v=0$. In our case of $j=7/2$, the four particles constitute just half a shell, $v-v'$ is 2, and the general selection rule for these matrix elements is $|v-v''|=0, 2$. Thus, for every term in (43), either $|v-v''|$ or $|v'-v''|$ is 0 and all these terms vanish. All that is left of (42) are the terms $T^0$ and $\tau_i^r\cdot\tau_i^r$, both of which are scalars, i.e., independent of all angle and spin coordinates. Since, then, wave functions for states of different seniorities are orthogonal, the entire matrix element of $G$ is zero and the seniority remains a good quantum number.

We shall now calculate the diagonal energy matrix element of $G$ in the state $(7/2)^4$ $v=2$ $J=2$, which in nuclear spectroscopy is expected to be the first excited state of this configuration. This matrix element is given by (37):

$$((7/2)^4, v=2, J=2|G|(7/2)^4, v=2, J=2)$$
$$=\sum_{J'} Z(J')((7/2)^2J'|G|(7/2)^2J'). \quad (45)$$

Equation (38) for $Z(J')$ contains the term

$$(2J'+1)[1+(-1)^{J'}]\begin{Bmatrix} jjJ' \\ jjJ \end{Bmatrix}.$$

This will be recognized as the major term in the formula for the fractional parentage coefficient for the configuration $j^3$ $J=j$, where $J$ (which is even) plays the role of $J_0$. Since we know that for $(7/2)^3$ $J=7/2$ there is only one state, and that one is of seniority $v=1$, we can use (17) and write directly

$$(2J'+1)[1+(-1)^{J'}]\begin{Bmatrix} jjJ' \\ jjJ \end{Bmatrix}$$
$$=-\delta(J',J)+C\left[\delta(J',0)-\frac{(2J'+1)}{2j+1}(1+(-1)^{J'})\right], \quad (46)$$

and setting $J'=0$ we have $C=-2/(2j-1)$. Substituting (46) into (38) we have

$$Z(J')=\delta(J',J)+\frac{8}{(2j-1)(2j-3)}\delta(J',0)$$
$$+\frac{4}{(2j+1)(2j-1)}(2J'+1)[1+(-1)^{J'}], \quad (47)$$

or

$$((7/2)^4 22|G|(7/2)^4 22)$$
$$=((7/2)^2 2|G|(7/2)^2 2)+\tfrac{1}{5}((7/2)^2 0|G|(7/2)^2 0)$$
$$+\tfrac{1}{12}\sum_{J'}(2J'+1)[1+(-1)^{J'}]((7/2)^2J'|G|(7/2)^2J').$$

For the state $(7/2)^4$ $v=0$ $J=0$, we get, using (A8), the matrix element

$$((7/2)^4 00|G|(7/2)^4 00)=(4/3)((7/2)^2 0|G|(7/2)^2 0)+\tfrac{1}{9}D,$$

but

$$D=\tfrac{1}{2}\sum_{J'}(2J'+1)[1+(-1)^{J'}](j^2J'|G|j^2J'). \quad (48)$$

Finally, for the $0-2$ energy difference we have

$$((7/2)^4 00|G|(7/2)^4 00)-((7/2)^4 22|G|(7/2)^4 22)$$
$$=((7/2)^2 0|G|(7/2)^2 0)-((7/2)^2 2|G|(7/2)^2 2). \quad (49)$$

Here we have the general result that for any two-body interaction the excitation energy from the ground to the first excited state is the same for two as for four particles in the $j=7/2$ shell.

An example of this result can be seen in the results of the explicit calculations of Kurath.[10]

The clearest data on this subject involves the pair of isotopes $Ca^{42}$ and $Ca^{44}$. Both nuclei have a magic number, 20, of protons, hence we can well ignore the effect of a mixing of neutron and proton configurations. The nuclei have, respectively, two and four neutrons in the $f_{7/2}$ shell. This shell is supposedly well isolated between the magic numbers 20 and 28 so that contributions from a second-order calculation would be very small.

The energy of the first excited state in these two nuclei are[11]

$Ca^{42}$—1.51 Mev,
$Ca^{44}$—1.16 Mev.

The large discrepancy between these two measured values indicates very strongly the limitations to which an individual-particle shell model for the nucleus must be restricted.

## APPENDIX

As was mentioned earlier, for work with $G$-type operators it is most convenient to describe a wave function for $n$ equivalent particles in the form:

$$\psi(j^n\alpha J)=\sum_{\alpha''J''J''}(j^{n-2}(\alpha''J'')j^2(J')J\,\|\,j^n\alpha J)$$
$$\times\psi(j^{n-2}(\alpha''J'')j^2(J')J). \quad (A1)$$

These two-particle fractional parentage coefficients are related to the one-particle coefficients by

$$(j^{n-2}(\alpha''J'')j^2(J')J\,\|\,j^n\alpha J)$$
$$=\sum_{\alpha'''J'''}(2J'+1)^{\frac{1}{2}}(2J'''+1)^{\frac{1}{2}}(-1)^{J+J'''+2j}$$
$$\times\begin{Bmatrix} jjJ' \\ JJ'''J''' \end{Bmatrix}(j^{n-2}(\alpha''J'')jJ'''\,\|\,j^{n-1}\alpha'''J''')$$
$$\times(j^{n-1}(\alpha'''J''')jJ\,\|\,j^n\alpha J), \quad (A2)$$

and in terms of seniority they obey the selection rule $\Delta v=0, \pm 2$. Putting Racah's recursion relations [reference 3, Eq. (58)] for the one-particle coefficients into (A2) we can get recursion relations for the two-particle

[10] D. Kurath, Phys. Rev. 91, 1430 (1953).
[11] G. Scharff-Goldhaber, Phys. Rev. 90, 587 (1953).

coefficients

$$(j^{n-2}(v''J'')j^2(J')J\|j^nvJ)$$
$$=\left[\frac{v(v-1)(2j+3-n-v)(2j+5-n-v)}{n(n-1)(2j+3-2v)(2j+5-2v)}\right]^{\frac{1}{2}}$$
$$\times(j^{n-2}(v-2J'')j^2(J')J\|j^nvJ)(v''=v-2)$$
$$=\left[\frac{(v+1)(v+2)(n-v)(2j+3-n-v)}{2n(n-1)(2j+1-2v)}\right]^{\frac{1}{2}}$$
$$\times(j^n(vJ'')j^2(J')J\|j^{n+2}vJ)(v''=v)$$
$$=\left[\frac{(v+3)(v+4)(n-v)(n-v-2)}{8n(n-1)}\right]^{\frac{1}{2}}$$
$$\times(j^{n+2}(v+2J'')j^2(J')j\|j^{n+4}vJ)(v''=v+2). \quad \text{(A3)}$$

We shall take matrix elements of the symmetric scalar operator $G=\sum_{i<j}g_{ij}$ with the wave function (A1) as follows:

$$(j^nvJ|G|j^nv'J)$$
$$=\frac{n(n-1)}{2}\sum_{J'J''v''}(j^2J'|g_{ij}|j^2J')$$
$$\times(j^nvJ\|j^{n-2}(v''J''),\ j^2(J')J)$$
$$\times(j^{n-2}(v''J''),\ j^2(J')J\|j^nv'J). \quad \text{(A4)}$$

We shall also need the relation

$$(j^{m-n}\alpha J|G|j^{m-n}\alpha'J)$$
$$=(j^n\alpha J|G|j^n\alpha'J)+\frac{2j+1-2n}{2j+1}D, \quad \text{(A5)}$$

where $m=2j+1$; and

$$D=(j^m,\ v=0,\ J=0|G|j^m,\ v=0,\ J=0)$$
$$=\tfrac{1}{2}m(m-1)\sum_{J'}(j^{m-2}(J'),\ j^2(J')0\|j^m0)^2$$
$$\times(j^2J'|g_{ij}|j^2J').$$

From a simple generalization of Racah's equation (19),[3] we have

$$(j^{m-2}(J'),\ j^2(J')0\|j^m0)^2$$
$$=\frac{2}{m(m-1)}(2J'+1)(j^0(0),\ j^2(J')J'\|j^2J'),$$

so

$$D=\sum_{J'}(2J'+1)\left(\frac{1+(-1)^{J'}}{2}\right)(j^2J'|g_{ij}|j^2J').$$

In (A4) the selection rule is $v-v'=0,\ \pm2,\ \pm4$. For $v'=v-4$, there is only one term in the sum over $v''$, namely $v''=v-2$; then using Eq. (A3), we can separate out the $n$-dependence of the matrix element and get

$$(j^nvJ|G|j^nv-4J)$$
$$=\left[\frac{(2j+3-n-v)(2j+5-n-v)(n-v+2)(n-v+4)}{8(2j+3-2v)(2j+5-2v)}\right]^{\frac{1}{2}}$$
$$\times(j^nvJ|G|j^nv-4J). \quad \text{(A6)}$$

For $v'=v-2$ there are two terms in the sum (A4), $v''=v,\ v-2$. Thus this matrix element for $n$ particles can be expressed in terms of that for $v$ particles and one other configuration. We take the other to be $2j+1-v$ particles and use (A5) to get

$$(j^nvJ|G|j^nv-2J)=\left[\frac{(2j+3-n-v)(n-v+2)}{2(2j+3-2v)}\right]^{\frac{1}{2}}$$
$$\times\left[(j^nvJ|G|j^nv-2J)+\frac{(n-v)}{2j+1}D\right]. \quad \text{(A7)}$$

For $v'=v$ we shall use the three configurations of $v$, $2j+1-v$, and $v+2$ particles to account for the three terms in the sum (A4). Substitution of the relations (A3) gives an expression which finally reduces to the earlier quoted result

$$(j^nvJ|G|j^nvJ)=\frac{(n-v)(2j+1-n-v)}{2(2j-1-2v)}$$
$$\times(j^{n+2}vJ|G|j^{n+2}vJ)-\frac{(n-v-2)(2j-1-n-v)}{2(2j-1-2v)}$$
$$\times(j^nvJ|G|j^nvJ)+\frac{(n-v)(n-v-2)}{(2j-1-2v)(2j+1)}D. \quad \text{(A8)}$$

These reduction equations play the same role in the study of two-particle operators as Eqs. (67) and (69) of Racah[3] for one-particle operators.

# Angular Distribution of Neutrons Scattered from Cadmium, Tin, and Bismuth*

S. C. Snowdon and W. D. Whitehead†
*Bartol Research Foundation of The Franklin Institute, Swarthmore, Pennsylvania*

(Received February 8, 1954)

The differential cross sections for the scattering of 3.7-Mev neutrons from cadmium, tin, and bismuth have been measured over an angular range between 13 degrees and 140 degrees with an angular resolution of about ±10 degrees. The effects due to higher-order scattering have been removed at each measured angle by extrapolation. Previous measurements of the differential cross sections of aluminum, iron, and lead gave a uniform shift of the position of the first minima in the curve with atomic weight. In the present measurements, the curves for cadmium and tin, while quite similar, do not fall uniformly between those of iron and lead. The curve for bismuth, however, is again quite similar to that for lead. Possible explanations of this behavior are discussed in light of the continuum theory of nuclear reactions.

## INTRODUCTION

THE measurement of the differential cross sections for the scattering of 3.7-Mev neutrons from cadmium, tin, and bismuth represents an extension of similar measurements[1] on aluminum, iron, and lead in order to establish the pattern of variation with atomic weight. In addition, the recent continuum theory of nuclear reactions given by Feshbach, Porter, and Weisskopf[2] has been used with a plausible extension to calculate the angular distribution of 3.7-Mev neutrons scattered from nuclei of atomic weight 115 and 209. This should be of value in assessing the possibilities of using the continuum theory in this energy range to give detailed information about neutron scattering.

## EXPERIMENTAL

In general, the arrangement used in this experiment is exactly the same as that used in our previous experiment.[1] Neutrons of about 3.7 Mev were produced by bombarding a deuterium gas chamber with 10 $\mu$a of deuterons of 0.65-Mev mean energy. A ring geometry was employed in which the angle of scattering was varied both by using different size rings and by an axial movement of each ring.

The previous experiments demonstrated that corrections of considerable magnitude must be made to allow for the higher-order scattering in order to obtain the correct differential cross sections from the apparent differential cross sections observed with a ring of finite thickness. They further demonstrated that, within the experimental accuracy, a linear extrapolation of the apparent differential cross section to zero axial thickness of the scatterer most probably gave the correct differential cross section. The present measurements, therefore, were carried out using only two ring thicknesses. However, unlike the previous experiments in which only a few selected angles were chosen to determine the higher-order scattering correction, in these experiments each ring thickness was used at all the angles of measurement. The result gives the apparent differential cross section as a function of angle for each of the two ring thicknesses used. The true differential cross section now can be found at each angle by a linear extrapolation of the apparent differential cross section to zero ring thickness.

Finally, the neutron flux monitor was changed from that previously used, a butane-filled proportional counter, to a Lucite-zinc sulfide scintillator detector[3] identical with that used in detecting the scattered neutrons. In the previous experiments[1] some difficulty was experienced in maintaining a constant 0°/90° neutron flux ratio. Changing the monitor detector improved this situation somewhat.

## DATA

Figure 1 shows the experimental points of the apparent differential cross section for the scattering of 3.7-Mev neutrons incident on the $\frac{3}{4}$-inch and 1-inch thick rings of cadmium. A point by point linear extrapolation to zero ring thickness gives the true differential cross section $\sigma(\theta)$. Figures 2 and 3 present similar information with regard to tin and bismuth. At every angle the apparent differential cross section for the 1-inch rings is larger than the apparent differential cross section for the $\frac{3}{4}$-inch rings, thus demonstrating that at each angle the higher-order scattering adds a positive contribution to the apparent differential cross section.‡ The total cross sections corresponding to $\sigma(\theta)$ have been calculated and are presented together with

* Assisted by the joint program of the U. S. Atomic Energy Commission and the U. S. Office of Naval Research.

† Present address: North Carolina State College, Raleigh, North Carolina.

[1] W. D. Whitehead and S. C. Snowdon, Phys. Rev. **92**, 114 (1953).

[2] Feshbach, Porter, and Weisskopf, Phys. Rev. **90**, 166 (1953); U. S. Atomic Energy Commission Reports NYO 3076, NDA Report 15B-4 (unpublished); Massachusetts Institute of Technology (Laboratory for Nuclear Science) Technical Report No. 62, 1953 (unpublished).

[3] W. F. Hornyak, Rev. Sci. Instr. **23**, 264 (1952). The authors are indebted to Dr. Hornyak for supplying them with Lucite-zinc sulfide molded buttons.

‡ *Note added in proof.*—This positive contribution of the multiple scattering depends upon the definition of the apparent differential cross section used. It is possible to change the definition of the apparent differential cross section in such a way that multiple scattering does not add any contribution on the average. In this case there will be negative as well as positive contributions to the apparent scattering, depending on the angle.

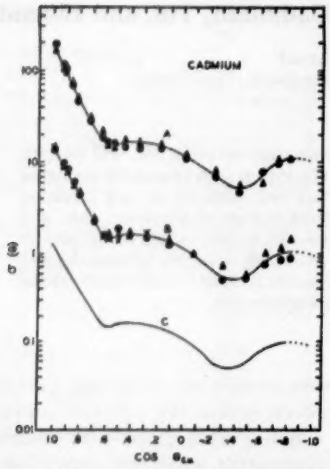


FIG. 1. Angular distribution of 3.7-Mev neutrons scattered from cadmium: (*A*) apparent differential cross section using 1-in. axial thickness ring scatterers; (*B*) apparent differential cross sections using ½-in. axial thickness ring scatterers; (*C*) true differential cross sections for elastic scattering obtained by a point-by-point linear extrapolation of curves (*A*) and (*B*) to zero-thickness scatterer. Ordinates are for curve (*C*) and are in units of barns/steradian. Curve (*B*) ordinate should be reduced by a factor of 10. Curve (*A*) ordinate should be reduced by a factor of 100.

the measured total cross sections in Table I. The measured total cross sections in each case are about 8–10 percent higher than those previously measured at an energy close to 3.7 Mev.[4] However, since both the differential and total cross sections were measured with the same experimental setup, at worst all measurements are systematically from 8–10 percent high which is within our over-all uncertainties of about 15 percent.

As was discussed previously,[1] the integrated cross section corresponding to $\sigma(\theta)$ does not accurately measure the total elastic cross section, since the neutron detector does not discriminate adequately against inelastically scattered neutrons. However, to within about 20 percent, it may be considered to represent this elastic cross section. Subject to this reservation, the difference between the measured total cross section and the integrated cross section corresponding to $\sigma(\theta)$ may be considered to equal the total inelastic cross section. Table I presents a summary of these calculations.

## THEORY

Since the neutron energy resolution in this experiment is about 200 kev, the angular distribution of scattered neutrons may be discussed in terms of a theory that averages the differential cross section over an energy interval of this magnitude. Generally, in our energy range there will be many resonance levels within this 200-kev energy interval, hence we may average the differential cross section over many resonance levels. Feshbach and Weisskopf[5] and Feshbach, Porter, and Weisskopf[2] have provided two distinct theories that discuss total neutron cross sections averaged in this manner. The total neutron cross-section measurements of Barschall *et al.*[6] generally show agreement with the theory of Feshbach, Porter, and Weisskopf[2] and are definitely at variance with the theory of Feshbach and Weisskopf.[5] Therefore, we will compare our measurements with the theory of Feshbach, Porter, and Weisskopf suitably formulated to exhibit the angular distribution of neutrons elastically scattered from nuclei.

The theory first will be formulated, assuming that there are no reaction products (i.e., no inelastic scattering, etc.). In general, the differential cross section for elastic scattering is given by[7]

$$\sigma_{se}(\theta)=\tfrac{1}{4}\lambda^2\sum_l\sum_m(2l+1)(2m+1)(1-\eta_l)\times(1-\eta_m^*)P_l(\cos\theta)P_m(\cos\theta), \quad (1)$$

where $\lambda$ is the deBroglie wavelength of the neutron, divided by $2\pi$, $\eta_l$ is the phase constant, and $P_l(\cos\theta)$ is the Legendre polynomial. The relation between the phase constant $\eta_l$ and the corresponding logarithmic derivative $f_l$ is given by[7]

$$\eta_l=\exp(2i\xi_l)\cdot[(f_l-\Delta_l+is_l)/(f_l-\Delta_l-is_l)], \quad (2)$$

where $\xi_l$ is the phase determining the potential scattering, and $\Delta_l+is_l$ is the logarithmic derivative of the outgoing wave in the entrance channel.

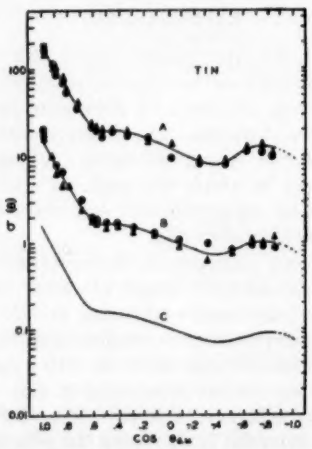


FIG. 2. Angular distribution of 3.7-Mev neutrons scattered from tin: (*A*) apparent differential cross section using 1-in. axial thickness ring scatterers; (*B*) apparent differential cross section using ½-in. axial thickness ring scatterers; (*C*) true differential cross section for elastic scattering obtained by a point-by-point linear extrapolation of curves (*A*) and (*B*) to zero-thickness scatterer. Remarks concerning ordinates are the same as in Fig. 1.

[4] *Neutron Cross Sections*, Atomic Energy Commission Report AECU-2040 (U. S. Office of Technical Services, Department of Commerce, Washington, D. C., 1952); N. Nereson and S. Darden, Phys. Rev. **89**, 775 (1953).

[5] H. Feshbach and V. F. Weisskopf, Phys. Rev. **76**, 1550 (1949); Feld, Feshbach, Goldberger, Goldstein, and Weisskopf, U. S. Atomic Energy Commission Report NYO-636, 1951 (unpublished).

[6] H. H. Barschall, Phys. Rev. **86**, 431 (1952); Miller, Adair, Bockelman, and Darden, Phys. Rev. **88**, 83 (1952).

[7] J. M. Blatt and V. F. Weisskopf, *Theoretical Nuclear Physics* (John Wiley and Sons, Inc., New York, 1952), Chap. VIII.

We now average Eq. (1) over an energy interval that includes many resonance levels:

$$\sigma_{sc}(\theta)=\tfrac{1}{4}\lambda^2\sum_l\sum_m(2l+1)(2m+1)[(1-\bar{\eta}_l)(1-\bar{\eta}_m^*)+(\langle\eta_l\eta_m^*\rangle_{Av}-\bar{\eta}_l\bar{\eta}_m^*)]P_l(\cos\theta)P_m(\cos\theta), \quad (3)$$

where all quantities such as $\lambda$, $\xi_l$, $s_l$, and $\Delta_l$ that only vary slowly with the energy are treated as constants. The distribution obtained from the term $(1-\bar{\eta}_l)\times(1-\bar{\eta}_m^*)$ is called the "shape elastic" scattering and the distribution obtained from the term $(\langle\eta_l\eta_m^*\rangle_{Av}-\bar{\eta}_l\bar{\eta}_m^*)$ is called the "compound elastic" scattering.[2]

In order to calculate $\eta_l$, first it is necessary to choose a model that will provide a logarithmic derivative which includes a description of resonances. Feshbach, Porter, and Weisskopf introduce a simplified version of a nuclear reaction. The zero-order approximate problem is described by a Hamiltonian,

$$H^{(0)}=H_T+H_n, \quad (4)$$

where $H_T$ is the Hamiltonian describing the complicated internal motions of the target nucleus, and $H_n$ describes the relative motion of the neutron and the target and is given by

$$H_n=-(\hbar^2/2m)\nabla^2+V(r), \quad (5)$$

where $m$ is the reduced mass, $\nabla^2$ is the Laplacian in the relative coordinate of the neutron and the target system. $V(r)$ is given by

$$V(r)=-V_0 \text{ for } r<R; \quad 0 \text{ for } r>R, \quad (6)$$

where $R$ is the nuclear radius.

The formation of the compound nucleus is described in the next approximation by adding an interaction operator $H'$ to give for the total Hamiltonian,

$$H=H_T+H_n+H'. \quad (7)$$

For a convenient choice of the matrix elements of $H'$ in the basis determined by the eigenfunctions of $H_T$, the value of the logarithmic derivative may be found. It is shown then that this rather complicated expression for the logarithmic derivative may be approximated by

$$f_l=w_{1l}+w_{2l}\cot z_l(\epsilon), \quad (8)$$

where $w_{1l}$ and $w_{2l}$ are slowly varying functions of the energy $\epsilon$ of the neutron. The phase $z_l(\epsilon)$ is taken as proportional to the energy. If this expression for the logarithmic derivative is inserted into Eq. (2) and averaged over many resonances, the result is

$$\bar{\eta}_l=\exp(2i\xi_l)\cdot[(w_{1l}-iw_{2l}-\Delta_l+is_l)]/(w_{1l}-iw_{2l}-\Delta_l-is_l)]. \quad (9)$$

TABLE I. Total cross sections. The value of $\int\sigma(\theta)d\Omega$, subject to the reservations in the text, is the total elastic cross section.

| Element | $\sigma_{tot}$ in barns This exp. | Ref. 4 | Theory | $\int\sigma(\theta)d\Omega$ barns |
|---|---|---|---|---|
| Cadmium | 4.5 | ~4.0 | 5.6 | 2.5 |
| Tin | 4.6 | ~4.2 | | 2.5 |
| Bismuth | 8.3 | 7.6 | 7.7 | 6.9 |

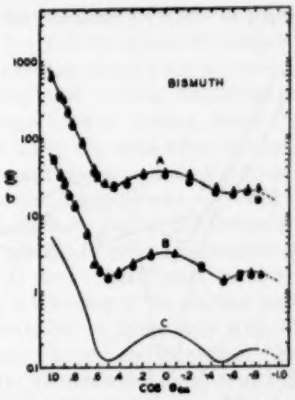


FIG. 3. Angular distribution of 3.7-Mev neutrons scattered from bismuth: (*A*) apparent differential cross section using 1-in. axial thickness ring scatterers; (*B*) apparent differential cross section using ½-in. axial thickness ring scatterers; (*C*) true differential cross section for elastic scattering obtained by a point-to-point linear extrapolation of curves (*A*) and (*B*) to zero-thickness scatterer. Remarks concerning the ordinates are the same as in Fig. 1.

Thus the averaging results in replacing the $\cot z_l$ in Eq. (8) by $-i$. The expressions obtained for $w_{1l}$ and $w_{2l}$ in the perturbation calculation are such that they may be approximated by the real and imaginary parts of the logarithmic derivative of the following non-Hermitean problem in the relative coordinates of the neutron and the target:

$$H=-(\hbar^2/2m)\nabla^2+V(r),$$

where

$$V(r)=-V_0(1+i\xi) \text{ for } r<R; \quad 0 \text{ for } r>R. \quad (10)$$

Thus all quantities in Eq. (3) are provided for except $\langle\eta_l\eta_m^*\rangle_{Av}$. To obtain this, we assume in Eq. (8) that $z(\epsilon)$ is a linear function of the energy,

$$z_l=\pi\epsilon/d_l+\beta_l, \quad (11)$$

where $d_l$ is the average level separation. The product $\eta_l\eta_m^*$ is then averaged with respect to $\epsilon$ as in the case of $\eta_l$. In particular the result will depend on the unknown parameters $\beta_l$. Since we are only interested in statistical results, the average of $\eta_l\eta_m^*$ with respect to $\epsilon$ is again averaged with respect to $\beta_l$. The result is then

$$\langle\eta_l\eta_m^*\rangle_{Av}=\bar{\eta}_l\bar{\eta}_m^* \text{ for } l\neq m; \quad =1 \text{ for } l=m. \quad (12)$$

Thus the average phase constant in Eq. (9) completely defines an angular distribution of the elastic scattering averaged over many resonances. The non-Hermitean problem defined by Eq. (10), which is used to provide an approximate expression for the average phase, may be solved by a method due to Lax and Feshbach.[6] We

[6] M. Lax and H. Feshbach, J. Acoust. Soc. Am. **20**, 108 (1948); Morse, Lowan, Feshbach, and Lax, "Scattering and Radiation from Circular Cylinders and Spheres" (Reprinted by U. S. Navy Department Office of Research and Inventions, Washington, D. C., 1946).

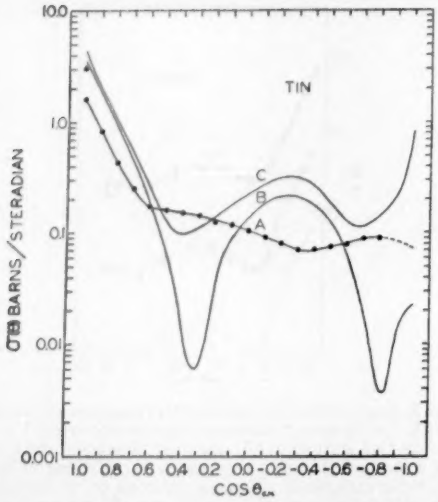


FIG. 4. Comparison of the experimental differential cross section for elastic scattering of 3.7-Mev neutrons from cadmium with the predictions of the continuum model for a nuclear radius of $7.1\times10^{-13}$ cm and a complex potential constant of $-19(1+0.05i)$ Mev: (*A*) experimental results from Fig. 1(*C*); (*B*) "shape elastic" differential cross section; (*C*) "compound elastic" plus "shape elastic" differential cross section using Eq. (12) to determine the "compound elastic" scattering. Solid triangle is $\sigma_{se}(0)$ from first version of the continuum theory.

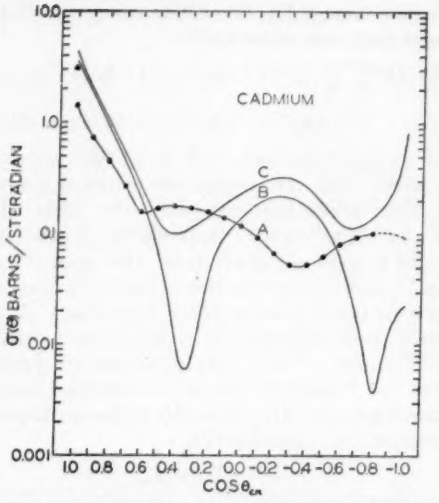


FIG. 5. Comparison of the experimental differential cross section for the elastic scattering of 3.7-Mev neutrons from tin with the predictions of the continuum model for a nuclear radius of 7.1 $\times10^{-13}$ cm and a complex potential constant of $-19(1+0.05i)$ Mev; (*A*) experimental results from Fig. 2(*C*); (*B*) "shape elastic" differential cross section; (*C*) "compound elastic" plus "shape elastic" differential cross section using Eq. (12) to determine the "compound elastic" scattering. Solid triangle is $\sigma_{se}(0)$ from first version of the continuum theory.

have used for the potential within the nucleus,

$$V=-19(1+0.05i)\text{ Mev};\qquad(13)$$

and for the nuclear radius,

$$R=1.45\times10^{-13}A^{\frac{1}{3}}\text{ (cm)}.\qquad(14)$$

These values give good agreement with the total cross-section measurements of Barschall.[2,6]

In the preceding theory, it was assumed that no reaction products were present in the decay of the compound nucleus. This restriction may be removed by realizing that the effect of these reaction products upon the entrance channel can be accounted for approximately by introducing an imaginary part to the energy. Thus Eq. (11) is changed to

$$z_l=(\pi/d_l)(\epsilon+\tfrac{1}{2}i\Gamma_r^{(l)})+\beta_l,\qquad(15)$$

where $\Gamma_r^{(l)}$ is the reaction width.[2,9] When this is done, it will be found that Eq. (9) for the average phase $\bar{\eta}_l$ is unchanged, and that Eq. (12) for the average phase product $\langle\eta_l\eta_m^*\rangle_{Av}$ is unchanged for $l\neq m$, but that for

TABLE II. $\sigma_{se}$ is the integrated "shape elastic" cross section. $\bar{\sigma}_c$ is the average cross section for the formation of the compound nucleus. $\bar{\sigma}_{tot}$ is the total neutron cross section. The "compound elastic" cross section plus the average reaction cross section add up to $\bar{\sigma}_c$.

| $R(10^{-13}$ cm) | $\sigma_{se}$(barns) | $\bar{\sigma}_c$(barns) | $\bar{\sigma}_{tot}$(barns) |
|---|---|---|---|
| 7.1 (Cd, Sn) | 4.0 | 1.6 | 5.6 |
| 8.6 (Bi) | 6.1 | 1.6 | 7.7 |

[9] Feshbach, Peaslee, and Weisskopf, Phys. Rev. **71**, 145 (1947).

$l=m$:

$$\langle\eta_l\eta_m^*\rangle_{Av}=1-[\exp(2\pi\Gamma_r^{(l)}/d_l)-1]\times\frac{1-\bar{\eta}_l\bar{\eta}_l^*}{\exp(2\pi\Gamma_r^{(l)}/d_l)-\bar{\eta}_l\bar{\eta}_l^*}.\qquad(16)$$

Hence the preceding formulation may be used throughout except for this one change. Table II and Figs. 4–6 present the chief numerical results of the above theory.

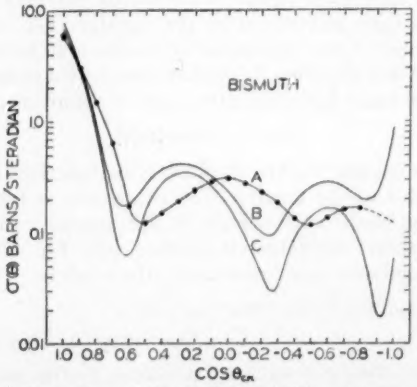


FIG. 6. Comparison of the experimental differential cross section for the elastic scattering of 3.7-Mev neutrons from bismuth with the predictions of the continuum model for a nuclear radius of $8.6\times10^{-13}$ cm and a complex potential constant of $-19(1+0.05i)$ Mev: (*A*) experimental results from Fig. 3(*C*); (*C*) "shape elastic" differential cross section; (*B*) "compound elastic" plus "shape elastic" differential cross section using Eq. (12) to determine the "compound elastic" scattering. Solid triangle is $\sigma_{se}(0)$ from first version of the continuum theory.

## DISCUSSION

A comparison in Figs. 4–6 of the experimental differential cross section for the elastic scattering of 3.7-Mev neutrons from cadmium, tin, and, bismuth with the theoretical predictions of the continuum model shows that the main features of the experimental curves are reproduced by the theory. In general, the theoretical results give a better fit with bismuth than with cadmium or tin. If one were to use Eq. (16) in the determination of the "compound elastic" scattering, there is no choice of the ratio of reaction width to level separation $\Gamma_r^{(l)}/d_l$ that would make the fit much better. The addition of "compound elastic" scattering, however, does adjust the "shape elastic" scattering to a distribution that more nearly resembles the experimental curve than does the "shape elastic" scattering alone. In particular, this "compound elastic" scattering shifts the position of the first minima in the "shape elastic" scattering. Since different nuclei have different amounts of "compound elastic" scattering, this may account for the lack of a uniform shift in the position of the first minima in the experimental elastic scattering distributions as one proceeds from iron to bismuth.

Since the largest discrepancy between theory and experiment occurs in the differential cross section for forward scattering, $\sigma_{sc}(0)$, it is of interest to consider possible adjustments of $\sigma_{sc}(0)$ in the theory. The minimum theoretical value of $\sigma_{sc}(0)$ is given by a theory that does not include "compound elastic" scattering and has the maximum possible cross section for the formation of the compound nucleus. These conditions are met in the first version of the continuum theory.[5] The values of $\sigma_{sc}(0)$ from this theory agree with the experimental value of $\sigma_{sc}(0)$ in the case of bismuth but are too high in the case of cadmium and tin. In the case of bismuth, however, the subsequent form of $\sigma_{sc}(\theta)$ does not offer any possibility of giving a detailed fit. Therefore, it is not possible to obtain a useful value of $\sigma_{sc}(0)$ that agrees with experiment by adjusting only the value of $\xi$ in Eq. (10) and the value of $\Gamma_r^{(l)}/d_l$ in Eq. (16). It can be argued that the double average used to obtain $\langle\eta_l\eta_m^*\rangle_{Av}$ in Eq. (12), strictly speaking, is not a necessary feature of the continuum theory and that one should insert some function of $l$ for the parameter $\beta_l$ in Eq. (11). To get some idea of the restriction introduced by this average over $\beta_l$, the value of $\eta_l\eta_m^*$ was averaged with respect to $\epsilon$ with the value of $\beta_l$ set equal to zero. For bismuth the difference between this method and the double-average method was quite small. For cadmium and tin the difference was somewhat larger but still not large enough to alter appreciably the results of the double average method. Hence, it is not likely that significantly better fits between theory and experiment would be obtained if $\beta_l$ were known as a function of $l$.

Since the theoretical value of $\sigma_{sc}(0)$ can be made to agree with experiment by adjusting the nuclear radius, it is of interest to estimate the magnitude of the change necessary to bring about this agreement. The nuclear radius used for bismuth [$A=209$ in Eq. (14)] would have to be lowered by about 6 percent since $\sigma_{sc}(0)$ varies approximately as the fourth power of the radius. This also would move the first theoretical minima closer to the first experimental minima. Since this change in radius would lower the total cross section by approximately 15 percent and since the total cross section is in fair agreement with experiment, it would be necessary to raise the imaginary part of the potential in Eq. (13) by about 15 percent in order to maintain agreement of the theoretical and experimental total cross section. Furthermore, a lowering of the nuclear radius by about 6 percent would be in agreement with the measurements of Coon, Graves, and Barschall,[10] in which they find for 14-Mev neutrons and for elements above barium that the nuclear radius as measured by $(\sigma_{tot}/2\pi)^{\frac{1}{2}}$ falls below the value predicted by $R=1.5\times10^{-13}A^{\frac{1}{3}}$ cm.

In order to adjust the theory to the experimental value of $\sigma_{sc}(0)$ for cadmium and tin it would be necessary to lower the nuclear radius chosen [$A=115$ in Eq. (14)] by about 30 percent. Corresponding to this, it would be necessary to increase the parameter $\xi$ by a large amount to give a sufficiently large total cross section if, indeed, a large change in $\xi$ is capable of adjusting the total cross section by a correspondingly large amount. This large adjustment of the nuclear radius is not very palatable in view of the general experimental agreement of the nuclear radius with the formula in Eq. (14) for 14-Mev neutrons and for values of $A$ near 115.[10] It is conceivable that the theory as it stands would give better agreement if it were applied to an ellipsoidal-shaped target nucleus. However, since only 20–25 percent of the cadmium and tin isotopes have odd neutron numbers and since nuclear eccentricities in the region of $A=115$ are only about 6 percent,[11] it is not likely that the use of an ellipsoidal target nucleus can produce the desired change. Hence, we are reduced to the necessity of a modification of the theory as the only means by which a sufficiently large adjustment can be accomplished. Within the general framework of the theory, it might be possible to choose the matrix elements of $H'$ in Eq. (7) to be a function of the relative coordinate $r$, or to let the potential in Eq. (6) be a function of the spins of the neutron and the target nucleus.[12] In any case, however, it would be necessary that these changes introduce little effect on the present results in the neighborhood of $A=209$.§

[10] Coon, Graves, and Barschall, Phys. Rev. **88**, 562 (1952).

[11] J. M. Blatt and V. F. Weisskopf, *Theoretical Nuclear Physics* (John Wiley and Sons, Inc., New York, 1952), pp. 29, 776.

[12] N. C. Francis and K. M. Watson, Phys. Rev. **92**, 291 (1953).

§ *Note added in proof.*—Although the computations of the angular distributions were stated to be found using $R=1.45\times10^{-13}A^{1/3}$ cm, the nuclear radius was inadvertently chosen using $R=1.50\times10^{-13}A^{1/3}$ cm. Since both of these formulas for the nuclear radius have been used in the arguments presented in the discussion, and since the accuracy of the data limits the comparison of the data with theory to within 4 percent in the nuclear radius, it was not considered necessary to change the computations to correspond to a nuclear radius of $R=1.45\times10^{-13}A^{1/3}$ cm. All of the arguments stated in the discussion are essentially valid despite the interchangable use of the two formulas for nuclear radius.

In summary then, it may be said that the continuum theory may be brought into rather detailed agreement with the measured angular distribution of 3.7-Mev neutrons scattered from bismuth. The theory in the case of cadmium and tin exhibits only the general features of the experimental results and possibly demonstrates a need for a revision of the theory.

ACKNOWLEDGMENT

In conclusion, the authors wish to express their appreciation to Dr. L. Eisenbud for many helpful conversations, to Mr. H. S. Hans for help with the computations, and to Dr. W. F. G. Swann, Director of the Bartol Research Foundation, for his continuing interest in this problem.

PHYSICAL REVIEW VOLUME 94, NUMBER 5 JUNE 1, 1954

# A Study of the Interaction of Neutrons with Moderating Materials

G. F. von Dardel
*Department of Physics, AB Atomenergi, Stockholm, Sweden*
(Received October 16, 1953)

In the theoretical part of this paper we consider the time dependence of the slowing-down process for certain simple cases: (1) For free nuclei at rest an approximate expression is found for the velocity distribution. (2) The existence of a bond in one direction while the motion is unhindered in other directions is found to have little influence on the slowing-down process. (3) The slowing-down process in a monatomic gas is discussed quantitatively on the assumption of a Maxwellian neutron velocity distribution. The experimental part of the paper reports measurements with a pulsed neutron source and a time analyzer, in which the variations of the neutron velocity spectrum with time were studied by transmission measurements. Measurements on water show that the neutrons approach thermal equilibrium with the moderator at a rate which is in agreement with the theoretical predictions. The equilibrium temperature of the neutrons is found to agree with the moderator temperature over a wide temperature range. At low temperatures evidence is found for the effect of the lattice forces on the slowing-down process. Measurements on the initial slowing-down process for neutrons in heavy water indicate satisfactory agreement with the theory for slowing down by free deuterons at rest. The various factors which determine the rate of decay of the neutron intensity in a moderator are discussed, and the feasibility of using measurements of the decay rate to determine the diffusion and absorption properties of the moderating material as well as the geometrical buckling of complicated moderating systems is considered. In an appendix tables are given for the absorption of thermal neutrons in $1/v$ absorbers.

MODERATING materials are used for the production of thermal neutrons from a fast neutron source, and are required to slow down neutrons to thermal energies in a time which is small compared to the lifetime of the neutrons. The slowing-down time is therefore of considerable practical interest. Since the slowing-down times are of the order of 10 or 100 $\mu$sec, the process can be readily studied by the technique of the pulsed neutron source and detector developed mainly for neutron time-of-flight spectroscopy.[1] It is the purpose of the present article to discuss briefly a number of experiments performed with this method, and their theoretical interpretation. A more detailed account of the subject is given in the author's thesis, published elsewhere.[2]

## PART I. THEORY

### A. General

We consider the case of neutrons produced with the initial velocity $v_{in}$ in an infinite uniform moderator during an infinitely short time interval. The subsequent slowing-down process is in principle uniquely defined by the probability $g(v_0,v)dv$ per unit path for a neutron to suffer a collision in which the velocity is changed from $v_0$ to the velocity interval $dv$ at $v$. The velocity distribution $f(v,t)$ at the time $t$ after the production of neutrons is given by the space- and angle-independent Boltzmann equation

$$\frac{\partial f(v,t)}{\partial t}=-\frac{vf(v,t)}{l(v)}+\int v_0 f(v_0,t)g(v_0,v)dv_0 +\delta(v_{in}-v)\delta(t), \quad (1)$$

where $l(v)$ is the total mean free path including absorption of the neutrons in the moderator. In the case when the absorption cross sections are inversely proportional to the relative neutron velocity, the velocity distribution at a given time is the same as for no absorption, since neutrons of all energies are absorbed at the same rate. Since we will in the following consider only this case, we may consider $l(v)$ to be the mean free path for scattering alone.

Except for the problem of solving the integro-differential equation (1) for an arbitrary slowing-down kernel $g(v_0,v)$, the main difficulty lies in the fact that for moderators of practical interest, where in general

[1] Rainwater, Havens, Wu, and Dunning, Phys. Rev. 71, 65 (1947).
[2] G. F. von Dardel, Trans. Roy. Inst. Technol. Stockholm No. 75 (1954).

account has to be taken of the chemical bonds and thermal excitation in the substance, the expression for the kernel becomes exceedingly complicated. For the theoretical interpretation of the present measurements, the actual moderating substance was therefore replaced by simple idealized structures for which the theory leads to manageable expressions for the slowing-down kernel.

As long as the neutron energy is much higher than the thermal excitation and binding energy of the atoms in the substance, the problem is reduced to the relatively simple case of slowing down against free nuclei at rest, which will be discussed in Sec. B. As the neutron energy decreases, the forces which keep the nuclei together in molecules begin to make themselves noticeable, and the slowing down process will proceed more slowly. Fermi[3] has studied the case of nuclei bound by an isotropic oscillator potential. In this case the energy loss occurs in multiples of the oscillator quanta. In practice the quantum energies of the various degrees of freedom of the molecule may well differ considerably from each other, so that the case of an anisotropic binding is of some interest and will be discussed in Sec. C, neglecting thermal motion.

When the neutron energy has dropped below the value necessary to excite the vibrational and rotational degrees of freedom of polyatomic molecules, the subsequent slowing-down process will occur by energy transfer to the translational degrees of freedom of the molecule as a whole, if the bonds between the molecules can be neglected as is the case in gases and, approximately, in liquids and solids for temperatures above the Debye temperature. A monatomic gas of nuclei having the mass of the molecules should be a good substitute for the actual substance. This case will be discussed in Sec. D.

When the temperature of the moderator is lower than the Debye temperature of the substance, the model of a gas is no longer a good approximation. Kleinman[4] has derived expressions for the differential cross section of a Debye crystal which in principle makes it possible to calculate the slowing-down process.

### B. Moderator Containing Free Nuclei at Rest

The time-dependent velocity distribution for this case has been studied by Marshak[5] and Walen.[6] If the initial energy of the neutrons is very high, their velocity distribution can, for dimensional reasons, be written in the form

$$f(v,t)dv=\varphi(x)dx, \tag{2}$$

which depends only on the dimensionless parameter $x=vt/l_0$. $l_0$ is the mean free path in the moderator, which we assume to be independent of the neutron velocity. It is shown in reference 2 that the velocity distribution at time $t$, $\varphi(x)$, is related to the time distribution of neutrons with the velocity $v$, $F(x)$, as introduced by Marshak,[5] by the relation

$$F(x)=\frac{\xi}{2}x\cdot\varphi(x), \tag{3}$$

where $\xi=1+[r^2/(1-r^2)]\log r^2$ is the average logarithmic energy loss per collision, and $r$ is the ratio $(M-m)/(M+m)$, $m$ and $M$ being the masses of the neutron and the scattering nucleus, respectively.

Introducing (2) and the proper kernel into (1), it is easy to obtain expressions for the $n$th positive and negative moments of $\varphi(x)$,

$$\langle x^{+n}\rangle=\frac{2}{\xi}\prod_{\nu=1}^{n-1}\nu\left\{1-\frac{2(1-r^{\nu+2})}{(\nu+2)(1-r^2)}\right\}^{-1}, \tag{4}$$

$$\langle x^{-n}\rangle=\prod_{\nu=1}^{n}\frac{1}{\nu}\left\{\frac{2(r^{2-\nu}-1)}{(\nu-2)(1-r^2)}-1\right\}. \tag{5}$$

As in Marshak's[5] treatment, it has been attempted to find an approximate expression for $\varphi(x)$ of the form

$$\varphi(x)=Ax^{2/(1-r^2)-1}e^{-x-b/x}. \tag{6}$$

As is shown in Fig. 1, quite good agreement was obtained between the moments of this function and the required moments, Eqs. (4) and (5), with the values for $A$ and $b$ given in Table I. For nuclei of unit mass, Eq. (6) is the exact solution.

The form of the function (6) for best fit in the cases $M/m=2$, 9, and 15 is shown in Fig. 2 and compared to curves derived from Marshak's[5] article.

### C. Incompletely Bound Nuclei

As a simple example of the incompletely bound nucleus, we consider the case of a nucleus which is

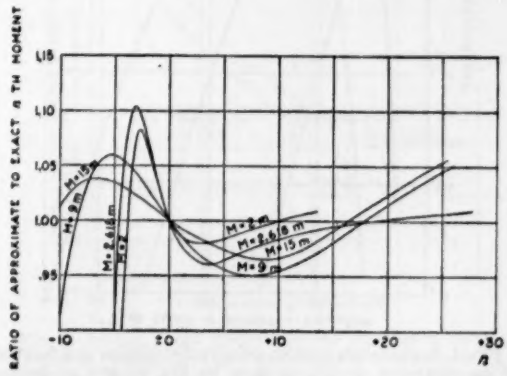


FIG. 1. Ratio of the moments of the trial function (6) to the required moments (4) and (5) of the time dependent neutron velocity distribution in the case of free nuclei at rest.

[3] E. Fermi, Ricerca sci. 7, 13 (1936).
[4] D. A. Kleinman, Phys. Rev. 90, 355 (1953).
[5] R. E. Marshak, Revs. Modern Phys. 19, 185 (1947).
[6] R. Walen, "Recueil de travaux de l'institut de recherches sur la structure de la matière," Belgrad, July 1952 (unpublished).

bound to a plane by a harmonic restoring force but is free to move parallel to the plane. The angular frequency of the harmonic motion perpendicular to the plane is $\omega$.

By integration, over the proper volume in momentum space and over the orientations of the plane, of the matrix element[7] for the energy transfer $n\hbar\omega$ to the motion perpendicular to the plane and $\Delta\hbar\omega$ to the unquantized motion parallel to the plane, we obtain the differential scattering cross section for the energy loss $E_0-E=(n+\Delta)\hbar\omega$

$$\sigma_n(E_0,E)=\frac{1}{n!}\frac{1}{1-r^2}\frac{\sigma_f}{E_0}\int_{\cot\theta'}^{\cot\theta''}(\Delta t^2)^n \times\exp(-\Delta t^2)(1+t^2)^{-1}dt. \quad (7)$$

$\sigma_f$ is the scattering cross section of the free nucleus at rest. The limits of integration are given by

$$\sin\theta'=(\Delta\hbar\omega\cdot M/m)^{\frac{1}{2}}/(E_0^{\frac{1}{2}}-E^{\frac{1}{2}}); \qquad \sin\theta''=(\Delta\hbar\omega\cdot M/m)^{\frac{1}{2}}/(E_0^{\frac{1}{2}}+E^{\frac{1}{2}}). \quad (8a,b)$$

The expression (7) has been calculated numerically for initial neutron energies up to $2.2\times\hbar\omega$ and for a number of masses $M$ of the nuclei. Figure 3 shows the result for $M=4m$.

The effect of the incomplete bond on the slowing-down process was studied by the Monte-Carlo process

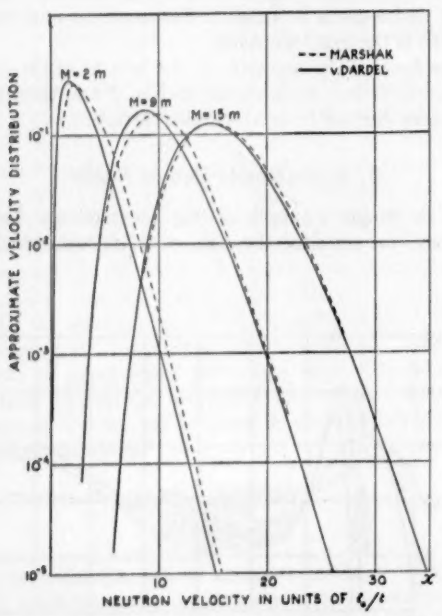


FIG. 2. Approximate neutron velocity distribution as a function of the parameter $x=v\ell/l_0$ as given by Eq. (6) and as derived from the curves in reference 5.

[7] G. Placzek, Phys. Rev. 86, 377 (1952).

TABLE I. Optimum parameters in the trial function (6) for best fit to the required moments (4) and (5).

| $M/m$ | | 1 | 2 | 2.618 | 9 | 15 |
|---|---|---|---|---|---|---|
| $2/(1-r^2)$ | exact | 2.00 | 2.25 | 2.50 | 5.5556 | 8.533 |
| | approx. | 2.00 | 2.25 | 2.50 | 5.500 | 8.500 |
| $y=2\sqrt{b}$ | | 0 | 1.9 | 2.8 | 12.0 | 20.5 |
| $b$ | | 0 | 0.903 | 1.96 | 36.0 | 105.1 |
| $A$ | | 1.000 | 1.528 | 1.929 | 3.610 | 0.681 |

and gives a rather insignificant decrease in the speed of the process. In consequence, we may neglect the effects of the bonds to a first approximation until the neutron energy is below the quantum energy of the weakest bond.

### D. The Slowing Down of Neutrons in a Monatomic Gas

The differential cross section per molecule of a monatomic gas of temperature $T$ for a collision which changes the neutron energy from $E_0=\omega_0^2kT$ to $dE$ at $E=\omega^2kT$ is given by Wigner and Wilkins,[8]

$$\sigma(E_0,E)=\frac{1}{(1-r^2)}\frac{\sigma_f}{E_0}\frac{1}{\sqrt{\pi}}\{\exp(\omega_0^2-\omega^2)\,\mathrm{Erf}(b\omega_0-a\omega) -\mathrm{Erf}(a\omega_0-b\omega)-|\exp(\omega_0^2-\omega^2)\,\mathrm{Erf}(b\omega_0+a\omega) -\mathrm{Erf}(a\omega_0+b\omega)|\}, \quad (9)$$

where

$$a=\tfrac{1}{2}[(M/m)^{\frac{1}{2}}-(m/M)^{\frac{1}{2}}]; \qquad b=\tfrac{1}{2}[(M/m)^{\frac{1}{2}}+(m/M)^{\frac{1}{2}}]. \quad (10a,b)$$

A derivation of this formula is also given in reference 2.

It is of interest to calculate the total cross section,

$$\sigma_t(E_0)=\sigma_f\frac{1}{\beta^2\sqrt{\pi}}[\beta\exp(-\beta^2)+(2\beta^2+1)\,\mathrm{Erf}\beta], \quad (11)$$

and the mean energy loss per collision,

$$(E_0-E)_{Av}=-\frac{4kT}{(M/m)+1}+\frac{2kT}{[(M/m)+1]^2} \times\frac{[\beta^3+(5/2)\beta]\exp(-\beta^2)+(2\beta^4+6\beta^2+\frac{3}{2})\,\mathrm{Erf}\beta}{\beta\exp(-\beta^2)+(2\beta^2+1)\,\mathrm{Erf}\beta}, \quad (12)$$

where $\beta=(ME_0/mkT)^{\frac{1}{2}}$. Expression (11) was first derived by Tait.[9]

Since the integral equation (1) cannot be solved explicitly for the kernel corresponding to (9), we have recourse to the following approximate treatment. We assume the neutron velocity spectrum to be Maxwellian at all times, characterized by a single parameter, the neutron temperature $T_n$, which we expect to de-

[8] E. P. Wigner and J. F. Wilkins, U. S. Atomic Energy Commission Report AECD-2275 (unpublished).

[9] P. G. Tait, Trans. Roy. Soc. (Edinburgh) 33, 74 (1886).

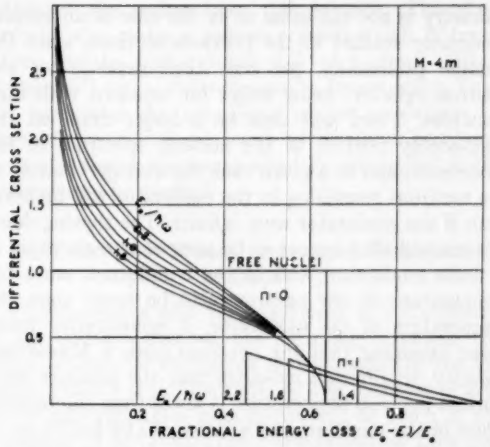


FIG. 3. Average differential cross section as a function of the fractional energy loss for an incompletely bound nucleus of mass $M=4$ m in units of the value for the free nucleus. Parameter: Initial neutron energy in units of the quanta $\hbar\omega$ of the bond. Upper curves: elastic collisions ($n=0$). Lower curves: collisions exciting the nucleus to the first excited state ($n=1$).

crease during the slowing-down process and eventually to approach the temperature $T$ of the moderator.

From (11) and (12) we find for the average rate of energy transfer from the neutrons to the moderating gas the equation:

$$\frac{d\bar{E}_n}{dt}=-\frac{8}{\sqrt{\pi}}\frac{(2kT/m)^{\frac{1}{2}}}{l_b}\cdot\frac{(M/m)^{5/2}}{(M/m+1)^{7/2}}\times\left[1+\frac{T_n-T}{T(1+m/M)}\right]^{\frac{1}{2}}k(T_n-T), \quad (13)$$

where $l_b$ is the mean free path if the nuclei were rigidly bound. In analogy to heat transfer problems, we define as the (asymptotic) heat transfer coefficient between the neutrons and the moderator gas

$$\alpha_0=\frac{8}{\sqrt{\pi}}\frac{(2kT/m)^{\frac{1}{2}}}{l_b}\cdot\frac{(M/m)^{5/2}}{(M/m+1)^{7/2}}k. \quad (14)$$

Since the average neutron energy $\bar{E}_n$ for a Maxwellian spectrum is $\frac{3}{2}kT_n$, Eq. (13) is a differential equation for $T_n$, with the solution

$$\frac{T_n-T}{T}=\frac{2(1+m/M)}{\cosh(c+\alpha_0 t/\frac{3}{2}k)-1}. \quad (15)$$

If we require the solution to describe correctly the fact that at zero time the neutron energy is infinite, we have to put the integration constant $c=0$.

The result of this simplified argument will be in error if the true velocity distribution during the slowing-down process is markedly different from a Maxwellian spectrum. For neutron energies large compared to thermal energies the velocity distribution is approximately given by Eq. (6), which is definitely not Maxwellian. It is reasonable to assume that the shape of the velocity distribution becomes more and more Maxwellian as the neutrons approach thermal equilibrium with the gas. An upper limit on the errors committed in the simplified theory will therefore be obtained if we compare the time dependence of the average neutron energy as derived from Eq. (15) and, for free nuclei at rest, from Eq. (4). The result is that for energies large compared to $kT$, Eq. (15) predicts a time scale for the slowing-down process, which in the case of a proton gas is too slow by a factor of 1.3 and for very heavy nuclei too fast by a factor of 0.8, whereas for nuclei of mass four the two models agree. The best picture for the variation of the average neutron energy with time is probably obtained if we use Eq. (4) for the slowing-down process down to an energy where we expect the thermal motion to become of importance, say $5kT$, and join a curve of the form (15) at this point by a proper choice of the constant of integration $c$.

In order to further check the simplified theory, an approximate solution of the integral equation (1) with the kernel corresponding to the differential cross section (9) has been evaluated for the case $M=m$, by the Monte-Carlo method. From the result the time variation of the mean neutron energy is calculated and compared with the approximate expression (15) in Fig. 4. This comparison confirms the expectation that the initial rate of energy loss predicted by Eq. (15) is too slow but that the subsequent approach to equilibrium with the moderating gas is quite accurately described.

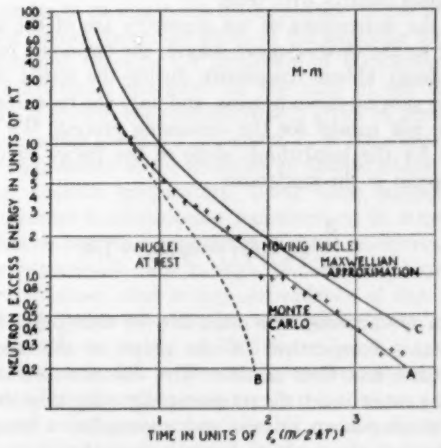


FIG. 4. Average excess energy over the equilibrium value $\frac{3}{2}kT$ of neutrons slowing down in a proton gas of temperature $T$ as a function of time. Curve $A$: smoothed result of Monte-Carlo calculation. Curve $B$: calculated neglecting the thermal motion of the protons [Eq. (4)]. Curve $C$: calculated on the assumption of a Maxwellian neutron velocity distribution [Eq. (15)].

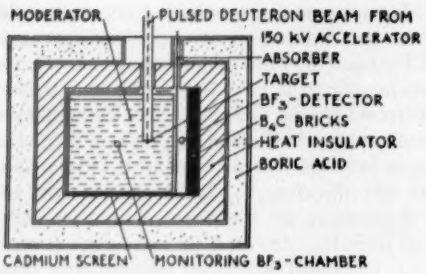


FIG. 5. Experimental arrangement.

### E. Effect of the Finite Size of the Moderator

In a finite geometry the time dependence at position $\mathbf{r}$ of the neutron density due to a burst of neutrons at time $t=0$ can be written[10]

$$n(\mathbf{r},t)=Z_0(\mathbf{r})\exp\left(-\kappa_0^2\int Ddt-1/\theta\right)+\sum_{\nu=1}^{\infty}Z_\nu(\mathbf{r})\exp\left(-\kappa_\nu^2\int Ddt-1/\theta\right), \quad (16)$$

where $D(t)$ is the diffusion coefficient of the neutrons at time $t$, $\kappa_0^2$ and $\kappa_\nu^2$ are the eigenvalues (geometrical buckling) corresponding to the eigenfunctions $Z_0(\mathbf{r})$ and $Z_\nu(\mathbf{r})$ for the fundamental and harmonic modes of the boundary problem, and $\theta$ is the mean life for absorption.

The integral $\int Ddt$ is identical to the Fermi age[3] which during the slowing-down process increases from zero to the value $L_s^2$, $L_s$ being the slowing-down length. After the neutrons have become thermal the age increases linearly with time.

If the dimensions of the geometry are of the same order as the slowing-down length, the harmonic modes will decay almost completely during the initial phase of the slowing-down process, and only the fundamental mode will subsist for the remaining process. We then have for the logarithmic slope of the decay curve at any point in the moderator

$$-\frac{\partial}{\partial t}[\log n(\mathbf{r},t)]=\kappa_0^2D(t)+1/\theta. \quad (17)$$

For a $1/v$ absorber the mean life for absorption $\theta$ is a constant, independent of the shape of the neutron spectrum and thus of time. The diffusion coefficient, on the other hand, decreases rapidly with time during the slowing-down process and approaches a constant value when the neutrons become thermal.

The velocity spectrum of the neutrons in a finite geometry is not the same as in the case of an infinite moderator studied in the previous sections, since the leakage probability per unit time depends on the neutron velocity, being larger for neutrons with high velocities. There will thus be a larger drain on the high-energy portion of the neutron spectrum in the moderator, and at a given time the average velocity of the neutrons remaining in the moderator will be lower than if the moderator were infinite. The slowing-down process will thus appear to be somewhat more rapid in a finite moderator, and in the equilibrium state the temperature of the neutrons will be lower than the temperature of the moderator. A quantitative treatment assuming that the neutrons have a Maxwellian velocity distribution indicates that the absolute equilibrium neutron temperature is lower than the temperature of the moderator by a factor of $(1+\frac{1}{2}\kappa_0^2Dk/\alpha_0)^{-1}$. Here $\kappa_0^2D$ is the leakage probability per unit time, $k$ is Boltzmann's constant, and $\alpha_0$ is the heat transfer coefficient between the neutrons and the moderator which in the case of a moderating monatomic gas is given by Eq. (14). The effect will be quite important if the amount of moderator is small.

## PART II. EXPERIMENT

### A. Apparatus

The experimental arrangement is shown in Fig. 5. The moderator is contained in a cubical tank of about 19-cm side, and is surrounded by a double-walled plywood box, the interspace between the walls being filled with boric acid for protection against stray neutrons from outside. For experiments at temperatures other than room temperature, the moderator can be surrounded by a 5-cm thick heat-insulating layer. The moderator is screened against neutrons diffusing in this layer by 0.05-cm cadmium sheets, except at one face of the tank where there is an empty space lined with boron carbide bricks. At this face is positioned a small $BF_3$ chamber (sensitive volume about 1 cm³) which measures the flux from the surface. The spectrum of the flux can be investigated by interposing absorbers between the emitting surface and the detector. A list of the boron absorbers used in the experiment is given in Table II. The value $k_0$ of a boron absorber is defined as the neutron velocity for which the transmission for perpendicular incidence is $1/e$. In the last column is given the corresponding neutron temperature $T_a=mk_0^2/2k$. Measurements were also made with a 0.05-cm cadmium absorber. The measurements were monitored with a monitoring chamber placed in a position where the flux is not influenced by the absorbers, usually in a central channel through the tank.

A block diagram of the apparatus is given in Fig. 6.

A 40-channel time-analyzer described in a separate publication[11] is used for the analysis of the time distri-

[10] S. Glasstone and M. C. Edlund, *The Elements of Nuclear Reactor Theory* (D. Van Nostrand Company, Inc., New York, 1952).

[11] G. F. von Dardel, Appl. Sci. Research **B3**, 209 (1953).

bution of the pulses from the detector. The time-analyzer also emits a reference pulse which is transmitted to the high-voltage side of a small 150-kv accelerator[12] by a radio-frequency transmission link[13] and modulates the ion source of the accelerator. A burst of neutrons is produced by deuteron bombardment of a heavy ice target which is submerged in the moderator to be studied.

### B. Methods of Measurement and Treatment of Data

A measurement with the equipment is characterized by the width, $c$ μsec, of the detecting channels, the length, $ic$ μsec, of the pulses which modulate the ion source, and the repetition time, $Rc$ μsec, between pulses. In the following these parameters will be given in the convenient code $(i/R)\cdot c$ μsec. The repetition time was usually 20 channel widths. The shortest channel width of the time analyzer is 2 μsec.

For intensity reasons it is not economical to choose the repetition time so long that all neutrons from the preceding pulse have disappeared before the next is applied. A certain overlap between cycles must be tolerated, and an overlap correction is easily obtained by extrapolation of the measured time distribution exponentially into the next cycle (see Fig. 8).

The procedure in treating the data is to refer the number of counts measured with and without absorbers to a constant number of monitor counts, plot the time distribution on a semilogarithmic plot, determine and apply the overlap correction, and from the corrected values calculate the transmission curves as a function of time after the neutron burst.

The transmission measurements were not sufficiently accurate and extensive to allow the neutron velocity spectrum to be determined by a direct analysis of the transmission curve, as indicated by Eckart.[14] Instead certain assumptions were made concerning the shape of the spectrum, and the calculated transmission compared with the experimental values.

During the first interval of time, which we define as the *epicadmium* period, the energies of most neutrons

TABLE II. Boron absorbers.

| No. | Material | g B/cm² | $k_0$[a] cm/sec | $T_a$°K |
|---|---|---|---|---|
| $B1$ | Boron carbide | 0.0110 | $0.97\times10^5$ | 56 |
| $B2$ | "Hysil" glass | 0.0244 | $2.12\times10^5$ | 270 |
| $B3$ | "Hysil" glass | 0.0248 | $2.16\times10^5$ | 279 |
| $B1+B2$ | | 0.0354 | $3.09\times10^5$ | 572 |
| $B2+B3$ | | 0.0492 | $4.28\times10^5$ | 1100 |

[a] On the basis of $\sigma_B = 710\times10^{-24}$ cm² for a neutron velocity of $2.2\times10^5$ cm/sec.

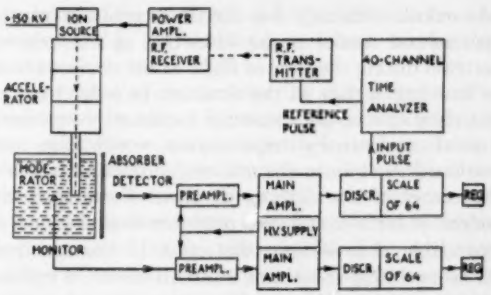


FIG. 6. Block diagram.

are above the cadmium absorption limit. The velocity distribution should be approximately given by the function (6) derived for slowing down against free nuclei at rest, since the chemical bonds and the thermal motion can be neglected. During the subsequent *transition* period to thermal equilibrium, the shape of the velocity distribution is assumed to be Maxwellian, this being the basis for the theory discussed in Part I, Sec. D. In both cases the angular distribution of the neutrons emitted from a surface element is assumed to be proportional to $(\cos\vartheta+\sqrt{3}\cos^2\vartheta)$ as predicted by Fermi.[3] With this law the angular distribution of the neutron flux at the detector would be proportional to $(1+\sqrt{3}\cos\vartheta)$ if the emitting surface were infinite and the flux density uniform. Under the conditions of the experiment some deviations from this angular distribution are expected for neutrons arriving at very oblique angles, which originate near the edge of the surface of the moderator where the neutron flux is lower. These deviations, which will at most result in an increase of the transmission by 6 percent, will, however, be neglected in the treatment.

In order to facilitate the interpretation of the transmission values, tables are given in the appendix for the transmission through $1/v$ absorbers of monoenergetic and Maxwellian neutrons. In the case of the Maxwellian spectrum the transmission is given in terms of the parameter $x=(T_a/T_n)^{\frac{1}{2}}$, where $T_a$ is the characteristic temperature of the absorber as defined above and $T_n$ the neutron temperature. Using these tables, one can interpret a transmission measurement in terms of an effective neutron temperature. For the interpretation of the transmission data through the cadmium absorber, the complicated true energy dependence of the cadmium-absorption cross section was approximated with a constant cross section of 2300 barns below a certain cutoff velocity and a zero cross section above this velocity. In interpreting data for the epicadmium period the cutoff velocity chosen is $9.7\times10^5$ cm/sec, for which the transmission is 50 percent. In the transition period, where the transmission is low, a lower value $7.5\times10^5$ cm/sec is used. The measured cadmium transmission values can also be transformed to effective neutron temperatures.

[12] E. Blomsjö and G. F. Von Dardel, Appl. Sci. Research **B4**, 1 (1954).
[13] von Dardel, Hellstrand, and Taylor, Appl. Sci. Research **B3**, 35 (1953).
[14] C. Eckart, Phys. Rev. **45**, 851 (1934).

A serious difficulty for the interpretation of the experimental results is the distortion of the velocity spectrum during the time of flight of the neutrons from the emitting surface to the detector. In order to minimize these effects, the volume of the detector was made as small as intensity requirements would allow and positioned as close to the emitting surface as possible. The center of the detector is about 1 cm from the moderator surface, and even over this small distance an appreciable time-of-flight distortion of the spectrum will occur during those time intervals when the emitted spectrum is changing rapidly. The effect is serious chiefly for hydrogenous substances. The flux from a light water moderator measured with the detector at various distances from the surface, the parameters being $(1/20)\times 11$ μsec in our notation, is given in Fig. 7, which shows that time-of-flight effects are appreciable only during the first 10–20 μsec of the slowing-down process. If the velocity spectrum is known it is possible to calculate the expected time-of-flight delay of the various parts of the spectrum, and the apparent transmission. The velocity distribution of neutrons emitted by a hydrogenous moderator has previously been studied by Rainwater and Havens[15] by the time-of-flight method. Whereas this method gives the average distribution over the whole neutron lifetime, the present measurements allow the changes in the velocity distribution during the lifetime to be studied.

### C. Measurements on Light Water

Due to the high proton scattering cross section and the large energy loss per collision, the slowing-down process in light water will be very rapid, and it is necessary to use the highest available resolution.

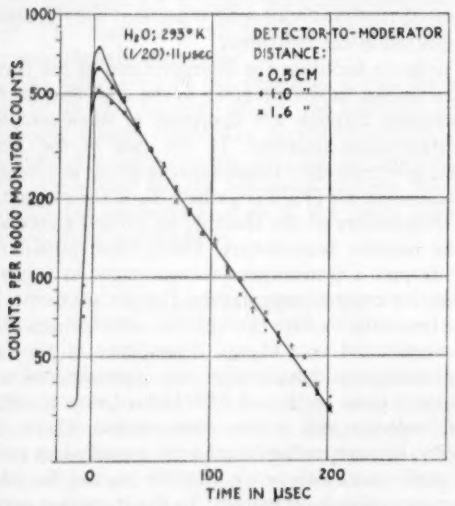


FIG. 7. Neutron flux from light water moderator at room temperature with the detector 0.5, 1.0, and 1.6 cm from the moderator surface.

[15] L. J. Rainwater and W. W. Havens, Jr., Phys. Rev. **70**, 136 (1946).

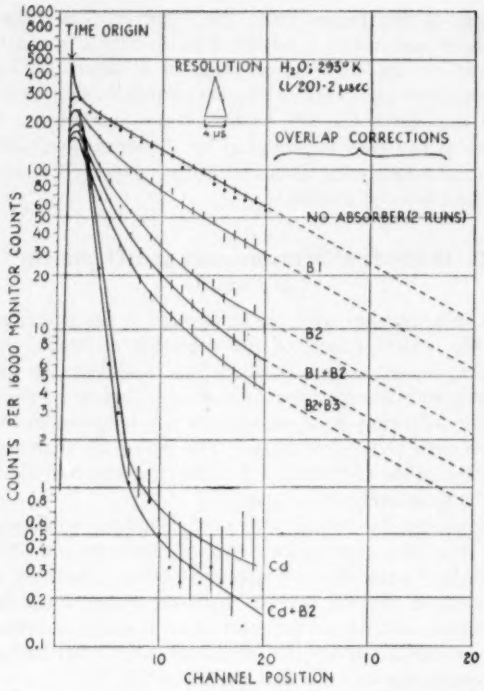


FIG. 8. Neutron flux from ordinary water with 20 g/liter boric acid

In Fig. 8 are reported the results of 2 μsec channel-width measurements of the neutron flux from the tank filled with water at room temperature, and in Fig. 9 the corresponding transmission curves. In order to avoid excessive overlap between periods, about 20 grams of boric acid per liter were dissolved in the water so that the period of the exponential decay was decreased from about 70 μsec to 23 μsec. Measurements could then be repeated with 40 μsec intervals.

When the neutron energy is high and absorption negligible, the transmission is near unity for all curves. During the slowing down process the transmission decreases with neutron energy, and finally approaches a constant value when the neutrons have become thermal.

For the initial, epicadmium, part of the process the experimental curves of Fig. 9 for the cadmium absorber and the boron absorber *B2* should be compared with the theoretical curves I and III, respectively, which are calculated for the velocity distribution given by Eq. (6). The agreement is not very good, mainly due to the time-of-flight distortion of the spectrum. In curves II and IV this effect has been taken into account, and we obtain satisfactory agreement with the initial part of the experimental curves.

During the transition period to thermal equilibrium the neutron energy is too low to excite the vibrations

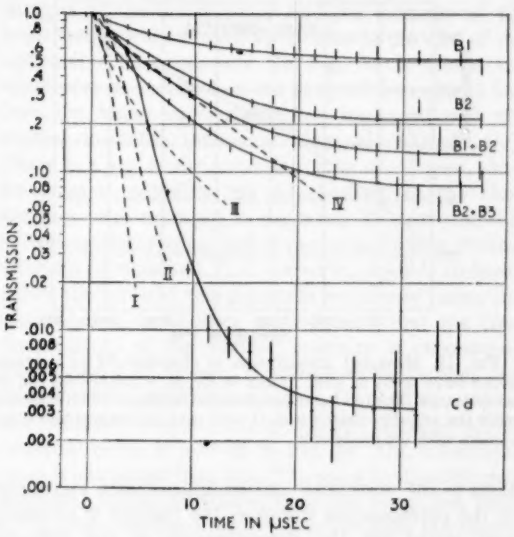


FIG. 9. Transmission of neutrons slowing down in ordinary water with 20 g/liter boric acid. Full curves: experimental transmission through the boron absorbers of Table II and through 0.438 g/cm² cadmium. Broken curves: Calculated transmission through cadmium and through absorber *B2*, neglecting time-of-flight distortion (I and III) and taking time of flight into account (II and IV).

within the water molecule at 0.45, 0.46, and 0.20 ev[16] and the water molecules may therefore be regarded as rigid structures. The neutron will soon also lose ability to excite the hindered rotations of the water molecules with quantum energies of about 0.10 ev,[17] and the main energy transfer is then to the Debye waves in which the water molecules move as rigid units. Since, on the other hand, at room temperature the temperature of the liquid is not small compared to the Debye temperature, which is about 300°K,[17] we may expect the model of a monatomic gas of nuclei having the weight of the water molecules to be a fair approximation. As described in Sec. B, the transmission data of Fig. 9 for the various absorbers were transformed, by means of Table VIII, to the effective neutron temperature values shown in Fig. 10. Except for the thinnest $1/v$ absorber *B1*, the neutron temperature values obtained from measurements with different absorbers are scattered around a single curve, which indicates that the neutron velocity distribution is indeed Maxwellian within the admittedly large experimental uncertainty limits. The time dependence of the experimentally determined temperature variations has the same character as the predicted theoretical curve for a monatomic gas of nuclei of mass 18. The discrepancy is adequately accounted for by the effect of the experimental resolution, time-of-flight effects, and the fact that for water molecules Eq. (15) predicts an initial slowing-down process which is too fast.

The failure of the data for the thin absorber *B1* to conform to the rest of the data would indicate that the true spectrum contains less slow neutrons than a Maxwellian distribution. As is shown by other measurements, this abnormal behavior of the thin absorber data persists even after the neutrons have become thermal. Since thermal neutrons should certainly have a Maxwellian distribution, we attribute the anomaly to some systematic errors in the method to which the thin absorber data would be particularly sensitive, such as departures from the angular distribution $(1+\sqrt{3}\cos\vartheta)$ and errors in the composition of the absorber.

A number of measurements were also made on the effect of temperature on the slowing-down process. Figure 11 shows the transmission through the $1/v$ absorber *B2* of the neutron flux from an ice moderator kept at 98°K and 273°K and from water heated to 354°K. We expect the temperature of the moderator not to influence the initial slowing-down process appreciably when the energy of the neutrons is large compared to thermal energies. The curves for 98°K and 273°K coincide indeed during the initial part, and the failure of that for 354°K to do so can be attributed to an observed erratic behavior of the monitoring chamber at this temperature. We correct for this monitoring error by shifting the curve so that the initial part coincides with the 98°K and 273°K curve (broken

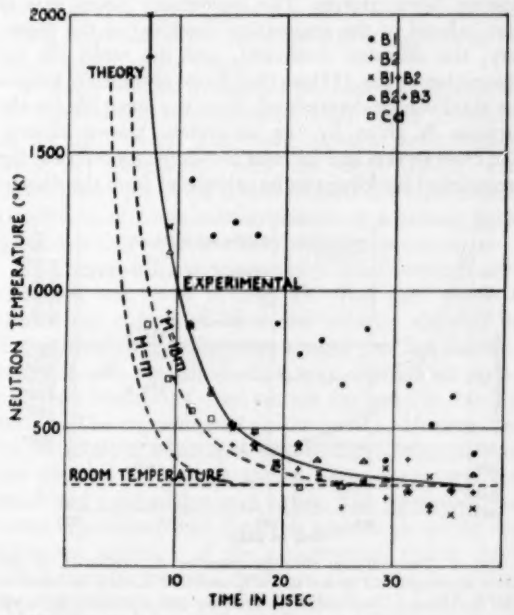


FIG. 10. Effective neutron temperature. Broken curves: theoretical [Eq. (15)]. Full curve drawn through points, calculated from the transmission measurements of Fig. 9.

[16] G. Herzberg, *Infrared and Raman Spectra of Polyatomic Molecules* (D. Van Nostrand Company, Inc., New York, 1947).
[17] N. Bjerrum, Kgl. Danske Videnskab Selskab, Mat.-fys. Medd. **27**, 1 (1951).

curve $C'$). The curves $A$, $B$, and $C'$ should be compared with the theoretical curves $D$, $E$, and $F$, calculated from Eq. (15). For the higher temperatures the resolution is not high enough to resolve the approach to the asymptotic value, but the data are consistent with the conclusion from Fig. 9, that the slowing-down process at room temperature proceeds as if the moderator were a monatomic gas of nuclei of mass 18. The experimental results for 98°K, however, indicate an approach which is substantially slower than what would be predicted for a monatomic gas. This is a strong indication that the model of a monatomic gas is a poor approximation to actual conditions for temperatures which are low compared to the Debye temperature.

The asymptotic transmission values approached after the conclusion of the slowing-down process are in close agreement with the values expected for thermal neutrons in temperature equilibrium with the moderator, and having the angular distribution $(1+\sqrt{3}\cos\vartheta)$. A special investigation was made of the variation of the asymptotic transmission with the moderator temperature over the entire temperature range from 98°K to 354°K. The results are reproduced in Fig. 12 and compared with the curve expected for thermal neutrons in temperature equilibrium with the moderator. The agreement is essentially within the experimental errors.

Manley, Haworth, and Luebke[18] calculated the mean life for absorption $\theta$ from decay measurements. In the small geometries, used in the present measurements only the fundamental mode of the neutron distribution will be present, since the harmonics decay during the slowing down process. The logarithmic decay rate is then related to the geometrical buckling of the geometry, the diffusion coefficient, and the mean life for absorption by Eq. (17), so that if two of these are known the third can be determined. Since the mean life for absorption is given by the accurately known absorption cross section and (at least for simple geometries) the geometrical buckling can be calculated from the dimensions of the moderator and an approximate knowledge of the extrapolation distance, the method is probably best suited for the determination of the diffusion coefficient which is not easily determined directly by other methods. The experimental conditions of the present measurements were, however, not chosen with this application in mind, and neither the mean life for absorption nor the geometrical buckling of the moderating system is readily calculated. Only qualitative conclusions can therefore be drawn from the decay-rate data. The measured asymptotic decay rate due to leakage and absorption of neutrons increases markedly with moderator temperature in the range from 98°K to 354°K. Since the mean life for absorption is independent of the temperature of the neutrons and depends only slightly on the temperature of the moderator, the leakage term $H_0^2D$ in Eq. (17) must be responsible for this increase. An attempt was made to estimate the magnitude of the diffusion coefficient at room temperature from the measured decay rate, using rough estimates of the mean life for absorption and geometrical buckling of the moderating geometries. The value obtained was larger by almost a factor of two than the value derived from the diffusion length[19] and the mean life for absorption,[20] but in view of the uncertainty of the estimates this discrepancy may not be significant.

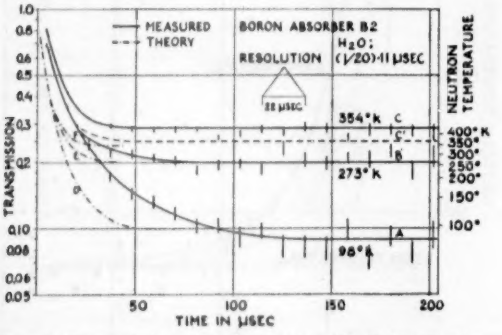


FIG. 11 Transmission through absorber $B2$, Table II, of neutrons slowing down in ice of 98°K and 273°K, and in water of 354°K. Curve $C'$ is the 354° K measurement corrected for a suspected normalization error. Curves $D$, $E$, and $F$ are calculated by Eq. (15).

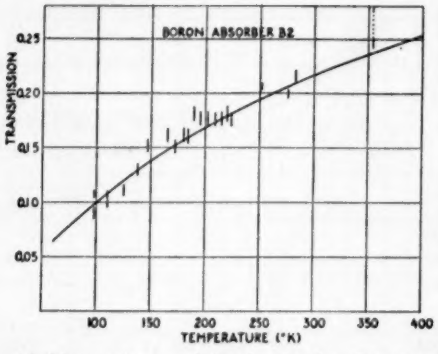


FIG. 12. Measured transmission in absorber $B2$ of neutrons which have spent at least 72 μsec in ice, as a function of the ice temperature. The full curve is calculated for Maxwellian neutrons with the angular distribution $(1+\sqrt{3}\cdot\cos)$ in temperature equilibrium with the moderator.

*Note added in proof.*—In later more accurate measurements good agreement was found with the expected value for the diffusion correction.

### D. Measurements on Heavy Water at Room Temperature

Measurements were made on a quantity of 6.2 liters of heavy water, 99.7 percent pure, in a cubical aluminum vessel with a central cavity. In this small volume only a small fraction of the neutrons will reach low

[18] Manley, Haworth, and Luebke, Phys. Rev. **61**, 152 (1941).

[19] E. Fermi, Atomic Energy Commission Report AECD-2664 (unpublished).

[20] G. F. von Dardel and A. W. Waltner, Phys. Rev. **91**, 1284 (1953).

energies in the heavy water and the intensity of the neutron flux will be much lower than in the case of the light-water measurements. In Fig. 13 is shown the result of measurements on the decay of the neutron flux from the heavy-water moderator, measured with the highest available resolution (channel-width 2 μsec). There is a gap in the curve for times 25–65 μsec, since for greater reliability the 40 channels of the time analyzer were arranged to duplicate 20 time intervals in the most interesting part of the cycle, leaving 20 time intervals unmeasured. It is, however, possible to interpolate the curve in this gap quite accurately, using the fact obtained in another measurement that the continued decay of the neutron intensity is exponential with a period of 84 μsec. A smooth curve through the experimental points is corrected for overlap, whose determination is shown in Fig. 13, and the slope of the corrected curve is plotted in Fig. 14. The theoretical curve is calculated from Eq. (17), using for the diffusion coefficient values calculated from the mean free path and average neutron velocity, obtained from the theory for slowing down by free nuclei at rest. The two curves agree surprisingly well over the initial part of the slowing-down process, where the theory for free nuclei at rest is expected to describe the process well. In the subsequent process the experimental curve approaches a value due to absorption and leakage of thermal neutrons, whereas the theoretical decay constant goes towards a very small value due to absorption alone.

An attempt was made to determine the diffusion coefficient for thermal neutrons in heavy water by a measurement of the asymptotic decay rate. The cavity in the container was filled with heavy water in order to make the moderating geometry more regular, and the target was positioned outside the container, so as not to influence the decay of the neutron distribution in

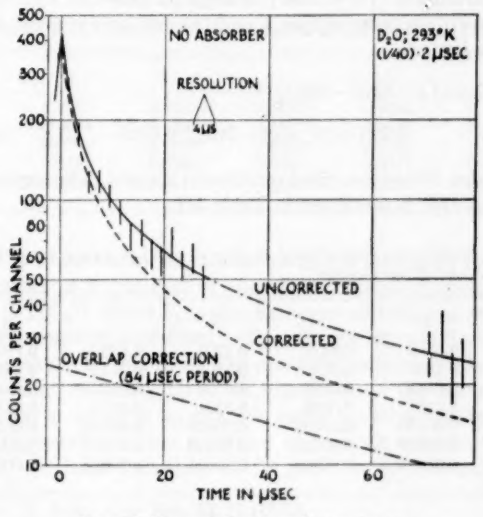


FIG. 13. Neutron flux from heavy water.

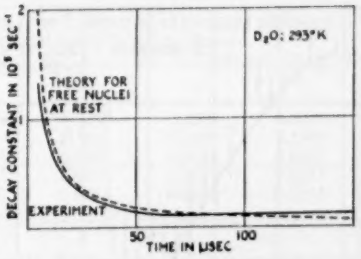


FIG. 14. Theoretical and experimental decay rate of the flux from the heavy water moderator.

the heavy water. The measured decay rate, 10 300±150 $sec^{-1}$, corrected for an estimated absorption rate of 90 $sec^{-1}$, and combined with the geometrical buckling, calculated for the volume of the heavy water extended by the extrapolation length of Auger, Munn, and Pontecorvo,[21] yields for the diffusion coefficient of thermal neutrons in 99.7 percent heavy water the value $1.52 \cdot 10^5$ $cm^2/sec$. If we combine this value with Auger's *et al.*[21] value for the transport mean free path we find a mean neutron velocity of about 2000 m/sec, corresponding to a neutron temperature about 100°K below room temperature. This estimate is rather uncertain since the transport mean free path is energy dependent and the value which relates the diffusion coefficient to the mean neutron velocity may not be the same as the value which results from the measurements of Auger *et al.* The theoretical arguments of Sec. E, Part I, predict that the equilibrium neutron temperature should be about 50°K below the moderator temperature which at least is of the same order of magnitude as the rough experimental value.

It is also possible to measure the neutron temperature by transmission measurements with boron absorbers, as for light water. The result of such measurements while not inconsistent with the above results, were inconclusive due to the presence under the experimental conditions of these measurements of a strong background, which made the interpretation uncertain.

The result of other transmission measurements with cadmium are given in Fig. 15. The solid curve is theoretical, calculated from the velocity distribution Eq. (6) for the slowing down against free deuterons at rest and with the schematic energy dependence of the cadmium absorption cross section discussed in Part II, Sec. B. The experimental points have to be corrected for the effect of resolution, time-of-flight delay, and for the effect of the oxygen atoms. These corrections are small and compensate each other. The agreement between experiment and theory is essentially within the statistical accuracy of the experimental points, indicating that the neutron spectrum above 0.4 ev and its time dependence are not appreciably influenced by the thermal motion and chemical bonds.

[21] Auger, Munn, and Pontecorvo, Can. J. Research **A25**, 143 (1947).

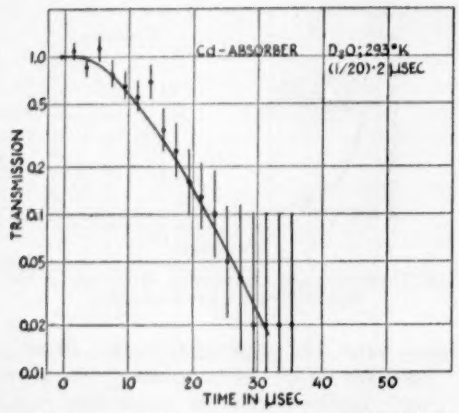


FIG. 15. Transmission through cadmium as a function of time for neutrons slowing down in heavy water. Experimental points normalized to unity for first point. Theoretical curve derived for free deuterons at rest.

## CONCLUSION

The pulsed neutron source technique used in the present investigation seems to be capable of giving interesting information concerning the slowing-down process for neutrons in a moderator. The present investigation has mainly been concerned with a rapid survey of the possibilities and limitations of this technique and the accuracy of the experimental results can undoubtedly be improved upon considerably. With a maximum resolution of 2 μsec, the slowing-down process from initial energies to the cadmium absorption limit will not be very well resolved, at least not for hydrogenous materials, and the results will further be invalidated by time-of-flight distortion of the spectrum. For improved measurements designed to study this phase of the slowing-down process, the time scale for the process can be increased by dilution of the moderating substance with a nonmoderating substance and the time-of-flight effects reduced by the use of a thin neutron detector, e.g., of the type described by Alburger.[22] It would, however, appear that more refined measurements in the energy range above the cadmium absorption limit have little of interest to offer for the understanding of the slowing-down process since in this energy range, where the thermal motion and chemical bonds have little effect, the theory is fairly complete. Below the cadmium absorption limit, on the contrary, the complications introduced by the chemical bonds and the thermal motion make a satisfactory theoretical treatment exceedingly difficult, and an experimental study of the slowing-down process in this range by the present method is of considerable interest. A comparison of the slowing-down processes in different hydrogenous substances, as for example the various types of hydrocarbons, may contribute to the understanding of the effect of the chemical bond. Other substances of interest would be crystalline materials of well-defined structure, e.g., beryllium, for which Kleinman[4] has calculated the necessary data to predict theoretically the slowing-down process and approach to thermal equilibrium.

A sufficiently long time after the neutron burst, the neutron spectrum has reached a well-defined equilibrium state which can be studied by transmission measurements. The temperature of these neutrons will depend somewhat on the size of the moderator, but for reasonably large amounts of material the neutron temperature is very close to the moderator temperature and the neutrons are thus thermal neutrons in the true sense of the word.

The diffusion coefficient of these thermal neutrons in the moderator can be determined from the decay rate of the neutron intensity as shown in this investigation, and thermal neutron absorption cross sections can be determined for strong absorbers either by transmission measurements in bad geometry, or by mixing the absorber intimately with the moderator and measuring the increase in decay rate.

The author wishes to thank Dr. G. Placzek for stimulating advice and Dr. S. Eklund for active support.

## APPENDIX

The transmission of neutrons with the angular distribution $(1+\sqrt{3}\cos\vartheta)$ through an absorber with the absorption cross section $\Sigma$ cm$^2$ per cm$^2$ area is given by the formula

$$T(\Sigma)=[1-(2\sqrt{3}-3)\Sigma]e^{-\Sigma} - \mathrm{Ei}(-\Sigma)[-(4-2\sqrt{3})\Sigma+(2\sqrt{3}-3)\Sigma^2], \quad (18)$$

where $\mathrm{Ei}(-x)$ is the logarithmic integral. The expression (18) is tabulated in Table III.

TABLE III. Transmission of monoenergetic neutrons having an angular distribution proportional to $(1+\sqrt{3}\cos\vartheta)$ as a function of the macroscopic cross section $\Sigma$ cm$^2$/cm$^3$ of the absorber.

| $\Sigma$ | 0 | 1 | 2 | 3 | 4 | 5 | 6 | 7 | 8 | 9 |
|---|---|---|---|---|---|---|---|---|---|---|
| 0.0 | 1.0000 | 0.9640 | 0.9358 | 0.9106 | 0.8875 | 0.8659 | 0.8456 | 0.8263 | 0.8080 | 0.7904 |
| 0. | 1.0000 | 0.7736 | 0.6344 | 0.5299 | 0.4475 | 0.3807 | 0.3258 | 0.2800 | 0.2416 | 0.2091 |
| 1. | 0.1814 | 0.1577 | 0.1375 | 0.1200 | 0.1049 | 0.0918 | 0.0805 | 0.0707 | 0.0621 | 0.0546 |
| 2. | 0.0481 | 0.0424 | 0.0374 | 0.0330 | 0.0291 | 0.0257 | 0.0228 | 0.0201 | 0.0178 | 0.0158 |
| 3. | 0.0140 | 0.0124 | 0.0110 | 0.00977 | 0.00867 | 0.00770 | 0.00684 | 0.00608 | 0.00540 | 0.00481 |
| 4. | 0.00427 | 0.00381 | 0.00336 | 0.00302 | 0.00269 | 0.00239 | 0.00214 | 0.00190 | 0.00169 | 0.00151 |
| 5. | 0.00135 | 0.00120 | 0.00108 | 0.00096 | 0.00086 | 0.00076 | 0.00068 | 0.00061 | 0.00055 | 0.00049 |

[22] D. E. Alburger, Rev. Sci. Instr. **23**, 769 (1952).

TABLE IV. Transmission of thermal neutrons through a $1/v$ absorber. Case I: Detector of constant efficiency. Isotropic angular distribution. The values for $x \geqslant 3.3$ were determined by extrapolation.

| $x$ | 0 | 1 | 2 | 3 | 4 | 5 | 6 | 7 | 8 | 9 |
|---|---|---|---|---|---|---|---|---|---|---|
| 0. | 1.0000 | 0.8527 | 0.7395 | 0.6476 | 0.5711 | 0.5064 | 0.4509 | 0.4031 | 0.3615 | 0.3251 |
| 1. | 0.2931 | 0.2649 | 0.2399 | 0.2176 | 0.1978 | 0.1800 | 0.1641 | 0.1499 | 0.1370 | 0.1254 |
| 2. | 0.1149 | 0.1054 | 0.0968 | 0.0890 | 0.0819 | 0.0754 | 0.0695 | 0.0641 | 0.0592 | 0.0547 |
| 3. | 0.0506 | 0.0469 | 0.0435 | 0.0400 | 0.0370 | 0.0343 | 0.0318 | 0.0297 | 0.0277 | 0.0257 |
| 4. | 0.0239 | 0.0222 | 0.0206 | 0.0192 | 0.0179 | 0.0167 | 0.0156 | 0.0145 | 0.0135 | 0.0126 |

TABLE V. Transmission of thermal neutrons through a $1/v$ absorber. Case II: $1/v$ detector. Perpendicular incidence. The values for $x \geqslant 4.0$ were determined by extrapolation.

| $x$ | 0 | 1 | 2 | 3 | 4 | 5 | 6 | 7 | 8 | 9 |
|---|---|---|---|---|---|---|---|---|---|---|
| 0. | 1.0000 | 0.8959 | 0.8063 | 0.7281 | 0.6596 | 0.5992 | 0.5450 | 0.4969 | 0.4538 | 0.4151 |
| 1. | 0.3802 | 0.3488 | 0.3204 | 0.2946 | 0.2711 | 0.2498 | 0.2304 | 0.2128 | 0.1965 | 0.1817 |
| 2. | 0.1682 | 0.1558 | 0.1444 | 0.1340 | 0.1243 | 0.1154 | 0.1073 | 0.0985 | 0.0929 | 0.0862 |
| 3. | 0.0804 | 0.0751 | 0.0697 | 0.0651 | 0.0603 | 0.0567 | 0.0529 | 0.0491 | 0.0461 | 0.0431 |
| 4. | 0.0403 | 0.0375 | 0.0352 | 0.0330 | 0.0310 | 0.0290 | 0.0272 | 0.0256 | 0.0240 | 0.0225 |

TABLE VI. Transmission of thermal neutrons through a $1/v$ absorber. Case III: Detector of constant efficiency. Perpendicular incidence. The values for $x \geqslant 3.9$ were determined by extrapolation.

| $x$ | 0 | 1 | 2 | 3 | 4 | 5 | 6 | 7 | 8 | 9 |
|---|---|---|---|---|---|---|---|---|---|---|
| 0. | 1.0000 | 0.9161 | 0.8408 | 0.7729 | 0.7114 | 0.6557 | 0.6051 | 0.5591 | 0.5168 | 0.4784 |
| 1. | 0.4432 | 0.4109 | 0.3813 | 0.3540 | 0.3290 | 0.3058 | 0.2847 | 0.2650 | 0.2469 | 0.2301 |
| 2. | 0.2146 | 0.2003 | 0.1870 | 0.1747 | 0.1633 | 0.1527 | 0.1428 | 0.1336 | 0.1251 | 0.1171 |
| 3. | 0.1097 | 0.1029 | 0.0965 | 0.0905 | 0.0849 | 0.0796 | 0.0747 | 0.0700 | 0.0656 | 0.0621 |
| 4. | 0.0585 | 0.0550 | 0.0518 | 0.0485 | 0.0455 | 0.0429 | 0.0403 | 0.0380 | 0.0357 | 0.0337 |

TABLE VII. Transmission of thermal neutrons through a $1/v$ absorber. Case IV: Detector of constant efficiency. Angular distribution $(1+\sqrt{3}\cos\vartheta)$. The values for $x \geqslant 3.9$ were determined by extrapolation.

| $x$ | 0 | 1 | 2 | 3 | 4 | 5 | 6 | 7 | 8 | 9 |
|---|---|---|---|---|---|---|---|---|---|---|
| 0. | 1.0000 | 0.8671 | 0.7608 | 0.6724 | 0.5974 | 0.5299 | 0.4775 | 0.4285 | 0.3866 | 0.3491 |
| 1. | 0.3160 | 0.2866 | 0.2604 | 0.2370 | 0.2159 | 0.1972 | 0.1802 | 0.1649 | 0.1511 | 0.1386 |
| 2. | 0.1269 | 0.1170 | 0.1076 | 0.0991 | 0.0914 | 0.0843 | 0.0778 | 0.0719 | 0.0665 | 0.0615 |
| 3. | 0.0569 | 0.0528 | 0.0490 | 0.0455 | 0.0420 | 0.0393 | 0.0364 | 0.0337 | 0.0315 | 0.0294 |
| 4. | 0.0275 | 0.0257 | 0.0240 | 0.0223 | 0.0209 | 0.0195 | 0.0183 | 0.0171 | 0.0159 | 0.0149 |

TABLE VIII. Transmission of thermal neutrons through a $1/v$ absorber. Case V: $1/v$ detector. Angular distribution: $(1+\sqrt{3}\cos\vartheta)$.

| $x$ | 0 | 1 | 2 | 3 | 4 | 5 | 6 | 7 | 8 | 9 |
|---|---|---|---|---|---|---|---|---|---|---|
| 0. | 1.0000 | 0.7652 | 0.6282 | 0.5284 | 0.4508 | 0.3886 | 0.3376 | 0.2952 | 0.2595 | 0.2292 |
| 1. | 0.2031 | 0.1807 | 0.1612 | 0.1442 | 0.1294 | 0.1163 | 0.1048 | 0.0946 | 0.0856 | 0.0774 |
| 2. | 0.0703 | 0.0639 | 0.0581 | 0.0530 | 0.0483 | 0.0441 | 0.0403 | 0.0369 | 0.0338 | 0.0310 |
| 3. | 0.0285 | 0.0261 | 0.0240 | 0.0221 | 0.0204 | 0.0188 | 0.0173 | 0.0160 | 0.0148 | 0.0136 |
| 4. | 0.0126 | 0.0117 | 0.0108 | 0.0100 | 0.0093 | 0.0086 | 0.0080 | 0.0074 | 0.0069 | 0.0064 |

The transmission of thermal neutrons through a $1/v$ absorber is a function of the dimensionless quantity $x=(T_a/T_n)^{\frac{1}{2}}$, where $T_a$ is the characteristic temperature of the absorber as defined in Part II, Sec. B, and $T_n$ is the neutron temperature. The problem has been studied by Zahn[23] who has given an expansion of the transmission in terms of $x$, which is useful up to $x=1$, and by Laporte[24] who has given an asymptotic expansion valid for large values of $x$. In order to fill the gap between these two expressions, the author has extended the use of Zahn's power series, which converges for all values of $x$, to about $x=4$ by including more terms and recalculating the coefficients with higher accuracy. Laporte's results are then used for extrapolating to larger values of $x$. The results of the calculations for the 5 cases discussed by Zahn are given in Tables IV–VIII. For the highest values of $x$ the results may be in error by a few units in the last decimal.

[23] C. T. Zahn, Phys. Rev. **52**, 67 (1937).
[24] O. Laporte, Phys. Rev. **52**, 72 (1937).

# First-Forbidden Matrix Elements in β Decay*

R. W. KING, *National Research Council, Washington, D. C.*

AND

D. C. PEASLEE, *Columbia University, New York, New York*

(Received December 14, 1953)

An assumed form for the linear combination in $\beta$ decay ($S-T+\lambda_P P$), is used as a tool to explore the features of nuclear structure revealed by first-forbidden matrix elements. The assumptions made are sufficient to account for the observed fact that most first-forbidden transitions have log$ft$ values centering around 6.5, 7.5, and 8.5, according as $\Delta I=0$, 1, or 2. The squared matrix elements are reduced by an order of magnitude (i) when configuration mixing occurs, as in the usual, "unfavored" transitions, in contrast to the "favored" transitions around $A=208$; (ii) when the single-particle spin change $\Delta j$ predicted by the shell model exceeds the nuclear spin change $\Delta I$. From (i) and (ii) it is concluded that the elementary form of the shell model specifies individual particle orbitals with good accuracy but that configuration mixing is also of major importance, although it is not encompassed by the simple shell model. The $2^-\rightarrow 2^+$ transitions can be classified under (ii); their apparently straight spectra should average on the order of 10 percent $\alpha$ type. The only consistent interpretation of the RaE decay is as a $1^-\rightarrow 0^+$ transition; it is possible to predict that this kind of spectrum is unlikely to occur at any other mass number $A$. Evidence for the presence of the pseudoscalar interaction $P$ in the linear combination is then provided by the low $ft$ values of $\Delta I=0$ transitions.

## 1. INTRODUCTION AND SUMMARY

IF the linear combination of interactions in $\beta$ decay is known, we can use it as a tool in surveying observed $ft$ values to obtain information about the nuclear matrix elements. The present study analyzes first-forbidden transitions in this way. The linear combination ($S-T+\lambda_P P$) is assumed for this purpose. Included in the formulation are parameters to allow for the effect of pseudoscalar-coupled nuclear forces.

The nuclear matrix elements with correct statistical factors are most readily computed for single-particle transitions in the $j-j$ shell model. Failure of the extreme one-particle model is represented by introducing a factor of reduction in the matrix element to account for configuration mixing. For "favored" first-forbidden transitions near the closed shells at $A=208$, the squared nuclear matrix elements are an order of magnitude larger than for the "unfavored" transitions throughout the rest of the periodic table. For comparable unfavored transitions the reduction factors are the same for even-$A$ and odd-$A$ nuclei.

The distinction between "favored" and "unfavored" transitions is, as in the allowed case, qualitative and empirical. It signifies a difference of degree rather than of kind. The favored transitions are those with exceptionally low $ft$ values or hence good overlap of the nuclear wave functions; presumably this implies little mixing of configurations. For the unfavored transitions the configuration mixing is considerable; nevertheless, the individual orbitals in the configuration are specified with about 90 percent accuracy by the shell model. This conclusion results from the analysis of $2^-\rightarrow 2^+$ transitions.

* Work partly supported by the research program of the U. S. Atomic Energy Commission.

These conclusions about $\beta$-decay matrix elements illustrate both the virtues and limitations of the simple shell model. On the one hand, the shell model specification of individual orbitals is accurate to a high degree; on the other hand, an important role is played by the mixing of configurations, about which the elementary shell model has nothing to say.

A survey of the unfavored transitions shows that the log$ft$ values group around 6.5, 7.5, and 8.5 for $\Delta I=0$, 1 and 2, respectively (the $ft$ value is corrected for the unique spectrum shape when $\Delta I=2$). This difference is ascribed to several factors: the $\Delta I=0, 1$ transitions contain factors of $(\alpha Z/2R)^2$, which make them faster than the $\Delta I=2$ transitions. The difference between $\Delta I=0$ and $\Delta I=1$ arises from partial cancellation of these large factors for $\Delta I=1$, and the presence of a substantial contribution from the pseudoscalar terms for $\Delta I=0$. Both of these effects require the presence of pseudoscalar-coupled forces in the nucleus, and the $\Delta I=0$ enhancement implies the presence of $P$ in the linear combination. The various nuclear parameters obtained in this way have values consistent with those obtained from analysis of second forbidden spectral shapes.

The $2^-\rightarrow 2^+$ transitions to the first excited states of even-even nuclei are surveyed as a special class. Correlation is found between the matrix element for this transition and that of the corresponding $2^-\rightarrow 0^+$ ground-state transition in a given nucleus. Although these are $\Delta I=0$ transitions, their average log$ft$ value is around 7.5, suggesting that the shell model specification of individual orbitals is 90 percent valid. These $2^-\rightarrow 2^+$ spectra should contain an average of about 10 percent $\alpha$-type spectrum and might show deviations from allowed shape under careful observation.

The "favored" first-forbidden transitions show a

quite uniform value of the radial matrix element (squared) about 10 times larger than the average of the unfavored transitions. The information obtained about matrix elements can be summarized as follows, with $\Delta I$ the spin change of the whole nucleus, $\Delta j$ the single-particle change indicated by the shell model:

(i) for any region in the periodic table the matrix elements for transitions with $\Delta I=\Delta j$ are the same order of magnitude for $\Delta I=0, 1, 2$;
(ii) the matrix elements (squared) for $\Delta I<\Delta j$ are an order of magnitude smaller than those with $\Delta I=\Delta j$ in this same region;
(iii) the matrix elements (squared) are an order of magnitude smaller for "unfavored" than for "favored" transitions.

The only interpretation of the RaE spectrum consistent with this analysis requires the ground-state spin of RaE to be $I=1^-$. The peculiar shape then appears to result from a confluence of favorable conditions not likely to be repeated for any other value of $A$.

This interpretation of RaE would remove the direct evidence for the pseudoscalar interaction $P$ in the linear combination in $\beta$ decay. Statistically sounder indirect evidence for $P$ is provided, however, by the low $ft$ values for $\Delta I=0$ transitions.

## 2. FIRST-FORBIDDEN $ft$ FORMULAS

First-forbidden $\beta$ transitions involve a change of nuclear parity and $\Delta I=0, 1, 2$. The $\Delta I=2$ transitions have a unique ($\alpha$-type) shape and have markedly larger $ft$ values than the other first forbidden transitions. The $\Delta I=0, 1$ transitions all have allowed shapes with perhaps a few exceptions like RaE. An allowed shape for $\Delta I=0, 1$ (yes) indicates the dominance of a few selected terms[1,2] in the spectrum shape formula. By retaining only these dominant terms, we can write a simple expression for the $ft_1$ values of first-forbidden transitions. This approximation should be as valid for fitting the absolute $ft_1$ values as for fitting the apparently allowed shapes; and since we compare only log$ft$ values, any errors in the approximation should be of no consequence. Taking the linear combination for $\beta^-$ decay to be $(S-T+\lambda_P P)$,[2] we have:

$$(ft_1)^{-1}=\lambda_0\left\{|B_{ij}|^2(f_1/f)+\left(\frac{\alpha Z}{2R}\right)^2\left|\int \mathbf{r}\right|^2 \times[(\Lambda-\Delta_1')t+\Delta_1]^2+\left(\frac{\alpha Z}{2R}\right)^2\left|\int \boldsymbol{\sigma}\cdot\mathbf{r}\right|^2\Delta_0^2\right\}. \quad (1)$$

The nuclear matrix elements $B_{ij}$, $\int \mathbf{r}$, $\int \boldsymbol{\sigma}\cdot\mathbf{r}$ have the usual definitions;[3] they involve a change of nuclear parity and the removal of a total angular momentum $J=2$, 1, and 0, respectively, by the light particles. The quantity $|B_{ij}|^2(f_1/f)$ is considerably smaller than the other terms in Eq. (1); we therefore neglect it except when it is the only nonvanishing term ($\Delta I=2$, yes). The factor $(f_1/f)$ accounts for the unique spectrum shape associated with $B_{ij}$.

The factors $(\alpha Z/2R)^2$ in Eq. (1) are characteristic of the dominant terms (in low-$Z$ approximation) that cause the first-forbidden transitions to have allowed shapes. The remaining factors arise from expressing certain nuclear matrix elements in terms of others with identical selection rules: e.g., $\int \beta\boldsymbol{\alpha}$ and $\int \boldsymbol{\sigma}\times\mathbf{r}$ in terms of $\int \mathbf{r}$, and $\int \beta\gamma_5$ in terms of $\int \boldsymbol{\sigma}\cdot\mathbf{r}$. They therefore depend on the linear combination of interactions responsible for $\beta$ decay. Using the notation and results of reference 2 and Appendix I below, we have:

$$\begin{aligned}\Lambda&=\chi/B,\\ \Delta_1&=\Lambda\delta_1-1,\\ \Delta_1'&=\Lambda\delta_1'-1,\\ \Delta_0&=\lambda_P\Lambda\delta_0-1.\end{aligned} \quad (2)$$

It is expected[4] that $\Lambda\approx 1-2$ with some fluctuation from one nucleus to the next. The $\delta$ are factors to account for the influence of pseudoscalar-coupled nuclear forces on the nuclear matrix elements. These quantities are difficult to estimate, and we cannot even be sure that they are the same for both matrix elements; hence the distinction of $\delta_1$ and $\delta_0$. The meager empirical evidence from second-forbidden spectrum shapes suggests $\Lambda\delta\sim 1$ to 2. The quantity $t$ in Eq. (1) is defined as $t=(1/\hbar)\times[(\boldsymbol{\sigma}\cdot\mathbf{L})_f-(\boldsymbol{\sigma}\cdot\mathbf{L})_i]$. The choice of $(S-T+\lambda_P P)$ for mirror-image transitions leads to a decay constant of $\log(\lambda_0^{-1})=3.7$.

It is not possible to say anything about the ratios of nuclear matrix elements with different selection rules ($B_{ij}$, $\int \mathbf{r}$, $\int \boldsymbol{\sigma}\cdot\mathbf{r}$) without having recourse to a specific nuclear model. We shall attempt to use the $j-j$ coupling shell model with some modification for the many-particle character of the wave function in medium and heavy nuclei. For the extreme odd-$A$ model of a single particle outside a spinless core, the angular and statistical factors of the nuclear matrix elements are evaluated explicitly in Appendix II. For the more general case we regard the initial and final nucleus wave functions as linear combinations of products of single-particle $j-j$ orbitals:

$$\begin{aligned}\Psi_I&=\sum a(I',i)\psi_{I'}\varphi^{(i)},\\ \Psi_F&=\sum a(F',f)\psi_{F'}\varphi^{(f)}.\end{aligned} \quad (3)$$

Here $\varphi^{(i)}$, $\varphi^{(f)}$ refer to the nucleon making the transition; even though the $\beta$-decay operator involves a sum over all nucleons in the nucleus, $O=\sum_j O_j$, the matrix element of $O$ can always be written as a sum of matrix

[1] H. M. Mahmoud and E. J. Konopinski, Phys. Rev. **88**, 1266 (1952).
[2] D. C. Peaslee, Phys. Rev. **91**, 1447 (1953).
[3] E. J. Konopinski and G. E. Uhlenbeck, Phys. Rev. **60**, 308 (1941).
[4] T. Ahrens and E. Feenberg, Phys. Rev. **86**, 64 (1952); D. L. Pursey, Phil. Mag. **42**, 1193 (1951).

elements like that generated by Eq. (3). In Eq. (3) the "core" wave functions are also expansible as sums of products:

$$\psi_{I'}=\sum a(i_1,\cdots i_{n-1})\varphi^{(i_1)}\cdots\varphi^{(i_{n-1})};$$
$$\psi_{F'}=\sum a(f_1,\cdots f_{n-1})\varphi^{(f_1)}\cdots\varphi^{(f_{n-1})}. \quad (3a)$$

This means that in general, with random phasing of the coefficients,

$$\int\psi_{F'}^{*}\psi_{I'}\leq 1, \quad (4)$$

even though the spins $F'$ and $I'$ are identical. For the case of a constant core spin $J'$ the matrix element $M_{IF}$ of an operator is related to the single-particle matrix element by:[5]

$$|M_{IF}(J)|^2=(2F+1)(2i+1)\times W^2(ifIF;JJ')|M_{if}(J)|^2, \quad (5)$$

where $J$ is the total angular momentum of the electron-neutrino field, and the coefficient $W$ represents[6] a sum over Clebsch-Gordan coefficients.

By arguments of this sort we can write the matrix element in the most general form:

$$|M_{IF}(J)|^2=|aM_{if}(J)+a'M_{i'f'}(J)+\cdots|^2. \quad (6)$$

The coefficients $a$ contain sums over many coefficients: with assumed random phasing, conditions like Eq. (4) obtain, so that we may generally expect $|a|^2\ll 1$. This corresponds to "unfavored" transitions. In order to make Eq. (6) tractable, we assume the $j-j$ shell model to be sufficiently good so that only one term is dominant on the right-hand side. The assignments of $i$ and $f$ in this dominant $M_{if}$ are just those indicated by the shell model. This procedure receives some justification from the analysis in Sec. 4; it is not identical with assuming a single-particle model, since $|a|^2$ can account for a number of equivalent particles in $i$ and $f$ orbits.[7]

In addition to "unfavored" first-forbidden transitions, there fortunately exist a few "favored" ones. Over a limited region near $A=208$, where both neutrons and protons form closed shells of opposite parity, we may expect one-particle wave functions to be a good approximation, so that $|a|^2$ approaches unity. Indeed, some log$ft$ values around 5.0 to 5.5 appear in this region for what must be parity change transitions. These $ft$ values are at least an order of magnitude smaller than the usual $ft$ for first-forbidden transitions,[8] presumably reflecting exceptionally large $|a|^2$ values.

### 3. "UNFAVORED" TRANSITIONS

Except in the region of closed shells, the mixture of configurations in Eq. (6) is expected to be considerable, with corresponding $|a|^2\ll 1$. These are the "unfavored" first-forbidden transitions. Because of the presumed high complexity of the wave functions involved, we cannot hope to compute accurate, detailed values of the coefficients. We therefore make a simple statistical survey to determine average matrix elements for these unfavored cases.

The survey comprises only transitions with $A<200$, in order to exclude the "favored" cases. Only cases where the decay scheme and the shell model permit fairly definite assignments have been included.[9] For $\Delta I=0$ and 1 this effectively limits the sample to odd-$A$ nuclei; for $\Delta I=2$, the unique shape and exceptionally large first-forbidden $ft$ are identifying features, so that both even- and odd-$A$ transitions are included. Table I gives the mean values of log$ft$ for $\Delta I=0$, 1 (yes) transitions, and the mean values of log$f_1t$ for the $\Delta I=2$ (yes) cases, where $f_1$ takes into account the special shape of these spectra. The errors given are the standard deviations of the mean values, computed by the usual statistical procedure; the figures in parentheses are the total number of transitions involved in each group. These transitions are catalogued in Table II.

Table I shows the remarkable feature[9,10] that the $\Delta I=0$, 1, and 2 transitions fall into well-defined groups with matrix elements separated by an order of magnitude.

We apply the values in Table I to extract information about the radial matrix elements. For this purpose write Eq. (1) in the form:

$$(ft_1)^{-1}=\lambda_0(\tfrac{1}{2}\alpha Z)^2\{(f_1/f)(1/B)^2S_2|J_2|^2+FS_1|J_1|^2[(\Lambda-\Delta_1')t+\Delta_1]^2+F|J_0|^2\Delta_0^2\}. \quad (7)$$

Here $B=(\alpha Z/2R)$ is the Coulomb barrier height in Mev, and $F$ is a correction to allow for the finite charge distribution in the nucleus,[11] which has an appreciable effect for heavy elements. The quantity $F$ is roughly the reduction factor in the $\beta$-spectrum coefficient[3] $M_0$, or the square of the reduction factor in the coefficient $N_0$. The value computed for $Z=83$ is $F\approx\frac{1}{2}$, with $F\to 1$ as $Z\to 0$. The quantity $|J|^2=|a|^2|\int r/R|^2$ is a radial matrix element. The factor $\int r/R$ is supposed to represent the average one-particle integral, while

TABLE I. First-forbidden log$ft$ values (unfavored).

| | $\Delta I=0$ | $\Delta I=1$ | $\Delta I=2$ |
|---|---|---|---|
| Odd $A$ | 6.5±0.4 (12) | 7.5±0.3 (13) | 8.4±0.4 (19) |
| Even $A$ | ...[a] | ... | 8.5±0.5 (17) |

[a] A certain exceptional class of even-$A$, $\Delta I=0$ transitions is excluded here and discussed separately in Sec. 4.

[5] H. Brysk, Phys. Rev. **90**, 365 (1953).
[6] G. Racah, Phys. Rev. **62**, 438 (1942).
[7] A more extensive discussion of this model is given by A. de-Shalit and M. Goldhaber, Phys. Rev. **92**, 1211 (1953). These authors have independently observed the existence of "favored" first-forbidden transitions.
[8] King, Dismuke, and Way, Oak Ridge National Laboratory Report ORNL-1450, 1952 (unpublished).
[9] R. W. King, thesis, Washington University, 1952 (unpublished).
[10] R. King and E. Feenberg, Phys. Rev. **87**, 218 (1952).
[11] M. E. Rose and D. K. Holms, Oak Ridge National Laboratory Report ORNL-1022 (unpublished) and Phys. Rev. **83**, 190 (1951).

$|a|^2$ accounts for the many-particle character of the wave function.

The statistical factors $S$ for one-particle transitions are given in Appendix II; their average values are:

$$S_2=\frac{4(j+j'+1)^2}{(j+j')(j+j'+2)}\approx 4, \quad \Delta j=2;$$
$$S_1=\frac{(2j'+1)}{2(j+j'+1)}\approx \tfrac{1}{2}, \quad \Delta j=1; \tag{8}$$
$$S_1=\frac{1}{(2j)(2j+2)}, \quad \Delta j=0.$$

The dispersions of the $S$ about their mean values will be small in comparison with the dispersions in Table I and are therefore neglected.

For the cases included in Table I, a survey shows that:

$$\langle \log F(\alpha Z/2)^2\rangle_{\text{Av}}=-1.5\pm 0.2, \quad \Delta I=0;$$
$$=-1.6\pm 0.2, \quad \Delta I=1; \tag{9}$$
$$\langle \log(\alpha Z/2B)^2\rangle_{\text{Av}}=-3.6\pm 0.1, \quad \Delta I=2,$$

where the errors are again the statistical standard deviations. The values for $\Delta I=2$ are to this precision identical for even and for odd $A$.

The quantity $t$ in (7) is $\pm(2j+1)$ for a $\Delta j=0$ transition. For a $\Delta j=1$ transition, the one-particle values of $t$ is $\pm 1$, although this may be modified by contributions from other configurations. The list of $\Delta j=1$ transitions shows no significant difference between $t=+1$ and $t=-1$ cases; but the sample is small and consists predominantly of $t=-1$ transitions.

Combining the values of Table I with (8)–(9), we obtain:

$$\log\{|J_1|^2[(\Lambda-\Delta_1')+\Delta_1]^2/(2j)(2j+2)+|J_0|^2\Delta_0^2\}$$
$$=-1.3\pm 0.5, \quad \Delta j=\Delta I=0;$$
$$\log\{|J_1|^2[(\Lambda-\Delta_1')t+\Delta_1]^2\} \tag{10}$$
$$=-1.9\pm 0.5, \quad \Delta j=\Delta I=1;$$
$$\log\{|J_2|^2\} \quad =-1.8\pm 0.5, \quad \Delta j=\Delta I=2.$$

If we assume the average $|J|^2$ to be all the same, (10) is consistent with:

$$|J|^2\approx 0.02,$$
$$\Lambda\approx 1\approx\Delta_1'\approx|\Delta_1|, \tag{11}$$
$$\Delta_0^2\approx 3.$$

These are only crude averages, possibly subject to appreciable fluctuations.

We conclude from this survey that $\Lambda\approx 1$ for these mixed configurations, as predicted by a statistical model.[4] Both correction factors $\Delta$ appear to be positive and of average order 1, which is consistent with the second-forbidden transitions.[2] The difference between $\log ft$ values for $\Delta I=0$ and $\Delta I=1$ transitions, although not outside statistical error, is interpreted as a real effect. It arises from the substantial contribution of the $\Delta_0^2$ terms, the statistical factor of $\frac{1}{2}$ in $S_1$, and the tendency for $\Lambda$ and $\Delta_1'$ to cancel. The tendency to cancellation suggests that $\Delta I=1$ transitions are more likely to show deviations from the allowed shape than $\Delta I=0$ transitions. It also explains why no difference is found between $t=+1$ and $t=-1$ for $\Delta I=\Delta j=1$ transitions.

### 4. THE $2^-\rightarrow 2^+$ TRANSITIONS

The even-$A$, $\Delta I=2$ transitions of Table I are generally to the ground states of even-even nuclei, coming from a $2^-$ ground state of an odd-odd nucleus. Since the first excited state of practically all these even-even nuclei is $2^+$, a number of these decay schemes also show a $2^-\rightarrow 2^+$ branch to the first excited state. These could have been included as even-$A$, $\Delta I=0$ transitions in Table I; but they appear to be exceptional and are therefore better discussed separately.

Thirteen cases of this type listed in Table II give the average result:

$$\log ft'=7.55\pm 0.47. \tag{12}$$

This is an order of magnitude larger than the usual $ft$ value for $\Delta I=0$, but is still an order of magnitude smaller than that for $\Delta I=2$. We may therefore neglect the $\Delta I=2$ matrix elements to a first approximation and write:

$$\log[|J_1'|^2S_1[(\Lambda-\Delta_1')t+\Delta_1]^2+|J_0'|^2\Delta_0^2]$$
$$=-2.2\pm 0.4. \tag{13}$$

It is not very clear what the value of the first term in (13) should be for this case; but taking both terms to be about the same order of magnitude, we have:

$$|J_1'|^2, \quad |J_0'|^2\approx 10^{-3}. \tag{14}$$

The $|J'|^2$ values in (14) are an order of magnitude smaller than the unfavored $|J|^2$ in (11). For all these cases, however, the orbitals indicated for the transition by the shell model have $\Delta j=\pm 2$. Hence if the shell model were strictly valid, we should have $|J_1'|^2=|J_0'|^2=0$. The order-of-magnitude reduction in $|J_1'|^2$ and $|J_0'|^2$ from their normal "unfavored" values suggests that the (squared) deviations from the shell model orbitals amount to about 10 percent. In spite of this, the $J_0'$, $J_1'$ matrix elements account for about 90 percent of the $\beta$-transition rate, so that the spectrum shape appears to a high degree allowed. Some of these transitions may by fluctuation have an especially large ratio of $|J_2'|^2$ to $|J_0'|^2$ and $|J_1'|^2$, in which case deviations of the spectrum from an allowed shape could be observed. A possibility of this type is $As^{76}$.

It is of interest to consider the correlation of the matrix elements $|J|^2$ and $|J'|^2$ for the respective transitions to the ground and first excited states of a given even-even nucleus. Define $x=\log ft'$, $y=\log f_1t$,

$z=\log(ft'/f_1t)$; then, for the thirteen cases considered:

$$\begin{aligned}\bar{x}&=7.55\pm0.47,\\ \bar{y}&=8.51\pm0.46,\\ \bar{z}&=-0.96\pm0.33.\end{aligned}\tag{15}$$

The figures given are the average and the standard deviation $\sigma$, found by summing the quantities $x$ and $(x-\bar{x})^2$, etc., over the distribution of thirteen cases in the usual statistical fashion. Defining the correlation coefficient $\rho$ of $x$ and $y$ by

$$\sigma_z^2=\sigma_x^2+\sigma_y^2-2\rho\sigma_x\sigma_y,\tag{16}$$

we have, from (15):

$$\rho=0.75.\tag{17}$$

This apparent high degree of correlation between $|J|^2$ and $|J'|^2$ for transitions to a given final nucleus leads us to write:

$$|a'|^2=|a|^2|b|^2,\quad |b|^2\approx0.1.\tag{18}$$

Here, $|a|^2$ is a reduction factor for configuration mixing when the individual orbitals in the transition are those allowed by the shell model, and $|b|^2$ is an additional reduction factor when the orbitals involved are not in accord with the shell model. The value (17) suggests that to a zero approximation $|a|^2$ and $|b|^2$ can be treated as independent. The value of $|b|^2$ in (18) suggests that the shell model specification of orbitals is about 90 percent valid. We therefore expect condition (18) to hold whenever the single-particle spin change $\Delta j$ exceeds the total nuclear spin change $\Delta I$.

## 5. "FAVORED" FIRST-FORBIDDEN TRANSITIONS

For the "favored" transitions around $A=208$ we try to extract an estimate of $|J|^2$ for comparison with the unfavored cases. The spin and parity assignments used for even-$A$ decay schemes in this region are discussed in Appendix IV. No $\alpha$-type spectra are considered, so the term in $|J_2|^2$ will be dropped from (7). We use the results of section three that the $\Delta I=\Delta j=0$ transitions have the lowest $ft_1$ values by an order of magnitude as a means of assigning quantum numbers in some transitions.

(i) $0^-\leftrightarrow0^+$ transitions. These include $Pb^{210}\rightarrow Bi^{210*}$ (RaD), $Pb^{212}\rightarrow Bi^{212*}$, and $Tl^{206}\rightarrow Pb^{206}$. The $\log ft_1$ values range from 5.2 to 5.4. Equation (7) becomes

$$(ft_1)^{-1}=\lambda_0(\tfrac{1}{2}\alpha Z)^2F|J_0|^2\Delta_0^2.\tag{19}$$

Substituting numerical values, we get

$$|J_0^2|=0.6/\Delta_0^2\approx0.2,\tag{20}$$

using $\Delta_0^2\approx3$, as indicated by (11).

(ii) $\Delta j=\Delta I=0$, not $0-0$. These include $Hg^{205}\rightarrow Tl^{205}$, $Tl^{207}\rightarrow Pb^{207}$, $Pb^{209}\rightarrow Bi^{209}$, with $\log ft_1$ values ranging from 5.2 to 5.5. In Eq. (19) we make the replacement

$$|J_0|^2\Delta_0^2\rightarrow[|J_1|^2\{(\Lambda-\Delta_1')t+\Delta_1\}^2/(2j)(2j+2)+|J_0|^2\Delta_0^2]\approx|J_0|^2\Delta_0^2,\tag{21}$$

so that these cases again lead to the result (20).

(iii) $0^+\rightarrow1^-\rightarrow0^+$. The shape and large $ft$ value of the RaE decay indicate cancellation of the first order terms included in Eq. (1). If we interpret RaE as a $0^-\rightarrow0^+$ transition, this implies $\Delta_0^2\approx0$, in considerable contrast to (11) and (19)–(21). On the other hand, if RaE is $1^-\rightarrow0^+$, cancellation means that

$$\begin{aligned}&(\Lambda-\Delta_1')t+\Delta_1\approx0,\\ &\Lambda\approx\Delta_1'-\Delta_1/t\approx\Delta_1',\end{aligned}\tag{22}$$

since here $t=-10$. This is in complete accord with (11). The $ft_1$ value will be reduced from that in (19) by a factor of order $(2I_i+1)\Delta_0^2(\alpha Z/2R)^2\approx10^3$. The corresponding $\log ft_1\approx8$, as observed.

The $0^+\rightarrow1^-\rightarrow0^+$ ground-state decay scheme of $Pb^{212}\rightarrow Bi^{212}\rightarrow Po^{212}$, with $\log ft$ values of 6.8 and 7.2 for the successive decays should and does exhibit somewhat similar behavior to the RaE transition. That is, the large $ft$ values in the region of favored first-forbidden transitions speak for the tendency of (22) to hold. The fact that the $ft$ values are somewhat reduced from that of RaE indicates that the cancellation is not perfect. This may arise from a moderate configuration admixture of $\Delta j=\Delta I=1$ or a very modest variation in $\Lambda$ and/or $\delta$. Equation (22) represents a very delicate balance, and the $Pb^{212}\rightarrow Bi^{212}$ transitions can be fit with minor fluctuations in any of the three nuclear parameters $t$, $\Lambda$, or $\delta$. Thus, $A=212$ fits well into the general scheme; the larger $ft$ for the $Bi^{212}$ decay is consistent with the extra statistical factor of $1/(2I_i+1)$.

From (20) it appears that the difference between "favored" and "unfavored" transitions is about one order of magnitude in $|J|^2$. It does not seem particularly surprising that $|J|^2<1$ even for the most favored transitions. There may be some configuration mixing even here (the magnetic moments show bad deviations from the Schmidt limits in this region), and the overlap of one-particle radial functions associated with orbits of different parity should not be perfect.

## 6. RARITY OF RaE-TYPE SHAPES

Further, if indirect evidence in favor of the $1^-\rightarrow0^+$ assignment for RaE is provided by the observed scarcity of such spectra. If RaE were $0^-\rightarrow0^+$, it would be difficult to construct an explicit argument to show why none of the other known $0^-\leftrightarrow0^+$ transitions display a similar tendency to cancellation. For a $1^-\rightarrow0^+$ assignment, however, we can immediately see why such perfect cancellation is unlikely to be found in any other first-forbidden transition (except perhaps the identical ground-state transition of RaD). The conditions for cancellation are that $t$ be large and that the $\Delta_0^2$ term be absent; these conditions are satisfied only if: (a) $\Delta j=0$,

$\Delta I=1$; (b) $j$ is large; and (c) the configuration admixture is small. If the requirement (c) is not satisfied, a moderate admixture of $\Delta j=\Delta I=1$ transition may occur, producing a straight-line spectrum. The only region where all these conditions (24) can be satisfied is for $A$ slightly larger than 208; i.e., at $A=210$.

The assignment of $1^-$ as the ground state of RaE is bolstered slightly by the observations on its $\alpha$ decay.[12] If the transition is predominantly to the ground state of $Tl^{206}$, the $Q$ value for $\alpha$ decay would be $Q_\alpha=5.06$ Mev. The observed partial half-life is most consistent with the energy-lifetime relationships for the Bi emitters[13] if $Q_\alpha$ is about 0.2–0.3 less than this value. This suggests that the $\alpha$ decay proceeds to an excited state in $Tl^{206}$, although no direct observation has been made. If RaE had $I=0^-$ in its ground state, the transition to the $I=0^-$ ground state of $Tl^{206}$ could proceed with $s$-wave $\alpha$ particles; but if $I=1^-$ for RaE, spin and parity cannot be conserved in an $\alpha$-particle transition to a $0^-$ state in $Tl^{206}$. The $\alpha$ decay must then proceed to an excited state, as seems to be the case.

The arguments against $I=1^-$ for the ground state of RaE are not conclusive.[14]

## 7. THE LINEAR COMBINATION

The assignment of $I=1^-$ to RaE would remove what has been the sole evidence for the presence of the pseudoscalar interaction $P$ in the linear combination. Furthermore, if first-order effects due to the $P$ term can be observed, this implies strong corrections to the matrix element $\beta\gamma_5$ because of pseudoscalar-coupled forces in the nucleus.[15] For the sake of both the $P$ term and the pseudoscalar force corrections, it is desirable to find other evidence for $P$ to replace that of RaE.

Indirect evidence of this sort is provided by the observation that the $\Delta I=0$, yes, transitions have low $ft$ values, which in turn must be ascribed to a large value of $\Delta_0^2$. The most straightforward interpretation of this large $\Delta_0^2$ is in terms of $\beta\gamma_5$ with pseudoscalar force corrections, as assumed above. This evidence for $P$ has the advantage of being a statistic based on some 25 cases, whereas the RaE interpretation place excessive weight on a single instance. Unfortunately, the evidence drawn from $\Delta_0^2$ does not provide any information about the algebraic sign of $\lambda_P$, although its magnitude appears to be of order unity.

The authors wish to thank Dr. K. Way for helpful discussions of the experimental data.

## APPENDIX I

The matrix element estimate (35) of reference 2 is revised here. The need for revision can be seen from the following example: for a one-particle transition with $\Delta j=0$, the matrix element $|\int\mathbf{r}|^2$ is reduced from its value for $\Delta j=1$ by a statistical factor of order $1/[j(2j+2)]$, which is much less than unity for moderate $j$. On the other hand, $|\int\boldsymbol{\sigma}\times\mathbf{r}|^2$ is about the same for $\Delta j=0$ as for $\Delta j=1$, because $t=\pm(2j+1)$ in first case, $t=\pm1$ in the second. Thus the matrix element $|\int\mathbf{r}|^2$ is peculiar in suffering a substantial reduction for $\Delta j=0$ transitions.

This effect is special to $|\int\mathbf{r}|^2$ and presumably does not occur for $|\int\beta\boldsymbol{\alpha}|^2$. In fact, the nonrelativistic approximation to $\int\beta\boldsymbol{\alpha}$ without pseudoscalar force corrections is just proportional to $\int\boldsymbol{\sigma}\times\mathbf{r}$. The correction term for pseudoscalar coupling of nuclear forces should also be more or less constant, independent of whether $\Delta j=0$ or 1. The approximations leading to (35) of reference 2 yielded a pseudoscalar correction term proportional only to $\int\mathbf{r}$. The discussion above makes it seem likely that the pseudoscalar correction should include a term proportional to $\int\boldsymbol{\sigma}\times\mathbf{r}$.

Such a term is not hard to find. If in reference 2 we omit the symmetrizing step in Eq. (31) and repeat the argument leading to (32) we obtain:

$$\sum_{k\neq j}[\boldsymbol{\sigma}^j\cdot\mathbf{p}^j,\boldsymbol{\sigma}^k\cdot\boldsymbol{\nabla}^k R_n{}^k U^{jk}]\approx\sum_{k\neq j}[\mathbf{p}^j\cdot\boldsymbol{\nabla}^j+i(\boldsymbol{\sigma}^j\times\mathbf{p}^j)\cdot\boldsymbol{\nabla}^j R_n{}^j,U^{jk}],\quad\text{(I.1)}$$

whence

$$\langle Q\beta\boldsymbol{\alpha}\cdot\boldsymbol{\nabla}R_n\rangle\approx-i[t/n+\delta(1-t/n)]\int QR_n,\quad\text{(I.2)}$$

with $\delta=\rho(m_0M/\mu^2)f_r$ (2.4B). Equation (I.2) differs from (35) of reference 2 by addition of the term $-\delta t/n$ inside the brackets, which arises from the presence of a $\int\boldsymbol{\sigma}\times\mathbf{r}$ term in the pseudoscalar correction.

The use of (I.2) instead of (35) makes no change in the conclusions of reference 2, except for a slight improvement in consistency. Only Eqs. (49) and (51) of reference 2 have to be changed, becoming:

$$a=-\chi[\tfrac{1}{2}t+\delta(1-\tfrac{1}{2}t)],\quad\text{(49')}$$

$$\begin{aligned}&\delta=1-2\quad Cl^{36}\\&\delta=1-1.5\quad I-Cs\end{aligned}\quad\text{(51')}$$

The apparent range of variations of $\delta$ is thus reduced.

In order not to relay too heavily upon the rather heuristic procedures used to obtain (I.2), we use for application in the text above the general phenomenological form:

$$\langle Q\beta\boldsymbol{\alpha}\cdot\boldsymbol{\nabla}R_n\rangle\approx-i[t/n+\delta-\delta' t/n]\int QR_n,\quad\text{(I.3)}$$

where $\delta$ and $\delta'$ are not necessarily equal. The survey of experimental data resulting in (11) is in fact consistent with $\delta=\delta'$.

[12] E. Broda and N. Feather, Proc. Roy. Soc. (London) **190**, 20 (1947).
[13] Perlman, Ghiorso, and Seaborg, Phys. Rev. **77**, 26 (1950).
[14] R. W. King and D. C. Peaslee, Phys. Rev. **74**, 795 (1954).
[15] M. Ruderman, Phys. Rev. **89**, 1227 (1953).

## APPENDIX II[16]

### 1. The Matrix Element $|\int \boldsymbol{\sigma}\cdot\mathbf{r}|^2$

$$\left|\int \boldsymbol{\sigma}\cdot\mathbf{r}\right|^2=\left|\int r\right|^2\left|\int \sigma_r d\omega\right|^2, \tag{II.1}$$

where $\sigma_r=\boldsymbol{\sigma}\cdot\mathbf{r}/r$. Here $\int r$ is a radial integral only, and $|\int d\omega|^2$ involves all angular integrals and spin summations. Now, since $\sigma_r$ is a pseudoscalar,

$$\sigma_r\psi_{jl}=\psi_{jl'}, \tag{II.2}$$

where $l'=2j-l$; that is, the operator $\sigma_r$ applied to any initial (angular) state can lead only to a single final (angular) state. We may therefore apply sum rules:

$$\begin{aligned}\langle\sigma_r\rangle_{if}^2&=\langle\sigma_r\rangle_{if}\langle\sigma_r\rangle_{fi}=\textstyle\sum_f\langle\sigma_r\rangle_{if}\langle\sigma_r\rangle_{fi}\\&=\langle\sigma_r^2\rangle_{ii}=1.\end{aligned} \tag{II.3}$$

Equation (II.3) holds for a fixed value of $m_i$, the projection of the initial spin, but includes a summation over all $m_f$. The average of (II.3) over all $m_i$ is $(2j_i+1)^{-1}\sum_{m_i}0=1$. Therefore,

$$\left|\int \boldsymbol{\sigma}\cdot\mathbf{r}\right|^2=\left|\int r\right|^2. \tag{II.4}$$

### 2. The Matrix Element $|\int \mathbf{r}|^2$

$$\begin{aligned}\left|\int \mathbf{r}\right|^2&=\left|\int r\right|^2\frac{1}{(2j+1)}\\&\times\sum_{m,m'M}\left|\int\Omega_{j'}^{m'*}\left(\frac{4\pi}{3}\right)^{\frac{1}{2}}Y_1^M\Omega_j^m d\omega\right|^2\\&=\left|\int r\right|^2(2j'+1)(2l'+1)(2l+1)\\&\quad\times V^2(l1l';000)W^2(ll'jj';1\tfrac{1}{2});\end{aligned} \tag{II.5}$$

the coefficients $V$ and $W$ are defined in reference 6 and have been tabulated.[17] Evaluation for $l'-l=\Delta l=\pm1$ yields:

$$(2l+1)(2l'+1)V^2(l1l';000)=l_>, \tag{II.6}$$

where $l_>$ is the larger of $l, l'$. And with $j'-j=\Delta j=0, \pm1$, we have:

$$\begin{aligned}\left|\int \mathbf{r}\right|^2&=\left|\int r\right|^2\frac{1}{2j(2j+2)},\quad \Delta j=0;\\&=\left|\int r\right|^2\frac{2j'+1}{2(j+j'+1)},\quad \Delta j=\pm1.\end{aligned} \tag{II.7}$$

### 3. The Matrix Element $|B_{ik}|^2$

$$\begin{aligned}\sum_{i,k}|B_{ik}|^2&=\frac{1}{(2j+1)}\sum_{mm'M}\left|\int\psi_{j'}^{m'*}Y_2^M(\boldsymbol{\sigma},\mathbf{r})\psi_j^m\right|^2,\\&=C_{jj'}^2\sum_{mm'M}V^2(j2j';mM-m'),\\&=C_{jj'}^2,\end{aligned} \tag{II.8}$$

where $Y_2^M(\boldsymbol{\sigma},\mathbf{r})$ is a polarized solid harmonic.[18] Since these harmonics transform like second-rank tensors, it is possible to separate out the $m$ dependence by writing:

$$\int\psi_{j'}^{m'*}Y_2^M\psi_j^m=(2j+1)^{\frac{1}{2}}C_{jj'}V(j2j';mM-m'). \tag{II.9}$$

We are interested only in the transition $\Delta j=j'-j=\pm2$, $\Delta l=l'-l=\pm1$ and can evaluate $C_{jj'}$ by considering a special case. Let $\Delta j=-2$, and take:

$$\begin{aligned}&\int\psi_{j'}^{j'*}Y_2^{-2}\psi_j^j\\&\quad=C_{jj'}(2j+1)^{\frac{1}{2}}V(j2j';j-2-j'),\\&\quad=C_{jj'},\\&\quad=\int r\int\Omega_{j'}^{j'*}\left(\frac{8\pi}{3}\right)^{\frac{1}{2}}Y_1^{-1}(\sigma_x-i\sigma_y)\Omega_j^j d\omega,\end{aligned} \tag{II.10}$$

where the last relation follows from Eq. (39) of reference 18. In this case:

$$\begin{aligned}\Omega_j^j&=\chi_{\frac{1}{2}}^{\frac{1}{2}}Y_l^l,\quad \Omega_{j'}^{j'}=\left(\frac{2j'+1}{2l'+1}\right)^{\frac{1}{2}}\chi_{\frac{1}{2}}^{-\frac{1}{2}}Y_{l'}^{l'}\\&\qquad-\left(\frac{1}{2l'+1}\right)^{\frac{1}{2}}\chi_{\frac{1}{2}}^{\frac{1}{2}}Y_{l'}^{l'-1}.\end{aligned} \tag{II.11}$$

The $\chi$ are spin functions, so that (II.10) becomes:

$$\begin{aligned}C_{jj'}&=2\left(\frac{8\pi}{3}\right)^{\frac{1}{2}}\left(\frac{2j'+1}{2l'+1}\right)^{\frac{1}{2}}\int Y_{l'}^{l'*}Y_1^{-1}Y_l^l d\omega,\\&=2\sqrt{2}\left(\frac{2j'+1}{2l'+1}\right)^{\frac{1}{2}}[(2l'+1)(2l+1)]^{\frac{1}{2}}\\&\quad\times V(l1l';000)V(l1l';l1-l'),\\&=2\left(\frac{2j'+1}{2l'+1}\right)^{\frac{1}{2}}\left(\frac{2l_>}{2l_>+1}\right)^{\frac{1}{2}}.\end{aligned} \tag{II.12}$$

This result is made to apply generally to $\Delta j=\pm2$ by recognizing the factor $2l'+1$ as $2l_<+1=2l_>-1$. Substituting $l_>=\frac{1}{2}(j+j'+1)$, we have:

$$\sum_{i,k}|B_{ik}|^2=4\frac{(2j'+1)(j+j'+1)}{(j+j')(j+j'+2)}\left|\int r\right|^2,\ \Delta j=\pm2. \tag{II.13}$$

[16] An extensive study has been made of these statistical factors: M. E. Rose and R. K. Osborn, Phys. Rev. **93**, 1326 (1954).

[17] L. C. Biedenharn, Oak Ridge National Laboratory Report ORNL-1098, 1952 (unpublished).

[18] D. L. Falkoff and G. E. Uhlenbeck, Phys. Rev. **79**, 323 (1950).

TABLE II. The β transitions used for the surveys in Secs. 3 and 4. While some of the assignments may prove to be in error, the groups as a whole should lend themselves to legitimate statistical interpretation. *m* indicates a metastable state, the end point energy is given in Mev, and the sign of the β emission precedes the end-point energy. Except where indicated, the classification and values quoted are from references 8 and 9.

*Note added in proof.*—The assignment of $Ta^{185}$ now appears questionable, and $Pr^{145}$ should be deleted. Three other $\Delta I=\pm1$ transitions would be added, however ($Sm^{153}$, $Hf^{181}$, and $Os^{191}$), with no significant change in the analysis.

1. Odd $A$, $\Delta I=0$ (yes).

| Parent | Energy | log $fst$ | Parent | Energy | log $fst$ |
|---|---|---|---|---|---|
| $Ag^{111}$ | −1.04 | 7.34 | $In^{119m}$ | −2.7 | 6.20 |
| $Ag^{113}$ | −2.1 | 6.95 | $Dy^{165}$ | −1.25 | 6.21 |
| $Ag^{115}$ | −3 | 6.40 | $Er^{169}$ | −0.33 | 6.09 |
| $Cd^{115}$ | −1.12 | 7.13 | $Tm^{171}$ | −0.10 | 6.36 |
| $In^{115m}$ | −0.84 | 6.66 | $Ta^{185}$ | −1.7 | 6.26 |
| $In^{117m}$ | −1.77 | 6.58[a] | $Au^{199}$ | −0.25 | 6.16 |

2. Odd $A$, $\Delta I=\pm1$ (yes).

| Parent | Energy | log $fst$ | Parent | Energy | log $fst$ |
|---|---|---|---|---|---|
| $Ge^{77}$ | −2.20 | 7.55 | $Pr^{143}$ | −3.2 | 7.87 |
| $Br^{87}$ | −8.0 | 7.30 | $Pm^{147}$ | −0.229 | 7.42 |
| $Kr^{87}$ | −3.63 | 7.31 | $Lu^{177}$ | −0.475 | 6.75 |
| $Ag^{111}$ | −0.70 | 7.76 | $Lu^{177}$ | −0.366 | 6.95 |
| $Ce^{141}$ | −0.581 | 7.72 | $W^{187}$ | −1.318 | 7.86 |
| $Ce^{143}$ | −1.37 | 7.72 | $Au^{199}$ | −0.46 | 7.73 |
| $Pr^{143}$ | −0.932 | 7.61 | | | |

3. Odd $A$, $\Delta I=\pm2$ (yes).

| Parent | Energy | log $fst$ | Parent | Energy | log $fst$ |
|---|---|---|---|---|---|
| $S^{37}$ | −4.3 | 7.68 | $Pd^{107}$ | −0.035 | 8.54 |
| $Cl^{38}$ | −2.96 | 7.86 | $Ag^{111}$ | −0.80 | 8.16 |
| $A^{39}$ | −0.565 | 8.74 | $Sn^{123}$ | −1.42 | 8.82 |
| $A^{41}$ | −2.55 | 8.72 | $Sn^{125}$ | −2.37 | 9.00 |
| $Kr^{85}$ | −0.695 | 8.24 | $Sb^{125}$ | −0.62 | 8.57 |
| $Sr^{89}$ | −1.50 | 8.33 | $I^{131}$ | −0.810 | 8.50 |
| $Sr^{91}$ | −2.66 | 8.24 | $I^{133}$ | −1.5 | 8.86 |
| $Y^{91}$ | −1.54 | 8.51 | $Cs^{137}$ | −0.52 | 8.88 |
| $Zr^{95}$ | −0.887 | 8.93 | $Er^{171}$ | −1.49 | 7.84 |
| $Tc^{95}$ | +0.65 | 7.84 | | | |

4. Even $A$, $\Delta I=\pm2$ (yes).

| Parent | Energy | log $fst$ | Parent | Energy | log $fst$ |
|---|---|---|---|---|---|
| $N^{16}$ | −10.5 | 8.23 | $Rb^{88}$ | −5.13 | 8.14 |
| $Cl^{38}$ | −4.81 | 8.13 | $Sr^{90}$ | −0.535 | 8.82 |
| $K^{42}$ | −3.58 | 8.50 | $Y^{90}$ | −2.18 | 8.02 |
| $As^{73}$ | +3.38 | 9.28 | $Sb^{122}$ | −2.01 | 8.59 |
| $As^{74}$ | +1.53 | 8.57 | $I^{134}$ | +2.20 | 8.01 |
| $As^{74}$ | −1.36 | 8.32 | $I^{136}$ | −1.24 | 8.51 |
| $As^{76}$ | −2.98 | 8.75 | $Pr^{142}$ | −2.15 | 7.83 |
| $Rb^{84}$ | +1.629 | 9.56[b] | $Tl^{204}$ | −0.783 | 9.05 |
| $Rb^{86}$ | −1.760 | 8.38 | | | |

5. Even $A$, $(2-)\rightarrow(2+)$ excited state transitions. (Each of the transitions listed here has a higher energy branch listed in the even $A$, $\Delta I=2$ (yes) table that goes to the $0+$ ground state.)

| Parent | Energy | log $fst$ | Parent | Energy | log $fst$ |
|---|---|---|---|---|---|
| $Cl^{38}$ | −2.77 | 6.91 | $Rb^{86}$ | −0.670 | 7.53 |
| $K^{42}$ | −2.05 | 7.45 | $Rb^{88}$ | −3.29 | 7.10 |
| $As^{72}$ | +2.50 | 7.77 | $Sb^{122}$ | −1.45 | 7.66 |
| $As^{74}$ | +0.92 | 6.89 | $Sb^{122}$ | −0.73 | 7.68 |
| $As^{74}$ | −0.69 | 7.55 | $I^{134}$ | +1.50 | 7.41 |
| $As^{76}$ | −2.41 | 8.18 | $I^{136}$ | −0.85 | 7.86 |
| $Rb^{84}$ | +0.822 | 8.63[b] | $Pr^{142}$ | −0.64 | 7.19 |

[a] C. L. McGinnis (private communication).
[b] This value is based on the assumption $K/\beta^+\approx2$.

## APPENDIX III

Figures 1, 2, and 3 illustrate the even-$A$ decay schemes in the region $A\sim208$ and contain the proposed new

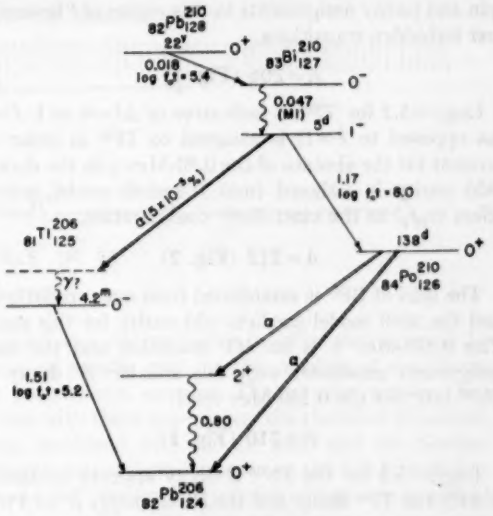


FIG. 1. Decay schemes and level assignments for $A=206$ and $A=210$.

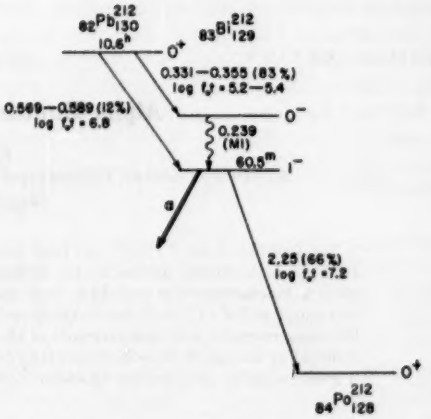


FIG. 2. Decay schemes and level assignments for $A=212$.

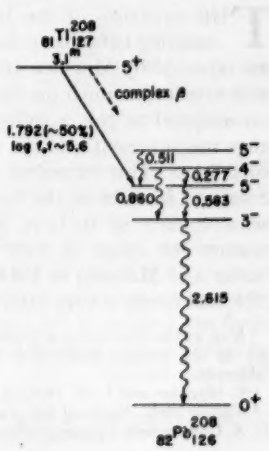


FIG. 3. Decay schemes and level assignments for $A=208$.

spin and parity assignments in this region of "favored" first forbidden transitions.

### $A=206$ (Fig. 1)

Log$ft$=5.2 for $Tl^{206}$ is indicative of $\Delta I=0$ or 1. $I=0$ (as opposed to $I=1$) is assigned to $Tl^{206}$ in order to account for the absence of the 0.80-Mev $\gamma$ in the decay. Odd parity is assigned from the shell model, which offers $(s_{\frac{1}{2}}p_{\frac{1}{2}})$ as the most likely configuration.

### $A=212$ (Fig. 2)

The spin of $Bi^{212}$ is established from $\alpha$-$\gamma$ correlation,[19] and the shell model predicts odd parity for this state. The 0.239-Mev $\gamma$ is an $M1$ transition and the only assignment consistent with this and the $\beta^-$ decay of $Pb^{212}$ is $0^-$ for the 0.239-Mev level.

### $A=210$ (Fig. 1)

Log$ft$=5.4 for the $Pb^{210}$ $\beta$ decay appears to classify it with the $Tl^{206}$ decay and the lower-energy $\beta^-$ of $Pb^{212}$, both of which are $0\rightarrow0$, parity change transitions. Section 5 of the text argues for the $1^-$ assignment for the 5-day $Bi^{210}$ state, and the $M1$ character of the 47-kev $\gamma$ is in complete accord.

### $A=208$ (Fig. 3)

The decay of $Tl^{208}$ and the recently determined[20] excited states of $Pb^{208}$ appear to offer another example of a "favored" first-forbidden transition. An $(s_{\frac{1}{2}},g_{9/2})$ configuration is quite plausible for $Tl^{208}$. This offers a $4^+$ or $5^+$ assignment. Because of the absence of a $\beta^-$ transition to the $3^-$ excited state, the $5^+$ assignment is preferred. Thus, another $\Delta I=0$ (yes) transition in the $A\approx208$ range appears to yield an anomalously low $ft$ value. This is completely consistent with the rest of the region if the $5^-$ state is formed by exciting the 82nd proton from an $s_{\frac{1}{2}}$ orbit to an $h_{9/2}$ orbit, thus making the single particle transition $g_{9/2}\rightarrow h_{9/2}$, as is found elsewhere in this region.

[19] J. Horton and R. Sherr, Phys. Rev. **90**, 388 (1953).

[20] Elliott, Graham, Walker, and Wolfson, Phys. Rev. **93**, 356 (1954).

PHYSICAL REVIEW VOLUME 94, NUMBER 5 JUNE 1, 1954

# Alpha-Emitting Isomer: Polonium-211

FRED NOEL SPIESS*
*Radiation Laboratory, Department of Physics, University of California, Berkeley, California*
(Received November 9, 1953)

The half-life of AcC′ ($Po^{211}$) has been measured for the first time, and is 0.52 second rather than the 1/200 seconds widely quoted in the literature. Three short-lived alpha emitters resulting from alpha-particle bombardment of lead have been studied. They have been identified as $Bi^{211}$ ($T_{\frac{1}{2}}=2.16$ min) and two states of $Po^{211}$ ($T_{\frac{1}{2}}=25$ sec and 0.52 sec) by means of chemical separations, excitation functions, half-life measurements, and measurements of the energies of the emitted alpha particles. The energy measurements show that the 0.52-second state is an excited state of $Po^{211}$, with an excitation energy of about 0.3 Mev. A group of alpha particles having about 9-Mev energy was observed but not identified.

## I. INTRODUCTION

THE existence of the isotope $Po^{211}$ as an alpha-emitting beta-decay daughter of actinium C was first reported by Marsden and Perkins[1] in 1914. In the same article the much quoted half-life of 1/200 second was assigned to this activity on the basis of a rough range measurement and the application of the Geiger-Nuttall law. This estimated value has persisted in the literature[2] in spite of the fact that until this time no measurements of it have been made. Attempts to measure the range of these particles were made by Varder and Marsden in 1914, by Bates and Rogers in 1924, and finally a very careful measurement was made by Rutherford, Wynn-Williams, and Lewis[3] in 1931. They obtained a mean range of 6.506 cm. This value was corrected by Holloway and Livingston[4] to a value of 6.555 cm.

In 1940 Corson, MacKenzie, and Segrè[5] found this same actinium C′ as the $K$-capture daughter of $At^{211}$. The identification was made by observation of polonium x-rays having the same half-life as the $At^{211}$ (7.5 hours), and by the presence of an alpha group having 6.55 cm range, in agreement with the measurements made by Lord Rutherford *et al.*[3]

The work reported here utilized $Po^{211}$ as it occurs following $At^{211}$ decay as well as that produced directly from cyclotron bombardment of lead and bismuth. As a

* Now at the University of California Marine Physical Laboratory of the Scripps Institution of Oceanography, San Diego, California.

[1] E. Marsden and P. B. Perkins, Phil. Mag. **27**, 690 (1914).

[2] *Nuclear Data*, National Bureau of Standards Circular No. 499 (U. S. Government Printing Office, Washington, D. C., 1950).

[3] Rutherford, Wynn-Williams, and Lewis, Proc. Roy. Soc. (London) **A133**, 351 (1931).

[4] M. G. Holloway and M. S. Livingston, Phys. Rev. **54**, 18 (1938).

[5] Corson, MacKenzie, and Segrè, Phys. Rev. **58**, 672 (1940).

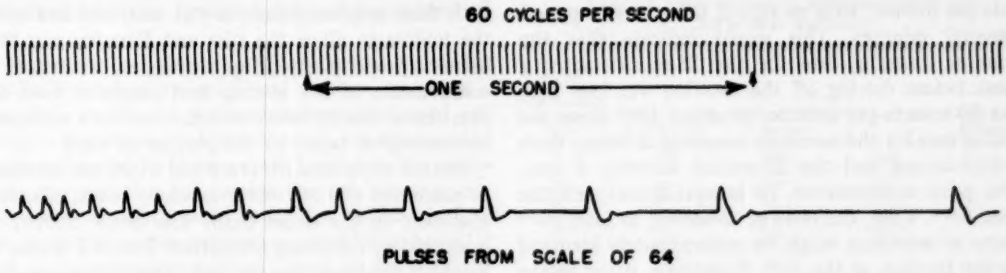


FIG. 1. Actinium C′ decay.

result of these investigations the half-life of the 6.55-cm alphas was determined directly as 0.52 second. In addition, it was found that when the AcC′ was formed from bombardment of lead or bismuth targets a second group of alphas appeared. These alphas had somewhat lower energy and a half-life of 25 seconds. Further work showed that this latter decay takes place from the ground state of $Po^{211}$. It thus appears that, although the 0.52-second state is the only one observed following the $K$-capture decay of $At^{211}$, it is nevertheless an excited state which decays almost entirely by direct alpha emission.

This work falls naturally into several parts: first, the measurement of the half-life of AcC′ as it occurs following $K$-capture decay in $At^{211}$; second, the study of the production of the short-lived alpha groups by bombardment of lead and bismuth; third, the measurement of the energies of the observed alpha particles; and fourth, the chemical separation experiments used in identifying the longer-lived products of bombardment.

## II. ACTINIUM C′ HALF-LIFE

In facing the problem of measuring the half-life of AcC′ as it occurs in the $At^{211}$ decay scheme two very different modes of approach presented themselves. If the half-life were actually about 1/200 second as quoted in the literature based on the Geiger-Nuttall law, then one should measure delayed coincidences between the $Po^{211}$ x-rays (following $K$-capture in $At^{211}$) and the ensuing alpha emissions. However, experiments reported below had indicated the possibility that the half-life was of the order of 0.5 second or more, in which case some chemical separation method might be applicable. A method for making such a separation was devised based on the observation by Ghiorso[6] that while polonium will stick to platinum at dull red heat, astatine evaporates off quite easily.

One part of the experimental apparatus was a thin platinum strip (1.2 and 0.7 mils were both used) about one centimeter wide and five centimeters long. It was connected through a switch to a transformer in order that it could be brought rapidly to a dull red heat by the passage of a large current pulse. The strip was mounted on a sliding holder in order that it could be positioned rapidly over the thin window of a methane flow proportional counter. The counter window was covered with three one-quarter mil sheets of aluminum which, combined with the air path and the window thickness, was sufficient to cut out the 5.9-Mev alphas from the $At^{211}$ decay. The counter output was amplified and fed to a scale of 64, from which output pulses were fed to a Brush recorder.

The $At^{211}$ was made by bombarding a thick bismuth target with 28-Mev alphas from the 60-inch cyclotron. The bismuth was then heated in a vacuum and the evaporating astatine was caught in a liquid air trap. The astatine in the trap was dissolved in nitric acid. For each run a few drops of this solution were put on the platinum filament and allowed to evaporate to dryness. The amount of astatine used was such as to give an initial counting rate of 20 000 to 40 000 counts per minute through the absorber.

The procedure was to position the strip away from the counter, pass a single pulse of current through it to drive off the astatine and then slide it over the counter window in order to observe the decaying $Po^{211}$ activity which would be recorded on the tape of the Brush recorder. Two runs were made in inverse fashion by performing the evaporation over the counter window, catching the astatine on a thin silver foil placed over the counter window, and then removing the polonium laden filament in order to watch the activity grow into the astatine again with the appropriate half-life.

The Brush recorder data were analyzed[7] and the resulting half-life was determined to be 0.52 second. A section of the Brush recorder tape for a typical run is shown in Fig. 1.

When the isomerism of the 25-second activity with the 0.52-second activity became apparent, additional runs were made in order to find out whether the 25-second period might be present in the $Po^{211}$ as it occurs upon decay of $At^{211}$. The best such run showed a counting rate of 465 000 AcC′ counts per minute prior to evaporating off the astatine. After separation, the half-second activity was allowed to die out and the steady background counting rate which resulted was 520

[6] A. Ghiorso (private communication).

[7] F. N. Spiess, University of California Radiation Laboratory Unclassified Report, UCRL-1494 (unpublished).

counts per minute, with no sign of decay over a period of several minutes. This would indicate that the maximum counting rate for the 25-second activity present before driving off the astatine was less than about 50 counts per minute, or about $10^{-4}$ times the counting rate for the normally occurring activity. Both the 0.52-second and the 25-second activity, if any, would, prior to separation, be in equilibrium with the parent $At^{211}$. Thus, the ratio of 25-second to total $Po^{211}$ activity at zero time would be approximately identical with the fraction of the $At^{211}$ $K$-captures going to the state having the 25-second half-life, plus the fraction going to the 0.52-second state and decaying by gamma emission to the lower state prior to alpha emission. The sum of these two is then less than one part in $10^4$.

Some mention should be made here of the fact that the half-life of 0.52 second is considerably longer than the old estimated value. This is, however, to be expected in view of recent studies of the systematics of alpha decay.[8,9] These show that the degree of prohibition of alpha decay increases appreciably as one approaches nuclei having $Z$ near 82 and $N$ near 126. Presumably the effect is in part related to an actual decrease in the radius of the daughter nucleus relative to the radius predicted from other alpha decay data ($r=1.57A^{\frac{1}{3}}\times10^{-13}$ cm).[10] In addition the high stability of the closed shell configurations may make very low the probability of formation of an alpha particle in a nucleus not having at least two neutrons and two protons beyond the closed shells. This would then multiply the probability of barrier penetration, for which detailed calculation can be made,[11] by an additional probability of alpha-particle formation, with consequent increase in half-life.

### III. PRODUCTION OF $Po^{211}$ FROM ALPHA-PARTICLE BOMBARDMENT OF LEAD AND BISMUTH

The experimental arrangements used in measuring the cross sections for production of these activities at various energies can be divided into three parts: beam collimating and measuring system, ionization chamber, and amplifiers and scalers.

The beam collimating and measuring system is substantially the same as that described by Kelly and Segrè.[12] It consists of an evacuated tube down which the cyclotron beam can travel, a rotating absorber carriage and a Faraday cup. These are arranged so that the deflected cyclotron beam, upon emerging from the exit port passes through a slit at one end of a pipe about 70 cm long and 7 cm in diameter. At the other end of the pipe there is a second collimating slit. Since the entire system is located in the fringing magnetic field of the cyclotron (about 2000 gauss), the pipe is fitted with three sylphon joints, one at each end and one at the middle to allow the slits and Faraday cup to be oriented properly to pick up the maximum current. The combination of slit system and magnetic field thus provides a velocity selection which insures a sufficiently monoenergetic beam for the purpose at hand.

Behind the second slit is a wheel which can be rotated to place any one of twenty carefully made, aluminum absorbers in the beam path. The beam current was measured by collecting the current from a Faraday cup in which the beam was stopped. The dimensions of the cup were such that, in the fringing cyclotron field, no secondary electrons liberated at the back wall could escape collection. The entire system of pipe, foil wheel, and Faraday cup were connected to the cyclotron tank vacuum system.

The ionization chamber used[7] was basically a parallel plate chamber with Frisch grid. The spacing from sample to grid was about $2\frac{1}{2}$ inches, while the grid to collector spacing was $\frac{1}{8}$ inch. The main difference between this and other chambers previously used was that the sample holder was mounted on one end of a sliding rod which allowed the target to be placed either in the cyclotron beam, which passed through an extension of the chamber, or in the active volume of the chamber, or in an intermediate position in which the sample in the holder could be replaced with a different sample previously loaded in the target changing magazine. The sample holder was driven from the counting to the bombarding position and back again by the action of compressed air on a piston connected to the external end of the sample holding rod. The transit time from one position to the other was about 0.1 second.

Electron collection was employed and the grid to plate voltage ratio used was such as to eliminate electron collection at the grid.[13] In order to obtain fast rising pulses the chamber was filled with a mixture of about 95 percent argon and 5 percent $CO_2$.[14] The pressure of the gas used was dictated by the range of the alpha particles involved and the dimensions of the chamber, and in most runs was between 20- and 25-psi gauge pressure.

The pulses were amplified by a pre-amp and amplifier system having a rise time of about 0.1 microsecond. The pre-amp was operated in the fringing field of the cyclotron (about 1000 gauss). At first the iron tube shields previously employed when the pre-amp had been operated in smaller fields were used, but without success. The final arrangement had no magnetic shielding, but utilized instead the fact that the $6AK5$'s could be oriented in such a manner that the principal electron flow was along the lines of force of the field. Under these conditions the amplification remained virtually

[8] Perlman, Ghiorso, and Seaborg, Phys. Rev. **77**, 26 (1950).
[9] I. Perlman and T. J. Ypsilantis, Phys. Rev. **79**, 30 (1950).
[10] I. Kaplan, Phys. Rev. **81**, 962 (1951).
[11] M. A. Preston, Phys. Rev. **71**, 865 (1947).
[12] E. L. Kelly and E. Segrè, Phys. Rev. **75**, 999 (1949).
[13] Bunemann, Cranshaw, and Harvey, Can. J. Res. **A27**, 191 (1949).
[14] B. Rossi and H. H. Staub, *Ionization Chambers and Counters: Experimental Techniques* (McGraw-Hill Book Company, New York, 1949).

unchanged when the cyclotron magnet was turned off or on.

The cyclotron beam entered an extension of the chamber through a one-mil Dural window, traversed a short path in the gas of the chamber and passed out through a second one mil Dural window into the Faraday cup. A collimated $Po^{210}$ source was located in the chamber on the end of a rod passing through the chamber wall. Since the source could be rotated to point into or away from the active volume, it provided a beam of alpha particles which could be turned on or off at will in order to check the operation of the system.

Data were recorded using a two-channel Brush recorder. The output of the Faraday cup, amplified with a Brush dc amplifier, was fed to one channel, while the output of the pulse amplifier, scaled down by a factor of 4, 16, or 64 was fed to the other. In addition a signal was supplied to the latter pen to indicate the time at which the target entered and left the beam.

The ordinary lead and bismuth targets were made by evaporating a thin layer onto one-mil aluminum in a high vacuum chamber. In this way highly uniform, thin (0.1-mg/cm²) samples were produced. Since only small amounts of enriched lead were available these targets were made by electroplating, in spite of the fact that the resulting samples did not have the high uniformity shown by the evaporated samples.

As a result of the work done with the equipment described above, it was found that when ordinary lead targets were bombarded with alphas from the 60-inch cyclotron three different alpha-decaying products resulted. The half-lives of these alpha emitters were 0.5, 25, and 130 seconds.

Since the 0.5-second alphas were found to have the same energy as the AcC′ alphas following $At^{211}$ decay, and since the half-life was the same as that determined as described above for $Po^{211}$, it was evident that this was $Po^{211}$ produced by the only possible reaction—$Pb^{208}(\alpha,n)Po^{211}$. The 130-second half-life agreed with that for $Bi^{211}$ (AcC), and subsequent chemical separations verified that this was actually bismuth, which must have been formed by the reaction $Pb^{208}(\alpha,p)Bi^{211}$.

Identification of the 25-second activity was the only remaining problem. Chemical separations, to be described below, showed that these alphas came from polonium. The final assignment of this activity to $Po^{211}$ rests on the measurements of the variation of the yields of all three of these activities as the lead isotope content was varied. In these measurements it was found that the ratio of yield of 130-second to yield of 25-second activity at an alpha bombarding energy of 35 Mev was independent of lead isotope ratio over a wide range (30 to 90 percent in $Pb^{208}$, 8 to 60 percent in $Pb^{207}$, and 2 to 25 percent in $Pb^{206}$). The same was found at both 18 and 20 Mev for the ratio of 0.5-second to 25-second activity. Since both the 130- and 0.5-second activities resulted from the presence of $Pb^{208}$ only, then it was apparent that the 25-second activity was the result solely of bombardment of the $Pb^{208}$ also. The only polonium isotope which could be produced from $Pb^{208}$ and not from $Pb^{207}$, would be $Po^{211}$ (neglecting possibility of an $\alpha,\gamma$ reaction). The conclusion was thus forced that the 25-second activity was isomeric with the 0.52-second activity.

TABLE I. Cross sections in millibarns ($10^{-27}$ cm²) for several reactions.

| Alpha particle bombarding energy Mev | $Pb^{208}(\alpha,n)Po^{211}$ 0.52-second | $Pb^{208}(\alpha,n)Po^{211}$ 25-second | $Pb^{208}(\alpha,p)Bi^{211}$ | $Bi^{209}(\alpha,pn)Po^{211}$ 25-second |
|---|---|---|---|---|
| 18 | 2.6 | 0.01 | <0.01 | |
| 20 | 15 | 0.17 | <0.01 | |
| 21½ | 90 | 2.3 | <0.01 | |
| 23 | 46 | 4.6 | 0.01 | |
| 24½ | 30 | 5.5 | 0.07 | |
| 26 | 25 | 4.7 | 0.11 | |
| 27 | 11.5 | 2.7 | 0.54 | |
| 28 | 9.6 | | | |
| 30½ | 8.2 | | | <0.1 |
| 33 | | | | 0.3 |
| 33½ | 5.9 | | | |
| 34 | | | | 0.4 |
| 36 | 5.2 | | | 0.6 |
| 37½ | 4.8 | | | |
| 39 | 4.1 | 2.3 | 3.7 | 1.2 |

Absolute cross sections for production of both $Po^{211}$ states from the reaction $Pb^{208}(\alpha,n)Po^{211}$ were determined at several energies. In addition cross sections for the $Pb^{208}(\alpha,p)Bi^{211}$, and $Bi(\alpha,pn)Po^{211}$, (25-second state only) were measured. The results of these measurements are listed in Table I, and will be discussed in Sec. VI, below.

## IV. ALPHA-PARTICLE ENERGY MEASUREMENTS

The energies of the alpha particles from both the 0.52- and the 25-second emitters were determined using the argon-filled parallel-plate ionization chamber, with Frisch grid, described above. The output pulses from the chamber were amplified by a linear amplifier and the output of the amplifier was fed through a delay line (40 or 60 feet of RG65U) to the $y$-deflection plates of a Dumont 248 oscilloscope. The same pulse was put through a pulse shaper and discriminator to provide sharp pulses to trigger the sweep of the scope and square pulses to intensify the trace briefly. The pulses displayed on the scope were photographed on Super XX or Linagraph Pan film using a General Radio oscillograph recording camera. Drive motors were used which provided film speeds from 5 ft/sec to 1½ in./sec, in order that speeds appropriate to the level of activity would be available. After processing, the film was viewed using a microfilm viewer, and the pulse heights were measured.

Since the voltage produced at the pre-amp input by each alpha pulse is known to be proportional to the alpha energy with this type chamber, a curve of pulse generator output voltage *vs* oscilloscope pulse height could be used to give the alpha energy *vs* pulse-height relationship under these operating conditions if the energy corresponding to one particular pulse height were known. However, since three well-defined alpha

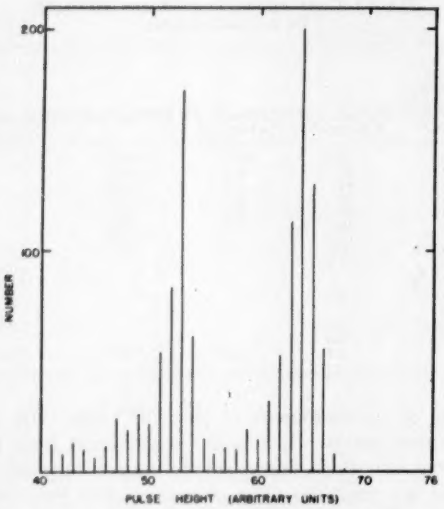


FIG. 2. Astatine pulse-height distribution.

groups were readily available, it was possible to construct directly a pulse height *vs* alpha energy curve covering the necessary energy range. The three groups used were $Po^{210}$ (5.30 Mev), $At^{211}$ (5.9 Mev), and $Po^{211}$ (7.43 Mev) from an astatine source. The pulse-height distributions for these three calibrating points are shown in Figs. 2 and 3A. The shape of the resulting pulse height *vs* energy curve agreed within the experimental error with the pulse height *vs* pulse generator voltage curve, so it was possible to extend the energy curve upward by using the pulse generator points, and thus find the energy of the long-range alphas which were observed.

The most important energy measurement was that of the 25-second activity since it would determine the excitation energy of the $Po^{211}$ isomer. This determination was made by bombarding a thin (0.1-mg/cm$^2$) lead sample with 22-Mev alphas for 30 seconds, waiting about 20 seconds, and then photographing the resulting pulses occurring over a period of about a minute. At this bombarding energy very little AcC is formed. Figure 3B shows the resulting pulse-height distribution, with peak at 62.0 divisions. This indicates that the energy of these alphas is 7.14±0.05 Mev. This same pulse height distribution shows, in contrast to the $Po^{210}$ and astatine calibration samples, alphas with energies as high as 9 Mev. At this date not much is known about these groups except that they must be in cascade with some other activity, since it would be difficult to imagine a 9-Mev alpha emitter with half-life long enough to allow its observation as long as a half minute after its production. This group may be the same as that reported[15] to occur somewhere in the natural decay chain following actinium B.

[15] M. Curie and W. A. Lub, J. phys. et radium **4**, 513 (1933).

## V. CHEMICAL SEPARATION EXPERIMENTS

These separations were made in order to determine the element to which each of the two longer-lived activities should be assigned. It could be assumed that after a bombardment with alphas of less than 40 Mev, the heavy elements present in a lead target would be lead, bismuth, and polonium. Two different separations were thus made. In the first, polonium was extracted alone from the combination, and the 25-second activity was observed to go with the polonium fraction. In the second, bismuth and polonium together were extracted from lead, and in this case both the 130- and the 25-second activities were in the bismuth-polonium portion.

In both separations the target material used was lead carbonate, since it was easily soluble in either warm hydrochloric or nitric acid. A slurry of the carbonate was spread on a strip of 10-mil aluminum and allowed to dry. It was then covered with $\frac{1}{4}$ mil aluminum in order that the active material would not be lost during the transfer from the bombarding area to the working area.

The sample was attached to a piece of aluminum rod, which, upon completion of the bombardment was blown by compressed air through a pipe to a point outside the cyclotron shielding where the chemical and counting equipment were set up.

The counter used was a methane flow proportional counter into which the samples could be inserted rapidly by means of a tight-fitting sliding panel. The output pulses were amplified and then fed to a scale of 64. The scaled-down pulses were recorded on a Brush recorder.

The analysis for polonium[16] was relatively simple. The lead carbonate was dissolved in hot, 6*N* HCl containing 1.0 mg per liter of Bi as a holdback. A piece of

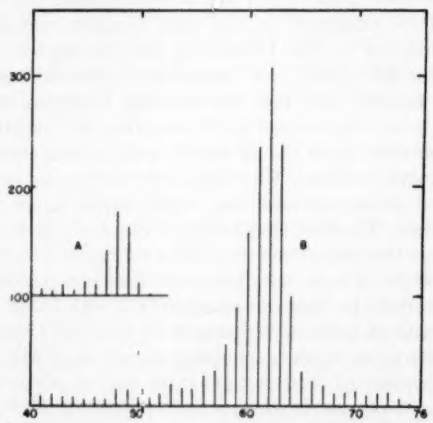


FIG. 3. (A) Polonium-210 pulse-height distribution. (B) Pulse-height distribution for intermediate-lived activity. (No pulses observed above 75.)

[16] W. W. Meinke, University of California Radiation Laboratory Report, UCRL-432 (unpublished), p. 84–1 (under remarks).

silver foil was inserted in the solution and stirred in it for about one minute, after which it was removed, washed in distilled water, and finally counted in the proportional counter. This process could be completed with sufficient rapidity to give an initial counting rate of more than 600 counts per minute of the 25-second activity, following a 30-second bombardment with about 2 microamperes of 30-Mev alphas.

The separation of polonium and bismuth from lead[17] went as follows. The lead carbonate was dissolved in about 5 cc of hot $HNO_3$, and about 20 mg of Bi in solution was added. The solution was boiled to concentrate the $HNO_3$, at which point a large part of the lead precipitated as $PbNO_3$. The solution was decanted into a centrifuge cone containing NaOH to neutralize the $HNO_3$ and then two drops of a one percent solution of Thionalide (Thioglycollic acid $\beta$-amino napthalide) were added. This precipitated the Bi as an organic complex which carried the Po with it. The solution was centrifuged and the liquid was poured off. The precipitate was first washed and then completely dissolved in acetone. The acetone solution was then dropped onto a hot platinum disk to evaporate the liquid. The disk was then flamed and finally placed in the counter. This process was completed in about 4 minutes from the end of the bombardment, which was fast enough to allow observation of the tail of the 25-second activity after a bombardment at 25 Mev.

The method given by Meinke[18] for separating Bi and Po from Pb by chemical plating on Ni was tried. Although both decay periods could be crudely identified, the yields obtainable in the available times were not sufficient to give counting rates comparable to those obtained as outlined above by Prodinger's method.[17]

The data obtained from the Po extractions showed the half-minute activity clearly, thus allowing an opportunity for determining that it was exactly 25 seconds. After decay of the 25-second activity only, a steady counting rate (about 300 counts per minute, attributable to the $Po^{210}$) was observed, with no trace of the 2.2-minute activity. Thus this experiment showed that the 25-second decay period should be assigned to some isotope of Po, while the 2.2-minute activity should not.

The results of the Po and Bi extraction clearly showed both the 25-second and the longer activity, whose half-life was accurately measured as 2.15 minutes. Here the 2.2-minute activity was present in the separated sample with a counting rate (extrapolated back to the end of the bombardment) 640 times as great as that of the $Po^{210}$, in contrast with the polonium separation experiment in which the same ratio was less than 0.4. Thus the 2.2-minute material was apparently a Bi isotope, and the agreement between the observed half-life and that known for AcC ($Bi^{211}$) indicated that this reaction could definitely be assigned as $Pb^{208}(\alpha,p)Bi^{211}$.

## VI. CONCLUSIONS

In this section three topics will be discussed in some detail. They are first, the excitation functions for the production of the two $Po^{211}$ states; second, the identification of the 0.52- and 25-second alpha-decay periods as arising from isomeric nuclear states; and third, a comparison of the information regarding the two isomeric states, particularly the implications bearing on spin assignments.

A rough excitation function for the reaction $Pb^{208}(\alpha,n)Po^{211}$ is presented in Table I above. It is desirable to compare this excitation function with others of the same sort and with theoretically predicted $(\alpha,n)$ excitation functions, but to date no other $(\alpha,n)$ reactions in this portion of the periodic table have been investigated. One can, however, assume that an $(\alpha,n)$ reaction should have a cross section which behaves in a way similar to a $(p,n)$ and use for comparison the results of Kelly[19] for the $Bi^{209}(p,n)Po^{209}$ reaction. Both show a steep rise limited by the barrier, followed by a sharp drop at the onset of the competing $2n$ reaction and a long, high-energy tail in which the cross section falls off quite slowly, having a magnitude roughly one-tenth of that at the peak.

A method of comparison with theory is to use the total cross sections for alpha bombardment as calculated by Weisskopf.[20] This can be compared directly with the lowest two or three experimental points, which are in a region not too heavily influenced by the competing $(\alpha,2n)$ and $(\alpha,p)$ reactions. Such a comparison shows that the experimental points give agreement with theory if a nuclear radius of $1.4A^{\frac{1}{3}}\times10^{-13}$ cm is used. This value is close to the $1.43A^{\frac{1}{3}}\times10^{-13}$ cm found in a similar way by Kelly[19] for $Bi^{209}+\alpha$ based on excitation functions for the $(\alpha,2n)$ and $(\alpha,3n)$ reactions.

The excitation function for the production of the 25-second state alone is depressed considerably below that for the more normal appearing curve for the 0.52-second activity at the low-energy end, but takes on comparable values at the high-energy end. One logical assumption as to the reason for this behavior is that it is due to an appreciable centrifugal barrier, indicating that this state (25-second) probably has a high angular momentum.

The following argument, based on the lack of variation in 25-second to 0.52-second yield ratio with change in isotopic concentration shows that the 25-second activity should be assigned to $Po^{211}$: Consider two targets, $a$ and $b$, each of thin lead, but having different

[17] Wilhelm Prodinger, *Organic Reagents Used in Quantitative Inorganic Analysis* (Elsevier Publishing Company, New York, 1940).

[18] W. W. Meinke, University of California Radiation Laboratory Report, UCRL-432 (unpublished), p. 83–1.

[19] E. L. Kelly, Ph.D. thesis, University of California, 1951 (unpublished).

[20] V. F. Weisskopf *et al.*, Lecture Series in Nuclear Physics, Atomic Energy Commission Report, MDDC-1175 (U. S. Government Printing Office, Washington, D. C., 1947).

percentages of the various stable isotopes. When each of these is bombarded with a constant alpha current for a time, $T$, at an energy such that only the $(\alpha,n)$ reaction contributes, then the ratio of the number of 0.52-second to the number of 25-second nuclei formed would be

$$R_a=\left(\frac{N_{0.52}}{N_{25}}\right)_a=\frac{0.52\sigma_{0.52}(1-e^{-1.33T})}{25\sigma_{25}(1-e^{-0.028T})}\left(\frac{p_{208}}{p_x}\right)_a;$$

$$R_b=\left(\frac{N_{0.52}}{N_{25}}\right)_b=\frac{0.52\sigma_{0.52}(1-e^{-1.33T})}{25\sigma_{25}(1-e^{-0.028T})}\left(\frac{p_{208}}{p_x}\right)_b;$$

where $p_{208}$ is the percent of $Pb^{208}$ in the target, and $p_x$ is the percent of the lead isotope from which the 25-second activity is formed by an $(\alpha,n)$ reaction. The $\sigma$'s are the appropriate cross sections. If both targets are bombarded at the same energy and for the same length of time then $\sigma_{25}$, $\sigma_{0.52}$, and $T$ will be the same in both equations above and the following relation will hold:

$$\left(\frac{N_{0.52}}{N_{25}}\right)_a\left(\frac{N_{2.5}}{N_{0.52}}\right)_b=\frac{R_a}{R_b}=\left(\frac{p_{208}}{p_x}\right)_a\left(\frac{p_x}{p_{208}}\right)_b.$$

The two targets used were (a) natural lead and, (b) lead enriched in $Pb^{207}$. Inserting the appropriate values for the isotope percentages, one finds that the possible values of $R_a/R_b$ are: for $x=208$, the ratio should be unity. For $x=207$, the ratio is 5. If $x=206$, the ratio is 0.5. The experimentally determined yield ratios are given below for two different bombarding energies. The ratios of the $R$'s are seen to be essentially

| Bombarding energy | $R_a$ | $R_b$ | $R_a/R_b$ |
|---|---|---|---|
| 18 Mev | 11.5 | 10.2 | 1.1 |
| 20 Mev | 3.3 | 3.6 | 0.9 |

one within the accuracy of these runs. The result, then, is to show that the 25-second, as well as the 0.52-second activity, is produced from an alpha-particle bombardment of $Pb^{208}$ at energies near and below the threshold for the $(\alpha,2n)$ reaction. Taken with the chemical identification of the 25-second activity as polonium, this means that the best assignment of the state decaying by 25-second alpha emission is to $Po^{211}$ isomeric with the state giving rise to the 0.52-second activity.

In addition, this is the only polonium isotope to which the 25-second, 7.14-Mev activity can be assigned without assuming it to arise from a state having at least 1.9-Mev excitation above the ground state. This would require a very highly forbidden gamma transition to the ground state, and from what is known of nuclear energy levels there would in such an energy range be several intermediate states to which jumps could be made, not all of which could involve highly forbidden transitions also. Thus again the only possible assignment consistent with the chemical identification is to $Po^{211}$.

Some information is available which makes possible a tentative assignment of spins to the two states of $Po^{211}$. The usual data on which such assignments are made, are lacking in this case. Nothing is known of the conversion coefficients for the unobservable (in these experiments) transition between the two states, nor of more than a lower limit on the half-life for such a transition. Neither of the two spins has been measured directly, and the $K$-capture decay from $At^{211}$ to the 0.52-second state gives no information, since the $At^{211}$ spin is itself unknown. The information available concerns alpha decay to a well-known nucleus, limit on half-life for decay from upper to lower state, and relative cross sections for production of the two states.

In the ensuing discussion it will be assumed that both decays terminate at the ground state of $Pb^{207}$, which in turn allows the assignment of the entire 0.3-Mev energy difference to excitation of the 0.52-second state above the 25-second state. This assumption is made in view of the fact that the first level above the ground state in $Pb^{207}$ is at about 0.5 Mev.[21–23]

Observation of alpha half-lives and energies shows that if a nuclear radius[10] of $1.57A^{\frac{1}{3}}\times10^{-13}$ cm is used in the decay formula of Preston[11] with the observed alpha-decay energies, then the calculated decay constant for most even-even nuclides agrees with the observed. This is not the case, however, for odd-even, even-odd, or odd-odd nuclei, or for nuclei in the vicinity of the closed shells at 82 or 126 protons or neutrons.[8] In these cases the calculated value is greater than the observed, indicating that the actual decay is inhibited in some way relative to the simple decay of the even-even types.

In the case of $Po^{211}$, since it seems that both states decay to the ground state of $Pb^{207}$, the nuclear radius should be the same for both decays and should be somewhat below the $A^{\frac{1}{3}}$ law prediction. By applying the most rigorous available development of the barrier penetration theory including angular momentum change,[11] and using the observed energies and several assumed radii (from 1.27 to $1.47A^{\frac{1}{3}}\times10^{-13}$ cm), it was found that the prohibition of the 25-second relative to the 0.52-second decay is accounted for by assuming an angular momentum change of 5 or 6 units for the 25-second decay, and 0 or 1 for the 0.52-second activity. This in turn implies (from the $Pb^{207}$ spin of $\frac{1}{2}$) that the spin of the 25-second state is large (9/2 to 13/2), while the spin of the $\frac{1}{2}$-second state is small (1/2 or 3/2). These calculations do not single out a well-defined nuclear radius unless some assumption is made with regard to the retardation due to even-odd nuclear character, but indicate that values between 1.3 and $1.4A^{\frac{1}{3}}\times10^{-13}$ cm are the most acceptable.

The lack of observed decay of the 0.52-second to the 25-second state, as noted above, indicates again that

[21] J. A. Harvey, M.I.T. Progress Report, Office of Naval Research Report, ONR-NP-1586, April 1, 1950 (unpublished).
[22] E. C. Campbell and M. Goodrich, Phys. Rev. **78**, 640 (1950).
[23] M. Goldhaber and R. D. Hill, Revs. Modern Phys. **24**, 179 (1952).

there is a large spin difference between the two states. Theoretical calculations of the decay constants for gamma emission,[24] including the large effects of $K$ and $L$ conversion as one must for large $Z$, are not particularly reliable for this case; however, they indicate that at least a $2^5$-pole transition would be required. Comparison with the assignments made by Goldhaber and Sunyar[25] for the isomers of $Pa^{234}$, $Hg^{199}$, and $Hg^{197}$ indicate that electric $2^4$-pole or any higher order transition should suffice to give the necessary decay constant of less than $10^{-4}$ $sec^{-1}$. These limits do not contradict the spin difference which is required by the alpha decay considerations, above, nor do they indicate which state has the higher spin.

A third indication of the large difference in spin comes from the different forms which the excitation functions for the production of the two activities take. The contrast can be most easily explained by postulating that the centrifugal barrier depresses the probability of formation of the 25-second activity for low bombarding energies. This argument agrees with the alpha-decay discussion also in the assignment of the larger spin to the 25-second state.

The one-particle model of the nucleus, particularly as developed by Mayer[26] using the assumption of strong coupling, gives an explanation of the magic numbers and predicts the spins properly in most instances for even-odd and odd-even nuclides. Goldhaber and Sunyar,[25] by making an additional assumption to cover a few special cases, are able to assign spins to a large number of isomers in such a way that they agree with the predicted sequence of levels given by Mayer. In the region in which we are interested (127 neutrons, beginning of a new shell) nothing is known of the magnitude of the splitting due to the spin-orbit coupling, but the order of levels is thought to be $1i_{11/2}$, $2g$, $3d$, $4s$, etc.

This sequence of levels would make the appearance of isomers very unlikely, and indeed the shell model predicts isomers when the odd nucleons are a few units *less* than the magic numbers, and excludes them when the nucleons are a few more than the magic numbers. This is borne out very clearly by the "islands" of isomerism. Now $Po^{211}$, with 84 protons and 127 neutrons, is positively out of a possible island of isomerism. There are indications of such an island for $N<126$ and, e.g., $Pb^{207}$ belongs to it, but $N=127$ is definitely outside of it.

We have thus to look for another type of explanation for this isomerism, and this is most likely given by the "core isomerism" first indicated by Goldhaber[27] for the case of $Mo^{93}$. Applying the ideas of Goldhaber to our case, we consider, according to the shell model, that our odd neutron is $i_{11/2}$ or $g_{9/2}$, whereas the last 2 protons in the "core" are either $(h_{9/2})^2$ or $(f_{7/2})^2$. In the ground state of the isomer, in which the core is not excited, the core has $I_{core}=0$, and $I$ for the whole nucleus is the $I_{o.n.}$ of the odd neutron; hence the $I$ of the nucleus as a whole is 11/2 or 9/2 according to whether the odd neutron is in the $i_{11/2}$ or $g_{9/2}$ state. By exciting one of the protons of the core, possibly to a configuration $(h_{9/2}f_{7/2})$, the core can assume a spin up to 8 (even parity). The ground state and the excited state of the nucleus as a whole have thus the same parity and can have a spin difference up to 8 units.

All the evidence presented here indicates that the 25-second state is the lower, and thus probably has its core in the ground state. This would mean that the spin to be assigned to this state would be most probably 9/2 in view of recent work[28] indicating the 127th neutron to be a 9/2 state. If the excited core should combine with this to give a very low spin for the 0.52-second state, all would be well, except for one sizeable difficulty, namely the very strong preference of the electron capture decay of $At^{211}$ for the 0.52-second state, which, if the spin of $At^{211}$ were $\sim 9/2$ as expected, would not seem logical with the spins postulated here.

In any event it seems quite probable that this is the second known case of core isomerism as well as the first clear-cut example of an alpha-decaying isomer.

## VII. ACKNOWLEDGMENTS

This work was guided from the start by Professor E. Segrè. In addition many helpful discussions were held with Dr. O. Chamberlain, Dr. C. Wiegand, and Dr. E. Kelly. Particular thanks are due to Dr. R. F. Leininger for his direct aid in devising and carrying out the many chemical separations described above, as well as for advice and assistance throughout the remainder of the work. Discussions with Dr. M. Goldhaber on the interpretation of the $Po^{211}$ isomerism were most valuable.

Thanks are also due to Dr. J. G. Hamilton, T. Putnam, B. Rossi and the sixty-inch cyclotron crew for their considerable cooperation and assistance. Dr. T. J. Thompson rendered able assistance in setting up and operating equipment during cyclotron bombardments.

A portion of this work was carried out while the author was a U. S. Atomic Energy Commission Pre-Doctoral Fellow.

[24] E. Segrè and A. C. Helmholz, Revs. Modern Phys. **21**, 271 (1949).
[25] M. Goldhaber and A. W. Sunyar, Phys. Rev. **83**, 906 (1951).
[26] M. G. Mayer, Phys. Rev. **78**, 16 (1950).
[27] M. Goldhaber, Phys. Rev. **89**, 1146 (1953).
[28] Fred, Tomkins, and Barnes, Phys. Rev. **92**, 1324 (1953).

# Proton-Proton Scattering at 9.7 Mev

BRUCE CORK AND WALTER HARTSOUGH
*Radiation Laboratory, Department of Physics, University of California, Berkeley, California*
(Received February 5, 1954)

The differential cross section for scattering of 9.7-Mev protons from hydrogen gas has been measured. Angles over the range from 27° to 112° in the center-of-mass system have been measured with a statistical error of less than ±1.0 percent and a probable error of ±1.1 percent has been assigned to the absolute values of differential cross section.

It is observed that within the accuracy of the measured cross section, the scattering can be described as pure $S$ wave. The phase shift analysis is reported in a following paper.

## I. INTRODUCTION

THE new 9.8-Mev Berkeley proton linear accelerator, which is to be used as an injector for the Bevatron, has been used to do proton-proton scattering. Although this energy range has been investigated by others,[1,2] the accuracy of the measurements is not sufficient to allow a critical analysis of the data.

The new proton linear accelerator[3] has a well-collimated monoenergetic beam of protons with low background radiation. It is a very stable and reliable accelerator, thus it is possible to make long runs while investigating any systematic errors that may be present in the scattering apparatus.

## II. SCATTERING AND DETECTION APPARATUS

The proton beam from the linear accelerator was focused with a set of four magnetic quadruple strong-focusing magnets[4] and then deflected 24° by a double-focusing wedge magnet (Fig. 1). The beam was then collimated by a three-slit system having graphite slits of circular cross section and of 1.00 mm thickness (Fig. 2).

The beam entered the scattering chamber through two layers of 0.0002-inch thick rubber hydrochloride.

Since the protons are scattered only in the forward direction, it is reasonable to arrange a set of fixed counter telescopes to detect the scattered protons. This greatly simplifies the scattering chamber and the detection apparatus.

A drawing of the scattering chamber is shown in Fig. 3. Pure hydrogen is admitted to the scattering chamber through a hot palladium tube, until a pressure of approximately 5-cm Hg is reached. The scattered protons are then selected by each of the several telescopes, which define the solid angle for scattering. The scattered protons leave the telescopes through a 0.001-inch thick aluminum window and enter a NaI(Tl) crystal scintillator through another 0.001-inch thick aluminum window. For large angles, the windows were made of 0.0005 Mylar. An RCA 6199 photomultiplier, followed by a linear amplifier, supplies the signals to a

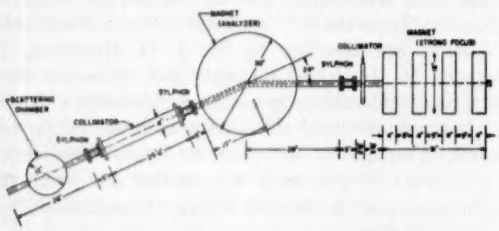

FIG. 1. Proton-proton scattering apparatus.

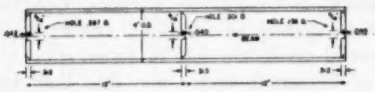

FIG. 2. Beam collimator geometry.

pulse-height discriminator and scale of 16. Three angles were measured simultaneously.

The beam current is monitored with an ionization chamber coaxial with the beam. The beam then leaves the scattering chamber through a 0.001-inch aluminum foil and enters the Faraday cup, which is used as a current integrator.

## III. SOLID-ANGLE CALCULATIONS

Since the scattering volume is defined by the counter detector telescopes, the formula of Critchfield[5] can be applied. The product of the effective scattering length $S$ and the solid angle $\Omega$ is given by the relation

$$\Omega S=\frac{HA^2}{lR_0\sin\theta}\left[1-\frac{A^2}{4l^2}+\frac{A^2}{12R_0^2}\cot^2\theta+\cdots\right],$$

where $H$ is the height of the back slit, $A$ is the width, $l$ is the separation between the front and rear slits, and $R_0$ is the distance from the back slit to the center of the scattering chamber.

The front and rear slits in the counter telescopes (Fig. 3) were made of brass ½-mm thick with 0.250-inch

[1] R. R. Wilson, Phys. Rev. **71**, 384 (1947).
[2] Allred, Armstrong, Bondelid, and Rosen, Phys. Rev. **88**, 433 (1952).
[3] Bruce Cork, University of California Radiation Laboratory Report UCRL-2385 (in preparation).
[4] Bruce Cork and Emery Zajec, University of California Radiation Laboratory Report UCRL-2182, April 15, 1953 (unpublished).
[5] Jack Benveniste and Bruce Cork, Phys. Rev. **89**, 422 (1953).

square holes accurately broached and aligned. The baffles, located as indicated, were $\frac{3}{4}$-inch diameter apertures. The telescopes define an angle of $\pm 2.0$ degrees.

## IV. METHOD OF ALIGNMENT

The center of the scattering chamber was used as the reference point, and a simple alignment jig was used in order that each counter telescope could be inserted into the wall of the chamber with its axis passing through the center of the chamber. While the jig was in place, the telescopes were soldered into the wall of the scattering chamber. After all the telescopes were soldered into place, the chamber was centered on a calibrated dividing head, and the angles were accurately measured relative to the entrance and exit ports.

The beam collimator, scattering chamber, and Faraday cup were aligned by observing the position of a spot "burned" on a glass plate where the proton beam struck it. The 12-inch diameter chamber was centered to within $\pm\frac{1}{16}$ inch or $\pm 0.6$ degree by this method.

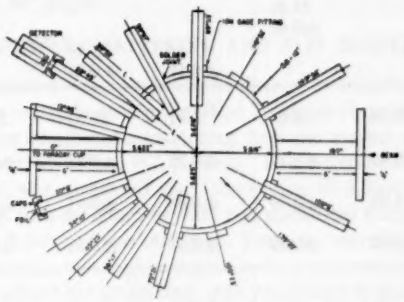

FIG. 3. Geometry of the proton-proton scattering chamber.

The differential cross section at 60° in the center-of-mass system was measured on both the left and right sides of the chamber, and the cross sections were observed to agree within the statistics of $\pm 1.0$ percent.

## V. COUNTING PROCEDURE

Since the background radiation was low and the crystal counters could easily be well shielded, the background counts were very low. This greatly simplified the procedure for obtaining counter thresholds. The RCA 6199 photomultipliers were operated at 800 volts and the linear amplifier gains were adjusted so that the proton pulses were 70 volts. Pulse-height discriminator runs were made first with protons entering the crystals and then with shutters inserted between the counter telescopes and the crystal detectors. The background was usually measured in this manner, but on occasions the hydrogen was pumped out of the scattering chamber so that if protons were scattered from the beam collimator and entered the detector telescope, they could be detected.

The discriminators were usually set to detect any

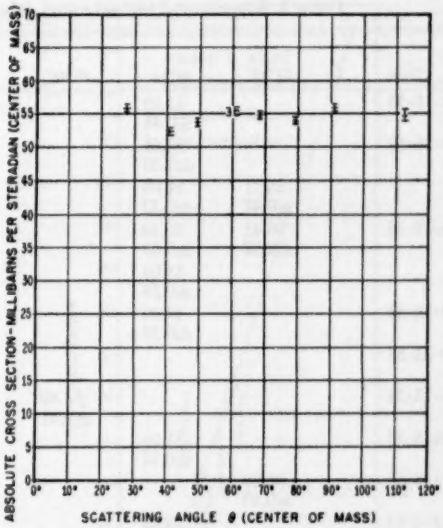


FIG. 4. Angular distribution of the absolute cross section for 9.7 Mev incident protons.

pulse height greater than 60 percent of the peak proton pulses.

However, runs were always made with discriminators adjusted over a range of 35 volts or 50 percent of the elastic proton pulse height. After the proper discriminator pulse-height settings were determined, the number of counts and background in each of three counters was measured until a total of over 10 000 counts per counter was observed. Two of the counters were then rearranged, the third left as a monitor. Seven angles could be measured to a statistical accuracy of $\pm 1.0$ percent during a ten hour day.

## VI. MEASUREMENT OF ENERGY

The scattering chamber was filled with $He^4$ to a pressure of 10-cm Hg, and a triple coincidence counter[5] was arranged to detect the protons elastically scattered from $He^4$ at an angle of 30°. The front two counters were arranged in coincidence, the third counter in anticoincidence. The elastic peak was measured by determining the amount of aluminum absorber required ahead of the counters such that protons would stop in the 1.9 mg/cm² foil separating the second and third counters. The energy was observed to be 9.73 $\pm 0.05$ Mev, and the energy spread of the elastic peak was observed to be less than $\pm 0.1$ Mev. The measurement of the energy spread was limited by the energy straggling in the aluminum absorber that was used to determine the range of the protons. Thus the actual energy spread was probably less than $\pm 0.1$ Mev.

The magnet current of the analyzing magnet was regulated and was kept constant to $\pm 0.2$ percent. Care was taken to approach the proper current in the same manner for each run, and the stability of the

TABLE I. Experimental proton-proton differential cross section $\times 10^{-27}$ cm$^2$ *versus* $\theta_{c.m.}$ at 9.73 Mev.

| Date | $\theta_{c.m.}$ 27°32′ | 40°16′ | 49°48′ | 59°38′ | 60°8′ | 68°20′ | 79°44′ | 90°50′ | 112°34′ |
|---|---|---|---|---|---|---|---|---|---|
| 9–15–53 | | 52.20 ±0.48 | | 54.82 ±0.62 | | 53.26 ±0.66 | | | |
| 9–16–53 | | 52.59 ±0.30 | | 56.22 ±0.37 | | 55.87 ±0.42 | | | |
| | 55.21 ±0.48 | 54.08 ±0.52 | | | | | | 60.02 ±1.02 | |
| 9–17–53 | 56.41 ±0.52 | 55.10 ±0.63 | | | | | | 55.60 ±1.06 | |
| | | 53.04 ±0.28 | | | | | 54.72 ±0.40 | 57.16 ±0.49 | |
| 9–18–53 | | 49.89 ±0.28 | | | | | 53.58 ±0.41 | 54.98 ±0.49 | |
| 9–23–53 | | | | | | | 55.83 ±0.44 | | 54.52 ±0.58 |
| 10–13–53 | | | 53.89 ±0.31 | | 55.38 ±0.40 | | | | |
| 11–5–53 | | 51.66 ±0.32 | | 54.25 ±0.40 | | | | 55.54 ±0.54 | |
| 11–6–53 | 56.06 ±0.30 | | | | | 53.81 ±0.47 | 52.31 ±0.48 | | |
| 12–1–53 | | 53.28 ±0.42 | | | | | | 55.52 ±0.71 | |
| 12–3–53 | | 52.61 ±0.35 | | 54.05 ±0.48 | | 55.20 ±0.49 | | | |
| | | 52.61 ±0.36 | | | | | 51.62 ±0.51 | 55.49 ±0.61 | |
| Average millibarns | 55.95 | 52.46 | 53.89 | 55.06 | 55.38 | 54.84 | 53.91 | 56.11 | 54.52 |
| Statistical error mb | ±0.23 | ±0.10 | ±0.31 | ±0.22 | ±0.40 | ±0.24 | ±0.20 | ±0.23 | ±0.58 |
| Absolute error in percent | ±0.90 | ±0.83 | ±1.00 | ±0.90 | ±1.08 | ±0.89 | ±0.88 | ±0.91 | ±1.34 |
| Absolute error millibarns | ±0.50 | ±0.43 | ±0.54 | ±0.49 | ±0.60 | ±0.49 | ±0.47 | ±0.51 | ±0.73 |

magnet was checked by using a bismuth probe[6] cooled with liquid nitrogen.

## VII. MEASUREMENT OF PRESSURE AND TEMPERATURE

The pressure of the hydrogen in the scattering chamber was measured by reading the difference in heights of a closed mercury manometer. The difference could be measured with a precision cathetometer to an accuracy of ±0.3 percent. Corrections were made for the change in density of the mercury with temperature. Since a slight amount of hydrogen leaked through the thin foil, the pressure and temperature were measured at frequent intervals. Comparison was made with another manometer and the two agreed within an accuracy of ±0.1 percent.

The temperature of the top of the scattering chamber was measured with a mercury thermometer to an accuracy of ±0.1 percent.

## VIII. MEASUREMENT OF INTEGRATED CHARGE

The Faraday cup used for these measurements has been described.[7] The charge was collected on a low-leakage 0.1-microfarad polystyrene condenser and the potential measured by connecting the Faraday cup to the grid of a 5803 electrometer tube used as a null indicator. The feedback voltage was applied to a Leeds and Northrup recording voltmeter which was self-calibrating against a standard cell. The voltmeter was also calibrated against a Leeds and Northrup potentiometer and voltage could be measured to ±0.2 percent.

The capacitance of the 0.1-microfarad condenser was measured with a General Radio 1000-cycle bridge by comparing the capacitance with a General Radio mica condenser that was calibrated by the National Bureau of Standards. The capacitance could be measured to an accuracy of ±0.2 percent.*

During runs, the pressure in the Faraday cup was always less than $10^{-5}$ mm Hg; and a bias of −90 volts was applied to the guard cylindrical electrode. It was demonstrated, by using the scattered protons as a monitor, that a bias of greater than 20 volts was required to prevent secondary electrons from leaving

[6] H. B. Keller, University of California Radiation Laboratory Report UCRL-2249, June 9, 1953 (unpublished).

[7] Cork, Johnston, and Richman, Phys. Rev. **79**, 71–80 (1950).

* *Note added in proof.*—The capacitance of these condensers was compared with a polythene condenser recently measured by the National Bureau of Standards and observed to agree within 0.2 percent.

the Faraday cup. Over the range from $-20$ volts to $-300$ volts, the "plateau" was flat to $\pm 0.4$ percent, limited by the statistical accuracy.

## IX. MEASUREMENT OF CONTAMINATION

Care was taken to keep all the internal parts of the apparatus clean. The chamber was pumped with a well trapped pump to less than $10^{-4}$ mm Hg and the rate of rise was measured with the system sealed off. The contamination over a 5-hour period was estimated to be less than 2 parts in $10^5$. Hydrogen was admitted through a directly heated palladium tube, which had been well outgassed.

Contamination was measured by inserting an aluminum foil ahead of the 40° counter. This foil was thick enough to stop protons elastically scattered from hydrogen, but protons elastically scattered from $He^4$ or heavier nuclei would be detected. Assuming the proton-proton cross section and the contamination cross section were the same in the laboratory system, the contamination background was less tha 0.3 percent at the 40° angle.

## X. MULTIPLE SCATTERING AND SLIT SCATTERING

Estimates were made of the change in counting rate due to multiple scattering. The Williams formula[8] was used for small-angle scattering, and the largest correction was less than 0.2 percent. The differential cross section was measured over the region of 3.0 cm to 30 cm Hg, and no effect beyond the statistical fluctuation of $\pm 1.0$ percent was observed. Thus, no correction was made.

To reduce slit scattering, care was taken to make the defining slits just sufficiently thick to stop the elastic protons. Also the slit widths were fairly large. The Williams formula was used to estimate the number of protons scattered from the front analyzer slit. The corrections for these scattered protons were estimated to be less than 0.2 percent for all except the 28° center-of-mass angle. Background runs were made with no gas in the scattering chamber, with the shutter ahead of the counter both in and out. The number of protons scattered from the collimator slits was less than 0.2 percent for all angles measured except 28° in the center-of-mass system. For this angle, a correction of 1.0 percent for slit scattering was made.

Table II. Summary of experimental uncertainties.

| | | Probable error (percent) |
|---|---|---|
| Proton current | a. Capacitance | $\pm 0.3$ |
| | b. Voltage | $\pm 0.2$ |
| | c. Leakage | $+0.0$ |
| Proton energy | | $\pm 0.5$ |
| Gas contamination | | $\pm 0.1$ |
| Slit scattering | | $\pm 0.2$ |
| Solid angle calculations | | $\pm 0.2$ |
| Multiple scattering | | $\pm 0.2$ |
| Statistics | | $< \pm 1.0$ |
| Pressure | | $\pm 0.3$ |
| Temperature | | $\pm 0.1$ |
| Counting losses | | $\pm 0.2$ |
| Angular resolution | | 0.0 |

[8] E. J. Williams, Proc. Roy. Soc. (London) **A169**, 531 (1939).

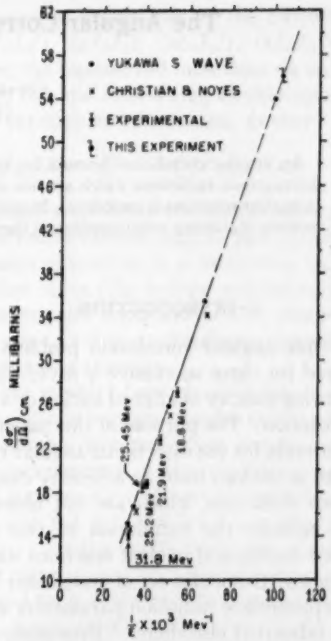


FIG. 5. Variation of the absolute differential cross section at 90° (center-of-mass system) as a function of the reciprocal of the energy of the incident protons.

## XI. RESULTS

The differential cross section in the center-of-mass system and the probable errors are listed in Table I and plotted in Fig. 4.

The 60° center-of-mass cross section to the left and to the right of the beam are observed to agree within statistics, also the 68° and 112° center-of-mass cross sections—the symmetrical angles about 90°—are observed to have the same differential cross section within statistics.

Figure 5 is an extension of previous cross section data[9,10] for the 90° center-of-mass angle.

The phase shift analysis of these data has been made by Dr. Harold Hall, and it has been observed that within the experimental accuracy of these measurements, the scattering cross section can be described by pure $S$ wave scattering.

The known errors are listed in Table II, expressed in percent.

[9] Bruce Cork, Phys. Rev. **80**, 321 (1950).

[10] J. L. Yntema and M. G. White, Princeton University Technical Report NYO-3478 (unpublished).

# The Angular Correlation of Three Nuclear Radiations

G. R. SATCHLER
*Clarendon Laboratory, Oxford, England*
(Received December 4, 1953)

An angular correlation formula for any three nuclear radiations is given, including the effects of other intermediate radiations which are not observed. Emission from aligned nuclei is also covered. Application to nuclear reactions is considered. In particular the correlation formula is given for $\gamma$ rays following inelastic neutron scattering when continuum theory is applied to the compound nucleus state.

## I. INTRODUCTION

THE triple angular correlation problem has been treated for three successive $\gamma$ rays,[1] and for two $\gamma$ rays following $\beta$ decay of aligned nuclei[2] or a deuteron-stripping reaction.[3] The purpose of this paper is to give a general formula for the directional angular correlation of any three radiations from an arbitrary cascade, with intermediate radiations which are not observed. The formalism includes the correlation of two radiations from aligned nuclei, and nuclear reactions with aligned targets. For any particular set of transitions we merely insert the appropriate radiation parameters which have been fully tabulated elsewhere.[1,3] Previously published results are then included as special cases.

Not all three radiations need be emitted. Absorption from a beam is equivalent for the purpose of defining a direction. Hence the application to a nuclear reaction followed by several emissions [such as $(p,\gamma\gamma)$ or $(n,n'\alpha)$], provided there is no interference between compound nucleus states of different spin.

Mixtures of radiation multipoles or orbital angular momenta are considered but not polarization detection. The latter would increase the complexity of the results prohibitively.

## II. CORRELATION FORMULAS

Consider the decay scheme $J_0(L_0)J_1(L_1)\cdots J_\tau(L_\tau)\times J_{\tau+1}\cdots J_s(L_s)J_{s+1}$, where the $J$ are nuclear spins and the $L$ are the total angular momenta carried away or absorbed at each transition. Using standard techniques[1] we find the angular correlation between radiations $L_0$, $L_\tau$, and $L_s$, taking the direction of $L_0$ as polar axis:

$$W(\theta,\theta_s,\phi)=\sum_{\mu\nu\lambda}A_\mu(J_0J_1)A_\lambda(J_{s+1}J_s)R_{\mu\nu\lambda}(J_\tau J_{\tau+1})\times S_{\mu\nu\lambda}(\theta,\theta_s,\phi)U_\mu(L_1J_1J_2)U_\mu(L_2J_2J_3)\cdots\times U_\mu(L_{\tau-1}J_{\tau-1}J_\tau)U_\lambda(L_{\tau+1}J_{\tau+1}J_{\tau+2})\cdots\times U_\lambda(L_{s-1}J_{s-1}J_s),\quad(1)$$

where $\phi$ is the difference in azimuth of the directions of $L_\tau$ and $L_s$. The $A_\mu$ depend only on the details of the first transition, the $A_\lambda$ only on the final transition, and the coupling term $R_{\mu\nu\lambda}$ depends only on the intermediate radiation $L_\tau$.

All dependence on unobserved radiations is thrown into the (normalized) Racah functions:[4]

$$U_\mu(LJ_1J_2)=[(2J_1+1)(2J_2+1)]^{\frac{1}{2}}(-)^{J_1+J_2-1}W(J_1J_1J_2J_2;\mu L),$$

one for each transition. If any of these radiations is "mixed" (two or more $L$ values) we have to sum over $L$ with appropriate amplitudes, but the sum is incoherent and interference terms do not appear. The *nature* of unobserved radiations is irrelevant.

The $A_{\mu,\lambda}$ have been tabulated for all forms of radiation of interest. For example, for spin-$\frac{1}{2}$ particles,

$$A_\mu(J_0J_1)=\sum_{LL'}B(L)B^*(L')\eta_\mu(LL'J_0J_1),\quad(2)$$

$$\eta_\mu=(-)^{J_0-J_1-\frac{1}{2}}[(2J_1+1)(2L+1)(2L'+1)]^{\frac{1}{2}}\times C(LL'\mu;\tfrac{1}{2}-\tfrac{1}{2})W(J_1J_1LL';\mu J_0),$$

where $\eta_\mu$ has been tabulated,[3] and the $B(L)$ are reduced matrix elements so that the fraction of intensity with $L$ is $|B(L)|^2$. $B(L)$ is real if Coulomb effects are neglected; these will introduce a phase factor $e^{i\delta l}$, where $l$ is the corresponding orbital momentum. If the only $L$'s involved are those for a single $l$, i.e., $L=l\pm\frac{1}{2}$, this phase factor drops out.

For $\gamma$ rays, in the notation of tabulated parameters,[1]

$$A_\mu(J_0J_1)=\sum_{LL'}C(L)C(L')\lambda_\mu(LL'J_0J_1),\quad(3)$$

$$\lambda_\mu=F_\mu(LJ_0J_1)\quad\text{if}\quad L'=L,$$

$$=(-)^{J_0-J_1-1}[(2J_1+1)(2L+1)(2L+3)]^{\frac{1}{2}}\times G_\mu(LJ_0J_1)\quad\text{if}\quad L'=L+1.$$

Again the fraction of intensity with $L$ is $[C(L)]^2$, with $C(L)$ real.

For conversion electrons, $\beta$ and $\alpha$ rays, we obtain $A_\mu$ by multiplying the value for $2^L$-pole $\gamma$ rays, Eq. (3), by the appropriate tabulated[1,5,6] correction factors $b_\mu(L)$.

If the nucleus is initially aligned and of spin $J_1$, the density matrix describing its orientation may always be expressed as a series of statistical tensors,[7] $B_\mu(J_1)$. In this case we omit the $L_0$ transition and replace its

[1] L. C. Biedenharn and M. E. Rose, Revs. Modern Phys. **25**, 729 (1953).
[2] J. A. M. Cox and H. A. Tolhoek, Physica **18**, 359 (1952).
[3] G. R. Satchler, Proc. Phys. Soc. (London) **A66**, 1081 (1953).
[4] L. C. Biedenharn, Oak Ridge National Laboratory Report 1098 (unpublished).
[5] Rose, Biedenharn, and Arfken, Phys. Rev. **85**, 5 (1952).
[6] M. E. Rose and L. C. Biedenharn, Oak Ridge National Laboratory Report No. 1324 (unpublished).
[7] U. Fano, Natl. Bur. Standards Rept. No. 1214 (1951) (unpublished). Our $B_\mu(J)$ is his $\langle|(JJ)\mu 0\rangle$.

parameter $A_\mu(J_0J_1)$ by $B_\mu(J_1)$. (If aligned in sense as well as direction, odd values of $\mu$ may now appear.)

$$B_\mu(J)=\sum_M(-)^{J-M}(2J+1)^{\frac{1}{2}}C(JJ\mu;M-M)W_M,$$

where $W_M$ is the relative population of the $M$ magnetic substate[8] (for example, a Boltzmann factor $ae^{\beta M}$). Then $B_0=1$ if $\sum_M W_M=1$.

The coupling term $R_{\mu\nu\lambda}$ is given by

$$R_{\mu\nu\lambda}(J_aJ_b)=\sum_{LL'}F_\nu(LL')[(2J_a+1)(2J_b+1)(2L+1)(2L'+1)]^{\frac{1}{2}}\times X(J_aJ_a\mu;LL'\nu;J_bJ_b\lambda),\quad(4)$$

$$F_\nu(LL')=C(L)C(L')(-)^{L'-1}C(LL'\nu;1-1)\quad\text{for }\gamma\text{ rays},\quad(4a)$$

or

$$F_\nu(LL')=\sum'_{ll'}S(Ll)S^*(L'l')C(ll'\nu;00)(i)^{l'-l}\times(-)^{L'-s}[(2l+1)(2l'+1)]^{\frac{1}{2}}W(LL'll';\nu s)=\sum'_{ll'}S(Ll)S^*(L'l')(-)^{L'-s}(-)^{\nu/2}\times Z(l'L'lL;s\nu),\quad(4b)$$

for particles of spin $s$ and orbital momentum $l$. The $Z$ functions are tabulated in reference 4. The primed sum over $l$, $l'$ indicates we take only even or only odd values, according to the parity change. Again the $S(Ll)$ are reduced matrix elements, real except for any Coulomb phase factor $e^{i\delta l}$. For $s=\frac{1}{2}$ (neutron or proton emission), (4b) reduces to

$$F_\nu=B(L)B^*(L')(-)^{L'-\frac{1}{2}}C(LL'\nu;\tfrac{1}{2}-\tfrac{1}{2}).\quad(4c)$$

$R_{\mu\nu\lambda}$ for pure dipole $\gamma$ rays, and the Wigner coefficients $C(LL'\nu;\frac{1}{2}-\frac{1}{2})$, have been tabulated in reference 3, and the Fano recoupling symbol $X$[7,9] defined. As before, if the $L_\tau$ radiation consists of conversion electrons, $\alpha$ or $\beta$ rays, we multiply the $F_\nu$ for $2^{L_\tau}$-pole $\gamma$ rays by the appropriate $b_\nu(L_\tau)$.[1]

The angular factor is explicitly

$$S_{\mu\nu\lambda}=4\pi\sum_m C(\nu\lambda\mu;m-m)Y_\nu^m(\theta_\tau,0)Y_\nu^{-m}(\theta_s,\phi),\quad(5)$$

where the $Y_\nu^m$ are Condon and Shortley spherical harmonics.

$R_{\mu\nu\lambda}S_{\mu\nu\lambda}$ assume very simple forms when all $(\mu\nu\lambda)\leqslant 2$ and the radiations are unmixed. These are given in reference 3 for $\gamma$ rays; for spin-$\frac{1}{2}$ particles we just replace the $F_\nu$ occurring there by the corresponding $\eta_\nu$.

Integration over the direction of any one of the three radiations immediately reduces Eq. (1) to the general double correlation formula (Appendix IV of reference 3).

The angular complexity of the correlation is restricted by the largest values of $\mu$, $\nu$, and $\lambda$. These are limited by the usual requirements for the nonvanishing of Racah functions.[4] They are always even (except for nuclear alignment, when $\mu$ may be odd) and have to satisfy triangular inequalities in the following triads: $(\mu\nu\lambda)$, $(\mu L_0L_0')$, $(\mu J_1J_1)$, $(\nu L_\tau L_\tau')$, $(\lambda L_sL_s')$, $(\lambda J_sJ_s)$. In addition, the unobserved radiations do not limit the complexity, but the intervening nuclear spins still act as "gates" for angular information, so that

$$\mu\leqslant 2J_2,\ 2J_3\cdots 2J_\tau,\quad \lambda\leqslant 2J_{\tau+1},\ 2J_{\tau+2}\cdots 2J_s.$$

To avoid possible confusion we should point out that if two unobserved radiations (e.g., $L_1$ and $L_2$) are replaced by a crossover transition in a competing cascade, one of the nuclear spins ($J_2$) is then omitted and does not restrict the angular complexity. The observed correlation, of course, is then an incoherent superposition of the two competing cascades.

Also, it has recently been shown[10] that a cascade of "basic" transitions between nuclear states whose spins form a monotonic sequence gives angular correlations which are independent of the nuclear spins and the number of intervening unobserved radiations. That is to say, if $J_1=J_2+L_1$, $J_2=J_3+L_2\cdots$ or $J_1=J_2-L_1$, $J_2=J_3-L_2\cdots$ for the unobserved part of our cascade, the angular correlation is the same as if these transitions were replaced by a single crossover with $J_1=J_\tau+L$ or $J_1=J_\tau-L$, respectively, where $L=L_1+L_2\cdots+L_{\tau-1}$. In this case, the two competing cascades mentioned above give the same correlation.

If the three observed transitions also form part of the monotonic sequence ($J_0=J_1+L_0$, etc.) reference 10 is easily extended to show that the *triple* correlation is now independent of nuclear spins and unobserved radiations; it depends only on $L_0$, $L_\tau$, and $L_s$. In fact, *any* multiple correlation from such a sequence depends only on the nature of the observed radiations.

Practical interest centers on the correlation when only one angular momentum is concerned in each transition (e.g., pure multipole $\gamma$ rays). The correlation function (1) then simplifies and gives unambiguous results which depend only on angular momenta. All dependence on unknown matrix elements $B(L)$, $C(L)$, etc., disappears.

## III. NUCLEAR REACTIONS

Blatt and Biedenharn[11] have given expressions for the angular distribution of nuclear reaction products ("double correlation"). It is clear from the complexity of their results that little is to be gained by generalizing to reactions followed by cascades of radiation. However, our formulas are easily applied when there are no

[8] N. R. Steenberg, Proc. Phys. Soc. (London) **A66**, 399 (1953).
[9] H. A. Jahn and J. Hope, Phys. Rev. **93**, 318 (1954). There, $X$ is called the "Wigner 9$j$ symbol."

[10] J. Weneser and D. R. Hamilton, Phys. Rev. **92**, 321 (1953). While the conclusions they draw are correct, the formulas contain a misprint; $j_f$ should be $j_a$ everywhere except in the last column of their paper. Their $j_f$ is defined by $j=L_n+j_f$ and is not the same as $j_n$. The products of Racah functions representing unobserved radiations reduce (in their notation) to $W(j_1j_1j_{n-1}j_{n-1};\nu L)$, where $L=L_1+L_2\cdots+L_{n-1}$; i.e., all unobserved radiations may be replaced by a single unobserved crossover with angular momentum $L$ without observable effects.
[11] J. M. Blatt and L. C. Biedenharn, Revs. Modern Phys. **25**, 258 (1953).

interference terms between compound nucleus states of different spin and parity. This occurs

(i) at resonance when the reaction proceeds through a compound state of definite spin $J_1$ and parity. The correlation formula (1) is used as it stands, the $L_0$ transition representing the capture process. Values of the matrix elements $B(L)$ for neutrons or protons when the initial and compound nuclear states obey **j-j** or **L-S** coupling rules have been given in reference 3.

(ii) if we apply continuum theory[12,13] the interference terms disappear on taking a statistical average, and the outgoing partial waves are incoherent. We may then replace the matrix elements by "transmission coefficients"[12] for the incoming and outgoing particles at energy $E$:

$$S(Ll)S^*(L'l')\rightarrow\delta(ll')T_l(E).$$

For spin-$\frac{1}{2}$ particles each $L$ implies a definite orbital $=L+\frac{1}{2}$ or $l=L-\frac{1}{2}$, but not both by parity considerations. Then the matrix elements $B(L)\equiv B(Ll)$ are a special case of $S(Ll)$, and we put

$$B(L)B^*(L')\rightarrow\delta(ll')T_l(E).$$

The sums over $L$ now reduce to two values $L=l\pm\frac{1}{2}$. The final angular correlation is then an incoherent sum of functions like (1) for different $J_1$, parity, $l_0$, and $l_1$. All unknown matrix elements have disappeared; assuming a definite nuclear model (the statistical model) we have been able to replace them by calculable transmission coefficients.

An example of interest is the $(n',\gamma)$ correlation following inelastic scattering of neutrons. Making the above assumptions, we find for emission of a $2^L$-pole $\gamma$ ray:

$$W(\theta_1\theta_2\phi)=\sum T_{l_0}(E_0)T_{l_1}(E_1)(2J_1+1)\times\sum\eta_\mu(L_0L_0'J_0J_1)F_\lambda(LJ_2J_2)\times R_{\mu\nu\lambda}(J_2J_1)S_{\mu\nu\lambda}(\theta_1\theta_2\phi), \quad (6)$$

summed over $l_0$, $l_1$, $J_1$, $\mu$, $\nu$, and $\lambda$, and $L_0$, $L_0'=l_0\pm\frac{1}{2}$, where now

$$R_{\mu\nu\lambda}=\sum(-)^{L_1'-1}[(2J_1+1)(2J_2+1)(2L_1+1)(2L_1'+1)]^{\frac{1}{2}}\times C(L_1L_1'\nu;\tfrac{1}{2}-\tfrac{1}{2})X(J_1J_1\mu;L_1L_1'\nu;J_2J_2\lambda),$$

summed over $L_1$, $L_1'=l_1\pm\frac{1}{2}$, where $E_0$, $E_1$ are the energies of the incident and scattered neutrons, respectively. Expressions for $T_l(E)$ are given in Blatt and Weisskopf.[12]

Equation (6) simplifies if the target nucleus is even-even, so that $J_0=0$, (+), and $J_1=L_0$. For fairly low $E_0$ (say about 2 Mev and below) we need only consider $s$, $p$, and $d$ waves. If the first state $J_2=2$, (+), is excited, followed by $E2$ emission ($L=2$), the $n'-\gamma$ correlation (6) becomes

$$\begin{aligned}W(\theta_1\theta_2\phi)=&T_0(E_0)T_2(E_1)[2+1.421P_2(\cos\gamma)\\&-0.571P_4(\cos\gamma)]+T_1(E_0)T_1(E_1)\{5+P_2(\cos\theta_2)\\&-1.200P_2(\cos\theta_1)+0.500P_2(\cos\gamma)\\&-0.004[\cos2\phi P_2^2(\cos\theta_1)P_2^2(\cos\theta_2)\\&-2\cos\phi P_2^1(\cos\theta_1)P_2^1(\cos\theta_2)-12P_2(\cos\theta_1)P_2(\cos\theta_2)]\\&-0.020[\cos2\phi P_2^2(\cos\theta_1)P_4^2(\cos\theta_2)\\&+12\cos\phi P_2^1(\cos\theta_1)P_4^1(\cos\theta_2)\\&+72P_2(\cos\theta_1)P_4(\cos\theta_2)]\}+T_2(E_0)T_0(E_1)\\&\times[2+2.713P_2(\cos\theta_2)-1.716P_4(\cos\theta_2)].\end{aligned}$$

The $P_\nu^m$ are (un-normalized) associated Legendre polynomials,[14] $P_1^1=\sin\theta$, etc.$\cdots$.

Since the compound state is formed isotropically by $S$ waves, the first bracket depends only on the angle $\gamma$ between the scattered neutron and the $\gamma$ ray:

$$\cos\gamma=\cos\theta_1\cos\theta_2+\sin\theta_1\sin\theta_2\cos\phi.$$

The constant terms and terms in $\theta_2$ alone are together the same as the angular distribution of the $\gamma$ rays alone, when the scattered neutrons are not observed, as may be seen by integrating over $\theta_1$, the neutron angle. Proton scattering would only mean different $T_l$'s to account for the Coulomb barrier.

Finally we note that reactions involving aligned nuclei may also be considered, provided again we have no interference between different compound nucleus spins. If we replace the $L_0$ transition by alignment according to the prescription given above, and take the $L_\nu$ radiation to be captured, not emitted, we have immediately the angular distribution of the reaction products when an unpolarized beam is fired at a target of aligned nuclei.

The author wishes to thank Dr. J. A. Spiers for advice on this problem.

[13] J. M. Blatt and V. W. Weisskopf, *Theoretical Nuclear Physics* (John Wiley and Sons, Inc., New York, 1952), Chapter VIII.

[12] O. Hittmair, Phys. Rev. 87, 375 (1952). The transmission coefficient for the outgoing neutrons, $Tl_1(E_1)$, and a factor $W(j_3s_2j_2s_1;i_2\nu)$, appear to have been omitted.

[14] E. Jahnke and F. Emde, *Tables of Functions* (Dover Publications, New York, 1945).

# Magnetic Moment of $K^{40}$ in Intermediate Coupling

G. E. TAUBER* AND TA-YOU WU
*National Research Council, Ottawa, Canada*

(Received January 15, 1954)

The $K^{40}$ nucleus is of interest since its spin $I=4$ forms a notable exception to Nordheim's rule while the observed value $\mu=-1.29\mu_N$ for the magnetic moment seems to favor the $j-j$ coupling. The theory of intermediate coupling is applied to the configuration $d^{-1}f$ with the view of accounting for the spin and the observed magnetic moment. It is found that a small spin-orbit interaction will lead to a negative magnetic moment. A central nucleon-nucleon interaction of the form $(mP+nQ)V(r_{12})$, where $P$ denotes the Majorana and $Q$ the Bartlett operator, is assumed and calculations have been carried out for the exponential, Yukawa and Gaussian types of potential $V(r_{12})$ with various "ranges." For a suitable choice of the spin-orbit interaction parameter $\zeta$, the observed magnetic moment can be obtained, the exact value of $\zeta$ depending on the type of potential and range used.

## 1. INTRODUCTION

THE spin $I=4$ of the ground state of the $K^{40}$ nucleus forms a notable exception to Nordheim's empirical rule[1] and might indicate that pure $j, j$ coupling does not hold for that nucleus. On the other hand, the negative magnetic moment $\mu=-1.29\mu_N$ observed[2] for $K^{40}$ seems to favor the $j, j$ coupling, since none of the $L, S$ states having the observed spin $I=4$, namely, $^3H_4$, $^3G_4$, $^3F_4$, and $^1G_4$, gives rise to a negative magnetic moment, whereas of the four configurations $(d_{5/2})^{-1}f_{5/2}$, $(d_{3/2})^{-1}f_{5/2}$, $(d_{5/2})^{-1}f_{7/2}$, and $(d_{3/2})^{-1}f_{7/2}$ in $j, j$ coupling, the last does give rise to a negative magnetic moment $\mu=-1.70\mu_N$.[3] It was suggested by Feenberg[3] that a possible explanation of the observed moment might be found in an intermediate coupling. In the present note, calculations of the energy levels and the magnetic moment for intermediate coupling have been carried out in the manner of a previous work of the authors.[4]

## 2. ENERGY LEVELS OF THE $d^{-1}f$ CONFIGURATION

It is reasonable, on the nuclear shell model, to take the proton-neutron configuration of the incomplete shell in the nucleus $K^{40}$ to be $d^{-1}f$, i.e., one $d$ particle missing from a closed shell and an $f$ particle. The 140 states of this configuration can be grouped in the $L, S$ limit into the levels

$$^3H_{6,5,4},\quad ^3G_{5,4,3},\quad ^3F_{4,3,2},\quad ^3P_{2,1,0},$$
$$^1H_5,\quad ^1G_4,\quad ^1F_3,\quad ^1D_2,\quad ^1P_1. \qquad (1)$$

The matrix elements of the particle-particle interaction can be calculated with the aid of the theorem of trace invariance for the case of a $d$ and an $f$ particle, if for the $d$ particle one uses the $m_l$ and $m_s$ value of the "missing" particle in the complete shell and changes the sign of the resulting matrix element.[5] This will give the correct matrix element up to an additive constant. Consider, for example, a state in the $m_l$, $m_s$ representation in which the missing $d$ particle from the closed shell $d^{10}$, denoted by $d'$ for the moment, has the quantum numbers $m_l'$, $m_s'$. The matrix elements of the particle-particle interactions in the configuration $d^{-1}f$, $d^{10}f$ are related by

$$E(d^{-1}f)=E(d^9f),$$
$$E(d^9f)=E(d^{10}f)-E([d^9]d')-E(d'f),$$

where $E([d^9],d')$ means the interaction energy between the $d'$ particle and the other nine $d$ particles. This may be written

$$E(d^9f)=E(d^{10}f)-E(d^{10})+E(d^9)-E(d'f).$$

Since the first 3 terms on the right are independent of the $m_l'$, $m_s'$ of the missing $d$ particle, we may write

$$E(d^9f)=\text{const}-E(d'f), \qquad (2)$$

in so far as relative energies of the various states in (1) are concerned.

A general nucleon-nucleon interaction of the form

$$V_{12}=(mP+nQ)V(|\mathbf{r}_1-\mathbf{r}_2|) \qquad (3)$$

has been assumed, where $P$ and $Q$ are the Majorana and Bartlett operators, respectively, and $V$ is a central potential. As we are dealing only with central interactions, the potential can be expanded in a series of Legendre polynomials and the resulting interaction expressed in terms of the Slater integrals defined by

$$F^k(a_1,a_2)=\int\int R_{a_1}^2(r_1)R_{a_2}^2(r_2)f_k(r_1r_2)dr_1dr_2$$

$$G^k(a_1,a_2)=\int\int R_{a_1}(r_1)R_{a_2}(r_2)f_k(r_1r_2)R_{a_1}(r_2)R_{a_2}(r_1)dr_1dr_2$$

where

$$f_k=\frac{2k+1}{2}\int V(|\mathbf{r}_2-\mathbf{r}_1|)P_k(\cos\omega_{12})d\cos\omega_{12}. \qquad (4)$$

* National Research Laboratories Postdoctorate Fellow.

[1] L. W. Nordheim, Phys. Rev. **78**, 294 (1950); A. de Shalit, Phys. Rev. **91**, 1479 (1953).

[2] P. F. Klinkenberg, Revs. Modern Phys. **24**, 63 (1952); Eisinger, Bederson, and Feld, Phys. Rev. **86**, 73 (1952) give $\mu=-1.30\mu_N$.

[3] E. Feenberg, Phys. Rev. **76**, 1275 (1949); I. Talmi, Phys. Rev. **83**, 1248 (1951); H. M. Schwarz, Phys. Rev. **89**, 1293 (1953).

[4] G. E. Tauber and Ta-You Wu, Phys. Rev. **93**, 295 (1954).

[5] E. U. Condon and G. H. Shortley, *Theory of Atomic Spectra* (Cambridge University Press, Cambridge, 1951), second edition.

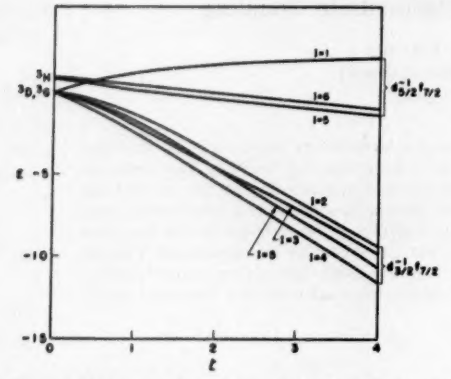


FIG. 1. Energy levels of $K^{40}$ as a function of spin-orbit parameter $\zeta$ for Yukawa potential, $r_0=1.0\times10^{-13}$ cm. Scales in Mev. Only the lowest levels are shown.

The energies of the various states in the $L-S$ limit for the $d^{-1}f$ configuration are given in Table I. The accidental degeneracy of some of these states (and vanishing matrix elements) is due to the fact that on introducing the missing particle all triplet states $(m_1m_s, m_1'm_s'|Q|m_1m_s, m_1'm_s')$ vanish on account of the spin wave functions, and that the sum of $(m_1m_s, m_1'm_s'|P|m_1m_s, m_1'm_s')$ is the same for a given value of $M$ and $S$.[6]

To evaluate the integrals $F_i$ and $G_i$, we shall assume for the radial wave functions $R$ the harmonic oscillator wave functions. The Slater integrals can be expressed in terms of the Talmi integrals $I_l$ for harmonic oscillator wave functions,[7]

$$I_l=N_l^2\int_0^\infty \exp(-\nu r^2)r^{2l+2}V(r)dr, \tag{5}$$

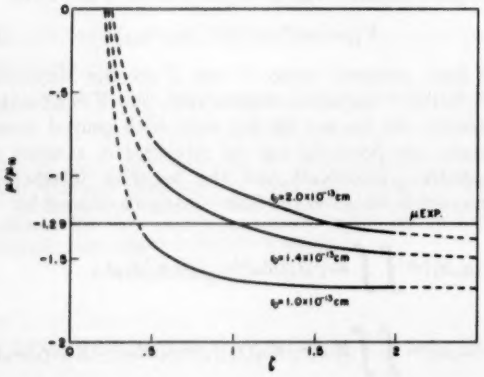


FIG. 2. Magnetic moment of $K^{40}$ as a function of spin-orbit parameter $\zeta$ for exponential potential and various ranges. Magnetic moment in units of $\mu_N$. The parameter $\zeta$ is in Mev. Dotted parts of the graphs indicate results near $L$, $S$ and $j$, $j$ limits.

[6] See reference 5, Chapter 6, Table I.
[7] I. Talmi, Helv. Phys. Acta **25**, 185 (1952).

as follows:

$$\begin{aligned}
160\,G^1&=99(I_0-I_5)+9(I_1-I_4)+38(I_2-I_3), & G_1&=G^1/35,\\
160\,G^3&=21[11(I_0-I_5)-19(I_1-I_4)+2(I_2-I_3)], & G_3&=G^3/315,\\
160\,G^5&=363[(I_0-I_5)-5(I_1-I_4)+10(I_2-I_3)], & G_5&=G^5/1524.6,\\
160\,F^0&=33(I_0+I_5)+21(I_1+I_4)+26(I_2+I_3), & F_0&=F^0,\\
160\,F^2&=15[11(I_0+I_5)-5(I_1+I_4)-6(I_2+I_3)], & F_2&=F^0/105,\\
160\,F^4&=297[(I_0+I_5)-3(I_1+I_4)+2(I_2+I_3)], & F_4&=F^4/693.
\end{aligned} \tag{6}$$

A general method for obtaining the coefficients in (6) in any problem of this kind is given in Appendix I.[8]

TABLE I. Energy states for $d3^1f$ configuration in $L-S$ limit.

| State | $P$ | $Q$ |
|---|---|---|
| $^3H$ | $-210G_5$ | 0 |
| $^1H$ | $-210G_5$ | $-2F_0-20F_2-6F_4$ |
| $^3G$ | 0 | 0 |
| $^1G$ | 0 | $-2F_0+30F_2+44F_4$ |
| $^3F$ | $-60G_3$ | 0 |
| $^1F$ | $-60G_3$ | $-2F_0+22F_2-132F_4$ |
| $^3D$ | 0 | 0 |
| $^1D$ | 0 | $-2F_0-12F_2+198F_4$ |
| $^3P$ | $-35G_1$ | 0 |
| $^1P$ | $-35G_1$ | $-2F_0-48F_2-132F_4$ |

To carry out the calculation, we have confined ourselves to the following types of potentials:[4]

$$\begin{aligned}
&\text{(i)}\quad \text{Exponential} && V(r)=V_0{}^E e^{-r/r_0},\\
&\text{(ii)}\quad \text{Yukawa} && V(r)=V_0{}^Y e^{-r/r_0}(r_0/r),\\
&\text{(iii)}\quad \text{Gaussian} && V(r)=V_0{}^G \exp(-r^2/r_0^2),
\end{aligned} \tag{7}$$

where $V_0$ is the depth and $r_0$ the "range" of the potential. These constants and $m$ and $n$ appearing in the interaction can be estimated from the data of two free nucleons.[9] With these values the Talmi integrals $I_l$ for the various interactions and ranges can be calculated, and finally the energies of the various states (Table I) can be obtained by inserting the appropriate expressions for the $F$'s and $G$'s.

In order to obtain the energy levels for any intermediate coupling between the $L$, $S$ and $j$, $j$ limits, the secular equations must be solved. From (1) it is seen that there are three equations of order 4 ($I=4$, 3 and 2), two of order 3 ($I=5$ and 1) and two linear ones ($I=6$ and 0). The spin-orbit matrices for two nucleons are known[10] and can be given in terms of two parameters

[8] A more general method, but not as readily adaptable for numerical calculations, has been given by E. H. Kronheimer, Phys. Rev. **90**, 1003 (1953).
[9] See reference 4, Table II.
[10] G. Racah, Physica **16**, 651 (1950).

$\zeta_1=\zeta_d$ and $\zeta_2=\zeta_f$. As in the shell-model of Mayer *et al.*[11] the spin-orbit interaction is to be assumed negative for particles and positive for "holes," one can write

$$\begin{aligned}&\zeta_d=\zeta, \quad (\zeta>0),\\ &\zeta_f=-a\zeta,\end{aligned} \tag{8}$$

where $a$ is an arbitrary positive constant $a\geq 1$. The secular equations are particularly simple for $a=1$ and already give a splitting of the correct order for the $d$ and $f$ levels;[12] they are given in Appendix II. The energy levels as functions of the spin-orbit parameter $\zeta$ for the various ranges and potentials considered can then be obtained by inserting the corresponding values of the $L-S$ energies and solving them numerically. Figure 1 shows the energy levels for one range in the Yukawa potential. It is seen that the lowest level has the spin $I=4$ in agreement with observation. The levels for the other types of interactions and ranges are similar.

### 3. MAGNETIC MOMENT OF $K^{40}$

The magnetic moment is given by the expectation value of the operator

$$\mu=\sum_{i=P,N}(m_l{}^i g_l{}^i+m_s{}^i g_s{}^i)\mu_N, \tag{9}$$

where $m_l{}^i$ and $m_s{}^i$ are the orbital and spin angular momentum operators of the nucleons, respectively, and $g_l{}^i$ and $g_s{}^i$ are the gyromagnetic ratios of orbit and spin, respectively, and are given by

$$\begin{aligned}&g_l{}^P=1, \qquad g_l{}^N=0,\\ &g_s{}^P=5.58, \quad g_s{}^N=-3.82.\end{aligned}$$

In order to adapt (9) to a hole-particle configuration, it is again sufficient to consider only the missing particle instead of the nearly completed shell, provided the eigenvalues of the operators $m_l{}^P$ and $m_s{}^P$ are replaced by their negatives. The appropriate wave function is found from the solution of the secular equation. For $I=4$ it is a linear combination of the (zeroth-order) wave functions corresponding to the states $^3H_4$, $^3G_4$, $^3F_4$, and $^1G_4$ and can be written as

$$\psi(4_14)=\alpha\psi(^3H_4)+\beta\psi(^1G_4)+\gamma\psi(^3F_4)+\delta\psi(^3G_4), \tag{10}$$

where the coefficients $\alpha$, $\beta$, $\gamma$, $\delta$ are obtained from the appropriate solution of the secular equation for $I=4$, and satisfy the requirement that $\alpha^2+\beta^2+\gamma^2+\delta^2=1$. The (zeroth-order) wave functions are obtained by properly combining the states corresponding to the various values of $M_l$ and $M_s$ into multiplets and are given in Appendix III. The phases have been so chosen as to give the known expressions for the spin-orbit matrices.[10]

Applying the operator $\mu$ in (9) to the wave function (10) one obtains for the magnetic moment:

$$\begin{aligned}\langle\mu\rangle/\mu_N=&1.47\alpha^2+1.4\beta^2+1.63\gamma^2+1.51\delta^2\\ &+0.43\alpha\delta-8.41\beta\delta+0.645\gamma\delta.\end{aligned} \tag{11}$$

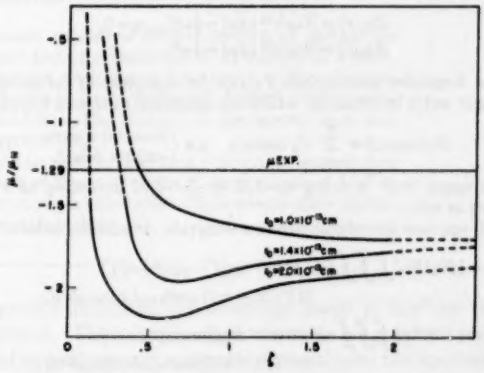


FIG. 3. Magnetic moment of $K^{40}$ as a function of spin-orbit parameter $\zeta$ for Yukawa potential and various ranges. For scale and notation see Fig. 2.

The magnetic moment as a function of the spin-orbit parameter $\zeta$ has been plotted for the various potentials and ranges considered (Figs. 2–4). From these figures it is seen that for large values of the spin-orbit parameter the $j-j$ coupling value $\mu=-1.70\mu_N$ is obtained as an asymptotic limit, and also that a comparatively small amount of spin-orbit coupling is sufficient to give the (observed) negative magnetic moment $\mu=-1.29\mu_N$. This is due to the appearance of cross terms in Eq. (11) which do not appear in the $L-S$ limiting case.[13]

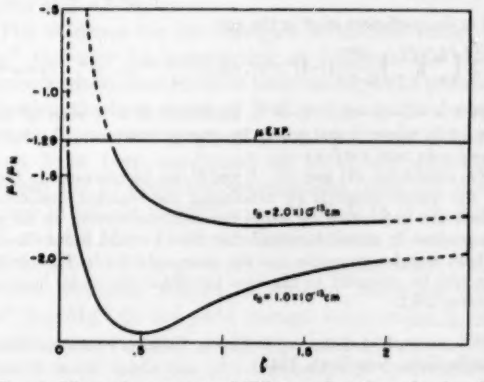


FIG. 4. Magnetic moment of $K^{40}$ as a function of spin-orbit parameter $\zeta$ for Gaussian potential and various ranges. For scale and notation see Fig. 2.

### ACKNOWLEDGMENT

We wish to express our appreciation to Miss E. Motard for carrying out the numerical calculations involved.

[11] M. G. Mayer, Phys. Rev. **74**, 235 (1948); **75**, 1969 (1949); **78**, 16 (1950). Haxel, Jensen, and Suess, Phys. Rev. **75**, 1766 (1949).

[12] The case for $a=2$ has also been considered without changing the final results materially.

[13] In the $L$, $S$ limit, the lowest level $^3G_4$ has $\mu=1.51\mu_N$.

## APPENDIX I. CALCULATION OF SLATER INTEGRALS IN TERMS OF TALMI INTEGRALS

The Slater integrals occuring in calculations of $L-S$ limit matrix elements are given by Eq. (4) of the test, where for the radial wave function we use harmonic oscillator wave functions

$$R_{n_1}(r)=Nl_1r^{l_1+1}\exp(-\tfrac{1}{2}\nu r^2),\quad n=0,$$
$$R_{n_2}(r)=Nl_2r^{l_2+1}\exp(-\tfrac{1}{2}\nu r^2).$$

The Legendre polynomials $P_k$ can be expressed in terms of a power series in $\cos\omega_{12}$ for which the coefficients are well known.[14]

$$P_k(\cos\omega_{12})=\sum_{a=0,1}^{m} C_a\cos^a\omega_{12},\quad a=\begin{cases}\text{even for } k \text{ even},\\ \text{odd for } k \text{ odd},\end{cases} \tag{12}$$

the upper limit $m$ being $m=k/2$ or $(k-1)/2$ according as $k$ is even or odd.

If one now introduces two new integrals, $A^a$ and $B^a$, defined by

$$A^a=\tfrac{1}{2}Nl_1{}^2Nl_2{}^2\int\!\!\int\!\!\int (r_1r_2)^{l_1+l_2+2}\exp[-\nu(r_1{}^2+r_2{}^2)]\times V(|\mathbf{r}_1-\mathbf{r}_2|)\cos^a\omega_{12}d\cos\omega_{12}dr_1dr_2,$$
$$B^a=\tfrac{1}{2}Nl_1{}^2Nl_2{}^2\int\!\!\int\!\!\int r_1{}^{2l_1+2}r_2{}^{2l_2+2}\exp[-\nu(r_1{}^2+r_2{}^2)]\times V(|\mathbf{r}_1-\mathbf{r}_2|)\cos^a\omega_{12}d\cos\omega_{12}dr_1dr_2, \tag{13}$$

$F$ and $G$ can be expressed as sums involving the new integrals

$$F^k=(2k+1)\sum_{a=0}^{m} C_aB^a,\quad G^k=(2k+1)\sum_{a=1}^{m} C_aA^a. \tag{14}$$

Following Talmi one now introduces new coordinates defined by

$$\mathbf{r}=\mathbf{r}_2-\mathbf{r}_1,\quad 2\mathbf{R}=\mathbf{r}_1+\mathbf{r}_2,\quad \cos\vartheta=(\mathbf{r}\cdot\mathbf{R})/rR.$$

The $R$ and $\vartheta$ integration can be done immediately, and one finally obtains for $A$ and $B$ the series

$$A^a=\sum_{s=0}^{L} K_sb_s{}^aI_s,\quad B^a=\sum_{s=0}^{L} K_sd_s{}^aI_s, \tag{15}$$

where

$$K_s=2^{-L}(1+2s)!!(2p-1)!!/(1+2l_1)!!(1+2l_2)!!;$$

$b_s{}^a$ is the coefficient of $y^a$ in the sum

$$\sum_{\sigma=0}^{(L-a)/2}\binom{(L-a)/2}{\sigma}\frac{2^{2\sigma}}{2\sigma+1}(-1)^\sigma x^\sigma y^\sigma(x+y)^{L-a-2\sigma}(x-y)^a;$$

$d_s{}^a$ is the coefficient of $y^a$ in the sum

$$\sum_{\sigma}^{L_1}\sum_{\tau}^{L_2}\binom{L_1}{\sigma}\binom{L_2}{\tau}\frac{2^{2\rho}}{2\rho+1}(-1)^\sigma x^\rho y^\rho(x+y)^{L-a-2\rho}(x-y)^a,\quad 2\rho=\sigma+\tau;$$

$n!!=n(n-2)\cdot(n-4)\cdots 2$ or 1, according as $n$ is even or odd; $L=l_1+l_2$, where $l_1$ and $l_2$ are the angular momenta, $L_1=l_1-\frac{1}{2}a$, $L_2=l_2-\frac{1}{2}a$, and $p=L+1-s$.

On combining (4) and (5), $F$ and $G$ can be expressed in terms of the Talmi integrals by tabulating the required coefficients, which are obtainable by inspection without having to do any integration. It should be noted that $B^a=A^a$ (and hence $F^k=G^k$) if both angular momenta are the same, i.e., $l_1=l_2$. The method can also be extended to the case for which the radial quantum number $n\neq 0$.

[14] See, e.g., E. Jahnke and F. Emde, *Tables of Functions* (Dover Publications, New York, 1943).

## APPENDIX II. SECULAR EQUATIONS FOR $d^{-1}f$ CONFIGURATION [FOR $a=1$ IN (8)]

$I=6$, $\quad E={}^3H-\frac{1}{2}\zeta$

$I=5$,
$$\begin{vmatrix} {}^1H-E & 0 & -\frac{1}{2}\zeta\sqrt{30}\\ 0 & {}^3G-\frac{1}{2}\zeta-E & 6\zeta/5\\ -\frac{1}{2}\zeta\sqrt{30} & 6\zeta/5 & {}^3H+\zeta/10-E\end{vmatrix}=0,$$

$I=4$,
$$\begin{vmatrix} {}^3H+3\zeta/5-E & 0 & 0 & \zeta\sqrt{88}/\sqrt{75}\\ 0 & {}^1G-E & 0 & -\zeta\sqrt{5}\\ 0 & 0 & {}^3F-3\zeta/4-E & \zeta\sqrt{125}/\sqrt{48}\\ \zeta\sqrt{88}/\sqrt{75} & -\zeta\sqrt{5} & \zeta\sqrt{125}/\sqrt{48} & {}^3G+3\zeta/20-E\end{vmatrix}=0,$$

$I=3$,
$$\begin{vmatrix} {}^3G+3\zeta/4-E & 0 & 0 & 15\zeta/\sqrt{112}\\ 0 & {}^1F-E & 0 & -\zeta/\sqrt{3}\\ 0 & 0 & {}^3D-\zeta-E & \zeta\sqrt{24}/\sqrt{7}\\ 15\zeta/\sqrt{112} & -\zeta/\sqrt{3} & \zeta\sqrt{24}/\sqrt{7} & {}^3F+\zeta/4-E\end{vmatrix}=0.$$

$I=2$,
$$\begin{vmatrix} {}^3F+\zeta-E & 0 & 0 & \zeta\sqrt{12}/\sqrt{5}\\ 0 & {}^1D-E & 0 & -\sqrt{6}\zeta/2\\ 0 & 0 & {}^3P-3\zeta/2-E & \sqrt{18}\zeta/\sqrt{5}\\ \zeta\sqrt{12}/\sqrt{5} & -\zeta\sqrt{6}/2 & \sqrt{18}\zeta/\sqrt{5} & {}^3D+\zeta/2-E\end{vmatrix}=0,$$

$I=1$,
$$\begin{vmatrix} {}^3P+3\zeta/2-E & 0 & \sqrt{2}\zeta\\ 0 & {}^1P-E & -\zeta/\sqrt{2}\\ \sqrt{2}\zeta & -\zeta/\sqrt{2} & {}^3P+3\zeta/2-E\end{vmatrix}=0,$$

$I=0$, $\quad E={}^3P+3\zeta.$

Here ${}^3H$ stands for the energy in the $L$, $S$ limit in Table I, etc.

## APPENDIX III. WAVE FUNCTIONS FOR $d^{-1}f$ CONFIGURATION

The 140 wave functions can be grouped together in states of definite $M_l$ and $M_s$ enumerated in Eq. (1) in the text. The corresponding wave functions are linear combinations of the above and can be found either by direct diagonalization or using the operators[15]

$$\mathfrak{L}_\pm=L_x\pm iL_y,\quad \mathfrak{S}_\pm=S_x\pm iS_y,\quad \mathfrak{J}_\pm=J_x\pm iJ_y.$$

The wave functions required in calculating the magnetic moment are those for which $I=M=4$ and are given in the following:[16]

$$\psi({}^3H_4)=\Big\{\frac{3}{\sqrt{20}}[\sqrt{6}(-2^-,2^-)+\sqrt{6}(-2^+,2^+)-2(-1^-,3^-)-2(-1^+,3^+)]-3\sqrt{5}(-2^+,3^-)-\frac{1}{\sqrt{30}}\times[\sqrt{10}(-2^-,1^+)-4(-1^-,2^+)+2(0^-,3^+)]\Big\}\Big/\sqrt{55},$$

$$\psi({}^3G_4)=-[\sqrt{2}(-2^-,2^-)+\sqrt{3}(-1^-,3^-)-\sqrt{2}(-2^+,2^+)-\sqrt{3}(-1^+,3^+)]/\sqrt{10},$$

$$\psi({}^3F_4)=-[\sqrt{2}(-2^-,1^+)+\sqrt{5}(-1^-,2^+)+\sqrt{5}(0^-,3^+)]/\sqrt{12},$$

$$\psi({}^3G_4)=\{2\sqrt{2}[\sqrt{2}(-2^-,2^-)+\sqrt{2}(-2^+,2^+)+\sqrt{3}(-1^-,3^-)+\sqrt{3}(-1^+,3^+)]-[\sqrt{10}(-2^-,1^+)+(-1^-,2^+)-3(0^-,3^+)]\}/10.$$

[15] N. M. Gray and L. A. Wills, Phys. Rev. **38**, 248 (1931).

[16] The first figure in each parenthesis gives the $m$ value of the "missing" proton, with the + or − denoting the $z$ component of the spin equal to $+\frac{1}{2}$ or $-\frac{1}{2}$, respectively. The second figure gives the corresponding information for the neutron.

# Scintillation Counter Study of Gamma Rays from Proton Capture in Sodium*

R. R. Carlson, E. H. Geer, and E. B. Nelson
*State University of Iowa, Iowa City, Iowa*

(Received February 26, 1954)

The spectrum of the gamma rays produced by the resonant capture of 305-kev protons by sodium has been studied with a single-crystal scintillation spectrometer having a resolution of 21 percent at 6 Mev, and with a three-crystal scintillation pair spectrometer having a resolution of 7 percent at 6 Mev. Gamma rays of energies 10.61±0.05 Mev, 7.9±0.2 Mev, 6.7±0.2 Mev, 4.2±0.1 Mev, and 1.38±0.03 Mev were observed. Cascades were found from coincidence measurements. The energies of the gamma rays and cascades are consistent with transitions between known levels of $Mg^{24}$.

The alpha decay of the 11.99-Mev $Mg^{24}$ state to the ground state of $Ne^{20}$ has been observed to be much less probable than its gamma decay. The direct gamma transition of this state to the $0^+$ ground state of $Mg^{24}$ is absent. The angular distribution of the most energetic gamma ray is anisotropic. These results allow limitations to be placed on the spin and parity of the 11.99-Mev state in $Mg^{24}$.

## INTRODUCTION

THE nuclear energy states of $Mg^{24}$ have been studied in a number of reactions and processes. The energies, spins, and parities of some of the lower states have been determined with certainty, but relatively little is known about states of higher excitation. We have studied the gamma-ray spectrum of the excited $Mg^{24}$ formed by resonant capture of 305-kev protons.

Measurements of the energies of the $Mg^{24}$ gamma rays following the beta decay of $Na^{24}$ give a precise determination of the energies of two of the lower states, at 1.38 and 4.14 Mev. The spins and parities of these states are known from gamma-gamma angular correlation[1] and internal pair conversion[2] measurements to be $2^+$ and $4^+$, respectively.

Studies of the energies of inelastically scattered proton groups from natural magnesium by Fulbright and Bush[3] were made at bombarding energies of 6.08, 9.64, and 15.30 Mev. They detected the scattered protons with photographic plates, using the magnetic field of the cyclotron for energy analysis. They observed levels at 1.00, 1.33, 1.58, 3.97, 4.17, 5.51, and 7.32 Mev and some others whose origin they question. Most of their data are consistent with previously reported values[4] within their probable error of ±0.2 Mev. Using 9.6-Mev protons, Baker, Dodd, and Simmons[5] measured the ranges of scattered protons with aluminum foils and proportional counters. They found $Mg^{24}$ levels at 1.34, 4.17, and 6.38 Mev. The first two are in good agreement with known levels, and the third agrees with results on inelastic deuteron scattering[6] from separated $Mg^{24}$. Hausman *et al.*[7] have made the most accurate determination of energy levels in $Mg^{24}$ by this method. They bombarded natural magnesium with 8-Mev protons and magnetically analyzed the scattered protons, obtaining levels at 1.38±0.02, 4.13±0.02, and 4.24±0.02 Mev, which were uniquely assigned to $Mg^{24}$ by a study of the reaction $Al^{27}(p,\alpha)Mg^{24}$.

Mandeville[8] measured the energies of the neutrons from the reaction $Na^{23}(d,n)Mg^{24}$ by the ranges of recoil protons in Ilford C2 emulsions. He found states at 0.83, 1.24, 1.66, 4.16, 7.70, and 8.64 Mev. The energies of the three higher states agree well with previous data, but the lower ones have not been observed in other reactions.

Gamma rays of many different energies result from the reaction $Na^{23}(p,\gamma)Mg^{24}$. Using a single NaI(Tl) crystal, Casson[9] found gamma rays of 10.3±0.3, 7.5 ±0.2, 6.84±0.24, 1.38±0.04 Mev, a probable gamma of 3.6±0.2 Mev, and other unresolved radiation in the region of 2–4.5 Mev.

The evidence for the energies of excited states in $Mg^{24}$ can now be summarized as follows. The most accurate measurements have been made on the gammas following the beta decay of $Na^{24}$ and on natural magnesium by scattering experiments, and some of these levels have been confirmed by work on separated isotopes and by other nuclear reactions. Thus the levels known to belong to $Mg^{24}$ are at 1.38, 4.14, 4.24, 6.38, 7.3, and 8.6 Mev. Other levels have been observed at 1.0, 1.6, and 5.5 Mev, whose isotopic assignment is uncertain. Previous studies of gamma radiation from $Na^{23}(p,\gamma)Mg^{24}$ do not yield enough information to say anything more about the energy level structure. The present work made use of a three-crystal spectrometer to improve the resolution for the higher-energy gamma-ray measurements.

## THREE-CRYSTAL SCINTILLATION SPECTROMETER

A gamma ray of energy two Mev or greater may interact in a number of different ways with a scintil-

* Supported in part by the U. S. Atomic Energy Commission.

[1] E. L. Brady and M. Deutsch, Phys. Rev. **78**, 558 (1950).
[2] S. Bloom, Phys. Rev. **88**, 312 (1952).
[3] H. W. Fulbright and R. R. Bush, Phys. Rev. **74**, 1323 (1948).
[4] T. R. Wilkins, Phys. Rev. **60**, 365 (1941); R. H. Dicke and J. Marshall, Phys. Rev. **63**, 86 (1943).
[5] Baker, Dodd, and Simmons, Phys. Rev. **85**, 1051 (1952).
[6] Massachusetts Institute of Technology Progress Report, July, 1950 (unpublished), p. 174.
[7] Hausman, Allen, Arthur, Bender, and McDole, Phys. Rev. **88**, 1296 (1952).
[8] C. E. Mandeville, Phys. Rev. **76**, 436 (1949).
[9] H. Casson, Phys. Rev. **89**, 809 (1953).

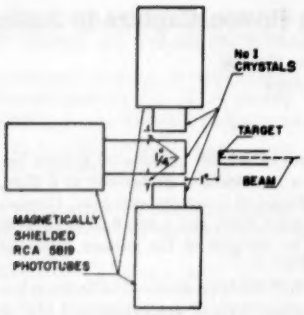


FIG. 1. Physical arrangement of three NaI crystals forming the three-crystal scintillation pair spectrometer.

lating crystal. The broad distribution of the Compton recoil electrons has a high-energy edge at about $E_\gamma - 0.5$ Mev, where $E_\gamma$ is the gamma-ray energy. From the pair process, in general, one may obtain peaks at $E_\gamma$, $E_\gamma - 0.51$ Mev, or $E_\gamma - 1.02$ Mev, as none, one, or both of the annihilation quanta escape from the crystal. The resulting confusion may be alleviated at the sacrifice of the counting rate by the use of a three-crystal pair spectrometer.[10] The annihilation radiation is detected in two crystals placed on opposite sides of a center crystal, on which the gamma ray is incident. A triple coincidence between the three crystals corresponds to an energy loss of $E_\gamma - 1.02$ Mev in the center crystal, and an analysis of the coincident pulses from the center counter yields a spectrum which is much easier to analyze than the single-crystal distribution.

A three-crystal spectrometer was arranged as in Fig. 1 in order to study the $Mg^{24}$ gamma radiation. Commercially potted NaI(Tl) crystals[11] 1½ in. in diameter, 1 in. thick, were used for the annihilation radiation detectors; the center crystal was 1½ in. in diameter and either 2 in. or 4 in. long. The RCA 5819 photomultipliers were operated at 1000 volts. The block diagram of the electronic circuits for the detection of triple coincidences and pulse-height analysis is given in Fig. 2. The pulses from the annihilation radiation crystals were limited[12] in height, their maximum height being equal to that produced by a 750-kev gamma ray, in order to detect the annihilation radiation in the presence of radiation of energy extending up to 10 Mev without overloading the amplifier, and to expand the voltage scale in the region of interest. The pulses from the three crystals were amplified by Atomic Instrument Company Model 204B amplifiers, and triple coincidences were detected by an Atomic Instrument Company Model 502, 0.5-microsecond resolving time, coincidence circuit. The spectrum of the pulses from the center crystal was analyzed with a 10-channel pulse-height analyzer,[13] which was gated by the 3-fold coincidence pulse. The pulses from the center crystal were delay-line clipped so that they were fairly flat on top for 0.5 microsecond, and then delayed by 1 microsecond before amplification in order to allow time for the gating triple coincidence pulse to open the 2-microsecond gate of the analyzer. The counting rate in the side crystal was usually several thousand per second, and about one thousand per second in the center crystal. The insertion of a 4-microsecond delay in one of the coincidence channels showed that the number of accidental triple coincidences was negligible.

The resolution of the three-crystal spectrometer has been studied with gamma rays at 4.43, 6.13, and 11.67

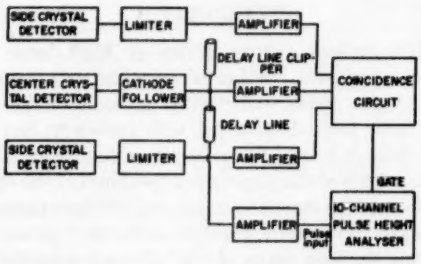


FIG. 2. Block diagram of the electronic circuits for the detection of triple coincidences in the three-crystal spectrometer and pulse-height analysis of the coincident pulses from the central crystal.

Mev, from the $B^{11}(p,\gamma)C^{12}$ and $F^{19}(p,\alpha\gamma)O^{16}$ reactions. The single-crystal and three-crystal spectra of the 6.13-Mev gamma ray detected with a 2-in. long crystal are given in Fig. 3. The requirement of a triple coincidence rejects the two higher-energy peaks, leaving the single pair peak at (6.13−1.02) Mev. The width at half-maximum of the "pair" peak has been reduced from 21 percent to 7 percent and the Compton background suppressed. At 11.67 Mev and with a 4-in. long center crystal, the three-crystal pair peak is 11 percent wide at half-maximum. The width of the three-crystal pair peak is due to photomultiplier statistics, difficulties in light collection, escape of electrons and positrons from the crystal, and bremsstrahlung produced in the crystal by the positron-electron pair. The width due to photomultiplier statistics and poor light collection should decrease for higher-energy gamma rays. The escape of the positron, electron, and bremsstrahlung would tend to broaden the peak and could account for the long tail on the low-energy side. Campbell and Boyle[14] have performed "Monte Carlo" calculations to determine the distribution in pulse height obtained with a single NaI crystal, of nearly the same size as we have used, for incident gamma-ray energies of

[10] J. K. Bair and F. C. Maienschein, Rev. Sci. Instr. **22**, 343 (1951); S. A. E. Johansson, Nature **166**, 794 (1950); Phil. Mag. **43**, 249 (1952).
[11] Harshaw Chemical Company, Cleveland, Ohio.
[12] W. C. Elmore, Rev. Sci. Instr. **20**, 963 (1949).
[13] W. C. Johnstone, Nucleonics **11**, No. 1, 36 (1953).
[14] J. G. Campbell and A. J. F. Boyle, Australian J. Phys. **6**, 171 (1953).

6 Mev, 12 Mev, and 18 Mev. They find that, for gamma-ray energies greater than 10 Mev, a significant fraction of the incident gamma-ray energy escapes from the crystal and that the fraction fluctuates. This limitation on the resolution of a single-crystal spectrometer is also present in the three-crystal spectrometer. We have observed a considerable increase in the asymmetry of the peak toward the low-energy side as $E_\gamma$ increases from 6 Mev to 12 Mev.

Accidental coincidences among the three crystals of the spectrometer have not been important at the counting rates used in our experiments. The existence of triple-gamma cascades has been established in the $Mg^{24}$ decay, and these spurious true coincidences contribute to the background. When the side counters were moved away from the center crystal so that the annihilation radiation would not contribute to triple coincidences, and the counter-target distance kept constant, the threefold coincidence rate decreased to less than 20 percent of the original value for lower-energy gamma rays and was negligible for higher-energy gamma rays. The spurious rate can be made small by moving the three crystals farther from the source, and it was this

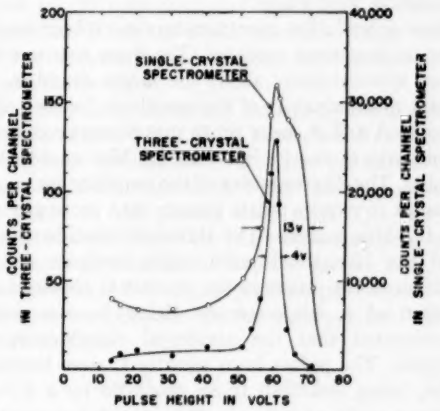


FIG. 3. Single-crystal spectrometer and three-crystal pair spectrometer measurements of the 6.13-Mev gamma ray produced in the $F^{19}(p,\alpha\gamma)O^{16}$ reaction. The 3:1 improvement in resolution and 3:1 improvement in peak-to-valley ratio are attained at a sacrifice of 250:1 in peak counting rate.

difficulty which determined the choice of distances shown in Fig. 1.

From the data shown in Fig. 3 it can be seen that the ratio of the peak counting rate of the three-crystal spectrometer to that of the single-crystal spectrometer is as 1 to 250 at 6.13 Mev. The differential pulse-height analyzer window width was 2.5 volts. Another way to express the efficiency of the three-crystal spectrometer is to give the number of counts observed in the peak per gamma ray emitted. The yield of fluorine gamma rays from a thick target is 0.1 rutherford per $\mu$a of protons. About $2.5\times10^{-6}$ count is obtained in our apparatus in the triple-coincidence peak for every 6.13-Mev gamma ray emitted. Gamma rays of energy less than about 3.0 Mev cannot be detected in our experiment because of the decrease in pair-production cross section with decreasing energy.

## PROCEDURE AND RESULTS

Protons from an rf ion source[15] were accelerated by a 500-kv Cockcroft-Walton accelerator.[16] The beam was analyzed and its energy determined by a 90° deflection magnet. The magnet was calibrated using the $B^{11}(p,\gamma)C^{12}$ reaction at 163 kev and the $F^{19}(p,\alpha\gamma)O^{16}$ reaction at 340 kev.

### 1. Energy of Gamma Radiation

Thick targets of $Na_3PO_4$ were pressed mechanically into the ends of thin-walled brass tubes and bombarded by beam currents of approximately 200 $\mu$a. The yield curve shows resonances at 225 kev and at 305 kev in agreement with Tangen.[17] The 305-kev resonance is about 100 times stronger than the 225-kev resonance, and all the gamma radiation observed was attributed to it. Particular care was taken to avoid fluorine contamination as it exhibits the strong $F^{19}(p,\alpha\gamma)O^{16}$ reaction at 340 kev. The lowest resonance in phosphorus is at 355 kev.[18] The only gamma ray produced in the $O^{16}(p,\gamma)F^{17}$ reaction has an energy less than 1 Mev.

The results of a typical run with the three-crystal spectrometer are shown in Fig. 4. The slow counting rate makes it impractical to use it for energies below about 3 Mev in this reaction. The three-crystal spectrum was obtained in about 3 hours. The width of the channels of the 10-channel analyzer, 2 volts, was checked with pulses from a mercury relay pulse generator.[19] The stability of the entire electronic system was checked frequently by increasing the signal level 8-fold by an input attenuator which precedes the amplifier,

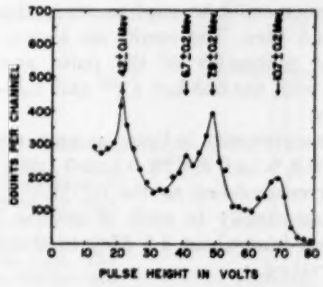


FIG. 4. Results of a three-crystal spectrometer study of gamma rays from the 11.99-Mev state of $Mg^{24}$.

[15] Moak, Reese, and Good, Nucleonics **9**, No. 3, 18 (1951).
[16] W. R. Arnold, Rev. Sci. Instr. **21**, 796 (1950).
[17] R. Tangen, Kgl. Norske Videnskab. Selskabs Skrifter, No. 1 (1946).
[18] D. E. Alburger and E. M. Hafner, Revs. Modern Phys. **22**, 373 (1950).
[19] W. C. Johnstone (private communication).

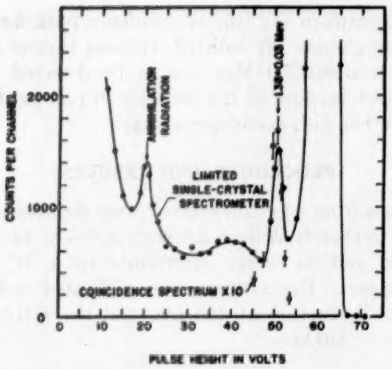


FIG. 5. The full circles show the results of a single-crystal spectrometer study of the low-energy part of the $Mg^{24}$ gamma spectrum when the pulses have been limited in height. The open circles show the results of the measurement of the energy of the low-energy gamma ray in twofold coincidence with the highest energy gamma ray of the $Mg^{24}$ spectrum.

and measuring the photopeak of the $Cs^{137}$ (663 kev) gamma ray. Shifts of the photopeak were not more than 2 percent during any of the runs. The three-crystal spectrometer was calibrated at 4.43 Mev, 6.13 Mev, and 11.67 Mev and was linear within the accuracy of measurement of the calibration points. The reaction was monitored by an integral discriminator on the center crystal of the spectrometer.

A careful search was made for the gamma radiation which would result from the direct transition to the ground state of $Mg^{24}$, at an energy of 11.99 Mev.[20] The single-crystal and three-crystal spectrometers were calibrated with the 11.67-Mev radiation from $B^{11}(p,\gamma)C^{12}$. The direct transition to the ground state was not observed, and it is estimated that its intensity is less than 2 percent of the $10.7\pm0.2$ Mev radiation.

A single-crystal spectrometer was used to study the lower-energy part of the spectrum in detail. The pulses were limited in height so that the entire voltage range of the analyzer could be used to study the spectrum from 0 to 1.5 Mev. The results are shown in Fig. 5. The energy calibration of the pulse analyzer was established with the 663-kev $Cs^{137}$ and 1.33-Mev $Co^{60}$ gamma rays.

These measurements indicate gamma rays of $10.7\pm0.2$, $7.9\pm0.2$, $6.7\pm0.2$, $4.2\pm0.1$, and $1.38\pm0.03$ Mev. The peak corresponding to the 6.7-Mev gamma ray appeared consistently in each of several runs. The energy region from about 1.5 Mev to about 3.5 Mev was not surveyed.

## 2. Coincidence Counting

The number and energies of the gamma rays emitted in $Mg^{24}$ suggest a number of cascades. Some of these were studied by coincidence counting. Two single-crystal NaI detectors and single-channel differential pulse-height analyzers (Atomic Instrument Company, Model 510) were used to show that the $10.7\pm0.2$ and $1.38\pm0.03$ Mev gamma rays are emitted in cascade. One scintillator-analyzer detected the $10.7\pm0.2$ Mev peak and the other scanned the low-energy region. The pulses from the low-energy detector were limited in height to those equivalent to 1.75 Mev, permitting greater accuracy in scanning this part of the spectrum. The number of coincidence counts as a function of the analyzer setting is given in Fig. 5. A more precise determination than from the pair spectrometer of the energy of the highest-energy gamma ray can be obtained knowing that it is in cascade with the $1.38\pm0.03$ Mev gamma rays and the energy of excitation of $Mg^{24}$. The result is $10.61\pm0.05$ Mev.

The same arrangement, minus the limiter, was used to show that the $7.9\pm0.2$ Mev gamma radiation is in cascade with $4.2\pm0.2$ Mev gamma radiation. One scintillator-analyzer detected the $7.9\pm0.2$ Mev peak and the other scanned the spectrum. The number of coincidence counts as a function of analyzer setting has the same shape as the single-crystal pulse-height distribution up to pulse heights corresponding to $4.2\pm0.2$ Mev gamma-ray energy. Beyond this point, no coincidences were found.

Three scintillation spectrometers have been used to detect triple-gamma cascades. The three counters were located symmetrically about the target chamber. The integral discriminators of the amplifiers for two of the counters, A and B, were set so that pulses produced by gamma rays of energy less than 1.4 Mev could not be detected. The discriminator of the amplifier for counter C was set to require pulses greater than those produced by a 0.7-Mev gamma. The threefold-coincidence pulse gated the 10-channel pulse-height analyzer and the spectrum of the pulses in the counter C obtained. The insertion of a 4-microsecond delay in one channel demonstrated that the accidental coincidences were negligible. The pulses from counter C were limited in height, being less than those produced by a 2.3-Mev gamma ray. The triple-coincidence peak for counter C agrees exactly with that of the 1.38-Mev gamma obtained in the single-crystal spectrometer and demonstrates that at least one triple cascade occurs via the 1.38-Mev level in $Mg^{24}$. The bias on counter C was increased so that only gamma rays of energy greater than 1.38 Mev could be counted in any counter and a significant number of triple coincidences detected.

## 3. Angular Distribution of 10.6-Mev Gamma Ray

The angular distribution with respect to the proton beam of the highest-energy gamma ray, at 10.61 Mev, was measured by discriminating against pulses from the 2-in. NaI counter produced by gamma rays of lower energy. A thick $NaAlO_2$ target on a 0.01-in. tantalum backing was bombarded with a 60-$\mu$a beam. A yield curve showed only the sodium resonance and

[20] C. W. Li, Phys. Rev. 88, 1038 (1952).

the pulse-height distribution of the gamma rays was the same as previously obtained from the $Na_3PO_4$ targets. The target disk was placed at 45° to the beam. There was a small asymmetry in the system which could be corrected by comparison with the apparent asymmetry in the angular distribution of the gamma radiation from $F^{19}(p,\alpha\gamma)O^{16}$, which is known to be isotropic.[21] The function $W=1+A\cos^2\theta$ fits the data reasonably well for measurements in the forward quadrant. The most precise result of the measurement is the anisotropy, $W(0°)/W(90°)=0.76\pm0.05$.

### 4. Alpha Decay of $Mg^{24}$

A resonance in the reaction $Na^{23}(p,\alpha)Ne^{20}$ was sought in the neighborhood of 305-kev proton energy. The alpha-particle energy would be 2.24 Mev. The target was $NaAlO_2$ on a thick brass backing at right angles to the beam, and the alpha counter was a NaI(Tl) flake on the end of a Lucite light pipe placed at an angle of 105° to the beam. The brass backing could be rotated to give target spots of $NaAlO_2$, $CaF_2$, and graphite with the same geometry in order to compare alpha and gamma yields from sodium and fluorine and to measure the background. Scattered protons were stopped by 50 microinches of nickel foil in front of the counter. Polonium alpha particles whose energy had been reduced by aluminium foils were used to calibrate the detector.

We measured A: the ratio of the alpha yield to gamma yield from sodium with a 20-$\mu$a beam, and B: the corresponding ratio for fluorine with a 3-$\mu$a beam. Let $f$ be the fraction of disintegrations of $Mg^{24}$ which proceed by alpha decay to the ground state of $Ne^{20}$, $\epsilon_1$ be the efficiency of detection of the $Mg^{24}$ alpha particles, $\eta_1$ be the efficiency of detection of the $Mg^{24}$ gamma rays, and $N_1$ be the number of disintegrations per second. For the fluorine reaction, we use the same symbols with a subscript 2. Then

$$A=N_1f\epsilon_1/[N_1(1-f)\eta_1],$$
$$B=N_2\epsilon_2/N_2\eta_2.$$

Consequently,

$$f/(1-f)=(A/B)(\eta_1/\eta_2)(\epsilon_2/\epsilon_1).$$

The ratio $\epsilon_2/\epsilon_1$ is about 0.5 and the ratio $\eta_1/\eta_2$ of the gamma efficiencies is about one. The yield of alpha particles in the $Mg^{24}$ decay did not show a resonance at 305 kev which was significantly larger than the background, while the gamma yield showed a clear resonance. After subtracting the background, our values for $A$ and $B$ are

$$A=0\pm0.03,\quad B=0.063\pm0.002,$$

from which we conclude that $f$ is at most equal to $\frac{1}{3}$.

[21] F. Ajzenberg and T. Lauritsen, Revs. Modern Phys. **24**, 321 (1952).

## DISCUSSION OF RESULTS

### 1. Gamma Radiation

The number and energies of the gamma rays observed in this study are in general agreement with the results of Casson.[9] The pair spectrometer is not suited to a study of this radiation in the 1–3 Mev region, and the single-crystal spectrum is so complex and poorly resolved that one cannot be certain of the energy of the radiation in this region. The results of a Compton spectrometer are also confused because of the large number of pulses from gamma rays of higher energy and cascade gammas of higher energy. The uncertainty in the energy measurements with the three-crystal spectrometer arises about equally from the instability of the electronic apparatus, the width of the pair peak, and the lack of adequate calibration points in the 6–10 Mev region.

The observed gamma rays may be fit into a decay scheme involving the known levels in $Mg^{24}$ as shown in Fig. 6, but the lack of precision in the knowledge of the energy of the higher states and in the gamma-ray measurements make a unique fit of all the radiation impossible. The $10.61\pm0.05$ Mev and $1.38\pm0.03$ Mev gammas are in cascade. Since the energy of the 1.38-Mev gamma ray corresponds so closely to that of the 1.38-Mev level, it appears that the decay proceeds by way of the well-known 1.38-Mev state which has spin and parity of $2^+$. The $4.2\pm0.1$ Mev gamma probably does not arise from a direct transition from the $4^+$ state at 4.14 Mev as the crossover transition is not observed in the gamma radiation following the $Na^{24}$ beta decay.[22] The discovery of the level at 4.24 Mev which is not reached in the beta decay provides a convenient explanation for the observed 4.2-Mev radiation. The 7.9 $\pm0.2$ Mev radiation may result from a transition from the capture state to the 4.24-Mev state, since it is in cascade with the 4.2-Mev gamma ray.

The triple cascade involving the 1.38-Mev gamma ray is energetically consistent with a cascade by way

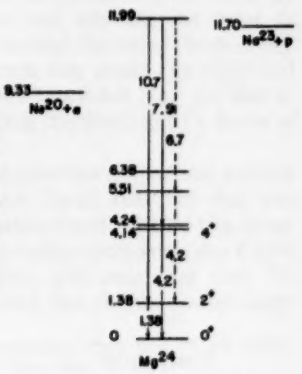


FIG. 6. The horizontal lines indicate known energy levels of $Mg^{24}$ and related nuclear configurations with their energies on the left in Mev and their spins and parities on the right. The transitions indicated are consistent with the measured gamma-ray energies and coincidences.

[22] Bishop, Wilson, and Halban, Phys. Rev. **77**, 416 (1950).

of the 5.51-Mev and 1.38-Mev levels. The triple cascades involving higher than 1.38-Mev gammas may proceed in a number of different ways which have not been identified.

### 2. Proton Capture State

The ground state of $Na^{23}$ has[23] spin $\frac{3}{2}$ and even parity.[24] For *s*-wave proton capture this limits the 11.99-Mev level in $Mg^{24}$ to $1^+$, $2^+$; for *p*-wave, to $0^-$, $1^-$, $2^-$, $3^-$; for *d* wave, to $0^+$, $1^+$, $2^+$, $3^+$, $4^+$. From the observed anisotropy of the 10.6-Mev gamma ray, we can conclude that the spin is not zero and pure *s*-wave capture does not occur. Spin values of 1 are also ruled out by the failure to observe a gamma transition to the $0^+$ ground state of $Mg^{24}$. Isotopic spin selection rules would not replace the angular momentum selection rules in this argument since it is not expected that pure isotopic spin states would be found at 11.99-Mev excitation.[25] Spin values of $3^+$ and $4^+$ would require pure *d*-wave capture which is unlikely at these bombarding energies. This leaves us with the possibilities $2^+$, $2^-$, $3^-$. Goldberg *et al.* have observed a $2^+$ level at 11.985-Mev excitation in $Mg^{24}$ in alpha scattering experiments[26] on $Ne^{20}$. Since the 11.99-Mev level in $Mg^{24}$ has a width of less than 0.5 kev and is separated by about 50 kev from nearby levels,[17] it is reasonable to identify the level studied here with that studied in the alpha-scattering experiments. This requires that both *s*- and *d*-wave protons contribute to the capture. The failure to observe alpha particles implies that the penetrability is sufficiently low for alpha particles to allow gamma radiation to compete successfully.

[23] I. I. Rabi and V. W. Cohen, Phys. Rev. **46**, 707 (1934).
[24] P. Shapiro, Phys. Rev. **93**, 290 (1954).
[25] L. Radicati, Phys. Rev. **87**, 521 (1952).
[26] Goldberg, Haeberli, Galonsky, and Douglas, Phys. Rev. **93**, 799 (1954).

# Time and Directional Study of Primary Heavy Nuclei*†

G. W. ANDERSON,‡ P. S. FREIER, AND J. E. NAUGLE
*University of Minnesota, Minneapolis, Minnesota*
(Received September 28, 1953)

The "plate mover" technique has been used in two emulsion studies of the time dependence of the flux of primary heavy nuclei ($Z \geq 10$). No evidence for the previously reported "day-night" effect was found. The angular distribution was studied on an oriented flight, and some statistically significant azimuthal asymmetries were noted, but these showed no obvious trend in time. The absorption mean free path was found to be 19 g/cm², independent of depth in the atmosphere for depths $\geq 18.5$ g/cm².

## I. INTRODUCTION

DECISIVE checks on some theories of the origin of cosmic rays would be furnished by measurements of the intensity of the primary radiation as a function of time and direction of incidence. Such measurements have been attempted often in the past,[1] but until recently, they were made only at great depths in the atmosphere where the behavior of the primary rays is obscured by that of the secondaries. The development of high-altitude, constant-level balloons has lately made it convenient to study the primary beam directly for long periods of time, so that a new approach to the time and directional measurements is possible.

The heavy-nucleus component of the primary radiation has some properties which made it especially well suited for these measurements. In the first place, the heavy nuclei observed are known either to be primary or to be fragments of heavier primary nuclei, so that at reasonably high altitudes and with sufficiently heavy nuclei one deals directly with primary particles only, while ambiguities arising from multiplication and albedo are absent from heavy nucleus measurements. Second, the lower charge-to-mass ratio for heavy nuclei allows them to pass through the earth's magnetic field at energies below the cutoff for protons, extending the range of energies over which the time and directional measurements can be made. Third, heavy nuclei can be efficiently detected with nuclear emulsions, so that the well known advantages for balloon work of this modern tool can be utilized. Special techniques for time measurements using emulsions have been developed, and are described briefly below and in more detail elsewhere.[2]

For the study of directional effects, emulsions continue to be highly effective, accepting particles from all directions at once and permitting the direction of incidence of any particular particle to be measured with great accuracy. As with any detector, however, it is necessary to know the attitude of the plates with respect to the earth in order to reduce the observed directions to geomagnetic directions.

On the other hand, by selecting heavy nuclei instead of protons for study, one sacrifices statistical accuracy in the observations, since protons are roughly 500 times more abundant in the primary flux than are heavy nuclei with charges $Z \geq 10$. In the present experiments, the counting rate was of the order of 50 particles per hour, but could have been increased simply by exposing more area of emulsion and by devoting more scanner time to the analysis.

## II. EARLIER WORK

Earlier emulsion measurements of time fluctuations in the flux of primary heavy nuclei have been quite conflicting. In 1949, the Minnesota group[3] first reported evidence for a night-time decrease in the flux of nuclei with $Z \geq 10$. The flux was found to be lower than previously measured daytime values by a factor of two to three, but the results were considered to be tentative because of the poor altitude record of the balloon. Also in 1949, Lord and Schein[4] reported similar results based on two night flights at depths in the atmosphere of 47 and 87 g/cm². They performed a more thorough experiment in 1950,[5] exposing two stacks of plates during the night, dropping one of them by parachute about sunrise, and allowing the other to remain with the balloon through the rest of the morning. By a subtraction technique they found the night and day fluxes separately, and concluded that the flux at night was lower than during the morning by a factor of $2.5 \pm 0.26$.

The Minnesota group studied the results from another night flight in 1950, and found that the flux was consistent with their daytime fluxes. In 1951 this group published a survey[6] of flux values from seven day flights and the two night flights, and concluded that the spread of the values was such that the low measurement

* This work was supported by the joint program of the U. S. Office of Naval Research and the U. S. Atomic Energy Commission.

† This paper is based on a dissertation presented by one of the authors (GWA) to the University of Minnesota in partial fulfillment of the requirements for the degree of Doctor of Philosophy.

‡ Now at Sandia Corporation, Albuquerque, New Mexico.

[1] H. Elliot, *Progress in Cosmic Ray Physics* (North Holland Publishing Company, Amsterdam, 1952), Chapter VIII.

[2] Anderson, Ney, and Thorness, Rev. Sci. Instr. **24**, 997 (1953).

[3] Freier, Ney, Naugle, and Anderson, Phys. Rev. **79**, 206 (1950).

[4] J. J. Lord and M. Schein, Phys. Rev. **78**, 484 (1950).

[5] J. J. Lord and M. Schein, Phys. Rev. **80**, 304 (1950).

[6] Freier, Anderson, Naugle, and Ney, Phys. Rev. **84**, 322 (1951).

TABLE I. Previous emulsion work on day-night effect in heavy nucleus flux.

| Date | Observer | Av. pressure ($g/cm^2$) | Method | Day flux / Night flux |
|---|---|---|---|---|
| Oct. 26–27, 1949 | Minn.[a,b] | 25 | Night flight | 2–3 (?) |
| Oct. 31–Nov. 1, 1949 | Chicago[c] | 45 | Night flight | 2.1 ±0.6 |
| Nov. 30–Dec. 1, 1949 | Chicago[c] | 87 | Night flight | 3.0 ±1.1 |
| April 13–14, 1950 | Minn.[b] | 14 | Night flight | 1.0 ±0.2 |
| May 22–23, 1950 | Chicago[a] | 15 | Drop load | 2.55±0.26 |

[a] See reference 3.
[b] See reference 6.
[c] See reference 4.

on the first night flight could have been a fluctuation consistent with fluctuations in the daytime measurements. These fluctuations could reasonably be attributed to various experimental and statistical uncertainties.

Table I summarizes the data from these emulsion experiments.

Although it did not deal with the day-night effect discussed above, the experiment of Ney and Thon[7] is relevant to the later discussion. In 1950, they employed a scintillation counter telescope to measure the flux and charge spectrum for $Z \geq 1$ at 10 $g/cm^2$. It was found that the frequency of pulses of magnitude greater than 16 times the average proton pulse increased by 35 percent between the morning (10:30 A.M.–12:20 P.M.) and the afternoon (1:20 to 3:30 P.M.) while the frequency of proton pulses remained constant within 3 percent.

## III. THE PRESENT EXPERIMENT

In view of the importance of this problem to theories of the origin of cosmic rays and of the conflicting results reviewed above, it was apparent that a more direct and more detailed measurement of the flux as a function of time was needed. The two experiments described here were designed for this purpose. The balloon flights for these experiments took place on July 31-August 1, 1952, and August 28–29, 1952. They will be referred to as the *A* experiment and the *B* experiment, respectively. Both of these experiments, as well as all others discussed in this paper, were performed at geomagneitc latitudes between 54° and 56° north.

An effect worthy of further investigation noted on both of the Minnesota night flights listed in Table I, but not found on a similar day flight, was an asymmetry in the azimuthal distribution of the heavy nucleus flux.[8] However, the evidence for this asymmetry was considered to be preliminary, since the record of the orientation on both flights was incomplete. Furthermore, on the first night flight the sphere was known to have been tilted, but an exact record of the positioning was not made during either flight. After making the most plausible corrections, it was found that on October 26, 1949, the flux as a function of azimuth varied roughly sinusoidally about the mean with an amplitude of about 50 percent of the mean and with the maximum near the west. On April 13, 1950, the asymmetry was about 10 percent with the maximum 20° west of south. Since time variations in the flux, at least any due to the rotation of the earth, would probably have such asymmetries associated with them, a further study of the azimuthal dependence of the flux was made an additional objective of experiment *A*.

## IV. APPARATUS

To obtain the heavy-nucleus flux as a function of time, a device called a "plate mover" was used. The principle of the method was first suggested by Lord and Schein,[5] while Yngve and Schein[8] have used the idea in a measurement of time variations during the daytime. The idea is simply to move one plate slowly across another during the high altitude exposure, so that the relative separation of the two segments of the track of any particle which penetrates both plates indicates the time of incidence of the particle. Details of the plate mover built for use at Minnesota are described elsewhere.[2]

In order to study directional effects, it is necessary to hold the plates in a fixed orientation with respect to the earth. The device designed for this purpose used a magnetic compass for the sensing element and coupled it to the orienting motor through a light beam and photocell system. Four plate movers arranged around the sides of a square were kept oriented to within ±10° by this system on the *A* flight, but no attempt was made to orient the *B* flight.

Among the auxiliary data recorded on both flights were the residual pressure, the history of movement of the plate movers, the levelness of the plates, and

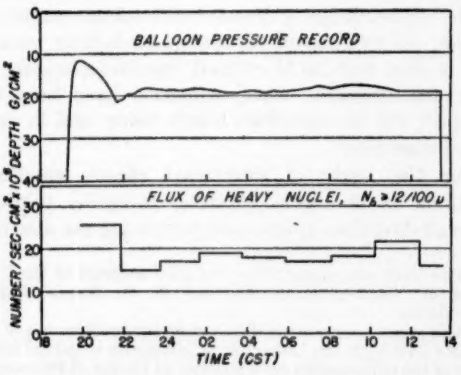


FIG. 1. The residual atmospheric pressure and heavy nuclei flux as a function of time for the July 31, 1952 flight.

[7] E. P. Ney and D. M. Thon, Phys. Rev. **81**, 1068 (1951).

[8] V. H. Yngve and M. Schein, Phys. Rev. **92**, 428 (1953).

direction of facing of the plates. Accuracy and reliability in the pressure measurements are especially important in heavy nucleus studies, because of the rapid rate of decrease of the flux with increasing atmospheric depth. Wallace and Tiernan aneroid gauges reading directly in mm Hg absolute pressure were used on both flights and were calibrated both before and after the flights by laboratory standards. Standard errors of 0.2-mm Hg for both flights were assigned to the pressure data. In addition, the pressure readings were verified by secondary instruments, a General Mills barograph on July 31 and a telemetered aneroid gauge on August 28.

A check on the levelness of the plates during exposure has been made standard practice in the Minnesota laboratory since the discovery that on two occassions the plates were tilted during the flight in spite of preflight precautions. One of these occasions was the *A* flight described herein. The recording level showed that the apparatus was tilted a constant 9 degrees from the vertical throughout the flight, in a known but varying direction with respect to the plates, the plates themselves being kept oriented in azimuth. It was estimated that owing to the rapid decrease of the heavy nucleus flux with zenith angle, a spurious azimuthal asymmetry of as much as 34 percent could have appeared in the data if the tilt had not been detected or had remained uncorrected. From the attitude of the plates as a function of time, however, the corrections were made, with the result that the directional data are believed to be free of large systematic errors arising from the tilt, but are somewhat less accurate because of the introduction of experimental errors in measurement of the parameters of the tilt. The time-variation data are negligibly affected by the tilt, since the plates were arranged symmetrically around the sides of a square, and equal areas were scanned on each plate. The recording level on the August 28 flight showed that the plates were vertical within one degree.

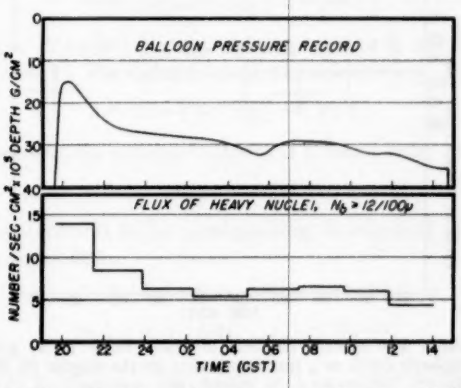


FIG. 2. The residual atmospheric pressure and heavy nuclei flux as a function of time for the August 28, 1952 flight.

TABLE II. Relative flux of heavy nuclei as a function of time.

| Flight | Period | Time start CST | *N* | *dN/dtdA* (corr.) percent of average |
|---|---|---|---|---|
| *A* (July 31) | 2 | 1956 | 158 | 106±9 |
| | 3 | 2151 | 92 | 86±9 |
| | 4 | 2346 | 105 | 96±10 |
| | 5 | 0142 | 127 | 109±10 |
| | 6 | 0347 | 121 | 104±9 |
| | 7 | 0554 | 117 | 94±9 |
| | 8 | 0803 | 127 | 98±9 |
| | 9 | 1013 | 148 | 120±10 |
| | 10 | 1223 | 59 | 92±11 |
| *B* (Aug. 28) | 3–4 | 1929 | 151 | 101±8 |
| | 5–6 | 2126 | 118 | 101±9 |
| | 7–8 | 2354 | 91 | 91±10 |
| | 9–10 | 0226 | 79 | 87±10 |
| | 11–12 | 0502 | 88 | 112±12 |
| | 13–14 | 0730 | 83 | 108±12 |
| | 15–16 | 0943 | 74 | 114±13 |
| | 17–18 | 1153 | 53 | 92±13 |

## V. TIME VARIATION MEASUREMENTS

Ilford G-5 plates of 400-micron thickness were used in both experiments, and were processed by the temperature cycle method. The plates were scanned for tracks having at least 12 delta rays per 100 microns, which corresponds to accepting only those heavy nuclei having an atomic number of at least 10.[6] A total area of 179.4 cm² was searched on the *A*-flight plates, and 213.2 cm² on the *B*-flight plates. The total numbers of $Z \geq 10$ tracks analyzed were 1110 and 773, respectively, for the two flights.

Pressure-*versus*-time curves for the two flights are given in the upper parts of Figs. 1 and 2, while in the lower parts are plotted the numbers of particles per unit time and unit area on the plates, for qualitative comparison with the upper graphs. Since the flux data are dependent on the instantaneous atmospheric depth of the plates, it is necessary to reduce them to corresponding data at a common reference depth in order to search for time variations in the primary flux. The expected variation of the flux with depth can be deduced from the observed variation with zenith angle, described in part VIII. The desired reduction function results from integrating Eq. (8), part VIII, with the aid of the Bessel-Integral functions tabulated by Bickley and Nayler.[9]

The relative numbers of particles per unit time after correction for altitude changes are given in Table II and are plotted in Figs. 3 and 4. It may be noted on the altitude record of the *A* flight that except for the initial overshoot, the balloon remained at a depth between 18 and 19 g/cm² throughout the flight, so that the corrections for altitude changes amounted to less than four percent during this level part. In contrast, the relatively small overshoot of 3 g/cm² necessitated a correction of 35 percent, illustrating the importance of accurate pressure measurements on experiments dealing

[9] W. G. Bickley and J. Nayler, Phil. Mag. **20**, 343 (1935).

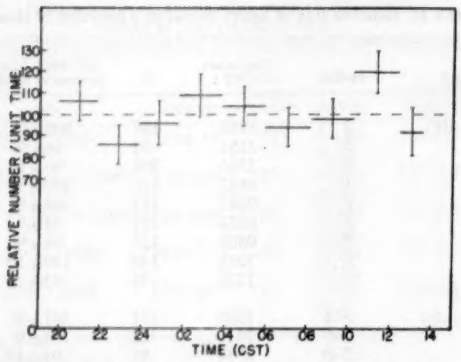


FIG. 3. The relative numbers of a heavy nuclei at 18.5 g/cm² atmospheric depth as a function of time on the July 31, 1952 flight.

with heavy nuclei. For the *B* flight, the corrections were at most 15 percent, except during the initial overshoot of the balloon.

There is clearly no evidence for a large nighttime decrease in the flux on either of the dates of these two experiments. For quantitative comparison with previous work, the "night" may be defined as the period from about midnight until about 6 A.M., and the "day" as the period from about 6 A.M. until about noon, the exact times being determined by the times at which the plate movers moved. Thus defined, the daytime flux is found to be 6±8 percent higher than the nighttime flux during the July 31 flight and 15±9 percent higher during the August 28 flight. The latter figure, however, is subject to experimental uncertainties of the order of 5 percent in addition to the statistical uncertainty quoted, because relatively large and somewhat approximate corrections for altitude changes were necessary. These figures may be contrasted with previous results of 100 to 200 percent cited above.

The small fluctuations about the mean of the points in Figs. 3 and 4 are possibly significant, however, and must be tested statistically. The direct test given by Jánossy[10] is applicable to the main part of the July 31 data since the corrections for altitude changes are small. From this test it is concluded that there is a probability of 71 percent that fluctuations this great or greater would be observed in a purely random flux having a constant average value.

For the *B*-flight data, it is necessary to apply the less direct $\chi^2$ test since the atmospheric depth at the plates changed appreciably with time. Referred to a constant at the top of the atmosphere, the probability of the observed value of $\chi^2$ is 40 percent, while a value of this probability of less than 5 percent is usually considered necessary to prove that the assumed and observed distributions are different.

These tests show, therefore, that within the statistical errors, the flux was constant in time during both flights.

[10] L. Jánossy, *Cosmic Rays* (Oxford University Press, London, 1948), p. 377.

Special attention may be directed to the anomalous flux observed at about noon on August 1 (Fig. 3), since the Chicago group has recently reported a similar deviation also at about noon.[8] The probability of occurrence of a deviation at least this great (two standard deviations) sometime during the *A* flight is 30 percent. This figure is large enough that it is not possible to assert firmly that the deviation is due to a real physical process. Furthermore, comparison of Figs. 3 and 4 shows that there is no trend to the fluctuations which is common to the data of both our *A* and *B* flights. If we consider the Chicago and Minnesota results together, however, and in addition consider the results of Ney and Thon[7] cited above, it appears that further measurements of time variations with greater statistical accuracy and with attention centered on the period about noon would be worthwhile.

Simpson[11] has reported that no special activity was recorded by his neutron monitoring network on either of the dates of these experiments. The neutron flux on July 31-August 1 was reported to be higher than average, however, since these dates occurred a few days after a 27-day maximum in the neutron intensity.

Since no evidence for the "day-night" effect was found in these experiments, it may be supposed that the effect is a sporadic one, due, say, to some sporadic solar phenomenon. However, as shown above, without plate movers or without accurate and reliable pressure information, the measurement is quite liable to error. Perhaps, therefore, the hypothesis of large sporadic day-night effects should be withheld until further evidence for them is found by the new techniques.

## VI. AZIMUTHAL ASYMMETRY MEASUREMENTS

As noted before, a search for azimuthal effects could not be undertaken until corrections were made for the effects of the tilted sphere. The result of the corrections was to define a new zenith and azimuth angle for each track, these new angles being on the average closer to

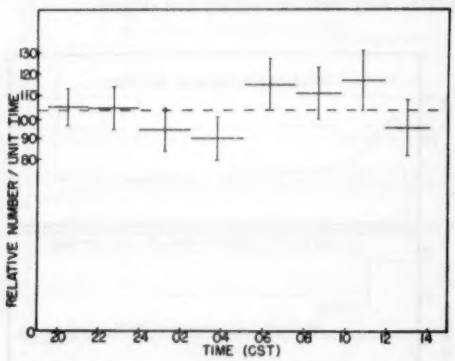


FIG. 4. The relative numbers of heavy nuclei at 30 g/cm² atmospheric depth as a function of time on the August 28, 1952 flight.

[11] Dr. J. A. Simpson (private communication).

the correct angles in an untilted system. Each track was then assigned a weighting factor $L=R/t$, where $R$ is the range of the track in the emulsion and $t$ is the thickness of the emulsion. It may easily be seen that $L$ is inversely proportional to the effective area of the plate as seen by the incoming particle, so that the tilt-corrected, weighted data are no longer dependent on the attitude of the plates. In order to reduce the number of unduly large fluctuations due to single large weights, it was desirable to assign to each track an additional weight of $\sin\theta$, where $\theta$ is the particle's zenith angle of incidence. This may be regarded as the projection of each track onto a horizontal plane on which azimuthal effects can be studied in two dimensions.

In brief, the angles measured with respect to the plates have been replaced by angles measured with respect to the earth, and the plain numbers of particles have been replaced by sums of $L'\equiv L\sin\theta$.

Geomagnetic azimuth angles $\phi$ are defined from 0–360° in the N-E-S-W sense. The azimuthal asymmetry is defined as follows:

$$\mathbf{A}=2(\Sigma\mathbf{L}'/\Sigma L'), \tag{1}$$

where $\mathbf{L}'$ is a vector denoting a track of weight $L'$ and direction of incidence $\phi$. The physical significance of this definition is that $A(=|\mathbf{A}|)$ is the ratio of the amplitude of the first Fourier component of the flux, when analyzed by azimuth angle, to the average flux per unit angle of azimuth. That is, if

$$dN/d\phi=a+b\cos(\phi-\phi_0), \tag{2}$$

then

$$a=\Sigma L'/2\pi, \quad b=|\Sigma\mathbf{L}'|/\pi, \tag{3a}$$

and

$$A=b/a. \tag{3b}$$

The direction of $\mathbf{A}$ is denoted by $\phi_0$.

Some statistical characteristics needed in the analysis are found as follows. If the angles $\phi$ for $N$ particles having *unit* weight are randomly distributed, the distribution for $A$ is given by[12]

$$P(A<A')=1-\exp[-NA'^2/4], \tag{4}$$

where $P(A<A')$ is the probability that $A$ is less than a given $A'$. The differential distribution is

$$dP/dA=\tfrac{1}{2}NA\exp[-NA^2/4]. \tag{5}$$

From this, the expected value of $A$ is found to be

$$A_{\text{exp}}=(\pi/N)^{\frac{1}{2}}. \tag{6}$$

The statistical limits corresponding to standard errors are found from

$$\begin{aligned} &P(A<A_L)=0.16, \quad A_L=0.84/N^{\frac{1}{2}}, \\ &P(A<A_U)=0.84, \quad A_U=2.70/N^{\frac{1}{2}}. \end{aligned} \tag{7}$$

[12] J. V. Uspensky, *Introduction to Mathematical Probability* (McGraw-Hill Book Company, Inc., New York, 1937), pp. 314 ff.

TABLE III. Analysis of azimuthal data, July 31–August 1, 1952.

| Period | Time, CST | $N$ | $A_{\text{exp}}$ (%) | $A_L$ (%) | $A_U$ (%) | $A_{\text{observed}}$ (%) | $\phi_0$ |
|---|---|---|---|---|---|---|---|
| 4 | Start 2346 | 97 | 22 | 11 | 32 | 34 | 290 |
| 5 | Start 0142 | 116 | 20 | 10 | 30 | 7 | 330 |
| 6 | Start 0347 | 116 | 20 | 10 | 30 | 21 | 320 |
| 7 | Start 0554 | 109 | 21 | 10 | 31 | 46 | 115 |
| 8 | Start 0803 | 121 | 20 | 10 | 31 | 9 | 315 |
| 9 | Start 1013 | 140 | 18 | 9 | 28 | 32 | 010 |
| 10 | Start 1223 | 57 | 28 | 13 | 42 | 34 | 220 |
| | End 1333 | | | | | | |
| 4–10 | 2346–1333 | 756 | 8 | 4 | 14 | 7 | 345 |

The data used to find the observed $A$ are not of unit weight, as assumed in the above analysis. A more detailed calculation taking into account the weights shows that the above distribution should be broadened by the factor $(0.53+0.20\ln N)^{\frac{1}{2}}$, so that $A_L$, $A_{\text{exp}}$ and $A_U$ as given above are increased somewhat, e.g., by a factor of 1.20 when $N=100$.

Table III gives the results of the azimuthal analysis for each plate mover period during the level part of the flight, as well as for all of these periods considered together.

The observed asymmetries are seen to vary considerably, including values both larger and smaller than the statistical limits calculated for a symmetrical random process. The smaller values are clearly statistical fluctuations, since no easily imagined physical process would produce a flux of particles coherently symmetrical in their directions of incidence. In periods 4, 7, and 9, the asymmetries observed are larger than those expected in a random process, and may represent real physical effects. However, there is no obvious trend from period to period in either the magnitude or the direction of the effect. This fact prevents explaining the effect by the simplest type of mechanism for producing asymmetries, namely, an anisotropic flux which appears on earth to change direction because of the earth's rotation. The observed asymmetry for the combined periods agrees with the value predicted on the basis of a symmetrical random flux.

It should be noted that under the conditions of this experiment, it would be impossible to detect asymmetries due to geomagnetic effects. At 55° geomagnetic latitude the energy cutoffs for a zenith angle of 60° for the eastern and western directions are, respectively, 0.33 and 0.25 Bev/nucleon, which means for $Z\geq 10$, ionization range cutoffs of 12.8 and 8 g/cm². Therefore, none of the particles in this geomagnetic-sensitive energy region would reach the plates at a depth of 18.5 g/cm².

## VII. ABSOLUTE FLUX

The heavy nucleus flux in absolute units as determined by these experiments is shown in Fig. 5 along with the daytime flux previously measured in this laboratory.

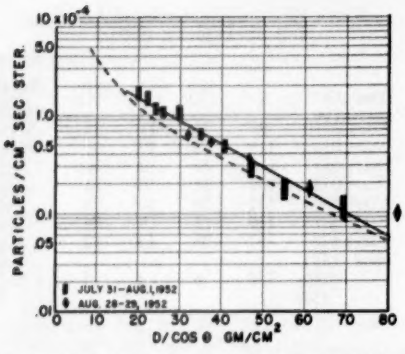


FIG. 5. The flux of $Z \geq 10$ nuclei at geomagnetic latitude of 55°N on the July 31 and August 28 flights. The dashed curve is the average of seven other flights reported in reference 6.

Whereas the time and directional variation results of these experiments depend essentially on internal comparisons within a body of data, the absolute flux determinations requires a knowledge of several additional factors. One of these is the absolute residual atmospheric pressure; this was known with relatively good accuracy and reliability for these experiments, as discussed before. Further, the use of plate movers made it possible to eliminate from the data those tracks formed during the nonlevel parts of the flights, so that the measurements are for nearly unique altitudes.

Another factor is the time of exposure; the uncertainty in time was negligible in these experiments. Previous measurements without plate movers, however, required a somewhat ambiguous designation of the time when the balloon reached "altitude" with a consequently great uncertainty in time of exposure on short balloon flights.

The agreement between the absolute flux measurements of these experiments and the average of the other experiments shown in Fig. 5 may be considered satisfactory, in view of the spread of the previous points.[6] The agreement between the two present experiments is especially good, and it may be hoped that the spread of the flux values on future flights will be reduced through the use of plate movers to remove some of the former experimental uncertainties.

## VIII. ZENITH ANGLE DISTRIBUTION

The exceptionally level balloon flight on July 31 offered a better than usual opportunity to study the zenith angle distribution of the flux. Only those tracks formed during the last 14 hours of the flight were used; during this time the plates remained at a depth of 18.5 g/cm² within 0.5 g/cm².

The amount of air traversed by a particle incident at zenith angle $\theta$ is $d \sec\theta$, where $d$ is the vertical depth in g/cm². The number of nuclei per unit zenith angle observed in the plates would be (for untilted plates)

$$dN/d\theta = K \exp[-d(\sec\theta)/\lambda] \sin^2\theta, \qquad (8)$$

where $\lambda$ is the attenuation mean free path of the flux. Although this distribution is derived by considering collision losses only, it is found to fit the experimental data satisfactorily for $d \sec\theta \geq 15$ g/cm², so that the effects of stopping by ionization appear as a constant addition to the parameter $\lambda$. In Eq. (8), one factor of $\sin\theta$ enters to convert from solid angle to angle increments, and the other to account for the effective area of the vertical plate as seen by the flux. In the case of tilted plates, the second factor becomes $\sin\theta'$, where $\theta'$ is the zenith angle with respect to the plates.

A least squares fit to the data was found by putting Eq. (8) in the form

$$\log I(d \sec\theta) = \log I_0 - (d/\lambda) \sec\theta + \epsilon \sec^2\theta, \qquad (9)$$

and determining the constant coefficients $\log I_0$, $d/\lambda$, and $\epsilon$. $I(d \sec\theta)$ is the flux of $Z \geq 10$ particles/sec-cm²-sterad at the depth $d$ and zenith angle $\theta$, while $I_0$ is this flux at the top of the atmosphere. The value of $I_0$ was found experimentally to be $4.5 \times 10^{-4}$/sec-cm²-sterad, but this is of course an extrapolated value which assumes that the same absorption law holds for $d \sec\theta < 18.5$ g/cm² as does for $d \sec\theta \geq 18.5$ g/cm². There is evidence[6] that the law is in fact different at smaller depths because of ionization stopping of very low-energy particles, so that the value for $I_0$ obtained here will be useful for comparison with direct measurements at $d \approx 0$ to corroborate this evidence.

The attenuation mean free path $\lambda$ was found to be 19 g/cm² using $d = 18.5$ g/cm². The third parameter $\epsilon$ is a measure of the departure of the attenuation law from the simple exponential law, Eq. (8). Experimentally, $\epsilon$ is found to be $-0.02$, which is not significantly different from zero. Within the accuracy of this experiment, therefore, the flux is found to be absorbed truly exponentially with a mean free path of 19 g/cm² at depths greater than 18.5 g/cm².

The authors wish to express sincere thanks to Dr. E. P. Ney and Mr. R. Thorness for their part in designing the plate movers, to Dr. John Linsley for designing the prototype orienter, to Mr. A. T. Bauman and the General Mills crew for the excellent balloon flight, and to Mrs. Dawn Copeland and Mrs. La Donna Wagner for help in scanning the plates.

# Some Studies of the Products of the High-Energy Fission Process*

M. LINDNER† AND R. N. OSBORNE†
*Livermore Research Laboratory, California Research and Development Company, Livermore, California*
(Received October 16, 1953)

The energy dependence of the formation cross section of certain nuclides formed in fission of uranium and thorium has been studied. Excitation functions in the hundred-Mev region are given for $Ni^{66}$, $Zr^{97}$, $Ag^{111}$, $Ba^{131}$, and $Ba^{139}$. Protons, deuterons, and alpha particles from the Berkeley 184-inch frequency-modulated synchrocyclotron were used to induce the activities.

It was found that the yields of neutron-deficient fission products increase with energy; those with an excess of neutrons decrease in yield. Helium ions impart greater nuclear excitation than do protons of the same energy. Neutron-deficient fission products have nearly identical cross sections for formation in uranium and thorium; those with an excess of neutrons are formed in higher yield in uranium. The results indicate that some of the fissioning events may be preceded by the evaporation of about twenty-five nucleons.

## INTRODUCTION

IT has been recognized that fission induced by particles accelerated to high energies differs from low-energy induced fission. Newton,[1] in bombarding thorium with 38-Mev helium ions obtained a peak-to-valley ratio of less than two in the fission yield curve, in contrast to a value of 600 for thermal fission of $U^{235}$,[2] and of about 300 obtained by Turkevich[3] for fission of $Th^{232}$ induced by pile neutrons of average energy estimated as 2.7 Mev. It is evident, therefore, that in the range from several Mev to 38 Mev, the nature of the fission process has changed. The first radiochemical investigations of fission induced in the hundred-Mev region were made on bismuth with 190-Mev deuterons by Goeckermann and Perlman.[4] It was found that symmetrical fission was the most probable mode, and that the fission products did not all necessarily contain an excess of neutrons. O'Connor and Seaborg[5] using 380-Mev helium ions on uranium, and Folger[6] using 340-Mev protons on uranium, studied the fission product distribution, and reached conclusions similar to those of Goeckermann and Perlman. By counting fission recoils, Jungermann[7] obtained excitation functions for total fission induced in thorium and uranium with alpha particles, deuterons, and protons from threshold into the hundred-Mev region. He concluded that the total cross sections rise to constant values in this region, being largest for alpha particles, smallest for protons.

In view of the lack of information on the manner in which individual fission reactions change from threshold to the hundred-Mev region, a radiochemical study of the excitation functions for certain chosen fission products was made for uranium and thorium. The reactions were induced with helium ions, deuterons, and protons at energies from 50 Mev to 380, 190, and 340 Mev, respectively. The fission products chosen for study were $Ba^{139}$, $Ba^{131}$, $Ag^{111}$, $Zr^{97}$, and $Ni^{66}$. $Ba^{139}$, $Ag^{111}$, and $Zr^{97}$ were selected because these nuclides were considered indicative of the "symmetry" of the fission process. Since $Ni^{66}$ was found to occur as a fission product only in hundred-Mev fission,[4,6] the excitation function for this nuclide was established. $Ba^{131}$ was chosen for study because its occurrence in fission[6] was felt to be associated with an increasing yield of neutron-deficient isotopes as the available excitation energy was increased. In order to investigate further the appearance of neutron-deficient isotopes in high-energy fission, a short study was made on the isotope $Ba^{128}$ as a fission product. The $Ba^{131}$ and $Ba^{128}$ had to be detected through their respective cesium daughters because of the preponderance of $Ba^{140}$ in the barium fraction.

## EXPERIMENTAL PROCEDURE

### Bombardments

Uranium and thorium foils from one to ten mils thick were bombarded for from several minutes to several hours with helium ions, deuterons, or protons in the 184-inch cyclotron at Berkeley.

Proton and deuteron bombardments were always made in the internal circulating beam. Probe position determined the bombarding energy. Owing to the likelihood of deuteron contamination of the circulating alpha particle beam, helium-ion bombardments were carried out using the pulse-deflected helium ion beam synchronized with the pulsed-arc source. The stacked-foil technique was used with aluminum absorbers to achieve the various energies needed to establish the excitation function.

* This work was performed under a contract with the U. S. Atomic Energy Commission.
† Now at the University of California Radiation Laboratory, Livermore, California.
[1] A. S. Newton, Phys. Rev. **75**, 17 (1949).
[2] A. S. Newton, J. Am. Chem. Soc. **68**, 2411 (1946).
[3] J. Niday and A. Turkevich, U. S. Atomic Energy Commission Report AECD-2862 (unpublished).
[4] R. H. Goeckermann and I. Perlman, Phys. Rev. **76**, 628 (1949).
[5] P. R. O'Connor and G. T. Seaborg, Phys. Rev. **74**, 1189 (1948).
[6] R. L. Folger, University of California Radiation Laboratory Report UCRL-1195 (unpublished).
[7] J. Jungerman, University of California Radiation Laboratory Report UCRL-436 (unpublished).

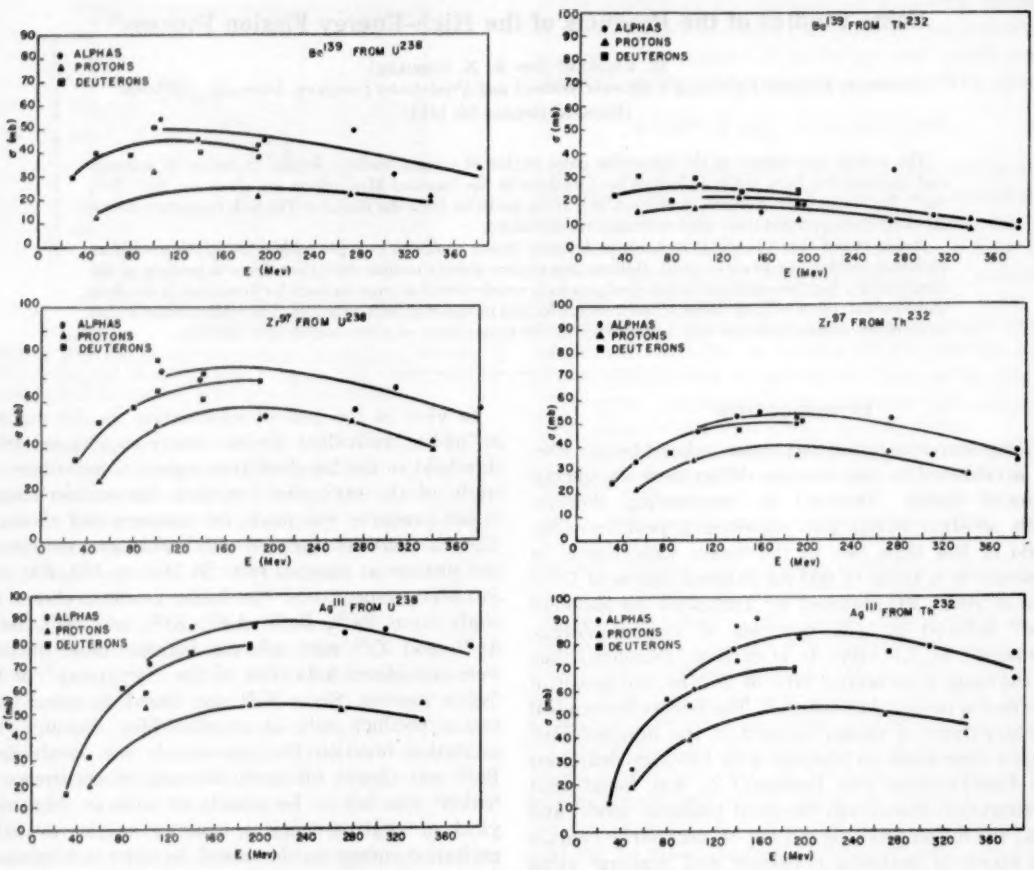


FIG. 1. Energy dependence of cross sections for formation of certain fission products of $U^{238}$ and $Th^{232}$.

All bombardments were monitored with aluminum foils; cross sections for $Na^{24}$ production from aluminum are based upon data of Stevenson and Folger for protons,[8] of Batzel and Crane for deuterons,[9] and of the authors for helium ions.[10]

## Chemical Procedures

### *A. $Ba^{139}$, $Ag^{111}$, and $Zr^{97}$*

The irradiated uranium or thorium target was dissolved in concentrated nitric acid which contained the barium, zirconium, and silver carriers.

Barium was precipitated with fuming nitric acid, purified by precipitation with ether-hydrochloric acid mixture, and finally separated from radium isotopes by elution with *p*H 7.8 citrate solution from a "Dowex 50" cation exchange column. It was finally weighed as the chromate.

Zirconium was extracted from the diluted nitric acid into a benzene solution of thenoyltrifluoracetone. It was then extracted into and precipitated by dilute metaphosphoric acid, ignited, and weighed as the pyrophosphate.

Silver was isolated as the chloride and repurified by a series of chloride precipitations alternated with an acid sulfide precipitation in the presence of iodide and several ferric hydroxide scavenges. It was finally weighed as the chloride.

### *B. $Ba^{131}$ and $Ni^{66}$*

The irradiated uranium and thorium targets were dissolved in concentrated nitric acid which contained barium and nickel carriers.

Barium was isolated and purified by one nitrate and two chloride precipitations (above). It was then weighed as the carbonate. After standing for two weeks the carbonate was dissolved, cesium and lanthanum carriers added, and the cesium isolated and weighed as the perchlorate.

[8] P. C. Stevenson and R. L. Folger (unpublished data).
[9] Batzel, Crane, and O'Kelley, Phys. Rev. **91**, 939 (1953).
[10] M. Lindner and R. N. Osborne, Phys. Rev. **91**, 342 (1953).

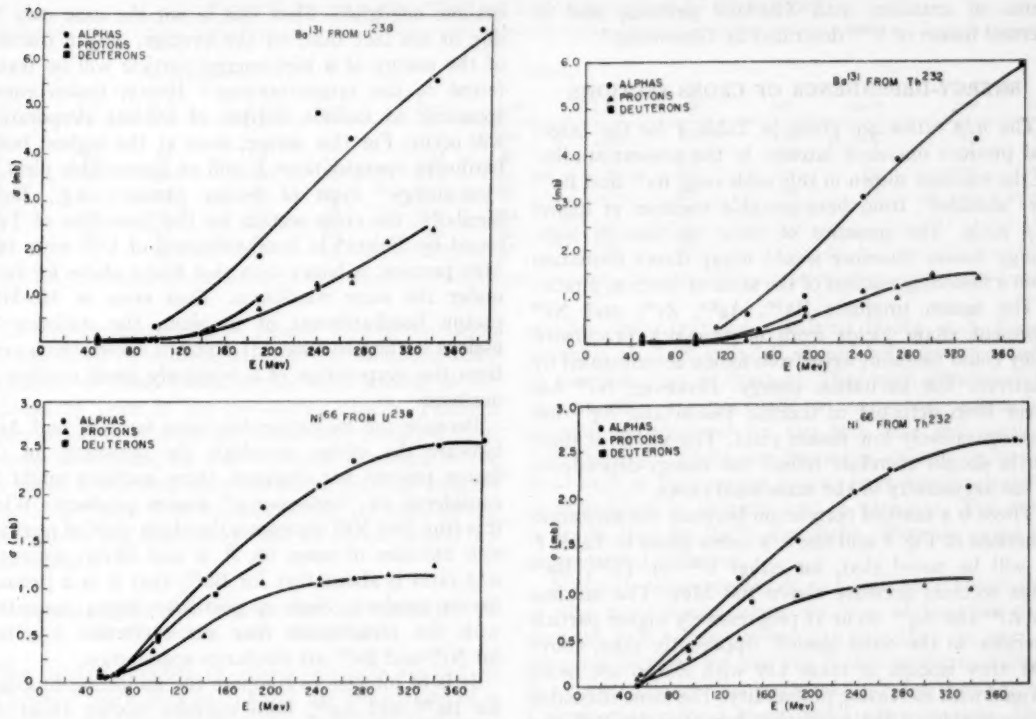


FIG. 1.—*Continued.*

Nickel was isolated and purified by repeated precipitations with dimethylglyoxime from ammoniacal solution. Palladium contamination was removed by absorption of this fission product on a Dowex A-2 anion exchange resin from a *3N* hydrochloric acid solution of the isolated nickel. The nickel was then precipitated from ammoniacal solution as the dimethylglyoxime and weighed in this form.

### *$Ba^{128}$*

The chemical procedure was similar to that for $Ba^{131}$ except that the barium fraction was allowed to stand for half an hour only, and the cesium perchlorate was rapidly dissolved and reprecipitated twice in the presence of barium and lanthanum carriers in water-free fumed perchloric acid solution.

### *Counting Techniques*

All counting of beta radiation was performed with an argon-alcohol-filled Tracerlab-type TGC-3A counter, using saturation back-scattering from aluminum. Since all counting rates were relative to an aluminum monitor, the cross sections were independent of counter geometry, and only slightly dependent upon backscattering, self-scattering, and air-window absorption corrections because all radioisotopes investigated emitted reasonably energetic beta radiations.

In the case of the $Cs^{131}$ daughter of $Ba^{131}$, the nuclide was detected by counting all the *K*-x-rays on a sodium iodide scintillation counter of known geometry coupled with a single-channel pulse analyzer. The disintegration rate of the aluminum monitor was in this case determined on a proportional counter of 100 percent geometry.

Corrections for fission recoil losses were made on all bombardments of one-mil foils. These corrections, determined experimentally for $Ag^{111}$, $Ba^{139}$, and $Zr^{97}$, amounted to from 10 to 18 percent.

Nuclear absorption corrections were made in the stacked-foil helium ion bombardments. For this purpose the calculated geometrical cross section of 0.64 barn for the aluminum constituting the absorber was used.

## DISCUSSION OF RESULTS

### The Fission Model

The model described by Goeckermann and Perlman[4] for the fission of bismuth with 190-Mev deuterons, will be adopted. It is also assumed that for a given mass chain, a distribution of primary fission products exists, and that this distribution roughly approximates a Gaussian. This assumption is consistent with independent mass yield studies made by Folger[6] on isobars of masses 83, 111, 140, 156, and 166 in bombard-

ments of uranium with 340-Mev protons, and in thermal fission of $U^{235}$ described by Glendenin.[11]

## ENERGY-DEPENDENCE OF CROSS SECTIONS

The $n/p$ ratios are given in Table I for the target and product nuclei of interest in the present studies. Of the nuclides shown in this table only $Ba^{131}$ and $Ba^{128}$ are "shielded" from beta-unstable nuclides of higher $n/p$ ratio. The presence of these nuclides in high-energy fission therefore would imply direct formation from a fissioning nucleus of the same or lower $n/p$ ratio.

The fission products $Ba^{139}$, $Ag^{111}$, $Zr^{97}$, and $Ni^{66}$ represent chain yields from neutron-rich precursors. They could therefore arise from fission accompanied by relatively low excitation energy. However, $Ni^{66}$ has never been detected in thermal fission and $Ag^{111}$ has a comparatively low fission yield. The yields of these nuclei should therefore reflect the energy-dependence of the asymmetry of the mass-yield curve.

There is a marked correlation between the excitation functions of Fig. 1 and the $n/p$ ratios given in Table I. It will be noted that, for either $U^{238}$ or $Th^{232}$, $Ba^{139}$ cross sections decrease above 100 Mev. The maxima for $Zr^{97}$ and $Ag^{111}$ occur at progressively higher particle energies, in the order named. Apparently then, above 100 Mev isobars of mass 139 with $Z>56$ are being formed with increasing probability. The same reasoning is applicable to the excitation functions for $Zr^{97}$ and $Ag^{111}$.

In order to determine whether the negative slope of the excitation functions for fission products with a high $n/p$ ratio ($Ba^{139}$, $Zr^{97}$) corresponds to increasing formation of neutron-deficient nuclides, the behavior of $Ba^{131}$ was studied. The excitation functions shown in Fig. 1 for both $U^{238}$ and $Th^{232}$ indicate thresholds of about 50 Mev. $Ba^{128}$, with an $n/p$ ratio of 1.28, should arise from a fissionable nucleus resulting from even higher nuclear excitation. A single value of 0.2 mb was determined for the activation cross section of this nuclide in fission of uranium with 340-Mev protons.

The simplified explanation of trends in high-energy fission would seem to imply that the yield of any fission product should not only reach a maximum, but as the available excitation energy is further increased, it should become negligible. That this is not the case may be due to the fact that, on the average, only a fraction of the energy of a high-energy particle will be transferred to the target nucleus.[12] Hence, fission corresponding to various degrees of nuclear evaporation will occur. For this reason, even at the highest bombardment energies there is still an appreciable yield of "low-energy" type of fission product, e.g., $Ba^{139}$. Similarly, the cross section for the formation of $Te^{131}$ found by Folger[6] in bombardments of $U^{238}$ with 340-Mev protons, is larger than that found above for $Ba^{131}$ under the same conditions. Thus even in 340-Mev proton bombardment of uranium, the majority of fissions leading to mass 131 occur in nuclei which arise from the evaporation of a relatively small number of nucleons.

Because the excitation functions for $Ni^{66}$ and $Ag^{111}$ indicate the extent to which the symmetry of the fission process has changed, these nuclides might be considered as "high-energy" fission products. While it is true that $Ni^{66}$ represents the chain yield of neutron-rich nuclides of mass 66, it is also likely, since the $n/p$ ratio is about that for $Ba^{131}$, that it is a primary fission product. Such a postulate seems consistent with the observation that the excitation functions for $Ni^{66}$ and $Ba^{131}$ are similar in appearance.

It is of interest to compare the excitation functions for $Ba^{131}$ and $Ag^{111}$, both nuclides having about the same $n/p$ ratio. The former is shielded from neutron-rich nuclides, the latter from neutron-deficient nuclides only, under the conditions of the experiment. Presumably the $Ag^{111}$ formed directly (primary fission product) rather than through chain yield would exhibit an excitation function not unlike those for $Ba^{131}$ or $Ni^{66}$.

TABLE I. The $n/p$ ratios for target and product nuclei.

| Nuclide | $n/p$ |
|---|---|
| $U^{238}$ | 1.59 |
| $Th^{232}$ | 1.58 |
| $Ba^{139}$ | 1.48 |
| $Zr^{97}$ | 1.42 |
| $Ag^{111}$ | 1.36 |
| $Ni^{66}$ | 1.36 |
| $Ba^{131}$ | 1.34 |
| $Ba^{128}$ | 1.28 |

## THE FISSIONING NUCLEUS

For the cases of the shielded nuclides $Ba^{128}$ and $Ba^{131}$, it is possible to speculate as to the fissionable precursors if the original assumption of preservation of $n/p$ ratio is valid. Thus at $Z=92$, and $n/p=1.34$, the nucleus responsible for fission would be $U^{215}$. This would imply a nuclear reaction such as $U^{238}(p,p^{23n})U^{215}$ or $U^{238}(\alpha,\alpha 23n)U^{215}$. Since it is doubtful that the evaporation of neutrons would occur to the exclusion of protons, such reactions as $U^{238}(p,2p24n)Pa^{213}$ and $U^{238}(p,3p26n)Th^{210}$ might be postulated as giving rise to such fission products as $Ba^{131}$. Although this represents a very large number of nucleons to be evaporated, evidence of another nature indicates that this may be the case. Douthett,[13] in a radiochemical study of the ranges of fission recoils of uranium in aluminum, found that the ranges of $Sr^{89}$, $Ag^{111}$, and $Ba^{140}$ were actually smaller in 335-Mev proton-induced fission than

[11] L. E. Glendenin, U. S. Office of Naval Research Technical Report NP-1242 (unpublished).

[12] R. Serber, Phys. Rev. 72, 1114 (1947).

[13] E. M. Douthett and D. H. Templeton, University of California Radiation Laboratory Report UCRL-1244 (unpublished).

TABLE II. Percent yields of $Ba^{139}$ and $Zr^{97}$ relative to $Ag^{111}$ for $U^{238}$ and $Th^{232}$.

| | Alpha particles | | | | Protons | | | | Deutrons | | | |
|---|---|---|---|---|---|---|---|---|---|---|---|---|
| | U | | Th | | U | | Th | | U | | Th | |
| Mev | $Zr^{97}$ | $Ba^{139}$ | $Zr^{97}$ | $Ba^{139}$ | $Zr^{97}$ | $Ba^{139}$ | $Zr^{97}$ | $Ba^{139}$ | $Zr^{97}$ | $Ba^{139}$ | $Zr^{97}$ | $Ba^{139}$ |
| 50 | | | | | 132 | 74 | 110 | 79 | 120 | 100 | 85 | 76 |
| 100 | 96 | 68 | 69 | 31 | 120 | 58 | 85 | 43 | 95 | 69 | 76 | 43 |
| 150 | 89 | 59 | 65 | 26 | 114 | 51 | 80 | 35 | 91 | 59 | 75 | 36 |
| 200 | 84 | 53 | 63 | 23 | 107 | 47 | 77 | 31 | 89 | 51 | 73 | 27 |
| 250 | 80 | 48 | 61 | 20 | 104 | 44 | 71 | 27 | | | | |
| 300 | 76 | 45 | 58 | 18 | 95 | 42 | 65 | 22 | | | | |
| 340 | 74 | 43 | 55 | 16 | 87 | 41 | 60 | 20 | | | | |

in 18-Mev deuteron-induced fission. This phenomenon was explained by considering that the complementary fragments of these fission recoils were smaller in the high-energy than in the low-energy fission. Through conservation of momentum Douthett calculated that, in order to account for the difference in ranges in the two cases, it was necessary to assume that the complement of $Sr^{90}$ must have been lighter in the high-energy case than in the low-energy case by about twenty six mass units.

## COMPARISON OF SYMMETRY OF FISSION IN THORIUM AND URANIUM

The limited number of fission products studied in the present work does not permit the elucidation of a mass-yield curve for a given energy. It follows, therefore, that no information can be obtained concerning the total fission cross sections. However, certain high-energy-induced fission characteristics of thorium and uranium can be compared from the values in Table II. In this, the yields of $Ba^{139}$ and $Zr^{97}$ have been expressed in percent of the yield of $Ag^{111}$, the values being taken directly from the curves of Fig. 1.

In all cases, the increasing "symmetry," as measured by decreasing relative yields of $Zr^{97}$ and $Ba^{139}$, is evident.

The comparatively small relative values for $Ba^{139}$ have been discussed in terms of the high $n/p$ ratio for this nuclide.

It might be pointed out that the values in Table II are always highest for the proton- and lowest for the alpha-particle-induced fission. This phenomenon will be discussed later.

It is significant that the values in Table II are always lower for thorium than for uranium. In short, thorium appears to exhibit a more "symmetrical" type of fission than does uranium. A possible explanation for this might be that the fission products $Ba^{139}$ and $Zr^{97}$, both characteristic of fission induced at low excitation energies, arise as a result of collisions involving transfer of only a small fraction of the energy of the high-energy particle. It is known[14] that the fission cross section of thorium at or near its threshold is considerably smaller than that for uranium. Hence such fission products as $Ba^{139}$ and $Zr^{97}$ should be more prominent in uranium than in thorium. That such differences in cross section are not valid at very high excitation energies is suggested by the fact that the nuclides $Ni^{66}$ and $Ag^{111}$, which are formed in greatly increased yield only in high-energy fission, have nearly identical cross sections in thorium and in uranium. The same is nearly true for $Ba^{131}$; the slight difference could be experimental variation.

Although these studies do not lead to a knowledge of the total fission cross sections of uranium and thorium, it is of some interest to note that the sum of the cross sections for the five fission products studied is somewhat larger for uranium than for thorium, at a given energy for a given bombarding particle. This is in accord with the work of Jungerman,[7] who found that in fission induced with 190-Mev deuterons, $U^{238}$ had a cross section about twenty percent greater than that for $Th^{232}$.

## COMPARISON OF ALPHA-PARTICLE-, DEUTERON-, AND PROTON-INDUCED FISSION

The curves in Fig. 1 show another feature of interest. Without exception for a given energy, proton-induced fission cross sections are smallest, while the alpha-particle-induced cross sections are, with one exception, largest. This exception is probably due to experimental error. Deuteron-induced cross sections are intermediate. The explanation of this phenomenon may lie in the concept of nuclear transparency. Since, for a given energy a proton possesses twice the velocity of an alpha particle, the latter should, because of its shorter mean free path, be more effective in causing nuclear excitation; the nucleus will be more transparent to protons. Deuterons would assume an intermediate role.

The effect of nuclear transparency manifests itself not only in the magnitude of the respective cross sections, but also in the comparative yields of the fission products. This is shown rather effectively in the values of Table II. For any given energy and target nucleus, the values in Table II are invariably smallest for alpha particles, largest for protons; that is, fission

[14] *Neutron Cross Sections*, U. S. Atomic Energy Commission Report AECU-2040 (Technical Information Service, Department of Commerce, Washington, D. C., 1952).

appears to be more symmetrical when induced by helium ions than by protons of the same energy. It has already been pointed out that a large relative yield of $Ag^{111}$ is accentuated at higher nuclear excitation; large relative yields of $Zr^{97}$ and $Ba^{139}$ are indicative of relatively low-energy fission. High-energy helium ions are thus more effective in causing nuclear excitation than are protons of the same energy. Deuterons again appear to occupy an intermediate situation. One may, from the values in Table II, estimate roughly that helium ions of 150-Mev energy induce about the same distribution of the fission products $Zr^{97}$, $Ag^{111}$, and $Ba^{139}$ as do protons of about 300 Mev.

### ACKNOWLEDGMENTS

We wish to thank Mr. James T. Vale and the crew of the 184-inch cyclotron of the University of California Radiation Laboratory for the bombardments which made this work possible. Thanks are also due Miss M. Gallagher for technical assistance.

PHYSICAL REVIEW VOLUME 94, NUMBER 5 JUNE 1, 1954

# *K*-Meson and Hyperon Decays*

PAUL H. BARRETT†
*Cornell University, Ithaca, New York*
(Received Februrary 18, 1954)

A stack of 400$\mu$ Ilford G-5 nuclear emulsion surrounded by 5.5 cm of brass was flown at 85 000 feet for 10 hours at $\lambda=41°$N. While scanning 409 cm$^2$ of these emulsions the decay of seven $K$ particles and one $\tau$ meson have been observed. A hyperon produced in a star is seen to decay into an $L$ meson. For the decay scheme $Y^{\pm}\rightarrow\pi^{\pm}+n+Q$ this event gives $Q=(48\pm20)$ Mev. A heavy nuclear fragment ($Z\sim5$) from an eight-prong star decays into $Li^8$, a proton, and a particle that is probably a deuteron. An event has been observed that could be interpreted as an example of the decay of a $\tau$ meson by the decay scheme $\tau^+\rightarrow\pi^+ +2\pi^0$.

## INTRODUCTION

DURING the last three years a large number of observations have been reported on the decay at rest in photographic emulsions and cloud chambers of charged heavy mesons ($K$ mesons) and there have been reports of unstable particles (hyperons)[1] and nuclear fragments[2] more massive than the proton.

Further examples of the masses and modes of decay of these particles have been obtained from a stack of 400$\mu$ Ilford G-5 nuclear emulsions which was surrounded by 5.5 cm of brass and flown at 85 000 feet for 10 hours by a high-altitude balloon. The balloon was launched on July 18, 1952 from Holloman Air Force Base, New Mexico (geomagnetic latitude 41°N).

In a systematic scanning of 409 cm$^2$ of emulsion the decay of seven $K$ particles, one $\tau$ meson, one hyperon, and one heavy nuclear fragment have been identified. A heavy particle is observed to stop in the emulsion and decay into a $\pi$ meson which is identified by the characteristic $\pi$-$\mu$-$e$ decay in the emulsion.

## CHARGED *K* MESONS

The results of the measurements on seven $K$ particles are shown in Table I. $K$-1 to $K$-6 were found in scanning 370 cm$^2$ of emulsion that was inside the brass and $K$-7 was found during the scanning of 39 cm$^2$ of emulsion that was outside but near the brass. The masses of the $K$ particles are determined from range-scattering measurements. $g^*$ is the ratio of the grain density to the plateau grain density.

The event $K$-2 is consistent with being the decay of a $\chi$ meson ($\chi\rightarrow\pi+$neutral particle). The value of $p\beta$ for the secondary of $K$-2 agrees well with the value $p\beta=179\pm7$ Mev/$c$ obtained by the Bristol group.[3]

The emulsions used in this experiment had glass backing and were placed emulsion-to-emulsion. Events $K$-4 and $K$-5 were traced from one emulsion to the next; however, there was a gap between the exit point in one emulsion and the entrance point of the next. This could have been due to two causes: (a) a gap between the emulsions in the vicinity of the tracks due to the emulsion surface being uneven; (b) removal of a surface layer of emulsion in processing. As the relative contributions of (a) and (b) are unknown and thus the correction to the range in going from one emulsion to the other, only the result of the mass measurement in the emulsion containing the decay is given. The mass values in parentheses are from scattering and grain

* Supported in part by the U. S. Office of Naval Research and the U. S. Atomic Energy Commission. Part of the data analysis was done at Syracuse University and was supported by a grant from the Research Corporation.
† Now at Syracuse University, Syracuse, New York.
[1] Levi-Setti, Peters, and Ceccarelli, Cosmic-Ray Conference, Bagnères, 1953 (unpublished).
[2] M. Danysz and J. Pniewski, Phil. Mag. **44**, 348 (1953); Tidman, Davis, Herz, and Tennent, Phil. Mag. **44**, 350 (1953); J. Crussard and D. Morellet, Compt. rend. **236**, 64 (1953).
[3] M. Menon and C. O'Ceallaigh, Cosmic-Ray Conference, Bagnères, 1953 (unpublished).

TABLE I. Results of measurements on $K$ mesons. The masses of the primaries were computed from range-scattering measurements except for those shown in parentheses which were computed from grain density and scattering measurements. $g^*$ is the ratio of the grain density of the track to the plateau grain density.

| | Primary | | Secondary | | | |
|---|---|---|---|---|---|---|
| | Range ($\mu$) | Mass ($m_e$) | Length ($\mu$) | $p\beta$ (Mev/$c$) | $g^*$ | Mass ($m_e$) |
| $K$-1 | 5000 | 1020±140 | 200 | ··· | 1.12±0.11 | ··· |
| $K$-2 | 520 | ··· | 4700 | 172±26 | 1.07±0.03 | 280±50 |
| $K$-3 | 120 | ··· | 2500 | 24.5±2.5 | 2.75±0.08 | 191±30 |
| $K$-4 | 11 300 | $1000^{+260}_{-190}$ | 130 | ··· | ~1 | ··· |
| $K$-5 | 10 400 | (1080±150)<br>1190±400<br>(1030±250) | 340 | ··· | 1.15±0.40 | ··· |
| $K$-6 | 1700 | 1000 | 250 | ··· | 1.56±0.14 | ··· |
| $K$-7 | 440 | ··· | 640 | 111±35 | 1.1 ±0.1 | 190±60 |

density measurements near the points where the particles first entered the emulsion. $K$-3, $K$-6, and $K$-7 are consistent with being examples of the decay of $\kappa$ mesons ($\kappa \rightarrow \mu + 2$ neutral particles) and $K$-1, $K$-4, and $K$-5 could be either $\kappa$'s of $\chi$'s.

Ritson[4] has measured the masses of $K$-1 and $K$-4 by the method of gap-density *versus* range and has obtained the values $(1020\pm100)m_e$ and $(870\pm100)m_e$, respectively.

One example of a $\tau$ meson stopping and decaying in the emulsion has been identified. The three secondaries are coplanar within 2°. From grain density and scattering measurements they are all consistent with being $\pi$ mesons and it is not likely that they are $\mu$ mesons though this possibility cannot be excluded. Their observed track lengths in the emulsion are 310$\mu$, 2300$\mu$, and 315$\mu$, and the sum of their momenta is zero within the statistical errors of the measurements.

## PRODUCTION AND DECAY OF A HYPERON

Originating from a star (20+19$p$) (Fig. 1), a track of about five times minimum ionization goes a distance of 795$\mu$ (Track $A$) and then appears to decay at a right angle into a charged particle (Track $B$) and one or more neutral particles. The result of measurements on these tracks is given in Table II. The mass determination is from grain density-scattering measurements. The particle producing Track $A$ had a velocity $\beta=0.20$ and lived $(1.3\pm0.1)\times10^{-11}$ sec. If Track $B$ is assumed to be a $\pi$ meson it has an energy of (59±15) Mev. If a two-body decay is assumed with the neutral secondary being a neutron and Track $B$ a $\pi$ meson, then $Q=(72\pm20)$ Mev and $M=(2260\pm40)m_e$.

TABLE II. Results of measurements on the tracks shown in Fig. 1. The masses are computed from grain density and scattering measurements. See Table I for explanation of $g^*$.

| Track | $g^*$ | $p\beta$ (Mev/$c$) | Mass ($m_e$) | Length ($\mu$) |
|---|---|---|---|---|
| $A$ | 5.0±0.1 | 113±35 | 2500±900 | 800 |
| $B$ | 1.6±0.1 | 100±25 | 300±75 | 900 |
| $C$ | 6.0±0.1 | 55±8 | proton | 2360 |

[4] D. M. Ritson, Phys. Rev. **91**, 1572 (1953).

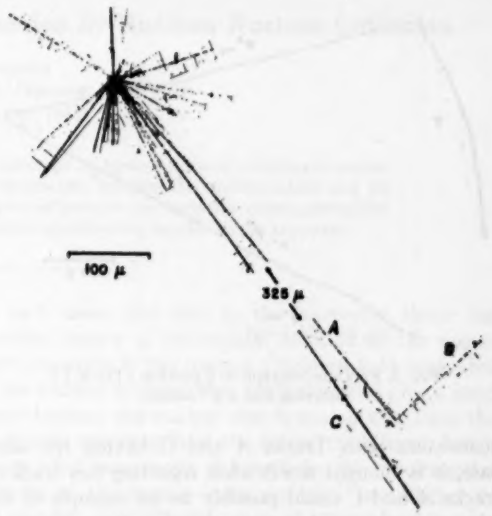


FIG. 1. Photomicrograph of a star in which one of the prongs (Track $A$) decays into a meson (Track $B$).

This event is similar to the case reported by Ceccarelli and Peters[1] which, in the new nomenclature of particles, is hypothesized as being the decay of a charged hyperon ($Y^{\pm} \rightarrow \pi^{\pm} + n + Q$). Ceccarelli and Peters give for this reaction $Q=131\pm24$ Mev and $Q=135\pm35$ Mev, respectively.

From the nuclear interaction that was the origin of Track $A$ there emerges another particle (Track $C$) that makes an angle of 3° with Track $A$. Track $C$ leaves the emulsion after traversing 2360$\mu$. Because of the high grain density of Track $C$ an accurate density counting of grains cannot be performed; therefore, the mass determination of this particle is quite uncertain. However, its mass can be estimated to be about protonic. Since the measurements are not

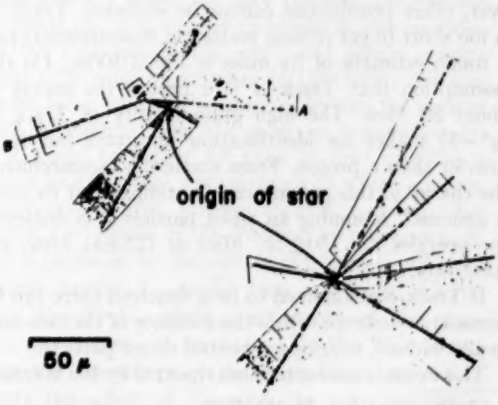


FIG. 2. Photomicrograph of an eight-prong star (one of the prongs might be the recoil nucleus). Seven of the prongs are shown in the lower right. The eighth prong is shown separately in the upper left along with several of the other prongs.

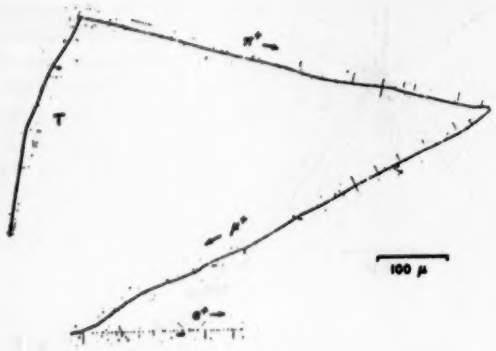


FIG. 3. Photomicrograph of a particle (Track $T$) decaying into a $\pi^+$ meson.

inconsistent with Tracks $A$ and $C$ having the same mass, it is thought worth while reporting this track as Tracks $A$ and $C$ could possibly be an example of the pair production of hyperons that has been suggested by Pais.[5]

## DECAY OF HEAVY NUCLEAR FRAGMENT

Figure 2 is a photomicrograph of an eight-prong star (one gray track and seven black tracks). The decay of one of the black tracks is shown in detail in the upper left of the figure. This prong appears to stop after traversing $27\mu$ of emulsion. Its ionization is greater than that of an $\alpha$ particle of similar range and its charge is estimated as being from four to six. From the end of its range three charged particles originate. Tracks $A$ and $B$ leave the emulsion after track lengths of $300\mu$ and $690\mu$, respectively. Track $C$ has a length of $4\mu$ and decays into two short heavy tracks and a light track which from its observed scattering is probably an electron. Track $C$ is consistent with being a $Li^8$ nucleus ($Li^8 \rightarrow Be^8 + e^-$, $Be^8 \rightarrow 2He^4$), giving the characteristic "hammer" track upon decaying; however, other possibilities cannot be excluded. Track $A$ is too short to get reliable scattering measurements but a rough estimate of its mass is $1500 \pm 500 m_e$. On the assumption that Track $A$ is a proton the energy is about 50 Mev. The high grain density of Track $B$ ($g^* \sim 8$) makes its identification uncertain but it is heavier than a proton. From scattering measurements the energy of this particle can be computed if its mass is assumed. Assuming an alpha particle or a deuteron the energies are $(50 \pm 10)$ Mev or $(25 \pm 5)$ Mev, respectively.

If Track $B$ is assumed to be a deuteron there can be momentum balance within the accuracy of the measurements without requiring a neutral decay particle.

This event is similar to those reported by the Warsaw, Bristol, and Paris groups[2] and these unstable heavy fragments have been interpreted as containing a bound $\Lambda^0$ (or $V_1^0$ in the old notation) in place of a neutron. The bound $\Lambda^0$ can then disappear either by the normal decay $\Lambda^0 \rightarrow p + \pi^- + 37$ Mev or by interacting with other nucleons and changing into a nucleon with the release of about 178 Mev. This latter process has been called by Cheston and Primakoff[6] "nonmesonic decay."

Applying this hypothesis to the event reported above, we have, resulting from a high-energy nuclear interaction, a carbon or boron nucleus ($A = 11$ to 13) with a neutron replaced by a $\Lambda^0$. The $\Lambda^0$ undergoes a "nonmesonic decay" after about $10^{-12}$ sec leaving the nucleus highly excited. The nucleus breaks up with the emission of $Li^8$, a proton, a particle of $Z = 1$ or 2 and $A = 2$, 3, or 4, and one or more neutral particles.

## $\pi$ MESON FROM DECAY OF HEAVY PARTICLE

In Fig. 3 a photomicrograph shows the decay of a particle (Track $T$) into a $\pi$ meson of range $536\mu$ (4.3 Mev) which decays upon coming to rest into a $\mu$ meson ($562\mu$) which in turn decays into an electron. The $\pi$ meson is assumed positive as it is not captured by a nucleus. Track $T$ enters the emulsion at the glass surface and has a track length in the emulsion of $320\mu$. Its mass can be only roughly estimated from inspection of its track and comparing it with the tracks of protons and mesons of similar range. Its mass is probably intermediate between those of the $\pi$ meson and the proton.

This event could be an example of the decay of a positive $\tau$ meson by the alternate decay scheme suggested by Pais[5] $\tau^{\pm} \rightarrow \pi^{\pm} + 2\pi^0$. Other possible examples of this mode of decay of the $\tau$ meson have been observed by Crussard *et al.*[7] and Amaldi[8] and co-workers.

One more possible example of this type of decay has been found in these emulsions but the "$\tau$ meson" track is short ($60\mu$) and the $\pi$ meson ($480\mu$) makes an angle of only 8° with the end of the "$\tau$ meson" track. The possibility that this event could be the scattering of a $\pi$ meson cannot be ruled out.

## ACKNOWLEDGMENTS

The author wishes to thank Mrs. Carol Sienko and Mrs. Gerry de Vesty who performed the exacting task of scanning the emulsions, and the personnel of the Aero-Medical Laboratory, Holloman Air Force Base for making the balloon flight possible.

[5] A. Pais, Phys. Rev. **86**, 663 (1952).

[6] W. Cheston and H. Primakoff, Phys. Rev. **92**, 1537 (1953).

[7] Crussard, Kaplon, Klarmann, and Noon, Phys. Rev. **93**, 253 (1954).

[8] Amaldi, Baroni, Castagnoli, Cortini, Franzinetti, and Manfredini (to be published).

PHYSICAL REVIEW VOLUME 94, NUMBER 5 JUNE 1, 1954

# Effect of Coulomb Barrier on Meson Production by Nucleon-Nucleus Collisions

TOICHIRO KINOSHITA
*The Institute for Advanced Study, Princeton, New Jersey*
(Received Februrary 19, 1954)

The effect of the Coulomb barrier on charged meson production by nucleon-nucleus collisions is studied by a classical and qualitative treatment of the Coulomb interaction between the emitted meson and the residual nucleus. Especially, the discrepancy in the behavior of positive and negative meson production cross sections as functions of atomic number can be understood qualitatively by this simple argument.

MEASUREMENTS have recently been performed on the variation of the positive and negative meson production cross sections with atomic number which result from the interaction of a 340-Mev proton beam with target nuclei.[1] The targets used are Be, C, Al, Cu, Ag, Pb, and the differential cross section is studied by photographic emulsion exposed at 90° to the direction of the proton beam in the laboratory system. The kinetic energy of the observed mesons ranges from 12.5 to 35 Mev.

A remarkable fact revealed by these observations is that there is a systematic difference in the behavior of the negative and positive production cross sections: the cross section per nucleus for $\pi^-$ production increases steadily as a function of the atomic number while that for $\pi^+$ production shows a tendency to level off or even decrease towards heavier nuclei for all observed meson energies. It would be very hard to understand this without referring to the Coulomb effect, since other effects such as the scattering and absorption of the incident proton and the secondary meson would work in the same direction for both $\pi^+$ and $\pi^-$.[2] There has, however, been no reliable method which gives the Coulomb effect on the meson production correctly even in a qualitative sense.

As is well-known in the theory of beta decay, a simple way of introducing the Coulomb correction is to multiply the uncorrected cross section by the correction factor $C=2\pi\xi/[1-\exp(-2\pi\xi)]$, $\xi=\pm Ze^2/hv$. This method cannot be used in our case, however, since the nuclear Coulomb field does not belong to a point charge but to an extended charge distribution.[3] In such cases, one uses as the correction factor the absolute square of the regular solution of the meson wave equation in the nuclear Coulomb field evaluated at the nuclear surface. This again does not give a good result because the nuclear size is not smaller than the de Broglie wavelength of the meson considered, which means that one needs a knowledge of the irregular solution of the meson wave equation in addition to the regular one. Finally, even the complete outside solution would not provide a satisfactory estimation of the Coulomb effect since this is essentially determined by the behavior of the meson inside the nucleus which belongs to the yet unknown properties of mesons. At the present stage, it is therefore almost useless to solve the meson wave equation exactly in the region outside of a nucleus. As is mentioned above, this is mostly due to the fact that the nuclear size is large compared to the meson wavelength. This, however, means at the same time that the magnitude of the Coulomb field is small compared to the meson kinetic energy, which leads us to another kind of approximation method.

As is well-known, the Coulomb effect can be understood qualitatively in the following way: it accelerates the $\pi^+$ and decelerates the $\pi^-$. Hence, the $\pi^+$ spectrum has fewer slow particles, and $\pi^-$ spectrum more slow particles, than they would have in the absence of the Coulomb effect. Now, one may describe the ejection of a meson out of a nucleus classically in our problem, since the Coulomb field is small and slowly varying compared to other quantities. In this sense, the momentum $k_0^\pm$ of $\pi^\pm$ at the moment of leaving the nucleus would be different from the observed momentum $k^\pm$, and it would be rather $k_0^\pm$ than $k^\pm$ that provides a measure for the initial momentum with which a meson is produced in the nucleon-nucleon collision. For example, a $\pi^+$ meson of the observed kinetic energy $E$, which is produced on the surface of a nucleus with the Coulomb barrier $V_c$ would have an initial kinetic energy $E_0=E-V_c$, while a $\pi^-$ meson of the same kinetic energy would have $E_0=E+V_c$. This would change the kinematics of the usual treatment which neglects the effect of $V_c$, and the atomic number dependence of the cross section for fixed $E$ would be considerably different from that of fixed $E_0$ as one goes towards heavier nuclei if the energy spectrum of the

[1] R. Sagane and W. Dudziak, Phys. Rev. **92**, 212 (1953); University of California Radiation Laboratory Reports UCRL-2284, 2304, 2317, 1953 (unpublished).

[2] Recently, S. Gasiorowicz [Phys. Rev. **93**, 843 (1954)] tried to explain this experiment by taking account of the energy degeneration of the incident proton in the nucleus and the reabsorption of the meson by the nucleus it traverses. His results depend, however, on an unestablished assumption that the protons tend to be confined to a region of somewhat smaller radius compared to the nucleus as a whole. The validity of Gasiorwicz's picture may be examined by considering meson production by *neutron*-nucleus collisions, photomeson production by nuclei, etc.

[3] For a meson of 33 Mev produced by lead, the correction factors $C_-$ and $C_+$ are about 6.3 and 0.012, respectively. It is to be noticed that use of $C_+$ for $\pi^+$ mesons would be especially meaningless since it describes the case where the momentum of the $\pi^+$ meson becomes imaginary at the point nucleus due to the infinitely high Coulomb potential, while in our problem the $\pi^+$ meson may preserve its wave character up to the center of the nucleus.

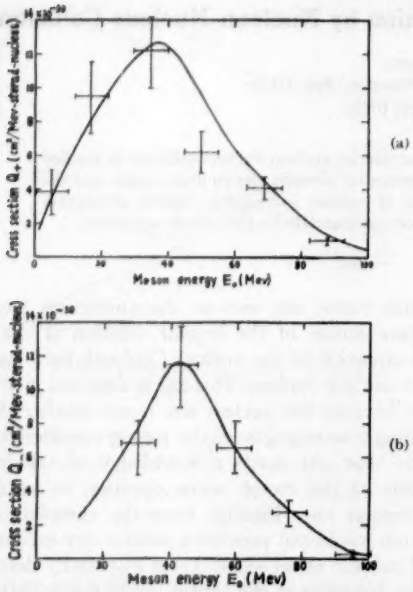


FIG. 1. (a) The energy spectrum $Q_+$(Pb) as a function of the initial kinetic energy $E_0$ based on the experimental data of reference 6. The solid curve is a hypothetical energy spectrum which is assumed to be valid for all elements in our analysis. (b) The energy spectrum $Q_-$(Pb) as a function of the initial kinetic energy $E_0$ based on the experimental data of reference 6. The solid curve is a hypothetical energy spectrum which is assumed to be valid for all elements in our analysis.

meson is strongly dependent on its energy. We shall show in the following that the principal feature of the above experiments can actually be understood in accordance with this idea by taking $E_0=E\mp V_e$ as the crudest approximation for the initial kinetic energy of the secondary meson.

First, we shall write the production cross section of a meson with the kinetic energy $E$ as

$$d\sigma_\pm(E;Z,N)/dEd\Omega=P_\pm(E;Z,N), \qquad (1)$$

where $Z$ and $N$ are the proton and neutron numbers of the target nucleus. This can be rewritten as the cross section for the *initial* kinetic energy $E_0$:

$$d\sigma_\pm(E_0\pm V_e;Z,N)/dE_0d\Omega=Q_\pm(E_0;Z,N), \qquad (2)$$

in conformity with the classical approximation mentioned above.[4] For fixed $Z$ and $N$, this gives the meson energy spectrum in terms of the initial kinetic energy $E_0$ and is therefore the one to be compared with the energy spectrum of the ordinary theoretical treatment in which the Coulomb effect is not taken into account.[5] In the same way, the atomic number dependence of $Q$ can be compared with the theoretical expectation. In order to derive the atomic number dependence of $Q$ from the experimental data $P$, however, one has to know the energy dependence of $Q$ for all elements considered.

The energy spectrum $P$ at 90° has heretofore been measured only for C and Pb.[6] Unfortunately, these are not accurate enough for our purpose. The corresponding spectrum $Q(E_0;\text{Pb})$ is found to be an increasing function of $E_0$ up to a maximum at ~40 Mev and then to decrease fairly rapidly for larger $E_0$ (Figs. 1). $Q(E_0;\text{C})$, on the other hand, has a very broad maximum at ~40 Mev. It is expected that the spectrum $Q$ for all heavy elements is not very different from $Q(E_0;\text{Pb})$. Meanwhile, $Q$ is nearly identical with $P$ for light elements irrespective of its energy dependence since $V_e$ is small in these cases. We may therefore assume without serious error that the energy spectrum is proportional to that of Pb for all elements. (The multiplicative factor is not important for our purpose.) We shall assume for simplicity that the energy spectra for all elements are given by the solid curves in Figs. 1, which are drawn more or less arbitrarily out of the multitude of curves which might fit experimental data just as well.

Once the energy spectrum is fixed, one can easily calculate the atomic-number dependence of $Q$ from that of $P$. In Figs. 2, the spectra $Q$ thus determined are given together with the experimental spectra $P$. It is seen that the atomic number dependence of $Q$ for both $\pi^+$ and $\pi^-$ can now be approximated by $A^{\frac{1}{3}}$-curves, as is expected from the interaction of the meson with the nucleus.[7] One may thus be lead to the conclusion that the Coulomb barrier is actually the agent which gives rise to the discrepancy between the $\pi^+$- and $\pi^-$-cross sections. One should, however, keep in mind that this is based upon many assumptions and approximations. Some of these points will be discussed in the following.

1. In the first place, it should be stressed that we have treated the effect of the Coulomb barrier in a classical way. Namely, we have treated $k$ and $k_0$ as simultaneously diagonal operators, and this introduces an error of the order of $[4\alpha Z/(kR)^2]\cdot[(\mu+E)/k]$ for sufficiently large $k$.[8] This is about 20 percent for a

[4] $Q_\pm$ as a function of $E_0$ is obtained by shifting $P_\pm$ as a function of $E$ to the left or right by the amount $V_e$ (for $\pi^+$ or $\pi^-$ mesons, respectively).

[5] E. M. Henley, Phys. Rev. **85**, 204 (1952); Passman, Block, and Havens, Phys. Rev. **83**, 167 (1951).

[6] C. Richman and H. Wilcox, Phys. Rev. **78**, 496 (1950); M. Weissbluth, Ph.D. thesis, University of California, 1950 (unpublished); Richman, Weissbluth, and Wilcox, Phys. Rev. **85**, 161 (1952).

[7] Better agreement may be obtained taking account of the collision mean free path of the incident proton and the absorption of the produced meson in the nucleus. Both effects will reduce the production cross section by a factor $A^{-\frac{1}{3}}$. More precisely, the latter is known to multiply the cross section by a factor

$$3\{\tfrac{1}{2}(1/X)-(1/X^2)+(1/X^3)(1+X)e^{-X}\},$$

where $X=2R/\lambda_a$, $R=a_0A^{\frac{1}{3}}$ being the nuclear radius, and $\lambda_a$ the absorption mean free path of a meson in the nucleus. See Brueckner, Serber, and Watson, Phys. Rev. **84**, 258 (1951).

[8] An estimate of this error is made by evaluating the upper limit for

$$\langle[\Delta,(\mu+E\pm\alpha Z/r)^2-\mu^2]_-\rangle/\langle\Delta\rangle\cdot\langle(\mu+E\pm\alpha Z/r)^2-\mu^2\rangle,$$

where $\langle\Delta\rangle$, etc., mean the expectation value of $\Delta$, etc., with respect to the meson wave function.

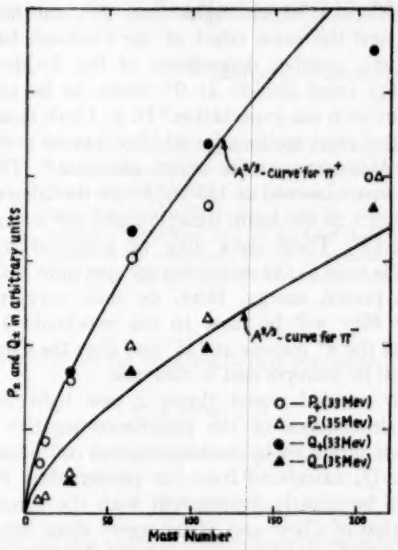


(a)

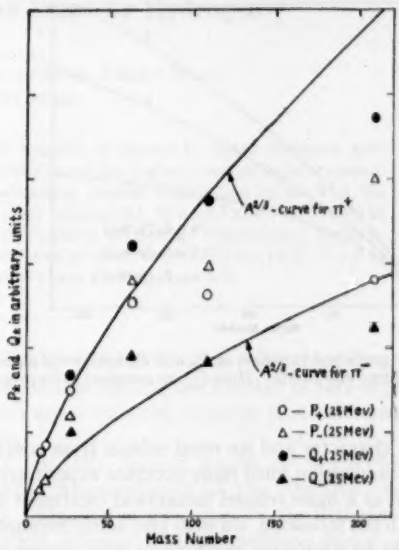


FIG. 2(b)

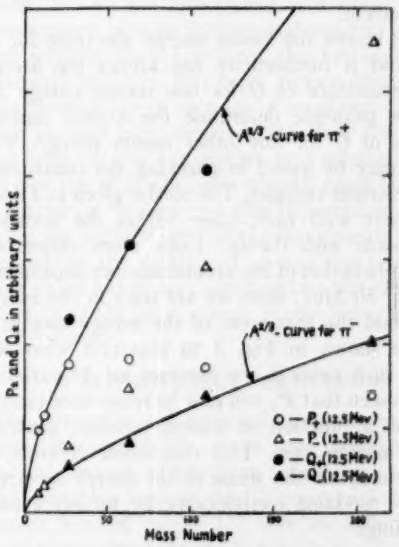


FIG. 2(c)

FIG. 2(a). The variation of $Q_+$(33 Mev) and $Q_-$(35 Mev) as well as the experimental data $P_+$(33 Mev) and $P_-$(35 Mev) with mass number. The $A^{\frac{2}{3}}$-curves are superimposed on the data for comparison. (b) The variation of $Q_\pm$(25 Mev) as well as the experimental data $P_\pm$(25 Mev) with mass number. The $A^{\frac{2}{3}}$-curves are superimposed on the data for comparison. (c) The variation of $Q_\pm$(12.5 Mev) as well as the experimental data $P_\pm$(12.5 Mev) with mass number. The $A^{\frac{2}{3}}$-curves are superimposed on the data for comparison.

meson of kinetic energy 33 Mev produced by lead. Obviously, the errors become larger for mesons of lower energies and thus our method cannot be applied to very low-energy mesons.

2. We do not know the nuclear radius exactly. Accordingly, we are not sure up to what point the pure Coulomb potential can be used. In this note, we have adopted $R=1.5\times10^{-13}\times A^{\frac{1}{3}}$ cm as the nuclear radius. The result of our analysis, however, would not vary very much for a slight change in the assumed nuclear radius.

3. In the formula (2), we have adopted the surface value $E\pm V_c$ as the initial kinetic energy of the produced meson. Strictly speaking, this is not correct since a meson can be produced at any place within the nucleus and we do not know anything at all about the "meson-nucleus potential." The situation is exactly the same in the case of the ordinary treatment where a meson is assumed to be produced in a hypothetical nucleus which has no surrounding Coulomb field.[6] In so far as one is confined to the analysis of the Coulomb effect in terms of the formulas (1) and (2), one need not worry about the details of the behavior of mesons within the nucleus since they will cancel each other, being common to both (1) and (2).

4. Finally, an objection might be raised against the assumptions we have imposed on the energy spectrum. The present experimental data are very crude so that they cannot determine the energy spectrum with sufficient accuracy. The spectrum used in our discussion is so chosen out of the variety of spectra which fit the data that the Coulomb effect is seen clearly. It is easy to see that another choice would modify our result to a considerable extent although it would not change the qualitative feature of our argument. One should also notice that the energy spectrum is slightly different for different elements. Since this is disregarded in our treatment, some amount of error will be involved systematically in the atomic number dependence of $Q$. It is therefore highly desirable to have accurate energy spectra for meson production in order to settle these points unambiguously.

Our treatment of the Coulomb effect is merely of a

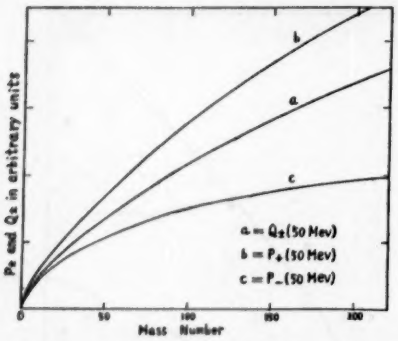


FIG. 3. The predicted variation of $P_+$ and $P_-$ with mass number at a meson energy $E=50$ Mev. Here $Q_\pm$ are assumed to be proportional to $A^{\frac{1}{3}}$.

provisional character and we must refrain from coming to the final conclusion until more accurate experimental data as well as a more refined theoretical treatment are available. In the following, we shall give some comments which might be useful for checking or establishing our way of approach.

1. If one knows the meson energy spectrum for all elements and if furthermore one knows the atomic number dependence of $Q$ for one meson energy $E_0$, one can in principle determine the atomic number dependence of $Q$ for any other meson energy. This statement may be useful in checking the consistency of data at various energies. The results given in Figs. 2 are consistent with each other within the accuracy of experiments and theory. Even more interesting will be the prediction of the atomic number dependence of $P$ for $E \gtrsim 50$ Mev, since we are then in the energy region beyond the maximum of the energy spectrum. Curves are shown in Fig. 3 to illustrate what will happen in such cases if one assumes an $A^{\frac{1}{3}}$ variation for $Q_\pm$. It is seen that $P_+$ will now increase more rapidly than $P_-$ as a function of atomic number, contrary to the low-energy case. This conclusion depends, of course, critically on the shape of the energy spectrum and will be modified considerably by further experimental findings.

2. From the observation of the meson production cross sections at other angles than 90°, one may be able to find the same effect of the Coulomb barrier. The atomic number dependence of the 53-Mev $\pi^+$-production cross section at 0° seems to be not inconsistent with our expectation.[9] D. L. Clark measured the relative cross sections for 40-Mev mesons produced by 240-Mev protons in seven elements.[10] The $\pi^+$ mesons were observed at 135°±15° (in the laboratory) with respect to the beam direction and the $\pi^-$ mesons at 45°±15°. These data may be analyzed by our method as soon as the meson energy spectrum is known for this proton energy. Here, we shall only remark that 40 Mev will be close to the maximum kinetic energy of the $\pi^+$ mesons at 135° and thus the Coulomb effect will be unimportant in this case.

3. Our method would throw a new light on the energy dependence of the positive-to-negative ratio of mesons produced by nucleon-nucleus collisions. The ratio $Q_-/Q_+$ calculated from the present data for Pb seems to be slightly inconsistent with the theoretical expectation of Chew and Steinberger[11] since this ratio is too large for high meson energies. In view of the crudeness of the present data, however, it would be premature to draw conclusions about this point.

4. Finally, it may be mentioned that a similar argument will hold in other problems such as the atomic number dependence of the cross section of various nuclei for photomeson production.

The author would like to thank Professor R. Sagane for informing him of the experimental results prior to publication, and Professor Y. Namu and Professor T. Miyazima for many valuable discussions. He would like to express his gratitude to Professor R. Oppenheimer for the hospitality extended to him at the Institute for Advanced Study.

[9] Hamlin, Jakobson, Merritt, and Schulz, Phys. Rev. **84**, 857 (1951). The meson spectrum in the direction of an incident 341-Mev proton beam has been measured only in the case of a carbon target by Cartwright [University of California thesis, April 16, 1951 (unpublished)]; and by Merritt, Schulz, and Heinz (unpublished).

[10] D. L. Clark, Phys. Rev. **87**, 157 (1952). He also measured the atomic number dependence of 20-Mev $\pi^+$ mesons produced by 240-Mev protons in several targets. See D. L. Clark, Phys. Rev. **81**, 313 (1951).

[11] G. Chew and J. Steinberger, Phys. Rev. **78**, 497 (1950).

# Scattering of 217-Mev Negative Pions by Hydrogen†*

MAURICE GLICKSMAN
*Institute for Nuclear Studies, University of Chicago, Chicago, Illinois*

(Received January 18, 1954)

The differential cross sections for scattering of 217-Mev negative pi mesons by liquid hydrogen have been observed at six angles. An analysis of the angular distribution of the ordinary scattering is consistent with a small $d$-wave contribution; the charge exchange scattering angular distribution agrees with the assumption of only $s$ and $p$ waves. The integrated total cross sections are $18.2\pm2.3\times10^{-27}$ cm² for the ordinary scattering and $35.8\pm3.4\times10^{-27}$ cm² for the charge exchange scattering. Transmission measurements of the total cross section gave values of $57.2\pm2.9\times10^{-27}$ cm² at 209 Mev and $52.1\pm2.3\times10^{-27}$ cm² at 220 Mev. An analysis of the angular distributions in terms of phase shifts is discussed.

A STUDY of the pion scattering reactions

$$\pi^+ + p \rightarrow \pi^+ + p, \quad (1)$$

$$\pi^- + p \rightarrow \pi^- + p, \quad (2)$$

$$\pi^- + p \rightarrow \pi^0 + n, \quad (3)$$

is of considerable value in understanding the interaction between pions and nucleons. Angular distributions for these reactions have been reported by a number of authors.[1–9] On the basis of charge independence, the scattering should be describable in terms of phase shifts. At low energies, angular momentum states higher than $s$ or $p$ waves may be assumed unimportant. One set of six phase shifts should then completely describe the scattering at a definite energy.

An extensive study of these reactions has been made at 120 and 135 Mev by AFMN.[5] Their results enable them to eliminate all but two possible sets of phase shifts. Observations of the scattering of negative pions alone at higher energies (up to 210 Mev) have been reported.[8] A phase shift analysis of these data is more difficult.[10] Because of the higher energy, it is quite possible that $d$ states contribute appreciably to the scattering and need to be included in the analysis. It is also not possible to calculate a unique set of phase shifts from the negative scattering data alone. Some positive scattering data at high energies have recently become available[9–12] and an analysis using these data may prove successful in limiting the number of sets of phase shifts which agree with the negative pion scattering observations.

It was felt that it would be worthwhile making detailed measurements of the negative and positive pion scattering at an energy in the 210-Mev region. A detailed differential cross section should give some information on the importance of $d$ waves and good measurements of both positive and negative differential cross sections should remove the ambiguity in the phase-shift analysis. This paper reports observations of the differential cross sections of reactions (2) and (3) for an incident pion energy of 217 Mev. The scattered pions from (2) and the gamma rays resulting from the decay of the $\pi^0$ in (3) (plus a small contribution from the reaction $\pi^- + p \rightarrow \gamma + n$) were observed at six angles. Within the limits of error of the experiment, this allows some test of the validity of an analysis in terms of $s$ and $p$ waves alone; an experiment on the positive pion scattering at the same energy is now being carried out here by others.

## I. EXPERIMENTAL ARRANGEMENT

The arrangement is essentially the same as that used in previous work.[5] The pions were produced by the bombardment of a beryllium target by the internal 450-Mev proton beam of the Chicago synchrocyclotron. Pions of nominal energy 227 Mev are deflected out of the cyclotron and focussed in a fairly parallel beam by the fringing magnetic field. They traverse a channel through the twelve feet of shielding and are then deflected by a steering magnet into the detecting scintillation counters. A description of the pion beams, target and steering magnet has been published.[13]

Details of the scattering geometry are given in Fig. 1. The pions incident on the liquid hydrogen were detected by two 2-inch diameter scintillation counters (No. 1 and No. 2) with the second counter 5.5 inches from the center of the liquid hydrogen cell. Scattered pions (and a small number of converted gamma rays)

† Research supported by a joint program of the U. S. Office of Naval Research and the U. S. Atomic Energy Commission.
* Submitted to the Department of Physics, the University of Chicago in partial fulfillment of the requirements for the Ph.D. degree.
[1] Anderson, Fermi, Nagle, and Yodh, Phys. Rev. **86**, 793 (1952).
[2] Fowler, Fowler, Shutt, Thorndike, and Whittemore, Phys. Rev. **86**, 1053 (1952).
[3] G. Goldhaber, Phys. Rev. **89**, 1187 (1953).
[4] Bodansky, Sachs, and Steinberger, Phys. Rev. **90**, 996, 997 (1953).
[5] Anderson, Fermi, Martin, and Nagle, Phys. Rev. **91**, 155 (1953), quoted here as AFMN.
[6] J. P. Perry and C. E. Angell, Phys. Rev. **91**, 1289 (1953).
[7] J. Orear, Phys. Rev. **92**, 156 (1953).
[8] Fermi, Glicksman, Martin, and Nagle, Phys. Rev. **92**, 161 (1953).
[9] Fowler, Lea, Shephard, Shutt, Thorndike, and Whittemore, Phys. Rev. **92**, 832 (1953).
[10] E. Fermi (private communication).
[11] Homa, Goldhaber, and Lederman, Phys. Rev. **93**, 554 (1954).
[12] R. A. Grandey and A. F. Clark (private communication).
[13] R. L. Martin, Phys. Rev. **87**, 1052 (1952).

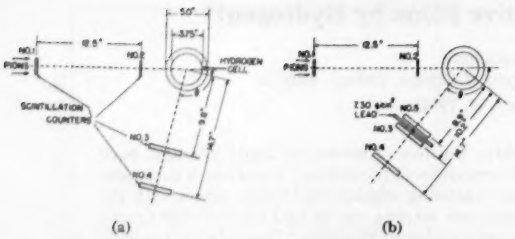


FIG. 1. Details of the scattering geometry. (a) Detection of scattered pions. Counters No. 1, 2, 3, and 4 are in coincidence. (b) Detection of gamma rays. Counters No. 1, 2, 3, and 4 are in coincidence, with counter No. 5 in anticoincidence.

were detected by two 4-inch wide by 6-inch high liquid scintillation counters (No. 3 and No. 4) placed at a variable angle with the incident beam. Gamma rays [coming mainly from the decay of the $\pi^0$ produced in reaction (3)] were detected using three 4-inch by 6-inch counters (No. 5, 3, and 4) with 7.30 g/cm² of lead placed between counters No. 5 and No. 3. A gamma ray was counted with about fifty-percent efficiency by the quadruple coincidence of counters No. 1, 2, 3, and 4, with counter No. 5 in anticoincidence. Observations were made at six angles. In the observation of scattered pions, absorbers were placed between counters No. 3 and 4 at the forward angles to remove the recoil protons. This amounted to 12.94 g/cm² aluminum at 25.7° and 6.19 g/cm² at 51.4°.

Pulses from the scintillation counter were fed into a preamplifier, amplified in a two-stage distributed amplifier, fed through some 150 feet of 100-ohm cable into another two-stage distributed amplifier and through a delay box into the coincidence circuits. The output of the coincidence circuits was counted in a Hewlett Packard high-speed decade scaler in cascade with an Atomic Instrument decade scaler.

The efficiency of the scintillation counters detecting the scattered particles was checked by observing: (1) the ratio of quadruple coincidences (counters No. 1, 2, 3, and 4) to double coincidences (counters No. 1 and 2) with the counters in line in the sequence No. 1, 3, 4, and 2, and (2) the ratio of quadruple coincidences (counters No. 1, 2, 3, and 4 in coincidence, with counter No. 5 in anticoincidence) to double coincidences (counters No. 1 and 2) with the counters in line in the sequence No. 1, 2, 5, 3, and 4. Results of measurement (1) were quite close to 100 percent; measurement (2) gave something less than 0.1 percent. The counters and the anticoincidence circuit were therefore taken to be 100-percent efficient.

The incident pion intensity was about 20 000 counts per minute. The scattered intensity was about 3 per minute for most of the measurements. Of this, from 20–70 percent was background which remained when the hydrogen was removed from the cell. A typical measurement would consist of (1) coincidences at 25.7° without hydrogen in the cell, (2) coincidences at 25.7° with hydrogen in the cell, (3) coincidences at 51.4° with hydrogen in the cell, (4) coincidences at 51.4° without hydrogen in the cell, etc., the complete sequence being repeated some five to eight times during one run. The coincidence (scattered pions) and anticoincidence (gamma rays) observations were not mingled; a run consisted of about twenty-four hours running time on the anticoincidence measurement followed by about forty hours running time on the coincidence measurement.

## II. EQUIPMENT

### a. Scintillation Counters

Counters No. 1 and 2 were made thin so that the energy loss of the pions in them would be small, and so that counter No. 2 would not contribute appreciably to the background by scattering pions into the other counters. Counter No. 1 was a liquid scintillator 2 inches in diameter and $\frac{3}{16}$ inch thick, contained in a Lucite cell with $\frac{1}{32}$-inch windows. The liquid used was phenylcyclohexane with 3 g/liter of terphenyl and 10 mg/liter of diphenylhexatriene dissolved in it.[14] The end of the Lucite cell was shaped to fit the photocathode of an RCA 5819 photomultiplier and good optical contact was maintained with a thin layer of silicone grease. The photomultiplier was housed in a cylindrical mu-metal shield to minimize the influence of the stray magnetic field present. Counter No. 2 was a $\frac{1}{8}$ inch thick, 2-inch diameter plastic scintillator making good optical contact with a Lucite light pipe $\frac{1}{8}$ inch thick. Silicone grease was used for the scintillator-Lucite and Lucite-photomultiplier contact and pressure was maintained to keep the sections in position. The cells of both counters were wrapped in 0.004-inch aluminum foil to increase their optical efficiency. Counters No. 3, 4, and 5 were 4 inches by 6 inches by $\frac{1}{2}$-inch thick over-all Lucite cells with $\frac{1}{16}$-inch windows, containing liquid scintillator; they have been described previously.[5]

### b. Electronic Equipment

The pulses from the counters were fed directly from the anode of the photomultiplier into an attached preamplifier[15] which produced pulses of a square shape and about $2.5\times10^{-8}$ second long. After amplification in two distributed amplifiers they went into the coincidence circuits.[15] For the coincidence (scattered pions) measurement, pulses from counters No. 1 and 2 were counted in double coincidence in one circuit $F$, counters No. 3 and 4 in another circuit $B$, and counters No. 1 and 3 in a third circuit $A$. The outputs of these three circuits, which were about $5\times10^{-8}$ second long, were then counted in triple coincidence in a coincidence circuit capable of recording double, triple, or quaduple coincidences. The anticoincidence (gamma rays) measure-

[14] H. Kallman and M. Furst, Phys. Rev. **81**, 853 (1951).
[15] Glicksman, Anderson, and Martin, Proceedings of the National Electronics Conference **9**, 483 (1953).

ment was similar, with the one change being the addition of pulses from counter No. 5 into the anticoincidence input of the double coincidence circuit $B$. The outputs of circuit $F$ and the triple coincidence circuit each led into a cascade combination of a Hewlett Packard high-speed decade scaler and an Atomic Instrument decade scaler, which then recorded the number $D$ of incident pions and the number $Q$ of interactions, respectively.

The resolving time of the equipment was small enough ($2.5\times10^{-8}$ second) to make the number of accidental coincidences a negligible correction. The counting rates were low enough and the dead time of the equipment (about $10^{-7}$ second) small enough that there was no need to correct the data for counting losses.

### c. Hydrogen Target

The hydrogen target differs from one previously described[6] only in the physical dimensions of the scattering cell. The cell has an inside diameter of 3.75 inches and walls of stainless steel 0.005 inch thick. Concentric with it are the radiation shield (0.002-inch thick aluminum) and the external duraluminum vacuum jacket, 5 inches in diameter and 0.015 inch thick. Purified hydrogen gas was used in the transfer of the liquid hydrogen from storage Dewar to target reservoir, and to apply the pressure required to remove the liquid hydrogen from the scattering cell during the experiment.

## III. ENERGY OF THE PIONS

The range of the pions in copper was observed by setting counters No. 1, 2, 3, and 4 in line in the beam and measuring the ratio $Q/D$ as a function of the thickness of the copper absorber placed between counters No. 2 and 3. A typical curve obtained is plotted in Fig. 2. To the mean range obtained from this curve is added 1.74-g/cm² aluminum equivalent as the contribution of counter No. 3 and part of No. 4 to the range; 1.02-g/cm² aluminum equivalent is subtracted to represent the contribution of half the hydrogen and the walls of the scattering cell. The result is the mean range of the pions in the center of the hydrogen cell. This is converted to energy using Aron's tables[16] and the value[17] 0.1488 for the ratio of the mass of the pion to the mass of the proton. Two runs were made on the angular distribution of the scattering; in the first of these, the mean energy so obtained was 216 Mev, in the second 218 Mev. The energy spread of the beam was estimated as ±4 Mev in each case. The two runs were averaged and the energy of the average was thus taken as 217 Mev with a spread of ±5 Mev.

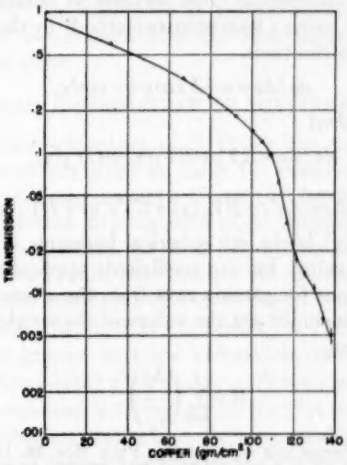


FIG. 2. Range curve in copper taken during Run 2.

TABLE I. Observed values of the fraction ($Q/D$) of pions interacting to give a gamma ray, in units of $10^{-4}$.

| Lab angle | With hydrogen | Without hydrogen | Net |
|---|---|---|---|
| | Run 1 | | |
| 25.7° | 530.1±14.5 | 155.2±9.6 | 374.9±17.4 |
| 51.4° | 251.4±10.0 | 35.4±5.2 | 216.0±11.3 |
| 77.1° | 137.4± 7.4 | 29.7±4.4 | 107.7± 8.6 |
| 102.8° | 113.6± 6.7 | 30.0±4.8 | 83.6± 8.2 |
| 128.6° | 140.4± 7.5 | 45.9±5.5 | 94.5± 9.3 |
| 154.3° | 164.4± 8.1 | 81.1±6.8 | 83.3±10.6 |
| | Run 2 | | |
| 25.7° | 453.3±18.9 | 118.7±12.2 | 334.6±22.5 |
| 51.4° | 186.5± 9.6 | 34.4± 6.2 | 152.1±11.4 |
| 77.1° | 124.0± 7.9 | 41.0± 6.4 | 83.0±10.2 |
| 102.8° | 106.0± 7.3 | 25.4± 5.3 | 80.6± 8.1 |
| 128.6° | 125.1± 7.9 | 39.9± 5.5 | 85.2± 9.3 |
| 154.3° | 161.5± 9.0 | 76.5± 7.6 | 85.0±11.8 |

Averaged values

| Lab angle | Net |
|---|---|
| 25.7° | 354.8±20.1 |
| 51.4° | 184.1±32.0 |
| 77.1° | 95.4±12.3 |
| 102.8° | 82.1± 5.8 |
| 128.6° | 89.8± 6.5 |
| 154.3° | 84.2± 7.9 |

From the range curve it is also possible to estimate the purity of the beam. The residual counts after the pions have been absorbed are due to muons (the muon momentum obtained from the range agreeing closely with that of the pions). For the geometry used, multiple scattering corrections to the muon intensity are large. An estimate of these gives 3±1 percent as a value for the muon contamination. A later curve (see Sec. VI) in which the corrections for multiple scattering are small gives a pion content of 97±1 percent, and this value was used throughout.

## IV. ANGULAR DISTRIBUTION OF GAMMA RAYS

The experiments of AFMN[5] detected the gamma rays and pions by measuring the coincidences $Q/D$ with and without lead in front of counter No. 3. The measurements without lead included the scattered pions plus some converted gamma rays; the lead measurement included the pions but added about one-half the gamma

[16] W. A. Aron, University of California Radiation Laboratory Report UCRL-1325, 1951 (unpublished).
[17] Smith, Birnbaum, and Barkas, Phys. Rev. 91, 765 (1953).

TABLE II. Differential cross sections for $\pi^-+p\rightarrow\gamma$.

| Laboratory angle $\theta$ (deg) | Angle in the barycentric system $\chi$ (deg) | Mean gamma-ray energy $\bar{\nu}_l$ (Mev) | Solid angle $\Delta\omega$ (sterad) | Gamma-ray detection efficiency $\epsilon_\gamma$ | Fraction of pions giving gamma ray in units of $10^{-6}$ $Q/D$ | Differential cross section in laboratory ($10^{-27}$ cm$^2$/sterad) | Differential cross section in the barycentric system, for $\gamma$ from $\pi^0$ ($10^{-27}$ cm$^2$/sterad) |
|---|---|---|---|---|---|---|---|
| 25.7 | 32.9 | 176 | 0.110 | 0.595 | 354.8±20.1 | 14.68±0.98 | 9.31±0.61 |
| 51.4 | 63.9 | 162 | 0.110 | 0.573 | 184.1±32.0 | 7.96±1.46 | 5.98±1.11 |
| 77.1 | 91.9 | 144 | 0.109 | 0.552 | 95.4±12.3 | 4.29±0.60 | 4.03±0.56 |
| 102.8 | 116.7 | 129 | 0.109 | 0.532 | 82.1± 5.8 | 3.84±0.31 | 4.53±0.36 |
| 128.6 | 139.2 | 118 | 0.110 | 0.516 | 89.8± 6.5 | 4.31±0.35 | 6.11±0.50 |
| 154.3 | 160.0 | 111 | 0.110 | 0.516 | 84.2± 7.9 | 4.02±0.41 | 6.40±0.66 |

rays. Because of the need for using both of the measurements to calculate either of the cross sections for process (2) or (3), the standard deviations of the results are somewhat larger than those for either one of the measurements. It is, however, possible to separate the two processes partially by using the anticoincidence technique described above, which detects only the gamma rays. The results of this give the cross section for production of gamma rays, directly. Not only does this eliminate the increased standard deviation due to the combination of measurements; the much decreased background of the anticoincidence observations increases the accuracy of the measurement itself. The observed values of $Q/D$ for the anticoincidence measurements are given in Table I. The errors quoted are the standard deviations.

The efficiency of the detecting telescope includes a large correction for the scattering and absorption of the electrons in the lead. The scattering correction can be reduced considerably by having the lead as close as possible to the last counter, and this was done here; in the previous experiment[5] the increased background prevented this. The probability of detecting the gamma rays by the electrons or positrons produced in the lead converter was calculated as a function of gamma-ray energy and scattering angle $\theta$, making approximate corrections for the absorption (which decreases the probability) and the large scattering (which increases the probability) of the electrons.[5] These corrections varied from 1.5 percent at the lowest energy to 14 percent at the highest energy. Corrections made in a similar manner in reference 5 gave a calculated efficiency in agreement with a measured value.

The resulting probabilities were multiplied by (a) 0.994 to correct for the gamma rays internally converted[18] and thus not detected, and (b) 0.973 to 0.975 depending on the energy, to correct for the gamma rays converted in the hydrogen, cell walls, and counter No. 5, and therefore not detected. To this was added 0.008 to 0.009 (depending on energy), the probability of conversion in counter No. 3 multiplied by the fraction of gamma rays reaching the counter, to give the probabilities for gamma detection $\epsilon_\gamma$ listed in the fifth column of Table II.

The differential cross section is then given by

$$\frac{d\sigma}{d\omega}=\frac{Q/D}{\epsilon_\gamma(0.993)(0.97)(3.82\times10^{23})\Delta\omega}=\frac{2.69\times10^3}{\epsilon_\gamma\Delta\omega}Q/D,$$

in units of $10^{-27}$ cm$^2$/sterad, where the 0.993 is a correction factor due to the attenuation of the beam in passing through the hydrogen, the 0.97 is the fraction of incident particles which are pions, $3.82\times10^{23}$ is the number of hydrogen atoms per square centimeter, and $\Delta\omega$ is the solid angle in steradians subtended by counter No. 4. Observations of the pion flux at the target indicated that the center of the beam did not coincide with the scattering center (see Sec. VI). This gives a small (one to two percent) correction to the solid angle, dependent on the scattering angle $\theta$. Table II contains the pertinent data: $\theta$ and $\chi$ are the angles of observation in the laboratory system and in the barycentric system, respectively, $\bar{\nu}_l$ is the mean energy of the gamma rays in the laboratory system, and the last column has the contribution of the reaction $\pi^-+p\rightarrow n+\gamma$ (which is estimated from the inverse process[19] as $0.05\times10^{-27}$ cm$^2$/sterad) subtracted.

The six differential cross sections so obtained have been fitted, using a least squares method[20] by the possible angular distributions

$$d\sigma/d\omega=a+b\cos\chi+c\cos^2\chi, \tag{4}$$

the equivalent

$$d\sigma/d\omega=AY_0+BY_1(\chi)+CY_2(\chi), \tag{5}$$

and

$$d\sigma/d\omega=AY_0+BY_1(\chi)+CY_2(\chi)+DY_3(\chi), \tag{6}$$

where $Y_n(\chi)$ is the $n$th spherical harmonic. Table III gives the values for the coefficients applicable to the cross sections for gamma rays from the $\pi^0$ and for the $\pi^0$'s. Also included are the values of the weighted least squares sum,

$$M=\sum_{i=1}^{6}\left(\frac{\Delta_i}{e_i}\right)^2, \tag{7}$$

[18] R. H. Dalitz, Proc. Roy. Soc. (London) **A64**, 667 (1951); Lindenfeld, Sachs, and Steinberger, Phys. Rev. **89**, 531 (1953).

[19] J. Steinberger and A. S. Bishop, Phys. Rev. **86**, 171 (1952); White, Jacobson, and Schulz, Phys. Rev. **88**, 836 (1952).

[20] M. E. Rose, Phys. Rev. **91**, 610 (1953).

TABLE III. Angular distribution of charge-exchange scattering.

| Process | $d\sigma/d\omega = a + b\cos\chi + c\cos^2\chi$ $a$ | $b$ | $c$ | Weighted least squares sum, $M$ |
|---|---|---|---|---|
| $\pi^- \to \gamma$ | 4.32±0.37 | 1.80±0.38 | 4.85±0.76 | 1.35 |
| $\pi^- \to \pi^0$ | 1.36±0.22 | 1.23±0.26 | 4.82±0.76 | |

| Process | $d\sigma/d\omega = AY_0 + BY_1(\chi) + CY_2(\chi) + DY_3(\chi)$ $A$ | $B$ | $C$ | $D$ | Weighted least squares sum, $M$ |
|---|---|---|---|---|---|
| $\pi^- \to \gamma$, $D=0$ | 21.06±0.88 | 3.67±0.80 | 5.12±0.80 | | 1.35 |
| $\pi^- \to \gamma$ | 20.65±1.03 | 3.55±0.83 | 5.54±0.96 | 0.79±1.02 | 0.78 |
| $\pi^- \to \pi^0$, $D=0$ | 10.53±0.44 | 2.52±0.54 | 5.10±0.80 | | |
| $\pi^- \to \pi^0$ | 10.33±0.51 | 2.42±0.57 | 5.51±0.96 | 1.18±1.52 | |

$Y_0 = 1/(4\pi)^{\frac{1}{2}}$,
$Y_1 = (3/4\pi)^{\frac{1}{2}}\cos\chi$,
$Y_2 = (5/4\pi)^{\frac{1}{2}}(\frac{3}{2}\cos^2\chi - \frac{1}{2})$,
$Y_3 = (7/4\pi)^{\frac{1}{2}}(5\cos^3\chi - 3\cos\chi)/2$.

which serve as an indication of the goodness of the fit. Here $\Delta_i$ is the deviation of the calculated $i$th cross section from the observed value and $e_i$ is the assigned error to the observed cross section.

If the coefficients for $(d\sigma/d\omega)_\gamma$ are represented by the subscripts $\gamma$ and those for $(d\sigma/d\omega)_{\pi^0}$ with subscript 0, it can be shown[5] that

$$A_\gamma = 2A_0,$$

$$B_\gamma = \left(\frac{2\gamma}{\eta} - \frac{1}{\eta^2}\ln\frac{\gamma+\eta}{\gamma-\eta}\right)B_0 = 1.464B_0,$$

$$C_\gamma = \left(2 + \frac{6}{\eta^2} - \frac{3\gamma}{\eta^3}\ln\frac{\gamma+\eta}{\gamma-\eta}\right)C_0 = 1.005C_0,$$

$$D_\gamma = \left[\frac{2\gamma}{\eta} + 15\frac{\gamma}{\eta^3} - \frac{3}{2}\left(\frac{5}{\eta^4} + \frac{4}{\eta^2}\right)\ln\frac{\gamma+\eta}{\gamma-\eta}\right]D_0 = 0.666D_0,$$

where $\eta$ and $\gamma$ are the momentum and energy of the $\pi^0$ in the barycentric system, in units of $\mu c$ and $\mu c^2$, respectively.

Figure 3 is a plot of the two fitted angular distributions, with the experimental points included. Good agreement is obtained with the first three spherical harmonics alone.

## V. ANGULAR DISTRIBUTION OF SCATTERED PIONS

The observed values of $Q/D$ for the coincidence measurement are given in Table IV. However, in this case each of these numbers is the sum of: (a) the number of pions emitted into the solid angle multiplied by an efficiency to account for their absorption in the hydrogen, target walls and counter No. 3, and (b) the gamma rays converted in the hydrogen, target walls and counter No. 3. The efficiencies for detecting the pions and gamma rays are included in Table V; the cross sections obtained from the anticoincidence measurement were used in correcting the data for the gamma-ray contribution. Table V is similar to Table II, with the first and second columns giving the angles of observation in the laboratory system and the barycentric system, respectively, the third and fourth columns the efficiencies for detecting the pions ($\epsilon_\pi$) and the gamma rays ($\epsilon_\gamma'$), and the last two columns giving the differential cross sections in the laboratory system and in the barycentric system, respectively. The reduced values for $\epsilon_\pi$ at 25.7° and 51.4° are caused by the absorption of the pions in the aluminum absorbers placed in front of counter No. 4 at these angles to keep all recoil protons from reaching the last counter.

The differential cross section in the laboratory is given by the relation

$$\frac{d\sigma}{d\omega} = 2.69\times10^3\frac{(Q/D)_\pi - (\epsilon_\gamma'/\epsilon_\gamma)(Q/D)_\gamma}{\epsilon_\pi\Delta\omega}10^{-27}\ \text{cm}^2/\text{sterad},$$

where $(Q/D)_\pi$ refers to the values in Table IV, $(Q/D)_\gamma$ to those given in Table I. The corrections due to the gamma ray sensitivity are from six to thirteen percent.

As in the case of the gamma-ray measurement, the differential cross sections were analyzed in the form of

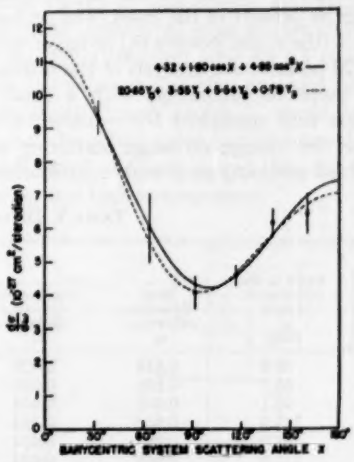


FIG. 3. Differential cross sections of $\pi^- \to \gamma$. The curves are least squares fits to the expressions $a_\gamma + b_\gamma\cos\chi + c_\gamma\cos^2\chi$ and $A_\gamma Y_0 + B_\gamma Y_1(\chi) + C_\gamma Y_2(\chi) + D_\gamma Y_3(\chi)$.

TABLE IV. Observed values of the fraction ($Q/D$) of pions elastically scattered, in units of $10^{-6}$.

| Lab angle | With hydrogen | Without hydrogen | Net |
|---|---|---|---|
| | Run 1 | | |
| 25.7° | 840.7±16.0 | 665.0±16.8 | 175.7±23.2 |
| 51.4° | 193.0± 7.5 | 96.8± 6.8 | 96.2±10.1 |
| 77.1° | 125.5± 5.3 | 83.4± 4.7 | 42.1± 6.9 |
| 102.8° | 111.5± 5.3 | 71.6± 4.9 | 39.9± 7.2 |
| 128.6° | 144.2± 5.9 | 97.5± 5.9 | 46.7± 8.3 |
| 154.3° | 248.6± 6.6 | 194.2± 6.6 | 54.4± 9.3 |
| | Run 2 | | |
| 25.7° | 587.3±11.2 | 463.1±11.5 | 124.2±16.1 |
| 51.4° | 169.5± 6.3 | 94.4± 5.4 | 85.1± 8.3 |
| 77.1° | 125.7± 5.1 | 100.1± 4.6 | 25.6± 6.9 |
| 102.8° | 105.0± 4.2 | 78.7± 4.1 | 26.3± 5.9 |
| 128.6° | 147.9± 6.1 | 106.7± 5.5 | 41.2± 8.2 |
| 154.3° | 278.4± 8.6 | 209.2± 7.6 | 69.2±11.5 |

Averaged values

| Lab angle | Net |
|---|---|
| 25.7° | 150.0±25.8 |
| 51.4° | 90.7± 6.6 |
| 77.1° | 33.9± 8.3 |
| 102.8° | 33.1± 6.8 |
| 128.6° | 43.9± 5.8 |
| 154.3° | 61.8± 7.4 |

Eqs. (4) and (6) using a least squares method. The results, including the values of the weighted least squares sum $M$, are given in Table VI and plotted in Fig. 4.

Rose has shown[20] that $M$ should be about equal to the number of data minus the number of parameters of the fit. For the angular distribution fitted here, $M$ should then be about 3. If it is considerably larger, there are two possible conclusions: either there are systematic errors in the experiment or the fit is being made with too few parameters. Bodansky, Sachs, and Steinberger[4] have made use of the Monte Carlo method to estimate the probability of a given value of $M$; this analysis gives the result that here $M$ is expected less than 2.3 in 50 percent of the cases. The probability of an $M$ of 4.3 (the $s$- and $p$-wave fit) or larger would then be about 20 percent. An analysis of the ordinary scattering is therefore compatible with a small $d$-wave contribution with coefficient $D=-0.80\pm0.43$; on the other hand the charge exchange scattering was adequately fitted assuming no $d$-wave contribution.

## VI. TOTAL CROSS SECTIONS

The differential cross-section measurements in the laboratory system can be integrated to give the total cross sections for ordinary and charge exchange scattering. Such an integration gives the values in the third line of Table VII. A comparison of these results with a previous angular distribution measurement[8] and a separate transmission measurement[21] indicates some disagreement in the ordinary scattering cross section. A third run was then made, in which the total cross section was measured by a transmission measurement and the differential cross section at 90° for process (2) was also observed at the same time, for pion energies of 209 and 220 Mev.

The electronic equipment and the hydrogen target used were the same as those used in Runs 1 and 2; however, a completely different set of counters was employed. The details of the geometry are given in Fig. 5. Counters No. 1 and 2 were $\frac{1}{8}$ inch thick by 2 inches by 2 inches plastic scintillators, with counter No. 2 three and three-quarters inches from the center of the hydrogen cell. Counters No. 3 and 4 were at 90° to the incident beam direction and counters No. 5 and 6 were in line with the first two counters. Counters No. 3 and 5 were plastic scintillators 7 inches wide, 9 inches high, and $\frac{1}{8}$ inch thick; counters No. 4 and 6 were liquid scintillation counters 8 inches in diameter and $\frac{3}{4}$ inch in overall thickness. Observations were made of the quadruple coincidences ($Q$) of counters No. 1, 2, 3, and 4, the quadruple coincidences ($Q'$) of counters No. 1, 2, 5, and 6, and the double coincidences ($D$) of counters No. 1 and 2.

The incident pion energy was measured by taking a range curve in copper as described above. This was done for the incident beam with no absorber and for the case where 5.0 g/cm² of polyethylene was placed in the pion beam between the steering magnet and counter No. 1. The energies of the beams in the two situations were calculated using the mean of the two range measurements and the calculated loss of energy in the polyethylene. The beam without absorber had an energy of 220±6 Mev and the beam with the polyethylene in it an energy of 209±6 Mev, where the ±6 Mev is an

TABLE V. Differential cross sections for $\pi^-+p\rightarrow\pi^-+p$.

| Laboratory angle $\theta$ (deg) | Angle in the barycentric system $\chi$ (deg) | Pion detection efficiency $\epsilon_\pi$ | Gamma-ray detection efficiency $\epsilon_\gamma'$ | Solid angle $\Delta\omega$ (sterad) | Fraction of pions elastically scattered units of $10^{-6}$ $Q/D$ | Differential cross section in laboratory ($10^{-27}$ cm²/sterad) | Differential cross section in barycentric system ($10^{-27}$ cm²/sterad) |
|---|---|---|---|---|---|---|---|
| 25.7 | 33.9 | 0.824 | 0.026 | 0.110 | 150.0±25.8 | 4.02±0.82 | 2.42±0.49 |
| 51.4 | 65.7 | 0.896 | 0.025 | 0.110 | 90.7± 6.6 | 2.28±0.20 | 1.67±0.15 |
| 77.1 | 94.1 | 0.968 | 0.024 | 0.109 | 33.9± 8.3 | 0.77±0.22 | 0.73±0.21 |
| 102.8 | 119.0 | 0.968 | 0.024 | 0.109 | 33.1± 6.8 | 0.76±0.18 | 0.93±0.22 |
| 128.6 | 141.0 | 0.968 | 0.024 | 0.110 | 43.9± 5.8 | 1.02±0.16 | 1.57±0.24 |
| 154.3 | 161.0 | 0.968 | 0.024 | 0.110 | 61.8± 7.4 | 1.47±0.19 | 2.62±0.35 |

[21] Anderson, Fermi, Long, Martin, and Nagle, Phys. Rev. 85, 934 (1952).

estimate of the spread of the beam energy taken from the absorption curve.

A check was made of the beam spread at the hydrogen target using a terphenyl crystal scintillation counter movable in the horizontal direction, with the crystal $\frac{3}{16}$ inch wide by 1 inch high. This distribution was integrated numerically over the cell to give an effective pion length in the hydrogen. This correction amounted to two percent.

From the observations of $Q'/D$, the cross section was calculated using the expression

$$e^{-N\sigma}=R-r(1-R),$$

where $N$ is the number of hydrogen nuclei per square centimeter, $3.69\times10^{23}$, $\sigma$ the total cross section, $r$ the ratio of the number of muons to pions in the beam, 0.03, and $R$ the ratio of $Q'/D$ with hydrogen to $Q'/D$ without hydrogen, $0.98056\pm0.00073$ at 209 Mev and $0.98213\pm0.00059$ at 220 Mev. A number of corrections were made to these values for $\sigma$. They have to be increased because of the scattered pions, gamma rays converted in the hydrogen target and counter No. 5, and the protons counted by counter No. 6. These corrections were made using the 210-Mev data[8] and the results reported above; they were about 1.5 percent, less than 0.1 percent, and 2.5 percent for the three kinds of particles, respectively. The values of $\sigma$ would be decreased by the corrections for the multiple scattering out of the pions in the hydrogen and scattering out of the beam from increased $\pi$–$\mu$ decay due to the hydrogen. However, these were less than 0.1 percent because of the large angle subtended by counter No. 6 at the hydrogen cell and were neglected. The corrected values for $\sigma$ are then $57.2\pm2.9\times10^{-27}$ cm² at 209 Mev and $52.1\pm2.3\times10^{-27}$ cm² at 220 Mev.

TABLE VI. Angular distribution of the scattering $\pi^-+p\rightarrow\pi^-+p$.

| $d\sigma/d\omega=a_-+b_-\cos\chi+c_-\cos^2\chi$ | | | | Weighted least squares sum, $M$ |
|---|---|---|---|---|
| $a_-$ | $b_-$ | $c_-$ | | |
| 0.85±0.15 | 0.75±0.22 | 2.36±0.44 | | 4.33 |
| $d\sigma/d\omega=A_-Y_0+B_-Y_1(\chi)+C_-Y_2(\chi)+D_-Y_3(\chi)$ | | | | |
| $A_-$ | $B_-$ | $C_-$ | $D_-$ | Weighted least squares sum $M$ |
| $D=0$ 5.80±0.35 | 1.53±0.44 | 2.50±0.47 | | 4.33 |
| 5.35±0.43 | 0.95±0.55 | 2.01±0.54 | −0.80±0.43 | 0.50 |

TABLE VII. Total cross sections.

| Energy (Mev) | $\sigma(\pi^-\rightarrow\pi^-)$ ($10^{-27}$ cm²) | $\sigma(\pi^-\rightarrow\gamma)$ ($10^{-27}$ cm²) | Total $\sigma(\pi^-)$ ($10^{-27}$ cm²) | Differential cross section at 90° in the laboratory for $\pi^-+p\rightarrow\pi^-+p$ ($10^{-27}$ cm²/sterad) |
|---|---|---|---|---|
| 210[a] | 28.7±3.1 | 69.1±7.2 | 64 ±5 | 1.47±0.29 |
| 217[b] | | | 60 ±6 | |
| 217 | 18.2±2.3 | 72.2±6.8 | 54.5±5 | 0.76±0.21 |
| 209 | | | 57.2±2.9 | 0.86±0.20 |
| 220 | | | 52.1±2.3 | 1.03±0.16 |

[a] See reference 8.
[b] See reference 21.

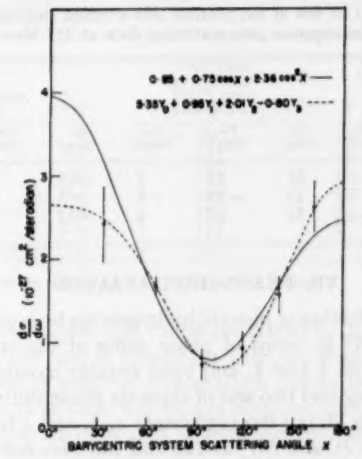


FIG. 4. Differential cross sections of $\pi^-\rightarrow\pi^-$. The curves are least squares fits to the expressions $a_-+b_-\cos\chi+c_-\cos^2\chi$ and $A_-Y_0+B_-Y_1(\chi)+C_-Y_2(\chi)+D_-Y_3(\chi)$.

The observations of $Q/D$ were treated as described previously, and the values of the differential cross-section at 90° in the laboratory system are given in Table VII. The corrections for gamma rays included in $Q/D$ were about eight percent.

The measurements of the total cross section given in Table VII thus seem to agree satisfactorily; there is some indication of a small decrease in the total cross section with energy in this energy interval. The observations of the differential cross section at 90° of the ordinary scattering reported here are all considerably lower than the value at 210 Mev reported previously[8] of $1.47\pm0.29\times10^{-27}$ cm²/sterad. It would be fair to conclude that the actual value in this interval is of the order of $0.9\times10^{-27}$ cm²/sterad, and that the figure reported earlier is a high measurement.

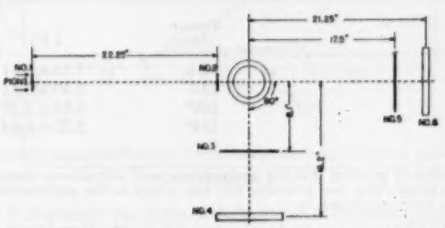

FIG. 5. Details of the geometry used in measuring the total cross section, and the differential cross section at 90° for the process $\pi^-+p\rightarrow\pi^-+p$. Counters No. 1, 2, 3, and 4 are in coincidence; counters No. 1, 2, 5, and 6 are also in coincidence.

TABLE VIII. A few of the possible sets of phase shift solutions to the negative pion scattering data at 217 Mev.

| $\alpha_3$ (deg) | $\alpha_1$ (deg) | $\alpha_{33}$ (deg) | $\alpha_{31}$ (deg) | $\alpha_{13}$ (deg) | $\alpha_{11}$ (deg) | Total cross sections for $\pi^+$ Calculated ($10^{-27}$ cm$^2$) |
|---|---|---|---|---|---|---|
| 20 | 7 | 72 | 12 | 2 | −15 | 157 |
| 20 | 7 | 42 | −79 | −5 | −5 | 160 |
| −69 | −3 | 33 | 45 | 4 | −12 | 160 |

## VII. PHASE-SHIFT ANALYSIS

The scattering of pions in hydrogen has been analyzed by AFMN[5] in terms of phase shifts of the states of isotopic spin $\frac{1}{2}$ and $\frac{3}{2}$, and total angular momentum $\frac{1}{2}$ and $\frac{3}{2}$. They find two sets of these six phase shifts which fit the nine data [the coefficients $a$, $b$, and $c$ for reactions (1), (2), and (3)] at 120 and 135 Mev fairly well, and these sets are given in reference 5. However, an analysis of the scattering of negative pions in hydrogen at higher energies in terms of these six phase shifts gives a large number of possible solutions because there are only six data to determine the six phase shifts. A graphical method[22] was used to obtain some of these sets as approximate solutions and these are given as examples in Table VIII, along with the predicted total positive pion cross sections. They are approximate in that they were checked against the cross sections to see that the fits were good, but they were not varied to make $M$ go all the way to zero or very near it. With the negative data alone, an analysis using the six phase shifts of $s$ and $p$ waves gives ambiguous results; if $d$ waves are to be included, the situation is still more confusing. The use of positive scattering data would help remove this ambiguity. The present positive data in this energy region consist of the observations of Homa, Goldhaber, and Lederman[11] at 188 Mev, and those of Fowler *et al.*[9] at a mean energy of about 235 Mev but with an energy spread from 210 to 330 Mev. Because of the difficulty of interpolating satisfactorily to data based on such a broad spectrum, an analysis using some interpolation of this data was not made.

Because of these difficulties, it was thought that an analysis in terms of fewer phase shifts might prove interesting. It should be stressed that the author presents this analysis only as an interesting calculation: there is no evidence that the assumption that some of the phase shifts are zero is correct, nor is there a sound theoretical basis for the choices made here.

The phase shifts used in reference 5 were labelled as $\alpha_3$, $\alpha_1$, $\alpha_{33}$, $\alpha_{31}$, $\alpha_{13}$, and $\alpha_{11}$ where the first subscript is twice the total isotopic spin, the second is missing for $s$ waves and is twice the total angular momentum for $p$ waves. The results of AFMN[5] indicate that $\alpha_{31}$, $\alpha_{13}$, and $\alpha_{11}$ are small in the "first" solution; it was considered worthwhile, seeing how good a fit could be obtained with $\alpha_{33}$, $\alpha_3$, and $\alpha_1$ alone.[23,24] The scattering at 120, 135, 169, 194, and 217 Mev was analyzed in this way; the data used are summarized in Table IX. Here $k$ is the wave number in the barycentric system, and the positive pion values are interpolated from the known data.[9,11,12,25]

As a trial set of phase shifts, $\alpha_{33}$, $\alpha_3$, and $\alpha_1$ were obtained from a graphical analysis[22] using the relations

$$|X+Y|^2=36k^2(a_-+b_-+c_-),$$

$$|X-Y|^2=36k^2(a_--b_-+c_-),$$

$$4\pi\left(a_-+\frac{c_-}{3}+a_0+\frac{c_0}{3}\right)=-\frac{4\pi}{6k^2}\,\mathrm{Re}(X+Y),$$

where the first two equations come from the expressions for the phase shifts, and the last from the "Optical

TABLE IX. Angular distributions used in phase-shift analysis.

| Energy (Mev) | Process $\pi^-+p\to\pi^-+p$: $d\sigma/d\omega=a+b\cos\chi+c\cos^2\chi$ | | | Process $\pi^-+p\to\pi^0+n$ | | |
|---|---|---|---|---|---|---|
| | $36\,k^2a_-$ | $36\,k^2b_-$ | $36\,k^2c_-$ | $18\,k^2a_0$ | $18\,k^2b_0$ | $18\,k^2c_0$ |
| 120 | 1.38±0.31 | 0.96±0.45 | 3.28±0.96 | 0.85±0.56 | −2.68±0.71 | 4.52±2.40 |
| 135 | 2.26±0.45 | 1.87±0.64 | 4.48±1.45 | 1.42±0.73 | −3.06±0.81 | 5.88±3.06 |
| 169 | 3.14±0.93 | 2.31±1.42 | 14.93±3.05 | 4.54±1.77 | −1.50±1.52 | 10.44±5.58 |
| 194 | 5.50±1.18 | 3.19±1.97 | 14.10±3.93 | 4.25±1.97 | −0.22±1.82 | 14.47±6.41 |
| 217 | 4.73±0.85 | 4.18±1.15 | 13.14±2.36 | 3.79±0.57 | 3.42±0.71 | 13.42±2.00 |

| Energy (Mev) | Process $\pi^++p\to\pi^++p$ | | |
|---|---|---|---|
| | $4\,k^2a_+$ | $4\,k^2b_+$ | $4\,k^2c_+$ |
| 120 | 1.16±0.41 | −1.79±0.50 | 3.67±1.22 |
| 135 | 1.40±0.82 | −2.54±1.00 | 6.45±2.44 |
| 169[a] | 3.85±1.40 | −1.95±1.00 | 7.3 ±2.3 |
| 194[a] | 5.20±1.84 | −1.3 ±1.0 | 8.8 ±3.5 |

[a] It should be noted that the positive data used here do not conform to the requirements of the "Optical Theorem" and analysis for the positive scattering phase shifts (see reference 22); this is due to the asymmetries of the measured angular distributions. The best-fit values, however, do of course satisfy these requirements.

[22] J. Ashkin and S. H. Vosko, Phys. Rev. **91**, 1248 (1953).

[23] The suggestion of an analysis in terms of only these three phase shifts was made to the author by Professor G. Wentzel.

[24] Dr. R. L. Martin of Cornell University has made a similar analysis (assuming however only $\alpha_{13}=\alpha_{11}=0$) using four phase shifts; see R. L. Martin, Phys. Rev. **94**, 765 (1954).

[25] I am grateful to Professor Fermi for making available his analysis and interpolation of the positive pion data.

TABLE X. A set of phase shifts assuming $\alpha_{31}=\alpha_{13}=\alpha_{11}=0$.

| Energy (Mev) | Pion momentum in barycentric system $\eta$ | $\alpha_{33}$ (deg) | $\alpha_3$ (deg) | $\alpha_1$ (deg) | Total cross section for $\pi^+$ ($10^{-27}$ cm$^2$) (calculated | Weighted least squares sum $M$ | $M$ (expected) |
|---|---|---|---|---|---|---|---|
| 120 | 1.24 | 32 | −13 | 9 | 100 | 3.9 | 6 |
| 135 | 1.33 | 40 | −11 | 11 | 121 | 4.7 | 6 |
| 169 | 1.51 | 65 | −15 | 10 | 174 | 6.1 | 6 |
| 194 | 1.63 | 84 | −5 | 14 | 184 | 4.3 | 6 |
| 194 | | 78 | −12 | −16 | 179 | 5.7 | 6 |
| 217[a] | 1.76 | 100 | −23 | −4 | 171 | 8 | 9 |

[a] The phase shifts at 217 Mev predict the angular distribution for positive pion scattering: $(d\sigma/d\omega)_{\pi^+}=7.3+5.4\cos\chi+18.8\cos^2\chi$.

Theorem"[22] which states that the total cross section is equal to $4\pi/k$ times the imaginary part of the forward elastic scattering amplitude. $X$ and $Y$ are given by

$$X=e^{2i\alpha_3}+2e^{2i\alpha_1}-3, \quad Y=2e^{2i\alpha_{33}}-2.$$

By using the $a$'s, $b$'s, and $c$'s in the above expressions, a set of three phase shifts can be calculated graphically; these values were then used to try to fit all nine coefficients except at 217 Mev, where they were tested against the twelve measured differential cross sections for negative pion scattering. It was found that the values of $M$ obtained were somewhat insensitive to small variations of the phase shifts, and there is some considerable scatter of the value of $\alpha_3$, for example. The phase shifts were calculated by numerically minimizing $M$; this was not exhaustive nor was a search for other possible solutions made. However, at 194 Mev, another similar set giving a poorer fit was found and is included in Table X, which gives the results of the analysis. The signs of the phase shifts were chosen so that $\alpha_3$ was negative, in agreement with present experimental evidence.[4,26] At 217 Mev, a positive $\alpha_3$ could correspond to $\alpha_{33}$, being 80° instead of 100°. The last column gives the value of $M$ expected from the least squares criterion[20] discussed in Sec. V. The total cross sections for positive pion scattering calculated from these best fits are included, as well as the expected values of $a_+$, $b_+$, and $c_+$ for the 217-Mev positive pion scattering. It is seen that all the calculations give fits within the $M$ criterion, indicating that this analysis is a good fit to the data.

The phase shifts obtained in this way are plotted in Fig. 6 against $\eta$, the pion momentum in the barycentric system. The phase shift $\alpha_{33}$ behaves as $18°\,\eta^3$ and passes through 90° in the vicinity of 200 Mev; $\alpha_3$ probably varies as $-8°\,\eta$, and $\alpha_1$ seems to be a constant 10° with some possibility of a decrease at the highest energy. The behavior of $\alpha_{33}$ in this particular solution would agree with the existence of a resonance in the $\frac{3}{2}$, $\frac{3}{2}$ state as suggested by Brueckner.[27]

In Fig. 7 the positive pion cross sections calculated from the above set of phase shifts are compared to the measured values. The values calculated in the 170–220-Mev region are in agreement with the data presently available. A check of this analysis can be made when positive pion data will be available for comparison of total cross sections and angular distributions in this region.

With a knowledge of the phase shifts it is possible to estimate the influence of the Coulomb scattering on the measured angular distribution: the main contribution at the smallest angle measured is from the interference between Coulomb scattering and the pion-nucleon scattering. A calculation has been made using the three phase shifts alone, as given in Fig. 6, and also using the last of the six phase-shift examples of solutions given in Table VIII. At an angle of 33.9° in the barycentric system the correction is −0.15 or 0.12 $\times10^{-27}$ cm$^2$/sterad, for the three phase-shift and six phase-shift analyses, respectively; this is to be compared with the observed cross section $2.43\pm0.49\times10^{-27}$ cm$^2$/sterad. A correction was therefore not made to the data in calculating the coefficients of the angular distribution.

## VIII. CONCLUSIONS

The differential cross sections for the processes $\pi^-\rightarrow\pi^-$, and $\pi^-\rightarrow\gamma$ have been measured at 217 Mev and the results fitted using a least squares method to an angular distribution $a+b\cos\chi+c\cos^2\chi$. The fit for the

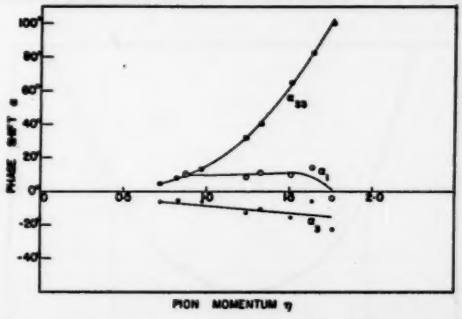


FIG. 6. A possible set of phase shifts obtained by setting $\alpha_{31}=\alpha_{13}=\alpha_{11}=0$, plotted *versus* pion momentum in the barycentric system. The values plotted for $\eta<1.0$ are the solutions of Bodansky, Sachs, and Steinberger, references 4 and 26 (58 and 65 Mev), Orear, Lord, and Weaver [Phys. Rev. 93, 575 (1954)] (45 Mev), and from AFMN, reference 5 (78 Mev).

[26] Bodansky, Sachs, and Steinberger, Phys. Rev. 93, 1367 (1954); J. Orear, Phys. Rev. 93, 918 (1954); Barnes, Angell, Perry, Miller, Ring, and Nelson, Phys. Rev. 92, 1328 (1953).

[27] K. A. Brueckner, Phys. Rev. 86, 106 (1952).

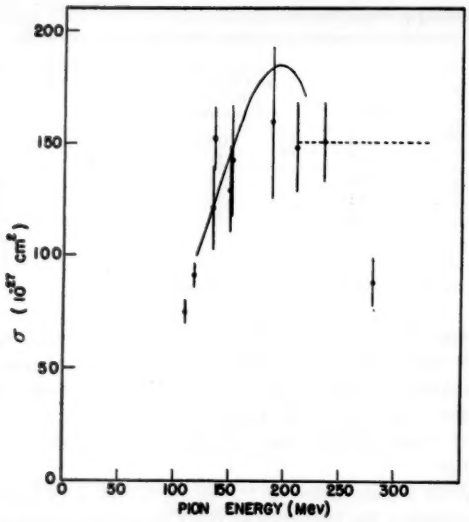


FIG. 7. Total cross sections of positive pions in hydrogen. The curve is that predicted by the three phase-shift sets given in Table X. Experimental values plotted include those of references 5, 9, 11, 12, and 28.

process $\pi^- \rightarrow \gamma$ is excellent, and the experimental results are compatible with assuming no $d$-wave contribution here. For the process $\pi^- \rightarrow \pi^-$, the fit is only fair, the value of the weighted least squares sum $M$ being 4.3 for six data fitted by three parameters; a value of $M$ as large as this has about 20 percent probability of occurring. Increasing the number of terms of the angular distribution to include $p$- and $d$-wave interference gives a good fit; the analysis is compatible with a small $d$-wave contribution.

A phase shift analysis of the type carried out by AFMN[5] is ambiguous for the negative scattering alone because of the large number of possible solutions. As an interesting exercise, three of the phase shifts were somewhat arbitrarily set equal to zero, and a solution attempted using only $\alpha_3$, $\alpha_1$, and $\alpha_{33}$. Such an analysis gives the curves plotted in Fig. 6. They are presented only as a *possible* set that does represent the data. When accurate data, both of positive and negative pion scattering, become available in this energy region, it should be possible to decide how the phase shifts behave between 135 and 220 Mev.

The integrated total cross sections are $18.2\pm2.3\times10^{-27}$ cm$^2$ for the ordinary scattering and $72.2\pm6.8\times10^{-27}$ cm$^2$ for the process $\pi^- \rightarrow \gamma$, giving a value for the total cross section of $54.5\pm5\times10^{-27}$ cm$^2$. Transmission measurements gave $57.2\pm2.9\times10^{-27}$ cm$^2$ at 209 Mev and $52.1\pm2.3\times10^{-27}$ cm$^2$ at 220 Mev, in good agreement with the value obtained from the differential cross sections. These values are also lower than the values $66\pm6\times10^{-27}$ cm$^2$ at 176 Mev[21] and $74\pm5\times10^{-27}$ cm$^2$ at 194 Mev,[8] indicating that the cross section has gone through a maximum in this energy region. The observations of Yuan and Lindebaum[28] in the energy range 265–700 Mev give the extent of the drop from the maximum: their results give a total cross section of about $25\times10^{-27}$ cm$^2$ in the region 340–500 Mev.

Observations of the differential cross section for process (2) disagree with the values obtained earlier at 210 Mev,[8] the measurements at 217 Mev being considerably lower than those at 210 Mev. The cross section was then measured at 90° at 209 and 220 Mev; the results agree with the measurement at 217 Mev and are compatible with the conclusion that the actual value in this energy region is probably about $0.9\times10^{-27}$ cm$^2$/sterad.

## IX. ACKNOWLEDGMENTS

I wish to thank Professor Herbert L. Anderson for his excellent advice and active encouragement throughout this research. I would also like to thank Dr. Ronald L. Martin and Mr. Gaurang B. Yodh for their assistance in assembling the equipment and conducting the experiment, and Mr. Joseph Fainberg for his aid during the experimental runs.

[28] L. C. L. Yuan and S. J. Lindenbaum, Phys. Rev. **93**, 917 (1954).

# Normalization of WKB-Type Approximations

S. C. MILLER, JR.
*Department of Physics, University of Colorado, Boulder, Colorado*
(Received January 22, 1954)

A method is developed for normalizing WKB-type approximations to wave functions for a simple potential well type of problem. The procedure closely resembles Furry's method of finding the normalization for the usual WKB approximations.

## I. INTRODUCTION

IN a recent paper[1] a WKB-type approximation for the solutions of the one-dimensional Schrödinger equation was described. The method was illustrated in that paper by using, as an example, the problem of a potential well with two classical turning points of the motion. In addition, for this example, an approximate method for normalizing the wave function was given. In the present paper an alternate method for obtaining the normalization is discussed. This treatment closely resembles one given by Furry[2] for the normalization of the usual WKB approximate wave functions in the case of a potential well problem with two turning points.

The function $\psi$ for which an approximation is found by Miller and Good[1] satisfies the one-dimensional Schrödinger equation,[3]

$$d^2\psi(x)/dx^2+p^2(x)\psi(x)=0, \tag{1}$$

where

$$p^2(x)=W-V(x). \tag{2}$$

Here $W$ is $2m$ times the total energy of a particle of mass $m$ moving in a potential $V(x)/2m$. The function $V(x)$ will be limited to the general form shown in Fig. 1, a potential well giving two turning points $x_1$ and $x_2$ with $x_1<x_2$. The approximation is based on the function $\phi(S)$ which satisfies a Schrödinger equation,

$$d^2\phi(S)/dS^2-P^2(S)\phi(S)=0, \tag{3}$$

for some function

$$P^2(S)=E-U(S), \tag{4}$$

in which the parameter $E$ is independent of $S$. The function $U(S)$ will here be taken qualitatively similar to $V(x)$, a potential well giving two turning points $s_1$ and $s_2$ with $s_1<s_2$. Moreover, it will be assumed that the normalizing constants of the bound states $\phi_n(S)$ are known. The approximate wave function is

$$\psi\cong S'^{-\frac{1}{2}}\phi(S), \tag{5}$$

where $S$ is given as a function of $x$ by

$$\int_{s_1}^{S}P(\sigma)d\sigma=\int_{x_1}^{x}p(\xi)d\xi. \tag{6}$$

Also the equation

$$\int_{s_1}^{s_2}P(\sigma)d\sigma=\int_{x_1}^{x_2}p(\xi)d\xi \tag{7}$$

gives the functional relationship between $W$ and $E$. If $E_n$ is the eigenvalue for the $n$th bound state of $U(S)$, the corresponding $W=W_n$ given by Eq. (7) is the approximate eigenvalue for the $n$th bound state of $V(x)$.

## II. NORMALIZATION

In this discussion $\psi_\alpha(x)$ corresponding to any $W$ will denote a solution of Eq. (1) which goes to zero as $x$ approaches minus infinity but which does not necessarily go to zero as $x$ approaches plus infinity. Likewise $\psi_\beta(x)$ is a solution which goes to zero as $x$ approaches plus infinity but not necessarily as $x$ approaches minus infinity. Furthermore the relative amplitudes of these two functions will be chosen so that when $W$ is an eigenvalue $W_n$ for the $n$th bound state, the functions $\psi_\alpha$ and $\psi_\beta$ are both the same function $\psi_n$. This function goes to zero as $x$ approaches either plus or minus infinity. Each of the functions $\psi_\alpha$ and $\psi_\beta$ satisfies Eq. (1)

$$\psi_\alpha''(x)+(W-V)\psi_\alpha(x)=0, \tag{8}$$

$$\psi_\beta''(x)+(W-V)\psi_\beta(x)=0. \tag{9}$$

Likewise, the complex conjugate of $\psi_n$ satisfies

$$\psi_n^{*\prime\prime}(x)+(W_n-V)\psi_n^*(x)=0. \tag{10}$$

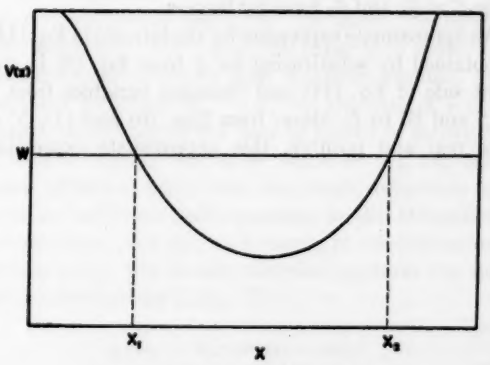


FIG. 1. Type of potential considered.

[1] S. C. Miller, Jr. and R. H. Good, Jr., Phys. Rev. **91**, 174 (1953).
[2] W. H. Furry, Phys. Rev. **71**, 360 (1947).
[3] Units have been chosen so that $\hbar=1$.

Upon multiplying Eq. (8) by $\frac{1}{2}\psi_n^*$ and Eq. (10) by $\frac{1}{2}\psi_\alpha$, subtracting one equation from the other, and integrating from $-\infty$ to a point $a$, one obtains

$$\tfrac{1}{2}\int_{-\infty}^{a}\psi_n^*\psi_\alpha dx=-\tfrac{1}{2}(W-W_n)^{-1}\times(\psi_n^*\psi_\alpha'-\psi_n^{*\prime}\psi_\alpha)_{x=a}, \quad (11)$$

since the term in parentheses on the right is zero at $x=-\infty$. If Eq. (11) is added to its complex conjugate, the result is

$$\tfrac{1}{2}\int_{-\infty}^{a}(\psi_n^*\psi_\alpha+\psi_n\psi_\alpha^*)dx=-\tfrac{1}{2}(W-W_n)^{-1}\times[\psi_n^*(\psi_\alpha'-\psi_n')-\psi_n'(\psi_\alpha^*-\psi_n^*)+\text{c.c.}]_{x=a}, \quad (12)$$

where terms have been added and subtracted on the right and c.c. means complex conjugate. Similarly using Eqs. (9) and (10), one obtains

$$\tfrac{1}{2}\int_{a}^{\infty}(\psi_n^*\psi_\beta+\psi_n\psi_\beta^*)dx=\tfrac{1}{2}(W-W_n)^{-1}\times[\psi_n^*(\psi_\beta'-\psi_n')-\psi_n'(\psi_\beta^*-\psi_n^*)+\text{c.c.}]_{x=a}. \quad (13)$$

In the limit as $W$ approaches $W_n$, a term such as $(\psi_\alpha'-\psi_n')/(W-W_n)$ becomes $\partial\psi_\alpha'/\partial W$. Therefore, the sum of Eqs. (12) and (13) in this limit is

$$\int_{-\infty}^{\infty}|\psi_n|^2dx=-\tfrac{1}{2}[\psi_n^*\partial(\psi_\alpha'-\psi_\beta')/\partial W-\psi_n'\partial(\psi_\alpha^*-\psi_\beta^*)/\partial W+\text{c.c.}]_{x=a}, \quad (14)$$

evaluted at $W=W_n$.

A similar expression holds for the integral of $|\phi_n|^2$ over $S$ in terms of $\phi_\alpha$ and $\phi_\beta$ and their derivatives with respect to $S$ and $E$, evaluated at $S(a)$ and $E_n$. The functions $\phi_\alpha$ and $\phi_\beta$ are to have the same properties for large $S$ as $\psi_\alpha$ and $\psi_\beta$ have for large $x$.

An approximate expression for the integral in Eq. (14) is obtained by substituting for $\psi$ from Eq. (5) in the right side of Eq. (14) and changing variables from $x$ to $S$ and $W$ to $E$. Since, from Eqs. (6) and (7), $S'$ is here real and positive, this approximate expression simplifies to

$$\begin{aligned}\int_{-\infty}^{\infty}|\psi_n|^2dx&=-\tfrac{1}{2}(dE/dW)[\phi_n^*\partial(d\phi_\alpha/dS-d\phi_\beta/dS)/\partial E\\&\quad-(d\phi_n/dS)\partial(\phi_\alpha^*-\phi_\beta^*)/\partial E+\text{c.c.}]_{S=S(a)}\\&=(dE/dW)\int_{-\infty}^{\infty}|\phi_n|^2dS,\end{aligned} \quad (15)$$

where each of the expressions is evaluated at $E=E_n$. With the definitions of $p^2$ and $P^2$ in Eqs. (2) and (4), differentiation of Eq. (7) leads to

$$dE/dW=\int_{x_1}^{x_2}[p(\xi)]^{-1}d\xi\Big/\int_{s_1}^{s_2}[P(\sigma)]^{-1}d\sigma. \quad (16)$$

If, then, $A_n$ is the approximate normalizing constant of $\psi_n$ and $A_n'$ is the normalizing constant of $\phi_n$, Eq. (15) can be written as

$$A_n^2/A_n'^2=\int_{s_1}^{s_2}[P(\sigma)]^{-1}d\sigma\Big/\int_{x_1}^{x_2}[p(\xi)]^{-1}d\xi. \quad (17)$$

This is the desired approximate expression giving the normalizing constant $A_n$.

For the particular $P(S)$ used in reference 1 for which $U(S)=S^2$,

$$\phi_n=H_n(S)\exp(-S^2/2), \quad (18)$$

where $H_n$ is the $n$th Hermite polynomial. Also for this case one has

$$\int_{s_1}^{s_2}[P(\sigma)]^{-1}d\sigma=\pi, \quad (19)$$

$$A_n'^2=(2^n\pi^{\frac{1}{2}}n!)^{-1}. \quad (20)$$

Therefore the normalizing constant is given by

$$A_n^2=\pi^{\frac{1}{2}}\left\{2^n n!\int_{x_1}^{x_2}[p(\xi)]^{-1}d\xi\right\}^{-1}. \quad (21)$$

For a representative case such as the potential $V(x)$ used in reference 1, the approximate normalizing constant is correct to about three significant figures. This method of normalization should give as accurate results for high-energy levels as for low ones with no appreciable change in the labor of computation. A possible defect in this method is that there appears to be no way to estimate the error in the approximation. Also there does not seem to be any way to generalize the method to give matrix elements of general functions.

# Relativistic Configuration Space Formulation of the Multi-Electron Problem. II

MARIAN GÜNTHER
*Institute of Theoretical Physics, University of Warsaw, Warsaw, Poland*
(Received January 19, 1953; revised manuscript received July 9, 1953)

This is the second part of a paper under the same title (quoted as I) and deals with an adaptation of the formalism developed there to the Dirac "hole theory." This adaptation is achieved by the application of methods which are based on the (relativistic) configuration space concept and, simultaneously, on second quantization. The electrons (and positrons) are thus divided into "configurational" and "background" electrons (and holes). This separation may be believed to give appropriate means for handling bound state problems with a finite number of configurational particles. The background is then the Dirac ("physical") vacuum.

## I. INTRODUCTION AND SUMMARY

It has been shown in I[1] that the many-time wave function for $\nu$ electrons $\varphi(x_1, \cdots x_\nu)$ can be given by

$$\varphi(x_1, \cdots x_\nu) = \sum_{n=0}^{\infty} [1/n!][1/ihc]^n \int_{-\infty}^{+\infty} \cdots \int_{-\infty}^{+\infty} d^4x^{(1)} \cdots d^4x^{(n)} \times P[\mathfrak{H}^{Ret}(x^{(1)}; x_1, \cdots x_\nu) \cdots \times \mathfrak{H}^{Ret}(x^{(n)}; x_1, \cdots x_\nu)]\chi(x_1, \cdots x_\nu), \quad (1)$$

and satisfies the equation

$$\chi(x_1, \cdots x_\nu) = \sum_{n=0}^{\infty \text{ (or } \nu)} [1/n!][-1/ihc]^n \int_{-\infty}^{+\infty} \cdots \int_{-\infty}^{+\infty} d^4x^{(1)} \cdots \times d^4x^{(n)} P^I[\mathfrak{H}^{Ret}(x^{(1)}; x_1, \cdots x_\nu) \cdots \times \mathfrak{H}^{Ret}(x^{(n)}; x_1, \cdots x_\nu)]\varphi(x_1, \cdots x_\nu), \quad (2)$$

only the first $\nu$ terms of the expansion of its right hand side being not identically zero, as it follows easily from the relation:

$$P^I[S^{Ret}(x'-x)Q(x'\to x), S^{Ret}(x''-x)Q(x''\to x)] = 0. \quad (3)$$

The following notation has been used here:

$$\mathfrak{H}^{Ret}(x; x_1, \cdots x_\nu) = -e \sum_{i=1}^{\nu} S_i^{Ret}(x_i - x)A_i(x)Q(x_i \to x), \quad (4)$$

the operators being defined by

$$Q(x_i \to x)f(x_1, \cdots x_\nu) = f(x_1, \cdots x_{i-1}, x, x_{i+1}, \cdots x_\nu), \quad (5)$$

$P$ and $P^I$ denoting the chronological and antichronological ordering operators, respectively. Further,

$$A(x) = \gamma^\mu A_\mu(x), \quad (6)$$

where $A_\mu(x)$ are the electromagnetic radiation field operators in the interaction representation, $\chi(x_1, \cdots x_\nu)$ being a function generated by the Dirac field-free operators $[\gamma^\mu(\partial/\partial x^\mu) + (mc/\hbar)]$ from the initial condition imposed on $\varphi(x_1, \cdots x_\nu)$ at $-\infty$. There is an obvious general disadvantage of the formalism based on the above equations. In the case of a finite number of physical particles one would actually have to deal with an infinite number of $x$ arguments. The "sea" of negative energy electrons would have to consist entirely of configurational "individuals," there being no place for the electron field aspect. In the formalism developed so far, use has nevertheless been made of the quantized electromagnetic field concept. Consequently, as repeatedly pointed out in I, the wave function $\varphi(x_1, \cdots x_\nu)$ should not be regarded as a function of the $x$ arguments only, but should depend on the radiation field variables also. The latter dependence of the wave function (i.e., as far as the radiation field only is concerned) is exactly of the same type as that of the state vector $\Psi[\sigma]$ of the Tomonaga-Schwinger theory. Therefore it would be most desirable to generalize this formalism by generalizing the wave function concept, so that it should become a function of the occupation numbers of a certain number of electrons, which we do not wish to treat configurationally, while it should still be possible to represent other electrons more explicitly by the $x$ arguments. The former we shall call in the sequel "background electrons," the latter "configurational electrons." The aim of this paper is to show that a generalization on these lines is indeed possible. The new wave function $v(x_1, \cdots x_\nu)$ (in the case of $\nu$ configurational electrons) will then be shown to satisfy an equation of exactly the same shape as (2), the only formal difference being that one should substitute for $A_\mu(x)$ the radiation field operators in the Heisenberg representation, and not, as hitherto, in the interaction representation. One should therefore perform the following substitutions in Eq. (2):

$$\varphi(x_1, \cdots x_\nu) \to v(x_1, \cdots x_\nu); \quad (7)$$
$$\mathfrak{H}^{Ret}(x; x_1, \cdots x_\nu) \to \mathfrak{H}^{(H)Ret}(x; x_1, \cdots x_\nu),$$

[1] Marian Günther, Phys. Rev. 88, 1411 (1952).

where, instead of (4),

$$\mathcal{H}^{(\mathrm{H})Ret}(x; x_1, \cdots x_\nu) = -e\sum_{i=1}^{\nu} S_i^{Ret}(x_i - x)\boldsymbol{A}^{(\mathrm{H})}{}_i(x)Q(x_i \to x), \quad (4')$$

$$\boldsymbol{A}^{(\mathrm{H})}(x) = \gamma^\mu A^{(\mathrm{H})}{}_\mu(x);$$
$$X^{(\mathrm{H})}(x) = U^{-1}[\sigma, -\infty]X(x)U[\sigma, -\infty], \quad (6')$$

and where the superscript (H) following an operator $X$ denotes $X$ in the Heisenberg representation. The well-known transformation matrix $U[\sigma,\sigma_0]$ will later be defined by Eqs. (24) and (25) of Sec. II. Our new formalism will furthermore enable us to introduce configurational positrons, so that in a still more general case of $\nu$ configurational particles one has instead of (4′),

$$\mathcal{H}^{(\mathrm{H})Ret}(x; x_1, \cdots x_\nu) = -\sum_{i=1}^{\nu} \epsilon_i S_i^{Ret}(x_i - x)\boldsymbol{A}^{(\mathrm{H})}{}_i(x)Q(x_i \to x), \quad (4'')$$

where $\epsilon_i = +e$ or $-e$ according to whether the $i$th particle is an electron or a positron. Equation (2) with the substitutions (7) and (4′) or (4″) performed will be referred to in the sequel as (2′) or (2″), respectively. The generalized formalism we shall call the "mixed representation formalism" to emphasize its intermediate character between the configurational representation and the methods of the second quantization. The Heisenberg operators $A^{(\mathrm{H})}{}_\mu(x)$ which appear here obviously cannot be expressed in terms of the free radiation field operators $A_\mu(x)$ only, the transformation formulas containing also the operators $\psi(x)$ and $\bar{\psi}(x')$ of the electronic background. The substitution (4′) or (4″) brings about a nontrivial modification of the formalism as the operators $A^{(\mathrm{H})}{}_\mu(x)$ when applied to the $v(x_1, \cdots x_\nu)$ function will induce changes of the occupation numbers of the background particles. The result of such an operation of $A^{(\mathrm{H})}{}_\mu(x)$ on $v(x_1, \cdots x_\nu)$ would in fact be a rather complicated expression, so that, whenever it needs to be explicitly computed, it should be given in terms of an $e$-power expansion, use being made of plane wave approximations for the background particles. This enables us also to get some information concerning the practical application of the mixed representation. One should use the configuration space to describe particles whenever their mutual interactions can be expected to be strong, and where the use of plane waves would lead to badly convergent or even divergent $e$-power expansions. For example, the bound state electrons of an atom are to be treated as configurational electrons. On the other hand, those particles whose motions either are only slightly influenced by the interactions, or else make their appearance in one or a few elementary processes (e.g., pair creation) are most conveniently chosen as background particles. The actual derivation of the mixed representation equations (2′) and (2″) is outlined in the following two sections respectively. The derivations are carried out for two-particle systems only (electron-electron and electron-positron problems) in order to avoid long formulas. A generalization leading to substitutions (4′) and (4″) will then be obvious. It might, however, be interesting to observe that in the two-body case some terms are absent which appear in the more general case. These are of the form

$$[e/ihc]^n \int_{-\infty}^{+\infty} \cdots \int_{-\infty}^{+\infty} S_1^{Ret}(x_1 - x^{(1)}) \times \cdots \times S_n^{Ret}(x_n - x^{(n)}) P^I[\boldsymbol{A}^{(\mathrm{H})}{}_1(x^{(1)}), \cdots \boldsymbol{A}^{(\mathrm{H})}{}_n(x^{(n)})] \times v(x^{(1)}, \cdots x^{(n)}, x_{n+1}, \cdots x_\nu) d^4x^{(1)} \cdots d^4x^{(n)}. \quad (8)$$

These terms correspond to many-body forces and appear before any approximation method has been applied, whereas in the case of the nonrelativistic configuration formalism such terms appear only after the elimination of virtual processes, formally as a result thereof. The method of elimination of the virtual processes is however still to be used in our relativistic formalism. This is explained in Sec. IV, which is devoted to the bound state problem of a two-particle system, the following two definitions being the starting point of its considerations: (*a*) A state of a number of configurational particles will be called stable if all components of its wave function $\langle V | v(x_1, \cdots x_\nu)\rangle$ with the exception of the one corresponding to the (physical) vacuum are permanently zero for all space-like configurations of the particles. (*b*) Such a stable state for which the wave function is normalizable, in the sense that the condition

$$\int_\sigma \langle \bar{v}(x_1, x_2) | V \rangle \gamma_1{}^\mu \langle V | v(x_1, x_2)\rangle d\sigma_1{}^\mu \neq 0 \quad (9)$$

does not imply

$$\langle V | v(x_1, x_2)\rangle = 0 \quad (10)$$

for all configurations on the $\sigma$-surface, will be called a bound state.

An example of a stable state which is not bound is the case of elastic scattering of two electrons. Although use has already been made of these definitions in I, it should be pointed out here that the "selection rule," forbidding emission of light quanta in a stable state, is here extended to the emission of background particles, so as not to allow for pair creation. Finally, it should be noted that the component of the mixed representation wave function for some $\nu$ electrons corresponding to the fictitious "completely empty space" (no background electrons even in the negative energy states) is simply equal to the wave function used in I. The wave function of the mixed representation in the case of no configurational particles is, on the other hand, equal to the state vector in the Heisenberg representation of the usual quantum electrodynamics.

## II. TWO-ELECTRON PROBLEM

To arrive at a proper definition of the wave function in the mixed representation describing two configurational electrons, it is most convenient to start with the case of space-like distances between these two electrons. Furthermore, we shall confine ourselves at first to the case where the occupation numbers of the background electrons refer to states on a space-like $\sigma$-surface which passes through both argument points of the configurational electrons. These two requirements can also be formulated simply by saying that what we are going to consider first is the case of space-like distances of all the electrons, background as well as configurational. For the purpose of the ultimate most general definition of the wave function, the above two limitations will be removed in different ways. The background particles will always "remain" on a given fixed surface, i.e., the occupation numbers of the background will always be referred to as corresponding to states it assumed on a fixed $\sigma_0$-surface. The argument points of the configurational electrons, on the other hand, are in general going to be "removed" from $\sigma_0$ and allowed to assume quite arbitrary space or time-like mutual configurations. The actual separation of all the electrons into configurational and background is explained as follows: Consider for simplicity the case of one electron and write

$$\varphi(x)=\sum_n u_n(x)\langle 0,\cdots 0,1_n,0,\cdots|\Psi[\sigma]\rangle. \quad (11)$$

This corresponds to the way we have introduced the configuration space in I, i.e., to there being no other electrons than just the single configurational one. $\varphi(x)$ represents the wave function of this electron. The right side of (11) is the sum of all products of the components $\langle 0,\cdots 0,1_n,0,\cdots|\Psi[\sigma]\rangle$ of the state vector satisfying the Tomonaga-Schwinger equation,

$$(ihc)[\delta/\delta\sigma(x)]\Psi(\sigma)=\mathrm{H}(x)\Psi[\sigma], \quad (12)$$

with

$$\mathrm{H}(x)=-ie\bar{\psi}(x)\boldsymbol{A}(x)\psi(x), \quad (13)$$

by the appropriate spatial (free-particle) wave functions $u_n(x)$. This means that it is the sum (extended over all states $n$ of the free electrons) of products of the following probability amplitudes: (1) The amplitude of the probability of finding an electron which is in the state $n$, at point $x$, by (2) the amplitude of the probability of finding an electron in state $n$. If we now were to deal with some $\mu+1$ electrons, we could still ask questions concerning the probabilities of finding only one electron at $x$, provided the states of the others are also somehow completely determined. The latter can be done by stating that the electrons are to be found at some other points, and our problem is reduced to that considered in I for the case of $\mu+1$ configurational particles. We can, however, also say that the electrons are to be found in the free-particle states $m_1,\cdots m_\mu$, respectively, in which case any question concerning our electrons can certainly be answered in terms of the state vector components $\langle 0,\cdots 0,1_{m_1},0,\cdots 0,1_n,0,\cdots 0,1_{m_\mu},0\cdots|\Psi[\sigma]\rangle$ only. In particular the probability amplitude of finding (any) one electron at $x$ is then easily seen to be

$$\langle 0,\cdots 0,1_{m_1},0,\cdots 0,1_{m_\mu},0,\cdots|v(\sigma)](x)\rangle$$
$$=\sum_n(-1)^{J_n}u_n(x)\langle 0,\cdots,1_{m_1},0,\cdots 0,1_n,0,\cdots$$
$$0,1_{m_\mu},0\cdots|\Psi[\sigma]\rangle, \quad (14)$$

where

$$J_n=\text{number of } m_\lambda<n, \quad (15)$$

the summation being extended over all states available to the $(\mu+1)$th electron, i.e., over all states except $m_1,\cdots m_\mu$. The right side of (14) is namely the sum of all products of probability amplitudes of finding an electron in the state $n$ provided other electrons occupy the states $m_1,\cdots m_\mu$, respectively, by the appropriate probability amplitudes of finding one electron at $x$ provided the latter is in the state $n$. The sum is extended over all states $n$. Using the following expansion of the electron field operators $\psi(x)$ and $\bar{\psi}(x)$:

$$\psi(x)=\sum_n a_n u_n(x),\quad \bar{\psi}(x)=\sum_n a_n^*\bar{u}_n(x), \quad (16)$$

where $a_n$ and $a_n^*$ are the well-known creation and annihilation operators of the electron field, we can rewrite (11) and (14) as

$$\varphi(x)=\langle 0,\cdots|\psi(x)\Psi[\sigma]\rangle, \quad (17)$$

and

$$\langle 0,\cdots 0,1_{m_1},0,\cdots 0,1_{m_\mu},0,\cdots|v[\sigma](x)\rangle$$
$$=\langle 0,\cdots 0,1_{m_1},0,\cdots,0,1_{m_\mu},0,\cdots|\psi(x)\Psi[\sigma]\rangle. \quad (18)$$

If the state of our background electrons $\Omega[\sigma]$ is a given superposition of the various possible $\langle 0,\cdots 0,1_{m_1},0,\cdots 0,1_{m_\mu},0,\cdots|$-states on $\sigma$, (18) reads

$$\langle\Omega[\sigma]|v[\sigma](x)\rangle=\langle\Omega[\sigma]|\psi(x)\Psi[\sigma]\rangle. \quad (19)$$

Therefore, we are naturally led to the following definition of the one-electron wave function in the mixed representation

$$v[\sigma](x)=\psi(x)\Psi[\sigma]. \quad (20)$$

The foregoing argument can be applied to the case of more configurational electrons. For two electrons in a completely empty space, we have instead of (11)

$$\varphi(x_1,x_2)=(\tfrac{1}{2})^{\frac{1}{2}}\sum_{n_1<n_2}[u_{n_1}(x_1)\times u_{n_2}(x_2)$$
$$-u_{n_2}(x_1)\times u_{n_1}(x_2)]$$
$$\times\langle 0,\cdots 0,1_{n_1},0,\cdots 0,1_{n_2},0,\cdots|\Psi[\sigma]\rangle \quad (21)$$

which can also be written as

$$\varphi(x_1,x_2)=(\tfrac{1}{2})^{\frac{1}{2}}\langle 0,\cdots|\psi(x_1)\times\psi(x_2)\Psi[\sigma]\rangle. \quad (22)$$

Consequently, the definition of the wave function in the mixed representation for two configurational elec-

trons is easily seen to be

$$v[\sigma](x_1,x_2)=(\tfrac{1}{2})^{\frac{1}{2}}\psi(x_1)\times\psi(x_2)\Psi[\sigma], \tag{23}$$

if the points $x_1$ and $x_2$ lie space-like with respect to each other. It must be pointed out that the $\sigma$-dependence of $v[\sigma](x)$ or $v[\sigma](x_1,x_2)$ is nontrivial, in the sense that they do change in general, even if a deformation of $\sigma$ outside $x_1$ and $x_2$ is being performed. This is because the state vector of the background particles $\Omega[\sigma]$ will undergo changes when passing from one $\sigma$-surface to another. This vector must also satisfy the Tomonaga-Schwinger equation (12), the only difference from $\Psi[\sigma]$ being, that the former corresponds to a lesser number of electrons than that represented by the latter. This difference in the number of electrons is obviously equal to the number of configurational ones. It should, however, be remarked in advance that we are going to introduce still more general wave functions in the mixed representation by means of which the configurational positrons can also be described, and that the difference of the number of electrons represented by $\Psi[\sigma]$ and $\Omega[\sigma]$ will then be equal to the number of configurational electrons minus the number of configurational positrons. It will therefore be either positive or negative in general. The functional $\sigma$-dependence of the wave functions defined by (20) or (23) makes them useless for our purposes, since we are still (as was the case in I) seeking for integral or integro-differential equations satisfied by "pure" functions of distinct points only. An application of a suitably chosen unitary transformation to these functions can however make them pure functions again. The transformation matrix used must obviously be $\sigma$-dependent itself in order to cancel the $\sigma$-dependence of $v[\sigma](x_1,x_2)$. It is most natural to assume therefore, that this transformation matrix be simply equal that defined by the well-known relations:

$$(ihc)[\delta/\delta\sigma(x)]U[\sigma,\sigma_0]=H(x)U(\sigma,\sigma_0], \tag{24}$$

and

$$U[\sigma_0,\sigma_0]=1, \tag{25}$$

and being equal to the $S$-matrix for $\sigma_0=-\infty$ and $\sigma=+\infty$. We are thus led to the following more general definition of the wave function for two configurational electrons

$$\begin{aligned} v(x_1,x_2)&=U^{-1}[\sigma,\sigma_0]v[\sigma](x_1,x_2)\\ &=(\tfrac{1}{2})^{\frac{1}{2}}U^{-1}[\sigma,\sigma_0]\psi(x_1)\times\psi(x_2)\Psi[\sigma]. \end{aligned} \tag{26}$$

This function will indeed turn out to be pure, so that the functional argument $\sigma$ has already been omitted on the left side of (26). It is nevertheless still understood that $x_1$ and $x_2$ lie space-like with respect to each other. As the space-like surface $\sigma_0$ on which the left side of of this equation still depends, we will choose a fixed one, most conveniently one corresponding to the remote past. The physical interpretation of the wave function defined by (26) is quite simple. To obtain probability amplitudes corresponding to a given state of background electrons and the radiation field on $\sigma$ (denoted by $\Omega[\sigma]$ )we must multiply our wave function from the left by the transformed "bra" $\langle\Omega[\sigma_0]$. Since

$$\Omega[\sigma_0]=U^{-1}[\sigma,\sigma_0]\Omega[\sigma] \tag{27}$$

is then simply a state of the background (including radiation field with all the interactions caused thereby being taken into account) on $\sigma_0$, the components of the new wave function refer always to the latter surface, notwithstanding the fact that the argument points of the configurational electrons are no longer compelled to remain on it. To conclude the preliminary remarks concerning the construction of the mixed representation, it should be pointed out that the separation of all electrons into configurational and background has indeed been performed in such a way as never to come in contradiction with Fermi statistics or with the principle that all the electrons should remain indistinguishable from one another, the configurational electrons being just any electrons we are supposed to try to find at the $x$-points. Further generalization of the definition of our wave function in the mixed representation which we have yet in view, namely, that of allowing the distance between $x_1$ and $x_2$ to be either space or time-like, will be of somewhat more formal character because we are mainly interested in its physical interpretation for space-like distances. As in I, it will be important to perform this, as it will lead us to an everywhere-compatible integral equation satisfied by our wave function. The method employed is now very similar to that already used in I and is based on solving some functional differential equations. Denoting by $x_{\mathrm{I}}$ and $x_{\mathrm{II}}$, respectively, the points $x_1$ and $x_2$ in chronological order of their occurrence in time, and by $\sigma_{\mathrm{I}}$ and $\sigma_{\mathrm{II}}$, two space-like surfaces passing through these points (either having no common points or else being identical), we can define the following functional

$$\Gamma[\sigma](x_1,x_2)=\pm(\tfrac{1}{2})^{\frac{1}{2}}$$
$$\times\begin{cases} U^{-1}[\sigma,-\infty]\psi(x_{\mathrm{II}})\times\psi(x_{\mathrm{I}})U[\sigma,-\infty]\Psi[-\infty] \\ \qquad \text{for } \sigma \text{ sooner than } x_{\mathrm{I}} \text{ and } x_{\mathrm{II}}, \\ U^{-1}[\sigma,-\infty]\psi(x_{\mathrm{II}})\times U[\sigma,\sigma_{\mathrm{I}}]\psi(x_{\mathrm{I}}) \\ \quad \times U(\sigma_{\mathrm{I}},-\infty]\Psi[-\infty] \text{ for } \sigma \text{ sooner than} \\ \qquad\qquad x_{\mathrm{II}} \text{ but later than } x_{\mathrm{I}}, \\ U^{-1}[\sigma_{\mathrm{II}},-\infty]\psi(x_{\mathrm{II}})\times U[\sigma_{\mathrm{II}},\sigma_{\mathrm{I}}]\psi(x_{\mathrm{I}}) \\ \quad \times U[\sigma_{\mathrm{I}},-\infty]\Psi[-\infty] \\ \qquad \text{for } \sigma \text{ later than } x_{\mathrm{I}} \text{ and } x_{\mathrm{II}}, \end{cases} \tag{28}$$

$-$ or $+$ being taken according to whether I, II is an even or odd permutation of the numbers 1, 2; where we have already put $\sigma_0=-\infty$. The idea underlying the construction of this functional can be explained as follows. Consider $x_{\mathrm{I}}$ and $x_{\mathrm{II}}$ as fixed and let the "interaction front" $\sigma$ advance towards the future. Before an $x$-point of an electron is reached by this front, it is represented by a free-particle operator $\psi(x)$. After

that, it gets "immersed" in the interaction, the corresponding operator $\psi(x_{II})$ being then "separated" from its nearest sooner neighbor $\psi(x_I)$ by the factor $U[\sigma_{II},\sigma_I]$. The latter can also be expressed by saying that the free electron operators $\psi(x)$ are one after another changed by the interaction into corresponding Heisenberg operators, because instead of (28) we can also write

$$\Gamma[\sigma](x_1,x_2)=(\tfrac{1}{2})^{\frac{1}{2}} \times\begin{cases} U^{-1}[\sigma,-\infty]\psi(x_{II})\times\psi(x_I)U[\sigma,-\infty]\Psi[-\infty] \\ \qquad \text{for } \sigma \text{ sooner than } x_I \text{ and } x_{II}, \\ U^{-1}[\sigma,-\infty]\psi(x_{II})\times U[\sigma,-\infty]\psi^{(H)}(x_I)\Psi[-\infty] \\ \qquad \text{for } \sigma \text{ sooner than } x_{II} \text{ but later than } x_I, \\ \psi^{(H)}(x_{II})\times\psi^{(H)}(x_I)\Psi[-\infty] \\ \qquad \text{for } \sigma \text{ later than } x_I \text{ and } x_{II}. \end{cases} \tag{29}$$

It is immediately clear from (28) that

$$v(x_1,x_2)=\Gamma[+\infty](x_1,x_2), \tag{30}$$

whenever $x_1$ and $x_2$ lie space-like with respect to each other and with $\sigma_0$ corresponding to the remote past. Therefore our most general definition of the wave function, describing two configurational electrons and valid for arbitrary configurations, suggests itself as

$$v(x_1,x_2)=\pm(\tfrac{1}{2})^{\frac{1}{2}}U^{-1}[\sigma_{II},-\infty]\psi(x_{II}) \times U[\sigma_{II},\sigma_I]\psi(x_I)U[\sigma_{II},-\infty]\Psi[-\infty], \tag{31}$$

or, according to (29),

$$v(x_1,x_2)=\pm(\tfrac{1}{2})^{\frac{1}{2}}P[\psi^{(H)}(x_1),\psi^{(H)}(x_2)]\Psi[-\infty], \tag{32}$$

and is now evidently $\sigma$-independent for both space and time-like distances between the electrons. The form (32) of the definition of our wave function could also, especially in view of its immediate physical interpretation for space-like interelectron distances, be postulated without introducing the functional $\Gamma[\sigma](x_1,x_2)$.[2] This functional, however, plays an important role in our derivation of the integral equation satisfied by $v(x_1,x_2)$. For that purpose we differentiate (28) with respect to $\sigma$ at some point $x$ lying on $\sigma$. Taking into account (24), we then get

$$(i\hbar c)[\delta/\delta\sigma(x)]\Gamma[\sigma](x_1,x_2)=\pm(\tfrac{1}{2})^{\frac{1}{2}} \times\begin{cases} U^{-1}[\sigma,-\infty][\psi(x_{II})\times\psi(x_I),H(x)]_- \\ \quad \times U(\sigma,-\infty]\Psi[-\infty] \\ \qquad \text{for } \sigma \text{ sooner than } x_I \text{ and } x_{II}, \\ U^{-1}[\sigma,-\infty][\psi(x_{II}),H(x)]_- \\ \quad \times U[\sigma,\sigma_I]\psi(x_I)U(\sigma,-\infty]\Psi[-\infty] \\ \qquad \text{for } \sigma \text{ sooner than } x_{II} \text{ but later than } x_I, \\ 0 \qquad \text{for } \sigma \text{ later than } x_I \text{ and } x_{II}. \end{cases} \tag{33}$$

[2] The component corresponding to the physical vacuum of a function defined in this way has already been introduced by M. Gell-Mann and F. Low [Phys. Rev. 84, 350 (1951)] as a suitable definition of a wave function for two-body bound state problems.

Because of the well-known anticommutation relations for the $\psi$ and $\bar\psi$-operators

$$[\bar\psi(x),\psi(x')]_+=(1/i)S(x-x'), \quad [\bar\psi(x),\bar\psi(x')]_+=[\psi(x),\psi(x')]_+=0, \tag{34}$$

we have

$$[\psi(x_{II},H(x)]_-=-eS(x_{II}-x)A(x)\psi(x);$$
$$[\psi(x_{II})\times\psi(x_I),H(x)]_- =-eS(x_{II}-x)A(x)\psi(x)\times\psi(x_I)+ -e\psi(x_{II})\times S(x_I-x)A(x)\psi(x), \tag{35}$$

and therefore

$$(i\hbar c)[\delta/\delta\sigma(x)]\Gamma[\sigma](x_1,x_2) =-eS_1^{Ret}(x_1-x)A^{(H)}{}_1(x)\Gamma[\sigma](x,x_2)+ -eS_2^{Ret}(x_2-x)A^{(H)}{}_2(x)\Gamma[\sigma](x_1,x), \tag{36}$$

where the $S^{Ret}$-function is defined by

$$S^{Ret}(x-x')=\eta(x,x')S(x-x'), \tag{37}$$

where

$$\eta(x,x')=\begin{cases}1 & \text{for } x \text{ later than } x' \\ 0 & \text{for } x \text{ sooner than } x'.\end{cases}$$

The appearance of the latter, somewhat unexpected at first sight, is caused by the fact that after the $\sigma$ front reaches point $x_I$, the corresponding $\psi(x_I)$ operator stands to the right of $U[\sigma,\sigma_I]$ in (33), so that in this case it does not get commuted with $H(x)$. Using the notations (4′) of the preceding section we can now write (36) in the form

$$(i\hbar c)[\delta/\delta\sigma(x)]\Gamma[\sigma](x_1,x_2) =\mathfrak{IC}^{(H)Ret}(x;x_1,x_2)\Gamma[\sigma](x_1,x_2).^3 \tag{38}$$

Solving the last equation by the Dyson method of chronological products we get

$$\Gamma[\sigma](x_1,x_2) =\sum_{n=0}^{\infty}[1/n!][1/i\hbar c]^n\int_{-\infty}^{\sigma}\cdots\int_{-\infty}^{\sigma}d^4x^{(1)}\cdots d^4x^{(n)} \times P[\mathfrak{IC}^{(H)Ret}(x^{(1)};x_1,x_2)\cdots \times\mathfrak{IC}^{(H)Ret}(x^{(n)};x_1,x_2)]\chi(x_1,x_2). \tag{39}$$

If we now let $\sigma$ tend to $+\infty$ and use the definition (31), we finally get

$$v(x_1,x_2)=\sum_{n=0}^{\infty}[1/n!][1/i\hbar c]^n\int_{-\infty}^{+\infty}\cdots\int_{-\infty}^{+\infty}d^4x^{(1)}\cdots d^4x^{(n)} \times P[\mathfrak{IC}^{(H)Ret}(x^{(1)};x_1,x_2)\cdots \times\mathfrak{IC}^{(H)Ret}(x^{(n)};x_1,x_2)]\chi(x_1,x_2) \tag{40}$$

[3] $\Gamma[\sigma](x_1,x_2)$ is not to be considered as a generalization of the functional $\Phi[\sigma](x_1,x_2)$ used in I because it does not in general obey the field-free Dirac equation as a function of the $x$-arguments. If it were otherwise, only the $S$-functions and not $S^{Ret}$ would appear on the right-hand side of Eq. (38).

where $\chi(x_1,x_2)$ satisfies the field-free Dirac equation,

$$[\gamma_i^{\mu}(\partial/\partial x_i^{\mu})+(mc/\hbar)]\chi(x_1,x_2)=0; \quad i=1,2, \quad (41)$$

as a function of every $x$-argument and is equal to $\Gamma[-\infty](x_1,x_2)$. To obtain an integral equation satisfied by $v(x_1,x_2)$, it is sufficient to "invert" the relation (40) and express $\chi(x_1,x_2)$ in terms of $v(x_1,x_2)$, getting

$$\chi(x_1,x_2)=\sum_{n=0}^{\infty\ (\text{or } 2)}[1/n!][-1/ihc]^n$$
$$\times\int_{-\infty}^{+\infty}\cdots\int_{-\infty}^{+\infty}d^4x^{(1)}\cdots d^4x^{(n)}$$
$$\times P^I[\mathfrak{C}^{(\mathrm{H})Ret}(x^{(1)};x_1,x_2)\cdots$$
$$\times\mathfrak{C}^{(\mathrm{H})Ret}(x^{(n)};x_1,x_2)]v(x_1,x_2). \quad (42)$$

As in I, we can now argue in favor of the greater usefulness of (42) compared with (40), especially in the case of bound states. Equation (40) is, namely, an expansion of $v(x_1,x_2)$ in a power series in the coupling constant $e$, corresponding to the building of the actual state of our system as a result of elementary scatterings of plane waves, whereas (41) is an exact equation written in a finite form (containing two terms in the case here considered). Even if $e$-power expansions are to be used again when practically solving (42), they may be made to correspond to the elimination of virtual processes of the background and of the radiation field only, and may be expected to be sufficiently rapidly convergent for bound states. In the case of two configurational electrons, (42) is identical with what we have called (2′) in the preceding section. At the same time, we may consider the general validity of (2′) as demonstrated also, since the generalization of the methods employed in deriving (42) can easily be extended to any number of configurational electrons.

## III. ELECTRON-POSITRON PROBLEM

We wish now to construct wave functions describing configurational positrons. In accordance with the basic principles of the hole-theory, the components of such wave functions must be understood as probability amplitudes of finding Dirac holes (no electrons) at their argument points. Using the word hole instead of the word electron and vice versa, we can construct the wave function in the mixed representation for one configurational positron in strict analogy to the case of one configurational electron. The definition of a component of this function which corresponds to the presence of holes in the states $m_1,\cdots m_\mu$, one extra hole at $x$ and all other states being occupied by electrons, is the following: the sum of products of probability amplitudes of finding a hole at $x$, provided a state $n$ is empty, by appropriate probability amplitudes of finding holes in the states $m_1,\cdots m_\mu$ and in the state $n$ only. This sum is to be extended over all states $n$ from which an electron can be removed. If we use charge-conjugated wave functions to describe positrons and denote the above-defined component by $\langle 1,\cdots 1,0_{m_1},1,\cdots 1,0_{m_\mu},1,\cdots|v[\sigma](x)\rangle$, we have instead of (14):

$$\langle 1,\cdots 1,0_{m_1},1,\cdots 1,0_{m_\mu},1,\cdots|v[\sigma](x)\rangle$$
$$=\sum_n(-1)^{J_n}u_n'(x)\langle 1,\cdots 1,0_{m_1},1,\cdots 1,0_n,1,\cdots 1,$$
$$0_{m_\mu},1\cdots|\Psi[\sigma]\rangle, \quad (43)$$

where the functions $u_n'(x)$ are the charge-conjugated free particle wave functions given by

$$u_n'(x)=L\bar{u}_n(x), \quad (44)$$

and where the operator $L$ satisfies the well-known relations

$$L^*L=1; \quad L^*\gamma^{\mu}L=-(\gamma^{\mu})^{\text{transposed}}. \quad (45)$$

Using the charge-conjugated electron field operators,

$$\psi'(x)=L\bar{\psi}(x)=\sum_n a_n^*u_n'(x), \quad (46)$$

we can rewrite (43) as

$$\langle 1,\cdots 1,0_{m_1},1,\cdots 1,0_{m_\mu},1,\cdots|v[\sigma](x)\rangle$$
$$=\langle 1,\cdots 1,0_{m_1},1,\cdots 1,0_{m_\mu},1,\cdots|\psi'(x)\Psi[\sigma]\rangle, \quad (47)$$

and therefore, exactly in the same way as that which led us to the definition of the one electron wave function (20), we can define the mixed representation wave function describing one configurational positron as

$$v[\sigma](x)=\psi'(x)\Psi[\sigma]. \quad (48)$$

By an easy generalization we can now construct wave functions in the mixed representation describing any number of electrons and positrons. They will be equal to diadic products of a number of the $\psi$ and $\psi'$-operators multiplied from the right by the state vector $\Psi[\sigma]$. Their components will be obtained by multiplying them by another state vector $\Omega[\sigma]$ corresponding to the background and the radiation field only, i.e., to a state which would result if the configurational particles were absent. As already mentioned in the preceding section, the state vector $\Omega[\sigma]$ does not need to correspond to a lesser number of electrons then those represented in $\Psi[\sigma]$, because not only configurational electrons are to be removed from $\Psi[\sigma]$, but also configurational holes must be filled. By exactly the same argument as in the preceding section, we arrive at the following most general definition of the wave function in the mixed representation for the electron-positron system:

$$v(x_1,x_2)=\pm(\tfrac{1}{2})^{\frac{1}{2}}P[\psi^{(\mathrm{H})}(x_1),\psi^{(\mathrm{H})\prime}(x_2)]\Psi[-\infty], \quad (49)$$

which corresponds to the definition (32) for two electrons and is likewise valid for all types of mutual configurations of our two particles. The function defined by (49) can again be obtained from a functional $\Gamma[\sigma](x_1,x_2)$ by letting $\sigma$ tend to $+\infty$. The functional

$\Gamma[\sigma](x_1,x_2)$ must here be defined as follows:

$$\Gamma[\sigma](x_1,x_2)=-(\tfrac{1}{2})^{\frac{1}{2}}$$
$$\times\begin{cases} U^{-1}[\sigma,-\infty]\psi'(x_2)\times\psi(x_1)U[\sigma,-\infty]\Psi[-\infty] \\ \qquad \text{for } \sigma \text{ sooner than } x_1 \text{ and } x_2, \\ U^{-1}[\sigma,-\infty]\psi'(x_2)\times U[\sigma,\sigma_1]\psi(x_1) \\ \quad \times U[\sigma_1,-\infty]\Psi[-\infty] \\ \qquad \text{for } \sigma \text{ sooner than } x_2 \text{ but later than } x_1, \\ U^{-1}[\sigma_{II},-\infty]\psi'(x_2)\times U[\sigma_{II},\sigma_1]\psi(x_1) \\ \quad \times U[\sigma_1,-\infty]\Psi[-\infty] \\ \qquad \text{for } \sigma \text{ later than } x_1 \text{ and } x_2, \end{cases} \tag{50}$$

for configurations where the argument point of the electron $x_1$ lies earlier in time than the argument point $x_2$ of the positron, and

$$\Gamma[\sigma](x_1,x_2)=+(\tfrac{1}{2})^{\frac{1}{2}}$$
$$\times\begin{cases} U^{-1}[\sigma,-\infty]\psi(x_1)\times\psi'(x_2)U[\sigma,-\infty]\Psi[-\infty] \\ \qquad \times \text{for } \sigma \text{ sooner than } x_1 \text{ and } x_2, \\ U^{-1}[\sigma,-\infty]\psi(x_1)\times U[\sigma,\sigma_1]\psi'(x_2) \\ \quad \times U[\sigma_1,-\infty]\Psi[-\infty] \\ \qquad \text{for } \sigma \text{ sooner than } x_1 \text{ but later than } x_2, \\ U^{-1}[\sigma_{II},-\infty]\psi(x_1)\times U[\sigma_{II},\sigma_1]\psi'(x_2) \\ \quad \times U[\sigma_1,-\infty]\Psi[-\infty] \\ \qquad \text{for } \sigma \text{ later than } x_1 \text{ and } x_2 \end{cases} \tag{51}$$

if the argument point of the positron is earlier than that of the electron. The indexes I and II of the $\sigma$-surfaces passing through the two argument points, unlike $x_1$ and $x_2$, do not refer to electron and positron, but are always connected with the earlier and later of the $x$-points, respectively. For spacelike distances between electron and positron definitions (50) and (51) are identical, because then the operators $\psi(x_1)$ and $\psi'(x_2)$ anticommute. It can now be easily seen that the functional $\Gamma[\sigma](x_1,x_2)$ satisfies the equation

$$(ihc)[\delta/\delta\sigma(x)]\Gamma[\sigma](x_1,x_2)$$
$$=-eS_1^{Ret}(x_1-x)\boldsymbol{A}^{(H)}{}_1(x)\Gamma[\sigma](x,x_2)$$
$$+eS_2^{Ret}(x_2-x)\boldsymbol{A}^{(H)}{}_2(x)\Gamma[\sigma](x_1,x). \tag{52}$$

A characteristic change of sign of the $S^{Ret}$-function referring to the positron is to be noticed when compared to the analogous Eq. (36). This is formally caused by the fact that for charge-conjugated $\psi$-operators we have, instead of (34),

$$[\psi'(x),\psi(x')]_+=(1/i)LS(x-x');$$
$$[\psi'(x),\bar{\psi}(x')]_+=0. \tag{53}$$

Consequently, instead of (35), we have

$$[\psi'(x_2),H(x)]_-=+eS(x_2-x)\boldsymbol{A}(x)\psi'(x);$$
$$[\psi(x_1)\times\psi'(x_2),H(x)]_-=-eS(x_1-x)\boldsymbol{A}(x)\psi(x)$$
$$\times\psi'(x_2)+e\psi(x_1)\times S(x_2-x)\boldsymbol{A}(x)\psi'(x). \tag{54}$$

Our wave function (49) therefore satisfies an integral equation of the form (42), except that we must put here

$$\mathfrak{K}^{(H)Ret}(x;x_1,x_2)=-eS_1{}^{Ret}(x_1-x)\boldsymbol{A}^{(H)}{}_1(x)Q(x_1\to x)$$
$$+eS_2{}^{Ret}(x_2-x)\boldsymbol{A}^{(H)}{}_2(x)Q(x_2\to x), \tag{55}$$

and this corresponds to the substitution (4″) for the case of one electron and one positron. The considerations of this section can now be easily extended to any number of configurational particles, so that the general validity of (2″) can also be considered as proved. This completes the derivation of our general "mixed representation formalism" outlined in Sec. I.

## IV. TIME INVERSION

Before outlining some more practical means of calculation with the help of our new formalism in Sec. V, we shall investigate its general transformation properties with respect to the inversion of the direction of time. These properties are not exactly identical with the transformation properties of the Feynman theory, notwithstanding the fact that the two formalisms are equivalent, since they are only two different formulations of quantum electrodynamics. This might lead to an interesting question (not dealt with, however, in this paper) of comparing methods based on these two ways of approach in some more practical cases, especially in view of the fact that several attempts have already been made to apply the Feynman theory to bound-state problems. To avoid once more all unnecessary complications, but to deal at the same time with the most interesting case of "coexistence" of configurational electrons and configurational positrons, we shall simply continue with the electron-positron problem of the preceding section. If $x_2$ is earlier than $x_1$, then a component of the function $v(x_1,x_2)$, corresponding to the state of the background in the remote past $\Omega[-\infty]$, is:

$$\langle\Omega[-\infty]|v(x_1,x_2)\rangle=(\tfrac{1}{2})^{\frac{1}{2}}\langle\Omega[+\infty]|U[+\infty,\sigma_{II}]\psi(x_1)$$
$$\times U[\sigma_{II},\sigma_I]\psi'(x_2)\times U[\sigma_I,-\infty]|\Psi[-\infty]\rangle. \tag{56}$$

Because of the diadic product which appears here, this is a two-index spinor and we can subject it to charge conjugation with respect to the spinor index, referring to either of the particles. To do so, we should take first the conjugate of (56),

$$(\tfrac{1}{2})^{\frac{1}{2}}\langle\Psi[-\infty]|U^{-1}[\sigma_I,-\infty]\psi'^*(x_2)$$
$$\times U^{-1}[\sigma_{II},\sigma_I]\psi^*(x_1)U^{-1}[+\infty,\sigma_{II}]|\Omega[+\infty]\rangle, \tag{57}$$

multiply it by $\gamma_1{}^4\times\gamma_2{}^4$ to obtain the corresponding "$v$-bar" expression,

$$(\tfrac{1}{2})^{\frac{1}{2}}\langle\Psi[-\infty]|U^{-1}[\sigma_I,-\infty]\bar{\psi}'(x_2)$$
$$\times U^{-1}[\sigma_{II},\sigma_I]\bar{\psi}(x_1)U^{-1}[+\infty,\sigma_{II}]|\Omega[+\infty]\rangle, \tag{58}$$

and finally multiply it again from the left by

$$L_1\times L_2,$$

where the operator $L$ is given by (45), the index "1" and "2" referring to the spinor index of the electron and positron respectively. The charge conjugate of (56) therefore is

$$(\tfrac{1}{2})^{\frac{1}{2}}\langle\Psi[-\infty]|U^{-1}[\sigma_{\rm I},-\infty]\psi(x_2)$$
$$\times U^{-1}[\sigma_{\rm II},\sigma_{\rm I}]\psi'(x_1)U^{-1}[+\infty,\sigma_{\rm II}]|\Omega[+\infty]\rangle. \quad (59)$$

If we now invert the direction of time, the above can be considered as a component of another "inverted" wave function in the mixed representation

$$v^{\rm inv}(x_1,x_2)=(\tfrac{1}{2})^{\frac{1}{2}}U[+\infty,\sigma_{\rm I}]\psi(x_2)$$
$$\times U^{-1}[\sigma_{\rm II},\sigma_{\rm I}]\psi'(x_1)U^{-1}[+\infty,\sigma_{\rm II}]\Omega[+\infty], \quad (60)$$

which has developed from the "initial condition"

$$\chi^{\rm inv}(x_1,x_2)=\psi(x_2)\times\psi'(x_1)\Omega[+\infty] \quad (61)$$

and which corresponds to the "final" state of the background $\Psi[-\infty]$. Equation (60) can now also be written as

$$v^{\rm inv}(x_1,x_2)=\pm P^{\rm I}[\psi_{\rm (H)}'(x_1)\times\psi_{\rm (H)}(x_2)]\Omega[+\infty], \quad (62)$$

where the $\psi_{\rm (H)}'(x_1)$ and $\psi_{\rm (H)}(x_2)$ operators are Heisenberg operators again, but are not identical with those hitherto used. They are defined, not by (6′), but by the relations:

$$X_{\rm (H)}(x)=U[+\infty,\sigma]X(x)U^{-1}[+\infty,\sigma]. \quad (63)$$

These operators are equal to the corresponding free particle operators for the infinite future, while those defined by (6′) were equal to the corresponding free particle operators in the remote past. There is, however, a simple relation between these two types of operators, expressible in terms of the $S$-matrix, namely

$$X_{\rm (H)}(x)=SX^{\rm (H)}(x)S^{-1}. \quad (64)$$

By introducing an auxiliary functional, analogous to that defined by (50) and (51), but with the domain of interaction beginning on the future side of the "interaction front" $\sigma$, we can show that the time inverted wave function (60) satisfies, instead of (42), the equation

$$\chi^{\rm inv}(x_1,x_2)=\sum_{n=0}^{\infty}{}^{\rm (or\ 2)}[1/n!][+1/i\hbar c]^n$$
$$\times\int_{-\infty}^{+\infty}\cdots\int_{-\infty}^{+\infty}d^4x^{(1)}\cdots d^4x^{(n)}$$
$$\times P[\mathfrak{H}_{\rm (H)}{}^{\rm Adv}(x^{(1)};x_1,x_2)\cdots$$
$$\times\mathfrak{H}_{\rm (H)}{}^{\rm Adv}(x^{(n)};x_1,x_2)]v^{\rm inv}(x_1,x_2), \quad (65)$$

with

$$\mathfrak{H}_{\rm (H)}{}^{\rm Adv}(x;x_1,x_2)=+eS_1{}^{\rm Adv}(x_1-x)A_{\rm (H)1}(x)$$
$$\times Q(x_1\to x)-eS_2{}^{\rm Adv}(x_2-x)A_{\rm (H)2}(x)Q(x_2\to x), \quad (66)$$

and with the advanced $S$-function defined by

$$S^{\rm Adv}(x-x')=[1-\eta(x,x')]S(x-x'), \quad (67)$$

and where now, contrary to (4″), the + sign refers to the positron and the − sign to the electron. The result of the time inversion can therefore be expressed within the framework of our formalism by saying that the symbols used to represent the electrons ($\psi$-operators, − sign of $e$) are to be replaced by symbols which hitherto referred to the positrons ($\psi'$-operators, + sign of $e$) and inversely. This obviously corresponds to the Feynman positrons as electrons "traveling backwards in time." The essential difference, however, seems to lie in the fact that all the particles have here to "travel" in a common direction in time, there being no electron world lines which are continued by positron world lines (i.e., whenever the former turns back in time). Furthermore we have, in our general formalism, not yet encountered the Feynman (causal) $S$-functions, as they will appear for the first time in the course of the elimination of the virtual processes.

## V. BOUND STATE PROBLEMS

As indicated in Sec. I, we will now develop some methods suitable for practical applications of the theory. Starting from the definitions of a bound and stable state adopted there, these methods will enable us to write down equations satisfied by a narrower class of wave functions describing these states. However, explicit methods of solving the resulting equations will not be given in this paper, as we are here chiefly concerned with developing further, namely up to the terms of the order of $e^4$, the method of eliminating the virtual processes, on lines strictly analogous to those already explained in Sec. III of I. The carrying out of such an elimination further than up to terms of the order of $e^2$ within the scope of a more rigid formalism of solely configurational particles would be meaningless because of the effects of the polarization of the vacuum. The resulting equations in the $e^4$-approximation cannot be given here because of their considerable length. Instead, stress is laid here on the generalization of the method of eliminating of virtual processes so as to cover all the processes of the background and not only those of the radiation field. We start with the exact two-body equation (40), which we now write in the form

$$\chi(x_1,x_2)=v(x_1,x_2)+[e/i\hbar c]$$
$$\times\int_{-\infty}^{+\infty}S_1{}^{Ret}(x_1-x)\gamma_1{}^{\mu}A^{\rm (H)}{}_{\mu}(x)v(x,x_2)a'^4x$$
$$\pm[e/i\hbar c]\int_{-\infty}^{+\infty}S_2{}^{Ret}(x_2-x)\gamma_2{}^{\mu}A^{\rm (H)}{}_{\mu}(x)v(x_1,x)d^4x$$
$$\mp[e^2/\hbar^2c^2]\int_{-\infty}^{+\infty}\int_{-\infty}^{+\infty}S_1{}^{Ret}(x_1-x^{\rm I})S_2{}^{Ret}(x_2-x^{\rm II})$$
$$\times\gamma_1{}^{\mu}\gamma_2{}^{\nu}P^{\rm I}[A^{\rm (H)}{}_{\mu}(x^{\rm I}),A^{\rm (H)}{}_{\nu}(x^{\rm II})]$$
$$\times v(x^{\rm I},x^{\rm II})d^4x^{\rm I}d^4x^{\rm II}, \quad (68)$$

where the upper and lower signs will refer to the two-electron and electron-positron problems, respectively. For problems involving more particles the corresponding exact equations will contain terms of the form of (8). The function $v(x_1,x_2)$ which appears in (68) is here assumed to correspond to a true two-body problem, the background corresponding to the Dirac (physical) vacuum. Equation (68) can also be rewritten as

$$\chi(x_1,x_2)=v(x_1,x_2)+[e/i\hbar c]\int_{-\infty}^{+\infty} S_1^{Ret}(x_1-x)\gamma_1^\mu \times\langle V|A^{(H)}{}_\mu(x)|V\rangle v(x,x_2)d^4x \pm[e/i\hbar c]\int_{-\infty}^{+\infty} S_2^{Ret}(x_2-x)\gamma_2^\mu\langle V|A^{(H)}{}_\mu(x)|V\rangle \times v(x_1,x)d^4x+I_1(x_1,x_2), \quad (69)$$

where

$$I_1(x_1,x_2)=[e/i\hbar c]\int_{-\infty}^{+\infty} S_1^{Ret}(x_1-x)\gamma_1^\mu \times[A^{(H)}{}_\mu(x)-\langle V|A^{(H)}{}_\mu(x)|V\rangle]v(x,x_2)d^4x \pm[e/i\hbar c]\int_{-\infty}^{+\infty} S_2^{Ret}(x_2-x)\gamma_2^\mu \times[A^{(H)}{}_\mu(x)-\langle V|A^{(H)}{}_\mu(x)|V\rangle]v(x_1,x)d^4x \pm[e^2/\hbar^2c^2]\int_{-\infty}^{+\infty}\int_{-\infty}^{+\infty} S_1^{Ret}(x_1-x^{\rm I}) \times S_2^{Ret}(x_2-x^{\rm II})\gamma_1^\mu\gamma_2^\nu P^{\rm I}[A^{(H)}{}_\mu(x^{\rm I}),A^{(H)}{}_\nu(x^{\rm II})] \times v(x^{\rm I},x^{\rm II})d^4x^{\rm I}d^4x^{\rm II}, \quad (70)$$

and where $\langle V|\cdots|V\rangle$ are expectation values corresponding to the physical vacuum. Equation (69) represents a division of the right side of (68) into two parts. The first part is simply equal to the vacuum expectation value of this right side, to which only the diagonal elements of the $A^{(H)}{}_\mu(x)$ operators contribute. The other, denoted by $I_1(x_1,x_2)$, is the "rest," and, consequently, the vacuum expectation value of its operator is equal to zero. The operators contained in $I_1(x_1,x_2)$ always induce changes of the occupation numbers of the radiation field and of the background. It will be with the help of $I_1(x_1,x_2)$ that we are going to perform the elimination of the virtual processes. As a consequence of (69), we can write

$$v(x_1,x_2)=\chi(x_1,x_2)-[e/i\hbar c]\int_{-\infty}^{+\infty} S_1^{Ret}(x_1-x)\gamma_1^\mu \times\langle V|A^{(H)}{}_\mu(x)|V\rangle v(x,x_2)d^4x \mp[e/i\hbar c]\int_{-\infty}^{+\infty} S_2^{Ret}(x_2-x)\gamma_2^\mu\langle V|A^{(H)}{}_\mu(x)|V\rangle \times v(x_1,x)d^4x-I_1(x_1,x_2), \quad (71)$$

and substitute its right side for $v(x_1,x_2)$ in $I_1(x_1,x_2)$ of (69). The equation which thus results will not contain $\chi(x_1,x_2)$ on its right side. The vacuum component of the expression $I_1(x_1,x_2)$, with $\chi(x_1,x_2)$ substituted instead of $v(x_1,x_2)$, vanishes. This is caused by the fact that $\chi(x_1,x_2)$ corresponds to completely uncoupled fields, all its components except $\langle V|\chi(x_1,x_2)\rangle$ being permanently equal to zero. The resulting equation will again contain terms of nonvanishing vacuum expectation value in addition to those already separated in (69). These terms correspond to virtual emission and subsequent reabsorption of photons and background pairs caused by the operators contained in $I_1(x_1,x_2)$ and applied twice. The next step of the procedure is to repeat the division of all terms in our resulting equation into those corresponding to the vacuum expectation value of its right side operators and the rest. This rest is now denoted by $I_2(x_1,x_2)$. It is done in exactly the same way as before. No details of the computation need be given here, as at this stage of the procedure, they are exactly the same as in I. The result, now in the form of an integral equation, is:

$$\langle V|\chi(x_1,x_2)\rangle=\langle V|v(x_1,x_2)\rangle \pm[ie^2/\hbar c]\int_{-\infty}^{+\infty}\int_{-\infty}^{+\infty} S_1^{Ret}(x_1-x^{\rm I})\gamma_1^\mu S_2^{Ret}(x_2-x^{\rm II}) \times\gamma_2^\mu D_F(x^{\rm I}-x^{\rm II})\langle V|v(x^{\rm I},x^{\rm II})\rangle d^4x^{\rm I}d^4x^{\rm II} +[ie^2/\hbar c]\int_{-\infty}^{+\infty}\int_{-\infty}^{+\infty} S_1^{Ret}(x_1-x^{\rm I})\gamma_1^\mu S_1^{Ret}(x^{\rm I}-x^{\rm II}) \times\gamma_1^\mu D_F(x^{\rm I}-x^{\rm II})\langle V|v(x^{\rm II},x_2)\rangle d^4x^{\rm I}d^4x^{\rm II} +[ie^2/\hbar c]\int_{-\infty}^{+\infty}\int_{-\infty}^{+\infty} S_2^{Ret}(x_2-x^{\rm I})\gamma_2^\mu S_2^{Ret}(x^{\rm I}-x^{\rm II}) \times\gamma_2^\mu D_F(x^{\rm I}-x^{\rm II})\langle V|v(x_1,x^{\rm II})\rangle d^4x^{\rm I}d^4x^{\rm II} +[ie^2/\hbar c]\int_{-\infty}^{+\infty}\int_{-\infty}^{+\infty} S_1^{Ret}(x_1-x^{\rm I})\gamma_1^\mu D^{Ret}(x^{\rm I}-x^{\rm II}) \times{\rm Tr}[\gamma^\mu S^{(+)}(x^{\rm II}-x^{\rm II})]\langle V|v(x^{\rm II},x_2)\rangle d^4x^{\rm I}d^4x^{\rm II} \pm[ie^2/\hbar c]\int_{-\infty}^{+\infty}\int_{-\infty}^{+\infty} S_2^{Ret}(x_2-x^{\rm I})\gamma_2^\mu D^{Ret}(x^{\rm I}-x^{\rm II}) \times{\rm Tr}[\gamma^\mu S^{(+)}(x^{\rm II}-x^{\rm II})]\langle V|v(x_1,x^{\rm II})\rangle \times d^4x^{\rm I}d^4x^{\rm II}+I_2(x_1,x_2), \quad (72)$$

$$S^{(+)}(x-x')=-S_F(x-x')+S^{Ret}(x-x').$$

The exact form of $I_2(x_1,x_2)$ need not be given here, as no explicit use is made of it in this paper. To proceed further we now insert $v(x_1,x_2)$ as determined by (71) in all terms of $I_2(x_1,x_2)$, perform a separation as in (68), etc. This then corresponds to the elimination of virtual

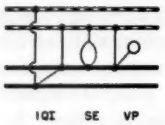


FIG. 1. The nets corresponding to the second order in $e$.

processes of the third order. The procedure is in general guided by the recursive rule,

After the elimination of virtual processes of the $n$th order is accomplished, one should use Eq. (71), in all terms of the corresponding rest $I_n(x_1,x_2)$, i.e., in all terms of the resulting equation, the vacuum expectation value of which vanishes.

Then, on taking the vacuum expectation value again, one obtains the stable state contributions due to virtual processes of the order of $(n+1)$. To be sure that all terms up to the order of $e^4$ are accounted for, all computations must be carried out to the fourth order in virtual processes. The remaining task is then to calculate the following vacuum expectation values:

$$\langle V|A^{(H)}{}_\mu(x)|V\rangle;\quad \langle V|A^{(H)}{}_\mu(x)A^{(H)}{}_\nu(x')|V\rangle;$$
$$\langle V|A_\mu(x)A_\nu(x')A_\lambda(x'')A_\nu(x''')|V\rangle. \quad (73)$$

Following the general idea of Sec. I of considering the background as representing weakly coupled particles, these expectation values are most naturally to be computed with the help of standard $S$-matrix methods. After all this has been done, the final equation satisfied by a wave function of a stable state (vacuum component of the wave function in the mixed representation) in the $e^4$-approximation will be a sum of a number of integrals involving argument points of this function. The kernel of every such integral will be in general itself an integral of products of $S$ and $D$ functions, and can easily be represented by ordinary Feynman diagrams. The only difference from those met in $S$-matrix computations is, that not only the Feynman (causal) $S$ and $D$ functions will appear but also $S^{Ret}$, $D^{Ret}$ and $S^{Adv}$, $D^{Adv}$. In case of our two configurational particles, every such kernel depends on one or two argument points, repeated on the left side of the equation as argument points of the $\langle V|\chi(x_1,x_2)\rangle$ function, and on one or two argument points, repeated as arguments of $\langle V|v(x^{I},x^{II})\rangle$ and then integrated over space-time. If we draw first all the diagrams corresponding to different kernels which appear in our equation, and then draw two thick dotted lines through all points corresponding to arguments of the former type and two thick continuous lines through all points corresponding to arguments of the later type, we obtain an easy graphic representation of our equations.[4]

[4] Interaction patterns corresponding to different kernels in our equation can also be represented by the so-called "ladder diagrams." We would get such a ladder diagram by drawing, one after another, a number of identical Feynman diagrams corresponding to a particular kernel, and then by joining the "free-particle ends" of every diagram with the corresponding "bound-particle ends" of the next. A ladder diagram makes clear to which part of the $S$-matrix a particular interaction pattern corresponds, in case the problem in question allows for the application of the usual $S$-matrix computation techniques.

The two thick dotted lines will represent two non-interacting particles, and the two thick continuous lines, the two particles with all the interactions taken into account. The latter lines will be connected with or "suspended" on the former two by means of various "nets" of thin lines representing the Feynman diagrams corresponding to different interaction patterns. The thin dotted lines correspond here, as usual, to virtual photons, and the continuous lines to virtual electrons. As not only $D_F$ and $S_F$ functions are to be represented by these lines, one should, to be strict, introduce further distinctions among them. As this is only a preliminary survey of the interaction patterns, we need not do so and will only give (in brackets) the number of different patterns corresponding to a given net. A few of these nets are given in Figs. 1–3. First of all (Fig. 1), there are the three corresponding to the second order in $e$ and, consequently, to terms already written down explicitly in (69). They represent the one-quantum interactions ($1QI$), the self-energy or self-action terms ($SE$), and terms corresponding to internal vacuum polarization ($VP$). The most important terms of the fourth order in $e$ are represented by the diagrams in Fig. 2. They represent two-quantum interaction terms ($2QI$), terms corresponding to the vacuum polarization corrections to one-quantum interactions ($VP$-$1QI$), and finally, three types of nets accounting for "Lamb-shift-like" corrections due to the mutual interactions of two particles ($MI$"$LS$"). As the latter are certainly the most interesting interactions of the fourth order, we shall write down the appropriate two integrals appearing in the equation for bound states and corresponding to the net marked $X$. They are

$$+[e^4/\hbar^2c^2]\int_{-\infty}^{+\infty}\int_{-\infty}^{+\infty}\int_{-\infty}^{+\infty}\int_{-\infty}^{+\infty} S_1{}^{Ret}(x_1-x^{I})\gamma_1{}^{\mu}$$
$$\times S_1{}^{Ret}(x^{I}-x^{II})\gamma_1{}^{\nu}S_1{}^{Ret}(x^{II}-x^{III})\gamma_1{}^{\mu}$$
$$\times S_2{}^{Ret}(x_2-x^{IV})\gamma_2{}^{\nu}D^{(-)}(x^{I}-x^{III})$$
$$\times[D^{(-)}(x^{II}-x^{IV})+D^{(-)}(x^{IV}-x^{II})]$$
$$\times\langle V|v(x^{III},x^{IV})\rangle d^4x^{I}d^4x^{II}d^4x^{III}d^4x^{IV}, \quad (74)$$
$$D^{(-)}(x-x')=D_F(x-x')+D^{Adv}(x-x').$$

Some techniques are yet to be applied to make all the above terms finite. If the infinities are entirely on account of some part of the net itself, as in the case of the $VP$-terms, the problem of their removal is exactly

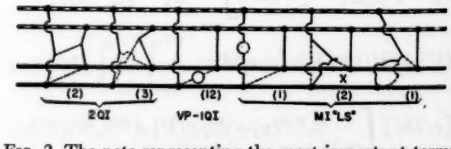


FIG. 2. The nets representing the most important terms of the fourth order in $e$.

the same as the corresponding one for the $S$-matrix. The regularized infinities will appear as some multiplicative constants and will not depend on the form of the wave function $\langle V|v(x_1,x_2)\rangle$. The terms like $SE$ and $MI"SL"$ on the other hand, seem to involve $\langle V|v(x_1,x_2)\rangle$ more deeply, the arguments of the latter being integration variables with respect to which the most dangerous integrations are being performed. The function $\langle V|v(x_1,x_2)\rangle$ certainly cannot be represented by plane waves, and by some particular choice of it the infinities can be even made to disappear. It seems therefore that some additional techniques have to be developed in order to regularize such terms for a wide enough class of wave functions. If on the other hand the $S$-matrix techniques were to turn out to be adequate for the above purposes, it would not be, in the author's opinion, without some adaptations made in the actual computation rules of the integrals concerned. In this case one might even hope to get a deeper insight into the physical meaning of these methods. In addition to those already given, Fig. 3 shows ten nets completing the interaction patterns in the $e^4$-approximation. These are less interesting, as they may be decomposed into simpler parts encountered before. It might, nevertheless, be of some interest to observe that the characteristic vacuum polarization loop "attached" to one photon line appears where the external potential would also appear, should it be postulated. The meaning of this loop is simply an (infinite) potential produced by the Dirac "sea," and it might be physically considered meaningless. With regard to all nets given above which are not already symmetric with respect to both particles, we finally observe that they are to be repeated with the roles of the particles exchanged.

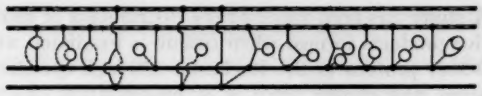

FIG. 3. Ten nets completing the interaction patterns in the $e^4$ approximation.

PHYSICAL REVIEW VOLUME 94, NUMBER 5 JUNE 1, 1954

# Reactions of Cesium with 240-Mev Protons*

RICHARD W. FINK† AND EDWIN O. WIIG
*Department of Chemistry, University of Rochester, Rochester, New York*

(Received February 23, 1954)

Absolute yields of radionuclides produced in the spallation of cesium with 240-Mev protons have been measured from barium to ruthenium. The yields are based on the known cross section for the monitor reaction $Al^{27}(p,3pn)Na^{24}$. In agreement with the well-established pattern for high-energy spallation yields, the results indicate that the majority of reactions occur as primary knock-on collisions in which the incident proton interacts with only a few nucleons. This primary interaction is followed by a dissipation of the residual nuclear excitation, whose energy spread is very broad, leading to a distribution of products which reach far down the nuclide chart.

Measurement of absolute x-ray counting efficiencies for the $K$ x-rays of $Xe^{131}$ and $Mn^{55}$ in a methane beta-proportional counter and in a helium-alcohol G-M tube is also reported.

## I. INTRODUCTION

THE nuclei which result when target nuclei are struck by high energy projectiles have been investigated in several instances by measurement of the yields of various radioactive products.[1]

An outstanding feature of high-energy reactions is the wide distribution of spallation products which result from dissipation of the excitation energy of the struck nuclei. In all cases where spallation has been studied at energies above 100 Mev, it has been found that while the distribution of products spreads far down the periodic chart from the target element, the distribution of yields is sharply accentuated in the region close to the target. A proposal by Serber and enlarged upon by Goldberger[2] gives a qualitative mechanism whereby fairly small excitation energies may be transferred to the target nucleus by projectiles of very great energy.

* This investigation was supported by the U. S. Atomic Energy Commission. Part of this work is taken from the doctoral thesis of R. W. Fink, who acknowledges with appreciation the award of an Atomic Energy Commission Predoctoral Fellowship in the Physical Sciences, 1951–1953.

† U. S. Atomic Energy Commission contract Postdoctoral Fellow, University of Rochester, 1953. Present address: Department of Chemistry, University of Arkansas, Fayetteville, Arkansas.

[1] Cunningham, Hopkins, Jr., Lindner, Miller, O'Connor, Perlman, Seaborg, and Thompson, Phys. Rev. **72**, 739 (1947); H. H. Hopkins, Jr., and B. B. Cunningham, Phys. Rev. **73**, 1406 (1948); M. Lindner and I. Perlman, Phys. Rev. **73**, 1124, 1202 (1948); **78**, 499 (1950); H. H. Hopkins, Jr., Phys. Rev. **77**, 717 (1950); L. Marquez, Phys. Rev. **88**, 225 (1952); Miller, Thompson, and Cunningham, Phys. Rev. **74**, 347 (1948); Rudstam, Stevenson, and Folger, Phys. Rev. **87**, 358 (1952); G. Wagner and E. O. Wiig, J. Am. Chem. Soc. **74**, 1101 (1952); S. G. Rudstam, Phil. Mag. **44**, 1131 (1953). See also the reviews by G. T. Seaborg and D. H. Templeton, Ann. Rev. Phys. Chem. **2**, 83 (1951) and G. W. Wilkinson, J. Chem. Soc. **S366** (1949).

[2] R. Serber, Phys. Rev. **72**, 1114 (1947); M. L. Goldberger, **74**, 1269 (1948).

A study has been made of the distribution of radioactive products formed when cesium is irradiated with 240-Mev protons in the Rochester 130-inch cyclotron. Cesium was chosen since it is monoisotopic ($Cs^{133}$), which enables specific reactions to be established even though the reaction path is not always known.

## II. EXPERIMENTAL PROCEDURE

Targets for irradiation consisted of approximately 200 milligrams of spectroscopically-pure cesium chloride[3] which was wrapped in a single sheet of aluminum foil 3.8 cm long, 0.3 cm wide, and 0.2 cm thick, covered by monitor foils 0.001-inch thick. To avoid errors caused by inexactitude in alignment of the target with the beam direction, the monitor and guard foils were placed both before and after the target proper. To minimize the error caused by recoil of $Na^{24}$ out of the monitor foil, a guard foil was placed in front of each monitor so that any loss of $Na^{24}$ by recoil out of the monitor foil would be offset by the gain in $Na^{24}$ from the guard foil. It was found that more accurate measurement of absolute cross sections could be made using a target square in cross section as illustrated in Fig. 1. This minimizes the effect of beam penetration cutoff in the aluminum foil surrounding the target. In this way, it was possible to increase the accuracy of measuring absolute cross sections by a factor of almost 1.5. Measurement of the cyclotron beam current was made using the $Al^{27}(p,3pn)Na^{24}$ reaction in the monitor foils.

After irradiations of about one hour, the target was processed chemically. The aluminum monitor foils were dissolved separately in 1 ml of concentrated hydrochloric acid. After dilution, an aliquot of each of these solutions was mounted on $\frac{7}{8}$-inch filter paper disks backed by 0.005-inch thick stainless steel counting plates one inch in diameter and counted in the standard manner adopted for spallation products under a high-resolution beta-proportional counter. In every case the activities observed were 2.0-hour $F^{18}$, 15.00-hour $Na^{24}$, and long-lived activity, presumably a mixture of $Be^{7}$ and $Na^{22}$.

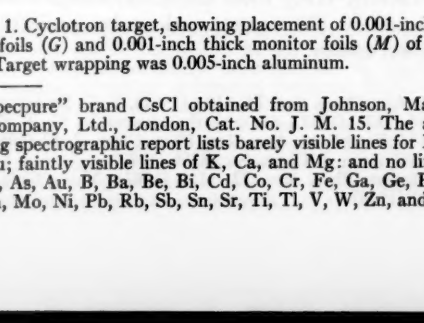


FIG. 1. Cyclotron target, showing placement of 0.001-inch thick guard foils ($G$) and 0.001-inch thick monitor foils ($M$) of aluminum. Target wrapping was 0.005-inch aluminum.

The CsCl target itself was dissolved in 6$N$ nitric acid for subsequent separation into various elemental fractions. Chemical exchange of radioelements with the inert carriers which were added was assured through vigorous oxidation-reduction steps. The general chemical methods employed were taken, with some modifications,[4] from the fission product procedures discussed by Coryell and Sugarman.[5] In various bombardments the following elements were separated and studied: lanthanum, barium, cesium, xenon, iodine, tellurium, antimony, tin, indium, cadmium, palladium, and ruthenium.

After chemical separation and successive repurifications of the desired elemental fraction, the final precipitate was vacuum filtered in a Hirsch funnel onto a weighed disk of Whatman No. 42 filter paper $\frac{7}{8}$ inch in diameter which had been treated previously with ethanol and dried under a heat lamp. The chemical yield was then determined gravimetrically. The disk containing the active deposit was cemented with Duco to a one-inch diameter stainless steel plate, covered with a thin film of collodion, dried under heat, and counted under a beta-proportional counter, sodium iodide scintillation counter, or beta-ray survey spectrometer.

Yields were computed starting with the raw counting yields obtained from an extremely-stable methane flow beta-proportional counter which is a duplicate of the Los Alamos model.[6] The electronic units were custom-built.[7] The counter consists of an aluminum cathode counting chamber with a $2\frac{1}{4}$-inch diameter window of thickness 4.9 mg/cm$^2$ and a 0.002-inch diameter stainless steel central anode wire held at a potential of 4600 volts. Pulses from this chamber pass through 4 feet of RG-13/U coaxial cable to the Model PA-2 pulse amplifier where they are amplified linearly, passed through a trigger circuit after amplification, and then equalized to about 1 volt in amplitude. These are then fed into a fast scaler. The chamber is flushed with pure methane gas[8] and operated at a slow flow rate giving

[3] "Specpure" brand CsCl obtained from Johnson, Matthey, and Company, Ltd., London, Cat. No. J. M. 15. The accompanying spectrographic report lists barely visible lines for Na, Si, and Cu; faintly visible lines of K, Ca, and Mg: and no lines for Ag, Al, As, Au, B, Ba, Be, Bi, Cd, Co, Cr, Fe, Ga, Ge, Hg, In, Li, Mn, Mo, Ni, Pb, Rb, Sb, Sn, Sr, Ti, Tl, V, W, Zn, and Zr.

[4] For detailed chemical separation procedures, see R. W. Fink, Ph.D. thesis, University of Rochester Library, 1953 (unpublished).

[5] C. D. Coryell and N. Sugarman, *Radiochemical Studies: Radiochemistry of the Fission-Product Elements*, (McGraw-Hill Book Company, Inc., New York, 1951 and 1952), National Nuclear Energy Series, Plutonium Project Record, Vol. 9.

[6] E. L. Kemp, Los Alamos Laboratory Report La-1207, 1950 (unpublished); J. H. Larkins, Los Alamos Laboratory Report La-1238, 1951 (unpublished); V. C. Rexroth, Los Alamos Laboratory Report La-1259, 1951 (unpublished).

[7] By Trott Electronics Company, 1944 Clinton Avenue North, Rochester, New York.

[8] "96 percent pure" methane with not more than 4 percent ethane, 2 percent nitrogen, and 0.1 percent oxygen, and sulfur-free. Obtained from Industrial Gas Department, Carbide and Carbon Chemicals Corporation, 30 East 42nd Street, New York 17, New York.

rise to a pressure slightly above atmospheric. With this arrangement, a plateau about 350 volts long with a slope of less than 1 percent per 100 volts was obtained. The resolving time, less than $(0.07\pm0.03)\times10^{-8}$ minute, was determined by using two $Y^{91}$ half-samples which together gave approximately 120 000 counts/minute. By using the decay of a very active source of $Na^{24}$, it was found that the coincidence correction was negligible up to 500 000 counts per minute. Above this, a small but increasing resolving time correction was found to apply. Saturation set in at $1.3\times10^6$ counts per minute. In all cases, where the counting rate of the sample was excessive, a lower geometry was used. Because a greater amount of active precipitate can be counted than with a G-M tube, the error in the chemical yield determination can be materially reduced with this instrument since weighing errors become less significant. The counting efficiency for gamma rays, x-rays, and particulate radiation is very similar to that of a standard helium-alcohol G-M tube. All samples were counted on a $\frac{7}{16}$-inch thick shelf of stainless steel and an appropriate estimate of the correction factor for saturation backscattering was applied.

It is worthwhile to give the method and assumptions under which yields were computed from the raw counting yield, $A^0$, obtained by back extrapolation of the decay curves to the time of cessation of bombardment.

The absolute disintegration rate, $N^0$, may be related to the observed raw yield, $A^0$, by the relation

$$N^0=\frac{A^0}{f_C f_W f_A f_B f_{SSA} G E}\ \text{dis/min},$$

where $f_C$=correction factor for counter resolution (taken as unity for beta-proportional and scintillation counters). $f_W$=correction factor for total air-window absorption. Under our conditions, the total air-window thickness was about 5 mg/cm². Values of $f_W$ were interpolated from data of Gleason, Taylor, and Tabern[9] for particles of various energies while for electromagnetic radiation a value of 0.99 was used. Where weak conversion electrons are present, this factor may constitute a serious correction. Values for each nuclide were computed as a weighted mean using known or estimated branching ratios for the respective radiations emitted. $f_A$=correction for air scattering of particles; taken as unity. $f_B$=correction factor due to backscattering in the source.[10] For saturation backscattering, $f_B$ varies with $Z$ of the backing material. Burtt[11] gives about 1.3 for beta-particles scattered from filter paper or cardboard of infinite thickness. In this work, the following values of $f_B$ were used: for negative electrons, 1.25; for positrons, 1.2; and for electromagnetic radiations, 1.0. That $f_B$ is definitely larger for negatrons than for positrons has been demonstrated by Seliger[12] for all cases. $f_H$=correction factor for scattering of particles from the housing (taken as unity for the Lucite and aluminum housing used). $f_{SSA}$=correction factor for effect of self-scattering and self-absorption owing to the finite source thickness. For each nuclide in each individual sample, a value of this factor was interpolated from the data of Nervik and Stevenson.[13] For electromagnetic radiations, $f_{SSA}$ was assumed to be unity. In cases of nuclides having known branching ratios between particles of various energies and electromagnetic radiations, or where these ratios could be estimated from absorption curves in aluminum, a weighted mean value was calculated. This factor becomes the more serious the weaker the particle energy and the thicker the sample. $G$=correction factor for geometry. $G$ is the solid angle fraction subtended by the sensitive volume of the counter. The value of $G$ was calculated from geometrical measurements as 0.347, while from an absolutely-calibrated $Co^{60}$ source, assuming 2 percent efficiency for $Co^{60}$ gamma rays, the value was 0.316. For all corrections used here, $G$ was taken as 0.32. $E$=correction factor for counting efficiency, defined as the ratio of the number of events recorded by the counter to the total number of particles or photons traversing the sensitive volume of the counter. This factor constitutes the largest over-all error to the determination of absolute cross sections. In order to establish the true counting efficiency for x-rays, samples of $Fe^{55}$ and $Cs^{131}$ were prepared and taken to Brookhaven National Laboratory[14] where they were calibrated using a high-pressure argon-methane x-ray proportional chamber and pulse analysis equipment. These calibrated x-ray standards were subsequently used to measure the x-ray counting efficiency of the beta-proportional counter and a helium-alcohol G-M Tube. The experimental results are shown in Table I. In this work, $E$ was taken as 0.25 percent for 30 kev x-rays, 1 to 2 percent for high-energy gamma

TABLE I. Experimental values for counting efficiencies of xenon and manganese x-rays.

| Detector | Values in percent: Xenon $K$ x-rays (30 kev) | Manganese $K$ x-rays (6.4 kev) |
|---|---|---|
| Methane beta-prop. counter | 0.25 | $0.8_3$ |
| Tracerlab TCG-2 GM tube, He-alcohol | $0.1_5$ | 0.2 |

[9] Gleason, Taylor, and Tabern, Nucleonics 8, No. 5, 12 (1951).
[10] See L. Yaffe and K. M. Justus, J. Chem. Soc. S341 (1941).
[11] B. P. Burtt, Nucleonics 5, No. 2, 28 (1949).
[12] H. H. Seliger, Phys. Rev. 78, 491 (1950); Phys. Rev. 88, 408 (1952).
[13] W. E. Nervik and P. C. Stevenson, Nucleonics 10, No. 3, 18 (1952).
[14] We appreciate the hospitality extended to us by the Brookhaven National Laboratory and assistance with the equipment provided by Dr. M. L. Perlman, of the Department of Chemistry.

TABLE II. Experimental results of 240-Mev Cs-$p$-spallation studies.

| Nominal half-life | Nuclide | Assumed counting efficiency, $E$ | Average absolute cross section in millibarns |
|---|---|---|---|
| 15.0 hr | $Na^{24}$ | 1.0 | 11.0 (Monitor) |
| 2.4 days | $Ba^{128}$ | 1.0 | 8.1 |
| 2.0 hr | $Ba^{129}$ | 1.0 | 3.6 |
| 12.0 days | $Ba^{131}$ | 0.72 | 5.3 |
| 5.5 hr | $Cs^{127}$ | 1.0 | 4.5 |
| 31 hr | $Cs^{129}$ | 0.39 | 15 |
| 9.8 days | $Cs^{131}$ | 0.0025 | 460 |
| 7.1 days | $Cs^{132}$ | 0.005 | 117 |
| 1.6 hr | $I^{120+121}$ | 1.0 | 11 |
| 13 hr | $I^{123}$ | 0.17 | 21 |
| 4.0 days | $I^{124}$ | 0.30 | 8.4 |
| 12.5 days | $I^{126}$ | 0.53 | 5.0 |
| 2.5 hr | $Te^{117}$ | 1.0 | 2.4 |
| 6.0 days | $Te^{118}$ | 1.0 | 4.8 |
| 16 hr | $Te^{119}$? | 0.002? | 50? |
| 17.0 days | $Te^{121}$ | 0.09 | ? |
| 90 days | $Te^{121m}$? | 1.0 | 0.3 |
| 2.8 hr | $Sb^{117}$ | 0.15? | 4.2 |
| 6.0 days | $Sb^{120}$ | 0.1? | 4 |
| 2.6 days | $Sb^{122}$ | 1.0 | 0.3 |
| 60 days | $Sb^{124}$ | 1.0 | 0.07 |
| 4.5 hr | $Sn^{108}$ | 0.05? | 0.3 |
| 2.0 hr | $In^{108,110}$ | 1.0 | 0.02 |
| 4.2 hr | $In^{109}$ | 0.9 | 0.05 |
| 6.7 hr | $Cd^{107}$ | 0.05 | 0.9 |
| 50 min | $Cd^{104,105}$ | 1.0 | 0.2 |
| 4.0 days | $Pd^{100}$ | 0.05 | 1.5 |
| 1.7 hr | $Ru^{95}$ | 1.0 | 0.2 |
| 2.8 days | $Ru^{97}$ | 0.07? | 3? |
| 4 hr | $La^{133}$? | 1.0 | 0.005? |

rays, and 99 percent for particulate radiation. The actual counting efficiency assumed for each nuclide is listed with the final results in Table II.

To convert the absolute counting rate $N^0$ into an absolute cross section, it is necessary to correct each yield to saturation bombardment. By assuming a constant rate of production in the cyclotron, we obtain the relation

$$N_\infty{}^0(A)=N^0(A)/(1-e^{-\lambda_A T}),$$

where $N_\infty{}^0(A)$ is the yield of species $A$ at infinite bombardment, $T$ is the actual duration of irradiation, and $\lambda_A$ is the decay constant of species $A$. Since $I^{126}$ was the only species determined in all bombardments, it was chosen as the internal monitor to which all other yields were compared. To convert these relative yields into absolute cross sections, it is first necessary to evaluate the absolute cross section of the internal monitor $I^{126}$ by comparison of its yield with that of $Na^{24}$ from the $Al^{27}(p,3pn)Na^{24}$ reaction[15] assuming thin target formulation. The result is

$$\frac{\sigma(I^{126})}{\sigma(Na^{24})}=\frac{N_\infty{}^0(I^{126})}{N_\infty{}^0(Na^{24})}\times f,$$

where $f=6.24\times$(weight of aluminum monitor/weight of CsCl target). The factor $f$ corrects for the fact that the total number of cesium atoms exposed to the proton beam is different from the total number of atoms of aluminum monitor. By this method, the absolute cross section for formation of $I^{126}$ from cesium at 240 Mev is 5.0 millibarns.

## III. DISCUSSION OF ERRORS

In addition to the error in the absolute cross sections due to errors in interpolating values of absolute counting correction factors, chemical yields, counting efficiencies, resolution of decay curves having many components, which lead to an estimated total indeterminate error of from 20 percent to 60 percent in general, there are some intangible effects which cannot be evaluated directly.

These effects are associated with the fact that in most cases one is dealing with short lived, highly neutron-deficient nuclides whose yield may be partly primary and partly the result of the decay of very short-lived parent nuclides produced as primary spallation products. For example, the cross sections of $I^{120+121}$, $Te^{117}$, $Cs^{127}$, and other neutron-deficient nuclides having unknown or very short-lived parent nuclides, may quite possibly be excessively large due to contributions from short-lived parents. It is clear that yields of those species subject to this effect are much more susceptible to such bombardment conditions as intermittent beam intensity fluctuations and variations in the duration of bombardment. Indeed, from bombardment to bombardment, the yields of $I^{124}$, $I^{126}$, $Cs^{132}$, and other shielded nuclides appear to be smoother and more reproducible than of such species as $I^{120+121}$, $Te^{117}$, $Cs^{127}$, and other similar species. It is known,[16] for example, that $Ba^{127}$ has a 12-minute half-life. Thus, during the 2 to 3 hours required for chemical separation, this nuclide decays out before the barium fraction can be separated from the cesium fraction. What the independent yield of $Cs^{127}$ is, therefore, has not been determined.

Errors can be caused by lack of radiochemical purity. In this work, the purity of the various elemental fractions was satisfactory as evidenced by decay curves and beta-ray spectrometer spectra. In the case of the

[15] Values of the cross section for $Al^{27}(p,3pn)Na^{24}$ were interpolated at 240 Mev from data of V. Peterson *et al*, University of California Radiation Laboratory file compiled by W. W. Meinke, Jr., 1950 (unpublished). Values are also published by N. H. Hintz and N. F. Ramsey, Phys. Rev. **88**, 19 (1952), and by L. Marquez, Phys. Rev. **88**, 225 (1952).

[16] M. Lindner and R. N. Osborne, Phys. Rev. **88**, 1422 (1952).

lanthanum fraction, however, that yield assigned to 4-hour $La^{133}$ may be due entirely to the carrying of 4-hour $In^{109}$ or $Sn^{108}$ even through the many steps and repurification procedures used. Although the question of whether $La^{133}$ was formed by a secondary $(\alpha,4n)$ reaction, not previously observed in spallation, is interesting, it has not been established in this study.

## IV. INTERPRETATION OF RESULTS

The experimental values of the absolute cross sections of various nuclides formed when cesium is bombarded with 240-Mev protons[17] are given in Table II.

These data indicate that the yield pattern of radioactive spallation products is as follows.

1. From mass numbers 131 to 127, a loss of up to 6 nucleons, the absolute cross sections drop by a factor of 50. The largest yields by far are represented by mass numbers 131 and 132, one and two neutrons removed from the target. Presumably this reflects the primary knock-on reaction whereby the incident proton interacts with only one or two nucleons according to the mechanism of Serber and Goldberger.[2] The struck nucleons are then emitted in the order of $10^{-22}$ second as high-energy secondaries sharply peaked in the forward direction. Forward peaked neutrons and charged particles[18] have been observed in high-energy spallation reactions. At an energy as high as 240 Mev, the contribution of the neutron "pickup" reactions $(p,d)$ and $(p,t)$ would not be expected to account appreciably for the very large yields of $Cs^{132}$ and $Cs^{131}$; rather, it would be expected that the instantaneous knock-on process caused by glancing collisions in which only a small excitation energy is imparted to the struck nucleus would be the responsible mechanism.

2. From mass numbers 127 to 120, a further loss of up to 7 nucleons from the excited nucleus, the yields are fairly constant and of the order of 10 millibarns. This constancy of yields reflects the fact that the residual excitation energies left to the struck nuclei after the primary knock-on process are broader in distribution and generally much larger than in typical low-energy cases where the Bohr-Wheeler compound nucleus mechanism[19] prevails. The wider and higher distribution of excitation energies results in a broad distribution of end products, a phenomenon which is in contrast to the narrow distributions prevailing in low-energy reactions.

3. From mass numbers 120 to 110, a further loss of up to 10 nucleons, the yields decrease by another factor of 10 and continue to decrease at the same rate down to mass number 95, the lowest measured. At still lower mass numbers, the yield curve should rise again because of the contribution from the competing process of fission. The study of cesium fission has not been included in the scope of this work.

4. Ordinarily, in a chemical study it is not possible to ascertain whether the nucleons ejected come off singly or in fragments. The fact, however, that such products as $Ru^{95}$, $Pd^{100}$, and $Cd^{107}$ are found chemically leads to the conclusion that fragmentation must play an important role in the evaporation process. For the formation of $Ru^{95}$, $Pd^{100}$, or $Cd^{107}$ from cesium by evaporation of single nucleons, the energetic requirement is much larger than the actual bombardment energy of 240 Mev. Thus, only by the emission of alpha particles and larger fragments can one account for the presence of $Ru^{95}$, $Pd^{100}$, $Cd^{107}$, etc., among the end products. Evidence for alpha-particle emission has been given by Wagner and Wiig,[1] while heavier fragments have been identified by Wright[20] and by Marquez and Perlman.[21]

Yields of those elements more likely to be formed through the evaporation process following the initial knock-on step are accentuated toward the most neutron-deficient nuclides. This is true for iodine, tellurium, antimony, and possibly barium nuclides, the latter arising from neutron evaporation from excited $Ba^{133}$ formed by the $(p,n)$ charge exchange reaction. It is decidedly not true for cesium isotopes whose yield pattern is mostly due to the primary knock-on process. Accentuation of the yields of the most neutron-deficient species is more marked the higher the energy and the heavier the target element as expected from the increase in the Coulomb barrier with increasing atomic number.

These data are in agreement with the general pattern for all cases studied. About 80 percent of all interactions leads to nuclides in the vicinity of the target element, followed by respectable and comparatively constant yields to about 15 or 16 mass numbers below the target, and finally a sharp and continuing drop in yields until the fission product region is reached where the yields are expected to rise again.

## V. ACKNOWLEDGMENTS

We are happy to acknowledge the cooperation of Professor S. W. Barnes, Mr. William Coombs, Mr. Kurt Enslein, and the crew of the Rochester 130-inch cyclotron.

[17] Results of excitation studies of 60 to 240-Mev protons on cesium will appear in a forthcoming paper.

[18] J. Hadley and H. York, Phys. Rev. **75**, 1467 (1949); Phys. Rev. **80**, 345 (1950).

[19] N. Bohr, Nature **137**, 344 (1936); Science **86**, 161 (1937); N. Bohr and J. A. Wheeler, Phys. Rev. **56**, 426 (1939).

[20] S. C. Wright, Phys. Rev. **79**, 838 (1950).

[21] L. Marquez and I. Perlman, Phys. Rev. **81**, 953 (1951).

# The Theory of Quantized Fields. VI

JULIAN SCHWINGER
*Harvard University, Cambridge, Massachusetts*
(Received January 22, 1954)

This paper treats the effect of a time-independent external electromagnetic field upon a Dirac field by constructing the transformation function in a representation adapted to the external field. In addition to the alteration of the Green's function, the structure of the transformation function differs from that of the zero field situation by a factor which describes the energy of the modified vacuum state. A formula for the vacuum energy is obtained and expressed in a form appropriate to a localized field, in terms of the energy eigenvalues of discrete modes, and of the phase shifts associated with continuum modes. Determinantal methods are then introduced, and the class of fields is established for which a certain frequency-dependent modified determinant is an integral function of the parameter measuring the strength of the field. The properties of the determinant are investigated in the two frequency regions $|p_0|<m$ and $|p_0|>m$, with regard to the zeros of the real determinant in the former region, which are the frequencies of the discrete modes, and to the phase of the complex determinant in the latter region. In the second situation, a connection is established with a unitary matrix defined for modes of a given frequency, and the phase of the determinant is expressed in terms of the eigenphases of this matrix. Following a discussion of the asymptotic behavior of the determinant as a function of $p_0$, the modified determinant is constructed in terms of the discrete mode energies and of the eigenphases. This yields a more precise version of the vacuum energy formula, in which a single divergent parameter is exhibited, for a suitable class of fields.

The scattering description is introduced by an evaluation of the Green's function, for a sufficiently large time interval, in terms of the discrete modes, and of linear combinations of free particle modes expressed by a unitary matrix which is an extension of that referring to modes of a single frequency. Transition probabilities are derived and summarized in a generating function that serves to evaluate occupation number expectation values for the final state, upon which is based the definition of differential and total scattering cross sections. A discussion is presented of various symmetry operations and the resulting properties of cross sections. Then, a determinantal formula for the individual transition probabilities is used to examine the probability for the persistence of a state, in its dependence upon occupation numbers. An incidental result of this analysis is a qualitative upper limit to total cross sections in relation to the character of the angular distribution. A section is devoted to the properties of eigenphases, including the demonstration of equivalence between phase shifts and eigenphases, and the discussion of alternative procedures for their evaluation in terms of quantities exhibited as convergent power series in the potential. Finally, the determinantal asymptotic behavior is used to obtain a high-energy approximation to the eigenphases for an isotropic scalar potential. The resulting high energy, small angle, form of the scattering cross section is discussed in the extreme quantum and classical limits. An alternative derivation of the high-energy scattering formula is provided in terms of an approximate construction of the Green's function.

THE influence of a time-independent external electromagnetic field upon a Dirac field can be discussed either by adapting the representation to the external field, or by considering that the given field is part of a larger time-dependent one that vanishes outside suitable boundaries. With the latter approach, the results of the previous paper[1] are applicable, and the question is recast as the problem of separating the properties of a system for a certain time interval from the known behavior over a larger interval. We shall defer consideration of this problem and employ the first method for the treatment of time-independent fields.

## TIME INDEPENDENT ELECTROMAGNETIC FIELDS

It is natural to use a gauge in which the potential vector is time-independent, $A_\mu(\mathbf{x})$. Since fields of physical interest are spatially localized, we also impose the convention of vanishing potential in field-free space. The field equations in the absence of sources can be written as equations of motion in the form (IV[2] 5), where $H$, acting on $\psi$, is

$$H=eA_0(\mathbf{x})+\gamma_0\gamma_k[-i\partial_k-eA_k(\mathbf{x})]+m\gamma_0. \quad (1)$$

We introduce a basic restriction on the class of time-independent fields by requiring that the spectrum of $H$ eigenvalues fall into two distinct sets, of positive and negative frequencies, with a finite interval separating each set from zero frequency. This excludes the homogeneous electric field,[3] for example, where the $H$ spectrum forms a continuum, extending from $-\infty$ to $\infty$.

The procedure employed in IV for zero electromagnetic fields is readily adapted to this class of static fields. Projection operators can be defined [IV 6] that separate $\psi$ and $\bar{\psi}$ into positive and negative frequency parts [IV 11]. One can construct generators of infinitesimal changes in the positive or negative frequency parts of $\psi$ and $\bar{\psi}$ [IV 17–22], and derive therefrom commutation relations referring to a given time [IV 23, 24]. Complete sets of anticommuting operators for a fixed time are provided by the positive frequency, or the negative frequency parts of the fields, and one can introduce their right or left eigenvectors. The construction of the transformation function describing a time translation, in terms of that referring to zero eigenvalues, is expressed by the substitution (IV 33). The dependence of $\mathcal{W}_0$ upon the sources is given, as in (V 2), in terms of a Green's function obeying the differential equations (V 4). But this Green's function depends only upon $x_0-x_0'$, and contains positive or

[1] J. Schwinger, Phys. Rev. **93**, 615 (1954).
[2] This refers to the fourth paper of the series, J. Schwinger, Phys. Rev. **92**, 1283 (1953).
[3] That is, fields of magnitude $E$ that are essentially homogeneous over distances greater than $m/eE$, where this distance is not many orders of magnitude in excess of $1/m$.

negative frequencies for $x_0>x_0'$, or $x_0<x_0'$, respectively. The principal deviation from the zero field situation is the occurrence of $w$, which characterizes the null eigenvalue transformation function in the absence of sources.

Concerning the dependence of $w$ upon the electromagnetic field, we must notice that the definition of the eigenvalues involves $A_\mu(\mathbf{x})$. Hence the change in the transformation function $(0\sigma_1|0\sigma_2)]_0$, induced by $\delta A_\mu$, arises from potential variations in the interior of the region and on the boundaries,

$$\delta_A(0\sigma_1|0\sigma_2)]_0=\delta_A e^{iw}$$
$$=i\left(0\sigma_1\left|\left[G_A(\sigma_1)-G_A(\sigma_2)+\int_{\sigma_2}^{\sigma_1}(dx)\delta A_\mu(x)j_\mu(x)\right]\right|0\sigma_2\right)\Big]_0. \quad (2)$$

The infinitesimal generators, $G_A(\sigma_1)$ and $G_A(\sigma_2)$, differ only in their dependence upon dynamical variables referring to the surfaces $\sigma_1$ (time $t_1$) and $\sigma_2$ (time $t_2$), respectively. But the zero eigenvalue state is the minimum energy state of the system and, as the phrase "stationary state" indicates, expectation values of dynamical variables in an energy eigenstate are independent of the time to which the dynamical variables refer. Hence,

$$(0\sigma_1|\,(G_A(\sigma_1)-G_A(\sigma_2))\,|0\sigma_2)]_0=0, \quad (3)$$

and the same development as in V yields

$$\delta w=\int_{\sigma_2}^{\sigma_1}(dx)\ \mathrm{tr}ie\gamma_\mu\delta A_\mu(x)G_+(x,x). \quad (4)$$

We shall suppose that the time-independence of $A_\mu(\mathbf{x})$ is maintained by any infinitesimal variation, $\delta A_\mu(\mathbf{x})$. Since the Green's function only contains $x_0-x_0'$, $G_+(x,x)$ is independent of $x_0$ and the integrand of (4) is time-independent. The time integral thus supplies the factor

$$T=t_1-t_2. \quad (5)$$

On writing

$$w=-TE(0), \quad (6)$$

we obtain the differential expression

$$\delta E(0)=-\int(dx)\ \mathrm{tr}ie\gamma_\mu\delta A_\mu(\mathbf{x})G_+(x,x), \quad (7)$$

which is to be integrated subject to the initial condition,

$$A_\mu=0:\quad E(0)=0. \quad (8)$$

The resulting transformation function describing a time translation differs in form from that given in IV only by the additional factor $\exp[-iE(0)T]$. When extended to include a phase transformation, the transformation function for a source-less system is given by [IV 66]

$$(\chi^{(-)'}\sigma_1\alpha_1|\chi^{(+)'}\sigma_2\alpha_2)]_0$$
$$=\exp\Big[-iE(0)T-i\int_{\sigma_1}d\sigma\int_{\sigma_2}d\sigma'\bar\psi^{(-)'}(x)\gamma_0$$
$$\times e^{ie\alpha}G_+(x,x')\gamma_0\psi^{(+)'}(x')$$
$$-i\int_{\sigma_2}d\sigma\int_{\sigma_1}d\sigma'\bar\psi^{(+)'}(x)\gamma_0G_+(x,x')$$
$$\times e^{-ie\alpha}\gamma_0\psi^{(-)'}(x')\Big]. \quad (9)$$

There are no terms in which both integrals refer to a common surface [IV 65], since the three-dimensional symbolic form of the Green's function, (IV 49), is still applicable in this static field situation.

Let us introduce a complete set of discretely labelled eigenfunctions for $H$,

$$H\psi_\kappa(\mathbf{x})=\epsilon_\kappa E_\kappa\psi_\kappa(\mathbf{x}),\quad \bar\psi_\kappa(\mathbf{x})\gamma_0H=\epsilon_\kappa E_\kappa\bar\psi_\kappa(\mathbf{x})\gamma_0,$$
$$\textstyle\sum_\kappa\psi_\kappa(\mathbf{x})\bar\psi_\kappa(\mathbf{x}')=\gamma_0\delta(\mathbf{x}-\mathbf{x}'), \quad (10)$$

where $E_\kappa>0$, and $\epsilon_\kappa=\pm1$ characterizes the positive and negative eigenvalues. Hence,

$$P^{(\pm)}\gamma_0\delta(\mathbf{x}-\mathbf{x}')=\textstyle\sum_\pm\psi_\kappa(\mathbf{x})\bar\psi_\kappa(\mathbf{x}'), \quad (11)$$

and, as the analog of (IV 55), we have

$$G_+(x,x')=i\textstyle\sum_+\psi_\kappa(x)\bar\psi_\kappa(x'),\qquad x_0>x_0'$$
$$=-i\textstyle\sum_-\psi_\kappa(x)\bar\psi_\kappa(x'),\quad x_0<x_0', \quad (12)$$

in which

$$\psi_\kappa(x)=\psi_\kappa(\mathbf{x})e^{-ie_\kappa E_\kappa x_0}. \quad (13)$$

With the notation

$$\chi_\kappa^{(-)'}=\int_{\sigma_1}d\sigma\bar\psi^{(-)'}(x)\gamma_0\psi_\kappa(\mathbf{x}),$$
$\epsilon_\kappa=1$:
$$\chi_\kappa^{(+)'}=\int_{\sigma_2}d\sigma\bar\psi_\kappa(\mathbf{x})\gamma_0\psi^{(+)'}(x),$$
$$\chi_\kappa^{(-)'}=\int_{\sigma_1}d\sigma\bar\psi_\kappa(\mathbf{x})\gamma_0\psi^{(-)'}(x), \quad (14)$$
$\epsilon_\kappa=-1$:
$$\chi_\kappa^{(+)'}=\int_{\sigma_2}d\sigma\bar\psi^{(+)'}(x)\gamma_0\psi_\kappa(\mathbf{x}),$$

the transformation function (9) is obtained as

$$\exp[-iE(0)T+\textstyle\sum_\kappa\chi_\kappa^{(-)'}\exp(-iE_\kappa T+ie\epsilon_\kappa\alpha)\chi_\kappa^{(+)'}]$$
$$=\textstyle\sum_n(\chi^{(-)'}|n)\exp(-iP_0'T+iQ'\alpha)(n|\chi^{(+)'}), \quad (15)$$

where

$$P_0'=E(0)+\textstyle\sum_\kappa n_\kappa E_\kappa,\quad n_\kappa=0,1,\quad Q'=\sum_\kappa n_\kappa e\epsilon_\kappa \quad (16)$$

and

$$(n|\chi^{(+)\prime})=\prod_\kappa(\chi_\kappa^{(+)\prime})^{n_\kappa},$$
$$(\chi^{(-)\prime}|n)=\prod_\kappa(\chi_\kappa^{(-)\prime})^{n_\kappa}. \tag{17}$$

Evidently, $E(0)$ represents the energy of the modified vacuum, the minimum energy state of the system, $n_\kappa=0$.

### The Vacuum Energy

To obtain a formula for $E(0)$, we remark that $\delta A_\mu(\mathbf{x})$ induces a modification of the Green's function which is described by

$$\{\gamma_\mu[-i\partial_\mu-eA_\mu(\mathbf{x})]+m\}\delta G_+(x,x') = e\gamma_\mu\delta A_\mu(\mathbf{x})G_+(x,x'). \tag{18}$$

The left side of this equation can also be written $(-i\gamma_0\partial_0+\gamma_0H)\delta G_+(x,x')$, and, therefore,

$$\delta E(0)=-\int(d\mathbf{x})\ \mathrm{tr}(\gamma_0\partial_0+i\gamma_0H)\delta G_+(x,x')]_{x'\to x}. \tag{19}$$

Now $H$ is a differential operator referring only to spatial coordinates, so that the averaged limit of equal times can be performed in the Green's function for the second term of (19),

$$-\int(d\mathbf{x})\ \mathrm{tr}i\gamma_0H\delta G_+(x,x')]_{x'\to x} = \tfrac{1}{2}\int(d\mathbf{x})\ \mathrm{tr}\gamma_0H\delta(\textstyle\sum_\kappa\epsilon_\kappa\psi_\kappa(\mathbf{x})\bar\psi_\kappa(\mathbf{x}'))]_{x'\to x}. \tag{20}$$

In virtue of the formal Hermitian property of $H$, which is assured by the use of discrete eigenfunctions, $\gamma_0H$ can always be applied to an unvaried eigenfunction in (20), whence the latter becomes

$$\tfrac{1}{2}\textstyle\sum_\kappa E_\kappa\delta\left(\int(d\mathbf{x})\bar\psi_\kappa\gamma_0\psi_\kappa\right)=0. \tag{21}$$

We can now integrate (19) to obtain

$$E(0)=-\int(d\mathbf{x})\ \mathrm{tr}\gamma_0\partial_0(G_+(x,x')-G_+^{\,0}(x,x'))]_{x'\to x}. \tag{22}$$

Since

$$\int(d\mathbf{x})\ \mathrm{tr}\gamma_0G_+(x,x')]_{x'\to x}=i\textstyle\sum_+e^{-iE_\kappa(x_0-x_0')},\quad x_0>x_0' \\ =-i\textstyle\sum_-e^{iE_\kappa(x_0-x_0')},\quad x_0<x_0', \tag{23}$$

the averaged limit is given by

$$E(0)=-\tfrac{1}{2}\textstyle\sum_\kappa(E_\kappa-E_\kappa^0). \tag{24}$$

A variation of this procedure that leads directly to (24), employs the eigenvalue property

$$\delta E_\kappa=-\epsilon_\kappa\int(d\mathbf{x})\bar\psi_\kappa e\gamma_\mu\delta A_\mu\psi_\kappa, \tag{25}$$

which is equivalent to (20) and (21).

For static fields that are effectively localized in a finite volume, the spectrum of $E_\kappa$ will consist of a continuum extending from $m$ to infinity, and possibly of discrete values less than $m$, which are associated with bound modes of the Dirac field. The completely discrete spectrum that we have employed can be attained by the familiar artifice of considering a large but finite volume of three-dimensional space, as defined by a radius $R$. An eigenfunction is specified by an energy eigenvalue $E$, and a set of other quantities $\gamma$. An eigenfunction of type $\gamma$ with $E>m$ will have an asymptotic form involving trigonometric functions of $p|\mathbf{x}|+\phi$, where $p=(E^2-m^2)^{\frac{1}{2}}$, and $\phi$ is a constant phase. If we impose some elementary boundary requirement at $|\mathbf{x}|=R$ (say $B\psi=0$, where $B$ is a matrix of rank two), the eigenvalue equation is obtained as

$$pR+\phi=n\pi+\beta,\quad n=0,1,2,\cdots, \tag{26}$$

where $\beta$ depends upon the particular boundary condition. Thus the number of eigenfunctions of type $\gamma$ in an interval $dE$ is

$$dn=\frac{1}{\pi}(dp/dE)RdE=dE/\Delta E, \tag{27}$$

where $\Delta E$ is the interval between adjacent eigenvalues.

The eigenvalue equation for zero external field similarly reads

$$p^0R+\phi^0=n\pi+\beta, \tag{28}$$

so that the static field produces an energy displacement of a given mode,

$$E-E^0=(dE/dp)R^{-1}(p-p^0)R=-\Delta E(\delta/\pi), \tag{29}$$

where $\delta_{\gamma E}$ is the phase shift, $\phi-\phi^0$. Thus, if $\delta=\nu\pi$, $\nu=1,2,\cdots$, the effect of the static field has been to displace the $n$th mode to the level occupied by the $(n-\nu)$th unperturbed mode. Otherwise expressed, $\nu$ modes (of type $\gamma$) have been pushed below the energy level $E$. Let us think of a bound mode as one which has been displaced below the minimum unperturbed energy, $E=m$, and become detached as a true discrete mode. If there are $\nu_\gamma$ bound modes of type $\gamma$, that many modes have been pushed below $E=m$, and we must have

$$\delta_{\gamma m}=\nu_\gamma\pi. \tag{30}$$

In consequence of this remark on the origin of the bound modes from the unperturbed modes with $E$ differing infinitesimally from $m$, we see that the contribution of the bound modes to (24) is $-\frac{1}{2}\sum(E_\kappa'-m)$, where we have written $E_\kappa'$ for the discrete eigenvalues, $E_\kappa'<m$. For modes with $E>m$, we combine (27) and (29). Thus, for a given type $\gamma$,

$$dn(E-E^0)=-dE(\delta/\pi), \tag{31}$$

and $E(0)$ is obtained as

$$E(0)=\tfrac{1}{2}\textstyle\sum_\kappa(m-E_\kappa')+\dfrac{1}{2\pi}\displaystyle\int_m^\infty dE\sum_\gamma\delta_{\gamma E}, \tag{32}$$

in terms of the discrete energy eigenvalues and the phase shifts for the continuum modes.

### Determinantal Methods

We shall now obtain more precise results by using a three-dimensional version of the techniques developed in the previous paper for space-time localized fields. Let us introduce the Fourier transform of the Green's function,

$$G_+(\mathbf{x},\mathbf{x}',p_0)=\int_{-\infty}^{\infty}dx_0e^{ip_0(x_0-x_0')}G_+(x,x'), \tag{33}$$

or, in terms of the eigenfunction representation of the Green's function,

$$G_+(\mathbf{x},\mathbf{x}',p_0)=i\int_0^{\infty}dt\sum\nolimits_+\psi_\kappa(\mathbf{x})\bar{\psi}_\kappa(\mathbf{x}')e^{-i(E_\kappa-p_0)t}$$

$$-i\int_0^{\infty}dt\sum\nolimits_-\psi_\kappa(\mathbf{x})\bar{\psi}_\kappa(\mathbf{x}')e^{-i(E_\kappa+p_0)t}, \tag{34}$$

in which we have placed $t=|x_0-x_0'|$. The characterization of $G_+$ by means of an infinitesimal negative imaginary addition to $m$ is useful here.

The effect of the latter on the energy eigenvalues of the continuum modes is expressed by $dE_\kappa/dm=m/E_\kappa>0$. For bound modes, we use the following form of the virial theorem (obtained by differentiating with respect to $m$ after introducing $1/m$ as the unit of length):

$$m(dE_\kappa'/dm)=E_\kappa'+\epsilon_\kappa\int(d\mathbf{x})\bar{\psi}_\kappa(\mathbf{x})(1+\mathbf{x}\cdot\boldsymbol{\nabla})\gamma_\mu A_\mu(\mathbf{x})$$
$$\times\psi_\kappa(\mathbf{x}). \tag{35}$$

Thus, for the Coulomb field, $m(dE_\kappa'/dm)=E_\kappa'$, and $dE_\kappa'/dm=0$ can only occur when $E_\kappa'=0$, which is prohibited. Incidentally, the latter situation exists for the lowest energy state at $Z=$'137'. Only for fields more singular than the Coulomb field will $dE_\kappa'/dm>0$ not be a consequence of $E_\kappa'>0$. Excluding such fields, we can assert that

$$dE_\kappa/dm>0,$$

and every energy eigenvalue acquires an infinitesimal negative imaginary part on replacing $m$ with $m-i\epsilon$, $\epsilon>0$. This means that all the time integrals in (34) are convergent, for real $p_0$, and

$$G_+(\mathbf{x},\mathbf{x}',p_0)=\sum_\kappa\frac{\psi_\kappa(\mathbf{x})\bar{\psi}_\kappa(\mathbf{x}')}{\epsilon_\kappa E_\kappa-p_0}. \tag{36}$$

We see that, as a function of $p_0$, $G_+(\mathbf{x},\mathbf{x}',p_0)$ has poles at $p_0=E_\kappa$, $\epsilon_\kappa=1$, and $p_0=-E_\kappa$, $\epsilon_\kappa=-1$, which are infinitesimally displaced below, and above the real axis, respectively. For the spatially localized fields that we are considering, there may be isolated poles, corresponding to the discrete bound modes, while the continuum modes produce two lines of poles, beginning at $\pm m$ and extending to infinity. That is to say, $\pm m$ constitute branch points of $G_+(\mathbf{x},\mathbf{x}',p_0)$, as a function of $p_0$. This Green's function obeys the differential equation

$$\{\gamma_\mu[p_\mu-eA_\mu(\mathbf{x})]+m\}G_+(\mathbf{x},\mathbf{x}',p_0)=\delta(\mathbf{x}-\mathbf{x}'),$$
$$p_k=-i\partial_k, \tag{37}$$

and we seek the solution that, for real $p_0$, is a regular function of the complex variable $m$ in the lower half-plane, $\mathrm{Im}m<0$. Of course, we are only interested in the limit of real $m$, approached from the lower half-plane. The transformation inverse to (33) is

$$G_+(x,x')=\frac{1}{2\pi}\int_{-\infty}^{\infty}dp_0e^{-ip_0(x_0-x_0')}G_+(\mathbf{x},\mathbf{x}',p_0). \tag{38}$$

That the function so described satisfies the outgoing wave condition, characteristic of $G_+(x,x')$, follows from the location of the singularities in (36), which reproduce the expansion (12).

The Green's function defined by ingoing wave conditions,

$$G_-(x,x')=i\sum\nolimits_-\psi_\kappa(x)\bar{\psi}_\kappa(x'),\qquad x_0>x_0'$$
$$=-i\sum\nolimits_+\psi_\kappa(x)\bar{\psi}_\kappa(x'),\quad x_0<x_0' \tag{39}$$

has the Fourier transform

$$G_-(\mathbf{x},\mathbf{x}',p_0)=i\int_0^{\infty}dt\sum\nolimits_-\psi_\kappa(\mathbf{x})\bar{\psi}_\kappa(\mathbf{x}')e^{i(E_\kappa+p_0)t}$$

$$-i\int_0^{\infty}dt\sum\nolimits_+\psi_\kappa(\mathbf{x})\bar{\psi}_\kappa(\mathbf{x}')e^{i(E_\kappa-p_0)t}, \tag{40}$$

and this exists if $m$ is given a positive imaginary part,

$$G_-(\mathbf{x},\mathbf{x}',p_0)=\sum_\kappa\frac{\psi_\kappa(\mathbf{x})\bar{\psi}_\kappa(\mathbf{x}')}{\epsilon_\kappa E_\kappa-p_0}. \tag{41}$$

The Green's function $G_-(\mathbf{x},\mathbf{x}',p_0)$ obeys the differential equation

$$\{\gamma_\mu[p_\mu-eA_\mu(\mathbf{x})]+m\}G_-(\mathbf{x},\mathbf{x}',p_0)=\delta(\mathbf{x}-\mathbf{x}'), \tag{42}$$

and is the solution which is a regular function of $m$ in the upper half-plane, $\mathrm{Im}m>0$. It is clear from (36) and (41) that $G_-$ is the analytic continuation of $G_+$ into the upper $m$ half-plane.

The discontinuity across the real $m$ axis is given by

$$G_-(\mathbf{x},\mathbf{x}',p_0)-G_+(\mathbf{x},\mathbf{x}',p_0)$$
$$=\sum_\kappa\psi_\kappa(\mathbf{x})\bar{\psi}_\kappa(\mathbf{x}')\{[\epsilon_\kappa E_\kappa(m+i\epsilon)-p_0]^{-1}$$
$$-[\epsilon_\kappa E_\kappa(m-i\epsilon)-p_0]^{-1}\} \tag{43}$$
$$=-2\pi i\sum_\kappa\delta(\epsilon_\kappa E_\kappa-p_0)\epsilon_\kappa\psi_\kappa(\mathbf{x})\bar{\psi}_\kappa(\mathbf{x}').$$

Hence, if $|p_0|<m$, we have $G_-=G_+$ almost everywhere,

the exceptions being delta-function discontinuities at $p_0=\epsilon_k E_k'$, which are associated with bound modes. The continuous spectrum yields a finite discontinuity for $|p_0|>m$. These statements are an expression of the nature of the Green's function's singularities, isolated poles and branch points. A simple illustration is provided by $G_\pm{}^0(\mathbf{x},\mathbf{x}',p_0)$, describing the zero field situation. Thus,

$$\begin{aligned}G_\pm{}^0(\mathbf{x},\mathbf{x}',p_0)&=(\gamma p+m\mp i\epsilon)^{-1}\delta(\mathbf{x}-\mathbf{x}')\\&=(m-\gamma p)(\mathbf{p}^2-(p_0^2-m^2\pm i\epsilon)]^{-1}\delta(\mathbf{x}-\mathbf{x}')\\&=(m+\gamma_0 p_0+i\boldsymbol{\gamma}\cdot\boldsymbol{\nabla})\{[1/(4\pi|\mathbf{x}-\mathbf{x}'|)]\\&\qquad\times\exp[\pm i(p_0^2-m^2)^{\frac{1}{2}}|\mathbf{x}-\mathbf{x}'|]\},\end{aligned}\tag{44}$$

where

$$\pm i(p_0^2-m^2)^{\frac{1}{2}}=-(m^2-p_0^2)^{\frac{1}{2}},\quad |p_0|<m.\tag{45}$$

We see that $G_-{}^0=G_+{}^0$ for $|p_0|<m$, corresponding to the absence of bound modes, while for $|p_0|>m$, $G_-{}^0-G_+{}^0$ is finite, marking the existence of a continuous spectrum extending from $m$ to infinity.

We now return to the differential expression for $E(0)$, and write

$$\begin{aligned}\delta E(0)&=-\frac{1}{2\pi}\int_{-\infty}^{\infty}dp_0\int(d\mathbf{x})\,\mathrm{tr}ie\gamma_\mu\delta A_\mu(\mathbf{x})G_+(\mathbf{x},\mathbf{x},p_0)\\&=-\frac{i}{2\pi}\int_{-\infty}^{\infty}dp_0\,\mathrm{Tr}e\gamma\delta AG_+(p_0),\end{aligned}\tag{46}$$

where the latter version represents the introduction of matrix notation for the spinor indices and space coordinates. In this notation, the differential equation (37) reads

$$[\gamma(p-eA)+m]G_+(p_0)=1,\tag{47}$$

while that for the field-free case is

$$[\gamma p+m]G_+{}^0(p_0)=1.\tag{48}$$

In analogy with the four-dimensional situation, we can construct integral equations [V 22] and use their formal solution [V 23] to evaluate

$$\begin{aligned}&\mathrm{Tr}e\gamma\delta AG_+(p_0)\\&\quad=\mathrm{Tr}e\gamma\delta AG_+{}^0(p_0)[1-e\gamma AG_+{}^0(p_0)]^{-1}\\&\quad=-\delta\log\det[1-e\gamma AG_+{}^0(p_0)].\end{aligned}\tag{49}$$

Thus,

$$E(0)=\frac{i}{2\pi}\int_{-\infty}^{\infty}dp_0\log\det[1-e\gamma AG_+{}^0(p_0)],\tag{50}$$

or

$$E(0)=\frac{i}{2\pi}\int_{-\infty}^{\infty}dp_0\,\mathrm{Tr}\log[1-e\gamma AG_+{}^0(p_0)].\tag{51}$$

We must notice that

$$D_+(p_0)=\det[1-e\gamma AG_+{}^0(p_0)]\tag{52}$$

is not an even function of $e$, in contrast with its four-dimensional counterpart. Rather, we have

$$D_+(p_0)=\det[1+e\gamma AG_+{}^0(-p_0)].\tag{53}$$

This is a consequence of the structure of the charge conjugate Green's function,

$${}_cG_+(\mathbf{x},\mathbf{x}',p_0)=CG_+{}^{\mathrm{tr}}(\mathbf{x}',\mathbf{x},-p_0)C^{-1},\tag{54}$$

where $-p_0$ appears as the Fourier equivalent for the interchange of $x_0$ and $x_0'$ in (V 6). Since

$${}_cG_+{}^0(\mathbf{x},\mathbf{x}',p_0)=G_+{}^0(\mathbf{x},\mathbf{x}',p_0),\tag{55}$$

the transposition of the matrix in (52) yields (53). Of course,

$$\begin{aligned}E(0)&=\frac{i}{2\pi}\int_{-\infty}^{\infty}dp_0\log D_+(p_0)\\&=\frac{i}{4\pi}\int_{-\infty}^{\infty}dp_0\log[D_+(p_0)D_+(-p_0)]\end{aligned}\tag{56}$$

is an even function of $e$.

In order to establish the nature of the functional dependence of $D_+(p_0)$ on $e$, or on the parameter measuring the strength of the external field, we write

$$\begin{aligned}D_+(p_0)=\exp\{&-\mathrm{Tr}[e\gamma AG_+{}^0(p_0)]\\&-\tfrac{1}{2}\mathrm{Tr}[e\gamma AG_+{}^0(p_0)]^2\}D_+{}''(p_0),\end{aligned}\tag{57}$$

where

$$D_+{}''(p_0)=\det{}''[1-e\gamma AG_+{}^0p_0],\tag{58}$$

and also

$$\begin{aligned}&[D_+(p_0)]^2\\&\quad=\det[1-e\gamma AG_+{}^0(p_0)]\det[1+e\gamma AG_+{}^0(-p_0)]\\&\quad=\det\{1-e\gamma A[G_+{}^0(p_0)-G_+{}^0(-p_0)]\\&\qquad-e\gamma AG_+{}^0(p_0)e\gamma AG_+{}^0(-p_0)\}\\&\quad=\exp\{-2\,\mathrm{Tr}[e\gamma AG_+{}^0(p_0)]-\mathrm{Tr}[e\gamma AG_+{}^0(p_0)\\&\qquad\times e\gamma AG_+{}^0(-p_0)]\}\det{}'(1+\lambda K).\end{aligned}\tag{59}$$

Here we have employed the charge symmetry relation

$$\mathrm{Tr}e\gamma AG_+{}^0(p_0)=-\mathrm{Tr}e\gamma AG_+{}^0(-p_0),\tag{60}$$

and introduced the symbol

$$\begin{aligned}\lambda K=&-e\gamma A[G_+{}^0(p_0)-G_+{}^0(-p_0)]\\&-e\gamma AG_+{}^0(p_0)e\gamma AG_+{}^0(-p_0).\end{aligned}\tag{61}$$

Hence

$$\begin{aligned}[D_+{}''(p_0)]^2=\exp\{&\tfrac{1}{2}\mathrm{Tr}[e\gamma A(G_+{}^0(p_0)\\&-G_+{}^0(-p_0))]^2\}\det{}'(1+\lambda K),\end{aligned}\tag{62}$$

and a demonstration that the right side is an integral function of $e$ establishes the same property for $D_+{}''(p_0)$.

We have shown that the criterion for $\det'(1+\lambda K)$ to be an integral function of $\lambda$ is the finiteness of $\mathrm{Tr}\lambda K(\lambda K)^\dagger$. To apply this test we need the information,

derived from (44), that

$$\mathbf{x}\sim\mathbf{x}': \quad G_+^0(\mathbf{x},\mathbf{x}',p_0)\sim|\mathbf{x}-\mathbf{x}'|^{-2},$$
$$G_+^0(\mathbf{x},\mathbf{x}',p_0)-G_+^0(\mathbf{x},\mathbf{x}',-p_0)\sim|\mathbf{x}-\mathbf{x}'|^{-1}. \tag{63}$$

We consider the question of convergence in the vicinity of a point $\mathbf{x}_0$, where

$$A(\mathbf{x})\sim|\mathbf{x}-\mathbf{x}_0|^{-(1-\beta)}. \tag{64}$$

The second term of (61) provides the three-dimensional analog of (V 74), and it will be seen from the discussion of the latter integral that the convergence criterion is now $12>4(1-\beta)+8$, or $\beta>0$. It is easily verified that the additional terms arising from the first part of (61) are more convergent, in virtue of the reduced singularity of $G_+^0(p_0)-G_+^0(-p_0)$. The same statement applies to the argument of the exponential function in (62).

We shall also give a more precise characterization of the restriction to spatially localized fields, by considering potentials that have the asymptotic behavior

$$|\mathbf{x}|\to\infty: \quad A(\mathbf{x})\sim|\mathbf{x}|^{-(2+\beta')}. \tag{65}$$

The corresponding property of the Green's function is

$$|\mathbf{x}-\mathbf{x}'|\to\infty: \quad G_+(\mathbf{x},\mathbf{x}',p_0),\ [G_+(\mathbf{x},\mathbf{x}',p_0) - G_+(\mathbf{x},\mathbf{x}',-p_0)]\sim|\mathbf{x}-\mathbf{x}'|^{-1} \times\exp[i(p_0^2-m^2)^{\frac{1}{2}}|\mathbf{x}-\mathbf{x}'|], \tag{66}$$

where $|\exp[i(p_0^2-m^2)^{\frac{1}{2}}|\mathbf{x}-\mathbf{x}'|]|\leq 1$. On considering the second term of (61), for example, we are led to examine the convergence at infinity of

$$\int(d\mathbf{x})(d\mathbf{x}')(d\mathbf{x}_1)(d\mathbf{x}_2)A(\mathbf{x})A(\mathbf{x}')A(\mathbf{x}_1)A(\mathbf{x}_2) \times[|\mathbf{x}-\mathbf{x}_1||\mathbf{x}_1-\mathbf{x}'||\mathbf{x}'-\mathbf{x}_2||\mathbf{x}_2-\mathbf{x}|]^{-1},$$

for which the condition is $12<4(2+\beta')+4$, or $\beta'>0$. All other relevant terms lead to the same condition. We conclude that, for potentials[4] not as singular as $|\mathbf{x}-\mathbf{x}_0|^{-1}$, which vanish at infinity more rapidly than $|\mathbf{x}|^{-2}$, $D_+''(p_0)$ is an integral function of the parameter measuring the strength of the field, and is represented by the convergent power series

$$D_+''(p_0)=1+\sum_{n=3}^{\infty}\frac{(-e)^n}{n!}\int(d\mathbf{x}_1)\cdots(d\mathbf{x}_n) \times\mathrm{tr}\left\{\prod_{i=1}^{n}[\gamma_i A(\mathbf{x}_i)]\det{}_{(n)}''G_+^0(\mathbf{x}_i,\mathbf{x}_j,p_0)\right\}. \tag{67}$$

[4] In the nonrelativistic limit, the singularity of the Green's function is reduced to $|\mathbf{x}-\mathbf{x}'|^{-1}$, $\mathbf{x}\sim\mathbf{x}'$, and the corresponding class of scalar potentials includes those less singular than $|\mathbf{x}-\mathbf{x}_0|^{-2}$, which vanish at infinity more rapidly than $|\mathbf{x}|^{-2}$. For potentials with a singularity only at the origin, these criteria are combined in $\int_0^\infty d|\mathbf{x}|\,|\mathbf{x}|\,|eA_0(\mathbf{x})|<\infty$, which agrees with the condition (46) of Jost and Pais (reference 5 of V).

We can now exploit (V 61), which yields the elements of the matrix

$$[1-e\gamma AG_+^0(p_0)]^{-1}-1-e\gamma AG_+^0(p_0) =e\gamma A[G_+(p_0)-G_+^0(p_0)], \tag{68}$$

in analogy with (V 69). We need only transcribe (V 70) into

$$D_+''(p_0)[G_+(\mathbf{x},\mathbf{x}',p_0)-G_+^0(\mathbf{x},\mathbf{x}',p_0)] =\sum_{n=1}^{\infty}\frac{(-e)^n}{n!}\int(d\mathbf{x}_1)\cdots(d\mathbf{x}_n)\,\mathrm{tr}\left\{\prod_{i=1}^{n}[\gamma_i A(\mathbf{x}_i)] \times\det{}_{(n+1)}''\begin{bmatrix}0, & G_+^0(\mathbf{x},\mathbf{x}_j,p_0)\\ G_+^0(\mathbf{x}_i,\mathbf{x}',p_0), & G_+^0(\mathbf{x}_i,\mathbf{x}_j,p_0)\end{bmatrix}\right\}, \tag{69}$$

which exhibits $G_+(\mathbf{x},\mathbf{x}',p_0)$ as the ratio of two integral functions. We can also present this result in terms of the matrix $I(p_0)$, defined by

$$G_+(p_0)=G_+^0(p_0)+G_+^0(p_0)I(p_0)G_+^0(p_0). \tag{70}$$

Thus,

$$D_+''(p_0)I(\mathbf{x},\mathbf{x}',p_0) =\sum_{n=1}^{\infty}\frac{(-e)^n}{n!}\int(d\mathbf{x}_1)\cdots(d\mathbf{x}_n)\,\mathrm{tr}\left\{\prod_{i=1}^{n}[\gamma_i A(\mathbf{x}_i)] \times\det{}_{(n+1)}''\begin{bmatrix}0, & \delta(\mathbf{x}-\mathbf{x}_j)\\ \delta(\mathbf{x}_i-\mathbf{x}'), & G_+^0(\mathbf{x}_i,\mathbf{x}_j,p_0)\end{bmatrix}\right\}. \tag{71}$$

The properties of $D_+''(p_0)$ differ in the two regions $|p_0|<m$ and $|p_0|>m$. We first notice that $D_+(p_0)$ and $D_+''(p_0)$ are real if $|p_0|<m$. This follows from the remark that

$$D_-(p_0)=D_+(p_0)^* \tag{72}$$

is obtained from $D_+(p_0)$ by substituting $G_-^0$ for $G_+^0$, which Green's functions are equal if $|p_0|<m$. A second statement applicable to the latter domain is that $D_+''(p_0)$ has at least one zero[5] as a function of the magnitude of the parameter measuring the strength of the field. This we shall prove for electrostatic fields where the potential $A_0$ has a single sign.

We begin with

$$D_+(p_0)D_+(-p_0) =\exp\{\mathrm{Tr}\log 1-(e\gamma AG_+^0(p_0))^2]\} =\exp\{-\mathrm{Tr}[e\gamma AG_+^0(p_0)]^2\}D_+''(p_0)D_+''(-p_0). \tag{73}$$

For sufficiently weak fields, we can expand the logarithm, and obtain

$$D_+''(p_0)D_+''(-p_0) =\exp\left\{-\sum_{n=2}^{\infty}\frac{1}{n}\mathrm{Tr}[e\gamma AG_+^0(p_0)]^{2n}\right\}, \tag{74}$$

[5] This is the analog of Schmidt's theorem, E. T. Whittaker and G. N. Watson, *Modern Analysis* (Cambridge University Press, Cambridge, 1927), p. 223.

where the individual traces are all finite. We are considering electrostatic fields for which $A_0(\mathbf{x})$ is of definite sign. Since (74) is an even function of $eA_0$, there is no restriction in taking the sign of the latter to be positive; reversing the sign of $A_0$ interchanges $D_+''(p_0)$ and $D_+''(-p_0)$. Now observe that

$$\mathrm{Tr}[e\gamma AG_+^0(p_0)]^{2n}=\mathrm{Tr}K^n, \tag{75}$$

where

$$K=[(eA_0)^{\frac{1}{2}}\gamma_0 G_+^0(p_0)(eA_0)^{\frac{1}{2}}]^2 \tag{76}$$

is Hermitian and positive-definite. Hence $\mathrm{Tr}K^n$ is real and positive. These traces obey the inequalities

$$\mathrm{Tr}K^{n+m}\leq \mathrm{Tr}K^n\,\mathrm{Tr}K^m, \tag{77}$$

$$(\mathrm{Tr}K^n)^2\leq \mathrm{Tr}K^{n-l}\,\mathrm{Tr}K^{n+l}, \tag{78}$$

from which we derive

$$\mathrm{Tr}K^n\leq(\mathrm{Tr}K^2)^{\frac{1}{2}n},\quad n=2,3,\cdots. \tag{79}$$

Thus, the expansion (74) is convergent if

$$\mathrm{Tr}K^2=\mathrm{Tr}[eA_0\gamma_0 G_+^0(p_0)]^4<1. \tag{80}$$

But the inequality (78) also asserts that

$$\frac{\mathrm{Tr}K^{n+1}}{\mathrm{Tr}K^n}\geq\frac{\mathrm{Tr}K^n}{\mathrm{Tr}K^{n-1}}\cdots\geq\frac{\mathrm{Tr}K^3}{\mathrm{Tr}K^2}, \tag{81}$$

and therefore the sum of positive terms in (74) is surely divergent if

$$\mathrm{Tr}K^3/\mathrm{Tr}K^2\geq 1, \tag{82}$$

which shows that $D_+''(p_0)D_+''(-p_0)$ vanishes for some strength of field, equal to or less than that determined by

$$\mathrm{Tr}[eA_0\gamma_0 G_+^0(p_0)]^6=\mathrm{Tr}[eA_0\gamma_0 G_+^0(p_0)]^4. \tag{83}$$

To establish which is the vanishing factor, for a given sign of $eA_0(\mathbf{x})$, we assume a sufficiently weak field, and examine

$$D_+''(p_0)/D_+''(-p_0)$$

$$=\exp\left\{-2\sum_{m=1}^{\infty}\frac{1}{2m+1}\mathrm{Tr}[e\gamma AG_+^0(p_0)]^{2m+1}\right\} \tag{84}$$

in its dependence upon $p_0$. For this purpose, we remark that

$$(\gamma p+m)(\partial/\partial p_0)G_+^0(p_0)=\gamma_0 G_+^0(p_0) \tag{85}$$

has the unique solution

$$(\partial/\partial p_0)G_+^0(p_0)=G_+^0(p_0)\gamma_0 G_+^0(p_0). \tag{86}$$

Let us suppose that $eA_0(\mathbf{x})$ is positive. Then

$$(\partial/\partial p_0)\log[D_+''(p_0)/D_+''(-p_0)]$$

$$=2\sum_{m=1}^{\infty}\mathrm{Tr}[(eA_0)^{\frac{1}{2}}(\gamma_0 G_+^0 eA_0)^m\gamma_0 G_+^0$$

$$\cdot\gamma_0 G_+^0(eA_0\gamma_0 G_+^0)^m(eA_0)^{\frac{1}{2}}] \tag{87}$$

is real and positive since each term is of the form $\mathrm{Tr}KK^\dagger$. Hence, the logarithm increases monotonically as $p_0$ is increased from zero, and

$$p_0>0:\quad D_+''(p_0)/D_+''(-p_0)>1, \tag{88}$$

which shows that, for positive $eA_0$, it is $D_+''(-p_0)$, $p_0>0$ that vanishes for a suitable strong field. Similarly, $D_+''(p_0)$, $p_0>0$ is the vanishing factor for negative $eA_0$. Thus, for any $p_0\neq 0$ in the interval $|p_0|<m$, there is a definite sign and strength of field for which $D_+''(p_0)=0$.

The qualitative dependence of this field magnitude upon $p_0$ can also be inferred from (87). Let $\lambda(p_0)$ be the value of the parameter specifying the strength of the field for which $D_+''(p_0)=0$. The expression (87) is valid for $\lambda<\lambda(p_0)$. Considered as a function of $\lambda$, $D_+''(p_0)$ evidently contains the factor $\lambda(p_0)-\lambda$, which contributes to the derivative (87) the term

$$[\lambda(p_0)-\lambda]^{-1}[d\lambda(p_0)/dp_0].$$

This dominates as $\lambda$ approaches $\lambda(p_0)$ from below, and must therefore be positive. We conclude that

$$d\lambda(p_0)/dp_0>0 \tag{89}$$

for positive $eA_0$. Thus, as $p_0$ increases from $-m$, the critical strength of the field must increase. If $eA_0$ is negative, the logarithmic derivative (87) is negative, and $d\lambda(p_0)/dp_0<0$; as $p_0$ decreases from $m$, the magnitude of the field must increase to maintain $D_+''(p_0)=0$.

We have obtained these results without reference to the fact that the roots of $D_+''(p_0)$ are the frequencies of the bound modes. The equation

$$G_+(p_0)-G_+^0(p_0)=G_+^0(p_0)e\gamma AG_+(p_0)$$

$$=G_+(p_0)e\gamma AG_+^0(p_0) \tag{90}$$

show that, at a zero of $D_+''(p_0)$, assumed nonmultiple for simplicity, $D_+''(p_0)G_+(\mathbf{x},\mathbf{x}',p_0)$ obeys the homogeneous integral equations

$$\psi(\mathbf{x})=\int(d\mathbf{x}')G_+^0(\mathbf{x},\mathbf{x}',p_0)e\gamma A(\mathbf{x}')\psi(\mathbf{x}'), \tag{91}$$

and

$$\bar{\psi}(\mathbf{x})=\int(d\mathbf{x}')\bar{\psi}(\mathbf{x}')e\gamma A(\mathbf{x}')G_+^0(\mathbf{x}',\mathbf{x},p_0), \tag{92}$$

which govern its dependence upon the variables $\mathbf{x}$ and $\mathbf{x}'$, respectively. Hence, in the neighborhood of a root $\epsilon_\kappa E_\kappa'$, we have

$$G_+(\mathbf{x},\mathbf{x}',p_0)\sim\frac{\psi_\kappa(\mathbf{x})\bar{\psi}_\kappa(\mathbf{x}')}{\epsilon_\kappa E_\kappa'-p_0}. \tag{93}$$

The implied normalization of the eigenfunction $\psi_\kappa(\mathbf{x})$ can be deduced from

$$(\partial/\partial p_0)\log D_+(p_0)$$

$$=-\mathrm{Tr}\{[1-e\gamma AG_+^0(p_0)]^{-1}e\gamma AG_+^0(p_0)\gamma_0 G_+^0(p_0)\}$$

$$=-\mathrm{Tr}\{[G_+(p_0)-G_+^0(p_0)]\gamma_0\}, \tag{94}$$

namely

$$\int (d\mathbf{x})\bar{\psi}_\kappa(\mathbf{x})\gamma_0\psi_\kappa(\mathbf{x})=1. \tag{95}$$

For real values of $p_0$ that exceed $m$ in magnitude, $D_+(p_0)$ is a complex number. Its phase is determined by

$$D_-(p_0)/D_+(p_0)=\det\{1+I(p_0)[G_+{}^0(p_0)-G_-{}^0(p_0)]\}, \tag{96}$$

as follows from the relation

$$[1-e\gamma AG_+{}^0(p_0)]^{-1}[1-e\gamma AG_-{}^0(p_0)] =1+I(p_0)[G_+{}^0(p_0)-G_-{}^0(p_0)]. \tag{97}$$

On interchanging $G_+{}^0$ and $G_-{}^0$, we get

$$D_+(p_0)/D_-(p_0)=\det\{1-\bar{I}(p_0)[G_+{}^0(p_0)-G_-{}^0(p_0)]\}. \tag{98}$$

The direct verification that the product of these two determinants is unity employs the Fourier transform of (V 94),

$$\begin{aligned} I(p_0)-\bar{I}(p_0)&=I(p_0)[G_+{}^0(p_0)-G_-{}^0(p_0)]\bar{I}(p_0)\\ &=\bar{I}(p_0)[G_+{}^0(p_0)-G_-{}^0(p_0)]I(p_0). \end{aligned} \tag{99}$$

The equation analogous to (96), relating to the phase of $D_+''(p_0)$, is

$$\begin{aligned} &D_-''(p_0)/D_+''(p_0)\\ &\quad=\exp\{-\mathrm{Tr}I^{(1)}(p_0)[G_+{}^0(p_0)-G_-{}^0(p_0)]\}\\ &\qquad\times\det\{1+I(p_0)[G_+{}^0(p_0)-G_-{}^0(p_0)]\}, \end{aligned} \tag{100}$$

in which we have introduced the abbreviation

$$I^{(1)}(p_0)=e\gamma A+e\gamma A\tfrac{1}{2}[G_+{}^0(p_0)+G_-{}^0(p_0)]e\gamma A. \tag{101}$$

On referring to (43) and (IV 55), we see that

$$\begin{aligned} &G_+{}^0(\mathbf{x},\mathbf{x}',p_0)-G_-{}^0(\mathbf{x},\mathbf{x}',p_0)\\ &\quad=2\pi i\sum_{\lambda\mathbf{p}}\delta(\epsilon(\lambda)E_\mathbf{p}-p_0)\epsilon(\lambda)\psi_{\lambda\mathbf{p}}(\mathbf{x})\bar{\psi}_{\lambda\mathbf{p}}(\mathbf{x}'), \end{aligned} \tag{102}$$

where (we have previously used the symbol $p_0$ for this quantity)

$$E_\mathbf{p}=(\mathbf{p}^2+m^2)^{\frac{1}{2}}, \tag{103}$$

and the $\psi_{\lambda\mathbf{p}}(\mathbf{x})$ are the eigenfunctions

$$\psi_{\lambda\mathbf{p}}(\mathbf{x})=\left[\frac{(d\mathbf{p})}{(2\pi)^3}\frac{m}{E_\mathbf{p}}\right]^{\frac{1}{2}}u_{\lambda\mathbf{p}}e^{i\epsilon(\lambda)\mathbf{p}\cdot\mathbf{x}}. \tag{104}$$

The summation in (102) is limited to modes of frequency $p_0$, that is, modes with $E_\mathbf{p}=|p_0|$ and $\epsilon(\lambda)=\epsilon(p_0)$. For this reason, it is convenient to replace the $\lambda\mathbf{p}$ specification of a mode with $p_0=\epsilon(\lambda)E_\mathbf{p}$ and an index $a$, which combines $|\lambda|$ and the direction of $\mathbf{p}$. We write

$$(d\mathbf{p})=p^2dpd\omega=pE_pdE_pd\omega, \tag{105}$$

where $d\omega$ is an element of solid angle, and

$$\psi_{\lambda\mathbf{p}}(\mathbf{x})=(dE_\mathbf{p})^{\frac{1}{2}}\phi_{ap_0}(\mathbf{x}), \tag{106}$$

so that

$$\phi_{ap_0}(\mathbf{x})=\left[\frac{mpd\omega}{(2\pi)^3}\right]^{\frac{1}{2}}u_{\lambda\mathbf{p}}e^{i\epsilon(p_0)\mathbf{p}\cdot\mathbf{x}}. \tag{107}$$

We can then perform the integration with respect to $E_\mathbf{p}$ in (102), and obtain

$$\begin{aligned} &G_+{}^0(\mathbf{x},\mathbf{x}',p_0)-G_-{}^0(\mathbf{x},\mathbf{x}',p_0)\\ &\qquad=2\pi i\epsilon(p_0)\textstyle\sum_a\phi_{ap_0}(\mathbf{x})\bar{\phi}_{ap_0}(\mathbf{x}'). \end{aligned} \tag{108}$$

The matrices defined by

$$I_{ab}(p_0)=\int(d\mathbf{x})(d\mathbf{x}')\bar{\phi}_{ap_0}(\mathbf{x})I(\mathbf{x},\mathbf{x}',p_0)\phi_{bp_0}(\mathbf{x}'), \tag{109}$$

$$\begin{aligned} I_{ab}{}^\dagger(p_0)&=\int(d\mathbf{x})(d\mathbf{x}')\bar{\phi}_{ap_0}(\mathbf{x})\bar{I}(\mathbf{x},\mathbf{x}',p_0)\phi_{bp_0}(\mathbf{x}')\\ &=I_{ba}(p_0)^*, \end{aligned}$$

possess the following property, according to (99) and (108),

$$\begin{aligned} I_{ac}(p_0)-I_{ac}{}^\dagger(p_0)&=2\pi i\epsilon(p_0)\textstyle\sum_b I_{ab}(p_0)I_{bc}{}^\dagger(p_0)\\ &=2\pi i\epsilon(p_0)\textstyle\sum_b I_{ab}{}^\dagger(p_0)I_{bc}(p_0). \end{aligned} \tag{110}$$

We thereby encounter the unitary matrix $s(p_0)$ with elements

$$s_{ab}(p_0)=\delta_{ab}+2\pi i\epsilon(p_0)I_{ab}(p_0). \tag{111}$$

Thus,

$$\begin{aligned} &\textstyle\sum_b s_{ab}{}^\dagger(p_0)s_{bc}(p_0)\\ &\quad=\textstyle\sum_b[\delta_{ab}-2\pi i\epsilon(p_0)I_{ab}{}^\dagger(p_0)][\delta_{bc}+2\pi i\epsilon(p_0)I_{bc}(p_0)]\\ &\quad=\delta_{ac}+2\pi i\epsilon(p_0)[I_{ac}(p_0)-I_{ac}{}^\dagger(p_0)\\ &\qquad-2\pi i\epsilon(p_0)\textstyle\sum_b I_{ab}{}^\dagger(p_0)I_{bc}(p_0)]=\delta_{ac}, \end{aligned} \tag{112}$$

and, similarly, we find that $s(p_0)s^\dagger(p_0)=1$, in which we might more properly write $1(p_0)$ to emphasize that the elements of $s(p_0)$ refer entirely to modes of frequency $p_0$.

To recognize that the determinant of (96) can be evaluated as $\det s(p_0)$, consider the traces of successive powers of $I(p_0)(G_+{}^0(p_0)-G_-{}^0(p_0))$. The first two,

$$\mathrm{Tr}\{I(p_0)[G_+{}^0(p_0)-G_-{}^0(p_0)]\}=\textstyle\sum_a 2\pi i\epsilon(p_0)I_{aa}(p_0), \tag{113}$$

and

$$\begin{aligned} &\mathrm{Tr}\{I(p_0)[G_+{}^0(p_0)-G_-{}^0(p_0)]I(p_0)[G_+{}^0(p_0)-G_-{}^0(p_0)]\}\\ &\qquad=\textstyle\sum_{ab}[2\pi i\epsilon(p_0)]^2I_{ab}(p_0)I_{ba}(p_0), \end{aligned} \tag{114}$$

indicate the general result, that $I(p_0)[G_+{}^0(p_0)-G_-{}^0(p_0)]$ is effectively replaced by the elements of the matrix $2\pi i\epsilon(p_0)I_{ab}(p_0)$. Therefore,

$$\begin{aligned} &\det\{1+I(p_0)[G_+{}^0(p_0)-G_-{}^0(p_0)]\}\\ &\qquad=\det[\delta_{ab}+2\pi i\epsilon(p_0)I_{ab}(p_0)]=\det s(p_0). \end{aligned} \tag{115}$$

We can also remark that the original matrix decomposes into a product of unit matrices associated with modes of frequency $\mp p_0$, and the matrix $s(p_0)$ for modes of frequency $p_0$. Thus,

$$D_-(p_0)/D_+(p_0)=\det s(p_0), \tag{116}$$

and

$$D_-''(p_0)/D_+''(p_0) =\exp[-2\pi i\epsilon(p_0)\textstyle\sum_a I_{aa}^{(1)}(p_0)]\det s(p_0). \tag{117}$$

Since the unitary matrix $s(p_0)$ has eigenvalues $s_A(p_0)$, of the form $\exp[2i\delta_A(p_0)]$, where the phases $\delta_A(p_0)$ are real, these results can also be expressed as

$$D_-(p_0)/D_+(p_0)=\exp[2i\textstyle\sum_A \delta_A(p_0)] \tag{118}$$

and

$$D_-''(p_0)/D_+''(p_0) =\exp\{2i[\textstyle\sum_A \delta_A(p_0)-\pi\epsilon(p_0)\sum_a I_{aa}^{(1)}(p_0)]\}. \tag{119}$$

The matrix elements $s_{ab}(p_0)$ and $I_{ab}(p_0)$ can be exhibited in terms of the eigenphases $\delta_A(p_0)$, and the transformation function $(a|A)_{p0}$. Thus

$$s_{ab}(p_0)=\textstyle\sum_A (a|A)_{p0}e^{2i\delta_A(p_0)}(A|b)_{p0}, \tag{120}$$

and

$$I_{ab}(p_0)=(1/\pi)\epsilon(p_0)\textstyle\sum_A (a|A)_{p0}e^{i\delta_A(p_0)} \times\sin\delta_A(p_0)(A|b)_{p0}. \tag{121}$$

The corresponding eigenfunction transformation equations are

$$\begin{aligned}\bar\phi_{ap0}(\mathbf{x})&=\textstyle\sum_A (a|A)_{p0}\bar\phi_{Ap0}(\mathbf{x}),\\ \phi_{ap0}(\mathbf{x})&=\textstyle\sum_A \phi_{Ap0}(\mathbf{x})(A|a)_{p0}.\end{aligned} \tag{122}$$

As a consequence of the latter, we have

$$\textstyle\sum_a \bar\phi_{ap0}(\mathbf{x})\phi_{ap0}(\mathbf{x}')=\sum_A \bar\phi_{Ap0}(\mathbf{x})\phi_{Ap0}(\mathbf{x}') \tag{123}$$

and

$$\textstyle\sum_a I_{aa}^{(1)}(p_0)=\sum_A I_{AA}^{(1)}(p_0), \tag{124}$$

which enables us to write (119) as

$$D_-''(p_0)/D_+''(p_0)=\exp[2i\textstyle\sum_A {}'\delta_A(p_0)], \tag{125}$$

or

$$\operatorname{Im}\log D_+''(p_0)=-\textstyle\sum_A {}'\delta_A(p_0), \tag{126}$$

where

$${}'\delta_A(p_0)=\delta_A(p_0)-\pi\epsilon(p_0)I_{AA}^{(1)}(p_0). \tag{127}$$

We must also study the asymptotic character of $D_+''(p_0)$ as a function of $p_0$. It is useful to consider first the class of potentials that have no singularity. Then a sufficiently large $p_0$ can be found so that a negligible fractional change of the potential occurs in the distance $(p_0^2-m^2)^{-\frac{1}{2}}$, which is the characteristic distance appearing in $G_+^0(\mathbf{x},\mathbf{x}',p_0)$. Let us write

$$G_+^0(\mathbf{x},\mathbf{x}',p_0)=\int\frac{(d\mathbf{p})}{(2\pi)^3}e^{i\mathbf{p}\cdot(\mathbf{x}-\mathbf{x}')}G_+^0(\mathbf{p},p_0), \tag{128}$$

$$G_+^0(\mathbf{p},p_0)=(\gamma p+m)^{-1},$$

and evaluate the typical trace

$$\operatorname{Tr}[e\gamma AG_+(p_0)]^n=\int(d\mathbf{x}_1)\cdots(d\mathbf{x}_n)\frac{(d\mathbf{p}_1)}{(2\pi)^3}\cdots\frac{(d\mathbf{p}_n)}{(2\pi)^3}$$
$$\times\operatorname{tr}[e\gamma A(\mathbf{x}_1)e^{i\mathbf{p}_1\cdot(\mathbf{x}_1-\mathbf{x}_2)}G_+^0(\mathbf{p}_1,p_0)e\gamma A(\mathbf{x}_2)$$
$$\times e^{i\mathbf{p}_2\cdot(\mathbf{x}_2-\mathbf{x}_3)}G_+^0(\mathbf{p}_2,p_0)\cdots$$
$$\times e\gamma A(\mathbf{x}_n)e^{i\mathbf{p}_n\cdot(\mathbf{x}_n-\mathbf{x}_1)}G_+^0(\mathbf{p}_n,p_0)] \tag{129}$$

with the asymptotically valid approximation of placing $A(\mathbf{x}_2)=\cdots A(\mathbf{x}_n)=A(\mathbf{x}_1)$. This yields

$$\operatorname{Tr}[e\gamma AG_+(p_0)]^n\sim\int\frac{(d\mathbf{x})(d\mathbf{p})}{(2\pi)^3}\operatorname{tr}[e\gamma A(\mathbf{x})G_+^0(\mathbf{p},p_0)]^n, \tag{130}$$

and therefore

$$\det[1-e\gamma AG_+^0(p_0)]=\exp\{\operatorname{Tr}\log[1-e\gamma AG_+^0(p_0)]\}$$
$$\sim\exp\left\{\int\frac{(d\mathbf{x})(d\mathbf{p})}{(2\pi)^3}\operatorname{tr}\log[1-e\gamma A(\mathbf{x})G_+^0(\mathbf{p},p_0)]\right\}. \tag{131}$$

The modified $\det''[1-e\gamma AG_+^0(p_0)]$ will be similarly exhibited in terms of the modified logarithm

$$\log''(1-z)=\log(1-z)+z+\tfrac{1}{2}z^2.$$

These asymptotic results evidently correspond to a classical approximation, with $(d\mathbf{x})(d\mathbf{p})/(2\pi)^3$ representing the number of modes in the corresponding volume of phase space.

The trace in (131) can be evaluated as

$$\operatorname{tr}\log[1-e\gamma A(\mathbf{x})G_+^0(\mathbf{p},p_0)]$$
$$=\operatorname{tr}\log\{[\gamma(p-eA)+M](\gamma p+m)^{-1}\}$$
$$=2\{\log[(p-eA)^2+m^2]-\log(p^2+m^2)\}, \tag{132}$$

and therefore,

$$\operatorname{tr}\log''[1-e\gamma A(\mathbf{x})G_+^0(\mathbf{p},p_0)]$$
$$=2\sum_{n=3}^{\infty}\frac{1}{n!}[-eA(\mathbf{x})\partial/\partial p]^n\log(p^2+m^2)$$
$$=2\sum_{n=3}^{\infty}\frac{1}{n!}[-e\mathbf{A}(\mathbf{x})\cdot\partial/\partial\mathbf{p}-eA_0(\mathbf{x})\partial/\partial p_0]^n$$
$$\times\log(\mathbf{p}^2+m^2-p_0^2). \tag{133}$$

On performing the convergent $\mathbf{p}$ integrations, we find that each term containing $\partial/\partial\mathbf{p}$ leads to a vanishing surface integral, whence

$$\int\frac{(d\mathbf{p})}{(2\pi)^3}\operatorname{tr}\log''[1-e\gamma A(\mathbf{x})G_+^0(\mathbf{p},p_0)]$$
$$=-\frac{i}{3\pi}\sum_{n=3}^{\infty}\frac{1}{n!}[-eA_0(\mathbf{x})]^n(\partial/\partial p_0)^n(p_0^2-m^2)^{\frac{3}{2}}, \tag{134}$$

and

$$\log D_+''(p_0)\sim-\frac{i}{3\pi}\int(d\mathbf{x})\{[(p_0-eA_0(\mathbf{x}))^2-m^2]^{\frac{1}{2}}$$
$$-(p_0^2-m^2)^{\frac{1}{2}}+3eA_0(\mathbf{x})p_0(p_0^2-m^2)^{\frac{1}{2}}$$
$$-\tfrac{3}{2}[eA_0(\mathbf{x})]^2[(p_0^2-m^2)^{\frac{1}{2}}+p_0^2(p_0^2-m^2)^{-\frac{1}{2}}]\}, \quad (135)$$

which is independent of $\mathbf{A}(\mathbf{x})$, as required by gauge invariance. We see that $\log D_+''(p_0)$ possesses a finite limit as $|p_0|\to\infty$,

$$\log D_+''(p_0)\to\frac{i}{3\pi}\epsilon(p_0)\int(d\mathbf{x})[eA_0(\mathbf{x})]^3, \quad (136)$$

while, according to the approximation (131), $D_+''(p_0)\times D_+''(-p_0)$ approaches unity as

$$\log[D_+''(p_0)D_-''(p_0)]\to$$
$$-\frac{i}{4\pi}\frac{m^4}{|p_0|^5}\int(d\mathbf{x})[eA_0(\mathbf{x})]^4. \quad (137)$$

Now consider potentials with the singularity

$$|\mathbf{x}-\mathbf{x}_0|^{-(1-\beta)}, \quad \beta>0.$$

The asymptotic form (130) remains valid for the contributions of distances from the singularity

$$\gtrsim(p_0^2-m^2)^{-\frac{1}{2}}\to|p_0|^{-1}.$$

The contribution of smaller distances in (129) can be verified to have the asymptotic $p_0$ dependence, $|p_0|^{-n\beta}$, for $|p_0|\to\infty$. Hence the finite limiting value (136) is still valid for potentials that are not as singular as $|\mathbf{x}-\mathbf{x}_0|^{-1}$, but the statement (137) is replaced by

$$|p_0|\to\infty: \quad \log[D_+''(p_0)D_+''(-p_0)]\sim|p_0|^{-4\beta}. \quad (138)$$

We are going to show that the above discussed properties of $D_+''(p_0)$ suffice to determine completely this quantity. Let us remark first that the source of the complex values assumed by $D_+''(p_0)$, for real $p_0$ in the interval $|p_0|>m$, can be transferred from $m$ to $p_0$. Thus, with $\epsilon\to+0$, we can write

$$\begin{aligned} p_0>m: &\quad D_+''(p_0)=D''(p_0+i\epsilon)\\ &\quad D_-''(p_0)=D''(p_0-i\epsilon),\\ p_0<-m: &\quad D_+''(p_0)=D''(p_0-i\epsilon)\\ &\quad D_-''(p_0)=D''(p_0+i\epsilon),\end{aligned} \quad (139)$$

where $m$ is a real parameter in the function $D''(p_0)$. These relations assert the equivalence of, say, having a line of poles infinitesimally displaced below $p_0$, which is on the real axis, and finding $p_0$ infinitesimally above a line of poles occupying the real axis. The function $\log D''(p_0)$ is regular in the upper half-plane, $\mathrm{Im}\,p_0>0$, approaches the constant $(i/3\pi)\int(d\mathbf{x})[eA_0(\mathbf{x})]^3$ at infinity, and has its imaginary part assume the following values on the section of the real axis $|p_0|>m$ (reached from the upper half-plane),

$$\begin{aligned} p_0>m: &\quad \mathrm{Im}\log D''(p_0+i\epsilon)=-\textstyle\sum_A{}'\delta_A(p_0),\\ p_0<-m: &\quad \mathrm{Im}\log D''(p_0-i\epsilon)=+\textstyle\sum_A{}'\delta_A(p_0).\end{aligned} \quad (140)$$

If $p_0$ is on the real axis with $|p_0|<m$, the function $D''(p_0)=D_\pm''(p_0)$ is real and has zeros at the points $\epsilon_x E_x'$. Hence $\mathrm{Im}\log D''(p_0)$ is constant between the roots, but discontinuously decreases by $\pi$ as an increasing $p_0$ moves through a root (by a detour into the upper half-plane). We must add the remark that $\mathrm{Im}\log D''(p_0)=0$, in the neighborhood of $p_0=0$. For zero field, $D''(p_0)=1$ and $\mathrm{Im}\log D''(p_0)=0$. As the strength of the field increases, roots can appear at the boundaries of the interval $|p_0|<m$ and move toward the origin. But we have excluded the possibility that a root reach the origin, and thus the phase of $D''(p_0)$, in the vicinity of the origin, must be unchanged from its zero field value, which verifies our remark. Now let us follow the course of $\mathrm{Im}\log D''(p_0)$ from $p_0=0$ to $p_0=m$. The initial value of this quantity is zero. As we pass the first root, it acquires the value $-\pi$, and after traversing the zeros associated with the $\nu_+$ positive frequency bound modes, it will have the value $-\nu_+\pi$. Therefore,

$$\nu_+=(1/\pi)\textstyle\sum_A{}'\delta_A(m)=(1/\pi)\sum_A\delta_A(m), \quad (141)$$

where the second part of this statement is based upon the vanishing of the normalization constant in $\phi_{ap_0}$ at $p_0=m$, $\mathbf{p}=0$. The number of negative frequency bound modes similarly determines the value of $\mathrm{Im}\log D''(p_0)$ at $p_0=-m$, namely $\nu_-\pi$. Hence

$$\nu_-=(1/\pi)\textstyle\sum_A{}'\delta_A(-m)=(1/\pi)\sum_A\delta_A(-m). \quad (142)$$

With the introduction of a notation in which $|p_0|=E$ is indicated separately from the sign of $p_0$, $\delta_A(p_0)=\delta_{\gamma E}$, we recognize in (141) and (142) consequences of the relation (30), which was obtained by more elementary arguments. Of course, this agreement is based upon the assumed equivalence of the two definitions of phases, which we have yet to establish.

A function of a complex variable, $\phi(z)=u(x,y)+iv(x,y)$, which is regular in the upper half-plane and approaches an imaginary constant at infinity, is exhibited in terms of its imaginary part on the real axis by

$$\mathrm{Im}z>0: \quad \phi(z)=\frac{1}{\pi}\int_{-\infty}^{\infty}dx'\frac{v(x',0)}{x'-z}, \quad (143)$$

where the infinite integral is to be understood in the sense of $\int_{-X}^{X}$, $X\to\infty$. This statement can be derived from the Cauchy integral theorem, applied at the point $z$, and at the image point $z^*$. We shall use it to construct the function $\log D''(p_0)$. We thereby encounter the integral

$$\frac{1}{\pi}\int_{-m}^{m}dp_0'\frac{\mathrm{Im}\log D''(p_0')}{p_0'-p_0},$$

which we subject to an integration by parts. Since

$$(d/dp_0)\ \mathrm{Im}\ \log D''(p_0) = -\pi \sum_\kappa \delta(p_0 - \epsilon_\kappa E_\kappa') \quad (144)$$

and

$$\mathrm{Im}\ \log D''(m) = -\nu_+\pi, \quad \mathrm{Im}\ \log D''(-m) = \nu_-\pi, \quad (145)$$

we get

$$-\nu_+ \log(m-p_0) - \nu_- \log(-m-p_0) + \sum_\kappa \log(\epsilon_\kappa E_\kappa' - p_0),$$

and therefore

$$\log D''(p_0) = \log\left[\prod_\kappa \left(\frac{\epsilon_\kappa E_\kappa' - p_0}{\epsilon_\kappa m - p_0}\right)\right] - \frac{1}{\pi}\int_m^\infty \frac{dp_0'}{p_0' - p_0} \sum_A {}'\delta_A(p_0') + \frac{1}{\pi}\int_{-\infty}^{-m} \frac{dp_0'}{p_0' - p_0} \sum_A {}'\delta_A(p_0'). \quad (146)$$

On introducing the notation ${}'\delta_A(p_0) = {}'\delta_{\gamma E}$, $\epsilon(p_0) = \epsilon_\gamma$, we find that

$$D''(p_0) = \prod_\kappa \left(\frac{\epsilon_\kappa E_\kappa' - p_0}{\epsilon_\kappa m - p_0}\right) \times \exp\left[-\frac{1}{\pi}\int_m^\infty dE \sum_\gamma \frac{\epsilon_\gamma\, {}'\delta_{\gamma E}}{\epsilon_\gamma E - p_0}\right]. \quad (147)$$

The connection between the number of bound modes and the phases at $E=m$ insures the absence of any singularity at $p_0 = \pm m$. The function $D_+''(p_0)$, for real $p_0$, is given by the same formula with $m$ resuming its infinitesimal negative imaginary part.

We now return to the discussion of

$$E(0) = \frac{i}{2\pi}\int_{-\infty}^\infty dp_0\, \log D_+(p_0) = e^2 E^{(1)} + \frac{i}{2\pi}\int_{-\infty}^\infty dp_0\, \log D_+''(p_0), \quad (148)$$

in which we have used (60), and written

$$E^{(1)} = -\frac{i}{4\pi}\int_{-\infty}^\infty dp_0\, \mathrm{Tr}(\gamma A G_+^0(p_0)\gamma A G_+^0(p_0)) = -\tfrac{1}{2} i \int (d\mathbf{x})(d\mathbf{x}')dx_0' \times \mathrm{tr}[\gamma A(\mathbf{x}) G_+^0(x,x')\gamma A(\mathbf{x}') G_+^0(x',x)]. \quad (149)$$

On examining (V 68) and its value (V 88) for a field that is time-independent over a long interval, we observe that one time integration can be removed to yield

$$E^{(1)} = C\int (d\mathbf{x})\tfrac{1}{4}F_{\mu\nu}^2(\mathbf{x}) - \tfrac{1}{2}\int (d\mathbf{x})(d\mathbf{x}') \times \partial_\nu F_{\mu\nu}(\mathbf{x})\omega(\mathbf{x}-\mathbf{x}')\partial_\lambda' F_{\mu\lambda}(\mathbf{x}'), \quad (150)$$

where

$$\omega(\mathbf{x}-\mathbf{x}') = \int_{-\infty}^\infty dx_0'\, \omega(x-x') = \frac{1}{4\pi^2}\int_{2m}^\infty \frac{d\kappa}{\kappa}\left[\left(1-\left(\frac{2m}{\kappa}\right)^2\right)^{\frac{1}{2}} - \frac{1}{3}\left(1-\left(\frac{2m}{\kappa}\right)^2\right)^{\frac{3}{2}}\right]\frac{e^{-\kappa|\mathbf{x}-\mathbf{x}'|}}{4\pi|\mathbf{x}-\mathbf{x}'|}. \quad (151)$$

The finiteness of the second term in (150) depends upon the convergence of the integral

$$\int^\infty d\kappa \kappa^{-1}\int (d\mathbf{x})(d\mathbf{x}')\,|x-x_0|^{-(3-\beta)}\,|\mathbf{x}-\mathbf{x}'|^{-1} \times e^{-\kappa|\mathbf{x}-\mathbf{x}'|}\,|\mathbf{x}'-\mathbf{x}_0|^{-(3-\beta)} \sim \int^\infty d\kappa \kappa^{-2\beta},$$

which requires that $\beta > \frac{1}{2}$. Accordingly, the squares of the field strengths should not be as singular as $|\mathbf{x}-\mathbf{x}_0|^{-4}$, and this class of external fields can be characterized as possessing finite total energy. Hence, the coefficient of $C$ is also finite.

The second term of (148) is likewise finite for this class of field, as is evident from (138). By applying a partial integration to the contribution of the discrete modes, we get

$$\int_{-\infty}^\infty dp_0\, \log D_+''(p_0) = \int_{-\infty}^\infty dp_0\left[\sum_\kappa\left(\frac{\epsilon_\kappa E_\kappa'}{\epsilon_\kappa E_\kappa' - p_0} - \frac{\epsilon_\kappa m}{\epsilon_\kappa m - p_0}\right) - \frac{1}{\pi}\int_m^\infty dE \sum_\gamma \frac{\epsilon_\gamma\, {}'\delta_{\gamma E}}{\epsilon_\gamma E - p_0}\right], \quad (152)$$

and a residue calculation can be performed by averaging the results of closing the contour in the upper and lower half-planes. This gives[6]

$$E(0) = e^2 E^{(1)} + \tfrac{1}{2}\sum_\kappa (m - E_\kappa') + \frac{1}{2\pi}\sum_\gamma \int_m^\infty dE\, {}'\delta_{\gamma E}, \quad (153)$$

which, with its exhibition of the single divergent quantity $C$, for a suitable class of fields, replaces the formal expression (32).

[6] For a remark on the order of operations in the last term, see reference 8.

### The Scattering Description

We have used the transformation function (9) to obtain eigenvalues and eigenfunctions, with the aid of a representation of the Green's function that puts all modes on the same footing. But this is somewhat artificial for localized potentials, where the continuum modes differ profoundly from the bound modes and are most naturally described in terms of the physical picture of scattering. We shall now proceed to introduce this viewpoint.

The Green's function for $x_0-x_0'=T>0$,

$$G_+(x,x')=\frac{1}{2\pi}\int_{-\infty}^{\infty}dp_0e^{-ip_0T}G_+(\mathbf{x},\mathbf{x}',p_0), \quad (154)$$

can be evaluated by deforming the path of integration so that it encircles, in the negative sense, the discrete poles at $p_0=E_\kappa'<m$, and the branch line extending from $m$ to infinity. As we see from (93), the contribution of each isolated pole is $i\psi_\kappa(\mathbf{x})\bar{\psi}_\kappa(\mathbf{x}')e^{-iE_\kappa'T}$, so that

$$G_+(x,x')-i\sum\nolimits_+\psi_\kappa(\mathbf{x})\bar{\psi}_\kappa(\mathbf{x}')e^{-iE_\kappa'T}$$
$$=\frac{1}{2\pi}\int_{\infty}^{(m,-)}dp_0e^{-ip_0T}G_+(\mathbf{x},\mathbf{x}',p_0), \quad (155)$$

where the path of integration begins at infinity, encircles the point $m$ in the negative sense, and returns to infinity. We insert

$$G_+(\mathbf{x},\mathbf{x}',p_0)=G_+^0(\mathbf{x},\mathbf{x}',p_0)+\int(d\mathbf{x}_1)(d\mathbf{x}_2)G_+^0(\mathbf{x},\mathbf{x}_1,p_0)$$
$$\times I(\mathbf{x}_1,\mathbf{x}_2,p_0)G_+^0(\mathbf{x}_2,\mathbf{x}',p_0), \quad (156)$$

and remark that

$$\frac{1}{2\pi}\int_{\infty}^{(m,-)}dp_0e^{-ip_0T}G_+^0(\mathbf{x},\mathbf{x}',p_0)=G_+^0(x,x'), \quad (157)$$

as one may verify directly from

$$G_+^0(\mathbf{x},\mathbf{x}',p_0)=\sum_{\lambda\mathfrak{p}}\frac{\psi_{\lambda\mathfrak{p}}(\mathbf{x})\bar{\psi}_{\lambda\mathfrak{p}}(\mathbf{x}')}{\epsilon(\lambda)E_{\mathfrak{p}}-p_0}. \quad (158)$$

In the contribution to (155) of the second term in (156), we encounter the integral

$$\frac{1}{2\pi}\int_{\infty}^{(m,-)}dp_0e^{-ip_0T}\frac{1}{\epsilon(\lambda)E-p_0}I(p_0)\frac{1}{\epsilon(\lambda')E'-p_0}. \quad (159)$$

It is here that we introduce the scattering picture by evaluating this integral only for large $T$, such that

$$T\gg1/\Delta E, \quad (160)$$

where $\Delta E$ measures the smallest change of $p_0$ that is discernible in $I(p_0)$. We may say that $T$ is chosen to be large compared with the duration of the collision. Then the variation of $I(p_0)$ with $p_0$ can be ignored, and the integral (159) acquires the value

$$-iI(E)[e^{-iET}-e^{-iE'T}]/(E-E'), \quad (161)$$

provided, of course, that $\epsilon(\lambda)=\epsilon(\lambda')=1$. We have not distinguished between $I(E)$ and $I(E')$ since the condition for (161) to be relatively large is that $E-E'\sim1/T\ll\Delta E$. We thus obtain

$$G_+(x,x')=i\sum\nolimits_+\psi_\kappa(\mathbf{x})\bar{\psi}_\kappa(\mathbf{x}')e^{-iE_\kappa'T}$$
$$+i\sum\nolimits_+\psi_{\lambda\mathfrak{p}}(\mathbf{x})S_{\lambda\mathfrak{p},\lambda'\mathfrak{p}'}\bar{\psi}_{\lambda'\mathfrak{p}'}(\mathbf{x}')e^{-iET}, \quad (162)$$

and the analogous statement for $x_0'-x_0=T$ is

$$G_+(x,x')=-i\sum\nolimits_-\psi_\kappa(\mathbf{x})\bar{\psi}_\kappa(\mathbf{x}')e^{-iE_\kappa'T}$$
$$-i\sum\nolimits_-\psi_{\lambda\mathfrak{p}}(\mathbf{x})S_{\lambda\mathfrak{p},\lambda'\mathfrak{p}'}\bar{\psi}_{\lambda'\mathfrak{p}'}(\mathbf{x}')e^{-iET}. \quad (163)$$

Here,

$$S_{\lambda\mathfrak{p},\lambda'\mathfrak{p}'}=\delta_{\lambda\mathfrak{p},\lambda'\mathfrak{p}'}+2\pi i\epsilon(p_0)\delta_T(E-E')$$
$$\times\int(d\mathbf{x})(d\mathbf{x}')\bar{\psi}_{\lambda\mathfrak{p}}(\mathbf{x})I(\mathbf{x},\mathbf{x}',p_0)\psi_{\lambda'\mathfrak{p}'}(\mathbf{x}')$$
$$=\delta_{\lambda\mathfrak{p},\lambda'\mathfrak{p}'}+2\pi i\epsilon(p_0)\delta_T(E-E')$$
$$\times(dEdE')^{\frac{1}{2}}I_{ab}(p_0), \quad (164)$$

and

$$\delta_T(E-E')=\frac{i}{2\pi}\frac{1-e^{i(E-E')T}}{E-E'}=\frac{1}{2\pi}\int_0^Tdte^{i(E-E')t}. \quad (165)$$

We also have

$$S^\dagger_{\lambda\mathfrak{p},\lambda'\mathfrak{p}'}=S^*_{\lambda'\mathfrak{p}',\lambda\mathfrak{p}} \quad (166)$$
$$=\delta_{\lambda\mathfrak{p},\lambda'\mathfrak{p}'}-2\pi i\epsilon(p_0)\delta_T(E-E')(dEdE')^{\frac{1}{2}}I_{ab}^\dagger(p_0),$$

in view of the relation

$$\delta_T(E'-E)^*=\delta_T(E-E'). \quad (167)$$

Other properties of $\delta_T(E-E')$ are

$$\int dE'\delta_T(E-E')\delta_T(E'-E'')=\delta_T(E-E''), \quad (168)$$
$$\delta_T(0)=T/2\pi,$$

and

$$|\delta_T(E-E')|^2=\frac{T}{2\pi}\frac{1}{2\pi}\int_{-T}^{T}dt(1-|t|/T)e^{i(E-E')t}$$
$$\to(T/2\pi)\delta(E-E'), \quad (169)$$

where the latter statement expresses the limiting form for increasing $T$.

One can verify, in the manner of (112), that the $S_{\lambda\mathfrak{p},\lambda'\mathfrak{p}'}$ form a unitary matrix. This matrix is defined over the complete mode domain, but its nonvanishing elements are confined to an energy range $E-E'\sim1/T$. With the understanding that the selection of modes with equal energy is limited to the accuracy $1/T(\ll\Delta E)$, we can write $\delta_T(E-E')(dEdE')^{\frac{1}{2}}=\delta_{E,E'}$, which shows the connection with the unitary submatrix $s_{ab}(p_0)$,

$$S_{\lambda\mathfrak{p},\lambda'\mathfrak{p}'}=\delta_{E,E'}s_{ab}(p_0). \quad (170)$$

As a special consequence of the unitary property, we have

$$|S_{\lambda\mathbf{p},\lambda\mathbf{p}}|^2=1-\sum_{\lambda'\mathbf{p}'\neq\lambda\mathbf{p}}|S_{\lambda\mathbf{p},\lambda'\mathbf{p}'}|^2$$
$$=1-\sum_{\lambda'\mathbf{p}'\neq\lambda\mathbf{p}}|S_{\lambda'\mathbf{p}',\lambda\mathbf{p}}|^2, \quad (171)$$

where

$$|S_{\lambda\mathbf{p},\lambda\mathbf{p}}|^2=1-2TdE\epsilon(p_0)\,\mathrm{Im}I_{aa}(p_0), \quad (172)$$

and

$$\lambda\mathbf{p}\neq\lambda'\mathbf{p}': \quad |S_{\lambda\mathbf{p},\lambda'\mathbf{p}'}|^2=2\pi TdEdE'$$
$$\times\delta(E-E')|I_{ab}(p_0)|^2. \quad (173)$$

We recognize here the diagonal element of the matrix relation (110),

$$2\,\mathrm{Im}I_{aa}(p_0)=2\pi\epsilon(p_0)\textstyle\sum_b|I_{ab}(p_0)|^2$$
$$=2\pi\epsilon(p_0)\textstyle\sum_b|I_{ba}(p_0)|^2. \quad (174)$$

We now insert the Green's function representations (162) and (163), in (9) (omitting the phase transformation). The notation (14) for the discrete modes is retained, and we write $\chi_{\lambda\mathbf{p}}{}^{(\pm)'}$ for the analogous quantities constructed from the free particle mode functions, $\psi_{\lambda\mathbf{p}}(\mathbf{x})$. Then,

$$(\chi^{(-)'}\sigma_1|\chi^{(+)'}\sigma_2)$$
$$=e^{-iE(0)T}\exp[\textstyle\sum_\kappa\chi_\kappa{}^{(-)'}\chi_\kappa{}^{(+)'}e^{-iE_\kappa'T}$$
$$+\textstyle\sum_+\chi_{\lambda\mathbf{p}}{}^{(-)'}S_{\lambda\mathbf{p},\lambda'\mathbf{p}'}\chi_{\lambda'\mathbf{p}'}{}^{(+)'}e^{-iET}$$
$$+\textstyle\sum_-\chi_{\lambda\mathbf{p}}{}^{(-)'}S_{\lambda\mathbf{p},\lambda'\mathbf{p}'}{}^{\mathrm{tr}}\chi_{\lambda'\mathbf{p}'}{}^{(+)'}e^{-iET}], \quad (175)$$

where, for the negative frequency modes, there occurs

$$S_{\lambda\mathbf{p},\lambda'\mathbf{p}'}{}^{\mathrm{tr}}=S_{\lambda'\mathbf{p}',\lambda\mathbf{p}}. \quad (176)$$

This is a generating function for the transformation function $(n\sigma_1|n'\sigma_2)$, in which the states are specified by the occupation numbers of the bound modes, and of free particle modes. We represent this transformation function in terms of the elements of a unitary matrix,

$$(n\sigma_1|n'\sigma_2)=\exp(-iE(n)t_1)(n|S|n')\exp(iE(n')t_2),$$
$$E(n)=E(0)+\textstyle\sum_\kappa n_\kappa E_\kappa'+\sum_{\lambda\mathbf{p}}n_{\lambda\mathbf{p}}E_\mathbf{p}, \quad (177)$$

which matrix elements,

$$(n|S|n')=\delta_{n_\kappa,n_\kappa'}(\det{}_{(n_+)}S_{\lambda\mathbf{p},\lambda'\mathbf{p}'})$$
$$\times(\det{}_{(n_-)}S_{\lambda\mathbf{p},\lambda'\mathbf{p}'}{}^{\mathrm{tr}}), \quad (178)$$

still depend upon $T$. In the first determinant, $\lambda\mathbf{p}$ and $\lambda'\mathbf{p}'$ range in standard order over the $n_+$ occupied positive frequency modes of the final and initial state, respectively. The second determinant refers similarly to the negative frequency modes. The factor $\delta_{n_\kappa,n_\kappa'}$ describes the stationary character of the bound modes.

The probability of a transition between states is thus given by

$$|(n|S|n')|^2=\delta_{n_\kappa,n_\kappa'}p_+(n,n')p_-(n,n'), \quad (179)$$

where

$$p_+(n,n')=|\det{}_{(n_+)}S_{\lambda\mathbf{p},\lambda'\mathbf{p}'}|^2 \quad (180)$$

and

$$p_-(n,n')=|\det{}_{(n_-)}S_{\lambda\mathbf{p},\lambda'\mathbf{p}'}{}^{\mathrm{tr}}|^2 \quad (181)$$

are the independent probabilities for the two types of particles. A generating function for $p_+(n,n')$, say, is provided by

$$\det(1+xSyS^\dagger)=\det(1+S^\dagger xSy)$$
$$=\sum_{n,n'}\Pi_+(x_{\lambda\mathbf{p}})^n p_+(n,n')\Pi_+(y_{\lambda'\mathbf{p}'})^{n'}. \quad (182)$$

Thus, the expansion of the infinite determinant yields

$$\det(1+xSyS^\dagger)$$
$$=\sum_{n_+=0}^{\infty}\frac{1}{n_+!}\sum_{\lambda\mathbf{p}_i}\det{}_{(n_+)}(\sum_{\lambda'\mathbf{p}'}x_{\lambda\mathbf{p}_i}S_{\lambda\mathbf{p}_i,\lambda'\mathbf{p}'}y_{\lambda'\mathbf{p}'}S_{\lambda'\mathbf{p}',\lambda\mathbf{p}_j}{}^\dagger)$$
$$=\sum_{n_+=0}^{\infty}(\frac{1}{n_+!}\sum_{\lambda\mathbf{p}_i}\frac{1}{n_+!}\sum_{\lambda\mathbf{p}_k}\Pi(x_{\lambda\mathbf{p}_i})|\det{}_{(n_+)}S_{\lambda\mathbf{p}_i,\lambda\mathbf{p}_j}|^2\Pi(y_{\lambda\mathbf{p}_k})$$
$$=\sum_{n,n'}\Pi_+(x_{\lambda\mathbf{p}})^n|\det{}_{(n_+)}S_{\lambda\mathbf{p},\lambda'\mathbf{p}'}|^2\Pi_+(y_{\lambda'\mathbf{p}'})^{n'}, \quad (183)$$

in which the $\lambda\mathbf{p}_i$ and $\lambda\mathbf{p}_k$ range independently over all (positive frequency) modes. If we place every $x_{\lambda\mathbf{p}}=1$ in (182), we get

$$\sum_{n,n'}p_+(n,n')\Pi_+(y_{\lambda'\mathbf{p}'})^{n'}=\det(1+y)=\Pi_+(1+y_{\lambda\mathbf{p}})$$
$$=\textstyle\sum_{n'}\Pi_+(y_{\lambda\mathbf{p}})^{n_{\lambda\mathbf{p}'}}, \quad (184)$$

which verifies that

$$\textstyle\sum_n p_+(n,n')=1. \quad (185)$$

We similarly find, on putting $y_{\lambda\mathbf{p}}=1$, that

$$\textstyle\sum_{n'}p_+(n,n')=1. \quad (186)$$

A partial generating function, for given initial occupation numbers, can be obtained by rewriting the determinant (182) as

$$\det\left(1-\frac{y}{1+y}+S^\dagger xS\frac{y}{1+y}\right)\det(1+y), \quad (187)$$

and placing $y_{\lambda\mathbf{p}}=0$ for all except certain modes ($n_{\lambda\mathbf{p}}{}'=1$) where $y_{\lambda\mathbf{p}}\to\infty$. This yields

$$\textstyle\sum_n\Pi_+(x_{\lambda\mathbf{p}})^n p_+(n,n')=\det(1-n'+S^\dagger xSn'). \quad (188)$$

To get a useful alternative form we make the substitution $x\to1+x$, and remark that $(1+x)^n=1+nx$, since $n(n-1)=0$. Hence,

$$\textstyle\sum_n\Pi_+(1+n_{\lambda\mathbf{p}}x_{\lambda\mathbf{p}})p_+(n,n')=\det(1+S^\dagger xSn')$$
$$=\det(1+xSn'S^\dagger), \quad (189)$$

which acts as a generating function for the expectation values of occupation numbers, or products of occupation

numbers, in the final state. Since (189) is identical in form with (182), we see that

$$\sum_n \Pi_{(k)}(n_{\lambda\mathbf{p}})p(n,n') = \langle \Pi_{(k)}(n_{\lambda\mathbf{p}})\rangle_{n'}$$
$$= \frac{1}{k!}\sum_{\lambda'\mathbf{p}'} |\det{}_{(k)} S_{\lambda\mathbf{p},\lambda'\mathbf{p}'}|^2 \Pi_{(k)}(n'_{\lambda'\mathbf{p}'}), \quad (190)$$

where the $\lambda\mathbf{p}$ are $k$ arbitrary modes. In particular,

$$\sum_n n_{\lambda\mathbf{p}} p(n,n') = \langle n_{\lambda\mathbf{p}}\rangle_{n'} = \sum_{\lambda'\mathbf{p}'} |S_{\lambda\mathbf{p},\lambda'\mathbf{p}'}|^2 n_{\lambda'\mathbf{p}'}. \quad (191)$$

The latter result is also expressed by

$$\langle n_{\lambda\mathbf{p}}\rangle_{n'} - n_{\lambda\mathbf{p}}' = \sum_{\lambda'\mathbf{p}'} |S_{\lambda\mathbf{p},\lambda'\mathbf{p}'}|^2 (n_{\lambda'\mathbf{p}'} - n_{\lambda\mathbf{p}}')$$
$$= T\sum_{\lambda'\mathbf{p}'} 2\pi\delta(E-E')dE\,|I_{ab}(E)|^2 dE'(n_{\lambda'\mathbf{p}'} - n_{\lambda\mathbf{p}}'). \quad (192)$$

Now

$$dE\,|I_{ab}(p_0)|^2 dE'$$
$$= \frac{(d\mathbf{p})}{(2\pi)^3}\frac{m}{E}|(\lambda\mathbf{p}|I(E)|\lambda'\mathbf{p}')|^2 \frac{(d\mathbf{p}')}{(2\pi)^3}\frac{m}{E}, \quad (193)$$

in which we have defined (with $p_0 = +E$)

$$(\lambda\mathbf{p}|I(p_0)|\lambda'\mathbf{p}')$$
$$= \int (d\mathbf{x})(d\mathbf{x}')\bar{u}_{\lambda\mathbf{p}} \exp[-i\epsilon(p_0)\mathbf{p}\cdot\mathbf{x}]$$
$$\times I(\mathbf{x},\mathbf{x}',p_0) u_{\lambda'\mathbf{p}'} \exp[i\epsilon(p_0)\mathbf{p}'\cdot\mathbf{x}']. \quad (194)$$

We further remark that, according to (IV 103), the expectation value of the electric current vector, in the initial state, is given by

$$\langle \tfrac{1}{2}e[\bar{\psi}(x), \gamma\psi(x)]\rangle = \sum_{\lambda\mathbf{p}} e\epsilon(\lambda)\bar{\psi}_{\lambda\mathbf{p}}(\mathbf{x})\gamma\psi_{\lambda\mathbf{p}}(\mathbf{x}) n_{\lambda\mathbf{p}}'$$
$$= \sum_{\lambda\mathbf{p}} e\epsilon(\lambda)\mathbf{J}_{\lambda\mathbf{p}}', \quad (195)$$

where, accordingly,

$$\mathbf{J}_{\lambda\mathbf{p}}' = (\mathbf{p}/E)[(d\mathbf{p})/(2\pi)^3] n_{\lambda\mathbf{p}}' \quad (196)$$

is the contribution of a mode to the average flux of *particles*. Hence, (192) can be written

$$\langle n_{\lambda\mathbf{p}}\rangle_{n'} - n_{\lambda\mathbf{p}}' = T\sum_{\lambda'\mathbf{p}'} \delta(E-E')dE d\sigma(\lambda\mathbf{p},\lambda'\mathbf{p}')J_{\lambda'\mathbf{p}'}'$$
$$- T\sigma(\lambda\mathbf{p})J_{\lambda\mathbf{p}}', \quad (197)$$

which exhibits the average change in the occupation number of a given mode, in the time interval $T$, as a balance of particles scattered into and out of the mode. Here

$$d\sigma(\lambda\mathbf{p},\lambda'\mathbf{p}')/d\omega = \left|\frac{m}{2\pi}(\lambda\mathbf{p}|I(E)|\lambda'\mathbf{p}')\right|^2 \quad (198)$$

is the differential scattering cross section, per unit solid angle, for the indicated scattering process, and

$$\sigma(\lambda\mathbf{p}) = \sum_{\lambda'}\int d\omega' \left|\frac{m}{2\pi}(\lambda\mathbf{p}|I(E)|\lambda'\mathbf{p}')\right|$$
$$= \sum_{\lambda'}\int d\omega' \left|\frac{m}{2\pi}(\lambda'\mathbf{p}'|I(E)|\lambda\mathbf{p})\right|^2$$
$$= (2m/p)\,\mathrm{Im}(\lambda\mathbf{p}|I(E)|\lambda\mathbf{p}) \quad (199)$$

is the total scattering cross section. The equivalence of the various expressions for $\sigma(\lambda\mathbf{p})$ follows from (174).

The scattering cross sections for the negative frequency modes are

$$d\sigma(\lambda\mathbf{p},\lambda'\mathbf{p}')/d\omega = \left|\frac{m}{2\pi}(\lambda'\mathbf{p}'|I(-E)|\lambda\mathbf{p})\right|^2$$
$$= \left|\frac{m}{2\pi}(\lambda\mathbf{p}|\bar{I}(-E)|\lambda'\mathbf{p}')\right|^2, \quad (200)$$

and

$$\sigma(\lambda\mathbf{p}) = -(2m/p)\,\mathrm{Im}(\lambda\mathbf{p}|I(-E)|\lambda\mathbf{p})$$
$$= (2m/p)\,\mathrm{Im}(\lambda\mathbf{p}|\bar{I}(-E)|\lambda\mathbf{p}). \quad (201)$$

For the situation in which the incident particles form a beam that is well-defined in momentum and polarization (spin), (197) asserts that the number of particles, which are deflected into a solid angle $d\omega$ with a particular polarization, is given by

$$\sum_{d\omega}\langle n_{\lambda\mathbf{p}}\rangle_{n'} = Td\sigma(\lambda\mathbf{p},\lambda'\mathbf{p}')J', \quad (202)$$

where $J'$ is the total particle current. This is in accordance with the conventional definition of differential cross sections. One can construct cross sections referring to unpolarized particles with the aid of the relations

$$\sum_{\lambda>0} u_{\lambda\mathbf{p}}\bar{u}_{\lambda\mathbf{p}} = (m-\boldsymbol{\gamma}\cdot\mathbf{p}+\gamma_0 E)/(2m),$$
$$-\sum_{\lambda<0} u_{\lambda\mathbf{p}}\bar{u}_{\lambda\mathbf{p}} = (m+\boldsymbol{\gamma}\cdot\mathbf{p}-\gamma_0 E)/(2m). \quad (203)$$

Thus

$$\sigma_+(\mathbf{p}) = \tfrac{1}{2}\sum_+ \sigma(\lambda\mathbf{p})$$
$$= (1/2p)\,\mathrm{Im}\int (d\mathbf{x})(d\mathbf{x}')\,\mathrm{tr}\exp[-ip\cdot(\mathbf{x}-\mathbf{x}')]$$
$$\times(m-\boldsymbol{\gamma}\cdot\mathbf{p}+\gamma_0 E)I(\mathbf{x},\mathbf{x}',E), \quad (204)$$

and

$$\sigma_-(\mathbf{p}) = \tfrac{1}{2}\sum_- \sigma(\lambda\mathbf{p})$$
$$= (1/2p)\,\mathrm{Im}\int (d\mathbf{x})(d\mathbf{x}')\,\mathrm{tr}\exp[ip\cdot(\mathbf{x}-\mathbf{x}')]$$
$$\times(m+\boldsymbol{\gamma}\cdot\mathbf{p}-\gamma_0 E)I(\mathbf{x},\mathbf{x}',-E). \quad (205)$$

The latter can also be written as

$$\sigma_-(\mathbf{p}) = (1/2p)\ \mathrm{Im}\int (d\mathbf{x})(d\mathbf{x}')\ \mathrm{tr}\exp[-i\mathbf{p}\cdot(\mathbf{x}-\mathbf{x}')] \times(m-\boldsymbol{\gamma}\cdot\mathbf{p}+\gamma_0 E)_o I(\mathbf{x},\mathbf{x}',E). \quad (206)$$

The result of averaging over all incident directions of motion, with a given energy, can be expressed by

$$\begin{aligned}\sigma_\pm(E) &= (1/4\pi)\int d\omega\sigma_\pm(\mathbf{p}) = \sigma(p_0)\\ &= (\pi/2p^2)\ \mathrm{Tr}\{[G_-{}^0(p_0)-G_+{}^0(p_0)] \times[I(p_0)-\bar{I}(p_0)]\}\\ &= (\pi/2p^2)\ \mathrm{Tr}\{[G_-{}^0(p_0)-G_+{}^0(p_0)] \times\bar{I}(p_0)[G_+{}^0(p_0)-G_-{}^0(p_0)]I(p_0)\},\end{aligned} \quad (207)$$

or, equivalently, by

$$\begin{aligned}\sigma(p_0) &= (2\pi/p^2)\epsilon(p_0)\ \mathrm{Im}\textstyle\sum_a \pi I_{aa}(p_0)\\ &= (2\pi/p^2)\textstyle\sum_{ab}|\pi I_{ab}(p_0)|^2.\end{aligned} \quad (208)$$

The insertion of (71) and (67) will yield explicit expressions for these cross sections as ratios of convergent power series in the potential.

Some invariance properties of the scattering cross sections are worthy of note. For an electrostatic field, a combination of charge conjugation and time reflection[7] leaves the Green's function invariant,

$$\gamma_0\gamma_5 C G_+{}^{\mathrm{tr}}(\mathbf{x}',\mathbf{x},p_0)(\gamma_0\gamma_5 C)^{-1} = G_+(\mathbf{x},\mathbf{x}',p_0). \quad (209)$$

Since this property certainly applies to $G_+{}^0$, it also holds for $I(\mathbf{x},\mathbf{x}',p_0)$, and

$$(\lambda\mathbf{p}|I(p_0)|\lambda'\mathbf{p}') = (\lambda_{\mathrm{rev}}'-\mathbf{p}'|I(p_0)|\lambda_{\mathrm{rev}}-\mathbf{p}), \quad (210)$$

where

$$u_{\lambda_{\mathrm{rev}}-\mathbf{p}} = \bar{u}_{\lambda\mathbf{p}}\gamma_0\gamma_5 C, \quad \bar{u}_{\lambda_{\mathrm{rev}}-\mathbf{p}} = (\gamma_0\gamma_5 C)^{-1}u_{\lambda\mathbf{p}} \quad (211)$$

are related by

$$\bar{u}_{\lambda_{\mathrm{rev}}-\mathbf{p}} = u_{\lambda_{\mathrm{rev}}-\mathbf{p}}{}^*\gamma_0, \quad (212)$$

and describe the reversed mode, $(\lambda_{\mathrm{rev}}, -\mathbf{p})$, which has the same frequency as the original mode $(\lambda,\mathbf{p})$. In consequence of the invariance of $G_+{}^0$, we have $(\lambda, \lambda_{\mathrm{rev}}>0$ or $<0)$

$$\textstyle\sum_\lambda u_{\lambda\mathbf{p}}\bar{u}_{\lambda\mathbf{p}} = \sum_{\lambda_{\mathrm{rev}}} u_{\lambda_{\mathrm{rev}}\mathbf{p}}\bar{u}_{\lambda_{\mathrm{rev}}\mathbf{p}}, \quad (213)$$

which implies the following reciprocity property for differential cross sections referring to unpolarized particles,

$$\sum_{\lambda,\lambda'}|(\lambda\mathbf{p}|I(p_0)|\lambda'\mathbf{p}')|^2 = \sum_{\lambda,\lambda'}|(\lambda'-\mathbf{p}'|I(p_0)|\lambda-\mathbf{p})|^2. \quad (214)$$

With regard to total cross sections, we learn that

$$\sigma(\lambda\mathbf{p}) = \sigma(\lambda_{\mathrm{rev}}-\mathbf{p}) \quad (215)$$

and that

$$\sigma_\pm(\mathbf{p}) = \sigma_\pm(-\mathbf{p}). \quad (216)$$

For a potential with the space reflection behavior

$$A_0(\mathbf{x}) = A_0(-\mathbf{x}), \quad \mathbf{A}(\mathbf{x}) = -\mathbf{A}(-\mathbf{x}), \quad (217)$$

we have the Green's function invariance property

$$\gamma_0 G_+(-\mathbf{x},-\mathbf{x}',p_0)\gamma_0 = G_+(\mathbf{x},\mathbf{x}',p_0), \quad (218)$$

which implies that

$$(\lambda\mathbf{p}|I(p_0)|\lambda'\mathbf{p}') = (\lambda_{\mathrm{refl}}-\mathbf{p}|I(p_0)|\lambda_{\mathrm{refl}}-\mathbf{p}'). \quad (219)$$

Here

$$u_{\lambda_{\mathrm{refl}}-\mathbf{p}} = \gamma_0 u_{\lambda\mathbf{p}}, \quad \bar{u}_{\lambda_{\mathrm{refl}}-\mathbf{p}} = \bar{u}_{\lambda\mathbf{p}}\gamma_0 \quad (220)$$

describe the reflected mode $(\lambda_{\mathrm{refl}}, -\mathbf{p})$. Statements about cross sections derived from (219) are

$$\sum_{\lambda,\lambda'}|(\lambda\mathbf{p}|I(p_0)|\lambda'\mathbf{p}')|^2 = \sum_{\lambda,\lambda'}|(\lambda-\mathbf{p}|I(p_0)|\lambda'-\mathbf{p}')|^2 \quad (221)$$

and

$$\sigma(\lambda\mathbf{p}) = \sigma(\lambda_{\mathrm{refl}}-\mathbf{p}). \quad (222)$$

With an electrostatic field, the combination of both transformations (space-time reflection and charge conjugation) gives

$$(\lambda\mathbf{p}|I(p_0)|\lambda'\mathbf{p}') = (\lambda_{\mathrm{comp}}{}'\mathbf{p}'|I(p_0)|\lambda_{\mathrm{comp}}\mathbf{p}), \quad (223)$$

where the complementary (reversed-reflected) mode is described by

$$u_{\lambda_{\mathrm{comp}}\mathbf{p}} = \bar{u}_{\lambda\mathbf{p}}\gamma_5 C, \quad \bar{u}_{\lambda_{\mathrm{comp}}\mathbf{p}} = (\gamma_5 C)^{-1}u_{\lambda\mathbf{p}}. \quad (224)$$

The basis for this designation is the remark that

$$(\bar{u}_{\lambda\mathbf{p}}u_{\lambda_{\mathrm{comp}}\mathbf{p}}) = (\bar{u}_{\lambda\mathbf{p}}\gamma_5 C\bar{u}_{\lambda\mathbf{p}}) = 0, \quad (225)$$

since $\gamma_5 C$ is an antisymmetrical matrix. Hence $(\lambda_{\mathrm{comp}},\mathbf{p})$ is the mode with the complementary polarization to $(\lambda,\mathbf{p})$. Indeed, the $u_{\lambda\mathbf{p}}$ can be chosen so that

$$u_{\pm 2\mathbf{p}} = \bar{u}_{\pm 1\mathbf{p}}\gamma_5 C, \quad u_{\pm 1\mathbf{p}} = -\bar{u}_{\pm 2\mathbf{p}}\gamma_5 C. \quad (226)$$

We deduce from (223) the validity of the detailed balancing principle for the scattering of unpolarized particles in an electrostatic field,

$$\sum_{\lambda,\lambda'}|(\lambda\mathbf{p}|I(p_0)|\lambda'\mathbf{p}')|^2 = \sum_{\lambda,\lambda'}|(\lambda'\mathbf{p}'|I(p_0)|\lambda\mathbf{p})|^2, \quad (227)$$

and the fact that

$$\sigma(\lambda\mathbf{p}) = \sigma(\lambda_{\mathrm{comp}}\mathbf{p}), \quad (228)$$

which expresses the spin-independence of the total scattering cross section for an electrostatic field.

If an electrostatic field is such that

$$A_0(\mathbf{x}) = A_0(\mathbf{R}\cdot\mathbf{x}), \quad (229)$$

where the orthogonal dyadic $\mathbf{R}$ describes an arbitrary

[7] This is the analog of the nonrelativistic concept of time reflection [E. Wigner, Gött. Nachr. **31**, 546 (1932)].

rotation, we have the invariance property

$$R^{-1}G_+(\mathbf{R}\cdot\mathbf{x},\mathbf{R}\cdot\mathbf{x}',p_0)R=G_+(\mathbf{x},\mathbf{x}',p_0) \quad (230)$$

provided the unitary matrix $R$ satisfies

$$R\gamma_0R^{-1}=\gamma_0, \quad R\boldsymbol{\gamma}R^{-1}=\boldsymbol{\gamma}\cdot\mathbf{R}. \quad (231)$$

Then

$$(\lambda\mathbf{p}|I(p_0)|\lambda'\mathbf{p}')=(\lambda\mathbf{R}\cdot\mathbf{p}|I(p_0)|\lambda'\mathbf{R}\cdot\mathbf{p}'), \quad (232)$$

where

$$u_{\lambda\mathbf{R}\cdot\mathbf{p}}=Ru_{\lambda\mathbf{p}}, \quad \bar{u}_{\lambda\mathbf{R}\cdot\mathbf{p}}=\bar{u}_{\lambda\mathbf{p}}R^{-1} \quad (233)$$

describe the rotated mode. We have not written $\lambda_{\text{rot}}$, with the understanding that the two modes of polarization are to be distinguished by the eigenvalues of $\boldsymbol{\sigma}\cdot\mathbf{p}/p$, which are unchanged under rotations. A rotation of $\pi$ about the axis of $\mathbf{p}+\mathbf{p}'$ will result in $\mathbf{R}\cdot\mathbf{p}=\mathbf{p}'$ and $\mathbf{R}\cdot\mathbf{p}'=\mathbf{p}$, so that

$$(\lambda\mathbf{p}|I(p_0)|\lambda'\mathbf{p}')=(\lambda\mathbf{p}'|I(p_0)|\lambda'\mathbf{p}), \quad (234)$$

which leads again to the detailed balancing principle (227). The result of combining (234) with (223) is

$$(\lambda\mathbf{p}|I(p_0)|\lambda'\mathbf{p}')=(\lambda_{\text{comp}}'\mathbf{p}|I(p_0)|\lambda_{\text{comp}}\mathbf{p}'), \quad (235)$$

which includes the statement

$$(\lambda\mathbf{p}|I(p_0)|\lambda\mathbf{p}')=(\lambda_{\text{comp}}\mathbf{p}|I(p_0)|\lambda_{\text{comp}}\mathbf{p}'). \quad (236)$$

A rotation of $\pi$ about the axis of $\mathbf{p}-\mathbf{p}'$ gives

$$(\lambda\mathbf{p}|I(p_0)|\lambda'\mathbf{p}')=(\lambda-\mathbf{p}'|I(p_0)|\lambda'-\mathbf{p}), \quad (237)$$

from which we can derive the reciprocity principle (214). We deduce from (232) that the differential cross sections for unpolarized particles depend only upon the scattering angle, and that the total cross section is independent of the incident direction. Since the total cross section is also spin-independent, it is identical with the averaged cross section $\sigma(p_0)$.

A determinantal formula for the individual transition probabilities can be obtained from (188) by placing $x_{\lambda\mathbf{p}}=0$ for all except $n_+=n_+'$ modes where $x_{\lambda\mathbf{p}}=1$. In view of the fixed number of particles, this isolates the transition probability for the final state with occupation numbers $n_{\lambda\mathbf{p}}=x_{\lambda\mathbf{p}}$,

$$\begin{aligned}p_+(n,n')&=\det(1-n'+S^\dagger nSn')\\&=\det[1-S^\dagger(1-n)Sn'].\end{aligned} \quad (238)$$

We shall apply this formula to find the probability that no change in state occurs,

$$p_+(n,n)=\det[1-nS^\dagger(1-n)Sn], \quad (239)$$

which form is distinguished by the fact that diagonal elements of $S_{\lambda\mathbf{p},\lambda'\mathbf{p}'}$ do not appear, since $n(1-n)=0$. It will be noted that $p_+(n,n)=1$ in the two extreme situations where no mode is occupied or where every mode is occupied. Indeed, this probability is unchanged by the substitution $S\leftrightarrow S^\dagger$, $n\leftrightarrow 1-n$ (more generally, $n'\leftrightarrow 1-n$). We shall be concerned with the usual physical situation in which there are but a finite number of occupied modes, or "almost all" modes are unoccupied. This results in a rapidly converging expansion for the logarithm of the determinant (239),

$$\begin{aligned}-\log p_+(n,n)=&\sum_{\lambda\mathbf{p}}n_{\lambda\mathbf{p}}\Big[\sum_{\lambda'\mathbf{p}'}S^\dagger{}_{\lambda\mathbf{p},\lambda'\mathbf{p}'}(1-n_{\lambda'\mathbf{p}'})S_{\lambda'\mathbf{p}',\lambda\mathbf{p}}\Big]\\&+\tfrac{1}{2}\sum_{\lambda\mathbf{p},\lambda'\mathbf{p}'}n_{\lambda\mathbf{p}}n_{\lambda'\mathbf{p}'}\Big|\sum_{\lambda''\mathbf{p}''}S^\dagger{}_{\lambda\mathbf{p},\lambda''\mathbf{p}''}\\&\times(1-n_{\lambda''\mathbf{p}''})S_{\lambda''\mathbf{p}'',\lambda'\mathbf{p}'}\Big|^2+\cdots,\end{aligned} \quad (240)$$

which is dominated by

$$\sum_{\lambda'\mathbf{p}'\neq\lambda\mathbf{p}}n_{\lambda\mathbf{p}}|S_{\lambda\mathbf{p},\lambda'\mathbf{p}'}|^2=T\sum_{\lambda\mathbf{p}}\sigma(\lambda\mathbf{p})J_{\lambda\mathbf{p}}. \quad (241)$$

We shall examine (240) for a polarized beam of particles that move within a solid angle $\delta\omega$, which is sufficiently small to produce negligible changes in differential cross sections, and for which the occupation numbers vary slowly with energy, on the scale defined by $1/T$. Then the first term of (240) is

$$T\sum_{\lambda\mathbf{p}}\sigma'(\lambda\mathbf{p})J_{\lambda\mathbf{p}}=T\int dE\sigma'(\lambda\mathbf{p})J_\lambda(E), \quad (242)$$

where

$$dEJ_\lambda(E)=\textstyle\sum_{\delta\omega}J_{\lambda\mathbf{p}}=dE\sum_{\delta\omega}n_{\lambda\mathbf{p}}[p^2/(2\pi)^3]d\omega \quad (243)$$

is the incident particle current in the energy range $dE$, and $\sigma'(\lambda\mathbf{p})$ is the total scattering cross section computed with the omission of all transitions to initially occupied modes. Since the latter modes have identical polarizations and indiscernibly different directions of motion, we find that the second term of (240) is

$$\pi T\int dE[\sigma'(\lambda\mathbf{p})J_\lambda(E)]^2, \quad (244)$$

and, indeed, the complete expansion is represented by

$$\begin{aligned}&-\log p_+(n,n)\\&\quad=-(T/2\pi)\int dE\log[1-2\pi\sigma'(\lambda\mathbf{p})J_\lambda(E)].\end{aligned} \quad (245)$$

The form of this result can be understood directly from (239) with the aid of the representation $S_{\lambda\mathbf{p},\lambda'\mathbf{p}'}=\delta_{E,E'}s_{ab}$, which enables one to present the determinant as a product of determinants associated with each energy,

$$p_+(n,n)=\textstyle\prod_E\det[\delta_{ab}-n_a\sum_c s_{ac}^\dagger(1-n_c)s_{cb}n_b]. \quad (246)$$

We should note that, according to

$$\begin{aligned}&\textstyle\sum_{E'}|\delta_T(E-E')(dEdE')^{\frac{1}{2}}|^2\\&\quad=(T/2\pi)dE\int dE'\delta(E-E')=(T/2\pi)dE,\end{aligned} \quad (247)$$

the interval between adjacent energy values is $2\pi/T$.

Since all occupied modes of a given energy have essentially identical properties, we have

$$\sum_c s_{ac}^\dagger(1-n_c)s_{cb}=(d\omega_a d\omega_b)^{\frac{1}{2}}(p/2\pi)^2\sigma', \quad (248)$$

and

$$p_+(n,n)=\prod_E \det[\delta_{ab}-n_a d\omega_a{}^{\frac{1}{2}}n_b d\omega_b{}^{\frac{1}{2}}(p/2\pi)^2\sigma']. \quad (249)$$

Now, all terms in the expansion of an individual determinant vanish after the second one, so that

$$\begin{aligned} p_+(n,n)&=\prod_E[1-\sum_a n_a d\omega_a(p/2\pi)^2\sigma'] \\ &=\prod_E[1-2\pi\sigma'(\lambda\mathbf{p})J_\lambda(E)]. \end{aligned} \quad (250)$$

On taking the logarithm and replacing the sum by an integral, with the aid of (247), we arrive at (245).

An upper limit to total cross sections is implied by (250). Let $\Delta\omega$ be the solid angle associated with the deviation in direction of modes $a$ and $b$ for which (248) is not seriously in error. If every mode in this angular range is equally occupied, a factor in (250) is given approximately by

$$1-n(1-n)\Delta\omega(p/2\pi)^2\sigma. \quad (251)$$

Since $n(1-n)\leq\frac{1}{4}$, we conclude that

$$\sigma\lesssim(4\pi/p^2)(4\pi/\Delta\omega). \quad (252)$$

The same result is obtained from (199), in the following way,

$$\begin{aligned} \sigma(\lambda\mathbf{p})&=(2m/p)\ \mathrm{Im}(\lambda\mathbf{p}|I(E)|\lambda\mathbf{p}) \\ &\gtrsim\Delta\omega[(m/2\pi)\ \mathrm{Im}(\lambda\mathbf{p}|I(E)|\lambda\mathbf{p})]^2 \\ &\lesssim\frac{(2m/p)^2}{\Delta\omega(m/2\pi)^2}=(4\pi/p^2)(4\pi/\Delta\omega). \end{aligned} \quad (253)$$

We see thereby that

$$2\pi\sigma'(\lambda\mathbf{p})J_\lambda(E)<4\sum_{\delta\omega}n_{\lambda\mathbf{p}}(d\omega/\Delta\omega)\ll1, \quad (254)$$

since $\delta\omega<\Delta\omega$, and only a small fraction of the modes in $\delta\omega$ will be occupied, under ordinary circumstances. The fractional difference between $\sigma(\lambda\mathbf{p})$ and $\sigma'(\lambda\mathbf{p})$ has the same order of magnitude. Indeed, we derive from

$$\sigma'(\lambda\mathbf{p})=\sigma(\lambda\mathbf{p})-[(2\pi)^3/p^2][d\sigma(\lambda\mathbf{p},\lambda\mathbf{p})/d\omega]J_\lambda(E), \quad (255)$$

and the estimate

$$\sigma(\lambda\mathbf{p})\gtrsim\Delta\omega[d\sigma(\lambda\mathbf{p},\lambda\mathbf{p})/d\omega], \quad (256)$$

that

$$\begin{aligned} (\sigma-\sigma')/\sigma&\lesssim[(2\pi)^3/p^2\Delta\omega]J_\lambda(E) \\ &=\sum_{\delta\omega}n_{\lambda\mathbf{p}}(d\omega/\Delta\omega)\ll1. \end{aligned} \quad (257)$$

We have thus justified the expression

$$p(n,n)=\exp\left[-T\int dE\sigma(\lambda\mathbf{p})J_\lambda(E)\right], \quad (258)$$

for the low-density beams ordinarily encountered. Having demonstrated the statistical independence of the modes under the latter conditions, we can write the more general formula [Eq. (241)]

$$p(n,n)=\exp[-T\sum_{\lambda\mathbf{p}}\sigma(\lambda\mathbf{p})J_{\lambda\mathbf{p}}]. \quad (259)$$

### The Eigenphases

We must still prove the equivalence of the phase shifts defined by means of the asymptotic form of eigenfunctions, with the eigenphases defined in terms of the eigenvalues of the matrix $s_{ab}(p_0)$. For this purpose, we examine the asymptotic form of the Green's function and represent it as an eigenfunction expansion. For $x_0-x_0'=T>0$, we have

$$\begin{aligned} G_+(x,x')\sim i\sum_+\int_m^\infty dE\phi_{aE}(\mathbf{x})\bar{\phi}_{aE}(\mathbf{x}')e^{-iET} \\ +\frac{1}{2\pi}\int_\infty^{(m,-)}dp_0e^{-ip_0T}\sum\frac{\psi_{\lambda\mathbf{p}}(\mathbf{x})}{\epsilon(\lambda)E-p_0} \\ \times\left[\int\bar{\psi}_{\lambda\mathbf{p}}I(p_0)\psi_{\lambda'\mathbf{p}'}\right]\frac{\bar{\psi}_{\lambda'\mathbf{p}'}(\mathbf{x}')}{\epsilon(\lambda')E'-p_0}, \end{aligned} \quad (260)$$

since the contributions of the discrete modes decrease exponentially with increasing distance from the localized field. Our concern with the limiting form as $|\mathbf{x}|$, $|\mathbf{x}'|\to\infty$ enters decisively through the remark that $\psi_{\lambda\mathbf{p}}(\mathbf{x})$ and $\bar{\psi}_{\lambda'\mathbf{p}'}(\mathbf{x}')$ are rapidly varying functions of $E$ and $E'$, in comparison with $\int\bar{\psi}_{\lambda\mathbf{p}}I(p_0)\psi_{\lambda'\mathbf{p}'}$. Hence,

$$\begin{aligned} G_+(x,x')\sim i\sum_+\int_m^\infty dE\phi_{aE}(\mathbf{x})\bar{\phi}_{aE}(\mathbf{x}')e^{-iET} \\ +\frac{1}{2\pi}\int_\infty^{(m,-)}dp_0e^{-ip_0T}\sum_{ab}\int_m^\infty dEdE'\frac{\phi_{aE}(\mathbf{x})}{E-p_0} \\ \times I_{ab}(p_0)\frac{\bar{\phi}_{bE'}(\mathbf{x}')}{E'-p_0}, \end{aligned} \quad (261)$$

in which we have omitted the contribution of negative frequency modes, and introduced $I_{ab}(p_0)$, which refers entirely to modes of frequency $p_0$, in virtue of the fact that the integrals

$$\begin{aligned} \frac{1}{\pi}\int_m^\infty dE'\frac{\phi_{aE'}(\mathbf{x})}{E'-E\mp i\epsilon}&=\phi_{aE}{}^{(\pm)}(\mathbf{x}), \\ \frac{1}{\pi}\int_m^\infty dE'\frac{\bar{\phi}_{aE'}(\mathbf{x})}{E'-E\mp i\epsilon}&=\bar{\phi}_{aE}{}^{(\pm)}(\mathbf{x}). \end{aligned} \quad (262)$$

are dominated by the immediate neighborhood of $E$, as $|\mathbf{x}|\to\infty$. Since the $p_0$ integration path encircles the

section of real axis from $m$ to infinity, we get

$$G_+(x,x')\sim i\int_m^\infty dE e^{-iET}\Big\{\sum_a \epsilon(p_0)\phi_{ap_0}(\mathbf{x})\bar{\phi}_{ap_0}(\mathbf{x}')$$
$$-\frac{\pi i}{2}\sum_{ab}[\phi_{ap_0}{}^{(+)}(\mathbf{x})I_{ab}(p_0)\bar{\phi}_{bp_0}{}^{(+)}(\mathbf{x}')$$
$$-\phi_{ap_0}{}^{(-)}(\mathbf{x})I_{ab}(p_0)\bar{\phi}_{bp_0}{}^{(-)}(\mathbf{x}')]\Big\}, \quad (263)$$

which we have written in a form that is also valid for $x_0'-x_0=T$, where $\epsilon(p_0)=-1$.

The relation

$$\left[\frac{1}{E'-E-i\epsilon}-\frac{1}{E'-E+i\epsilon}\right]=2\pi i\delta(E-E'),\ \epsilon\to+0 \quad (264)$$

shows that

$$\phi_{ap_0}{}^{(+)}-\phi_{ap_0}{}^{(-)}=2i\phi_{ap_0}. \quad (265)$$

We also have

$$\phi_{ap_0}{}^{(+)}+\phi_{ap_0}{}^{(-)}=2\phi_{ap_0}{}^{(1)}, \quad (266)$$

where the definition

$$\phi_{ap_0}{}^{(1)}(\mathbf{x})=\frac{1}{\pi}P\int_m^\infty dE'\frac{\phi_{ap_0'}(\mathbf{x})}{E'-E} \quad (267)$$

involves the principal part of the integral. The representation of $\phi_{ap_0}(\mathbf{x})$ provided by (265) is a decomposition into divergent and convergent waves. The integral operations (262), applied to the plane wave $e^{i\mathbf{p}\cdot\mathbf{x}}=\exp(ip|\mathbf{x}|\cos\vartheta)$, yield asymptotically

$$\frac{1}{2i}[\exp(ip|\mathbf{x}|\cos\vartheta)]^{(+)}\sim\frac{1}{2\pi i}\int dp'\frac{\exp[ip'|\mathbf{x}|\cos\vartheta]}{p'-p-i\epsilon}$$
$$=\begin{cases}\exp(ip|\mathbf{x}|\cos\vartheta), & \cos\vartheta>0\\ 0, & \cos\vartheta<0\end{cases} \quad (268)$$

and

$$-\frac{1}{2i}[\exp(ip|\mathbf{x}|\cos\vartheta)]^{(-)}$$
$$\sim-\frac{1}{2\pi i}\int dp'\frac{\exp[ip'|\mathbf{x}|\cos\vartheta]}{p'-p+i\epsilon}$$
$$=\begin{cases}0, & \cos\vartheta>0\\ \exp(ip|\mathbf{x}|\cos\vartheta), & \cos\vartheta<0\end{cases} \quad (269)$$

which shows that the phases of the waves $\phi_{ap_0}{}^{(+)}$ and $\phi_{ap_0}{}^{(-)}$ increase and decrease, respectively, with increasing distance. A related statement is

$$\int dE e^{-iET}\phi_{ap_0}{}^{(-)}(\mathbf{x})\sim 0, \quad (270)$$

which follows from the integral representation (262), or from the absence of a stationary phase point in (270). The latter argument also indicates the validity of the statement

$$\int dE e^{-iET}\phi_{ap_0}{}^{(-)}(\mathbf{x})\bar{\phi}_{bp_0}{}^{(-)}(\mathbf{x}')\sim 0, \quad (271)$$

for large $|\mathbf{x}|$ and $|\mathbf{x}'|$.

We can now bring (263) into eigenfunction form with the aid of the following rearrangement,

$$\frac{1}{2i}\sum[\phi_{ap_0}{}^{(+)}I_{ab}(p_0)\bar{\phi}_{bp_0}{}^{(+)}-\phi_{ap_0}{}^{(-)}I_{ab}(p_0)\bar{\phi}_{bp_0}{}^{(-)}]$$
$$=\sum[\phi_{ap_0}{}^{(+)}I_{ab}(p_0)\bar{\phi}_{bp_0}+\phi_{ap_0}I_{ab}{}^\dagger(p_0)\bar{\phi}_{bp_0}{}^{(-)}]$$
$$+\pi\epsilon(p_0)\sum\phi_{ap_0}{}^{(+)}I_{ac}(p_0)I_{cb}{}^\dagger(p_0)\bar{\phi}_{bp_0}{}^{(-)}$$
$$-\pi\epsilon(p_0)\sum\phi_{ap_0}{}^{(-)}I_{ac}(p_0)I_{cb}{}^\dagger(p_0)\bar{\phi}_{bp_0}{}^{(-)}, \quad (272)$$

in which use has been made of (110). If we discard the last term of (272) on the basis of (271), we get

$$G_+(x,x')\sim i\int_m^\infty dE e^{-iET}\sum_a \epsilon(p_0)\psi_{ap_0}(\mathbf{x})\bar{\psi}_{ap_0}(\mathbf{x}'), \quad (273)$$

with

$$\psi_{ap_0}(\mathbf{x})\sim\phi_{ap_0}(\mathbf{x})+\epsilon(p_0)\sum_b\phi_{bp_0}{}^{(+)}(\mathbf{x})\pi I_{ba}(p_0)$$
$$=\frac{1}{2i}[-\phi_{ap_0}{}^{(-)}(\mathbf{x})+\sum_b\phi_{bp_0}{}^{(+)}(\mathbf{x})s_{ba}(p_0)], \quad (274)$$

and

$$\bar{\psi}_{ap_0}(\mathbf{x})\sim\bar{\phi}_{ap_0}(\mathbf{x})+\epsilon(p_0)\sum_b\pi I_{ab}{}^\dagger(p_0)\phi_{bp_0}{}^{(-)}(\mathbf{x})$$
$$=\psi_{ap_0}(\mathbf{x})^*\gamma_0. \quad (275)$$

These eigenfunctions correspond to the stationary state viewpoint of scattering. In particular, the matrix $s_{ab}(p_0)$ appears as the one-particle scattering matrix that relates radially diverging waves to converging waves.

The introduction of the eigenfunctions $\phi_{Ap_0}$ replaces (273) and (274) with

$$G_+(x,x')\sim i\int_m^\infty dE e^{-iET}\sum_A \epsilon(p_0)\psi_{Ap_0}(\mathbf{x})\bar{\psi}_{Ap_0}(\mathbf{x}'), \quad (276)$$

and

$$\psi_{Ap_0}(\mathbf{x})\sim\frac{1}{2i}[-\phi_{Ap_0}{}^{(-)}(\mathbf{x})+\phi_{Ap_0}{}^{(+)}(\mathbf{x})e^{2i\delta_A(p_0)}]$$
$$=e^{i\delta_A(p_0)}\frac{1}{2i}[\phi_{Ap_0}{}^{(+)}(\mathbf{x})e^{i\delta_A(p_0)}$$
$$-\phi_{Ap_0}{}^{(-)}(\mathbf{x})e^{-i\delta_A(p_0)}], \quad (277)$$

where the functions $\phi_{Ap_0}{}^{(\pm)}$ are obtained from $\phi_{ap_0}{}^{(\pm)}$ by means of

$$\phi_{Ap_0}{}^{(\pm)}(\mathbf{x})=\sum_a\phi_{ap_0}{}^{(\pm)}(\mathbf{x})(a|A)_{p_0}, \quad (278)$$

which implies an integration with respect to propagation direction. The asymptotic behavior of these integrals

will be determined by the stationary phase point in angle, $\vartheta=0,\ \pi$ [Eqs. (268), (269)]. Hence the asymptotic expressions for $\phi_{Ap_0}{}^{(\pm)}(\mathbf{x})$ contain radial functions of the form $|\mathbf{x}|^{-1}\exp[\pm i(p|\mathbf{x}|+\phi^0)]$. The resulting asymptotic expressions for $\psi_{Ap_0}(\mathbf{x})$ involve trigonometric functions of $p|\mathbf{x}|+\phi^0+\delta_A(p_0)$, which establishes the equivalence of the two definitions,

$$\delta_A(p_0)=\delta_{\gamma E}. \tag{279}$$

It may be noted that the differential cross section, total cross section, and averaged total cross section, have the following expressions in terms of eigenphases,

$$d\sigma(\lambda\mathbf{p},\lambda'\mathbf{p}')/d\omega=(1/p^2)\left|\sum_A(\lambda\mathbf{p}|A)e^{i\phi(p_0)\delta_A(p_0)}\right.$$
$$\left.\times\sin\delta_A(p_0)(A|\lambda'\mathbf{p}')\right|^2, \tag{280}$$
$$\sigma(\lambda\mathbf{p})=(4\pi/p^2)\sum_A\sin^2\delta_A(p_0)\,|(A|\lambda\mathbf{p})|^2,$$

and

$$\sigma(p_0)=(2\pi/p^2)\sum_A\sin^2\delta_A(p_0), \tag{281}$$

in which we have written

$$(a|A)_{p0}=(d\omega/4\pi)^{\frac{1}{2}}(\lambda\mathbf{p}|A), \tag{282}$$

so that

$$\sum_\lambda\int\frac{d\omega}{4\pi}(A|\lambda\mathbf{p})(\lambda\mathbf{p}|B)=\delta_{AB}. \tag{283}$$

We also want to remark upon the construction of the phases from the elements of the diagonal matrix $I_{AB}(p_0)$,

$$\int(d\mathbf{x})(d\mathbf{x}')\bar{\phi}_{Ap0}(\mathbf{x})I(\mathbf{x},\mathbf{x}',p_0)\phi_{Bp0}(\mathbf{x}')$$
$$=\delta_{AB}(1/\pi)\epsilon(p_0)e^{i\delta_A(p_0)}\sin\delta_A(p_0), \tag{284}$$

which involves the awkward feature of evaluating a complex function of a single real parameter. We can avoid this difficulty by returning to the definition

$$I(p_0)=e\gamma A[1-G_+{}^0(p_0)e\gamma A]^{-1}, \tag{285}$$

and writing

$$G_+{}^0(p_0)=\mathbf{G}^0(p_0)+\tfrac{1}{2}[G_+{}^0(p_0)-G_-{}^0(p_0)], \tag{286}$$

where the Green's function

$$\mathbf{G}^0(p_0)=\tfrac{1}{2}[G_+{}^0(p_0)+G_-{}^0(p_0)] \tag{287}$$

is self-adjoint. Now

$$1-G_+{}^0(p_0)e\gamma A=\{1-\tfrac{1}{2}[G_+{}^0(p_0)-G_-{}^0(p_0)]\mathbf{I}(p_0)\}$$
$$\times[1-\mathbf{G}^0(p_0)e\gamma A], \tag{288}$$

in which the self-adjoint matrix

$$\mathbf{I}(p_0)=e\gamma A[1-\mathbf{G}^0(p_0)e\gamma A]^{-1} \tag{289}$$

is constructed from $\mathbf{G}^0$ in the same way that $I(p_0)$ involves $G_+{}^0$. Therefore,

$$I(p_0)=\mathbf{I}(p_0)\{1-\tfrac{1}{2}[G_+{}^0(p_0)-G_-{}^0(p_0)]\mathbf{I}(p_0)\}^{-1}$$
$$=\{1-\mathbf{I}(p_0)\tfrac{1}{2}[\mathbf{G}_+{}^0(p_0)-G_-{}^0(p_0)]\}^{-1}\mathbf{I}(p_0), \tag{290}$$

or, equivalently,

$$I(p_0)-\mathbf{I}(p_0)=I(p_0)\tfrac{1}{2}[G_+{}^0(p_0)-G_-{}^0(p_0)]\mathbf{I}(p_0)$$
$$=\mathbf{I}(p_0)\tfrac{1}{2}[G_+{}^0(p_0)-G_-{}^0(p_0)]I(p_0). \tag{291}$$

The matrix of $\mathbf{I}(p_0)$, referring to modes of frequency $p_0$, is Hermitian,

$$\mathbf{I}_{ab}(p_0)=\int(d\mathbf{x})(d\mathbf{x}')\bar{\phi}_{ap0}(\mathbf{x})\mathbf{I}(\mathbf{x},\mathbf{x}',p_0)\phi_{bp0}(\mathbf{x}')$$
$$=\mathbf{I}_{ba}{}^*(p_0), \tag{292}$$

and is related to $I_{ab}(p_0)$ by

$$I_{ac}(p_0)-\mathbf{I}_{ac}(p_0)=\pi i\epsilon(p_0)\sum_b I_{ab}(p_0)\mathbf{I}_{bc}(p_0)$$
$$=\pi i\epsilon(p_0)\sum_b\mathbf{I}_{ab}(p_0)I_{bc}(p_0), \tag{293}$$

according to (108) and (291). On introducing the common eigenfunctions of these matrices, we get the eigenvalue relation

$$I_A(p_0)-\mathbf{I}_A(p_0)=\pi i\epsilon(p_0)I_A(p_0)\mathbf{I}_A(p_0), \tag{294}$$

or

$$I_A(p_0)=\mathbf{I}_A(p_0)[1-\pi i\epsilon(p_0)\mathbf{I}_A(p_0)]^{-1}, \tag{295}$$

from which we obtain

$$s_A(p_0)=1+2\pi i\epsilon(p_0)I_A(p_0)$$
$$=\frac{1+\pi i\epsilon(p_0)\mathbf{I}_A(p_0)}{1-\pi i\epsilon(p_0)\mathbf{I}_A(p_0)}=e^{2i\delta_A(p_0)}. \tag{296}$$

The real numbers $\mathbf{I}_A(p_0)$ are thus connected with the eigenphases by

$$\mathbf{I}_A(p_0)=(1/\pi)\epsilon(p_0)\tan\delta_A(p_0). \tag{297}$$

By appropriately modifying (67) and (71), we get the following equation for the construction of the eigenphases,

$$\delta_{AB}(1/\pi)\epsilon(p_0)\tan\delta_A(p_0)$$
$$=\frac{1}{\mathbf{D}''(p_0)}\sum_n(-e)^n\frac{1}{n!}\int(d\mathbf{x}_1)\cdots(d\mathbf{x}_n)$$
$$\times\mathrm{tr}\left\{\prod_{i=1}^n[\gamma_iA(\mathbf{x}_i)]\det{}_{(n+1)}{}''\right.$$
$$\left.\times\begin{bmatrix}0, & \bar{\phi}_{Ap0}(\mathbf{x}_j)\\ \phi_{Bp0}(\mathbf{x}_i), & \mathbf{G}^0(\mathbf{x}_i,\mathbf{x}_j,p_0)\end{bmatrix}\right\}, \tag{298}$$

where

$$\mathbf{D}''(p_0)=1+\sum_n(-e)^n\frac{1}{n!}\int(d\mathbf{x}_1)\cdots(d\mathbf{x}_n)$$
$$\times\mathrm{tr}\left\{\prod_{i=1}^n[\gamma_iA(\mathbf{x}_i)]\det{}_{(n)}{}''\mathbf{G}^0(\mathbf{x}_i,\mathbf{x}_j,p_0)\right\}. \tag{299}$$

It should be realized that the eigenfunctions $\phi_{Ap0}$ are dependent upon the strength of the potential, in general, since they are defined by the requirement that (298) shall be a diagonal matrix, for a given potential. Further simplification is possible when this is not true, by virtue of the complete determination of the eigenfunctions from the symmetry properties of the potential. The familiar illustration is the angular momentum classification for a spherically symmetric scalar potential. Under these conditions, the Green's function $\mathbf{G}^0(\mathbf{x},\mathbf{x}',p_0)$ is composed additively of terms $\mathbf{G}_A{}^0(\mathbf{x},\mathbf{x}',p_0)$ that only contain free particle modes of type $A$, and the determinant $\mathbf{D}''(p_0)$ corresponding decomposes into a product of determinants, each referring entirely to a particular type of mode. In the expression (298) for the $A$ diagonal element, all contributions of modes other than $A$ will cancel, therefore, and $\mathbf{G}^0$ can be replaced by $\mathbf{G}_A{}^0$ in (298) and (299).

The necessity for using modified determinants stems from the singularity of $\mathbf{G}^0(\mathbf{x},\mathbf{x}',p_0)$ at $\mathbf{x}=\mathbf{x}'$. As one can verify for the example of the isotopic scalar potential, this singularity is attributable to the divergence of the $A$ summation; each $\mathbf{G}_A{}^0(\mathbf{x},\mathbf{x},p_0)$ is finite, except at the origin. Hence, one need not use modified determinants in the version of (298) and (299) that employs $\mathbf{G}_A{}^0(\mathbf{x},\mathbf{x}',p_0)$. The criterion for the existence of each unmodified determinant is found to be the finiteness of $\int_0^\infty d|\mathbf{x}|\,|eA_0|$, in the above example. Thus, the individual phases exist for arbitrary magnitude of a potential that is not as singular as $|\mathbf{x}|^{-1}$, and that vanishes at infinity more rapidly than $|\mathbf{x}|^{-1}$. The latter is less stringent then the condition for the existence of $D''(p_0)$.

### The High-Energy Limit

Finally, we shall give the simple high-energy limiting forms of the differential and total cross sections, for an isotopic scalar potential, $A_0(r)$. If $R$, the effective range of the potential, is sufficiently great, as measured by

$$pR\gg 1, \tag{300}$$

large values of the orbital angular momentum $l$ are important. Then the precise coupling of orbital and spin angular momentum is not significant and the quantum numbers $A$, specifying the various types of modes, may be chosen as $lm\lambda$. The determinant referring to modes of given angular momentum, $D_+(lm\lambda p_0)$, can be constructed for sufficiently high energy by the analog of the classical approximation for $D_+''(p_0)$. On remarking that $p^2\simeq p_r{}^2+l^2/r^2$, it will be seen that

$$\begin{aligned}&\log D_+(lm\lambda p_0)\\ &\sim\int\frac{dr\,dp_r}{2\pi}\{\log[p_r{}^2+(l^2/r^2)+m^2-(p_0-eA_0(r))^2]\\ &\quad-\log[p_r{}^2+(l^2/r^2)+m^2-p_0{}^2]\}\\ &=-i\int_0^\infty dr\{[(p_0-eA_0(r))^2-(l^2/r^2)-m^2]^{\frac12}\\ &\qquad-[p_0{}^2-(l^2/r^2)-m^2]^{\frac12}\}.\end{aligned} \tag{301}$$

As a check, we verify that[8]

$$\begin{aligned}&\log D_+''(p_0)\\ &=\sum_{lm\lambda}\log D_+''(lm\lambda p_0)\sim 2\int_0^\infty 2ldl(-i)\int_0^\infty dr\\ &\quad\times\sum_{n=3}^\infty\frac{1}{n!}[-eA_0(r)]^n(\partial/\partial p_0)^n[p_0{}^2-(l^2/r^2)-m^2]^{\frac12}\\ &=-\frac{i}{3\pi}\int_0^\infty 4\pi r^2dr\sum_{n=3}^\infty\frac{1}{n!}[-eA_0(r)]^n\\ &\qquad\times(\partial/\partial p_0)^n(p_0{}^2-m^2)^{\frac12},\end{aligned} \tag{302}$$

in agreement with (135). Hence

$$\begin{aligned}&\delta_l(p_0)=-\operatorname{Im}\log D_+(lm\lambda p_0)\\ &\sim\int_0^\infty dr\{([p_0-eA_0(r)]^2-(l^2/r^2)-m^2)^{\frac12}\\ &\qquad-[p_0{}^2-(l^2/r^2)-m^2]^{\frac12}\},\end{aligned} \tag{303}$$

where the radial integration is extended only over the region where the individual square roots are real. For $l$ not equal to zero (which is effectively ensured by the more precise statement, $p^2\simeq p_r{}^2+(l+\frac12)^2/r^2$) the second integral in (303) is restricted to values of $r$ greater than $l/p$. There is also a smallest nonzero value of $r$ in the first integral for any strength of potential, provided the latter is not so singular as $1/r$.

Now let the energy be so great that

$$pv\gg|eA_0(r\sim 1/p)|, \tag{304}$$

where

$$v=p/|p_0|, \tag{305}$$

and $r\sim 1/p$ indicates the smallest distance that occurs in (303). Then one can approximate (303) by

$$\begin{aligned}\delta_l(p_0)&=-p_0\int_{l/p}^\infty dr\frac{eA_0(r)}{(p^2-l^2/r^2)^{\frac12}}\\ &=-\epsilon(p_0)\frac{1}{v}\int_\rho^\infty\frac{r\,dr}{(r^2-\rho^2)^{\frac12}}eA_0(r)=\delta(\rho),\end{aligned} \tag{306}$$

in which

$$\rho=l/p. \tag{307}$$

---

[8] It should be remarked that, in this approximation

$$\begin{aligned}&\int_{-\infty}^\infty dp_0\log D_+''(lm\lambda p_0)\\ &=-i\sum_{n=3}^\infty\frac{1}{n!}\int_0^\infty dr(-eA_0(r))^n\int_{-\infty}^\infty dp_0(\partial/\partial p_0)^n\\ &\qquad\times[p_0{}^2-(l^2/r^2)-m^2]^{\frac12}=0,\end{aligned}$$

as required by gauge invariance, whereas (135) yields a finite gauge dependent result. This suggests that difficulties in maintaining gauge invariance will be avoided in the expression for $E(0)$, Eq. (153), if the energy integration is performed prior to the $\gamma$ summation.

The condition (304) can be satisfied for arbitrary strength of a potential that is not so singular as $1/r$. Thus, let $|eA_0(r)|\sim\lambda r^{-(1-\beta)}$. Then (304) reads

$$p^\beta v\gg\lambda, \tag{308}$$

and the left side can indeed be made arbitrarily large, provided $\beta>0$. If we write $r=(\rho^2+z^2)^{\frac{1}{2}}$, (306) assumes the form

$$\delta(\rho)=-\epsilon(p_0)(1/2v)\int_{-\infty}^{\infty}dzeA_0[(\rho^2+z^2)^{\frac{1}{2}}], \tag{309}$$

which corresponds to the picture of a particle moving along a classically describable trajectory that approximates to a straight line. At the limit of infinite energy, for arbitrary fixed $l$, the eigenphases have the universal, nonvanishing[9] value

$$\delta_l(p_0)\longrightarrow-\epsilon(p_0)\int_0^{\infty}dreA_0(r). \tag{310}$$

In the requirement that this quantity be finite, we recognize the previously stated criterion for the existence of the individual eigenphases.

The transformation function satisfying the normalization condition (283) is, evidently,

$$(\lambda\mathbf{p}|lm\lambda')=\delta_{\lambda\lambda'}(4\pi)^{\frac{1}{2}}Y_{lm}(\mathbf{p}), \tag{311}$$

so that, according to (280) and (281),

$$d\sigma(\lambda\mathbf{p},\lambda'\mathbf{p}')/d\omega\sim\delta_{\lambda\lambda'}(1/p^2)$$
$$\times|\textstyle\sum_l(2l+1)P_l(\cos\vartheta)e^{i\epsilon(p_0)\delta_l(p_0)}\sin\delta_l(p_0)|^2, \tag{312}$$

and

$$\sigma(p_0)\sim(4\pi/p^2)\textstyle\sum_l(2l+1)\sin^2\delta_l(p_0). \tag{313}$$

On replacing the summations by integrals with respect to $l=p\rho$, and using the limiting form of $P_l(\cos\vartheta)$ for small angles, $J_0(l\vartheta)$, (which can be obtained by comparing the respective differential equations) we get[10]

$$d\sigma(\lambda\mathbf{p},\lambda'\mathbf{p}')/d\omega\sim\delta_{\lambda\lambda'}4p^2$$
$$\times\left|\int_0^{\infty}\rho d\rho J_0(p\vartheta\rho)e^{i\epsilon(p_0)\delta(\rho)}\sin\delta(\rho)\right|^2, \tag{314}$$

and

$$\sigma(p_0)\sim8\pi\int_0^{\infty}\rho d\rho\sin^2\delta(\rho). \tag{315}$$

In order that the total cross section exist, $\delta(\rho)$ must approach zero with increasing $\rho$ more rapidly than $1/\rho$, which requires that $eA_0(r)$ vanish more rapidly than $1/r^2$, in agreement with the previously obtained condition for the effective localization of the field. We should also note that $\sigma$ has a nonzero limit for infinite energy.

The magnitude of $\delta(\rho)$ for $\rho<R$ is roughly indicated by

$$\delta(\rho)\sim(|eA_0|/pv)(pR), \tag{316}$$

of which the first factor is small and the second large. Depending upon the relation between these quantities, the eigenphases can assume arbitrary values. Should the maximum value of $\delta(\rho)$ be small compared with unity, the angular distribution deduced from (314) will be essentially determined by the oscillatory character of the Bessel function, and thus is confined to the angular interval measured by

$$\vartheta_0\sim1/pR\ll1. \tag{317}$$

The situation is different (and constitutes the classical limit) when $\delta(\rho)$ attains values that are large compared with unity. We shall now designate as $R$, the range of the potential, the distance at which $\delta(\rho)$ has decreased from large values for $\rho<R$ to values less than unity for $\rho>R$. If we neglect the contribution of distances greater than $R$, we can write (314) and (315) as ($\lambda=\lambda'$)

$$\frac{d\sigma}{d\omega}\sim p^2\left|\int_0^R\rho d\rho J_0(p\vartheta\rho)e^{2i\epsilon(p_0)\delta(\rho)}-\int_0^R\rho d\rho J_0(p\vartheta\rho)\right|^2, \tag{318}$$

and

$$\sigma\sim2\pi R^2, \tag{319}$$

in which we have used the average value of $\sin^2\delta(\rho)$. The major contribution to the first integral in (318) occurs in the neighborhood of the point of stationary phase (assuming $p\vartheta\rho\gg1$), which is given by

$$p\vartheta=2|(d/d\rho)\delta(\rho)|=(1/v)\left|\int_{-\infty}^{\infty}dz(\partial/\partial\rho)eA_0\right|. \tag{320}$$

This is just the high-energy approximation to the classical connection between impact parameter and angle of deflection. In order to satisfy the condition $p\vartheta\rho\gg1$, we must restrict $\rho$ to such values that

$$(1/v)\left|\int_{-\infty}^{\infty}dz\rho(\partial/\partial\rho)eA_0\right|\sim(\rho/R)\delta(\rho)\gg1. \tag{321}$$

Only a small fraction of the range $0<\rho<R$ will be excluded if $\delta(\rho)$ is sufficiently large. We also note that the magnitude of the angles obtained from (320) is given by

$$\vartheta_c\sim|eA_0|/pv\ll1, \tag{322}$$

whereas the second term of (318) is effectively confined

[9] This has been noticed by G. Parzen, Phys. Rev. **80**, 261 (1950).
[10] Similar results have previously been derived by G. Moliere, Z. Naturforsch. **2a**, 133 (1947) and R. J. Glauber, Phys. Rev. **91**, 459 (1953).

to angles of the order $\vartheta_q \sim 1/pR$. But

$$\vartheta_c/\vartheta_q \sim (|eA_0|/pv)(pR) \sim \delta(\rho), \tag{323}$$

which is large compared with unity for $\rho < R$. On performing the integrations in (318) and neglecting the interference between the two essentially nonoverlapping angular distributions, we get

$$d\sigma/d\omega = (\rho d\rho/\vartheta d\vartheta)_c + R^2[J_1(pR\vartheta)/\vartheta]^2, \tag{324}$$

in which the first term is the classically computed differential cross section, and the second represents the familiar shadow scattering. Both parts contribute $\pi R^2$ to the total cross section, in agreement with (319). Indeed the neglect of the interference between classical and shadow scattering corresponds precisely to the approximation $4\sin^2\delta = |e^{2i\delta}-1|^2 \sim 1+1$.

Other derivations can be given for the limiting forms of the cross sections (314) and (315). In particular, one can avoid explicit reference to eigenphases by a direct construction of the Green's function from its defining differential equation, in high-energy approximation. If we write

$$G_+(\mathbf{x},\mathbf{x}',p_0) = \int \frac{(d\mathbf{p})}{(2\pi)^3} e^{i\mathbf{p}\cdot(\mathbf{x}-\mathbf{x}')} g_+(\mathbf{x},p), \tag{325}$$

the Green's function differential equation reads

$$[\gamma p + m - i\boldsymbol{\gamma}\cdot\boldsymbol{\nabla} + \gamma_0 e A_0(\mathbf{x})] g_+(\mathbf{x},p) = 1, \tag{326}$$

and multiplication with $m-\gamma p$ converts this into

$$[p^2+m^2-2i\mathbf{p}\cdot\boldsymbol{\nabla}+2p_0 eA_0 + (-i\boldsymbol{\gamma}\cdot\boldsymbol{\nabla}+\gamma_0 eA_0)(\gamma p+m)] g_+(\mathbf{x},p) = m-\gamma p. \tag{327}$$

For zero potential, $g_+(\mathbf{x},p)$ is independent of $\mathbf{x}$,

$$A_0 = 0: \quad g_+(\mathbf{x},p) = (m-\gamma p)/(p^2+m^2), \tag{328}$$

and has a singularity at $p^2+m^2=0$, being the eigenvalue equation for free particles. Since the factor $\gamma p+m$ removes this singularity, it will be clear that the high-energy approximation is the replacement of (327) with the simplified equation

$$[p^2+m^2-2i\mathbf{p}\cdot\boldsymbol{\nabla}+2p_0 eA_0(\mathbf{x})] g_+(\mathbf{x},p) = m-\gamma p. \tag{329}$$

With $\mathbf{p}$ directed along the $z$ axis, the solution of this differential equation is

$$g_+(\mathbf{x},p) = (m-\gamma p)(i/2|p_0|v) \times \int_{-\infty}^{z} dz' \exp\left[-(i/2|p_0|v) \times \int_{z'}^{z} dz''(p^2+m^2+2p_0 eA_0)\right], \tag{330}$$

in which the choice of $-\infty$ for the lower limit of integration stems from the requirement that $G_+$ be regula in the lower $m$ half-plane, since this demands that $z-z'$ never be negative for arbitrary $z$. For $A_0=0$, the integrations can be performed and we regain (328). As $p^2+m^2 \to 0$, the major contribution to (330) comes from large negative values of $z'$, and

$$g_+(\mathbf{x},p) \to \frac{m-\gamma p}{p^2+m^2} \exp\left[-ie(p_0)(1/v)\int_{-\infty}^{z} dz' eA_0\right], \tag{331}$$

which quantity has constant limiting values for $|z|>R$,

$$\begin{aligned} g_+(\mathbf{x},p)(\gamma p+m) &\to 1, && z<-R \\ &\to e^{2i\delta(\rho)}, && z>R. \end{aligned} \tag{332}$$

A notation analogous to (325), namely

$$I(\mathbf{x},\mathbf{x}',p_0) = \int \frac{(d\mathbf{p})}{(2\pi)^3} e^{i\mathbf{p}\cdot(\mathbf{x}-\mathbf{x}')} i(\mathbf{x},p), \tag{333}$$

enables us to write $I(p_0)G_+^0(p_0) = e\gamma A G_+(p_0)$ as

$$\begin{aligned} i(\mathbf{x},p) &= -\gamma_0 eA_0(\mathbf{x}) g_+(\mathbf{x},p)(\gamma p+m) \\ &= \gamma_0(1/2p_0)(p^2+m^2-2i\mathbf{p}\cdot\boldsymbol{\nabla})[g_+(\mathbf{x},p) \times (\gamma p+m)-1] \to -i\gamma_0 e(p_0)v(\partial/\partial z) \times [g_+(\mathbf{x},p)(\gamma p+m)-1], \end{aligned} \tag{334}$$

where the latter form corresponds to $p^2+m^2 \to 0$. On using the reflection property (219), we can replace (194) with

$$\begin{aligned} &(\lambda\mathbf{p}|I(p_0)|\lambda'\mathbf{p}') \\ &= \int (d\mathbf{x})(d\mathbf{x}')\bar{u}_{\lambda\mathbf{p}} e^{-i\mathbf{p}\cdot\mathbf{x}} I(\mathbf{x},\mathbf{x}',p_0) u_{\lambda'\mathbf{p}'} e^{i\mathbf{p}'\cdot\mathbf{x}'} \\ &= \int (d\mathbf{x}) e^{-i(\mathbf{p}-\mathbf{p}')\cdot\mathbf{x}} \bar{u}_{\lambda\mathbf{p}} i(\mathbf{x},p') u_{\lambda'\mathbf{p}'}, \end{aligned} \tag{335}$$

and by remarking that the longitudinal factor of $e^{-i(\mathbf{p}-\mathbf{p}')\cdot\mathbf{x}}$ varies relatively little in a distance $\sim R$, for sufficiently small scattering angles, evaluate (335) as

$$\begin{aligned} &(\lambda\mathbf{p}|I(p_0)|\lambda'\mathbf{p}') \\ &= -i\delta_{\lambda\lambda'}(p_0 v/m)\int (d\boldsymbol{\varrho}) \exp[-i(\mathbf{p}-\mathbf{p}')\cdot\boldsymbol{\varrho}](e^{2i\delta(\rho)}-1) \\ &= \delta_{\lambda\lambda'} 4\pi\epsilon(p_0)(p/m)\int_0^\infty \rho d\rho J_0(p\vartheta\rho) e^{i\delta(\rho)} \sin\delta(\rho). \end{aligned} \tag{336}$$

Here $\boldsymbol{\varrho}$ is the transverse (to $\mathbf{p}'$) component of $\mathbf{x}$, and the axial symmetry of $\delta(\rho)$ has been invoked for the second form of (336). It is worth noticing that this approximation is consistent with the general property

[Eq. (110)]

$$(\lambda\mathbf{p}|I(p_0)|\lambda'\mathbf{p}')-(\lambda\mathbf{p}|\bar{I}(p_0)|\lambda'\mathbf{p}')$$
$$=2\pi i\epsilon(p_0)\sum_{\lambda''}\int(\lambda\mathbf{p}|I(p_0)|\lambda''\mathbf{p}'')\frac{m}{E''}\frac{(d\mathbf{p}'')}{(2\pi)^3}$$
$$\times\delta(E''-E)(\lambda''\mathbf{p}''|\bar{I}(p_0)|\lambda'\mathbf{p}')$$
$$\simeq i(m/p)\epsilon(p_0)\sum_{\lambda''}\int(\lambda\mathbf{p}|I(p_0)|\lambda''\mathbf{p}'')\frac{(d\mathbf{p}_\rho'')}{(2\pi)^2}$$
$$\times(\lambda''\mathbf{p}''|\bar{I}(p_0)|\lambda'\mathbf{p}'), \quad (337)$$

in the latter, small angle scattering version. One easily verifies, using the first form of (336), that either side of (337) yields

$$\delta_{\lambda\lambda'}4i(p/m)\epsilon(p_0)\int(d\boldsymbol{\varrho})$$
$$\times\exp[-i(\mathbf{p}-\mathbf{p}')\cdot\boldsymbol{\varrho}]\sin^2\delta(\rho). \quad (338)$$

The differential and total cross sections, computed from (336) according to Eqs. (198)–(201), are identical with (314) and (315).

PHYSICAL REVIEW VOLUME 94, NUMBER 5 JUNE 1, 1954

# *V* Particles and the Gamma Decay of a Neutral Pion

TOICHIRO KINOSHITA
*The Institute for Advanced Study, Princeton, New Jersey*
(Received Februrary 18, 1954)

It is shown that the previous theoretical calculations of the lifetime for the gamma decay of the $\pi^0$ meson must be subject to an obvious modification because of the presence of new particles recently discovered experimentally. This may be regarded as an example of the fact that, in some cases, the meson-nucleon system cannot be treated as being isolated from the rest of the elementary particles. We cannot give an accurate numerical prediction for the lifetime until sufficient knowledge about the new particles is accumulated. Some features of Pais' theory of the *V* particles are discussed in connection with this problem.

THE purpose of this note is to point out that meson theory has to be examined seriously not only with respect to the mathematical aspects of describing various processes, but also in the light of the new situation that many elementary particles have recently been discovered in nature. We shall illustrate how greatly the results of the ordinary meson theory will be modified by the presence of various particles by taking the gamma decay of a neutral pion as an example.

It is well known that a $\pi^0$ meson decays into two photons, the lifetime being of the order of $5\times10^{-15}$ sec.[1] Phenomenologically this process can be treated by introducing into the photon-pion system an interaction Hamiltonian which is linear in the pion operator and quadratic in the photon operators. In view of the strong interaction of the pion with the nucleon field, however, many authors have attempted to explain this process as one in which the $\pi^0$ meson creates a virtual proton-antiproton pair which are annihilated together to emit two gamma quanta.[2] In the case of a pseudoscalar $\pi^0$ coupled to the nucleon field by pseudoscalar interaction, for instance, the lifetime for the gamma decay calculated by the lowest order perturbation theory is given by

$$\frac{1}{\tau}=\frac{\alpha^2}{16\pi^2}\frac{g^2}{4\pi\hbar c}\frac{\mu c^2}{\hbar}\left(\frac{\mu}{M}\right)^2, \quad (1)$$

where $\alpha$ is the fine structure constant, $g$ is the strength of coupling of pion and nucleon fields, and $\mu$ and $M$ are the masses of the $\pi^0$ meson and nucleon, respectively. Comparing (1) with experiment, one finds that

$$g^2/4\pi\hbar c\approx0.14. \quad (2)$$

This is much smaller than the value $g^2/4\pi\hbar c\gtrsim10$ deduced from the theory of other processes such as the photonic and nucleonic production of mesons. Other assumptions about the interaction also lead to similar conclusions.

Of course, one can enumerate several possible reasons for such discrepancy. First, it may be owing to the general failure of perturbation calculation in meson problems that one finds different effective coupling constants for different processes. The apparent smallness of the coupling constant (2), though it seems to favor the use of perturbation method for this case, might simply be a result of misuse of the theory, and higher-order corrections to (1) may lead to a quite different result. Secondly, it may happen that the nucleon cannot be described by the Dirac equation or similar ones. This may be related to the question of

[1] B. M. Anand, Proc. Roy. Soc. (London) **A220**, 183 (1953). Previous estimates of the lifetime of the neutral pion are summarized in this paper.

[2] S. Sakata and Y. Tanikawa, Phys. Rev. **57**, 548 (1940); R. J. Finkelstein, Phys. Rev. **72**, 415 (1947); J. Steinberger, Phys. Rev. **76**, 1180 (1949); H. Fukuda and Y. Miyamoto, Progr. Theoret. Phys. Japan **4**, 347 (1949).

the existence of the antinucleon and cannot be answered at present.

Until lately, this was almost the only picture of the $\pi^0-2\gamma$ decay process and the above two points were thought to be the only ones which needed to be examined. This would be correct if there were no other particles than nucleons that interact strongly with a pion. It is now known, however, that this is not the case since there are actually several such particles among a variety of elementary particles discovered in recent years. Insofar as one treats the problem on the basis of the present theory of quantized fields, there is no reason to restrict oneself to the former picture and one has rather to take account of the effects of all particles in the decay process. Contributions to the decay matrix element from various channels will be of the same order of magnitude provided their couplings with a pion, as well as their masses, are comparable. This means that the lifetime of the $\pi^0$ meson given by (1) might be modified by a nontrivial factor due to the presence of several particles which interact strongly with a pion. Namely, (1) may not give a correct lifetime even if perturbation theory is applicable to this case.[3] It may thus be concluded that paying attention to such particles might be as important as the other two points in understanding the meson-theoretical aspect of the gamma decay of the $\pi^0$ meson.

Actually, our present knowledge about the elementary particles is far from satisfactory and thus we cannot go beyond a mere guess. It would nevertheless be instructive to estimate the lifetime of $\pi^0-2\gamma$ decay by taking only the proton and the $V^+$ particle into account.[4] If we assume that the coupling constant of a $V^+$ particle with a pion is the same as that of the pion-nucleon interaction, the lifetime of the $\pi^0$ meson is given by

$$\frac{1}{\tau_\pm}=\frac{\alpha^2}{16\pi^2}\frac{g^2}{4\pi\hbar c}\frac{\mu c^2}{\hbar}\left(\frac{\mu}{M}\pm\frac{\mu}{M'}\right)^2, \tag{3}$$

where $M'$ is the mass of the $V^+$ particle; the $+$ or $-$ sign corresponds to the case where the matrix elements for these two processes are of the same or opposite signs. Adopting $M'\approx 2200m_e$, one finds from (3) and the observed lifetime that

$$g^2/4\pi\hbar c\approx 0.04, \tag{4}$$

or

$$g^2/4\pi\hbar c\approx 5, \tag{5}$$

for the two cases, respectively. The large difference in the coupling constants determined by (1) and (3) indicates that ignorance of the existence of several channels may eventually lead to a meaningless result in such problems. The coupling constant (5) is much more consistent than (2) with the values determined by other processes. This is not to be taken too seriously, however, since such a picture may not be realistic and the perturbation theory may not give a reliable lowest-order approximation for such a large couple constant.

It may be interesting to notice that the theory recently proposed by Pais[5] gives matrix elements of different sign for the proton and the $V^+$ particle and thus leads to (5). If one takes account of all excited states predicted by his theory, however, the matrix element for the gamma decay of the $\pi^0$ meson is found to be badly divergent in spite of the partial cancellation among various intermediate states. It is seen that this is due to the large degeneracy with respect to the charge in the highly excited states. In other words, this is a divergence coming from the freedom in the $\omega$ space for which no method of disposal has yet been obtained.[6] If it is found in future that this divergence is unrenormalizable in any sense, it might suggest to us the necessity of departing from the theories which admit too many excited states or modifying some of the basic parts of the present formulation of field theories.

The author would like to express his gratitude to Professor R. Oppenheimer for his kind hospitality at the Institute for Advanced Study and for the stimulating interest which he has taken in this work. He is also very indebted to Professor A. Pais for many valuable discussions.

[3] It may be interesting to point out that the gamma decay of the $\pi^0$ meson is one of the rare events in which the presence of various particles in the intermediate states may possibly have a large influence on the over-all results. In most cases, such effects appear only as small corrections or unobservable quantities.

[4] One may be allowed to assume that neutral particles do not give major contributions to the lifetime of the $\pi^0$ meson. The existence of a positively charged $V$ particle heavier than a nucleon is reported by York, Leighton, and Bjornerud, Phys. Rev. **90**, 167 (1953).

[5] A. Pais, Physica **19**, 869 (1953).

[6] A. Pais, Progr. Theoret. Phys. Japan **10**, 457 (1953).

# Letters to the Editor

*PUBLICATION of brief reports of important discoveries in physics may be secured by addressing them to this department. The closing date for this department is five weeks prior to the date of issue. No proof will be sent to the authors. The Board of Editors does not hold itself responsible for the opinions expressed by the correspondents. Communications should not exceed 600 words in length and should be submitted in duplicate.*

## Observation of Exchange Interaction Effects in Ferromagnetics by Spin Wave Resonance*

G. T. RADO AND J. R. WEERTMAN
*Naval Research Laboratory, Washington, D. C.*
(Received April 5, 1954)

NO previous experiments at any temperature have revealed exchange interaction effects in ferromagnetic resonance, and semitheoretical estimates[1] have indicated that at room temperature the fractional "exchange shift," $\Delta H/H$, of the static resonance field is too small to be observable. The "spin wave resonance" experiments reported herein show, however, that an easily measurable $\Delta H/H$ ($\sim$20 or 30 percent) can be obtained at room temperature if appropriate experimental conditions are established. Our experiments also include an actual measurement of the important exchange factor (or "exchange stiffness constant") $A$, and show that in the present case both the width and shape of the absorption and dispersion curves can be described by using *not* the usual phenomenological damping terms (of the Landau and Lifschitz, or Bloch, type) but rather the physical mechanism of exchange stiffness in the skin depth of a ferromagnetic metal. Thus the energy losses near resonance are, in this case, almost exclusively due to eddy current dissipation.

The ideas underlying our experiments are the following. We increase $\Delta H/H$ by making the resonance field $H$ rather small ($\sim 10^3$ oersteds) and $\Delta H$ reasonably large, the latter being accomplished by producing a fairly small skin depth $\delta$. Because of the relatively low frequency necessitated by the small $H$, a small $\delta$ requires a very large $\mu_2$($\sim 10^3$) at resonance. We obtain a resonance despite the small $H$, and achieve a very large $\mu_2$, by bringing about in our present polycrystals a magnetocrystalline anisotropy, $K$, of about zero; in monocrystals, however, a small $K(\neq 0)$ should be usable.

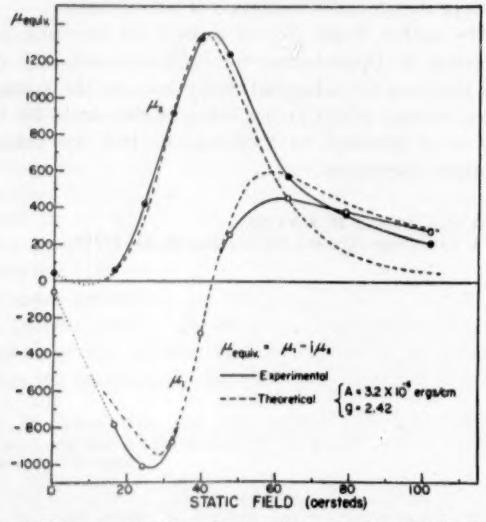


FIG. 1. Measured and calculated values of $\mu_{equ} = \mu_1 - i\mu_2$ at 3000 Mc/sec.

We used a long, electropolished rod of a 66 percent nickel-34 percent iron alloy (by weight) which had been slowly cooled (at $\approx$60°C/hr) to obtain[2] $K \approx 0$, then covered with gold foil except near the center, and mounted in a strain-free manner as the inner conductor in a (half wave or full wave) coaxial cavity. Using an improved version of a pulse method,[3] supplemented by the axial static $H$ which is normal to the microwave field, we measured the complex "equivalent isotropic permeability," $\mu_{equ} = \mu_1 - i\mu_2$, as a function of $H$.

In Fig. 1 the measured results for 3000 Mc/sec, corrected for static demagnetization,[4] are shown by the points on the solid lines, and the calculated results, based on the reasonable constants $g = 2.42$ and $A = 3.17 \times 10^{-6}$ erg/cm, are shown by dashed lines. These calculations, by Ament and Rado,[5] required a combined solution of the precession equation [including the spin-wave, or exchange, term $(2A/M_s^2)\mathbf{M} \times \nabla^2\mathbf{M}$] and Maxwell's equations, because the perturbation approach[1] is not valid in our case and does not yield the line shape. The agreement between the data and the exchange effect calculations is seen to be good, particularly when one considers that neither the characteristic asymmetries of the $\mu_1$ and $\mu_2$ curves, nor their width for a given height, could have been represented by means of the phenomenological Landau-Lifshitz damping. Furthermore, even though the samples are not quite saturated for small $H$ (<15 oersteds), the unprecedented negative values of $\mu_2$ obtained both experimentally (dotted lines) and theoretically (not shown) over part of that range do not violate thermodynamics but constitute, in fact, evidence of exchange effects. Since in the presence of exchange effects $\mu_{equ}$ is not an induction/field ratio but a measure of the surface impedance, $\mu$[2] can be negative and only the attenuations must be (and are) positive.

We obtained similar line width and line shape agreement with the exchange stiffness picture at 6000 Mc/sec. Here we found $\mu_{equ} \approx 1$ for $H = 0$, and a $g$ value only slightly above 2. However, within the present experimental error of $A$ ($\approx$30 percent), $A$ is the same at 6000 as at 3000 Mc/sec. These and other matters (e.g., the determination of $A$ from the Bloch $T^{\frac{3}{2}}$ law) are discussed by us elsewhere.[6]

* Presented at the Detroit meeting of the American Physical Society, March 18, 1954 [Bull. Am. Phys. Soc. **29**, No. 3, 13 (1954)].

[1] C. Kittel and C. Herring, Phys. Rev. **77**, 725 (1950).
[2] R. M. Bozorth and J. G. Walker, Phys. Rev. **89**, 624 (1953).
[3] M. H. Johnson and G. T. Rado, Phys. Rev. **75**, 841 (1949); the pulsing method described in this reference was used in the present work to establish a reference point ($\mu_{equ} = 1$) for the $Q$ and frequency shift measurements by saturating the rod parallel to the microwave field.
[4] R. M. Bozorth and D. M. Chapin, J. Appl. Phys. **13**, 320 (1942).
[5] W. S. Ament and G. T. Rado, Bull. Am. Phys. Soc. **29**, No. 3, 13 (1954). Also, paper in preparation.
[6] G. T. Rado and J. R. Weertman (paper in preparation).

## Bound States in Dislocations

ROLF LANDAUER
*Research Department, International Business Machines Corporation, Poughkeepsie, New York*
(Received April 2, 1954)

SHOCKLEY[1] has pointed out that an edge dislocation in germanium may give rise to acceptor levels, and recent measurements[2] support this prediction. Dislocations may, however, have other effects in semiconductors, in addition to providing Shockley's "dangling" levels. Dislocations can affect the distribution of impurities.[3] Furthermore, edge dislocations are accompanied by lattice dilations and contractions, which in turn cause the top of the valence band and the bottom of the conduction band to be displaced from their normal positions. We have therefore attempted to estimate the trapping energy associated with the elastic distortions. In the case of a semiconductor in which a volume change causes the bottom of the conduction band and the top of the valence band to move in opposite directions, these

elastic distortions will provide traps for holes and electrons which coincide spatially, and therefore may influence recombination processes and exciton motion.

In the case of both metals[4] and semiconductors[5] the potentials involved are of the form $-A\sin\theta/r$, where $\theta$ is the angle with the slip plane and $r$ is the distance from the dislocation axis. It can be shown that this two-dimensional dipole potential distribution contains an infinite number of bound states. This, however, is true only if the dislocation field is really infinite in extent. To get more realistic information we have applied the variational method to this problem. The minimum value of

$$\int\psi^*\left(-\frac{\hbar^2}{2m^*}\nabla^2+V\right)\psi d\sigma$$

was found, for a trial function to be described, and for $V=-A\times\sin\theta/r$. The integration here is over the two-dimensional plane perpendicular to the dislocation. The trial function we have used is $(2/\pi)^{\frac{1}{2}}\alpha\exp(-\alpha^2 s^2)$, where $s$ is the distance from a line parallel to the dislocation axis. This second line is taken to be at $\theta=\pi/2$ and at a distance $d$ from the dislocation axis. The undetermined parameters are $\alpha$ and $d$. The integrals that have to be evaluated in this variational procedure can be made trivial by applications of Green's theorem. The minimum expectation value of the energy occurs when

$$d=1.76\hbar^2/Am^*,\quad \alpha=0.451Am^*/\hbar^2.$$

The energy at this minimum is

$$-0.204m^*A^2/\hbar^2.$$

These results are illustrated in Fig. 1.

For a given value of $m^*$, as the binding strength $A$ is increased, the state becomes more strongly localized, and the binding energy increases more rapidly than $A$. In the case of a semiconductor, the equation for $A$ has been given by Dexter and Seitz,[5] based on the theory of deformation potentials,[6] which neglects all the more recently suggested complications in the germanium band structure. To represent electrons in germanium we have used $\lambda=4.0\times10^{-8}$ cm, $(1-2\nu)/(1-\nu)=\frac{1}{2}$ and an effective mass of $\frac{1}{4}$ the electronic mass. $E_1$ was taken to be 2 ev. These values give a bound state $3\times10^{-3}$ ev below the bottom of the conduction band and centered at a distance $d=8\times10^{-7}$ cm from the dislocation axis. In view of the uncertainty of the relevant constants these numerical results do not have much significance. For all reasonable combinations of the relevant constants we do find that the state is sufficiently localized (within $10^{-5}$ cm) so that it is within the field of a single dislocation, at the densities of dislocations which might be expected in semiconductors. Furthermore, the state is always sufficiently spread out so that it is not likely to be just a consequence of the fictitious singularity at the origin.

The method of deformation potentials as used by Dexter and Seitz takes into account how the band edges are displaced in the absence of holes and electrons. If holes or electrons are present, the carriers can redistribute themselves, and thereby screen the deformation potential. If we are well within a Debye length of the dislocation axis, then the method of deformation potentials, which predicts a band edge shift of $E_1\Delta$, is justified. Since the Debye length $(\epsilon kT/4\pi ne^2)^{\frac{1}{2}}$, for 1-ohm cm germanium is $10^{-5}$ cm and larger for purer material, our lowest state is well within this range for all reasonable purities.

Since the bound states can presumably have momentum along the dislocation axis, we cannot expect to find discrete states. If the edge dislocations are parts of sharply curved rings, the two-dimensional picture we have given breaks down completely, and there may be no bound states. In this discussion it has also been assumed that there are no extra "dangling" electrons to give a repulsive Coulomb field.

In the case of metals, bound states are implicitly assumed in the argument leading to the potential $-A\sin\theta/r$. Using the constants from earlier calculations,[4] we find that in Cu the lowest of these states is at an energy of 0.016 ev below the bottom of the conduction band in the undeformed metal. The wave function is centered at a distance $d=1.4\times10^{-7}$ cm from the dislocation axis. The corrugations in the bottom of the conduction band arising from dislocations may reduce the number of electrons which are free to move as conduction electrons. To estimate this total number of trapped electrons we shall try to find the number of bound levels in our potential $-A\sin\theta/r$. For lack of a better method we have used the Fermi-Thomas approximation (which has already been used implicitly in deriving the potential $-A\sin\theta/r$ in the metallic case). This tells us that there are $1.41\alpha R$ bound states in the two-dimensional potential, $-A\sin\theta/r$, between $r=0$ and $r=R$. For a heavily cold-worked metal we can take $\pi R^2=10^{-12}$ cm$^2$ which gives about four bound states per dislocation in heavily cold-worked Cu. This does not take into account that each of these states in the two-dimensional potential can also have momentum along the dislocation axis. If we assume that the $n$ electrons per cc in the occupied part of the conduction band have spatial wave functions which can be factored into one-dimensional wave functions, then there will be $(3n/\pi)^{\frac{1}{2}}$ different possible one-dimensional wave functions per unit length within the energy range occupied in the conduction band. For heavily cold-worked Cu this means that about 1 out of 500 electrons is confined to motion along the dislocation axis. The presence of jogs, solute atoms, and vacancies near the dislocation axis may

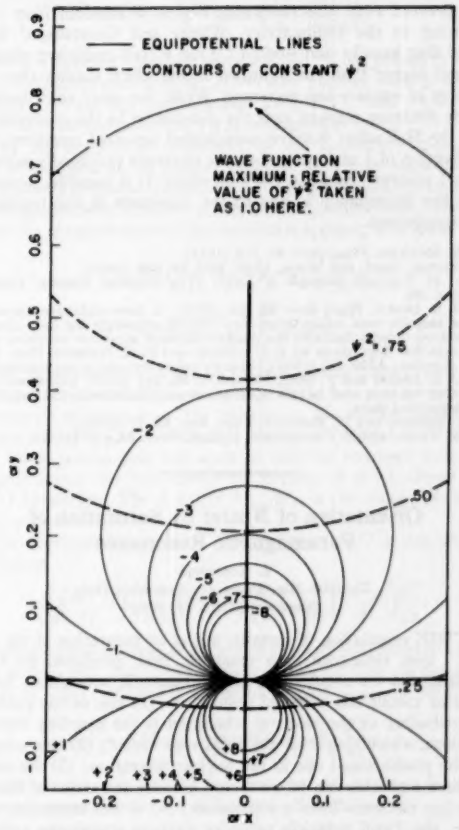


FIG. 1. Variation of the best trial wave function for the lowest state in a potential $-A\sin\theta/r$. The vertical axis $y$ measures the distance perpendicular to slip plane; the horizontal axis $x$ measures the distance in the direction of the slip vector. The dislocation axis is taken to be at (0,0) and perpendicular to the plane of the paper. The values given for $\psi^2$ are not normalized; they must be multiplied by $2\alpha^2/\pi$ to normalize them. The solid circles are equipotentials. The integral values with which they are labeled give relative potential values. These values must be multiplied by $1.25\alpha A$ to give actual potential values.

well prevent even this remaining degree of freedom from contributing to the conductivity. Wiener and Groetzinger[7] have found that heavily cold-worked Cu has a Hall coefficient about 1 percent higher than the annealed metal which implies that the number of carriers has decreased. While the exact contributions of the electrons trapped near the dislocation to the conductivity and the Hall effect involve complicated unsolved questions, the localization of $\frac{1}{2}$ of 1 percent of the electrons can hardly account for a 1 percent change in the Hall effect. It is possible, however, that the discrepancy is due to the crudeness of our remaining approximations.

[1] W. Shockley, Phys. Rev. **91**, 228 (1953).
[2] Pearson, Read, and Morin, Phys. Rev. **93**, 666 (1954).
[3] A. H. Cottrell, *Strength of Solids* (The Physical Society, London, 1948), p. 30.
[4] D. L. Dexter, Phys. Rev. **85**, 936 (1952). A more elaborate discussion of the metallic case, which takes into account explicitly not only changes in electron density but also the changes in band structure resulting from dilations, has been given by S. C. Hunter and F. R. Nabarro, Proc. Roy. Soc. (London) **A220**, 542 (1953). Dexter's values are used in our calculations.
[5] D. L. Dexter and F. Seitz, Phys. Rev. **86**, 964 (1952). Undefined symbols that we have used in this letter are in accordance with the definitions of Dexter and Seitz.
[6] J. Bardeen and W. Shockley, Phys. Rev. **80**, 72 (1950).
[7] B. Wiener and G. Groetzinger, J. Appl. Phys. **23**, 441 (1952).

## Orientation of Nuclei by Saturation of Paramagnetic Resonance

J. KORRINGA
*The Ohio State University, Columbus, Ohio*
(Received March 25, 1954)

THE orientation of metallic nuclei by saturation of the electron resonance in a magnetic field, predicted by Overhauser,[1] has its counterpart in paramagnetic substances. In the case of metals the essential points are: (1) one of the processes contributing to the electron relaxation is the coupling with the nucleus, which conserves the total spin vector; (2) this coupling is the predominant one in the nuclear relaxation; (3) the energy in such a process can be conserved because the states of the conduction electrons form a continuum; (4) in the saturated situation, the Pauli principle provides electron transitions with decrease of magnetic energy with a larger *a priori* probability than the inverse transitions.

We wish to point out here that the conditions prevailing in paramagnetic salts in which the nuclei of the paramagnetic ion have a spin, are such that requirements equivalent to those mentioned above are satisfied: (1) through the coupling $\alpha(\boldsymbol{\sigma}\cdot\mathbf{I})$ between the electronic spin $\boldsymbol{\sigma}$ and the nuclear spin $\mathbf{I}$, the nuclear and electronic systems can exchange energy under conservation of total angular momentum; (2) its contribution to the electronic relaxation process is a minor one, because, as is well known, the most probable electronic relaxation process comes from the interaction of the electron spin with the lattice vibrations; but it certainly is responsible for practically the entire heat-contact of the nuclear spins with the crystal. This is seen, for example, from the fact that the very long nuclear relaxation times found in pure diamagnetic crystals are greatly reduced[2] by small amounts of paramagnetic impurities; (3) in the processes of spin-exchange between nucleus and electron the energy can be conserved by a simultaneous absorption or emission of a lattice quantum $2\mu_0 H$; (4) the difference in the *a priori* probabilities of absorption (increase of magnetic energy of the electron) and emission comes from from the fact that these probabilities are proportional to $\nu$ and $\nu+1$, respectively, where $\nu$ is the number of lattice quanta of magnitude $2\mu_0 H$ present at the temperature $T$, which is given by the Bose-Einstein distribution law.

An upper limit for the resulting nuclear orientation can be obtained as follows: In the equilibrium state in an external magnetic field in the absence of electron resonance radiation, we have

$$|a|^2 n_+ N_m(\nu+1) = |a|^2 n_- N_{m+1}\nu; \tag{1}$$

here $n_\pm$ are the occupation probabilities for the electronic spin states (we assume an effective spin 1/2 for simplicity) in thermal equilibrium, $n_\pm = \exp(\mp\mu_0 H/kT)$; $N_m = \exp(-2m\mu_n H/kTI) \approx 1$ are the corresponding quantities for the nucleus with spin $I$, and $\nu$ is the number of excited lattice vibrations of magnitude $2\mu_0 H$; and $|a|^2$ is a combination of matrix elements for this transition. Equation (1) expresses the principle of detailed balancing. In the steady state formed under constant absorption of resonance radiation, we can write, when all other relaxation processes for the nucleus can be neglected,

$$|a|^2 n_+' N_m'(\nu'+1) = |a|^2 n_-' N_{m+1}'\nu', \tag{2}$$

where the primed quantities are those reached in the steady state. Equation (2) is the condition for a steady state in this case. Under the assumption that (a) the electron resonance is completely saturated ($n_+' = n_-'$) and (b) the lattice-lattice relaxation time is so short that we can put $\nu' = \nu$, we find, from (1) and (2):

$$N_m'/N_{m+1}' = n_+/n_-, \tag{3}$$

i.e., the nuclei are orientated at the temperature $T$ to the extent as if they had a magnetic moment $\mu_0 I$. In view of the small mutual interaction of lattice vibrations, the validity of $\nu' = \nu$ is doubtful if the temperature is low; it would then perhaps only be approximated in *dilute* paramagnetic salts. At high temperatures the Raman-type process between the electron spin and lattice vibrations eliminates this difficulty, but then, of course, the nuclear orientation is always small. This limiting value[3] is the same as that obtained by Overhauser in the case of metals; a small energy leak for the nucleus, a shift in the distribution of lattice quanta, or an only partial saturation may decrease this orientation.

This nuclear orientation should be detectable by a narrowing and shift of the electron resonance line near saturation if the width of that line is predominantly produced by the interaction with the nucleus. If, in a dilute salt, the hfs is resolved, a change of the relative intensities of the components may be expected. Whether direct detection could be made by measuring the nuclear resonance absorption in the paramagnetic ion, depends on the rate of energy-exchange between the electron and the nucleus. The time average of the diagonal part of the interaction, i.e., the effective internal field for the nucleus, would be reduced to zero by saturation. This possibility of varying the internal field might be useful experimentally.

*Note added in proof:* After this manuscript was submitted, it was brought to my attention that a similar suggestion has been made independently by F. Bloch at the Stanford Meeting [Phys. Rev. **93**, 944 (1954); see also Physics Today, April 1954, p. 30] and by A. W. Overhauser at the New York Meeting [Phys. Rev. **94**, 768 (1954)].

[1] A. W. Overhauser, Phys. Rev. **92**, 411 (1953).
[2] N. Bloemberger, Physica **15**, 386 (1949).
[3] J. H. Van Vleck, Phys. Rev. **59**, 724 (1941).

## Electron Resonance in *F* Centers

J. KORRINGA
*The Ohio State University, Columbus, Ohio*
(Received March 25, 1954)

IN the preceding note attention has been drawn to the possibility of nuclear orientation by saturation of the electron resonance in paramagnetic salts. An application of particular interest is offered by the electrons of $F$ centers in alkali halides. As a paramagnetic substance it is very dilute; therefore, the lattice oscillators will have the equilibrium distribution at low temperatures also, and the electron resonance line width is mainly due to the interaction with the 6 neighboring alkali nuclei. In this case the process of nuclear orientation is more complicated because it involves two different relaxation times. According to Kip and co-workers,[1] the interaction between the electron and the nuclei is given by $\alpha(\boldsymbol{\sigma}\cdot\Sigma\mathbf{I}_i)$, where $\boldsymbol{\sigma}$ is the electronic spin and $\mathbf{I}_i (i=1\cdots6)$ are the nuclear spins. Clearly, in any process due to

this operator the absolute value of the total nuclear angular momentum, $|\Sigma \mathbf{I}_i|$, is conserved. Therefore, instead of the orientation $N_m'/N_{m-1}' = n_-/n_+$ of the individual nuclei (see the preceding note), one obtains an orientation in which each of the nuclear states with well-defined value of $(\Sigma \mathbf{I}_i)^2$ is oriented, with conservation, however, of their statistical weights found in thermal equilibrium. There are, of course, processes that may cause a change $\Delta|\Sigma \mathbf{I}_i| = \pm 1$, but these are due to corrections to the previously mentioned interaction, and therefore are much less probable. One possibility is a nuclear spin exchange back and forth with the neighboring alkali nuclei not belonging to the $F$ center. Another effect, which might be more important, is produced by a deformation of the $F$ center of static nature or due to thermal or zero point vibrations, which cause slight differences of the coupling constants, $\alpha(1+\delta_i)$ of the electron with the nuclei. The relaxation time corresponding to a transition from the original partial orientation to the orientation of the individual nuclei is proportional to $1/(\delta^2)_{Av}$, and can be of the order of seconds instead of microseconds. Inversely, if the electron resonance radiation causing saturation is suddenly decreased in intensity, first an isotropic distribution of nuclear spin states of predominantly the largest $|\Sigma \mathbf{I}_i|$-value is obtained, which then changes gradually into the equilibrium distribution. If the second relaxation time is microscopically long, one could observe this phenomenon in different ways, for example by first saturating the electron system and then observing resonance absorption under small amplitude. Then $(2I_{\max}+1)$ lines would appear with approximately equal intensity (provided $\mu_0 H/kT$ is not too small), and this pattern would gradually change into the conventional Gaussian line corresponding to random nuclear orientation. Perhaps the 19 equidistant and equi-intense lines observed by Schneider[2] in the hfs of $F$ centers in LiF could be explained in terms of this or a similar process. A promising possibility for observing the nuclear orientation is offered by the spin exchange with neighboring alkali nuclei, which has been mentioned already. By this process the nuclear orientation diffuses into the space between the $F$ centers, where a direct observation by nuclear resonance is not limited by the perturbation from the electron.

[1] Kip, Kittel, Levy, and Portis, Phys. Rev. 91, 1066 (1953).
[2] E. E. Schneider (private communication).

## Diffusion of Lattice Defects in a Temperature Gradient

ROBERT W. KEYES
*Westinghouse Research Laboratories, East Pittsburgh, Pennsylvania*
(Received March 31, 1954)

SHOCKLEY[1] has recently pointed out that in a crystal in which there is a temperature gradient there is also a gradient in the concentration of lattice defects, and that observable macroscopic deformation may result from the flow of defects due to this concentration gradient. Le Claire[2] and Brinkman[3] have called attention to another driving force acting on the defects, that due to the interaction between the flow of heat toward low temperatures and the flow of vacancies, but comment by Shockley[4] shows that they have used an incorrect interpretation of the heat of transport. The purpose of the present communication is to adapt existing treatments of the Kirkendall effect to a detailed comparison of the statistical and thermodynamic interpretations of the phenomenon discussed by these authors and thereby to relate the heat of transport to some statistically significant quantities.

Seitz[5] has made a statistical analysis of the Kirkendall effect; we replace his concentration-dependent functions by temperature-dependent ones and use a similar notation: Let $p(T_1,T_2)$ = probability per unit time that a vacancy on plane 1, where the temperature is $T_1$, changes places with an atom on an adjacent plane, 2, where the temperature is $T_2$. Then the result for the vacancy current, analogous to that obtained by Seitz, is

$$J_v = -p\lambda^2 \frac{dN_v}{dx} + N_v\lambda^2\left(\frac{\partial p}{\partial s} - \frac{\partial p}{\partial r}\right)\frac{dT}{dX}, \tag{1}$$

where $x$ = distance measured perpendicular to the planes in question, $\lambda$ = interplanar spacing, $N_v$ = mean volume density of vacancies, $T$ = average temperature, $p = p(T,T)$, and $\partial p/\partial s$ and $\partial p/\partial r$ are the derivatives of $p(r,s)$ evaluated at $r = s = T$.

The thermodynamic treatment[6] of the Kirkendall effect can also be adapted to the present problem. In a pure substance, if the currents of atoms, vacancies, and energy are written in terms of the gradients of chemical potentials and temperature,[7] and the condition of conservation of lattice sites is applied,[8] it is found that

$$J_v = M_{vv} T \frac{d}{dx}\left(\frac{\mu_v - \mu_l}{T}\right) - M_{vu}\frac{1}{T}\frac{dT}{dx},$$

$$J_u = M_{vu} T \frac{d}{dx}\left(\frac{\mu_v - \mu_l}{T}\right) - M_{uu}\frac{1}{T}\frac{dT}{dx},$$

where the subscript $v$ refers to vacancies, $u$ to energy, and $l$ to atoms of the crystal. The potential $\mu_v$ is the free energy required to remove an atom from the interior to the surface, leaving a vacant site, and $\mu_v - \mu_l$ is the free energy of (crystal of $N$ atoms and $N_v$ vacancies plus one atom at rest far removed from the crystal) minus the free energy of (crystal of $N+1$ atoms and $N_v - 1$ vacancies). The quantity $M_{vu}/M_{vv}$ is the energy of transport, $q$.[7]

The thermodynamic force, $T(d/dx)[(\mu_v - \mu_l)/T]$, can be rewritten as

$$T\frac{d}{dx}\left(\frac{\mu_v - \mu_l}{T}\right) = \frac{\partial}{\partial N_v}\left(\frac{\mu_v - \mu_l}{T}\right)\frac{dN_v}{dx} + T\frac{\partial}{\partial T}\left(\frac{\mu_v - \mu_l}{T}\right)\frac{dT}{dx}.$$

For small concentrations of vacancies the only contribution to the first term is that due to the entropy of mixing. The coefficient of $dT/dx$ is $-h/T$, where $h$ is the enthalpy part of $\mu_v - \mu_l$. Thus,

$$J_v = -M_{vv}\frac{kT}{N_v}\frac{dN_v}{dx} + M_{vv}(h-q)\frac{1}{T}\frac{dT}{dx}. \tag{2}$$

Comparing this with Eq. (1), it is seen that $M_{vv}kT/N_v = p\lambda^2 = D_v$, the usual expression for the diffusion coefficient, and

$$\frac{M_{vv}}{T}(h-q) = N_v\lambda^2\left(\frac{\partial p}{\partial s} - \frac{\partial p}{\partial r}\right),$$

or

$$q = h - \frac{kT^2}{p}\left(\frac{\partial p}{\partial s} - \frac{\partial p}{\partial r}\right).$$

Thus, in addition to $h$, $q$ includes a "heat of transport," $q^* = -(kT^2/p)(\partial p/\partial s - \partial p/\partial r)$, and Eq. (2) can be written in terms of $q^*$ and $D_v$:

$$J_v = -D_v\frac{dN_v}{dx} - D_v\frac{N_v}{kT^2}q^*\frac{dT}{dx}. \tag{3}$$

The first term of Eqs. (1), (2), and (3) is that originally envisaged by Shockley and ordinarily leads to a flow of vacancies toward low-temperature regions. The direction of the flow due to the second term depends on $q^*$; not even the sign of this quantity can be deduced from available experimental data. According to a model suggested by Wirtz,[8] $p$ should be written as

$$p(T_1,T_2) = p_0 \exp\left(-\frac{q_1}{T_1} - \frac{q_{1,2}}{\frac{1}{2}(T_1+T_2)} - \frac{q_2}{T_2}\right),$$

where $q_1$, $q_{1,2}$, and $q_2$ are the energies supplied at temperatures $T_1$, $\frac{1}{2}(T_1+T_2)$, and $T_2$, respectively. This leads to $q^* = q_1 - q_2$, whereas the activation energy for motion of a defect is $q_1 + q_{1,2} + q_2$.

[1] W. Shockley, Phys. Rev. 91, 1563 (1953).
[2] A. D. Le Claire, Phys. Rev. 93, 344 (1954).
[3] J. A. Brinkman, Phys. Rev. 93, 345 (1954).
[4] W. Shockley, Phys. Rev. 93, 345 (1954).
[5] F. Seitz, Acta Cryst. 3, 355 (1950); Acta Met. 1, 355 (1953).
[6] J. Bardeen and C. Herring, *Atom Movements* (American Society for Metals, Cleveland, 1951).
[7] K. Denbigh, *Thermodynamics of the Steady State* (Methuen and Company, Ltd., London, 1951).
[8] K. Wirtz, Physik. Z. 44, 221 (1943).

## Effect of Plastic Flow upon Color Centers in Alkali Halide Crystals*

MASAYASU UETA AND WERNER KÄNZIG
*Department of Physics, University of Illinois, Urbana, Illinois*
(Received April 7, 1954)

GYULAI and Hartly[1] found an enhancement of charge drift in NaCl when the crystal was deformed plastically. Seitz[2] has interpreted this effect in terms of an electrolytic current associated with the generation of positive- and negative-ion vacancies during plastic flow. He estimated that a vacancy concentration of approximately $10^{18}$ per cc was produced by a strain of ten percent. On the other hand it is well known that isolated negative-ion vacancies and simple clusters of vacancies can trap electrons to form $F$ and other centers; e.g.,

the $F'$ center, a negative-ion vacancy+two electrons;
the $M$ center, and $F$ center+one pair of vacancies;
the $R$ centers, two negative-ion vacancies+one or two electrons.

One expects, therefore, that plastic flow will affect the absorption spectrum of a crystal containing color centers. We have found that the yellow color of a NaCl crystal containing $F$ centers changes to blue after plastic deformation and simultaneous exposure to white light, whereas the undeformed crystal maintains its coloration for a long time. The change of color occurs more quickly the greater the magnitude of the plastic deformation. This effect has been investigated in the following experiments.

In a synthetic (Harshaw) NaCl crystal, $F$ centers were produced electrolytically with a concentration of about $3\times10^{16}$ per cc. The crystal was then irradiated with intense blue light through a filter, the transmission maximum of which coincided approximately with the $F$-absorption maximum, until the growth of the $M$ and $R$ bands ceased. (Curve $I$ in Fig. 1, measured at room temperature.) Then the crystal was subjected at room temperature to a plastic strain of six percent under a red light. No observable change in the absorption bands occurred after this treatment. However, if the deformed crystal was irradiated with $F$ light, the $F$ band bleached rapidly and the $M$ and $R$ bands were enhanced. Curves $IIa$ and $IIb$, measured at room and liquid $N_2$ temperature, respectively, illustrate this effect. After further irradiation curves $IIIa$ and $IIIb$ were obtained. Complete bleaching of $F$ centers was possible by prolonged irradiation with $F$ light. This indicates that vacancies are generated by the plastic flow and that their concentration is larger than that of the original $F$ centers.

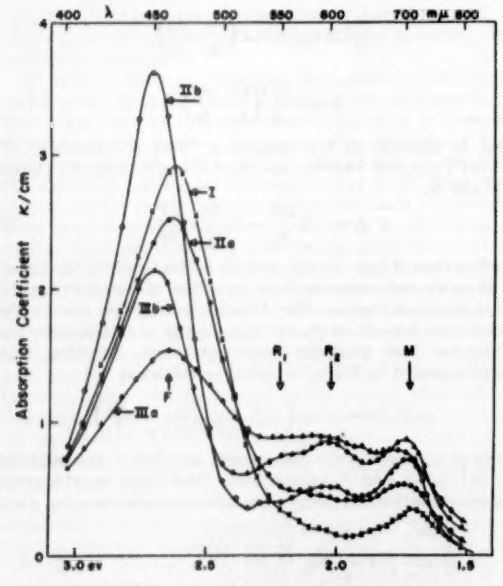


FIG. 1. Optical bleaching of $F$ centers in NaCl crystal after plastic deformation. Curve $I$: absorption spectrum of the crystal previous to $F$ light irradiation. Curve $II$: after two hours irradiation with $F$ light. Curve $III$: after further four hours irradiation with $F$ light. $a$, $b$ indicate the measurements at room and liquid $N_2$ temperature, respectively.

Somewhat different results were obtained if the crystal (irradiated at room temperature with blue light as before) was subjected to plastic flow at liquid $N_2$ temperature and kept at this temperature. Complete bleaching of the $F$ band could not be obtained by irradiation of $F$ light under these circumstances.

The observed partial bleaching of the $F$ band was accompanied by the formation of $F'$ centers in this case and no enhancement of the $M$ and $R$ bands occurred. If the crystal was warmed to room temperature in the dark, however, a slight enhancement of the $M$ band was observed. Subsequent irradiation at this temperature with $F$ light produced the same effect as in a crystal deformed at room temperature. Hence it appears that the vacancy aggregates generated by the plastic flow at low temperature do not act as effective traps for electrons released optically from the $F$ center. After the warming up, the vacancy aggregates decompose and migrate.

More quantitative experiments with NaCl and KCl crystals containing different concentrations of $F$ centers will be carried out with different magnitudes of plastic deformation.

The authors are indebted to Professor R. J. Maurer and Professor F. Seitz for many stimulating discussions during the course of this work.

* Partially supported by the U. S. Office of Naval Research.
[1] Z. Gyulai and D. Hartly, Z. Physik **51**, 378 (1928).
[2] F. Seitz, Phys. Rev. **80**, 239 (1950).

## Superconductivity of Pure Metallic Rhenium

JOHN K. HULM
*Institute for the Study of Metals, The University of Chicago, Chicago, Illinois*
(Received April 1, 1954)

THE occurrence of superconductivity in rhenium was first reported by Aschermann and Justi,[1] who observed a sharp drop in the electrical resistance of a sintered rhenium rod at about 0.95°K. In later measurements upon rhenium powder Goodman[2] and Daunt and Smith[3] found magnetic evidence for the onset of superconductivity in the neighborhood of 2.4°K. In view of the discrepancy between the sintered rod and powder results, it was thought to be worth while to prepare a solid rod of metallic rhenium so that reliable data could be obtained on the superconducting transition temperature and other superconducting properties of the bulk metal. We have, therefore, fabricated a rhenium rod of length 2 inches and of diameter $\frac{1}{4}$ inch by zone-melting compressed rhenium powder[4] in an argon arc furnace. Spectrographic analysis of this rod indicated that the total impurity content was less than 0.01 percent; the high purity of the material may also be judged from its residual resistance value, which was only 0.00068 of the ice-point resistance.

Both electrical resistance and magnetic induction measurements indicated that the pure rhenium rod became superconducting at 1.699°K. Below this temperature the destruction of superconductivity by a magnetic field occurred quite sharply at well-defined values of the field strength which could be represented by the equation

$$H_c = 188[1-(T/1.699)^2] \text{ oersteds.} \quad (1)$$

At the lowest temperature, 1.16°K, the induction rose to about 95 percent of the normal value just above the critical field strength, and the removal of a field of about five times the critical value caused the expulsion of more than 99 percent flux. This tendency of rhenium to exhibit nearly ideal superconducting behavior is

interesting in view of the fact that the nearby superconducting transition metals, vanadium, niobium, and tantalum, usually exhibit very broad magnetic field transitions unless great care is taken to avoid contamination of these metals by small amounts of nitrogen and oxygen.[5,6] The absence of such effects in rhenium may perhaps be due to the low solubility of nitrogen and oxygen in this metal; it may be noted that rhenium has a close-packed hexagonal structure in contrast to the more open, body-centered cubic structure of the group 5A metals.

In comparing the present data with previous results, it seems possible that the low transition temperature (0.95°K) reported by Aschermann and Justi may have been due to chemical impurities in their sintered rod, as evidenced by a rather high residual resistance, 0.017 of the ice-point value. However, the somewhat high transition temperature (2.4°K) reported for the powder specimens cannot be attributed to chemical impurities, as the materials were believed to be spectroscopically pure. In seeking the origin of this anomalous behavior, we have observed that untreated rhenium powder samples received from the University of Tennessee (reduced from ammonium perrhenate) undergo a superconducting transition which is spread out over the range from 2.4°K down to 1.7°K. However, after such samples have been compressed and heated for 12 hours at 1460°C, the entire superconducting transition takes place between 1.8° and 1.7°K, in good agreement with the behavior of the bulk metal. It seems likely that these effects are due to the existence in the untreated rhenium powder of appreciable amounts of very finely divided metal with transition temperatures higher than that of bulk rhenium, perhaps for reasons similar to those responsible for the elevated transition temperatures found by Buckel and Hilsch[7] for thin films of tin condensed at low temperatures. The occurrence of such finely divided metal is possible because of the low temperature at which the ammonium perrhenate reduction takes place, 300°C, well below the melting temperature of rhenium, 3170°C. Annealing at quite high temperatures is necessary to permit the aggregation of metal fragments and the removal of imperfections so that crystals are produced with superconducting transition temperatures close to that of bulk rhenium.

I am grateful to H. Charbnau and S. Foldes for assisting in the fabrication of the rhenium rod. A detailed account of the work will be published later.

[1] G. Aschermann and E. Justi, Physik. Z. **43**, 207 (1942).
[2] B. B. Goodman, Natl. Bur. Standards Circ. 519 (U. S. Government Printing Office, Washington, D. C., 1952), p. 72.
[3] J. G. Daunt and T. S. Smith, Phys. Rev. **88**, 309 (1952).
[4] Obtained from Professor A. D. Melaven, University of Tennessee.
[5] A. Wexler and W. S. Corak, Phys. Rev. **85**, 85 (1952).
[6] H. Preston-Thomas, Phys. Rev. **88**, 325 (1952).
[7] W. Buckel and R. Hilsch, Z. Physik **132**, 420 (1952).

## Localized Perturbations*

MELVIN LAX
*Physics Department, Syracuse University, Syracuse, New York*
(Received April 15, 1954)

THERE are many problems in physics characterized by a strong local perturbation on an otherwise solvable problem. One such problem that has been treated by Smith and the author is the vibration of a lattice in the neighborhood of an impurity center.[1] More recently, Slater[2] has treated the problem of electronic impurity levels using difference equations. Since many other applications are possible, it seems worthwhile to present the procedure used to solve such problems in its most general and abstract form.

We are required to find the eigenvector $x$ and eigenvalues $\lambda$ of the matrix $A+b$:

$$\Sigma_j(A+b)_{ij}x_j=\lambda x_i, \tag{1}$$

where the matrix $A=A_{ij}$ has elements $i, j=1, 2, \cdots N$, and all elements of the matrix $b_{ij}$ vanish except $b_{rs}$ for $r, s=1, 2, \cdots k$. It is assumed that the eigenvectors $S_p$ and eigenvalues $E(p)$ of $A$ are known:

$$\Sigma_j A_{ij}S_{jp}=E(p)S_{ip}. \tag{2}$$

Equation (1) can be rewritten in the form $x=(\lambda-A)^{-1}bx$, or

$$x_i=\sum_{r,s}(\lambda-A)^{-1}_{ir}b_{rs}x_s, \tag{3}$$

expressing all elements $x_i$ of the eigenvector in terms of the few components $x_s$ associated with the localized perturbation. The latter components may be obtained by specializing $i$ to any of the values $1, 2, \cdots k$ and solving $k$ equations in $k$ unknowns—a problem whose order is small if the perturbation is localized.

The reciprocal matrix elements in (3) can be obtained from (2) by regarding $S$ as the matrix of a similarity transformation

$$\begin{aligned}(\lambda-A)^{-1}_{ij}&=[S(\lambda-E)^{-1}S^{-1}]_{ij}\\&=\Sigma_p S_{ip}[\lambda-E(p)]^{-1}(S^{-1})_{pj}\\&=\Sigma_p S_{ip}S_{jp}^*/[\lambda-E(p)].\end{aligned} \tag{4}$$

In the last part of (4) we have utilized the fact that $S$ will be unitary if $A$ is Hermitian.

A particularly simple special case arises if the matrix $b$ has only one nonvanishing element

$$b_{ij}=b_0\delta_{i0}\delta_{j0}. \tag{5}$$

This case has particular usefulness for the vibration of a lattice one of whose atoms differs in mass from that of a pure lattice. In this case the $k\times k$ problem reduces to a single equation obtained from (3) by setting $i=0$ (and cancelling $x_0$):

$$1=b_0\Sigma_p|S_{0p}|^2/[\lambda-E(p)]. \tag{6}$$

If the matrix $A$ is cyclic, then $S$ will have Bloch form,

$$S_{jp}=N^{-\frac{1}{2}}\exp(i\mathbf{p}\cdot\mathbf{R}_j), \tag{7}$$

where $\mathbf{R}_j$ is the position of atom $j$ in the lattice. For this cyclic case, Eqs. (4) and (6) reduce to those obtained by Slater.

Equation (6) can be rationalized to an algebraic equation of degree $N$ for $\lambda$. The $N$ roots for $\lambda$ will interlace the unperturbed roots $E(p)$. For positive $b_0$, each $\lambda$ will exceed the corresponding $E(p)$, but not the next higher $E(p)$. The largest $\lambda$ is not limited, however, and can separate from the other roots if $b_0$ is large enough. For the calculation of a separated root the sum in (6) can be replaced by an integral.

Each intermediate eigenvalue will differ by an amount of order $N^{-1}$ from one $E(p)$. Thus one term in the sum (6) will be of finite size. Since unperturbed eigenvalues neighboring to $E(p)$ will differ from it by an amount of order $N^{-1}$ in three dimensions and $N^{-\frac{1}{2}}$ in two dimensions, the neighboring terms in the sum will all be infinitesimal. It will therefore be possible to replace (6) by an isolated term plus a principal-valued integral. This procedure is similar to that used in the spherical-model saddle-point condition.[3]

In one dimension, the eigenvalue separation is of order $N^{-1}$, so that if $\lambda$ differs from one eigenvalue $E(p_1)$ by an amount of order $O(N^{-1})$ its distance from the neighboring eigenvalues is similar. This difficulty may be overcome by considering separately the contributions to the sum for which $|p-p_1|>N^{-\frac{1}{2}}$ and for which $|p-p_1|<N^{-\frac{1}{2}}$. The former contribution may be replaced by a principal-valued integral since a symmetric interval about $p_1$ is excluded, and the terms now vary sufficiently slowly for the sum to be replaced by an integral. The latter contribution must be handled as a sum, but only the properties of $E(p)$ in the neighborhood of $p_1$ are involved. The number of terms in this sum (of order $N^{\frac{1}{2}}$) can then be allowed to go to infinity. Equation (6) can, for one dimension, therefore be written:

$$(b_0)^{-1}=(2\pi)^{-1}\mathrm{P}\int_0^{2\pi}\frac{dp}{E(p_1)-E(p)}+\frac{N|S_{0p_1}|^2\cot\pi\epsilon}{\pi dE/dp_1}, \tag{8}$$

where the eigenvalue $\lambda(p_1)$ has been written in the form

$$\lambda(p_1)=E(p_1+2\pi N^{-1}\epsilon), \tag{9}$$

so that $\epsilon$ is the fraction of the separation between $E(p_1)$ and the

next eigenvalue that $\lambda(p_1)$ has been shifted relative to $E(p_1)$. Since $\cot\pi\epsilon$ covers the range from infinity to zero as $\epsilon$ changes from zero to one-half, the eigenvalues are never shifted more than half an interval.

Application of the above techniques to vibrations of imperfect lattices will be discussed in more detail later.

* This research was supported in part by the United States Air Force, through the Office of Scientific Research of the Air Research and Development Command.

[1] J. M. Smith and M. Lax, Progress Report, August 1, 1953 (unpublished).

[2] J. C. Slater, Technical Report No. 5, Solid-State and Molecular Theory Group, Massachusetts Institute of Technology, December 15, 1953 (unpublished).

[3] M. Lax, J. Chem. Phys. **20**, 1351 (1952).

## Wave Functions for Impurity Levels*

G. F. Koster† and J. C. Slater
*Massachusetts Institute of Technology, Cambridge, Massachusetts*
(Received April 15, 1954)

UNDER the title above, a paper is being submitted to *The Physical Review*, containing material some of which has been presented in the unpublished Technical Report No. 5 of the Solid-State and Molecular Theory Group of Massachusetts Institute of Technology. Further material on the same subject will be incorporated in two further papers. These treat the technique of handling the motion of electrons in perturbed periodic lattices, by expanding the perturbed solutions in terms of Wannier functions, and setting up and solving the equations for the coefficients of the Wannier functions, which take the form of difference equations. Previous treatments of this problem[1] have usually approximated the difference equations by differential equations, thereby leading to the concept of an effective mass. This approximation, though sometimes satisfactory, is not rigorous, and we feel that the difference equation method is preferable.

Our attention has now been called by Professor Melvin Lax to the fact that he and a student of his, Mr. James H. Smith, of Syracuse University, have been independently using similar mathematical methods for handling problems in the vibrations of a lattice containing local impurities and imperfections. Lax describes these methods in an accompanying Letter to the Editor. The purpose of the present letter is merely to point out that our work, and that of Lax and Smith, were carried out independently, both leading to a mathematical technique which appears to have wide applicability, in problems of quantum theory of solids an in the mathematical theory of difference equations. The application to the vibrations of a lattice, which Lax and Smith are treating, had also occurred to us as a useful application of the method, but we have not made wide use of this application.

* Supported in part by the U. S. Office of Naval Research, in part by the Army, Navy, and Air Force.

† Staff Member, Lincoln Laboratory, Massachusetts Institute of Technology, Cambridge, Massachusetts.

[1] G. Wannier, Phys. Rev. **52**, 191 (1937); J. C. Slater, Phys. Rev. **76**, 1592 (1949); and various other papers. See, however, for instance, P. Feuer, Phys. Rev. **88**, 92 (1952), in which the difference equations are treated directly.

## Spin Resonance of Donors in Silicon

R. C. Fletcher, W. A. Yager, G. L. Pearson, A. N. Holden, W. T. Read, and F. R. Merritt
*Bell Telephone Laboratories, Murray Hill, New Jersey*
(Received April 15, 1954)

RESONANCE absorption believed associated with the spin of electrons bound to Group V donor atoms has been observed in several different samples of silicon. The absorption was measured on a Zeeman modulation spectrometer operating at a frequency of 24 000 Mc/sec. The samples were cut from single crystals in the form of bars 0.420 in.×0.170 in.×0.030 in. They were mounted on the narrow side of a rectangular resonant cavity kept at a temperature of 4.2°K.

The first resonances were observed in arsenic-doped silicon which had been plastically deformed by compression at 1000°C.[1] Four fairly sharp absorption lines (*ca* 10 oersteds between inflection points) appeared, equal in amplitude and spaced uniformly 73 oersteds apart. These are shown schematically in Fig. 1(a), (b), (c), where a line roughly indicating relative magnitude is plotted against its gyromagnetic ratio ($g$). The gyromagnetic ratio was determined by introducing diphenyl picryl hydrazyl into the system and comparing its resonance absorption line ($g=2.0036$[2]) with the newly observed lines.

These four lines did not appear in undoped silicon (10 ohm-cm, $p$ type at room temperature) either compressed or uncompressed. Neither did they appear in an arsenic-doped sample ($5\times10^{16}$ atoms/cm$^3$) which had not been compressed. In all of these samples, however, one weak line was observed with a $g\doteq2.006$, approximately coinciding with one of the four strong lines previously observed. This line was strongly affected by etching and is thus presumably associated with the crystal surface.

Four lines with the same separation and appearance as the ones described above have also been found in silicon in which the

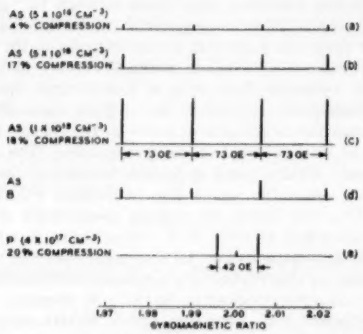


FIG. 1. The gyromagnetic ratio of the spin resonance absorption lines for various specimens of silicon.

arsenic donors have been compensated with boron acceptors [Fig. 1(d)]. In this sample the lines were fairly weak, and the line with $g=2.006$ was larger and broader than the other three. This is probably caused by the presence of the same single weak line observed in the control samples.

In this compensated crystal the lines only showed up in that part of the crystal where the arsenic concentration exceeded the boron concentration. In addition the four lines were observed in an uncompressed silicon sample with $10^{18}$ arsenic atoms/cc. These observations lead us to believe that the lines are associated with neutral arsenic atoms. Why the compression enhances the lines is not understood.

The presence of four lines associated with arsenic strongly suggests that this is hyperfine structure caused by the $As^{75}$ nucleus of spin 3/2. In order to verify this suggestion, phosphorus was used to replace the arsenic as the donor material. Phosphorus has the single isotope $P^{31}$ with a nuclear spin of 1/2 and thus should give a twofold hyperfine splitting. A sample containing $4\times10^{17}$ cm$^{-3}$ phosphorus atoms was plastically deformed and measured. Two strong lines of about equal amplitude appeared with a separation of 42 oersteds [Fig. 1(e)]. This supports the interpretation that we are observing hyperfine splitting. In addition to the two strong lines there was a slight suggestion of a weak line midway between them, as shown in the figure. At the present time we are not certain whether this is real or not.

We have also examined $p$-type silicon with $10^{17}$ boron atoms/cc, both compressed and uncompressed. No lines were observed.

Aluminum-doped silicon ($3\times10^{17}$ atoms/cc) was similarly unproductive.

We are indebted to W. H. Brattain for stimulating discussion, to N. B. Hannay and E. D. Kolb for the special silicon crystals, and to P. Breidt and W. F. Flood for preparing the silicon samples.

[1] C. J. Gallagher, Phys. Rev. **88**, 721 (1952).
[2] Holden, Kittel, Merritt, and Yager, Phys. Rev. **77**, 147 (1950).

## Energy of the High-Lying Acceptor Level in Copper-Doped Germanium

J. F. Battey and R. M. Baum
*Electronics Division, Sylvania Electric Products, Ipswich, Massachusetts*
(Received April 5, 1954)

IN addition to the much investigated[1] level at about 0.037 ev above the valence band, it has been reported that copper introduces another higher-lying acceptor level[2] in the forbidden energy gap of germanium. If this is the case, the level should make itself very evident in Hall and resistivity data at room temperature and below if it can be arranged that the lower-lying level is substantially completely populated and the higher level is partially populated at these temperatures. This requires the Fermi level to be within a few $kT$ of the upper level and will lead to an exponential variation of carrier density in the temperature region where the carrier concentration of a sample doped only with Group III and Group V atoms is approximately constant.

This situation may be achieved by diffusing copper into an originally $n$-type sample of Group V impurity concentration $N_d$. If a density of copper atoms, $N_a$, between $\frac{1}{2}N_d$ and $N_d$ is introduced, the lower copper level will be entirely filled and the upper level partially filled with the Group V donor electrons. The solid solubility of copper in germanium as a function of temperature may be estimated from the work of Fuller and Struthers,[3] and Finn,[3] and the time necessary to achieve a reasonable approximation of solid solubility may be estimated from a knowledge of the diffusion coefficient as a function of temperature.[3]

The sample for which data are shown in Fig. 1 was $1.5\times0.58\times0.27$ cubic centimeters and had about $1.2\times10^{15}$ Group V donors per cc. It was copper plated, held at 630°C for about ten days in an argon atmosphere, then quenched rapidly to room temperature to try to introduce about $8\times10^{14}$ copper atoms/cc. Room-temperature measurement following this treatment showed the sample to be high-resistivity $p$ type.

The condition for electrical neutrality in this semiconductor at room temperature and below requires that $p+p_a=2N_a-N_d$, where $p$ is the hole density in the valence band and $p_a$ is the density of empty upper copper levels. This may be written as

$$N_v\exp[-(F-E_v)/kT]+N_a/\{1+\exp[(F-E_a)/kT]\}=2N_a-N_d,$$

where $N_v$ is the effective density of states in the valence band, $F$ is the Fermi energy level, $E_v$ is the energy of the top of the valence band, and $E_a$ is the upper copper energy level. For the sample measured $N_a\simeq8\times10^{14}$/cc, $2N_a-N_d\simeq4\times10^{14}$/cc, and at room temperature $p\simeq9\times10^{13}$/cc. Thus for values of $p$ smaller than the room-temperature value, the Fermi level should coincide with the upper copper level to within an energy of the order of $kT$, and $p=N_v\exp[-(E_a-E_v)/kT]$.

Hall and resistivity data are shown in Fig. 1. The curves exhibit a temperature dependence below the intrinsic range which is consistent with the premise of a partially populated level at about 0.3 ev above the valence band. Both Hall coefficient and resistivity curves show a very steep activation energy below room temperature where $F$ and $E_a$ coincide. Both curves go into the usual intrinsic line above room temperature, and the Hall curve exhibits a reversal of sign at about 355°K. The activation energy for the upper copper level is 0.304 ev from the Hall curve and 0.308 ev from the resistivity curve if other temperature dependences in these expressions are neglected. If it is assumed that $N_v$ goes as $T^{1.5}$, $\mu_H/\mu$ as $T^{0.5}$,[4] and $\mu$ as $T^{-2.3}$,[5] where $\mu$ is the drift mobility, and $\mu_H$ the Hall mobility, a plot of $\rho T^{-0.8}$ or $RT^{1.0}$ *versus* $1/T$ should be proportional to $\exp[(E_a-E_v)/kT]$. Using this procedure the Hall data give $E_a-E_v=0.285$ ev and the resistivity data $E_a-E_v=0.315$ ev.

The authors wish to give thanks to Robert Carye for help in preparation of the samples and taking of the data.

[1] See for instance F. J. Morin and J. P. Maita, Phys. Rev. **90**, 337 (1953); W. C. Dunlap, Bull. Am. Phys. Soc. **29**, No. 3, 21 (1954).
[2] W. Kaiser and H. Y. Fan, Phys. Rev. **93**, 977 (1954); J. A. Burton *et al.*, J. Phys. Chem. **57**, 853 (1953); W. C. Dunlap, Bull. Am. Phys. Soc. **29**, No. 3, 21 (1954).
[3] C. S. Fuller and J. D. Struthers, Phys. Rev. **87**, 526 (1952); G. B. Finn, Phys. Rev. **91**, 754 (1953).
[4] E. M. Conwell, Bull. Am. Phys. Soc. **29**, No. 3, 18 (1954).
[5] F. J. Morin, Phys. Rev. **93**, 62 (1954).

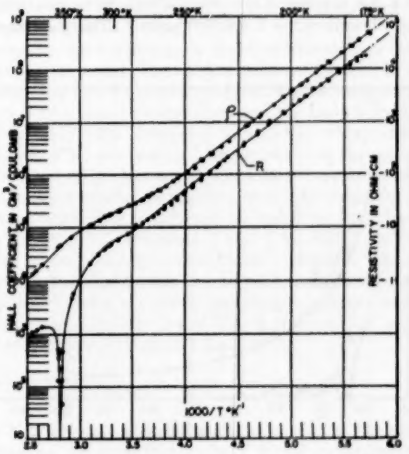


FIG. 1. Temperature dependence of Hall coefficient $R$ and resistivity $\rho$ for a germanium sample doped with $1.2\times10^{15}$ arsenic atoms per cc and approximately $8\times10^{14}$ copper atoms per cc.

## Doppler Line-Width Reduction*

M. W. P. Strandberg and H. Dreicer
*Research Laboratory of Electronics and Department of Physics, Massachusetts Institute of Technology, Cambridge, Massachusetts*
(Received April 13, 1954)

WE have succeeded in observing a large reduction in the Doppler width of a molecular absorption line by using a combination of microwave spectroscopic and molecular beam techniques.[1] This procedure, utilizing the effect of the matter on the electromagnetic radiation, solves the onerous detection problem encountered in the usual molecular beam experiments where the effect of the radiation on the matter is observed. The high resolution of molecular beam experiments afforded by the interaction of the radiation field and the transverse molecular beam is thus made available for microwave spectroscopic use.

In the exploratory study reported here the ammonia inversion absorption transition for the rotational state $J=3$, $K=3$ was observed with the microwave radiation propagated transverse to a beam of ammonia molecules. The radiation was detected and displayed by conventional techniques.[2] However, because of the resulting narrow line width the microwave oscillator was swept in saw-tooth fashion only over a region 80 kc/sec wide, centered at about 23 870 Mc/sec. Figure 1 shows the absorption signal of the

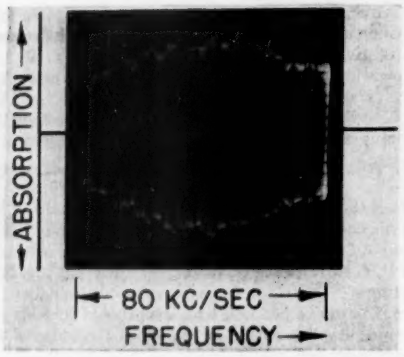


FIG. 1. The 23 870-Mc/sec $NH_3$ inversion absorption line exhibiting the limiting Doppler breadth with conventional observation ($2\Delta\nu = 72$ kc/sec).

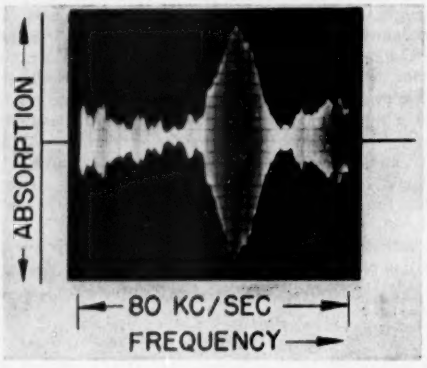


FIG. 2. The 23 870-Mc/sec $NH_3$ inversion absorption line exhibiting a large reduction in Doppler width from observation of a transverse beam.

ammonia inversion line ($J=3, K=3$) as observed in a conventional absorption cell of such dimensions and with the gas at such a pressure that essentially only the Doppler width ($\Delta\nu$ = half-power − half-width = 36 kc/sec) remains; i.e., the radiation is swept in frequency between the half-power absorption points. Figure 2 shows the simultaneous record of the absorption of the same radiation as observed transverse to an ammonia molecular beam of the same temperature. A reduction of the Doppler width by a factor of about six is apparent. Further line-width reduction will be accomplished in the future by available experimental means. The signal-to-noise ratio shown here is readily attained with a system noise band width of the order of 10 cps. An improved value for this transition frequency has not yet been obtained, since the possible precision afforded by this experimental arrangement is beyond our present frequency-determining facilities.

We feel that the use of these techniques will bring a large and new field of problems within the reach of microwave spectroscopic methods; e.g., spectra of the more refractory materials, the study of fine structure beyond present resolution, and the study of free radicals and substances of evanescent existence.

We wish to acknowledge the laboratory assistance of J. D. Kierstead.

* This work was supported in part by the U. S. Signal Corps, the U. S. Air Materiel Command, and the U. S. Office of Naval Research.

[1] For earlier work with different apparatus see H. R. Johnson and M. W. P. Strandberg, Phys. Rev. 85, 503 (1952).

[2] M. W. P. Strandberg, *Microwave Spectroscopy* (Methuen Publishing Company, London, 1954).

## Magnetothermoelectric Behavior of Bismuth at Liquid Helium Temperatures

M. C. STEELE AND J. BABISKIN
*United States Naval Research Laboratory, Washington, D. C.*
(Received April 15, 1954)

THE previously observed anomalous magnetic properties of bismuth at low temperatures[1-3] suggested that the thermoelectric properties of this metal be studied in a magnetic field. Such magnetothermoelectric measurements have now been made on a single crystal of bismuth.

The crystal was grown from Cerro de Pasco Copper Company bismuth (99.99 percent pure) in a furnace described by Schubnikow.[4] It was a cylinder 57 mm long and 1.7 mm in diameter. The distance between the bismuth-copper thermoelectric junctions was 47 mm. By cleaving the crystal it was found that the trigonal axis was parallel to the crystal length to within 1.5°. The measurements were taken with the magnetic field, $H$, perpendicular to the crystal length (and heat current). The binary axes were located from magnetoresistance measurements. Thermoelectric data were obtained for two orientations of the field relative to a binary axis, parallel and perpendicular. Because of the more complicated nature of the results for the perpendicular orientation (due to beats resulting from more than one oscillating term) only the data for the parallel orientation will be discussed in this paper. Figure 1 shows the results for $H$ parallel to a binary axis. The graph gives the thermoelectric voltage observed as a function of $H^{-1}$ for a constant temperature difference of 0.0055°K ±0.0002°K between junctions (mean temperature 4.379°K). Temperatures at both junctions were measured with carbon resistance thermometers[5] throughout the entire experiment. In order to depict the oscillatory nature of the thermoelectric voltage more clearly, the differences, $\delta$, between the experimental points and the envelope curve are shown at the bottom of Fig. 1. Positions for maxima and minima in $\delta$ are indicated by arrows on the graph. In Fig. 2 the values of $H^{-1}$ corresponding to these positions are plotted against integers. The resulting straight line indicates that the thermoelectric oscillations are periodic in $H^{-1}$ as are the magnetic susceptibility (de Haas-van Alphen effect),[1] magnetoresistance[2] and Hall Coefficient.[3] From the slope of the line in Fig. 2 we obtain a value of $7.3\times10^{-5}$ gauss$^{-1}$ for $\beta^*/E_0$ (where $\beta^*$ is the double effective Bohr magneton and $E_0$ is the Fermi energy for the de Haas-van Alphen electrons). The calculated value of $\beta^*/E_0$ (from susceptibility data) for an orientation with $H$ perpendicular to the trigonal axis and parallel to a binary axis (within a few degrees of our orientation), using the parameters given by Shoenberg,[6] is $7.1\times10^{-5}$ gauss$^{-1}$. The good agreement

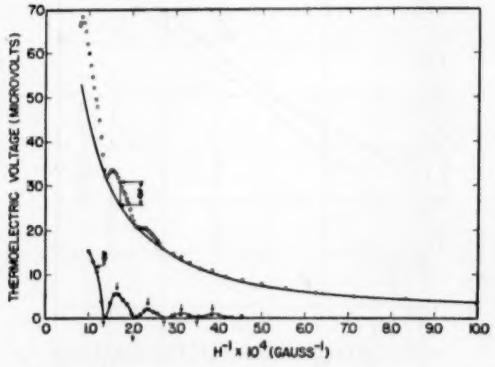


FIG. 1. Thermoelectric voltage of a bismuth single crystal as a function of $H^{-1}$ for a temperature difference of 0.0055°K between bismuth-copper junctions (mean temperature of 4.379°K). $\delta$ is the difference between the experimental points and the solid curve.

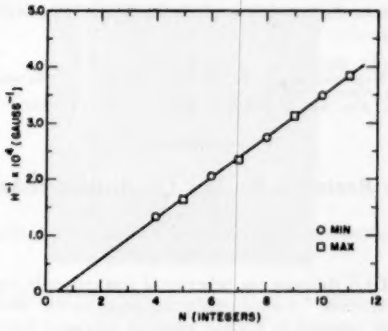


FIG. 2. Values of $H^{-1}$ corresponding to maxima and maxima and minima of $\delta$, plotted against integers.

between the two values of $\beta^*/E_0$ is further evidence for a one-to-one correspondence between the various magneto-oscillatory effects in bismuth.

Further work is in progress and will be reported in a later date. We wish to acknowledge the benefit of discussions with Dr. T. G. Berlincourt.

[1] D. Shoenberg, Proc. Roy. Soc. (London) **A170**, 341 (1939).
[2] P. B. Alers and R. T. Webber, Phys. Rev. **91**, 1060 (1953).
[3] Reynolds, Leinhardt, and Hemstreet, Phys. Rev. **93**, 247 (1954).
[4] L. W. Schubnikow, Proc. Koninkl. Ned. Akad. Wetenschap. **33**, 327 (1930); Leiden Comm. **207b**.
[5] J. R. Clement and E. H. Quinnell, Rev. Sci. Instr. **23**, 213 (1952).
[6] D. Shoenberg, Trans. Roy. Soc. (London) **A245**, 1 (1952).

## Multiphonon Transitions in the *F* Center

JORDAN J. MARKHAM
*Research Department, Zenith Radio Corporation, Chicago, Illinois*
(Received April 16, 1954)

KLICK[1] has shown that transitions from the excited state of an $F$ center to the ground state occur without photon emission. The possibility of that center transferring its energy to a close by foreign atom ("sensitized luminescence") seems slight since the crystals Klick used have no known appropriate activator. One seems forced to the conclusion that the system transfers its energy directly to the lattice by a spontaneous emission of about 50 phonons. This process must occur in less than $10^{-8}$ sec to suppress the emission of photons. At present the mechanism by which this process occurs is not understood.

The author has constructed a model to indicate how this multiphonon process occurs. The model consists of an electron attached to a vibrating ion. Transition probabilities between state $e$ (the electron is in a bound excited state and the ionic degrees of freedom have only their zero-point vibrational energy—this corresponding to 4°K) and state $g$ (the electron is in the ground state, and the ionic vibrations are excited) have been calculated. The results indicate relative probability of a single, double, triple$\cdots$ phonon process. This is achieved by assuming that the electron energy interval between state $e$ and $g$ increases, requiring the emission of one, then two, then three$\cdots$phonons. The model is sufficiently simplified so that one does not need special summation procedures.[2,3] Using the Born-Oppenheimer approximation, one may show the transition probability is governed by matrix elements of the type [reference 2 Eq. (15)]:

$$\int \zeta_{0e}\zeta_{ng}dX \quad \text{and} \quad \int \zeta_{0e}P_X\zeta_{ng}dX,$$

where $X$ is a degree of freedom of the ion; $\zeta_{ne}$ is the vibrational eigenfunction corresponding to the $X$ degree of freedom when the electron is in the excited state and the ion has the energy $(n+\frac{1}{2})h\nu_e$; $\zeta_{ng}$ is the corresponding function for the ground state; $P_X$ is the momentum operator corresponding to the $X$ degree of freedom; and $\nu_e$ is the ionic frequency in the excited state.

One might at first expect that these matrices restrict the absorption of energy per degree of freedom to zero or one phonon. This would be true if the frequency and rest position of the ion are independent of the electron state. Recently, Kubo[2] has indicated how the frequency changes with the electronic state. The equilibrium position also depends on the electronic distribution. For example, calculations on the self-trapped electrons[4] indicate that the nearest neighbors shift about 0.05 A during the trapping process. The average zero-point displacement of an ion is about 0.04 A. Since the rest position and frequency do depend on the electronic state, a degree of freedom can absorb more than one phonon.

One would like to know if 1 ev of energy, about 50 phonons, could be absorbed rapidly by the lattice when the electron jumps from the excited state to the ground state. Kubo's frequency shift alone does not explain Klick's observation. The equilibrium position shift, however, seems to. In our model we have artificially displaced the "central ion" (which actually does not exist in an $F$ center) instead of the neighboring ions. A 10-phonon process is more rapid than a single-phonon process. The model does not give an absolute life time for the process. If one assumes that single-phonon processes occur in $10^{-12}$ sec, one would expect from the calculation that a process involving up to 50 phonons might occur more rapidly than a photon mission. As the energy gap between the $e$ and $g$ states increases, the probability of a multiphonon process eventually decreases, and for a large enough energy the system will emit a photon. The transition point cannot be estimated from this simple model.

Huang and Rhys's calculation of a multiphonon process disagrees with Klick's results and the calculations presented here. Due to the brevity of their paper, the author is not sure where the disagreement lies. Huang and Rhys attempt to calculate absolute rates (this, it seems, would require a more accurate model of the $F$ center than is available at present) and use a simplified summation procedure which neglects some important terms. Pekar[5] has calculated the Stokes' shift for Klick's experiment but he did not consider the competitive multiphonon process.

Details of the calculation will be submitted for publication in the near future. The author would like to thank Professor F. Seitz for several discussions of this problem, Dr. Klick for the detailed discussion of his results, and Mr. Clavier and Mr. Bronstein for help in the calculations.

[1] C. C. Klick, same issue [Phys. Rev. **94**, 1438 (1954)].
[2] R. Kubo, Phys. Rev. **86**, 929 (1952).
[3] K. Huang and A. Rhys, Proc. Roy. Soc. (London) **A204**, 406 (1950).
[4] J. J. Markham and F. Seitz, Phys. Rev. **74**, 1014 (1948).
[5] S. I. Pekar, J. Exptl. Theoret. Phys. (U.S.S.R.) **22**, 641 (1952).

## Existence of a $3.7\times10^{-8}$-sec Metastable State in $Pa^{233}$

D. ENGELKEMEIR AND L. B. MAGNUSSON
*Chemistry Division, Argonne National Laboratory, Lemont, Illinois*
(Received March 8, 1954)

A METASTABLE state of $Pa^{233}$ having a half-life of $3.69\pm0.04$ $\times10^{-8}$ sec has been observed by a study of delayed conversion electrons following the alpha decay of $Np^{237}$.

Stilbene scintillation counters were used as detectors. After amplification with Hewlett Packard 480A wide-band amplifiers, the pulses were shaped to 0.03-$\mu$sec duration with shorted delay lines and mixed in a coincidence circuit similar to that described by Garwin.[1] Pulse delay was accomplished by introducing measured lengths of 184-ohm cable (Transradio C.22) between the cathode follower preamplifier and the first amplifier. The velocity of propagation in this cable was found to be $0.91c$ ($1.12m$ $\mu$sec/ft) by measurement of the resonant frequencies of shorted cables. Single channel pulse-height analyzers driven by separate cathode

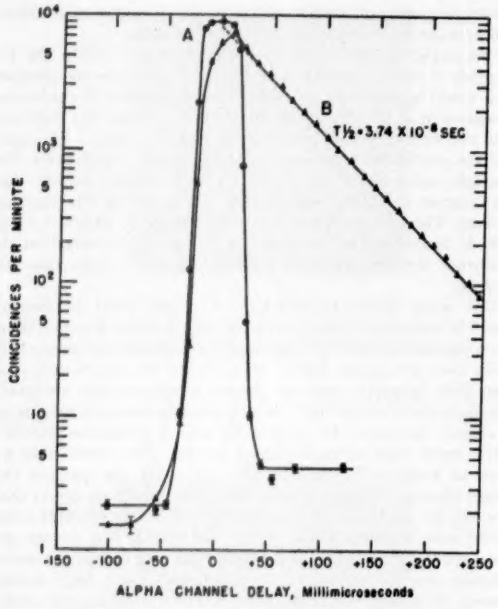


FIG. 1. Delay curve of $\alpha-e^-$ coincidences in $U^{234}$ ($A$) and $Np^{237}$ ($B$).

followers in the preamplifiers permitted the selection of alpha pulses from one detector and conversion electrons from the other. The discrimination against conversion electron pulses in the alpha detector was complete; however, some alpha pulses were counted by the conversion electron detector.

The $Np^{237}$ samples were separated from their 27.4-day $Pa^{233}$ daughter by solvent extraction and were evaporated onto plastic films 0.6 mg/cm² thick which were inserted between the two counters with the sample facing the conversion electron crystal. An aluminum light reflector 0.2 mg/cm² thick was located between the sample and the alpha counter. The delay curves were determined within one day after separation of the $Pa^{233}$.

Curve $A$, Fig. 1, is the delay curve for the prompt $U^{234}$ alpha-conversion electron coincidences. The limiting slope on the positive alpha delay side corresponds to a maximum half-life of $1.4\times10^{-9}$ sec. The delay curve for $Np^{237}$ is given by Curve $B$. The slope corresponds to a half-life of $3.74\times10^{-6}$ sec. The average half-life obtained from four such determinations was $3.69\pm0.04\times10^{-6}$ sec. The slight increase in slope near the peak of the curve is probably attributable to a small prompt coincidence contribution.

The energy of the metastable state in $Pa^{233}$ was not determined in these measurements since the energy resolution of a stilbene counter is very poor for low energy conversion electrons. Only a single broad peak with a maximum at 30 kev and extending up to 100 kev appears in the delayed coincidence spectrum. The energy of the metastable state may be inferred from measurements of the alpha-gamma coincidence spectrum now in progress,[3] which indicate that the most abundant level of $Pa^{233}$ populated by alpha decay is 87 kev above the ground state. Since few, if any, prompt coincidences or other periods are seen, the 87-kev level is probably the metastable level.

It is noteworthy that the half-life of $3.7\times10^{-6}$ sec observed here for the metastable state of $Pa^{233}$ is very similar to those found in $Np^{237}$ ($6.3\times10^{-6}$ sec)[3] and in $Ac^{227}$ ($4.2\times10^{-6}$ sec),[4] both of which are also odd-$Z$, odd-$A$ nuclides. In the latter two examples, the transition to the ground state is believed to be by electric dipole radiation.

[1] Richard L. Garwin, Rev. Sci. Instr. 24, 618 (1953).
[2] L. B. Magnusson and D. Engelkemeir, Phys. Rev. (to be published).
[3] Beling, Newton, and Rose, Phys. Rev. 87, 670 (1952).
[4] Teillac, Riou, and Desneiges, Compt. rend. 237, 41 (1953).

## "Slow Beats" in Nuclear Quadrupole Induction*

M. BLOOM
*Department of Physics, University of Illinois, Urbana, Illinois*
(Received April 15, 1954)

WHILE studying the behavior of spin echoes in quadrupole systems,[1,2] a phenomenon analogous to the "slow beats" previously reported in nuclear magnetic resonance has been observed. In nuclear magnetic resonance, the term "slow beats" refers to a periodic modulation of the echo envelope, the modulation frequencies being closely related to the splitting frequencies in the hyperfine structure of the resonance.

In nuclear quadrupole induction, a similar modulation of the echo envelope appears when a small magnetic field is applied. While the explanation of nuclear magnetic resonance "slow beats" required an interaction between neighboring nuclear spins, the "slow beats" thus far observed in quadrupole induction can be explained solely in terms of the splitting and mixing of the degenerate electric quadrupole energy levels by the interaction of the nuclear magnetic moment with the external magnetic field. By means of theory outlined previously,[1,2] it may be shown that for two rf pulses at the quadrupole resonant frequency separated by a time $\tau$, the voltage induced in the coil at $t=2\tau$ is given by

$$V(2\tau)\propto\sin(\Omega_1 t_\omega)\sin^2\left(\frac{\Omega_1 t_\omega}{2}\right)\left\{\frac{f^2+1}{2f^2}+\frac{f^2-1}{2f^2}[\cos(3\Omega_0\tau\cos\theta_0)+\cos(\Omega_0\tau f\cos\theta_0)+\cos(3\Omega_0\tau\cos\theta_0)\cos(\Omega_0\tau f\cos\theta_0)]\right\}$$

+terms identified with free induction signals following each of the pulses. Here $\Omega_1=\sqrt{3}\gamma H_1\sin\theta_1$; $\Omega_0=\gamma H_0$; $f=(1+4\tan^2\theta_0)^{\frac{1}{2}}$; $H_1$ and $H_0$ are the amplitudes of the rf and static magnetic fields, respectively; $\theta_1$ and $\theta_0$ are the angles they make with the symmetry axis of the electric field gradient $\nabla E$; $t_\omega$ is the duration of the pulses; $\gamma$ is the nuclear gyromagnetic ratio.

The identification of this expression as the echo was made by introducing in the theory a distribution of $|\nabla E|$ corresponding to a line width $\approx\Delta\omega$ and averaging the calculated signal over this distribution for $t\ll2\pi/\Delta\omega$. The distribution of $|\nabla E|$ therefore has the same function in quadrupole induction as an inhomogeneous magnetic field in magnetic induction.

The term independent of $\tau$ in Eq. (1) represents the ordinary echo studied by Hahn and Herzog[3] in $NaClO_3$. The other terms give rise to the "slow beats" and should decay with a time constant $\approx2\pi/\gamma H_{\text{loc}}$, where $H_{\text{loc}}$ is the average value of the internal magnetic fields at the nuclear sites. Note that these terms vanish

FIG. 1. Multiple exposure showing echo envelope for single crystal of $NaClO_3$. $H_0$ in (0,0,1) direction and equal to 15.5 gauss. Sweep length is 1500 μsec.

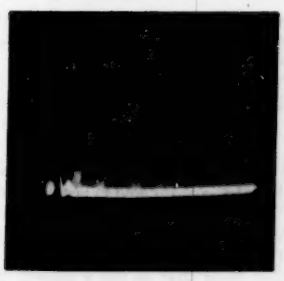

FIG. 2. $H_0$ in $(1/\sqrt{2},1/\sqrt{2},0)$ direction and equal to 15.5 gauss. Sweep length is 1500 μsec.

for $\theta_0=0$ or $\pi$. This corresponds to the condition that $H_0$ does not cause "mixing" of the $m=\pm\frac{1}{2}$ states so that the $+m$ and $-m$ states form two independent systems. An analogous system in nuclear magnetic resonance is that of two groups of identical nuclei, chemically shifted with respect to one another, but which do not interact with one another.

In order to verify the theory in detail, the $Cl^{35}$ quadrupole resonance in a single crystal of $NaClO_3$ was studied. A distribution of $|\nabla E|$ was artificially set up by introducing a temperature gradient across the sample. Otherwise, the induction signal from the first pulse would still have a large amplitude in the interesting region ($2\tau \lesssim 2\pi/\gamma H_{\text{loc}}$), since the natural line width is solely due to internal magnetic fields, causing the echo, which is randomly phased (for a pulsed oscillator) relative to the first induction decay, to flutter.

In applying Eq. (1) to $NaClO_3$, contributions from the four different directions of $\nabla E$ in the unit cell must be added. As shown previously,[1] $H_0$ and $H_1$ oriented along the (0,0,1) axis is the simplest case since the $\theta_0$'s for each of the $\nabla E$'s are identical. For this case, Eq. (1) predicts

$$V(2\tau) \propto (5/9)+(4/9)[2\cos(\sqrt{3}\gamma H_0\tau)+\cos^2(\sqrt{3}\gamma H_0\tau)],$$

which explains within experimental error the frequency of the "slow beats" shown in Fig. 1 and, approximately, the amplitudes if the term in square brackets is assumed to decay with a time constant $\approx 2\pi/\gamma H_{\text{loc}}$.

The more complicated echo envelope shown in Fig. 2, corresponding to $H_0$ along the $(1/\sqrt{2},1/\sqrt{2},0)$ axis, is also explained by Eq. (1) which predicts

$$V(2\tau) \propto (5/3)+[\cos(2\gamma H_0\tau)+\tfrac{1}{3}\{2\cos(\sqrt{2}\gamma H_0\tau)+\cos^2(\sqrt{2}\gamma H_0\tau)\}].$$

When a crystalline powder is used, the beat structure also persists for a time $\approx 2\pi/\gamma H_{\text{loc}}$, even though the electric field gradients are oriented at random angles to $H_0$. It is expected that a numerical integration over the complicated angular dependence will illustrate this. Figure 3 shows the slow beat in a crystalline powder of $NaClO_3$. The individual induction signals have a decay time $\approx 2\pi/\gamma H_0$, which is also the period of the slow beat here so that it is unnecessary to induce a temperature gradient in the sample in order to observe the effect. Similar patterns were observed in $CH_3CCl_3$, $(CH_3)_3CCl$, and $CHCl_3$.

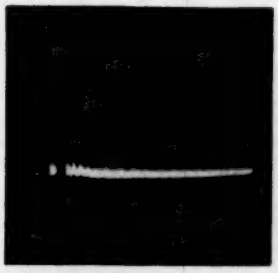

FIG. 3. Crystalline powder of $NaClO_3$. $H_0=15.5$ gauss. Sweep length is 1340 μsec.

I would like to thank Professor C. P. Slichter and Dr. R. E. Norberg for many helpful discussions during the course of this work and Dr. E. L. Hahn for valuable correspondence.

* Supported by the U. S. Office of Naval Research.

[1] M. Bloom and R. E. Norberg, Phys. Rev. **93**, 638 (1954).
[2] E. L. Hahn and B. Herzog, Phys. Rev. **93**, 639 (1954).
[3] McNeil, Slichter, and Gutowsky, Phys. Rev. **84**, 1245 (1951); E. L. Hahn and D. E. Maxwell, Phys. Rev. **84**, 1246 (1951); **88**, 1070 (1952).

## Interference of Rayleigh and Nuclear Thomson Scattering

A. M. CORMACK
*Physics Department, University of Cape Town, Rondebosch, Cape Town, South Africa*
(Received April 14, 1954)

THE differential cross sections $\sigma_T$ and $\sigma_R$ for elastic scattering of gamma rays by the nucleus (nuclear Thomson scattering), and by the atomic electrons (Rayleigh scattering) have been given and discussed by Moon.[1] Since both of these scattering processes are elastic, interference effects are to be expected, and calculations have been made to determine the effect of this interference on the combined differential cross section for the atom $\sigma_{R+T}$ for scattering by either the nucleus or by the electrons of the atom.

This combined cross section is given by (see Heitler[2])

$$\sigma_{R+T}(\theta)=\left(\frac{1+\cos^2\theta}{2}\right)\left|\left(\frac{e^2}{mc^2}\right)\int|\psi_e|^2\exp[i(\boldsymbol{\kappa}-\boldsymbol{\kappa}_0)\cdot\mathbf{R}_e]dv_e+\frac{Z^2e^2}{Mc^2}\exp[i(\boldsymbol{\kappa}-\boldsymbol{\kappa}_0)\cdot\mathbf{R}_n]\right|^2, \quad (1)$$

where the angle of scattering is $\theta$, $\boldsymbol{\kappa}_0$ and $\boldsymbol{\kappa}$ are the propagation vectors of the incident and scattered photons, $m$ and $M$ are the masses of the electron and the nucleus, and $\mathbf{R}_n$ and $\mathbf{R}_e$ are vectors to the nucleus and to a typical point of the electron distribution which has the wave function $\psi_e$. It has been assumed that the wavelength of the radiation is much larger than the dimensions of the nucleus. Taking the square moduli of the two terms separately gives $\sigma_R$ and $\sigma_T$, respectively. The matrix element for the Rayleigh scattering has been evaluated by Franz[3] assuming a Thomas-Fermi atom, and he finds that

$$\int|\psi_e|^2\exp[i(\boldsymbol{\kappa}-\boldsymbol{\kappa}_0)\cdot\mathbf{R}_e]dv_e=\frac{Z}{u}(\pi/2u)^{\frac{1}{2}}, \quad (2)$$

$$u=(5.86/\lambda Z^{\frac{1}{3}})\sin(\theta/2), \quad (3)$$

$\lambda$ being the wavelength of the radiation in angstroms. Equation (2) is valid for gamma-ray energies of up to a few Mev and for $Z<40$. For $Z>40$, relativity effects become noticeable but only amount to 16 percent for $Z=90$, so (2) will be adequate for the purpose in hand.

If $\psi_e$ is symmetrical about the nucleus and we write $\mathbf{R}_e=\mathbf{R}_n+\mathbf{r}$, then (1) gives

$$\sigma_{R+T}=\sigma_R+\sigma_T+2(\sigma_R\sigma_T)^{\frac{1}{2}}, \quad (4)$$

which represents the classical reinforcement of the two kinds of scattering, in agreement with a remark of Moon. If $\psi_e$ is not symmetrical about the nucleus, a phase term will occur within the modulus signs in (1), and this will give rise to an angle-dependent modification of (4) which represents classical destructive interference effects between the scattering processes. The curves given by Moon for $\sigma_R$ and $\sigma_T$ show that they are comparable in magnitude only at large scattering angles, and since, in addition, observations of these types of scattering would have to be made with a biased scintillation counter at large scat-

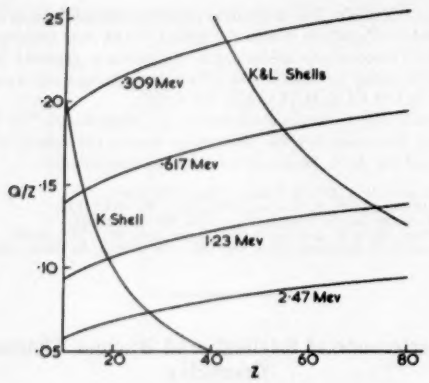


FIG. 1. The charge $Q$ contributing 90 percent of the Rayleigh scattering as a function of the atomic number $Z$ for various gamma-ray energies.

tering angles to eliminate the large background of inelastically scattered Compton gamma rays, it will be sufficient to consider only $\theta \approx 180°$. The fraction of the total number of electrons which contribute a given fraction $F^2$ of the Rayleigh scattered intensity at 180° was found by solving the equation,

$$\int_0^{r_0} |\psi_a|^2 \exp[i(\kappa - \kappa_0)\cdot r] r^2 dr = (FZ/u)(\pi/2u)^{\frac{1}{2}}, \qquad (5)$$

numerically for $r_0$, for $F^2 = 90$ percent and for various values of $\lambda$ and $Z$ using the Thomas-Fermi distribution for the atom. The charge contained within the sphere of radius $r_0$ about the nucleus was calculated and the results are shown in Fig. 1 where the fraction of the number of electrons contributing 90 percent of the Rayleigh scattering is plotted against $Z$ for various values of the energy of the gamma rays. The curves for all values of $\lambda$ and $F$ satisfying $\lambda/(1-F)^{\frac{1}{2}} = \text{constant}$ will be the same, so that the curves given may be used for values of $\lambda$ and $F$ other than those shown. For comparison, the fraction of the atomic number represented by the $K$ electrons and the $K$ and $L$ electrons together are also shown as a function of $Z$.

For destructive interference effects to be observable, appreciable deviations from spherical symmetry will have to occur within the radii containing the charges calculated above, and it will be seen that the most favorable conditions for the occurrence of these deviations from spherical symmetry (due to effects such as molecular binding) are low $Z$ and low gamma ray energy. But the ratio of the Thomson to the Rayleigh cross sections, $\sigma_T/\sigma_R \sim ZE^2$, so that when deviations from spherical are most likely to occur $\sigma_T/\sigma_R$ is so small, and in fact $\sigma_R$ itself is so small, as to preclude the possibility of the observation of any interference effects.

It may therefore be concluded that for all gamma-ray energies and values of $Z$ at which either of the scattering processes may be observed, Eq. (4) gives the correct differential cross section for the atom.

[1] P. B. Moon, Proc. Phys. Soc. (London) **A63**, 1189 (1950).
[2] W. Heitler, *Quantum Theory of Radiation* (Clarendon Press, Oxford, 1944), second edition, p. 133.
[3] W. Franz, Z. Physik **98**, 314 (1930).

## Decay of the $\chi$ Meson

SEIICHI SUEOKA[a]
*Division of Physics, National Research Council, Ottawa, Canada*
(Received April 16, 1954)

RECENTLY many experiments[1] have shown that the $\chi$ meson possibly undergoes the following two-body mode of decay, $\chi^{\pm} \to \pi^{\pm} + N^0$, since the secondary $\pi$ meson very probably has uniform energy. Here $N^0$ denotes an unknown neutral particle. If for $N^0$ we take the known neutral particles, we have three possibilities, namely,

$$\begin{aligned} \chi^{\pm} &\to \pi^{\pm} + \gamma; \quad m_\chi \sim 945 m_e, \\ &\to \pi^{\pm} + \pi^0; \quad m_\chi \sim 1019 m_e, \\ &\to \pi^{\pm} + \theta^0; \quad m_\chi \sim 1610 m_e. \end{aligned}$$

The only other possibility, $N^0 = \nu^0$, is omitted, because then the $\chi$ meson would have to be considered to be a fermion. The approximate values of the mass of the $\chi$ meson corresponding to each scheme are given above. In the first two cases the mass is very close to that of the $\tau$ meson, but in the last the mass seems to differ considerably from that of the $\tau$ meson. Because of this experimental fact, a suggestion was put forward at the Cosmic Ray Congress[2] held at Bagnères-de-Bigorre, France (July, 1953) that the $\chi$ and $\kappa$ mesons are possibly identical with the $\tau$ meson but have alternative decay modes instead of the usual $3\pi$ decay of the $\tau$ meson.

Goldhaber[3] has speculated on the possibility of finding a correlation between the various particles by considering the $\theta^0$ meson as the fundamental meson in nucleon-nucleon reactions. As far as the hyperons and $\tau$ mesons are concerned, this idea is natural and helpful, and does not lead to any contradictions. Goldhaber brings the $\chi$ meson and $\kappa$ meson into this scheme by assuming the following decay schemes proposed at the above-mentioned Bagnères Congress:

$$\chi \text{ mode: } \tau^{\pm} \to \pi^{\pm} + \begin{cases} \gamma \\ \pi^0 \end{cases},$$

$$\kappa \text{ mode: } \tau^{\pm} \to \mu^{\pm} + \nu^0 + \begin{cases} \gamma \\ \pi^0 \end{cases}.$$

These decay modes are consistent with the usual $3\pi$ decay. But here we wish to point out that the identification of $\chi^{\pm}(\chi^{\pm} \to \pi^{\pm} + \pi^0)$ with $\tau^{\pm}(\tau^{\pm} \to \pi^{\pm} + \pi^+ + \pi^-)$ leads to a difficulty from the point of view of the selection rules for the decay modes of bosons based on the principles of charge conjugation and charge symmetry.[4-6] The relevant theorem for our purpose can be stated as follows: the reaction between charged and neutral mesons through a nucleon field is forbidden if the total number of vector and tensor couplings is odd. Further, the conservation of angular momentum and parity leads to the absolute selection rules which are stronger than those mentioned above. Using all these selection rules, we can easily get the permitted kind of meson for various decaying mesons (bosons). Here we consider only the case that $\tau$ and $\chi$ mesons do not have higher spin than unity and we assume that these mesons are not composite structures but elementary bosons.

Denoting by $A$, $P$, and $T$ the decay schemes forbidden by the conservation of angular momentum, the conservation of parity, and the extension of Furry's theorem, respectively, we get the results listed in Table I, which shows the forbiddenness of each decay scheme of $\tau$ meson and $\chi$ meson for various mesonic properties. Here we assume that the $\pi$ meson is a pseudoscalar meson.[7] Here $S$, $V$, $PV$, and $PS$ denote, respectively, the scalar, vector, pseudovector, and pseudoscalar meson and $s$, $v$, $l$, $pv$, and $ps$ denote, respectively, the scalar, vector, tensor, pseudovector and pseudoscalar coupling of the meson with the nucleon field. $\tau_{(0)}$ or $\tau_{(3)}$ means that the neutral $\pi$ meson couples with the nucleon field through the $\tau_{(3)}(=1)$ or $\tau_{(s)}$ component of the isotopic spin.[8]

TABLE I. Selection rules for the decay of $\tau$ and $\chi$ mesons.

| Decay mode \ Property of meson | $S_s$ | $S_v$ | $V_s$ | $V_t$ | $PV_t$ | $PV_{pv}$ | $PS_{ps}$ | $PS_{pv}$ |
|---|---|---|---|---|---|---|---|---|
| $\tau^{\pm} \to \begin{cases} \pi^{\pm}+\pi^{+}+\pi^{-} \\ \pi^{\pm}+\pi^{0}+\pi^{0} \end{cases}$ | $P$ | $P$ | $T$ | $T$ | $T$ | · | · | · |
| $\chi^{\pm} \to \pi^{\pm} + \gamma$ | $A$ | $A$ | · | · | · | · | $A$ | $A$ |
| $\chi^{\pm} \to \pi^{\pm} + \pi^0 \begin{cases} \tau_{(3)} \\ \tau_{(s)} \end{cases}$ | · $T$ | $T$ · | $T$ · | $T$ · | $P$ $P$ | $P$ $P$ | $P$ $P$ | $P$ $P$ |

The cases permitted by these selection rules are represented by dots.

From this table, we can deduce some properties of the meson; for instance, the $\tau$ meson should be $PS$ or $PV_{pv}$, the $\chi$ meson decaying into a $\pi$ meson and $\gamma$ should be $V$ or $PV$, and the $\chi$ meson decaying into $\pi^{\pm}$ and $\pi^0$ should be $S$ or $V$. Therefore if we wish to identify the $\chi$ meson with the $\tau$ meson, we see that this is possible only if $\chi^{\pm}(\chi^{\pm}\to\pi^{\pm}+\gamma)$ is $PV_{pv}$, but it is not possible for us to identify $\chi^{\pm}(\chi^{\pm}\to\pi^{\pm}+\pi^0)$ with the $\tau$ meson. In other words, we may have the possibility that $\chi^{\pm}\to\pi^{\pm}+\gamma$ is an alternative decay scheme of the $\tau$ meson, but $\chi^{\pm}(\chi^{\pm}\to\pi^{\pm}+\pi^0)$ should be regarded as different from the $\tau$ meson. The above argument is valid under the assumption, now well established, that the $\pi$ meson is a pseudoscalar.

The author is greatly indebted to Dr. T. Y. Wu, Dr. L. Voyvodic, and Dr. S. Shanmugadhasan for their kind advice and discussion.

* National Research Laboratories Postdoctoral Fellow.

[1] M. G. K. Menon and C. O'Ceallaigh, Proc. Roy. Soc. (London) **A221**, 292 (1954).
[2] For instance, L. Leprince-Ringuet, Ann. Rev. Nuclear Sci. **3**, 39–66 (1953).
[3] M. Goldhaber, Phys. Rev. **92**, 1279 (1953).
[4] H. Fukuda and Y. Miyamoto, Progr. Theoret. Phys. (Japan) **4**, 389 (1949).
[5] A. Pais and R. Jost, Phys. Rev. **87**, 871 (1952).
[6] L. Michel, Nuovo cimento **10**, 319 (1953).
[7] R. E. Marshak, *Meson Physics* (McGraw-Hill Book Company, Inc., New York, 1952).

## Rotational Nuclear Energy Levels from Coulomb Excitation

G. M. TEMMER AND N. P. HEYDENBURG
*Department of Terrestrial Magnetism, Carnegie Institution of Washington, Washington, D. C.*
(Received April 16, 1954)

ONE of the predictions of the so-called collective model of the nucleus[1] concerns the existence of a low-lying rotational level spectrum in strongly deformed nuclei encountered in regions between closed shells. In the simplest strong-coupling approximation, the positions of these levels are given by the following expressions involving the spin $I$ and moment of inertia $\Im$ (~square of nuclear deformation):

(a) even-even nuclei: $E_I=\dfrac{\hbar^2}{2\Im}I(I+1)$; $\quad I=0^+, 2^+, 4^+\cdots$,

(b) odd-$A$ nuclei: $\quad E_I=\dfrac{\hbar^2}{2\Im}[I(I+1)-I_o(I_o+1)]$;

$$I=I_o, I_o+1, I_o+2, \cdots \text{ (same parity as } I_o).$$

Bohr and Mottelson in their original article[1] pointed out that Coulomb excitation was especially suited to investigate this level system, and the celebrated case of $Ta^{181}$ discovered by Huus and Zupančič[2] exhibits the first two excited states where predicted. Because of the limitation to $E2$ transitions in the excitation process[3,4] we expect only two levels to be excited in odd nuclei, and only one ($2^+$) in even-even nuclei. A number of cases of great regularity in the even-even nuclei of the heavy element region studied by alpha and gamma spectroscopy have been noted.[5,6] Encouraged by one more apparent case of agreement with rotational interpretation ($Eu^{168}$) in our last publication,[4] called to our attention by Bohr and Mottelson,[7] we have carefully reexamined the nuclei of mass number between 150 and 190 (mainly rare earth region) where excessively large quadrupole moments (strong deformations) are known to exist. We used alpha particles as in our previous work[3,4]; since only the oxides of the rare earths are available, this turns out to be the only way to avoid prohibitive gamma-ray backgrounds. We raised our bombarding energy to 3.4 Mev, thus gaining a factor of two or more in the excitation cross section[8] of energy levels lying between 200 and 300 kev; we also used some 30 mils of copper absorber to cut down on the x-ray as well as the first excited state gamma intensity. Our work was of course done with ordinary isotopic mixtures of the elements (some separated isotopes are on order), but the inherent difference in the spectra of even and odd nuclei permits a rather simple identification in most cases. In Table I we present the results obtained. We list in turn: the element; the number and total percent abundance of the even-even isotopes; the number and total percent abundance of the odd isotopes; the spins $I_o$ of the latter; the theoretically predicted ratio $\rho=(2I_o+3)/(I_o+1)$ of second excited state energy to first excited state energy for the odd isotopes; the experimental values of the energies of the gamma rays; and finally, the predicted value for the second excited state energy, considering the lowest-energy gamma ray to come from the first excited state. It is likely that the latter gamma peak contains not only the odd first excited states, but also the even-even gamma rays in some cases, so that the intensities observed are not directly meaningful. However, there seems to be a systematic difference between the moments of inertia of neighboring even and odd nuclei, in such a direction as to depress the first excited states of the odd species (larger $\Im$). In the cases of Sm and Lu we were able to resolve the higher-energy gamma ray probably belonging to the even nuclei. In addition to the nuclei listed in Table I, we have preliminary evidence concerning similar agreement in $_{64}$Gd; this case as well as $_{60}$Nd and $_{72}$Hf will be reexamined with separated isotopes. In the case of $_{65}$Tb the results are inconclusive; in $_{69}$Tm there seem to be no higher excited states. It is perhaps interesting that the latter nucleus has spin 1/2 and is not expected to exhibit simple regularities.[1]

TABLE I. Summary of results on rotational energy levels in the region $150<A<190$. $Z$ = element; $A(e-e)$ = number and (total percent abundance of even-even isotopes); $A(o)$ = number and (total percent abundance of odd isotopes); $I_o$ = ground-state spin of odd isotopes; $\rho$ = theoretical ratio of second to first excited state energies for odd isotopes; $E$ = observed gamma-ray energies; $E_{I_o+2}$ = energy predicted for second excited state. Italicized numbers designate second excited state gamma rays.

| $Z$ | $A(e-e)$ | $A(o)$ | $I_o$ | $\rho$ | $E_\gamma$ | $E_{I_o+2}$ |
|---|---|---|---|---|---|---|
| $_{60}$Nd[a] | 5(79.5) | 2(20.5) | $7/2^-$ | 2.222 | 70,[b] 128, *290* | 285 |
| $_{62}$Sm | 5(71.1) | 2(28.9) | $7/2^-$ | 2.222 | 82, 122,[b] *186* | 182 |
| $_{63}$Eu | ··· | 2(100) | $5/2^+$ | 2.286 | 81, 108,[c] *189* | 185 |
| $_{66}$Dy | 5(56.1) | 2(43.9) | $7/2^-$ | 2.222 | 76, *166* | 169 |
| $_{67}$Ho | ··· | 1(100) | $7/2^+$ | 2.222 | 93, *205* | 207 |
| $_{68}$Er | 5(77.1) | 1(22.9) | $7/2^-$ | 2.222 | 79, *174* | 175 |
| $_{70}$Yb | 5(69.6) | 2(30.4) | $5/2^-$, $1/2^-$[d] | 2.286 | 81, 114,[b] *180* | 185 |
| $_{71}$Lu | ···[e] | 1(97.4) | $7/2^+$ | 2.222 | 113, 183,[f] *248* | 251 |
| $_{72}$Hf[a] | 4(67.8) | 2(32.2) | $3/2^-$ or $1/2^-$ | 2.400 | 93,[b] 112, *250* | 269 |
| $_{73}$Ta | ··· | 1(100) | $7/2^+$ | 2.222 | 137, 167,[c] *303* | 304 |
| $_{77}$Ir | ··· | 2(100) | $3/2^+$ | 2.400 | 133, 219,[c] *360* | 319 |

[a] Tentative pending study with separated isotopes.
[b] Known or presumed first excited state(s) of even-even isotope(s).
[c] Probable or known cascade gamma ray from second to first excited state.
[d] $Yb^{171}$ (14.3 percent) has spin $1/2^-$ and hence uncertain level positions (see reference 1).
[e] Odd-odd nucleus $Lu^{176}$ (2.6 percent).
[f] Unassigned line.

Since the ratios are not far from two, it is difficult to resolve the cascade transition (if any) between second and first excited states; we were able to see it only in the cases of Ta (167 kev),[9] Eu (108 kev), and possibly in Ir (219 kev). We intend to locate these transitions by coincidence studies. They are of course important in determining absolute transition probabilities. Within the limits of our rough preliminary results, the relative excitation cross sections of first and second excited states also agree with the simple predictions of the collective model in terms of the intrinsic quadrupole moment $Q_0$.[1] By way of summary, we would like to point out the following:

(1) The upward trend of the positions of the first excited states is clearly discernible as we approach the 82-neutron and 126-neutron closed shells, being more rapid toward the former than toward the latter. This trend, for even-even nuclei, has been variously noted.[10,11]

(2) In spite of these variations, and the variations in the ground-state spin from 3/2 to 7/2, the second excited state positions seem to agree with the simple predictions within our experimental

errors in all cases except Hf and Ir. The rotational character of these levels seems difficult to refute.

(3) If the rotational interpretation is accepted, we of course automatically obtain spin and parity assignments for all levels. The second rotational states will probably never be observed except in Coulomb excitation because of their high spins.

We are indebted to Dr. Bohr and Dr. Mottelson for informative correspondence. Mr. E. L. Weise of the National Bureau of Standards and Professor F. H. Spedding of the Ames Laboratory made these experiments complete by generously supplying us with an unbroken line of high-purity rare earth oxide samples.

[1] A. Bohr and B. R. Mottelson, Kgl. Danske Videnskab. Selskab, Mat.-fys. Medd. 27, No. 16 (1953).
[2] T. Huus and Č. Zupančič, Kgl. Danske Videnskab. Selskab, Mat.-fys. Medd. 28, No. 1 (1953).
[3] G. M. Temmer and N. P. Heydenburg, Phys. Rev. 93, 351 (1954).
[4] N. P. Heydenburg and G. M. Temmer, Phys. Rev. 93, 906 (1954).
[5] A. Bohr and B. R. Mottelson, Phys. Rev. 90, 717 (1953).
[6] F. Asaro and I. Perlman, Phys. Rev. 91, 763 (1953).
[7] A. Bohr and B. R. Mottelson (private communication).
[8] K. Alder and A. Winther, Phys. Rev. 91, 1578 (1953).
[9] This has also been observed by the group at the Rice Institute (C. M. Class).
[10] G. Scharff-Goldhaber, Phys. Rev. 90, 587 (1953).
[11] P. Staehelin and P. Preiswerk, Nuovo cimento 10, 1219 (1953).

## Mean Lives of Positive and Negative Mu Mesons*

N. N. Biswas and M. S. Sinha
*Bose Institute, Calcutta, India*

(Received March 1, 1954; revised manuscript received April 19, 1954)

It is now well established that the apparent mean life of negative mu mesons decreases very rapidly as the atomic number of the absorbing medium increases and that this is entirely due to the rapid increase in the capture probability of the mu mesons by the gradually increasing positive charge of the nucleus.[1-5] The mean life for free decay of negative mu mesons is the same as that of the positives, and the apparent mean life of negative mesons is given by $1/\tau_-=1/\tau_++\Lambda$, where $\Lambda$ is the capture probability of the negatives by the nucleus. Under these circumstances the number of mesons remaining undecayed at any time $t$ is given by

$$N_t=N_0^+\exp(-t/\tau_+)+N_0^-\exp(-t/\tau_-), \qquad (1)$$

where $N_0^+$ and $N_0^-$ are the number of positive and negative mu mesons available for decay at $t=0$. The number of negatives remaining undecayed after a time $t$ equal to three times its apparent mean life is less than five percent. Hence if an integral decay curve is plotted with points close together, starting from a time as small as possible avoiding counter lags, we expect that the line joining the first few points would show a slope much sharper than that joining the points where the number of negative decays has fallen to a very low value. The slope of the latter part of the curve, in fact, would give the mean life of positives as has been shown by Morewitz and Shamos[6] in the case of sulfur.

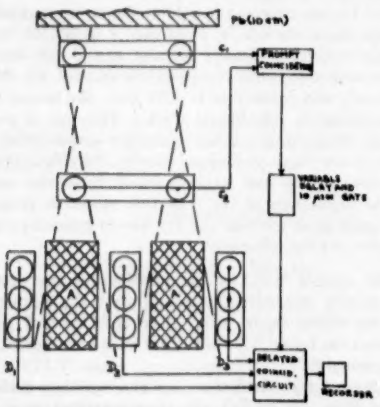


Fig. 1. Experimental arrangement.

The integral decay curves for a composite beam of mesons in Al, S, C, and Pb have been obtained in this laboratory by the delayed-coincidence technique. In the experimental arrangement as shown in Fig. 1, the twofold counter telescopes select an almost vertical beam of mesons and the trays $D_1$, $D_2$, $D_3$ detect the decay electrons. The meson-absorbing medium has been split up into two $(A,A)$ in order to reduce the path length that a decay electron has to traverse to enter any of the $D$ trays. The arrangement as a whole favors to increase the counting rates of the decay events.

Of the decay curves shown in Fig. 2, those for Al and S show

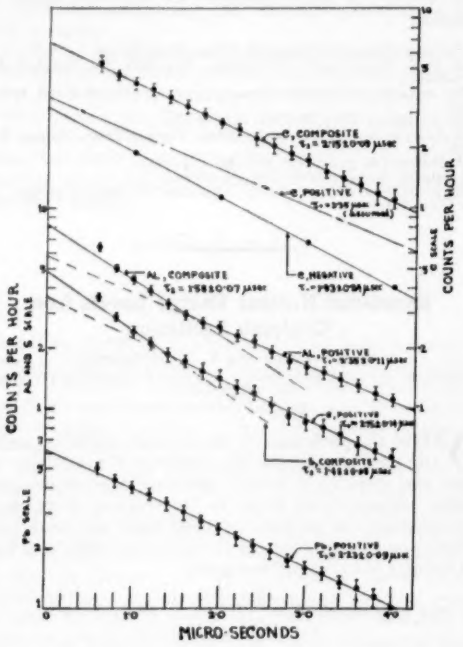


Fig. 2. Decay curves for $\mu$ mesons in C, Al, S, and Pb.

distinctly two separate slopes while those for C and Pb with the same experimental setup show only one. This is expected since the apparent mean life of negatives in C is not much less than that of the positives, which implies that the negatives were still available for decay at 4.0 microseconds. In the case of Pb the decay curve yields a mean life of $2.23\pm0.09$ microseconds, which can be attributed to the decay of positives alone, because the number of negatives recorded in this case is negligible on account of their high capture probability by the lead nucleus. The point corresponding to 0.6 $\mu$sec was not given much importance because it is suspected to include some spurious events due to the distribution of random lags in the discharge of the G.M. counters.[7] This has also been the case with curves obtained by Rossi and Nereson[8] and Sigurgeirsson and Yamakawa.[9]

For elements of $Z\leq16$, the composite decay mean lives show a gradual increase with decrease of $Z$, thereby indicating that $\tau_-$ increases as $Z$ decreases and reaches the limit of $\tau_+$ for $Z<6$. In Al and S, the determination of the mean lives of negatives alone could be done by subtracting the extrapolated dashed line (positive decays) from the composite curve, but this was not attempted since the statistical errors were too large to estimate the values of

$\tau_-$ with reasonable accuracy. Further experiments are in progress to evaluate $\tau_-$ by this method.

The value of $\tau_-$ in C has been determined in the following way. We chose the thickness of the carbon absorber such that it stopped the same number of mesons as in the case of Al. Hence the same number of positives must have decayed in C as in Al in the same time although the number of decay electrons recorded due to positives alone were smaller in C than in Al, because the solid angle subtended by the $D$ trays with respect to the total thickness of the absorber was smaller in case of C due to its larger thickness. The positive decay curve in Al has been reduced by a factor equal to the ratio of the solid angles and this reduced curve represents the positive decay curve in C as shown in Fig. 2. The mean life of negatives evaluated by subtraction, gives the value $1.93\pm0.24$ $\mu$sec.

Only a fraction $\tau_-/\tau_+$ of the negative mesons present in the cosmic-ray beam can decay in an absorber. Since the number of negative and positive mesons decaying in the interval $t=0$ to $t=\infty$ are separately known in the case of C, the ratio of positive to negative mu mesons can be determined from the equation

$$\mu^+/\mu^- = (n_0{}^+\tau_-)/(n_0{}^-\tau_+), \qquad (2)$$

where $n_0{}^+$, $n_0{}^-$ are the number of decay electrons recorded from $t=0$ to $t=\infty$. Substituting the relevant values from the decay curves of C, the value of this ratio is found to be $0.95\pm0.16$, agreeing well with the value $1.06\pm0.03$ obtained recently by Morewitz and Shamos.[6]

A detailed report of the experiment will be published in the Transactions of the Bose Research Institute. The authors acknowledge with thanks the advice and encouragement from Professor D. M. Bose, Director, Bose Institute during the course of the experiment.

* Work performed under a grant received from the Atomic Energy Commission, Government of India.

[1] Conversi, Pancini, and Piccioni, Phys. Rev. **71**, 209 (1947).
[2] G. E. Valley and B. Rossi, Phys. Rev. **73**, 177 (1948).
[3] H. K. Ticho, Phys. Rev. **74**, 1337 (1948).
[4] Keuffel, Harrison, Godfrey, and Reynolds, Phys. Rev. **87**, 942 (1952).
[5] W. E. Bell and E. P. Hincks, Phys. Rev. **88**, 162 (1952).
[6] H. A. Morewitz and M. H. Shamos, Phys. Rev. **92**, 136 (1953).
[7] B. Rossi and N. Nereson, Phys. Rev. **62**, 417 (1942).
[8] B. Rossi and N. Nereson, Phys. Rev. **64**, 200 (1943).
[9] T. Sigurgeirsson and K. A. Yamakawa, Revs. Modern Phys. **21**, 126 (1949).

## Phenomenology of the Pion-Nucleon $S$ Waves*

H. P. Noyes and A. E. Woodruff
*Department of Physics, University of Rochester, Rochester, New York*
(Received April 14, 1954)

As was pointed out by Anderson and Fermi,[1] knowledge of the cross section for photoproduction of $\pi^+$ mesons from hydrogen at threshold combined with the $\pi^-/\pi^+$ ratio for photoproduction from deuterium and the ratio of radiative capture to charge exchange capture of $\pi^-$ mesons in hydrogen as measured by Panofsky[2] allows one to calculate the difference in slope between the pion-nucleon $S$ phase shifts at zero energy. Calling these phase shifts $\alpha_1$ and $\alpha_3$ for the states of $I=1/2$ and $I=3/2$, respectively, Bernardini[3] reported at the Fourth Rochester Conference that recent photoproduction results give $\alpha_1-\alpha_3=(0.16\pm0.04)p/\mu c$, where $p$ is the center-of-mass momentum of the pion and $\mu$ its mass. However, pion-nucleon scattering experiments at 33,[4] 40,[5,6] 46,[7] and 58 [8] Mev all indicate that near 40 Mev $\alpha_1$ is about 10° while $\alpha_3$ lies between $-1°$ and $-4°$. The assumption that 40 Mev is a low enough energy for the pion-nucleon system to insure that the phase shifts below 40 Mev are simply proportional to momentum would therefore predict that $\alpha_1-\alpha_3=(0.3-0.35)p/\mu c$, and hence a zero energy cross section differing by a factor of four from the observed result. Further confirmation of the peculiar behavior of these phase shifts at low energy is given by Lederman's observation[3] of five scatterings of 5-Mev $\pi^-$ mesons in hydrogen, corresponding to a cross section of 20 to 25 mb. In spite of poor statistics, this positive result is by no means trivial, since linear extrapolation from 100 Mev would predict 0.1 mb, and from 40 Mev, 5 mb. The combination of these two results, namely that $\alpha_1-\alpha_3$ is small and $\alpha_3+2\alpha_1$ is large near threshold clearly shows that $\alpha_3$ *and* $\alpha_1$ *must have the same sign near threshold* and not opposite signs as observed at higher energies.

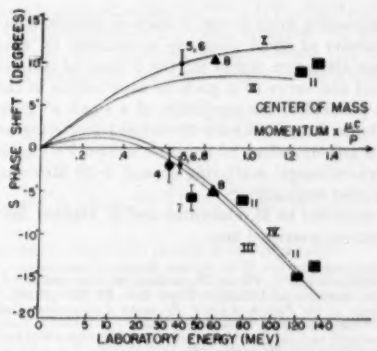


FIG. 1. $S$ phase shifts *vs* center-of-mass momentum for models given in Table I. Numbers indicate references for data.

The purpose of this note is to point out that this is precisely the behavior predicted by the $S$-wave potential model proposed by Marshak[9] as extended by Woodruff.[10] The predictions of this model, which uses an attractive exponential for $\alpha_1$ and a hard-core attractive exponential tail potential for $\alpha_3$ (see Table I), are compared with experiment[4-8,11] in Fig. 1. Comparison with the threshold data is given in Table II. Since 20 mb is reached near 5.5 Mev, and the energy in Lederman's experiment is probably not as closely defined as this, the agreement with experiment is clearly very good.

It must be emphasized that the present success of this model does not justify taking it seriously in a quantitative sense. There is no good theoretical reason to expect a static potential model to hold up to energies equal to the rest mass of the pion, and as has already been pointed out in the nucleon-nucleon case,[12] a hard core, attractive tail potential is peculiarly sensitive to kinematic relativistic corrections. Further, until it is shown experimentally that the $S$ phases are positive around 5 Mev, the possibility exists that both are negative, which would imply an energy dependence that could not be readily duplicated by any simple potential model. If this possibility is ignored, the results presented here are rather to be taken to indicate the qualitative features that a successful theory of the meson-nucleon force should exhibit, namely

TABLE I. Parameters for the potentials $\alpha_1$: $V=-V_0\exp(-r/r_0)$; $\alpha_3$: $V=\infty$, $r\leq r_c$; $V=-V_0\exp[-(r-r_c)/r_0]$, $r>r_c$.

| Phase shift | Model No. | $V_0$ (Mev) | $r_0$ $(\mu c)/\hbar$ | $r_c$ $(\mu c)/\hbar$ |
|---|---|---|---|---|
| $\alpha_1$ | I | 277 | 0.336 | ... |
| | II | 105 | 0.465 | ... |
| $\alpha_3$ | III | 187 | 0.428 | 0.386 |
| | IV | 163 | 0.460 | 0.375 |

TABLE II. Predictions at low energy.

| $\alpha_1$ Model | $\alpha_3$ | $\lim_{E\to0}(\alpha_1-\alpha_3)\mu c/p$ | $\sigma_{\pi^0\pi^-}$ (5 Mev), mb |
|---|---|---|---|
| I | III | 0.241 | 15 |
| II | III | 0.211 | 12 |
| I | IV | 0.185 | 17 |
| II | IV | 0.154 | 14 |
| Experiment | | $0.16\pm0.04$ | 20–25 |

a purely attractive force in the $S$ state of isotopic spin $\frac{1}{2}$ and a strong repulsion at short distances surrounded by a somewhat longer-range attractive region for the $S$ state of isotopic spin $\frac{3}{2}$. They should also serve as a guide to experiments in this energy region. In particular, the prediction of a small $\pi^+$ cross section which switches from backward to forward scattering around 20 Mev and a greatly enhanced $\pi^-$ cross section for elastic (rather than charge-exchange) scattering around 5–10 Mev should now be taken rather seriously.

We are indebted to H. Gelernter and E. Halbert for many of the calculations presented here.

* Work supported by the U. S. Atomic Energy Commission.
[1] H. L. Anderson and E. Fermi, Phys. Rev. **86**, 794 (1952).
[2] Panofsky, Aamodt, and Hadley, Phys. Rev. **81**, 565 (1951).
[3] *Proceedings of the Fourth Annual Rochester Conference* (University of Rochester Press, Rochester, to be published).
[4] S. L. Leonard and D. H. Stork, Phys. Rev. **93**, 568 (1954).
[5] S. W. Barnes *et al.*, Phys. Rev. **92**, 1327 (1953).
[6] J. Tinlot and A. Roberts, Phys. Rev. (to be published).
[7] Orear, Lord, and Weaver, Phys. Rev. **93**, 575 (1954).
[8] Bodansky, Sachs, and Steinberger, Phys. Rev. (to be published).
[9] R. Marshak, Phys. Rev. **88**, 1208 (1952).
[10] A. E. Woodruff, Phys. Rev. **92**, 855 (1953).
[11] Anderson, Fermi, Martin, and Nagle, Phys. Rev. **91**, 155 (1953).
[12] H. P. Noyes and H. G. Camnitz, Phys. Rev. **88**, 1206 (1952).

## Shower Structure in the Higher Shower Maxima

W. Bothe and H. Kraemer
*Institut für Physik im Max-Planck-Institut für Medizinische Forschung, Heidelberg, Germany*
(Received April 5, 1954)

In an attempt to shed more light on the production of showers in connection with the second, third, and fourth maxima of the shower curve, the experimental arrangement as described previously[1] was slightly modified. In Fig. 1, Pb is the lead radiator of variable thickness, I and II are the two crossed counter trays which determine the apparent shower angle, and III is a counter tray that may be shifted between I and Pb. Fivefold coincidences (I, I, II, II, III) as well as anticoincidences (I, I, II, II, −III) were counted as a function of lead thickness Pb. The results, some of which are reproduced in Fig. 2, are clear cut though rather surprising. If tray III is arranged immediately beneath Pb ($a=82$ cm), the second and third maximum only appear in the anticoincidence curve. The inverse holds if III is lowered to practically $a=0$ cm. In intermediate positions of III the maxima are divided up between the two curves.

The simplest interpretation of these results is this: The particles emerging from the Pb are *neutral* ones; a considerable fraction of them decay before reaching tray I, thus giving rise to the charged showers or pairs recorded by trays I+II. So these neutral particles have at least some of the characteristics of neutral $V$ particles.

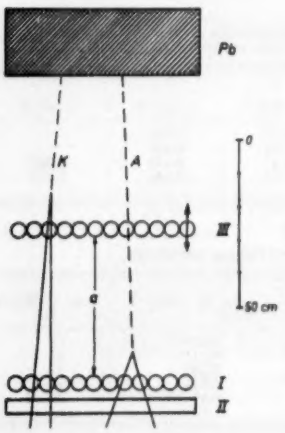


Fig. 1. Experimental arrangement. $K$: case of coincidence; $A$: case of anticoincidence.

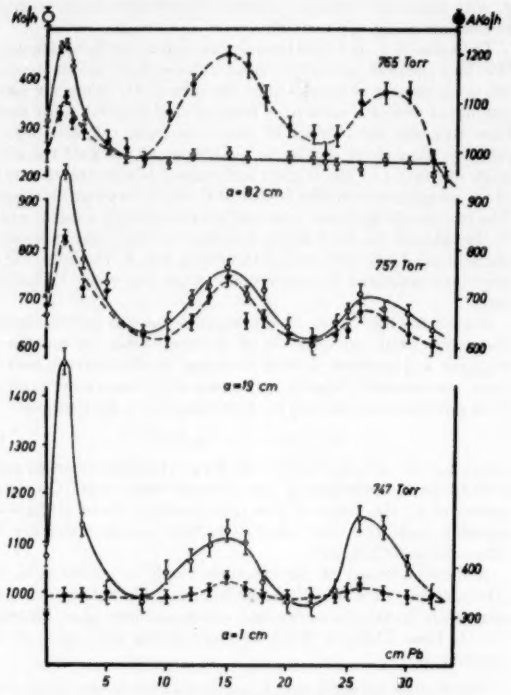


Fig. 2. Shower curves. Full curve: coincidence. Dashed curve: anticoincidence. (1 Torr = 1 mm mercury).

In the light of these results, a number of discrepancies that seemed to exist between the works of different authors now readily disappear. Since the apex of a shower does not lie in the lead layer but is more or less below, the real shower angle is considerably larger than supposed in our previous work. In fact Broussard and Graves[2] have observed in a cloud chamber that the second maximum occurs only for rather wide angle showers.

If a counter tray III is arranged beneath Pb and coincidences (I, I, III) or (I, I, II, II, III) are counted, the second and third maximum cannot appear. Likewise the higher maxima must be strongly suppressed, if trapezoidal counter arrangements are used fixing the shower apex within the lead layer. Investigations with both kinds of arrangements have been described and regarded as proof against the existence of higher shower maxima.

This counter work is being continued in combination with a cloud chamber.

[1] W. Bothe and H. Thurn, Phys. Rev. **79**, 544 (1950); H. Thurn and W. Bothe, Z. Naturforsch. **6a**, 576 (1951); H. Thurn, Z. Naturforsch. **7a**, 497 (1952); H. Thurn, Z. Naturforsch. **8a**, 134 (1953).
[2] L. Broussard and A. Graves, Phys. Rev. **60**, 413 (1941).

## Perturbation Theory with Sommerfeld-Maue Wave Function

G. K. Horton and E. Phibbs
*Department of Mathematics, University of Alberta, Edmonton, Alberta, Canada*
(Received March 29, 1954)

It has been implicitly assumed by a number of authors[1] that the matrix element in the differential cross section for a process is the same whether Sommerfeld-Maue wave functions or non-

relativistic wave functions[2] are employed. That this is not so may be seen as follows.

Given[3] that the Sommerfeld-Maue solutions of the iterated Dirac equation,

$$\nabla^2\psi+\left\{\left(E+\frac{Zze^2}{r}\right)^2-m^2\right\}\psi=iZze^2\boldsymbol{\alpha}\cdot\boldsymbol{\nabla}_r\left(\frac{1}{r}\right)\psi, \tag{1}$$

is

$$\psi(\mathbf{r})=\frac{N}{(2\pi)^{\frac{3}{2}}}e^{i\mathbf{k}\cdot\mathbf{r}}\left\{1+\frac{ik}{2Er}\boldsymbol{\alpha}\cdot\boldsymbol{\nabla}_k+O(n^2\beta^2)\right\}$$
$$\times F(ia,1;ikr-i\mathbf{k}\cdot\mathbf{r})u(\mathbf{k}), \tag{2}$$

it may be shown[4] that the $\psi(\mathbf{r})$ do not form a complete set of orthonormal functions but satisfy

$$\int_{\Delta}d\mathbf{k}'\int\psi''^{*}\left[1+\frac{2Zze^2}{(E'+E'')r}\right]\psi'd\tau=1 \text{ or } 0, \tag{3}$$

according as $\Delta$ includes $\mathbf{k}''$ or not. $\psi''$ and $\psi'$ are the solutions of (1) for $E=E''$ and $E'$, respectively. We employ the notation of reference 1.

Relation (3) gives $N'=[2\pi a'/(e^{2\pi a'}-1)]^{\frac{1}{2}}$, which is exactly the same as in the nonrelativistic case.[5] Relation (3) implies that when using the wave functions of Sommerfeld and Maue in a perturbation calculation, one must replace the matrix element

$$H_{if}'=\int\psi_{\text{initial}}^{*}H'\psi_{\text{final}}d\tau \tag{4}$$

by

$$H_{if}'=\int\psi_{\text{initial}}^{*}H'\left[1+\frac{2Zze^2}{r(E'+E'')}\right]\psi_{\text{final}}d\tau. \tag{5}$$

A paper employing these results is in preparation.

[1] H. A. Bethe and L. C. Maximon, Phys. Rev. **93**, 768 (1954); L. Bess, Phys. Rev. **77**, 550 (1950); Davies, Bethe, and Maximon, Phys. Rev. **93**, 788 (1954).

[2] W. Heitler, *Quantum Theory of Radiation* (Oxford University Press, London, 1944), second edition, p. 96.

[3] G. K. Horton and R. T. Sharp, Phys. Rev. **89**, 885 (1953).

[4] This was already known to Sommerfeld. See A. Sommerfeld, *Atombau und Spektrallinien* (F. Vieweg and Son, Braunschweig, 1939), Vol. 2, p. 214. See also F. J. Dyson, Phys. Rev. **73**, 617 (1948).

[5] This is probably the reason why the difference between (4) and (5) has so far been overlooked.

# Proceedings of the American Physical Society

## MINUTES OF THE 1954 MARCH MEETING HELD AT DETROIT AND ANN ARBOR, MARCH 18–20, 1954

(Corresponding to *Bulletin of the American Physical Society*, Volume 29, No. 3)

THE 1954 March meeting of the American Physical Society was held in two cities: Detroit on Thursday and Saturday, the eighteenth and twentieth of March, Ann Arbor on the intervening Friday. Conforming with young but firmly founded tradition, the executives of our Divisions of High-Polymer Physics and Solid-State Physics concentrated upon this meeting their principal efforts of the year in making programmes of invited papers, and their members followed suit by providing contributed papers in abundance from both fields. Thus the March meeting has become the major solid-state and high-polymer conclave of the Society's calendar. This is the best feasible solution of the problem posed by the immensity of the Annual Meeting and the Washington meeting, which would long since have been unmanageable had the March meeting not been authorized and interposed. Semiconductors and the effects of irradiation on solids predominated in the solid-state sessions. Mention should be made here of the first instance of what it is hoped to make an annual institution, *viz.* the lecture by the most recent winner of the Oliver E. Buckley Solid-State Physics Prize (John Bardeen). The subject of the Symposium in high-polymer physics was the properties of amorphous polymers in bulk. For invited speakers in other than the Divisional fields we sought principally at the University of Michigan, with excellent results. Special mention must be made of the fascinating historical address by Professor H. M. Randall, a Past President of our Society, who told the story of the evolution of infrared spectroscopy at his University as it was initiated and guided by himself, and spoke also of the famous Summer School of Theoretical Physics at Ann Arbor.

The registration amounted to 741. (There were 900 registrants at the 1953 March meeting; the difference is more than covered by the fact that the members of our Southeastern Section were with us then, not now.) Upwards of 800 attended sessions at Ann Arbor. The attendance at the banquet was 233; the after-dinner speakers were E. F. Barker for the University of Michigan, W. F. Busse for the Division of High-Polymer Physics, and Clarence Zener for the Division of Solid-State Physics. We are grateful to Wayne University for accommodating the sessions of the Division of High-Polymer Physics on the Thursday, and to the University of Michigan for providing halls for five sessions on the Friday morning and again on the Friday afternoon; other sessions were housed in the Sheraton-Cadillac Hotel. The Secretary did not always guess right in the ticklish business of forecasting which sessions would need the biggest halls.

We owe this "Michigan" meeting to the same man who brought about our 1941 meeting in the same two cities. His labors were tremendous, and probably much bigger than he foresaw—the Secretary was a better guesser than he in respect to the eventual size of the meeting. Especially to be commended was his provision and management of a special train (no less!) that conveyed 440 members of the Society from Detroit to Ann Arbor and back, together with buses at both ends of the run (we think that we owe the Ann Arbor buses to the courtesy of the University of Michigan). The name of G. P. Brewington should be gratefully remembered by the Society. Daniel Harmon and E. R. Phelps were those who helped him most. These three are of the Lawrence Institute of Technology, the University of Detroit, and Wayne University, respectively.

The Council met in Detroit on the Thursday afternoon. It elected to Membership 141 candidates and to Fellowship 2 candidates; their names are appended.

*Elected to Fellowship:* Kurt Lehovec and S. O. Morgan.

*Elected to Membership:* Charles Montie Aker, M. M. Atalla, *William L. Bade, Albert Baril, Jr., *Elbert White Bennett, *David Berley, *Richard Stephen Berry, John Ludwig Bjorkstam, *Mark Bolsterli, Wilson E. L. Boyce, Warren Eugene Bulman, Ray Aaron Burnstein, Edward Francis Carome, Gilbert William Castellan, *Stanley H. Charap, *Richard Allen Connell, *John Thomas Cox, Richard Pascoe Day, Harry Harroun Denman, Robert William DeSio, John Barber Dicks, Jr., Paul Brendel Dorain, *James Arthur Earl, Walter P. Eatherly, *John Allan Eisele, Robert William Ellison, William Paul Evans, *Richard Dwight Ewing, *Charles Alvin Fenstermacher, Andrzej Folkierski, *Peter J. Frank, *Jack Cavitt Fuller, Elliott David Friedman, Raymond Titus Gabler, Lawrence Allen Goldmuntz, Carroll Keller Gordon, *Andrew Vincent Granato, Tovy Grjebine, Lee Grodzins, Hermann Karl Gummel, *Mohamed Abdul Hakeem, George L. Hall, *Maclin S. Hall, Georg Hass, Victor Philippe Henri, Robert Ledyard Henry, Kuo-chu Ho, *Lothar Otto Hoeft, *William McClure Hooke, Frank A. Horak, Jr., Rudolf Bruno Horst, *Lawrence Paul Horwitz, *Raymond Howard Hoskins, Daisuke Ito, Bernard Jacrot, Philip Ord Johnson, Robert Howard Johnson, *Sidney Kahana, William Alexander Kemper, Aaron L. Kestenbaum, Walter Drew Kinsolving, Ernest Lee Kirkpatrick, Philip S. Klebanoff, *Bruce Winton Knight, Jr., *Leo A. Ch. Koerts, Yoshiaki Koshikawa, Bohdan Kostyshyn, Arnold Martin Kuethe, Anthony David Kurtz,

Joshua Ladell, *Oliver Harris LeBlanc, Jr., William C. Levengood, *Arnold David Levine, Raphael Berg Levine, *Robert Richards Lewis, Jr., *Louis F. Libelo, Jr., Torsten Lindqvist, David Aaron Lowitz, Francois Claude Lurcat, Edward Frank Mackey, Lachlan Mackinnon, George Mannig, Claude Manus, Rudolph Arthur Marcus, Herbert Franz Matare, *Robert M. Mazo, *David Bowen McCandlish, Richard Gordon McCarty, Robert Harrison Mellen, David Meneghetti, Jack Merritt, George Edward Metcalf, Nils Lilienberg Muench, Tsuneo Nagata, Henry Winston Newson, Robert Norton Noyce, Gerald Oster, *Elio Passaglia, Gordan Derby Patterson, *Donald Charles Peckham, *Paul John Persiani, Donald Allen Peterson, Byron Blake Phillips, *Irwin Abraham Pless, Colin Arnold Plint, Robert Charles Plumb, Amedeus Edward Profio, Robert Lloyd Reed, Robert Kilpatrick Riel, *William Howard Rosenfeld, *Donald Alexander Ross, *Allen Gershon Rubin, *Allan Melvin Russell, *Herman Emanuel Saffran, Mitsuo Sakai, *Murray Scheibe, *Robert Gardner Schmidt, Erich Ernst Schneider, *Theodore David Schultz, *Arthur Z. Schwarzschild, Johannes Coenraad Severiens, *Andrew Skumanich, Lester Anah Smith, *Gerald Speisman, Herbert Adrian Stahl, *Richard Steven Strzelecki, Pierre Taglang, *Clement Austin Tatro, Edwin Harold Tompkins, Jacob Israel Trombke, Carroll E. Tschiegg, Masayasu Ueta, *Wesley Johnson Van Sciver, Mary Bondurant Warren, Yukihiko Watanabe, *Jesse Leo Weil, *Kennedy Lunt Wilson, *Herman Winick, Ernest Carl Wurst, Jr., Tsunenobu Yamamoto, and Toshio Yokota.

*—Student

KARL K. DARROW, *Secretary*
American Physical Society
Columbia University
New York 27, New York

---

## Errata Pertaining to Papers B4, E4, G6, and R11

**B4**, by A. deBretteville and E. D. Harris. In line 13, −47 cal/mole should read −43.5 cal/mole. In line 14, 121.7°C should read 122.8°C. The remainder of that sentence should be deleted. Lines 15 through 20 and reference 1 should also be deleted.

**E4**, by Lindsey M. Hobbs, Douglas E. Brown, and David W. Pletcher. Mr. Hobbs' name was incorrectly written as M. Hobbs Lindsey.

**G6**, by F. A. D'Altroy and H. Y. Fan. The last sentence should read: The values of $\tau$ and the mobility give an average value of 0.43 m for the effective mass.

**R11**, by Selby M. Skinner. In line 7 after "poorly conducting materials," insert "such as high polymer." A footnote should be added, reading "With the support of the U. S. Office of Ordnance Research."

# PROGRAMME

THURSDAY MORNING AT 10:00

Crystal Ballroom

(CYRIL S. SMITH presiding)

## *Metals, I. (Lattice-Defects, Diffusion)*

**A1. On the Nature of Lattice Defects in Metals.** FREDERICK SEITZ, *University of Illinois.*—In spite of the interest of the topic, we do not have at present satisfactory experimental demonstrations of the nature of the defects which occur thermally in metals such as copper, silver, and gold. The most elementary procedure, based on measurement of density and lattice parameters at high temperatures, could, in principle at least, distinguish between vacancy-type, interstitial-type, and Frenkel-type disorder. It is unlikely, however, that this procedure will prove feasible for most metals because of the precision required. Shockley has proposed a method based on the determination of a Kirkendall shift in the presence of a thermal gradient in a chemically homogeneous material. This seems to require the assumption, however, that the defects will always migrate in the direction $-\text{grad}T$, as if the mixing entropy necessarily determined the direction of migration. It is proposed that one search for deviations in the applicability of the Matano formalism in the early stages of diffusion of two different metals which exhibit a strong Kirkendall effect of the normal type when the concentration gradient between specimens is very steep. One might expect the measured diffusion coefficients to be abnormally large on one side of the boundary and abnormally small on the other if $d$, the thickness of the diffusion layer, is not greater than $a\sqrt{\omega}$, where $a$ is the lattice parameter and $\omega$ is the number of jumps a vacancy makes between birth and death.

**A2. Formation Energy of Vacancies in Gold.** C. J. MEECHAN AND R. R. EGGLESTON, *North American Aviation, Inc.*—Determinations of the formation energy of vacancies in copper have been previously reported.[1] Recently these determinations of vacancy energy of formation have been made for pure gold, and the results of these new measurements will be reported. The experimental data taken below 500°C were fitted to the expression $R=A+BT+CT^3$. At higher temperatures the measured resistance values exceeded the extrapolated quadratic function by an amount $\Delta R$, which had the following temperature dependence: $\Delta R=A\exp(-E/kT)$. The additional resistance has been attributed to the presence of vacancies existing in thermodynamic equilibrium at the high temperatures. By plotting $\log\Delta R$ *vs* $1/T$, a formation energy for vacancies in gold of $0.67\pm0.07$ ev was obtained. This paper is based on studies conducted for the U. S. Atomic Energy Commission.

[1] Stanford Meeting, American Physical Society, December, 1953.

**A3. Imperfections in Copper in Terms of Electrical Resistivity and Thermoelectric Power.** G. W. RODEBACK, *North American Aviation, Inc.*—Certain types of imperfections in copper may be studied by including the degeneracy energy dependence[1] of their electron scattering in the expressions for electrical resistivity and thermoelectric power. Measurements of electrical resistivity and thermoelectric power from 130°K to 3000°K have been made on variously annealed states of cold-worked copper. Data were also taken from a sample bombarded at 150°K with 15 $\mu$amp-hr/cm$^2$ of 35-Mev alpha particles and subsequently annealed at room temperature. Two types of imperfections which contribute to the nonthermal scattering of conduction electrons are considered: fixed point scatterers whose scattering probability per unit time is assumed to have a one-half power dependence on degeneracy energy, and boundary scatterers whose scattering probability is assumed to be energy independent. If the imperfections due to cold work are assumed to be fixed point scatterers (perhaps vacancies) application of the free electron theory yields a degeneracy energy constant over the ranges of annealing and temperatures of measurement. The same degeneracy energy is approached above 200°K by the radiation-damaged copper if the imperfections are assumed to be boundary scatterers; this is in agreement with the view that point scatterers (vacancies and interstitials) are annealed below room temperature.

This paper is based on studies conducted for the U. S. Atomic Energy Commission.

[1] G. W. Rodeback and W. P. Eatherly, Phys. Rev. 91, 237 (1953).

**A4. Annealing Kinetics of Lattice Imperfections Using Evaporated Metal Films,*** R. W. HOFFMAN AND N. S. RASOR, *Case Institute of Technology.*—Copper films deposited in high vacuum onto glass substrates held at temperatures ranging from $-150$ to $-100$°C have been used to study the annealing kinetics of the lattice imperfections thus formed, utilizing the electrical resistivity as an index of the degree of imperfection. By varying the temperature of the film after deposition, isothermal anneals, tempering anneals, and activation energy determinations have been performed. A film 1200A thick deposited at $-150$°C anneals from an initial resistance of 17 ohms ($20\times10^{-6}$ ohm-cm) at $-150$°C to a resistance of 2 ohms after a 275°C anneal. This is a much larger effect than the 10 percent changes in resistivity reported for radiation damaged and cold-worked copper. However, the time dependence of the resistivity decay, the annealing states which occur, and the phenomenologically determined activation energies for the annealing of the films are not unlike those reported for radiation damaged[1] and cold-worked copper. Consideration of the annealing data, its dependence on deposition temperature, and the possible effect of internal stresses allow interpretation of the phenomena in terms of the migration of lattice imperfections.

* Supported by the U. S. Office of Naval Research.
[1] A. W. Overhauser, Phys. Rev. 90, 393 (1953).

**A5. Diffusion in Silver Single Crystals.*** C. T. TOMIZUKA AND L. SLIFKIN, *University of Illinois.*—Coefficients for the diffusion of radioactive tracers of cadmium, indium, and tin in silver single crystals were determined at an extremely dilute solute concentration. These results[1] together with those on diffusion of antimony in silver[2] show a systematic decrease of

$H$ and $D_0$ as the atomic number increases from that of silver. Since these diffusing elements are all neighbors of silver in the periodic table with larger atomic number, a transition element ruthenium which precedes silver is now being investigated. Preliminary results will be presented and discussed.

* Supported in part by the U. S. Atomic Energy Commission.
[1] C. T. Tomizuka and L. Slifkin, to be published.
[2] E. Sonder, L. Slifkin and C. T. Tomizuka, Phys. Rev. (to be published).

**A6. Solute Diffusion in Metals.** D. LAZARUS, *University of Illinois.*—It has been shown conclusively that even in extremely dilute solutions, solute ions may diffuse at a rate markedly different from the rate of self-diffusion of the solute.[1] A simple theory is proposed to explain this difference based on the effects of screening of the solute ions by the Fermi electrons of the lattice. Calculations made using a Thomas-Fermi model[2] give good agreement with the experimental data for solute diffusion in silver, if a vacancy mechanism is assumed.

[1] C. T. Tomizuka and L. Slifkin, Bull. Am. Phys. Soc. **29**, No. 3, 8 (1954) (this meeting).
[2] N. F. Mott, Proc. Cambridge Phil. Soc. **32**, 281 (1936).

**A7. A Comparison of Diffusion Techniques Employing Radioisotopes.*** R. L. SMITH, F. E. JAUMOT, JR., AND L. A. ARNÉ, JR., *The Franklin Institute Laboratories for Research and Development.*—The two radioactive tracer techniques generally used in the study of diffusion are the "sectioning" and "absorption" techniques. In the former, the diffusion coefficient is obtained from a curve of concentration *versus* the square of the penetration distance; in the latter, $D$ is obtained from the surface activity before and after diffusion. these two techniques have been compared in a study of self-diffusion in zinc over a temperature range from 200 to 400°C, using single crystal samples. The activation energies $Q$, obtained for diffusion parallel and perpendicular to the "$C$" axis agree for the two methods and with the most recent published data[1] within experimental error. The scatter in the data and the error is larger in the absorption technique. The effects of electroplating *versus* evaporation of the tracer onto the sample were studied and found to be negligible. The application of very large and very small amounts of tracer produced interesting anomalies in particular samples, but caused serious error in the calculation of $D$ only in the case of the absorption technique. The two methods were compared using polycrystal samples with various grain sizes and will be discussed.

* Supported by the U. S. Atomic Energy Commission.
[1] Shirn, Wajda, and Huntington, Acta Met. 1, 513 (1953).

**A8. Diffusion of $Co^{60}$ in Some Ni-Al Alloys Containing Excess Vacancies.*** A. E. BERKOWITZ,† F. E. JAUMOT, JR., AND F. C. NIX, *University of Pennsylvania.*—Bradley and Taylor[1] have shown that in the δ-phase of the Ni-Al system those alloys containing an excess of aluminum exhibit a density of vacancies that is considerably greater than the normal equilibrium concentration. Measurements were made of the diffusion of $Co^{60}$ in six compositions in the δ-phase of Ni-Al at 1050, 1150, 1250, and 1350°C. Diffusion coefficients and activation energies were obtained. The data show increasing diffusion coefficients and decreasing activation energies with increasing concentration of vacancies. These results are apparently consistent only with the vacancy mechanism of diffusion. These data do not agree with previous measurements[2] made on the same alloy system. The results are in agreement with measurements made on a similar defect alloy.[3]

* This work was supported by the U. S. Office of Naval Research.
† Now at The Franklin Institute Laboratories for Research and Development, Philadelphia 3, Pennsylvania.
[1] A. J. Bradley and A. Taylor, Proc. Roy. Soc. (London) **159**, 56 (1937).
[2] R. Smoluchowski and H. Burgess, Phys. Rev. **76**, 309 (1949).
[3] F. C. Nix and F. E. Jaumot, Jr., Phys. Rev. **83**, 1275 (1951).

**A9. The Effect on Diffusion Measurements of Some Beta-Ray Absorption Phenomena.*** A. E. BERKOWITZ,† *University of Pennsylvania.*—In diffusion experiments, in which one measures the decrease in activity as a radioactive tracer diffuses into a sample, an important source of error is the determination of the characteristics of the absorption of the radiation from the tracer by the sample. Usually a simple exponential expression is found or assumed to describe the absorption. During recent experiments on the diffusion of $Co^{60}$ in alloys of Ni and Al, we measured the absorption of the beta rays from $Co^{60}$ in thin foils and evaporated layers of Ni and Al. In all cases the activity increased with increasing absorber thickness in the range from 0 to 4 mg/cm². The data for thin foils differed from those representing evaporated and electroplated layers. The data fit closely to a curve representing the difference of two exponential terms. The indications are that the increased activity results from preferential beta-ray scattering rather than from the production of secondary electrons. The effect of the complex absorption expression on the calculation of diffusion coefficients will be discussed.

* This work was supported by the U. S. Office of Naval Research.
† Now at The Franklin Institute Laboratories for Research and Development.

**A10. Electrostatic Energy Calculations for Sodium Tungsten Bronze ($Na_xWO_3$).*** J. F. SMITH, *Iowa State College* (introduced by G. C. Danielson).—Recent measurements of the activation energy for diffusion of sodium in the metallic sodium tungsten bronze, $Na_{0.75}WO_3$, gave a value of 51.8 kcal/mole. To determine whether ionic bonding could be responsible for this high activation energy, electrostatic energy calculations have been made. Calculated activation energies for sodium diffusion using a model with random sodium distribution do not agree well with the measured value, but this discrepancy may be caused by ordering of the sodium atoms, Such ordering has been suggested by Gardner and Danielson to account for the anomalous resistivity at $x=0.75$. Further calculations of the total electrostatic energy as a function of sodium concentration have been made on the basis of random sodium distribution; point charges of $Na^{+}$, $W^{+6}$, $O^{-2}$; and a uniform neutralizing charge of free electrons. These calculations indicate that cubic sodium tungsten bronze should be unstable or metastable below $x=0.35$. This calculated value is in good agreement with the known phase transition occurring between $x=0.30$ and $x=0.38$.

* Work was performed in the Ames Laboratory of the U. S. Atomic Energy Commission.

**A11. The Surface Migration of Carbon on Tungsten*†** RALPH KLEIN, *Bureau of Mines.*—The surface migration of carbon on tungsten was observed with the field emission microscope. The carbon source was a carefully outgassed 5-mil diameter graphite filament. The vacuum attained in the system, exclusive of helium, was of the order of $10^{-12}$ mm of Hg. The tungsten point was shadowed with carbon and heated to a given temperature, the migration being followed by observing the emission patterns at room temperature at various time intervals. The migration process occurs with a sharp boundary of a form which clearly shows that the 011 and 121 planes are avoided. By application of the theory of diffusion with a sharp moving boundary,[1] an activation energy was calculated for the migration.

* This research is a part of the work being done at the Bureau of Mines, supported by Headquarters, U. S. Air Research and Development Command, Office of Scientific Research.
† Paper to be presented at meeting of the American Physical Society, Ann Arbor, Michigan, March 18, 1954.
[1] H. Fujita, J. Chem. Phys. **21**, 700 (1953).

## THURSDAY MORNING AT 10:00

## Italian Gardens

## (A. P. DE BRETTEVILLE presiding)

### *DSSP Symposium on Ferroelectricity*

**B1. Some X-ray and Neutron Diffraction Investigations on Ferroelectric Crystal Transitions.** RAY PEPINSKY, *The Pennsylvania State University* (30 min.)

**B2. Properties of Very Small Ferroelectric Particles.** WERNER KAENZIG, *University of Illinois.* (30 min.)

**B3. Nuclear Resonance in Ferroelectric Crystals.** W. D. KNIGHT, *University of California, Berkeley.* (30 min.)

### *Contributed Papers*

**B4. Heat of Transition of Barium Titanate at the Curie Point.** A. DEBRETTEVILLE AND E. D. HARRIS, *U. S. Signal Corps Engineering Laboratories.*—The authors' free energy expression for the paraelectric-to-ferroelectric phase-induced transformation is $E_t(P_m-1.5P_t)Nv$, where $E_t$ is the threshold field strength, $P_m$ is the maximum value of the polarization in the ferroelectric state, $P_t$ is the threshold polarization ($\epsilon/4\pi E_t$), and $Nv$ is the molar volume. By substituting experimentally-determined values of $E_t$, $\epsilon$ and $P_m$ that we obtained as functions of temperature into the free energy equation and differentiating it with respect to temperature, the entropy—and hence the heat of transition $\Delta H$—can be found. At the Curie point (115.5°C) $\Delta H$ is $-47$ cal/mole; the value of $\Delta H$ becomes zero at 121.7°C and increases to 8.5 cal/mole at 127°C. The data published by Merz give no value for $P_m$; his data,[1] however, can be interpreted to yield a value for $P_m$ of $10.09\times10^{-4}$ coulombs/cm². This value corresponds to the point of inflection of his $P$ *vs* $E$ curve. The value of $\Delta H$ obtained at the Curie point 107.5°C is $-24$ cal/mole; it becomes zero at 114.7°C and increases to 2 cal/mole at 116°C. The apparent temperature variation of the heat of transition may be merely a manifestation of a number of domains undergoing transitions at slightly different temperatures within a small temperature interval.

[1] W. J. Merz, Phys. Rev. 91, 513–517 (1953).

**B5. Domain Clamping Effect in Barium Titanate Single Crystals.** M. E. DROUGARD AND D. R. YOUNG, *International Business Machines Corporation.*—We have found that the dielectric constant of good single crystals of barium titanate decreases as the average polarization is decreased by means of an electric field. This has been interpreted as being due to a domain clamping effect arising from the multidomain situation in the crystal that accompanies the reduction in polarization. The dielectric constant for a crystal with zero average polarization is that of a thickness clamped crystal while the dielectric constant of crystal polarized to saturation is that of a free crystal. These measurements give a coefficient of coupling of 0.5 at room temperature in good agreement with the predicted value using the published values for $d_{31}$ and our independent measurement of $S_{31}$. The temperature dependence of the coupling coefficient for thickness vibrations as determined from our dielectric constant experiments is shown to be similar to that calculated for longitudinal vibrations from measurements of Merz.[1]

[1] W. Merz, Phys. Rev. 80, 1084 (1950).

**B6. Measurements of Ferroelectric Transition in Single Crystals of $Cd_2Nb_2O_7$.*** F. JONA, G. SHIRANE, AND R. PEPINSKY, *The Pennsylvania State University.*—Ceramic $Cd_2Nb_2O_7$ has been reported as ferroelectric below $-90$°C,[1] with a further transition taking place at $-190$°C.[2] By replacing Cd with Pb or Ca, or Nb with Ta, the Curie temperature was lowered. Single crystals of $Cd_2Nb_2O_7$ have been grown as octahedra, or thin plates with the major surface perpendicular to (111). The dielectric constant of these plates is about 700 at 20°C and roughly 10 000 at the Curie temperature (approximately $-115$°C). The single-crystal Curie temperature is somewhat lower than that of the ceramic, probably due to impurity in the crystals. The spontaneous polarization measured along the cubic (111) axis is about 5 microcoulombs/cm² at $-180$°C. Weissenberg photographs about the (110) zone show a small splitting of spots due to domain formation in the ferroelectric region. Assuming the low-temperature structure to be tetragonal, the axial distortion at $-180$°C is about 0.1 percent. Preliminary optical measurements confirm a transition to a noncubic system, but the symmetry is not yet established.

* Development supported by Aeronautical Research Laboratory, Wright Air Development Center.

[1] W. R. Cook, Jr., and H. Jaffe, Phys. Rev. 88, 1426 (1952); 89, 1297 (1953).

[2] G. Shirane and R. Pepinsky, Phys. Rev. 92, 504 (1953); and J. K. Hulm, Phys. Rev. 92, 504 (1953).

---

## THURSDAY MORNING AT 10:00

## Ballroom

## (G. J. DIENES presiding)

### *Irradiation Effects, I (Nonmetals)*

**C1. Dielectric Changes in Crystalphosphor Condensers Irradiated with X-Rays.** RUDOLF FRERICHS, *Northwestern University.*—The changes in dielectric constant and dielectric loss produced in crystalphosphors by irradiation [first observed by Gudden and Pohl (1920) in optically excited phosphors] can be used as detector for x-rays and penetrating

particles.[1] Electrical condensers consisting of alternating layers of aluminum foil and crystalphosphors embedded in polystyrene can be easily made in any electrical and geometrical size with complete absorption for the most penetrating impinging radiation. If such a condenser is fully excited changes up to 100 percent of the original capacity value can be obtained. Condensers made with copper activated zinc sulfide of 2000 $\mu\mu f$ reach a final value of more than 4000 $\mu\mu f$ after irradiation with 200 kv x-rays for one minute with a rate of 48 r/min. The increase of the dielectric constant and the dielectric loss as the irradiation progresses and the decrease in time as it is interrupted will be discussed and compared with the present theories. As the measurement of the capacity changes affords neither amplifiers nor high voltage or high insulation such condensers can be used as permanent monitors for radiation levels of about 1 r/min and higher.

[1] R. Frerichs, J. Appl. Phys. 23, 697 (1952).

**C2. Change of Electrical Conductivity of Alkali Halides Upon Irradiation with 350 Mev Protons.*** EDGAR PEARLSTEIN, *Carnegie Institute of Technology.*—KCl and NaCl crystals were irradiated at room temperature in the Carnegie Institute of Technology synchrocyclotron with proton fluxes between $10^{14}$ and $10^{17}$ per square centimeter. Conductivity was then measured by an ac method over a large temperature range. Data to be given are an extension of work previously reported by the author.[1] When the amount of bombardment is small, the conductivity is decreased. For large amounts of bombardment, there is at first an increase in conductivity, which becomes a decrease as the temperature at which conductivity measurements take place is raised. Polarization in times of the order of $\frac{1}{10}$ sec complicates the measurements at some temperatures, so that an ac method is desirable. Polarization is usually considerably larger for bombarded crystals than for nonbombarded ones.

* Work supported by the U. S. Atomic Energy Commission.
[1] E. Pearlstein, Phys. Rev. 92, 881 (1953).

**C3. On the Influence of Nuclear Radiation on Electrical Conductivity of Alkali Halides.*** R. SMOLUCHOWSKI, *Carnegie Institute of Technology.*—The preceding abstract on the change of electrical conductivity of alkali halides upon irradiation by high-energy protons illustrates amply the complexity of the phenomena here encountered. Some earlier results by Sproull, Maurer, and others point in the same direction. A brief summary will be given of the various mechanisms which could play a role in these effects such as clustering, trapping, vacancy formation, etc. It will be pointed out that irradiation with the high-energy protons of the Carnegie Institute of Technology cyclotron requires taking into account the probability of the occurrence of nuclear transformations in the solid analogous to the formation of "stars" in cosmic ray studies. The prongs of these stars have the right energy to produce large effects in solids. It appears that the total effect produced by this mechanism may be more important than the other processes usually considered.

* Work supported by a U. S. Atomic Energy Commission contract.

**C4. Irradiation Induced Optical Absorption in $Al_2O_3$.*** PAUL W. LEVY AND G. J. DIENES, *Brookhaven National Laboratory.*—Hunt and Schuler[1] have shown that synthetic crystals of $\alpha$-$Al_2O_3$ were slightly colored in the ultraviolet by x-ray bombardment and observed saturation at small x-ray doses. Irradiation of this material by gamma rays produces similar coloring. A dose of 2 to $3\times10^4$ r produces as much coloring as $10^7$ r. Single crystals of $\alpha$-$Al_2O_3$ subjected to pile irradiation exhibit two additional well-defined absorption bands at 2040A and 2600A. The 2040A band is approximately 10 times as intense as the 2600A band. The transmission of the crystals at 2040A is about 90 percent after the gamma-ray coloring has reached saturation. Sixteen hours irradiation in the Brookhaven reactor reduces the transmission at this wavelength to less than 0.1 percent. The intensity of the absorption bands is unaltered by additional $\gamma$-irradiation which indicates that the absorption due to fast neutron damage is independent of the presence of ionizing radiation. The 2040A absorption increases with irradiation time according to the equation $dN/dt = K - fN$. At 100°C in the reactor $f$ is approximately 0.14. In contrast, thermal annealing at 100° and 200°C reduces the intensity by less than 0.5 percent.

* Work accomplished under contract with the U. S. Atomic Energy Commission.
[1] R. Allan Hunt and Robert H. Schuler, Phys. Rev. 89, 664 (1953).

**C5. Magnetic Susceptibility of Fast Neutron Bombarded Ge.** D. K. STEVENS, J. W. CLELAND, AND J. H. CRAWFORD, JR., *Oak Ridge National Laboratory.*—The magnetic susceptibility of $n$-type Ge subjected to various periods of bombardment in the Oak Ridge Graphite Reactor has been measured as a function of temperature in the range 65° to 300°K. According to present concepts the free current carriers add a diamagnetic contribution to the total susceptibility due to the orbital motion imparted to the carriers by the magnetic field.[1] Because of the small effective mass of electrons[2] this contribution is quite large in Ge. The effect of irradiation is to decrease the diamagnetism of material with an initial large concentration of electrons in a manner consistent with the removal of electrons from the conduction band by bombardment introduced traps. Changes in electron concentration resulting from bombardment determined from susceptibility measurements agree within experimental error with the values obtained from Hall constant measurements. Implications concerning the magnetic nature of electron traps will also be discussed.

[1] Busch and Mooser, Z. physik Chem. 198, 23 (1951).
[2] D. K. Stevens and J. H. Crawford, Jr., Phys. Rev. 92, 1065 (1953).

**C6. Bombardment Damage of Ge Crystals by Fast Electrons.** W. KOHN,* *Bell Telephone Laboratories.*—It has been found[1] that the conductivity of $n$-type Ge is reduced by bombardment with electrons whose energy exceeds 0.63 Mev. This effect and its disappearance by annealing has been studied in detail by Fletcher, Brown, and Wright.[2] The experimental facts are consistent with the picture that the reduction of conductivity is due to the formation of acceptor levels associated with vacancy-interstitial pairs produced by the bombardment. The threshold of 0.63 Mev implies that at least 30.5 ev must be imparted to a Ge atom to produce an acceptor level. Theoretical considerations are presented which lead to the conclusion that some of the nearest interstitial positions can be reached by atoms with substantially smaller energies. This is consistent with the reported threshold of 25 ev for interstitial production in the much more closely packed Cu lattice.[3] One is thus led to the picture that in Ge the most easily accessible interstitial positions are either unstable or, if stable, do not give rise to acceptor levels.

* On summer leave from Carnegie Institute of Technology, Pittsburgh, Pennsylvania.
[1] E. E. Klontz and K. Lark-Horovitz, Phys. Rev. 86, 643 (1952).
[2] R. C. Fletcher and W. L. Brown, Phys. Rev. 92, 585 (1953); Brown, Fletcher, and Wright, Phys. Rev. 92, 591 (1953).
[3] D. T. Eggen and M. J. Laubenstein, Phys. Rev. 91, 238 (1953).

**C7. Minority Carrier Lifetime in Semiconductors as a Sensitive Indicator of Radiation Damage.*** P. RAPPAPORT, *Radio Corporation of America.*—Studies of beta-particle bombardment of semiconductors indicate that minority carrier lifetime constitutes an extremely sensitive indicator of radiation damage. In studies of the electron-voltaic behavior of $p$-$n$ junctions[1] bombarded by beta particles from a 50 millicurie Sr90-Y90 source, it was observed that the open circuit voltage decreased by as much as a factor of two in 1 hour. This effect decreases as one goes in the direction of intrinsic

material. This corresponds to a change of $10^{11}/cm^3$ in the number of defects. So small a change would not appreciably affect the conductivity of the samples studied. Observations on the junction rectifier characteristics which can also be markedly affected by beta bombardment suggest that the major physical basis for the change in both rectifier and electron-voltaic effects resides in an alteration of the minority carrier lifetime ($\tau$). This appears to be borne out by actual measurements which show that $\tau$ can change by an order of magnitude when the defects are increased by $10^{11}/cm^3$.

* Work supported by Wright Air Development Center, U. S. Air Force.
[1] P. Rappaport, Phys. Rev. 93, 1954.

**C8. Radiation Effects in Indium Antimonide.** J. W. CLELAND AND J. H. CRAWFORD, JR., *Oak Ridge National Laboratory.*—Measurements of the effect of reactor irradiation on the electrical properties of InSb[1] have been extended. Single crystal[2] specimens have been irradiated in the Oak Ridge graphite reactor at ~30°C. Since transmutation effects are comparable to or greater than lattice disordering effects for the neutron energy spectrum employed, all samples were shielded with Cd and In foil. Measurements of the Hall constant at liquid nitrogen temperature indicate that the rate of removal of holes for $p$-type material is about four times the rate of removal of electrons for low-resistivity $n$-type material. Since the hole removal process is predominant, $p$-type InSb can be converted to $n$-type by lattice disorder and both $p$-type and low-resistivity $n$-type arrive at a final high-resistivity $n$-type saturation with a liquid nitrogen carrier concentration of $\sim 1\times10^{16}$ electrons/cm$^3$. It is therefore concluded that lattice defects introduced by fast neutrons act as electron traps in $n$-type material and as hole traps in $p$-type material, the hole traps being about four times as efficient.

[1] J. W. Cleland and J. H. Crawford, Jr., Phys. Rev. (to be published).
[2] We are indebted to M. Tanenbaum of the Bell Telephone Laboratories for the samples used in these experiments.

**C9. Hall and Resistivity Measurements During Electron Bombardment of Germanium and Indium-Antimony.*** R. PEPPER, E. KLONTZ, K. LARK-HOROVITZ, AND J. MACKAY, *Purdue University.*—Electrons from the linear accelerator (4.5 Mev) were used for irradiating Ge and In-Sb semiconductors near liquid nitrogen temperatures (87°K). By bombarding between the poles of a magnet, the Hall effect $R$ and resistivity $\rho$ were measured during bombardment, thus allowing changes in mobility during irradiation to be followed. $p$-type Ge (In doped) exhibits monotonically increasing $R$ and $\rho$ values with little change in $R/\rho$ during bombardment. However in a 5.5 ohm-cm sample doped with Au, with an impurity activation energy of 0.21 ev, both $R$ and $\rho$ decrease. The ratio $R/\rho$ decreases first by a factor of three but finally increases to a value slightly greater than the initial value. In $p$-type In-Sb, $R$ and $\rho$ increase monotonically and $R/\rho$ decreases slightly during bombardment. In a 4 ohm-cm $n$-type Ge sample both $R$ and $\rho$ increase initially and $R$ passes through a maximum negative value for a flux of about $1.3\times10^{14}$ electrons/cm$^3$. Continued bombardment changes $R$ to positive values. On warming up to room temperature $R$ again becomes negative for a total flux of $5\times10^{15}$ electrons/cm$^3$.

* Supported by a U. S. Atomic Energy Commission contract.

**C10. The Elastic Constants of Silicon Before and After Neutron Bombardment from X-Ray Diffuse Scattering.*** W. P. BINNIE AND A. M. LIEBSCHUTZ,† *Purdue University.*—Using a Geiger counter the diffuse scattering of $CuK_\alpha$ x-rays from a single crystal of silicon was measured before and after a neutron bombardment of $3\times10^{19}$ n.v.t. From these data the elastic constants have been determined using Wooster and Ramachandran's method.[1] The elastic constants before irradiation agree with the values obtained by ultrasonic methods but after bombardment striking changes occur particularly in the values of $C_{11}$ and $C_{12}$. From the elastic constants Young's Modulus, compressibility and the Debye temperature can be calculated. The values calculated from the elastic constants before irradiation agree with those measured directly. The change in Debye temperature observed after neutron irradiation has been calculated from the changes of the elastic constants and is in agreement with the experiments.

* Supported by a U. S. Atomic Energy Commission contract.
† Now at Convair, Fort Worth, Texas.
[1] G. M. Ramachandran and W. A. Wooster, Acta Cryst. 3, 335, 431 (1915).

---

## THURSDAY MORNING AT 10:00

## Normandy Room

## (J. K. GALT presiding)

### *Magnetic Resonance and Spin-Wave Theory*

**D1. Paramagnetic Resonance Absorption in Carbons.*** J. G. CASTLE, JR., *University of Buffalo.*—Paramagnetic resonance absorption characteristic of natural and artificial graphite was found[1] as a single resonance line close to the gyromagnetic ratio of the spin moment of a free electron. The investigations have been extended to carbons of smaller crystallite size. The carbon was prepared by grinding soft coke to particles with mean diameters of one to two microns and then heat-treating a single batch of the powder to a series (starting around 1000°C) of successively higher temperatures until artificial graphite was formed (2500°C and higher). No resonance absorption was observed after the lower heat-treatments, but after treatment to around 1400°C a very broad line corresponding to $g=2.00$ was found. The line sharpens as heat-treatment temperature is increased. The width is $11\pm3$ gauss for polycrystalline graphite in agreement with the earlier measurements. The position of the peak absorption is essentially constant and the intensity of resonance absorption per unit mass is the same within an order of magnitude. Absorption may be present in the baked carbons, but a line with a half-width greater than 200 gauss would have gone undetected.

* Supported by the U. S. Office of Naval Research.
[1] J. G. Castle, Jr., Phys. Rev. 92, 1062 (1953).

**D2. Pure Quadrupole Spectrum of Methyl Iodide Vapor.*** FRED STERZER, *New York University and Newark College of Engineering,* AND YARDLEY BEERS, *New York University.*—In a symmetric top molecule transitions can take place between quadrupole hyperfine levels of the same $J$ and $K$ provided that $K\neq0$. Because of its large quadrupole-coupling constant, $CH_3I^{127}$ has several lines of this type with computed intensities sufficient for observation in the uhf region. Using the spectrometer reported previously,[1] we have observed the

following lines: $J=K=3$, $F=11/2\rightarrow 9/2$, 444.76±0.10 Mc/sec; $J=K=4$, $F=13/2\rightarrow 11/2$, 481.05±0.10 Mc/sec; $J=K=5$, $F=15/2\rightarrow 13/2$, 503.05±0.15 Mc/sec. The identities of the first two lines were confirmed from Stark splittings. These measured frequencies are perfectly consistent with the quadrupole coupling constant obtained from microwave rotational spectra[2] if second-order theory is employed.

* Supported by the U. S. Office of Naval Research and by the U. S. Air Force, through the Office of Scientific Research of the U. S. Air Research and Development Command.

[1] Y. Beers and S. Weisbaum, Phys. Rev. 91, 1014 (1953).

[2] Gordy, Simmons, and Smith, Phys. Rev. 74, 243 (1948).

**D3. Nuclear Magnetic Relaxation in Semiconductors.** N. BLOEMBERGEN, *Harvard University.*—The theory of nuclear relaxation in metals by the interaction with conduction electron spins is extended to semiconductors. When the carriers obey Maxwell-Boltzmann statistics, the relaxation time is inversely proportional to the concentration of carriers and to the square root of the temperature. In a degenerate Fermi-Dirac gas of carriers the relaxation time is inversely proportional to the absolute temperature and to the two-thirds power of the concentration. The degeneracy temperature and the hyperfine interaction in semiconductors may be determined from the nuclear relaxation time, which will usually be rather long. When most electrons or holes are bound in the impurity levels, another relaxation mechanism will be more important. Spin-diffusion toward the bound paramagnetic impurities may result in a relaxation time which is independent of the temperature. Applications of the theory to grey tin and to silicon and germanium will be discussed.

**D4. Proton Magnetic Resonance in Compounds Having Several Liquid Crystal Phases.** R. EWING AND J. C. LEE, *Michigan State College.*—According to Bernal and Crowfoot, the compounds ethylanisal *para*-aminocinnamate and ethylphenyl benzylamino cinnamate exhibit three and four liquid crystal phases, respectively. We have attempted to relate these phases with the changes in line shape of the proton resonance signal. In the three-phase compound the line shape in the highest temperature phase consists of a triplet similar to those reported[1] for compounds having only a single liquid crystal phase. As the temperature is decreased the line shape changes radically and at lower temperatures emerges as a single narrow line on a broad base. The changes of the line shape with temperature for the four phase compound are much less spectacular. Some of the observed line shapes may arise from crystalline phases which co-exist with the liquid crystal phases.

[1] Jain, Moses, Lee, and Spence, Phys. Rev. 92, 844(A) (1953).

**D5. Ferromagnetic Resonance Relaxation Times in Single Crystals of Nickel and Iron.*** J. A. COWEN AND R. D. SPENCE, *Michigan State College.*—We have measured the reciprocal relaxation time $1/T_2$ for samples cut from nickel and iron single crystals from room temperature up to their respective Curie temperatures, at a frequency of 9400 Mc. At room temperature (111) and (100) cuts of nickel yield a value of $1/T_2$ approximately 5/3 of its value for a polycrystalline sample ($3.2\times10^{-9}$ sec$^{-1}$). As the temperature is increased $1/T_2$ decreases and at 300°C is about the same as for a polycrystalline sample. As the temperature approaches the Curie point $1/T_2$ increases rapidly following a curve of the same shape as that for polycrystalline samples. For (111) samples of iron the room temperature value of $1/T_2$ is $14\times10^{-9}$ sec$^{-1}$. In such samples $1/T_2$ reaches a maximum at 250°C and then decreases to $5\times10^{-9}$ sec$^{-1}$ at the Curie point.

* Supported by the U. S. Office of Ordnance Research.

**D6. Study of Exchange Interactions by Spin Wave Resonance.** G. T. RADO AND J. R. WEERTMAN, *Naval Research Laboratory.*—No previous experiments have revealed exchange interaction effects in ferromagnetic resonance, and semi-theoretical estimates[1] have indicated that at room temperature the "exchange shift" $\Delta H$ is indeed only about 0.2 percent of the static field $H$ required for resonance. It is now shown that an easily measurable exchange shift of about 20 percent can be obtained at room temperature by using an unusually small $H$ (~100 oersted) in conjunction with a zero-anisotropy polycrystal (or low-anisotropy monocrystal) possessing a large $\mu_2$ (~1000) at resonance. The samples used by us to date are properly heat-treated cylinders of 66 percent Ni—34 percent Fe alloy. By using an improved, modified version of a technique described earlier,[2] measurements are obtained at 3000 and 6000 Mc/sec of both parts of the "equivalent isotropic permeability" ($\mu=\mu_1-i\mu_2$) as a function of the axially-applied static field. Tentative results demonstrate the existence of exchange effects in this "spin wave resonance" by exhibiting the characteristic line shapes calculated in the following abstract (Ament and Rado) and yielding reasonable values of the spectroscopic splitting factor $g$ and exchange factor $A$.

[1] C. Kittel and C. Herring, Phys. Rev. 77, 725 (1950).

[2] M. H. Johnson and G. T. Rado, Phys. Rev. 75, 841 (1949).

**D7. Electromagnetic Effects of Spin Wave Resonance.** W. S. AMENT AND G. T. RADO, *Naval Research Laboratory.*—Maxwell's equations, and the "precession equation" supplemented by the exchange torque $(2A/M_s^2)\mathbf{M}\times\nabla^2\mathbf{M}$, determine the microwave propagation inside a saturated ferromagnet. In a metal, the exchange factor $A$ gives rise to three propagation constants, $k_1$, $k_2$, $k_3$, for waves with both propagation vector and magnetic vector perpendicular to the static magnetic field $H_s$. When such waves are excited externally, the three wave-amplitudes are determined through the usual continuity conditions at the air-metal interface, plus two new boundary conditions, the vanishing of the normal derivatives of the $x$ and $y$ components of the microwave magnetization. These new conditions, shown to be equivalent to the delta-function picture,[1] are explained physically. The surface impedance $E_x/H_x$ is calculated from the boundary conditions and the solutions of the cubic secular equation for $k_1^2$, $k_2^2$, $k_3^2$. The "equivalent isotropic permeability," $\mu$, derived from $E_x/H_x$, depends on $A$, $g$, and $\lambda$, as well as on the known parameters $\omega$, $\sigma$, $M_s$, and $H_s$. For $A\neq0$, resonance shift and line broadening are found in the calculated $\mu$ even when the damping factor $\lambda$ vanishes.

[1] C. Kittel and C. Herring, Phys. Rev. 77, 725 (1950).

**D8. Theory of $g$ Factor and Spin-Lattice Relaxation Time in Alkali Metals.** HARVEY BROOKS, *Harvard University.*—A quantitative theory of the $g$ factor in alkali metals has been developed which permits calculations based only on a knowledge of the spectroscopic term values of the free atom, including the fine structure intervals in the $p$ terms. The method is an extension of that employed in a recent calculation of the cohesive energy of the alkalis, and the approximations involved are equivalent to those employed in a similar calculation by Yafet.[1] The result for sodium is $\Delta g=-3.2\times10^{-4}\sin^2\theta_0$ as compared with $\Delta g=-3.7\times10^{-4}\sin^2\theta_0$ computed by Yafet. Here $\theta_0$ is the angle between the $k$ vector and the magnetic field. Numerical results will be given for the other alkali metals. The new method has also been used to investigate the spin-lattice relaxation time, using essentially a model proposed by R. J. Elliott in which spin flops accompanying lattice scattering result from the contamination of each spin state by its opposite via the spin-orbit interaction. It is found that the principal contributions to the matrix element can be evaluated without recourse to explicit wave functions and ionic potentials and so can be deduced from spectroscopic data of the free atoms.

[1] Harvey Brooks, Phys. Rev. 91, 1027 (1953); Y. Yafet, Phys. Rev. 85, 478 (1952).

**D9. Spin Waves in Antiferromagnetic Face-Centered Cubic Lattices.** FRANK STERN,* *Bell Telephone Laboratories.*—Anderson's[1] treatment of spin waves in antiferromagnetic lattices is modified by expanding in the deviation of the $z$ component of spin from $S$ instead of from $[S(S+1)]^{\frac{1}{2}}$. The modified method is applied to face-centered cubic lattices with antiferromagnetic ordering of the second and third kinds. The energy and the mean spin per sublattice are evaluated at absolute zero and some of the resulting integrals are very crudely estimated in terms of the ratio of nearest to next nearest neighbor interactions. The lattice becomes disordered at the transition between ordering of the second and third kinds. There are two forms of ordering of the second kind—Case $A$ has alternating trigonal planes of up and down spins, as observed in MnO;[2] Case $B$ has spins in the trigonal planes alternately in the ratio 3:1 and 1:3, with no trigonal planes singled out.

* Now at the U. S. Naval Ordnance Laboratory.
[1] P. W. Anderson, Phys. Rev. **86**, 694 (1952).
[2] Shull, Strauser, and Wollan, Phys. Rev. **83**, 333 (1951).

**D10. Dipolar Ferromagnetism in Cubic Lattices.** M. H. COHEN, *University of Chicago,* AND F. KEFFER, *University of Pittsburgh.*—A critical examination of the Holstein-Primakoff spin-wave technique[1] has yielded explicit criteria for the stability of ferromagnetic arrays. These criteria have been applied to point dipoles on the three primitive cubic lattices for the shape most favorable for ferromagnetism, that of a long, thin sample. The results are as follows: (1) dipolar ferromagnetism cannot occur on the simple cubic lattice; (2) the ferromagnetic state can be the lowest, or at least a metastable, state on the face-centered and body-centered cubic lattices. The lowest energies of ferromagnetic states were calculated for the ⟨100⟩, ⟨011⟩, and ⟨111⟩ directions, thus obtaining two anisotropy constants, $K_1$ and $K_2$, for each lattice. This anisotropy is quantum-mechanical in nature, originating in the zero point energy of the spin waves. Comparison with previous classical[2] and quantum-mechanical[3] considerations will be made. This work is based on calculations of dipolar sums to be published shortly.

[1] T. Holstein and H. Primakoff, Phys. Rev. **58**, 1098 (1940).
[2] J. M. Luttinger and L. Tisza, Phys. Rev. **70**, 954 (1946).
[3] J. Tessman, Phys. Rev. **85**, 752 (1952).

## THURSDAY MORNING AT 10:00

State Hall 101, Wayne University

(T. G. Fox presiding)

### *Invited Papers in High-Polymer Physics*

**E1. Effect of High-Energy Radiation on Polymers.** A. CHARLESBY, *Harwell.* (30 min.)

**E2. Theory of Orientation and Double Refraction in Polymers.** E. F. GURNEE, *Dow Chemical Company.* (30 min.)

**E3. Measure of Orientation in Polystyrene Monofilaments by Means of Double Refraction.** R. D. ANDREWS, *Dow Chemical Company.* (30 min.)

### *Contributed Papers*

**E4. Effects of $Co^{60}$ Gamma Radiation on Formation and Degradation of Polymers.** M. HOBBS LINDSEY, DOUGLAS E. BROWN, AND DAVID W. PLETCHER, *University of Michigan.*—The composition of product of the gamma catalyzed polymerization of an equimolar mixture of styrene and methyl methacrylate is identical to that formed in the presence of benzoyl peroxide and quite different from those formed in the presence of sodium and stannic chloride. This result may be interpreted to mean, by the scheme of Mayo and Walling, that the gamma catalyzed polymerization is of the free radical type. The gamma catalyzed polymerization is promoted by several of the conventional antioxidants and inhibitors and certain vulcanization accelerators and is retarded by several materials including sulphur compounds. Consideration is given to the possible relationship of these observations with, (1) free radical polymerization and (2) polymer degradation in the presence of light, oxygen, ozone, and heavy metals.

**E5. Dielectric High-Frequency Method for Molecular Weight Determinations.*** P. DEBYE, P. P. DEBYE,† AND B. H. ECKSTEIN, *Cornell University.*—If an inhomogeneous electric field $E$ is applied to a solution whose constituents have different polarizabilities, the more polarizable one will accumulate to excess in the region of maximum field energy. Consider a polymer solution, the polymer having the greater polarizability, in a cylindrical condenser with a fine wire, centrally located, as one electrode. If a high field is applied, the concentration of polymer near the wire will exceed the macroscopic concentration and a "polymer atmosphere" will be formed about the wire, having a Boltzmann distribution corresponding to a potential energy $V=\frac{1}{2}\alpha E^2$. In the presently employed arrangement the condenser is made part of a circuit oscillating at 5 mc. The small change in frequency resulting when the potential is applied is measured by beating this variable frequency oscillator against a fixed frequency monitor. At low concentrations, the change in frequency is directly proportional to the molecular weight of the polymer and to $E^2$. However, the change in frequency is not instantaneous; it can be followed quite closely. From the manner in which the change occurs conclusions may be drawn about the distribution of mobilities, and hence of molecular weights and dimensions, in the polymer.

* This work is supported by the Office of Synthetic Rubber of the RFC.
† Present address: Raytheon Manufacturing Company, Waltham, Massachusetts.

**E6. A Field-Induced Diffraction Method for Molecular Weight Determinations.*** W. A. BARBER, P. DEBYE, AND B. H. ECKSTEIN, *Cornell University.*—When ultrasonic vibrations from a crystal are transmitted through a liquid, periodic inhomogeneities in density, and hence in refractive index, are created and may be discerned by using them as a diffraction grating for light. Another way of creating such a grating is to introduce periodic variations in the refractive index of a solution by other means. In this study, the effect of an inhomogeneous electric field, discussed in the preceding paper, is utilized. A stack of uniformly spaced razorblades with sharp edges serves as one electrode, a brass plate about 5 mm away

as the other. When the whole assembly is submerged in a polymer solution and a strong electric field is applied, again a Boltzmann atmosphere of polymer is built up in the vicinity of the blade edges, where the field is strongest. A parallel beam of monochromatic light is passed through the space between the electrodes, its direction parallel to the blade edges. The spectrum visible first, due to the blades alone, is blocked out. Then the field is applied, and the spectrum reappears, now due to the polymer aggregations. The intensity of the first-order line is proportional to $M^2$ and $E^4$, and it is measured by reading the output of a photomultiplier tube on a cathode-ray oscilloscope.

* This work is supported by the Office of Synthetic Rubber, of the RFC.

**E7. Gamma-Ray Polymerization of Acrylamide in the Solid State.*** ROBERT B. MESROBIAN AND PAUL ANDER, *Polytechnic Institute of Brooklyn*, AND DAVID S. BALLANTINE AND G. J. DIENES, *Brookhaven National Laboratory*.—The polymerization of vinyl monomers can be initiated by heat, ultraviolet radiation, and various catalysts. More recently ionizing radiation has been shown to initiate effectively vinyl polymerization.[1] However, polymerization in the solid state by any of the above means is not reported in the literature. Some experiments will be described which demonstrate that crystalline acrylamide undergoes polymerization upon irradiation with $\gamma$ rays from an intense $Co^{60}$ source. Sublimed acrylamide was irradiated in vacuo and the polymer isolated by methanol precipitant. Viscosity, osmotic pressure, and turbidity measurements were performed on water solutions of the polymer. Conversion *vs* time curves were obtained at several irradiation temperatures with the temperature maintained constant at ±1°C. At 5°C or below a long induction period was observed. Radicals are "frozen-in" at these temperatures since upon warming violent polymerization occurs. Residual crystallinity of the bulk sample was determined by measuring the integrated intensity of several x-ray reflections. The residual crystallinity decreases with irradiation. However, appreciable crystallinity remains even at high conversion indicating that the monomer crystalline domains are not strongly disturbed by the newly formed polymer chains.

* Work partially done under contract with the U. S. Atomic Energy Commission.

[1] F. S. Dainton and E. Collinson, Ann. Rev. Phys. Chem. 2, 99 (1951).

**E8. Static Electrification of Filaments: Dependence of Charge Transferred on Normal Force and Velocity.** S. P. HERSH* AND D. J. MONTGOMERY,† *Textile Research Institute*.—An apparatus has been constructed to permit short lengths of single filaments to be rubbed against each other under controlled ambient and mechanical conditions. The net charge transferred in a single rub is measured with an electrometer. Among the materials studied were various metals and the nonmetals, glass, wool, cotton, Nylon, viscose, polyethylene, and Teflon. With respect to dependence on normal force for both metals on insulators and insulators on insulators, the charge increases linearly from nonvanishing intercept to a limiting value, presumably as a result of electrical breakdown of the atmosphere. A similar behavior is found for the velocity dependence, except that for some insulators on insulators the charge appears to be independent of velocity within the range available for the apparatus.

* Union Carbide and Carbon Fellow at Textile Research Institute.
† Present address: Michigan State College, East Lansing, Michigan.

---

## THURSDAY AFTERNOON AT 2:00

## State Hall 101, Wayne University

## (J. D. FERRY presiding)

### *High-Polymer Physics*

**F1. Dynamic Mechanical Properties of Polyvinyl Acetate.** MALCOLM L. WILLIAMS AND JOHN D. FERRY, *University of Wisconsin*.—A sample of polyvinyl acetate (AYAX) of number-average molecular weight 140 000 has been investigated both in the undiluted state and as a 50 percent solution (by volume) in tri-*m*-cresyl phosphate. The real and imaginary parts of the complex compliance were measured with the double transducer of Fitzgerald and Ferry between 30 and 4500 cps. The temperature ranges were 50° to 90°C for the undiluted polymer and −10° to 40°C for the solution, and the values of the real component of the compliance ranged in each case from $10^{-6}$ to $10^{-9.6}$ cm²/dyne, corresponding to the transition from soft to glasslike consistency. The data for both components could be combined at various temperatures by the method of reduced variables. Relaxation distribution functions and apparent heats of activation for the relaxation process have been calculated and are compared with similar data for other polymers in the undiluted state as well as for solutions of polyvinyl acetate in a solvent of much lower viscosity.

**F2. Slow Relaxation Mechanisms in Concentrated Polymer Solutions.** JOHN D. FERRY, MALCOLM L. WILLIAMS, AND DONALD M. STERN, *University of Wisconsin*.—The distribution of relaxation mechanisms in concentrated polymer solutions at the slow end of the time scale can be derived from dynamic viscosity, stress relaxation, and (according to a new theory of DeWitt) the non-Newtonian viscosity. The results of such measurements are compared for several samples of polyisobutylene, polystyrene, and polyvinyl acetate, and in general they agree well. A modification of the Rouse theory is used to predict the slow time-dependent behavior from the steady flow viscosity (at vanishing stress) and the molecular weight; the agreement is close for a sharp fraction. The elastic compliance of a polymer solution in steady-state flow is dominated by the slow relaxation mechanisms; according to the modified Rouse theory, it is $J=(2/5)M_{w+1}M_z/M_w cRT$, where $c$ is the concentration in g/cc.

**F3. A Calculation of the Dynamic Bulk Modulus of Polyisobutylene.** ROBERT S. MARVIN, *National Bureau of Standards*, AND H. S. SACK AND R. ALDRICH,* *Cornell University*.†—The complex dynamic bulk (dilational) modulus ($K^*$) of a polyisobutylene of viscosity average molecular weight $1.35\times10^6$ has been computed from measured shear ($G^*$)[1] and compressional ($M^*$) moduli and the relation $M^*=K^*+4/3G^*$. The results demonstrate the existence of an imaginary (viscous) component of the bulk modulus of this material, and similarity between the temperature dependence of the apparent activation energy in dilatation and that in shear. There is a less certain indication that the maximum loss occurs at the same temperature and frequency in both shear and dilatation.

* Present address, General Electric Company, Syracuse, New York.
† The work at Cornell University was supported by the U. S. Office of Naval Research.

[1] R. S. Marvin, Second International Congress on Rheology, Oxford, England, 1953.

**F4. Steady-State Elastic Shear Compliance and Molecular Weight Distribution in Polyisobutylene.** HERBERT LEADERMAN AND M. WALES, *National Bureau of Standards.*—The steady-state elastic shear compliance $J$ of two polyisobutylene fractions ($\bar{M}_w$ $2\times10^4$ and $13.5\times10^4$) and of five blends of these fractions has been measured. Values for 0, 11.5, 19.9, and 100 percent weight fraction of the high molecular weight component are 1.1, 17.3, 16.0, and $3.3\times10^{-6}$ cm²/dyne. The maximum value of $\bar{M}_z/\bar{M}_w$ corresponds to a blend containing about 15 percent of the high molecular weight fraction. Preliminary data suggest that $J$ is proportional to $(\bar{M}_z/\bar{M}_w)^3$ for these blends. The parameter $1/G_i$ used to specify non-Newtonian flow shows the same trend.

**F5. Multiple Dispersion Regions in Rigid Polymeric Systems.** ROLF BUCHDAHL AND LAWRENCE E. NIELSEN, *Monsanto Chemical Company.*—It is shown how chemical and colloidal heterogeneity can result in multiple dispersion regions of the mechanical or electrical loss factor as a function of temperature. Heterogeneity can be produced in several ways: (a) mechanical blending (mixing) of certain polymers, (b) nonuniform copolymerization, (c) block or graft polymerization, (d) external plasticization, and (e) certain types of molecular weight distribution. Specific examples are given to demonstrate the effect.

**F6. The Effect of Crystallinity on the Dynamic Mechanical Properties of Polyethylenes.** LAWRENCE E. NIELSEN, *Monsanto Chemical Company.*—Six polyethylenes which differed widely in the degree of crystallinity were studied. The crystallinity was determined from density measurements. Both the density and the dynamic mechanical measurements were made over the temperature range from 25°C to above the melting point of the material. The dynamic shear modulus drops off rapidly as the melting point is approached. The mechanical damping goes through a maximum near 60°C and then through a minimum just below the melting point. It is possible to predict the density of any point from the value of the shear modulus at the same temperature. The more crystalline materials have the higher shear moduli and the higher melting points.

**F7. Elastic and Dielectric Losses of some High Polymers Near and Below the Second-Order Transition Temperature.*** H. S. SACK, T. R. CUYKENDALL, AND T. J. WOODS,† *Cornell University.*—While many high polymers (polyvinylacetate, GRS, etc.) exhibit peaks of the elastic and electric losses as a function of temperature in the region of the second-order transition, no such peaks were found for cellulose-acetate and nitrate, though samples of the same preparation show the characteristic second-order transition behavior of the expansion coefficient. However, peaks were found at very much lower temperatures, accompanied by changes in the elastic modulus. The dependence on frequency is that of a relaxation phenomenon similar to that observed above the transition temperature for polyvinylacetate (and others). The elastic and electric measurements are very similar, and the activation energies that can be calculated from the data are the same, though the absolute values of the relaxation times may be different. The low-temperature relaxation may be due to the mobility of relatively small groups, while above the transition temperature the motion of large sections of the whole molecule plays the important role.

* This research was supported by the U. S. Office of Naval Research.
† Now with Pratt & Whitney, Hartford, Connecticut.

**F8. Ultrasonic Properties of Hycar OS-10 and Paracril 35.*** J. L. MELCHOR† AND A. A. PETRAUSKAS, *University of Notre Dame.*—Ultrasonic propagation properties of Hycar OS-10 and Paracril 35 have been studied from 250 kc to 10 mc and from −50°C to +70°C. Sound velocity was found to decrease with increasing temperature and to exhibit two relatively sharp slope changes in the temperature range studied. Sound velocity increased with increasing frequency. Attenuation was found to peak in this temperature range for each of the frequencies employed. These peaks shifted to higher temperatures with increasing frequency. The temperature region of maximum attenuation and dispersion was assumed to represent the region of second-order transition. Activation energies of 38 kcal/mole for Hycar OS-10 and 40 kcal/mole for Paracril 35 were determined from the temperature variation of this region with frequency. Propagation properties of swollen Hycar OS-10 were observed. The effect of increasing swelling was found to be roughly the same as that of decreasing frequency.

* Supported in part by the U. S. Office of Naval Research, and by the United States Rubber Company.
† Now at Sylvania Corporation, California.

**F9. Stress-Temperature-Time Studies through the Second-Order Transition Region.** D. G. IVEY AND A. KWEI, *University of Toronto.*—Previous measurements of stress in elastomers held at a constant extension have shown strong relaxation effects in the region of the second-order transition temperature $T_m$, but have not been carried to temperatures much below $T_m$. In the work here reported, materials exhibiting a transition at about −30°C have been used, and the measurements carried out in the range +20° to −80°C. Stress is observed to increase linearly with temperature above $T_m$, as others have reported. Linear behavior is also observed below the transition region, stress increasing rapidly with decreasing temperature. It is felt that the intersection of the two straight lines might be used to define $T_m$ for the process. This definition would be unique, as opposed to $T_m$ defined by the point at which departures from the high-temperature linear behavior are observed. Because of relaxation effects in this region, $T_m$ so defined is dependent on the rate at which the experiment is performed. Values of stress less than those defined by the straight lines were not observed, hence these lines seem to represent the lower limit of the stress at a given temperature. Consequently, $T_m$ as defined by the line intersection may have some physical reality.

**F10. Measurement of Nuclear Induction Relaxation Times in Polymers.*** V. R. HONNOLD,† F. MCCAFFREY,† AND B. A. MROWCA, *University of Notre Dame.*—Both spin-lattice ($T_1$) and spin-spin ($T_2$) relaxation times of nuclear magnetic moments were studied for several polymers over a temperature range which included the second-order transition region. In this region the absorption line widths decreased by several gauss with increasing temperature. Average values of correlation times in this temperature range were estimated to be of the order of microseconds. Barrier height potentials against the thermal motion leading to absorption line narrowing were obtained from the $T_1$ and $T_2$ curves. Typical values obtained were 2 kcal/mole for Butyl and 7 kcal for Paracril 35. The line-width transition for polypropylene occurred at a temperature considerably higher than that for polypropylene oxide indicating a decreased steric hindrance to quasi-free rotation for the oxide. Silicone samples were characterized by narrow absorption lines limited by magnetic field inhomogeneity down to temperatures as low as −50°C. $T_1$ and $T_2$ data were also obtained for two low molecular weight hydrocarbons through the first- and second-order transition regions.

* Supported in part by the U. S. Office of Naval Research and by Research Corporation of America.
† Now at U. S. Naval Ordnance Test Station, Inyokern, California.

***Business Meeting of the Division of High-Polymer Physics***

THURSDAY AFTERNOON AT 2:00

Ballroom

(R. C. DUNLAP presiding)

## *Semiconductors, I (Germanium)*

**G1. Pressure Dependence of the Hall Effect in Germanium.*** W. PAUL, G. B. BENEDEK,† AND H. BROOKS, *Harvard University.*—The pressure dependence of the Hall constant and resistivity of *n*- and *p*-type samples of germanium of different impurity concentration has been measured from 0 to 12 000 kg/cm². In *n*-type samples chosen so that the carriers are all of one type and their density remains constant—a condition deducible from the known dependence of energy gap on pressure[1]—the Hall constant increases by some 8 percent to 12 000 kg/cm². Assuming constant carrier concentration, this can be interpreted as an increase in the ratio of Hall to drift mobility for electrons. Taken in conjunction with the resistivity data this implies a decrease in both Hall and drift mobility for electrons under pressure. The results for *n*-type germanium with a considerable number density of minority carrier are not inconsistent with this explanation. The changes in the Hall constant and resistivity in the *p*-type samples under pressure are smaller than in the *n*-type but do indicate an increase of both Hall and drift mobility for holes under pressure, with a decrease in their ratio.

* Supported in part by U. S. Army, U. S. Navy and U. S. Air Force under contracts with Harvard University and with M.I.T.
† Staff Member, Lincoln Laboratory, M.I.T.
[1] W. Paul, Phys. Rev. **90**, 336 (1952).

**G2. Hall Effect and Resistivity of Germanium at Low Temperatures.*** H. FRITZSCHE, *Purdue University.*—The anomalous behavior of the Hall coefficient *R*—maximum at low temperature—and the resistivity at low temperatures first observed in 1950[1] has been reexamined. New experiments show that surface effects can be eliminated by etching the sample. *R* and $\rho$ are independent of electric fields below 0.5 v/cm in the whole temperature range to 2°K. At helium temperatures *R* depends strongly on the magnetic field strength. Fields of 250 gauss alter *R* appreciably; at 3500 gauss the error is as large as 70 percent for some samples. However, after the magnetic field effect has been subtracted, the Hall curve still exhibits the maximum and the decrease at low temperatures. The magnetoresistive ratio also behaves abnormally by decreasing sharply with temperature in the same low-temperature range in which *R* decreases with temperature. Explanations offered so far will be discussed in the light of our experiments.

* Work supported by U. S. Signal Corps.
[1] C. S. Hung and J. R. Gliessman, Phys. Rev. **79**, 726 (1950).

**G3. Thermal Conductivity and Thermoelectric Power of Germanium at Low Temperatures.*** E. FAGEN, J. GOFF, AND N. PEARLMAN.—The effect on low-tempe ature thermal conductivity, *k*, and thermoelectric power, *Qr* of semiconductors, due to neutron bombardment, is being inv,estigated. Measurements of both these quantities, as well as resistivity, $\rho$, are made simultaneously by determining heat input, thermal emf, voltage drop due to current flow, and temperature gradient (the last by means of phosphor bronze thermometers in the liquid helium range and gas thermometers at higher temperatures, the thermometers in each case being attached directly to the sample). Preliminary results have been obtained for several Ge samples before bombardment. For a low-resistivity sample (*n* type, 0.005 ohm-cm at room temperature), *k* varies approximately as $T^4$ from 1.5°K to 4.2°K, where it is 0.36 watt-units; *Q* rises from 25 to 100 $\mu$v/degree, approximately linearly, in the same temperature range. For two other samples (*p* type, 0.2 ohm-cm at room temperature; *n* type, 0.013 ohm-cm at room temperature), *k* was about 2.5 watt-units at 80°K, rising at 5.0 at 55°K in the former, and to 4.0 in the latter. Measurements will be repeated on these samples after neutron irradiation, and are being extended to other samples of germanium and other semiconductors.

* Assisted by a U. S. Atomic Energy Commission contract.

**G4. Optical Properties of Germanium in the Far Infrared.*** E. J. JOHNSON AND W. G. SPITZER, *Purdue University.*—Reflection and transmission measurements have been made on germanium from 41 to 150 microns using residual ray arrangement[1] and a Golay detector. The samples were polished on both sides. The reflection from high-resistivity ($>10^{-1}$ ohm-cm) samples, *n* type and *p* type, give a constant reflectivity 0.36 over the entire wavelength range corresponding to a dielectric constant of 16. For low-resistivity ($<10^{-2}$ ohm-cm) samples the reflection increases with wavelength up to 117 microns (90 percent for 0.003 ohm-cm *n* type sample) dropping again at 152 microns.[1] These results are difficult to interpret on the basis of the Drude-Kronig free carrier theory.[2] Transmission measurements on *p* type samples show that the high absorption coefficient beginning at about 10 microns remains substantially constant up to 80 microns, then rises again sharply to much higher values. This result adds another interesting characteristic to the absorption spectrum of *p* type germanium.

* Work supported by a U. S. Signal Corps contract.
[1] K. Lark-Horovitz and K. W. Meissner, Phys. Rev. **76**, 1530 (1949).
[2] H. Y. Fan and M. Becker, *Semiconducting Materials* (London, 1951).
[3] Kaiser, Collins, and Fan, Phys. Rev. **91**, 1380 (1953).

**G5. Effective Mass and Degeneracy of Carriers in Ge from Diamagnetic Behavior.** J. H. CRAWFORD, JR., AND D. K. STEVENS, *Oak Ridge National Laboratory.*—Recent studies of the magnetic susceptibility of Ge[1] in the temperature range from 65 to 300°K have yielded values for the effective masses of electrons and holes ($m_e^*/m = 0.15 \pm 0.02$, $m_h^*/m = 0.23 \pm 0.03$) which considering the different experimental conditions, are in reasonable agreement with the results obtained from diamagnetic or cyclotron resonance absorption.[2] These effective mass values have been used to calculate the experimental susceptibility *vs* temperature curves, thereby testing the usual assumption of spherical energy surfaces. For both *n*- and *p*-type Ge, the use of the density of states for quasi-free carriers predicts an onset of degeneracy much higher in temperature than observed experimentally. The $\chi$ *vs* $T$ curve for *n*-type Ge can be fitted reasonably well under the usual assumption if the states in the conduction band are considered to be sixfold degenerate, thus lending support to the calculations of Herman and Callaway.[3] The data for *p*-type Ge, however, also require the assumption of a sixfold degeneracy for an acceptable fit, a result not borne out by the calculated band scheme.

[1] Stevens and Crawford, Phys. Rev. **92**, 1065 (1953).
[2] Dresselhaus, Kip, and Kittel, Phys. Rev. **92**, 827 (1953).
[3] Herman and Callaway, Phys. Rev. **89**, 518 (1953).

**G6. Microwave Transmission in *P*-Type Germanium.*** F. A. D'ALTROY AND H. Y. FAN, *Purdue University.*—Microwave transmission measurements ($\lambda = 3$ cm) on germanium[1] have been extended to 20°K. From the power transmission and the phase shift in the sample the conductivity $\sigma$ and

dielectric constant $K$ are calculated. The contribution of free carriers, $\Delta K$, is taken to be $(K-16)$. The values of the relaxation time $\tau$ (in $10^{-12}$ sec) calculated from $\Delta K/\sigma$ according to the Drude-Kronig theory (without strictly correct averaging) are 1.0, 1.75, 7.6, and 12.2 for 300°K, 200°K, 77°K, and 20°K, respectively. The two high-temperature values do not differ much from the results of Benedict.[3] The lower temperature values are considerably lower than those given by the extrapolation of his expression. The ratio $\sigma/\sigma_0$, $\sigma_0$ being the dc conductivity, is 0.81 at 77°K and 0.62 at 20°K, which values are in good agreement with the values of $\tau$. It should be pointed out that at these temperatures the impurity scattering is becoming dominant. The values of $\tau$ and the mobility give an average value of 0.63m for the effective mass.

* Work supported by a U. S. Signal Corps contract.
[1] F. A. D'Altroy and H. Y. Fan, Proc. Natl. Electronics Conf. **8**, 522 (1952).
[3] T. S. Benedict, Phys. Rev. **91**, 1565 (1953).

**G7. Electrical Properties of *P*-Type Germanium.** ESTHER M. CONWELL,* *Sylvania Electric Products, Inc.*—Hall and resistivity data for a set of $p$-type germanium samples with widely varying impurity concentration[1] are compared with theory. For the purest samples it is found that conductivity in the range 150°K to 300°K varies with temperature as $T^{-2.4}$,[2] as does the drift mobility $\mu$ of holes.[3] The Hall mobility $\mu_H$ varies as $T^{-1.4}$ in this range, however. This leads to $\mu_H/\mu \cong 0.1\sqrt{T}$ for high-resistivity samples, as compared with the theoretical prediction of a constant value of $3\pi/8$. Resistivity values for the more impure samples are calculated from carrier concentration, etc., and compared with experimental values. It is concluded that the impurity mobility increases less rapidly with temperature than predicted theoretically. The results of fitting the theoretical formula to curves of $\log_e$ of carrier concentration *vs* temperature will be discussed.

* On leave from Brooklyn College, Brooklyn, N. Y.
[1] P. P. Debye, Phys. Rev. **91**, 208(A) (1953).
[2] Reported also by W. C. Dunlap, Phys. Rev. **79**, 286 (1950).
[3] M. B. Prince, Phys. Rev. **91**, 208(A) (1953).

**G8. Measurement of Lifetimes and Diffusion Constants in Germanium.*** D. T. STEVENSON AND R. J. KEYES, *Lincoln Laboratory, M.I.T.*—The decay of photoconductivity has been used to measure the lifetime of excess carriers in rectangular samples of germanium in the range of 0.2 to 2500 μsec. A xenon spark tube provided by Professor H. E. Edgerton giving an intense light pulse ~0.1 μsec long is used for short lifetimes. For longer lifetimes a tungsten lamp and rotating mirror arrangement is used. The sample lifetime is obtained from an oscilloscope display of the decay of photoconductivity. Analysis of the solution of the diffusion equation yields methods of measuring the bulk lifetime, the surface recombination velocity, and the diffusion constant.[1] The ambipolar diffusion constant in intrinsic germanium from 300°K to 400°K and the diffusion constant of holes in $n$-type germanium from 100°K to 300°K have been measured. The results are in agreement with those calculated from the mobility data of Prince.[2] Bulk lifetimes up to 2500 μsec have been measured.

* The research in this document was supported jointly by the U. S. Army, U. S. Navy, and U. S. Air Force under contract with the Massachusetts Institute of Technology.
[1] Navon, Bray, and Fan, Proc. Inst. Radio Engrs. **40**, 1342 (1952).
[2] M. B. Prince, Phys. Rev. **91**, 208 (1953).

**G9. Variation of the Recombination Velocity of Germanium Surfaces with Ambient Gases.*** R. J. KEYES AND T. G. MAPLE, *Lincoln Laboratory, M.I.T.*—A study of the variation of surface recombination velocity, $s$, by observation of the decay of photoconductivity[1] has been carried out on high lifetime ($\tau \sim 2000$ μsec.) $n$-type germanium. All surfaces were CP-4 etched to obtain initial values of recombination velocity of about 50 cm/sec. The gaseous ambient was varied from wet oxygen to dry oxygen with ozone being introduced during the dry oxygen part of the cycle. This cycle as used by Brattain and Bardeen[2] in their study of contact potential charges with ambient. Consistent cyclic changes in $s$ were observed with $s$ being roughly twice as high in dry oxygen as in wet oxygen and with a slight upward trend in both ambients over many cycles. The same cycling without ozone gave about the same changes in $s$ but there was a downward trend over many cycles. Other changes in $s$ with surface treatment will be discussed.

* The research in this document was supported jointly by the U. S. Army, U. S. Navy, and U. S. Air Force under contract with the Massachusetts Institute of Technology.
[1] D. T. Stevenson and R. J. Keyes, abstract this meeting.
[2] W. H. Brattain and J. Bardeen, Bell System Tech. J. **32**, 1 (1953).

**G10. "Channels" in *n-p-n* Junction Transistors: New Results and a Proposed Model.*** R. H. KINGSTON, *Lincoln Laboratory, M.I.T.*—Further measurements of "channel" conductance[1] give the following results. If a transistor is first etched in hydrofluoric acid and then exposed to repeated short cycles of wet nitrogen and wet oxygen, the conductance at a fixed voltage decreases by a factor of approximately twenty when oxygen is substituted for nitrogen. However, after cycling for approximately one hour the conductance in either ambient has increased by a factor of one hundred. Exposure to wet nitrogen only, after etching, produces no measurable "channel" even after several hours. It is therefore proposed that an oxide layer on the germanium surface is necessary for "channel" formation. Revising the previous model[1] to include the variation of mobility with "channel" thickness indicates that the equilibrium value of the channel conductance corresponds to a fixed position of the Fermi level at the surface, which is independent of applied bias, but a definite function of surface treatment and gaseous ambient. The decrease in conductance in an oxygen ambient thus corresponds to a shift of the Fermi level toward the valence band.

* The research in this document was supported jointly by the U. S. Army, U. S. Navy, and U. S. Air Force under contract with the Massachusetts Institute of Technology.
[1] R. H. Kingston, Phys. Rev. (to be published).

---

## THURSDAY AFTERNOON AT 2:00

Crystal Ballroom

(R. V. POUND presiding)

### *DSSP Symposium on Nuclear and Electronic Resonance in Solids*

**H1. Nuclear Magnetic Resonance and the Structure of Metals and Alloys.** N. BLOEMBERGEN, *Harvard University.* (30 min.)

**H2. Nuclear Magnetic Resonance in Alkali Metals.** R. E. NORBERG, *University of Illinois.* (30 min.)

**H3. Electron Spin Resonance in Semiconductors and Metals.** A. F. KIP, *University of California, Berkeley.* (30 min.)

### *Post-Deadline Papers, If Any*

THURSDAY AFTERNOON AT 2:00

Italian Gardens

(J. H. CRAWFORD, JR. presiding)

## *Irradiation Effects, II (Mostly Metals)*

**I1. Effect of Radiation Damage on the Thermal Conductivity of Graphite.*** ALAN W. SMITH, *North American Aviation, Inc.*—The thermal conductivity of a number of graphite types, artificial and natural, has been measured from 10°K to 300°K. Several of these types have been subjected to radiation damage. The thermal conductivity was measured over the whole temperature range for varying amounts of damage. The results are compared among various graphite types and ungraphitized coke. Similar measurements have been made on bromgraphite compounds and these results are compared with the radiation-damaged samples. The anomaly in the temperature dependence of the thermal conductivity is discussed and also the variation of the conductivity and in its temperature dependence due to different thermal scattering mechanisms.

* This work is based on studies conducted for the U. S. Atomic Energy Commission.

**I2. Crystal Structure as a Factor in Radiation Damage.*** D. WRUCK AND C. WERT, *University of Illinois*.—An attempt has been made to determine the importance of crystal structure on the amount of damage produced in a metal by heavy particle bombardment. Three metals were used: iron, nickel, and cobalt, similar in most properties except crystal structure. During bombardment at −150°C with 10-Mev deuterons, the electrical resistivity of foils of these metals was measured at intervals at −180°C. For a total flux of $10^{17}$ particles/cm$^2$, the fractional increase in resistivity of iron was 0.5; that of nickel and cobalt about 0.1. Further, wires of iron and nickel were bombarded with neutrons for two months at ambient temperatures in the Brookhaven reactor. The resulting fractional changes in resistivity (at −195°C) were 0.1 and 0.01, respectively. Both experiments show that the resistivity change in nickel, a close-packed lattice, is less than that in iron, which is more loosely packed; the first shows further that close-packed cobalt behaves about like nickel. Further measurements were made on vanadium and titanium, though these metals are somewhat different in properties from the others; these measurements will be discussed. Possible interpretation of the entire investigation will be presented.

* Sponsored in part by the U. S. Atomic Energy Commission.

**I3. Neutron Irradiation Effects at Low Temperature—Cu and Al.*** A. W. MCREYNOLDS, W. AUGUSTYNIAK, AND M. MCKEOWN, *Brookhaven National Laboratory*, AND D. B. ROSENBLATT, *Frankford Arsenal*.—A general facility for low-temperature irradiations in the Brookhaven reactor has been developed. Temperature in a Dewar flask surround multiple samples is maintained at −150° to −195°C for long periods by periodic automatic refilling with liquid nitrogen. Provision is included for insertion and removal of active samples at low temperature. In this apparatus irradiations of $1.3\times10^{19}$ nvt were made on samples of Cu, Al, Cu−Si, and Be. After storage at −195°C for radioactive decay, low-temperature measurements of electrical and mechanical properties were made on wire samples. Largest effects observed were increases of 15–25 percent in electrical resistivity and several hundred percent in critical shear stress. Kinetics of recovery was studied in detail by measurement at −195°C at intervals during stepwise annealing. Data on copper indicate several types of lattice defects. Increased resistivity partly anneals out in two lower-temperature processes −60° to 0°C, and 0–300°C. Critical shear stress is unaffected but anneals simultaneously with a further resistivity decrease from 300°–400°C. In aluminum both properties anneal simultaneously in the range −80° to −20°C as in the high-temperature copper annealing.

* Work done under contract with the U. S. Atomic Energy Commission

**I4. The Effect of Short Time Moderate Flux Neutron Irradiation on the Mechanical Properties of Some Metals.** F. W. KUNZ AND A. N. HOLDEN, *Knolls Atomic Power Laboratory*.*—Single crystals of iron, lead, and zinc were irradiated at room temperature to a total flux of $10^{18}$ nvt to determine the effect of neutron irradiation on the mechanical properties of these metals. The flow stress of the iron and zinc crystals as measured from load *versus* elongation curves was markedly increased after the neutron exposure. The flow stress of the lead crystals remained unchanged after irradiation. Irradiated iron crystals were annealed at temperatures ranging from 200°C to 500°C for times ranging from one to $10^4$ minutes, following which they were tested in tension to determine the extent of recovery of the mechanical properties. The extent of recovery was determined by comparing the observed yield strength of the partially recovered crystals with the yield strength of crystals in both the irradiated and unirradiated condition. Using these data, an activation energy of 3.1 electron volts was determined from the slope of the line relating the natural logarithm of the recovery time to the reciprocal of the temperature. The determined activation energy for recovery is equal to the activation energy for self-diffusion in iron. X-ray measurements of irradiated copper, brass, and magnesium and elastic constant measurements of irradiated copper and aluminum were also made.

* Under contract with the U. S. Atomic Energy Commission.

**I5. Radiation Induced Changes in the Electrical Resistivity of α Brass.*** D. B. ROSENBLATT,† *Frankford Arsenal*, R. SMOLUCHOWSKI, *Carnegie Institute of Technology*, AND G. J. DIENES, *Brookhaven National Laboratory*.—Nucleon irradiation of pure metals results in an increase of the electrical resistivity. In the case of certain order-disorder alloys (copper-gold system) decreases in resistivity upon irradiation have been observed and attributed to additional ordering. It has been pointed out that a decrease in resistivity may also occur though a change in Debye temperature caused by radiation induced changes in the elastic moduli.[1,2] In an effort to separate these two effects, experiments were performed on α brass, which is presumably a random alloy. Samples of 10, 20, and 30 percent Zn content were irradiated at +50°C for one week in the Brookhaven reactor and the changes in resistivity measured at room, liquid nitrogen, and liquid helium temperatures. A decrease in resistivity was found at all these temperatures. The decrease in residual resistivity indicates that an interpretation based entirely on changes in the thermal part of the resistivity cannot be adequate. Annealing experiments will also be described which indicate that the resistivity is restored to the unirradiated value in the +170°C temperature range.

* Work done under contract with the U. S. Atomic Energy Commission.
† Guest Scientist at Brookhaven National Laboratory.
[1] R. Smoluchowski, Phys. Rev. **93**, 392 (1954).
[2] G. J. Dienes, Phys. Rev. **86**, 228 (1952).

**I6. Experimental Evidence for Melted Regions in Metal Crystals Resulting from Particle Bombardment.*** J. M. DENNEY, *North American Aviation, Inc.*—Theoretical consider-

ations by Brinkman indicate the existence of "melted" regions (displacement spikes) in metals as a result of bombardment with energetic particles. In order to distinguish conclusively the effects due to these melted regions from other radiation defects in the metal lattices a highly specialized experiment is necessary. It is believed that such an experiment is afforded by use of a metastable alloy of iron in copper. In this alloy of 2.4-weight percent iron in copper, aging at 700°C causes precipitation of iron within the solid solution. This thermally-induced precipitate is paramagnetic and structurally metastable and transforms to the ferromagnetic form upon plastic deformation or particle bombardment. It is observed experimentally that the ferromagnetic precipitate is stable with respect to any further thermal or mechanical treatments except resolution in solid solution by heating above the two-phase region. Alloy samples with the precipitate in the ferromagnetic form were irradiated in the Crocker Laboratory 60-inch cyclotron at the University of California. The ferromagnetic precipitate was found to decrease at an initial rate of $\frac{1}{2}$ percent per $\mu$ amp-hr/cm$^2$ of 9-Mev protons. It is felt that these results offer direct evidence in support of the displacement spike concept since, at present, it provides the only available explanation of the experimental results.

* This paper is based on studies conducted for the U. S. Atomic Energy Commission.

**I7. Shear Modulus of Irradiated Copper.*** H. DIECKAMP AND E. C. CRITTENDEN, JR., *North American Aviation, Inc.*—Polycrystalline copper wires of 99.999 percent purity have been irradiated at −175°C with 20-Mev deuterons to an integrated exposure of approximately 8$\mu$ amp-hr/cm$^2$. The recovery of the radiation-induced changes in the shear modulus has been observed at 25°C intervals throughout the temperature range of −196°C to +300°C. The annealing time at each temperature was 15 minutes, and all the measurements were made at −196°C. The recoverable changes indicate about a 1.5 percent decrease upon irradiation. About one-third of this change is removed after annealing at −125°C. Further annealing at −100°C and −75°C causes very little additional recovery. The final two-thirds is recovered steadily upon annealing between −50°C and +100°C. The shape of the shear modulus *vs* annealing temperature curve suggests that the recovery at low temperatures occurs by the loss or rearrangement of dislocations until the remaining ones are pinned down by the radiation-induced interstitials and vacancies. Further recovery is thus temporarily halted until these point defects move. The final portion of the recovery occurs when the interstitials move and annihilate vacancies, thus releasing the remaining dislocations to seek their desired configuration.

* This paper is based on studies conducted for the U. S. Atomic Energy Commission.

**I8. Radiation Ordering by Cyclotron Particles.*** C. E. DIXON AND D. B. BOWEN, *North American Aviation, Inc.*—Blewitt and Coltman[1] have shown the ordering process in $Cu_3Au$ can be accelerated by irradiation with pile neutrons. They attributed this effect to accelerated diffusion resulting from radiation-induced Frenkel defects. A similar experiment has been performed with cyclotron particles and the same effect was found. Ordered $Cu_3Au$ was irradiated with 36-Mev alpha particles at −180°C, and the initial disordering rate was found to be 0.37 micro-ohm-cm/($\mu$ amp-hr/cm$^2$). If one assumes the volume disordered is proportional to the resistivity change, 4.5 percent of the alloy is disordered by 1$\mu$ amp-hr/cm$^2$. The disordering rate of an identical specimen irradiated at 220°C with an average beam of 1$\mu$ amp/cm$^2$ was found to be smaller by a factor of 6. The difference between these two rates must be due to ordering which occurs simultaneously with the disordering. The ordering rate observed at 220°C with the beam off could account for only 5 percent of the difference; hence, it is concluded that the vacancies created by the irradiation are responsible for the ordering.

* This paper is based on studies conducted for the U. S. Atomic Energy Commission.

[1] T. H. Blewitt and R. R. Coltman, Phys. Rev. 85, 385 (1952).

**I9. Interstitial Content of Radiation Damaged Metals from Precision X-ray Lattice Parameter Measurements.** C. W. TUCKER, JR., AND J. B. SAMPSON, *Knolls Atomic Power Laboratory.**—An x-ray method for determining the interstitial content of irradiated metals is suggested and analyzed. This approach offers the following advantages: (a) the x-rays "see" mainly the interstitial atoms since their effect outweighs that of vacancies by a 5:1 ratio, (b) the interpretation is straightforward and may be made quantitative, and (c) the method is sensitive since 0.01 atomic percent, and perhaps less, of interstitials may be detected. These conclusions are based on a combination of theory and experiment. The theory is based upon an elasticity interpretation which predicts Vegard's law and several other experimentally confirmed x-ray effects. It is important to relate changes in physical properties due to irradiation and subsequent annealing to changes in basic crystal defects. The x-ray method promises to measure the concentration of one important defect with less ambiguity than other current methods (electrical resistivity is about equally affected by both interstitials and vacancies). The x-ray approach should therefore provide information of intrinsic interest and also help in interpreting observed changes in other physical properties. The possibilities of the x-ray method are born out by preliminary observations in this Laboratory of x-ray detected lattice expansions of several neutron-irradiated metals.

* Operated by the General Electric Company for the U. S. Atomic Energy Commission.

**I10. Dimensional Changes of Alpha Brass on Dezincification and Lattice Strain in Copper Introduced by Vacancies.** DAVID D. VAN HORN AND WILLIAM C. COOLEY, *Knolls Atomic Power Laboratories.**—Small wires of high-purity 70–30 brass were dezincified in vacuum at various temperatures and the dimensional changes were followed as a function of the amount of zinc removed. It is found that the length and the diameter changes are about the same, being linear functions of the amount of zinc removed, and it is further found that the relationship between dimension change and zinc loss is independent of temperature. Starting with samples containing thirty percent by weight of zinc, it is found that $\Delta L/L_0 = 0.173\Delta W/W_0$ and $\Delta D/D = 0.227\Delta W/W_0$. Since these relations are temperature independent, it is reasonable to assume that all of the vacancies introduced by the diffusion of zinc out of the specimen remain within the material, "precipitating" out of the lattice to form the observed porosity. If one assumes that no net volume change takes place when the vacancies agglomerate, then it is calculated from the observed dimension changes that the lattice strain introduced by the vacancies is 0.15 times the fractional concentration of vacancies. This figure is in substantial agreement with results of Tucker and Sampson reported elsewhere at this meeting.

* Under contract with the U. S. Atomic Energy Commission.

THURSDAY EVENING AT 7:00

Sheraton-Cadillac Hotel, Ballroom

(H. A. BETHE presiding)

***Banquet of the American Physical Society***

After-dinner speakers: E. F. BARKER, W. F. BUSSE, AND CLARENCE ZENER

---

FRIDAY MORNING AT 10:00

Rackham Lecture Hall

(J. A. HORNBECK presiding)

***Lecture by the 1954 Buckley Prize Winner***

**K1. Surface Barrier Effects in Semiconductors.** JOHN BARDEEN, *University of Illinois.* (30 min.)

***Semiconductors, II; Contributed Papers***

**K2. Properties of Zinc-, Copper-, and Platinum-Doped Germanium.** W. C. DUNLAP, JR., *General Electric Research Laboratory.*—Hall effect and resistivity measurements between 15°K and 400°K have been made on a number of samples of germanium cut from ingots doped with high-purity zinc,[1] copper, and platinum. All three were found to be high-energy acceptors. $\Delta E$ for zinc was 0.029, for copper 0.037, and for platinum 0.04 ev. Studies were also made on copper-diffused specimens. The copper-doped specimens had the same ionization energy as thermally treated material.[2,3] A zinc content as high as $10^{16}$ atoms/cm$^3$, copper $10^{16}$, and platinum $5\times10^{14}$ was produced. The Hall and resistivity curves, below 20°K, no longer followed the simple exponential dependence, but tended to become constant. This is not taken to indicate low-ionization energy states, but more probably results from extraneous effects. An unsuccessful search was made for acceptor states in the upper half of the forbidden band.[4] However, evidence for an impurity state in copper-diffused germanium lying at about the middle of the forbidden region[5] is discussed.

[1] W. C. Dunlap, Jr., Phys. Rev. **85**, 945 (1952).
[2] W. DeSorbo and W. C. Dunlap, Jr., Phys. Rev. **83**, 869 (1951).
[3] F. J. Morin and J. P. Maita, Phys. Rev. **90**, 337 (1953).
[4] W. C. Dunlap, Jr., Phys. Rev. **91**, 1282 (1953).
[5] Burton, Hull, Morin, and Severiens, J. Phys. Chem. **57**, 853 (1953).

**K3. Some Properties of Germanium Doped with Iron or Cobalt.** W. W. TYLER, H. H. WOODBURY, AND R. NEWMAN, *General Electric Research Laboratory.*—Dunlap has shown that gold introduces acceptor levels in germanium at ~0.15 ev above the valence band and ~0.20 ev below the conduction band. Evidence that nickel and copper introduce impurity levels in germanium at ~0.25 ev above the valence band has been given by Burton *et al.* Recently, evidence has been obtained that iron and cobalt introduce deep levels in germanium, giving rise to properties in some respects similar to those reported for gold, copper, and nickel. Although the solid solubilities of iron and cobalt are low compared with copper and gold, samples of germanium doped with iron and cobalt have been prepared which show very high resistivities and high photosensitivity at liquid nitrogen temperatures. At room temperatures the principal observable effect of the iron or cobalt impurity is the reduction of life-time due to the introduction of recombination centers. Studies of pulse photoconductivity at nitrogen temperatures indicate that cobalt-doped germanium samples show characteristic decay times of several milliseconds, whereas iron-doped samples show characteristic decay times as long as 30 seconds. There is evidence for several trapping levels in iron-doped germanium. Preliminary experiments at hydrogen and helium temperatures confirm the existence of thermal traps in iron-doped germanium and give rise to interesting nonequilibrium properties.

**K4. Photoconduction in Fe-, Co-, and Ni-Doped Germanium.** R. NEWMAN AND W. W. TYLER, *General Electric Research Laboratory.*—Iron, cobalt, and nickel introduce deep impurity levels in germanium (see preceding abstract). This paper reports some observations of the infrared photoconductivity for germanium samples doped with these impurities.[1] The impurity photoconductive edge, defined as the point for which the response is $\sim10^{-3}$ of the plateau value, is 0.20 ev for Ni ($p$-type), 0.25 ev for Co ($p$-type), and 0.30 ev for Fe ($n$-type). These are preliminary values. Quenching of the photoconductivity was observed. The quench effects appear only in samples which exhibit traps.

[1] Burton, *et al.*, J. Phys. Chem. **57**, 853 (1953), quote some unpublished work of Briggs on the photoconductivity of nickel-doped germanium.

**K5. Thermal Ionization of Trapped Electrons.** HERMANN GUMMEL AND MELVIN LAX, *Syracuse University.*—A comparison is made between the Born and Born-Oppenheimer treatments of the ionization probability of an impurity-trapped electron in Si and Ge due to the thermal agitation of the lattice. For the interaction between the electron and the lattice the Bardeen-Shockley deformation potential is taken. In the Born approximation only one-phonon processes are possible. In the Born-Oppenheimer approximation a transition from one electronic state to another results in a shift of the equilibrium positions of the normal coordinates; this shift makes multiphonon processes possible. The summation over all final lattice states including many-phonon processes is performed in closed form using a method previously presented.[1] The contribution of transitions involving $n$ phonons may be obtained as the $n$th term in an expansion in powers of a certain parameter whose size determines the importance of multiphonon processes. This parameter is proportional to the square of the deformation potential interaction constant and to an averaged lattice vibration energy. If the temperature is low enough so that only one-phonon processes are important, the

Born and Born-Oppenheimer treatments give the same result, provided that the maximum phonon energy is larger than the ionization energy.

[1] M. Lax, J. Chem. Phys. 20, 1752 (1952).

**K6. Effective Carrier Mobility in Surface Well.*** J. ROBERT SCHRIEFFER, *University of Illinois* (introduced by John Bardeen).—Carriers held to a region near the surface by the potential well of a space-charge layer may have their mobility reduced by surface scattering, if the width of the well is less than a mean free path. An effective mobility, which may differ from the bulk mobility by as much as a factor of ten, has been obtained from a one-dimensional solution of Boltzmann's equation with random scattering assumed at the surface. Solutions have been obtained for two types of potential functions: (1) a linear variation corresponding to a constant electric field, and (2) a solution of Poisson's equation obtained by considering the carrier density much greater than the impurity density in the well. Results have been used to calculate changes in surface conductance of Ge with changes in surface potential for various impurity densities.

* Supported by a Grant from Motorola, Inc.

**K7. Electron Traps on Germanium Surfaces Produced by Heating in Oxygen.** EDWARD N. CLARKE, *Sylvania Electric Products.*—It has been suggested[1,2] that localized energy levels or traps exist on the surface of germanium. However, there has been no detailed knowledge of the source of these traps. In the present work, the electrical conductivity of very thin single crystals is measured. Surface conductivity is produced by a method to be described. This surface conductivity is reduced by heating the germanium in the presence of oxygen. The surface conductivity is increased to its original value by heating the germanium in a vacuum of $10^{-7}$ mm Hg. The results suggest that germanium surface traps are produced by heating a relatively clean surface in the presence of oxygen. The traps may be associated with adsorbed oxygen or with the lattice discontinuity existing at a germanium-to-germanium oxide interface.

[1] J. Bardeen, Phys. Rev. 71, 717 (1947).
[2] W. H. Brattain and J. Bardeen, Bell System Tech. J. 32, 1 (1953).

**K8. Growth of Long Lifetime Germanium Crystals.** MILTON BECKER, *Hughes Aircraft Company.*—A furnace has been developed which is capable of growing intrinsic crystals with lifetimes of several milliseconds. The basic feature is a water-cooled copper jacket which surrounds the seed holder and extends to within half an inch of the quartz crucible. The grown part of the crystal is quenched within half an hour of growth if a gaseous atmosphere is used. Draws made in vacuum are not efficiently quenched and show marked deviations from expected resistivities and lifetimes. These can be correlated with the length of time the crystal is heated in the course of the draw. Crystals made with various impurities show lifetimes which agree well with those reported by Burton.[1] We have used both zone melt and pig metal for starting charges and find no difference in final lifetimes. This seems to indicate the limiting values obtained are due to thermal rather than chemical causes. The atmospheres apparently act as heat exchangers with the cooling walls and also serve to suppress evaporation of impurities from the walls of the furnace.

[1] J. A. Burton *et al.*, J. Phys. Chem. 57, 102 (1953).

---

## FRIDAY MORNING AT 10:00

## West Physics Lecture Room

## (C. S. BARRETT presiding)

## *Metals, II*

**L1. Anisotropic Debye-Waller Factors in Cubic Crystals.** R. J. WEISS, J. J. DEMARCO, AND G. WEREMCHUK, *Ordnance Materials Research Office,* AND J. HASTINGS AND L. CORLISS, *Brookhaven National Laboratories.*—Neutron and x-ray diffraction studies on $\alpha$ brass (70–30 f.c.c.) have revealed that the integrated intensities are reduced by a Debye-Waller temperature factor $\exp[-2B(\sin\theta/\lambda)^2]$ where $B$ is not only a function of the characteristic temperature $\theta$ and the absolute temperature $T$, but also a function of crystal direction, contrary to present theories. The effect is very marked in comparing the 222 and 400 peaks both as to their relative intensities and their change in intensity with temperature from liquid nitrogen to room temperatures. If one artificially invokes in the Debye-Waller expression a characteristic temperature dependent on crystalline direction, then a $\theta$ of 380 for the 111 direction $\alpha$, a $\theta$ of 215 for the 100 direction is required to fit the data as compared to a $\theta$ of 310 commonly expected from specific heat and elastic constants. The reduction in $\theta$ from 310 to 215 for the 100 direction reduces the intensity of the 400 peak by 40 percent. At present writing no theoretical explanation is available.

**L2. On a Peculiarity of the Electron Density Near an Impurity in a Metal and its Effect on X-Ray Spectra.** J. S. PLASKETT,* *University of Virginia.*—All the methods at present devised for finding wave functions in a metal in which there is an impurity atom present reduce to the problem of solving a Schrödinger equation in which the potential $V(r)$ is constant beyond a certain distance $a$ ($\sim$1 a.u.) from the impurity and becomes infinite at a distance $R(\sim 10^8$ a.u.) from the impurity (this is equivalent to having a zero boundary condition in this sphere). For $r<a$ the external potential may for example be that of the impurity atom (Friedel, 1952), or the difference between the potential of the solute and solvent atoms (Huntington, 1942), or a constant (Mott, 1936; Huang, 1948). The self-consistent solution of this problem involves the calculation of the electron density in the potential $V(r)$ for a number of slightly different $V(r)$'s. It might be thought that, when the potential well $V(r)$ is deepened so as to contain a bound state, the electron density might suddenly increase. We prove that this is not true. The proof is by means of Gamow's complex eigenvalues and we can see also that these eigenvalues will have an important effect on the fine structure of the x-ray spectra of a metal. The explanation of the fine structure in these terms is similar to Friedel's (1952) explanation of the fine structure.

* Part of a University of London Ph.D. thesis supported by a grant from the Department of Scientific and Industrial Research.

**L3. Elastic Spectrum of Copper from Temperature Scattering of X-Rays.*** E. H. JACOBSEN, *M.I.T.*—Measurements have been made of the temperature diffuse scattering of x-rays

from a single crystal of copper at 300°K using crystal monochromated CuKα radiation. The measurements were analyzed by the method of Laval and James to give frequency *vs* wave vector curves for longitudinal and transverse waves in the 100, 110, and 111 directions. These results were then expressed in terms of the force constants of the Born theory. By considering the interaction of first, second, and third neighbors, nine force constants are involved, and these have been evaluated from the frequency curves. The values of these nine force constants constitute the necessary data for computing a complete frequency distribution curve.

* Assisted by National Science Foundation and Armco Foundation.

**L4. Change of Elastic Constants of Copper on Annealing after Plastic Deformation at 78°K.*** E. C. CRITTENDEN, JR., *U. S. Naval Postgraduate School*, AND H. DIECKAMP, *North American Aviation*.—Twisting 0.010-in. polycrystalline wire of 99.999 percent purity copper at 77°K to a shear strain of 0.5 produces a shear modulus decrease of 15 percent, measured at low frequency. Measuring the shear modulus at 77°K after 15-min annealing periods at 25°K temperature intervals shows a rapid rise between 77°K and 150°K and a slower rise between 220°K and 290°K. These regions are separated by a plateau and the second rise is followed by another plateau. The lowering of modulus on cold work probably results from small displacements of dislocations.[1] The annealing behavior suggests the presence of two types of imperfections able to form Cottrell atmospheres. On this model the rapid rise, 77°K to 150°K, would be associated with clustering of imperfections near dislocations. The rise, 220°K to 290°K, may include clustering, near dislocations, of a second imperfection type. Yield points should be observed in these regions, and have been by Blewitt[2] after annealing at 78°N and 300°K. The plateaus may be regions of inactivity or may result from loss of imperfections together with reduction of total dislocation length.

* Supported in part by the U. S. Atomic Energy Commission.
[1] A. D. N. Smith, Phil. Mag. **44**, 433 (1953).
[2] T. H. Blewitt, Phys. Rev. **91**, 1115 (1953).

**L5. The Elastic Constants of Copper Alloys.*** JOHN R. NEIGHBOURS† AND CHARLES S. SMITH, *Case Institute of Technology*.—The elastic constants of single crystals of dilute solutions of Al, Si, Zn, Ga, and Ge in Cu have been determined by the ultrasonic pulse method. Alloying causes a decrease in all the fundamental constants, $C_{44}$, $(C_{11}-C_{12})/2$ and $(C_{11}+2C_{12})/3$, the relative decrease in $(C_{11}-C_{12})/2$ being the greatest. The changes in shear constants $C_{44}$ and $(C_{11}-C_{12})/2$ have been interpreted in terms of the known electrostatic and ionic contributions to these constants for copper. The large decrease in $(C_{11}-C_{12})/2$ is attributed to the change in ion-ion interactions upon alloying. The electrostatic shear stiffness of an alloy is found to be nearly equal to the electrostatic term for copper times the square of the electron atom ratio.

* This work was supported by the U. S. Office of Naval Research.
† Now at Rensselaer Polytechnic Institute, Troy, New York.

**L6. X-Ray Measurements of Cold-Worked Alpha Brass.*** E. P. WARekois, *M.I.T.*—Filings of (90–10), (80–20), (70–30), and (65–35) brass pressed into briquets served as cold-worked samples. Peak shapes and shifts were measured with a Norelco spectrometer using filtered CoKα. Fourier coefficients were determined and instrumental broadening corrected by Stokes' method. Log plots of the coefficients were used to separate particle size and distortion broadening; average particle size dimensions were $L_{111}=260$, 175, 160, and 145A; $L_{100}=150$, 100, 95, and 75A with increasing zinc content. Distortions corresponded to rms strains of the order of 0.007. Stacking fault probabilities for the (111) planes calculated from peak shifts indicate, on the average, one fault every 200 layers in the 90–10 brass and every 57, 40, and 25 layers in the other brasses, respectively. These data indicate that in cold-worked brass there is both particle size and distortion broadening, but a major portion of the particle size broadening must be attributed to faulting. The susceptibility to faulting appears to increase as the composition approaches the boundary of the alpha phase. Data will be presented on the changes with annealing.

* Research sponsored by the U. S. Atomic Energy Commission.

**L7. Internal Friction in Single Metal Crystals at Audio Frequencies.*** T. R. CUYKENDALL, T. BERESOVSKI,† AND H. S. SACK, *Cornell University*.—The internal friction in high-purity single crystals of Al, Cu, and Zn has been measured at 1000 cps and lower and at temperatures up to 550°C in the case of Cu. Several crystals of each metal were studied. Lateral vibration of thin reeds, mounted on specially designed supports, was employed. The amplitude of vibration could be varied by a factor of 100 and its approximate magnitude calculated. Maximum strains were about $10^{-6}$. The elastic losses observed are one order of magnitude greater than those observed by other investigators at 20–60 kc. The losses increase with increasing amplitude of vibration; the increase occurs both more steeply and at lower amplitudes as the temperature is increased, and in the case of copper, approach a limiting value at high amplitudes. No definite variation with crystal orientation was found. The dependence on temperature for small amplitude can be represented by one activation energy of about 5 kcal for Zn, and by two activation energies of about 1 and 10 kcal for Cu at low and high temperature, respectively.

* This work was supported by U. S. Office of Naval Research.
† Now with Pratt and Whitney Aircraft Division, Hartford, Connecticut.

**L8. Internal Friction Associated with Precipitation in an Al–Ag Alloy.** A. C. DAMASK* AND A. S. NOWICK,† *Frankford Arsenal*.—Internal friction and elastic aftereffect measurements have been made on wire specimens of an Al–Ag (20 percent Ag) alloy at various stages in the precipitation process. A specimen quenched from the solid solution region and aged at 155°C shows an internal friction peak at 140°C for a vibration frequency of 0.25 cps. The decrement at the maximum is 0.02. This peak is unaffected by short anneals at successively higher temperatures up to 170°C. For successive anneals above this temperature, the peak first migrates toward higher temperatures while increasing in height, then returns toward lower temperatures with a decrease in height. During this migration the peak is not completely reversible with respect to heating and cooling. Upon further annealing, sufficient to carry precipitation almost to completion, the peak becomes stable again at 148°C. The activation energy associated with this internal friction peak is 25.0±0.5 kcal/mole. The relation between these observations and the mechanism of precipitation will be discussed.

* Now at Iowa State College.
† Permanent address: Yale University, New Haven, Connecticut.

**L9. Thermoelectric Power and Resistivity of Dilute Cu–Si, Ni–Si, and Fe–Si Alloys.*** C. A. DOMENICALI AND F. A. OTTER, *The Franklin Institute Laboratories for Research and Development*.—We have measured the thermoelectric power and resistivity of the dilute alloys Cu–Si, Ni–Si, and Fe–Si from −195°C to +500°C. The results for Cu–Si have already been reported.[1] The Ni–Si alloys show a knick in the thermopower *versus* temperature curve at the Curie temperature of each alloy. The Fe–Si alloys contain Si up to 2 atomic percent, and their thermopowers against pure copper are all positive from −195°C up to a temperature which increases

from +15°C for 2-atomic-percent Si to 250°C for pure Fe. The resistivity of the Ni–Si and Fe–Si alloys increases faster than linearly with temperature. The change in resistivity with increasing Si content is much greater (factor of 2) in Fe–Si than in Ni–Si, but only slightly greater in Ni–Si than in Cu–Si. We are attempting to study electron scattering in these alloys on the basis of their thermoelectric and resistance properties.

* Supported by Squier Signal Laboratory, Fort Monmouth, New Jersey.
[1] C. Domenicali and B. Boyd, Phys. Rev. 91, 220 (1953).

**L10. The β→α Transformation in Tin.*** JEROME FLEEMAN, *Brookhaven National Laboratory.*—We have used a volume dilatometer to measure the rate of transformation of white to gray tin. The observations were made using tin cylinders of approximately 0.5 cc seeded with gray tin powder. In addition, we have compared these rates with the rates from similar tin samples irradiated in the Brookhaven pile at liquid nitrogen temperatures. Both of these rates are measured relative to the rate of transformation of an annealed tin capsule of approximately the same dimension. The annealed sample showed no evidence of transformation in the time required to transform the seeded and irradiated samples. The growth curves of both seeded and irradiated tin are characterized by an initial nucleation period in which there is a small volume change; this is followed by a linear portion to the final value of the transformation. The growth process in both cases can be characterized by a zero-order reaction. We find that the curves differ in two respects. First, the nucleation period for the irradiated sample is greater than for the seeded sample, and secondly, the rate of transformation is less for the irradiated than for the seeded sample. Typical curves will be presented and discussed.

* Work done under contract with the U. S. Atomic Energy Commission.

**L11. The Change of Resistivity of Copper with Elastic Strain.** D. B. BOWEN AND H. HORI, *North American Aviation, Inc.*—The reversible change in electrical resistivity that occurs on elastic strain has been measured at selected temperatures from 4.2°K to room temperature. The specimens are copper foils strained in tension. The value of $d\ln\rho/d\ln l$ measured at room temperature agrees with the value obtained by previous investigators and is approximately 3. Values measured below room temperature are up to twice as large. These large values at low temperatures imply that the principal effect of the strain is on the number of carriers rather than on the spectrum of lattice oscillations. Lattice imperfections introduce strains in the lattice that are reflected in the resistivity changes. These preliminary data indicate that these strains increase as the temperature is increased. This may be due to an anisotropy of thermal expansion around the defect. This paper is based on studies conducted for the Atomic Energy Commission.

**L12. The Electrical Resistivity of Cold-Worked Aluminum Single Crystals.*** A. SOSIN AND J. S. KOEHLER, *University of Illinois.*—High-purity (99.99+ percent) single crystals of aluminum have been pulled in tension in liquid nitrogen and helium baths. The electrical resistivity after deformation was measured as a function of direction and the behavior of the resistivity and stress-strain curves following annealing examined. Within the experimental error, the resistivity behavior can be described as follows: at liquid helium temperature the resistivity changes are isotropic. For 15 percent extension the increase was about $8\times10^{-9}$ ohm-cm. On annealing to liquid nitrogen overnight, approximately 10 percent of the resistivity change recovers isotropically; on annealing to room temperature overnight, approximately 65 percent of the total resistivity change recovers isotropically, leaving a "permanent" 25 percent. The stress-strain curve for a specimen pulled in helium is linear in the range investigated. On annealing to room temperature no softening occurs and an upper yield point is developed. The resistivity remains constant until plastic flow starts again, rising sharply. The resistivity changes for a crystal strained in nitrogen are isotropic, with a single anneal of about 65 percent on warming to room temperature.

* Supported by the U. S. Office of Ordnance Research and by the U. S. Office of Naval Research.

**L13. The Effective Mass of Conduction Electrons in Ag, Au, and Cu.*** L. G. SCHULZ, *University of Chicago.*—The effective mass $m^*$ of conduction electrons in Ag, Au, and Cu was determined by optical methods. In the wavelength range of $1\mu$ to $2\mu$ the optical constants $n$ and $k$ were obtained from measurements of the reflectivity and transmissivity of thin films formed by evaporation and deposition in a vacuum. The experimental values of $n$ and $k$ thus obtained were found to agree with the values predicted by the Drude free electron theory.[1] To obtain this agreement the ratio $m^*/m$ ($m$ is the free mass) was taken equal to unity for Ag and Au, and to 1.45 for Cu. In these calculations it was assumed that the density of the conduction electrons was equal to the atomic density. Reflectivity experiments lead to lower values of $k$ than those given by transmission experiments, a result which can be explained as a consequence of the anomalous skin effect.[2] Possibilities and limitations of the optical method will be presented.

* Supported in part by U. S. Air Force.
[1] F. Seitz, *The Modern Theory of Solids* (McGraw-Hill Book Company, Inc., New York, 1940), chapter 17.
[2] E. H. Sondheimer, Adv. in Phys. 1, 1 (1952).

**L14. The Hall Effect of the Palladium-Silver Alloy System.** A. I. SCHINDLER, *Naval Research Laboratory.*—Recently, a comparison of the electric, magnetic, and thermoelectric properties of the Cu–Ni and Pd–Ag alloy systems has been made.[1] Although the Pd–Ag alloy system follows theory relatively well, the Cu–Ni system shows well-marked and consistent deviations. The Hall constants of the Cu–Ni system are available,[2] but no such data exists for the Pd–Ag system. Consequently, the Hall constants of several alloys of Pd and Ag were measured at room temperature. The absolute value of the Hall constant rises slowly as Pd is added to Ag, reaches a maximum at roughly 50 percent Pd and then falls approximately linearly as the alloy composition approaches pure Pd. The Hall constant *versus* composition curve is asymmetric with composition and is very similar in appearance to the resistivity *versus* composition curve for the same alloy system. These results will be discussed and compared with the Hall data previously obtained on the Cu–Ni alloy system.

[1] B. R. Coles, Proc. Phys. Soc. (London) 65, 221 (1952).
[2] A. I. Schindler and E. M. Pugh, Phys. Rev. 89, 295 (1953).

FRIDAY MORNING AT 10:00

1400 Chemistry

(D. M. DENNISON presiding)

## *Molecular and Chemical Physics*

**M1. A General Method for High-Speed Machine Computation of Ideal Gas Thermal Properties. The Isotopic Water Molecules.** ABRAHAM S. FRIEDMAN AND LESTER HAAR, *National Bureau of Standards.*—A procedure is developed for the machine computation of the partition functions for non-rigidly rotating anharmonic oscillators. Vibrational-rotational coupling terms and low-temperature rotational corrections are included. A general code has been designed to permit the calculation of the ideal gas thermodynamic functions for a large variety of molecular structures on the National Bureau of Standards digital computor—SEAC. The method is illustrated by evaluating the thermodynamic functions for an asymmetric top molecule. Tables of $C_p^0/R$, $(H^0-E_0^0)/RT$, $(E_0^0-F^0)/RT$, and $S^0/R$ have been evaluated for $H_2O$, HDO, $D_2O$, HTO, DTO, and $T_2O$ at close intervals from 50° to 5000°K. The time required for these computations is of the order of several minutes per molecule. The results for $H_2O$ are in good agreement with those obtained by direct summation.[1]

[1] Glatt, Adams, and Johnston, O. S. U. Tech. Report No. 316-8 (1953).

**M2. Intensities, Electronic Transition Moments, and Vibrational Transition Probabilities of Diatomic Molecules.*** R. W. NICHOLLS, P. A. FRASER, R. G. TURNER, AND W. R. JARMAIN, *University of Western Ontario.*—Methods have been developed which enable accurately calculated values of overlap integrals $\int\psi_{v'}\psi_v dr$ of diatomic molecular vibrational wave functions[1] to be used together with experimentally determined band intensities to determine the form of the electronic transition moment $R_e(r)$ of the electronic transition concerned. Vibrational transition probabilities $|\int\psi_{v'}R_e\psi_{v''}dr|^2$ in which the conventional simplifying assumption that $R_e(r)$ is independent of $r$ has not been made, have thereby been determined for a number of transitions. Reliable values of such vibrational transition probabilities for molecular band systems are of great importance in the interpretation of spectra from inaccessible sources, usually of astrophysical interest.[2] Results so far obtained from band systems of $N_2$, $C_2$, and CN will be presented.

* This work is supported by contract with The Air Force Cambridge Research Center.

[1] Nicholls, Fraser, and Jarmain, Can J. Phys. 31, 1019 (1953); Jarmain, Fraser, and Nicholls, Astrophys. J. 118, 228 (1935); P. A. Fraser and W. R. Jarmain, Proc. Phys. Soc. (London) A66, 1145, (1953); W. R. Jarmain and P. A. Fraser, Proc. Phys. Soc. (London) A66, 1153 (1953).

[2] J. A. Hyneck, editor; P. Swings, "Molecular Spectra in Cosmic Sources," Chapter 4 of *Astrophysics* (McGraw-Hill Book Company, Inc., 1951).

**M3. Configuration Interaction Applied to the Hydrogen Molecule.*** EARL CALLEN, *M.I.T.*—The electronic wave function for the hydrogen molecule has been described as a sum of three configurations, each of which is expressed in terms of one-electron symmetry orbitals, which are written as variational functions of the elliptic coordinates. To a state due to Coulson,[1] made up of orbitals which are individually even under inversion, we first added an odd-odd state, thus improving the predicted binding energy from 3.535 ev to 4.125 ev. The addition of a third state, of a somewhat different nature, increases the binding energy to 4.276 ev. The experimentally observed binding energy is 4.72 ev. The role of the several configurations is explained in terms of the concept of spatial correlation, following the work of Lennard-Jones and coworkers.[2]

* This work has been supported by the U. S. Office of Naval Research.

[1] C. A. Coulson, Proc. Cambridge Phil. Soc. 34, 204 (1938).

[2] J. E. Lennard-Jones and J. A. Pople, Discussions Faraday Soc. No. 10 9 (1951).

**M4. The 2.7μ Bands of $CO_2$.** W. L. FRANCE AND F. P. DICKEY, *Ohio State University.*—The absorption spectra due to the $CO_2$ bands (02°1) and (101) in the 2.7μ region have been remeasured using a high-resolution prism grating spectrometer. A 15 000 lines per inch echelette grating ruled by Bausch and Lomb and a lead sulfide photoconductive detector were used in the spectrometer. The spectrometer was first evacuated and then dried $CO_2$ was introduced into it. The pressure of the $CO_2$ was 5 mm of Hg and the length of the absorbing path was approximately 7 meters. All of the lines in the band (02°1) from $P(62)$ to $R(66)$ have been identified and measured, and all of the lines in the band (101) from $P(62)$ to $R(66)$ have been identified and measured. Values of the band centers and the rotational constants have been determined.

**M5. The Absorption Spectra of Water Vapor in the 2.7 μ and 6.0μ Regions.*** F. W. DALBY, H. H. NIELSEN, AND F. P. DICKEY, *Ohio State University.*—The absorption spectra of water vapour has been obtained in the regions 2.7μ and 6.0μ with the new Ohio State vacuum spectrometer. In the region of 2.7μ a Bausch and Lomb 15 000 lines per inch grating and a lead sulfide photoconductor detector were employed. With the air pressure in the spectrometer reduced to a few millimeters, resolutions of better than 0.1 $cm^{-1}$ were achieved. Using a Bausch and Lomb 4500 lines per inch grating, a thermocouple detector, and similar pressures led to resolutions of better than 0.2 $cm^{-1}$ in the 6.0μ region. The substantial improvement in resolution, which resulted largely from the reduction of pressure broadening, leads to some revision in the molecular constants of the water molecule. Detailed reproductions will be presented and discussed.

* This work was assisted by the U. S. Office of Naval Research.

**M6. The Infrared Spectrum of Hydrogen Sulfide in the 5100 $cm^{-1}$ Region.** HARRY C. ALLEN, JR.,* *Harvard University,* AND EARLE K. PLYLER, *National Bureau of Standards.*—The absorption of hydrogen sulfide in the region near 2μ has been measured under high resolution. The rotational fine structure has been analyzed with the use of published energy tables for the rigid rotor. A classical centrifugal distortion correction was applied to the rigid rotor energy levels. The absorption can be accounted for by three bands plus overlapping water vapor absorption. The three bands are the $(n_1n_2n_3) = (1,0,1)$ at 5147.36 $cm^{-1}$, the (0,2,1) at 4939.23 $cm^{-1}$ and the lower component of the resonating pair (2,0,0) and (0,0,2) at 5145.12 $cm^{-1}$. The excited state inertial parameters in $cm^{-1}$ giving the best fits are

| | $A^*$ | $B^*$ | $C^*$ |
|---|---|---|---|
| (1, 0, 1) | 10.076 | 8.709 | 4.668 |
| (2, 0, 0) | 10.059 | 8.719 | 4.612 |
| (0, 2, 1) | 10.871 | 9.332 | 4.562 |

With the location of the (0,2,1) band it is possible to place the (0,0,1) band at 2628 $cm^{-1}$.

* U. S. Atomic Energy Commission Postdoctoral Fellow. Present address, Michigan State College.

**M7. The Effect of Foreign Gas Broadening on the Total Absorption by the 6.3μ Band of Water Vapor.** D. E. BURCH, J. N. HOWARD, AND DUDLEY WILLIAMS, *The Ohio State University.**—The total absorption of the 6.3 micron band of water vapor has been measured with a low-resolution spectrometer and a 22 meter, multipie-traversal absorption cell. Water vapor concentrations between 0.02 and 16 precipitable centimeters in the absorption path have been studied. In addition, the water-vapor band was pressure-broadened with nitrogen to various total pressures up to atmospheric pressure. With this apparatus, the absorption path length, the partial pressure of the absorbing gas, and the total pressure can be varied independently, and the effects of self-broadening and foreign gas broadening can be separately evaluated. Temperature was not varied in this study. Empirical relationships have been fitted to these data in order to permit the calculation of the total absorption by the 6.3 micron water vapor band for many problems of meterological interest.

* Work supported by Air Force Cambridge Research Center.

**M8. Generalized Absorption Coefficients of Water Vapor.*** HAROLD DAW.—The Pfund-type absorption cell of the ONR project at Johns Hopkins University is being used to study dependence of water vapor absorption on both the amount of absorber and the total pressure (produced by $N_2$). The optical path is 625 feet. In contrast with former work with that cell the author is using low dispersion (a Perkin-Elmer spectrometer with KBr and NaCl prisms) in order to get averaged absorption coefficients leading to generalized transmission functions. Pressures range up to 64 cm Hg; water vapor ranges from 0.004 to 0.064 precipitable cm. It was necessary to develop a special analysis for water vapor in the tube since water vapor in oil-pumped dry nitrogen gas and water adsorbed within the tube introduce significant errors if one simply uses liquid water added. Progress to date will be reported.

* This work is carried out under Air Force Cambridge Research Center contract. The cooperation of Professor John Strong and his U. S. Office of Naval Research contract is acknowledged and appreciated.

**M9. Shape of Collision-Broadened Spectral Lines,** E. P. GROSS,* *M.I.T.*—Van Vleck and Weisskopf and Fröhlich have derived a microwave line-shape by studying the interruption by collisions of the motion of a classical oscillator. They assume that after the instantaneous impact the oscillator variables are distributed according to a Boltzmann distribution appropriate to the value of the applied field at collision. In contrast to the earlier theory of Lorentz, they obtain the correct static polarization. The procedure involves an assumption of very large velocity during collision. This is unreasonable since the duration of collision is short compared to the resonant period and energy exchanges are of the order of $kT$. We have derived a line-shape formula assuming that the oscillator velocities have a Maxwellian distribution after impact but that the positions are unchanged. For collision frequency much less than the resonant frequency, the polarization is reached as a result of kinematic motion between collisions and the line-shapes agree. For collision frequency comparable to resonant frequency a less distorted line-shape results. Correct static polarization is obtained; for zero resonant frequency we obtain the behavior of free particles. For testing the theories experiments on foreign-gas broadening in the microwave region at pressures of the order of an atmosphere are required.

* Present address: Physics Department, Syracuse University, Syracuse, New York.

**M10. The Role of the Principal Quantum Number ($n$) in the Calculations of Radii for the Ions with High (4, 5, 6, 7) Valence.*** N. EFREMOV, *1061 Intervale Ave., New York, New York.*—The proposed periodic system of ions may be used as a system of coordinates in which each ion has its own ordinate $n$ (principal quantum number) and abscissa $K$. Abscissas $K$ may be derived from ordinates $n$ by means of the following equations: $K=n+8$, $K=n+9$, etc. The $K$ value of an ion increases by 1, when its atomic number is decreased by 1. The $F^7$-ion which has the smallest ionic radius is the primary ion, and its $K(F^7)=n+8$, while $K(O^8)=n+9$. Let us consider the ordinates and abscissas for the first quadruple group of high-valence ions belonging to the He period: C−N−O−F.

| Ions: | C | N | O | F |
|---|---|---|---|---|
| Valence: | 4 | 5 | 6 | 7 |
| Ordinate ($n$): | 1 | 1 | 1 | 1 |
| Abscissa ($K$): | $(n+11)$ | $(n+10)$ | $(n+9)$ | $(n+8)$ |
| Abscissa ($K$): | 12 | 11 | 10 | 9 |

The general formula for the calculation of ionic radius of any element ($X$) of this quadruple groups is the following: $R_i(X) = /n(n+Y)/P$, where $X$ is the given ion, $Y=8$, 9, 10, or 11, and $P=0.014692369$A, e.g. $R_i(F^7) = /1(1+8)/P = 9P = 0.13$A; $R_i(Cl^7) = /2(2+8)/P = 20P = 0.29$A.

* Paper given at the September 1953 meeting of the American Physical Society in Albuquerque, New Mexico.

**M11. The Cooling of a Gas by Radiation.*** ERNEST BAUER, *New York University* AND TA-YOU WU, *National Research Council, Canada.*—We consider a gas composed of atoms having two electronic states. Transitions between these two states can take place by collisions, and by emission or absorption of radiation. When the radiative transition probabilities are small compared with those due to collisions, a "temperature" may be defined for the translational motion. We formulate the general problem for the case where the total concentration of the gas depends on the space coordinates (altitude) in a given way, and the possibility of the "imprisonment" of the radiation emitted is taken into account. In this case the problem leads to a pair of coupled integro-differential equations, from which the "temperature" and the relative concentration of atoms in the excited states are obtained as functions of space and time. Neglecting the imprisonment of the resonance radiation and the variation of concentration with height, we have made calculations for the case when the energy difference between the two states is of the order $kT$, for a number of values of the ratio between radiative and collisional transition probabilities. The results are applied to the cooling of the atmospheric gas at high altitudes (100 Km) at night, as a result of the magnetic dipole transitions of the oxygen atom.

* This work was supported in part by Contract with the United States Air Force through sponsorship of the Geophysics Research Directorate of the Air Force Cambridge Research Center, Air Research and Development Command.

**M12. Note on the Theory of Directed Valence.** TA-YOU WU, *National Research Council, Canada.*—The recent observation by Zimmerman and Rysselberghe[1] and by Linnett and Pöe[2] that the wave functions of the free atoms when put in the determinant form exhibit the directional property of valence has been examined. It is shown that whatever directional properties the $\psi$ of the free atoms may have, a consistent theory of directed valence cannot be based on them, for the following reasons: (1) As long as one works on the Heitler-Londer theory of electron-pair bonds and the criterion of maximum overlap for the stability of a bond, one must work with wave functions antisymmetrized in the electrons of the atoms forming a bond, but not of the free atom alone. (2) It is not possible in general to associate the directional property of valence with the wave function of a particular state of the free atom. (3) Even if a particular state of the free atom contributes predominantly to the valence state, the fact that that state is degenerate must be taken into account. The nature of the assumption of hybridization in the Slater-Pauling theory is clarified and emphasized.

[1] H. K. Zimmerman and P. Rysselberghe, J. Chem. Phys. 17, 598 (1949).
[2] J. W. Linnett and J. Pöe, Trans. Faraday Soc. 47, 1033 (1951).

FRIDAY MORNING AT 10:00

130 Business Administration

(R. S. MARVIN presiding)

## *Symposium of the Division of High-Polymer Physics*

## *The Properties of Amorphous Polymers in Bulk*

**O1. Introductory Remarks.** R. S. MARVIN, *National Bureau of Standards.* (10 min.)
**O2. The Nature of the Liquid and Glassy States.** W. D. KAUZMAN, *Princeton University.* (40 min.)
**O3. The Effect of Structural Variables on the Specific Volume and Glass Temperature.** T. G. FOX, *Rohm & Haas Company.* (20 min.)
**O4. Some Physical Properties of Polymeric Glasses.** R. F. BOYER, *Dow Chemical Company.* (30 min.)
**O5. The Mechanics of the Molecular Motion in Bulk Polymers.** F. BUECHE, *Rohm & Haas Company.* (40 min.)

---

FRIDAY AFTERNOON AT 2:00

130 Business Administration

(R. S. MARVIN AND R. F. BOYER presiding)

## *Symposium on Amorphous Polymers (continued)*

**P1. A Theory of Viscoelastic Behavior.** W. G. HAMMERLE, *Textile Research Institute* (40 min.)
**P2. The Dynamic Properties of High Polymers.** E. A. W. HOFF, *Imperial Chemical Industries.* (30 min.)

## *Invited Paper*

**P3. Rotation of Chain Molecules in Crystals.** J. D. HOFFMAN, *National Bureau of Standards.* (30 min.)

## *Contributed Papers*

**P4. Experimental Investigation of the Statistical Theory of Rubber Elasticity.*** F. P. BALDWIN,† J. IVORY, AND R. L. ANTHONY, *University of Notre Dame.*—A careful experimental study of the dependence of stress upon temperature, for extensions ranging from 0 to 15 percent, was made for two rubbers, GR-I-18 and Paracril-35. Four-inch specimens, cut from standard tensile sheets, were stretched to various constant lengths at the highest temperature to be employed, and the stress permitted to relax at that temperature until a semi-equilibrium condition was reached. The temperature was then lowered in steps, and the dependence of stress upon temperature observed. Stretched specimen lengths were held constant to $\pm 0.05$ percent, both during the initial relaxation period and also during the stress-temperature run. In agreement with the predictions of the James-Guth theory, the stress-temperature characteristics were observed to be curved, and not linear. The predicted shift in the thermoelastic inversion extension with temperature was also observed. The experimental equipment will be described.

* Supported in part by U. S. Office of Naval Research, and by the United States Rubber Company.
† Now at Esso Laboratories, Linden, New Jersey.

**P5. Energy Requirements of Mechanical Shear Degradation in Concentrated Polymer Solutions.** A. B. BESTUL, *National Bureau of Standards.*—Molecular weight decrease by mechanical shearing results when solutions of around 10 percent of polyisobutenes having average molecular weights above 500 000 are forced through a capillary at nominal rates of shear above 10 000 $sec^{-1}$. Comparison of observed plots of shear load *versus* duration of shearing during this degradation process with the corresponding estimated plots which would be expected to obtain if degradation did not occur provide a means of evaluating the amount of applied shearing energy which is used up by the degradation process. The result is several hundred thousand kilocalories per mole of broken bonds, which is several thousand times the bond energy of carbon-carbon bonds. This finding is explained by the hypothesis that whenever a bond breaks the system loses much of the energy temporarily stored as potential energy in bonds located in a comparatively large volume surrounding the broken bond; these bonds having been involved in concentrating the required activation energy into the ruptured bond.

**P6. Concentration Dependence of Mechanical Shear Degradation.** P. GOODMAN,* *National Bureau of Standards.*—The rates of mechanical shear degradation of polyisobutene in cetane solutions have been studied for 3 and 20 percent solutions at various rates of shear. The data show that the rate constant for degradation in solutions of 5–20 percent concentration is independent of concentration at a fixed rate of shear energy input. The slope of the straight line relating the logarithm of the rate constant to the reciprocal of the rate of shear energy application decreases markedly in absolute value in the concentration range 5–3 percent and this decrease is

thought to be the result of a decreased efficiency of the intermolecular entanglements in temporarily concentrating mechanical energy in the less concentrated solution.

* Present address: Naval Powder Factory, Indian Head, Maryland.

**P7. Analysis of Reduced Viscosity Equations.** WILFRIED HELLER, *Wayne University.*—A detailed analysis of the various existing interrelated reduced viscosity equations is carried out using suitable data. Reliable graphical extrapolations of $[\eta]$ are possible only with the commonly used equation (1): $\eta_{sp}/c=[\eta]+K_1[\eta]^2c+\cdots$ or with the new equation (2): $c/\eta_{sp}=1/[\eta]-K_1c$—which is the function of the preceding infinite series—if combined with the corresponding auxiliary equations (1a): $\ln\eta_{rd}/c=[\eta]-K_3[\eta]^2c$ and (2a): $c/\ln\eta_{rd}=1/[\eta]+K_3c$, respectively. An advantage of (2) is the heretofore impossible direct graphical determination of the limiting value of $k_1$ by means of $d(c/\eta_{sp})/dc=f(c)$. The number of significant figures obtained from a graphical extrapolation to $[\eta]$ from either pair of equations can be increased, in the unfavorable case of good solvents, by plotting the apparent intercepts as a function of concentration. No truly satisfactory equation exists for the reproduction of data over a wide concentration range ($\Delta c>5$ g/100 ml) and none can be expected. The best approximations are generally obtained with a binomial expression of the form (3): $\eta_{rd}=(1+K_4c)^x$ (Baker). Less suitable, but often acceptable is the exponential expression (4): $\eta_{sp}/c=[\eta]e^{K_5c}$ (Staudinger-Martin). The logarithmic form of either allows the best graphical representation of data over a wide concentration range excepting $c<2$ g/100 ml. The generally rapid increase or decrease in slope towards $c\to0$ excludes its use for extrapolations to $[\eta]$.

**P8. The Infrared Spectrum of Polyethylene.** S. KRIMM, *University of Michigan.*—Previous studies on paraffins[1] and polarized studies on single crystals of *n*-paraffins[2] indicate that the splitting of the 725 $cm^{-1}$ and 1460 $cm^{-1}$ bands in polyethylene is due to interactions between neighboring chains in the crystalline phase. This is substantiated by present results on solid solutions of a *n*-paraffin, $C_{44}H_{130}$, in a deutero paraffin: a single band at 725 $cm^{-1}$ in the dilute solution splits, as the concentration is increased, finally into components at 721 $cm^{-1}$ and 731 $cm^{-1}$. Assignments of polyethylene bands in the 1300–1375 $cm^{-1}$ region are clarified by the solid solution spectra as well as by studies on melted paraffins. Solid $C_{44}H_{130}$ has only a single band at 1375 $cm^{-1}$. When melted, bands appear at 1363, 1350, and 1300 $cm^{-1}$. As the temperature is increased the 1375 $cm^{-1}$ band diminishes in intensity. These results, plus the relative decrease in intensity at 1375 $cm^{-1}$ in the solid solutions, are consistent with an assignment of the 1300, 1350, 1363, and most of the 1375 $cm^{-1}$ bands to $CH_2$ wagging modes in disordered and ordered phases of polyethylene.

[1] R. S. Stein and G. B. B. M. Sutherland, J. Chem. Phys. **21**, 370 (1953).
[2] S. Krimm, J. Chem. Phys. (to be published).

---

FRIDAY AFTERNOON AT 2:00

West Physics Lecture Room

(H. A. BETHE presiding)

### *Invited Papers*

**Q1. Early Days of Infrared Spectroscopy at the University of Michigan.** H. M. RANDALL, *University of Michigan.* (30 min.)

**Q2. Design of a Precision Experiment on the Gyromagnetic Ratio of the Free Electron.** H. R. CRANE, *University of Michigan.* (30 min.)

**Q3. Solid State at Low Temperatures: A Survey of the 1953 International Congress on Low Temperature-Physics.** C. F. SQUIRE, *Rice Institute.* (30 min.)

**Q4. Infrared Analysis of the Structure of Large Molecules.** G. B. B. M. SUTHERLAND, *University of Michigan.* (30 min.)

**Q5. Structure and Function in Molecular Biophysics.** CYRUS LEVINTHAL, *University of Michigan.* (30 min.)

---

FRIDAY AFTERNOON AT 2:00

Rackham Lecture Hall

(H. M. JAMES presiding)

### *Semiconductors, III*

**R1. Graphical Representation of the Semiconductor Hall Effect.** L. P. HUNTER, *International Business Machines Corporation.*—W. C. Dunlap[1] has given a graphical representation of the semiconductor Hall effect in terms of an ellipse relating the Hall mobility and resistivity at constant temperature. Various uses and extensions of this representation will be given which serve to correlate the important features of the Hall effect in semiconductors. The constant temperature limitation is removed and the effects of excess current carrier lifetime and the nonequality of the Hall and drift mobility ratios will be discussed. The question of determining the intrinsic activation energy of a semiconductor with a high-mobility ratio, from Hall coefficient measurements raises special problems which will be used to illustrate the application of this analysis.

[1] W. C. Dunlap, Phys. Rev. **79**, 286 (1950).

**R2. Hall Effect and Thermoelectric Power of Pure Tellurium at the Melting Point and in the Liquid State.*** A. EPSTEIN AND H. FRITZSCHE, *Purdue University.*—At the melt-

ing point, the thermoelectric power $Q$ and the Hall effect $R$ of spectroscopically pure tellurium show a discontinuous drop at the solid-liquid transition indicating an increase in carrier concentration. Depending on the crystal orientation of the solidified material, $Q$ ranges between +100 and +260 microvolts/degree and $R$ between +0.2 and +0.4 cm³/coulomb in the solid at the melting point, in the liquid the values are +9 microvolts/degree and +0.02 cm³/coulomb, respectively. Both quantities continue to decrease with increasing temperature in the liquid and become negative in the temperature range between 575°C and 625°C.

* Supported by Signal Corps contract.

**R3. Resistivity, Thermoelectric Power, and Hall Effect in a Semiconductor with Hexagonal Structure.*** V. A. JOHNSON, *Purdue University.*—In an anisotropic semiconductor, electron and hole masses are dyadics, and it follows that other quantities, including the mobility and Thomson coefficient, are also dyadics. For hexagonal structure, such as that of tellurium, this leads to a thermoelectric power $Q=Q_p\cos^2\theta+Q_n\sin^2\theta$, where $\theta$ is the angle between $c$ axis and temperature gradient ($p$ denotes parallel, $n$ normal to $c$ axis). In the impurity range, $Q_p=Q_n$ and thermoelectric power is independent of direction of temperature gradient. In the intrinsic range, a difference between $Q_p$ and $Q_n$ arises if $m_p/m_n$ has different values for electrons and holes. For the Hall coefficient, $R_p=R_n$ in the impurity range, but the values differ in the intrinsic range if $(m_p/m_n)_e\neq(m_p/m_n)_h$. It has been found for the intrinsic range that $2|R_n/R_p|=1+|Q_p/Q_n|$. The resistivity in the impurity range is dependent on orientation according to $\rho_n/\rho_p=m_n/m_p$. The corresponding resistivity ratio in the intrinsic range depends on the relative values of $(m_p/m_n)_e$ and $(m_p/m_n)_h$, as do the relations between $\rho$ and $R$, and $\rho$ and $Q$, in the intrinsic range.

* Work assisted by Signal Corps contract.

**R4. Infrared Absorption of Tellurium.*** R. S. CALDWELL AND H. Y. FAN, *Purdue University.*—Infrared absorption in single crystals of tellurium was investigated with polarized light from 4 to 25 microns. For both directions of polarization a small band was observed at 24.5 microns, apparently a lattice band. With the electric vector perpendicular to the $C$ axis the absorption increased smoothly with wavelength, whereas for the electric vector parallel to the $C$ axis a sharp band with a peak at about 11 microns was observed; with decreasing temperature this peak shifts to shorter wavelengths. In the impurity range, where all samples are $p$ type, this band in different samples increased with the hole concentration. The oscillator strength based on the hole concentration is close to one. When the temperature is raised into the intrinsic range this band increased. These observations indicate that this band is due to holes in the valence band, similar to the band structure in $p$-type germanium. The fact that this absorption is observed only with electric vector parallel to the $C$ axis gives some insight into the wave functions of the overlapping bands. No additional bands were observed in the intrinsic range, which might be ascribed to the conduction electrons.

* Work supported by a Signal Corps contract.

**R5. Metal-Insulator-Metal Junction.** G. H. SUITS, *University of Michigan* (introduced by E. Katz).—A present theory of solid rectifiers is based upon the idea that a high-resistance barrier layer is formed at the metal-semiconductor surface. The rest of the semiconductor plays the role of an ordinary conductor. The solution of the diffusion equation for this model predicts a rectifying chtracteristic. Approximate solutions of the diffusion equation for the metal-insulator-metal junction have also predicted a rectifying characteristic. So far, no conclusive experiments have been done which adequately test these predictions for the metal-insulator-metal junction. This paper presents the exact solution of the diffusion equation for the metal-insulator-metal junction where trapping of charge carriers may occur, and a description of the present experimental limitations preventing the construction of suitable test junctions by the vacuum evaporation technique.

**R6. The Transient Response of $P-N$ Junction Rectifiers.*** B. R. GOSSICK, *Purdue University.*—The rise time $T_R$ and delay time $T_D$ have been derived using the ac admittance[1] as:

$$T_D=T(v_0)+\frac{I_{p_0}\tau_p+I_{n_0}\tau_n}{2(I_{p_0}+I_{n_0})} \quad (1)$$

$$T_R=\left\{2\pi\left[T_D{}^3+\frac{I_{p_0}\tau_p{}^3+I_{n_0}\tau_n{}^3}{4(I_{p_0}+I_{n_0})}\right]\right\}^{\frac{1}{3}}. \quad (2)$$

$T(v_0)$ denotes the $RC$ time constant of the barrier with bias voltage $v_0$. It may be seen by (1) and (2) that the saturation currents $I_{p_0}$ and $I_{n_0}$ lead to the appropriate determination of the average effect of the lifetimes $\tau_p$ and $\tau_n$. Current *versus* barrier voltage characteristic curves which were measured using the post injection barrier emf[2] are presented.

* Supported by Signal Corps contract.

[1] W. Shockley, Bell System Tech. J. **28**, 435–489 (1949).
[2] B. R. Gossick, Phys. Rev. **91**, 1012 (1953).

**R7. Evaporated Multiple Layers with Semiconductor Properties.** J. C. M. BRENTANO AND J. D. RICHARDS,* *Northwestern University.*—Sintered materials, pressed powders, and thin evaporated films show the significance of boundaries in determining semiconductor properties. Alternate evaporations of two metals in high vacuum yield multiple layers ranging from distinct strata to highly dispersed deposits. Their microscale characteristics are short-range order long-range disorder, large number of internal boundaries, and eventual trapping centers. Distinctive from single thin layers, effects of external boundaries and support can be reduced with the total layer thickness. The mechanism of multiple layer formation is illustrated with deposits of indium and antimony. The metals when deposited in thin layers at room temperature form indium antimonide. When the individual layers are more than two atoms thick, a very thin layer of indium antimonide retards further reaction, which thus can be followed up by the change of conductivity. Deposited at −160°C, separate thin layers of indium and antimony are stable with a negative temperature coefficient. Increasing the temperature causes a sudden irreversible decrease in conductivity which may be explained by the formation of InSb; the temperature coefficient is then also negative, but resistance and temperature coefficient assume different values.

* Milwaukee Gas Specialty Company Fellow.

**R8. Hall Effect and Magnetoresistivity in Carbons.*** S. MROZOWSKI AND A. CHABERSKI, *University of Buffalo.*—Samples of a soft carbon were heat-treated (h.t.) to different temperatures (h.t. from 1200°C up to 3100°C) and investigated at liquid nitrogen and at room temperature. The Hall constant is negative for h.t. smaller than 1700°C or greater than 2400°C and positive for intermediate heat treatments, reaching a sharp peak in this range. In general the Hall constant is greater at liquid nitrogen temperature; the difference is slight for h.t. below 1800°C (neglecting irregularities probably caused by evaporation of impurities) and quite large in ranges of h.t. between 2100–2300°C and above 3000°C. The positive peak is located at h.t.=2050°C at room temperature and at h.t.=2140°C at liquid nitrogen temperature. This behavior agrees with expectations. No measurable magnetoresistance was found below h.t.=1800°C. For higher heat treatments, first a small negative effect is observed which further changes sign and steadily increases up to the highest h.t. The magnetoresistance is larger at liquid nitrogen temperature; the positions of the minimum (negative peak)

coincide with those of the positive peak in the Hall effect. Negative magnetoresistance occurs, therefore, in a range where not too many excess holes are present so that some electrons are thermally excited into the conduction band, but only as long as this latter number is small.

* Supported by the U. S. Office of Naval Research.

**R9. Effect of Impurities on the Conductivity of Gray Tin.** A. W. EWALD, *Northwestern University.*—The electrical conductivity of pure gray tin and of gray tin doped with antimony, indium, aluminum, and zinc has been measured in the temperature range from 77 to 273°K. Filamentary specimens were prepared by the method previously described.[1] The conductivity of 99.998 percent pure gray tin free of antimony does not show the minimum reported by Busch, Wieland, and Zoller,[2] but with the addition of 0.001 atomic percent Sb a minimum occurs at 140°K. For higher Sb concentrations the rise at low temperatures is more pronounced, suggesting that this rise is due in part to an increase in the number of carriers with decreasing temperature. This has been verified through magnetoresistance determinations of the mobility. Doping with Al, In, or Zn produces *P*-type conductivity, In and Zn being more effective than Al. Samples containing low concentrations of In or Zn (~0.001 atomic percent) show a nearly linear $\ln\sigma$ *vs* $1/T$ curve over the full temperature range similar to that reported by Kendall.[3]

[1] A. W. Ewald, Phys. Rev. **91**, 244 (1953).
[2] Busch, Wieland, and Zoller, Helv. Phys. Acta **24** (No. 1), 49 (1951).
[3] J. T. Kendall, Proc. Phys. Soc. (London) **B63**, 821 (1950).

**R10. Interaction of Impurities and Mobile Carriers in Semiconductors.*** GUY W. LEHMAN AND HUBERT M. JAMES, *Purdue University.*—The effect of the interaction between mobile carriers and impurities in semiconductors on the activation energy of impurity atoms has been investigated by an extension of the hydrogenic model; the theory thus applies only to impurities with low activation energies. Electrons trapped by impurity ions move in a resultant field due to the ion (treated as a point charge) and the surrounding distribution of untrapped carriers; the untrapped carriers move in a field because of neutral impurity atoms, impurity ions, and other carriers. Orbitals for trapped and untrapped carriers have been determined by approximate solution of appropriate Hartree equations. Because of the temperature dependence of the distribution over states of mobile carriers, the orbitals of the theory depend on the temperature as a parameter. For given temperature and impurity concentration $\bar{N}$, the electron concentration depends on the activation energy, and the activation energy depends on the electron concentration; these two quantities are thus determined by a consistency relation. The theory predicts that the activation energy will decrease with increasing $\bar{N}$ in a temperature-dependent way; if $\bar{N}$ is large the decrease will be smaller the lower the temperature.

* Work supported by Signal Corps contract.

**R11. Contact Potential, Work Function, and Surface States.** SELBY M. SKINNER, *Case Institute of Technology.*—Myerhof[1] and others have found that measured contact potential difference between electrode and semiconductor does not necessarily show correlation with work function difference. Bardeen[2] has explained this in terms of surface (Tamm) states. A consideration of current flow through poorly conducting materials taking into account thermodynamic equilibria within the material and at the contact with the metal, and space charge and diffusion effects, indicates that such lack of correlation is to be expected whenever the volume density of charge in the material in the vicinity of the boundary is large, irrespective of whether there are surface states. For small volume density near the boundary, i.e., large potential barrier, essentially the usual relationship is valid.

[1] W. E. Meyerhof, Phys. Rev. **71**, 727 (1947).
[2] J. Bardeen, Phys. Rev. **71**, p. 717.

---

## FRIDAY AFTERNOON AT 2:00

## 1400 Chemistry

## (F. C. NIX presiding)

### *Metals, III (Including Order-Disorder)*

**S1. Size Effects Found in the Nucleation of Fracture Origins.** E. A. MCLEAN AND WALLER GEORGE, *Naval Research Laboratory.*—Studies of the processes of nucleation of fracture origins in metals have been made using a centrally notched zinc foil model loaded in tension normal to the notch.[1] The fracture length observed was always less than the critical length at which extension is accelerated by the release of strain energy in excess of the specific fracture work. Fracture growth is accomplished in these regions by the initiation of nuclei in advance of the main crack, the subsequent growth of the nuclei, and the joining up of the nuclei with the main fracture. Interest in this experiment is primarily concerned with the time rate of appearance of these nuclei. Studies of foils in which the shape, the thickness, and the initial load per unit of width remain constant while the length and width are varied indicate a pronounced "size effect" as shown by plots of the total number of fracture nuclei formed as a function of time. The time to create a given number of fracture nuclei under equal specific loading is observed to increase with decreasing specimen size.

[1] E. A. McLean and W. George, Bull. Am. Phys. Soc. **29**, No. 1, 24 (1954).

**S2. On the Origin of Recrystallization Nuclei.** JOHN P. NIELSEN, *New York University.*—A theory has been developed for grain growth from a minimum of assumptions; no more than were used by Gibbs in his discussion of surfaces of discontinuity in his equilibrium of heterogeneous substances paper. It turns out that there are several components that contribute to the over-all growth rate curve that is observed. The outstanding discovery in this analysis is that the origin of recrystallization nuclei is a direct logical development of the application of the ideas of Gibbs. The origin of recrystallization nuclei was discussed in a report[1] circulated from this laboratory in 1949 and the essential requirement was stated therein. In that report slip plane intersections were used to satisfy the requirement and in the present theory, no such artificial mechanism is needed. A microstructure showing the

manner of selection for a secondary recrystallization nucleus has been obtained in an 8.4 percent nickel-titanium alloy. The process accounting for one of the components of the growth rate curve has been reproduced in a nonmetallic system. The frequency of recrystallization nuclei in textures can be accurately predicted.

[1] Comments on Paper by C. S. Smith, Trans. Am. Inst. Mining Met. Engrs. 175, 15 (1948).

**S3. Order-Disorder and Cold-Work Phenomena in Cu–Pd Alloys.*** F. E. JAUMOT, JR., AND A. SAWATZKY, *The Franklin Institute Laboratories for Research and Development.*—X-ray and resistivity measurements on samples of Cu-Pd alloys containing up to 29 atomic percent Pd indicate that there are four regions to be considered when the samples are slowly cooled (2°C per day) from 550°C. Below about 10 and above 28 percent Pd the alloys are disordered f.c.c.; between 10 and 19 percent Pd they are ordered f.c.c.; and between 19 and 27 percent Pd, ordered tetragonal. The tetragonality is quite marked at 400°C but the degree of order is increased on cooling to 285°C. Room temperature resistivities of samples slowly cooled, quenched from 800°C (disordered f.c.c.), and furnace cooled from 800°C were studied as a function of cold-work (drawing). The quenched samples exhibited a marked decrease in resistivity with cold work; the others showed a sharp rise initially, and then a decrease, eventually joining the curve for the quenched samples. Similar maxima are observed in curves of resistivity *versus* time of anneal for cold-worked samples and annealing temperatures from 100°C to 400°C. The temperature coefficients of resistivity (between room temperature and −190°C) exhibit no anomalies, regardless of the state of cold work of the sample.

* Supported by the Office of Ordnance Research, U. S. Army.

**S4. Diffraction Studies of Possible Ordering in α Brass.*** D. T. KEATING, *Brookhaven National Laboratory.*—A study of the possible ordering in the α-brass system has been conducted concurrently with the study of radiation induced changes in the electrical resistivity of α brass.[1] Masumoto, Saito, and Sugihara have concluded from their specific heat measurements that there is a possibility of ordering in the α brasses.[2]

A single crystal of 70–30 α brass annealed at 190°C for six weeks has been studied with both x-rays and neutrons. Any degree of long-range order in the crystal would produce a sharp (110) superlattice reflection, the integrated intensity being proportional to the Bragg and Williams long-range order parameter. Local or short-range ordering would be expected to produce a diffuse reflection centered about the (110) position. The diffracted intensities in the region of the expected (110) superlattice reflection have been carefully examined, and within the limits of error of the data no ordering was observed with either x-rays or neutrons.

* Work done under contract with the U. S. Atomic Energy Commission.
[1] Rosenblatt, Smoluchowski, and Dienes, Bull. Am. Phys. Soc. **29**, No. 3, 19 (1954) (this meeting).
[2] Masumoto, Saito, and Sugihara, Science Rep. Research Insts. Tohoku Univ., Ser. A4, 481 (1952).

**S5. Kinetics of the Ordering and Disordering Process in $Cu_3Au$.** F. P. BURNS, *Columbia University.**—The isothermal variation of electrical resistivity with time following rapid change of specimen temperature from an initial value $T_i$ to a final (constant) value $T_f$ is described. The experimental arrangements permit observation within one minute after initiation of the change. When $T_i > 390°C$ and $390°C > T_f > 360°C$ the resistivity first increases, then decreases monotonically. The time required to reach the maximum decreases and the subsequent rate of fall increases as $T_f$ is lowered. When $360°C > T_f > 326°C$ an initial rise is not observed and the rate of fall decreases as $T_f$ is lowered. The true kinetics of the ordering and disordering processes as they occur in a single domain, freed from effects due to the evanescence of antiphase domain boundaries, are revealed by similar observations made upon a specimen held at 388°C until such boundaries have nearly disappeared. Isothermals corresponding to various values of $T_f$, with $T_i < T_f < 390°C$ and $T_f < T_i < 390°C$ are reported. The observation of Sykes and Evans that the temperature coefficient of resistivity decreases with decreasing temperature immediately above the critical temperature is confirmed.

* Permanent address: The College of the City of New York, New York.

**S6. Application of Bimolecular Kinetics to Relaxation of Order Below the Curie Point.** JEROME ROTHSTEIN, *Columbia University.*—Ordering binary alloys below the Curie point have wrong pairs in analogy to Frenkel defects, with wrong pair activation energy of formation independent of density $n$ of wrong pairs for small $n$. Bimolecular kinetics at constant temperature can then be written $dn/dt = \alpha n_\infty - (\alpha/n_\infty)n^2$ with $\alpha$, $n_\infty$ constants. If $n = n_0$ at $t = 0$, then for $n_0 < n_\infty$ (heating) $n(t) = n_\infty \tanh[\alpha t + \tanh^{-1}(n_0/n_\infty)]$, while for $n_0 > n_\infty$ (cooling), $n(t) = n_\infty \coth[\alpha t + \coth^{-1}(n_0/n_\infty)]$. If temperature dependence of resistivity $\rho$ at constant $n$ is small compared to its $n$ dependence, then $\rho = \rho_0 + (d\rho/dn)_0 n$ whence tanh and coth resistivity relaxation laws are expected. From $T$ dependence of $\alpha$ and $n_\infty$ activation energies for formation and destruction of a wrong pair can be estimated. Theory agrees with experiments on $Cu_3Au$ of the preceding paper.

**S7. Long-Range Order in Cu–Au Alloys of Nonstoichiometric Compositions.*** C. H. SUTCLIFFE† AND F. E. JAUMOT, JR., *University of Pennsylvania.*—The degree of long-range order present as a function of temperature in samples of Cu-Au alloys containing from 15.5 to 34.2 atomic percent Au has been determined by measurement of the integrated x-ray intensities of the (3,0,0) superstructure reflections. Measurements were made from room temperature to temperatures above the ordering temperature, using monochromatic $CuK_\alpha$ radiation. The data indicate that the order parameter begins to decrease at a proportionately lower temperature for nonstoichiometric compositions than for $Cu_3Au$. Also, the slope of the curve of order parameter *versus* temperature is less steep for compositions appreciably different from $Cu_3Au$. Values of the long-range order parameter as a function of temperature will be given for each composition.

* Supported by the Office of Flight Research, U. S. Air Force.
† Present address: The Philco Corporation, Philadelphia, Pennsylvania.

**S8. The Nature of the Order-Disorder Transformation in Cu–Au Alloys of Nonstoichiometric Compositions.*** C. H. SUTCLIFFE† AND F. E. JAUMOT, JR., *University of Pennsylvania.*—The nature of the order-disorder transformation in Cu-Au alloys containing from 15.5 to 34.2 atomic percent Au has been studied by observing high angle fundamental x-ray reflections from single crystals. Measurements were made at temperatures ranging from room temperature to 450°C. The anomalous broadening and splitting of the (4,0,0) reflections from samples containing more than 25 atomic percent gold indicate that the transformation is a classical phase transformation rather than a homogeneous one, at least for gold-rich samples. The (4,0,0) reflections from samples containing less than 25 percent gold did not split and exhibited only slight broadening in the region of the so-called critical temperature. A possible explanation of the cause of this unusual behavior, based on the atomic sizes of the constituents, will be discussed.

* Supported by the Office of Flight Research, U. S. Air Force.
† Present address: The Philco Corporation, Philadelphia, Pennsylvania.

# SESSION T

SATURDAY MORNING AT 9:30

Ballroom

(E. BURSTEIN presiding)

## *Semiconductors, IV (Compounds)*

**T1. Electrical Properties of Single Crystals and Thin Films of PbTe.*** SEARL J. SILVERMAN AND HENRY LEVINSTEIN, *Syracuse University.*—A comparison was made of the electrical properties of single crystals of PbTe and subsequently evaporated thin films formed from the original material. Hall constants and resistivities were measured as a function of temperature from 300° to 77°K. Crystals were grown by the Stockbarger technique. Films were formed and measured without exposure to air. Regardless of whether the original crystal was "*n*" or "*p*" type, all films were "*n*" type, having carrier concentrations within the same order of magnitude for most cases. This observation was attributed to a limited amount of dissociation during evaporation, resulting in an inhomogeneous distribution of Te agglomerates throughout the film. Room temperature mobilities were about ½ that of the single crystal values. In general, carrier mobilities in films were markedly affected by substrate temperature during film formation, subsequent annealing, and limited oxygenation.

* This work was supported by the Wright Air Development Center.

**T2. The Effect of Oxygen on Lead Telluride Films.*** DONALD E. BODE AND HENRY LEVINSTEIN, *Syracuse University.*—The electrical properties of lead telluride films were studied as a function of the degree of oxygenation. Films of PbTe formed by high vacuum evaporation have a large affinity for oxygen at pressures above $10^{-4}$ mm of Hg. The quantity of oxygen adsorbed by a particular film depends on several factors: (1) substrate temperature during the initial film formation, (2) the pressure of the oxygen admission, (3) the time of exposure to oxygen, and (4) the film temperature during exposure to oxygen. By addition of calibrated pulses of oxygen at room temperature it was possible to transform PbTe films from *n*-type to *p*-type and obtain a point for point correlation of their electrical properties. In this manner it was possible to study in detail the change of a film's resistance, thermoelectric power, photoconductive sensitivity, time constants, and spectral characteristics with increasing oxygenation. It is felt that when oxygen atoms are adsorbed on PbTe films they permanently capture electrons first from the conduction band, then the impurity centers, and eventually the valence band to transform the film from *n* to *p*. Oxygen does not seem to play a primary role in the photoconductive effect at long wavelengths.

* This work was supported by the Wright Air Development Center.

**T3. Current Oscillations in Photoconductive Films of Lead Telluride.*** DEAN L. MITCHELL, WERNER J. BEYEN, AND DONALD E. BODE, *Syracuse University.*—During a study of the noise characteristics of PbTe cells it was found that the current through some of the films would break into oscillation at applied fields between about 500 to 4000 volts/cm. The frequency range for oscillations of this type was from $10^2$ to $10^4$ cycles/second. The amplitudes of these oscillations measured across a one-megohm load resistor ranged between $10^{-6}$ and $10^{-4}$ volts. The wave shape of an individual oscillation is sawtooth in appearance. It was possible for several different frequencies to exist simultaneously in a particular film. It was found that the frequency and amplitude of these oscillations increase when the applied voltage is increased. Above certain applied voltages all oscillations cease and only the characteristic flicker noise of the semiconductor is present. The results of this investigation indicate that the phenomenon is similar to that of a modified relaxation oscillator. The effect is probably associated with a certain type of inhomogeneity within the film. The presence of these inhomogeneities in films having this behavior is supported by several other types of phenomena which will be described.

* This work was supported by the Wright Air Development Center.

**T4. Interdiffusion in Lead Sulfide Crystals.** R. F. BREBRICK AND W. W. SCANLON, *U. S. Naval Ordnance Laboratory.*—In pure compound semiconductors such as lead sulfide the electrical properties are determined by slight deviations from the stoichiometric composition. A single crystal containing a slight excess of lead is *n* type. If such a crystal is exposed to sufficiently high temperature and pressure of sulfur vapor it will change its composition to excess sulfur by a diffusion process and become *p* type. A plane between *p* and *n* type material moves inward from the surface as diffusion progresses. Upon quenching the crystal the junctions can be located by rectification, thermoelectric force, or photoeffects. For fixed temperature and pressure conditions it is possible to calculate a diffusion coefficient from the movement of *p-n* junctions in two crystals of different compositions. With a sulfur pressure corresponding to the vapor pressure of sulfur at 123°C and a crystal temperature of 550°C the *p-n* junction in two *n*-type crystals ($n_1 = 1.5 \times 10^{17}$, $n_2 = 12 \times 10^{17}$) moved inward a distance of 0.67 mm and 0.11 mm, respectively, in one hour. Assuming that the composition at the *p-n* junction is the same in both crystals and that the sulfur concentration is the same at the surfaces a diffusion constant of $4.6 \times 10^{-6}$ cm²/sec is calculated from the solution of the appropriate diffusion boundary value problem.

**T5. The Preparation of Lead Sulfide Crystals of Controlled Electrical Properties.** W. W. SCANLON AND R. F. BREBRICK, *U. S. Naval Ordnance Laboratory.*—In theory a crystal of a binary ionic compound can exist as a single phase over a small range of composition. For such a crystal the system, crystal-vapor, has two degrees of freedom by the Gibbs phase rule. Therefore, at a temperature high enough for the crystal to come to equilibrium in a reasonable time with the vapor phase, the composition of the crystal and its electrical properites can be varied by varying the pressure of one of the constituents of its vapor. Small natural crystals of PbS were exposed at 500°C to various fixed pressures of sulfur vapor for 20 hours and then quenched to room temperature. The pressures used corresponded to the vapor pressures of sulfur in the range from 100°C to 120°C. Hall effect and resistivity data were taken from −190°C to +200°C. Both *p*-type and *n*-type crystals were made by this method with carrier concentrations between $10^{18}$ and $10^{19}$. The intrinsic activation energy for PbS is 0.37 ev and extrapolated resistivity data indicates that intrinsic material has a resistivity of about 3.0Ω cm at room temperature. The ratio of electron to hole mobility is 1.4.

**T6. The Mobility and Mean Free Path of Electrons and Holes in Lead Sulfide Crystals.** R. L. PETRITZ, W. W. SCANLON, AND F. L. LUMMIS, *U. S. Naval Ordnance Laboratory.*—Using the formulas for the two-carrier semiconductor, $\mu_e$ and $\mu_h$ were calculated from Hall effect and resistivity data for several crystals of *n*-type and *p*-type PbS. Impurity concentrations ranged from $10^{19}$/cc to $10^{18}$/cc. No evidence for im-

purity scattering was observed in the temperature range −190°C to +200°C. The mobility data was fitted over the entire temperature range by the expression:

$$\frac{1}{\mu}=\frac{1}{A(e^{\theta/T}+1)}+\frac{T^{\frac{3}{2}}}{B},\ \frac{\text{volt-sec}}{\text{cm}^2},$$

where the first term is the polar scattering formula of Mott and Fröhlich and is associated with the optical modes of the lattice vibrations. The second term is due to scattering by interactions with acoustical modes and is important only at low temperatures. We find that the mean values for the constants are approximately $\theta=1100°K$, $A=18$, and $B=3.5\times10^6$. From $A$ we find that $m^*/m$ is 0.17. The electron mobility at room temperature is approximately 400 and the corresponding mean free path is 120A.

**T7. Optical Absorption of AlSb.** R. F. Blunt, H. P. R. Frederikse, and J. H. Becker, *National Bureau of Standards.*—The absorption spectrum of AlSb has been measured at room temperature at 78°K and near 4.2°K. Two samples with carrier-concentrations of $2\times10^{17}$/cc ($p$-type) and $5\times10^{17}$/cc ($n$-type) have been investigated. The $n$-type sample is slightly polycrystalline and doped with tellurium; the $p$-type sample is a single crystal. Both samples show a sharp absorption edge corresponding to a forbidden gap of 1.55 ev at room temperature[1] in good agreement with electrical data.[2] The temperature dependence of the gap is about $-4\times10^{-4}$ ev/deg between 300°K and 78°K. A small absorption band at 0.75 ev is observed in the $p$-type sample in addition to the free carrier absorption. This band becomes sharper but not higher at lower temperatures. The $n$-type specimen shows a broad band with a maximum at 0.33 ev. The height of this band increases appreciably on cooling. The free-carrier absorption at longer wavelength appears to be larger at 78°K and 4.2°K than at room temperature in this sample. Possible interpretation will be discussed.

[1] See also Briggs, Cummings, Hrostowski, and Tanenbaum, Bulletin Am. Phys. Soc. **28**, No. 6.
[2] H. Welker, Z. Naturforschung **8a**, 248 (1953).

**T8. The Anomalous Optical Absorption Limit in InSb.** Elias Burstein, *Naval Research Laboratory.*—The anomalous shift of the absorption limit to shorter wavelengths with increasing impurity content in InSb[1] is attributed to the unusually small effective mass of the electrons, rather than to a specific impurity effect. The small effective mass of the electrons is associated with a small effective density of states and with a small degeneracy concentration. Consequently, InSb behaves as a degenerate semiconductor at relatively low electron densities, and the height of the Fermi level above the bottom of the conduction band in degenerate $n$-type material increases rapidly with increasing electron density. The optical absorption limit involves vertical transitions from the filled band to the lowest unfilled level in the conduction band. The optical energy gap of a degenerate $n$-type sample is, accordingly, given by the energy separation between the lowest unfilled level in the conduction band (which lies approximately $4kT$ below the Fermi level) and the corresponding level in the filled band, and not just simply by the minimum separation between the bands. The optical energy gap of an $n$-type sample containing $5\times10^{18}$ electrons/cm$^3$ is calculated on this basis to be 0.4 ev in agreement with the observed value of 0.39 ev.

[1] M. Tanenbaum and H. B. Briggs, Phys. Rev. **91**, 1561 (1953).

**T9. Optical and Electrical Measurements on InAs.** Robert M. Talley and Dorothy Enright, *U. S. Naval Ordnance Laboratory.*—InAs has been prepared by fusion of the elements in an evacuated Vycor container. Polycrystalline samples which appeared to be homogeneous and free from cracks and pits were cut from the melt. It was not possible to zone refine this compound because of a decomposition which begins at about 500°C. InAs melts at 942°C and crystallizes in the zincblende structure with a lattice spacing of 6.058A.[1] The infrared transmission agrees with the results reported by Briggs.[2] Hall effect and conductivity measurements will be reported.

[1] T. S. Liu and E. A. Peretti, Trans. Am. Soc. Metals **45**, 677 (1953).
[2] Briggs, Cummings, Hrostowski, and Tanenbaum, Bull. Am. Phys. Soc. **28**, No. 6, 8 (1953).

**T10. Infrared Properties of Indium Antimonide.*** W. Kaiser and H. Y. Fan, *Purdue University.*—Infrared transmission of indium antimonide has been measured at different temperatures. Samples with $10^{17}$ cm$^{-3}$ effective impurity concentration, both $n$ type and $p$ type, have an absorption edge at 7.1 microns at 300°K shifting with temperature between 520°K to 4°K by $-2.8\times10^{-4}$ ev/degree K.[1] Samples with $\sim5\times10^{18}$ cm$^{-3}$ carriers have an absorption edge at 3.5 microns at 300°K, 2.5 microns at 78°K, hardly changing between 78°K and 4°K. Samples with the lower carrier concentrations, both $n$ type and $p$ type, show the same absorption in the intrinsic range, increasing with temperature. In the impurity range $n$-type samples show absorption increasing with wavelength whereas the $p$-type samples give essentially flat absorption up to 30 microns. In both cases the absorption increases with decreasing temperature, more strongly for the $p$ type. For a $p$-type sample the transmission changed from 21 percent at 300°K to 2 percent at 78°K and <1 percent at 20°K. This behavior might be expected from excitations between the valence or conduction band and energy states <0.01 ev from the band edge.

* Work supported by a Signal Corps contract.
[1] See M. Tanenbaum and H. B. Briggs, Phys. Rev. **91**, 1561 (1953).

**T11. Conductivity, Hall Effect, and Rectification of Gallium Antimonide.*** D. P. Detwiler, *The Franklin Institute Laboratories for Research and Development.*—Gallium antimonide of relatively high purity has been prepared by zone-refining the compound and growing single crystals by pulling from the melt. As prepared under a hydrogen atmosphere in silica crucibles, this material exhibits in general $p$-type conductivity. The electrical conductivity and Hall constant of a number of samples, both $n$-type and $p$-type, have been measured between −190°C and 650°C. Room temperature conductivity ranged from a few ohm$^{-1}$ cm$^{-1}$ to 100 ohm$^{-1}$ cm$^{-1}$. The room temperature Hall mobility of holes in relatively pure specimens is about 2000 cm$^2$ volt$^{-1}$ sec$^{-1}$, while that of electrons is appreciably higher. The intrinsic energy gap is somewhat greater than that of germanium. Rectifying $p$-$n$ junctions have been grown from the melt by adding tellurium to a $p$-type melt. It has been found that these junctions may be located by chemical etching with a mixture of hydrochloric and nitric acids. Early junctions show a room temperature rectification ratio of several hundred at one volt with, however, considerable "softening" of the reverse characteristic. Although much smaller reverse currents are obtained at 77°K, saturation is still poor in the units tested.

* This work was supported by the Air Research and Development Command, U. S. A. F.

**T12. Some Properties of *P*-type Gallium Antimonide Between 15°K and 925°K.** H. N. Leifer and W. C. Dunlap, Jr., *General Electric Research Laboratory.*—Single crystals[1] of gallium antimonide were produced by the Czochralski technique from zone-refined material made by direct combination of the elements. The product was $p$ type, with resistivities of the order 0.1 ohm cm. Hall coefficient and resistivity were measured from 15°K to 925°K. The slope of the Hall curve at low temperatures yielded the value 0.024 ev for the carrier

ionization energy. The room temperature mobility was near 800 cm²/volt sec. The Hall mobility varied as $T^{-0.87}$ below room temperature, changing slope at room temperature and going over to a nearly $T^{-1}$ law at higher temperatures. An electron-to-hole mobility ratio of 5 was determined from the ratio of extrapolated extrinsic conductivity to actual conductivity at the Hall coefficient conversion temperature (357°C). From resistivity data, the intrinsic band gap at 0°K was estimated as 0.80 ev. From infrared data the best value for room temperature band gap was taken to be 0.71 ev. Based upon the assumption of spherical Fermi surfaces and assuming consistency of these data, the following are calculated: $3\times10^{-4}$/°C as the coefficient of band gap with temperature; 0.20 m and 0.39 m for the effective mass of electrons and holes, respectively.

[1] Tannenbaum, Pearson, and Feldmann, paper A10 and Briggs, Cummings, Hrostowaki, and Tannenbaum, paper A9, Bulletin of the Am. Phys. Soc. **28**, 6 (1953).

---

SATURDAY MORNING AT 9:30

Crystal Ballroom

(CYRIL S. SMITH presiding)

## *DSSP Symposium on Irradiation Effects*

**U1. Theory of Radiation Damage.** F. SEITZ, *University of Illinois.* (40 min.)
**U2. Stored Energy in Irradiated Copper.** A. W. OVERHAUSER, *Cornell University.* (20 min.)
**U3. Nucleon Bombardment of Semiconductors.** K. LARK-HOROVITZ, *Purdue University.* (30 min.)
**U4. Radiation Effects in Ionic and Valence Crystals.** R. SMOLUCHOWSKI, *Carnegie Institute of Technology.* (30 min.)
**U5. Radiation Damage Effects on Electronic Properties of Graphite.** W. P. EATHERLY, *North American Aviation, Inc.* (30 min.)

## *Business Meeting of the Division of Solid-State Physics*

(to be convoked during Session U whenever the Chairman of the Division shall see fit)

---

SATURDAY MORNING AT 9:30

Italian Gardens

(C. G. SHULL presiding)

## *Magnetism, I*

**V1. Ferromagnetic Properties and Order-Disorder in Fe–Pd Alloys.*** V. J. FOLEN AND F. C. NIX, *University of Pennsylvania,* AND F. E. JAUMOT, JR., *The Franklin Institute Laboratories for Research and Development.*—The saturation moment, Curie temperature, and magnetostriction of alloys of Fe-Pd near the composition $FePd_3$ were studied as a function of order. For disordered samples, the Curie point and saturation moment at room temperature exhibit a sharp decrease in value in the region of 75 atomic percent Pd. The saturation magnetostriction decreases with increasing palladium content. Partial order lowers the Curie temperature considerably in samples containing less than 75 percent Pd, and raises it slightly for samples containing more than 75 percent Pd. This result is consistent with the increase in volume on ordering of the low palladium samples and the negligible change in volume of the high palladium samples. Isothermal anneal studies indicate that the effect of order on the saturation moment is complete in the early stages of ordering.

* Supported by the U. S. Office of Naval Research and the Air Research and Development Command.

**V2. Ferromagnetism and Order in Fe–Pt Alloys Near $Fe_3Pt$.*** A. D. FRANKLIN, A. E. BERKOWITZ, AND E. KLOKHOLM, *The Franklin Institute Laboratories for Research and Development.*—The Fe-Pt alloys near the composition $Fe_3Pt$ exhibit an irreversible transition between b.c.c. $\alpha$ and f.c.c. $\gamma$ phases. Both are ferromagnetic, but the $\gamma$-phase Curie point lies much lower than that of the $\alpha$ phase. It is known[1] that ordering in these alloys moves the $\gamma$-phase Curie point to higher and the $\gamma\rightarrow\alpha$ transition to lower temperatures, without having an appreciable effect on the $\alpha\rightarrow\gamma$ transition. These ordering effects have been studied in greater detail, using a B-H curve tracer to follow the transitions magnetically. During the irreversible transitions, especially $\alpha\rightarrow\gamma$, isothermal changes in magnetization occur. In cold-worked specimens, the beginning of the $\gamma\rightarrow\alpha$ transition lies above liquid $N_2$ temperatures out to 27 atomic percent Pt. The increase in the $\gamma$-phase Curie temperature and the decrease in the $\gamma\rightarrow\alpha$ transition temperature with ordering occurs to an appreciable extent in the early stages of ordering, before superstructure lines appear in the x-ray patterns.

* Supported by the U. S. Air Research and Development Command.
[1] A. Kussmann and G. Rittberg, Z. Metallkunde **41**, 470–7 (1950).

**V3. Resistance Studies of the Phase Transformations in Fe–Pt Alloys Near the Composition $Fe_3Pt$.*** R. P. STEIJN AND F. J. DONAHOE, *The Franklin Institute Laboratories for*

*Research and Development.*—The γ-phase Fe-Pt alloys containing approximately 25 atomic percent platinum are known to develop superstructure of the type formed in $Cu_3Au$.[1] In addition, the f.c.c. γ phase transforms at low temperatures to a b.c.c. α phase in alloys containing $\lesssim 27$ atomic percent platinum. The resistance changes which are produced by these phase transformations have been studied in alloys ranging from 14 to 30 atomic percent platinum. In $Cu_3Au$ the formation of long range order is accompanied by a decrease in resistance which may be observed at the temperature at which order formation occurs. No such effects are observed in $Fe_3Pt$. This seems to be generally true in ferromagnetic alloys of this type. The progress of the ordering reaction during isothermal aging at elevated temperatures can be followed by quenching and measuring the resistance at some fixed temperature below the ferromagnetic Curie point of the disordered alloy. The irreversible $\alpha \rightarrow \gamma$ transition also produces large changes in resistance which are superposed on those caused by changes in the degree of order.

* Supported by the U. S. Air Research and Development Command.
[1] A. Kussmann and G. Rittberg, Z. Metallkunde **41**, 470–7 (1950).

**V4. Magnetization in the Nickel Ferrite Indates.** LOUIS R. MAXWELL AND STANLEY J. PICKART, *U. S. Naval Ordnance Laboratory.*—Trivalent indium has been substituted in nickel ferrite ($NiO \cdot Fe_2O_3$) to give the system $NiO \cdot Fe_{2-t}In_tO_3$ where $t$ varies from 0 to 1.875. The materials were prepared in powdered form and annealed at a cooling rate of 1° per minute from 1400°C. The lattice constant $a_0$ increased linearly with increasing $t$ from 8.332A to 8.708A at $t=1.5$; for greater values of $t$ the size of unit cell remains constant. At these higher values of $t$, x-ray lines caused by the uncombined NiO and $In_2O_3$ were present indicating that the remaining spinel structure was held together by the trivalent iron present. At $t=2$ no solid solution was formed. Thermal magnetization curves showed only the $Q$ type as classified by Néel. The saturation magnetization, obtained by extrapolation from liquid nitrogen temperature to absolute zero, increased with increasing $t$ to a maximum at $t=ca$, 0.5 beyond which the magnetization decreased toward zero. No crossover was found that would indicate a reversal in the dominance of the intrinsic magnetization as observed for the nickel ferrite aluminates.[1] The Curie temperatures decreased nearly linearly with increasing $t$ with values running systematically below corresponding Curie temperatures[1] when trivalent aluminum and trivalent gallium are substituted for trivalent iron.

[1] L. R. Maxwell and S. J. Pickart, Phys. Rev. **92**, 1120 (1953).

**V5. Magnetic Neutron Diffraction in $Fe_3O_4$.** T. RISTE AND A. W. MCREYNOLDS, *Joint Establishment for Nuclear Energy Research, Norway.*—The intensity of magnetic diffraction from the (111) planes of $Fe_3O_4$ has been studied as a function of temperature in order to investigate (1) the shape of the magnetization *vs* temperature curve, and particularly, (2) effects in the region of the Curie point. For thin crystals the diffracted intensity from a set of crystallographic planes is proportional to reflectivity $F^2=C^2+q^2D^2$ where C and D are, respectively, the nuclear and magnetic scattering amplitudes and $q$ a vector determined by direction of magnetization. By measurement with the crystal first unmagnetized then magnetized parallel to the scattering vector, reflectivity becomes, respectively, $F^2=C^2+\frac{2}{3}D^2$ and $F^2=C^2$, allowing elimination of the nuclear component. The remaining magnetic component is proportional to intensity of magnetization. The magnetization *vs* temperature curve thus measured on an *unmagnetized* material shows a sharply defined Curie point and may be compared with theory. A further decrease of scattering slightly above the Curie point indicates continued short-range correlation of magnetic moments.

**V6. Permeability and Magnetostriction of Cation-Substituted Magnetite.*** L. R. BICKFORD, JR.,† J. PAPPIS,‡ AND J. L. STULL, *New York State College of Ceramics.*—The temperature spectrum of initial permeability for magnetite traverses a sharp peak at 130°K, which has been identified with a change in sign of the first-order cubic anisotropy constant. We found that the substitution of small amounts of cobalt for divalent iron causes a marked shift upwards in the temperature of the peak. Substitution of other transition elements does not produce this effect. For cobalt additions the temperature shift is linear with respect to cobalt ferrite content, the rate being 140°C/mole percent. We have obtained convincing evidence from magnetostriction measurements that the shifted peak is still associated with a change in direction of easy magnetization. Apparently the spins of the cobalt ions are strongly coupled to the lattice parallel to the [100] direction, and the presence of a small amount of cobalt is sufficient to align the entire spin system in this direction. It is predicted that the first order anisotropy constant for cobalt ferrite itself is positive in sign and very large.

* Supported in part by the U. S. Office of Naval Research.
† Now at Research Laboratories, I.B.M.
‡ Now at M.I.T.

**V7. The Magnetization of $CuK_2(SO_4)_2 \cdot 6H_2O$ at Liquid Helium Temperatures and in Strong Magnetic Fields.** WARREN E. HENRY, *Naval Research Laboratory.*—Experimental study of the magnetization of copper potassium sulphate hexahydrate has been carried out in the liquid helium temperature range (1.3°–4.2°K) and in magnetic fields up to 60 000 gauss. From the fractional variation of the magnetic moment with H/T and the superposition of magnetic moment isotherms within experimental error in fields under 50 000 gauss it is concluded that a Brillouin function (not spin only) is followed. Above 50 000 gauss, a slight departure from the Brillouin function is suggested. It is possible to compare these results with previous measurements on copper sulphate pentahydrate[1] in which there is a pronounced dispersion of the magnetic isotherms caused by the large exchange interaction between copper ions. From a comparison of these results, one may see the decrease in exchange energy with increase in distance between interacting ions. The comparison is in agreement with the Van Vleck prediction[2] that an increase in exchange coupling can increase the sharpness of paramagnetic resonance absorption which was shown experimentally by Arnold and Kip.[3]

[1] W. E. Henry, Phys. Rev. **87**, 1133 (1952).
[2] J. H. Van Vleck, Phys. Rev. **74**, 1168 (1948).
[3] R. D. Arnold and A. F. Kip, Phys. Rev. **75**, 1199 (1949).

**V8. Note on Magneto Resistance.** L. P. KAO AND E. KATZ, *University of Michigan.**—Results of calculation are presented for the magneto resistance in cases more general than those discussed by L. Davis[1] and F. Seitz,[2] referring to anisotropic materials in arbitrary orientation.

* Research supported by the U. S. Lab. Procurement Office of the Signal Corps Supply Agency.
[1] L. Davis, Phys. Rev. **53**, 93 (1939).
[2] F. Seitz, Phys. Rev. **79**, 372 (1950).

**V9. Low Temperature Magnetoresistance of Gold in Fields up to 50 Kilogauss.** JOHN K. LOGAN, *Naval Research Laboratory.*—Measurements have been made of the magnetoresistance of a sample of gold in the temperature range from 1.2°K to 4.2°K, and in fields up to 50 kilogauss. These steady magnetic fields were provided by a Bitter-type air-core solenoid. The ratio of zero-field resistance to resistance at 300°K was $1.8 \times 10^{-3}$ at 4.2°K. This value was greater by 3.3 percent at the lowest temperature. At 50 kilogauss the resistance increased by 55 percent and 47 percent, at 4.2°K and 1.2°K, respectively, over the zero-field resistance. At intermediate temperatures and this field, the percentage increase

was linear with zero-field resistance. In addition, at constant temperature and high fields, the resistance ratio was linear in magnetic field, with a coefficient of 1.25 percent per kilogauss. This coefficient was independent of temperature. Above approximately 20 kilogauss, the resistance at constant field was a monotonically increasing function of temperature.

### *Invited Paper*

**V10. The Hall Effect in Ferromagnetics.** J. M. LUTTINGER, *University of Michigan.* (30 min.)

---

## SATURDAY MORNING AT 9:30

## Normandy Room

## (CHARLES S. SMITH presiding)

### *Nonmetallic Solids*

**W1. The Relation between Refractive Index and Density in Glass.** H. N. RITLAND, *Corning Glass Works.*—The refractive index and density have been measured on a large number of samples of a borosilicate crown optical glass (Corning Code 8370). The samples were cut from a large piece of homogeneous glass, and given various thermal treatments. The refractive indices of the treated samples range from about 1.511 to 1.517, and the densities from 2.50 to 2.53 g/cc. The refractive index is a single valued function of the density within about $3\times10^{-5}$ in refractive index. The Lorentz-Lorenz refractivity does not remain constant during this structural change; instead the data follow closely the Newton-Drude equation, $(n^2-1)/d=$constant. This equation corresponds to no contribution of the polarization to the local electric field. Data on other glasses indicate that this result is generally valid. This may imply that the polarization contribution is much less than the Lorentz value $4\pi P/3$, or alternatively that the ionic polarizabilities are considerably decreased as the density of the glass increases.

**W2. Multiple Diffraction Patterns in Glass Produced by Ultrasonic Waves of High Intensity.** J. M. BARNES, *Michigan State College.*—The multiple diffraction of light produced by two ultrasonic waves of different wavelengths in a transparent medium[1] can be considered as the superposition of the effects of the individual waves, if only first diffraction orders are created.[2] For higher intensities and for the special case of a strong longitudinal and a weak transverse wave a theory given by Nath[3] has to be used. In the case of six primary diffraction orders due to longitudinal waves and one primary diffraction order due to transverse waves, up to fifteen diffraction orders were obtained.

[1] L. Bergmann and E. Fues, Z. Physik. **109**, 1 (1938).
[2] Hans Mueller, Z. Krist. Abt. **A99**, 122 (1938).
[3] N. S. Nath, Proc. Cambridge Phil. Soc. **34**, 213 (1938).

**W3. Determination of the Ratio of the Photoelastic Constants of Glasses by Means of Ultrasonic Waves.** HALBERT GATES, *Michigan State College.*—The ratio of the two photoelastic constants of glass can be determined by means of the diffraction of light by ultrasonic waves.[1] The two known methods, the intensity method[2] and the polarization angle method[3] have been used for the measurement of a series of optical glasses and for a comparison of the methods.

[1] Hans Mueller, Z. Krist. Abt. **A99**, 122–141 (1938).
[2] L. Bergmann and E. Fues, Naturwissenschaften **24**, 492 (1936).
[3] E. Hiedemann, Z. Physik. **108**, 592 (1938).

**W4. The Simon Melting Equation and the Effective Intermolecular Potential.** L. SALTER, *Wabash College* (introduced by F. E. Throw).—Recent experiments[1] on solid helium have made plausible a connection[2] between the Simon empirical melting equation, $p_m/a=(T_m/T_0)^c-1$, the Grüneisen equation of state for a solid, and the well known Lindemann melting relation. Further equations satisfied by the macroscopic melting line parameters are derived, and, introducing the lattice dynamical expression for $\theta_m$, a differential equation for the effective intermolecular potential on the melting curve is obtained. On the assumptions underlying the derivation, the potential is of "reduced" form, $p(r_m)=\text{const}kT_0(r_m/r_0)^{-n}$, ($T_0$ and $r_0$ the temperature and lattice constant at the triple point), $n=3/(c-1)$; the constant involves the Simon constant $c$, parameters characteristic of the lattice structure, and and the Lindemann constant.

[1] Dugdale and Simon, Proc. Roy. Soc. (London) **A218**, 291 (1953).
[2] Salter (to be published).

**W5. Electronic Energy Bands in Crystals.** EDMOND BROWN, *Cornell University.*—A method of obtaining valence states of the Schroedinger equation with a prescribed crystal potential is discussed. A set of secular equations is obtained from an expansion of the wave function in a finite number of plane waves plus an auxiliary function. In the treatment of alkali metals this auxiliary function may be determined from the Wigner-Seitz[1] solution. The solution then reduces to that of W-S when the number of plane waves chosen is reduced to zero. Because of the orthogonality of the chosen functions the energy eigenvalue appears only in diagonal terms of the secular matrix. One difficulty which appears in the present method is due to the fact that the desired energy is not the lowest eigenvalue of the secular equations. However, an iteration technique is proposed which enables one to find the proper eigenvalue. The method is applicable to problems for which the OPW method[2] converges very slowly (*viz.*, those in which the desired state is the lowest of its symmetry type).

[1] E. Wigner and F. Seitz, Phys. Rev. **43**, 804 (1933).
[2] C. Herring, Phys. Rev. **57**, 1169 (1940).

**W6. Influence of Charge Distribution on Repulsive Forces and Internuclear Distances between Ions.** GILBERT BEGUIN AND KASIMIR FAJANS, *University of Michigan.*—According to M. Born (1918), repulsive forces acting within an ionic crystal must depend on the spatial charge distribution of the electronic systems of the ions. In fact, if the ions would remain spherical in the crystal, no repulsion would result from the mutual Coulombic interaction between the electrons and the nuclei. However, the deformation of the wave mechanical charge distribution of interpenetrating ions lowers the symmetry of the latter and gives rise to repulsive forces. K. Fajans and K. F. Herzfeld considered (1920) a model of a crystal consisting of ions, the outer eight electrons of which are at the corners of a cube. At equilibrium, an appreciable distance separates the electron cubes due to the repulsion between these charge distributions. This result is confirmed by computations made with a higher degree of approximation on models of molecules consisting of cubical rigid ions $X^+$ and $Y^-$ of variable edge length ratio and at different orientations. For instance, for the ratio 1:1, the fraction 0.78 of the internuclear distance

lies within the cubes when their space diagonals are in line and only 0.39 when their faces are parallel.

**W7. Evaluation of Statistical Approach to Phase Determination in X-Ray Analysis.*** V. VAND AND R. PEPINSKY, *The Pennsylvania State University.*—Statistical formulas for probabilities of signs of structure factors have been developed by Hauptman and Karle.[1] They claim that with a sufficient number of structure factors the probabilities converge to certainties. This is claimed for space-group $P\bar{1}$. General examples can be found, however, for which this leads to an incorrect structure. It is shown that the statistical formulas, although correct individually (within limits of approximations used), can bias the results toward wrong structures when applied jointly. Formulas for $\Sigma_1$ and $\Sigma_4$ were studied in detail, since these alone are useful in first attack in $P\bar{1}$. $\Sigma_1$ is related to a sharpened Patterson with origin removed, and tends to converge to the highest peaks of the Patterson—which differs from the structure. $\Sigma_4$ corresponds to a squared (origin-removed) Patterson, and its convergence to the highest Patterson peaks is more pronounced. The above does not apply to more complicated space groups for which the H-K formulas are related to Harker sections (see, for example, naphthalene, which structure is apparent directly in a Harker section.) It would appear that the practical crystallographic problem has not yet been generally solved.

* Development supported by the National Institute of Health.
[1] H. Hauptman and J. Karle, A.C.A. Monograph No. 3 (1953).

**W8. Interferometric Study of the Surface of X-Ray and Proton Irradiated KCl Crystals.*** W. J. SMITH, W. J. LEIVO, AND R. SMOLUCHOWSKI, *Carnegie Institute of Technology.*—Irradiation of potassium chloride crystals by x-rays is known to produce a density decrease of about $10^{-4}$. It was thought interesting to check whether this effect is associated with any definite changes on the surface. This is conveniently done by multiple beam interferometry which permits an analysis of a crystalline surface with an accuracy of the order of ten angstroms. Such a study has been made on x-ray and proton irradiated KCl single crystals. A comparison of the position and contour of the interference fringes in the x-ray irradiated and nonirradiated neighboring section of the crystal seems to indicate that the change of density does not occur to any extent by means of diffusion of individual atoms or vacancies. Thus it suggests that an internal mechanism along the lines suggested by Seitz is operative. This may be related to slip lines which are often visible in the irradiated area and point to a possible role of dislocations. In certain cases evidence of epitaxy was observed. The effect of proton irradiation is similar to x-rays except at high intensities when the surface is severely altered.

* Work supported by a U. S. Atomic Energy Commission contract.

**W9. Small-Angle Scattering of X-Rays by Irradiated Diamond.*** W. H. ROBINSON, YIN-YUAN LI, AND R. SMOLUCHOWSKI, *Carnegie Institute of Technology.*—Recent measurements of the intensity of x-rays scattered at small angles from diamond irradiated by 360 Mev protons at the Carnegie Institute of Technology synchrocyclotron have indicated an unexpected weak maximum in the scattered intensity at approximately 0.02 radian. A tentative interpretation of this maximum will be given. Further results using a focusing small-angle scattering camera will be reported. Also a description of the design of the focusing camera using a bent crystal monochromator will be given.

* Work supported by a U. S. Atomic Energy Commission contract.

**W10. The Fourier Analysis of X-Ray Small-Angle Scattering.*** YIN-YUAN LI AND R. SMOLUCHOWSKI, *Carnegie Institute of Technology.*—It is pointed out that a Fourier inversion of the intensity distribution of x-ray scattering taking the small-angle scattering alone gives the electron density function of the continuum approximation. The procedure of including only the central scattering is practicable, when none of the peaks of the lattice diffraction occurs at such a small angle that their scattered intensity overlaps the central scattering. A general discussion of the choice of the sign of the phase factor is given for the case that the scattering center has an even or an odd symmetry in its electron density function. The analysis is employed in discussing some of the approximate formulas used in fitting experimental data. The meaning of this Fourier method is further illustrated by comparing with that used by Walker and Guinier[1] in explaining the scattering in a supersaturated AlAg alloy. It is remarked that our electron density function remains the same as long as the small-angle scattering is the same, while the physical meaning of this function must be sought from other observations.

* Work supported by a U. S. Atomic Energy Commission contract.
[1] C. B. Walker and A. Guinier, Acta Metallurgica 1, 568 (1953).

**W11. Neutron Diffraction Studies of Rochelle-Salt Single Crystals.*** B. C. FRAZER, MARILYN MCKEOWN, AND RAY PEPINSKY,† *Brookhaven National Laboratory.*—The ferroelectric structure of Rochelle salt is examined by neutron diffraction. Observation of "forbidden" odd (OKO) peaks demonstrate departure from orthorhombic $P2_12_12$ symmetry. These disappear at both Curie points. Samples containing just enough deuterium to cancel coherent hydrogen scattering fail to show odd peaks. These results along with the fact that the odd peaks are not observed with x-rays indicate reorientations in the hydrogen bond network. It appears that these are not the only structural alterations. As will be reported elsewhere, a concurrent x-ray study by Rao and Pepinsky has detected other changes of considerable interest. Working in close cooperation with the x-ray investigation, we have been able to concentrate on the hydrogen bond network and have now established its principal features by difference maps on (001). The results differ somewhat from the network suggested by Beevers and Hughes.[1] The main difference occurs in the $O_3$ linkage. Analysis of the pseudo-symmetry is not complete at this writing, but it seems definite now that the $O_{1,10}$ bond, which has so often been used to explain ferroelectricity in this crystal, will not prove to be significant.

* Work done under the auspices of the U. S. Atomic Energy Commission.
† The Pennsylvania State College, State College, Pennsylvania.
[1] C. A. Beevers and W. Hughes, Proc. Roy. Soc. (London) A177, 251 (1941).

**W12. Two-Phase Graphitization.*** E. E. LOEBNER,† *University of Buffalo.*—The x-ray structure, resistance, and thermoelectric power of a hard coke prepared from a phenol-benzaldehyde resin have been investigated as a function of heat treatment $H$. The (002) diffraction ring is composed of a very broad line and a sharp peak. The relative intensities of these two components change with $H$. The sharp peak appears around 1400°C and increases in intensity, seemingly reaching a saturation at 2100°C. Above 2800°C the intensity of the sharp peak begins to increase again rapidly at the expense of the broad component. The electrical resistance shows two definite plateaus, the first ending about 250°C higher than for soft carbons, the second above 2800°C. The thermoelectric power shows one maximum in the region of the end of the first plateau and apparently a second one at the end of the second plateau. The temperature dependence of the first plateau's termination and of the position of the thermoelectric power maximum is similar to the dependence found previously for soft cokes. The graphitization of the material seems to proceed in two stages with about ½ of the substance starting to graphitize around 2000°C and the rest of the material not beginning to graphitize until the temperature is above 2800°C.

* Supported by the U. S. Office of Naval Research.
† Now with Sylvania Electric Products, Inc., Buffalo, New York.

SATURDAY MORNING AT 10:00

State Hall 101, Wayne University

(E. F. BARKER presiding)

## *Nuclear Physics*

### *Invited Paper*

**WA1. Recent Experimental Results from Stripping Reactions.** W. C. PARKINSON, *University of Michigan.* (20 min.)

### *Contributed Papers*

**WA2. Double Scattering of Electrons with Magnetic Perturbation.*** H. MENDLOWITZ AND K. M. CASE, *University of Michigan.*—In connection with the experiments of Crane, Pidd, and Louisell[1] for measuring the gyromagnetic ratio of a free electron by means of a double-scattering experiment with magnetic perturbation, the change in asymmetry after the second scattering has been investigated as a function of the magnitude of the magnetic field and its relative orientation with respect to the initial incident beam and the direction of the first scattered beam. In the case where the field is parallel with the direction of the first scattered beam, the asymmetry is altered in a manner which is readily obtained from semiclassical considerations. For other relative orientations, the change in asymmetry does not behave in as simple a manner. The way in which the asymmetry is altered in various special cases suggests a geometrical model which is helpful in describing the effects of the magnetic field on the asymmetry of the second cross section in the double-scattering experiment.

* Supported by the U. S. Atomic Energy Commission.
[1] Crane, Pidd, and Louisell, Phys. Rev. 91, 475 (1953).

**WA3. Design Features of a High-Current Cyclotron.** ROBERT S. LIVINGSTON AND ROYCE J. JONES, *Oak Ridge National Laboratory.*—Experience with fixed frequency cyclotrons at this Laboratory indicates that the design features most important for achieving high currents are: (1) an oscillator with adequate power output, (2) a high-$Q$ resonant dee structure, (3) a dee voltage very large compared with the threshold voltage, (4) a high potential gradient for initial acceleration of ions, and (5) a dee aperture (thickness) large enough to provide a high transmission factor for ions perturbed by variations in the magnetic and electric median planes. These features are being incorporated in the ORNL 44-inch cyclotron to provide for operation at proton currents $\gg$1 ma. This cyclotron operates at a relatively low magnetic field, 6400 oersteds, with a corresponding frequency of 9.7 megacycles. The energy of the protons at the maximum radius, 20 inches, is $\sim$5 Mev. A vacuum tank extension can be inserted to shift the dee system with respect to the magnetic center to permit operation at a radius of 11 inches or an energy of $\sim$1.5 Mev. The oscillator has a dc power input rating of 450 kw and will provide 100-kv dee-to-dee voltage. The ratio of dee thickness to radius is 1/3.1 for 5 Mev and 1/1.7 for 1.5 Mev. The biased quarter-wave resonant dee system is contained entirely in vacuum. Design features of the cyclotron will be illustrated.

**WA4. An Electromechanical Analog for the Study of Strong-Focusing Orbits.*** L. W. JONES AND K. M. TERWILLIGER, *University of Michigan and Midwest Accelerator Conference.*—An electromechanical analog[1] has been constructed to study orbits of particles in a strong-focusing synchrotron and in particular to investigate locked-in orbits in nonlinear fields. The device is essentially a galvanometer with a laminated, current-driven field magnet. A voltage signal proportional to the armature displacement is derived by causing an rf oscillator to be tuned by means of small condenser plates attached to the armature and by means of an FM receiver. The current in the armature coil is then made proportional to the discriminator output voltage. With one sign of field current, the motion is simple harmonic, with the other, exponential. Strong-focusing conditions are achieved with an alternating square-wave field current. Nonlinearities may easily be introduced into the feedback loop to simulate the effects nonlinear fields in the synchrotron. The coil displacement is presented on an oscilloscope screen and photographed on moving film. The analog operation and difficulties encountered will be discussed. Orbits locked into resonance in nonlinear cases have been observed. Traces will be presented and analyzed.

* Supported in part by the Michigan Memorial Phoenix Project.
[1] H. R. Crane, Midwest Accelerator Conference Report No. 8, September 4, 1953.

**WA5. The Activities of $Zn^{71}$.** J. M. LEBLANC, J. M. CORK,* AND S. B. BURSON, *Argonne National Laboratory.*—The activities of $Zn^{71}$ have been investigated with a 10-channel coincidence scintillation spectrometer. Sources were obtained by the irradiation of enriched $Zn^{70}$ and normal Zn in the Argonne heavy-water reactor. Two activities were found to be present in $Zn^{71}$; these decay with half-lives of 2.2 min and 3 hr. The 3-hr state of $Zn^{71}$ decays by the emission of beta rays followed by three gamma rays of energies 0.38, 0.49, and 0.61 Mev. The attenuation by Al of the beta rays in coincidence with each of the gamma rays was measured and found to be the same in each case and to represent a beta ray of maximum energy of 1.5$\pm$0.1 Mev. In addition each gamma ray is found to be in coincidence with the remaining two gamma rays. It is therefore concluded that the three gamma rays found in this activity are in cascade and the upper level is fed by a beta ray of 1.5 Mev. The 2.2-min state of $Zn^{71}$ is found to decay by the emission of a 2.4$\pm$0.2-Mev beta ray which is followed by a 0.51-Mev gamma ray. Additional weak gamma rays of energies 0.12, 0.90, and 1.05 Mev were also found to be associated with this activity and to follow beta emission. Gamma-gamma coincidence studies indicate that the 0.51 and 0.12-Mev gamma rays are not in coincidence.

* University of Michigan.

**WA6. Inelastic Scattering of Charged Particles in Electric Excitation Processes.** HANS MARK, *M.I.T.*—The recent discovery of electric excitation[1,2] by observing the $\gamma$ rays emitted by nuclei under proton bombardment raises the question of whether it would be useful instead to observe the inelastically-scattered charged particles. Using the semiclassical theory of Ter-Martirosyan,[3] it is found (for quad-

rupole excitation in the limit $E \gg \Delta E$) that the ratio $R$ of inelastically to elastically scattered particles is proportional to the radiative transition probability of the state under investigation and a function of the scattering angle which has its maximum in the backward direction. The advantage of measuring $R$ rather than the $\gamma$ rays coming from the nuclei is that detector efficiencies and internal conversion coefficients would not appear as factors in the evaluation of transition probabilities from experimental data. Numerical values of $R$ have been calculated for several nuclei for which experimental data are available.

* This work has been supported by the joint program of the U. S. Office of Naval Research and the U. S. Atomic Energy Commission.
[1] C. L. McClelland and C. Goodman, Phys. Rev. **91**, 760 (1953).
[2] Huus and Zupančič, Kgl. Danske Videnskab. Selskab Mat. fys. Medd. **28**, No. 1 (1953).
[3] K. A. Ter-Martirosyan, J. Exptl. and Theoret. Phys. U.S.S.R. **22**, 284 (1952).

**WA7. Electric Excitation of Platinum.*** C. L. McCLELLAND AND CLARK GOODMAN, *M.I.T.*—We have observed[1] evidence for electric excitation of 97-kev and 126-kev levels in $Pt^{198}$ (34 percent). Subsequently, we reported[2] levels at 215 kev and 330 kev using protons of higher energy. ($E_p = 2.46$ Mev). Heydenburg and Temmer have confirmed these levels with 3-Mev alphas.[3] The 330-kev line probably corresponds to the known[4] 328-kev level in $Pt^{194}$. If this is a rotational state, the Bohr-Mottelson theory predicts similar levels in $Pt^{196}$ and $Pt^{198}$ at somewhat higher energies. We have not observed the known[4] level at 358 kev in $Pt^{196}$ using natural platinum, and the low abundance of $Pt^{198}$ (7 percent) is probably insufficient for detection of the predicted level. We have requested separated isotopes for further study of this problem with a technique similar to that used for the separated isotopes of wolfram.[5]

* Supported in part by U. S. Office of Naval Research and U. S. Atomic Energy Commission.
[1] McClelland and Goodman, Phys. Rev. **91**, 760 (1953).
[2] C. L. McClelland, Phys. Rev. **92**, 1092 (1953).
[3] G. M. Temmer and N. P. Heydenburg, Phys. Rev. **93**, 351 (1954).
[4] Steffen, Huber, and Humbel, Helv. Phys. Acta **22**, 167 (1949).
[5] McClelland, Mark, and Goodman, Phys. Rev. (to be published).

**WA8. Initiation of the Discharge in a $CO_2$ Filled GM Counter by Negative Ions.*** H. R. CRANE, *University of Michigan*.—Because of the high energy of electron attachment (3.8 ev) by $CO_2$ to form $CO_2^-$, electrons produced by an ionizing particle passing through a $CO_2$ filled counter have little chance of reaching the wire as free electrons, and the counting efficiency is, consequently, low. However, it is known that the addition of a small amount of $CS_2$ raises the efficiency to virtually 100 percent. The mechanism is not understood. By making use of a new type GM counter[1] which can operate with $CO_2$ in the absence of a quench vapor, we have been able to obtain some additional facts. The passage of a CR meson through counters above and below the $CO_2$ counter triggers the sweep of a synchroscope. The discharge of the $CO_2$ counter gives a pip on the time axis, indicating the drift time. In $CO_2$ only about 20 percent of the mesons produced counts, but few were delayed. In $CO_2$ plus 1 percent $CS_2$ over 98 percent of the mesons produced counts and about 80 percent had delays characteristic of ion drift times (milliseconds). Conclusions: In $CO_2$, negative ions initiate the discharge rarely or not at all, while a small addition of $CS_2$ enables them to do so with high efficiency.

* Supported by the Michigan Memorial Phoenix Project.
[1] H. R. Crane, Bull. Am. Phys. Soc. **28**, No. 6 (1954).

## SATURDAY AFTERNOON AT 1:30

Ballroom

(HARVEY BROOKS presiding)

### *Invited Paper*

**X1. Avalanche Breakdown in Silicon.** K. G. McKAY, *Bell Telephone Laboratories*. (30 min.)

### *Semiconductors, V; Electron Physics*

**X2. Electrical Breakdown Paths in Nonpolar Crystals.** J. W. DAVISSON, *Naval Research Laboratory*.—According to the theory of Offenbacher and Callen,[1] the orientation of electrical breakdown paths in polar crystals is caused by the discontinuity at the Brillouin zone borders in the scattering of electrons by the polar modes of lattice vibration. In nonpolar crystals, on the other hand, the discontinuity in scattering at the zone border should either disappear or be greatly reduced because scattering by the "Umklapp" process is allowed for the non-polar modes. Thus, the Offenbacher-Callen theory should not apply to non-polar crystals, and orientation effects should be the result of some other mechanism for anisotropic electron scattering. Breakdown patterns have accordingly been studied in rhombic sulfur over a wide range of temperature. In agreement with the above considerations, the breakdown paths are found to be independent of temperature and do not seem to be related to the Brillouin zone borders. Orientation effects not attributed to the zone borders are also observed in the alkali halides.

[1] E. L. Offenbacher and H. B. Callen, Phys. Rev. **90**, 401 (1953).

**X3. Decay in Photoconductivity Associated with Deep Electron Traps in *P*-Type Silicon.** J. A. HORNBECK AND J. R. HAYNES, *Bell Telephone Laboratories*.—The transient decay in photoconductivity associated with the "deep" electron traps in $p$-type silicon[1] has been studied in crystals having a wide range of resistivity, lifetime ($\tau_r$), and trap concentration ($N$). All the data are consistent quantitatively with the multiple trapping hypothesis[1] and the existence in these crystals of a single deep trapping level 0.78 ev below the conduction band. If the traps are filled at zero time, this model leads to the decay formula: $\exp(-t/\tau) = (n_1/N) \exp[(1-n_1/N)(1+1/\tau_r N\sigma v)^{-1}]$ where $n_1$ equals concentration of trapped electrons, $t$ is time, $\tau = \tau_\theta + \tau_r \tau_\theta N\sigma v$, $\tau_\theta$ is mean time in a trap, $\sigma$ is the trapping cross section, and $v$ is thermal velocity. The photoconductivity induced by the trapped electrons equals $(n_1 e \mu_+)$, where $\mu_+$ is hole mobility, since there is one additional free hole for each trapped electron. From our data $\sigma\tau_\theta$, a property of the trap itself, equals $(0.81 \pm 0.25) \times 10^{-13}$ cm$^2$ sec and $\tau_\theta \cong 0.3$ sec. In low resistivity crystals there is evidence of a loss mechanism for electrons in addition to recombination from the conduction band, *viz.*,

recombination from the trap at a rate found to be proportional to (hole concentration)[2]. Trap concentration is roughly proportional to sample conductivity.

[1] J. R. Haynes and J. A. Hornbeck, Phys. Rev. 90, 152 (1953).

**X4. Decay in Photoconductivity Associated with Hole Traps in *N*-Type Silicon.** J. R. HAYNES AND J. A. HORNBECK, *Bell Telephone Laboratories.*—Preliminary photoconductivity measurements on *n*-type silicon indicate that hole traps behave differently in several respects from electron traps in *p*-type silicon.[1] The hole traps decay with nearly a single time constant, showing that multiple trapping is not an important mechanism. At room temperature the trap concentration ($N$) varies from $2\times10^{9}>N>10^{15}$ cm$^{-3}$ among specimens and is not correlated with resistivity. Decay times ($\tau$) are found in the range $7\times10^{-3}$ to 500 sec, and there is evidence for at least two and probably more trapping levels. More detailed studies have been carried out with two similar specimens having two trapping levels. In these, $N$ varies with temperature ($T$) in accordance with a "deep" trap 0.3 ev from the conduction band, and measurements of trapping cross section ($3\times10^{-18}$ cm$^2$) and $\tau$ place the trap 0.71 ev from the valence band. Investigation of $\tau$ *vs* temperature shows that the simple relation $1/\tau=\nu\exp(-U/kT)$ is obeyed, but $U$ is not the trap depth; the measurements also indicate that at room temperature and lower some recombination occurs in the trap causing a deviation from this relationship. Measurements on one sample place a shallow trap ~0.64 ev from the valence band with a cross section $\sim40\times10^{-16}$ cm$^2$.

[1] J. R. Haynes and J. A. Hornbeck, Phys. Rev. 90, 152 (1953).

**X5. The Photoconduction of Zinc Oxide Semiconductor: an Oxygen Adsorption Process.** DONALD A. MELNICK, *University of Pennsylvania.**—The photoconductive process of porous, sintered, semiconducting zinc oxide has been studied as a function of time (0.3 to $10^7$ sec), pressure of ambient oxygen ($10^{-5}$ to 760 mm), temperature (110° to 373°K), intensity (factor of $10^3$), and duration of excitation. The following conclusions are reached: (1) confirmation is given to the postulate[1] that physically adsorbed oxygen forms an acceptor impurity, removing electrons from the interstitial zinc donors. The oxygen thus becomes chemically adsorbed and tightly bound. The narrow "necks," which connect the sintered grains and control the sample's resistance, have a sufficiently high surface to volume ratio for the acceptor concentration to exceed the donor concentration. (2) The oxygen can be desorbed by light of forbidden gap energy, presumably because holes are attracted to the charged chemically adsorbed oxygens, converting them to weakly bound physically adsorbed. (3) The rate of chemical adsorption of oxygen is given by the Elovich equation, $dq/dt=a\exp(-bq)$. (4) The nature of the adsorption equation causes inner more weakly illuminated layers to represent longer time constants and to contribute appreciably to the final photoconductance. The array of time constants usually assumed for photoconductive processes is, therefore, found to be unnecessary.

* This work partially supported by the U. S. Office of Naval Research.
[1] S. R. Morrison. (Submitted to J. Chem. Phys.)

**X6. Photoresponse of Aromatic Films.*** J. F. ANDREW AND S. MROZOWSKI, *University of Buffalo.*—The variation of resistance of charred organic films under infrared illumination studied previously and believed to be a mixed photo and bolometric type response[1] has been investigated further and the study extended to much thinner films. It was suspected that charred films have a very porous structure and that the time constant is determined by the heat losses into the pores. Liquid backings were used which penetrate into these pores. It has been found that the response (limiting value for long illumination) is cut down by the presence of the liquid as much as by a factor 4 in some cases. In general, liquids with higher thermal conductivity are more effective in reducing the response, the effect being, however, also a function of the ability of the liquid to penetrate the pores. Films mounted in vacuum show a somewhat larger response; for very thin films a slight change caused by solid backing could also be established. The dependence of the response on the intensity of illumination, dark current and temperature were studied. Response in region of purely vibrational absorption (7–8$\mu$) was found. All findings lead to the conclusion that the response of charred organic films is of an essentially bolometric nature.

* Supported by the U. S. Office of Naval Research.
[1] Mrozowski, McMichael, and Kmetko, Phys. Rev. 91, 234 (1953).

**X7. Dielectric Constants of Powders at uhf.*** ROBERT S. SMITH, *University of Pennsylvania.*—A new approximate method of calculating the dielectric constant of powder has been devised to treat the case of inhomogeneous particles of various shapes. It yields the usual Clausius-Mossotti relationship for homogeneous spherical particles. For a matrix composed of homogeneous randomly-oriented cylinders the measured dielectric constant $\epsilon$ is

$$\epsilon=1+\frac{\delta\frac{1}{3}\left(4\frac{\epsilon_0-1}{\epsilon_0+1}+\epsilon_0-1\right)}{\delta\frac{1}{3}\left(\frac{4}{\epsilon_0+1}+1\right)+(1-\delta)\left(1+\frac{8}{9}\frac{\epsilon_0-1}{\epsilon_0+1}\frac{\ln\delta^{-1}}{(\delta^{-1}-1)}\right)}, \quad (1)$$

where $\epsilon_0$ is the bulk dielectric constant and $\delta$ the fractional density. For a matrix composed of conducting spheres coated with a dielectric shell of constant $\epsilon_0$,

$$\epsilon=1+\frac{3\delta(\epsilon_0-1)(1-\delta')+9k\delta'}{(1-\delta)(\epsilon_0+2)+3\delta(1-\delta')}, \quad (2)$$

where $\delta'$ is the conducting fraction of the spherical particle. Measurements of powdered zinc oxide at several hundred megacycles in the range $0<\delta<0.5$ fit either formulas (1) or (2) within the experimental error but are inconsistent with those of Clausius-Mossotti, Weiner, Bruggeman, or Bottcher.

* Supported in part by the U. S. Office of Naval Research.

**X8. $R'$, Colloidal, and Z Bands in KCl.** D. R. WESTERVELT, *North American Aviation, Inc.*—The thermally induced absorption peak which has been termed the $Z$ band in photochemically colored alkali halides[1] and the colloidal band in those additively colored[2] has been further studied. In both cases the band is destroyed by 35-kev x-rays. $R_1$ and $R_2$ bands are not an initial step in its formation, since these are immediately destroyed by heating. The broad $R'$ band forms rapidly during simultaneous annealing and $F$-light exposure; during continued heating, however, the $R'$ band narrows and the final results of annealing in the light and of the much slower process in the dark are the same. Once the $F\leftrightarrow Z$ equilibrium is established, prolonged annealing at the same temperature has no effect on the $Z$-peak location or band width, but raising the annealing temperature shifts the peak to longer wavelengths. Cooling to liquid nitrogen temperature sharpens the peak, although less than in the case of the $F$ band; and in some cases the peak is shifted to longer wavelengths by cooling, contrary to all previously observed behavior in the alkali halides. Observed differences in the colloidal and $Z$ bands apparently result from unavoidable thermoluminescence and the competition of recombination processes in bombarded crystals. This paper is based on studies conducted for the Atomic Energy Commission.

[1] D. R. Westervelt, Phys. Rev. 91, 218 (1953).
[2] Scott, Smith, and Thompson, J. Phys. Chem. 57, 757 (1953).

**X9. A Search for Luminescent Emission from the *F* Center.** CLIFFORD C. KLICK, *Naval Research Laboratory.*—Measurements have been made on the quantum efficiency of lu-

minescence from *F* centers in x-rayed LiF and additively colored KCl at 4°K. An upper limit of 3 percent efficiency is found for the emission from LiF should it fall in the wavelength range from 3000A to 20 000A. At 25 000A the upper limit is 10 percent. Similar results are found for *F* centers in KCl in the wavelength range from 6500A to 25 000A. These results are in disagreement with theoretical predictions that the *F* center should luminesce with high efficiency in the wavelength region near 10 000A.

**X10. Thermionic Emission and Semiconduction in Single Crystals of Barium Oxide.*** EVAN O. KANE, *Cornell University.*—Thermionic emission from single crystals of barium oxide has been activated by five orders of magnitude from $10^{-7}$ a/m² to $4\times10^{-2}$ a/cm² at 1000°K. Activation procedures used were heat and dc electrolysis. Both appear necessary to achieve maximum activity. During activation the Richardson slope decreases from 2.6 ev to 1.0 ev. The value of the work function computed from the absolute value of the emission at 1000°K decreases from 3.0 ev to 1.9 ev. Simultaneous measurements of conductivity by two-electrode and four-electrode methods show little correlation between conductivity and emission during activation. At the beginning of activation the emission at 1000°K increases by a factor of 6000 while the conductivity increases by only a factor of 3. The conductivity shows a break to a region of lower slope at high temperatures. The high-temperature slope decreases from 0.45±0.04 ev to 0.00±0.06 ev during activation and the break between slopes moves from 850°K to 500°K. The low-temperature slope is initially 0.75±0.05 ev. The absolute value of the conductivity at 1000°K increases from $10^{-4}$ ohm$^{-1}$ cm$^{-1}$ to $4\times10^{-2}$ ohm$^{-1}$ cm$^{-1}$.

* Supported in part by the U. S. Office of Naval Research.

**X11. Note on the Theory of Thermionic Emission.** KURT LEHOVEC, *Sprague Electric Company.*—Thermionic emission removes "fast" electrons from the surface of a solid. These electrons are replenished by "slow" electrons which gain energy from lattice vibrations and from the electric field. The theory of the process is similar to that of breakdown theory in insulators, where one is concerned also with the rate at which "slow" electrons become "fast" electrons. The deviation from thermal equilibrium distribution of electrons at the surface of a semiconducting cathode under current flow will be estimated and its implications on the thermionic emission will be discussed. At high current densities, the rate of energy gain of slow electrons in the cathode may become the current limiting process. The increase of this rate by the electric field may enhance the emission current more than the well-known decrease of the surface barrier by the field.

---

## SATURDAY AFTERNOON AT 1:30

Italian Gardens

(J. E. GOLDMAN presiding)

### *Magnetism, II*

**Y1. Neutron Diffraction Observations on Iron at High Temperatures.** M. K. WILKINSON AND C. G. SHULL, *Oak Ridge National Laboratory.*—Neutron diffraction patterns have been taken for iron at a series of elevated temperatures ranging up to 1000°C in order to establish the magnetic scattering effects through the Curie temperature ($T_c$) and also in the $\gamma$-phase region. The change in diffuse scattering above and below $T_c$ is accounted for mostly by the normal crystal lattice thermal scattering and the excess scattering is very much smaller than the calculated paramagnetic scattering. Pronounced small angle scattering is noticed however indicating a strongly modified paramagnetic scattering with short-range order characteristics. The patterns taken for iron in the face-centered cubic region offer no evidence for an antiferromagnetic structure.

**Y2. Small Angle Neutron Scattering by Iron at High Temperatures.** C. G. SHULL AND M. K. WILKINSON, *Oak Ridge National Laboratory.*—Pronounced small angle scattering of slow neutrons has been obtained for iron at temperatures up to and through the Curie temperature ($T_c$). This scattering which is magnetic in origin indicates a gradual disruption of the magnetic lattice into smaller domains as the temperature is increased until at $T_c$ only a few unit cells are magnetically coherent. Above $T_c$ the domain small angle scattering transforms gradually into short-range order scattering and this persists into the gamma-phase region up to the highest temperature of observation about 1000°C. Quantitative data on the small angle scattering and domain sizes will be presented.

**Y3. Equations for Magnetostriction and Anisotropic Energy for a Hexagonal Crystal of Class $D_{6h}$(6/m, 2/m, 2/m).** W. P. MASON AND J. A. LEWIS, *Bell Telephone Laboratories.*—In order to determine what measurements are necessary to specify completely the magnetostriction and anisotropic magnetic energy in a cobalt crystal, as discussed by Bozorth and Sherwood in the following abstract, a calculation is given for the energy terms for both cylindrical and hexagonal symmetry. Up to fourth-rank tensors the results are the same. For sixth-rank tensors, a characteristic hexagonal term enters. Out to fourth-rank terms the magnetostrictive strain can be written in the simple form

$$\begin{aligned}\lambda=\lambda_1[&(\alpha_1\beta_1+\alpha_2\beta_2)^2-(\alpha_1\beta_1+\alpha_2\beta_2)\alpha_3\beta_3]\\&-\lambda_2[(\alpha_1\beta_1+\alpha_2\beta_2)^2+(\alpha_3^2-1)(1-\beta_3^2)]\\&-\lambda_3[\beta_3^2(\alpha_3^2-1)+(\alpha_1\beta_1+\alpha_2\beta_2)\alpha_3\beta_3]\\&+4\lambda_4(\alpha_1\beta_1+\alpha_2\beta_2)\alpha_3\beta_3,\end{aligned}$$

where $\alpha_1$, $\alpha_2$, $\alpha_3$ are the direction cosines of the saturation magnetization, and $\beta_1$, $\beta_2$, $\beta_3$ the direction cosines of the direction of magnetostriction measurement, all with respect to orthogonal axes for which $X$ corresponds to one of the hexagonal axes and $Z$ to the unique $c$ axis. The introduction of the sixth-rank tensor gives a term with hexagonal symmetry but 11 constants are required unless the saturation magnetization is parallel or perpendicular to the direction of magnetostriction measurements. With this simplification, 8 constants suffice.

**Y4. Magnetostriction of Cobalt.** R. M. BOZORTH AND R. C. SHERWOOD, *Bell Telephone Laboratories.*—Magnetostriction at saturation ($\lambda$) has been measured in various crystallographic directions in a single crystal of cobalt, fields of 20 000 oersteds being required. Magnetostriction resulting from magnetiza-

tion along the $c$-axis is zero within the errors of measurement. Magnetization perpendicular to the hexagonal axis causes a contraction of $\lambda = -45 \times 10^{-6}$, while magnetization at 60° to the axis gives a larger contraction, $\lambda = -100 \times 10^{-6}$, when $\lambda$ is measured parallel to the magnetization. When $\lambda$ is at right angles to the magnetization, expansion is as large as $+145 \times 10^{-6}$. When the magnetization is perpendicular to the $c$-axis the fractional change in volume resulting from domain orientation is $-30 \times 10^{-6}$. Magnetostriction in any direction ($\beta$) in a hexagonal crystal, resulting from applying a saturating field in a given direction ($\alpha$) has been expressed in terms of the direction cosines of $\alpha$ and $\beta$ by W. P. Mason and J. A. Lewis. The cylindrical symmetry obtained when terms beyond the 4th power are excluded is a good approximation for cobalt. The 4 constants, $\lambda_1$ to $\lambda_4$, are evaluated as $-45$, $-95$, $+110$, and $-100$, each $\times 10^{-6}$.

**Y5. Magnetostriction in the Nickel Ferrite-Aluminates and Nickel Ferrite-Gallates.** D. F. Bleil and A. R. Butz, *U. S. Naval Ordnance Laboratory.*—Magnetostriction determinations of the systems, nickel ferrite-aluminate ($NiOFe_{2-t}Al_tO_3$), and nickel ferrite-gallate ($NiOFe_{2-t}Ga_tO_3$), have been made using a system of compensated strain gages[1]; the active gage is secured to a small rod of the sintered material. For the aluminates we find that the room-temperature saturation magnetostrictive constants ($\lambda_s = \Delta l/l$) decreases with increasing $t$, approaching zero at $t = 0.67$. For values of $t < 0.67$ the magnetization of the ions on the $B$ sites predominates and for $t > 0.67$ the $A$ sites are stronger.[2] At the crossover point where the magnetization of the ions on the $A$ and $B$ sites are equal, we have the situation where the magnetostrictive constant is also zero. As $t$ increases beyond this point the value of $\lambda_s$ goes through a maximum at approximately $t = 1$ and approaches zero at $t = 1.5$. The gallium series shows a gradual decrease in $\lambda_s$ with increasing values of $t$, approaching zero at $t = 1.5$. There is no abrupt drop to zero at $t = 0.67$ as found in the aluminates. This is due to the fact that in the gallates the ions on the $B$ sites always predominate.

[1] J. E. Goldman, Phys. Rev. **72**, 529 (1947).
[2] L. R. Maxwell and S. J. Pickart, Phys. Rev. **92**, 1120 (1953).

**Y6. Factors Determining the Permanent Magnet Properties of Single Crystals of $Fe_2NiAl$.** E. A. Nesbitt, H. J. Williams, and R. M. Bozorth, *Bell Telephone Laboratories.*—It is shown that fine precipitated particles present in single crystals of $Fe_2NiAl$ are elongated and that the shape anisotropy of these particles is a major factor in determining the coercive force of $Fe_2NiAl$. For fields of less than 7000 oersteds in the (110) plane, ⟨111⟩ directions are the directions of easy magnetization of the crystal and this is because of the shape effect of the precipitate oriented in three mutually perpendicular directions. At higher fields, the torque due to this effect decreases and then the [001] direction is the direction of easy magnetization because of intrinsic crystal anisotropy. These conclusions are based on an analysis and on measurements of the torque on three mutually perpendicular rods of magnetic material. These rods simulate the rods of precipitate in the actual crystal.

**Y7. Rapid Remagnetization of Thin Molybdenum Permalloy Strips.** H. Ekstein and J. Kelly, *Armour Research Foundation.*—Molybdenum Permalloy strips of ½- to 2-mil thickness have been subjected to approximately square pulses of 0.08 to 3 oersted after saturation magnetization by a strong opposite field. The time rate of magnetization was projected on an oscilloscope. The curves are monotonically decreasing for strong fields, but they exhibit a secondary maximum for weak fields. The total "switching time" is a power function of the difference between applied field $H$ and coercive force $H_c$, the exponent varying slightly between $-1.3$ and $-2.9$. The switching time as a function of tape thickness is closely approximated by parabolas, if corrections for the finite rise time of the pulse are made. Most properties can be understood on the following assumptions: (1) the strip is at any time divided into regions of opposite magnetization, the dividing plane walls moving from the surface toward the center, (2) the velocity of the wall is proportional to the difference between the field at the wall and $H_c$. If these assumptions are introduced into the eddy-current equations, a good approximate solution can be obtained, which agrees with experiments for strong fields. No satisfactory explanation for the secondary maximum of the switching curve for low fields is known.

**Y8. Effects of Anisotropy on the Thermodynamic Properties of Antiferromagnets.*** J. A. Eisele and F. Keffer, *University of Pittsburgh.*—In antiferromagnets, because of interplay with exchange energy, a small anisotropy energy can have a huge effect on thermodynamic properties. For example, in both $MnF_2$ and $CuCl_2 \cdot 2H_2O$ the characteristic spin temperatures of the anisotropy-exchange energy are about ¼ of the (respective) Curie temperatures. When this energy is taken into account, spin-wave theory is in reasonable agreement with existing experimental data on $CuCl_2 \cdot 2H_2O$ between 1°K and 2°K, including specific heat[1] and spontaneous magnetization of a sublattice.[2] Experiments are suggested on the relatively large spin specific heats of antiferromagnets with low Curie points.

* Work supported in part by U. S. Air Force Research and Development Command.
[1] S. A. Friedberg, Physica **18**, 714 (1952).
[2] N. J. Poulis and G. E. G. Hardeman, Physica **19**, 391 (1953).

## Saturday Afternoon at 1:30

Crystal Ballroom

(Otto Laporte presiding)

### *Invited Paper*

**YA1. Magnetohydrodynamics of the Earth and Sun.** W. M. Elsasser, *University of Utah.* (40 min.)

### *General Physics*

**YA2. Dimensional Relations in Magnetohydrodynamics.*** W. M. Elsasser, *University of Utah.*—A systematic study of dimensionless parameters in the magnetohydrodynamics of cosmic fluids shows that they are almost invariably very large, or small numerically, as the case may be. This results in significant simplifications of the theory. On calculating the thermal dissipation in such fluids it is found to result entirely from mechanical friction for interstellar gas, but to be entirely

in the form of Joule's heat for the interior of the stars. In the absence of instabilities (e.g., plasma oscillations, as sometimes postulated) the conditions for potentials leading to the higher cosmic-ray energies appear the more favorable, the larger the linear dimensions involved. A number of arguments can be adduced to show that theories which postulate acceleration in volumes of galactic size (e.g., Fermi's theory) encounter less difficulty than theories that require acceleration in confined spaces such as the neighborhood of stars. A detailed account is to be published.

* Supported by the U. S. Office of Naval Research.

**YA3. The Tensor Virial Equations.*** E. N. PARKER, *University of Utah.*—The conventional method of deriving the virial theorem by multiplying the equations of motion with the corresponding coordinates and summing is capable of generalization. On forming all such products one obtains the tensor virial equations from which the scalar virial results by contraction. The tensor virial equations are the equations of motion of the moment-of-inertia tensor of a swarm of particles relative to a fixed Cartesian frame. If the origin coincides with the center of mass of the swarm, these equations of motion are independent of the motion of the center of mass. The method appears to be very powerful. Applications have been made to the diffusion of charged particles in a magnetic field, to turbulence theory and to the derivation of the Navier-Stokes equations from elementary mechanics, and to certain astrophysical problems. A detailed account is to be published.

* Supported by the U. S. Office of Naval Research.

**YA4. Theory of the Photographic Intermittence Effect at Low Light Intensities.** E. KATZ, *University of Michigan.*—The present calculations are based on two assumptions: (1) the "order principle" which connects single grain processes with required plate exposures for isodense effects; (2) a trap depth distribution required to give a straight low intensity reciprocity failure of slope $x$, leading to a survival function for photoelectrons of the form $F(t)\sim t^{-x}$, as explained in a previous paper.[1] The low intensity intermittence effect is now calculated as a function of the transmission $p$ of the rotating sector, the average light intensity $I$, the average grain area $a$, chopping frequency $f$, and the low intensity reciprocity failure slope $x$. The statistics of interquantic times in a chopped beam are used. The results are given in terms of converging expansions, both for high and for low numbers of quanta per flash per grain $n=Iap/f$. For isodense exposures at relatively high frequencies the log exposure, $(\log It)_f$, differs from its limiting value $(\log It)_\infty$ by an amount proportional to $f^{x-1}$.

[1] E. Katz, J. Chem. Phys. **17**, 1132 (1949).

**YA5. Measurements of the Vibrational Relaxation Times in $Cl_2$ and $Cl_2$–He Mixtures.*** E. F. SMILEY, *U. S. Naval Ordnance Laboratory.*—Measurements have been made of vibrational relaxation times in $Cl_2$ and $Cl_2$–He mixtures. These measurements have been made using a shock tube and a Mach Zehnder interferometer.[1,2] The method and the accuracy to be expected in using it are discussed. Measured values of the vibrational relaxation times for $Cl_2$–$Cl_2$ and for $Cl_2$–He collisions at temperatures up to 1500°K are given. These data together with the data of Eucken are compared with the temperature dependence predicted for the probability of vibrational excitation by Schwartz, Slawsky, and Herzfeld.[3]

* Supported by the U. S. Office of Naval Research.
[1] W. Griffith, Phys. Rev. **87**, 234 (1952).
[2] Smiley, Winkler, and Slawsky, J. Chem. Phys. **20**, 923 (1952).
[3] Schwartz, Slawsky, and Herzfeld, J. Chem. Phys. **20**, 1591 (1952).

**YA6. Theoretical Determination of Shock Distances in Ideal and Real Gases.** W. H. HEYBEY, *U. S. Naval Ordnance Laboratory.*—A method is presented to determine theoretically the distance at which a detached shock will be found in front of a symmetrical body placed at zero incidence into supersonic uniform flow of an ideal gas. Agreement with experimental evidence on spheres in air and argon is satisfactory. The theory is extended to the more general case where the jump in temperature across the shock alters the internal molecular state of the gas. The shift in shock distance caused thereby can be predicted and may be used to obtain information on molecular excitation and dissociation if measured distances are compared with those indicated by theory.

**YA7. Study of Real Gas Effects by the Measurement of a Shock Detachment Distance.*** R. N. SCHWARTZ AND J. ECKERMAN, *U. S. Naval Ordnance Laboratory.*—An experimental study was carried out to determine the applicability of a shock wave detachment distance theory to the study of real gas effects. It had been shown theoretically[1] that the distance which a bow shock wave is detached from a blunt missile depends on the Mach number and the thermodynamic state of the gas before and after the shock. Studies were first carried out on spheres at Mach numbers 1.5 to 10 in monatomic gases. The small scatter in the experimental data indicated that it would be possible to observe nonequilibrium processes in selected gases. One such process is the excitation of a vibrational mode in a gas passing through a shock wave. Spheres were fired in chlorine. Whether the vibrational energy adjusted quickly or remained frozen in the region behind the shock wave could be recognized in the change of the detachment distance. Results indicated vibrational relaxation times were consistent with theory,[2] and those measured in a shock tube.[3]

* Supported by AEDC.
[1] W. H. Heybey, Bull. Am. Phys. Soc. **29**, No. 3, 43 (1954) (preceding abstract).
[2] R. N. Schwartz, Z. I. Slawsky and K. F. Herzfeld, J. Chem. Phys. **20**, 1591 (1952).
[3] E. F. Smiley, Bull. Am. Phys. Soc. **29**, No. 3, 43 (1954) (this meeting).

---

## SATURDAY AFTERNOON AT 1:30

## Normandy Room

## (G. E. UHLENBECK presiding)

## *Theoretical Physics*

**Z1. Symmetric Modes of the Tapered Reed.*** A. LEITNER AND E. A. HIEDEMANN, *Michigan State College.*—The tapered reed, used in ultrasonic whistles,[1] is a symmetric and homogeneous bar of rectangular cross section, uniform in the center and uniformly tapered to a sharp edge at each end. It is vibrating transversely under free-free conditions in the plane of the taper, and in its lowest symmetric mode; i.e., it must be mounted at the nodes. We have calculated the frequencies, positions of the nodes, and vibration curves for such bars, combining the exact methods of Rayleigh[2] and Kirchhoff[3] for bars of uniform and tapered cross sections, respectively. The main problem is that of joining the two different solutions at

the junction of the two regions. Results were obtained for a representative range of values of the ratio of length of tapered portion to total length.

* Supported by Detroit Ordnance District Office.
[1] Janovsky and Pohlman, Z. Angew. Phys. 1, 222 (1948).
[2] Rayleigh, *Theory of Sound* (Dover Publications, New York), Vol. I, p. 160.
[3] Kirchhoff, Ann. Physik, 10, 501 (1880).

**Z2. The Propagation of a Sound Pulse in a Medium with a Complex Elastic Modulus.** SALAH I. TAHSIN AND R. D. SPENCE, *Michigan State College.*—General restrictions on the form of the complex propagation constant can be derived from an application of the causality principle and other simple assumptions. We choose a simple form of complex elastic modulus which is consistent with these restrictions and whose dispersion results from a single relaxation process, and discuss the propagation of a sound pulse in such a medium. The precursors of the pulse for such a case are exponential in form in contrast to the oscillating precursors arising from a resonance process such as discussed by Sommerfeld and Brillouin.

**Z3. A Note on Basic Principles of Quantum Statistical Mechanics.** P. T. LANDSBERG, *University of Pennsylvania.**—The following principles and concepts are often convenient tools in statistical mechanics: microscopic reversibility, detailed balancing, equal *a priori* probabilities, random *a priori* phases, equilibrium, $H$-theorem. The interrelations between some of these have recently been discussed.[1] These ideas will be developed further in the following respects: (a) the distinction between coarse-grained and fine-grained probabilities is introduced; (b) the assumption of the interconnection of states is dropped, and discussed separately; (c) the assumption that, in equilibrium, ensemble averages do not exhibit fluctuations is also dropped, and discussed separately; (d) the extent to which any of these principles can be regarded as direct consequences of quantum mechanics is discussed. It is emphasized that, if the method of transition probabilities is used, none of these principles can be regarded as following directly from quantum mechanics. In this method they all need an additional statistical postulate. The conceptual basis, and some of the conclusions, of the paper cited[1] would therefore seem to need some revision along lines which will be suggested

* On leave of absence from University of Aberdeen, Scotland.
[1] J. S. Thomsen, Phys. Rev. 91, 1263 (1953).

**Z4. One-Dimensional Walk with Correlation by Saturation for the Description of Diffusion Phenomena.** C. M. TCHEN, *National Bureau of Standards.*—We distinguish two types of correlations to be introduced in the one-dimensional random walk: the partial correlation and the correlation by "saturation." The former is an intrinsic bond, inherent to the steps, and independent of the positions and the density of the steps in the space. The latter is an interaction between the steps created by saturation during the development of the walk. More specifically, a position becomes saturated, if it is visited by a prescribed critical number of steps, and a correlation by saturation arises between a pair of steps visiting the saturation point. In this way the walk will not allow the steps to sojourn or to return too often to individual positions, and therefore will be dispersed. As a dispersive property of the diffusion phenomena, the asymptotic value of the mean square distance $\langle x^2 \rangle$ between the $n$th step and the origin of the walk is calculated. In the case of partial correlations, $\langle x^2 \rangle \sim n$, and the asymptotic distribution of $x$ is Gaussian. Such a walk leading to the result of Brownian motion cannot explain the law of diffusion by irregular movements following a non-Gaussian distribution. For diffusion of non-Gaussian nature, we have to consider the correlation by saturation.

**Z5. Solutions of the Helmholtz and Schrödinger Equations in Sphero-Conal Coordinates.** OLEN KRAUS, *Michigan State College* (introduced by A. Leitner).—The coordinate surfaces of sphero-conal coordinates consists of spheres and two sets of cones of elliptical cross section which are orthogonal to each other and to the spherical surfaces. The axes of the cones coincide with two of the Cartesian axes. Such a system of coordinates separates the Helmholtz equation and the Schrödinger equation for a spherically symmetrical potential. The "angular" solutions can be represented as polynomials which may be expressed as linear combinations of conventional surface harmonics. The process of constructing the polynomial solutions leads to a set of eigenvalues which may be irrational numbers. An attempt is made to interpret these eigenvalues and the problem of quantization of angular momentum in this system of coordinates.

**Z6. The Nonrelativistic Limit of Half-Integral Spin-Wave Equations.** K. M. CASE, *University of Michigan.*—To investigate the properties of higher spin particles the nonrelativistic limit of the Dirac-Pauli-Fierz half-integral spin equations was considered. An expansion of the Hamiltonian operator for the essential components of the wave function is readily obtained in inverse powers of the mass. By means of Foldy-Wouthuysen type transformations a form is obtained which is independent of "odd" operators. To order $1/m^2$ the terms in the Hamiltonian are strictly analogous to those resulting from the spin-$\frac{1}{2}$ equation. The gyromagnetic ratio can be read off immediately and is

$$g=\frac{1}{2k+1}\,\frac{e}{mc},$$

where the spin is $k+\frac{1}{2}$. This is in agreement with Belinfante's conjecture that for arbitrary spin the expectation value of the magnetic moment operator for the state of highest $z$ component of the angular momentum is independent of the spin.

**Z7. The Determination of a Perturbation from the Scattering Operator.*** H. E. MOSES, *New York University.*—Jost and Kohn,[1] Levinson,[2] and others have discussed the problem of obtaining a radially symmetric potential from the scattering phases for the case of the radial equation corresponding to zero angular momentum. Through the use of the scattering operator formalism we have tried to generalize their discussion in order to see to what extent a perturbation can be obtained from a known scattering operator and a zero-order Hamiltonian. It appears that even when the spectrum of the perturbed Hamiltonian is prescribed, the perturbation is not unique unless additional conditions are imposed upon the perturbation. One such condition could be the assignment of the representation in which the perturbation is diagonal. This consideration leads to the question as to whether there are experiments from which the representation in which the perturbation is diagonal could be determined.

* The research reported in this paper has been sponsored by the Geophysics Research Division of the Air Force Cambridge Research Center, U. S. Air Research and Development Command.
[1] R. Jost and W. Kohn, Phys. Rev. 87, 977 (1952).
[2] N. Levinson, Phys. Rev. 89, 755 (1953).

**Z8. Nonadiabatic Corrections to Scalar Theory.** E. A. POWER, *Cornell University.*—We have investigated, by the method of Lévy,[1] the nonadiabatic term in order $g^4$ in the Tamm-Dancoff approximation to the interaction between two nucleons and their relationship to the no-pair terms of higher order. An examination of the well-known cancellation in the neutral scalar theory between the static $g^4$ potential and the iterated velocity dependent potential is considered in relation to the work of Cini and Fubini.[2] Further the Lévy claim that similar effects occur in the symmetric theory is found not to be substantiated; the remaining static potential being

$$-\lambda^2\tau_1\cdot\tau_2\frac{8\pi\kappa_0(2\omega)}{r}.$$

[1] M. M. Lévy, Phys. Rev. 88, 72 (1952).
[2] M. Cini and S. Fubini, Nuovo cimento 10, 12 (1953).

## Author Index to Papers Presented at the Detroit and Ann Arbor Meeting


Allen, Harry C., Jr., and Earle K. Plyler—M6
Ament, W. S. and G. T. Rado—D7
Andrew, J. F. and S. Mrozowski—X6
Andrews, R. D.—E3
Baldwin, F. P., J. Ivory, and R. L. Anthony—P4
Barber, W. A., P. Debye, and B. H. Eckstein—E6
Bardeen, John—K1
Barnes, J. M.—W2
Bauer, Ernest and Ta-You Wu—M11
Becker, Milton—K8
Beguin, Gilbert and Kasimir Fajans—W6
Berkowitz, A. E.—A9
——, F. E. Jaumot, Jr., and F. C. Nix—A8
Bestul, A. B.—P5
Bickford, L. R., Jr., J. Pappis, and J. L. Stull—V6
Binnie, W. P. and A. M. Liebschutz—C10
Bleil, D. F. and A. R. Butz—Y5
Bloembergen, N.—D3, H1
Blunt, R. F., H. P. R. Frederikse, and J. H. Becker—T7
Bode, Donald E. and Henry Levinstein—T2
Bowen, D. B. and H. Hori—L11
Boyer, R. F.—O4
Bozorth, R. M. and R. C. Sherwood—Y4
Brebrick, R. F. and W. W. Scanlon—T4
Brentano, J. C. M. and J. D. Richards—R7
Brooks, Harvey—D8
Brown, Edmond—W5
Buchdahl, Rolf and Lawrence E. Nielsen—F5
Bueche, F.—O5
Burch, D. E., J. N. Howard, and Dudley Williams—M7
Burns, F. P.—S5
Burstein, Elias—T8
Caldwell, R. S. and H. Y. Fan—R4
Callen, Earl—M3
Case, K. M.—Z6
Castle, J. G., Jr.—D1
Charlesby, A.—E1
Clarke, Edward N.—K7
Cleland, J. W. and J. H. Crawford, Jr.—C8
Cohen, M. H. and F. Keffer—D10
Conwell, Esther M.—G7
Cowen, J. A. and R. D. Spence—D5
Crane, H. R.—Q2, WA8
Crawford, J. H., Jr., and D. K. Stevens—G5
Crittenden, E. C., Jr., and H. Dieckamp—L4
Cuykendall, T. R., T. Beresovski, and H. S. Sack—L7
Dalby, F. W., H. H. Nielsen, and F. P. Dickey—M5
D'Altroy, F. A. and H. Y. Fan—G6
Damask, A. C. and A. S. Nowick—L8
Davisson, J. W.—X2
Daw, Harold—M8
deBretteville, A. and E. D. Harris—B4
Debye, P., P. P. Debye, and B. H. Eckstein—E5
Denny, J. M.—I6
Detwiler, D. P.—T11
Dieckamp, H. and E. C. Crittenden, Jr.—I7
Dixon, C. E. and D. B. Bowen—I8
Domenicali, C. A. and F. A. Otter—L9
Drougard, M. E. and D. R. Young—B5
Dunlap, W. C., Jr.—K2
Eatherly, W. P.—U5
Efremov, N.—M10
Eisele, J. A. and F. Keffer—Y8
Ekstein, H. and J. Kelly—Y7
Elsasser, W. M.—YA1, YA2
Epstein, A. and H. Fritzsche—R2
Ewald, A. W.—R9
Ewing, R. and J. C. Lee—D4
Fagen, E., J. Goff, and N. Pearlman—G3
Ferry, John D., Malcolm L. Williams, and Donald M. Stern—F2
Fleeman, Jerome—L10
Folen, V. J., F. C. Nix, and F. E. Jaumot, Jr.—V1
Fox, T. G.—O3
France, W. L. and F. P. Dickey—M4
Franklin, A. D., A. E. Berkowitz, and E. Klokholm—V2
Frazer, B. C., Marilyn McKeown, and Ray Pepinsky—W11
Frerichs, Rudolf—C1
Friedman, Abraham S. and Lester Haar—M1
Fritzsche, H.—G2
Gates, Halbert—W3
Goodman, P.—P6
Gossick, B. R.—R6
Gross, E. P.—M9
Gummel, Hermann and Melvin Lax—K5
Gurnee, E. F.—E2
Hammerle, W. G.—P1
Haynes, J. R. and J. A. Hornbeck—X4
Heller, Wilfried—P7
Henry, Warren E.—V7
Hersh, S. P. and D. J. Montgomery—E8
Heybey, W. H.—YA6
Hobbs, Lindsey, M., Douglas E. Brown, and David W Pletcher—E4
Hoff, E. A. W.—P2
Hoffman, J. D.—P3
Hoffman, R. W. and N. S. Rasor—A4
Honnold, V. R., F. McCaffrey, and B. A. Mrowca—F10
Hornbeck, J. A. and J. R. Haynes—X3
Hunter, L. P.—R1
Ivey, D. G. and A. Kwei—F9
Jacobsen, E. H.—L3
Jaumot, F. E., Jr., and A. Sawatzky—S3
Johnson, E. J. and W. G. Spitzer—G4
Johnson, V. A.—R3
Jona, F., G. Shirane, and R. Pepinsky—B6
Jones, L. W. and K. M. Terwilliger—WA4
Kaenzig, Werner—B2
Kaiser, W. and H. Y. Fan—T10
Kane, Evan O.—X10
Kao, L. P. and E. Katz—V8
Katz, E.—YA4
Kauzman, W. D.—O2
Keating, D. T.—S4
Keyes, R. J. and T. G. Maple—G9
Kingston, R. H.—G10
Kip, A. F.—H3
Klein, Ralph—A11
Klick, Clifford C.—X9
Knight, W. D.—B3
Kraus, Olen—Z5
Krimm, S.—P8
Kohn, W.—C6
Kunz, F. W. and A. N. Holden—I4
Landsberg, P. T.—Z3
Lark-Horovitz, K.—U3
Lazarus, D.—A6
Leaderman, Herbert and M. Wales—F4
LeBlanc, J. M., J. M. Cork, and S. B. Burson—WA5
Lehovec, Kurt—X11
Lehman, Guy W. and Hubert M. James—R10
Leifer, H. N. and W. C. Dunlap, Jr.—T12
Leitner, A. and E. A. Hiedemann—Z1
Leivo, W. J.—U4
Levinthal, Cyrus—Q5
Levy, Paul W. and G. J. Dienes—C4

Li, Yin-Yuan and R. Smoluchowski—W10
Lindsey, M. Hobbs, Douglas E. Brown, and David W. Pletcher—E4
Livingston, Robert S. and Royce J. Jones—WA3
Loebner, E. E.—W12
Logan, John K.—V9
Luttinger, J. M.—V10
Mark, Hans—WA6
Marvin, Robert S., H. S. Sack, and R. Aldrich—F3
Marvin, R. S.—O1
Mason, W. P. and J. A. Lewis—Y3
Maxwell, Louis R. and Stanley J. Pickart—V4
McClelland, C. L. and Clark Goodman—WA7
McKay, K. G.—X1
McLean, E. A. and Waller George—S1
McReynolds, A. W., W. Augustyniak, and M. McKeown—I3
Meechan, C. J. and R. R. Eggleston—A2
Melchor, J. L. and A. A. Petrauskas—F8
Melnick, Donald A.—X5
Mendlowitz, H. and K. M. Case—WA2
Mesrobian, Robert B., Paul Ander, David S. Ballantine, and G. J. Dienes—E7
Mitchell, Dean L., Werner J. Beyen, and Donald E. Bode—T3
Moses, H. E.—Z7
Mrozowski, S. and A. Chaberski—R8
Neighbours, John R. and Charles S. Smith—L5
Nesbitt, E. A., H. J. Williams, and R. M. Bozorth—Y6
Newman, R. and W. W. Tyler—K4
Nicholls, R. W., P. A. Fraser, R. G. Turner, and W. R. Jarmain—M2
Nielsen, John P.—S2
Nielsen, Lawrence—F6
Norberg, R. E.—H2
Overhauser, A. W.—U2
Parker, E. N.—YA3
Parkinson, W. C.—WA1
Paul, W., G. B. Benedek, and H. Brooks—G1
Pearlstein, Edgar—C2
Pepinsky, Ray—B1
Pepper, R., E. Klontz, K. Lark-Horovitz, and J. MacKay—C9
Petritz, R. L., W. W. Scanlon, and F. L. Lummis—T6
Plaskett, J. S.—L2
Power, E. A.—Z8
Rado, G. T. and J. R. Weertman—D6
Randall, H. M.—Q1
Rappaport, P.—C7
Riste, T. and A. W. McReynolds—V5
Ritland, H. N.—W1
Robinson, W. H., Yin-Yuan Li, and R. Smoluchowski—W9
Rodeback, G. W.—A3
Rosenblatt, D. B., R. Smoluchowski, and G. J. Dienes—I5
Rothstein, Jerome—S6
Sack, H. S., T. R. Cuykendall, and T. J. Woods—F7
Salter, L.—W4
Scanlon, W. W. and R. F. Brebrick—T5
Schindler, A. I.—L14
Schrieffer, J. Robert—K6
Schulz, L. G.—L13
Schwartz, R. N. and J. Eckerman—YA7
Seitz, Frederick—A1, U1
Shull, C. G. and M. K. Wilkinson—Y2
Silverman, Searl J. and Henry Levinstein—T1
Skinner, Selby M.—R11
Smiley, E. F.—YA5
Smith, Alan W.—I1
Smith, J. F.—A10
Smith, R. L., F. E. Jaumot, Jr., and L. A. Arné, Jr.—A7
Smith, Robert S.—X7
Smith, W. J., W. J. Leivo, and R. Smoluchowski—W8
Smoluchowski, R.—C3, U4
Sosin, A. and J. S. Koehler—L12
Squire, C. F.—Q3
Steijn, R. P. and F. J. Donahoe—V3
Stern, Frank—D9
Sterzer, Fred and Yardley Beers—D2
Stevens, D. K., J. W. Cleland, and J. H. Crawford, Jr.—C5
Stevenson, D. T. and R. J. Keyes—G8
Suits, G. H.—R5
Sutcliffe, C. H. and F. E. Jaumot, Jr.—S7, S8
Sutherland, G. B. B. M.—Q4
Tahsin, Salah I. and R. D. Spence—Z2
Talley, Robert M. and Dorothy Enright—T9
Tchen, C. M.—Z4
Tomizuka, C. T. and L. Slifkin—A5
Tucker, C. W., Jr., and J. B. Sampson—I9
Tyler, W. W., H. H. Woodbury, and R. Newman—K3
Van Horn, David D. and William C. Cooley—I10
Vand, V. and R. Pepinsky—W7
Warekois, E. P.—L6
Weiss, R. J., J. J. DeMarco, G. Weremchuk, J. Hastings, and L. Corliss—L1
Westervelt, D. R.—X8
Wilkinson, M. K. and C. G. Shull—Y1
Williams, Malcolm L. and John D. Ferry—F1
Wruck, D. and C. Wert—I2
Wu, Ta-You—M11, M12